Jangmyung Lee
Min Cheol Lee
Honghai Liu
Jee-Hwan Ryu (Eds.)

LNAI 8103

Intelligent Robotics and Applications

6th International Conference, ICIRA 2013
Busan, South Korea, September 2013
Proceedings, Part II

2 Part II

Springer

Lecture Notes in Artificial Intelligence 8103

Subseries of Lecture Notes in Computer Science

Jangmyung Lee Min Cheol Lee
Honghai Liu Jee-Hwan Ryu (Eds.)

Intelligent Robotics and Applications

6th International Conference, ICIRA 2013
Busan, South Korea, September 25-28, 2013
Proceedings, Part II

Springer

Volume Editors

Jangmyung Lee
Pusan National University
Department of Electronics Engineering, Busan, South Korea
E-mail: jmlee@pusan.ac.kr

Min Cheol Lee
Pusan National University
School of Mechanical Engineering, Busan, South Korea
E-mail: mclee@pusan.ac.kr

Honghai Liu
University of Portsmouth
School of Creative Technologies, Portsmouth, UK
E-mail: honghai.liu@port.ac.uk

Jee-Hwan Ryu
KOREATECH
School of Mechanical Engineering, Cheonan, South Korea
E-mail: jhryu@koreatech.ac.kr

ISSN 0302-9743 e-ISSN 1611-3349
ISBN 978-3-642-40848-9 e-ISBN 978-3-642-40849-6
DOI 10.1007/978-3-642-40849-6
Springer Heidelberg New York Dordrecht London

Library of Congress Control Number: 2013947376

CR Subject Classification (1998): I.2.8-11, I.5.3-4, I.4.8-9, K.4.2, J.2, J.3, C.3, C.2, G.1.10

LNCS Sublibrary: SL 7 – Artificial Intelligence

Typesetting: Camera-ready by author, data conversion by Scientific Publishing Services, Chennai, India

Printed on acid-free paper

Springer is part of Springer Science+Business Media (www.springer.com)

Preface

The organizing committee for the 6th International Conference on Intelligent Robotics and Applications has been committed to facilitating the interactions among members in the field of intelligent robotics, automation and mechatronics. Through this conference, the committee intends to enhance the sharing of individual experiences and expertise in intelligent robotics with particular emphasis on technical challenges associated with varied applications such as biomedical application, industrial automations, surveillance, and sustainable mobility.

The 6th International Conference on Intelligent Robotics and Applications was most successful in attracting 184 submissions on addressing the state-of-the-art developments in robotics, automation, and mechatronics. Owing to a lot of valuable submission papers, the committee was faced with the difficult challenge of selecting the most deserving papers for inclusion in these lecture notes. For this purpose, the committee undertook a rigorous review process. Despite the high quality of most of the submissions, a total of 147 papers were selected for publication in 2 volumes of Springer's Lecture Notes in Artificial Intelligence as subseries of Lecture Notes in Computer Science. The selected papers will also be presented during the 6th International Conference on Intelligent Robotics and Applications to be held during September 25-28, 2013 in Busan, South Korea.

The selected articles represent the contributions from the scientists from 20 different countries. The contributions of the technical program committee and the referees are deeply appreciated. Most of all, we would like to express our sincere thanks to the authors for submitting their most recent works and the Organizing Committee for their enormous efforts to turn this event into a smoothly-running meeting. Special thanks go to Pusan National University for the generosity and direct support. We particularly thank Mr. Alfred Hofmann and Ms. Anna Kramer of Springer-Verlag for their enthusiastic support in this project.

We sincerely hope that these volumes will prove to be an important resource for the scientific community.

July 2013

Jangmyung Lee
Min Cheol Lee
Honghai Liu
Jee-Hwan Ryu

Conference Organization

International Advisory Committee

Jorge Angeles	McGill University, Canada
Suguru Arimoto	Ritsumeikan University, Japan
Hegao Cai	Harbin Institute of Technology, China
Tianyou Chai	Northeastern University, China
Clarence De Silva	University of British Columbia, Canada
Han Ding	Huazhong University of Science and Technology, China
Sabina Jesehke	RWTH Aachen University, Germany
Ming Li	National Natural Science Foundation of China, China
Zhongqin Lin	Shanghai Jiao Tong University, China
Ding Liu	Xi'an University of Technology, China
Jinping Qu	South China University of Technology, China
Bruno Siciliano	University of Naples, Italy
Mark W. Spong	University of Texas at Dallas, USA
Guobiao Wang	National Natural Science Foundation of China, China
Kevin Warwick	University of Reading, UK
Ming Xie	Nanyang Technological University, Singapore
Youlun Xiong	Huazhong University of Science and Technology, China
Mohammad Siddique	Fayetteville State University, USA

General Chair

Jangmyung Lee	Pusan National University, Korea

General Co-chairs

Hee-Je Kim	Pusan National University, Korea
Chun-Yi Su	Concordia University, Canada
Xiangyang Zhu	Shanghai Jiao Tong University, China

Program Chairs

Min Cheol Lee	Pusan National University, Korea
Youngsun Ryuh	KITECH, Korea

Program Co-chairs

Subhash Rakheja	Concordia University, Canada
Shuzhi Sam Ge	National University of Singapore, Singapore

Publicity Chairs

Tongwen Chen	University of Alberta, Canada
Li-Chen Fu	National Taiwan University, Taiwan
Kok-Meng Lee	Georgia Institute of Technology, USA
Hideki Hashimoto	Chuo University, Japan
Ning Xi	City University of Hong Kong, Hong Kong
Xiaohua Xia	University of Pretoria, South Africa
Peter Xu	University of Auckland, New Zealand
Huayong Yang	Zhejiang University, China
Bin Yao	Purdue University, USA
Xinghuo Yu	Royal Melbourne Institute of Technology, Australia
Chaohai Zhang	Harbin Institute of Technology, China
Jae-Bok Song	Korea University, Korea
Jin-Woo Ahn	Kyungsung University, Korea

Organized Session Chairs

Seul Jung	Chungnam University, Korea
Weidong Chen	Shanghai Jiao Tong University, China
Youmin Zhang	Concordia University, Canada
Daniel Schilberg	RWTH Aachen University, Germany
Feng-Li Lian	National Taiwan University, Taiwan
Caihua Xiong	Huazhong University of Science and Technology, China
Kyung Taik Park	KIMM, Korea
In-So Kweon	KAIST, Korea

Exhibition Chairs

Hyunjea Ryu	Busan Robot Industry Association, Korea
Sung-Hyun Han	Kyungnam University, Korea
Samtae Gang	Robotech Co., Ltd., Korea
Young-Im Cho	Suwon University, Korea

Publication Chairs

Honghai Liu	University of Portsmouth, UK
Joonyoung Choi	Pusan National University, Korea
Jee-Hwan Ryu	KOREATECH, Korea

Local Arrangement Chairs

Sungshin Kim	Pusan National University, Korea
Jong-Wook Kim	DongA University, Korea
Byoung-Ho Kim	Kyungsung University, Korea

Finance Chair

Jangmok Kim	Pusan National University, Korea

Secretariat

Yunji Kim	SPENALO Center, Korea
Myungja Cho	SPENALO Center, Korea

Organized Session Committee

Shengyong Chen	Zhejiang University of Technology, China
Xinkai Chen	Shibaura Institute of Technology, Japan
Mingcong Deng	Tokyo University of Agriculture and Technology, Japan
Jun Fu	Massachusetts Institute of Technology, USA
Xin Fu	Zhejiang University, China
Haibo Gao	Harbin Institute of Technology, China
Yueming Hu	South China University of Technology, China
Danwei Wang	Nanyang Technological University, Singapore
Limin Zhu	Shanghai Jiao Tong University, China
Joonbum Bae	UNIST, Korea
Hyeungsik Choi	Korea Maritime University, Korea
Jungwon Yun	Gyeongsang National University, Korea
Yangmin Li	University of Macau, Macao
Zhijun Li	South China University of Technology, China
Guangjun Liu	Ryerson University, Canada
Xinjun Liu	Tsinghua University, China
Yandong Tang	Shengyang Institute of Automation, CAS, China
Simon Yang	University of Guelph, Canada
Jianhua Zhang	Shanghai University, China
Enrong Wang	Nanjing Normal University, China
Kang-Bak Park	Korea University, Korea
John M. Dolan	Carnegi Mellon University, USA
Joachim Horn	Helmut-Schmidt-University, Germany

International Program Committee

Amir Aghdam	Concordia University, Canada
Dongpu Cao	Lancaster University, UK
Qixin Cao	Shanghai Jiao Tong University, China
Guangren Duan	Harbin Institute of Technology, China
Shumin Fei	Southeast University, China
Peihua Gu	University of Calgary, Canada
Shuxiang Guo	Kagawa University, Japan
Liu Hsu	Federal University of Rio de Janeiro, Brazil
Chunqing Huang	Xiamen University, China
Sining Liu	Concordia University, Canada
Peter X. Liu	Carleton University, Canada
Derong Liu	University of Illinois at Chicago, USA
Jun Luo	Shanghai University, China
Tao Mao	Dartmouth College, USA
Daniel Miller	University of Waterloo, Canada
Yuichiro Oya	University of Miyazak, Japan
Hailong Pei	South China University of Technology, China
Juntong Qi	Chinese Academy of Sciences, China
Joe Qin	University of Southern California, USA
Yaohong Qu	Northwestern Polytechnical University, China
Gang Tao	University of Virginia, USA
Didier Theilliol	University of Lorraine, France
Hong Wang	University of Manchester, UK
Bugong Xu	South China University of Technology, China
Jianxin Xu	National University of Singapore, Singapore
Deyi Xue	University of Calgary, Canada
Bin Zhang	University of South Carolina, USA
Keitaro Naruse	University of Aizu, Japan
Seok Jo Go	Dongeui institute of Technology, Korea
Jie Chen	Beijing Institute of Technology, China
Zuomin Dong	University of Victoria, Canada
Wei Lin	Case Western Reserve University, USA
Andrew A. Goldenberg	University of Toronto, Canada
Guoying Gu	Shanghai Jiao Tong University, China
Jason J. Gu	Dalhousie University, Canada
Lina Hao	Northeastern University, China
Henry Hong	Concordia University, Canada
Qinglei Hu	Harbin Institute of Technology, China
Min Liu	Tsinghua University, China
Inna Sharf	McGill University, Canada
Yang Shi	Victoria University, Canada
Gangbing Song	University of Houston, USA
Jing Sun	University of Michigan, USA
Yonghong Tan	Shanghai Normal University, China

Yong Tang	South China University of Technology, China
Xingsong Wang	Southeast University, China
Pak Kin Wong	University of Macau, China
Shaorong Xie	Shanghai University, China
Zhenhua Xiong	Shanghai Jiao Tong University, China
Yanzheng Zhao	Shanghai Jiao Tong University, China
Huijun Gao	Harbin Institute of Technology, China
Zijiang Yang	Ibaraki University, Japan
Dingguo Zhang	Shanghai Jiao Tong University, China
Luis E. Garza C.	Tecnológico de Monterrey, Mexico
Ruediger Spillner	Technische University München, Germany
Weidong Chen	Shanghai Jiao Tong University, China
Jaemin Byun	ETRI, Korea

List of Reviewers

We would like to acknowledge the support of the following people who contributed to peer review of articles from ICIRA2013.

Dalei Pan	Derong Liu
Joonyoung Choi	Yinfeng Fang
Keitaro Naruse	Chao Liu
Yanzheng Zhao	Dingguo Zhang
Hailong Pei	John M. Dolan
Yuehui Wang	Bugong Xu
Wei Zeng	Kiattisin Kanjanawanishkul
Zhaojie Ju	Tadeusz Szkodny
Jae Min Byun	Taeyong Choi
Jason J. Gu	Shan Jiang
Hee-Je Kim	Chun-Yi Su
Hui Yu	Mingcong Deng
Ju Jang Lee	Ronglei Sun
Kai Xu	Sungshin Kim
Wenwei Yu	Jong-Wook Kim
Weidong Chen	Weiting Liu
Zhenhua Xiong	Jeehwan Ryu
Min Cheol Lee	Qinchuan Li
Jangmyung Lee	Seok Jo Go
Honghai Liu	Zainah Md Zain
Xuguang Zhang	Mihoko Otake
Po-Ying Lai	Shuzhi Sam Ge
Bin Zhang	Kang-Bak Park
SAM Farhchi	HENTOUT Abdelfetah
Yonghong Tan	Dong-Yun Gu
Mahmod Frajchi	Huayong Yang

Jangmok Kim
Young-Im Cho
Joonbum Bae
Byoung-Ho Kim
Hyeungsik Choi
Hyunmin Do
Dongkyoung Chwa
Caihua Xiong
Chaohai Zhang
Jianhua Zhang
Yaohong Qu
Shitao Zhan
Pi-Ying Cheng
Yangmin Li
Wenlong Li
Seul Jung
Guangren Duan
Feng-Li Lian
Juntong Qi
Enrong Wang
Yuding Cui
Xinjun Sheng
Xinyong Mao
Xinkai Chen
Zicheng Li
Wenbin Chen
Liu Yong-Hua
Guoying Gu
Min-Kyu Park
Jaesung Hong
Zhijun Li
Deqing Mei
Syed Hassan
Zhang Jianjun
Myung-Jin Chung
Jacek Czeczot
Taeseok Jin
Joon Young Choi
Can Wang
Guo-Ying Gu
Kalyana Chakravarthy Veluvolu
Xiaogang Duan
Yandong Tang
Tao Mao
Jianjun Meng
Jie Chen

Table of Contents – Part II

Mechanism Desing and Control

Design and Inverse Kinematics of Three Degree of Freedom Mine Detection Manipulator 1
Nauman K. Haider, Shiraz Gulraiz, Ayaz Mehmood, and Umer Izhar

The Modeling and Simulation of Kinetic Analysis of Nonholonomic Systems for the Omni-Directional Wall Climbing Robot 16
W.X. Yan, H.F. Zhou, Yan-Zheng Zhao, Z. Fu, and Y. Wang

A Rolling Sarrus Mechanism 33
Chao Liu, Hao Wang, Mei-Li Zhai, and Yan-An Yao

A New Euclidian Distance Based Approach to Measure Closeness to Singularity for Parallel Manipulators 41
Jianyu Mao, Yalei Guo, Jie Ren, and Weizhong Guo

Framework Based Path Planning, A Novel Approach 54
Morteza Aghaei and Seyyed Mohammad Reza Farshchi

Kinematics and Dynamics for a 3-DOF Parallel Manipulator with Limbs of Embedding Structures 63
Jianjun Zhang, Xiaohui Wang, Ning Jiang, and Weimin Li

High-Speed Tracking Control of Parallel Kinematic Machine for Pick-and-Place 74
Hyun Min Do, Chanhun Park, Byung In Kim, Tae Yong Choi, and Jin Ho Kyung

Ultrasound Based Object Detection for Human-Robot Collaboration . . . 84
Christoph Glowa and Thomas Schlegl

Exponential Stabilization of Second-Order Nonholonomic Chained Systems 96
Zainah Md. Zain, Keigo Watanabe, Kiyotaka Izumi, and Isaku Nagai

Development of an Autonomous RC-car 108
Daniel Claes, Joscha Fossel, Bastian Broecker, Daniel Hennes, and Karl Tuyls

Modeling, Control and Simulation of a 6-DOF Reconfigurable Space Manipulator with Lockable Cylindrical Joints 121
Pooya Merat, Farhad Aghili, and Chun-Yi Su

Mechanical Design of a Lower Extremity Exoskeleton with Hybrid Legs for Power Augmentation 132
Yunjie Miao, Feng Gao, and Dalei Pan

Design of Selectively Controllable Micro Actuators Powered by Remote Resonant Magnetic Fields 143
Kai Xu and Guoqing Liu

Mechanical Home Position Setting Method of the Manipulator with Two Encoders 155
Tae Yong Choi, Hyun-Min Do, Doo-Hyung Kim, Kyung-Taik Park, and Kwangcho Chung

Using Growth Curve in Trajectory Planning for Industrial Manipulator 166
Hua Jiang, Yonghua Yan, Mingyong Zhang, Jianrong Zhang, and Jiahang Xu

Motion and Optimal Control

Practical Implementation of the Nonlinear Control of the Liquid Level in the Tank of Irregular Shape 178
Witold Klopot, Tomasz Klopot, Piotr Laszczyk, Jacek Czeczot, and Mieczyslaw Metzger

An Optimal Feedback Approach for the Stabilization of Linear Systems Subject to Input Saturation and Magnitude-Bounded Disturbances 189
S.T. Zhan, W.X. Yan, Z. Fu, J.H. Liu, W.H. Deng, and Yan-Zheng Zhao

Estimation of Road Adhesion Coefficient Using Higher-Order Sliding Mode Observer for Torsional Tyre Model 202
J.J. Rath, K.C. Veluvolu, D. Zhang, Q. Zhang, and M. Defoort

Stability Domain Analysis for Input-Saturated Linear Systems Subject to Disturbance via Popov Criterion: An LMI Approach 214
S.T. Zhan, W.X. Yan, Z. Fu, and Yan-Zheng Zhao

Humanoid Robot

Synergetic Control Strategy for a Hybrid FES-Exoskeleton System: A Simulation Study 226
Yong Ren, Qing Zhang, and Dingguo Zhang

A Balance Control Method of a Walking Biped Robot under a Continuous External Force 237
Yeoun-Jae Kim, Joon-Yong Lee, and Ju-Jang Lee

Design and Control of a Four-Link Mechanism for High Speed and Dynamic Locomotion 246
Huiyang Yu, Ronglei Sun, Hua Nie, and Guohua Qin

A Six-Legged Walking Robot Inspired by Insect Locomotion 257
Yeongtae Jung and Joonbum Bae

A Stable Walking Control of Two – Legs Biped Robot 265
Won Sung Ki, Byung Kyun Shim, Won Jun Hwang, Eun Uk Kang, Woo Song Lee, and Sung Hyun Han

Underwater and Space Robot

Design of a Time-Delayed Controller for Attitude Control of a Quadrotor System 274
Jeong Geun Lim and Seul Jung

Brain Flow in Application for SYNAP New Robotic Platform 281
Alberto Rovetta

Design and Analysis on a New Underwater Robot 289
Ngoc-Huy Tran, Hyeung-Sik Choi, Sang-Seob Lee, and Ba-Loc Mai

Design and Manufacturing a Bio-inspired Variable Stiffness Mechanism in a Robotic Dolphin 302
Yong-Jai Park and Kyu-Jin Cho

Design and Control of 3-DOF Robotic Fish 'ICHTHUS V5.5' 310
Gi-Hun Yang, Kyung-Sik Kim, Sang-Hyo Lee, Chullhee Cho, and Youngsun Ryuh

Power Conversion Technology for Robotics

High Efficiency Isolated Bidirectional AC-DC Power Converter 320
Ho-Sung Kim, Myung-Hyo Ryu, Ju-Won Baek, Jong-Hyun Kim, and Hee-Je Kim

Dynamic Analysis and Optimal Design of High Efficiency Full Bridge LLC Resonant Converter 327
Dong-Keun Jeong, Myung-Hyo Ryu, Joo-Won Baek, and Hee-Je Kim

A Boost PFC Rectifier with a Passive Lossless Snubber Circuit Using Coupled Inductors Methodes 334
Hyeok-Jin Yun, Jong-Hyun Kim, Myung-Hyo Ryu, and Hee-Je Kim

Experimental Investigation on the Hybrid Smart Green Ship 338
Kyoung-Jun Lee, Dongsul Shin, Jong-Pil Lee, Tae-Jin Kim, and Hee-Je Kim

Hybrid Control Scheme for a Half-Bridge LLC Resonant Converter with a Wide Input Range 345
Dongsul Shin, Kyoung-Jun Lee, Jong-Pil Lee, and Hee-Je Kim

Mechatronics and Automation

A Relay Shaping Method for Servo Mechanical System Identification ... 353
Chao Liu, Jia Liu, Jian-hua Wu, Hui Wang, and Zhenhua Xiong

Optimal Cross-Coupled Synchronization Control of a Precision Motion Stage Driven by Dual Linear Motors 365
Gang Zhang, Jian-hua Wu, Pin-kuan Liu, and Han Ding

Genetic-Based k-Nearest Neighbor for Chaff Echo Detection 375
Jonggeun Kim, HyeYoung Han, Jungwon Yu, Hansoo Lee, and Sungshin Kim

Design and Analysis of a Spatial Remote Center of Compliance Mechanism 385
Lei-Jie Lai, Guo-Ying Gu, Hang Zhou, and Li-Min Zhu

A Novel Conductive Particle Dispersing Method via EHDA for POB-COG Packaging 397
Z. Ba, X. Yuan, L. Jia, X. Sheng, Zhenhua Xiong, and Han Ding

Performance Prediction of Hard Rock TBM Based on Extreme Learning Machine 409
Chengjun Shao, Xiuliang Li, and Hongye Su

A Sensor for Large Strain Deformation Measurement with Automated Grid Method Based on Machine Vision 417
Yi Jin, Mingchi Feng, Tao Luo, and Chao Zhai

A 6-Axis Sensor for Minimally Invasive Robotic Surgery 429
Jun Jiang, Le Xie, and Hailong Yu

Industrial Application of Actuator and Sensor

Mechanical Safety of Automatic Door by Using PFVA Based on 2-Stage Star Compound Gear 436
Min-Kyu Park and Delbert Tesar

Development of Smart Actuator and Its Application 442
Seok-Jo Go, Min-Kyu Park, and Young-Jin Lee

Development of Single Channel Interrogator for Optical Sensors 450
Jang Sik Park, Jong Kwan Song, and Byung Woo Yoon

In-network RFID Data Filtering Scheme in RFID-WSN for RFID Applications 454
Ali Kashif Bashir, Myong-Soon Park, Sang-Il Lee, Jinseop Park, Wongryol Lee, and Sayed Chattan Shah

Optimal Design of MR Shock Absorber for Passenger Vehicle 466
Kum-Gil Sung and Min-Kyu Park

Fractional-Order PID Control of Hydraulic Thrust System for Tunneling Boring Machine 470
Ling Fei, Jingcheng Wang, Langwen Zhang, Yang Ge, and Kang Li

Finite Element Research on Cutting Force and Temperature in Milling 300M Steel 481
Sen Lin, Fangyu Peng, Yizhi Liu, Sheng Yang, and Rong Yan

Multi-axis NC Machining Dynamics Analysis and Control

Experimental Study of Surface Integrity of Aluminum Lithium Alloy by Face Milling 491
Haikuo Mou, Xinda Huang, Xiaoming Zhang, and Han Ding

Research on Active Vibration Control of Thin-Walled Workpiece in Milling Based on Voice Coil Motor 503
Puwei Chen, Jie Zhai, Xiaoming Zhang, Hai-Tao Zhang, and Han Ding

A Complete Methodology for Estimating Dynamics of the Heavy Machine Tool Structure 513
Hui Cai, Bin Li, Xinyong Mao, Bo Luo, and Fangyu Peng

Adaptive LQR Control to Attenuate Chatters in Milling Processes 525
Hai-Tao Zhang, Zhiyong Chen, and Han Ding

Robot Surgery Simulation System for Soft Tissue Cutting 535
Hesheng Wang, Maojiao Cai, Weidong Chen, Meng Li, and Kang Li

A Novel PWM Scheme for Position Sensorless Control of BLDC Motor Drives Based on Back EMF 545
Zicheng Li, Zhouping Yin, and You-lun Xiong

Aviation Blade Inspection Based on Optical Measurement 555
Wen-long Li, Li-ping Zhou, and You-lun Xiong

Computer Integrated Manufacturing and Automation

Programmable Automation of Soccer Ball Stiching through Open Loop Control of a Path Tracing Gripper 569
Majid Munawar, Khurram Butt, Waseem Shahzad, Mehran Ahmad, and Kamal Yousaf

A Design and Development of Robotics Integrated Curriculum Based on Storytelling for Elementary School Student 580
Ji-Hun Sung, Young-Hoon Sung, and Wae-Shik Moon

Cutting Force Prediction of Plunge Milling Based on Precise Cutting Geometry 592
Kejia Zhuang, Xiaoming Zhang, and Han Ding

Distributed Coordination of Multiple Robot Systems Based on Hierarchical Petri Net Models 602
Gen'ichi Yasuda

Study on Collaborative Simulation of Excavation System of the Shield Machine in Composite Strata 614
Yanmin Zhao, Jianfu Zhang, and Pingfa Feng

Modeling and Control of Smart Material Actuating Systems

Robust Adaptive Control of a Class of Nonlinear Systems with Unknown Hysteresis Nonlinearity 623
Yong-Hua Liu, Ying Feng, and Chun-Yi Su

A Prandtl-Ishlinskii Model for Characterizing Asymmetric and Saturated Hysteresis of Smart Material Actuators 635
Omar Aljanaideh, Subhash Rakheja, and Chun-Yi Su

Improving Tracking Precision of Piezoceramic Actuators Using Feedforward-Feedback Control 644
Guo-Ying Gu, Chun-Xia Li, Lei-Jie Lai, and Li-Min Zhu

A Novel Analytical Inverse Compensation Approach for Preisach Model 656
Zhi Li, Sining Liu, and Chun-Yi Su

High Precision Control for Nano-stage Driven by Magnetostrictive Actuator 666
Xinkai Chen and Chun-Yi Su

Development of a Parallel-Kinematic High-Speed XY Nanopositioning Stage 678
Chun-Xia Li, Guo-Ying Gu, Mei-Ju Yang, and Li-Min Zhu

Full-Face Tunnel Boring Machine

Dynamical Behavior of Redundant Thrusting Mechanical System in Shield Machines with Various Grouping Strategies 690
Chunzhang Zhao, Haidong Yu, and Yong Zhao

Cutters Layout Design of the Full-Face Rock Tunnel Boring Machine Based on Physical Programming 700
Xu Zhang, Wei Sun, Junzhou Huo, and Jingxiu Ling

Analysis of Multi-sensor Attitude Measurement System on TBM 710
Chuncao Zhang, Guoli Zhu, Jianbo Zhang, and Minghua Pan

Endocrine Intelligent Control of Thrust Hydraulic System for TBM 720
Jin Yao, Xia Yimin, Cheng Yongliang, and Zhang Huan

A Cutter Layout Optimization Method for Full-Face Rock Tunnel Boring Machine 727
Geng Qi, Wei Zhengying, Du Jun, and Tang Yiping

Author Index 739

Table of Contents – Part I

Application of High Frequency Systems for Robotics

Development of Power Supply System for Medical Ruby Laser 1
Jae-Hun Jeong, Kook-Sung Hur, and Hee-Je Kim

Corrosion Protection Using High-Voltage and High-Frequency System 8
Seung-Hwa Baek, Hyun-Min Kim, and Hee-Je Kim

An Analysis on the Particular Pulse Related to the Human Bio-signal by Using Photoplethysmography(PPG) 18
Myong-hwan Kim and Hee-Je Kim

Bunker Oil C Heating Using Induction Heating 25
Dong-Hyun Kim, Ki-Ryong Kim, and Hee-Je Kim

Magnetic Resonance Wireless Power Transmission Using a LLC Resonant Circuit for a Locomotion Robot's Battery Charging 31
Ki-Ryong Kim, Dong-Hyun Kim, and Hee-Je Kim

Research on the MPPT Simulation of Mini Photovoltaic System for the Robotic Vacuum Cleaner Battery Charging 38
Seong-Min Heo, Ki-Ryong Kim, and Hee-Je Kim

Intelligent Robots and Autonomous Systems

VDC of In-Wheel EV Simulation Based on Precise Wheel Torque Control 45
Hyunuk Ha, Jongmoo Kim, and Jangmyung Lee

Vibration Pattern for the Implementation of Haptic Joystick 56
Kyung-Wook Noh, Sun-Kyun Kang, Dong-Hyuk Lee, and Jangmyung Lee

Outdoor Precision Position Estimation System Using Multi-GPS Receivers 66
Seunghwan Choi, Kijung Kim, Yunki Kim, and Jangmyung Lee

Low Complexity MAP Algorithm for Turbo Decoder 77
Jonghyun Seo and Jangmyung Lee

Force Feedback Implementation Based on Recognition of Obstacle for the Mobile Robot Using a Haptic Joystick 85
Dong-Hyuk Lee, Kyoung-Taik Park, Sun-Kyun Kang, and Jangmyung Lee

Position Detection Performance Improvement for LSM Control in Super Speed Maglev 97
Jinho Lee, Jeongmin Jo, Youngjae Han, and Changyoung Lee

Network Aware Resource Allocation Scheme for Mobile Ad Hoc Computational Grid 105
Sayed Chhattan Shah, Myong-Soon Park, Wan Sik Choi, Sajjad Hussain, and Ali Kashif Bashir

Single Camera Motion Estimation: Modification of the 8-Point Method 117
Mohammad Hossein Mirabdollah and Bärbel Mertsching

A Biomimetic Earthworm-Like Micro Robot Using Nut-Type Piezoelectric Motor 129
Maoying Zhou, Yuebang Tao, Liling Cheng, Wei-ting Liu, and Xin Fu

A Robust Control of Intelligent Mobile Robot Based on Voice Command 136
Sung Won Jung, Moon Yeol Park, In Man Park, Yang Keun Jung, and Hang Bong Shin

Vision Based People Tracking Using Stereo Camera and Camshift 145
Kang-Il Park, Chan-Ik Park, and Jangmyung Lee

Bio-Medical Robotics and Its Application

Analysis of Active Haptic Feedback Effects on Standing Stability 154
Muhammad Raheel Afzal, Yasir Jan, Syed Hassan, and Jungwon Yoon

Speed Adaptation of a Small Size Treadmill Using Impedance Control Approach for Rehabilitation 165
Jungwon Yoon, Auralius Manurung, and Irfan Hussain

Design and Simulation of a 3D Actuation System for Magnetic Nano-Particles Delivery System 177
Mohammad Dadkhah, Naveen Kumar, and Jungwon Yoon

Optimal Kinematic Design of a Novel Robotic Knee Device for Gait Rehabilitation with Stance Control 188
Sanghun Pyo, Mingyun Oh, and Jungwon Yoon

Neuro Invasive Multi-targeted Drug Delivery Approach Using Swarm of Nano-robotic Carriers 204
Syed Hassan, Ikram Ullah, Myeong Ok Kim, and Jungwon Yoon

A Novel EMG Control Method for Multi-DOF Prosthetic Hands with Electrical Stimulation Feedback 216
Qi Huang, Li Jiang, Dapeng Yang, and Hong Liu

Sliding Perturbation Observer Based Reaction Force Estimation Method in Surgical Robot Instrument 227
Sung Min Yoon, Min-Cheol Lee, and Chi Yen Kim

Design of a Novel Single Incision Laparoscopic Surgery Robot with Increased Tissue Handling Force 237
DaeKeun Ji, Byungsik Cheon, Makoto Hashizume, Morimasa Tomikawa, and Jaesung Hong

Vertical Collaborative Fuzzy C-Means for Multiple EEG Data Sets 246
Mukesh Prasad, Chin-Teng Lin, Chien-Ting Yang, and Amit Saxena

Comparison of Exoskeleton Robots and End-Effector Robots on Training Methods and Gait Biomechanics 258
Pi-Ying Cheng and Po-Ying Lai

TCP Performance in LTE Network 267
Hyun-Chul Yi, Hyoung-Woo Kim, and Joon-Young Choi

Analysis of Functional Components for a Robotic Patient Lift Based on Chinese Clinical Demands 273
Yu Wu, Dong-Yun Gu, and Jian-He Wei

Robotics for Rehabilitation and Assistance

Lower Limb Exoskeleton Using Recumbent Cycling Modality for Post-stroke Rehabilitation 284
Hua Yan and Canjun Yang

An Open-Source Development and Simulation Platform for Smart Wheelchairs 295
Wenlong Liao, Weidong Chen, Zhixuan Wei, Wenxi Zhang, Jingchuan Wang, and Kang Li

Semantic Mapping for Safe and Comfortable Navigation of a Brain-Controlled Wheelchair 307
Zhixuan Wei, Weidong Chen, Jingchuan Wang, Huiyu Wang, and Kang Li

Control Strategies and Particle Filter for RGB-D Based Human Subject Tracking and Behavior Recognition by a Bio-monitoring Mobile Robot 318
Nevrez Imamoglu, Myagmarbayar Nergui, Yuki Yoshida, Jose Gonzalez, and Wenwei Yu

CTS Rehabilitation Training Robot Using Motor Control 330
Heein Jeong, Sangyong Lee, and Jangmyung Lee

A Principle of Mechanical Implementing the Kinematic Synergy for Designing Anthropomorphic Hand 339
Wenbin Chen and Caihua Xiong

Design Simulations of the SJTU Continuum Arm Exoskeleton (SCAX) 351
Kai Xu, You Wang, and Dong Qiu

A Novel 10-DoF Exoskeleton Rehabilitation Robot Based on the Postural Synergies of Upper Extremity Movements 363
Kai Liu and Caihua Xiong

An ANN Based Approach for Gait Prediction of a Lower-Limb Exoskeleton with Plantar Pressure Sensors 373
Yuzhang Liu, Can Wang, Duan Zheng, Gang Wang, and Xinyu Wu

Optimal Kinematic Calibration of the 6-UPS Parallel Manipulator 384
Genliang Chen, Hao Wang, and Zhongqin Lin

Bio-Mechatronics

Effects of Long-Term Myoelectric Signals on Pattern Recognition 396
Jiayuan He, Dingguo Zhang, Xinjun Sheng, and Xiangyang Zhu

Development of a Surface EMG Acquisition System with Novel Electrodes Configuration and Signal Representation 405
Yinfeng Fang, Xiangyang Zhu, and Honghai Liu

Hybrid Force-Position Fuzzy Control for a Prosthetic Hand..... 415
Gaoke Zhu, Xiaogang Duan, and Hua Deng

Simulation of a Hydraulic System Duplicating the Human Circulatory System 427
Feng Huang, Wenwei Qian, Xiaodong Ruan, and Xin Fu

An Overview of Wearable Sensing and Wearable Feedback for Gait Retraining 434
Pete B. Shull, Wisit Jirattigalachote, and Xiangyang Zhu

Quantifying Roughness Sensation by an Active Touch Model for Vibrotactile Stimulation 444
Zhongyi Qiu, Dingguo Zhang, and Xiangyang Zhu

Visual Stimulus Background Effects on SSVEP-Based Brain-Computer Interface 453
Xiaokang Shu, Lin Yao, Jianjun Meng, Xinjun Sheng, and Xiangyang Zhu

Mechanical Implementation of Postural Synergies of an Underactuated Prosthetic Hand 463
Kai Xu, Yuheng Du, Huan Liu, Xinjun Sheng, and Xiangyang Zhu

A Micro-wires Based Tactile Sensor for Prosthesis 475
Guanhao Liang, Deqing Mei, Yancheng Wang, Yu Dai, and Zichen Chen

An Anti-aliasing and De-noising Hybrid Algorithm for Wavelet Transform 484
Yuding Cui, Caihua Xiong, and Ronglei Sun

Simultaneous and Proportional Estimation of Finger Joint Angles from Surface EMG Signals during Mirrored Bilateral Movements 493
Lizhi Pan, Xinjun Sheng, Dingguo Zhang, and Xiangyang Zhu

A Mechatronic Platform for Studies of Tactile Sensory System on Prosthesis Hand 500
Xiaoying Cheng, Qingchuan Shan, Ping Yu, Liling Cheng, Wei-ting Liu, and Xin Fu

Simulation Study of Dipole Localization in MEG-Based BCI Using Magnetic Field Reconstruction 509
Liang Hu, Hui-Min Shen, Wei-ting Liu, Kok-Meng Lee, and Xin Fu

Environment Recognition and Localization/Navigation

Fully Decentralized Cooperative Localization of a Robot Team: An Efficient and Centralized Equivalent Solution 520
Hua Mu, Mengyuan Dai, Ming Gao, and Xianfei Pan

Development of a Sound Source Localization System for Assisting Group Conversation 532
Mihoko Otake, Myagmarbayar Nergui, Seong-eun Moon, Kentaro Takagi, Tsutomu Kamashima, and Kazuhiro Nakadai

Adaptive Tracking Controller Based on the PID for Mobile Robot Path Tracking 540
Hyunjin Chang and Taeseok Jin

A New Non-Gaussian Filtering Approach to Monocular SLAM Problem 550
Mohammad Hossein Mirabdollah and Bärbel Mertsching

Object Following Robot Using Vision Camera, Single Curvature Trajectory and Kalman Filters 562
Shin-nyeong Heo, Hyun-Seop Lim, Seungik Hwang, and Jangmyung Lee

Accurate Localization with COAG Features and Self-adaptive Energy Region 576
Dong-Il Kim and Jae-Bok Song

2D Multi-class Occupancy Grid Map for a Mobile Security Robot in Urban Environments 584
Yungeun Choe and Myung Jin Chung

Trajectory Optimization Using Virtual Motion Camouflage and Particle Swarm Optimization 594
Dong Jun Kwak, Byunghun Choi, and H. Jin Kim

3D Probability Map Building for UGV Navigation in Special Environment 605
Min-Ho Kim, Hee-Mu Lee, and Min-Cheol Lee

Method and Development of Magnetic Positioning Device for Magnetic Guided Vehicle 615
Hyunhak Cho, Jaeyong Kim, Hajun Song, Moonho Park, and Sungshin Kim

Relative Pose Estimation for an Integrated UGV-UAV Robot System ... 625
Yongseop Jeong and In So Kweon

The Algorithm Camera Computing the Object Location 637
Tadeusz Szkodny

Quantitative Assessment of Uniformity in Particle Distribution 649
Xin Yuan, Lei Jia, Zhengyu Ba, Xinjun Sheng, and Zhenhua Xiong

Hand Gesture Recognition for Human-Computer Interaction Using Moment Invariants and Neural Network Classifier 661
Ran Chen, Shuangyuan Wang, Liang Gong, and Chengliang Liu

Sum of Squares Based Range Estimation for Camera Systems 668
Cheol-Joong Kim and Dongkyoung Chwa

Multi-Agent Fuzzy-Based Control Architecture for Autonomous Mobile Manipulators: Traditional Approaches and Multi-Agent Fuzzy-Based Approaches 679
Abdelfetah Hentout, Mohamed Ayoub Messous, Saliha Oukid, and Brahim Bouzouia

Robot Motion Analysis and Planning

Geometric Modeling of Any Obstacle Shapes for Robot Motion Planning 693
Md Nasir Uddin Laskar, Seung Y. Choi, Ishtiaq Ahmed, and TaeChoong Chung

Path Planning Approach for Redundant Manipulator Based on Jacobian Pseudoinverse-RRT Algorithm 706
Yang Qian and Ahmed Rahmani

Dynamic Research of a Novel Exoskeleton with Level Walking 718
Dalei Pan and Feng Gao

Mobility Analysis of Two Exechon-Liked Parallel Mechanisms 730
Xinxue Chai, Qiaohong Chen, Jigang Ma, and Qinchuan Li

A Method for Inverse Kinematic Solutions of 3R Manipulators with Coupling 742
Byoung-Ho Kim

Author Index 751

Design and Inverse Kinematics of Three Degree of Freedom Mine Detection Manipulator

Nauman K. Haider, Shiraz Gulraiz, Ayaz Mehmood, and Umer Izhar

Department of Mechatronics Engineering
College of Electrical and Mechanical Engineering,
National University of Sciences and Technology, Rawalpindi, Pakistan
nauman_khurshid@yahoo.com, gulshiraz@hotmail.com

Abstract. Every year hundreds of people lose their lives because of land mine explosions. The objective of this paper is to design a manipulator on which a mine detector can be mounted as its end effector and can effectively perform mine detection operation. In this paper the major factors for designing a 3 degree of freedom manipulator are discussed. These include design considerations, inverse kinematics, torque, velocity, stress, deformation analysis and centre of mass calculations are presented. A numerical approach is presented here for a manipulator design to achieve the required task. This robotic manipulator can support a robotic end effector (specifically mine detector) up to 2 kg.

Keywords: manipulator design, inverse kinematics, 3 DOF manipulator, stress analysis, deformation analysis, torque requirement calculations, centre of mass calculation.

1 Introduction

Currently more than 100 million mines are buried across the word. These mines not only effect the economic development of a nation but they also become reason for injuring and killing thousands of people each year [1][2]. Currently mostly manual mine detection techniques are employed that threaten the life of the operator. Many researchers have worked on designing a suitable manipulator for the purpose of mine detection, most of which involved three degree of freedom manipulators[1][2]. Some among them also used four degree of freedom manipulator to achieve the task [3].A generic manipulator is one that can support variety of end effectors with minimum or no alterations required. In designing a manipulator the first need is to define the task specifications of the manipulator. Task specifications include operating range of the manipulator and the kind of operation it is supposed to perform [3]. The operating range of manipulator is simply the workspace i.e. the points in space where a manipulator can reach effectively. To keep things simple operating angles here are kept constant but different combinations for link lengths and operating angles can be tried to find maximum operating range of the manipulator with minimum torque

J. Lee et al. (Eds.): ICIRA 2013, Part II, LNAI 8103, pp. 1–15, 2013.

requirements. Torque and force requirements of a manipulator can simply be calculated by inverse kinematic techniques. The type of operation that a manipulator has to perform is the application of that manipulator. Stress and deformation analysis are a good measure of the feasibility and durability of a manipulator. In this paper, a comprehensive approach is presented to design a manipulator to hold a mine detector as an end effector that can be mounted on an unmanned ground vehicle (UGV).

2 Design Considerations

Link lengths and operating range are the basic attributes of a manipulator. The operating range depends on the user or task requirements whereas the link lengths depend on the operating range and the operating angles of the manipulator links. In the considered case of manipulator design for UGV mine detector, the operating range found was 122 cm. The required extension out of UGV is 60 cm to avoid any interference of UGV's contents with the mine detector operation. The height of end effector from ground must be 5 cm and the height of UGV's upper surface is 29 cm from ground. Height of link 1 above the ground is also 29 cm. The degree of freedom required is 3, one for the sweeping motion of mine detector and other two to retract the manipulator back inside the UGV. Link 1 has to perform two motions [3] (lift and sweep) while link 2 has lift motion. Links and their motions are shown in Figure 1.

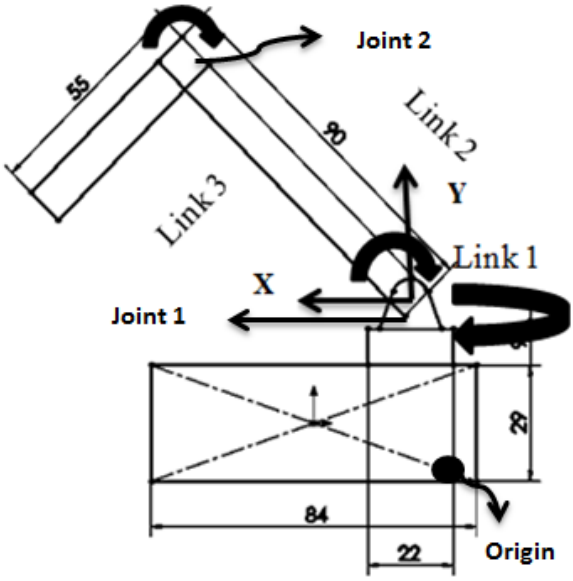

Fig. 1. Schematic representation of manipulator on UGV block (all dimensions are in cm)

2.1 Link Length Calculations

The operating point of end effector is (122, 5) cm (taking origin at the base of link 1). (122, 5) is the operating coordinate of end effector, meaning distance of end effector from origin in x direction is 122 cm (keeping link2 at an angle ofθ_2 and link3 at an angle of θ_3 (sweeping occurs when mine detector, end effector, reaches the coordinates of (122, 5)). The link lengths, L2 and L3, of link 2 and 3 respectively can be calculated by applying trigonometric ratios as given below:

$$L2*\cos\theta_2 + L3*\cos\theta_3 = 122 \quad (1)$$

$$L3*\sin\theta_3 = 29-5 \quad (a)$$

$$L3*\sin\theta_3 = 24 \quad (2)$$

Looking at equation (1) and (2) we have four unknowns thus to solve it we assume that when end effector reaches coordinates of (122, 5) angles will be $\theta_2=15^o$and $\theta_3=59.3^o$ thus corresponding lengths are found to be:

$$L2 = 90 \text{ cm}$$

$$L3 = 55 \text{ cm}$$

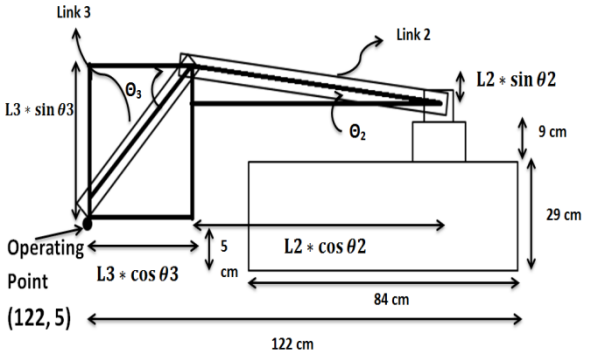

Fig. 2. Trigonometric distribution of links for calculation of link lengths

2.2 Workspace of Manipulator

Workspace of a manipulator is the boundary limit of the manipulator (operating range). Workspace can be easily checked with Matlab® using surface plot. Maximum range of the manipulator is simply $L_2 + L_3$ and it forms a semi-sphere [3] as shown in figure 3

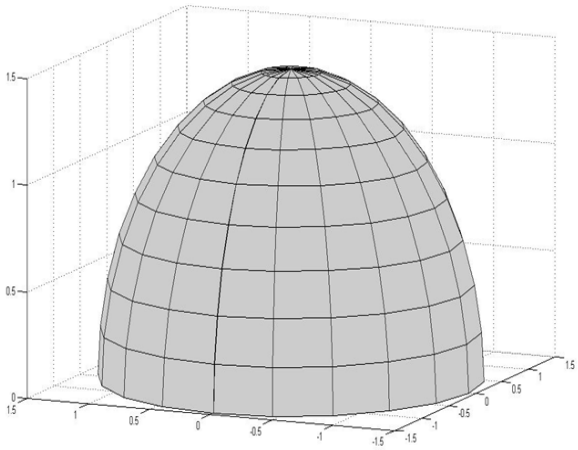

Fig. 3. Workspace of manipulator

Figure 3 is mere representation of outer boundary of the manipulator and also shows that it has equal reach in space (x, y and z axis).

3 Denavit Hartenberg Table

The best way to formulate the characteristics of a manipulator is to construct a *Denavit-Hartenberg* (DH) table for that manipulator. DH table not only provides all the information regarding link lengths and angles but also helps in calculating velocity and acceleration of links along with the torque analysis. Frames for the links are shown in figure 4:

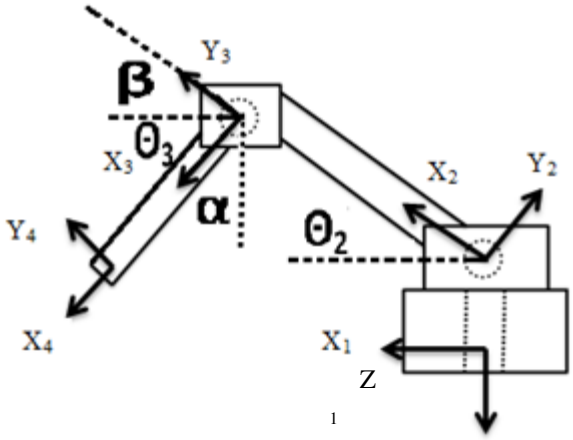

Fig. 4. Frames assignment to links for DH Table

In the figure above:

α = Angle of link 3 with vertical axis

θ_2 = Angle of link 2 with horizontal axis

θ_3 = Angle of link 3 with horizontal axis

$\beta = 90^o - \theta_3$

DH table for this particular link is:

Table 1. DH Table

I	α_{i-1}	a_{i-1}	d_i	Θ_i
1	0	0	0	Θ_1
2	-90	0	0	$-\Theta_2$
3	0	L_1	0	Θ_3
4	0	L_2	0	0

Above DH table shows all the characteristics and parameters of all the links of the manipulator. Here:

α_i = angle between $Z_i$and Z_{i+1}measured about X_i

a_i = distance between $Z_i$and Z_{i+1}measured along X_i

d_i = distance between X_{i-1} and X_i measured along Z_i

α_i = angle between X_{i-1} and X_i measured about Z_i

4 Torque Requirements

In designing a manipulator, amount of torque required to operate the mechanism is a critical variable to cater for the reaction forces and weights acting on the mechanism and then selecting appropriate motors. Conventional torque calculation techniques [4][5][6], that include the weights of the links are used here unlike those methods which ignore its effects and calculate joint torques using torque sensors [7]. Advantage of the technique incorporated in this paper over the one presented in [7] is that it is not only easier to implement but because it does not need electric equipment it provides a low cost solution. Another disadvantage of the technique in [7] is that user has to cater for ripple effects in sensor readings to get accurate results.

The force acting on joint 1 will be a resultant of the weights of link 2, link 3 and mine detector while for joint 2 it will be the weight of link 3 and mine detector.

Torque obtained from the numerical analysis is the maximum torque required to operate the link and motors are thus selected to have a higher torque value than this. Factor of safety for this link is 2.2.

Thus torque required for operating the mechanism successfully can be estimated from equation(s) below:

4.1 Torque Required for Joint 1

Torque required for operating link 2 (joint 1) can be calculated by:

$$\mathbf{T_1}= [(\frac{L2*\cos(\theta 2)}{2} * m2g\ j\grave{}+[(L2\cos(\theta 2) + \frac{L3*\cos(\theta 3)}{2}\ j) *(m_3g)] + (x * F) \quad (3)$$

In above equation:

x = distance of operating point from origin in horizontal direction

g = gravitational acceleration

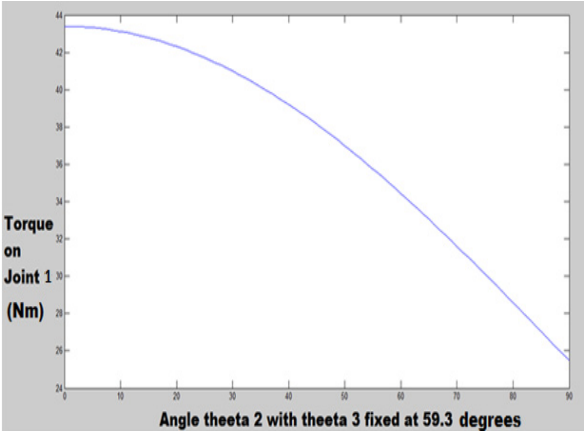

Fig. 5. Relationship between torque on joint 1 and θ_2

Figure 5 shows the relationship between torque and angle of link 2 (θ_2). Value of angle$\theta_2$ranges from 0 to 90^o and resulting torque is found using equation (3). Maximum torque is observed when θ_3 becomes 0^o (point where link 2 becomes parallel to the axis of rotation of link 1 and singularity [8] occurs).

4.2 Torque Required for Joint 2

Torque required for operating link 3 (joint 2) is calculated by following equation:

$$\mathbf{T_2} = F*L_3*\sin(\alpha) + \frac{m3g*L3*\sin(\alpha)}{2} \quad (4)$$

In above equation:

g = gravitational acceleration

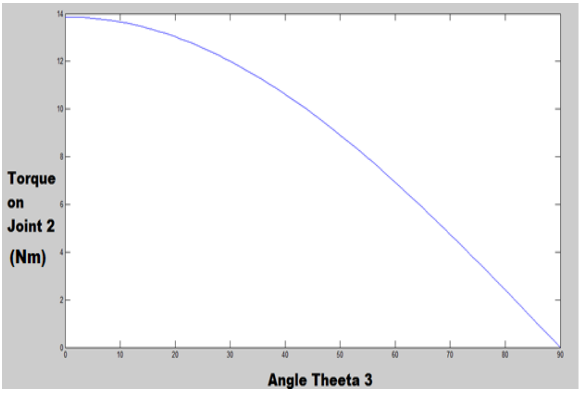

Fig. 6. Relationship between torque T_2 and θ_3

Figure 6 shows the relationship between torque and angle of link 3 (θ_3). Value of angle θ_3 ranges from 0 to 90^o and resulting torque is found using equation (4). Maximum torque is observed when θ_3 becomes 90^o (point where link 2 and link 3 become parallel and singularity occurs).

5 Centre of Mass

For the stability of UGV (over which the manipulator has to be mounted) the key is that during its manoeuvring the centre of mass must always remain within UGV. Centre of mass of any mechanism can be found by dividing it into different geometrical parts then find the centre of mass for those parts, after that find the effective centre of mass for whole structure. The dimensions of UGV in x and y axis are 84 and 42 cm respectively whereas distance of top surface from ground is 29 cm.

Effect of change in angles θ_2 and $\theta_3$on centre of mass is found by first keeping θ_2 constant (15^o) and varying θ_3 from 0 to 90^o and then keeping θ_3 constant (59.3^o) while varying θ_2 from 0 to 90^o.

5.1 X-axis Centroid

The x-component of mass centroid can be found by applying following formula [9]:

$$\bar{y} = \frac{\sum Ai * yi}{\sum Ai} \tag{5}$$

Where A_i= Area of UGV, Area of link2 and link 3

y_i = length of i-components in y-direction

The above equation was used to plot the relationship of (change in) θ_2 and θ_3 with the centre of mass and plots were generated on Matlab. For the stability of UGV during its maneuver the centre of mass of manipulator in x-direction must remain between 0 and 84 cm. For better stability conditions it must remain close to 44 cm.

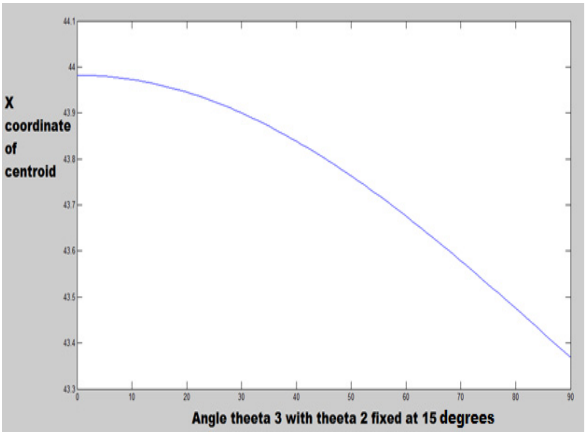

Fig. 7. Effect of change in θ_3 on centre of mass while keeping θ_2 constant

The result of change in centre of mass by varying angle θ_3 is shown in figure 7. It is apparent from the graph that centre of mass of manipulator remains well within the limits of UGV and its variation is form (43.3 to 44.1 cm) where dimension of UGV in x is 84 cm.

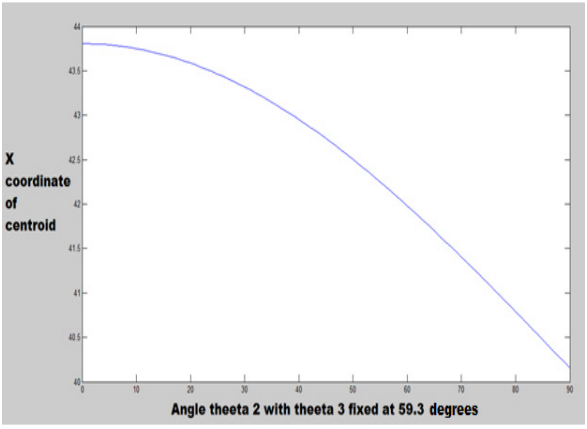

Fig. 8. Effect of change in θ_2 on centre of mass while keeping θ_3 constant

The result of change in centre of mass by varying angle θ_2 is shown in figure 8. It is apparent from the graph that centre of mass of manipulator remains well within the limits of UGV and its variation is form (40.5 to 43.5 cm) where dimension of UGV in x is 84 cm.

5.2 Y-axis Centroid

Y-component of mass centroid can be found by following equation [9]:

$$\bar{x} = \frac{\sum Ai * xi}{\sum Ai} \tag{6}$$

Where A_i= Area of UGV, Area of link2 and link 3

x_i = length of i-components in x-direction

Above equations were used to plot the relationship of (change in) θ_2 and θ_3 with the centre of mass and plots were generated on Matlab. For the stability of UGV during its manoeuvre the centre of mass of manipulator in y-direction must remain between 0 and 42 cm. For better stability conditions it must remain close to 21 cm.

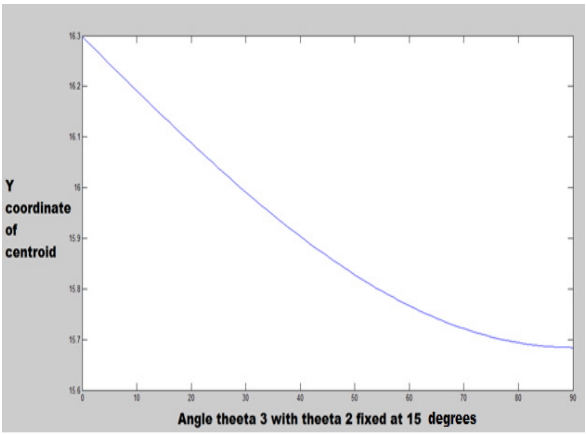

Fig. 9. Effect of change in θ_3 on centre of mass while keeping θ_2 constant

The result of change in centre of mass in y direction by varying angle θ_2 is shown in figure 9. It is apparent from the graph that centre of mass of manipulator remains well within the limits of UGV and its variation is form (14.8 to 18.5 cm) where dimension of UGV in x is 42 cm.

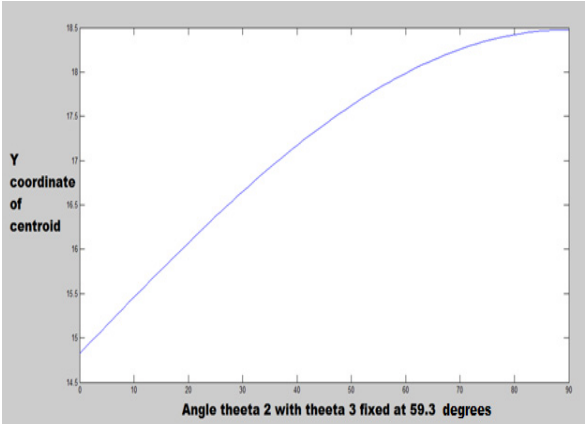

Fig. 10. Effect of change in θ_2 on centre of mass while keeping θ_3 constant

The result of change in centre of mass in y direction by varying angle θ_2 is shown in figure 10. It is apparent from the graph that centre of mass of manipulator remains well within the limits of UGV and its variation is form (14.8 to 18.5 cm) where dimension of UGV in x is 42 cm.

6 Velocity Analysis

Besides torque requirement calculations for the links of manipulator, it is also better to find the angular and linear velocity of the links so that motor of required rpm can be used for application. Laws of Robotics are used with the help of the DH table it is easier to find the velocity and acceleration of the links.

6.1 Angular Velocity

Angular velocity of links can be estimated from [10]:

$$ {}^{1}_{1}\omega = {}^{1}_{0}R\,{}^{0}_{0}\omega + \dot{\theta}1 * {}^{1}_{1}\hat{Z} \tag{7} $$

$$ {}^{2}_{2}\omega = {}^{2}_{1}R\,{}^{1}_{1}\omega + \dot{\theta}2 * {}^{2}_{2}\hat{Z} \tag{8} $$

$$ {}^{2}_{1}R = {}^{1}_{2}R^{\mathrm{T}} = \begin{bmatrix} cos\theta 2 & -sin\theta 2 & 0 \\ 0 & 0 & -1 \\ sin\theta 2 & cos\theta 2 & 0 \end{bmatrix}^{T} $$

Thus

$$ {}^{2}_{2}\omega = \begin{bmatrix} 0 \\ 0 \\ \dot{\theta}2 \end{bmatrix} $$

$$ {}^{3}_{3}\omega = {}^{2}_{2}\omega $$

6.2 Linear Velocity

Linear velocity computation of links is done by using following equations [10]:

$$ \mathbf{{}^{1}_{1}V = {}^{1}_{1}R\,({}^{0}_{0}V + {}^{0}_{0}\omega \times {}^{0}_{0}P)} \tag{9} $$

As linear velocity of joint 0 ($\mathbf{{}^{0}_{0}V}$) and angular velocity $\mathbf{{}^{0}_{0}\omega}$ is also zero thus:

$$ {}^{1}_{1}V = 0 $$

$$ \mathbf{{}^{2}_{2}V = {}^{2}_{1}R\,({}^{1}_{1}V + {}^{1}_{1}\omega \times {}^{1}_{2}P)} \tag{10} $$

Putting:

$$ \mathbf{{}^{1}_{2}P = \begin{bmatrix} L1 * \cos(\theta 1) \\ 0 \\ L1 * \sin(\theta 1) \end{bmatrix}} $$

$$ {}^{2}_{1}R = {}^{1}_{2}R^{\mathrm{T}} = \begin{bmatrix} cos\theta 2 & -sin\theta 2 & 0 \\ 0 & 0 & -1 \\ sin\theta 2 & cos\theta 2 & 0 \end{bmatrix}^{T} $$

$$ {}^{1}_{1}\omega = \begin{bmatrix} 0 \\ 0 \\ \dot{\theta 1} \end{bmatrix} $$

Velocity of joint 2:

$$ {}^{2}_{2}V = \begin{bmatrix} 0 \\ 0 \\ -L1cos\theta 1 * \dot{\theta 1} \end{bmatrix} $$

Velocity of joint 3 (end effector):

$$ {}^{3}_{3}V = {}^{3}_{2}R\ ({}^{2}_{2}V + {}^{2}_{2}\omega \mathrm{x} {}^{2}_{3}P) \tag{11} $$

Putting:

$$ {}^{3}_{2}R = {}^{2}_{3}R^{\mathrm{T}} = \begin{bmatrix} 1 & 0 & 0 \\ 0 & 1 & 0 \\ 0 & 0 & 1 \end{bmatrix}^{T} $$

$$ {}^{2}_{2}\omega = \begin{bmatrix} 0 \\ \dot{\theta 2} * L2 \\ -cos(\dot{\theta 2}) * \dot{\theta 1} * L2 \end{bmatrix} $$

$$ {}^{3}_{3}V = \begin{bmatrix} 0 \\ 0 \\ -L1cos\theta 1 * \theta 1 - cos(\dot{\theta 2}) * \dot{\theta 1} * L2 \end{bmatrix} $$

7 Link Designs

Material selection is the first step in designing a physical system. For this manipulator Aluminum Alloy 1060 is selected because of easy availability, good strength to weight and strength to size ratio and light weight. Two possible options were considered as

Table 2. Comparison between Cylindrical and Parallel Links

Cylindrical Links	Parallel Plate Links
Advantages 1. Stress distribution is uniform. 2. Links are easy to manufacture. 3. Quite cost effective for smaller link lengths.	Advantages 1. Stress distribution is normal to plane of plates and is parallel to the axis of trusses. 2. Stress endurance can be increased by adding more trusses. 3. Expensive for small link lengths but become cost effective in case of large link lengths. 4. Easier to assemble 5. Easy repair and maintenance 6. Suitable for higher loads

Table 2. (*Continued*)

Cylindrical Links	Parallel Plate Links
Disadvantages 1. Maximum stress endurance is less 2. Not suitable for higher loads 3. Quite costly when larger link lengths are required 4. Mechanism becomes heavy weight for support supporting high loads.	Disadvantages 1. Links are difficult to manufacture.

link designs for the particular manipulator which was either the using cylindrical links or going for parallel plate links reinforced with trusses made of nylon in between them. Thickness of both cylindrical and parallel plate links were kept 3 mm. In parallel plate links multiple trusses (in shape of cylindrical rods were inserted at a distance of 15 cm apart). Pros and Cons of the two types were found to be:

7.1 Stress Analysis

To check for the feasibility and practicality of manipulator it must be ensured that the stress endurance of whole system is more than the stresses acting on it. If a case arises where stresses on a system are greater than that a material can endure than material can fracture. For the purpose of stress analysis Solid Works® was used. Both the (cylindrical and parallel plate) links were created in the solid works then fixtures and weights were applied on it and results were generated accordingly. In this paper stress analysis of Link 2 is shown as it is under maximum loading due to link 3 and mine detectors weight.

7.1.1 Stress Analysis of Cylindrical Link

Figure 11 displays the side view of cylindrical design for link 2 of manipulator where point A is fixed and load of 40 N is applied on point B (that is the collective mass due to link 3 and end effector).

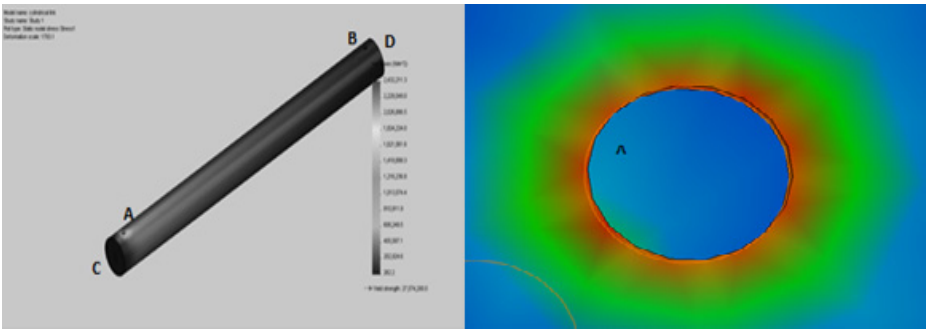

Fig. 11. Top: Stress result of cylindrical link 2, Bottom: Close up view of pin joint where stress is maximum

After fixing point A and applying load of 40 N on point B simulation results showed that maximum stresses occur at point A (one that is fixed). Value of stress everywhere except and near point A was observed to be around 262.2 N/m^2 where around point A it around 810,911.0 N/m^2, maximum value observed at point A was around 2,026,866 N/m^{2}which is not onlyless than yield strength of Aluminium 1060 alloy (yield strength = 27,574,200.0 N/m^2) and also it is very low compared to fracture point (i.e. 2,432,211.0 N/m^2).

7.1.2 Stress Analysis of Parallel plate Link

Similar to figure 11, figure 12 displays the side view of cylindrical design for link 2 of manipulator where point A is fixed and load of 40 N is applied on point B (that is the collective mass due to link 3 and end effector).

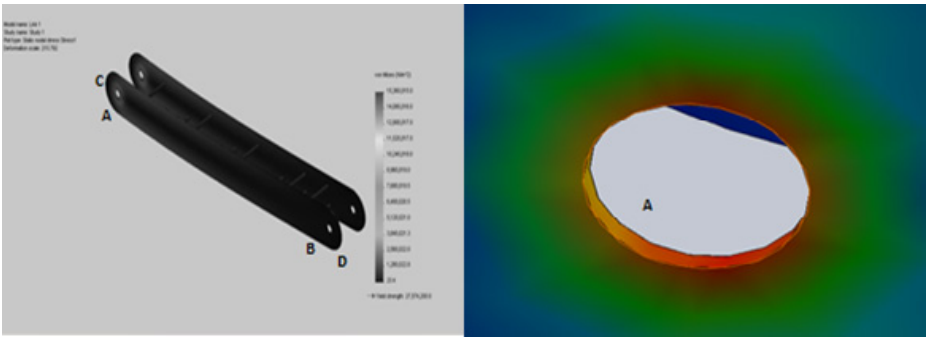

Fig. 12. Left: Stress result of parallel plate link 2, Right: Close up view of pin joint where stress is maximum

After the fixing point A and applying load of 40 N on point B simulation results showed that maximum stresses occur at point A (one that is fixed). Value of stress everywhere except and near point A was observed to be around 23.4 N/m^2 where around point A it is around 3,840,021 N/m^2, maximum value observed at point A was around 11,520,017.0 N/m^2 which is not only less than yield strength of Aluminium 1060 alloy (yield strength = 27,574,200.0 N/m^2) but also it is less compared to fracture point (i.e. 15,360,015 N/m^2).

7.2 Deformation Analysis

Deformation in both type of links were also studied due to loading as the obtained results are discussed in the following sections.

7.2.2 Deformations in Cylindrical Link

Application of load is same as in case of stress analysis in cylindrical links (see section 7.1.1, figure 11). Simulation result for deformation (in case of cylindrical link) is shown in figure 13.

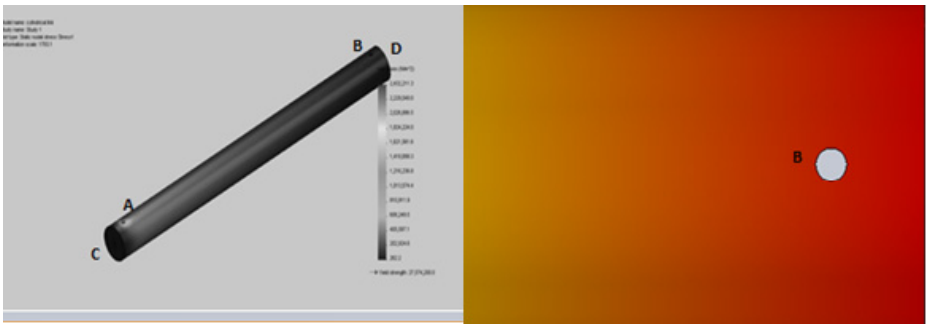

Fig. 13. Left: Deformation result for cylindrical link, Right: Close up of the highest deformation point (Point B is pin joint, point D is edge of link)

From simulation result it was observed that maximum deformation occurs at the edge point D (present near point B) and they tend to decrease from point B to point A. No deformations occur at point A and C. Value of deformation at point D were recorded around 1.7 mm.

7.2.2 Deformations in Parallel plate Link

Application of load is same as in case of stress analysis in cylindrical links (see section 7.1.2, figure 11). Deformation result of cylindrical link is shown in figure 14 and 15.

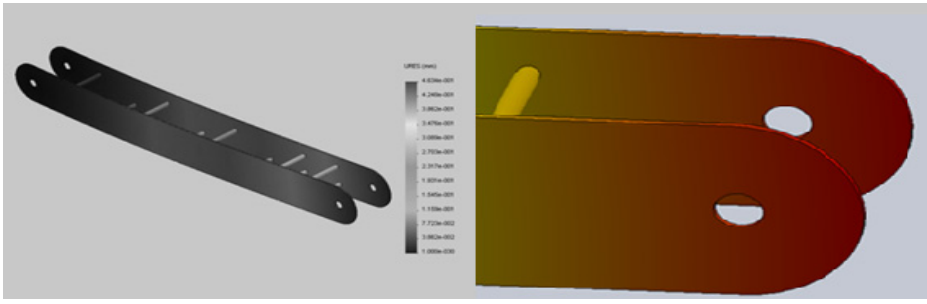

Fig. 14. Left: Deformation result for parallel plate link, **Right:** Close up of the deformation result for parallel plate link

From simulation results it was observed that maximum deformations occur at the edge point D (present near point B) and they tend to decrease from point B to point A. No deformations occur at point A and C. Value of deformation at point D were recorded around 0.46 mm.

8 Conclusion

In this paper a straightforward but comprehensive design for a 3DOF manipulator is presented. The design is presented with inverse kinematics, torque and velocity

calculations. The stability of the manipulator was established by calculating centre of masses. Feasibility and durability of design is checked by running simulations for stress and material deformation on Solid Works and parallel plate truss reinforced links are selected for final design. For physical design parallel plate links were preferred on the cylindrical links because of higher stress endurance, lesser deformation and parallel plate links can be lighter by introducing nylon trusses.

Simpler solution in terms of mechanical design has been presented in this paper contrast to some other researches. Design proposed in this paper is not only generic and simple unlike the designs presented in [1] and [2] besides it also provides more generic and conventional approach. It also achieves the task with one less degree of freedom unlike [3] thus reducing the complexity of design.

References

[1] Nonami, K.: Development of mine detection robot Comet-II and Comet-III. In: SICE 2002, Proceedings of the 41st SICE Annual Conference, vol. 1. IEEE (2002)

[2] Hirose, S., Kato, K.: Development of quadruped walking robot with the mission of mine detection and removal-proposal of shape-feedback master-slave arm. In: Proceedings of the 1998 IEEE International Conference on Robotics and Automation, vol. 2. IEEE (1998)

[3] Binoy, B.N., Kaushik, A., Keerthana, T., Sathees, A., Barani, P.R., Nair, A.S.: A GSM-based versatile Unmanned Ground Vehicle. In: 2010 International Conference on Emerging Trends in Robotics and Communication Technologies (INTERACT), December 3-5, pp. 356–361 (2010)

[4] Meriam, J.L., Kraige: Engineering Mechanics - Statics, 5th edn., pp. 73–76

[5] Papadopoulos, E., Abu-Abed, A.: Design and motion planning for a zero-reaction manipulator. In: Proceedings of the 1994 IEEE International Conference on Robotics and Automation, May 8-13, vol. 2, pp. 1554–1559 (1994)

[6] Craig, J.J.: Introduction to Robotics Mechanics and Control, 2nd edn., pp. 189–191

[7] Kim, I.-M., Kim, H.-S., Song, J.-B.: Design of joint torque sensor and joint structure of a robot arm to minimize crosstalk and torque ripple. In: 2012 9th International Conference on Ubiquitous Robots and Ambient Intelligence (URAI), November 26-28, pp. 404–407 (2012)

[8] Ceccarelli, M., Carbone, G., Ottaviano, E.: An optimization problem approach for designing both serial and parallel manipulators. In: Proc. of MUSME 2005, the Int. Sym. on Multibody Systems and Mechatronics (2005)

[9] Gere, J.M., Goodno, B.J.: Mechanics of Materials, 8th edn., pp. 958–959

[10] Craig, J.J.: Introduction to Robotics Mechanics and Control, 2nd edn., pp. 179–180

The Modeling and Simulation of Kinetic Analysis of Nonholonomic Systems for the Omni-Directional Wall Climbing Robot

W.X. Yan[1], H.F. Zhou[2], Yan-Zheng Zhao[1], Z. Fu[1,2], and Y. Wang[2]

[1] Shanghai JiaoTong University, State Key Lab of Mechanical System and Vibration, Shanghai, 200240, P.R. China
[2] State Key Lab of Robotics and System (HIT), Harbin, 150001, P.R. China
{yz-zhao,xiaogu4524,hfzhou,zhfu}@sjtu.edu.cn

Abstract. This paper studies the modeling and simulation of kinetic analysis for the omin-directional wall climbing robot system. The kinetic equation is necessary for the robot control. Based on Apell equation, dynamic model of the robot is established and the positive and inverse solutions are obtained, the result is proved correct simulated by simulating with Matlab. Finally, it obtained its purpose of the acceleration control and satisfies the requirements of precise motion control.

Keywords: wall climbing robot, omni-directional mechanism, modeling and simulation, Sheth-Uicher transform, Apell equation.

1 Introduction

In this paper, Wall climbing robot is a kind of robot which can be used in limiting environment, such as detection, service, rescue under dangerous and inaccessible conditions, for example, radial, high temperature, high pressure, upright wall, etc… Therefore it is important to research this kind of robot which has increasingly aroused focus around the world(Zhang Yi, 2003, Lal Tummala R. , 2002).

Yoshida, Y. presents a wall-climbing robot which adopts passive suction cups as the attaching components. Using only one motor, this robot can not only move on a wall but also attach suction cups to the wall and remove them from the wall (Yoshida, Y., 2010). But it's hard for it to carry heavy load because of its special structure.

Jun Li has been primarily proposed a brand new climbing robot suction method called "NPT method", which is based on compositive effect of negative pressure force and thrust(Jun Li, 2008).

Shanqiang Wu study a sliding wall climbing robot using a novel negative adsorption device that can be well adopted in small irregular places, such as brick walls, cement walls, ship hulls and oil storage tank surfaces so that the robot could be used where direct access by a human operator is very expensive or very dangerous due to the presence of a hostile environment(Shanqiang Wu, 2011).

J. Lee et al. (Eds.): ICIRA 2013, Part II, LNAI 8103, pp. 16–32, 2013.

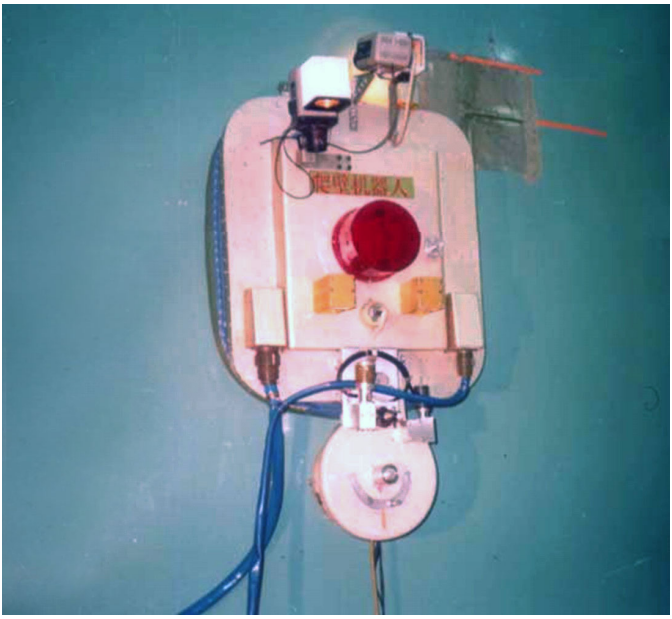

Fig. 1. Picture of the omni-directional wall climbing robot

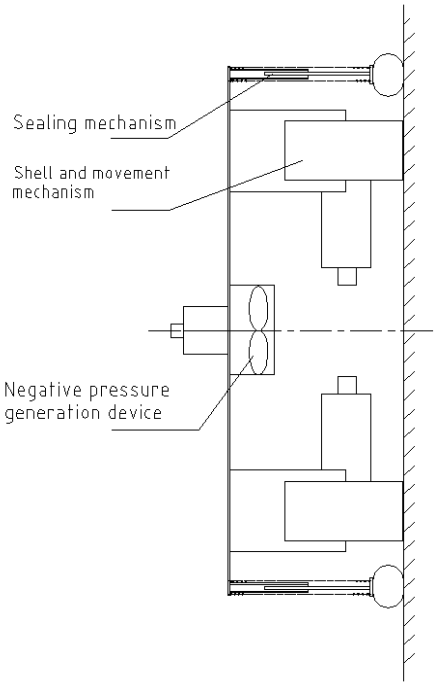

Fig. 2. Structure of robot

An omni-directional wall climbing robot is designed because the robot must walk along the welding lines with the ultrasonic detector on the austenitic stainless steel arc wall and detect deficiencies ultrasonically(Wang Y. et al. 1999). With adhering negative pressure of single suction cup, the robot can move onmi-directionally and precisely. Adaptive to the arc wall, the robot is of compact structure, light weight, precise movement, convenient control, and can climb over the welding lines(Chen I-M., 2003).

Figure 1 is the picture of the omni-directional wall climbing robot. As you can see, sucking, sealing, moving are three main functions and key techniques of this kind of robots. Figure 2 is the structure of omni-directional wall climbing robot, which includes four parts: negative pressure generation device (Fans), sealing mechanism, shell and movement mechanism. The robot is equipped with inclinometer, proximity sensor, CCD, ultrasonic detection devices to ensure the reliability and security of the running also(Zhao Y.Z., 2004, Zhao Y.Z., 1999).

The establishment of mathematical model is the kernel of kinetic analysis. Yinfeng Fang use kinematics graph theory to take a mathematical model for the robot, this paper utilized the Sheth-Uicher transform and Apell equation to establish the kinematic and dynamic model for the robot(Fang Y., 2010).Firstly, Sheth-Uicher transform is used to build the kinematics equation of omni-directional wall climbing robot(P.N.Shetch, 1991). And then the positive and inverse solutions are gained. This equation will devote to the motion control. Secondly, dynamic model of the robot is established based on Apell equation and the positive and inverse solutions are obtained. Finally, the result is proved correct simulated by simulating with Matlab. This method obtained its purpose of the acceleration control and satisfies the requirements of precise motion control(Kim Wheekuk, 2004, Yi Byung-Ju, 2002).

2 The System of the Omni-Directional Wall Climbing Robot

2.1 Working Environment

Elevation: below 2000m

Operating ambient temperature: 10℃~40℃

Operating relative humidity: 40%~85%

2.2 Technical Requirements

1) The robot system should be equipped with the crawling mechanism of adsorbing wall, the vacuum suction equipment, the detecting instrument, positioning device, the communication and expert system.

2) The robot system should be equipped with the dedicated carrying trolley and the remote operation module. It can crawl the surface of the wall safely, accurately and reliably when carry out the task of measure.

3) The robot system should be provided with the high degree of reliability and the ability of the stability of long period of time for continuous work of.
4) No matter what happens, such as power failure, earthquake and so on, the accident of robot falling must not take place. The robot system should have the ability of accident prevention and accident elimination.
5) The positioning accuracy of robot : less than ±2mm.
6) The size requirement :
The size of robot noumenon: ≤ 550×650×250mm ;
Dedicated carrying trolley: ≤ 750×1000×1500mm ;
7) The weight of robot noumenon < 300N

2.3 System Composition

Figure 3 is the assembly picture of the omni-directional wall climbing robot. To realize the functions mentioned above, the omni-directional wall climbing robot at least have six essential parts: wall-climbing robot subsystem, remote control subsystem, carrying trolley subsystem, manipulator subsystem, safety devices and vision system.

Fig. 3. The assembly Picture of the omni-directional wall climbing robot

Figure 4 is the posture of robot on the wall. Wall-climbing robot subsystem is the kernel of the omni-directional wall climbing robot, it can carry kinds of detecting instruments to accomplish the special works.

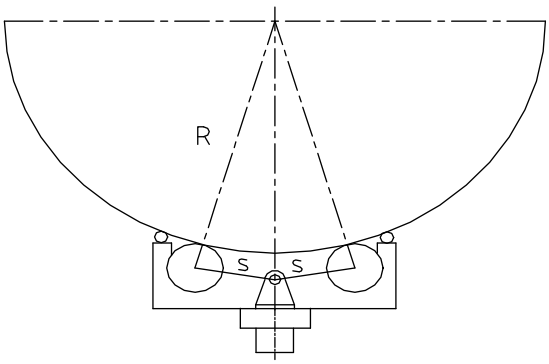

Fig. 4. Posture of robot on the wall

Remote control subsystem is used to operate every subsystem remotely, it is divided into two levels : management computer and executing computer.

The task of dedicated carrying trolley is to carry the wall-climbing robot noumenon and its' attached device between the wall and control station.

Figure 5 is the diagram of manipulator. It is installed in the carrying trolley, which can grab the robot and carry it before climb the wall, and unload it before carry out the detection task.

Safety devices is installed in the carrying trolley, which can limit the movement range of climbing robot by using safety rope when accidents occur.

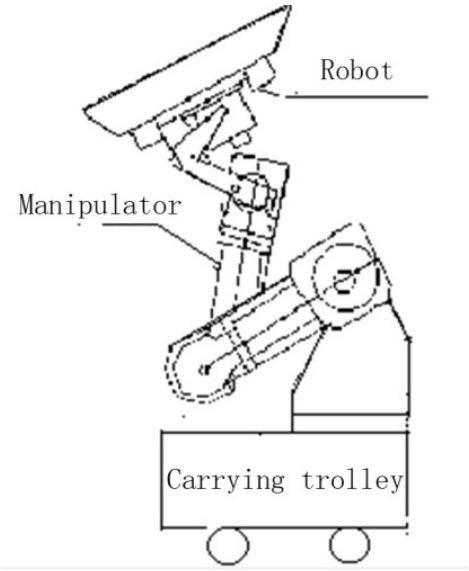

Fig. 5. Diagram of manipulator

Vision system is installed in the surface of robot which can send the vision signal from wall-climbing robot to romote base station. The vision system has come into wide use in the field of robotics, espeically the active vision, active perception mostly encourages the idea of moving a sensor to constrain interpretation of its environment (Chen S., 2011).

3 The Modeling of Kinetic Analysis for the Omni-Directional Wall Climbing Robot

The usual wheeled travel mechanism is nonholonomic system in which the position of the movement mechanism and the wheel corner has no direct algebraic relation. Here the Apell equation is used for research of its dynamic characteristics(F.P.J. Rimrott, 1995).

3.1 Apell Equation

A mechanical system which has n general coordinates and g nonholonomic constraints can be described as the equation below:

$$\sum_{j=1}^{n} A_{\beta j}\dot{q}_j + B_\beta = 0, (\beta = 1,..., g) \tag{1}$$

Choose the $\varepsilon = n - g$ $\dot{\pi}_\sigma (\sigma = 1, 2,..., \varepsilon)$, which are the linear combinations of the generalized linear velocities $\dot{q}_j\ (j = 1, 2,..., n)$,as independent variables. They can be described with the equation below:

$$\dot{\pi}_\sigma = \sum_{j=1}^{n} f_{\sigma j}\dot{q}_j, (\sigma = 1,..., \varepsilon) \tag{2}$$

Eq. (1) and Eq. (2) formed the $n = \varepsilon + g$ algebraic equations linearly independent about the generalized velocities. Solutions of the equation set are generalized velocities expressed by the pseudo velocities $\dot{q}_1,...,\dot{q}_\varepsilon$. The dependent generalized velocities $\dot{q}_{1+1},...,\dot{q}_{\varepsilon+\beta}$ can be expressed as independent generalized velocity function described with nonholonomic constraint equations:

$$\dot{q}_j = \sum_{\sigma=1}^{\varepsilon} h_{j\sigma}\dot{\pi}_\sigma + h_j, (\sigma = 1,..., \varepsilon) \tag{3}$$

The Apell equation obtained from the general dynamics equations is as below:

$$\begin{cases} \dfrac{\partial \dot{S}}{\partial \ddot{\pi}_\sigma} = F_\sigma, (\sigma = 1,..., \varepsilon) \\ S = \sum_{i=1}^{n} \dfrac{1}{2} m_i \ddot{\vec{r}}^2 \\ F_\sigma = \sum_{j=1}^{n} Q_j h_{j\sigma} \end{cases} \tag{4}$$

3.2 Acceleration of Robot in Fixed-Coordinate System

The Apell equation which takes acceleration energy as dynamic function is appropriate for nonholonomic mechanical system. To build a dynamical model with the Apell equation, the systemic acceleration energy expressed by the pseudo velocities is necessary. Climbing robot in this paper has 3 DOFs, the corresponding $V_1\left(V_1 = {}^{\bar{R}}\dot{X}_R\right)$、$V_2\left(V_2 = {}^{\bar{R}}\dot{Y}_R\right)$ and $\dot{\psi}_2\left(\dot{\psi}_2 = {}^{\bar{R}}\dot{\psi}_R\right)$ are chosen as the system pseudo velocities.

Figure 6 is the coordinate systems for wall-climbing robot, the coordinate system L of robot noumenon is dynamic coordinate system which is fixed in the geometric center of robot noumenon. Global coordinate system G is fixed coordinate system which is fixed in the working plane.

Figure 7 shows 3 coordinate systems: absolute coordinate system $\overline{O\,\overline{XYZ}}$, dynamic coordinate system $O'X'Y'Z'$ fixed in the body centre and the instantaneous static coordinate system OXYZ correspond with $O'X'Y'Z'$. Corresponding axes of the 3 systems are in the same direction(J. Denavit, 1995). Relative velocity of $O'X'Y'Z'$ in OXYZ could be represented as transition $\vec{V}' = [V_1, V_2, 0]^T$ along the axis and rotation $\dot{\vec{\psi}}' = [0, 0, \dot{\psi}]^T$. Coordinate of the centre of gravity G is (e1,e2,0) , the vector $\vec{r}'$ from point O' to G in $O'X'Y'Z'$ could be represented as $\vec{r} = \overrightarrow{OG}$ with velocity $\vec{V}$ and acceleration $\vec{a}$ in *OXYZ*. $\vec{V}$ and $\vec{a}$ could be represented with $\vec{V}'$, $\vec{\psi}'$ and $\vec{r}'$: $\frac{d'\vec{r}'}{dt} = 0$, $\frac{d\vec{r}'}{dt} = \frac{d'\vec{r}'}{dt} + \dot{\vec{\psi}}' \times \vec{r}' + \vec{V}'$ (Shown as Fig. 8). because $\vec{r}'$ is a constant vector in $O'X'Y'Z'$. Then the equation is obtained as below:

$$\vec{V} = \frac{d'\vec{r}'}{dt} + \dot{\vec{\psi}}' \times \vec{r}' + \vec{V}' = 0 + \begin{bmatrix} 0 \\ 0 \\ \dot{\psi} \end{bmatrix} \times \begin{bmatrix} e_1 \\ e_2 \\ 0 \end{bmatrix} + \begin{bmatrix} V_1 \\ V_2 \\ 0 \end{bmatrix} = \begin{bmatrix} V_1 - \dot{\psi} e_2 \\ V_2 + \dot{\psi} e_1 \\ 0 \end{bmatrix}$$

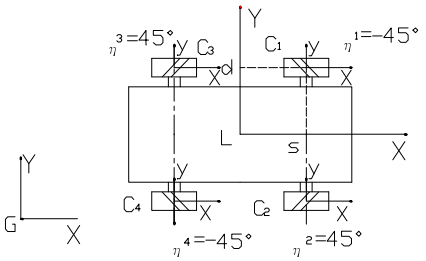

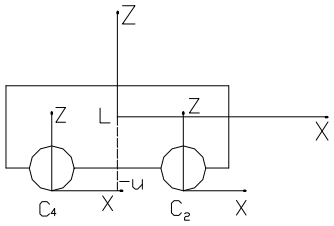

Fig. 6. Coordinate systems for wall-climbing robot

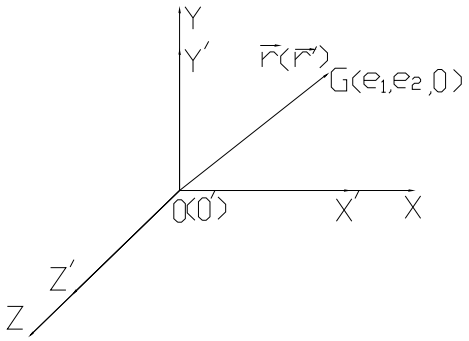

Fig. 7. Coordinate systems

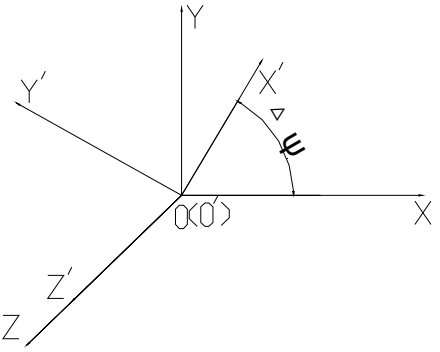

Fig. 8. Rotation between two coordinate systems

$\vec{a}$ is gained through differentiation of $\vec{V}$ in OXYZ:

$$\begin{aligned}\vec{a} &= \frac{d\vec{V}}{dt} = \frac{d}{dt}\left(\frac{d'\vec{r}'}{dt} + \dot{\vec{\psi}}' \times \vec{r}'\right) + \frac{d\vec{V}'}{dt} \\ &= \frac{d'^2\vec{r}'}{dt^2} + \dot{\vec{\psi}}' \times \left(\dot{\vec{\psi}}' \times \vec{r}'\right) + \frac{d\dot{\vec{\psi}}'}{dt} \times \vec{r}' + \frac{d\vec{V}'}{dt}\end{aligned}$$

The relative motion between $O'X'Y'Z'$ and OXYZ during a time interval Δt could be derived through the equations below:

$$\begin{cases}\Delta X = \left[V_1 \cos(\Delta\psi) - V_2 \sin(\Delta\psi)\right]\Delta t \\ \qquad = \left(V_1 - V_2\Delta\psi - \frac{1}{2}V_1\Delta\psi^2 + \frac{1}{6}V_2\Delta\psi^3 + \ldots\right)\Delta t \\ \Delta Y = \left[V_1 \sin(\Delta\psi) + V_2 \cos(\Delta\psi)\right]\Delta t \\ \qquad = \left(V_2 + V_1\Delta\psi + \frac{1}{2}V_2\Delta\psi^2 - \frac{1}{6}V_2\Delta\psi^3 + \ldots\right)\Delta t\end{cases}$$

Cause $\lim\limits_{\Delta t \to 0} \frac{\Delta\psi}{\Delta t} = \dot{\psi}$, then:

$$\begin{cases}V_x' = \lim\limits_{\Delta t \to 0} \frac{\Delta X}{\Delta t} = V_1, a_x' = \lim\limits_{\Delta t \to 0} \frac{\Delta X/\Delta t - V_1}{\Delta t} = \dot{V}_1 - V_2\dot{\psi} \\ V_y' = \lim\limits_{\Delta t \to 0} \frac{\Delta Y}{\Delta t} = V_2, a_y' = \lim\limits_{\Delta t \to 0} \frac{\Delta Y/\Delta t - V_2}{\Delta t} = \dot{V}_2 + V_1\dot{\psi}\end{cases}$$

$$\frac{d\vec{V}'}{dt} = \begin{bmatrix}a_x' \\ a_y' \\ 0\end{bmatrix} = \begin{bmatrix}\dot{V}_1 - V_2\dot{\psi} \\ \dot{V}_2 + V_1\dot{\psi} \\ 0\end{bmatrix}$$

V_x' and V_y' are components of V' along the coordinate axes, a_x' and a_y' are components of translational acceleration along the axes of OXYZ in $O'X'Y'Z'$. Cause $\frac{d'^2\vec{r}'}{dt^2} = 0$, $\vec{a}$ is obtained as the equation below:

$$\begin{aligned}\vec{a} &= \dot{\vec{\psi}} \times \left(\dot{\vec{\psi}} \times \vec{r}'\right) + \frac{d\dot{\vec{\psi}}}{dt} \times \vec{r}' + \frac{d\vec{V}'}{dt} \\ &= \begin{bmatrix} 0 \\ 0 \\ \dot{\psi} \end{bmatrix} \times \begin{bmatrix} 0 \\ 0 \\ \dot{\psi} \end{bmatrix} \times \begin{bmatrix} e_1 \\ e_2 \\ 0 \end{bmatrix} + \begin{bmatrix} 0 \\ 0 \\ \ddot{\psi} \end{bmatrix} \times \begin{bmatrix} e_1 \\ e_2 \\ 0 \end{bmatrix} + \begin{bmatrix} \dot{V}_1 - V_2\dot{\psi} \\ \dot{V}_2 + V_1\dot{\psi} \\ 0 \end{bmatrix} \\ &= \begin{bmatrix} \dot{V}_1 - \ddot{\psi}e_2 - \dot{\psi}V_2 - \dot{\psi}^2 e_1 \\ \dot{V}_2 + \ddot{\psi}e_1 + \dot{\psi}V_1 - \dot{\psi}^2 e_2 \\ 0 \end{bmatrix}\end{aligned} \tag{5}$$

$\vec{a}$ is translational component of acceleration of the robot body gravity centre. V_1, V_2, $\dot{V}_1$ and $\dot{V}_2$ are translational velocities and accelerations of the robot body relative to instantaneous static coordinate system, $\dot{\psi}$ and $\ddot{\psi}$ are angular velocity and angular acceleration of the robot body relative to Z axis of instantaneous static coordinate system.

3.3 Calculation of the Acceleration Energy

Acceleration energy of the robot body is:

$$\begin{aligned}S &= S_1 + S_2 + S_3 = \frac{1}{2}m\left|\vec{a}\right|^2 + \frac{1}{2}I_0\left|\ddot{\vec{\psi}}\right|^2 + \sum_{i=1}^{4}\frac{1}{2}I_A\ddot{\theta}_i^2 \\ &= \frac{1}{2}m[\dot{V}_1^2 + \dot{V}_2^2 - 2\dot{V}_1\ddot{\psi}e_2 + 2\dot{V}_2\ddot{\psi}e_1 - 2\dot{V}_1\dot{\psi}\left(V_2 + \dot{\psi}e_1\right) + \\ &\quad 2\dot{V}_2\dot{\psi}\left(V_1 - \dot{\psi}e_2\right) + 2\dot{\psi}\ddot{\psi}\left(e_2V_2 + e_1V_1\right)] + \\ &\quad \frac{1}{2}I_0\ddot{\psi}^2 + \frac{1}{2}\sum_{i=1}^{4}I_A\ddot{\theta}_i^2 + \ldots\end{aligned} \tag{6}$$

In the equation above, S_1 is translational acceleration energy of the body, S_2 is the rotational acceleration energy, m is the body mass, I_o is moment of inertia of noumenon around the Z axis of instantaneous static coordinate system, I_A is rotary inertia of wheels. Eq. (6) can be expressed by the matrix below:

$$S = \frac{1}{2}\begin{bmatrix}\dot{V}_1 & \dot{V}_2 & \ddot{\psi}\end{bmatrix} M \begin{bmatrix}\dot{V}_1 \\ \dot{V}_2 \\ \ddot{\psi}\end{bmatrix} + \dot{\psi}\begin{bmatrix}V_1 & V_2 & \dot{\psi}\end{bmatrix} Q \begin{bmatrix}V_1 \\ V_2 \\ \dot{\psi}\end{bmatrix} + \ldots \tag{7}$$

$$M = M' + W^T [I_A] W \tag{8}$$

$$M' = \begin{bmatrix} m & 0 & -me_2 \\ 0 & m & me_1 \\ -me_2 & me_1 & I_o \end{bmatrix}, \quad [I_A] = \begin{bmatrix} I_{A1} & 0 & 0 & 0 \\ 0 & I_{A2} & 0 & 0 \\ 0 & 0 & I_{A3} & 0 \\ 0 & 0 & 0 & I_{A4} \end{bmatrix}$$

$$W = \frac{1}{R} \begin{bmatrix} 1 & -1 & -(s+d) \\ 1 & 1 & (s+d) \\ 1 & 1 & -(s+d) \\ 1 & -1 & (s+d) \end{bmatrix}, \quad Q = \begin{bmatrix} 0 & -m & -me_1 \\ m & 0 & -me_2 \\ me_1 & me_2 & 0 \end{bmatrix}$$

3.4 Kinetic Equation of the Robot

According to the Apell equation: $\frac{\partial S}{\partial \ddot{\vec{\pi}}} = \vec{F}^*$, from the Eq. (7): $M \begin{bmatrix} \dot{V}_1 \\ \dot{V}_2 \\ \ddot{\psi} \end{bmatrix} + \dot{\psi} Q \begin{bmatrix} V_1 \\ V_2 \\ \dot{\psi} \end{bmatrix} = \vec{F}^*$,

according to kinetic virtual work principle, equation as below is gained:

$$[\delta X \quad \delta Y \quad \delta\psi] \vec{F}^* = [\delta\theta_1 \quad \delta\theta_2 \quad \delta\theta_3 \quad \delta\theta_4] \begin{bmatrix} T_1 \\ T_2 \\ T_3 \\ T_4 \end{bmatrix} +$$

$$[\delta X \quad \delta Y \quad \delta\psi] \begin{bmatrix} G_x \\ G_y \\ 0 \end{bmatrix} + [\delta X \quad \delta Y \quad \delta\psi] \begin{bmatrix} f_x \\ f_y \\ T_\varphi \end{bmatrix}$$

And because:

$[\delta\theta_1 \quad \delta\theta_2 \quad \delta\theta_3 \quad \delta\theta_4] = [\delta X \quad \delta Y \quad \delta\psi] W^T$, so

$\vec{F}^* = W^T \begin{bmatrix} T_1 \\ T_2 \\ T_3 \\ T_4 \end{bmatrix} + \begin{bmatrix} G_x \\ G_y \\ 0 \end{bmatrix} + \begin{bmatrix} f_x \\ f_y \\ T_\varphi \end{bmatrix}$ is obtained, then the kinetic equation of robot could be derived as below:

$$M\begin{bmatrix}\dot{V}_1\\ \dot{V}_2\\ \ddot{\psi}\end{bmatrix}+\dot{\psi}Q\begin{bmatrix}V_1\\ V_2\\ \dot{\psi}\end{bmatrix}=W^T\begin{bmatrix}T_1\\ T_2\\ T_3\\ T_4\end{bmatrix}+\begin{bmatrix}G_x\\ G_y\\ 0\end{bmatrix}+\begin{bmatrix}f_x\\ f_y\\ T_\varphi\end{bmatrix} \tag{9}$$

Solution of kinetic positive problem:

$$\begin{bmatrix}T_1\\ T_2\\ T_3\\ T_4\end{bmatrix}=\left(W^T\right)^+\left(M\begin{bmatrix}\dot{V}_1\\ \dot{V}_2\\ \ddot{\psi}\end{bmatrix}+\dot{\psi}Q\begin{bmatrix}V_1\\ V_2\\ \dot{\psi}\end{bmatrix}-\begin{bmatrix}G_x\\ G_y\\ 0\end{bmatrix}-\begin{bmatrix}f_x\\ f_y\\ T_\varphi\end{bmatrix}\right) \tag{10}$$

Solution of kinetic inverse problem:

$$\begin{bmatrix}\dot{V}_1\\ \dot{V}_2\\ \ddot{\psi}\end{bmatrix}=M^{-1}\left(W^T\begin{bmatrix}T_1\\ T_2\\ T_3\\ T_4\end{bmatrix}-\dot{\psi}Q\begin{bmatrix}V_1\\ V_2\\ \dot{\psi}\end{bmatrix}+\begin{bmatrix}G_x\\ G_y\\ 0\end{bmatrix}+\begin{bmatrix}f_x\\ f_y\\ T_\varphi\end{bmatrix}\right) \tag{11}$$

$\left(W^T\right)^+=A^{-1}W\left(W^TA^{-1}W\right)^{-1}$ is the pinv[2,3] of W^T, if A is unit matrix, equation is gained:

$\left(W^T\right)^+=W\left(W^TW\right)^{-1}=\frac{R}{4}\begin{bmatrix}1 & -1 & -1/l_{ab}\\ 1 & 1 & 1/l_{ab}\\ 1 & 1 & -1/l_{ab}\\ 1 & -1 & 1/l_{ab}\end{bmatrix}$, combined with Eq. (8), equations are obtained as follows:

$$M=\begin{bmatrix}m+4I_a/R^2 & 0 & -me_2\\ 0 & m+4I_a/R^2 & me_1\\ -me_2 & me_1 & I_o+4I_Al^2{}_{ab}/R^2\end{bmatrix} \tag{12}$$

$$\begin{bmatrix}\dot{V}_1\\ \dot{V}_2\\ \ddot{\psi}\end{bmatrix}=\begin{bmatrix}m+4I_a/R^2 & 0 & -me_2\\ 0 & m+4I_a/R^2 & me_1\\ -me_2 & me_1 & I_o+4I_Al^2{}_{ab}/R^2\end{bmatrix}^{-1}$$
$$\left(\frac{1}{R}\begin{bmatrix}1 & 1 & 1 & 1\\ -1 & 1 & 1 & -1\\ -l_{ab} & l_{ab} & -l_{ab} & l_{ab}\end{bmatrix}\begin{bmatrix}T_1\\ T_2\\ T_3\\ T_4\end{bmatrix}-\dot{\psi}\begin{bmatrix}0 & -m & -me_1\\ m & 0 & -me_2\\ me_1 & me_2 & 0\end{bmatrix}\right. \tag{13}$$
$$\left.\begin{bmatrix}V_1\\ V_2\\ \dot{\psi}\end{bmatrix}+\begin{bmatrix}G_x\\ G_y\\ 0\end{bmatrix}+\begin{bmatrix}f_x\\ f_y\\ T_\varphi\end{bmatrix}\right)$$

$$\begin{bmatrix} T_1 \\ T_2 \\ T_3 \\ T_4 \end{bmatrix} = \left(\frac{R}{4} \begin{bmatrix} m+\frac{4I_A}{R^2}+\frac{me_2}{l_{ab}} & -\left(m+\frac{4I_A}{R^2}+\frac{me_1}{l_{ab}}\right) & -\left[m(e_1+e_2)+\left(I_o+\frac{4I_A l_{ab}}{R^2}\right)/l_{ab}\right] \\ m+\frac{4I_A}{R^2}-\frac{me_2}{l_{ab}} & m+\frac{4I_A}{R^2}+\frac{me_1}{l_{ab}} & m(e_1-e_2)+\left(I_o+\frac{4I_A l_{ab}}{R^2}\right)/l_{ab} \\ m+\frac{4I_A}{R^2}+\frac{me_2}{l_{ab}} & m+\frac{4I_A}{R^2}+\frac{me_1}{l_{ab}} & -\left[m(e_1+e_2)+\left(I_o+\frac{4I_A l_{ab}}{R^2}\right)/l_{ab}\right] \\ m+\frac{4I_A}{R^2}-\frac{me_2}{l_{ab}} & -\left(m+\frac{4I_A}{R^2}+\frac{me_1}{l_{ab}}\right) & -\left[m(e_1+e_2)-\left(I_o+\frac{4I_A l_{ab}}{R^2}\right)/l_{ab}\right] \end{bmatrix} \right. \\ \left. + \dot{\psi}\frac{R}{4} \begin{bmatrix} -m-\frac{me_1}{l_{ab}} & -m-\frac{me_2}{l_{ab}} & m(e_2-e_1) \\ m+\frac{me_1}{l_{ab}} & -m+\frac{me_2}{l_{ab}} & -m(e_2+e_1) \\ m-\frac{me_1}{l_{ab}} & -m-\frac{me_2}{l_{ab}} & -m(e_2+e_1) \\ -m+\frac{me_1}{l_{ab}} & -m+\frac{me_2}{l_{ab}} & m(e_2-e_1) \end{bmatrix} \right) \begin{bmatrix} V_1 \\ V_2 \\ \dot{\psi} \end{bmatrix} - \left(W^T\right)^+ \begin{bmatrix} G_x - f_x \\ G_y - f_y \\ -T_\varphi \end{bmatrix} \tag{14}$$

4 The Simulation of Kinetic Analyse for the Omni-Directional Wall Climbing Robot

Two states of motion in the simulation:

1) The body does constant circular motion at the speed of 0.2m/s while keeps stance.
2) The body does 0.1m/s2 uniform acceleration 2m-radius-circular motion while the X axis of the body keeps tangent with the circle of the body position.

Simulation parameters of the two states of motion are as below:

Table 1. References in simulation of case No. 1

s(m)	d(m)	e1(m)	e2(m)	R(m)
0.138	0.085	0.00	-0.01	0.056
V(m/s)	IA(kg.m2)	I0(kg.m2)	m(kg)	
0.20	0.012	1.50	30	

Table 2. References in simulation of case No. 2

s(m)	d(m)	e1(m)	e2(m)	R(m)
0.138	0.085	0.00	-0.01	0.056
V(m/s)	IA(kg.m2)	I0(kg.m2)	m(kg)	
2.0	0.012	1.50	30	

Reasons for choice of the two states are as follows:

1) To keep stance in movement is an unusual feature of the omni-directional robot. With the omni-wheels the robot body could make translational motion freely while keeps stance.

2) As a typical case in the applied mechanics models, uniformly accelerated motion state is the state which could make exact description of problems.
3) Circular motion, making the status of motion more actual by enriching the acceleration factors and providing better icon of torque curves, could describe the problem clearly and precisely.
4) Making discussion of the two statuses separately would make the requirement for driving torque of the two statuses clear and definite.

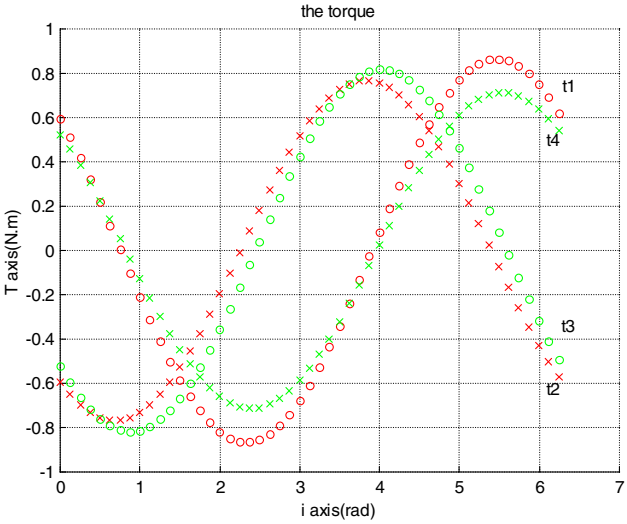

Fig. 9. Torque curve in case No.1

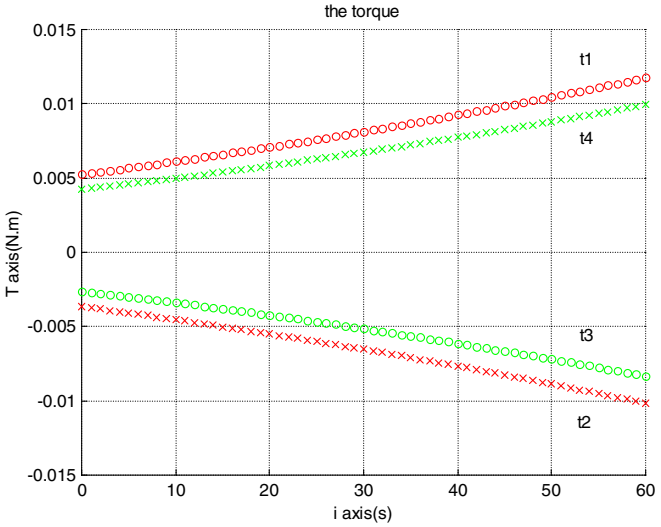

Fig. 10. Torque curve in case No.2

Figure 9 and 10 show the torque curves of the four wheels with no concern of gravity and friction, while figure 11 and 12 show torque curves of the four wheels with concern of gravity and friction.

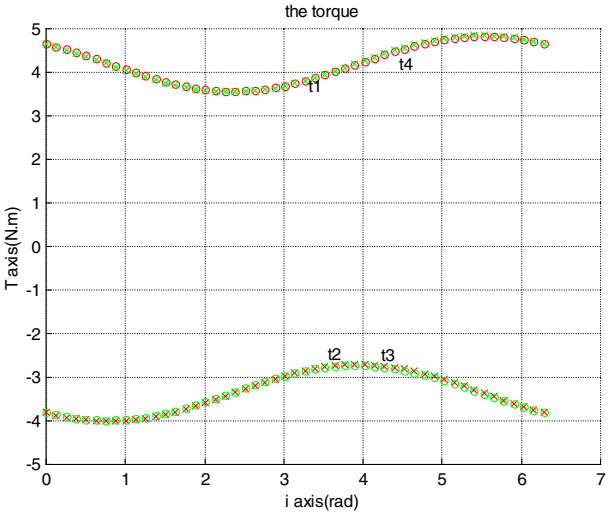

Fig. 11. Torque curve in case No.1

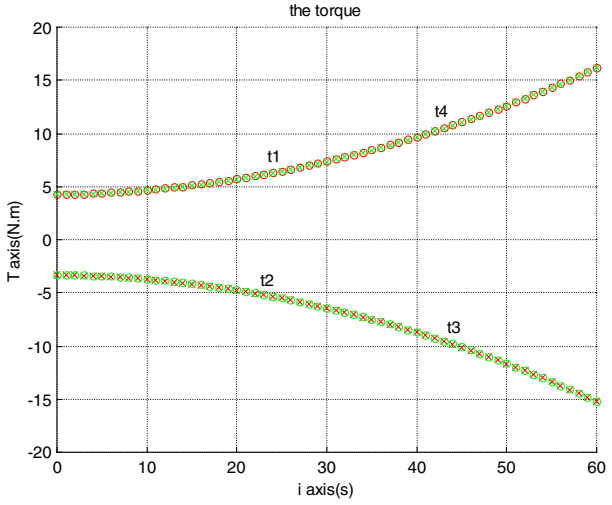

Fig. 12. Torque curve in case No.2

From the figures above conclusion could be made:

1) Trends of the torque change of wheel 1 and wheel 4 are coincident, so are these of wheel 2 and wheel 3;

2) In uniformly accelerated motion, torques of wheel 1 and wheel 2, wheel 3 and wheel 4 are respectively equivalent and reverse, in constant circular motion while the body keep stance, all of the torques vary, and the variation on wheel 2 and wheel 3 are ahead of that on wheel 1and wheel 4 by 1/4 cycle.

3) Torques from motor to wheels should be increased to ensure the capability of climbing upon walls of robot cause gravity and friction have great influence on the torques of wheels.

5 Conclusion

In this paper, Apell equation is used to form the kinetic model of the omni-directional wall climbing robot non-holonomic system, obtained the solutions of kinetic positive and reverse problems. According to the solution of kinetic positive problem, torques which the known motion needs are applied to the target. Two types of typical motion of kinetic positive problems are simulated and torque change curves of wheels are obtained and analysed.

Acknowledgments. This work was partially supported by the Research Fund of State Key Lab of MSV, China (Grant No. MSV-MS-2010-03), the State Key Laboratory of Robotics and System (HIT) (Grant No. SKLRS-2010-ZD-06), and the National Natural Science Foundation of China under Grant No. 61105101, 61075086, 60875058.

References

1. Zhang, Y., Nishi, A.: Low-pressure air motor for wall-climbing robot actuation. Mechatronics 14(4), 377–392 (2003)
2. Lal Tummala, R., Mukherjee, R., Ning, X., et al.: Climbing the walls [robots]. Robotics & Automation Magazine 9(4), 10–19 (2002)
3. Yoshida, Y., Shugen, M.: Design of a Wall-Climbing Robot with Passive Suction Cups. In: 2010 IEEE International Conference on Robotics and Biomimetics (ROBIO), pp. 1513–1518 (2010)
4. Li, J., Gao, X., Fan, N., et al.: Wall Climbing Robot Based on Negative Pressure-Thrust Suction Method. In: Proceedings of 2008 IEEE International Conference on Mechatronics and Automation, pp. 604–609 (2008)
5. Wu, S., Wu, L., Liu, T.: Design of a Sliding Wall Climbing Robot with a Novel Negative Adsorption Device. In: 2011 8th International Conference on Ubiquitous Robots and Abient Intelligence (Ul), pp. 97–100 (2011)
6. Wang, Y., Liu, S.L., Xu, D.G., et al.: Development and application of wall-climbing robots. In: Proc. of IEEE International Conference on Robotics and Automation, pp. 1207–1212 (1999)

7. Chen, I.-M., Yeo, S.H.: Locomotion of a two-dimensional walking-climbing robot using a closed-loop mechanism: From gait generation to navigation. International Journal of Robotics Research 22(1), 21–40 (2003)
8. Zhao, Y.Z., Fu, Z., Cao, Q.X., Wang, Y.: Development and applications of wall-climbing robots with a single suction cup. Robotica 22, 43–648 (2004)
9. Zhao, Y.Z., Shao, H., Wang, Y.: Wall-climbing robot with negative pressure suction cup used for cleaning work. High Technology Letters 5(2), 85–88 (1999)
10. Fang, Y., Zhang, H., Li, X., Chen, S.Y.: The mathematical model and control scheme of a four-legged robot based on GZ-I and note module. In: Liu, H., Ding, H., Xiong, Z., Zhu, X. (eds.) ICIRA 2010, Part I. LNCS, vol. 6424, pp. 300–309. Springer, Heidelberg (2010)
11. Shetch, P.N., Uicher, J.J.: A Generalized Symbolic Notation for Mechanisms. Journal of Engineering for Industry 70, 102–112 (1991)
12. Kim, W., Yi, B.-J., Dong, J.L.: Kinematic modeling of mobile robots by transfer method of augmented generalized coordinates. Journal of Robotic Systems 21(6), 301–322 (2004)
13. Yi, B.-J., Kim, W.: The kinematics for redundantly actuated omnidirectional mobile robots. Journal of Robotic Systems 19(6), 255–267 (2002)
14. Chen, S., Li, Y., Kwok, N.M.: Active vision in robotic systems: A survey of recent developments. The International Journal of Robotics Research 30(11), 1343–1377 (2011) AID: 0278364911410755
15. Rimrott, F.P.J., Tabarrok, B.: Complementary Formulation of the Appell Equation. Technische Mechanik 15, 187–196 (1995)
16. Denavit, J., Hartenberg, R.S.: A cinematic notation for lower-pair mechanisms based on matrices. Journal of Applied Mechanics 77(2), 215–221 (1995)

A Rolling Sarrus Mechanism

Chao Liu[1,2,3], Hao Wang[1,2], Mei-Li Zhai[3], and Yan-An Yao[3]

[1] State Key Laboratory of Mechanical System and Vibration, Shanghai Jiao Tong University, Shanghai, 200240, P.R. China
[2] Shanghai City Key Laboratory of Sheet Metal Manufacturing, Shanghai Jiao Tong University, Shanghai, 200240, P.R. China
[3] School of Mechanical and Electronic Control Engineering, Beijing Jiaotong University, Beijing, 100044, P.R. China
chaochaosjtu@gmail.com

Abstract. A novel application of the Sarrus mechanism is proposed in this paper and is used as a moving mechanism. It can roll along a regular path by take advantage of its singular configuration. Mobility, rolling locomotion, rolling path and simulation analyses are performed respectively, and a prototype is developed to verify the feasibility of the proposed concept.

Keywords: Spatial six-revolute mechanism, Sarrus mechanism, Rolling mechanism.

1 Introduction

The Sarrus mechanism is a typical spatial six-revolute overconstrained mechanism. As the first overconstrained mechanism, it was proposed by Sarrus in 1953 [1]. It has two sets of three adjacent parallel axes and can be used to convert circular inputs into linear motion [2-5]. To our knowledge, the Sarrus mechanism is used in applications which require precise linear motion [6].

In this paper, we propose a novel application that the Sarrus mechanism can be used as a rolling mechanism. A rolling Sarrus mechanism is presented and its mobility, rolling character, and simulation analyses are performed successively. Eventually, in order to verify the concept, a prototype is developed.

2 Concept Description and the Walking Principle

2.1 Concept Description

The rolling Sarrus mechanism proposed in this paper is illustrated in Fig. 1. The 3-D model is shown in Fig. 1a, and the corresponding schematic diagram in Fig. 1b. It is a single-loop spatial mechanism consisting of six links which connected to each other with revolute joints. Links 1 and 2 are connected by a revolute joint J_{R1}; links 2 and 3 are connected by a revolute joint J_{R2}; links 3 and 4 are connected by a revolute joint J_{R3}; links 4 and 5 are connected by a revolute joint J_{R4}; links 5 and 6 are connected by a revolute joint J_{R5}; links 6 and 1 are connected by a revolute joint J_{R6}.

J. Lee et al. (Eds.): ICIRA 2013, Part II, LNAI 8103, pp. 33–40, 2013.

The joints axes of J_{R1}, J_{R2} and J_{R3} are parallel, the joints axes of J_{R3} and J_{R4} are intersect at an angle, and the joints axes of J_{R4}, J_{R5} and J_{R6} are parallel.

In this rolling Sarrus mechanism, two actuators labeled as M1 and M2 in Fig. 1a are used to drive the six links leave and land on the ground in turn to realize rolling gaits.

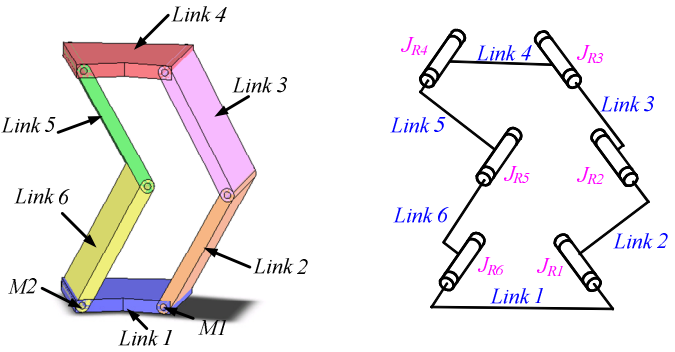

Fig. 1. The rolling Sarrus mechanism

2.2 Mobility Analysis

The sketch diagram of the rolling Sarrus mechanism is shown in Fig. 2. To analyze the motion screws, a Cartesian coordination system $oxyz$ is built and parameters are given.

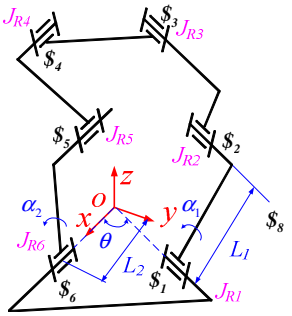

Fig. 2. The motion screws of the rolling Sarrus mechanism

Based on screw theory [7], the motion screws are built as noted in Fig. 2 and achieved as follows.

$$\$_1(\cos\theta \quad \sin\theta \quad 0 \quad , \quad 0 \quad 0 \quad 0)$$
$$\$_2(\cos\theta \quad \sin\theta \quad 0 \quad , \quad L_1\sin\theta\sin\alpha_1 \quad -L_1\cos\theta\sin\alpha_1 \quad L_1\cos\alpha_1(\cos^2\theta-\sin^2\theta))$$
$$\$_3(\cos\theta \quad \sin\theta \quad 0 \quad , \quad 2L_1\sin\theta\sin\alpha_1 \quad -2L_1\cos\theta\sin\alpha_1 \quad 0)$$
$$\$_4(1 \quad 0 \quad 0 \quad , \quad 0 \quad -2L_1\sin\alpha_2 \quad 0)$$
$$\$_5(1 \quad 0 \quad 0 \quad , \quad 0 \quad -L_1\sin\alpha_2 \quad L_1\cos\alpha_2)$$
$$\$_6(1 \quad 0 \quad 0 \quad , \quad 0 \quad 0 \quad 0)$$

While $\alpha_1 = \alpha_2 = \pm\pi/2$, the rank of the screw system's matrix is obtained as 4, and the reciprocal screws is $\$_1^r : (0,0,1;0,0,0)$ and $\$_2^r : (0,0,0;0,0,1)$, so the rolling Sarrus mechanism can neither translate along nor rotate around the z-axis. It is in the singular position. The number of the common constraints is 2. In other cases, the rank of the screw system's matrix is obtained as 5, and the reciprocal screws is $\$^r : (0,0,0;0,0,1)$, hence the rolling Sarrus mechanism cannot rotate around the z-axis. The number of the common constraints is 1.

The DOF (degree of freedom) F of a spatial mechanism is calculated as the following formula [7],

$$F = d(n - g - 1) + \sum_{i=1}^{g} f_i \tag{1}$$

where d is the rank of the screws system's matrix, n is the total number of links, g is the number of kinematic pairs and f_i is the number of the ith kinematic pair's DOFs.

Substituting the values of the parameters into the formula (1), F is obtained.

While $\alpha_1 = \alpha_2 = \pm\pi/2$,

$$F = d(n - g - 1) + \sum_{i=1}^{g} f_i = 2 \tag{2}$$

In other cases,

$$F = d(n - g - 1) + \sum_{i=1}^{g} f_i = 1 \tag{3}$$

2.3 Rolling Motion Analysis

According to the mobility analysis, the rolling mode can be planed and described in detail as follows. As show in Fig. 3a, when the DOF number of the rolling Sarrus mechanism is two, it is in singular position. The link 1 is stationary on the ground and the links 2 and 3 are on the same plane. The two actuators M1 and M2 must work simultaneously to determine the moving direction of all links. When the rotating directions of M1 and M2 are clockwise, the links 2 and 6 are moving in the same direction (Fig. 3b-Fig. 3d). After the rolling Sarrus mechanism through the singular position, the DOF number of the rolling Sarrus mechanism is one. It means that the rolling Sarrus mechanism can be driven to move only by one actuator (M1 or M2). When the actuator (M1 or M2) continue to rotate clockwise, the link 1 is lifted and the link 2 will land on the ground(Fig. 3d). Then the actuator (M1 or M2) rotate in counterclockwise（Fig. 3e-Fig. 3h）, the link 2 lands on the ground(Fig. 3h). Subsequently, this actuator (M1 or M2) adjust its rotating directions in order to let the links 3, 4, 5 and 6 land on the ground in turn. This process is displayed in Fig. 3i to Fig. 3l. Then, the actuator (M1 or M2) rotates counterclockwise(Fig. 3m and Fig. 3n) to make the rolling Sarrus mechanism reach its singular position(Fig. 3o). By successively repeating these sequences, the rolling motion of the rolling Sarrus mechanism is achieved.

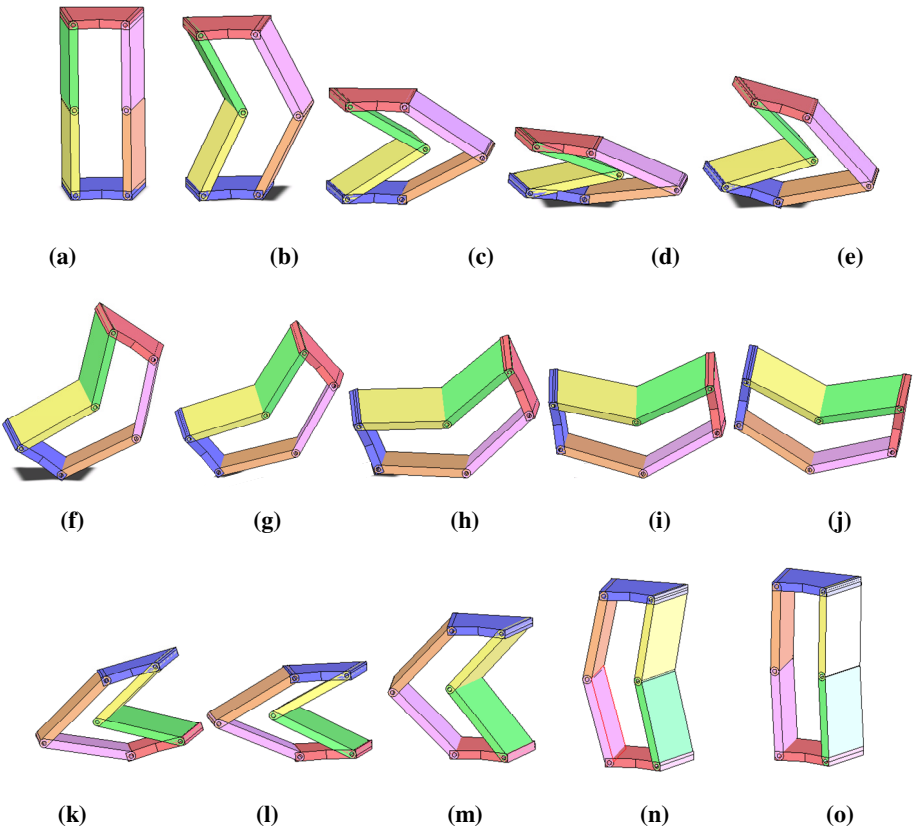

Fig. 3. Rolling locomotion

3 Rolling Path Analysis

The result of the rolling motion analysis indicates that this rolling Sarrus mechanism can only roll on its six links. The rolling path is a regular path which can be obtained as shown in Fig. 4. Concretely, it is a polyline which determined by the lengths of the six links. The angle between adjacent two lines is $\theta/2$.

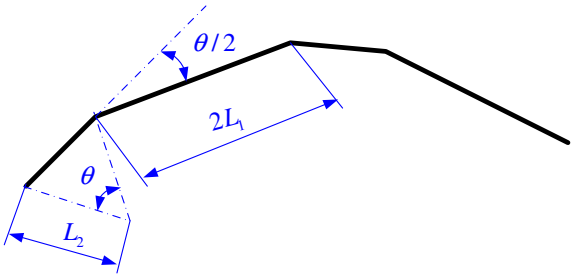

Fig. 4. Rolling path

4 Simulation Analysis

When the input angle value is given in Fig. 5(the angular velocity and the angular acceleration are given in Fig. 6 and Fig. 7 respectively), the rolling Sarrus mechanism can realize the rolling locomotion mentioned in Fig. 3. In order to describe the movement traces clearly, two reference points (A and B) are attached to links 1 and 4 as shown in Fig. 8a. The trajectories of the two reference points can be obtained in Fig. 8b. The Fig. 8a and Fig. 8c are differently corresponding with the initial and the last positions. The rolling direction could be adjusted through the change of the rotation direction of the input angle (M1 or M2). By successively repeating the sequences, the rolling Sarrus mechanism can roll along its regular rolling path (analyzed in Section 3).

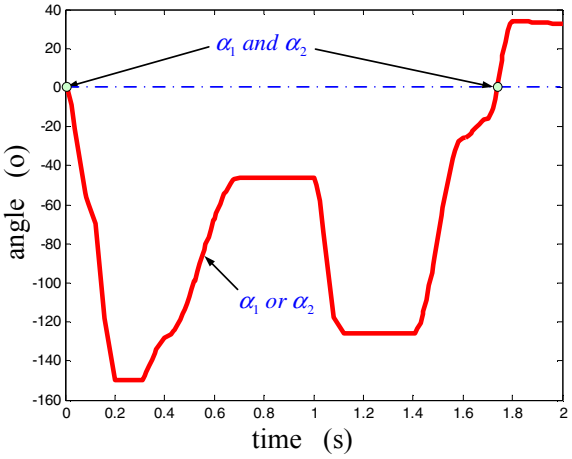

Fig. 5. The input angle value of the rolling Sarrus mechanism

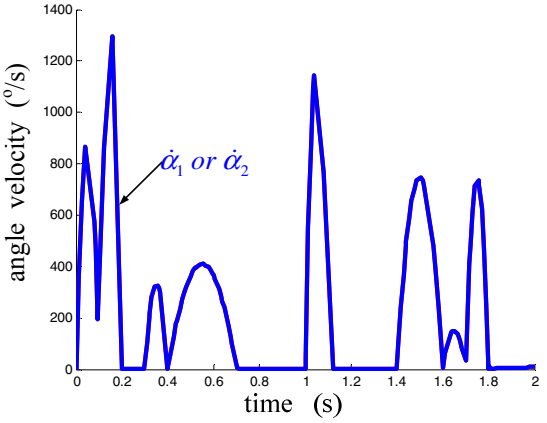

Fig. 6. The input angular velocity of the rolling Sarrus mechanism

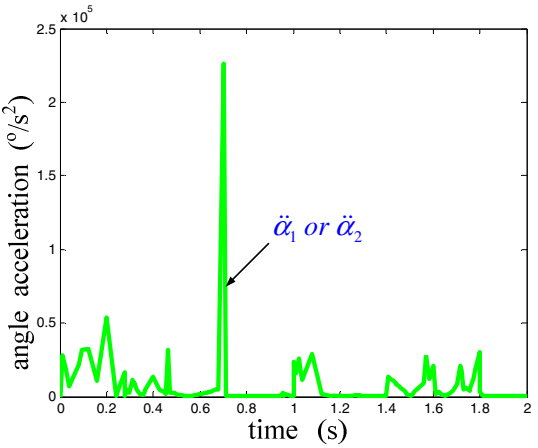

Fig. 7. The input angular acceleration of the rolling Sarrus mechanism

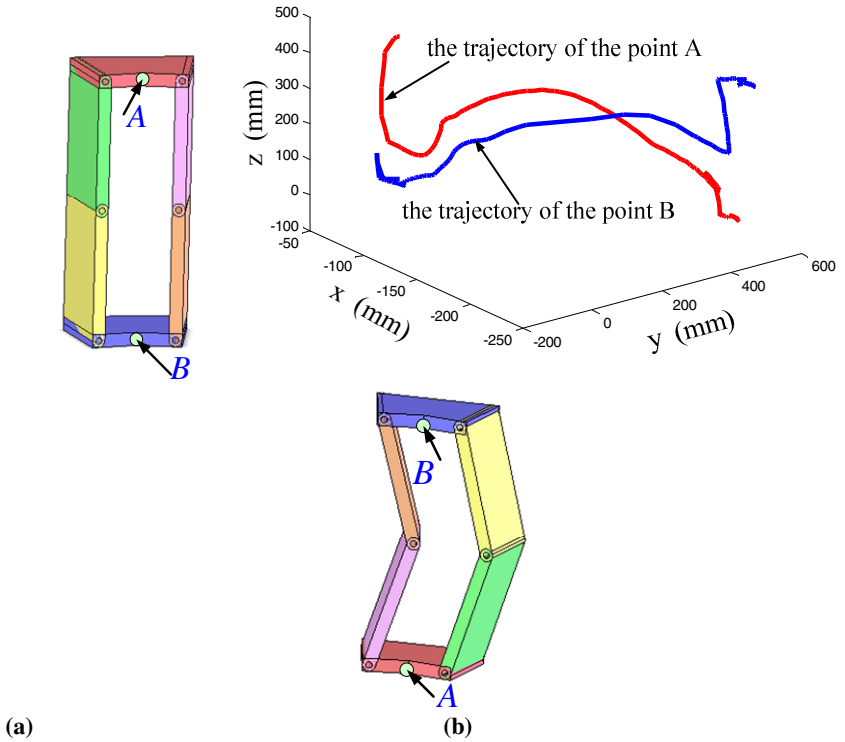

Fig. 8. The trajectories of the two reference points

5 Prototype

A prototype is built as shown in Fig. 9 and the rolling experiments are carried out. Figures 9a-9h shown the rolling process.

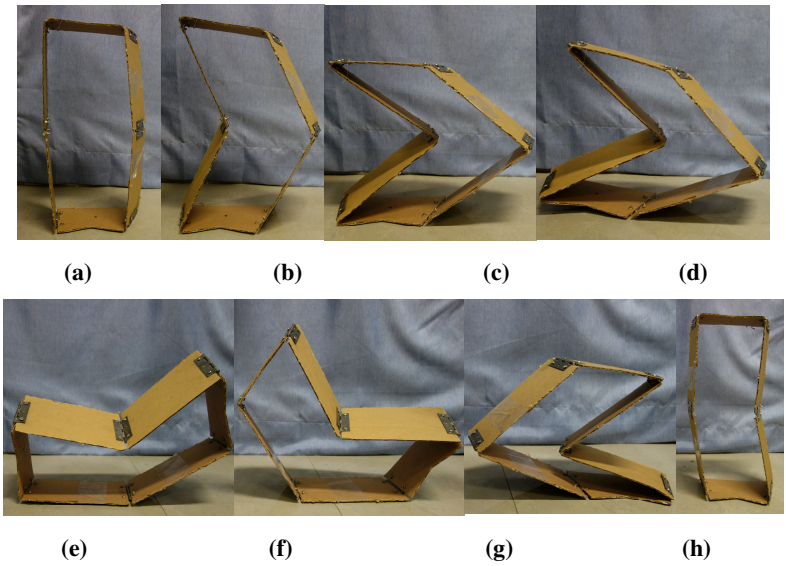

Fig. 9. Prototype of the rolling Sarrus mechanism

6 Conclusion

A novel rolling Sarrus mechanism is proposed in this paper. Its concept is described and the mobility is analyzed using screw theory. The rolling movement is planned and its analysis is preformed. The simulation analysis is achieved and the detailed moving trajectories of the two reference points are carried out. At last, a physical prototype is made and the proposed rolling Sarrus mechanism is proved to have the ability of rolling through corresponding experiment.

Acknowledgment. The research work is supported by China Postdoctoral Science Foundation (2013M531168), the National Science Foundation of China (51075259 and 51175030) and the Fundamental Research Funds for the Central Universities (2012JBZ002).

References

[1] Mavroidis, C., Roth, B.: Analysis and Synthesis of Overconstrained Mechanisms. In: Proceedings of the 1994 ASME Design Technical Conference, pp. 115–133 (1994)
[2] Lee, C.-C., Yan, H.-S.: Movable Spatial 6R Mechanisms with Three Adjacent Parallel Axes. Journal of Mechanical Design 115(3), 522–529 (1993)
[3] Zhao, J.-S., Chu, F., Feng, Z.-J., Zhao, S.: Synthesis of a Rear Wheel Suspension Mechanism With Pure Rectilinear Motion. Journal of Mechanical Design 131(10), 101007 (2009)
[4] Jin, Q., Yang, T.-L.: Synthesis and Analysis of a Group of 3-Degree-of-Freedom Partially Decoupled Parallel Manipulators. Journal of Mechanical Design 126(2), 301 (2004)
[5] Angeles, J.: The Qualitative Synthesis of Parallel Manipulators. Journal of Mechanical Design 126, 617–624 (2004)
[6] Lee, C.-C.: Kinematic Analysis and Dimensional Synthesis of General-Type Sarrus Mechanism. The Japan Society of Mechanical Engineers 39(4), 790–799 (1996)
[7] Hunt, K.H.: Kinematic Geometry of Mechanism. Clarendon Press Oxford (1978)

A New Euclidian Distance Based Approach to Measure Closeness to Singularity for Parallel Manipulators

Jianyu Mao, Yalei Guo, Jie Ren, and Weizhong Guo*

Laboratory of Mechanical System and Vibration, School of Mechanical Engineering
Shanghai Jiao Tong University, Shanghai, 200240, China
yaleiping@163.com,
wzguo@sjtu.edu.cn

Abstract. Singularity configurations are particular poses of end-effector, for which parallel manipulators lose inherent infinite rigidity and in which the end-effector lose control. Finding how close the manipulator is to a singularity is one of the most important issues of parallel manipulators, as well as explaining its physical meaning. Based on forward kinematic analysis and mathematical definition, this paper presents a new approach based on linear distance to measure closeness to singularity for parallel manipulators. By comparing with several singularity indices, the advantages and disadvantages of different indices can be easily identified, and the best index for different situations of various types of parallel manipulators can be derived.

Keywords: Singularity distance, Parallel manipulators, Linear distance.

1 Introduction

A parallel manipulator is made up of an end-effector with n degrees of freedom, and of a fixed base, linked together by at least two independent kinematic chains. Actuation takes place through n simple actuators [1]. There are several important issues involved in the field of parallel manipulators. Singularity analysis is a most important one. A parallel manipulator would gain or lose one or more degrees of freedom when it's at its singular configurations. So it will become out of control when singularity occurs which is improper even dangerous in practical processing. Therefore, singular configurations should be avoided in design and practical use of parallel manipulators.

Singularity analysis of parallel manipulators has been the research hotspot for years and many excellent studies [2–6] have been conducted. One of the most common methods for singularity analysis of parallel manipulators is using Jocabian matrix. In 1990, Gosselin and Angeles [2] addressed the analysis of singularities of parallel mechanisms and classified the singularities into three types based on the properties of the Jacobian matrices of the chain. Based on the nature of parallel

* Corresponding author.

J. Lee et al. (Eds.): ICIRA 2013, Part II, LNAI 8103, pp. 41–53, 2013.

manipulators, Ma and Angeles [7] proposed a different classification of singularities which consists of architecture singularity, configuration singularity, and formulation singularity. Using geometric framework, Park and Kim [8] presented a geometric singularity analysis of closed kinematic chains, including parallel manipulators and classified closed chain singularities into three types. However, all these methods and classifications cannot find a special singularity, i.e., the constraint singularity named by Zlatanov et al. [9]. Joshi and Tsai [10] proposed a methodology of obtaining the overall Jocabian matrix. Then, Merlet [11] investigated the singularities of 6–3 Gough–Stewart platform by line geometry. Zhao et al. [12] proposed a geometrical approach to singularity analysis of parallel manipulators based on screw theory.

For parallel manipulators, how to measure closeness between a pose and a singular configuration is still a challenging problem. There is no mathematical metric defining the distance between a prescribed pose and a singular pose if the parallel manipulator has translational and rotational DOFs. The local conditioning index (LCI) was used to define a good-condition workspace [13] or effective workspace [14] with respect to a specified minimum of LCI. The minimum of LCI is arbitrary or comparative since we cannot give it a uniform value for different types of parallel manipulators. Voglewede and Ebert-Uphoff [15,16] proposed three special measures for closeness to singularities of parallel manipulators but they did not consider the constraint singularity. Hubert and Merlet [17] presented an approach to measure closeness to singularity for a planar parallel manipulator based on a static analysis. It is unknown that the approach can be well applied to six-DOF spatial parallel manipulators.

This paper proposed a linear distance based approach to measure closeness to singularity for parallel manipulators. Section 2 describes position singularity and orientation singularity. Section 3 proposes definitions, theorem and measurement methods of singularity distance. Section 4 introduces three other indices and uses these four different approaches to describe closeness to singularity. Their performances are compared in this section. Finally we conclude in Section 5.

2 Singularity of Parallel Manipulators

Supposing the manipulator moves to (x, y, z) , if it is in singularity, it must be at one of the certain poses, including position and orientation. When it is not in singularity, namely there isn't any singular pose at this position (x, y, z).

2.1 Position Singularity

Definition: If a manipulator moves to (x, y, z), there exists one or more poses at which the manipulator will be in singularity, then this position (x, y, z) is a singular position (SP), and the manipulator is in position singularity at this position.

2.2 Orientation Singularity

Definition: When a manipulator is in position singularity at a SP, if there exist an orientation (α, β, γ) at which the manipulator will be in singularity at this SP, then this orientation (α, β, γ) is a singular orientation (SO), and the manipulator is in orientation singularity at this orientation in this position.

So if a manipulator is in orientation singularity, namely it is at a SO, then it must be in singularity. If only in position singularity, that is, the manipulator is at a SP, it may not be in singularity, because it may not at a SO.

3 The Definition and Measurement of Singularity Distance

In this section, an approach that utilizes Euclidean distance to represent closeness to singularity will be introduced for singularity analysis and closeness measure of parallel manipulators.

3.1 The "Wall"

For any parallel manipulators in a coordinate system $O-xyz$, x , y , z are the coordinates of working platform. θ is a variable quantity besides x , y , z , $l_i = l_i(x, y, z, \alpha, \beta, \gamma)$.

Supposing

$$\sqrt{\left|J^T J\right|} = f(x, y, z, \alpha, \beta, \gamma) \tag{1}$$

At a singularity, $\sqrt{\left|J^T J\right|} = 0$. So a singularity can be got when

$$f(x, y, z, \alpha, \beta, \gamma) = 0 \tag{2}$$

Suppose the solution of Eqn. (2) may be $P^6 \in R^6$.

$$\forall \vec{p} = \left(x_p, y_p, z_p, \alpha_p, \beta_p, \gamma_p\right)^T \in P^6 \tag{3}$$

Regardless of angle components in $\vec{p}$, the new vector shows as

$$\vec{e} = \left(x_p, y_p, z_p\right)^T \in E^3 \in R^3 \tag{4}$$

So there form a mapping $P^6 \to E^3$ which $E^3 \in R^3$.

In this method, the singular boundary is called as "wall" and the distance to singularity is the smallest Euclidean distance from a point (x, y, z) in workspace to the "wall". First of all, we define the "wall" as the singular boundary.

3.2 Related Definition

3.2.1 The Unit Sphere at Singularity Point Sr: In a **"hedgehog skin"**, all the singular orientations $(\alpha_i, \beta_i, \gamma_i)$ can be transformed to points $N_i(c\alpha_i s\beta_i c\gamma_i + s\alpha_i s\gamma_i, c\alpha_i s\beta_i s\gamma_i - s\alpha_i c\gamma_i, c\alpha_i c\beta_i)$ on a unit sphere, all those points compose set $\mathbf{S_r}$. In this case, letter s means sin, and letter c means cos. Specifically, $c\alpha s\beta c\gamma + s\alpha s\gamma$ means $\cos\alpha\sin\beta\cos\gamma + \sin\alpha\sin\gamma$. When the orientation of parallel manipulator is (α, β, γ), the normal direction of reference plane is

$$\begin{aligned}\vec{n} = R \bullet \overrightarrow{e_Z} &= \begin{pmatrix} c\beta c\gamma & s\alpha s\beta c\gamma - c\alpha s\gamma & c\alpha s\beta c\gamma + s\alpha s\gamma \\ c\beta s\gamma & s\alpha s\beta s\gamma + c\alpha c\gamma & c\alpha s\beta s\gamma - s\alpha c\gamma \\ -s\beta & s\alpha c\beta & c\alpha c\beta \end{pmatrix} \begin{pmatrix} 0 \\ 0 \\ 1 \end{pmatrix} \\ &= (c\alpha s\beta c\gamma + s\alpha s\gamma, c\alpha s\beta s\gamma - s\alpha c\gamma, c\alpha c\beta)^T \end{aligned} \tag{5}$$

So the three-dimensional vector $\vec{n}$ can describe the orientation of manipulator's working platform. In this way, any orientation (α, β, γ) of working platform can be corresponded to a point $N(c\alpha s\beta c\gamma + s\alpha s\gamma, c\alpha s\beta s\gamma - s\alpha c\gamma, c\alpha c\beta)$ on unit sphere in the normal direction.

In this case, every singular orientation can be corresponded to a point on unit sphere, these points compose set $\mathbf{S_r}$.

3.2.2 Unit Sphere Vector.

Definition: the vector which is started from original point $O(0,0,0)$ and ended on the surface of unit sphere $x^2 + y^2 + z^2 = 1$ with a length of 1, its set is called as $\overrightarrow{\Theta}$.

3.3 Singularity Distance

3.3.1 Definition

Definition 1: For any point A in a manipulator's workspace, its shortest geometrical distance to the "wall" is the point A 's **linear distance to singularity**.

Definition 2: When the manipulator is at a singular position, the minimum angle between the unit sphere vector that the manipulator's orientation corresponds to and the unit sphere vector that corresponds to point in Sr is called as the **angular distance to singularity** at this pose.

3.3.2 Theorem

Theorem: **In the measurement of singularity distance, angular distance to singularity needs to be measured if and only if the manipulator is in singular position.**

Corollary: When the manipulator is not in singular position, linear distance to singularity is only needed to be measured.

If studied the translation and orientation of the mechanism carefully, we can find it is likely to reach the orientation singularity when the mechanism is at position singularity, even if the rotation angel is very small. Hence, in case of orientation singularity, the calculation of angular distance to singularity is of great significance when the mechanism is at position singularity. Because linear distance is geometrical distance, if the manipulator is in singularity, it must be in orientation singularity, And if it is not at a singular position, it will not be in singularity.

Measurement Method of Definition 1:

If the manipulator moves to point O and its pose is $(x_0, y_0, z_0, \alpha, \beta, \gamma)$, build a sphere $S_r(O)$ with point O as its center and r as its radius.

$$(x-x_0)^2+(y-y_0)^2+(z-z_0)^2 \le r^2 \tag{6}$$

$$d=\min\left\{r\in R^+ \middle| S_r(O)\cap E\neq\varnothing\right\} \tag{7}$$

Measurement Method of Definition 2:

Any orientation pose (α,β,γ) of working platform can be corresponded to a point $N(c\alpha s\beta c\gamma+s\alpha s\gamma, c\alpha s\beta s\gamma-s\alpha c\gamma, c\alpha c\beta)\in\vec{\Theta}$ on unit sphere in the normal direction. Pick any singular point $M\in S_r$, the linear distance from point N to point M can be measured by its 2-norm $\|\bullet\|_2$ of $\overrightarrow{ON}$ to $\overrightarrow{OM}$ on unit sphere:

$$d'_{r\|\bullet\|_2}=\left\|\overrightarrow{ON}-\overrightarrow{OM}\right\|_2 \tag{8}$$

So if the manipulator is in singular position and at orientation pose (α,β,γ), then by the equation (5) we get its unit sphere vector $\vec{x}=(c\alpha s\beta c\gamma+s\alpha s\gamma, c\alpha s\beta s\gamma-s\alpha c\gamma, c\alpha c\beta)^T\in\vec{\Theta}$, and its angular distance to singularity can be measured by the minimum act length of the point in unit sphere corresponding to the vector **x** and **Sr**:

$$d_r(\vec{x})=2\arcsin\frac{d'_{r\|\bullet\|_2}(\vec{x},\vec{y})}{2} \tag{9}$$

3.4 Process

Our method is shown as the flow chart in Fig. 1. The detailed process may be presented as follows:

Step 1: As described above, all singularity position of a n-DOF parallel manipulator can be calculated out by our method above and form the "wall" of this manipulator's reachable workspace. So if the manipulator moves to point O and its

pose is $(x_0, y_0, z_0, \alpha, \beta, \gamma)$, using the measurement of definition 1, the linear distance to the "wall" can be decided, and it is shown as Euclidian distance in Eq. (9).

Step 2: After we got thelinear distance d which couldn't be negative since it describes Euclidian distance, then

1. If d isn't 0, it means the manipulator is not in singularity, there isn't any singular pose at this position (x_0, y_0, z_0), the manipulator must have a distance from singularity, and this distance is linear distance in geometric space. Linear distance from the position of manipulator to singular position is good enough to describe the distance from singularity.
2. If d is 0, the linear distance to singularity is 0, but the manipulator may not be in singularity, because its orientation (α, β, γ) may not be the singular one. So in this situation, (α, β, γ) decides the distance to singularity, namely angular distance to singularity.

Step 3: If d is not 0, the distance to singularity can be calculated by method 1, which is shown in Eq. (8)-(9) in the measurement method of definition 1. And the result shows the Euclidian distance to singularity.

If d is 0, the distance to singularity can be calculated by method 2, that is, the measurement method of definition 2.

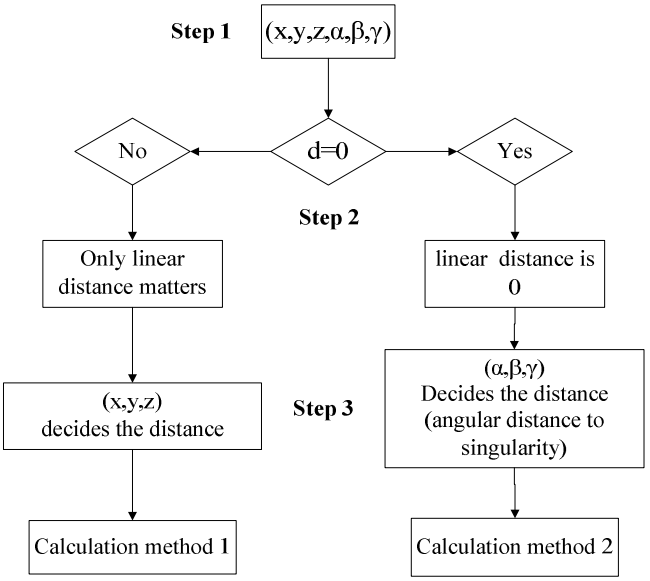

Fig. 1. Process of singularity distance calculation of parallel manipulators

4 Comparison of Singularity Indices

A parallel manipulator should work far from singularities since it always loses control at a singular configuration and in its neighborhood. In this section, some indices are described to measure the closeness to singular configurations, and compared with the index above in order to get the best index

Voglewede defines three conditions that a singularity index $S(X)$ should fulfill[1]:

$C_1 : S(X) = 0$ if and only if X is a singularity.

C_2 : If X is non-singular, $S(X) > 0$

$C_3 : S(X)$ must have a clear physical meaning

Here are kinematic indices may be used as singularity indices: the manipulability index $\sqrt{|JJ^T|}$ as defined by Yoshikawa [1], the inverse of the condition number $1/k$, and the smallest singular value of J_{fk}^{-1}, which will be 0 at a singularity. All these indices have variants according to the inverse jacobian matrix on which they are applied, and to the matrix norm that is used for their calculation [1].These indices, although they are commonly used, satisfy condition C_1, C_2, but not C_3.

In order to describe these methods performance in measuring closeness to singularities, applications on a PS-3-SPS parallel manipulator are taken as an example. This manipulator is shown in Fig. 2.

The whole body is fixed with the center of point O which is the center of Rotating disc body. Bar AA_1 is fixed with the platform $ABCD$, but bars BB_1, CC_1 and DD_1 are able to rotate with the center of B, C and D respectively. A, B, C and D are the

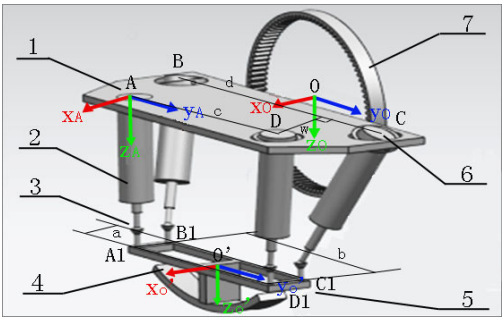

Fig. 2. The solid modeling of new segment erector with coordinate system and parameters 1.base frame 2.lift cylinder 3.spherical joint 4.segment 5.rotating disc body 6.revolute joint 7.moving platform

center of upper surface of bars AA_1, BB_1, CC_1 and DD_1. These four bars' length can be changed by the lift cylinders in them. Spherical joints are installed at points A_1, B_1, C_1 and D_1. Point O' is the center of $A_1B_1C_1D_1$. This PS-3-SPS parallel manipulator has four DOFs. If the manipulator rotates with the rotating disc body, then it will have six DOFs. By controlling four lift cylinders and rotating disc, this machine is used for segments assembling as a segment erector for shield machine.[18]

4.1 Euclidean Distance

Fig. 3 shows the reachable workspace and singular boundary of this PS-3-SPS manipulator, in which black circle lines represent the boundary of reachable workspace and the gray plane represents the singular boundary. No matter which index is used, these are the same.

After defining the "wall" and calculating distance, the danger surface on which all points are 5% length of reachable workspace away from singularities. The surface is portrayed as gray face in Fig. 3, the black circles are also the boundary of reachable workspace. It is showed in Fig. 3 that the closeness to singularity of every point in the body which is surrounded by the gray surface is more than 5% of the length of reachable workspace, namely, they are not in the danger area. And the manipulator can work properly.

According to this index, distance between a point and singularity is easy to and intuitive, just the Euclidean distance in coordinate system. This index meets Conditions C_1, C_2, C_3. Using this index can bring convenience and much benefit to manipulator design and actual working progress.

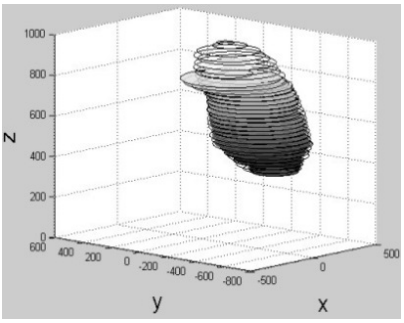

Fig. 3. Reachable workspace and singular boundary

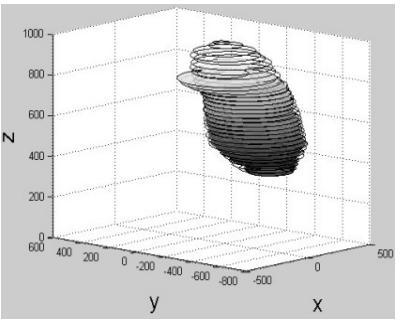

Fig. 4. Reachable workspace and surface of danger area

4.2 Manipulability Index $\sqrt{|JJ^T|}$

This is the index using Jacobin matrix. Yoshikawa proposed that this index was for manipulability measure, for measuring the manipulating ability of robotic arms in

positioning and orienting end-effectors. By calculating the value of $\sqrt{|JJ^T|}$, the best postures of various types of manipulators can be obtained. He also mentioned that when J is not a full rank matrix, the manipulator is in singularity [19].

In this situation, the "length" of a body means the largest value of $\sqrt{|JJ^T|}$ for all points in this body. The points whose value of $\sqrt{|JJ^T|}$ is 0.01854 form its danger area's surface, and they are showed in Fig. 6(a) and 6(b).

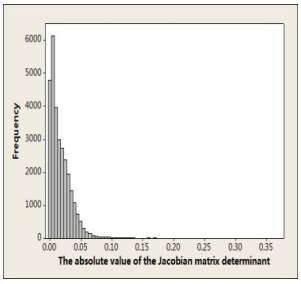

Fig. 5. Frequency of value of manipulability index

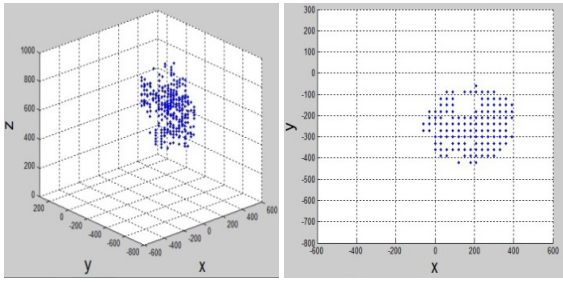

Fig. 6. (a) Points whose values of manipulability index are 5% of the largest value in reachable workspace; 6(b) top view

It can be seen that in Fig. 6(a), this index can't depict points well-proportioned, this index cannot show properties of points of which value are larger than 0.05. So the distances of these points to singularities are hard to be reflect by this index. And in Fig. 6(b), those points can only reflect the value in the workspace and hardly form a surface. So in actual working progress, it is difficult to figure out and be avoided.

4.3 Smallest Singular Value of J^{-1}_{fk}

This index uses the value of smallest singular value of inverse Jacobian matrix to describe the closeness to singularity. For the PS-3-SPS parallel manipulator showed in Fig. 2, Jacobian matrix is the same with it above.

When the point (x, y, z) is a singular point, $\min \lambda(J) = 0$. In this situation, the "length" of a body means smallest singular value of J^{-1}_{fk} for all points in this body. In Fig. 7, all points' value of J^{-1}_{fk} are showed, The largest value f is 0.0029. So the points whose value of J^{-1}_{fk} is 0.000145 form its danger area's surface, and they are showed in Fig. 8(a) and 8(b).

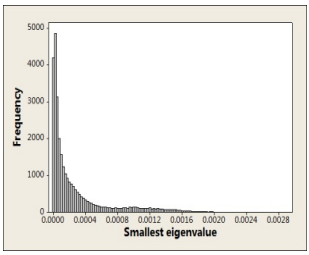

Fig. 7. Frequency of value of smallest singular value of J^{-1}_{fk}

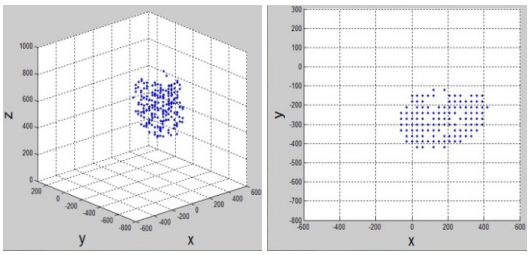

Fig. 8. (a)Points whose values of smallest singular value of J^{-1}_{fk} are 5% of the largest value in reachable workspace; 8(b) top view

It can be seen that in Fig. 8(a), this index can't describe points well-proportioned, this index cannot show properties of points of which value are larger than 0.0004. So the distances of these points to singularities are hard to be depicted by this index. In Fig. 8(b), those points can only reflect the value in the workspace and hardly form a surface. In actual working progress, it is difficult to figure out and be avoided.

4.4 Inverse of Condition Number $1/k$

The condition number of the Jacobian matrix was extended directly to the field of parallel manipulators. Points in the workspace that minimize the condition number of the Jacobian matrix are the best conditioned to minimize error propagation from input torques to output forces. We can find the best-conditioned point in the workspace of an existing manipulator design numerically[21]. So it is singularity when $1/k$ equals 0.

The "length" of a body means the value of $1/k$ for all points in this body. In Fig. 9, all points' value of $1/k$ are showed, So the points whose value of $1/k$ is 0.0000172, form its danger area's surface, and they are showed in Fig. 10(a) and 10(b).

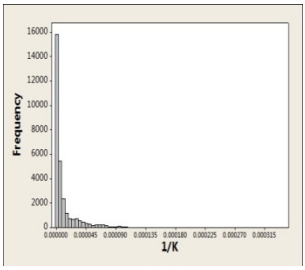

Fig. 9. Frequency of value of inverse of condition number

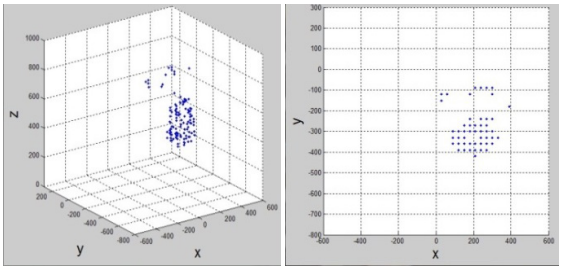

Fig. 10. (a) points whose values of inverse of condition number is 5% of the largest value in reachable workspace; 9(b) top view

It can be seen that in Fig. 10(a), this index can't describe points well, In Fig. 10(b), those points are separate, some of them even far away from others, so they can only reflect the value in the workspace and hardly form a surface.

4.5 Comparison of Indices

According to the statistics and charts above, we find that no matter which index is used, the Z coordinate value of most points are between 300 to 800, so they present consistency in a certain extent not only in identifying singularities, but also in describing the closeness as 5% to singularity. Besides, Results in four different indices have some overlap ratio. So these four indices have the same performance in some points' identification. It leads to the conclusion that these four indices are feasible to some extent.

As the transformation matrix of minus variable in mathematics, the Manipulability index keeps its high accuracy when the distance to singularity is not too large. Besides, the inverse of condition number plays a important role in error estimation, it has the best accuracy when the distance to singularity is small, and the worst accuracy when the distance to singularity becomes larger. However, the absence of a clear physical meaning makes those traditional index difficult to apply and not good enough to represent the distance to singularity.

One of the most prominent advantages of linear distance to singularity is that it has a very clear physical meaning. A visual expression can be seen without any complicated calculations. Based on the rigorous mathematical definition, the linear distance to singularity can be used to represent closeness to singularity perfectly. In addition, in the border of its working space its fault-tolerance-rate is much higher than the other three methods. The cause of this phenomenon is that when the closeness ε is given, the surface gotten from the other methods will in some place get to a minimum relative to the singular surface, and the position is undoubtedly very dangerous. But the linear distance to singularity has the constant distance relative to singular surface.

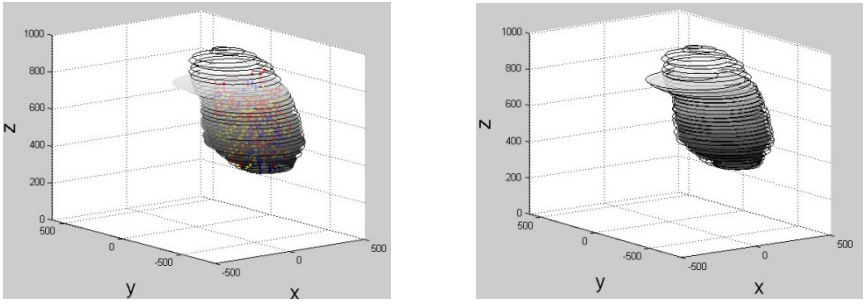

Fig. 11. (a)5% closeness by three indices;11(b) 5% closeness by new approach, the euclidean distance

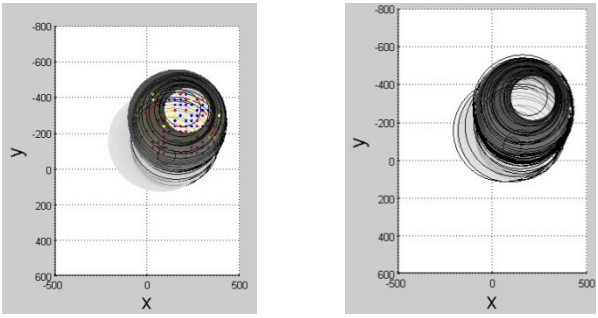

Fig. 11. (c) upward view of Fig. 11(a); 11(d) Upward view of Fig. 11(b)

5 Conclusion

In this paper, a new approach that uses Euclidean distance is introduced for singularity analysis of parallel manipulators. This approach is able to not only identify all singularities but also, the most important, quantitatively and qualitatively describe the closeness to singularity intuitively. The physical meaning is the geometrical distance to singularity. By introducing three usual indices, those four indices are discussed to measure the closeness to singularity respectively, and by comparing the results, the advantages and disadvantages of these indices are identified. These four indices are feasible to some extent and are better than others in some kind. The three usual indices all have problem in describing physical meanings and still need to be improved in separate aspect. However, for the advantage of new index is distinct, it will bring much benefits and convenience for manipulator design and actual working progress.

Acknowledgement. The authors thank the partial financial supports under the projects from the National Natural Science Foundation of China (NSFC Grant No. 51275284), Program for New Century Excellent Talents in University (Grant No. NCET-10- 0567)and the Research Fund of State Key Lab of MSV, China (Grant No. MSV-ZD-2010-02).

References

1. Merlet, J.-P.: Parallel Robots, 2nd edn. (2006)
2. Gosselin, C., Angeles, J.: Singularity Analysis of Closed-Loop Kinematic Chains. IEEE Trans. Rob. Autom 6(3), 281–290 (1990)
3. Liu, G., Lou, Y., Li, Z.: Singularities of Parallel Robots: A Geometric Treatment. IEEE Trans. Rob. Autom. 19(4), 579–594 (2003)
4. Liu, X.-J., Wang, J., Pritschow, G.: Kinematics, Singularity and Workspace of Planar 5R Symmetrical Parallel Mechanisms. Mech. Mach.Theory 41(2), 145–169 (2006)

5. Saglia, J., Dai, J.S., Caldwell, D.G.: Geometry and Kinematic Analysis of a Redundantly Actuated Parallel Mechanism That Eliminates Singularity and Improves Dexterity. ASME J. Mech. Des. 130(12), 124501 (2008)
6. Selvakumar, A.A., Karthik, K., Naresh Kumar, A.L., Sivaramakrishnan, R., Kalaichelvan, K.: Kinematic and Singularity Analysis of 3PRR Parallel Manipulator. Adv. Mater. Res. 403-408, 5015–5021 (2011)
7. Ma, O., Angeles, J.: Architecture Singularities of Platform Robots. In: IEEE International Conference on Robotics and Automation (ICRA 1991), Sacramto, CA, pp. 1542–1547 (1991)
8. Park, F.C., Kim, J.W.: Singularity Analysis of Closed Kinematic Chains. ASME J. Mech. Des. 121(1), 32–38 (1999)
9. Zlatanov, D., Bonev, I.A., Gosselin, C. M.: Constraint Singularities of Parallel Mechanisms. In: Proceedings of the IEEE International Conference on Robotics and Automation (ICRA 2002), Washington, DC, pp. 496–502 (2002)
10. Joshi, S.A., Tsai, L.W.: Jacobian Analysis of Limited-DOF Parallel Robots. ASME J. Mech. Des. 124(2), 254–258 (2002)
11. Merlet, J.P.: Singular Configurations of Parallel Robots and Grassmann Geometry. J. Robot. Res. 8(5), 45–56 (1989)
12. Zhao, J., Li, B., Yang, X., Yu, H.: Geometrical Method to Determine the Reciprocal Screws and Applications to Parallel Robots. Robotica 27(6), 929–940 (2009)
13. Liu, X.-J.: Optimal Kinematic Design of a Three Translational DOFs Parallel Robot. Robotica 24(2), 239–250 (2006)
14. Lou, Y.J., Liu, G.F., Chen, N., Li, Z.X.: Optimal Design of Parallel Robots for Maximum Effective Regular Workspace. In: Proceedings of IEEE/RSJ International Conference on Intelligent Robots and Systems, Edmonton,Canada, pp. 1208–1213 (2005)
15. Voglewede, P.A., Ebert-Uphoff, I.: Measuring 'Closeness' to Singularities for Parallel Robots. In: IEEE International Conference on Robotics and Automation (ICRA 2004), NewOrleans, pp. 4539–4544 (2004)
16. Voglewede, P.A., Ebert-Uphoff, I.: Overarching Framework forMeasuring Closeness to Singularities of Parallel Robots. IEEE Trans. Rob. 21(6), 1037–1045 (2005)
17. Hubert, J., Merlet, J.-P.: Static of Parallel Robots and Closeness toSingularity. ASME J. Mech. Rob. 1, .011011 (2009)
18. Guo, Y., et al.: Orientation Capability Analysis of a P-R-(PS-3-SPS)-type Segment Erector for Shield Machine. In: 2nd IFToMM Symposium on Mechanism Design for Robotics, Beijing, China, October 12-14 (2012)
19. Yoshikawa, T.: Manipulability of robotic mechanisms. Int. J. of Robotics Research 4(2), 39 (1985)
20. Wang, J., et al.: Performance evaluation of parallel manipulators: Motion/force transmissibility and its index. Mechanism and Machine Theory 45, 1462–1476 (2010)
21. Kenneth Salisbury, J., Craig, J.J.: Articulated Hands: Force Control and Kinematic Issues. The International Journal of Robotics Research 1(1) (1982)

Framework Based Path Planning, A Novel Approach

Morteza Aghaei[1] and Seyyed Mohammad Reza Farshchi[2,*]

[1] Department of Mathematics, Payame Noor University, Tehran, Iran
[2] Department of Control and Optimization, Department of Applied Mathematics, FUM University, Mashhad, Iran
Shiveex@Gmail.Com

Abstract. In this paper, we present a novel frameworks for robot path planning software development and deployment of multiple path planning for autonomous robots in an unstructured and unknown environment. This research covered applications ranging from scouting and reconnaissance, to search and rescue, to manipulation tasks, to cooperative localization and mapping, and formation control. Our software framework allows a modular and hierarchical approach to programming deliberative and reactive behaviors in autonomous operation. We demonstrate the algorithms and software on an experimental test bed that involves a group of carlike robots, each using a single omnidirectional camera as a sensor without explicit use of odometry. Experimental results of simulation show this improved algorithm can effectively improve the calculation speed of path planning and ensure the quality of path planning.

Keywords: Human-robot interaction, Visual processing, Wheeled robots, robot path planning.

1 Introduction

Robots are now being used in complex, unstructured environments, performing ever more sophisticated tasks. As the task and environmental complexity increases, the need for effective learning on such systems is becoming more and more apparent. Robot programmers often find it difficult to articulate their knowledge of how to perform a given task in a form suitable for robots to use. Even when they can, the limitations of robot sensors and actuators might render their intuitions less effective. Also, it is often not possible to anticipate (and code for) all environments in which the robot might find itself having to perform a certain task.
Therefore, it seems useful to have the robot be able to learn to act, in the hope of overcoming these two difficulties.

Mobile robots are increasingly being used in real-world application domains such as surveillance, navigation and healthcare due to the availability of high-fidelity sensors and the development of state of the art algorithms to process sensory inputs. As we move towards deploying robots in our homes and offices, i.e., domains with a

* Corresponding author.

J. Lee et al. (Eds.): ICIRA 2013, Part II, LNAI 8103, pp. 54–62, 2013.

significant amount of uncertainty, there is a need for enabling robots to learn from sensory cues and limited feedback from non-expert human participants. In the next sub section we review some important definition that extracted from Sagar Behere master thesis in [1].

1.1 Related Definition

A practical solution of a motion planning and control problem involves solving several sub problems.

This chapter gives an introduction to the main sub-problems, which are, Path planning, Trajectory generation, Motion control, Sensing and estimation.

Each sub-problem is a subject of extensive research and no attempt is made to provide a comprehensive survey of the field. Rather, the intention is to provide sufficient theoretical knowledge necessary for grasping the solutions which could be implemented in the framework. References are provided to sources of further, in-depth knowledge.

1.1.1 Path Planning

Physical objects in the workspace of a robot present potential obstacles to its motion. Path planning is the process of finding a path which the robot should follow, in order to avoid collisions with these obstacles. A path denotes the locus of points in the robot's configuration space, or in Cartesian space, which the robot has to follow in the execution of the assigned motion. Note that a path does not involve the notion of time, it is a purely spatial concept.

An in-depth discussion of robot motion planning is given in [2]. More general information on planning algorithms, with a specific section on motion planning is given in [3].

The output of typical path planning algorithms, however, is rarely in the form of a parameterized curve [4]. Path planning algorithms generally output a path as an ordered sequence of points. The distribution of these points is usually dependent on the distribution of obstacles in the workspace as well as the subset of the workspace through which motion is desired. In general, no assumptions can be made about the distribution of points output by the path planner. In this case, the task of building a parametric representation with continuity of the desired order is left to the trajectory generator. This is because the trajectory generator can perform this task while simultaneously optimizing some motion parameters.

Also, generating a continuous curve through the output of the path planner can be done in a variety of ways depending on the task being carried out. All these considerations do not affect the path planning process and hence an ordered set of collision free points is considered an acceptable output from a path planner.

1.1.2 Properties of Planning Algorithm

Characterizes a planning algorithm according to the task it addresses, properties of the robot solving the task and properties of the algorithm. This characterization helps in selecting an appropriate algorithm for the problem under consideration.

The task solved can be either of navigation, coverage, localization or mapping. Navigation involves handing a collision free path from one robot position to another. Coverage involves passing a sensor over all points in a workspace. Localization is the problem of using sensor data and a map to determine the position of the robot. Mapping refers to constructing a representation of an unknown environment which is useful for the other three tasks.

The representation is constructed from data obtained while the robot is moving around, and hence a good path for the motion must be determined. The framework under consideration in this thesis is mostly devoted to the navigation problem.

The effectiveness of a planning algorithm depends heavily on the robot utilizing that plan. This is because the robot characteristics determine the degrees of freedom available to the planner, the topology of the configuration space and the constraints on the robot motion (for example, holonomicity). If the robot is modeled with dynamic equations, the force and torque data can be used to compute paths optimized for these variables. An important characteristic of the planner is the space it works in. This could either be the robot's operational space (i.e. Cartesian space) or the robot's configuration space.

The space has an impact on the representation of obstacles. Specifically, the difficulty of representing an obstacle in configuration space [3, 4] increases with the number of degrees of freedom of the robot. A path generated in Cartesian space can be directly checked for intersection with workspace obstacles. However, configuration space paths provide an important advantage if the robot motion can be commanded in configuration space. This is because the problem of motion singularities can be avoided or easily resolved in configuration space.

1.2 Contribution

The contributions of this paper are twofold. On the one hand, we conducted a deep analysis of the issues that a robotic software framework should address, and how existing frameworks take their choices. On the other hand, we present our own framework, designed to meet the goals described above through its unique combination of design choices. In the other hand from the path planning view, in geometric modeling of an object may be focused on, at least, two representation levels. The former is called system representation and it consists of enveloping the whole robot by means of a sole model. The latter, called element representation, is based on modeling each link of the robot separately. So, the union of all parts models represents the whole object. Moreover, it is possible to use models of different complexity in each representation; in this way, increasing the complexity of a model implies improvement in accuracy. This approach is referred to as the hierarchical model.

1.3 Related Works

It has long been recognized that there are several tasks that can be performed more efficiently and robustly using multiple robots [4]. In fact, there is extensive literature

on control and coordination for multiple mobile robots, and application to tasks such as exploration [5], surveillance [6], search and rescue [7], mapping of unknown or partially known environments [8], distributed manipulation [9], distributed sensor fusion and localization [10], and transportation of large objects [11]. See, for instance, [12] for a review of contemporary work in this area. The problem of controlling a group of robots has been addressed in a series of papers: trajectory generation is addressed in [6].

The Voronoi concept has been used for four centuries. In his Traité de la Lumiére published in 1644, Descartes uses diagrams similar to Voronoi to show the disposition of matter in the solar system and its environment. Algorithms of Voronoi Diagrams have been appearing since the 1970s. See the surveys by author in [12, 5] on various algorithms, applications, and generalizations of Voronoi Diagrams.

From a theoretical point of view, the motion planning problem is well understood and formulated, and there is a set of classical solutions capable of computing a geometrical trajectory that avoids all known obstacles. Most of these general methods are not applicable if the environment is dynamic or there are no modelled obstacles. Hence, to avoid the problem of executing an unrealistic geometrical trajectory, in which the robot can collide with objects, obstacle avoidance algorithms have been developed to provide a robust way of coping with the problem.

One of the classical methods for dynamically solving the collision avoidance problem is the potential field approach. This approach is based on the creation of an artificial potential field in which the target is an attractive pole and the obstacles are repulsive surfaces. The robot follows the gradient of this potential toward its minimum. The derived force induces a collinear and proportional acceleration enabling easy dynamic and kinematic control actions. This technique can be used at a global or local level depending on the information used to generate the potentials. The major advantage of this method is its simplicity and its capability of being used dynamically because of the easy treatment of fixed and mobile obstacles. Its major disadvantage is the possible existence of local minima and the oscillations for certain configurations of obstacles. In spite of this problem, this technique has been used extensively in reactive architectures because of its natural ability to encapsulate specific robot behaviors.

In the navigation of mobile robots, many methods consist on a grid-based representation of the environment. This representation can have occupied or free cells (binary representation), or each cell can have an associated weight that represents the difficulty of traversing that area. This grid is usually approximated by a graph, with the nodes situated in the center of each cell. Many algorithms have been developed to find a path in the graph. Dijkstra's algorithm computes the optimal path between a single source points to any other point in the graph.

In the next section we describe problem definition and the adopted algorithm. Next we proposed our result and finally conclude the paper.

2 Problem Formulation

Since we are interested in topological, and not geometric, features of the world, we assume that our map is given to us in the form of a graph, representing the connectivity of free space for a single robot1. Because all our robots are alike, they all share this single roadmap.

We make some further simplifying assumptions about the map:

• The map is constructed such that two robots will only collide if they try to simultaneously occupy the same vertex in the graph. That is, the vertices must be spaced sufficiently far apart that two robots can occupy any pair of distinct vertices without colliding.

• A robot at vertex *a* can move to neighboring vertex *b* provided *a* is unoccupied, and no other robot is simultaneously entering or leaving *b*. Robots occupying other vertices in the graph do not affect this movement.

• The initial and goal locations of all robots lie on the roadmap. Obviously these assumptions do not always apply in an arbitrary roadmap, be with appropriate levels of underlying control, they should not be too difficult to achieve or approximate.

A simple centralized approach to computing *P* is given in Algorithm 1. This algorithm was adopted from [12]. The notation and symbol that used in Algorithm 1 was described in [12]. For simplicity, it has been expressed as a non-deterministic algorithm with choice points and failure. A complete implementation of this algorithm would require an appropriate search mechanism to evaluate the different paths of the algorithm and find one which terminates successfully.

For this paper we will assume that breadth-first search is used, with appropriate pruning of visited states, but other search techniques are also valid.

2.1 Planning with Subgraphs

Planning with the reduced graph is now a two-step process. First we plan a path between the connected subgraphs, from the subgraph containing the starting state to the subgraph containing the goal (see Algorithm 1). The difference is that checks need to be made when entering and exiting each subgraph to make sure that this action is permitted.

We have done a discrete mapping of obstacles in the configuration space to explore it. The obstacle in this case is only the other robot of the cell, this robot has four rotating links while the robot whose path is going to be calculated has only three degrees of freedom (three rotating links). This simple robot has been chosen because it is easier to visualize the configuration space. However, the approach can be extended to robots with more links, though in this case the search for appropriate planes would be more complicated.

The robots are works to transporting certain pieces from one working position to another. When the obstacle robot moves from its initial to its final point, we divide its trajectory in 4 equally spaced points and then we present the possible collisions with the other robot in the configuration space as it is shown in Figure 1.

Algorithm 1 A simple centralised planning algorithm

function PLAN(G, S_0, S^+)
  $P_r \leftarrow \emptyset, \forall r \in R$
  $\prec \leftarrow \emptyset$
  return PLAN(G, $\mathcal{P}$, S_0, S^+)
end function

function PLAN(G, $\mathcal{P}$, S_{curr}, S_{goal})
  if $S_{curr} = S_{goal}$ **then**
    return $\mathcal{P}$
  end if
  choose $r \in R$
  $v_f \leftarrow S_{curr}[r]$
  choose $v_t \in \{v \mid (v_f, v) \in G\}$
  $\mathcal{P} =$ MOVE($\mathcal{P}$, S_{curr}, r, v_f, v_t)
  return PLAN(G, $\mathcal{P}$, S_{curr}, S_{goal})
end function

function MOVE($\mathcal{P}$, S, r, v_f, v_t)
  if $\exists r' : S[r'] = v_t$ **then**
    fail
  end if
  add (v_f, v_t) to P_r
  $i \leftarrow \|P_r\|$
  set $E_r(i-1) \prec E_r(i)$
  if $\exists r', j : V_{r'}(j) = v_t$ **then**
    set $E_{r'}(j+1) \prec E_r(i)$
  end if
  $S[r] \leftarrow v_t$
  return $\mathcal{P}$
end function

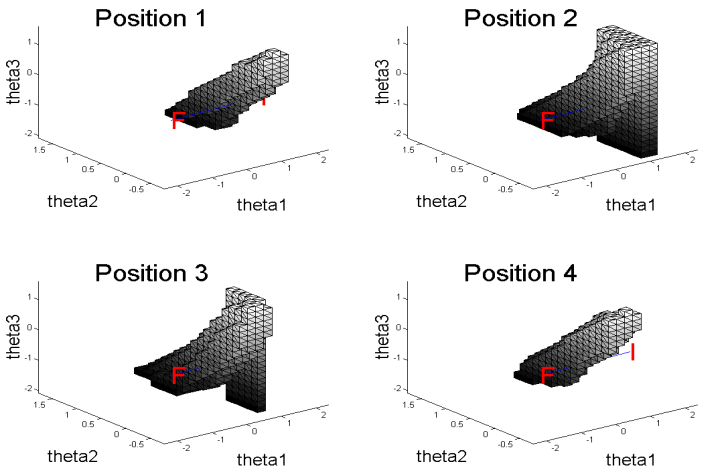

Fig. 1. Shapes of the obstacle in the configuration space for different positions

In Figure 2 we can see several planes that contain the *M* line for the second position in Figure 1. We can see that at each point some planes are more adequate than others. The planes that lead to a dead end in any position of the obstacle are eliminated from the list of possible planes, and the most appropriate at every position are stored.

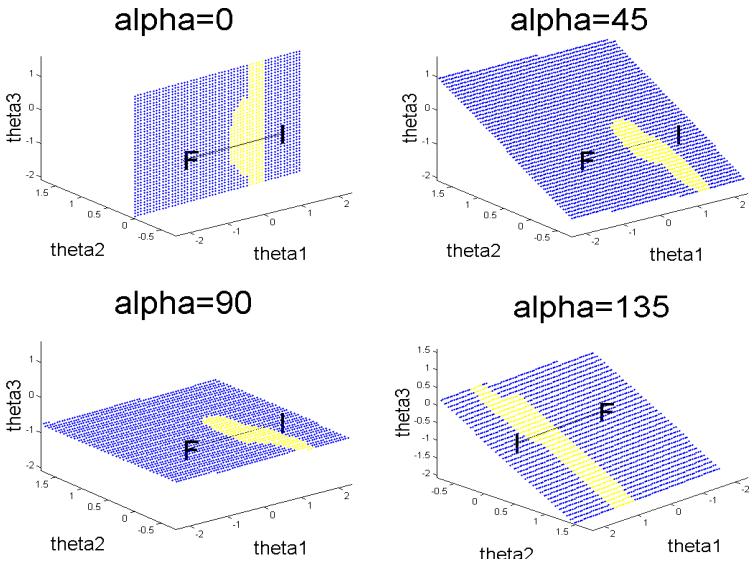

Fig. 2. The planes that contain the M line for the second position

The plane chosen for the path planning has no dead ends in any of the snapshots of the trajectory and has a good behaviour for all of them.

In this example we choose the plane with α=45º. Furthermore, if we use α=0º or α=135º we cannot solve the problem.

3 Simulation and Experimental Result

The Sadjad Laboratory Robotics (SLR) robots served as the testbed for all experiments. As a simplification for data gathering, we first examined the simpler problem of running from one end of the field to the other, with static robots acting as obstacles in the field. In filling in the domain dependent metrics, we first tried metrics that maintained continuous positional and angular velocity, continuous positional velocity only, and fixed curvature only. None of these worked well, substantially increasing planning times to unacceptable levels or failing to find it at all within a reasonable number of node expansions (N=2000). All metrics were written in terms of time and time steps so the planner would tend to optimize the time length of plans.

Although this was a substantial setback, we could still fall back on the obviously physically incorrect model of no kinematic constraints whatsoever and fixed time step sizes, which had been shown to work in simulation. The extension metric then became a model of a simple heuristic "goto-point" that had already been implemented for the robot.

The results are shown in Figure 3. Not only does the tree have better scalability to higher numbers of nodes due to its algorithmic advantage, but it provides an absolute performance advantage even with as few as 100 nodes. Using the tree, and the more efficient second implementation for the robot rather than the initial prototype simulator, planning was able to perform on average in 2.1ms, with the time rarely going above 3ms. This makes the system fast enough to use in our production SLR team, as it will allow 5 robots to be controlled from a reasonably powerful machine while leaving some time left over for higher level action selection and strategy.

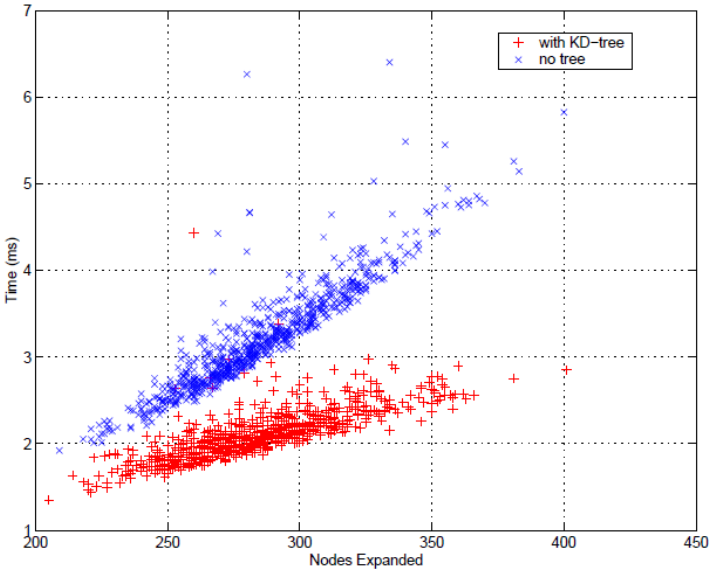

Fig. 3. Planning times vs. number of nodes expanded with and without a KD-tree for nearest neighbour lookup

4 Conclusion

A prototyping path planner is presented in this paper. The proposed method is able to deal simultaneously with both global and local planning requirements. The advantages of the approach can be summarized by the fact that the trajectories obtained are smooth and safe, and at the same time, free of local traps due to the integration of the real-time sensor information in the recalculation of the path. The method is easy to implement, the algorithm is very fast and can work online. It works

in cluttered and changing environments with moving obstacles. The method is complete, i.e., the method is capable of finding a trajectory if it exists. As demonstrated along this work, the method can perform in all types of environments without restrictions in the form of the obstacles. The planner works with curved forms, open environments (not totally enclosed by walls), and concavities.

References

1. Behere, S.: A Generic Framework for Robot Motor Planning and Control. Master of Science Thesis Stockholm, Sweden (2010)
2. Aurenhammer, F.: Voronoi Diagrams: A survey of a fundamental Geometric Data Structure. ACM Computing Surveys (23), 345–405 (1991)
3. Aurenhammer, F., Klein, R.: Voronoi Diagrams. In: Sack, J.R., Urrutia, J. (eds.) Handbook of Computational Geometry, ch. 5, pp. 201–290 (2000)
4. Biagiotti, L., Melchiorri, C.: Trajectory Planning for Automatic Machines and Robots. Springer Publishing Company, Incorporated (2008) ISBN 3540856285, 9783540856283
5. Le, D.V., Oh, H., Yoon, S.: RoCoMAR: Robots' Controllable Mobility Aided Routing and Relay Architecture for Mobile Sensor Networks. Sensors 13, 8695–8721 (2013)
6. Blum, H.: A transformation for extracting new descriptors of shape. In: Dunn, W.W. (ed.) Models for Perception of Speech and Visual Form, pp. 153–171. MIT Press, Cambridge (2012)
7. Breu, H., Gil, J., Kirkpatrick, D., Werman, M.: Linear time euclidean distance transform algorithms. IEEE Transactions on Pattern Analysis and Machine Intelligence 17(5), 529–533 (1995)
8. Chiang, C.S.: The Euclidean Distance Transform. Ph. D. Thesis, Dept. Comp. Sci., Purdue University (1992)
9. Choset, H.: Sensor Based Motion Planning: The Hierarchical Generalized Voronoi Graph. PhD thesis, California Institute of Technology, Pasadena, California (March 1996)
10. Choset, H., Burdic: Sensor-Based Exploration: The Hierarchical Generalized Voronoi Graph. The International Journal of Robotics Research 19, 96–125 (2000)
11. Choset, H., et al.: Principles of Robot Motion: Theory, Algorithms, and Implementations. The MIT Press (2005)
12. Ryan, M.: Multi-Robot Path-Planning with Subgraphs. In: Australian Conference on Robotics, pp. 189–250 (2012)

Kinematics and Dynamics for a 3-DOF Parallel Manipulator with Limbs of Embedding Structures

Jianjun Zhang, Xiaohui Wang, Ning Jiang, and Weimin Li

School of Mechanical Engineering, Hebei University of Technology,
Tianjin, CO. 300130 P.R. China
zhjjun@hebut.edu.cn

Abstract. The workspace of the parallel manipulators is relatively smaller than the serial manipulators, which results in lower translational or rotational capability and larger equipment fixing space. In order to improve this performance, a new type of parallel manipulators with special topology structures and special limbs is proposed. We name it similar-SCARA. The cylinder coordinate is used to describe the position and orientation of the mobile platform, and the kinematics equations of the similar-SCARA parallel manipulator is constructed. Then the dynamics modeling is developed with Lagrangian formulation. By aid of dynamics equations, the simulation curves denote the driving torque with time for the driving joint.

Keywords: Kinematics, Dynamics, Similar-SCARA, Parallel manipulator, Limbs of embedding structures.

1 Introduction

Parallel manipulators are always welcome in conditions where large payload capability, high stiffness and fine precision are needed. They have been studied intensively for more than a couple of decades and still attract attention from scholars of academe and industry [1-5]. To work in more complicated situations, many parallel manipulators with specified numbers and types of DOF have been proposed, and many researchers focused on the type synthesis of parallel manipulators. Because the workspace of the parallel manipulators is relatively smaller than the serial manipulators, many researchers have focused on new methods to avoid these disadvantages. Liu, Wang and Pritschow proposed a new family of spatial 3-DOF fully-parallel manipulators with high rotational capability [6]. Merlet's research showed that the joints' layout could have large influence on the workspace volume for robots [7]. Many serial-parallel manipulators were developed to achieve larger workspace [8, 9]. Also, Kim proposed an Eclipse-II parallel manipulator that used a circular leader rail to achieve the continuous 360-degree spinning [10].

Compared with the serial manipulators, a parallel manipulator is a kind of topological structure with multi-chains and possesses more components [11]. The complex movement of the components brings difficulty to dynamics modeling.

J. Lee et al. (Eds.): ICIRA 2013, Part II, LNAI 8103, pp. 63–73, 2013.

Among the methods for dynamics modeling [12-15], Lagrangian dynamics formulation is versatile and is wildly used in complex mechanical system, especially to the parallel manipulators.

In this paper, we will propose a new type of parallel manipulator, named similar-SCARA parallel manipulator, with special topology structures and special limbs to make their mobile platforms rotate continuously. The cylinder coordinate will be used to describe the position and orientation of the mobile platform, and the kinematics equations of the similar-SCARA parallel manipulator will be constructed. Based on the kinematics equations, the dynamics modeling will be developed with Lagrangian formulation. The simulation pictures will be obtained to denote the driving torque with time for the driving joints.

2 Mechanism Description and Kinematics

2.1 Mechanism Description

The 3-DOF parallel manipulator with limbs of embedding structures as shown in Fig. 1 possesses three limbs, i.e. a RHRPP (R-rotational joint, H-helix joint, P-prismatic joint) limb, a RPP limb and a RPRRR limb. The peculiarities of its structures are that the three limbs are embedding together. Concretely, the axis of the second R-joint in the RHRPP limb and the axis of the R-joint in the RPP limb are coincident, and the two limbs have two common P-joints. Moreover, the common P-joints run through the R-joint in the RPP limb whose axis is parallel to the translational direction of the P-joint. An actuator drives the first R-joint in the RHRPP limb, which makes the mobile platform translate along the *Z*-axis. And another actuator drives the R-joint in the RPP

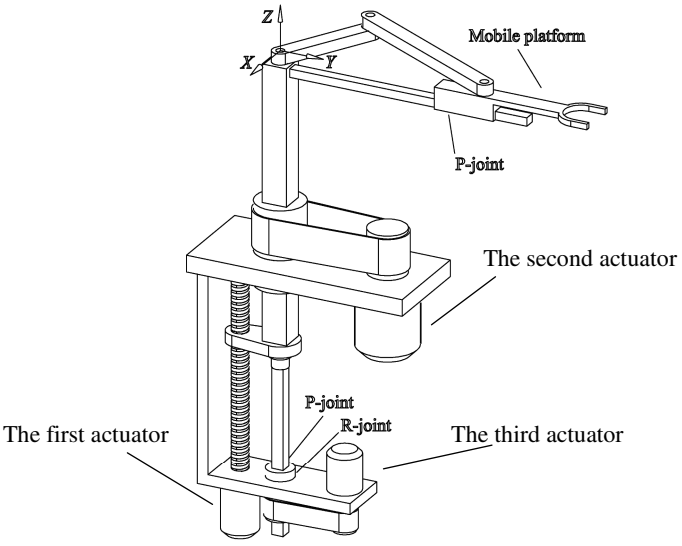

Fig. 1. A new 3-DOF parallel manipulator with limbs of embedding structures

limb by a belt (or the other driving mode), which makes the mobile platform rotate about the *Z*-axis continuously. Besides, the mobile platform can translate along a leader-rail in radial direction. Because the motion of the 3-DOF parallel manipulator is similar to SCARA serial manipulator, we name it similar-SCARA parallel manipulator.

2.2 Kinematics

For the mechanism of the 3-DOF similar-SCARA parallel manipulator in Fig.2, the outputs involve not only the z coordinate and the rotational angle α about the *Z*-axis but also the distance r between points O' and *C*. So the cylinder coordinate vector $(r \quad \alpha \quad z)^{\mathrm{T}}$ is used to denote the motion of the mobile platform. The inputs are three rotational angles which are θ_1 of the R-joint in point *O*, θ_2 of the R-joint in point *A* and θ_3 of the R-joint in point *B*. The outputs α and z are expressed by the equation

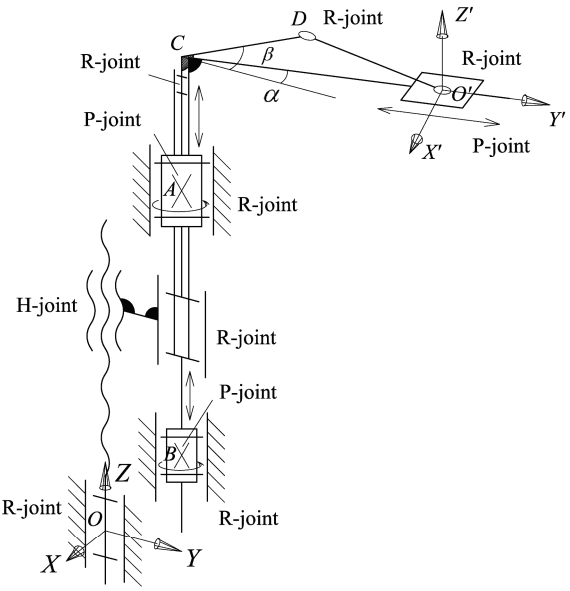

Fig. 2. Mechanism sketch of the 3-DOF similar-SCARA parallel manipulator

$$\begin{cases} z = z_0 + \dfrac{p}{2\pi}\theta_1 \\ \alpha = \theta_2 \end{cases} \tag{1}$$

Here, z_0 is the original distance in the *Z*-axis direction between points O and O', p is the pitch of the H-joint. Eq. (1) is differentiated with respect to time, velocity equations are obtained

$$\begin{cases} \dot{z} = \dfrac{p}{2\pi}\dot{\theta}_1 \\ \dot{\alpha} = \dot{\theta}_2 \end{cases} \tag{2}$$

The output r can be solved in the planar triangle CDO' where we have

$$b^2 = a^2 + r^2 - 2ar\cos(\beta - \alpha) \tag{3}$$

Here, a is the length of CD, b is the length of DO', β is the rotational angle of CD about the *Z*-axis and satisfies

$$\beta = \theta_3 \tag{4}$$

Differentiating Eq. (3) with respect to time and integrating with Eq. (4), we obtain

$$[2r - 2a\cos(\theta_3 - \theta_2)]\dot{r} = -2ar\sin(\theta_3 - \theta_2)(\dot{\theta}_3 - \dot{\theta}_2) \tag{5}$$

Combining Eqs. (2) and (5), we obtain a velocity equation of the similar-SCARA manipulator in a vector form, that is

$$\boldsymbol{A}\dot{\boldsymbol{q}} = \boldsymbol{B}\dot{\boldsymbol{X}} \tag{6}$$

Here, $\dot{\boldsymbol{X}} = \begin{pmatrix} \dot{r} & \dot{\alpha} & \dot{z} \end{pmatrix}^{\mathrm{T}}$ is the output velocity vector in which the elements are the translational and rotational velocities, respectively, $\dot{\boldsymbol{q}} = \begin{pmatrix} \dot{\theta}_1 & \dot{\theta}_2 & \dot{\theta}_3 \end{pmatrix}^{\mathrm{T}}$ is the input velocity vector. Matrices $\boldsymbol{A}$ and $\boldsymbol{B}$ can be expressed as

$$\boldsymbol{A} = \begin{pmatrix} 0 & 2ar\sin(\theta_3 - \theta_2) & -2ar\sin(\theta_3 - \theta_2) \\ 0 & 1 & 0 \\ \dfrac{p}{2\pi} & 0 & 0 \end{pmatrix} \tag{7}$$

$$\boldsymbol{B} = \begin{pmatrix} 2r - 2a\cos(\theta_3 - \theta_2) & 0 & 0 \\ 0 & 1 & 0 \\ 0 & 0 & 1 \end{pmatrix} \tag{8}$$

If $|\boldsymbol{B}| \neq 0$, Eq. (6) can be changed to

$$\dot{\boldsymbol{X}} = \boldsymbol{J}\dot{\boldsymbol{q}} \tag{9}$$

in which $\boldsymbol{J}$ is a velocity Jacobian matrix and satisfies

$$\boldsymbol{J} = \boldsymbol{B}^{-1}\boldsymbol{A} \tag{10}$$

3 Dynamics

For the purpose of the dynamics modeling, we name the number for the components of the 3-DOF similar-SCARA parallel manipulator, as shown in Fig.3. And we

choose the *OXY* plane as a zero potential energy surface. More, the frictions of all joints are omitted and all the components are regarded as rigid bodies.

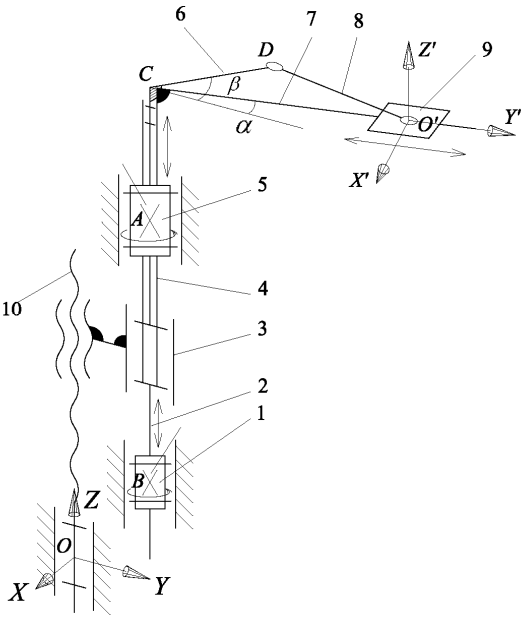

Fig. 3. Mechanism sketch of the 3-DOF similar-SCARA parallel manipulator

So the total kinetic energy of the manipulator is the sum contributions of the links and components,

$$K = \sum_{i=1}^{10} k_i \tag{11}$$

Here, the expression of k_i are as follows

$$k_1 = \frac{1}{2} I_1 \dot{\theta}_3^2 \tag{12}$$

$$k_2 = \frac{1}{2} I_2 \dot{\theta}_3^2 + \frac{1}{2} m_2 \dot{z}^2 \tag{13}$$

$$k_3 = \frac{1}{2} m_3 \dot{z}^2 \tag{14}$$

$$k_4 = \frac{1}{2} I_4 \dot{\theta}_2^2 + \frac{1}{2} m_4 \dot{z}^2 \tag{15}$$

$$k_5 = \frac{1}{2} I_5 \dot{\theta}_2^2 \tag{16}$$

$$k_6 = \frac{1}{2} I_6 \dot{\theta}_3^2 + \frac{1}{2} m_6 \dot{z}^2 \tag{17}$$

$$k_7 = \frac{1}{2} I_7 \dot{\theta}_2^2 + \frac{1}{2} m_7 \dot{z}^2 \tag{18}$$

$$k_8 = \frac{1}{2} I_8 \dot{\omega}_8^2 + \frac{1}{2} m_8 \dot{z}^2 \tag{19}$$

$$k_9 = \frac{1}{2} m_9 (\dot{z}^2 + \dot{r}^2 + (r\dot{\theta}_2)^2) \tag{20}$$

$$k_{10} = \frac{1}{2} I_{10} \dot{\theta}_1^2 \tag{21}$$

In Eqs.(12-21), m_i , I_i and $\dot{\theta}_i$ are masses, inertia, angular velocity of the corresponding components, $\dot{r}$ is the relative velocity of the 9th component, ω_8 is the angular velocity of the 8th component around the instantaneous center.

Let the z_i is the center of mass vector of i^{th} component distance from the mobile platform. Hence, the total potential energy of the manipulator is

$$U = \sum_{i=1}^{10} m_i g (z - z_i) \tag{22}$$

where g is the gravity acceleration and z possesses the same meaning in Eq.(1).

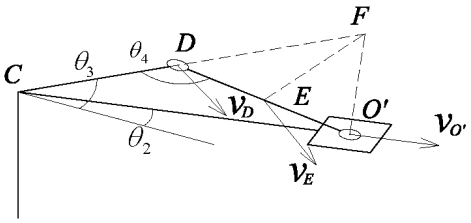

Fig. 4. The instantaneous centers of the 8th component

The dynamics modeling will be developed in joints space. We should describe the kinetic and potential energy with the joint variable. In Fig.4, the points *E* and *F* are the centroid and instantaneous center of the 8th component respectively. θ_4 is the angle between the 6th and the 8th component. According to the trigonometric relationship, we can be obtained

$$DF = CF - CD = \frac{r}{\cos(\theta_3 - \theta_2)} - a \tag{23}$$

$$\cos\theta_4 = \frac{a^2 + b^2 - r^2}{2ab} \tag{24}$$

$$EF^2 = DF^2 + \frac{b^2}{4} - (DF) b \cos(\pi - \theta_4) \tag{25}$$

$$r = a\cos(\theta_3 - \theta_2) + \sqrt{b^2 - a^2\sin^2(\theta_3 - \theta_2)} \tag{26}$$

$$I_8 = \frac{m_8}{12}b^2 + m_8 EF^2 \tag{27}$$

$$\omega_8 = \frac{v_D}{DF} = \frac{a\dot{\theta}_3\cos(\theta_3 - \theta_2)}{r - a\cos(\theta_3 - \theta_2)} \tag{28}$$

Combining the potential energy in Eq.(22) with kinetic energy in Eq.(11) and applying the other equations to the Lagrangian function, the necessary generalized torque T_i for the driving joint driven by the i^{th} actuator is educed

$$T_i = \frac{d}{dt}\frac{\partial(K-U)}{\partial\dot{\theta}_i} - \frac{\partial(K-U)}{\partial\theta_i}(i = 1,2,3) \tag{29}$$

Simplification, the general form and matrix form of torque can be obtained

$$\begin{cases} T_1 = D_{11}\ddot{\theta}_1 + D_{12}\ddot{\theta}_2 + D_{13}\ddot{\theta}_3 + \dot{D}_{111}\dot{\theta}_1^2 + \dot{D}_{122}\dot{\theta}_2^2 + \dot{D}_{133}\dot{\theta}_3^2 + D_{112}\dot{\theta}_1\dot{\theta}_2 + D_{123}\dot{\theta}_2\dot{\theta}_3 + D_{131}\dot{\theta}_3\dot{\theta}_1 + D_1 \\ T_2 = D_{21}\ddot{\theta}_1 + D_{22}\ddot{\theta}_2 + D_{23}\ddot{\theta}_3 + \dot{D}_{211}\dot{\theta}_1^2 + \dot{D}_{222}\dot{\theta}_2^2 + \dot{D}_{233}\dot{\theta}_3^2 + D_{212}\dot{\theta}_1\dot{\theta}_2 + D_{223}\dot{\theta}_2\dot{\theta}_3 + D_{231}\dot{\theta}_3\dot{\theta}_1 + D_2 \\ T_3 = D_{31}\ddot{\theta}_1 + D_{32}\ddot{\theta}_2 + D_{33}\ddot{\theta}_3 + \dot{D}_{311}\dot{\theta}_1^2 + \dot{D}_{322}\dot{\theta}_2^2 + \dot{D}_{333}\dot{\theta}_3^2 + D_{312}\dot{\theta}_1\dot{\theta}_2 + D_{323}\dot{\theta}_2\dot{\theta}_3 + D_{331}\dot{\theta}_3\dot{\theta}_1 + D_3 \end{cases} \tag{30}$$

The Eqs.(30) can be combined to

$$\begin{pmatrix} T_1 \\ T_2 \\ T_3 \end{pmatrix} = \begin{pmatrix} D_{11} & D_{12} & D_{13} \\ D_{21} & D_{22} & D_{23} \\ D_{31} & D_{32} & D_{33} \end{pmatrix}\begin{pmatrix} \ddot{\theta}_1 \\ \ddot{\theta}_2 \\ \ddot{\theta}_3 \end{pmatrix} + \begin{pmatrix} D_{111} & D_{122} & D_{133} \\ D_{211} & D_{222} & D_{233} \\ D_{311} & D_{322} & D_{333} \end{pmatrix}\begin{pmatrix} \dot{\theta}_1^2 \\ \dot{\theta}_2^2 \\ \dot{\theta}_3^2 \end{pmatrix} + \begin{pmatrix} D_{112} & D_{123} & D_{131} \\ D_{212} & D_{223} & D_{231} \\ D_{312} & D_{323} & D_{331} \end{pmatrix}\begin{pmatrix} \dot{\theta}_1\dot{\theta}_2 \\ \dot{\theta}_2\dot{\theta}_3 \\ \dot{\theta}_3\dot{\theta}_1 \end{pmatrix} + \begin{pmatrix} D_1 \\ D_2 \\ D_3 \end{pmatrix} \tag{31}$$

Here, D_{ii} is the effective inertia of the i^{th} joint, $D_{ij}(i \neq j)$ is the coupling inertia between the i^{th} joint and the j^{th} joint, $D_{ijj}\dot{\theta}_i^2$ is the torque due to the centripetal force which the velocity of the j^{th} joint effects on the i^{th} joint. And $D_{ijk}\dot{\theta}_j\dot{\theta}_k$ is defined as Coriolis touque which effect on the i^{th} joint and is caused by the interaction of $\dot{\theta}_j$ and $\dot{\theta}_k$. D_i is the torque which effect on the i^{th} joint and cased by the gravity. Supposed that

$$\begin{aligned} &\Delta\theta = \theta_3 - \theta_2 \\ &\varepsilon = \sqrt{b^2 - a^2\sin^2\Delta\theta} \\ &S_\theta = \sin\Delta\theta \\ &S_{2\theta} = \sin 2\Delta\theta \\ &C_\theta = \cos\Delta\theta \\ &C_{2\theta} = \cos 2\Delta\theta \end{aligned}$$

The effective inertias will be

$$D_{11} = \frac{p^2}{4\pi^2}(m_2 + m_3 + m_4 + m_6 + m_7 + m_8 + m_9 + m_{10}) + I_{10}$$

$$D_{22} = I_4 + I_5 + I_7 + m_9 a^2 C_\theta^2 + 2m_9 a\varepsilon C_\theta + m_9 b^2 + \frac{m_9 a^4 S_{2\theta}^2}{4\varepsilon^2} + \frac{m_9 a^3 S_\theta S_{2\theta}}{\varepsilon}$$

$$D_{33} = I_1 + I_2 + I_6 + m_9 a^2 S_\theta^2 + \frac{m_9 a^4 S_{2\theta}^2}{4\varepsilon^2} + \frac{m_9 a^3 S_\theta S_{2\theta}}{\varepsilon} + \frac{m_8 a^2 C_\theta^2}{\varepsilon^2}\left(\frac{b^2}{3} + \frac{\varepsilon^2}{C_\theta^2} + \frac{\varepsilon}{C_\theta}\frac{a - aC_{2\theta} - 2\varepsilon C_\theta}{2}\right)$$

The coupling inertia will be

$$D_{12} = D_{13} = D_{21} = D_{31} = 0$$

$$D_{23} = D_{32} = -m_9 a^2 S_\theta^2 - \frac{m_9 a^4 S_{2\theta}^2}{4\varepsilon^2} - \frac{m_9 a^3 S_\theta S_{2\theta}}{\varepsilon}$$

And the coefficients of centripetal term are that

$$D_{111} = D_{122} = D_{133} = D_{211} = D_{311} = 0$$

$$D_{222} = 2m_9 a^2 S_{2\theta} + \frac{2m_9 a S_\theta(-a^2 + b^2)}{\varepsilon} - \frac{m_9 a^2(2a^2 S_\theta C_{3\theta} + b^2 S_{2\theta})}{\varepsilon^2} + \frac{2m_9 a^3 S_\theta^3(-a^2 + b^2)}{\varepsilon^3} - \frac{m_9 a^4 S_\theta^2(a^2 S_{4\theta} + 2b^2 S_{2\theta})}{2\varepsilon^4}$$

$$D_{322} = \frac{3}{2}m_9 a^2 S_{2\theta} + m_9 a\varepsilon S_\theta + \frac{m_9 a^3 C_\theta S_{2\theta}}{2\varepsilon} + \frac{2m_9 a^4 \varepsilon^2 S_{4\theta} + m_9 a^6 S_{2\theta}^3}{8\varepsilon^4} - \frac{m_9 a^3 \varepsilon(C_\theta S_{2\theta} + 2S_\theta C_{2\theta})}{2\varepsilon^2} - \frac{m_9 a^5 S_\theta S_{2\theta}^2}{4\varepsilon^3}$$

$$D_{333} = m_8\left[\frac{1}{3}b^2 + \frac{\varepsilon^2}{C_\theta^2} + \frac{\varepsilon(a - aC_{2\theta} - 2\varepsilon C_\theta)}{2C_\theta}\right]\left(\frac{a^2 C_\theta^2}{\varepsilon^2} - 1\right) + \frac{m_8 a^2(a + \varepsilon)S_\theta C_\theta^2}{\varepsilon^2}\left[\frac{2(a + \varepsilon)}{C_\theta^3} - \frac{3a + aC_{2\theta} + 2\varepsilon C_\theta}{2C_\theta^2} + \frac{(a + \varepsilon)}{C_\theta} + \frac{a^2(1 - C_\theta)}{\varepsilon}\right.$$

$$D_{223} = -2m_9 a^2 S_{2\theta} - \frac{2m_9 a S_\theta[a^2(1 + 2C_\theta^2) + ab^2)}{\varepsilon} + \frac{2m_9 a^2(2a^2 S_\theta C_{3\theta} + b^2 S_{2\theta})}{\varepsilon^2} + \frac{4m_9 a^3 S_\theta^3(a^2 - b^2)}{\varepsilon^3} + \frac{m_9 a^4 S_\theta^2(a^2 C_{4\theta} + 2b^2 S_{2\theta})}{\varepsilon^4}$$

The coefficient of Coriolis term

$$D_{112} = D_{123} = D_{131} = D_{212} = D_{231} = D_{312} = D_{331} = 0$$

$$D_{233} = -D_{322}$$

$$D_{323} = -D_{333}$$

And then the gravity term

$$D_1 = \sum_{i=1}^{10} m_i g \frac{p}{2\pi}$$
$$D_2 = D_3 = 0$$

4 Numerical Simulation

By the former equations, the toque for the driving joint driven by the first actuator is

$$T_1 = \frac{p^2}{4\pi^2}\left(m_2 + m_3 + m_4 + m_6 + m_7 + m_8 + m_9 + m_{10}\right)\ddot{\theta}_1 + \sum_{i=1}^{10} m_i g \frac{p}{2\pi}$$

It is obvious that T_1 is depended on the angle acceleration of the first actuator's input for the given mechanical structure parameters of the similar-SCARA parallel manipulator. So we only simulate the toque curve for the driving joints driven by the second and third actuator.

Given the optimization kinematics parameters, $a = 0.33m$ and $b = 0.52m$, and the appropriate mechanical structure parameters of the 3-DOF similar-SCARA parallel manipulator, the geometrical model is established by Pro/E software. The inertia and mass of all the components can be obtained and numerical simulation can be developed by Pro/E software.

Let the driving joint driven by the second actuator follow the velocity of

$$\dot{\theta}_2 = 30 \times \cos\left(360 \times t/5 + 20\right) + 10 \quad \text{(deg/s)}$$

and the driving joint driven by the third actuator follow the velocity of

$$\dot{\theta}_3 = -30 \times \cos\left(360 \times t/5 + 20\right) + 10 \quad \text{(deg/s)}$$

We can get the curve for the input torques of the driving joints driven by the second actuator and the third actuator, as shown in Fig.5 and Fig.6.

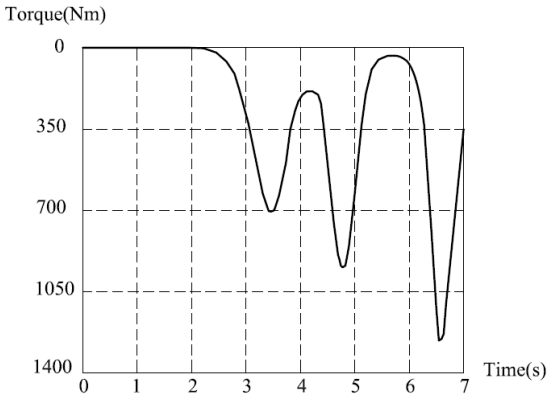

Fig. 5. Input torque of the second actuator

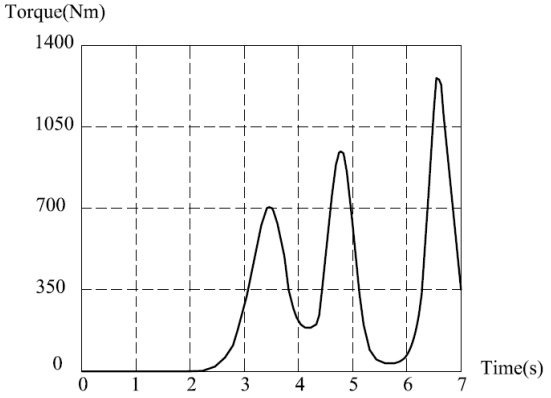

Fig. 6. Input torque of the third actuator

5 Conclusion

We have proposed a 3-DOF similar-SCARA parallel manipulator with limbs of embedding structures. The special topology structures and special limbs make the mobile platforms rotate continuously. The cylinder coordinate is used to describe the position and orientation of the mobile platform, and the kinematics equations of the similar-SCARA parallel manipulator have been constructed. Then, the dynamics modeling have been developed with Lagrangian formulation. The simulation pictures denote driving torque with time for the driving joint. What we studied will provide strong support for the selection of actuator parameters and the control of the parallel manipulator.

Acknowledgment. This research is supported by the National Natural Science Foundation of China (Grant No. 51175144), Tianjin Natural Science Foundation of China (Grant No.08JCYBJC03200).

References

1. Clavel, R.: DELTA: A fast robot with parallel geometry. In: 18th International Symposium on Industrial Robot, Lausanne, Switzerland, pp. 91–100 (1988)
2. Kim, H.S., Tsai, L.W.: Design optimization of a Cartesian parallel manipulator. Journal of Mechanical Design Transactions of the ASME 125(1), 43–51 (2003)
3. Kong, X.W., Gosselin, C.M.: Type synthesis of input-output decoupled parallel manipulators. Transactions of the CSME 28(2A), 185–196 (2004)
4. Gosselin, C.M.: Development and experimentation of a fast 3-DOF camera-orientating device. The International Journal of Robotics Research 16(5), 619–630 (1997)
5. Huang, T., Zhao, X., Whitehouse, D.J.: Stiffness estimation of a tripod-based parallel kinematic machine. IEEE Transactions on Robotics and Automation 18(1), 50–58 (2002)

6. Liu, X.-J., Wang, J.S., Pritschow, G.: A new family of spatial 3-DoF fully-parallel manipulators with high rotational capability. Mechanism and Machine Theory 40(4), 475–494 (2005)
7. Hervé, J.M.: The Lie group of rigid body displacements, a fundamental tool for mechanism design. Mechanism and Machine Theory 34(5), 719–730 (1999)
8. Russakow, J., Khatib, O., Rock, S.M.: Extended operational space formulation for serial-to-parallel chain (branching) manipulators. In: Proceedings of IEEE International Conference on Robotics and Automation, Nagoya, Japan, pp. 1056–1061 (1995)
9. Romdhane, L.: Design and analysis of a hybrid serial-parallel manipulator. Mechanism and Machine Theory 34(7), 1037–1055 (1999)
10. Kim, W., Hwang, J.C., Kim, J.S., Iurascu, C.C.: Eclipse-II: A new parallel mechanism enabling continuous 360-degree spinning plus three-axis translational motions. IEEE Transactions on Robotics and Automation 18(3), 367–373 (2002)
11. Dasgupta, B., Mruthyunjaya, T.S.: The stewart platform manipulator: a review. Mechanism and Machine Theory 35(1), 15–40 (2000)
12. Khal, L.W., Guegan, S.: Inverse and Direct Dynamic Modeling of Gough-Stewart Robots. IEEE Transactions on Robotics 20(4), 754–763 (2004)
13. Dasgupta, B., Choudhury, P.: A general strategy based on the Newton-Euler approach for the dynamic formulation of parallel manipulators. Mechanism and Machine Theory 34(6), 801–824 (1999)
14. Codourey, A.: Dynamic modeling of parallel robots for computed-torque control implementation. The International Journal of Robotics Research 17(12), 1325–1336 (1998)
15. Liu, M.J., Li, C.X., Li, C.N.: Dynamics analysis of the gough-stewart platform manipulator. International Transactions on Robotics and Automation 16(1), 94–98 (2000)

High-Speed Tracking Control of Parallel Kinematic Machine for Pick-and-Place

Hyun Min Do, Chanhun Park, Byung In Kim, Tae Yong Choi, and Jin Ho Kyung

Dept. of Robotics and Mechatronics, Korea Institute of Machinery and Materials,
156 Gajeongbukno, Yuseong-gu, Daejeon, 305-343, Korea
hmdo@kimm.re.kr

Abstract. Parallel robot has been usually used for pick-and place motion in very high speed and high precision environment to enhance the productivity. The high speed parallel robot is proposed for handling the solar cell in this paper. However the target processes are not just limited to the solar cell. The control algorithm is developed to achieve the high-speed tracking control of pick-and-place motion. Also the prototype machine is designed and the cycle time and the repeatability of the proposed robot are suggested. The method using the feedback and feedforward control is applied to the developed parallel robot and the performance is verified through the experiments. To improve the performance, both the tracking error and synchronization error are considered.

Keywords: Parallel robot, High-speed tracking, Pick-and-place motion, Synchronization error.

1 Introduction

Advantages of parallel robots are high stiffness, high speed, high accuracy and high payload compared to the serial robots and their closed-chain mechanism make it possible [1, 2]. These merits make parallel robots be proper for high speed and high payload motion and thus parallel robots are mainly used in the industrial area.

The important things are the design of a mechanism and the design of control systems to realize the high speed and high accuracy motion. Optimal design problem was studied in [3]. In this paper, we focus on the design of the control algorithm and the application of the developed algorithm to the experimental prototype. Conventionally, an independent control scheme is widely used, i.e., each actuator is controlled by each controller independently to track the reference trajectory. Thus the controller of each actuator does not receive the information of the tracking error from the others. However, since the mechanism of a parallel robot is closed-loop kinematic chain, each actuator takes effect on each other. Thus the tracking error of other manipulators should be considered to control each actuator precisely.

Many researches have been conducted in the field of control systems for parallel robots. Design of independent joint controllers was suggested in [4]. Some studies address the design for control to overcome difficulties of control problem [5]. Several studies on synchronized control of parallel robot have been done [6-9]. However, the

J. Lee et al. (Eds.): ICIRA 2013, Part II, LNAI 8103, pp. 74–83, 2013.

target model of those works was planar type parallel manipulator. A synchronization error was defined in several forms according to the purpose of a control in each approach.

In this paper, we propose a control approach to improve the accuracy of the tracking performance of parallel robot. A synchronization error was defined to measure the difference of errors between one joint and the others. A synchronization error and a tracking error have merged to form a coupled error which will be used in the feedback signal to PID controllers. Due to the PID controllers, both errors can be reduced and the position accuracy of each manipulator can be improved.

This paper is organized as follows. Section 2 describes the design and implementation of the prototype machine of parallel robot. The proposed control algorithm based on synchronization error is suggested in Section 3 and section 4 describes implementation and some experimental results to demonstrate the validity of the proposed approach. Conclusions are given in Section 5.

2 Design and Analysis of Mechanism

This paper considers a delta-type parallel manipulator, which is consisted of 3 arms and 1 additional rotating axis. This type of robot was patented and commercialized by ABB, Inc. and is now in the public domain. Recently, many companies like Fanuc, Yaskawa, Mitsubishi, et al., proposed their product, of which the type is a delta.

2.1 Derivation of the Required Specifications

Through numerical simulations, motion control of each joint was conducted with 60degress back and forth motion, which was derived from the so-called “Adept Cycle”. It represents a typical pick-and-place task, and first requires a vertical motion at the picking location (up 25mm), then a linear horizontal motion (305mm), a vertical motion at the placing location (down 25mm), and the same trajectory back [3]. The trajectory is shown in Fig. 1. To mimic the motion of “Adept cycle”, each joint moved for 60 degrees and back (1 cycle motion). To measure the maximum torque and maximum speed, 5 cycle motion was conducted. In the case of no payload, the required maximum torque is 150 Nm and maximum speed is 150 rpm. Fig. 2 shows the simulation results.

When it comes to “Adapt cycle”, the required maximum torque is more than 200 Nm and maximum speed is more than 200 rpm. According to the required specification, the motor and the reducer were selected considering a safety factor.

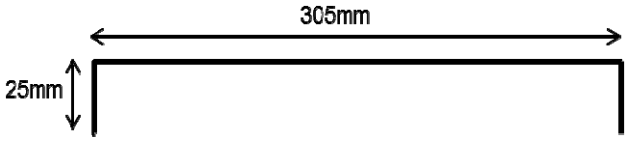

Fig. 1. Adept cycle motion

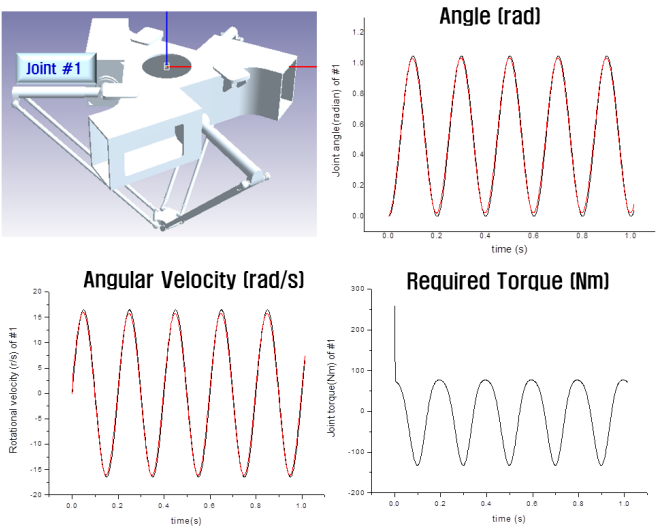

Fig. 2. Single joint motion (no payload)

2.2 Design of Mechanism

Base structure corresponds to a body of a robot and high stiffness is required, thus cast method is adopted because the welding method is not proper to maintain the consistency of the product quality. The base of a robot and the moving platform is connected with 3 arms, where each arm is consisted of 2 links. Inner arm is a first link which is connected to the motor attached to the base structure and thus high stiffness is required. Outer arm is a second link and it makes a parallelogram. To make a light weight robot, stainless steel is used. However, a link can be easily modified and connection part with ball joint can be broken. Ball joint is a very important part and it

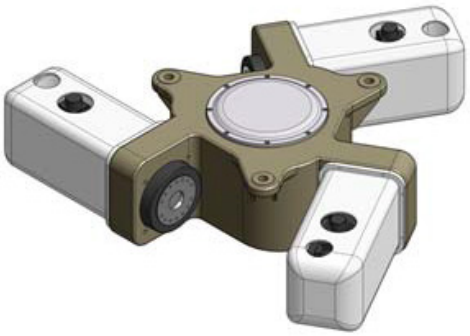

Fig. 3. Shape of the base structure

plays a role of joint in each link. Usually, an allowable angle of inclination of commercial products can not satisfy the requirement of ball joint in a parallel robot. Thus to increase an allowable angle of inclination of ball joint, the height of ball holder should be lowered. In this case, however, a ball and a ball holder can be separated. This problem can be solved by increasing the tensile force of spring in parallelogram structure. To increase a stiffness of ball joint, metallic material is adopted and to remove the problem of lubricant property, a coating on the surface is tried in the ball holder. The moving platform is a part in which 3 links are closed and will be equipped with a tool for an operation. Overall shape of the base structure is shown in Fig. 3.

2.3 Stress Analysis

Finite element analysis is conducted using ANSIS [10] for the stress analysis of the proposed robot. The developed model is shown in Fig. 4. By stress analysis, structurally weak points are found. Fixed condition is set at the lower part of main frame and gravity acceleration is defined at all parts of a robot system. Maximum stress level and displacement are verified through stress analysis and results are shown in Fig. 5 and Table 1. The calculated stress level satisfies the allowable stress level of the material at the contact area of the main housing which is bolted with upper plate.

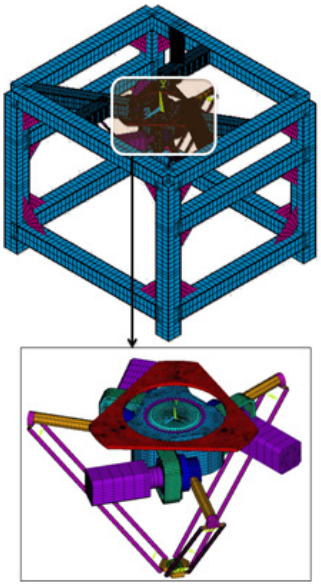

Fig. 4. Finite element model for stress analysis

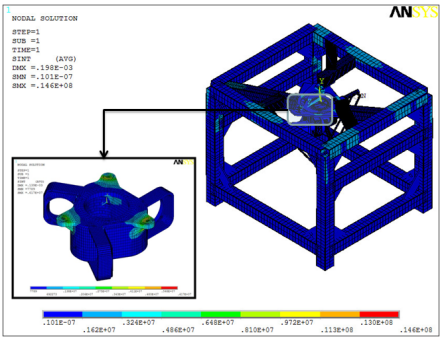

Fig. 5. Result of stress analysis of main housing

Table 1. Result of stress analysis of the proposed robot

allowable stress level of the material	maximum stress level of upper plate	maximum stress level of main housing	result
114MPa	14.6Mpa	6.17Map	soundness

3 Control Algorithm

3.1 Synchronization Error

As for parallel manipulators with *n* actuators, let $q_i\,(1 \le i \le n)$ be the position of *i*-th active joint and $q_i^d\,(1 \le i \le n)$ be the desired trajectory of q_i. Then the tracking error can be defined as

$$e_i = q_i^d - q_i,\ 1 \le \mathrm{i} \le \mathrm{n}. \tag{1}$$

From the concept of the synchronization among multiple manipulators, the synchronization error ε_i of the *i*-th active joint between two neighboring joints ((*i-1)*-th joint and (*i+1)*-th joint) can be defined as follows.

$$\begin{aligned} \varepsilon_i &= (e_i - e_{i-1}) + (e_i - e_{i+1}),\ 2 \le i \le n-1 \\ \varepsilon_1 &= (e_1 - e_n) + (e_1 - e_2),\ i = 1 \\ \varepsilon_n &= (e_n - e_{n-1}) + (e_n - e_1),\ i = n. \end{aligned} \tag{2}$$

Then, the tracking error and the synchronization error can be combined into the coupled error $e_i^{coupled}$ as (3).

$$e_i^{coupled} = e_i + \gamma \cdot \varepsilon_i, \ 1 \le i \le n, \tag{3}$$

where γ $(0 \le \gamma \le 1)$ is a constant parameter which means the portion of the synchronization error of overall error. Finally, the coupled error will be fed back to each active actuator, which contains the tracking error of each actuator and the degree of coordination of among multiple actuators.

3.2 Design of Controller

The controller was designed based on PID feedback controller and feedforward one and the overall scheme is described in Fig. 6.

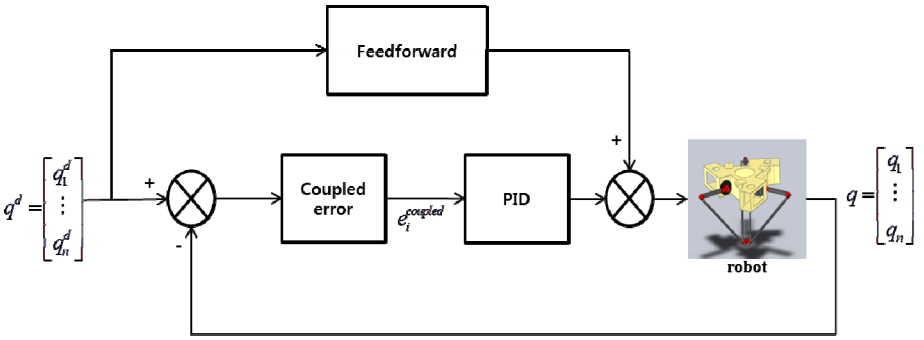

Fig. 6. Overall control scheme

In the proposed schemes, both the tracking error and the synchronization error were considered in the combined form, i.e., the coupled error, and such coupled error is used instead of the tracking error. Thus, the control input for i-th active joint can be written by (4),

$$\begin{aligned} u_i &= u_i^{feedback} + u_i^{feedforward} \\ &= \left[K_p e_i^{coupled} + K_d \dot{e}_i^{coupled} + K_i \int e_i^{coupled} \right] \\ &\quad + \left[K_{pff} q_i^d + K_{vff} \dot{q}_i^d + K_{aff} \ddot{q}_i^d \right], \end{aligned} \tag{4}$$

where K_p, K_d, K_i are feedback gains for PID control and K_{pff}, K_{vff}, K_{aff} mean gains for the position trajectory, velocity trajectory and acceleration trajectory in the feedforward control.

Since the considered parallel robot is a delta-type 3-DOF manipulator as described in section 2, the synchronization error can be defined as (5),

$$\begin{bmatrix} \varepsilon_1 \\ \varepsilon_2 \\ \varepsilon_3 \end{bmatrix} = \begin{bmatrix} (e_1 - e_3) + (e_1 - e_2) \\ (e_2 - e_1) + (e_2 - e_3) \\ (e_3 - e_2) + (e_3 - e_1) \end{bmatrix} = \begin{bmatrix} 2 & -1 & -1 \\ -1 & 2 & -1 \\ -1 & -1 & 2 \end{bmatrix} \begin{bmatrix} e_1 \\ e_2 \\ e_3 \end{bmatrix} = S \begin{bmatrix} e_1 \\ e_2 \\ e_3 \end{bmatrix}. \tag{5}$$

Then the coupled error can be written as

$$\begin{bmatrix} e_1^{coupled} \\ e_2^{coupled} \\ e_3^{coupled} \end{bmatrix} = \left(I + \gamma \cdot S \right) \begin{bmatrix} e_1 \\ e_2 \\ e_3 \end{bmatrix}, \tag{6}$$

where

$$S = \begin{pmatrix} 2 & -1 & -1 \\ -1 & 2 & -1 \\ -1 & -1 & 2 \end{pmatrix}.$$

4 Experiments

The designed prototype robot is implemented and is shown in Fig. 7. The performance of the proposed method is verified through some experiments, in which "Adept Cycle" was implemented. Pick-and-Place motion from (x = -152.5mm, y = 0, z = -775mm) to (x = +152.5mm, y=0, z=-775mm) was conducted and the cycle time for several payload condition was measured, where the payload condition was set as 0.1kg, 1kg, 2kg and 3kg. Results are shown in Table 2.

Table 2. Payload condition and achieved cycle time

payload (kg)	0.1	1	2	3
cycle time (sec)	0.3	0.36	0.4	0.5

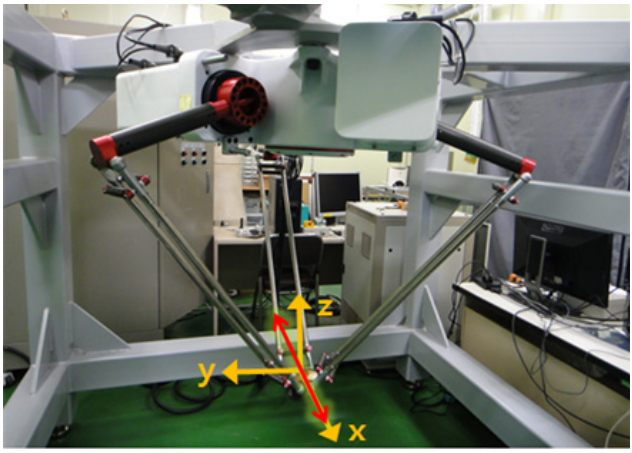

Fig. 7. Prototype robot and coordinate system

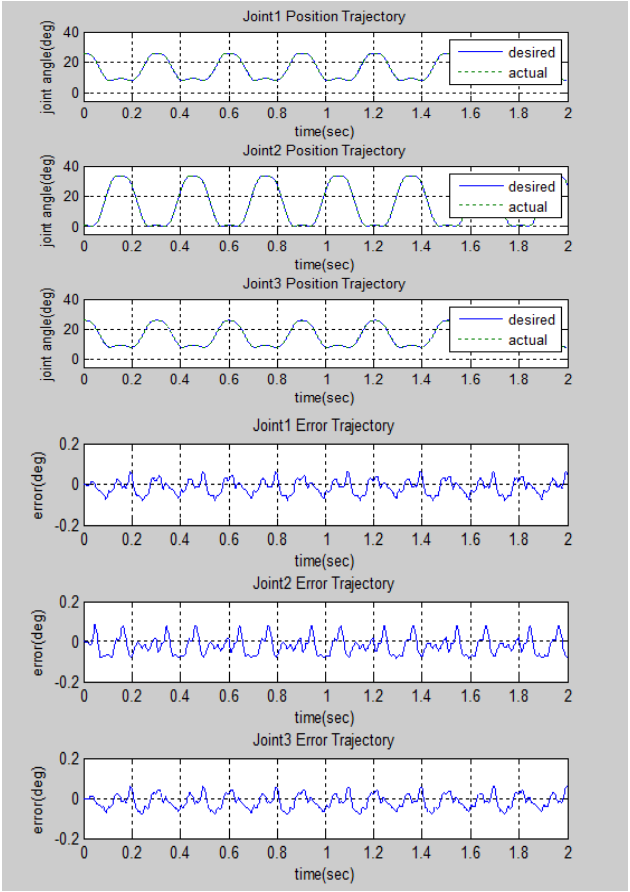

Fig. 8. Position and error trajectory of each joint

The position and error of an each joint angle and an end effector in pick-and –place motion are suggested in Fig. 8 and Fig. 9 respectively. Through experiments, we can see the maximum position error in 0.1kg-payload and 0.3sec-cycle motion is 0.85mm, which means about 0.3% error. From these results, we can see that the proposed system shows the satisfactory performance.

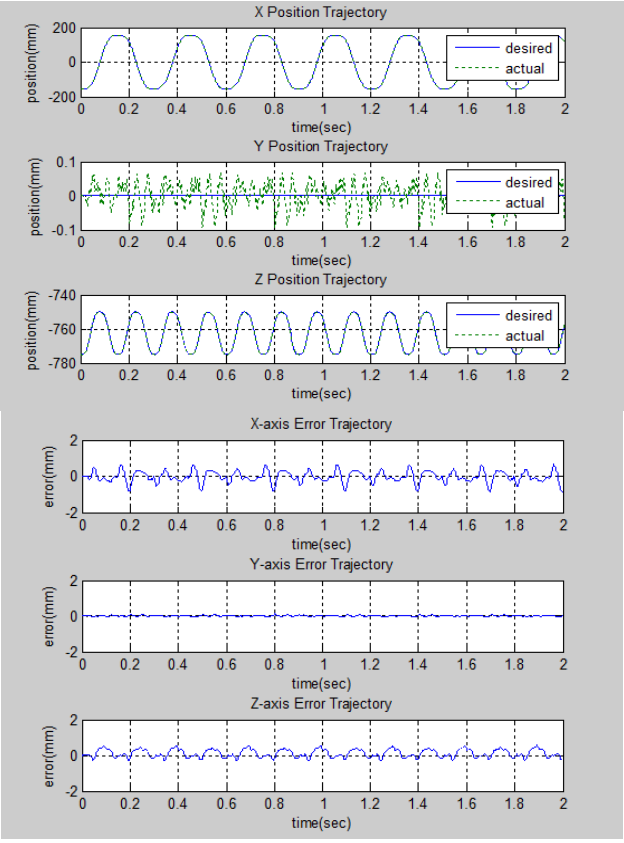

Fig. 9. Position and error trajectory of moving platform

5 Conclusion

In this paper, we have proposed the design method of the delta-type parallel robot for a pick-and-place motion and the control scheme for high-speed tracking motion based on the synchronization error. The prototype robot was implemented and the proposed method was tested on the designed platform. Through some experimental results, the performance can be verified.

References

1. Boër, C.R., Molinari-Tosatti, L., Smith, K.S.: Parallel Kinematic Machines. Springer (1999)
2. Merlet, J.-P.: Parallel Robots. Kluwer Academic Publishers (2000)
3. Peirrot, F., Nabat, V., Company, O., Krut, S., Poignet, P.: Optimal Design of a 4-DOF Parallel Manipulator: From Academia to Industry. IEEE Trans. Robot. 25(2), 213–224 (2009)
4. Chiacchio, P., Pierrot, F., Sciavicco, L., Siciliano, B.: Robust Design of Independent Joint Controllers with Experimentation on a High-Speed Parallel Robot. IEEE Trans. Ind. Electron. 40(4), 393–403 (1993)
5. Li, Q., Wu, F.X.: Control performance improvement of a parallel robot via the design for control approach. Mechatronics 14, 947–964 (2004)
6. Su, Y.X., Sun, D., Ren, L., Wang, X., Mills, J.K.: Nonlinear PD Synchronized Control for Parallel Manipulators. In: IEEE Int'l Conf. Robot. Automat., pp. 1386–1391 (2005)
7. Ren, L., Mills, J.K., Sun, D.: Performance Improvement of Tracking Control for a Planar Parallel Robot Using Synchronized Control. In: IEEE/RSJ Int'l Conf. Intelligent Robots and. Systems, pp. 2539–2544 (2006)
8. Ren, L., Mills, J.K., Sun, D.: Experimental Comparison of Control Approaches on Trajectory Tracking Control of a 3-DOF Parallel Robot. IEEE Trans. Contr. Syst. Technol. 15(5), 982–988 (2007)
9. Shang, W., Cong, S., Zhang, Y., Liang, U.: Active Joint Synchronization Control for a 2-DOF Redundantly Actuated Parallel Manipulator. IEEE Trans. Contr. Syst. Technol. 17(2), 416–423 (2009)
10. ANSYS Inc., Theory Reference Manual, vol. III (2003)

Ultrasound Based Object Detection for Human-Robot Collaboration

Christoph Glowa and Thomas Schlegl

Department of Mechanical Engineering,
Univ. of Applied Sciences Regensburg,
Galgenbergstraße 30, 93053 Regensburg, Germany
{Thomas.Schlegl,Christoph1.Glowa}@hs-regensburg.de
http://www.hs-regensburg.de

Abstract. For safe human-robot collaboration within a defined working area, a technologically diverse and redundant sensor system is developed, which comprises ultrasound sensors and two monocular cameras. The ultrasound sensor system, as well as the developed algorithms for the sensor system are proposed, which allow a distinction between objects. Detected objects within the working area are classified in static and dynamic objects. The sensor system is able to distinguish between these object types. Due to the safe detection of dynamic objects the robot system is enabled to react with an adaption of its trajectories to avoid undesired collisions. To ensure, that the manipulator only reacts on dynamic objects, distances caused by static objects are eliminated.

Keywords: Ultrasound sensor, human-robot collaboration, object detection.

1 Introduction

1.1 Project Framework

The research project "ManuCyte" [1] focuses on the realization of an industrial scale cultivation platform for human cells and tissues. To achieve this, a Hybrid Workplace (HW) is developed, which enables a human operator to work in collaboration with the CARo5X (**C**leanromm **A**pplication **Ro**bot **5** A**x**es). The developed facility is pictured in Fig. 1. The parts of the facility are described in detail in [1,2].

This paper lays focus on the object recognition due to ultrasound sensors which are mounted on the moving manipulator and are operated in a working area, which is defined by the dimensions of the HW. Also, algorithms are proposed which are able to distinguish, if a detected object is either static or dynamic. Based on this decision, the currently executed trajectory is interrupted to avoid physical contact with the dynamic object. If the detected object is static, the distances caused by these objects have to be suppressed, so that the manipulator is enabled to continue its path within the HW.

J. Lee et al. (Eds.): ICIRA 2013, Part II, LNAI 8103, pp. 84–95, 2013.

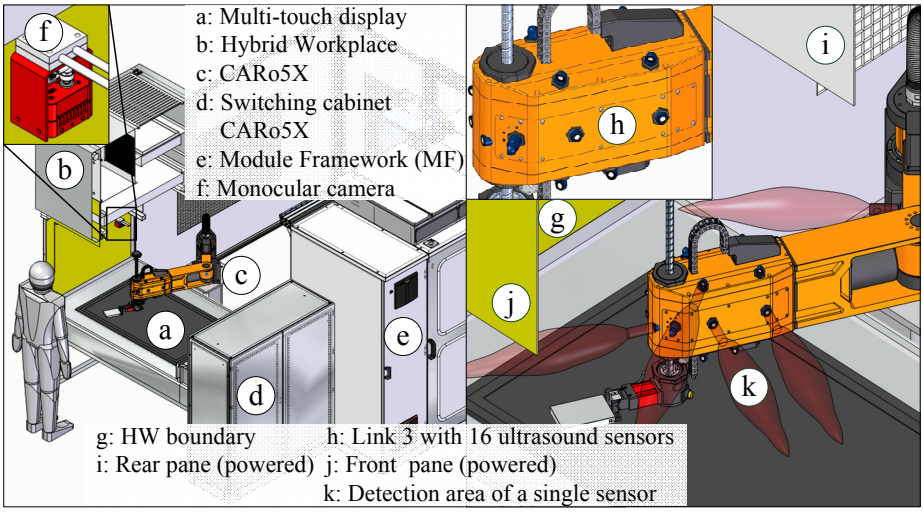

Fig. 1. Projekt "ManuCyte" - cell cultivation plant and sensor setup

1.2 Related Work

The realization of a safe man-machine collaboration using ultrasound sensors is uncommon. For example, the KR 3 SI and KR 5 SI robot, developed by KUKA [3], are operating with capacitive distance measuring sensors. Concerning the field of mobile robots, ultrasound sensors are often used for map generation of unknown environments [4]. Here the focus lies on optimizing the map generation process by eliminating measuring faults, such as specular reflections of ultrasonic waves on obstacles [5,6,7]. However, the frame conditions of the described system, concerning the Hybrid Workplace in conjunction with a collaborative manipulator and a human operator, require a different approach to deal with customary measuring faults like specular reflections or crosstalk-effects. The presented novel approach, concerning the establishment of a safe man-machine collaboration, is to enhance the detection of a human operator, due to the elimination of static objects from the ultrasound sensor signals, by including a-priori information about the manipulators environment in the obstacle detection algorithm.

1.3 Paper Organization

Section 2 outlines the general complex of problems. Section 3 discusses the hardware components and introduces the developed object recognition algorithms, which are discussed in detail in 4. Experimental results are shown and analyzed in Sect. 5. Finally, Sect. 6 concludes the article and gives an outlook on future work.

2 Complex of Problems

The problem to be solved is the safe detection of a human operator by the ultrasound sensor system. The frame conditions are the environmental influences of the HW and a moving manipulator inside the working area (see Fig. 2). Object

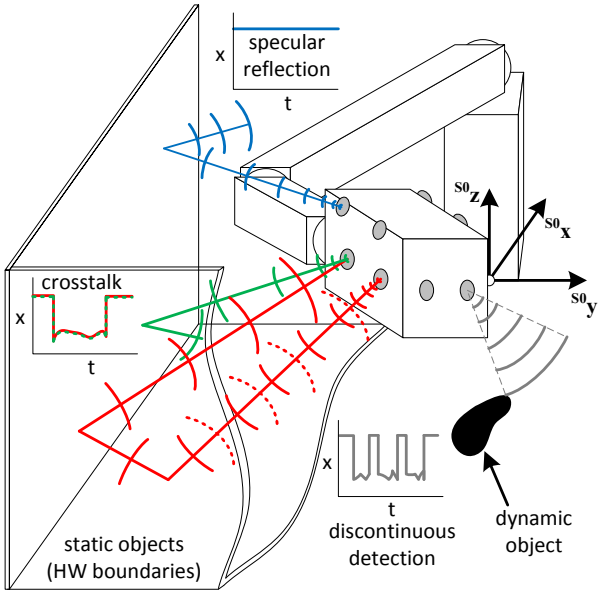

Fig. 2. Object detection and possible measurement errors within confined working area

recognition or rather distance determination via ultrasound sensors is difficult when the sensors are operating in a working area which is confined by reflective boundaries. These boundaries can cause the following measurement errors:

- Specular reflections: Here, ultrasonic waves are reflected from objects in a way that the sensors receive no echo (blue signal in Fig. 2).
- Crosstalk-effects: Due to specular reflections, sensors receive the ultrasonic waves from adjacent sensors as an echo (red and green signals in Fig. 2).
- Limited detection area: The continuous detection of a human operator is limited by the detection area of each sensor (grey signal in Fig. 2).

The aim is to generate an algorithm, which eliminates measurement errors and is also able to distinguish between the HW boundaries (static objects) and a human operator (dynamic object).

3 System Design

3.1 Hardware

Figure 1 shows the manipulator with the ultrasound sensor setup consisting of 18 ultrasound sensors. One can see that most sensors are located on the third axis,

the so called robot hand. The robot hand is the part of the manipulator, which most likely has the smallest distance to a human worker. Therefore, the area surrounding this axis, has to be particularly observed by the ultrasound sensor system. By having the ultrasound sensors mounted directly on the manipulator and not stationary in the HW, the robot becomes independent of the remaining facility and is able to react on nearby objects at any time.

The cuboid shaped hybrid working area is limited by flat plates consisting of stainless steel or glas. The form and orientation as well as the surface properties of these boundaries, affect the performance of the ultrasound sensor system, because ultrasonic waves are reflected directional. As pictured in Fig. 2, the reflection of ultrasonic waves is the main reason for two of the three mentioned measurement errors.

For the recognition of objects, ultrasound sensors of type *pico+35/U* and *pico+35/WK/U* from the company *Microsonic* are used. The time between two distance measurements is 16 ms. The sensors indicate the presence of an object with a distance of 65 mm or below (blind zone) by outputting a 0 V signal value. A signal of 10 V indicates that there is no detectable object present in the detection range of 350 mm. All sensors are working in *Synchronous Mode*, which means that ultrasonic waves of all sensors are emitted simultaneously. Except for the temperature compensation, all integrated filters are deactivated.

3.2 Software

The developed data processing algorithm (see Fig. 3) is running on the Control PC in real-time. It was developed using MATLAB/SIMULINK in combination with the toolboxes Simulink Coder and xPC.

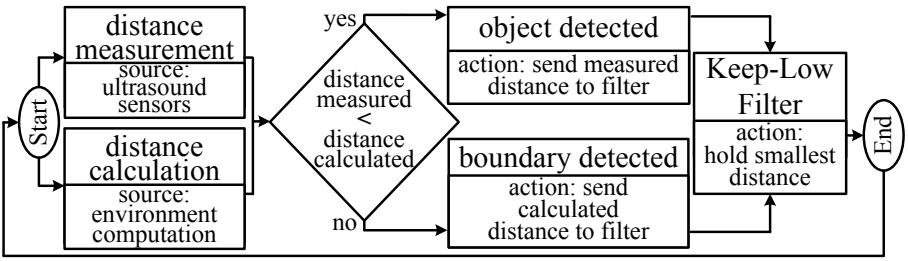

Fig. 3. Flow chart of distance processing algorithm

The pictured algorithm actually consists of two separate algorithms. At first, a distinction between static and dynamic objects takes place. Besides this, measurement errors due to specular reflections and crosstalk-effects are eliminated. The second algorithm is a directional selective filter which receives the processed signals from object elimination (OE) algorithm as an input. The output signal of the filter then is used for the adaption of the manipulators trajectory if a collision with a human operator is imminent.

4 Object Recognition Algorithms

4.1 Distance Calculation

Compared with mobile robots, the cultivation plant setup has the advantage that the manipulator as well as the HW is immobile. By knowing the kinematics of the manipulator in combination with the information from the optical encoders of each joint, the distances of each ultrasound sensor to the boundaries of the HW can be calculated. Figure 4 pictures the relevant coordinate systems (S) for the

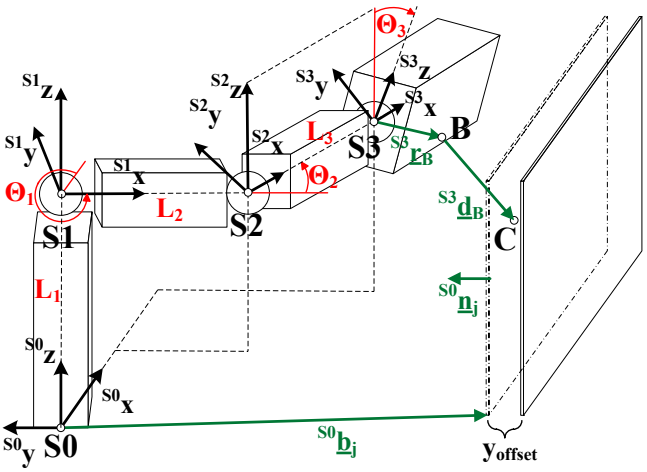

Fig. 4. Coordinate systems involved the distance calculation

distance calculation. With $i = [1, ..., 18]$, the positions ${}^{S3}\boldsymbol{r}_i$ and the orientations ${}^{S3}\boldsymbol{d}_i$ of each sensor i, are gathered from the CAD model of the robot. ${}^{S3}\boldsymbol{r}_i$ and ${}^{S3}\boldsymbol{d}_i$ are constant if referenced on the S3 System. With the rotationmatrix

$$ {}^{S0}\mathbf{R}_{S3} = {}^{S0}\mathbf{R}_{S3}\left(\Theta_1, \Theta_2, \Theta_3\right) \tag{1} $$

and the translational transformation

$$ {}^{S0}\mathbf{T}_{S3} = {}^{S0}\mathbf{T}_{S3}\left(L_1, L_2, L_3, \Theta_1, \Theta_2\right) \tag{2} $$

the homegenous transformation matix

$$ {}^{S0}\mathbf{A}_{S3} = \left[\begin{array}{ccc|c} & {}^{S0}\mathbf{R}_{S3} & & {}^{S0}\mathbf{T}_{S3} \\ \hline 0 & 0 & 0 & 1 \end{array}\right] \tag{3} $$

describes the sensor positions ${}^{S3}\boldsymbol{r}_i$ in the S0-System by

$$ {}^{S0}\boldsymbol{r}_i = {}^{S0}\mathbf{A}_{S3} \cdot {}^{S3}\boldsymbol{r}_i \ . \tag{4} $$

The sensor orientations ${}^{S3}\boldsymbol{d}_i$ are described in the S0-System by

$$ {}^{S0}\boldsymbol{d}_i = {}^{S0}\mathbf{R}_{S3} \cdot {}^{S3}\boldsymbol{d}_i \ . \tag{5} $$

Now, with the positions

$$ {}^{S0}\boldsymbol{b}_j = (x_j \ y_j \ z_j)^T \tag{6} $$

and orientations, defined by the normal vector ${}^{S0}\boldsymbol{n}_j$ of each boundary j, the vector ${}^{S0}\boldsymbol{r}_{BC}$ from every sensor i, to any boundary j, can be calculated with

$$ {}^{S0}\boldsymbol{r}_C = {}^{S0}\boldsymbol{r}_B + \frac{{}^{S0}\boldsymbol{n}_j \bullet \left({}^{S0}\boldsymbol{b}_j - {}^{S0}\boldsymbol{r}_B\right)}{{}^{S0}\boldsymbol{n}_j \bullet {}^{S0}\boldsymbol{d}_i} \cdot {}^{S0}\boldsymbol{d}_i \tag{7} $$

and

$$ {}^{S0}\boldsymbol{r}_{BC} = {}^{S0}\boldsymbol{r}_C - {}^{S0}\boldsymbol{r}_B \ . \tag{8} $$

Finally, the desired calculated distance x_{calc} results with

$$ x_{calc} = |{}^{S0}\boldsymbol{r}_{BC}| = \sqrt{{}^{S0}x_{BC}^2 + {}^{S0}y_{BC}^2 + {}^{S0}z_{BC}^2} \ . \tag{9} $$

The calculation of these distances allows the elimination of the HW boundaries from the distance measuring process, by replacing the distances in which the calculated distance is smaller than the actual measured distance, with a value of 350 mm (maximum detection range). With this approach, no avoiding action of the manipulator takes place, because the measured distance, caused by the HW boundary, is suppressed. In addition, specular reflections on the HW boundaries need no further consideration.

However, crosstalk-effects between adjacent sensors are still an issue which have to be considered. In order to eliminate crosstalk-effects, the algorithm is modified as following. By postponing the computed boundary, pictured in Fig. 4, away from the real boundary (${}^{S0}y_{offset} = 60\,\text{mm}$) and closer to the robot base (S0-System), also the influence of crosstalk-effects can be eliminated. The reason for this is, that whenever a sensor A receives the reflected ultrasonic waves from a adjacent sensor B, a distance, which is close to the real distance from a working area boundary, is indicated by sensor A. Depending on the orientation of the manipulator, this false distance can be bigger or smaller than the calculated distance to the computed boundary. Hence, by postponing the computed or rather simulated boundary from the real boundary, even the incorrect measured distances caused by crosstalk-effects are eliminated, because they are still bigger than the calculated ones.

4.2 Distance Filtering

The developed filter aims to improve the measured distance data concerning the signal quality, in order to use the processed data for plausibilization with the camera system and obstacle avoiding actions of the manipulator. The detection area of a single sensor is limited. So it is possible, that objects, which are located

at the edge of a detection area, are detected by the sensor in one time step and no more detected in the following time step. Another possibility is, that an object is within the detection area of a sensor, but, depending on its geometry, orientation and surface properties, not continuously detected by the sensor. The result of both cases is that the robot control receives a discontinuous signal from the sensor. Hence, a filter is designed to improve the signal quality. The behaviour of the filter is dependent on the following condition. Approaching obstacles must be detected as fast as possible, in order to enable the manipulator, to react quickly with an trajectory adaption action. Therefore, e. g. a PT1 filtering behaviour is disadvantageous, because, depending on the time constant, the obstacle avoiding algorithm of the manipulator would receive non actual distances.

To sum up, sensor signals with a decreasing obstacle to robot distance must not be filtered or modified by the filter. Signals, indicating a increasing distance to the robot must be filtered. Especially if the detected obstacle speed is physically implausible.

The algorithm of the resulting *Keep-Low-Filter* is pictured in Fig. 5. To fulfill the mentioned requirement, the filter has been designed directional selective. If an object is approaching on a sensor, the measured distances are not modified ($x_{i\_\mathrm{out}} = x_i$). On the other hand, if an object decreases its distance to a sensor, the smallest distance value ($x_{i\_\mathrm{out}} = x_{i-1}$) is hold for a certain amount of time steps (t_{hold}), if the change of the measured distance $|(x_i - x_{i-1})|$ between two time steps is bigger than the maximum velocity ($v_{\max} = 0.002\,\frac{\mathrm{m}}{\mathrm{ms}}$) of a human limb [8].

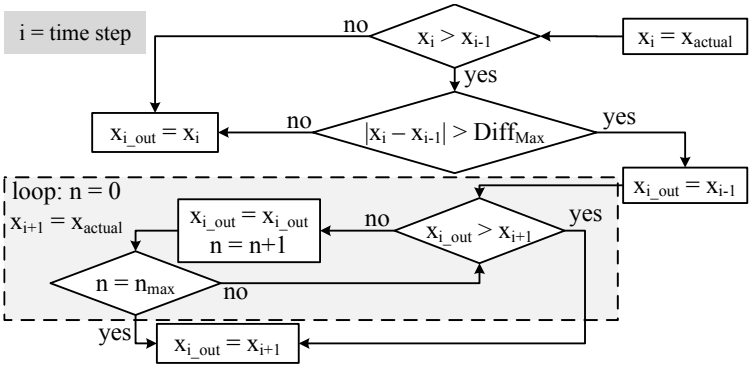

Fig. 5. Keep-Low-Filter algorithm

5 Experimental Results

In the following, the effective detection of a human operator in a confined space, by eliminating the measured distances from static objects, as well as the filtering of desired distances from dynamic objects, is validated by three experiments.

5.1 Object Elimination - Algorithm Validation

To validate the OE algorithm, the manipulator performed an approaching sequence to a single boundary. No objects except for the HW boundary were involved in the test. Hence, at the beginning of the movement, the two relevant sensors (Sensor A & B) in Fig. 6 indicate a distance of $x = 0.35$ m, which corresponds the maximum detection range. During the approach towards the boundary, the measured distances (solid lines), the calculated distances (dotted lines) as well as the resulting distances after the object elimination (dashed curves), have been recorded. In Fig. 6 one can see, that the OE algorithm eliminates distances which are caused by the presence of the HW boundary. Otherwise, the signals processed by the OE algorithm would indicate distances below the maximum detection range.

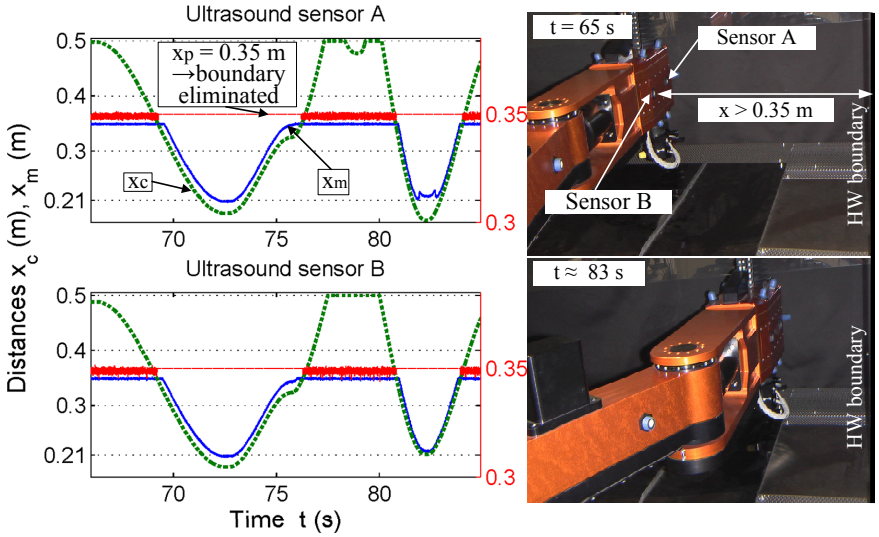

Fig. 6. Experimental validation of the OE algorithm

Also measurement errors are eliminated by the OE algorithm. In the top graph of Fig. 6, crosstalk-effects between both sensors can be seen in the time range between 80 s and 85 s. Due to specular reflections, ultrasound sensor A is not receiving an echo from its ultrasonic waves, but rather receives the ultrasonic waves from Sensor B, which were reflected from the boundary. The result is, that the signal value of sensor A is equal with the signal value from sensor B, as long as the ultrasonic waves from A do not return to sensor A.

5.2 Object Detection and Signal Filtering Validation

The next step, is to improve the detection of dynamic objects. The aim is to reduce a jumping of the distance signal. To validate the filtering algorithm,

a cylindrical shaped glass pipette, which is pictured in Fig. 8 C, was moved into the detection area of a ultrasound sensor. Both signals, filtered and not filtered, have been logged and compared. Concerning the geometry as well as the directly reflecting surface, the described evaluation is a worst case scenario for the ultrasound sensor system. Hence, it is concluded, that if the quality of the sensor signal can be sufficiently improved during the detection of the pipette, also the signals caused by every other object with bigger dimensions and better surface properties (e. g. a human hand) can be sufficiently improved. In Fig. 7 one can see, that the not filtered signal (thin curve) is unsteady and alternates between small and big distances. Due to specular reflections of the ultrasonic waves on the surface of the glas pipette the sensor receives no echo. Therefore, the signal jumps back to a distance of $x = 0.3\,\mathrm{m}$, which in this experiment is the maximum detection range of the ultrasound sensor.

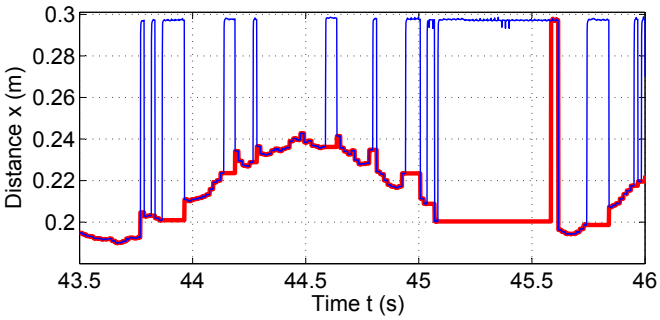

Fig. 7. Signal improvement due to the Keep-Low-Filter algorithm

The broad curve represents the resultant signal after the measured signal was processed by the filter. Whenever the sensor receives an ultrasonic echo from an obstacle in one sample, and no echo in the following sample, the filter holds the last distance value, until a distance, which is smaller than the actually hold value, is detected by the sensor, or the parameterised time ($t_{\mathrm{hold}} = 500\,\mathrm{ms}$), elapses. In this case, the originally held distance value is discarded and the filter outputs the actual measured distance.

This behaviour can be seen in Fig. 7 from $t_1 \approx 45.1\,\mathrm{s}$ to $t_2 \approx 45.6\,\mathrm{s}$. This approach is necessary to allow the robot to continue the movement, when a detected object is removed from the detection areas of the ultrasound sensors.

5.3 Object Elimination - Application Validation

To proof the functionality of the developed algorithms, a third experiment inside the final working area was conducted, in which the manipulator decreased the distance to the HW boundaries and also approached a human operator during a single moving sequence. Figure 8 shows trajectory of the end-effector in the S0-System. In this experiment, a interruption of the manipulators trajectory is

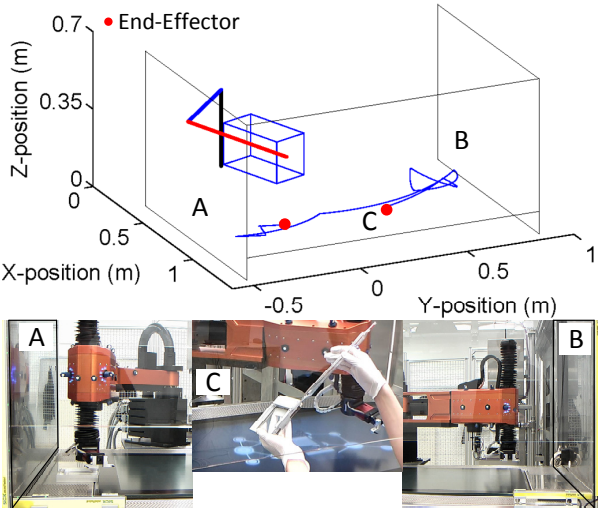

Fig. 8. Experimental validation of the OE algorithm within the facility

triggered (*TriggerStopSequence* in Fig. 10), if any ultrasound sensor is indicating a distance smaller than 0.30 m. The criteria for a successful validation of the algorithms are, that

- the manipulator is able to continue the movement, without any interruptions of the sequence caused by the presence of static objects (front pane and boundaries A & B in Fig. 8).
- a interruption of the trajectory is initiated as soon as the human operator is detected (see picture C in Fig. 8).

Figure 9 shows the calculated distances x_c (dotted lines), the measured distances x_m (solid lines) as well as the distances processed by the OE algorithm and the Filter x_p, during the approach of boundary A (time range 85 s to 120 s) and boundary B (time range 130 s to 150 s).

Both boundaries are successfully eliminated by the algorithm, because the calculated distances are smaller than the acutal measured distances at any time. Therefore, the processed distance, on which a trajectory adaption would be triggered, never falls below the maximum detection range of the ultrasound sensors. To analyse the detection of dynamic objects and the adaption of the sequence based on ultrasound sensor data, a human operator entered the HW during the experiment. The left plot in Fig. 10 pictures the end-effector position in the robot base coordinate system (S0) during the sequence. One can see, that the trajectory is interrupted at second 154 s, because the processed distance x_p of one ultrasound sensor (see the right plot in Fig. 10) decreased below the distance of 0.30 m (due to the presence of the human operator) and therefore triggered the interruption of the sequence.

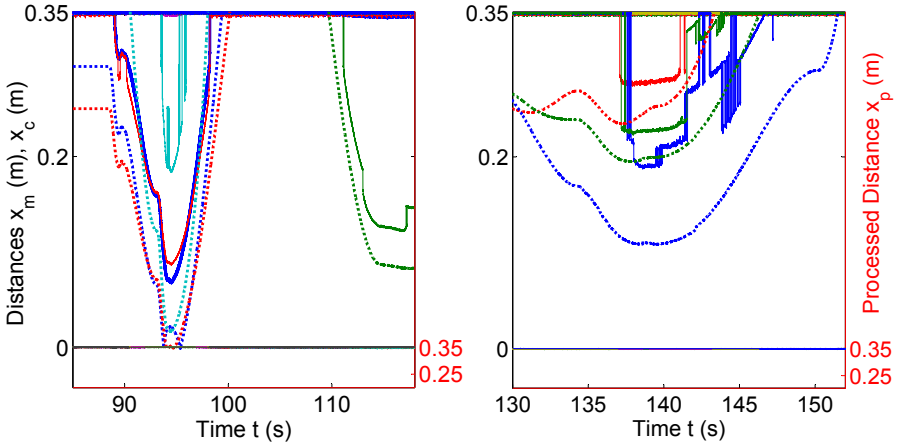

Fig. 9. Distance signals during the approach of boundary A (left plot) and boundary B (right plot)

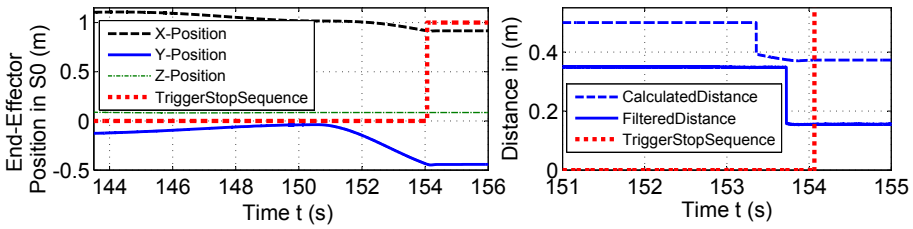

Fig. 10. Trajectory adaption due to detection of human operator

6 Conclusions and Outlook

Algorithms to support the detection of human extremities by an ultrasound sensor system have been developed. One algorithm suppresses measured distances of the ultrasound sensor system, if a static object is detected. Thus, the manipulator is enabled to react with an adaption of its trajectories, based on distances, caused by a human operator. A second algorithm improves the signal quality of the ultrasound sensor system, in order to avoid an undesired alternation between a interruption and a resumption of the manipulators trajectory. The concept of the elimination of undesired measured distances due to static objects was proved under experimental conditions and also under the frame conditions of the finalized facility. Until now, the OE algorithm is only able to distinguish the boundaries of the working area from other detected objects. A possible improvement of the OE algorithm is, that the cameras evaluate the positions and dimensions of the used tools inside the Hybrid Workplace and the gathered information is used to create computed areas, in which measured distances, caused

by the tools inside the HW, are suppressed. The resulting adaptable OE algorithm could suppress the detection of any non-human object inside the HW. A further enhancement of the algorithm is the fusion of the ultrasound sensor data with the camera data, in order to establish a plausibilization between the sensor systems and therefore increase the safety during the collaboration.

Acknowledgment. The authors would like to thank the European Commission for funding the work reported here within the framework of the ManuCyte Project (see [1]). The "Fraunhofer Institute for Manufacturing Engineering and Automation (IPA)" shall be thanked most sincerely as it is the leader of this project consortium within the Seventh Framework Programme (FP7).

References

1. ManuCyte: Modular Manufacturing Platform for Flexible, Patient-Specific Cell Cultivation. Fraunhofer Institute for Manufacturing Engineering and Automation (IPA). Nobelstr. 12, D-70569 Stuttgart, `http://www.manucyte-project.eu/`
2. Höcherl, J.: Recognition of Human Extremities in Monocular Camera Images for Human-Robot Collaboration. In: Applied Research Conference, pp. 236–244 (2012)
3. Heiligensetzer, P.: Aktuelle Entwicklungen bei Industrierobotern im Bereich der Mensch-Roboter Kooperation. Tag der Arbeitssicherheit in Fellbach (2009)
4. Leonard, J.J., Durrrant-Whyte, H.F.: Directed Sonar Sensing for Mobile Robot Navigation. Springer, Germany (1992)
5. Moravec, H.P., Elfes, A.: High Resolution Maps from Wide Angle Sonar. In: Proceedings of IEEE Conference on Robotics and Automation, pp. 116–121 (1985)
6. Yi, Z., Khing, H.Y., Seng, C.C., Wei, Z.X.: Multi-ultrasonic sensor fusion for mobile robots. In: Proceedings of the IEEE Intelligent Vehicles Symposium, pp. 387–391 (2000)
7. Xianzhang, Z., Junfang, Z., Yibo, G., Rui, G., Yiping, Y.: Multi-ultrasonic sensor fusion based on dezert-smarandache theory. In: International Technology and Innovation Conference, pp. 1858–1862 (2007)
8. Thiemermann, S.: Direkte Mensch-Roboter-Kooperation in der Kleinteilmontage mit einem SCARA-Roboter. Ph.D. dissertation, Faculty Mechanical Engineering. University Stuttgart (2005)

Exponential Stabilization of Second-Order Nonholonomic Chained Systems

Zainah Md. Zain[1,2], Keigo Watanabe[2], Kiyotaka Izumi[3], and Isaku Nagai[2]

[1] Faculty of Electrical and Electronic Engineering, Universiti Malaysia Pahang, Pekan Branch, 26600 Pekan, Pahang, Malaysia
[2] Department of Intelligent Mechanical Systems, Division of Industrial Innovation Sciences, Graduate School of Natural Science and Technology, Okayama University, 3-1-1 Tsushima-naka, Kita-ku, Okayama, 700-8530, Japan
[3] Department of Mechanical Engineering, Graduate School of Science and Engineering, Saga University, 1Honjomachi, Saga 840-8502, Japan
zainah@ump.edu.my

Abstract. In this paper, an underactuated control method is considered for an X4-AUV with four thrusters and 6-DOFs. A second-order chained form transformation is introduced to the dynamical model by separating a system into three parts of controller model. Then, the Astolfi's discontinuous control method is applied to realize an underactuated control method to stabilize the system. This approach is motivated by the fact that the discontinuous dynamic model without using a chained form transformation assures only a local stability (or controllability) of the dynamic based control system, instead of guaranteeing a global stability of the system. A computer simulation is presented to demonstrate the effectiveness of our approach.

Keywords: Nonholonomic system, underactuated control system, second-order chained form, discontinuous control.

1 Introduction

Second-order and high-order nonholonomic systems arise very often in the study of mechanical systems. Typical examples include redundant manipulators and underactuated systems [1]. Although the dynamics are well understood and many techniques have been investigated for these systems, controller design of these systems remains a challenging problem. Attempts were made to stabilize second-order or high-order nonholonomic systems recently. Among them, the most notable contribution is due to Laiou and Astolfi [2], who presented discontinuous state feedback laws to stabilize a class of high-order nonholonomic systems with two inputs.

Generally, a class of underactuated mechanical systems can be converted to a second-order chained form by constructing coordinate and input transformations explicitly in Laiou and Astolfi [2]. By converting the system to a second-order chained form, the dynamics are considerably simplified, and thus it is easy for controller design. A chained form is a canonical form for a class of nonholonomic

J. Lee et al. (Eds.): ICIRA 2013, Part II, LNAI 8103, pp. 96–107, 2013.

systems introduced by Murray and Sastry [3]. The class of nonholonomic systems to be studied in this paper is described in the following second-order chained form:

$$\begin{cases} \ddot{y}_1 = u_1 \\ \ddot{y}_2 = u_2 \\ \ddot{y}_3 = y_2 u_1 \end{cases} \tag{1}$$

In this paper, we consider a control problem based on a dynamic model for an underactuated X4-AUV with four inputs and 6-DOFs. To assure a globally asymptotic stability for the dynamic model based control system (or a global controllability for the controlled objective), a canonical form in a second-order chained form consisting of a dynamic model is obtained by separating the original dynamic model into three subsystems so as to use the canonical form studied in Laiou and Astolfi [2]. Here, two subsystems are subject to a second-order nonlinear model with two inputs and three states, and the other subsystem is subject to a linear second-order model with two inputs and two states. Note that the transformation algorithm presented by Laiou and Astolfi [2] cannot apply directly to nonlinear systems with three or more inputs, because of the theoretical inconvenience. Then, the Astolfi's discontinuous control approach is applied for such second-order chained forms, together with use of the controller design method studied by Xu and Ma [4]. The present method can only realize partially underactuated control, which controls five states out of six states by using four inputs.

2 X4-AUV

The X4-AUV with an ellipsoidal hull shape is shown in Fig. 1. The slenderness ratio of the body is 5. Therefore, parameters $r1$, $r2$ and $r3$ that are the lengths of the semi axes of the ellipsoidal vehicle are reduced to $r1 = 5r$ and $r2 = r3 = r$ [5][6]. It has four thrusters to control the position and attitude changes in the motion without using any

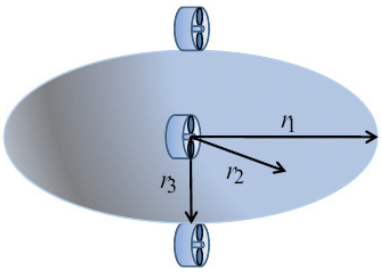

Fig. 1. X4-AUV with an ellipsoidal hull shape

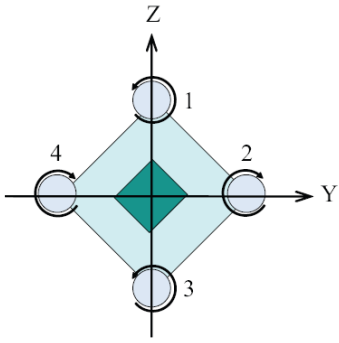

Fig. 2. X4-AUV thrusters (Back view)

steering rudders. It is categorized in underactuated AUVs and also has nonholonomic features. The consideration of nonholomic systems is an interesting study from a theoretical standpoint, because as pointed out in the earlier works of Brockett, they cannot be asymptotically stabilized to a fixed point in the configuration space using continuously differentiable, time-invariant and state feedback control laws [5][6]. As shown in Fig. 2, the arrows around the thrusters indicate the rotational direction of the thrusters. The rotational angles consist of roll, pitch and yaw angles commonly used in guidance and navigation.

2.1 X4-AUV Dynamic Model

Therefore, the dynamic equations of motion for an X4-AUV in Eq. (2) can be written as [5][6][7][8]:

$$\begin{aligned} m_1\ddot{x} &= \cos\theta\cos\psi u_1 \\ m_2\ddot{y} &= \cos\theta\sin\psi u_1 \\ m_3\ddot{z} &= -\sin\theta u_1 \\ I_x\ddot{\phi} &= \dot{\theta}\dot{\psi}(I_y - I_z) + u_2 \\ I_y\ddot{\theta} &= \dot{\phi}\dot{\psi}(I_z - I_x) - J_t\dot{\psi}\Omega + lu_3 \\ I_z\ddot{\psi} &= \dot{\phi}\dot{\theta}(I_x - I_y) - J_t\dot{\theta}\Omega + lu_4 \end{aligned} \tag{3}$$

Applying a partial linearizing technique, it gives

$$\begin{aligned} \ddot{x} &= w_1 \\ \ddot{y} &= \frac{m_1}{m_2}\tan\psi w_1 \\ \ddot{z} &= -\frac{m_1}{m_3}\tan\theta\sec\psi w_1 \\ \ddot{\phi} &= w_2 \\ \ddot{\theta} &= w_3 \\ \ddot{\psi} &= w_4 \end{aligned} \tag{4}$$

where

$$\begin{aligned} w_1 &= \left[\cos\theta\cos\psi u_1\right]/m_1 \\ w_2 &= \left[u_2 - I_z\dot{\theta}\dot{\psi} + I_y\dot{\theta}\dot{\psi}\right]/I_x \\ w_3 &= \left[lu_3 + I_z\dot{\phi}\dot{\psi} - \left(J_t\Omega + I_x\dot{\phi}\right)\dot{\psi}\right]/I_y \\ w_4 &= \left[lu_4 - I_y\dot{\theta}\dot{\phi} + \left(J_t\Omega + I_x\dot{\phi}\right)\dot{\theta}\right]/I_z \end{aligned}$$

In order to apply the algorithm for the conversion of a class of nonlinear systems with two inputs to a high-order chained form using standard tools from differential geometry as discussed in Laoiu and Astolfi,[2] we propose three controllers for subsystems as shown in Fig. 3, where we separate the original model in Eq. (4) into three parts such as

Part 1: x - ψ - y controller

$$\begin{aligned} \ddot{x} &= w_1 \\ \ddot{\psi} &= w_4 \\ \ddot{y} &= \frac{m_1}{m_2}\tan\psi w_1 \end{aligned} \tag{5}$$

Part 2: x - ψ - z controller

$$\begin{aligned} \ddot{x} &= w_1 \\ \ddot{\psi} &= w_4 \\ \ddot{z} &= -\frac{m_1}{m_3}\tan\theta\sec\psi w_1 \end{aligned} \tag{6}$$

Part 1: ϕ - θ controller

$$\begin{aligned} \ddot{\phi} &= w_3 \\ \ddot{\theta} &= w_4 \end{aligned} \tag{7}$$

Now, the subsystems Part 1 and Part 2 are in the form described by Laiou and Astolfi;[2] therefore, such subsystems can be controlled as discussed in Laiou and Astolfi[16] and Xu and Ma [4].

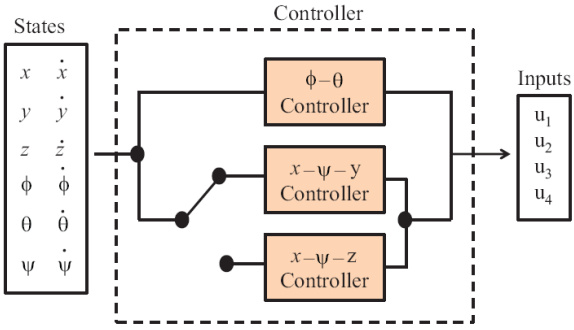

Fig. 3. Concept of the proposed controller

To facilitate the derivation of the stabilizing control law for the second-order form in Eq. (4), the following proposition and lemma are usefull. The proof of the Proposition 1 was presented in Xu and Ma [4].

Proposition 1. *For the linear system*

$$\dot{x}_1 = x_2, \qquad \dot{x}_2 = -s_1 s_2 x_1 - (s_1 + s_2) x_2,$$

if $s_2 > s_1 > 0$, *and the initial states* $(x_1(0), x_2(0))$ *satisfy* $(x_1(0)(s_2 x_1(0) + x_2(0)) > 0$, *then*

$$(1) \quad x_1(t) \neq 0 \quad (\forall t \in [0, \infty)),$$

$$(2) \lim_{t \to \infty} \left(\frac{x_2(t)}{x_1(t)} + s_1 \right) = 0 \tag{8}$$

$$(3) \int_0^\infty \left| \frac{x_2(t)}{x_1(t)} + s_1 \right| dt < \infty \cdot$$

Lemma 1. *For the linear time-varying system*

$$\dot{x} = (A_1 + A_2(t))x, \tag{9}$$

where A_1 *is a constant Hurwitz matrix, and* $A_2(t)$ *a time-varying matrix. If* $A_2(t)$ *satisfies*

$$\lim_{t \to \infty} A_2(t) = 0, \qquad \int_0^\infty \|A_2(t)\| dt < \infty, \tag{10}$$

then $\dot{x} = (A_1 + A_2(t))x$ *is exponentially stable.*

2.2 Converted Systems to Chained Forms and Their Stabilizing Controllers

This section presents the conversion of a two-input nonlinear system to a high-order chained form based on paper by Laiou and Astolfi [2] which we applied to an underactuated X4-AUV (Part 1 and Part 2).

Transformation of Part 1.
Eq. (5) can be written by the following affine system

$$\dot{\chi} = \boldsymbol{f}(\chi) + \boldsymbol{g}_1(\chi) w_1 + \boldsymbol{g}_2(\chi) w_4 \tag{11}$$

where $\chi = (x \quad \dot{x} \quad \psi \quad \dot{\psi} \quad y \quad \dot{y})^T \in \Omega_1 \underline{\Delta} \Re^2 \times \left(-\frac{\pi}{2}, \frac{\pi}{2} \right) \times \Re^3$ is the state vector and the vector fields $\boldsymbol{f}$, $\boldsymbol{g}_1$ and $\boldsymbol{g}_2$ are defined as follows:

$$\boldsymbol{f}(\chi) = [\dot{x} \quad 0 \quad \dot{\psi} \quad 0 \quad \dot{y} \quad 0]^T$$

$$\boldsymbol{g}_1(\chi) = \left[0 \quad 1 \quad 0 \quad 0 \quad 0 \quad \frac{m_1}{m_2} \tan\psi \right]^T$$

$$\boldsymbol{g}_2(\chi) = [0 \quad 0 \quad 0 \quad 1 \quad 0 \quad 0]^T$$

It can be easily shown that the choice $(n_1, n_2) = (2, 4)$ yields the distributions

$$
\begin{aligned}
\Delta_0 &= \operatorname{span}\{\boldsymbol{g}_1, \boldsymbol{g}_2, \operatorname{ad}_f \boldsymbol{g}_1, \operatorname{ad}_F \boldsymbol{g}_2, \operatorname{ad}_F^2 \boldsymbol{g}_2, \operatorname{ad}_F^3 \boldsymbol{g}_2\} \\
\Sigma_1 &= \operatorname{span}\{\boldsymbol{g}_1, \operatorname{ad}_f \boldsymbol{g}_1\} \\
\Sigma_2 &= \operatorname{span}\{\boldsymbol{g}_1\} \\
\Delta_1 &= \operatorname{span}\{\boldsymbol{g}_2, \operatorname{ad}_F \boldsymbol{g}_2, \operatorname{ad}_F^2 \boldsymbol{g}_2, \operatorname{ad}_F^3 \boldsymbol{g}_2\} \\
\Delta_2 &= \operatorname{span}\{\boldsymbol{g}_2, \operatorname{ad}_F \boldsymbol{g}_2, \operatorname{ad}_F^2 \boldsymbol{g}_2\}
\end{aligned} \tag{12}
$$

where $F = \boldsymbol{f} + \boldsymbol{g}_1$ and

$$
\begin{aligned}
\operatorname{ad}_f \boldsymbol{g}_1(\chi) &= \left[-1 \quad 0 \quad 0 \quad 0 \quad -\frac{m_1}{m_2}\tan\psi \quad \frac{m_1}{m_2}\frac{\dot{\psi}^2}{\cos^2\psi} \right]^T \\
\operatorname{ad}_F \boldsymbol{g}_2(\chi) &= \left[0 \quad 0 \quad -1 \quad 0 \quad 0 \quad 0 \right]^T \\
\operatorname{ad}_F^2 \boldsymbol{g}_2(\chi) &= \left[0 \quad 0 \quad 0 \quad 0 \quad 0 \quad \frac{m_1}{m_2}\frac{1}{\cos^2\psi} \right]^T \\
\operatorname{ad}_F^3 \boldsymbol{g}_2(\chi) &= \left[0 \quad 0 \quad 0 \quad 0 \quad -\frac{m_1}{m_2}\frac{1}{\cos^2\psi} \quad 2\frac{m_1}{m_2}\frac{\psi\dot{\psi}}{\cos^2\psi} \right]^T
\end{aligned}
$$

The distribution Δ_0 is full rank locally around the origin and it can be easily verified that the distributions $\sum_1$, $\sum_2$, Δ_1, and Δ_2 are involutive on Ω_1. The functions $h_1 = x$ and $h_2 = y$ satisfy conditions (C5) and (C6), respectively, for $(n_1, n_2) = (2, 4)$. In order to satisfy the condition (C5), h_1 should be

$$
\frac{\partial h_1}{\partial x} = \begin{bmatrix} 1 & 0 & 0 & * & 0 & 0 \end{bmatrix} \Rightarrow h_1 = x
$$

and h_2 should satisfy the condition (C6)

$$
\frac{\partial h_1}{\partial x} = \begin{bmatrix} * & * & 0 & 0 & 1 & 0 \end{bmatrix} \Rightarrow h_2 = y
$$

Then, it follows that

$$
\begin{aligned}
z_{11} &= h_1 = x \\
z_{12} &= L_f h_1 = \dot{x} \\
z_{21} &= L_{g_1} L_f h_1 = \frac{m_1}{m_2}\tan\psi \\
z_{22} &= L_f L_{g_1} L_f h_1 = \frac{m_1}{m_2}\frac{\dot{\psi}}{\cos^2\psi} \\
z_{31} &= h_1 = y \\
z_{32} &= L_f h_1 = \dot{y}
\end{aligned} \tag{13}
$$

which gives

$$v_1 = w_1$$
$$v_2 = 2\frac{m_1}{m_2}\tan\psi\frac{\dot{\psi}}{\cos^2\psi} + \frac{m_1}{m_2}\frac{1}{\cos^2\psi}w_4 \tag{14}$$

Note now that Step IV can also be positively completed.

Taking the time derivatives of the states z_{ij}, for $i = 1, 2, 3$ and $j = 1, 2$, yields the second-order generalized chained form

$$\begin{aligned} z_{11}^{(2)} &= v_1 \\ z_{21}^{(2)} &= v_2 \\ z_{31}^{(2)} &= z_{21}v_1 \end{aligned} \tag{15}$$

System in Eq. (15) is in the form described by Eq. (1) and it can, therefore, be controlled as discussed in Laiou and Astolfi [2].

Let

$$\begin{aligned} z_{11}^{(2)} &= \ddot{x}_1 = v_1 \\ z_{21}^{(2)} &= \ddot{x}_2 = v_2 \\ z_{31}^{(2)} &= \ddot{x}_3 = z_{21}v_1 \end{aligned} \tag{16}$$

and

$$\begin{aligned} x_1 &= y_1 \equiv z_{11} \\ x_2 &= \dot{y}_1 \equiv \dot{z}_{11} \underline{\underline{\Delta}} z_{12} \\ x_3 &= y_2 \equiv z_{21} \\ x_4 &= \dot{y}_2 \equiv \dot{z}_{21} \underline{\underline{\Delta}} z_{22} \\ x_5 &= y_3 \equiv z_{31} \\ x_6 &= \dot{y}_3 \equiv \dot{z}_{31} \underline{\underline{\Delta}} z_{32} \end{aligned} \tag{17}$$

the second-order chained form in Eq. (16) can be rewritten as

$$\begin{aligned} \dot{x}_1 &= x_2 \\ \dot{x}_2 &= v_1 \\ \dot{x}_3 &= x_4 \\ \dot{x}_4 &= v_2 \\ \dot{x}_5 &= x_6 \\ \dot{x}_6 &= x_3v_1 \end{aligned} \tag{18}$$

Designing the control input v_1 such as

$$v_1 = -(s_1 + s_2)x_2 - s_1s_2x_1 \tag{19}$$

where $s_2 > s_1 > 0$ are constants, then $x_1(t) \neq 0 \quad (\forall t \in [0,\infty))$ is guaranteed by Proposition 1, and so the coordinate transformations

$$\begin{aligned} z_i &= x_i && , (i = 1, 2, 3, 4) \\ z_i &= \frac{x_i}{x_1} && , (i = 5, 6) \end{aligned} \tag{20}$$

are well defined. In the new coordinates $z_i (i = 1, \cdots, 6)$, Eq. (18) becomes

$$\begin{aligned} \dot{z}_1 &= z_2 \\ \dot{z}_2 &= -(s_1 + s_2) z_2 - s_1 s_2 z_1 \\ \dot{z}_3 &= z_4 \\ \dot{z}_4 &= v_2 \\ \dot{z}_5 &= z_6 + s_1 z_5 - \left(\frac{z_2}{z_1} + s_1 \right) z_5 \\ \dot{z}_6 &= s_1^2 z_3 + s_1 z_6 - \left(\frac{z_2}{z_1} + s_1 \right) \left[(s_1 + s_2) z_3 + z_6 \right] \end{aligned} \tag{21}$$

Eq. (21) can be reorganized compactly as

$$\begin{aligned} \dot{z}_1 &= z_2 \\ \dot{z}_2 &= -(s_1 + s_2) z_2 - s_1 s_2 z_1 \\ \dot{Z}_{3-6} &= (A_1 + A_2(t)) Z_{3-6} + B_1 v_2 \end{aligned} \tag{22}$$

where $Z_{3-6} \underline{\Delta} [z_3, z_4, z_5, z_6]^T$, and

$$A_1 = \begin{bmatrix} 0 & 1 & 0 & 0 \\ 0 & 0 & 0 & 0 \\ 0 & 0 & s_1 & 1 \\ s_1^2 & 0 & 0 & s_1 \end{bmatrix} \quad A_2(t) = \left(\frac{z_2}{z_1} + s_1 \right) \begin{bmatrix} 0 & 0 & 0 & 0 \\ 0 & 0 & 0 & 0 \\ 0 & 0 & -1 & 0 \\ -(s_1 + s_2) & 0 & 0 & -1 \end{bmatrix} \quad B_1 = \begin{bmatrix} 0 \\ 1 \\ 0 \\ 0 \end{bmatrix}$$

By Proposition 1, we know

$$\lim_{t \to \infty} \left(\frac{z_2}{z_1} + s_1 \right) = 0, \int_0^\infty \left| \frac{z_2}{z_1} + s_1 \right| dt < \infty$$

It follows that

$$\lim_{t \to \infty} A_2(t) = 0, \int_0^\infty \| A_2(t) \| dt < \infty$$

Now let us check the controllability of $[A_1, B_1]$. Its controllability matrix can be calculated as $C_n = \left[B_1, A_1B_1, A_1^2B_1, A_1^3B_1\right]$, which gives the matrix described below,

$$C_n = \begin{bmatrix} 0 & 1 & 0 & 0 \\ 1 & 0 & 0 & 0 \\ 0 & 0 & 0 & s_1^2 \\ 0 & 0 & s_1^2 & s_1^3 \end{bmatrix}$$

which is nonsingular because $s_1 > 0$. Therefore, $[A_1, B_1]$ is controllable and we can choose a feedback gain matrix $L = [l_1, l_2, l_3, l_4]$ so that the matrix $A_1 + B_1L$ is a Hurwitz matrix, i.e., the control input

$$\begin{aligned} v_2 &= LZ_{3-6} = l_1z_3 + l_2z_4 + l_3z_5 + l_4z_6 \\ v_2 &= l_1\frac{m_1}{m_2}\tan\psi + l_2\frac{\dot{\psi}}{\cos^2\psi} + l_3\frac{y}{x} + l_4\frac{\dot{y}}{x} \end{aligned} \tag{23}$$

can exponentially stabilize the linear system

$$\dot{Z}_{3-6} = A_1Z_{3-6} + B_1v_2$$

From Lemma 1 in Xu and Ma [4], we can conclude that the system

$$\dot{Z}_{3-6} = (A_1 + B_1L + A_2(t))Z_{3-6}$$

is exponentially stable, i.e., system

$$\dot{Z}_{3-6} = (A_1 + A_2(t))Z_{3-6} + B_1v_2$$

can be exponentially stabilized to the origin by the following feedback control

$$v_2 = LZ_{3-6}$$

Since the states z_1 and z_2 are exponentially convergent to zeros, the whole states $z_i(i = 1, \cdots, 6)$ converge to zeros exponentially.

From $x_i = z_i$ (i = 1, 2, 3, 4); $x_i = z_iz_1$ (i = 5, 6), we can conclude that $x_i(i = 1, \cdots, 6)$ converge to zeros exponentially, and so do $(y, \dot{y})$. The above results are summarized in the following theorem.

Theorem 1. *If the initial states* $(y_1(0), \dot{y}_1(0))$, *satisfy* $y_1(0)(s_2y_1(0) + \dot{y}_1(0)) > 0$, *and* $L = [l_1, l_2, l_3, l_4]$ *is chosen such that* $A_1 + B_1L$ *is a Hurwitz matrix, then the second-order chained form in Eq.* (18) *can be exponentially stabilized to the origin by the following control law:*

$$\begin{aligned} v_1 &= -s_1s_2y_1 - (s_1 + s_2)\dot{y}_1 \\ v_2 &= l_1y_2 + l_2\dot{y}_2 + l_3\frac{y_3}{y_1} + l_4\frac{\dot{y}_3}{y_1} \end{aligned} \tag{25}$$

where $s_2 > s_1 > 0$ *are two constants.*

From the fact of

$$w_1 = v_1$$
$$w_4 = -\tan\psi\dot{\psi} - \frac{\dot{\psi}}{\cos^2\psi} - \frac{m_3}{m_1}\frac{v_2}{\tan\theta\sec\psi\tan\psi} \tag{26}$$

the actual control inputs can be calculated as

$$u_1 = \frac{m_1}{\cos\theta\cos\psi}w_1$$
$$u_4 = \frac{I_z}{l}w_4 - \dot{\phi}\dot{\theta}\frac{I_x - I_y}{l} - J_t\dot{\theta}\Omega \tag{27}$$

The transformation of Part 2 by using Eq. (6) follows the same steps as used in the transformation of Part 1.

3 Results and Analysis

To verify the proposed control scheme, the motion for the 6-DOFs of an X4-AUV is simulated in SCILAB. In this paper, Part 1 (x - ψ - y controller model) was simulated and the results are shown in Fig. 4. The system for x - ψ - y controller model started with an initial states $(x, \dot{x}, y, \dot{y}, z, \dot{z}, \phi, \dot{\phi}, \theta, \dot{\theta}, \psi, \dot{\psi}) = (1,0,0.5,0,1,0, \pi/6,0, \pi/4,0, \pi/4,0)$, and other parameters that are used in simulations are s_1 = 1/40, s_2 = 0.45, k_1 = 0.8, k_2 =1.2, k_3 = 0.6, k_4 = 0.7, l_1 = –0.1830, l_2 = –0.6845, l_3 = –1.7373, and l_4 = –38.7179. As shown in Figs. 4, the states related to the rotational angles and their rates converge to zero, while for positions, only the states related to the x- and y-positions for x - ψ - y controller model can be stabilized to origin.

The present method can only realize partially underactuated control, which controls five states out of six states by using four inputs. In order to realize full underactuated control, where all the states will converge to the origin by using four inputs, a switching strategy that combines two controllers, i.e., x - ψ - y controller and x - ψ - z controller should be implemented.

4 Conclusion and Future Works

We have presented a partially underactuated control method for stabilizing all attitudes and partial positions (x and y or x and z) out of full states of an underactuated X4-AUV with four thrusters and 6-DOFs. The system was separated into three parts of controller model to enable the system converted into second-order chained form by coordinate and input feedback transformations. A transformation to the control-affine form by applying a partial linearization technique helps to realize the application of this controller. A discontinuous time-invariant state feedback control law is derived to stabilize the second-order chained form. It has been proved that the proposed control

law is able to stabilize the second-order form exponentially, when the initial state is in or has been driven into certain regions of state space. Simulations on the X4-AUV were conducted to demonstrate the effectiveness of the proposed control scheme. In future work, we are going to develop a switching strategy that combines two controllers, i.e., x - ψ - y controller and x - ψ - z controller, to realize full underactuated control, where all the states will converge to the origin by using four inputs.

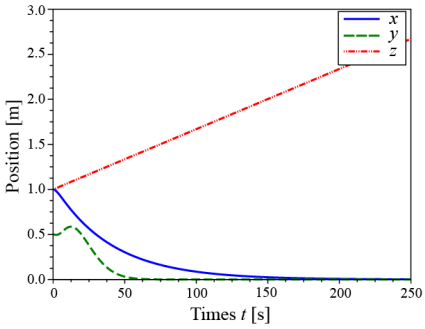

(a) Position control

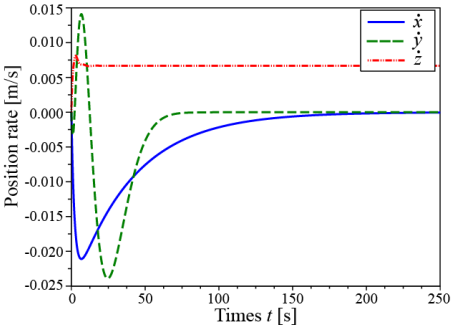

(b) Position rate control

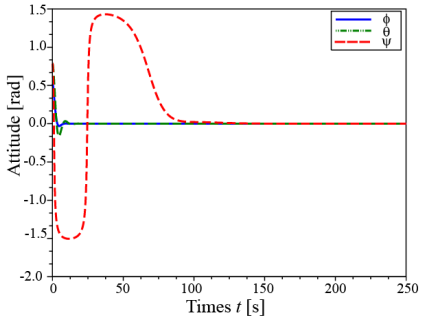

(c) Attitude control

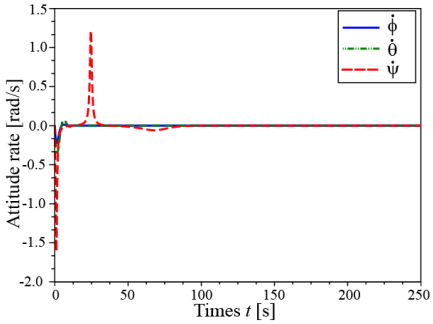

(d) Attitude rate control

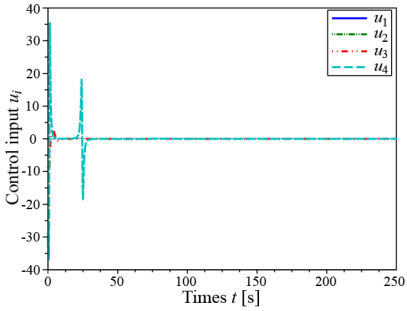

(e) Control inputs

Fig. 4. A case for stabilizing the orientation angles and x- and y-positions

References

1. Ge, S.S., Sun, Z., Lee, T.H., Spong, M.W.: Feedback Linearization and Discontinuous Control of Second-Order Nonholonomic Chained Systems. In: Proc. of the 2001 IEEE International Conference on Control Applications, pp. 5–7 (2001)
2. Laiou, M., Astolfi, A.: A Local Transformations to Generalized Chained Forms. In: Sixteenth International Symposium on Mathematical Theory of Networks and Systems, MTNS 2004 (2004)
3. Murray, R., Sastry, S.S.: Nonholonomic Motion Planning: Steering Using Sinusoids. IEEE Transactions on Automatic Control 38, 700–716 (1993)
4. Xu, W.L., Ma, B.L.: Stabilization of Second-order Nonholonomic Systems in Canonical Chained Form. Original Research Article Robotics and Autonomous Systems 34(4), 223–233 (2001)
5. Zain, Z.M., Watanabe, K., Danjo, T., Izumi, K., Nagai, I.: Modeling an Autonomous Underwater Vehicle with Four-thrusters. In: The Fifteenth International Symposium on Artificial Life and Robotics (AROB 2010), pp. 934–937 (2010)
6. Zain, Z.M., Watanabe, K., Danjo, T., Izumi, K., Nagai, I.: A nonholonomic control method for stabilizing an X4-AUV. Artificial Life and Robotics 16(2), 202–207 (2011)
7. Zain, Z.M., Watanabe, K., Izumi, K., Nagai, I.: A Discontinuous exponential stabilization law for an underactuated X4-AUV. Artificial Life and Robotics, 1–7 (December 11, 2012)
8. Zain, Z.M., Watanabe, K., Izumi, K., Nagai, I.: Stabilization of an underactuated X4-AUV using a discontinuous control law. Indian Journal of Geo-Marine Sciences (IJMS) 41(6), 589–598 (2012)

Development of an Autonomous RC-car

Daniel Claes, Joscha Fossel, Bastian Broecker, Daniel Hennes, and Karl Tuyls

Department of Knowledge Engineering
Maastricht University
Maastricht, The Netherlands
http://swarmlab.unimaas.nl

Abstract. In this paper we tackle the development of a robotic-car with hardware control, lane detection, mapping, localization and path planning capabilities. We aim for a completely independent, reliable and robust system that can traverse a single lane track bordered by white lines on an optimal path. To detect the track boundaries, we implement two different approaches. A RANSAC approach, which approximates the lines by random sampling of splines, and a polyline approach, which applies primitive image processing in combination with a road model. To map the environment, odometry and vision-based information is fused by a particle filter based Simultaneous Localization and Mapping system. The map is afterwards used in conjunction with Adaptive Monte Carlo Localization. For path planning, a one step continuous-curvature approach based on sensor or maps data is used. To offer more detailed information about the environment, we introduce a generic map analysis system. It is employed to evaluate the efficiency of certain paths on the track.

Keywords: Robot design, development and control, Planning, Navigation.

1 Introduction

In this paper we introduce the Autonomous RC-car (ARCC) as a car-like vehicle research platform. Car-like vehicles are defined as four wheeled vehicles with two fixed rear wheels and two directional front wheels. An advanatge of this concept over common differential drive vehicles is the lower friction of the wheels, which allows for higher speeds.

Car-like vehicles are an interesting subject regarding autonomy. Since cars are a standard concept for personal human transportation, the use of self-driving vehicles could reduce traffic congestions. To that extent, such a system might allow for shorter safety distances between vehicles. Furthermore, by communicating with other cars and acting accordingly exceeding road capacities could be avoided. (Semi-)autonmous cars could also assist people who are unable to drive, such as elderly or handicapped persons.

By combining various fields of research we aim to develop the ARCC so that it can detect street boundaries, map an unknown environment, locate its position, plan a path to a set target-state and follow this path. This system has to be completely autonomous without using any external computation or external motion

J. Lee et al. (Eds.): ICIRA 2013, Part II, LNAI 8103, pp. 108–120, 2013.

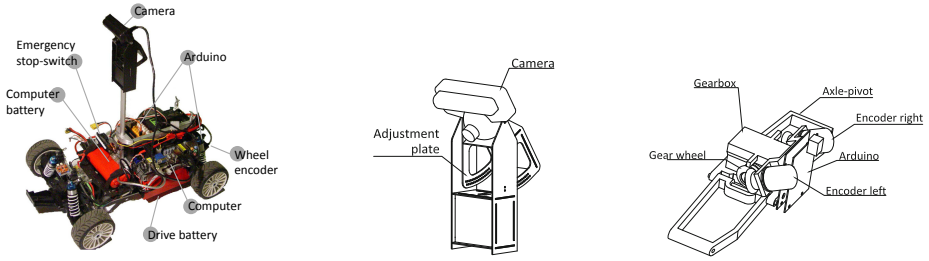

Fig. 1. Left: Final chassis. Center: Camera mount. Right: Wheel encoder mount.

capturing system. To provide similarity to real street scenarios, we define our test environment as a race-track bounded by white side lines. This environment is to be traversed autonomously by the vehicle. To increase the difficulty of the course, it contains curve combinations like S-curves and hairpin bends.

The ARCC is based on a standard 1 : 8 scale RC-car chassis additionally equipped with an onboard computer, RGB camera, wheel encoders and peripheral electronics. The motivation for using a RGB camera instead of time-of-flight sensors like laser or sonar based range scanners, is the lack of physical height of track boundaries in the target environment. Hence, we employ a visual sensor based line detection approach. Via a particle filter, wheel odometry and distance measurements provided by the line detection algorithm, are fused. The resulting map of the environment is the basis for adaptive monte carlo localization (AMCL). To navigate from start to destination the space is discretized, allowing for best-first search based planning. The mathematical model of the car used is kinematic, i.e. no slipping or sliding is considered.

2 The Autonomous RC-Car (ARCC)

This section introduces the autonomous RC-car (ARCC). The design and control are explained and shown.

Chassis. The chassis of a vehicle is an underlying frame, a running gear (engine, transmission, drive-shaft, differential and suspension) and a steering system. Our chassis includes a brushless DC electric motor, which is controlled by a proprietary drive controller. Commercially RC cars are designed to drive at full throttle so we have modified the car to operate at a slower speed. This modification includes an exchange of the drive controller and a maximisation of the gear ratio. The original setup is changed from a 45:15 to a 45:10 ratio; this reduces the maximum velocity by approximately 34%. Additionally a Camera, a computing unit and wheel encoders are attached to the car (Fig. 1 (left)). For safety and duration issues, drive and computer batteries are separate, as explained in more detail below.

Camera Mount. In order to transform a two dimensional image point into the three dimensional space of the car, we require the camera's extrinsic parameters

(tilt-, pitch-, yaw-angle and height above ground). In order to fulfil this requirement the camera is mounted at a fixed height of 43 cm. For more flexibility we construct a mount with an adjustable and measurable tilt angle. It can be set to angles between 0 and -45 degrees, with an incremental step width of one degree (see Figure 1 (center)).

Batteries. The energy supply is provided by two separate sets of batteries. One set provides electricity for the computer and the other provides electricity for the driving hardware (motor and servos). This separation allows us to cut-off the driving battery in the event of an emergency, but retains power to the computer. Both battery sets are a composition of $LiFePO_4$ batteries. In order to trigger an emergency cut-off a receiver is added to the robot. This receiver is completely independent from the rest of the system. A small servo is connected to the receiver. The servo can trigger a switch, which immediately cuts-off the energy to the motor.

Encoder Mount. Two encoders with the resolution of 200 ticks per revolution are connected to rear-left and the rear-right axis. Through their differential it is possible to compute the rotation of the car. A special mount is designed in order to attach these sensors to the car. Both sensors are mounted at a 45-degree angle to the back of the car. Gear wheels are installed on the axis and the shaft of the encoder to translate the rotation of the axis to the encoder (see Figure 1 (right)).

Steering Control. When steering at a fixed angle a car is traveling a path that can be described as a circle; its center is located on a line along the rear axis. The turning-radius depends on the wheel-base (distance between front- and rear-wheels) and the track. The robot uses a steering geometry that is commonly known as *Ackerman steering* [12]. Due to the use of Ackerman steering and mechanical backlash, the steering angle is not exactly equal to the rotation angle of the servo. To estimate the correlation between servo-angle and steering-angle we gather data via odometry in a test scenario. This results in a set of two-dimensional points, the servo-angle as X-component and the actual steering angle as Y-component. These points are approximated by a B-spline [5], which is then used to calculate the servo angle to a desired steering angle.

Velocity Control. The control of the robot's velocity is a feedback control system, which means it constantly compares current speed and target speed. If the two differ, it adjusts the current speed command. The current velocity can be determined by analyzing the odometry data. A Proportional Integral Derivative (PID) controller is used to regulate the speed; its parameter are tuned by applying the *Ziegler-Nichols Method*.

3 Vision System, Mapping and Localization

The main task of the vision system is to accurately detect the line markings even with sensor noise, reflections and while the ARCC is moving at high speeds. Furthermore, it forms the basis for mapping and localization. This section explains

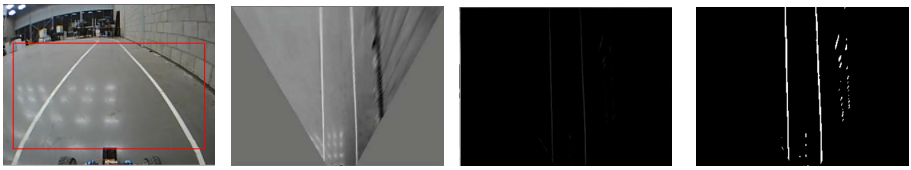

(a) Camera image (b) IPM (c) Threshold image (d) Binary image

Fig. 2. Preprocessing example

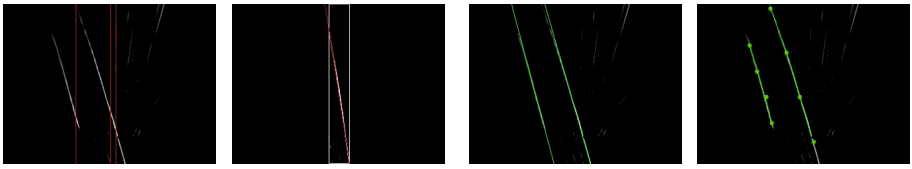

(a) Hough grouping (b) RANSAC detection window (c) RANSAC lines (d) Fitted splines

Fig. 3. RANSAC line detection

the two different algorithms used for detecting the line markings. Additionally, the approaches to tackle mapping and localisation are explained.

3.1 Vision System

Two different algorithms are used to detect road markings. The first approach uses a RANSAC [7] line fitting algorithm; the second approach uses a polyline approach with a road model. The perspective effect in a camera image causes parallel lines to appear to converge at the horizon. In order to eliminate this effect, both lane detection techniques apply Inverse Perspective Mapping (IPM) [2]. Further preprocessing involves two image filtering techniques, a threshold image and a binary image filter [11] (see Figure 2).

RANSAC Line Detection. After preprocessing the IPM image, the following techniques are used to detect the borderlines of the track: A simplified version of Hough Transformation to count the number of lines, followed by RANSAC [7] line fitting to robustly fit these lines.

The simplified Hough transform extracts a sum of values in each column of the threshold filtered image. This sum is then smoothed by a Gaussian filter, and local maxima are detected to determine the positions of lines. Lastly, nearby lines are grouped together to eliminate multiple responses to the same line. The algorithm applies RANSAC line fitting on a window around each of the detected lines.

The previous methods provide candidate lines that are refined via a spline fitting algorithm applied to an area around each line. For a detailed description of the spline fitting we refer to [1]. Figure 3 shows the steps of the algorithm.

Polyline Line Detection. In order to avoid dependence on the output of computationally expensive random processes as used in the previous RANSAC approach, a second approach is implemented.

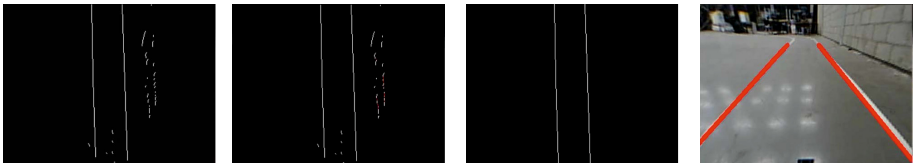

(a) Approximation (b) Fusion. (c) Road model filter (d) Projection result

Fig. 4. Polyline detection

This algorithm uses the IPM-binary image as input. The first step is to determine the near vertical lines in the image. It starts by scanning the picture horizontally line by line, from the bottom to the top to build chains of non-zero pixels. If a white pixel is found, the distance to the nearest extreme of a chain is calculated. If the distance is less than a given threshold, the pixel is assigned to the chain, otherwise a new chain is formed where the pixel is the start point. Afterwards, the chains are approximated by a sequence of lines (polylines) as illustrated in Figure 5 (left).

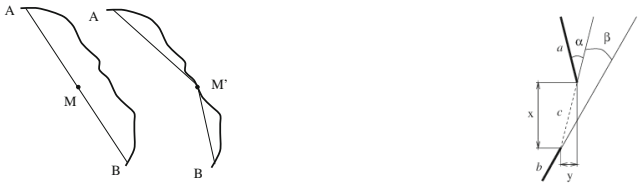

Fig. 5. Approximation and fusion. Left: Approximation of a pixel chain. If the horizontal distance between the midpoint M and the chain exceeds a certain threshold, the line is split into two new lines. Right: Fusion of two polylines. Only when the presented parameters are within a defined threshold, the lines are joined by the line c.

Further processing is sensible, since light conditions and light reflections on the ground can cause gaps in the detected lines. The system attempts to fuse polylines if they fulfil certain requirements as shown in Figure 5 (right).

Assuming the racetrack is a one-lane road, the system searches for two parallel polylines. The intersections among polylines and a set of equidistant horizontal lines are considered to compute the horizontal distances between each pair of polylines. The variance of these distances determines if two polylines are categorized as parallel.

The longer the polyline the higher the probability that it corresponds to a road marking, according to [3]. This fact is employed to validate if the two longest

lines are the most probable candidates for the lane markings. All steps of this algorithm are visualised in Figure 4.

3.2 Mapping and Localization

Creating maps of an environment and localization are fundamental tasks in the field of autonomous robotics. Simultaneous Localization And Mapping (SLAM) is considered to be a complex problem, because to localize itself a robot needs a consistent map and in order to acquire the map the robot requires a good estimate of its location.

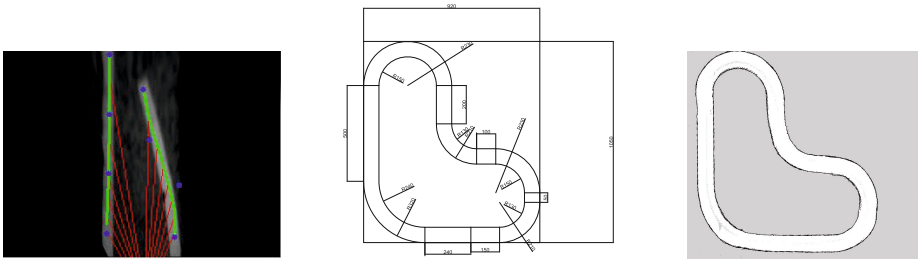

Fig. 6. Left: A simulated laser scan using the intersections of the ARCC's position to the detected lines. Center: Construction plan of the track. Right: Result of the mapping after driving three continuous laps.

This mutual dependency among the pose and the map estimates makes the SLAM problem particularly difficult to solve and requires searching for a solution in a high-dimensional space.

GMapping. We apply an implemented SLAM algorithm called GMapping. The algorithm is provided by the Robot Operating System (ROS) and is based on a *Rao Blackwellized Particle Filter* [6].

The basic idea of the SLAM Rao-Blackwellized particle filter is to estimate the joint posterior probability $p(x_{1:t}, m \,|\, z_{1:t}, u_{1:t-1})$ of the map m and the trajectory $x_{1:t} = x_1, \ldots, x_t$ of the car [10]. This estimation is achieved through the observations $z_{1:t} = z_1, \ldots, z_t$ and the odometry measurements $u_{1:t} = u_1, \ldots, u_{t-1}$. The observations are simulated laser-scans produced by calculating intersections between virtual rays origin at the car's position and the lines detected by the vision system (Figure 6 (left)). The center image represent the construction plan of the track and the right image illustrates the outcome of the mapping algorithm. This result was retained after three continuous laps of the robot. Each map completely overlays the map obtained from the previous lap. This indicates that the sensor data is reliable and provides consistent information for every lap.

Adaptive Monte Carlo Localization. Localization is used in the field of mobile robotics to identify a robot's position and orientation in a known environment. After the environment information is obtained, we apply a particle

filter based localization algorithm, more specifically adaptive monte-carlo localization (AMCL) [8]. Similar to GMapping, this method samples particles and resamples them based on their importance. Furthermore, AMCL has the ability to dynamically adapt the number of particles, where each particle represents a potential position and orientation of the robot.

4 Autonomous Drive and Map Analysis

This section explains the algorithms used for autonomous drive, namely sensor- and map-based continuous curvature path planning. Furthermore we introduce a general map analysis algorithm to efficiently calculate the covered track distance.

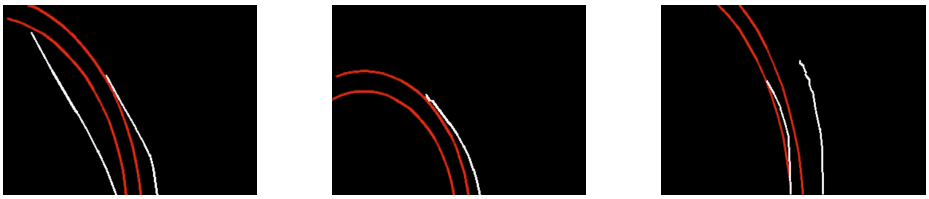

Fig. 7. Situations for sensor-based CCPP. Left: Normal situation. Center: Only one line detected. Right: One wheel is on the line marking.

4.1 Continuous Curvature Path Planning (CCPP)

We implement continuous curvature path planning (CCPP). The basic idea is to determine the steering angle that provides the longest path without any collisions with the track boundaries. The path can be a curve or a straight line depending on the steering angle. By calculating the intersection of the left-wheel- and the right-wheel path with the track, we can assure that the car does not leave the track. No dynamic constraints are considered, so we assume every curve can be driven at the same speed. The quality of a curve/straight line is thereby only evaluated in terms of its length and the longest continuous path is chosen for the next steering command. In the case of our robot, the steering angle is restricted by the car's steering geometry to a value between -31 and 24 degrees with an incremental step size of one degree.

Sensor-Based CCPP. As a preliminary control algorithm we implement an approach that does not require any map or localisation data. It is a reactive approach with the assistance of the visual data and a fixed velocity. This simple drive technique can be used in order to map an unknown environment or to gather enough data to localize the car.

Difficulties occur when one wheel leaves the track or is directly on the line. For example, in the case of Figure 7, the planned path will cause the car to leave the track or when only one line of the track is detected. Additionally, due to the camera's restricted view and inability to see long distances, this planning method is unsuitable for high-speed travel.

Map-Based CCPP. To improve the quality of the planning, we base the CCPP on the map obtained through GMapping in conjunction with pose estimates acquired by AMCL. In comparison to the previous method, where the scope was on the environment in the field of view of the camera, is it now possible to take into account the whole environment and its position relative to the robot. Similar to the raw sensor data approach, we calculate the intersection of the left-wheel- and the right-wheel path with the track, however, now based on the pose estimate of the ARCC in the known map.

The map is represented as a grid. In order to minimize the effort in collision detection, we decided to adapt the Bresenham line and circle algorithm [4]. This algorithm is used in the field of computer graphics to form a close approximation of straight lines or circles in grids. Figure 8 shows the Bresenheim algorithm for lines and circles and the map-based CCPP.

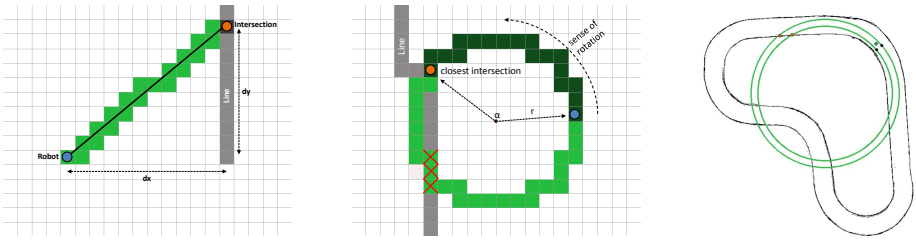

Fig. 8. Overview of map-based CCPP. Left: Bresenheim line intersection. Center: Bresenheim nearest circle intersection. Right: Map-based CCPP.

4.2 Map Analysis

As mentioned before, the current track representation is not suited for calculating intersections with standard linear algebra methods. A geometric characterization allows for a faster mathematical approach than the current iterative scan method. Additionally, it is difficult to determine which percentage of a lap is already completed by the car. However, this knowledge can be useful for path heuristics and to conclude how much of the track is covered by a certain path. This motivates the development of an approach to vectorize the track-information of the map. In the following we use the term *track-distance*, which we define as the percentage of the traveled lap multiplied by the total lap distance.

Vectorization. To transform the grid map format into a vector representation we use several methods: finding the lines, approximating the lines into vectors and dividing the new approximated track into areas. Dividing the track into areas is a key aspect for the *track-distance* calculation.

First, we try to find a continuous point chain, which represents one of the border lines of the track. We select a random occupied cell on the map. We validate with depth-first search, if it is connected to more occupied points on the map in one direction. If this is the case, we create a perpendicular barrier at

this point and select a target point next to the chosen point on the other side of the barrier. An A^* algorithm tries to determine a path from the start point to the target point without passing the defined "barrier". If a solution is found, we end up with an ordered sequence of points describing one of the two lines of the track. Otherwise the method restarts with a new initial point. This is continued until two distinct solutions are found. To avoid finding the same line twice, the obtained line and their neighbouring occupied cells are removed from the grid. After two lines are detected, we determine which one is the inner line and which one is the outer line of the track. We calculate the extremes x and y values of both lines. The line with the smaller minimal values and the larger maximal value is the outline. To approximate the point sequence with vectors, we use the same technique as used in line detection. As a result we get an array of line segments describing the outer and inner line of the track.

Track-Distance Calculation. To calculate the covered *track distance*, we first divide the track into areas. Normal vectors of the inner lines are created at both points of each line segment. The intersections of these normal vectors with the outer track line create trapezoid areas.

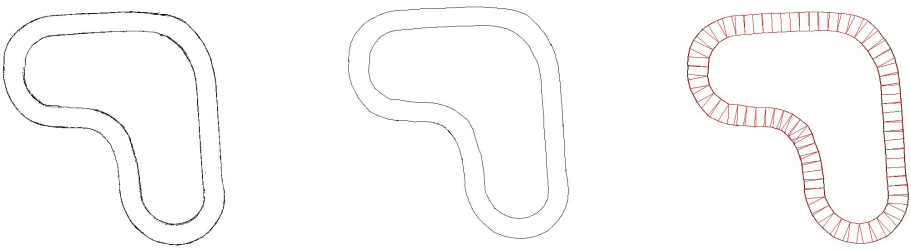

Fig. 9. Vectorization of the map data. Left: Raw map. Center: Both lines markings vectorized. Right: Track divided into areas.

We consider three possible configurations of two successive vectors: both have the same direction, the succeeding vector has a negative angle or has a positive angle relative to direction of the previous vector. If the relative angle is positive the areas overlap and nothing has to be added. The same applies for areas where the leading vectors have the same direction. But if the relative angle is negative it creates a gap between the two areas. In this case a new area is created by using the existing points of the trapezoid areas. This results in a triangle. The distance to the start-segment is stored for both directions of the track. This information is necessary for a fast computation of the *track-distance*.

In order to determine the *track-distance*, we have to calculate if start- and end-point of a certain route are inside the track and if so, in which track segment. After obtaining both areas, we calculate the *track-distance* between the start and the end point. The trapezoid shaped segment uses an approximation vector of the inner line as the base. In case of a triangular shaped segment the point

is used that belongs to the inner line. The *track-distance* is the accumulated distances of the vectors, which are between the start- and end-point.

As mentioned previously, some areas are overlapping, which means that more than one segment can contain the point. In this situation, the algorithm considers the area leading to the smaller distance between the start- and end-point in order to underestimate the *track-distance*.

5 Experiments and Results

This section presents the experiments and results[1]. We evaluate both the RANSAC and polyline based vision systems, as well as the different CCPP algorithms.

5.1 Comparison of the Line Detection Methods

In order to evaluate the performance of both approaches, we measure their runtime on a set of about 3000 images. Our results show that the polyline approach requires approximately 31.57% less time to process an image than the RANSAC technique. An advantage of the RANSAC technique is the matching of lines with splines, which result in a smooth curve. In contrast, the polyline approach results is only a sequence of straight lines. However, RANSAC uses a random process which is suboptimal most of the time. Using the RANSAC line detection approach, we encounter three unique disadvantages when compared to the polyline approach. These are illustrated in Figure 10. In conclusion, the polyline approach is faster and more robust, especially for the strongly arched curves of the test track. For these reasons, the polyline approach is favored over the RANSAC approach.

5.2 Comparison of Sensor-based and Map-based CCPP

In order to compare the different driving approaches, we apply the techniques on a dataset of different consecutive locations (position and image) in the map and measure the length of the calculated curvatures or *track distances*. The locations are recorded during two rounds of autonomous drive. For ease of reference, we split the track into 6 segments to give an intuition to which location in the track a datapoint belongs.

Figure 11 (left) illustrates that the approach based on the grid-map is able to find a longer arc than the vision-based approach in the majority of cases. However, one problem is that both algorithms do not factor in the traveled distance of the track, i.e. the calculated curve could result in an suboptimal route since a curve or line could exist that reaches the same endpoint in less time. Both methods try to maximize the arc length (distance between robot and intersection) of the curve, which is not always beneficial for the covered *track-distance*. The longest arc length is the curve covering the longest *track-distance*

[1] A video of the work can be found at:
`http://swarmlab.unimaas.nl/papers/icira-2013-autonomous-rc-car/`

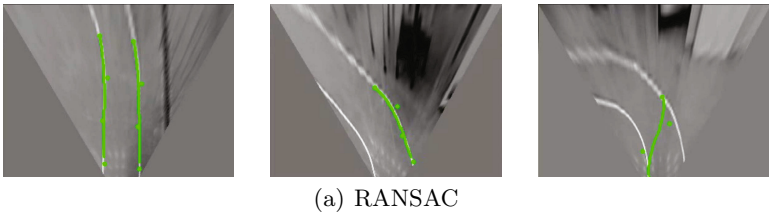

(a) RANSAC

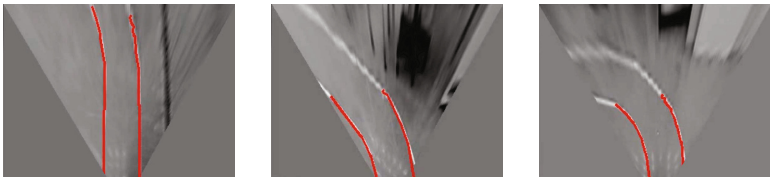

(b) Polyline

Fig. 10. Left: Commonly, the best-sampled spline is shorter than the polyline solution. Center: If all sampled splines do not exceed the required spline score, no line is detected. Right: Strongly curved lines can cause the spline to intersect with both markers.

most of the time. However, in the case shown in Figure 12(a) multiple steeper curves with the same *track-distance* could be chosen, thus the maximisation of the ARC-length yields a suboptimal result.

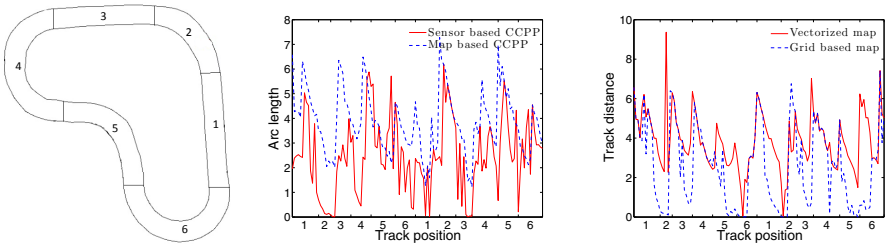

Fig. 11. Left: The track positions. Center: Comparison of arc lengths of the sensor based and the gridmap-based CCPP. Right: Comparison of the track distances of the vectorized map and gridmap CCPP.

Another drawback of this technique is its tendency to choose commands resulting in the robot manoeuvring near the borderlines of the track. Furthermore,

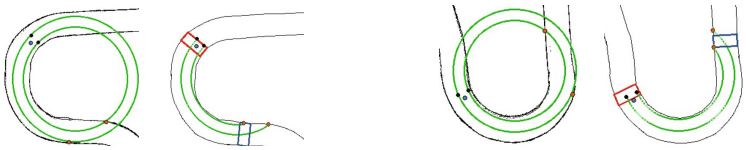

(a) Wide curve problem. (b) Unpolished map problem.

Fig. 12. Problems of the grid based approach compared to the vector based approach

if one wheel is directly over the line all steering angles result in the same intersection distance because the closest intersection for all options lies on the position of the wheel. Another problem appears when the robot leaves the track. Since the track is not represented by a geometry figure, like for instance a polygon, it is difficult to determine on which side of the track the car is located. This makes it more difficult to find a steering angle, which navigates the car back on the track. These issues are not present when using the vectorized map approach. We compared the vectorized map against the grid map on the same dataset and evaluated the resulting path by its track-distance. The result is illustrated in Figure 11 (right). Both approaches yield similar results, while the vectorized map approach yields longer track distances than the grid-based map approach in almost every setting.

Another advantage is the result of the more clean and polished track representation. This means the grid map contains noise, i.e. points scattered around a line. These points do not belong to the line, but effect the intersection calculation. The grid-map approach has to choose a wider path in order to avoid these points. The vectorized map represents the track by a sequence of lines with no actual width, which results in the curve being as close to the line as possible (Figure 12(b)).

Additionally, we compared the runtime of the optimal curvature calculation for the grid based approach and the map based approach. The average calculation time for the 200 consecutive location as shown above are recorded. The approach based on the vectorized map is about eight times faster than the approach that employs the raw map data. When using the grid map every point on the driving path has to be evaluated instead of using the fast geometric calculations enabled by vectorizing the map.

6 Conclusions and Future Research

This paper introduces and discusses the development of an Autonomous RC-car from scratch. This includes hardware design, two state of the art vision systems, as well as SLAM and localization algorithms. Autonomous drive is achieved by implementing various methods of CCPP. The systems for line analysis, mapping and localization are tested and yield satisfying results.

The focus of future research will be on more sophisticated path planning. The first step is to change the kinematic model into a dynamic model. Dynamic models take physical properties into account, which makes the prediction of the car's behavior more accurate. After the establishment of a dynamic model, we suggest to further explore state-of-the-art in planning with dynamic models. A Rapidly exploring Random Tree (RRT) is an algorithm designed for efficiently searching non convex, high-dimensional search spaces and is thereby a good choice for further investigation. Related research has already incorporated a dynamic vehicle model in RRT [9].

References

1. Aly, M.: Real Time Detection of Lane Markers in Urban Streets. In: IEEE Intelligent Vehicles Symposium (June 2008)
2. Bertozzi, M., Broggi, A.: Real-time lane and obstacle detection on the gold system. In: Proceedings of the IEEE Intelligent Vehicles Symposium, September 19-20, pp. 213–218. IEEE Press (1996)
3. Bertozzi, M., Broggi, A.: Gold: a parallel real-time stereo vision system for generic obstacle and lane detection. IEEE Transactions on Image Processing 7(1), 62–81 (1998)
4. Bresenham, J.E.: Algorithm for computer control of a digital plotter. IBM Syst. J. 4(1), 25–30 (1965)
5. De Boor, C.: A practical guide to splines. Appl. Math. Sci. (1978)
6. Doucet, A., Freitas, N., Murphy, K., Russell, S.: Raoblackwellised particle filtering for dynamic bayesian networks. In: The 16th Annual Conference on Uncertainty in Artificial Intelligence, pp. 176–183. Morgan Kaufmann Publishers (2000)
7. Forsyth, D.A., Ponce, J.: Computer Vision: A Modern Approach. Prentice Hall Professional Technical Reference (2002)
8. Fox, D.: Adapting the sample size in particle filters through kld-sampling. International Journal of Robotics Research 22 (2003)
9. Lavalle, S.M.: Rapidly-exploring random trees: A new tool for path planning. Technical report (1998)
10. Murphy, K.: Bayesian map learning in dynamic environments. In: Neural Info. Proc. Systems (NIPS), pp. 1015–1021. MIT Press (2000)
11. Nixon, M., Aguado, A.S.: Feature Extraction & Image Processing, 2nd edn. Academic Press (2008)
12. Norris, W.: Modern steam road wagons. Longmans, Green, and co. (1906)

Modeling, Control and Simulation of a 6-DOF Reconfigurable Space Manipulator with Lockable Cylindrical Joints

Pooya Merat[1], Farhad Aghili[2], and Chun-Yi Su[1]

[1] Concordia University, Montreal, QC, Canada
[2] Canadian Space Agency, St-Hubert, QC, Canada
{p_merat,cysu}@encs.concordia.ca,
farhad.aghili@asc-csa.gc.ca

Abstract. Reconfigurable manipulators can be very advantageous in dexterity-demanding tasks such as space operations. This paper presents the modeling, control and simulation of a robotic reconfigurable manipulator. The manipulator benefits from passive cylindrical joint design for its links which allows it to change the link parameters. The robot enters the reconfiguration phase in two steps; first, it forms a closed kinematic chain or in other words docks its end-effector to a fixed point in order to increase the constrained DOFs. Second, it releases the built-in locks of its cylindrical joints to enable the reconfiguration of the links. Then, the reconfiguration process is performed by using the proper control method. After achieving the desired configuration, the cylindrical joints are locked again, the end-effector is released and robot enters the operation mode. This paper only focuses on the reconfiguration process of a 6-DOF manipulator with two lockable passive cylindrical joints.

Keywords: Reconfigurable robotic manipulator, constrained multi-body, dynamic modeling.

1 Introduction

The space manipulators should be size efficient in order to be placed on the lunch vehicle. For example Canadarm II has a hinge at the middle of each of its links to be folded on the lunch vehicle, and then it has to be unfolded manually by the astronauts. For specific tasks that no human operator is present it is necessary for such manipulator to be unfolded automatically. Besides it is always desirable to have a multi-task manipulator that is able to change its parameters such as the links lengths or links twist angles, to have a suitable configuration for each particular task. For instance in space operations, large manipulators are suitable for inspection [1], or well-conditioned configurations are ideal for dexterous contact tasks [2].

Many space agencies agree that the reconfigurable space robots will be used in future for space applications. One option could be the modular reconfigurable robot that changes its configuration by making new connections between its robotic

J. Lee et al. (Eds.): ICIRA 2013, Part II, LNAI 8103, pp. 121–131, 2013.

modules [3–5]; however in these modular robots there is still difficulty in implementation of a robust and effective docking mechanism for connecting and releasing the modules [6]. Unlike the modular robots, the new design uses lockable passive cylindrical joints to change the robot configuration [7]. In this kind of manipulator, each cylindrical joint has two passive DOFs; one revolute and one prismatic with the same axes of the link. It is also equipped with an internal normally-passive [1] lock to prevent unwanted movements of these passive DOFs. The reconfiguration phase starts when the robot forms a closed chain by docking its end-effector (EE) to a fixed point. Then the cylindrical joints locks are released and using the proper control method the robot reconfigures its passive DOFs. When the process of reconfiguration is finished, the passive joints are locked again and the EE undocks. An example of the reconfiguration process of this manipulator is presented in Fig. **1**. It is worth mentioning that the reconfiguration process is performed with the same actuators and sensors used for normal operation of the manipulator, in other words the manipulator does not use any extra actuator or sensor during the reconfiguration; this results in a lighter manipulator design which is critical in space applications in order to reduce the lunch cost.

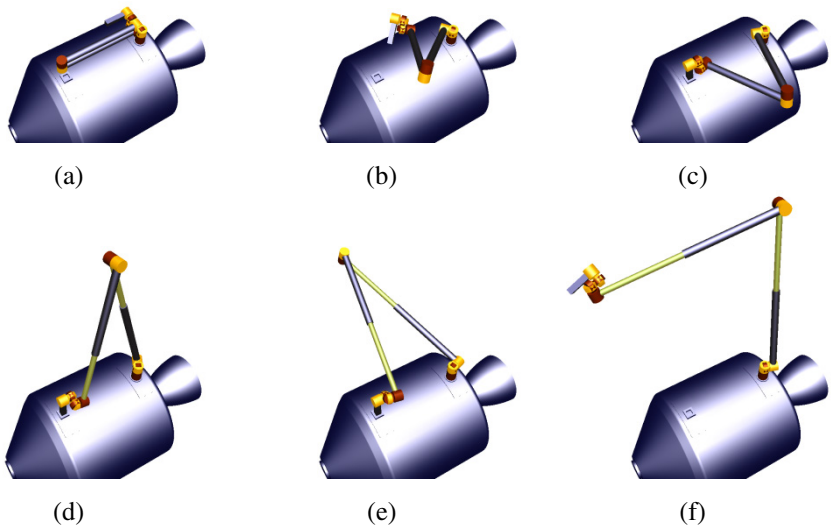

Fig. 1. Unfolding process of a reconfigurable 6-DOF manipulator installed on a satellite (a) The initial folded state; (b) the EE moving towards its docking position; (c) constraining the EE motion in dock and releasing both link locks; (d,e) reconfiguration process; (f) the final configuration.

[1] The lock consumes energy only during the state change from lock to unlock mode and vice versa [7].

In this paper the reconfiguration process of a 6-DOF reconfigurable manipulator with two cylindrical joints is presented. To enter the reconfiguration process first, the robot docks the EE to a fixed point and loses all its 6 DOFs (Fig. **1**- c). Second, both cylindrical joints are unlocked and 4 DOFs will be added to the system. Then the reconfiguration is performed (Fig. **1**-d,e) and then robot locks the cylindrical links and releases EE from the fixed docking position (Fig. **1**-f). The reconfiguration is done using 6 actuators to achieve 4 desired outputs (two link lengths and two link twist angles). The modeling, control and simulation of the manipulator before and after the reconfiguration process are not discussed in this paper and there are many papers in this regard [8].

2 Modeling

There are multiple ways to model a constrained multi-body system such as coordinate separation [9], augmented Lagrangian formulation [10] and projection-based method [11]. In this paper, the projection-based method is used to model and control the system. For this purpose, first the manipulator should be modeled without the presence of any constraints, which in the case this paper that would be the dynamic modeling of a 10-DOF manipulator. Afterwards, using the projection operator which is calculated from the constraint equation, the control law could be derived and the constrained model could be simulated. All the procedure is performed in MATLAB R2012b.

2.1 Dynamics

The first step for simulation of any mechanical system is to acquire the dynamic model. In this paper the iterative Newton-Euler formulation is used to derive dynamic equations. Unlike the widely used Lagrangian dynamic formulation, this method results in one of the simplest form of analytical equations which leads to dramatic reduction in computation time [12, 13].

When both locks of the 6-DOF manipulator are released, the manipulator has 10 DOFs without considering the constraints on EE i.e. the open-chain system. Using the projection-based method for simulation, it is only needed to calculate the open-chain manipulator dynamics. After forward kinematics calculation, the dynamic equation could be written in the following form:

$$M\ddot{q} + V = \tau \,. \tag{1}$$

where M is symmetric inertia matrix, V is non-linear vector, τ is vector of generalized force and q is generalized joint coordinates which is defined as:

$$q \triangleq [\theta^T \quad \psi^T]^T \,. \tag{2}$$

where θ is vector of active joints generalized coordinates and ψ is the vector of passive ones. After calculation of the dynamic equation, the symbolic parameters are written into *MATLAB m-functions* using the *matlabFunction* included in the *Symbolic Math Toolbox*. To speed up this process, the *MATLAB Parallel Computing Toolbox* was used.

2.2 Constraints

To implement the projection-based model it is necessary to formulate the constraint equation of the manipulator. Let denote the number of DOFs of the manipulator or number of active joints as *n*, the number of cylindrical joints that are unlocked at the same time as *m* and the number of constrained DOFs as *r*. In order to prevent the system from being under-actuated or over-constrained, the following inequalities must be kept satisfied [7]:

$$2m \le r \le \min(\mathrm{n}, 6)\,. \tag{3}$$

In the model studied in this paper, the manipulator has 6 DOFs (n = 6), both cylindrical joints will be reconfigured at the same time (m = 2), and EE is fully constrained by attaching to the satellite during reconfiguration (r = 6). Since the EE has no movements with respect to the satellite, the constraint equations could be extracted from the EE transform. The analytical transform of the EE could be calculated using forward kinematics in terms of q.

$${}^{B}_{EE}T = \left[\begin{array}{ccc|c} & {}^{B}_{EE}\mathrm{R} & & {}^{B}P_{EE} \\ \hline 0 & 0 & 0 & 1 \end{array}\right]. \tag{4}$$

where ${}^{B}_{EE}T$ and ${}^{B}_{EE}\mathrm{R}$ are transformation and rotation matrices from EE frame to the base frame and ${}^{B}P_{EE}$ is position of EE in the base frame.

The constraints equation could be written as:

$$\Phi = \begin{bmatrix} {}^{B}P_{EE} \\ {}^{B}O_{EE} \end{bmatrix} - \begin{bmatrix} {}^{B}P_{EE_0} \\ {}^{B}O_{EE_0} \end{bmatrix} = 0\,. \tag{5}$$

O_{EE} is the orientation of the EE in the form of the Euler angles:

$$O_{EE} = f({}^{B}_{EE}R) = \begin{bmatrix} \alpha & \beta & \gamma \end{bmatrix}^{T}\,. \tag{6}$$

and ${}^{B}P_{EE_0}$ and ${}^{B}O_{EE_0}$ are position and orientation of EE in the base frame when EE is fixed.

2.3 Projection Operator

Projection-based method is used as a basis for the simulation and control of the closed-chain robot during the reconfiguration process [14]. *Projection operator* is defined as:

$$P \triangleq I - A^{+}A \,. \tag{7}$$

where P, the projection operator, is a symmetric matrix and is the null-space orthogonal projector of A and A is the constraint Jacobian matrix:

$$A \triangleq \frac{\partial \Phi}{\partial q} \,. \tag{8}$$

Having the open-chain dynamic equation (**1**) the closed-chain dynamic formulation would be:

$$M_C \ddot{q} = P(\tau - V) + C_C \dot{q} \,. \tag{9}$$

where M_C and C_C could be calculated from:

$$\begin{aligned} M_C &= M + PM - (PM)^T \,. \\ C_C &= -MA^{+}\dot{A} \,. \end{aligned} \tag{10}$$

2.4 Control

The general control process of a reconfigurable manipulator is shown in Fig. 2. There are two control modes; the motion control mode which is not discussed in this paper and the reconfiguration control mode. For the reconfiguration control purpose a projection-based controller is used [7] which is a non-model-based controller. The projection operator and gravity term could be written as:

$$\begin{aligned} P &= \begin{bmatrix} P_{aa} & P_{ap} \\ P_{ap} & P_{pp} \end{bmatrix}. \\ G &= \begin{bmatrix} g_\theta \\ g_\psi \end{bmatrix}. \end{aligned} \tag{11}$$

where $P_{aa} \in \mathbb{R}^{n \times n}$ and $P_{pp} \in \mathbb{R}^{2m \times 2m}$. Also g_θ and g_ψ are the gravity terms of dynamic equation associated with the active and passive joints. Then the control law for the gravity-compensated PD controller would be:

$$\tau_\theta = P_{aa}^{-1} P_{ab} \left(K_d \dot{\psi} + K_p (\psi - \psi_d) + g_\psi \right) + g_\theta \,. \tag{12}$$

with τ_θ being the active joints torques and K_p and K_d being the PD controller gains [15]. Fig. 3 shows the overall control diagram of the reconfiguration process.

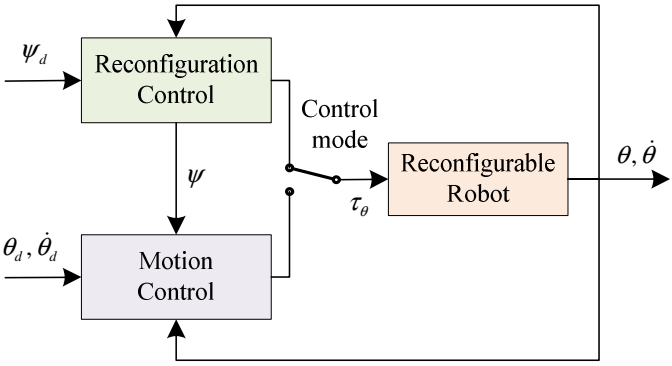

Fig. 2. Control modes of the reconfigurable manipulator [15]

2.5 Passive Joints Estimator

As mentioned before, no sensors or actuators are implemented for the passive joints. Thus, for the control purpose it is necessary to estimate the passive joints states with respect to the states of active joints that are instrumented with sensors.

Using the formula (13) passive joints states could be estimated:

$$\begin{aligned} \hat{\dot{\psi}} &= Q(\theta,\hat{\psi})\dot{\theta} - A_{\psi}^{T}(\theta,\hat{\psi})K_{\omega}\Phi(\theta,\hat{\psi}) . \\ \hat{\psi} &= \int \hat{\dot{\psi}} dt . \end{aligned} \tag{13}$$

where K_ω is the estimator gain obtained from a positive-definite matrix K and a weight matrix W.

$$K_{\omega} = W^{T} K W . \tag{14}$$

It can be proven that using the formula (**13**), the estimation error will exponentially approach to zero as t becomes large [15].

3 Simulation

The simulation of the reconfiguration process of the 6-DOF reconfigurable manipulator is implemented using MATLAB code instead of MATLAB SIMULINK, because of more programming flexibility. The variable time-step simulation method was also used to decrease the simulation computation. The variable time-step is designed to be a function of the maximum speed of the joints during the simulation.

3.1 Simulation Error Compensation

During simulation, the integration will lead to a drift error of q. It is possible that the constraint equation be no longer satisfied or in other words $\Phi(\tilde{q}) \neq 0$, with $\tilde{q}$ being

the drifted q. This can lead to instability of the system during simulation. By defining the drift error as:

$$\delta q = q - \tilde{q} \,. \tag{15}$$

and using the first two terms of the Taylor series for the constraint equation $\Phi = 0$ around $\tilde{q}$ we would have:

$$\Phi(q) \equiv \Phi(\tilde{q} + \delta q) \cong \Phi(\tilde{q}) + \frac{\partial \Phi(\tilde{q})}{\partial q} \delta q \,. \tag{16}$$

From (**8**) we know that $A(\tilde{q}) = \dfrac{\partial \Phi(\tilde{q})}{\partial q}$, and it can be concluded that

$$\Phi(\tilde{q}) + A(\tilde{q}) \delta q \cong \Phi(q) = 0 \,. \tag{17}$$

From (**17**) it can be inferred that if $\tilde{q}$ is close enough to q, by calculating the following two formulas iteratively $\tilde{q}$ will approach to q.

$$\begin{aligned} \delta q &\cong -A^{+}(\tilde{q}) \Phi(\tilde{q}) \,. \\ \tilde{q} &= q - \delta q \,. \end{aligned} \tag{18}$$

The error compensation of q does not necessarily lead to compensation of the error of $\dot{q}$ and so using the same concept it is possible to compensate the drift error of $\dot{q}$ by using the following formulas:

$$\begin{aligned} \delta \dot{q} &\cong -A^{+}(q) A(q) \tilde{\dot{q}} \,. \\ \tilde{\dot{q}} &= \dot{q} - \delta \dot{q} \,. \end{aligned} \tag{19}$$

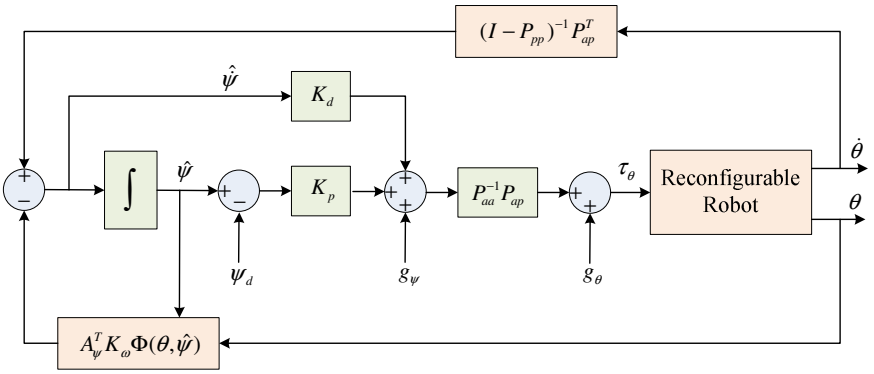

Fig. 3. The reconfiguration control diagram [15]

To validate the constrained manipulator model, the kinetic energy of the open-loop system was monitored without the presence of gravity. The model is excited only with an initial velocity of the joints, and no torque is exerted to the joints. It is expected

that the kinetic energy of the system doesn't change during time. The kinetic energy could be calculated from:

$$K = \frac{1}{2}\dot{q}^T M \dot{q} \,. \tag{20}$$

In a test with the simulation time-step of 5ms, an initial angular velocity was exerted which resulted in an initial kinetic energy of *K = 3.2e-2 J*. The kinetic energy was monitored over 10 seconds or 2000 iterations. The standard deviation of the monitored kinetic energy was *2.4e-5 J* which is a reasonable error for the simulation.

3.2 Results

The simulation results correspond to the process depicted in Fig. 1 which is the unfolding scenario of a space manipulator from a compact state to a manipulator with longer links. During the reconfiguration process, the length of both links are increased from *1m* (compacted state) to *1.9m* (unfolded state), i.e. an increase of 90% in length. The twist of first link also changes from 0 to π, but the second link twist angle remains the same. Each joint and each cylindrical joint have a mass of 2kg and the masses of the links are linearly distributed among their lengths. The satellite was considered as a fixed object and also to be on-orbit i.e. there is no gravity effect on the manipulator or $G = 0$. Controller gains for both length and twist angle are set to $K_p = 5,\ K_d = 30$. The simulation results are illustrated in the form of time histories of the passive DOFs (Fig. 4 and Fig. 5), active joints angles (Fig. 6), joint torques (Fig. 7) and joint velocities (Fig. 8). As could be seen the controller is able to reconfigure the manipulator to the desired configuration in about 60 seconds.

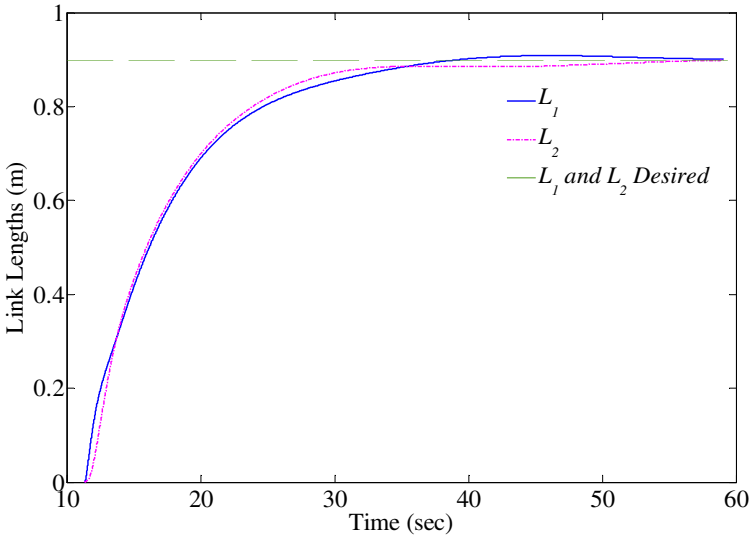

Fig. 4. During the reconfiguration process L_1 and L_2 (length of the first and second cylindrical joints) increase from *1m* to *1.9m*

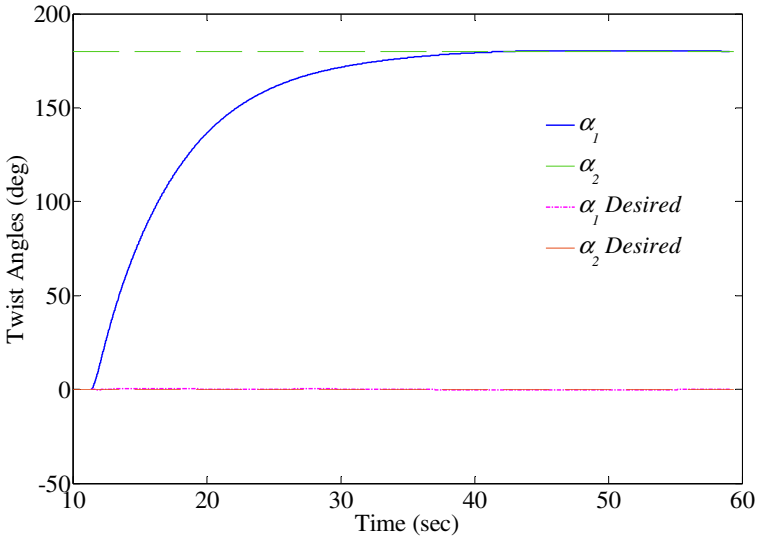

Fig. 5. During the reconfiguration process α_1 (twist angle of the first cylindrical joint) increases from *0* to π and α_2 (twist angle of the second cylindrical joint) remains *0* in this scenario

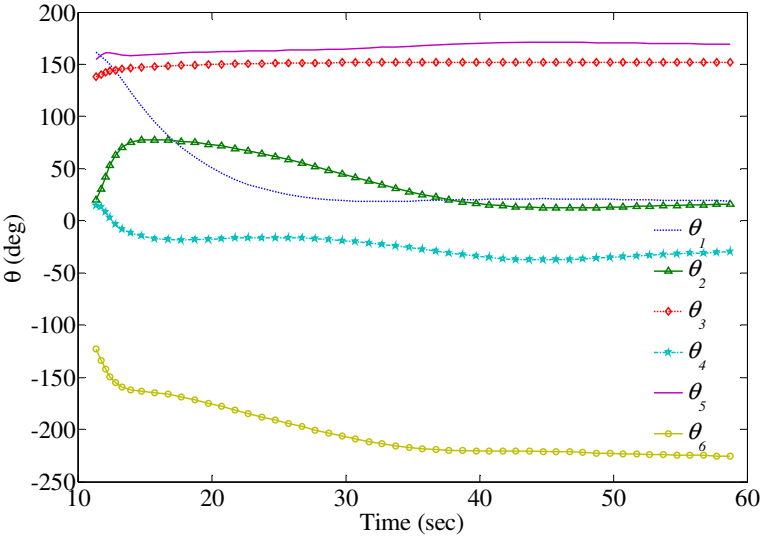

Fig. 6. Joint angles during the reconfiguration process

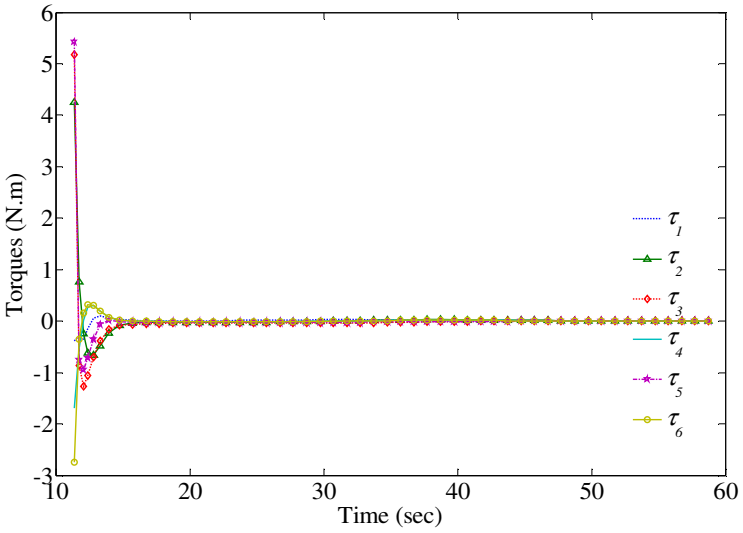

Fig. 7. Active joint torques during the reconfiguration process

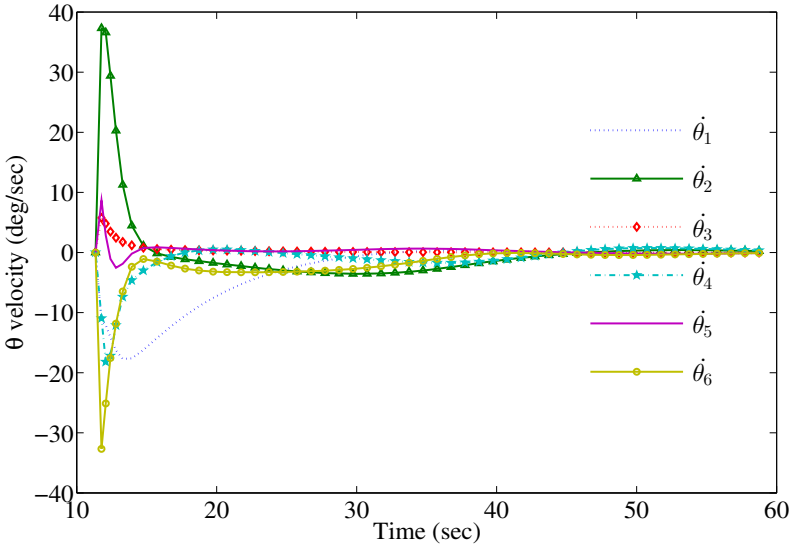

Fig. 8. Joint velocities during the reconfiguration process

4 Conclusion

In this paper the simulation results and the implementation methods of a 6-DOF reconfigurable manipulator are presented. Hence the manipulator controller might

lead the manipulator to singular configurations; therefore it is necessary to design a singularity avoidance algorithm to ensure the robustness of the controller. In addition, obstacle avoidance and joints limits avoidance must be also implemented in order to prevent the manipulator from hitting the satellite and clash on its joints limits.

Acknowledgments. This work was supported by NSERC under grant RGPIN/288255-2011.

References

1. Angeles, J.: Fundamentals of Robotic Mechanical Systems: Theory, Methods, and Algorithms. Springer (2007)
2. Merlet, J.-P.: Parallel Robots. Springer (2001)
3. Fukuda, T., Kawauchi, Y.: Cellular Robotic System (CEBOT) as one of the Realization of Self-Organizing Intelligent Universal Manipulator. In: Proceedings of the IEEE International Conference on Robotics and Automation, pp. 662–667. IEEE Comput. Soc. Press (1990)
4. Murata, S., Kurokawa, H., Kokaji, S.: Self-Assembling Machine. In: Proceedings of the IEEE International Conference on Robotics and Automation, pp. 441–448. IEEE Comput. Soc. Press (1994)
5. Ohkami, Y., Matunaga, S., Hayashi, R.: Operational Aspects of a Super Redundant Space Robot with Reconfiguration and Brachiating Capability. In: Proceedings of the IEEE International Conference on Systems, Man, and Cybernetics, SMC 1999, pp. 178–183 (1999)
6. Khoshnevis, B., Will, P.: Highly Compliant and Self-Tightening Docking Modules for Precise and Fast Connection of Self-Reconfigurable Robots. In: IEEE International Conference on Robotics and Automation (Cat. No.03CH37422), pp. 2311–2316 (2003)
7. Aghili, F., Parsa, K.: Design of a Reconfigurable Space Robot with Lockable Telescopic Joints. In: 2006 IEEE/RSJ International Conference on Intelligent Robots and Systems, pp. 4608–4614 (2006)
8. Lewis, F.L., Dawson, D.M., Abdallah, C.T.: Manipulator Control: Theory and Practice. CRC Press (2004)
9. McClamroch, N.H., Wang, D.: Feedback Stabilization and Tracking of Constrained Robots. IEEE Transactions on Automatic Control 33, 419–426 (1988)
10. Bayo, E., Garcia De Jalon, J., Serna, M.A.: A Modified Lagrangian Formulation for the Dynamic Analysis of Mechanical Systems. Computer Methods in Applied Mechanics and Engineering 71, 183–195 (1988)
11. Golub, G.H., Van Loan, C.F.: Matrix Computations. JHU Press (2012)
12. Craig, J.J.: Introduction to Robotics. Pearson Prentice Hall (2005)
13. Brady, M.: Robot Motion: Planning and Control. MIT Press (1982)
14. Aghili, F.: A Unified Approach for Inverse and Direct Dynamics of Constrained Multibody Systems Based on Linear Projection Operator: Applications to Control and Simulation. IEEE Transactions on Robotics 21, 834–849 (2005)
15. Aghili, F., Su, C.: Reconfigurable Space Manipulators for In-orbit Servicing and Space Exploration. In: International Conference on Intelligent Robotics and Applications (2012)

Mechanical Design of a Lower Extremity Exoskeleton with Hybrid Legs for Power Augmentation

Yunjie Miao[1], Feng Gao[2,*], and Dalei Pan[1]

[1] School of Mechanical Engineering, Shanghai Jiao Tong University, Shanghai, China
[2] State Key Laboratory of Mechanical System and Vibration,
Shanghai Jiao Tong University, Shanghai, China
fengg@sjtu.edu.cn

Abstract. An innovative lower extremity exoskeleton, SJTU-EX, is presented in Shanghai JiaoTong University, which mainly aims to help soldiers and workers to support a payload in motions. This paper summarizes the mechanical design of SJTU-EX. Each pseudo- anthropomorphic leg of SJTU-EX has four active joints and two passive joints and the joint ranges are optimized in consideration of both safety factors and realizations of typical motions. Springs are applied in the leg to eliminate the effect of gravity. The results of dynamic simulations are used to determine the actuated joints and the passive joints.

Keywords: exoskeleton, hybrid leg, diamond mechanism, mechanical design.

1 Introduction

Heavy objects are typically transported using wheeled vehicles. Many places in the world are too rugged or enclosed for vehicles to access, such as rocky terrains and staircases. Thus legged locomotion becomes an attractive method of transportation. In recent years, the research on lower extremity exoskeletons has become a hot topic. Lower extremity exoskeleton is a mobile machine worn by a person and supplies at least part of the activation-energy for limb movement. It combines the human intelligence and the machine power so that it enhances the intelligence of the machine and the power of the human operator. As a result, the human operator can achieve what he is not capable of by himself[1].

Several organizations all over the world have designed impressive exoskeletons for power augmentation, differing significantly in performance and technology used. They can be broadly categorized into two groups: passive or quasi-passive exoskeletons and powered exoskeletons.

The principle of a passive or quasi-passive exoskeleton is to store the energy at desired instances of the gait cycle and release the energy when more power is required. The leg exoskeleton[2] and the knee exoskeleton[3] presented in the Biomechatronics Group at the Massachusetts Institute of Technology Media

* Corresponding author.

J. Lee et al. (Eds.): ICIRA 2013, Part II, LNAI 8103, pp. 132–142, 2013.

Laboratory and the gravity balancing lower extremity exoskeleton[4] developed in University of Delaware, Newark are all passive or quasi-passive exoskeletons. With the help of springs, the energy during a gait cycle is redistributed and thus the peak values of human joints' powers are smaller. However, it is not possible to help support heavy loads for passive or quasi-passive exoskeletons because there is no additional power input. As for powered exoskeletons, they are mainly designed to help humans carry payloads, like the Berkeley Lower Extremity Exoskeleton (BLEEX)[5], the Sarcos exoskeleton WEAR[6] and the exoskeleton robot suit HAL[7] in University of Tsukuba. These most power consuming joints of the exoskeletons during gait cycles are set to be actuated while the left joints are passive, usually with springs to make wearers comfortable.

SJTU-EX is a powered lower extremity exoskeleton designed to assist and protect soldiers and construction workers. It is comprised of a rechargeable battery as the power supply, two pseudo-anthropomorphic legs and a backpack-like frame to mount varieties of loads. The parallel-series leg structure with four active joints and two passive joints can highly improve the load capacity. With the help of buffering springs on the legs, SJTU-EX can eliminate the effect of gravity during motions. Unlike most current exoskeletons with a fixed length distance between joints, SJTU-EX can automatically adapt to a wide range of human physical sizes when worn on. It allows the wearer to accomplish typical motions of human lower limbs, like walking, jogging, squatting and stairs climbing. It is our vision that SJTU-EX can be applied in rescue areas like nuclear plants. For example, SJTU-EX might help a rescue worker of Fukushima Nuclear Power Plant to support the weights of the lead coat and the devices so that the worker can manipulate faulty equipments inside the plant. It is convenient to protect the exoskeleton from dangerous environments like radiations because no devices and actuators are mounted along the legs.

2 Determination and Distribution of Degrees of Freedom

Fundamental to designing a lower extremity exoskeleton is to determine the degrees of freedom of the exoskeleton leg. To better follow human motions and minimize kinematic constraints experienced by the wearer, the exoskeleton leg should have sufficient degrees of freedom as compared to a human's leg. According to the Clinical Gait Analysis (CGA) Data[8] of a walking gait cycle, the movement of the human lower limb in the sagittal plane is the basic movement form. The hip and knee flexion/extension joints provide most of the torque to support the body weight while the ankle flexion/extension joint supplies the most torque to push the body forward.

As a result, a pseudo-anthropomorphic architecture is chosen for SJTU-EX which has ankle and hip joints similar to a human but no knee joints, as shown in Fig. 1. Each SJTU-EX leg has four degrees of freedom at the hip and two degrees of freedom at the ankle. The hip abduction/adduction axis R_1 and the two joint axes of the diamond mechanism R_3 and R_4 all pass through the human hip joint O. The hip rotation axis R_2 is chosen to be behind the wearer and thus it no longer passes through the human's hip joint. The SJTU-EX ankle has a flexion/extension axis R_5

and an abduction/adduction axis R_6. Both the two ankle axes are designed to pass through the human's ankle joint A. The degree of freedom of the ankle rotation is removed because its motion can be partly realized by the hip rotation. On the other hand, how to layout the two degrees of freedom of the hip and knee flexion/extension becomes critical for an exoskeleton specialized for load carrying. Traditional exoskeletons usually connect the hip joint and the knee joint in series as an anthropomorphic architecture in sacrifice of the load supporting capability. As for SJTU-EX, a parallel diamond mechanism with two rotational degrees of freedom is introduced and it works as the role of the hip and knee flexion/extension joints. The two joint angles between the two diamond sides and the sagittal axis are denoted as θ_1 and θ_2 which are clockwise negative. θ_1 and θ_2 determine the location of the ankle joint in sagittal plane together. The parallel diamond mechanism is prominent in the load supporting capability and can also provide a large workspace for the motion of human feet.

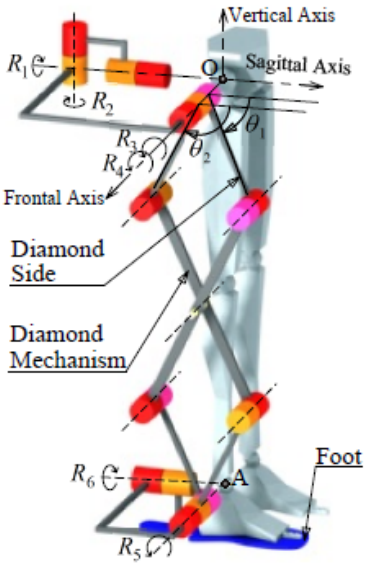

Fig. 1. Distribution of degrees of freedom

3 Determination and Optimization of Joint Ranges

SJTU-EX is designed to be worn by humans with the height from 1.60 m to 1.80 m. Thanks to the diamond mechanism, the exoskeleton can automatically adapt to the height of the wearer when worn on. For example, when a tall person puts on the SJTU-EX, the diamond angle α becomes small and hence the whole exoskeleton is lengthened. A smaller diamond angle α contributes to a better load supporting capability of the exoskeleton. So less torque and power is needed when worn by a tall person. The smallest diamond angle α is set to be 10°when a 1.80 m person wears

the exoskeleton and stands straight. The length of the diamond side L can then be determined by Eq. (1).

$$L=\frac{h_{H-A}}{4\cos(\frac{\alpha}{2})}=0.232\ m \tag{1}$$

where h_{H-A} is the distance between the hip and the ankle and approximately equals to 51.3% of the height of a person[9].

The joint ranges of SJTU-EX should be large enough to allow the wearers to accomplish typical motions of the lower limbs. On the other side, the SJTU-EX joints should also limit the mobility of the wears to some extent to prevent the wearers from moving beyond the maximum ranges of human joints. Otherwise it may cause damage to the wearers. So it is important to investigate the motion abilities of human joints.

Walking is the most fundamental human motion and must be realized by the SJTU-EX wearer without any difficulty. The data in Column 1[8] of Table 1 indicates the ranges of human joints during a walking cycle. The maximum ranges of human joints are shown in Column 2[9] of Table 1. The ranges of human joints with SJTU-EX (shown in Column 3 of Table 1) should be larger than the data in Column 1 and smaller than the data in Column 2.

Table 1. Human joint ranges of motion

	Human Walking Maximum(°)	Average Male Maximum(°)	Human with Exoskeleton(°)
Ankle Flexion/Extension	14/-12	20/-50	15/-25
Ankle Abduction/Adduction	10/-4	20/-35	10/-25
Knee Flexion/Extension	68/4	140/0	100/0
Hip Flexion/Extension	26/-10	120/-40	100/-15
Hip Abduction/Adduction	10/0	70/-20	25/0
Hip Rotation External/Internal	9/0	50/-31	20/-10

Table 2. Joint ranges of SJTU-EX

SJTU-EX Joint	Joint Angle Maximum(°)
Ankle Flexion/Extension	15/-25
Ankle Abduction/Adduction	10/-25
Hip Abduction/Adduction	25/0
Hip Rotation External/Internal	20/-10
Diamond Side 1	θ_1
Diamond Side 2	θ_2

SJTU-EX legs are similar to human lower limbs in kinematics, except for the hip and knee flexion/extension joints. So the joint ranges of SJTU-EX shown in Table 2 are set to be equal to the data in Column 3 of Table 1 for the hip abduction/adduction joint, the hip rotation joint and the two ankle joints. The joint angles θ_1 and θ_2 between the two diamond sides and the sagittal axis are determined by the hip flexion/extension joint angle θ_{hip} from -15°to 100°and the knee flexion/extension joint angle θ_{knee} from 0°to 100°. However a realistic workspace requires that the motions of the two joints are dependant to each other, especially near the boundary of the workspace. For example, Postures of ($\theta_{hip} = -15°, \theta_{knee} = 100°$) and ($\theta_{hip} = 100°, \theta_{knee} = 0°$) are not able to be accomplished by most people and thus should be removed from the workspace.

The workspace of the ankle relative to the hip is optimized by investigating the joint ranges of four typical human motions: walking, jogging, squatting and stairs climbing. Two limit postures for θ_1 and θ_2 are then determined in Fig. 2, which allow the wearer to accomplish the four typical motions[10]. $\theta_{1\min}$ and $\theta_{2\min}$ can be found in Limit Posture 1 when θ_{hip} equals to -10°and θ_{knee} equals to 45°. $\theta_{1\max}$ and $\theta_{2\max}$ can be found in Limit Posture 2 when θ_{hip} equals to 50°and θ_{knee} equals to 0°.

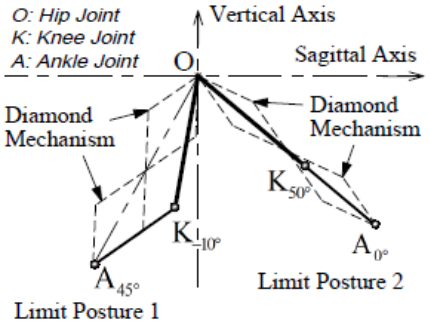

Fig. 2. Limit leg postures with SJTU-EX

Since SJTU-EX is designed for users from 1.60 m to 1.80 m, the determination of the ranges of θ_1 and θ_2 should also take into account the wearer's height. For a same posture with the same θ_{hip} and θ_{knee}, a taller wearer will result in a smaller θ_1 and a larger θ_2 of the exoskeleton. $\theta_{1\min}$ is determined by Eq. (2) when SJTU-EX is in Limit Position 1 and worn by a 1.80 m person.

$$\begin{cases} \dfrac{\theta_{1\min} + \theta_2}{2} = -119° \\ 4L\cos\left(\dfrac{\theta_{1\min} - \theta_2}{2}\right) = h_{H-A} \end{cases} \Rightarrow \theta_{1\min} = -96° \tag{2}$$

where L is the length of the diamond side and equals to 0.232 m,

h_{H-A} is the distance between the hip and the ankle and approximately equals to 0.854 m for a 1.80 m person.

$\theta_{1\max}$ is determined by Eq. (3) when SJTU-EX is in Limit Position 2 and worn by a 1.60 m person.

$$\begin{cases} \dfrac{\theta_{1\max}+\theta_2}{2} = -40° \\ 4L\cos\left(\dfrac{\theta_{1\max}-\theta_2}{2}\right) = h_{H-A} \end{cases} \Rightarrow \theta_{1\max} = -12° \tag{3}$$

where L is the length of the diamond side and equals to 0.232 m,

h_{H-A} is the distance between the hip and the ankle and approximately equals to 0.820 m for a 1.60 m person.

So the range of the joint angle θ_1 is $(-96°,-12°)$. In a same way, the range of the joint angle θ_2 can be found. $\theta_2 \in (-154°,-45°)$. θ_1 and θ_2 are dependent with each other and should also satisfy (4).

$$10° < \theta_1 - \theta_2 < 110° \tag{4}$$

where 10°is the minimum diamond angle α when SJTU-EX is worn by a 1.80 m person; 110°is the maximum diamond angle α when SJTU-EX is worn by a 1.60 m person. θ_1 and θ_2 determine the workspace of the ankle relative to the hip together and the optimized workspace with SJTU-EX is shown as the shaded area BCDEF in Fig. 3. C and F are the end points of the diamond mechanism at the two limit postures, as shown in Fig. 2. Curve CD is determined by increasing the angle of Diamond Side 1 θ_1 while keeping Diamond Side 2 still at Limit Posture 1 until the end point intersects with Arc $A'_{100°}A_{100°}$. In a similar way, Curve FE is determined by decreasing the angle of Diamond Side 2 θ_2 while keeping Diamond Side 1 still at Limit Posture 2 until the end point intersects with Arc $A'_{100°}A_{100°}$. Arc BC is centered

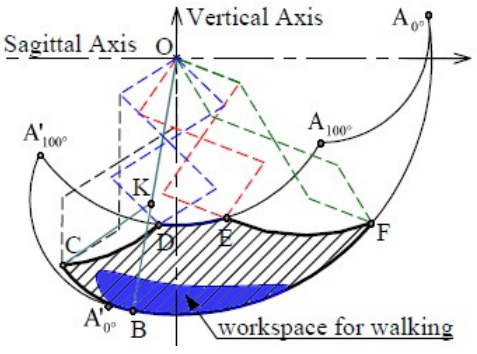

Fig. 3. Optimized workspace of the ankle with SJTU-EX

at the knee joint K when θ_{hip} equals to -10°. The optimized workspace BCDEF is inside of the human ankle workspace $A_{0°}A'_{0°}A'_{100°}A_{100°}$ without SJTU-EX and encompasses the blue region which indicates the ankle workspace for walking[11]. So both safety and a good motion ability of SJTU-EX can be guaranteed.

4 Determination of Actuated Joints and Passive Joints

Each SJTU-EX leg has six degrees of freedom to follow the motion of the lower limb well. However, actuating all of them would lead to high power consumption and control complexity. Instead, only joints that require substantial torque and power during motions should be actuated. Walking is considered as the principal human motion for exoskeletons and the corresponding joint torques and powers of SJTU-EX are chosen as the primary criterions to determine which joints to actuate.

A dynamic model of SJTU-EX is built to investigate the torques and the powers of the joints by the Lagrange equations of the second kind. The kinematic data for the two joints of the diamond mechanism is obtained from the motion data of human walking[12] by inverse kinematics so that the end point of the diamond mechanism can follow the motion of the human ankle. The kinematics of the other SJTU-EX joints is very similar to the kinematics of human joints, and thus can directly refer to the motion data of human walking. SJTU-EX is supposed to carry a payload of 70 kg including its own weight. The vertical ground reaction force (GFR) of SJTU-EX during a gait cycle has two peaks with the peak value about 120% of the total weight[13]. The leg of SJTU-EX is in swing phase at the first 40% of the cycle and in stance phase at the left 60% of cycle.

The dynamic simulations are performed on the condition that SJTU-EX is worn by a 1.80 m person at the walking speed of 1.3 m/s. The torque and power results of each joint during walking are shown in Fig. 4 and Fig. 5 respectively. The two joints of the diamond mechanism and the ankle flexion/extension joint all requires a peak torque more than $100\,N \cdot m$ and a peak power larger than 150 W. During a walking cycle, the diamond mechanism makes great contributions to supporting the whole body weight while the ankle flexion/extension joint is responsible to push the exoskeleton forward. As the most power consuming joints, the two joints of the diamond mechanism and the ankle flexion/extension joint all need to be actuated. The hip abduction/adduction joint of the exoskeleton requires a relatively small torque and power during walking. However, it provides the lateral balancing forces and does become a power consuming joint when walking sideways by abducting the leg to avoid obstacles. Consequently, it is also set to be actuated. Both the hip rotation joint and the ankle abduction–adduction joint require a small torque less than $10\,N \cdot m$ and a small power less than 10 W. They are mainly designed to help accomplish the wearer's motions in these two degrees of freedom.

In summary, each SJTU-EX leg has four powered degrees of freedom: the two joints of the diamond mechanism, the ankle flexion/extension joint and the hip

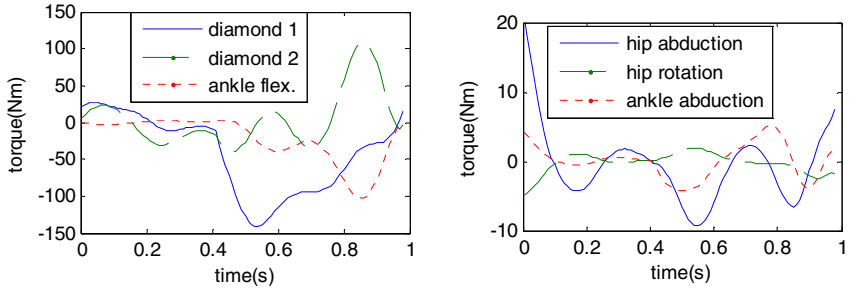

Fig. 4. Joint torques of SJTU-EX for walking with a payload of 70 kg

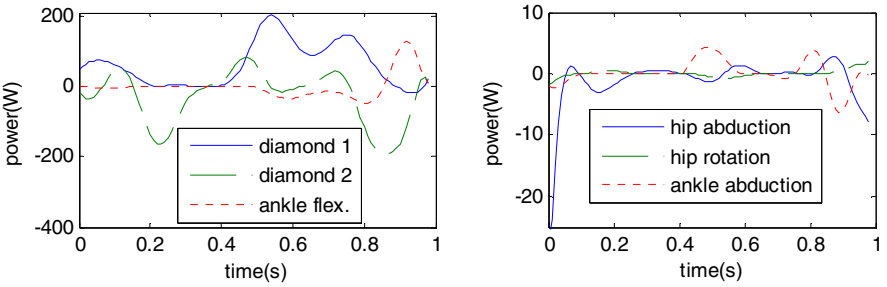

Fig. 5. Joint powers of SJTU-EX for walking with a payload of 70 kg

abduction–adduction joint. The hip rotation joint and the ankle abduction–adduction joint of SJTU-EX are left passive because they require small power consumptions. The necessary torques and powers of the two un-actuated joints are provided by the wearer. So springs are applied to reduce the load on human muscles and increase comfort.

5 Implement of Springs in the Diamond Mechanism

The required torques and powers of the actuated joints are the primary criterions to select proper actuators. However more torques would be needed for the two joints of the diamond mechanism if SJTU-EX is worn by a person shorter than 1.80 m. To compensate for the worse load supporting capability and eliminate the effect of gravity, extension springs are applied in the shorter diagonal of the diamond mechanism, as shown in Fig. 6.

The primary principle of the spring design is to shift an appropriate part of the torque from stance phase to swing phase so that the required peak torques for the two joints of the diamond mechanism are smaller. The selection of a proper spring should keep to the following three rules:

1. The spring is in the extension state when the wearer stands straight so that it helps the exoskeleton to support the load. A larger initial spring tension will lead to smaller driving torques for the diamond mechanism in stance phase and on the

other hand cause larger torques in swing phase which are originally close to 0. An appropriate spring initial tension should result in almost the same peak torques for the swing phase and the stance phase during a walking cycle.

2. The spring stiffness k should be small so that it won't cause a big torque undulation in swing phase. As a result, the initial spring elongation Δl_i must be large to provide the tension in Rule 1 according to the Hooke's law $F = k \times \Delta l$.
3. The spring stiffness k in Rule 2 must guarantee the spring elongation Δl within the spring elongation limit during the motion cycle.

According to the three rules, springs with different stiffnesses and initial lengths should be chosen for various applications, based on the height of the wearer, the payload and the motion type.

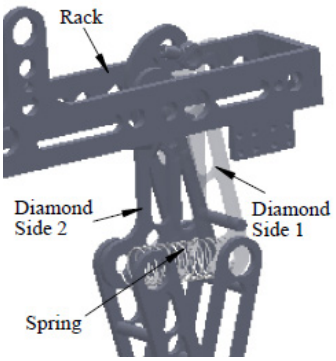

Fig. 6. Diamond mechanism with a spring in the diagonal

Table 3. Joint torques of the diamond mechanism with a payload of 70 kg

Height Of Wearer	Initial length and Stiffness of Spring	Joint Torque Range of Diamond Side 1 ($N \cdot m$)	Joint Torque Range of Diamond Side 2 ($N \cdot m$)
1.60 m	without Springs	$(-225, 24)$	$(-33, 192)$
	$l_0 = 0.15\ m, k = 4000\ N/m$	$(-155, 115)$	$(-114, 127)$
1.70 m	without Springs	$(-190, 26)$	$(-32, 160)$
	$l_0 = 0.1m, k = 2500N/m$	$(-146, 97)$	$(-88, 115)$
1.80 m	without Springs	$(-140, 27)$	$(-39, 109)$

Table 3 lists the simulation results for different wearers from 1.60 m to 1.80 m during walking. The implementation of the springs has an impressive effect on the reduction of the peak torques. The specifications of the springs in Table 3 can be referred to in practical use. The stiffness k in Table 3 means a total effective stiffness for the diamond mechanism. So it should be half of the stiffness for each

spring, if two springs are mounted in the diagonals of the two diamonds respectively. Springs are not necessary when the exoskeleton is worn by a 1.80 m person because the diamond mechanism remains a small diamond angle α less than 45°during walking. However, auxiliary springs should also be mounted in the diamond mechanism to help accomplish other human motions like squatting and stairs climbing when α becomes large and the load supporting capability goes worse. For example, the auxiliary spring will undertake more and more vertical load as the wearer squats and therefore obviously reduce the required torques for the two joints of the diamond mechanism.

6 Conclusions

In the paper, a pseudo-anthropomorphic exoskeleton SJTU-EX with six degrees of freedom is presented. Four joints with large power consumptions are actuated according to the dynamic simulations. A parallel diamond mechanism with two degrees of freedom is introduced in replace of the hip and knee flexion/extension joints for a better load supporting capability. Springs are mounted on both the active and passive joints of SJTU-EX, which can eliminate the effect of gravity as well as increase comfort. Human joint ranges when wearing SJTU-EX are first determined and then the corresponding exoskeleton joint ranges are optimized on the basis of typical human motions.

Future work will include the selection and layout of proper actuators and sensors.

Acknowledgements. This work is partially supported by the National Basic Research Program of China (973 Program, Grant No. 2013CB035501).

References

[1] Yang, C., Zhang, J., Chen, Y., Dong, Y., Zhang, Y.: A review of exoskeleton-type systems and their key technologies. Proceedings of the Institution of Mechanical Engineers, Part C: Journal of Mechanical Engineering Science 222(8), 1599–1612 (2008)

[2] Walsh, C.J., Endo, K., Herr, H.: A quasi-passive leg exoskeleton for load-carrying augmentation. International Journal of Humanoid Robotics 4(3), 487–506 (2007)

[3] Dollar, A.M., Herr, H.: Design of a quasi-passive knee exoskeleton to assist running, pp. 747–754. IEEE

[4] Agrawal, S.K., Banala, S.K., Fattah, A., Scholz, J.P., Krishnamoorthy, V., Hsu, W.L.: A gravity balancing passive exoskeleton for the human leg

[5] Kazerooni, H., Steger, R.: The Berkeley lower extremity exoskeleton. Journal of Dynamic Systems, Measurement, and Control 128, 14 (2006)

[6] Guizzo, E., Goldstein, H.: The rise of the body bots [robotic exoskeletons]. IEEE Spectrum 42(10), 50–56 (2005)

[7] Kawamoto, H., Sankai, Y.: Power assist method based on phase sequence and muscle force condition for HAL. Advanced Robotics 19(7), 717–734 (2005)

[8] Kirtley, C.: CGA Normative Gait Database. Hong Kong Polytechnic University (2005)

[9] Zheng, X., Jia, S., Gao, Y., Hou, M., Xi, D., Yang, H.: Modern sports biomechanics, pp. 100–163. National Defense Industry Press (2002)
[10] Rose, J., Gamble, J.G.: Human walking. Lippincott Williams & Wilkins (2006)
[11] Whittle, M.W.: Clinical gait analysis: A review. Human Movement Science 15(3), 369–387 (1996)
[12] Chu, A., Kazerooni, H., Zoss, A.: On the biomimetic design of the berkeley lower extremity exoskeleton (BLEEX), pp. 4345–4352. IEEE
[13] Keller, T., Weisberger, A., Ray, J., Hasan, S., Shiavi, R., Spengler, D.: Relationship between vertical ground reaction force and speed during walking, slow jogging, and running. Clinical Biomechanics 11(5), 253–259 (1996)

Design of Selectively Controllable Micro Actuators Powered by Remote Resonant Magnetic Fields

Kai Xu and Guoqing Liu

RII Lab (Lab of Robotics Innovation and Intervention), UM-SJTU Joint Institute,
Shanghai Jiao Tong University, Shanghai, 200240, China
{k.xu,novel_lau}@sjtu.edu.cn

Abstract. Micro actuators for tiny robots could lead to revolutionary advances in many cutting-edge applications (e.g. minimally invasive medicine). Many prototypes were hence developed, which were powered either by micro organism, by onboard mechatronic systems or by remote magnetic fields. This paper presents two evolving designs, aiming at fabricating micro actuators which can be selectively controlled by weak resonant magnetic fields. The core concept is to design a spring-mass structure to convert the vibrations of soft magnets into rotary outputs. The fabricated micro actuators could then drive propellers or revolute joints for locomotion or manipulation tasks. The proposed designs essentially directly harvest magnetic energy to perform mechanical work, avoiding complex system components from traditional motorized actuation units, such as windings, commutators, batteries, etc.

Keywords: Micro actuators, soft magnets, resonant magnetic fields, micro fabrication.

1 Introduction

Micro robots could find many potential applications in minimally invasive medicine, such as performing diagnosis and treatments in intracranial cavities and vascular systems [1, 2]. These visionary functions could not be realized unless micro actuators are integrated into micro robots for swimming through low-Reynolds-number regions [2, 3] and performing manipulation tasks. Both locomotion (such as intravascular swimming or crawling) and manipulation depend on properly integrated micro actuators. Actuation designs of many existing micro robots fall into one of the following categories:

- ✧ Engineered micro organisms (such as bacteria) were used to provide propelling actuation, as in [4-7]. Ensuring controllability and biological safety of such robots could be quite challenging.
- ✧ A standalone micro robot with an onboard power and a controller is also possible, such as the designs in [1, 8-10]. Fabrication complexity and difficulty might be a real obstacle when such a micro robot is further downsized.
- ✧ Strong magnetic fields could be used to drive micro robots. These micro robots made from magnetic materials could be dragged by a static magnetic gradient

J. Lee et al. (Eds.): ICIRA 2013, Part II, LNAI 8103, pp. 143–154, 2013.

(e.g. the designs in [11-13]). Or a rotating or an oscillating magnetic field can be used to spin or swing a micro robot so that its helical or flexible tail can generate thrusts for swimming (e.g. the designs in [14, 15] [16-18]). However, individual control of a swarm of robots can be quite difficult.

✧ A weak oscillating magnetic field could be used to trigger a resonant vibration between a micro robot's mass blocks made from soft magnetic materials. Then the collision could be modulated to provide thrusts, as presented in [19-21]. Different resonant frequencies can be used to control different robots. However, the aforementioned designs need a frictional surface to operate, which puts practical limitations for the designs' practical applications.

Inspired by the results from the work as in [19-21], this paper presents two evolving designs as shown in Fig. 3 and Fig. 7, aiming at fabricating a micro actuator which can be selectively remotely controlled by weak resonant magnetic fields. With such micro actuators fabricated and equipped, micro robots might then be able to actively navigate around (swim or crawl) and perform manipulation tasks.

The main contribution of this paper is the proposal of fabricating micro actuators which essentially directly harvest magnetic energy in space to perform mechanical work. These actuators consist of mass-spring structures using properly arranged soft magnetic and non-magnetic materials. Success of the proposed idea could lead to the development of micro actuators which could be remotely controlled by weak oscillating magnetic fields under different frequencies. And such micro actuators would find wide applications in both minimally invasive medicine and other fields.

The paper is organized as follows. Section 2 presents the working principle of the design concepts. Section 3 presents the coil design for generating oscillating magnetic fields. Section 4 and Section 5 present the alpha design and the beta design, including design simulations and fabrication attempts. Conclusions and future work are summarized in Section 6.

2 The Design Concept

Working principle of the design concepts is shown in Fig. 1. Mass blocks made from soft magnetic materials are connected by a non-magnetic spring. When an external magnetic field is applied, the mass blocks made from soft magnetic materials are magnetized. An attraction force is hence generated between the blocks to compress the non-magnetic spring. When the external magnetic field is removed, magnetization of the blocks disappears and so does the attraction force. The compressed spring generates a repulsive force to push the blocks apart.

When the external magnetic field is switched on and off at a frequency that matches the resonant frequency of the mass-spring system, mechanical energy (kinetic energy of the blocks and elastic potential energy of the spring) will accumulate within the system. When the accumulated energy exceeds a threshold, a designed structural feature will allow the output of the energy via a collision or modulated friction.

Following this working principle, two conceptual designs are presented in later sections, aiming at producing a micro actuator which can be selectively remotely controlled by resonant magnetic fields. The designs essentially directly harvest magnetic energy to perform mechanical work, avoiding complex system components from traditional motorized actuation units, such as windings, commutators, batteries, etc. With such micro actuators fabricated and equipped, micro robots might then be capable of swimming or crawling around and performing manipulation tasks.

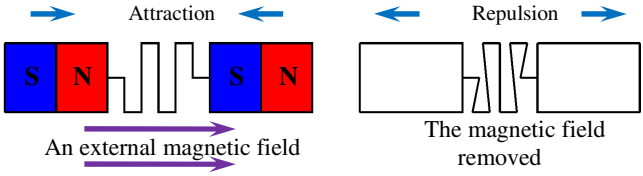

Fig. 1. Working principle of the design concept

3 The Coil Design

According to the working principle of the design concept, a fast switching magnetic field will be needed to actuate the micro actuators. This section presents the design of a coil system for such a magnetic field. Since the magnetic field will be primarily used to test the micro actuators that generate rotary outputs without moving around, the uniformity of the magnetic field is not much concerned. This work hence chose to apply a pair of Helmholtz coils due to its widely accepted effectiveness.

According to [20], a magnetic field with the magnetic flux density as weak as 2mT is capable of driving the micro robots with planar movements. 2mT is hence selected as the design goal of the coil system. Since the magnetic flux density matters the strength of the magnetization and hence affects how fast the harvested energy accumulates within an actuator, a slightly weaker or stronger magnetic field should be always capable of driving the actuators, as far as the principle works.

As shown in Fig. 2, a Maxon motor amplifier (LSC 30/2) working in its current mode was used to drive the pair of Helmholtz coils. Since the current output of the amplifier is limited to ±2A, the coils are assumed to have a 1.5A current while finalizing the coil parameters following the approach as in [22]. Each coil in the Helmholtz pair has a diameter of 30mm and 45 turns (distributed in 6 layers as 8-7-8-7-8-7 turns per layer). Distance between the center planes of the coils is also kept 30mm, as shown in Fig. 2-(b).

Referring to Fig. 2-(a), square-wave signals from the signal generator are connected to the V_{set+} and V_{set-} ports of the Maxon amplifier. Motor+ and Motor– ports of the Maxon amplifier are connected to the Helmholtz coils and a resistor serially. Voltage on the resistor is monitored by an oscilloscope to indicate the current flowing through the coils. P_{gain} and N_{max} knobs of the amplifier can be adjusted for the current to better follow the desired signal. Using this setup, an on/off current of 1.5A

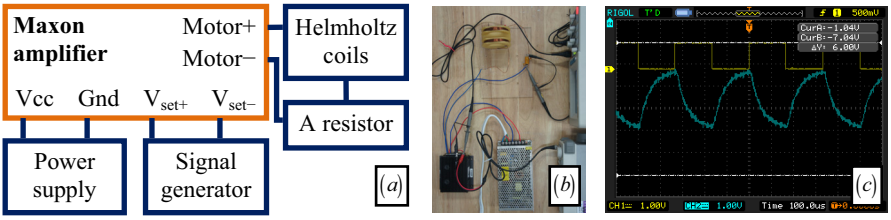

Fig. 2. The Helmholtz coils with the actuation circuit: (a) the schematic, (b) the actual system, and (c) wave form of the current in the Helmholtz coils following a 3.3KHz square-wave signal

can be driven to follow a square-wave signal with a frequency up to 3.3 KHz, as shown in Fig. 2-(c).

4 The Alpha Design

4.1 The Conceptual Structure

Following the aforementioned working principle, the alpha design is shown in Fig. 3. It consists of a base, an output rotor, two vibrators and two asymmetric planar springs. The vibrators are made from soft magnetic materials (electrically deposited nickel) and the springs are made from non-magnetic materials (electrically deposited copper). The nickel vibrators are sandwiched by the two copper springs.

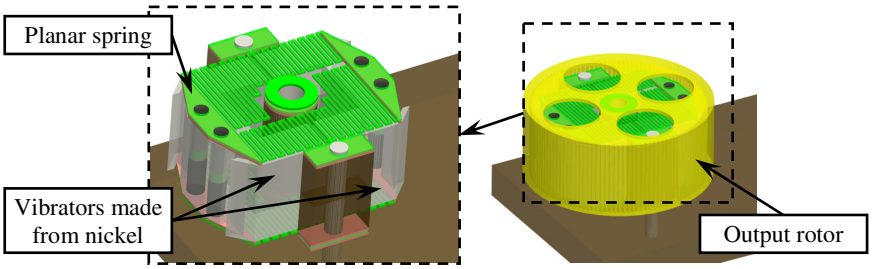

Fig. 3. The alpha design with a sandwiched spring-mass structure

When the spring-vibrator system is placed in an oscillating magnetic field (a fast switching on/off magnetic field), different resonant frequencies of the spring-vibrator system will lead to different vibration patterns. Making use of these different vibration patterns, the alpha design is expected to generate counterclockwise and clockwise rotary outputs when the magnetic field is switched on and off at different resonant frequencies.

Finite element simulations were then carried out to verify this conceptual structure.

4.2 Design Simulations

Back view of this alpha design is shown in Fig. 4-(a) for better indication of the geometrical dimensions of this design. The alpha design can be disassembled into i) the output rotor and ii) the sandwiched spring-mass structure.

- ✧ The output rotor has an outer diameter of 1 mm (1000 um).
- ✧ The Ni (nickel) vibrator blocks have a width of 600 um. The gap between the two Ni blocks is 20 um. An attraction force of about 1.2×10^{-6} N will be generated when the Ni blocks are magnetized in a magnetic field of 2 mT.
- ✧ Pointed corners (P_1, P_2, P_3 and P_4) are designed for the vibrators so that kinetic energy can be better transferred to the output rotor through collisions when the vibration amplitude becomes big enough under resonant frequencies.
- ✧ Width and layer thickness of the Cu spring are both 10 um. There are two holes with a diameter of 70um for relative positioning of the Cu spring and the Ni block.

Vibration patterns of the spring-mass structure under different resonant frequency were simulated in COMSOL.

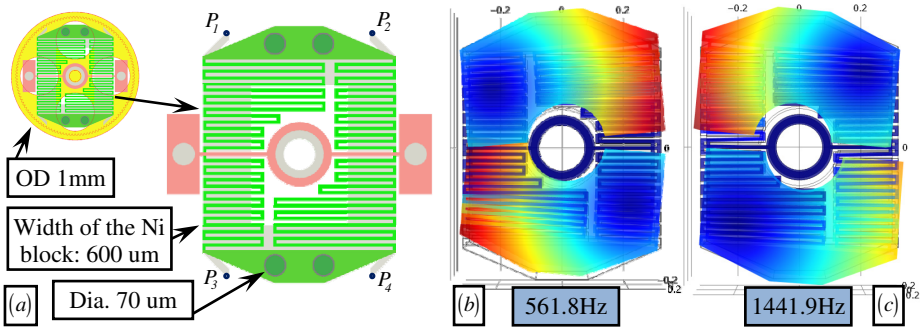

Fig. 4. Resonant vibrations of the alpha design: (a) geometrical dimensions, (b) the vibration pattern in an oscillating magnetic field at 561.8 Hz, and (c) the vibration pattern at 1441.9 Hz

As shown in Fig.4-(b), when the magnetic field is switched on/off at a resonant frequency of 561.8Hz, the nickel vibrator is oscillating in a rotary pattern with the center of motion located at the left side (indicated by the dark blue dot). When the vibration amplitude becomes bigger under this resonant excitation, the pointed corners P_1 and P_4 will hit the inner wall of the output rotor. A continuous counterclockwise rotation is then expected from such repeated collisions.

Similarly, at a higher resonant frequency of 1441.9Hz as shown in Fig. 4-(c), the nickel vibrator is oscillating with the center of motion located at the right side. At this higher frequency, the pointed corners P_2 and P_3 have bigger vibration amplitudes and they shall hit the inner wall of the output rotor. Such repeated collisions are then expected to generate continuous clockwise rotation outputs.

The gap between the pointed corners of the nickel vibrator and the inner wall of the output rotor is kept 6 to 10 um. At non-resonant frequencies of the spring-vibrator system, amplitudes of the vibrators will not be big enough to hit the inner wall of the

output rotor. Hence no rotation outputs are expected when the external magnetic field is switched on/off at non-resonant frequencies.

Cavities can be included in the nickel vibrators to change the mass distribution. This will lead to changes in the resonant frequencies. Then different micro actuators could be designed to work under different excitation frequencies.

4.3 Fabrication and Assembling Attempts

It will be a challenging and costly process to fabricate the alpha design from Fig. 3 as one piece going through consecutive micro fabrication steps. In order to lower the fabrication costs, it was decided to fabricate the components of the alpha design separately and assemble the components. Some fabrication results are shown in Fig. 5.

- ✧ The output rotor and the rectangular spacer blocks as in the insets (a) and (b) were fabricated via lithography using photoresist SU-8 (UV LIGA). The output rotor has been produced with various inner diameters.
- ✧ The nickel vibrator shown in the inset (c) was produced by lithography followed by electrical deposit of nickel. The thickness is 360 um.
- ✧ The copper spring and copper spacer as in the insets (d) and (e) were produced using lithography followed by electrical deposit of copper. The thickness is 10 um.

Tolerances of these fabricated components are all within ±5 um. After picking components with fitting tolerances, it is possible to assemble these components to form the alpha design using a micro positioning device.

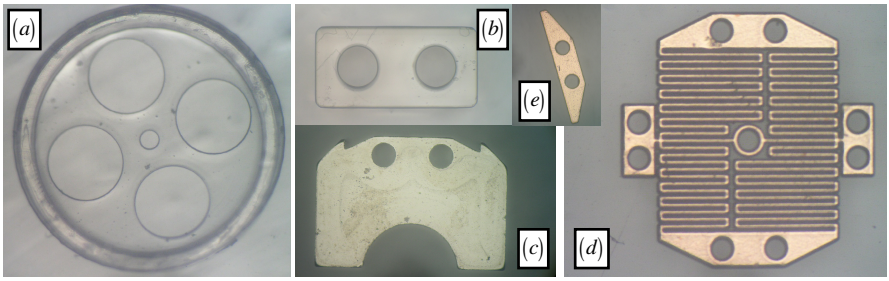

Fig. 5. Partial fabrication results of the alpha design

The proposed assembling process is shown in Fig. 6:

a) The connecting poles will be firstly inserted into the holes in the base; then the removable spacers (the blue ones) and the structural spacers (the pink ones) will then be placed;
b) The copper spring can now sit on top of the spacers; then another layer of the structural spacers (the pink ones) and the connecting pins (the blue ones) will be placed; glue droplets will be applied to bond the spring to the pins;
c) The rectangular block spacers (the brown ones) and the removable spacers (the blue ones) will be placed;

d) The nickel vibrator blocks will be placed on the connecting pins with another layer of the structural spacers (the pink ones); glue droplets will be applied again in the holes for the connecting pins;
e) The top spring can now be placed; and after the glue is set, the removable spacers (the blue ones) will be pulled out;
f) The output rotors will be assembled.

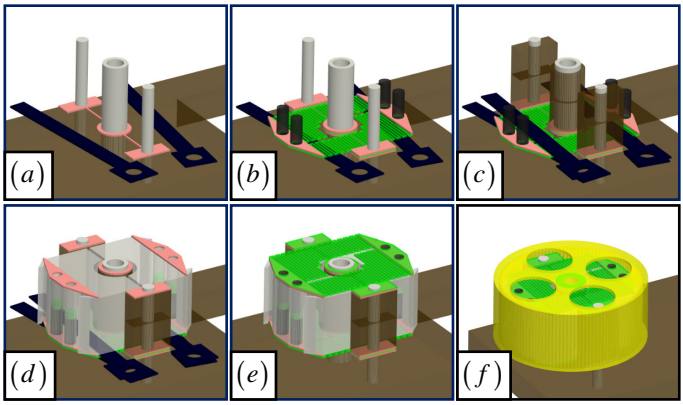

Fig. 6. Proposed assembling process of the alpha design

5 The Beta Design

It was planned to use a micro positioning device with a gripper to assemble the alpha design. Such suitable positioning devices are available from various suppliers (e.g. Thorlabs Inc.). However, a proper gripper was not identified. None of the home-made grippers using suctions, adhesives, or static electricity attractions could pick up and drop a component without affecting the components already in place. The alpha design was hence modified to form the beta design.

5.1 The Conceptual Structure

The beta design shown in Fig. 7 now has a layered spring-mass structure. It would be cheaper and easier to fabricate the layered spring-mass structure of the beta design than to fabricate the sandwiched structure of the alpha design as one piece

The beta design consists of i) a base, ii) an output rotor, and iii) a layered spring-mass structure. Similarly to the alpha design, the two nickel vibrators are expected to have various vibration modes under different resonant excitation frequencies to generate clockwise and counterclockwise rotations of the rotor.

A series of design simulations are presented in the next section to explain a minor revision of this design.

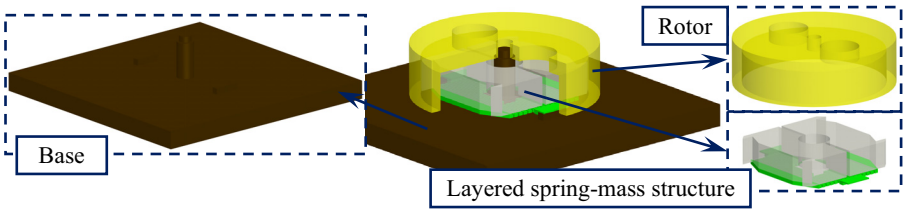

Fig. 7. The beta design with a layered spring-mass structure

5.2 Design Simulations

Vibrations of the layered spring-mass structure of the beta design are simulated in COMSOL to verify the existence of the desired vibration patterns. Geometrical parameters are listed as follows.

- ✧ The output rotor has an outer diameter of 1250 um.
- ✧ The nickel vibrator blocks have a width of 800 um and a thickness of 200 um. The gap between the two nickel blocks is 30 um.
- ✧ Width and layer thickness of the Cu spring are 10 um and 20 um respectively.

The simulated vibration patterns are presented in Fig.8. The patterns were exported to Matlab to plot the trajectories of the pointed corners. At an excitation frequency of 340 Hz, the vibration pattern is consistent with the design expectation: one side has considerably bigger amplitude to always trigger collisions on this side with the output rotor so as to generate a continuous rotary output. However at the second resonant frequency of 1797 Hz, the nickel vibrator has similar amplitudes at both sides. Continuous rotary output can hardly be expected since collisions on both sides would cancel out each other.

A series of simulations were carried out, trying to identify a beta design whose second resonant vibration mode meets the design requirement, by altering the mass distribution of the nickel vibrator and the layout of the spring. A proper spring-mass structure with such a desired second resonant vibration pattern was not identified.

A design compromise was made and the final beta design is shown in Fig. 9. Instead of having four pointed corners, the final design only features two pointed corners and only utilizes the first resonant vibration patterns.

The upper portion of the spring-mass structure has the first resonant frequency of 340 Hz, under which only the corner P_1 will collide with the rotor. The lower portion of the spring-mass structure has the first resonant frequency of 450 Hz, under which only the corner P_2 will collide with the rotor. Although the counterclockwise and clockwise rotations of the rotor could still be realized, efficiency of the final beta design could be relatively low. The reason is quite obvious: during resonant vibrations, only one vibrator mass (the upper one at 340 Hz or the lower one at 450 Hz) would transfer its kinetic energy to the rotor through collisions.

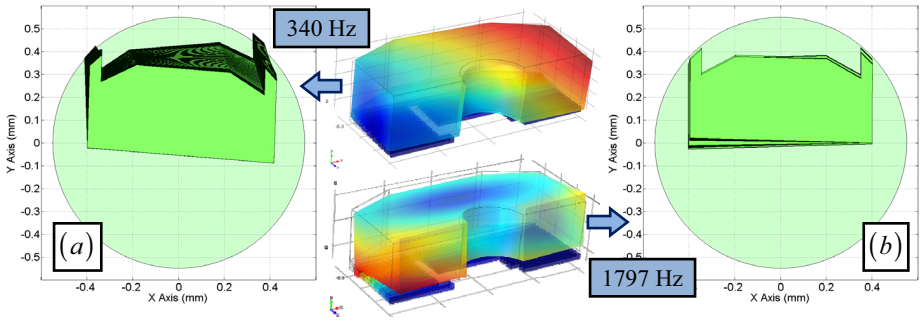

Fig. 8. Vibration patterns of the initial beta design: (a) 340 Hz and (b) 1797 Hz

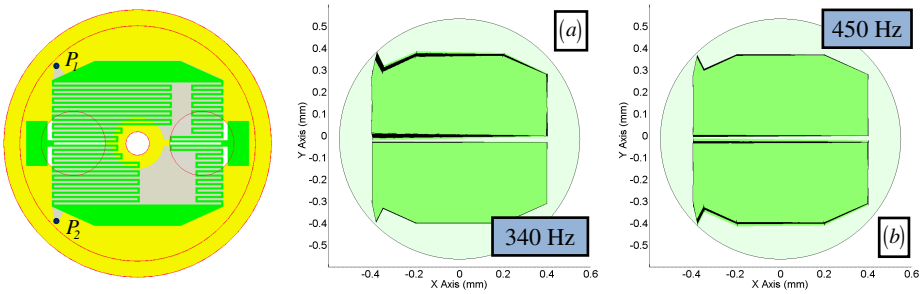

Fig. 9. The final beta design with its vibration patterns: (a) 340 Hz and (b) 450 Hz

5.3 Fabrication Attempts

The final beta design will be fabricated as three components as indicated in Fig. 7: i) the base, ii) the rotor, and iii) the layered spring-mass structure. Since no tiny components need to be placed and glued, this assembling task could be accomplishable.

The base and the rotor both have stepped structures and they would be fabricated by etching a silicon wafer through a series of masked lithography. The layered spring-mass structure would have the following fabrication steps, referring to Fig. 10:

a) A seed layer for nickel electroplating will firstly be sputtered on the backside of the wafer;
b) Lithography will be performed on the front side of the wafer to define the profile of the nickel blocks;
c) Silicon will then be removed by dry etching so that the nickel blocks could be electrically deposited;
d) The wafer will be polished and a layer of polycrystalline silicon will then be grown and etched to form the spacer layer to lift up the spring from the nickel blocks;

e) The Cu spring spacer was electroplated;
f) A Ti/Cu seed layer was applied and the spring defining photoresist will be formed;
g) The Cu spring will then be electroplated;
h) All silicon materials will be resolved to release the spring-mass structure.

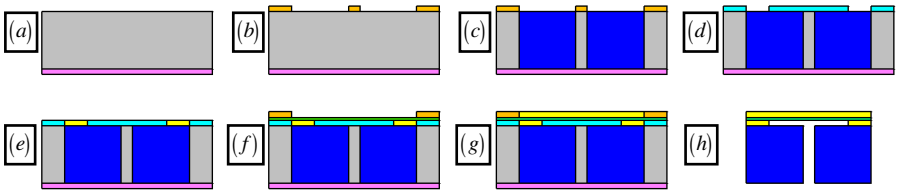

Fig. 10. Fabrication steps of the final beta design

6 Conclusions and Future Work

This paper presents two evolving designs, aiming at producing a micro actuator which can be selectively remotely actuated by weak resonant magnetic fields. If the proposed idea succeeds, these micro actuators can essentially directly harvest magnetic energy in space to perform mechanical work and they will find wide applications from MEMS manipulation to minimally invasive medicine.

The core design concept is to conceive various spring-mass structures where the mass blocks are made from soft magnetic materials and the springs are made from non-magnetic materials. A fast switching magnetic field will induce resonant vibrations of the mass blocks and the blocks would cause mechanical outputs via collisions or modulated friction when the vibrating amplitudes are big enough. Magnetic fields at different switching frequencies would then be capable of driving different rotary modes of different actuators.

Due to the fabrication and assembling challenges, the alpha design was evolved into the beta design. Design simulations and fabrication attempts for both designs were presented in detail.

The immediate future work is to finish fabricating the beta design. Then a series of experimental verifications and design characterizations could be carried out, investigating the i) feasibility, ii) speed of the rotation output versus strength of the magnetic field, iii) payload capability, iv) dynamic responses, v) further miniaturization possibility, etc.

Acknowledgments. This work was supported in part by the National Science Foundation of China Grant # 51005146, in part by the Program for New Century Excellent Talents in University (the NCET Program), and in part by the internal funds from the SJTU State Key Laboratory of Mechanical System and Vibration.

The authors would like to thank Gong Zhang from the Research Institute of Micro/Nano Science and Technology, Shanghai Jiao Tong University, and Yunfei Sun from the Suzhou Institute of Nano-Tech and Nano-Bionics, Chinese Academy of Sciences, for the help of fabricating various design components.

References

1. Cavalcanti, A., Shirinzadeh, B., Fukuda, T., Ikeda, S.: Nanorobot for Brain Aneurysm. International Journal of Robotics Research 28(4), 558–570 (2009)
2. Abbott, J.J., Nagy, Z., Beyeler, F., Nelson, B.J.: Robotics in the Small: Part I: Microrobotics. IEEE Robotics & Automation Magazine 14(2), 92–103 (2007)
3. Abbott, J.J., Peyer, K.E., Lagomarsino, M.C., Zhang, L., Dong, L., Kaliakatsos, I.K., Nelson, B.J.: How Should Microrobots Swim? International Journal of Robotics Research 28(12), 1434–1447 (2009)
4. Berg, H.C.: The Rotary Motor of Bacterial Flagella. Annual Review of Biochemistry 72, 19–54 (2003)
5. Behkam, B., Sitti, M.: Bacterial Flagella-Based Propulsion and on/off Motion Control of Microscale Objects. Applied Physics Letters 90(023902), 1–3 (2007)
6. Behkam, B., Sitti, M.: Characterization of Bacterial Actuation of Micro-Objects. In: IEEE International Conference on Robotics and Automation (ICRA), Kobe, Japan, pp. 1022–1027 (2009)
7. Steager, E., Kim, C.-B., Patel, J., Bith, S., Naik, C., Reber, L., Kim, M.J.: Control of Microfabricated Structures Powered by Flagellated Bacteria Using Phototaxis. Applied Physics Letters 90(263901), 1–3 (2007)
8. Zhang, H., Dong, S.-X., Zhang, S.-Y., Wang, T.-H., Zhang, Z.-N., Fan, L.: Ultrasonic Micro-motor Using Miniature Piezoelectric Tube with Diameter of 1.0 mm. Ultrasonics 441((s)1), e603-e606 (2006)
9. Watson, B., Friend, J., Yeo, L., Sitti, M.: Piezoelectric Ultrasonic Resonant Micromotor with a Volume of Less Than 1 mm3 for Use in Medical Microbots. In: IEEE International Conference on Robotics and Automation (ICRA), Kobe, Japan, pp. 2225–2230 (2009)
10. Yun, C.-H., Watson, B., Friend, J., Yeo, L.: A Piezoelectric Ultrasonic Linear Micromotor Using a Slotted Stator. IEEE Transactions on Ultrasonics, Ferroelectrics and Frequency Control 57(8), 1868–1874 (2010)
11. Yesin, K.B., Vollmers, K., Nelson, B.J.: Modeling and Control of Untethered Biomicrorobots in a Fluidic Environment Using Electromagnetic Fields. International Journal of Robotics Research 25(5-6), 527–536 (2006)
12. Floyd, S., Pawashe, C., Sitti, M.: Two-Dimensional Contact and Noncontact Micromanipulation in Liquid Using an Untethered Mobile Magnetic Microrobot. IEEE Transactions on Robotics 25(6), 1332–1342 (2009)
13. Pawashe, C., Floyd, S., Sitti, M.: Modeling and Experimental Characterization of an Untethered Magnetic Micro-Robot. International Journal of Robotics Research 28(8), 1077–1094 (2009)
14. Zhang, L., Abbott, J.J., Dong, L., Kratochvil, B.E., Bell, D., Nelson, B.J.: Artificial Bacterial Flagella: Fabrication and Magnetic Control. Applied Physics Letters 94(064107), 1–3 (2009)
15. Honda, T., Arai, K.I., Ishiyama, K.: Micro Swimming Mechanisms Propelled by External Magnetic Fields. IEEE Transactions on Magnetics 32(5), 5085–5087 (1996)
16. Troisi, C.S., Knaflitz, M., Olivetti, E.S., Martino, L., Durin, G.: Fabrication of New Magnetic Micro-Machines for Minimally Invasive Surgery. IEEE Transactions on Magnetics 44(11), 4488–4491 (2008)
17. Sudo, S., Segawa, S., Honda, T.: Magnetic Swimming Mechanism in a Viscous Liquid. Journal of Intelligent Material Systems and Structures 17(8-9), 729–736 (2006)

18. Guo, S., Pan, Q., Khamesee, M.B.: Development of a Novel Type of Microrobot for Biomedical Application. Microsystem Technology 14(3), 307–314 (2008)
19. Kratochvil, B.E., Frutiger, D., Vollmers, K., Nelson, B.J.: Visual Servoing and Characterization of Resonant Magnetic Actuators for Decoupled Locomotion of Multiple Untethered Mobile Microrobots. In: IEEE International Conference on Robotics and Automation (ICRA), Kobe, Japan, pp. 1010–1015 (2009)
20. Frutiger, D.R., Vollmers, K., Kratochvil, B.E., Nelson, B.J.: Small, Fast, and Under Control: Wireless Resonant Magnetic Micro-agents. International Journal of Robotics Research 29(5), 613–636 (2009)
21. Nagy, Z., Frutiger, D.R., Leine, R.I., Glocker, C., Nelson, B.J.: Modeling and Analysis of Wireless Resonant Magnetic Microactuators. In: IEEE International Conference on Robotics and Automation (ICRA), Anchorage, Alaska, USA, pp. 1598–1603 (2010)
22. Kirschvink, J.L.: Uniform Magnetic Fields and Double Wrapped Coil Systems: Improved Techniques for the Design of Bioelectromagnetic Experiments. Bioelectromagnetics 13(5), 401–411 (1992)

Mechanical Home Position Setting Method of the Manipulator with Two Encoders

Tae Yong Choi, Hyun-Min Do, Doo-Hyung Kim,
Kyung-Taik Park, and Kwangcho Chung

Department of Robotics and Mechatronics,
Korea Institute of Machinery & Materials, Daejeon, 305-343, Korea
{taeyongc,hmdo,kdh649,ktpark,ckc}@springer.com
http://www.kimm.re.kr

Abstract. Human rights at poor working condition is the severe problem in modern manufacturing system. The industrial dual-arm robot is being developed to meet these social issues fundamentally. The dual-arm robot we are developing has some merits compared with conventional dual-arm robots. It's size is similar to adult human size and payload is more than 5kg. We can not attach powerful position sensors at each joints to achieve small body with high torque property. With these constraints, we still want to achieve high precision position sensors with mechanical home positioning functions. The method is implemented with a absolute encoder without multi-turn function and a incremental encoder.

1 Introduction

Industrial robot systems, has been widely used for manufacturing such as laser welding, transfer and many repetitive process. They can work all day without stop and error. Conventional industrial robot is a single manipualtor robot. In case of serial robot, 6 degrees of freedom (DOF) commonly used to position the end-effector of robot to exact postion with orientation. However, they have limitation to replace human worker due to their low DOF in one arm. Recently, dual-arm robots such as [1–3] are becomming upcomming technology for manufacturing in cell line. They have almost same DOF as human. They can have 6 DOF or 7 DOF in one arm depending on shoulder motion. Cell line to assemble small product is good example for them to be used.

Yaskawa's motoman [1] is the leading robot. They already sells their products on the market for the purpose of assembly works. Kawada's nextage [2] shows insteresting example of the cooperation between human and robot. ABB's frida [3] is the promising robot as a coworker with human at production lines.

Aforementioned robots have their own advanates and disadvantaged. Yaskawa's motonman [1] has stength on its power. Its payload is more than 10Kg for each arm. However, its size is much bigger than the adults. The stength of ABB's frida [3] is the size. It is similar to human workers' body size. However, its payload is estimated small.

J. Lee et al. (Eds.): ICIRA 2013, Part II, LNAI 8103, pp. 155–165, 2013.

The robot with dual-arm is aimed to cowork with human workers. They have to have small body and high torque, even its size is not much bigger than the human size. To overcome conventional dual-arm robot's weakness, new dual-arm robot is being developed. The brief inductroduction is described in [4].

We used the hollow actuator to make the robot slim. Lines of the power and ethercat is embedded in the links and actuators. Our robot need to measure the contact force when it operate objects. However, force and torque sensors are somewhat corpulent. In this reason we attached two encoders for the out-stage and in-stage of the actuator. Out stage means the link actuated by the flexspline of the harmonic gears. In-stage means the link actuated by the wave generator. Position of the out-stasge is effected by the external forces. The position difference between out-stage and in-stage has direct relation with the external forces which must be measured. However, measureing the external forces with the two encoders is out of this research's focus.

Here we want to position the dual-arm robot based on the absolute position by combining two encoders adequately.

2 Background

We aim to develope the cell line for IT product manufacturing like Fig.1. Currently, IT products such as mobile phone and TV are made by human, who works all day at the designated area with standing. Their work is repetitive. Robot, specifically, Dual-arm robot which have functions like human can be a proper substitution for this kinds of tedious and repetitive works. In our senario, two or three robots cooperate to assemble mobile phone. Also, they can pack the mobile phone. Because dual-arm robot have two arms like human, then can manage objects as human do without additional tools for automation.

The dual-arm robot to apply the factory is on the development. Its physical properties are described in Tabel.1. It has 7 DOF in each arms and 2 DOF in waist. The payload to weight ratio will be at least 1/2. All actutors and sensors are communicated by ethercat protocol [5]. Ethercat is communication standard introduced by BECKHOFF inc.. It use the conventional local area network (LAN) physical layer and hardware, so user don't need to add any special equipments. It use the daisy chain topology for connection. In our robot, hollow axis actuators and sensors are used and all signals connected through the hole. In this reason serial connection method of ethercat is very useful.

Table 1. Dual-arm robot dimension

	DOF	Weight(Kg)	Length(mm)
Left arm	7	14.5	700
Right arm	7	14.5	700
Torse	2	21.4	720

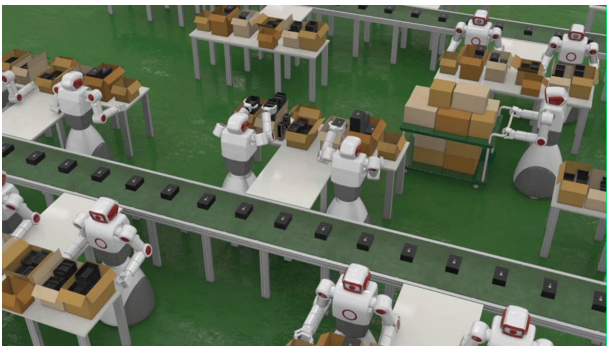

Fig. 1. Designed IT products manufacturing cell line

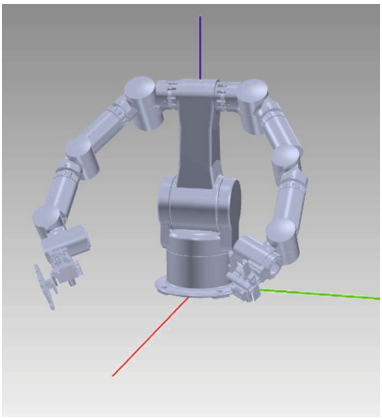

Fig. 2. Designed dual-arm robot

3 Constraints of the Positioning Sensors

Realization of the our dual-arm robot is shown in Fig.3. It is prototype. We are on developing, currently it has no torse axis, some wires are not embedded. Of course, it should be embedded and there are enough space for wiring. However, it is wired out the link for maintenance comfortability temporarily. Each link contains actuator of Fig.4. Its size is almost the adult's fist size. Internal structure is described in Fig.5.

Position sensor is essential to be controlled properly for all manipulators. For the exact and compliant usage high resolution absolute encoder with the multi-turn information is good solution. However, the size of absolute encoder with the multi-turn information is not small. Robots need absolute encoder for home positioning and high resolution encodoer for stable position control. In our dual-arm robot with the hollow actuator, there are not much spaces. To cope with these needs, absolute encoder without multi-turn information is attached

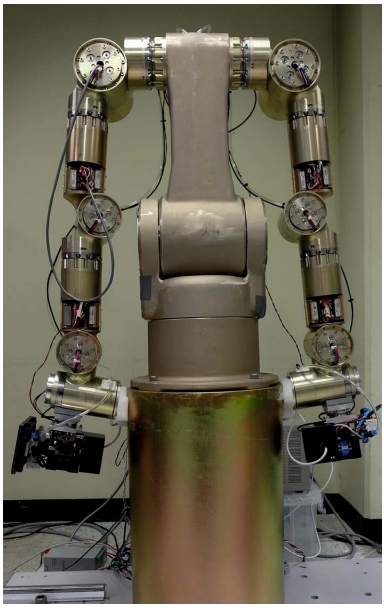

Fig. 3. The developed dual-arm robot

Fig. 4. The structure of actuators

to the out-stage, and the high resolution incremental encoder is attached to the in-stage. Of course the resolution of incremental encoder is low due to the given spaces. However, the final resolution is higher than the absolute encoder by multiplying gear ratio. Table. 2 shows the comparison between out-stage and in-stage.

We aim to get the arm position based on the absolute encoder. In industrial application robot have to know the mechanical origin of himself even though the power is down. So using the absolute encoder is absolutely nessasary. Meanwhile,

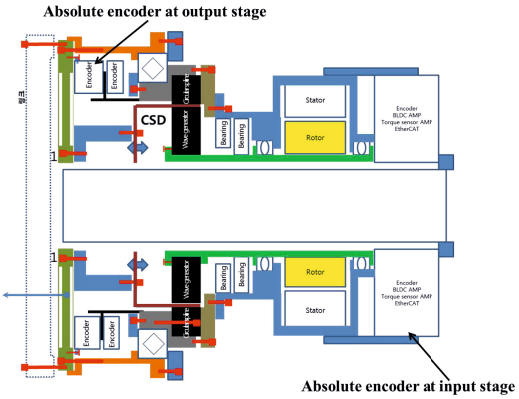

Fig. 5. The structure of actuators

Table 2. Comparison between out-stage and in-stage

	Out-Stage	In-Stage
Encoder	Absolute	Incremental
feature	Hollow type No multi-turn	Hollow type
Resolution	262,144	24,576
Gears	No	Yes
Gear ratio	-	160:1(Axis:1,2,3,4) 100:1(Axis:5,7,6)
Resolution with gear ratio	262,144	3,932,160 2,457,600
Motion range	-180∼+180	-

robot needs high resolution position sensor, in other words encoder. The resolution of industrial robot is very significant property. To meeth both property, we set the mechanical homeposition using the installed absolute encoder. we use the incremental encoder when robot moves. Also, we assume the angle range from -180 degrees to +180 degress. This assumption is available in case of the manipulator. Manipulator usually don't have the motion range more than 360 degrees.

4 Positioning Rules

To make the situation simple, a case is assumed. However, it is a representative and it is not belong to special case. A manipulator is postioned down aligned to gravity direction. This position is set as the mechanical home position abs_offset. Current manipulator's position is set as abs_q. Clockwise is defined plus direction. Case 1 is like this; abs_q is less than the end of absolute encoder,

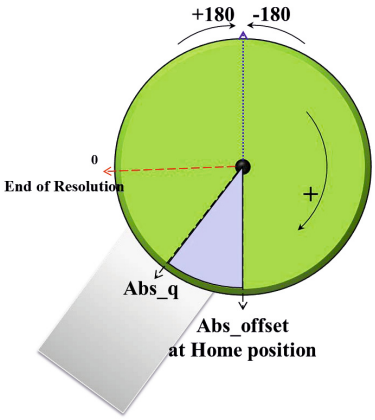

Fig. 6. Relation of the absolute encoder and incremental encoder. Case#1.

and the angle between abs_q and abs_offset is less than 180 degree, bigger than zero like (1). This configuration is displayed in Fig.6. This case is easy-thinkable case. Joint angle Q_{abs} is simply derived as (2). We aim to descride current angle in the incremental encoder domain. For the current incremental encoder value inc_q Q_{inc} in the incremental encoder domain is derived by (4)

$$180 > (abs_q - abs_{offset}) > 0 \tag{1}$$

$$Q_{abs} = (abs_q - abs_{offset}) \times 360/abs_{res} \tag{2}$$

where abs_{res} means the resolution (262,144).

$$offset_{inc} = Q_{abs} \times inc_{res}/360 \tag{3}$$

$$Q_{inc} = (inc_q + offset_{inc}) \times 360/inc_{res} \tag{4}$$

Case 2 of Fig.7 is somewhat different with case 1. Manipulator moved in negative direction, so (5) is valid. In case 2, (2),(3) and (4) is valid too.

$$0 > abs_q - abs_{offset} > -180 \tag{5}$$

Case 3 of Fig.8 is different with case 1 and 2. Manipulator moved in negative direction. However abs_q is much bigger than abs_{offset}. Relation (6) is derived. In case 3, Q_{abs} is derived as (7). (3) and (4) is valid.

$$(abs_q - abs_{offset}) > 180 \tag{6}$$

$$Q_{abs} = ((abs_q - abs_{offset}) - 360) \times 360/abs_{res} \tag{7}$$

Fig.9 displays case 4. Manipulator moved in positive direction. However abs_q is much smaller than abs_{offset}. Relation (8) is derived. In case 4, Q_{abs} is derived as (9). (3) and (4) is valid.

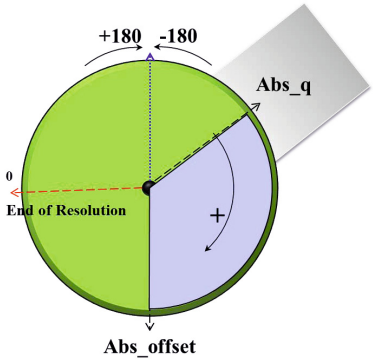

Fig. 7. Relation of the absolute encoder and incremental encoder. Case#2.

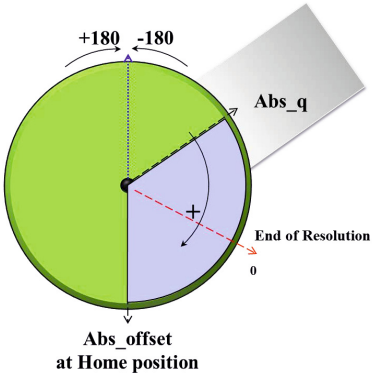

Fig. 8. Relation of the absolute encoder and incremental encoder. Case#3.

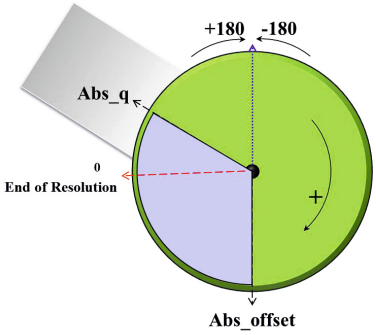

Fig. 9. Relation of the absolute encoder and incremental encoder. Case#4.

$$-180 > (abs_q - abs_{offset}) \tag{8}$$

$$Q_{abs} = ((abs_q - abs_{offset}) + 360) \times 360/abs_{res} \tag{9}$$

5 Experiments

Currently, prototype of dual-arm robot is developed. With him, we get the joint angles using the proposed method. Axis 2 of right arm is selected as experiments. We moved it to 30, 60 and 90 degrees. Each motion is displayed in Fig10, 13 and 16. In movements of 30 degrees trajectories are achieved in Fig.11. Black line is the reference trajectory. Red line is the joint trajectory in incremental encoder domain. Blue line is the joint trajectory in absolute encoder domain. In all cases reference trajectory, incremental encoder and absolute encoder shows similar trajectory, which means the proposed method is valid. Small difference

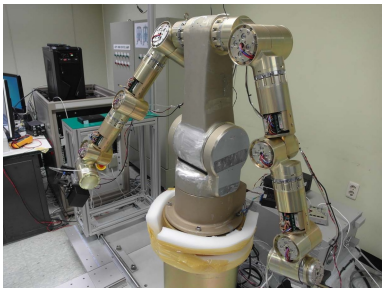

Fig. 10. Relation of the absolute encoder and incremental encoder. Case#1.

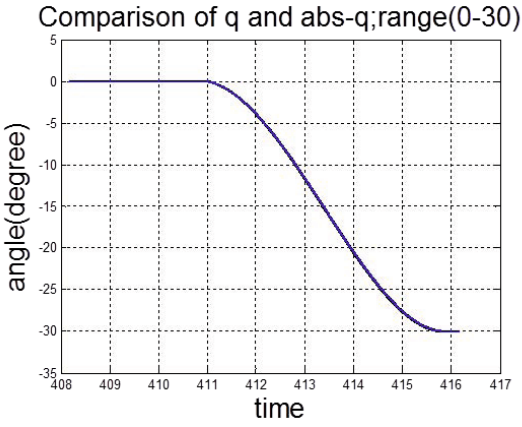

Fig. 11. Trajectory of the shoulder axis[0deg-30deg]. Desired trajectory[black]; q trajecotry[red]; abs-q trajecotry[blue].

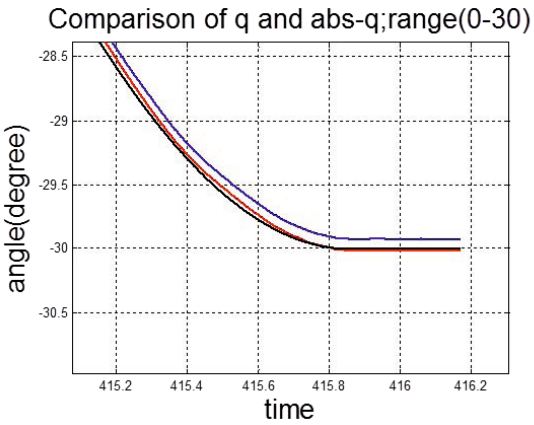

Fig. 12. Zoom of trajectory of the shoulder axis around 30deg. Desired trajectory[black]; q trajecotry[red]; abs-q trajecotry[blue].

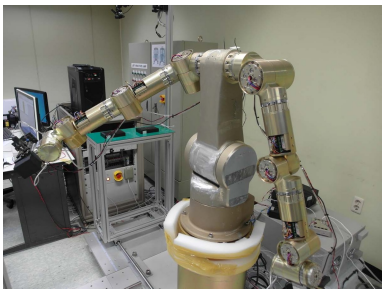

Fig. 13. Relation of the absolute encoder and incremental encoder. Case#1.

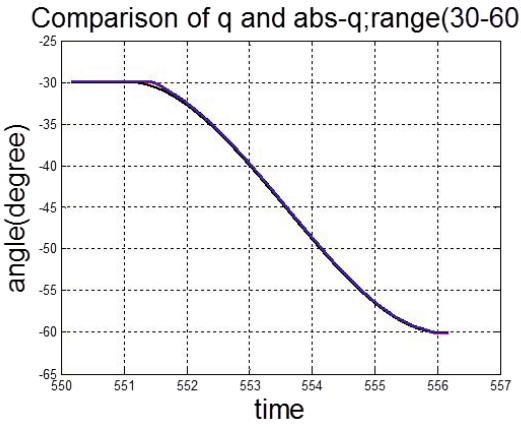

Fig. 14. Trajectory of the shoulder axis[30deg-60deg]. Desired trajectory[black]; q trajecotry[red]; abs-q trajecotry[blue].

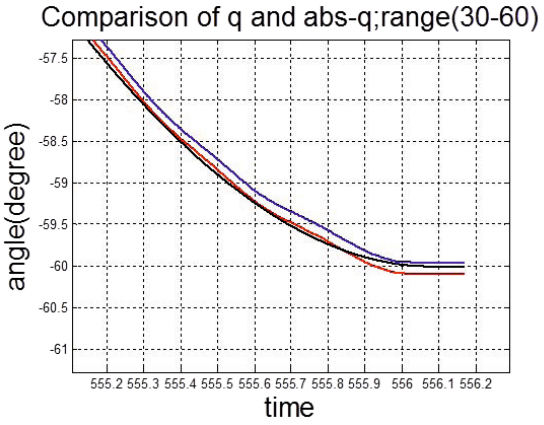

Fig. 15. Zoom of trajectory of the shoulder axis around 60deg. Desired trajectory[black]; q trajecotry[red]; abs-q trajecotry[blue].

Fig. 16. Relation of the absolute encoder and incremental encoder. Case#1.

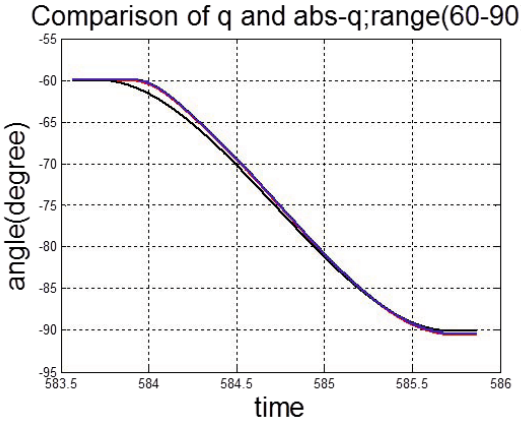

Fig. 17. Trajectory of the shoulder axis[60deg-90deg]. Desired trajectory[black]; q trajecotry[red]; abs-q trajecotry[blue].

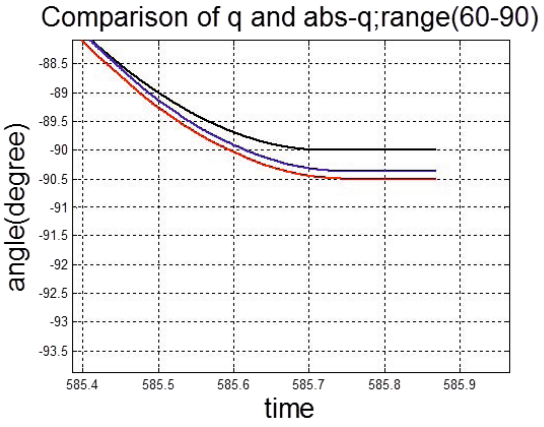

Fig. 18. Zoom of trajectory of the shoulder axis around 90deg. Desired trajectory[black]; q trajecotry[red]; abs-q trajecotry[blue].

between the angles in incremental encoder and the angles in absolute encoder is observed. These difference is owing to flexion of link and harmonic gears. In later research, we are supposed to measure the external force using this values.

6 Conclusion

We are developing the novel dual-arm robot. He has strength in the size and torque compared with the conventional robots. To achieve these strength, the actuator module has some constraints. Actuators have a absolute encoder with no multi-turn information and a incremenatal encoder. With the gears, incremental encoder can have high resolution. We aim to move manipulator using the incremental encoder with high resolution and we want to our robot have mechanical home positioning functions. To do that, complex relation is considered. Three cases are derived to cover all relations.

References

1. Yaskawa inc., Motoman Robotics, `http://www.motoman.com/products/robots/assembly-robots.php`
2. Kawada inc., Nextage Humanoids, `http://www.kawada-nextage-humanoids.com/`
3. ABB inc., FRIDA concept robot, `http://www.abb.com`
4. Choi, T.Y., Do, H.M., Park, C.H., Kyung, J.H.: Software platform for the Industrial Dual-arm Robot. In: ICHS 2012, Daejeon, Korea, August 16-18 (2012)
5. Ethercat Technology Group, `http://www.ethercat.org/en/technology.html`
6. RTX Real-Time Platform, `http://www.intervalzero.com/products/rtx-at-a-glance/`

Using Growth Curve in Trajectory Planning for Industrial Manipulator

Hua Jiang, Yonghua Yan, Mingyong Zhang, Jianrong Zhang, and Jiahang Xu

School of Mechanical Engineering, Shanghai Jiaotong University,
Mechanical Building 800 Dong Chuan Road. 200240 Shanghai, P.R. China
{stupid_ghost,yhyan,yongjun,jrzhang,henghang99}@sjtu.edu.cn

Abstract. The paper presents a new algorithm to solve the problem of trajectory planning in industrial manipulator, the growth curve which is well known in Biological Sciences. The growth curve is used to demonstrate the relationship between the quantities of a certain creature over the time, which is similar to the curve of velocity in trajectory planning for industrial manipulator. This papers purpose is to introduce the algorithm and derive the logistic formula from basic growth curve to fit the velocity curve, using to plan the trajectory in industrial manipulator controlling. Although the algorithm is very simple and easy which contains only three parameters, the logistic curve can easily solves the general cases in trajectory planning where there are the upper limits of velocity and acceleration.

Keywords: Growth Curve, Logistic Curve, Trajectory Planning, Industrial Manipulator, Time-Minimum Planning, Jerk-Limit Planning.

1 Introduction

It is so crucial to control the industrial manipulator efficiently and smoothly that many designers have devoted themselves to research new algorithms. Owing to different kinds of constraints in the manipulator controlling, the algorithms applied in this field should take all the factors into accounts. Taking the actuator for example, each actuator has its own upper bounds in several aspects that should be considered in trajectory planning, such as the velocity and acceleration. It is even more vital to achieve high-level operation performance in dynamic control with continuous velocity and acceleration. Otherwise, poor trajectory planning may cause the manipulator vibrate. What is worse, it may excite the mechanical resonances of robotic manipulator[1], thus the stability and accuracy cannot be guaranteed.

There have already been many algorithms used in trajectory planning that can be found in various journals. Among all the algorithms, cubic spline and B-spline are two widely used algorithms in this field. Many researchers proposed kinds of methods to optimize trajectory planning of industrial manipulator based on the two algorithms in different of situations. Gasparetto, Y.Xiao and Sahar went deep into the planning and provided some optical methods based on time

J. Lee et al. (Eds.): ICIRA 2013, Part II, LNAI 8103, pp. 166–177, 2013.

optical[2-4], energy optical and jerk optical[5, 6]. And some researchers even go further, they introduce the newly intelligent algorithm to the path planning[7].

To achieve a smoothness trajectory, we may firstly tend to use high-order polynomial, this is why cubic spline is more widely used than quadratic spline. However, high-order polynomial may cause tough problems. For instance, it may be difficult to solve the equation and have speed overshoot, this is why four-order polynomial is seldom used, not to mention the five-order or even higher-order polynomial.

The growth curve was firstly associated with the phenomenon of the population growth of the creatures in nature[8], which drew the attention of biologist. Due to this interesting phenomenon, Verhulst is the first researcher to introduce the logistic curve in the XIX century for the study of population growth[8]. Since then, the logistic curve spreads to other fields due to the type of growth with a saturation value is frequently observed in many cases. For example, the logistic curve applied in economic is usually to predict the possibility development of economy[9].

When planning the end-effectors trajectory of the manipulator, we mainly expect the velocity starting from zero since the manipulator body has inertia mass and the acceleration with a small value. In this way we can lower the jerk to make the manipulator moves smoothness. Then the values of acceleration and velocity begin to increase. But each actuator tends to have a certain saturation value of velocity and acceleration (The acceleration has a maximum value, so does the velocity.) which should be considered in trajectory planning. When the end-effectors velocity is close to the saturation value, the acceleration should be reduced and in the end the value should be zero. This process is just similar with the process of population growth. As a result, the logistic curve can be applied to the trajectory planning as the velocity curve.

There are several growth models, such as Pearl model and Gompertz model, and Kwasnicki has already analysed the features of different models[10], to use these model in various situation. Different growth models define different logistic curves, even though they are describe the similar phenomenon. A deterministic logistic model is defined in the form of the differential equation as follow[8]

$$\begin{cases} \frac{dx}{dt} = ax - bx^2 \\ x(t_0) = x_0 \end{cases}$$

Where a and b are two constants and is an initial value of the equation.

This paper contains five sections. The first section is introduction, describing the basic condition of trajectory planning and logistic curve. The paper presents the possibility of logistic curve when applying to the trajectory planning. In the second section, we find the integral of the differential form of the logistic model . In section 3, we describe the application of logistic curve in trajectory planning with respect to the certain constraints and derive the formulas based on the actual situation for the logistic formula to determine the values of variables. And in section 4, we give an examples to give a comparison between the cubic spline and the logistic curve with the aspect of velocity and acceleration in the

trajectory planning. And in the last section, we discuss the issues related to the logistic model and make a brief conclusion.

2 The Feature of the Logistic Curve

Because the logistic curve is stated in the form of differential equation. In order to apply the logistic curve to our situation, we must find the antiderivative of the equation through the process of integration and make the final formula as simple as possible.

According to the introduction, the differential equation of the growth model can be rewritten as follow:

$$\frac{dx}{dt} = ax - bx^2 \tag{1}$$

Considering $ax - bx^2 \neq 0$, both sides of the equation(1) divide by $ax - bx^2$

$$\frac{dx}{ax - bx^2} = dt \tag{2}$$

And the equation then be rewritten in the term of integrate

$$\int (\frac{1}{x} + \frac{b}{a - bx})dx = \int (a)dt \tag{3}$$

$$\frac{x}{a - bx} = \pm e^{at+k} = me^{at} \tag{4}$$

Where k is a constant and $m = \pm e^k$

Therefor the integrate of the differential equation above is

$$x = \frac{ame^{at}}{1 + bme^{at}} \tag{5}$$

Assume that $K = \frac{a}{b}$,$B = \frac{e^{-k}}{bm}$, and $A = a$

$$x = \frac{am}{e^{-at-k} + bm} = \frac{\frac{a}{b}}{\frac{e^{-k}}{bm}e^{-at} + 1} = \frac{K}{1 + Be^{-At}} \tag{6}$$

3 Logistic Curve in Trajectory Planning with Constraints

On the basic of the figures of the logistic curve and the conclusion above, we have known the features of the logistic curve. Because the logistic curve is a sigmoid curve and the ideal velocity curve in trajectory planning is also a sigmoid curve, in order to apply the logistic curve to the trajectory planning, the formula should be transform to a new form to satisfy the actual condition. And how to determine the value of the three variables in the equation associated to the constraints become the main task. This is what we do in this section.

In trajectory planning, the main factors should be considered is the upper limits of the velocity and the acceleration. To a certain industrial manipulator, the upper bounds of constraints in velocity and acceleration can be formulated as

$$\begin{cases} |v(t)| \leq V_{cj} (j = 1, \cdots, N) \\ |a(t)| \leq a_{cj} (j = 1, \cdots, N) \end{cases}$$

Where

j means the jth joint.

V_{cj} means the velocity bound for the jth joint.

a_{cj} means the acceleration bound for the jth joint.

As the conclusions in section 2 we get, we use the logistic curve to manifest the process of velocitys variation.

According to (6), the equation is supposed to be

$$\Delta v = \frac{K}{1 + Be^{-At}} \tag{7}$$

So the velocity that can be

$$v = v_{init} + \Delta v = v_{init} + \frac{K}{1 + Be^{-At}} \tag{8}$$

Where

v is the real-time value of velocity in the trajectory planning

v_{init} is the initial value of velocity in the trajectory planning.

Because v_{init} and v_{final} is known during the path planning, so we should begin with the Δv to calculate the variables of K, B and A.

Step1:Calculate the Value of K.

Because the value of Δv is the difference of v_{final} and v_{init} according to the (8), Δv always starts form zero. So the sign of A is always positive. Due to the property of logistic curve, we define that

$$K = \Delta v = v_{final} - v_{init} \tag{9}$$

Where v_{final} is the final value of velocity in the trajectory planning.

v_{init} is the initial value of velocity in the trajectory planning.

Because of the property of the logistic curve, the curve of Δv cannot be equal to the value of K (when A $>$ 0), even though it can get more and more close to K (The value of K is just an equilibrium value). Also we have to plan the path in finite time, so the value of t must be in a finite interval.

In order to make sure the velocity curve can reach the point with acquired value and the jerk is in a controlled range, we should define an infinitesimal , that the expression of K above can be rewritten in the form as follow

$$K = v_{final} - v_{init} + \varepsilon \tag{10}$$

Step2:Calculate the Value of B.
Because of the property of the logistic curve described in the (6) as above, the value of Δv cannot be zero even if $t \to -\infty$ (when A > 0). What is more, the value of t must start form zero in actual situation. In order to make the value of Δv zero or close to zero, we also define an infinitesimal δ, $\delta \to 0$, that when $t = 0$,the value of Δv is

$$\Delta v = \frac{K}{1+B} = \delta \tag{11}$$

Due to the fact that the value of δ is not zero, so

$$B = \frac{K-\delta}{\delta} \tag{12}$$

Because the value of K is certain and δ is an infinitesimal, the value of B can be very large.

Step3:The Equation of Δv.
Using the same method as step 2, we also use the same infinitesimal δ defined in step2 that when $t = t_f$,

$$\Delta v(t_f) = \frac{K}{1+Be^{-At_f}} = K - \delta \to K \tag{13}$$

However, because of the existence of δ, the velocity curve at the two distinct end points in the trajectory is no continuous, staring from a value no equal to zero and ending with a value not equal to zero. In order to smooth the curve, firstly we move down the curve at the distance of δ, then the (7) can be rewritten as

$$\Delta v = \frac{K}{1+Be^{-At}} - \delta \tag{14}$$

But the equation above leads to a problem that when $t = t_f$,

$$\Delta v(t_f) = \frac{K}{1+Be^{-At_f}} - \delta = K - 2\delta \tag{15}$$

And in order to make the velocity curve continuous at the point when $t = t_f$, the value of K should be enlarged by 2δ, that is

$$\Delta v = \frac{K+2\delta}{1+Be^{-At}} - \delta \tag{16}$$

But by doing this, the value of Δv is not zero when $t = 0$. Again we have to enlarge the value of δ and the K, and repeat the process.

So the formula of logistic curve can be as follow

$$\begin{aligned}\Delta v = &\frac{K}{1+Be^{-At}}(1 + \frac{2}{1+B} + \cdots + (\frac{2}{1+B})^n + \cdots) \\ &-\frac{K}{1+B}(1 + \frac{2}{1+B} + \cdots + (\frac{2}{1+B})^n + \cdots)\end{aligned} \tag{17}$$

Because the function of $1/(1-x)$ can be represent in the type of a sum of power series as

$$\frac{1}{1-x} = 1 + x + x^2 + \cdots + x^n + \cdots = \sum_{n=0}^{\infty} x^n \tag{18}$$

So the final formula of Δv is

$$\Delta v = \frac{B+1}{B-1}\left(\frac{K}{1+Be^{-At}} - \frac{K}{1+B}\right) \tag{19}$$

Where $2/(1+B) < 1$, that is $B > 1$
So the formula of can be written in the form as

$$\Delta v = \frac{B+1}{B-1}\left(\frac{K}{1+Be^{-At}} - \frac{K}{1+B}\right) \tag{20}$$

Where $B > 1$

Step4:The Equation of Acceleration.
According to the new form of logistic equation above, we can find the equation of acceleration, that is the derivative of Δv. And the final formula of acceleration is

$$a = \frac{B+1}{B-1}\frac{KABe^{-At}}{(1+Be^{-At})^2} \tag{21}$$

Where $B > 1$

Step5:The Value of A.
To calculate the value of A, we should find the maximum value of acceleration based on (21). And the maximum value of the (21) should be smaller than the constraint in the path planning. So we should do some transformation about the equation, that is

$$a = \frac{A}{K}\frac{B+1}{B-1}\left[-\left(\frac{K}{1+Be^{-At}} - \frac{K}{2}\right)^2 + \frac{K^2}{4}\right] \tag{22}$$

So when

$$\frac{K}{1+Be^{-At}} - \frac{K}{2} = 0 \tag{23}$$

That

$$t = \frac{lnB}{A} \tag{24}$$

The maximum value of acceleration is

$$a_{max} = \frac{KA}{4}\frac{B+1}{B-1} \tag{25}$$

Because each actuator in manipulator has a certain upper limit in acceleration, the acceleration we used in the trajectory planning must be in the range of the

limit. To make full use of the actuator and take the least time to reach the point with the acquired value of velocity, in the trajectory planning, we should make sure that the acceleration can be equal to the upper limit during the planning with the permit of the actuator. To a certain actuator, its acceleration satisfies the condition as

$$|a| \leq a_c \tag{26}$$

Where a_c is the maximum value of acceleration to a certain actuator.

So $a_{max} \leq a_c$, that is

$$\frac{KA}{4}\frac{B+1}{B-1} \leq a_c \tag{27}$$

The formula to calculate the value of A is

$$A = \frac{4a_c}{K}\frac{B-1}{B+1} \tag{28}$$

Step6:The Time to Reach the Final Point of Velocity.

To make sure the velocity curve continuous when $t = t_f$, the value of Δv should be K.

According to (11), when $t = t_f$

$$\Delta v = \frac{B+1}{B-1}\left(\frac{K}{1+Be^{-At}} - \frac{K}{1+B}\right) = K \tag{29}$$

That is

$$\frac{1}{1+Be^{-At}} = \frac{B}{1+B} \tag{30}$$

So the time taking to reach the final velocity point is

$$t_f = \frac{2}{A} lnB \tag{31}$$

Step7:The Distance in the Trajectory Planning.

In the point-to-point trajectory planning, based on the curve (8) of velocity, we can calculate the area of the region enclosed by the logistic curve, the line of $v = 0$, and $t = t_f$ (t_f is the time that takes from the beginning of the trajectory). The area of region is the distance that the actuator moves during the time from the beginning. The distance can be as the follow

$$s = v_{init}t_f + \frac{B+1}{B-1}\frac{K}{A}(\ln(1+Be^{-At}) + At)\Big|_0^{t_f} - \frac{K}{B-1}t_f \tag{32}$$

The final equation of s is

$$s = v_{init}t + \frac{B+1}{B-1}\frac{K}{A}(\ln(1+Be^{-At}) + At - \ln(1+B)) - \frac{K}{B-1}t \tag{33}$$

Where t_f is the time that takes the actuator to reach point with the certain value of velocity and v_{init} is the initial value of the velocity that starting the trajectory planning.

Form the above seven steps, we can calculate values of the basic variables in the equation that be used in the trajectory planning. Also include the distance that the actuator moves and the time taking the actuator to reach the acquired velocity can be calculated. Among the seven steps, especially step 3, we assume that the default value of time that starts a new trajectory is zero. In this way, we can simplify the process of the calculation, and if we must set the value of time when starting a new trajectory, we can do some transformation to make the initial value of t be zero.

4 Comparison Examples and Application

In order to show the advantages of logistic curve in the trajectory planning over traditional algorithm-cubic spline, a comparison example follows which subject to the constraints in the path planning. And to show how the logistic curve works, an example is showed that applied to the manipulator controlling based on the point-to-point trajectory planning.

In the path planning, the main factors that should be considered are the velocity and the acceleration. Also to the actuators driving the manipulators arm, they have their own upper limits on the velocity and acceleration. So we assume that to a certain actuator, the upper limits of velocity and acceleration are as

$$\begin{cases} v_{\max} = 500 pulse/ms \\ a_{\max} = 100 pulse/ms^2 \end{cases}$$

The value is defined in the term of the digital signal which can be used in the digital controller directly.

When used the cubic algorithm to plan the trajectory, the formula of s should define as

$$s = a_3 t^3 + a_2 t^2 + a_1 t + a_0 \tag{34}$$

$$v = \frac{ds}{dt} = 3a_3 t^2 + 2a_2 t + a_1 \tag{35}$$

$$a = \frac{dv}{dt} = 6a_3 t + 2a_2 \tag{36}$$

The initial condition of this path planning can be assumed that the value of s, s_{init} , begins with zero, the initial velocity v_{init} is $0 pulse/ms$ and the velocity at the end point of the path v_{final} is $500 pulse/ms$. Because the final velocity is a certain value, in order to smooth the path, the value of acceleration at the end point of the path, a_{final} , is $0 pulse/ms^2$. And due to the fact the curve of acceleration in this algorithm is a line and to make full use of the actuator and to take the shortest time to reach to the point with the acquired value of velocity, the initial value of the acceleration a_{init} is assumed to the maximum value of the motor, that is $100 pulse/ms^2$. Based on the initial condition assumed, the formulas of distance, velocity and the acceleration are

$$s = -5t^3/3 + 50t^2 \tag{37}$$

$$v = -5t^2 + 100t \tag{38}$$

$$a = -10t + 100 \tag{39}$$

When using the logistic equation to planning the trajectory, the values of the variables should be calculated firstly(K, B and A). In order to compare the logistic algorithm and the cubic algorithm in the path planning, the initial conditions used are as same as cubic algorithm. Thus the value of the three variables can be calculated followed from step 1 to step 6. Base on the (9), the value of K can be

$$K = v_{final} - v_{init} = 500 \tag{40}$$

Because the value of B should be based on the value of infinitesimal variable δ as in the formula, to make clear how the infinitesimal variation δ affect the curve in the path planning, there we set δ two values, $\delta = 1$ and $\delta = 10$ to find the differences of the two curves.

The values of B_1 and B_2 based on the formula are

$$B_1 = \frac{500 - 1}{1} = 499(\delta_1 = 1) \tag{41}$$

$$B_2 = \frac{500 - 10}{10} = 49(\delta_1 = 10) \tag{42}$$

And the values of A based on the (28)are

$$A_1 = \frac{B_1 - 1}{B_1 + 1}\frac{4a_{max}}{K} = \frac{498}{500}\frac{4 \times 100}{500} \approx 0.7968 \tag{43}$$

$$A_2 = \frac{B_2 - 2}{B_2 + 2}\frac{4a_{max}}{K} = \frac{48}{50}\frac{4 \times 100}{500} = 0.7680 \tag{44}$$

Finally, the equations of Δv are

$$\Delta v_1 = \frac{500}{498}(\frac{500}{1 + 498e^{-0.7968t}} - 1) \tag{45}$$

$$\Delta v_2 = \frac{50}{48}(\frac{500}{1 + 48e^{-0.7680t}} - 10) \tag{46}$$

Where the times that reach the point with the required value of velocity are The value of t_{f1} is

$$t_{f1} = \frac{2ln499}{0.7968} = 15.5939 \tag{47}$$

$$t_{f2} = \frac{2ln49}{0.7680} = 10.1349 \tag{48}$$

The final equations of acceleration, a, are

$$a_1 = \frac{500}{498}\frac{500 \times 0.7968 \times 499 \times e^{-0.7968t}}{(1 + 499e^{-0.7968t})^2} \tag{49}$$

$$a_2 = \frac{50}{48}\frac{500 \times 0.7680 \times 49 \times e^{-0.7680t}}{(1 + 49e^{-0.7680t})^2} \tag{50}$$

The final equation of s is

$$s_1 = \frac{500}{498}\frac{500}{0.7968}(ln(1+499e^{-0.7968t}) + 0.7968t - ln500) - \frac{500}{498}t \tag{51}$$

$$s_2 = \frac{50}{48}\frac{500}{0.7680}(ln(1+49e^{-0.7680t}) + 0.7680t - ln50) - \frac{500}{48}t \tag{52}$$

Under this condition of trajectory planning, the equations of velocity, acceleration and the distance have been at hand, the curves can be drawn as below.

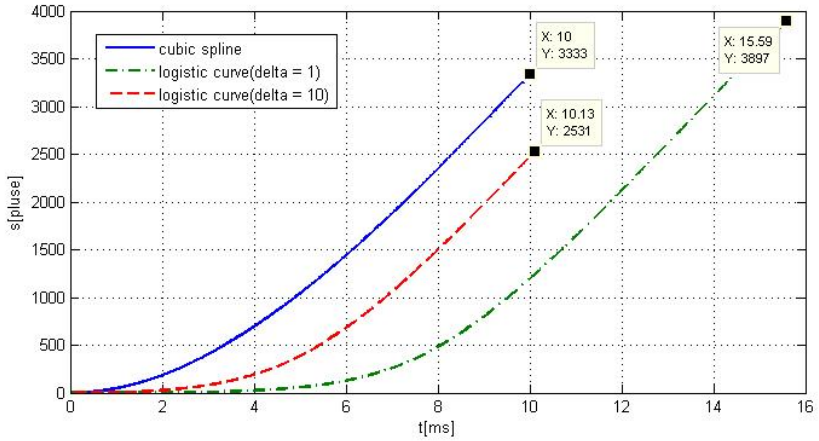

Fig. 1. The curves of distance in trajectory planning

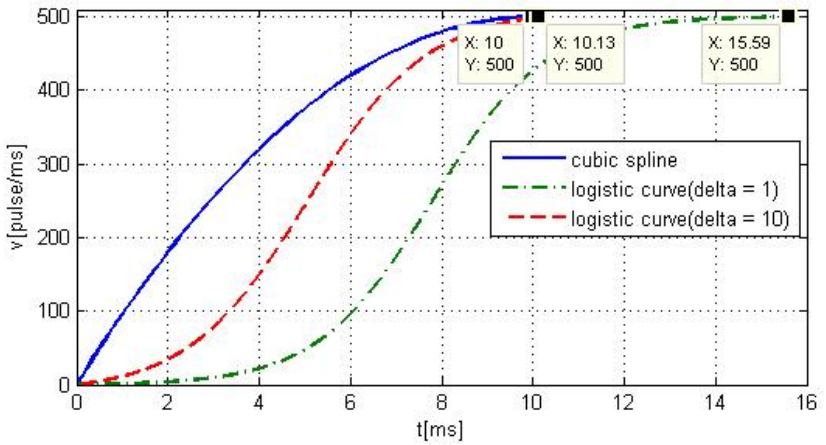

Fig. 2. The curves of velocity in trajectory planning

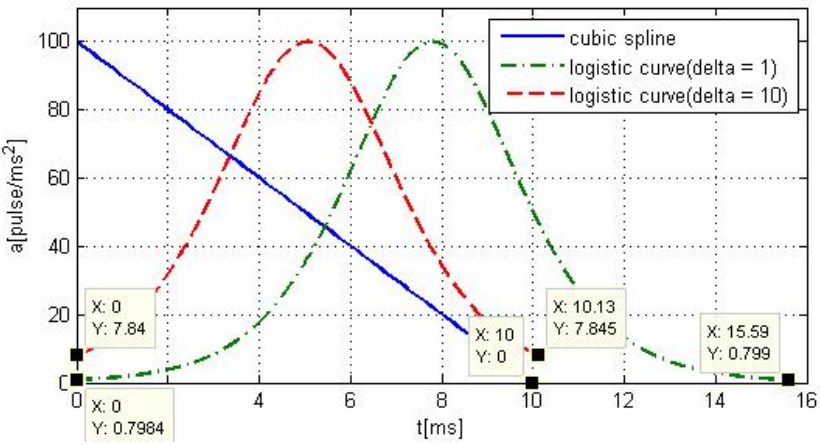

Fig. 3. The curves of acceleration in trajectory planning

From the figures, we observe that the curves of velocity in logistic curves are sigmoid curves and the accelerations in these two curves start almost from 0.7984 and 7.84 and end to 0.7984 and 7.84, there is almost no abrupt changes in the curve of acceleration using the logistic algorithm compare to the cubic spline, where at the beginning the value of acceleration starting from zero to 100. These changes in the logistic curve can suit to the actuator in the controlling.

However, we observe that the time to take the actuator reaching the desired velocity value (Fig 2) and the distances that the actuator moves(Fig 1) is longer than that in the cubic spline when $\delta = 1$. Especially at the beginning part and at the end part in the planning, the changing magnitude of velocity is smaller but the time it takes a little longer. This indicates that in this way, this method of planning wastes time. And the performance of the logistic curve is improved when $\delta = 10$ as we observe that the larger the value of δ , the shorter time taking to the get desired velocity and the shorter distance the actuator moves.

5 Discussion and Conclusion

A new algorithm-logistic curve, which is derived from the biology science is presented in this paper. The curve of the algorithm is used as velocity curve in trajectory planning that can satisfy the needs in manipulator controlling. Based on the examples in section 4, the performance of logistic curve is much better than that of the cubic spline, especially in the acceleration, that guaranteeing the curve of acceleration continuous from the beginning to the end.

Although, in the algorithm, there is an infinitesimal δ ,whose value should set firstly during the calculation, that determines the time taking the actuator to the required velocity and the value of abrupt change in the acceleration at the

beginning. However, the value of δ can be set in a certain value according to the actual condition in controlling.

After all, the logistic curve is excellent over the cubic spline.

References

1. Smith, T.F., Waterman, M.S.: Identification of Common Molecular Subsequences. J. Mol. Biol. 147, 195–197 (1981)
2. Gasparetto, A., Zanotto, V.: Optimal trajectory planning for industrial robots. Advances in Engineering Software 41, 548–556 (2009)
3. Xiao, Y., Du, Z., Dong, W.: Smooth and near time-optimal trajectory planning of industrial robots for online applications. Industrial Robot: An International Journal 39, 169–177 (2012)
4. Sahar, G., Hollerbach, J.M.: Planning of Minimum- Time Trajectories for Robot Arms. The International Journal of Robotics Research 5, 90–100 (1986)
5. Constantinescu, D., Croft, E.A.: Smooth and time-optimal trajectory planning for industrial manipulators along specified paths. Journal of Robotic Systems 17, 233–249 (2000)
6. Liu, H., Lai, X., Wu, W.: Time-optimal and jerk-continuous trajectory planning for robot manipulators with kinematic constraints. Robotics and Computer-Integrated Manufacturing 29, 309–317 (2013)
7. Huang, M.-S., Hsu, Y.-L., Fung, R.-F.: Minimum-Energy Point-to-Point Trajectory Planning. IEEE/ASME Transtractions on Mechatronics 17, 337–344 (2012)
8. Gasparetto, A., Lanzutti, A., Vidoni, R., Zanotto, V.: Experimental validation and comparative analysis of optimal time-jerk algorithms for trajectory planning. Robotics and Computer-Integrated Manufacturing 28, 164–181 (2011)
9. Roman-Roman, P., Torres-Ruiz, F.: Modelling logistic growth by a new diffusion process: application to biological systems. Biosystems 110, 9–21 (2012)
10. Kwasnicki, W.: Logistic growth of the global economy and competitiveness of nations. Technological Forecasting and Social Change 80, 50–76 (2012)
11. Tsoularis, A., Wallace, J.: Analysis of logistic growth models. Methematical Bilsciences 179, 21–55 (2002)

Practical Implementation of the Nonlinear Control of the Liquid Level in the Tank of Irregular Shape

Witold Klopot, Tomasz Klopot, Piotr Laszczyk,
Jacek Czeczot, and Mieczyslaw Metzger

Institute of Automatic Control, Silesian University of Technology,
44-100 Gliwice, Poland
{Witol.Klopot,Tomasz.Klopot,Piotr.Laszczyk,
Jacek.Czeczot,Mieczyslaw.Metzger}@polsl.pl

Abstract. In this paper, the control of the liquid level in the tank of irregular (partially conical) shape is considered. The process nonlinearities must be incorporated in the control law to ensure good tracking properties and disturbances rejection despite of the variations of the operating point defined by the desired liquid level. For this purpose, two control strategies are considered: PI+GS (gain scheduling) controller with scheduling function based on the preliminary process identification and B-BAController (Balance-Based Adaptive Controller), which is derived from the nonlinear but significantly simplified model of the process, without any preliminary identification. The control performance of both techniques is verified experimentally and the results show superiority of the latter.

Keywords: Nonlinear control, model-based control, liquid level control, nonlinear tank.

1 Introduction

In process industry (*e.g.* food industry, water treatment plants, petrochemical industry, paper making industry, etc.), reservoirs of different shapes and sizes are frequently used as storage tanks for liquids, dosing tanks, settling tanks, equalizing tanks, vessels of biochemical reactors, etc. Usually, the level of the liquid in such tanks has to be regulated at the desired set point, which can vary according to different technological conditions, such as *e.g.* the variations of the total amount of the liquid that has to be stored in the tank or the variations of the desired liquid level in the sequencing batch reactor depending on the operating mode (filling, reaction and settling, decanting).

The control of the liquid level in the tank becomes a challenge when the its shape is irregular – see *e.g.* [1], [2], [3]. It takes place frequently, when the shape of the tank is determined by its technological application or by the economical reasons. One example can be the spherical shape that can withstand higher tensions comparing to other shapes and it has the best ratio between the outside area and its storing volume, which economically justifies its application. The second frequently used example is the conical shape, that can significantly improve disposal of solids while mixing.

J. Lee et al. (Eds.): ICIRA 2013, Part II, LNAI 8103, pp. 178–188, 2013.

In both cases, the dynamical properties of the filling/decanting processes depend significantly on the operating point resulting from the volume of the liquid stored in the tank. These nonlinearities are strong and they significantly limit the application of the conventional control systems for level regulation.

In this paper, the control of the water level in the reservoir of irregular (partially conical) shape frequently used in industry [4] is considered. The tank is supplied by the pump whose flow rate is assumed as the process disturbance. The level is adjusted by manipulating the control valve located at the bottom of the tank. For this purpose, two controllers are derived and experimentally validated. The first is the PI+GS, (PI+gain scheduling), which is frequently suggested as the simplest way of improving control performance for strongly nonlinear processes [5]. In considered case, the scheduling function is based on the experimental identification of the dynamical properties of the process from the step responses collected at the most representative operating points. The second control strategy considered in this paper is the B-BAC (Balance-Based Adaptive Control) methodology [6], [7]. Its control performance has been already successfully validated by simulation (*e.g.* [8], [9], [10]) and experimentally [11]. It is based on the simplified first order dynamical equation written in the affine form, in which the known part of the model is completed with a single additive time-varying parameter representing all modeling inaccuracies. This parameter is estimated on-line from the measurement data, which ensures adaptability of the controller. The estimation always converges to the true value without any additional excitation of a process [8].

The paper is organized as follows. First, the problem is stated and the experimental setup is shortly described. Then, two different modeling approaches are presented and the synthesis of both considered controller is shown. In the next section, the experimental results are presented and discussed. Conclusions complete the paper.

2 Statement of the Problem

In this paper, the problem of the level control in the tank of the partially conical shape is considered. The experimental setup is presented schematically in Fig. 1 (left). The water is supplied into the tank by the peristaltic pump adjusted by the analog input 4 – 20 [mA] to manipulate the flow rate Q_{in} within the range 0 – 2.5 [L/min]. The outlet flow rate Q_{out} [L/min] can be adjusted by manipulating the control valve positioned by the Siemens SIPART PS2 electropneumatic positioner driven via the analog signal 4 - 20 [mA] corresponding to the valve opening X_g defined within the normalized range 0 – 1. Both flow rates are measurable by the magnetic-inductive flow sensors SM6000 from ifm with the analog output 0 – 10 [V]. The level of the water inside the tank H_{PV} [m] is measured by the pressure transmitter VEGABAR 14 with the analog output 4 – 20 [mA], exclusively modified by the producer for the corresponding pressure measurement range 0 - 0.13 [bar].

The control goal is to keep the controlled water level H_{PV} at the desired set point H_{SP} by manipulating the position of the control valve at the bottom of the tank X_g. The measurable disturbance is the supplying flow rate Q_{in}.

In the considered case, the most important difficulty for the control system results from the partially irregular shape of the tank. The large cross section of the upper cylindrical shape decreases smoothly in the conical part of the tank into the small one of the cylindrical part at the bottom of the tank. Consequently, the system is nonlinear and its dynamical properties strictly depend on the cross section of the tank at the operating point defined by the desired set point H_{SP}. Thus, the application of the conventional time-invariant PI controller is very limited and to improve its control performance, the nonlinear model-based control system must be designed.

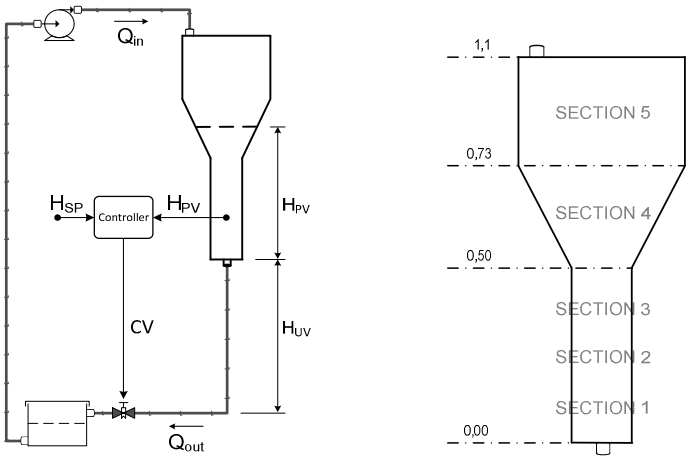

Fig. 1. Schematic diagram of the experimental setup (left) and dividing the tank for five sections (right)

3 Synthesis of the Control Systems

The control system discussed in this paper is based on two nonlinear control strategies. The PI+GS controller is considered as the benchmark. Consequently, its control performance is considered as the reference and compared with the performance of the model-based B-BAC strategy. Both control systems benefit from the adaptive action but for each case, the adaptability is applied in different way, which is described below.

3.1 PI+GS Controller

The gain scheduling technique is usually considered as the simplest way of incorporating the process nonlinearities into the control law [5]. In this paper, the synthesis of the PI+GS controller is based on the successive approximation of the dynamical properties of the considered system by the first order (FO) lag models derived experimentally from the step responses. For this purpose, the tank was

divided into five sections defined by the water level and shown in Fig. 1 (right). The number of sections and their thresholds have been determined experimentally to ensure the compromise between the complexity of the approximating model and its accuracy.

For each section, the step change of the manipulated variable X_g was applied and the step response was approximated to determine the corresponding gain K and time constant T of the respective local model. The results are presented in Table1.

Table 1. Parameters of the approximating First Order (FO) models

Tank section	Gain K	Time constant T [s]
section 1	-8.82	5.90
section 2	-9.44	6.70
section 3	-10.55	23.40
section 4	-13.30	284.90
section 5	-13.41	687.20

The gain K_r and the integral time T_r [s] for the PI+GS controller are scheduled by (1) according to the variations of the dynamical properties of the system that are presented in Table I. For each section, these tunings were determined using the simplest tuning rule derived for the PI control of the first order system [12] with the aggressivity factor T_C [s] defining the desired time constant of the closed loop response (1). To ensure stable and non-oscillatory behavior in the practical cases, the aggressivity factor was chosen as $T_C = 0.1\ T$.

$$K_r = \frac{T}{T_C \cdot K}; \qquad T_r = T. \tag{1}$$

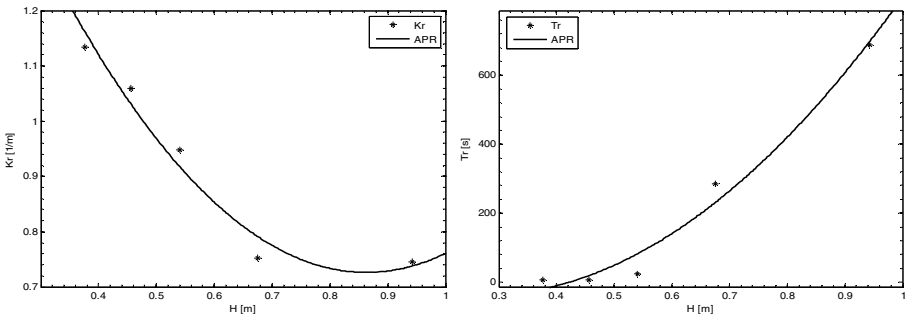

Fig. 2. Approximation of the PI controller gain K_r (left) and integral time T_r (right)

Fig. 2 shows the scheduling functions determined respectively for the controller gain K_r and integral time T_r based on the values calculated by Eqs. (1) for each section. The scheduling variable is the water level H_{PV}. For smooth gain-scheduling, the variations of the tunings were approximated by the second order polynomials (2).

$$K_r(H_{PV}) = 1597.5\,H_{PV}^2 - 840.55\,H_{PV} + 69.73$$
$$T_r(H_{PV}) = 1.83\,H_{PV}^2 - 3.16\,H_{PV} + 2.09 \tag{2}$$

3.2 B-BAController

The B-BAC methodology is dedicated for control of the nonlinear SISO (Single Input Single Output) systems that can be described by the simplified nonstationary dynamical model (3) of the first order describing directly the controlled variable *Y*:

$$\frac{dY}{dt} = f(Y,\underline{d}) + g(Y,\underline{d})u - R_Y^{\sim}. \tag{3}$$

The nonlinear functions *f(.)* and *g(.)*represent the known part of the model (3), *u* denotes the manipulated input and $\underline{d}$ are the measurable disturbances. In the practice, there is always modeling inaccuracy, which results from the uncertain values of the model parameters, presence of the not measurable disturbances and modeling simplifications. Thus, the additional time-varying parameter R_Y is included in the model (3) to compensate for these inaccuracies [6], [7].

After defining the control goal as regulating the controlled variable *Y* at the desired set point *SP* by manipulating the value of *u*, the synthesis of the final form of the B-BAController is based on the linearization technique [13] in the form dedicated to the systems whose relative order is one [14]. Assuming the stable first order reference model for the closed loop response with λ being the positive tuning parameter:

$$\frac{dY}{dt} = \lambda(SP - Y) \tag{4}$$

after combining Eqs. (3) and (4), the final explicit form of the B-BAController can be written in the discrete-time form:

$$u_i = \frac{\lambda}{g_i}(Y_{sp} - Y_i) + \frac{-f_i + \hat{R}_{Y,i}}{g_i} \tag{5}$$

where $f_i = f(Y_i, \underline{x}_i, \underline{d}_i)$, $g_i = g(Y_i, \underline{x}_i, \underline{d}_i)$ and *i* denotes the discretization instant. $\hat{R}_Y$ denotes the on-line estimate of the unknown parameter R_Y computed by the scalar form of the Weighted Recursive Least-Squares (WRLS) method based on the discretized model (3) [6], where T_S is the sampling time and α is the forgetting factor:

$$w_i = (Y_i - Y_{i-1}) - T_R(f_i - g_i u_i), \tag{6a}$$

$$P_i = \frac{P_{i-1}}{\alpha}\left(1 - \frac{T_S^2 P_{i-1}}{\alpha + T_S^2 P_{i-1}}\right), \tag{6b}$$

$$\hat{R}_{Y,i} = \hat{R}_{Y,i-1} - T_R P_i(w_i + T_S \hat{R}_{Y,i-1}). \tag{6c}$$

For the considered case, modeling of the dynamics of the water level in the tank is based on the simplified mass balance considerations. For the cross section of the tank varying according to the shape variations and for the assumed measurable quantities, this model has the following form:

$$\frac{d}{dt}\left(A(H_{PV})\,H_{PV}\right) = Q_{in} - K_{VM}\sqrt{\frac{H_{PV}+H_{uv}}{100\,[kPa]}}\,X_g \tag{7}$$

where $A(H_{PV})$ [m^2] is the cross section, K_{VM} = 2[m^3/h] is the valve sizing coefficient and H_{uv} = 1 [m] is the length of the pipe between the outlet of the tank and the valve (see Fig. 1 - left).

Nonlinear model (7) was simplified assuming constant averaged cross section A_M:

$$A_M = \frac{A_r + A_R}{2} \tag{8}$$

with A_r = 1.5 E-04 and A_R = 12.0 E-03 denoting respectively the cross sections of the lower and upper cylindrical parts of the tank. Consequently, after defining $Y = H_{PV}$ and $u = X_g$, the synthesis of the B-BAController was based on the simplified model (9) written in the form of (3) by direct application of Eqs. (5) – (6).

$$\frac{dH_{PV}}{dt} = \underbrace{\frac{Q_{in}}{A_M}}_{f(.)} + \underbrace{-\frac{K_{VM}}{A_M}\sqrt{\frac{H_{PV}+H_{uv}}{100\,[kPa]}}\,X_g}_{g(.)} \tag{9}$$

Tuning of the B-BAController requires adjusting the values of λ and α. The tuning procedure [15] is based on the equivalence between the linear approximation of the B-BAController and the conventional PI controller. Namely, the tunings adjusted by any PI tuning method for the conventional PI controller can be recalculated into the corresponding B-BAController tunings as:

$$\lambda = K_r\, g_0(.), \qquad \alpha = 1 - \frac{T_S}{T_r}, \tag{10}$$

which ensures equivalent closed loop performance with additional improvement resulting from the presence of the feedforward action and of the adaptability and gain scheduling provided by the B-BAC methodology. $g_0(.)$ denotes the value of the function $g(.)$ at the chosen operating point, for which the PI controller is tuned. In the considered case, this operating point was defined by Q_{in0} = 2.4 [L/min], H_{PV0} = 0.61[m] (in the middle of the conical part of the tank) and X_{g0} = 0.52, which results in the following tunings for the B-BAController: λ = 0.0275 and α = 0.9996.

4 Experimental Results

The experimental verification was carried out for the hardware configuration presented in Fig. 3. The sensors and the actuator of the laboratory installation shown

in Fig. 1 (left) are connected to the analog I/O modules of the SIMATIC S7 314C unit with CPU, which stands as the interface between the process and the SCADA system written in LabView environment and running on PC. Its front panel is presented in Fig. 4. The connection with the SIMATIC S7 314C unit is provided via an Ethernet module SIMATIC S7 CP 343-1 IT and the OPC Server running on the same PC.

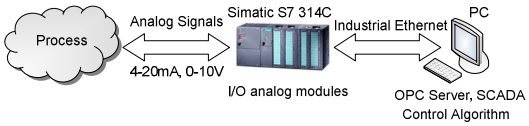

Fig. 3. Block diagram of the experimental setup

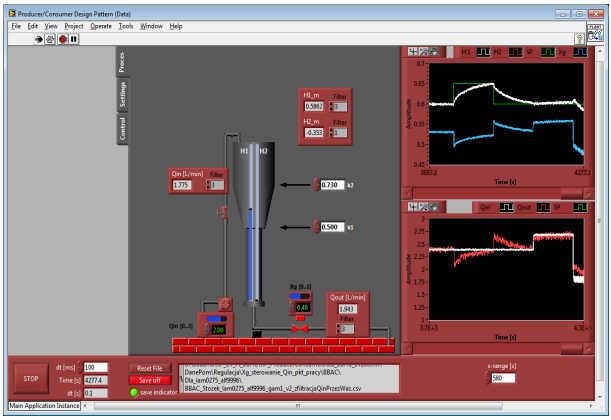

Fig. 4. Front panel of the LabView-based SCADA system

In the same SCADA system, the considered controllers were implemented as the exclusively written Virtual Instruments. For the PI+GS controller, the conventional PID function block was designed including the bumpless switching and anti-windup action. This block was completed with the gain-scheduling functionality by computing the scheduling functions according to Eqs. (2). The B-BAController was implemented as the general-purpose function block [16]. The idea of this block consists in encapsulating the calculations of the control law (5) and of the estimation procedure (6) with the bumpless switching functionality and the equivalence of the anti-windup action inside this block. The model-based calculations (namely, the functions $f(.)$ and $g(.)$) were computed separately basing on their definition in Eq. (9) and the resulting signals were wired to the appropriate inputs of this function block.

The results of the comparative experiments are presented in Figs. 5 – 7. The performance of each considered controller was verified for three representative sections of the tank presented in Fig. 1 (right): section 3 in the lower cylinder, section 4 in the middle of the conical part and section 5 in the upper cylinder. For each section, the experiments were carried out under the same scenario. First, the same

indicated successive step changes of the set point *SP* (increase of 0.05 and decrease of 0.05) were applied to the system to investigate the tracking properties. Then, the disturbance rejection was investigated by applying the same indicated successive step changes of the incoming flow rate Q_{in} (increase of 0.6 and decrease of 1.2). The performance of both considered controllers was also quantified separately for each section of the tank by calculating the respective ISE measures presented in Table 2.

Table 2. Comparison of the control performance

Tank section	SP_o	ISE_{PI}	ISE_{BBAC}	$1-\frac{ISE_{PI}}{ISE_{BBAC}}$
section 3	0.8	32.37	4.74	≈85%
section 4	0.6	10.55	1.55	≈85%
section 5	0.45	1.21	0.47	≈61%

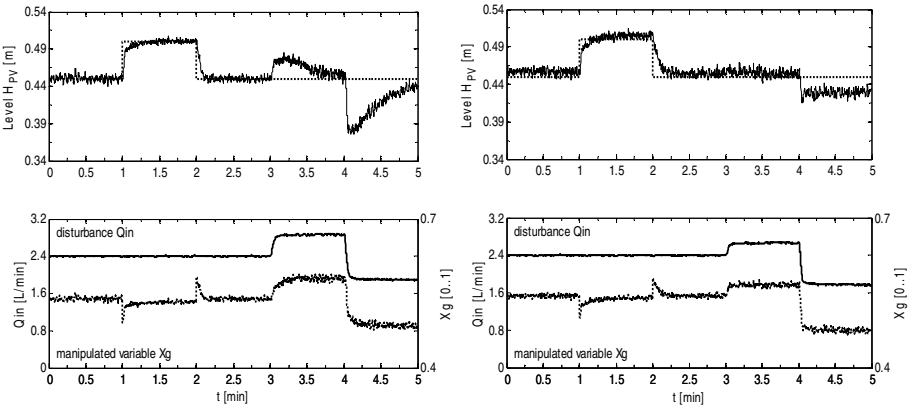

Fig. 5. Control performance of PI+GS (left) and of B-BAC (right) in section 3

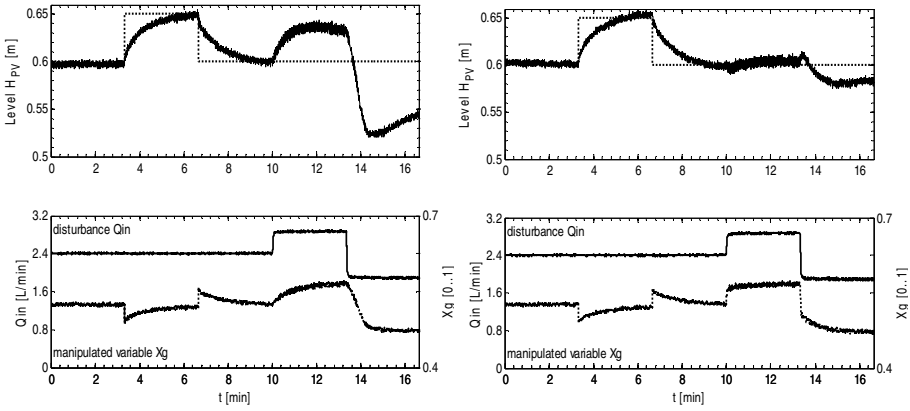

Fig. 6. Control performance of PI+GS (left) and of B-BAC (right) in section 4

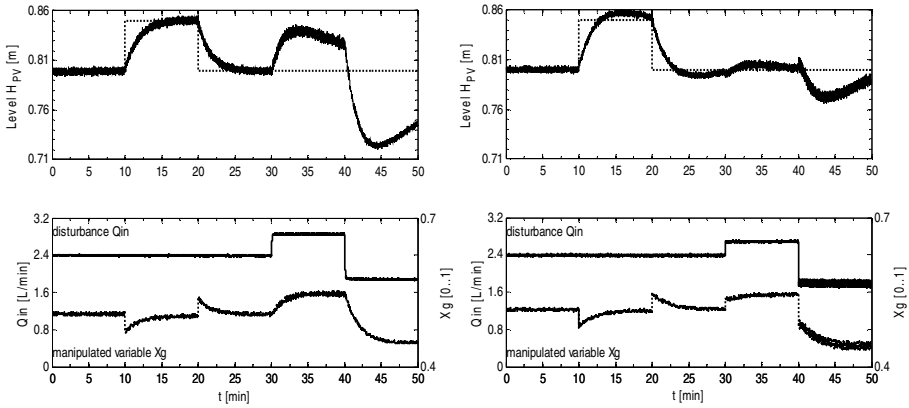

Fig. 7. Control performance of PI+GS (left) and of B-BAC (right) in section 5

The results of the experiments clearly show that even if the PI+GS controller ensures good tracking properties and disturbances rejection at each tank section, it can be significantly outperformed by the application of the suggested B-BAController. Even if the latter is derived on the basis of the simplified model (9), it provides better disturbances rejection (significantly smaller overregulations and settling time) with fully comparable tracking properties, which follow from:

- its adaptability resulting from the compensating properties of the estimation procedure (6),
- its feedforward action resulting from the direct inclusion of the measurable disturbance Q_{in} in the final control law,
- its gain-scheduling abilities resulting from direct incorporating the process nonlinearities into the final control law.

The last column of Table 2 additionally shows the relative measure of the improvement obtained by replacing the PI+GS controller with the B-BAController.

5 Conclusions

In this paper, the problem of control of the water level in the tank of the partially conical shape is considered. Due to the irregularity of this shape, the process is nonlinear and two nonlinear control strategies are suggested and validated experimentally: PI+GS controller and B-BAController. The first represents the conventional approach for regulating this kind of systems while the second is the model-based control algorithm that can be potentially considered as the interesting alternative for the PID controller in the industrial automation.

For PI+GS controller, the scheduling function was derived experimentally, which required preliminary open loop identification of the process dynamics from the step responses collected and approximated at different operating points. This approach is surely very effective but it has some important limitations when it is to be applied in the practical industrial cases:

- the preliminary identification is time-consuming and it requires intensive process excitation, which is not always is acceptable and sometimes even is impossible due to the technological conditions,
- the step responses should be collected for stable and constant disturbances, which practically is possible only for laboratory installations; in the industrial practice, one must expect that the disturbances vary and these variations can influence the identification accuracy.

In the case of the B-BAController, the preliminary experimental process identification is not requires because the control law is derived on the basis of the nonlinear model that incorporates process nonlinearities and the influence of the measurable disturbances. The results presented in this paper show that this model can be simplified and its inaccuracies does not degrade the control performance significantly due to the compensating properties of the estimation procedure. The form of the B-BAController provides gain-scheduling functionality resulting from incorporating the modeled process nonlinearities into the control law. It also provides the feedforward action from the measurable disturbances included in the model of the process.

To summarize, the B-BAController outperforms the PI+GS approach, in terms of both the implementation complexity and the control performance. Its synthesis does not require preliminary experimentation for the process identification. Accessibility of the simple tuning rules and possibility of application of the B-BAC general purpose function block [16], [17] additionally support its practical implementation. At the same time, experimental results show its superiority over PI+GS approach for the considered case.

Acknowledgments. This work was supported: partially by the National Science Center, project no. N N514 146438, 2010-2012, and partially by the Ministry of Science and Higher Education under grant BK-UiUA. Additionally, the work of Witold Klopot was supported under “DoktoRIS Scholarship for innovative Silesia”, co-financed by the European Union under the European Social Fund.

References

1. Wang, M., Crusca, F.: Design and implementation of a gain scheduling controller for a water level control system. ISA Transactions 41, 323–331 (2002)
2. Anandanatarajan, R., Mourougapragash, S.: Experimental evaluation of a controller using a variable transformation Smith predictor for a nonlinear process with dead time. ISA Transactions 47, 217–221 (2008)
3. Bhuvaneswari, N.S., Uma, G., Rangaswany, T.R.: Adaptive and optimal control of a non-linear process using intelligent controllers. Applied Soft Computing 9, 182–190 (2009)
4. El Damatty, A.A., Saafan, M.S., Sweedan, A.M.I.: Experimental study conducted on a liquid-filled combined conical tank model. Thin-Walled Structures 43, 1398–1417 (2005)
5. Åström, K.J., Wittenmark, B.: Adaptive control. Addison-Wesley Publishing Company (1995)

6. Czeczot, J.: Model-based Adaptive Predictive Control of Fed-Batch Fermentation Process with the Substrate Consumption Rate Application. In: Proc. of IFAC Workshop on Adaptive Systems in Control and Signal Processing, University of Strathclyde, Glasgow, Scotland, UK, pp. 357–362 (1998)
7. Czeczot, J.: Balance-Based Adaptive Control of the Heat Exchange Process. In: Proc. of 7th IEEE International Conference on Methods and Models in Automation and Robotics MMAR, Międzyzdroje, Poland, pp. 853–858 (2001)
8. Czeczot, J.: Balance-Based Adaptive Control of a Neutralization Process. International Journal of Control 79(12), 1581–1600 (2006)
9. Czeczot, J.: Balance-Based Adaptive Control Methodology and its Application to the Nonlinear CSTR. Chemical Eng. and Processing 45(5), 359–371 (2006)
10. Czeczot, J.: Modelling for the effective control of the electric flow heaters – Simulation validation. Simulation Modelling Practice and Theory 16, 429–444 (2008)
11. Czeczot, J., Laszczyk, P., Metzger, M.: Local Balance-Based Adaptive Control in the Heat Distribution System – Practical Validation. Applied Thermal Engineering 30(8-9), 879–891 (2010)
12. Preuss, H.P.: Robuste Adaption in Prozessreglern. Automatisierungstechnische Praxis 33(4), 178–187 (1991)
13. Isidori, A.: Nonlinear control systems. Springer, New York (1989)
14. Bastin, G., Dochain, D.: On-line estimation and adaptive control of bioreactors. Elsevier Science Publishers B.V. (1990)
15. Stebel, K., Czeczot, J.: General tuning procedure for the nonlinear Balance-Based Adaptive Controller. Int. Journal of Control (2012)
16. Laszczyk, P., Czubasiewicz, R., Czeczot, J.: LabVIEW-based Implementation of Balance-Based Adaptive Control Technique. In: Proc. of 17th International Conference on Methods and Models in Automation and Robotics MMAR, Międzyzdroje, Poland, pp. 516–521 (2012)
17. Klopot, T., Czeczot, J., Klopot, W.: Flexible Function Block For PLC-Based Implementation of the Balance-Based Adaptive Controller. In: Proc. of American Control Conference, Fairmont Queen Elizabeth, Montréal, Canada, pp. 6467–6472 (2012)

An Optimal Feedback Approach for the Stabilization of Linear Systems Subject to Input Saturation and Magnitude-Bounded Disturbances

S.T. Zhan[1], W.X. Yan[1], Z. Fu[1,2], J.H. Liu[1], W.H. Deng[1], and Yan-Zheng Zhao[1]

[1] Shanghai JiaoTong University, State Key Lab of Mechanical System and Vibration, Shanghai, 200240, P.R. China
[2] State Key Lab of Robotics and System (HIT), Harbin, 150001, P.R. China
{selproton,xiaogu4524,zhfu,yihongyishui,1110209041, yz-zhao}@sjtu.edu.cn

Abstract. Disturbance may severely degrade the control accuracy of an input-saturated system and even induce instability. This paper intends to present an approach to realize optimal disturbance attenuation for an input-saturated system subject to magnitude-bounded disturbance. Based on circle criterion and the techniques of linear matrix inequalities and convex optimization, stability properties of a system under a known feedback controller are analyzed and an linear approach of synthesizing optimal feedback controller is proposed. Illustrative examples are given and state trajectories of the system before and after stabilization are compared to examine the effectiveness of the proposed approach. The simulation results show that the synthesized controller is effective in stabilizing the system and realizing optimal disturbance attenuation.

Keywords: saturation; disturbance; linear feedback; LMIs; convex optimization.

List of Acronyms, Notations and Symbols

$a \in A$	:	element a belongs to set A
$A \subset B$	:	set A is a proper subset of set B
$\overline{A}$	:	complement of set A
$A \cap B$	:	intersection of set A and set B
$\mathbf{I}_n$	:	$n \times n$ identity matrix
LMIs	:	linear matrix inequalities.
$max(\mathbf{X})$	:	matrix resulted from every element of matrix $\mathbf{X}$ taking its maximum value
$\mathbf{R}$, $\mathbf{R}^n$ and $\mathbf{R}^{m\times n}$	:	fields of real numbers, n-dimensional real vector and $m \times n$ real matrices
$\boldsymbol{x}^{max}$ and $\boldsymbol{x}^{min}$	:	the maximum and the minimum values of variable $\boldsymbol{x}$
$\mathbf{X}^*$	:	the optimal value of matrix $\mathbf{X}$

J. Lee et al. (Eds.): ICIRA 2013, Part II, LNAI 8103, pp. 189–201, 2013.

$\mathbf{X}^T$	:	transpose of matrix $\mathbf{X}$
$\mathbf{X}_i$	:	ith row of matrix $\mathbf{X}$
$\mathbf{X} > \mathbf{Y}$	:	matrix $\mathbf{X}$-$\mathbf{Y}$ is positive definite
$\lvert\mathbf{X}\rvert$	:	matrix resulted from every element of matrix $\mathbf{X}$ taking its absolute value
□	:	end of proof

1 Introduction

In this paper, an approach is presented based on circle criterion to address the problem of controlling linear systems subject to input saturation and magnitude-bounded disturbance. The closed-loop local stability of an input-saturated system, which is under a given linear state feedback and with no disturbance input, has been studied in a lot of work [1]-[6]. Approaches of estimating the region of attraction proposed in these work utilize the absolute stability analysis methods, e.g., the circle and Popov criteria in [3] and the quadratic Lyapunov function in [7] and [8], and the conditions for local stability are expressed in terms of solvable linear matrix inequalities (LMIs).

Nevertheless, in the presence of disturbance input, the analysis of local stability and the estimation of region of attraction become more complicated. Solutions to such kind of problems are provided in [2] and [8] for the cases that disturbances are of finite energy. This paper, however, from another perspective considers the case that the disturbance is magnitude-bounded and intends to propose not only the condition for use in such a case to estimate the stability domain and region of attraction, but also the condition under which feedback controller would be synthesized and disturbance would be attenuated. Here disturbance attenuation is in the sense that there is a small (as small as possible) neighborhood of the origin such that all the trajectories starting from the origin will remain in it and the trajectories with non-zero initial states in region of attraction would converge into this neighborhood in a finite time and remain in it thereafter.

This paper is organized as follows. Section 2 states the problem in detail. Section 3 addresses the analysis of closed-loop stability. Section 4 addresses issues related to disturbance rejection. Section 5 presents illustrative examples and compares the state trajectories before and after stabilization. A brief concluding remark is given in Section 6.

2 Problem Statement

Consider the linear continuous-time system described by:

$$\dot{\boldsymbol{x}}(t) = \mathbf{A}\boldsymbol{x}(t) + \mathbf{B}\boldsymbol{u}(t) + \mathbf{E}\boldsymbol{w}(t) \tag{1}$$

where $\boldsymbol{x}(t) \in \mathbf{R}^n$ is the state, $\boldsymbol{u}(t) \in \mathbf{R}^m$ is the control input, $\boldsymbol{w}(t) \in \mathbf{R}^q$ is the disturbance. $\mathbf{A}$, $\mathbf{B}$ and $\mathbf{E}$ are known real matrices of appropriate dimensions, with pair $(\mathbf{A}, \mathbf{B})$ controllable and $\mathbf{E}$ the magnitude of disturbance. The vector $\boldsymbol{w}(t)$ is assumed to

take values in the compact set $\mathfrak{V} = \{\boldsymbol{w} \subset \mathbf{R}^q; \boldsymbol{w}^T \boldsymbol{w} \le 1\}$. The vector $\boldsymbol{u}(t)$ is assumed to take values in the compact set $\Omega = \{\boldsymbol{u} \subset \mathbf{R}^m; -\boldsymbol{u}_0 \le \boldsymbol{u} \le \boldsymbol{u}_0\}$, with $\boldsymbol{u}_0$ component-wise positive vector of $\mathbf{R}^m$.

The saturation function $sat(\mathbf{F}\boldsymbol{x}(t))$ is defined as:

$$sat(\mathbf{F}\boldsymbol{x}(t)) = [sat(\mathbf{F}\boldsymbol{x}(t))_1, sat(\mathbf{F}\boldsymbol{x}(t))_2, \cdots sat(\mathbf{F}\boldsymbol{x}(t))_m]^T$$

with for i=1,…,m:

$$sat(\mathbf{F}\boldsymbol{x}(t))_i = \begin{cases} -\boldsymbol{u}_{0i} & \text{if} \quad \mathbf{F}_i x < -\boldsymbol{u}_{0i} \\ \mathbf{F}_i x & \text{if} \quad -\boldsymbol{u}_{0i} \le \mathbf{F}_i x \le \boldsymbol{u}_{0i} \\ \boldsymbol{u}_{0i} & \text{if} \quad \mathbf{F}_i x > \boldsymbol{u}_{0i} \end{cases}$$

By implementing such a saturated state feedback control law $\boldsymbol{u}(t) = -sat(\mathbf{F}\boldsymbol{x}(t))$, the closed-loop system is

$$\dot{\boldsymbol{x}}(t) = \mathbf{A}\boldsymbol{x}(t) - \mathbf{B}sat(\mathbf{F}\boldsymbol{x}(t)) + \mathbf{E}\boldsymbol{w} \tag{2}$$

When the control inputs do not saturate, that is, for all $\boldsymbol{x}(t) \in L(\mathbf{F}, \boldsymbol{u}_0)$ defined as

$$L(\mathbf{F}, \boldsymbol{u}_0) = \{\boldsymbol{x} \in \mathbf{R}^n; -\boldsymbol{u}_0 \le \mathbf{F}\boldsymbol{x} \le \boldsymbol{u}_0\}$$

system (2) admits the linear model:

$$\dot{\boldsymbol{x}}(t) = (\mathbf{A} - \mathbf{BF})\boldsymbol{x}(t) + \mathbf{E}\boldsymbol{w}$$

Here the notation $L(\mathbf{F}, \boldsymbol{u}_0)$ denotes the region in the state space where the control is linear in $\boldsymbol{x}$.

Since system (1) is not necessary to be stable before feedback stabilization, no open-loop stability properties are assumed in this paper for representation (1). As a result, the local stabilization of the closed-loop saturated system (2) must be investigated. Local stabilization is in the sense that there exists a bounded set M_0 in R^n such that for $\forall \boldsymbol{x}_0 = \boldsymbol{x}(t=0) \in M_0$, the resulting trajectories under $\boldsymbol{w} \in \mathfrak{V}$, denoted by $\boldsymbol{x}(t, \boldsymbol{x}_0, \boldsymbol{w})$, would asymptotically converge into a bounded invariant set M_1 determined by disturbance $\boldsymbol{w}$ (note that set M_1 is the origin if $\mathbf{E}\boldsymbol{w}(t) = 0$ holds for $\forall t > 0$).

Definition 1. *The region of attraction of set* M_1 *is define as*

$$\Im(M_1) = \{\boldsymbol{x}_0 \in \mathbf{R}^n : \lim_{t \to \infty} l(\boldsymbol{x}(t, \boldsymbol{x}_0, \boldsymbol{w}), M_1) = 0, \forall \boldsymbol{w} \in \mathfrak{V}\}$$

where $l(\boldsymbol{x}(t, \boldsymbol{x}_0, \boldsymbol{w}), M_1) = \inf_{\forall \boldsymbol{\psi} \in M_1} \left\| \boldsymbol{x}(t, \boldsymbol{x}_0, \boldsymbol{w}) - \boldsymbol{\psi} \right\|$ *is a measurement of the distance from* $\boldsymbol{x}(t, \boldsymbol{x}_0, \boldsymbol{w})$ *to set* M_1.

Definition 2. *Let* $\mathbf{P} \in \mathbf{R}^{n\times n}$ *be a positive definite matrix and the ellipsoid* $\delta(\mathbf{P}, \rho)$ *be given as*

$$\delta(\mathbf{P}, \rho) = \{\boldsymbol{x} \in \mathbf{R}^n : \boldsymbol{x}^T \mathbf{P} \boldsymbol{x} \le \rho, \mathbf{P} > 0, \rho \ge 0\}$$

The ellipsoid $\delta(\mathbf{P}, \rho)$ *is said to be (strictly) invariant if for all* $\boldsymbol{x} \in \partial\delta(\mathbf{P}, \rho)$ *and* $\boldsymbol{w} \in \mathfrak{V}$, *the time-derivative of the function* $V(\boldsymbol{x}) = \boldsymbol{x}^T \mathbf{P} \boldsymbol{x}$ *along the trajectories of system (2) is non-positive (negative), that is*

$$\dot{V}(\boldsymbol{x}) = 2\boldsymbol{x}^T \mathbf{P}(\mathbf{A}\boldsymbol{x}(t) - \mathbf{B}sat(\mathbf{F}\boldsymbol{x}(t)) + \mathbf{E}\boldsymbol{w}) \le 0 (< 0)$$

where $\partial\delta(\mathbf{P}, \rho)$ *denotes the boundary of ellipsoid* $\delta(\mathbf{P}, \rho)$.

Definition 1 indicates that if set M_0 belongs to the domain $\Im(M_1)$, trajectories of system (2) will eventually converge into set M_1 and stay inside. Definition 2 makes it possible to estimate the invariant set M_1 by an ellipsoid of appropriate volume. Let the invariant ellipsoid δ_{min} be an estimation of set M_1, with $M_1 \subset \delta_{min}$, then for the concern of disturbance rejection, the ellipsoid δ_{min} is expected to be sufficiently small, so that trajectories starting from the origin will stay close to the origin. On the other hand, let the invariant ellipsoid δ_{max} be an estimation of set $\Im(M_1)$, with $\delta_{max} \subset \Im(M_1)$, then for the concern of local stability throughout a prescribed state space denoted by compact set $X_0 \in \mathbf{R}^n$, the ellipsoid δ_{max} is expected to be sufficiently large to include set X_0.

Therefore, the requirements on the optimal feedback stabilization of representation (1) can be stated as optimization objective (3): Design a controller **F**, such that the following requirements are satisfied simultaneously

$$\begin{aligned} &a) \quad M_1 \subset \delta_{min} \subset \delta_{max} \subset \Im(M_1) \\ &b) \quad \delta_{min} \text{ is minimized} \\ &c) \quad X_0 \subset \delta_{max} \end{aligned} \tag{3}$$

3 Stability Analysis

To deal with requirement (3a), it is necessary to find a way to determine whether an ellipsoid is invariant in the region of attraction. For this reason, based on the circle criterion and the sector condition proposed in section 3.1, a set invariance condition is proposed and thereafter proved in section 3.2 as Theorem 1 and Corollary 1. On the other aspect, it also hints in requirement (3a) that for $\forall \boldsymbol{x}_0 \in \delta_{max} \cap \overline{\delta}_{min}$ the trajectories should be able to converge into δ_{min}, hence a convergence condition based on Corollary 1 is proposed and thereafter proved in section 3.3 as Theorem 2, by which the trajectories' convergence between two invariant sets is guaranteed and requirement (3a) is actually satisfied.

3.1 Sector Condition

An equivalent form of the saturated system (2) is

$$\dot{\boldsymbol{x}}(t) = (\mathbf{A} - \mathbf{B}\mathbf{K}_1\mathbf{F})\boldsymbol{x}(t) - \mathbf{B}\varphi(t, \mathbf{F}\boldsymbol{x}) + \mathbf{E}\boldsymbol{w} \tag{4}$$

where $\mathbf{K}_1 \in \mathbf{R}^{m\times m}$ is a diagonal positive matrix such that $\mathbf{A} - \mathbf{B}\mathbf{K}_1\mathbf{F}$ is Hurwitz stable, $\varphi(t, \mathbf{F}\boldsymbol{x})$ is a decentralized nonlinear function described as

$$\varphi(t, \mathbf{F}\boldsymbol{x}) = sat(\mathbf{F}\boldsymbol{x}(t)) - \mathbf{K}_1\mathbf{F}\boldsymbol{x}(t)$$

Define the domain $L(\mathbf{F}, \boldsymbol{u}_0 / \mathbf{K}_1)$ as:

$$L(\mathbf{F}, \boldsymbol{u}_0 / \mathbf{K}_1) = \{\boldsymbol{x} \in \mathbf{R}^n; -\frac{\boldsymbol{u}_{0i}}{(k_1)_i} \le \mathbf{F}_i\boldsymbol{x} \le \frac{\boldsymbol{u}_{0i}}{(k_1)_i},$$
$$i = 1, ..., m\}$$

where $(k_1)_i$ denotes the ith diagonal element of matrix $\mathbf{K}_1$. Note that $\varphi(t, \mathbf{F}\boldsymbol{x})$ satisfies the sector condition defined in [9], thus for $\forall t \ge 0$ and $\forall \boldsymbol{x} \in L(\mathbf{F}, \boldsymbol{u}_0 / \mathbf{K}_1)$, there must exist another diagonal positive matrix $\mathbf{K}_2 (\ge \mathbf{K}_1 \in \mathbf{R}^{m\times m})$, such that

$$[sat(\mathbf{F}\boldsymbol{x}(t)) - \mathbf{K}_1\mathbf{F}\boldsymbol{x}(t)]^T [sat(\mathbf{F}\boldsymbol{x}(t)) - \mathbf{K}_2\mathbf{F}\boldsymbol{x}(t)] \le 0$$

which equals to

$$\varphi(t, \mathbf{F}\boldsymbol{x})^T (\varphi(t, \mathbf{F}\boldsymbol{x}) - (\mathbf{K}_2 - \mathbf{K}_1)\mathbf{F}\boldsymbol{x}(t)) \le 0 \tag{5}$$

Inequality (5) is said to be the sector condition for nonlinearity $sat(\mathbf{F}\boldsymbol{x}(t))$, and $sat(\mathbf{F}\boldsymbol{x}(t))$ is said to belong to the sector $[\mathbf{K}_1, \mathbf{K}_2]$.

3.2 A Set Invariance Condition

Based on the knowledge of sector condition, circle criterion and the results proposed in [8]-[10], the following Theorem can be stated:

Theorem 1. *Assume that there exists a triplet* $(\mathbf{F}, \mathbf{K}_1, \mathbf{K}_2)$ *with* $\mathbf{K}_1 < \mathbf{I}_m$, $\mathbf{K}_2 \ge \mathbf{I}_m$ *such that* $(\mathbf{F}, \mathbf{A}, \mathbf{B})$ *is controllable and observable, and* $sat(\mathbf{F}\boldsymbol{x}(t))$ *satisfies the sector condition in sector* $[\mathbf{K}_1, \mathbf{K}_2]$. *Given an ellipsoid* $\delta(\mathbf{P}, \rho)$, *if there exist a matrix* $\mathbf{Z} \in \mathbf{R}^{m\times n}$ *and a positive scalar* μ, *such that*

$$(\mathbf{A} - \mathbf{B}\mathbf{K}_1\mathbf{F})^T\mathbf{P} + \mathbf{P}(\mathbf{A} - \mathbf{B}\mathbf{K}_1\mathbf{F}) + \mathbf{Z}^T\mathbf{Z} + \frac{1}{\mu}\mathbf{P}\mathbf{E}\mathbf{E}^T\mathbf{P} + \frac{\mu}{\rho}\mathbf{P} < 0 \tag{6}$$

$$\mathbf{P}\mathbf{B} = \mathbf{F}^T(\mathbf{K}_2 - \mathbf{K}_1) - \sqrt{2}\mathbf{Z}^T \tag{7}$$

$$\delta(\mathbf{P},\rho) \subset L(\mathbf{F},\boldsymbol{u}_0 / \mathbf{K}_1) \tag{8}$$

then $\delta(\mathbf{P},\rho)$ *is a strictly invariant set for system (2).*

Proof. Select a quadratic Lyapunov function $V(\boldsymbol{x}) = \boldsymbol{x}^T\mathbf{P}\boldsymbol{x}$, then from the equivalent form of system (2) given in (4), it follows

$$\begin{aligned}\dot{V}(\boldsymbol{x}) = \boldsymbol{x}^T((\mathbf{A}-\mathbf{B}\mathbf{K}_1\mathbf{F})^T\mathbf{P}+\mathbf{P}(\mathbf{A}-\mathbf{B}\mathbf{K}_1\mathbf{F}))\boldsymbol{x}\\ -2\boldsymbol{x}^T\mathbf{P}\mathbf{B}\varphi(t,\mathbf{F}\boldsymbol{x})+2\boldsymbol{x}^T\mathbf{P}\mathbf{E}\boldsymbol{w}\end{aligned}$$

The relationship (8) leads to the satisfaction of sector condition (5), thus there is

$$\begin{aligned}\dot{V}(\boldsymbol{x}) < \boldsymbol{x}^T((\mathbf{A}-\mathbf{B}\mathbf{K}_1\mathbf{F})^T\mathbf{P}+\mathbf{P}(\mathbf{A}-\mathbf{B}\mathbf{K}_1\mathbf{F}))\boldsymbol{x}\\ -2\boldsymbol{x}^T\mathbf{P}\mathbf{B}\varphi(t,\mathbf{F}\boldsymbol{x})+2\boldsymbol{x}^T\mathbf{P}\mathbf{E}\boldsymbol{w}\\ -2\varphi(t,\mathbf{F}\boldsymbol{x})^T(\varphi(t,\mathbf{F}\boldsymbol{x})-(\mathbf{K}_2-\mathbf{K}_1)\mathbf{F}\boldsymbol{x}(t))\end{aligned}$$

If conditions (6) and (7) are both satisfied, it follows

$$\begin{aligned}&\boldsymbol{x}^T((\mathbf{A}-\mathbf{B}\mathbf{K}_1\mathbf{F})^T\mathbf{P}+\mathbf{P}(\mathbf{A}-\mathbf{B}\mathbf{K}_1\mathbf{F}))\boldsymbol{x}\\ &\quad -2\varphi(t,\mathbf{F}\boldsymbol{x})^T(\varphi(t,\mathbf{F}\boldsymbol{x})-(\mathbf{K}_2-\mathbf{K}_1)\mathbf{F}\boldsymbol{x}(t))\\ &\quad -2\boldsymbol{x}^T\mathbf{P}\mathbf{B}\varphi(t,\mathbf{F}\boldsymbol{x})\\ &< -\boldsymbol{x}^T(\frac{1}{\mu}\mathbf{P}\mathbf{E}\mathbf{E}^T\mathbf{P}+\frac{\mu}{\rho}\mathbf{P})\boldsymbol{x}-(\mathbf{Z}\boldsymbol{x}-\sqrt{2}\varphi(t,\mathbf{F}\boldsymbol{x}))^T(\mathbf{Z}\boldsymbol{x}-\sqrt{2}\varphi(t,\mathbf{F}\boldsymbol{x}))\\ &\le -\boldsymbol{x}^T(\frac{1}{\mu}\mathbf{P}\mathbf{E}\mathbf{E}^T\mathbf{P}+\frac{\mu}{\rho}\mathbf{P})\boldsymbol{x}\end{aligned}$$

Besides, since it is assumed $\boldsymbol{w} \in \mathfrak{V}$, there is

$$2\boldsymbol{x}^T\mathbf{P}\mathbf{E}\boldsymbol{w} \le \frac{1}{\mu}\boldsymbol{x}\mathbf{P}\mathbf{E}\mathbf{E}^T\mathbf{P}\boldsymbol{x}+\mu\boldsymbol{w}^T\boldsymbol{w} \le \frac{1}{\mu}\boldsymbol{x}\mathbf{P}\mathbf{E}\mathbf{E}^T\mathbf{P}\boldsymbol{x}+\mu$$

Hence

$$\dot{V}(\boldsymbol{x}) < -\mu\boldsymbol{x}^T\mathbf{P}\boldsymbol{x} / \rho+\mu$$

For all $\boldsymbol{x} \in \partial\delta(\mathbf{P},\rho)$, there is $\boldsymbol{x}^T\mathbf{P}\boldsymbol{x} = \rho$, hence $\dot{V}(\boldsymbol{x}) < 0$. It follows that $\delta(\mathbf{P},\rho)$ is a strictly invariant set for system (2). □

By writing conditions (6) and (7) in one inequality, the following corollary can be stated.

Corollary 1. *Assume that there exists a triplet* $(\mathbf{F},\mathbf{K}_1,\mathbf{K}_2)$ *with* $\mathbf{K}_1 < \mathbf{I}_m$, $\mathbf{K}_2 \ge \mathbf{I}_m$, *such that* $(\mathbf{F},\mathbf{A},\mathbf{B})$ *is controllable and observable, and sat*$(\mathbf{F}\boldsymbol{x}(t))$ *satisfies the sector condition in sector* $[\mathbf{K}_1,\mathbf{K}_2]$. *Given an ellipsoid* $\delta(\mathbf{P},\rho)$, *if there exist a matrix* $\mathbf{Z} \in \mathbf{R}^{m\times n}$ *and a positive scalar* μ , *such that*

$$(\mathbf{A}-\mathbf{B}\mathbf{K}_1\mathbf{F})^T\mathbf{P}+\mathbf{P}(\mathbf{A}-\mathbf{B}\mathbf{K}_1\mathbf{F})+\frac{1}{\mu}\mathbf{P}\mathbf{E}\mathbf{E}^T\mathbf{P}+\frac{\mu}{\rho}\mathbf{P}$$
$$+\frac{1}{2}[\mathbf{F}^T(\mathbf{K}_2-\mathbf{K}_1)-\mathbf{P}\mathbf{B}][(\mathbf{K}_2-\mathbf{K}_1)\mathbf{F}-\mathbf{B}^T\mathbf{P}]<0 \tag{9}$$

$$\delta(\mathbf{P},\rho)\subset L(\mathbf{F},\boldsymbol{u}_0/\mathbf{K}_1) \tag{10}$$

then $\delta(\mathbf{P},\rho)$ *is a strictly invariant set for system (2).*

3.3 A Convergence Condition for Two Invariant Sets

Theorem 2. *Assume that there exist a quaternion* $(\mathbf{F},\mathbf{K}_{\rho 1},\mathbf{K}_{\rho 2},\mathbf{K}_2)$ *with* $\mathbf{K}_{\rho 2}<\mathbf{K}_{\rho 1}<\mathbf{I}_m$ *and* $\mathbf{K}_2\geq\mathbf{I}_m$, *such that* $(\mathbf{F},\mathbf{A},\mathbf{B})$ *is controllable and observable, and sat*$(\mathbf{F}\boldsymbol{x}(t))$ *satisfies the sector condition in both sectors* $[\mathbf{K}_{\rho 1},\mathbf{K}_2]$ *and* $[\mathbf{K}_{\rho 2},\mathbf{K}_2]$. *Given two ellipsoids* $\delta(\mathbf{P},\rho_1)$ *and* $\delta(\mathbf{P},\rho_2)$, $\rho_2>\rho_1>0$, *if there exists a positive scalar* η, *such that*

$$(\mathbf{A}-\mathbf{B}\mathbf{K}_{\rho 1}\mathbf{F})^T\mathbf{P}+\mathbf{P}(\mathbf{A}-\mathbf{B}\mathbf{K}_{\rho 1}\mathbf{F})+\frac{1}{\mu}\mathbf{P}\mathbf{E}\mathbf{E}^T\mathbf{P}+\frac{\mu}{\rho_1}\mathbf{P}$$
$$+\frac{1}{2}[\mathbf{F}^T(\mathbf{K}_2-\mathbf{K}_{\rho 1})-\mathbf{P}\mathbf{B}][(\mathbf{K}_2-\mathbf{K}_{\rho 1})\mathbf{F}-\mathbf{B}^T\mathbf{P}]<0 \tag{11}$$

$$(\mathbf{A}-\mathbf{B}\mathbf{K}_{\rho 2}\mathbf{F})^T\mathbf{P}+\mathbf{P}(\mathbf{A}-\mathbf{B}\mathbf{K}_{\rho 2}\mathbf{F})+\frac{1}{\mu}\mathbf{P}\mathbf{E}\mathbf{E}^T\mathbf{P}+\frac{\mu}{\rho_2}\mathbf{P}$$
$$+\frac{1}{2}[\mathbf{F}^T(\mathbf{K}_2-\mathbf{K}_{\rho 2})-\mathbf{P}\mathbf{B}][(\mathbf{K}_2-\mathbf{K}_{\rho 2})\mathbf{F}-\mathbf{B}^T\mathbf{P}]<0 \tag{12}$$

$$\delta(\mathbf{P},\rho_1)\subset L(\mathbf{F},\boldsymbol{u}_0/\mathbf{K}_{\rho 1}) \tag{13}$$

$$\delta(\mathbf{P},\rho_2)\subset L(\mathbf{F},\boldsymbol{u}_0/\mathbf{K}_{\rho 2}) \tag{14}$$

then, for $\forall\rho\in[\rho_1,\rho_2]$, *there exists a positive definite diagonal matrix* $\mathbf{K}_1<\mathbf{I}_m$ *such that*

$$(\mathbf{A}-\mathbf{B}\mathbf{K}_1\mathbf{F})^T\mathbf{P}+\mathbf{P}(\mathbf{A}-\mathbf{B}\mathbf{K}_1\mathbf{F})+\frac{1}{\mu}\mathbf{P}\mathbf{E}\mathbf{E}^T\mathbf{P}+\frac{\mu}{\rho}\mathbf{P}$$
$$+\frac{1}{2}[\mathbf{F}^T(\mathbf{K}_2-\mathbf{K}_1)-\mathbf{P}\mathbf{B}][(\mathbf{K}_2-\mathbf{K}_1)\mathbf{F}-\mathbf{B}^T\mathbf{P}]<0 \tag{15}$$

$$\delta(\mathbf{P},\rho)\subset L(\mathbf{F},\boldsymbol{u}_0/\mathbf{K}_1) \tag{16}$$

Proof. Let $(k_1)_i$, $(k_{\rho 1})_i$ and $(k_{\rho 2})_i$ be the *i*th diagonal elements of matrix $\mathbf{K}_1$, $\mathbf{K}_{\rho 1}$ and $\mathbf{K}_{\rho 2}$, respectively, with $i \in [1, m]$. According to [11] and [12], conditions (13) and (14) are equivalent to inequalities (17) and (18), respectively,

$$\begin{bmatrix} 1/\rho_1 & (k_{\rho 1})_i \mathbf{F}_i / u_{0i} \\ (k_{\rho 1})_i \mathbf{F}_i^T / u_{0i} & \mathbf{P} \end{bmatrix} > 0 \tag{17}$$

$$\begin{bmatrix} 1/\rho_2 & (k_{\rho 2})_i \mathbf{F}_i / u_{0i} \\ (k_{\rho 2})_i \mathbf{F}_i^T / u_{0i} & \mathbf{P} \end{bmatrix} > 0 \tag{18}$$

Since $\rho \in [\rho_1, \rho_2]$, there must exist a $\lambda \in [0,1]$, such that $1/\rho = \lambda/\rho_1 + (1-\lambda)/\rho_2$. Let $(k_1)_i = \lambda(k_{\rho 1})_i + (1-\lambda)(k_{\rho 2})_i$, then $\lambda \times \text{Eq.}(17) + (1-\lambda) \times \text{Eq.}(18)$ leads to

$$\begin{bmatrix} 1/\rho & (k_1)_i \mathbf{F}_i / u_{0i} \\ (k_1)_i \mathbf{F}_i^T / u_{0i} & \mathbf{P} \end{bmatrix} > 0$$

which equals to condition (16).

On the other hand, note that conditions (11) and (12) are equivalent to inequalities (19) and (20), respectively,

$$\begin{bmatrix} \Gamma_{11} & \Gamma_{21}^T \\ \Gamma_{21} & -2\mathbf{I}_m \end{bmatrix} < 0 \tag{19}$$

$$\begin{bmatrix} \Gamma_{12} & \Gamma_{22}^T \\ \Gamma_{22} & -2\mathbf{I}_m \end{bmatrix} < 0 \tag{20}$$

where

$$\Gamma_{11} = (\mathbf{A} - \mathbf{B}\mathbf{K}_{\rho 1}\mathbf{F})^T \mathbf{P} + \mathbf{P}(\mathbf{A} - \mathbf{B}\mathbf{K}_{\rho 1}\mathbf{F}) + \frac{1}{\mu}\mathbf{P}\mathbf{E}\mathbf{E}^T\mathbf{P} + \frac{\mu}{\rho_1}\mathbf{P}$$

$$\Gamma_{21} = [(\mathbf{K}_2 - \mathbf{K}_{\rho 1})\mathbf{F} - \mathbf{B}^T\mathbf{P}]$$

$$\Gamma_{12} = (\mathbf{A} - \mathbf{B}\mathbf{K}_{\rho 2}\mathbf{F})^T \mathbf{P} + \mathbf{P}(\mathbf{A} - \mathbf{B}\mathbf{K}_{\rho 2}\mathbf{F}) + \frac{1}{\mu}\mathbf{P}\mathbf{E}\mathbf{E}^T\mathbf{P} + \frac{\mu}{\rho_1}\mathbf{P}$$

$$\Gamma_{22} = [(\mathbf{K}_2 - \mathbf{K}_{\rho 2})\mathbf{F} - \mathbf{B}^T\mathbf{P}]$$

Therefore $\lambda \times \text{Eq.}(19) + (1-\lambda) \times \text{Eq.}(20)$ leads to

$$\begin{bmatrix} \Gamma_1 & \Gamma_2^T \\ \Gamma_2 & -2\mathbf{I}_m \end{bmatrix} < 0$$

where

$$\Gamma_1 = (\mathbf{A} - \mathbf{B}\mathbf{K}_1\mathbf{F})^T \mathbf{P} + \mathbf{P}(\mathbf{A} - \mathbf{B}\mathbf{K}_1\mathbf{F}) + \frac{1}{\mu}\mathbf{P}\mathbf{E}\mathbf{E}^T\mathbf{P} + \frac{\mu}{\rho}\mathbf{P}$$

$$\Gamma_2 = [(\mathbf{K}_2 - \mathbf{K}_1)\mathbf{F} - \mathbf{B}^T\mathbf{P}]$$

which equals to condition (15).□

Theorem 2 implies that if conditions (11)-(14) are satisfied, the ellipsoid $\delta(\mathbf{P}, \rho)$ is strictly invariant for $\forall \rho \in [\rho_1, \rho_2]$, and the time-derivative of Lyapunov function $V(\boldsymbol{x})$ is negative throughout the domain $\delta(\mathbf{P}, \rho_2) \cap \delta(\mathbf{P}, \rho_1)$, so that for every initial state $x_0 \in \delta(\mathbf{P}, \rho_2) \cap \delta(\mathbf{P}, \rho_1)$, the trajectory will asymptotically converge into $\delta(\mathbf{P}, \rho_1)$. Therefore, to fulfill requirement (3a), the ellipsoids δ_{min} and δ_{max} can be selected as ellipsoids $\delta(\mathbf{P}, \rho_1)$ and $\delta(\mathbf{P}, \rho_2)$, respectively. Since ρ_2 can be absorbed into other parameters, it is for simplicity in the following sections to assume: $0 < \rho_1 < 1$, $\rho_2 = 1$.

4 Optimal Controller Synthesis

In this section, method of synthesizing the optimal feedback controller for system (1) is concerned. Based on Theorem 2 and the idea of convex theory, requirements (3a) to (3c) are transformed into LMIs constraints and the optimal controller is synthesized via convex optimization.

4.1 LMI Constraints

1) To fulfill requirement (3a), conditions (11)-(14) must hold. For inequality (19), which equals to condition (11), the following transformation holds

$$\begin{bmatrix} \mathbf{P}^{-1} & 0 \\ 0 & \mathbf{I}_m \end{bmatrix}^T \begin{bmatrix} \Gamma_{11} & \Gamma_{21}^T \\ \Gamma_{21} & -2\mathbf{I}_m \end{bmatrix} \begin{bmatrix} \mathbf{P}^{-1} & 0 \\ 0 & \mathbf{I}_m \end{bmatrix} < 0$$

which equals to

$$\begin{bmatrix} \mathbf{P}^{-1}\Gamma_{11}\mathbf{P}^{-1} & \mathbf{P}^{-1}\Gamma_{21}^T \\ \Gamma_{21}\mathbf{P}^{-1} & -2\mathbf{I}_m \end{bmatrix} < 0 \tag{21}$$

Let $\mathbf{Q} = \mathbf{P}^{-1}$ and $\mathbf{Y} = \mathbf{P}^{-1}\mathbf{F}^T$, then inequality (21) equals to the following constraint

$$\begin{bmatrix} \mathbf{H}_1 & \mathbf{Y}(\mathbf{K}_2 - \mathbf{K}_{\rho 1}) - \mathbf{B} \\ (\mathbf{K}_2 - \mathbf{K}_{\rho 1})\mathbf{Y}^T - \mathbf{B}^T & -2\mathbf{I}_m \end{bmatrix} < 0 \tag{22}$$

where

$$\mathbf{H}_1 = \mathbf{Q}\mathbf{A}^T + \mathbf{A}\mathbf{Q} - \mathbf{Y}(\mathbf{B}\mathbf{K}_{\rho 1})^T - (\mathbf{B}\mathbf{K}_{\rho 1})\mathbf{Y}^T + \frac{1}{\mu}\mathbf{E}\mathbf{E}^T + \frac{\mu}{\rho_1}\mathbf{Q}$$

Similarly, inequality (20), which equals to condition (12), can be transformed into the following constraint

$$\begin{bmatrix} \mathbf{H}_2 & \mathbf{Y}(\mathbf{K}_2 - \mathbf{K}_{\rho 2}) - \mathbf{B} \\ (\mathbf{K}_2 - \mathbf{K}_{\rho 2})\mathbf{Y}^T - \mathbf{B}^T & -2\mathbf{I}_m \end{bmatrix} < 0 \tag{23}$$

where

$$\mathbf{H}_2 = \mathbf{Q}\mathbf{A}^T + \mathbf{A}\mathbf{Q} - \mathbf{Y}(\mathbf{B}\mathbf{K}_{\rho 2})^T - (\mathbf{B}\mathbf{K}_{\rho 2})\mathbf{Y}^T + \frac{1}{\mu}\mathbf{E}\mathbf{E}^T + \frac{\mu}{\rho_2}\mathbf{Q}$$

From [13] and [14], for all $i \in [1, m]$, condition (13) equals to

$$\begin{bmatrix} \left(u_{0i} / (k_{\rho 1})_i\right)^2 & \mathbf{F}_i (\mathbf{P} / \rho_1)^{-1} \\ (\mathbf{P} / \rho_1)^{-1} \mathbf{F}_i^T & (\mathbf{P} / \rho_1)^{-1} \end{bmatrix} > 0$$

which can be transformed into the following constraint

$$\begin{bmatrix} \left(u_{0i} / (k_{\rho 1})_i\right)^2 & \rho_1 \mathbf{Y}^T \\ \rho_1 \mathbf{Y} & \rho_1 \mathbf{Q} \end{bmatrix} > 0 \tag{24}$$

Similarly, condition (34) can be transformed into the following constraint

$$\begin{bmatrix} \left(u_{0i} / (k_{\rho 2})_i\right)^2 & \rho_2 \mathbf{Y}^T \\ \rho_2 \mathbf{Y} & \mathbf{Q} \end{bmatrix} > 0 \tag{25}$$

2) To deal with requirement (3b), let $X_C \in \mathbf{R}^n$ denote a prescribed convex set, and define a linear transformation $\kappa X_C : \mathbf{R}^n \mapsto \mathbf{R}^n$ as $\kappa X_C = \{\tilde{\boldsymbol{x}} \in \mathbf{R}^n : \tilde{\boldsymbol{x}} = \kappa \boldsymbol{x}, \ \forall \boldsymbol{x} \in X_C, \kappa \in \mathbf{R}\}$, then the ellipsoid $\delta(\mathbf{P}, \rho_1)$ can be minimized via the following technique:

minimize κ
subject to $\delta(\mathbf{P}, \rho_1) \subset \kappa X_C$

If X_C is defined as $X_C = \delta(\mathbf{P}_C, 1) = \{\boldsymbol{x} \in \mathbf{R}^n : \boldsymbol{x}^T \mathbf{P}_C \boldsymbol{x} \le 1, \mathbf{P}_C = \mathbf{P}_C^T > 0\}$, the constraint would be in a LMI form, that is

$$\begin{bmatrix} \mathbf{P}_C / \kappa^2 & \mathbf{I}_n \\ \mathbf{I}_n & (\mathbf{P} / \rho_1)^{-1} \end{bmatrix} < 0 \Leftrightarrow \begin{bmatrix} \mathbf{P}_C / \kappa^2 & \mathbf{I}_n \\ \mathbf{I}_n & \rho_1 \mathbf{Q} \end{bmatrix} < 0 \tag{26}$$

3) To deal with requirement (3c), two types of set X_0 are considered, which are the ellipsoid

$$X_0 = \delta(\mathbf{P}_0, 1) = \{\boldsymbol{x} \in \mathbf{R}^n : \boldsymbol{x}^T \mathbf{P}_0 \boldsymbol{x} \le 1, \mathbf{P}_0 = \mathbf{P}_0^T > 0\} \tag{27a}$$

and the polyhedron designated by h points: $\boldsymbol{x}_1, \boldsymbol{x}_2, ..., \boldsymbol{x}_h$

$$X_0 = co\{\boldsymbol{x}_1, \boldsymbol{x}_2, ..., \boldsymbol{x}_h\} \tag{27b}$$

where "co" denotes the convex hull. For equations (27a) and (27b), requirement (3c) equals to constraints (28a) and (28b), respectively

$$\begin{bmatrix} \mathbf{P}_\infty & \mathbf{I}_n \\ \mathbf{I}_n & (\mathbf{P}/\rho_2)^{-1} \end{bmatrix} > 0 \quad \Leftrightarrow \quad \begin{bmatrix} \mathbf{P}_\infty & \mathbf{I}_n \\ \mathbf{I}_n & \rho_2 \mathbf{Q} \end{bmatrix} > 0 \tag{28a}$$

$$\begin{bmatrix} 1 & \boldsymbol{x}_i^T \\ \boldsymbol{x}_i & (\mathbf{P}/\rho_2)^{-1} \end{bmatrix} > 0 \quad \Leftrightarrow \quad \begin{bmatrix} 1 & \boldsymbol{x}_i^T \\ \boldsymbol{x}_i & \rho_2 \mathbf{Q} \end{bmatrix} > 0 \tag{28b}$$

where in inequality (28b), $\boldsymbol{x}_i \in X_0$ and there are totally h LMIs constraints.

4.2 Disturbance Rejection with Guaranteed Region of Attraction

Based on the analysis in section 4.1, the requirement (3) can be stated as the following optimization problem

$$\underset{\mathbf{Q}>0, \rho_1>0, \mu>0}{\text{minimize}} \quad \kappa \tag{29}$$

subject to
a) constraints (22)-(25).
b) constraint (26).
c) constraint (28a) or (28b).

Note that if μ, ρ_1, $\mathbf{K}_{\rho 1}$, $\mathbf{K}_{\rho 2}$ and $\mathbf{K}_2$ are fixed, constraints in problem (29) would be LMIs. Furthermore, if $\mathbf{K}_{\rho 1}$, $\mathbf{K}_{\rho 2}$ and $\mathbf{K}_2$ are assigned with values that satisfy the sector condition (5), the minimum of κ can be obtained by running iterations on ρ and μ/ρ from 0+ to $+\infty$, and the optimal controller $\mathbf{F}$ can be recovered from equation $\mathbf{F} = \mathbf{Y}^T \mathbf{Q}^{-1}$, once the matrices $\mathbf{Q}$ and $\mathbf{Y}$ are synthesized.

5 Illustrative Example

Consider the system (2) described by

$$\mathbf{A} = \begin{bmatrix} 0.6 & -0.8 \\ 0.8 & 0.6 \end{bmatrix}, \ \mathbf{B} = \begin{bmatrix} 2 \\ 4 \end{bmatrix}, \ \mathbf{E} = \begin{bmatrix} 0.1 \\ 0.1 \end{bmatrix}, \ u_0 = 1, \ w(t) = sign(0.2t)$$

The system is expected to be stable within the compact set X_0 defined by its vertices $X_0 = \{x_1, x_2, ..., x_6\}$, that is

$$X_0 = \begin{Bmatrix} [2,0], & [\sqrt{2},\sqrt{2}], & [0,2], & [-\sqrt{2},\sqrt{2}] \\ [-2,0], & [-\sqrt{2},-\sqrt{2}], & [0,-2], & [\sqrt{2},-\sqrt{2}] \end{Bmatrix}$$

The state feedback controller, which guarantees that the set set X_0 belongs to the region of attraction and the derived system has the maximal level of capacity in disturbance attenuation, can be derived by solving the optimization problem (29).

Let $\mathbf{K}_2 = 1$, $\mathbf{P}_C = \mathbf{I}_2$, then the optimal state feedback controller $\mathbf{F}^*$ can be solved in the MATLAB environment. The results are given as $\mathbf{F}^* = [-0.2711, \ 1.3174]$, with $\mathbf{K}^*_{\rho 1} = 0.86$, $\mathbf{K}^*_{\rho 2} = 0.12$, $\kappa^* = 0.4355$, $\rho_1^* = 0.0512$, $\mu^* = 4.7 \times 10^{-6}$ and

$$\mathbf{Q}^* = \begin{bmatrix} 0.4622 & 0.1769 \\ 0.1769 & 0.3079 \end{bmatrix}$$

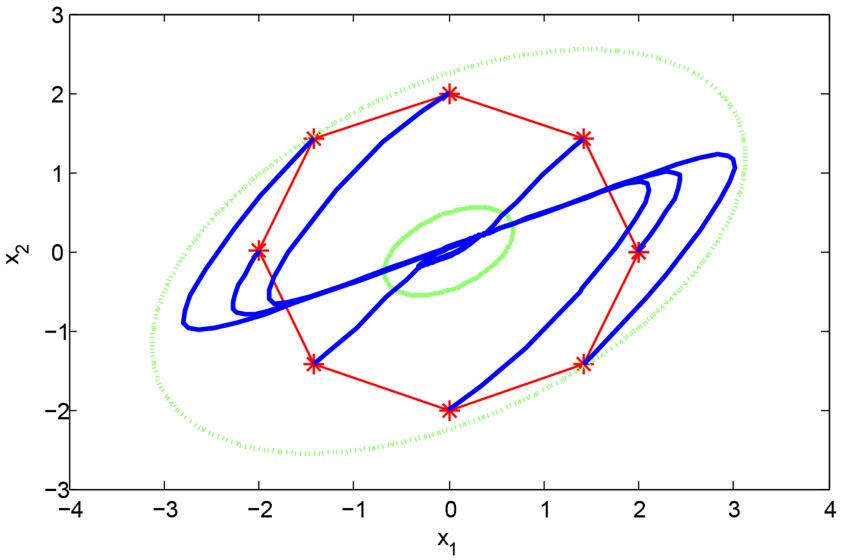

Fig. 1. The invariant ellipsoids and trajectories starting from vertices of the prescribed polyhedron

Figure 1 gives the trajectories starting from all vertices of the prescribed polyhedron X_0. The larger ellipsoid $\delta(\mathbf{Q}^{*-1}, 1)$ and the smaller ellipsoid $\delta(\mathbf{Q}^{*-1}, \rho_1)$ denote the stability domain and the capability of disturbance attenuation, respectively. All the trajectories converge asymptotically into the smaller ellipsoid in a few seconds.

6 Conclusions

In this paper, a methodology of designing optimal feedback controller is presented for linear systems subject to input saturation and magnitude-bounded disturbance. Based on circle criterion, a condition used to judge the invariance of an ellipsoid and a condition used to judge the contractiveness of trajectories starting between the two ellipsoids were proposed. These two conditions provided a possibility to synthesize the optimal controller which would realize disturbance attenuation with guaranteed region of attraction.

Reference

1. Gilbert, E.G., Tan, K.T.: Linear systems with state and control constraints: The theory and application of maximal output admissible sets. IEEE Transaction on Automatic Control AC-36, 1008–1020 (1991)
2. Hindi, H., Boyd, S.: Analysis of linear systems with saturation using convex optimization. In: Proceedings of IEEE Conference on Decision and Control, Tampa, US, pp. 903–908. IEEE, New York (1998)
3. Pittet, C., Tarbouriech, S., Burgat, C.: Stability regions for linear systems with saturating controls via circle and popov criteria. In: Proceedings of the 36th Conference on Decision & Control, San Diego, California, US, pp. 4518–4523 (December 1997)
4. Blanchini, F.: Ultimate boundedness control for uncertain discrete-time systems via set-induced Lyapunov function. IEEE Transaction on Automatic Control AC-39, 428–433 (1994)
5. Saberi, A., Lin, Z., Teel, A.R.: Control of linear systems with saturating actuators. IEEE Transaction on Automatic Control AC-41, 368–378 (1996)
6. Kladis, G.P., Economou, J.T., Knowles, K., et al.: Energy conservation based fuzzy tracking for unmanned aerial vehicle missions under a priori known wind information. Engineering Applications of Artificial intelligence 24, 279–294 (2011)
7. Davison, E.J., Kurak, E.M.: A computational method for determining quadratic Lyapunov functions fro non-linear systems. Automatica 7, 627–636 (1971)
8. Hu, T.S., Lin, Z.L., Chen, B.M.: An analysis and design method for linear systems subject to actuator saturation and disturbance. Automatica 38(2), 351–359 (2002)
9. Khalil, H.K.: Nonlinear Systems, 3rd edn., p. 339. Prentice-Hall, New Jersey (2002)
10. Fang, H.J., Lin, Z.L., Hu, T.S.: Analysis of linear systems in the presence of actuator saturation and L2-disturbance. Automatica 40(7), 1229–1238 (2004)
11. Hu, T.S., Lin, Z.L.: Practical stabilization of exponentially unstable linear systems subject to actuator saturation nonlinearities and disturbance. International Journal of Robust and Nonlinear Control 11(6), 555–588 (2001)
12. Hindi, H.: A tutorial on convex optimization. In: Proceedings of American Control Conference, Boston, US, pp. 3252–3265 (June 2004)
13. Boyd, S., Ghaoui, L., Feron, E., Balakrishnan, V.: Linear matrix inequality in system and control theory. In: Proceedings of Studies in Applied Mathematics, PA, Philadelphia, pp. 555–588 (June 1994)
14. Nguyen, T., Jabbari, F.: Disturbance attenuation for systems with input saturation: An LMI approach. IEEE Trans. Autom. Control 44(4), 852–857 (1999)

Estimation of Road Adhesion Coefficient Using Higher-Order Sliding Mode Observer for Torsional Tyre Model

J.J. Rath[1], K.C. Veluvolu[1,⋆], D. Zhang[2], Q. Zhang[2], and M. Defoort[3]

[1] School of Electronics Engineering, College of IT Engineering, Kyungpook National University, Daegu, South Korea 702-701
veluvolu@ee.knu.ac.kr
[2] State Key Laboratory of Mechanical System and Vibration, Shanghai Jiao Tong University, Shanghai 200240 China
[3] LAMIH, CNRS UMR 8201, Univ. Lille Nord de France, UVHC, F-59313 Valenciennes, France

Abstract. The estimation of friction coefficient for a vehicle when it traverses on different surfaces has been an important issue. In this paper, a super-twisting algorithm based sliding mode observer is proposed to estimate the road adhesion coefficient, treated as an unknown input in the dynamics of a quarter-vehicle. By estimating the road adhesion coefficient, the coefficient of friction can be estimated. Simulation results show the effectiveness of the proposed observer in estimation of the road adhesion coefficient that changes with surface variations.

Keywords: Super-twisting algorithm, LuGre friction model, torsional tyre model, road adhesion coefficient.

Nomenclature

v	Longitudinal velocity of the vehicle
w_w	Tyre hub angular velocity
w_r	Tyre ring velocity
θ_{rw}	Torsional angle
z	Internal friction state
J_w	Inertia of hub
J_r	Inertia of ring
κ	Constant representing distribution of force on a patch
r	Radius of tyre
F_x	Longitudinal friction force
F_N	Normal load
C_{av}	Drag coefficient
σ_v	Rolling resistance coefficient
K_t	Spring stiffness

⋆ Corresponding author.

J. Lee et al. (Eds.): ICIRA 2013, Part II, LNAI 8103, pp. 202–213, 2013.

C_t Damping coefficient
T_b Braking Torque
v_r Relative velocity
v_s Stribeck velocity
σ_0 Normalized longitudinal lumped stiffness
σ_1 Normalized longitudinal damping
σ_2 Normalized viscous damping
μ_c Coulomb friction coefficient
μ_s Static friction coefficient
ξ Road adhesion coefficient
g Acceleration due to gravity

1 Introduction

The steady emergence and rapidly evolving intelligent safety systems such as traction control systems(TCS), anti-lock break systems (ABS) etc., have contributed immensely to the development of automotive vehicle industry supplementing its rapid growth. The research in this field has been abundant and widespread ranging from hybrid control schemes that improvise the maneuverability and safety aspects of vehicle motion to different estimation techniques needed to extract information of different factors that are crucial for implementation of ABS. The implementation of controllers for these safety systems relies on availability of accurate information about real-time vehicle behavior which is subject to changing environmental aspects. The tyres of vehicle play a very significant role serving as the medium for transmitting traction forces necessary for vehicle motion. The generated tractive force mainly depends on the friction effect between the road surface and the tyres apart from depending on other factors such as quality of tyres, pressure of tyre etc. The friction effect varies dynamically depending on the type of road surface, normal load on the tyre etc leading to significant changes in the transmitted force by the tyres, affecting the control of safety systems implemented. To facilitate for accurate control of these safety systems, it becomes imperative to estimate the friction effect between tyres and road.

In [1], the nonlinear LuGre model was used for the estimation of road adhesion coefficient for a quarter-vehicle using a nonlinear observer with only wheel angular velocity as measurement under low slip velocity cases. The design of nonlinear adaptive observers was performed in [2] using the LuGre friction model with the wheel speed as measured quantity. Sliding mode based observers have been used to estimate the road friction coefficient. The first-order sliding mode observer (SMO) for a quarter wheel vehicle model and LuGre friction model with angular speed of wheel as measurement to estimate the road adhesion coefficient for varying surface conditions using output injection technique was performed in [3]. In this work by obtaining a robust estimate of the road adhesion coefficient, the advantage of sliding mode observers in comparison to adaptive observers was shown. Recently, considering the dynamics of the nonlinear full vehicle model undergoing longitudinal motion only, a first-order SMO was used for estimation of road adhesion coefficient to determine the maximum tractive torque at

different operating conditions in [4]. In all the works above, the tyre model considered was a rigid ring tyre model that did not take into consideration the effect of torsional properties of the tyre. An observer based on torsional tyre model to estimate the tyre friction coefficient was proposed in [5]. The use of torsional tyre model and a first-order SMO to estimate the tyre pressure and friction was done in [6]. By the use of torsional model of the tyre and the LuGre friction, it was determined how the torsional dynamics of the tyre affected the ABS protocol significantly in [7]. In [3] the nonlinearities in vehicle longitudinal motion were not considered, while in [6] the dynamically varying nature of friction was not accounted for. While these works included the use of SMOs', yet they had to use filtering to reduce the effect of chattering. The work proposed in this paper makes use of the torsional tyre dynamics, the LuGre friction model with corrected terms and the nonlinear quarter-vehicle model including the effects of drag and rolling resistance to estimate the road adhesion coefficients by the use of second order sliding mode observer, the super-twisting algorithm (STA) based observer that does not require any filtering.

2 Vehicle Dynamics Modeling

The dynamics of the longitudinal motion for the vehicle is given as:

$$m\dot{v} = -F_x - C_{av}v^2 - \sigma_v vmg \tag{1}$$

In the considered vehicle model, the nonlinear effects of the air drag force [8] and the effect of the rolling resistance are also considered. In this work, the normal load acting on the tyre is considered to be static. The equations which govern the dynamics of the tyre are given by [7]

$$\begin{cases} J_w\dot{w_w} = K_t(\theta_{rw}) + C_t(w_r - w_w) - T_b \\ J_r\dot{w_r} \;\; = F_x r - K_t(\theta_{rw}) - C_t(w_r - w_w) \end{cases} \tag{2}$$

The static coefficient of friction when a tyre interacts with the road is given as $\mu = \frac{F_x}{F_N}$. The coefficient of friction depends on many factors which influence the interaction between the surface and tyre. Many methods such as the Magic formula [9] etc., have been proposed to model the tyre road friction coefficient. In this work the LuGre model has been employed to model the interaction between tyre and road. The LuGre friction model dynamics is given as:

$$\begin{cases} v_r \;\; = v - rw_r \\ \dot{z} \;\; = v_r - \frac{\sigma_0|v_r|z}{h(v_r)}\xi(t) - \kappa r|w_r|z \\ g(v_r) = \mu_c + (\mu_s - \mu_c)\exp^{-|v_r/v_s|^{0.5}} \\ F_x \;\; = (\sigma_0 z + \sigma_1\dot{z} + \sigma_2 v_r)F_N \end{cases} \tag{3}$$

The dynamic LuGre friction model [10] is well suited to model the dynamic effects of friction. The LuGre model incorporates the effect of change in road conditions alongside representing the transient behavior during acceleration or

braking. In the LuGre friction model considered in [10], the distribution of the longitudinal force along the contact patch was considered to be constant. To improvise on that, in [11], a corrective term was introduced for the LuGre friction model. The same effect has also been included in the modeled LuGre dynamics.

3 Problem Formulation

A nonlinear model that integrates the torsional tyre model, LuGre dynamic friction model and the longitudinal dynamics of the vehicle are considered to estimate the road adhesion coefficient $\xi(t)$. The integrated dynamics (1)-(3) can be represented in the state space form as

$$\begin{cases} \dot{\mathbf{x}} = \mathbf{Ax} + \mathbf{B(x,u)} + \mathbf{Ef(t)} \\ \mathbf{Y} = \mathbf{Cx} \end{cases} \tag{4}$$

where

$$\mathbf{x} = \begin{bmatrix} x_1 \; x_2 \; x_3 \; x_4 \; x_5 \end{bmatrix}^{\mathrm{T}},$$

$$\mathbf{A} = \begin{bmatrix} a_{11} & 0 & a_{13} & 0 & -\sigma_0 g \\ 0 & -\frac{C_t}{J_w} & \frac{C_t}{J_w} & \frac{K_t}{J_w} & 0 \\ a_{31} & \frac{C_t}{J_r} & a_{33} & -\frac{K_t}{J_r} & \frac{rF_N\sigma_0}{J_r} \\ 0 & -1 & 1 & 0 & 0 \\ 1 & 0 & -r & 0 & 0 \end{bmatrix}, \; \mathbf{B(x,u)} = \begin{bmatrix} -\frac{f_1(\mathbf{x})-\sigma_1 F_N f_2(\mathbf{x})}{m} \\ -\frac{T_b}{J_w} \\ -\frac{rF_N\sigma_1}{J_r} f_2(\mathbf{x}) \\ 0 \\ -f_2(\mathbf{x}) \end{bmatrix} \; \mathbf{E} = \begin{bmatrix} \sigma_1\sigma_0 g \\ 0 \\ -\frac{rF_N\sigma_1\sigma_0}{J_r} \\ 0 \\ -\sigma_0 \end{bmatrix}$$

$a_{11} = -((\sigma_1 + \sigma_2)g + \sigma_v g)$, $a_{13} = (\sigma_1 + \sigma_2)gr$, $a_{31} = \frac{(\sigma_1+\sigma_2)rF_N}{J_r}$
$a_{33} = -\frac{C_t+(\sigma_1+\sigma_2)F_N r^2}{J_r}$, and

$$f_1(\mathbf{x}) = C_{av}{x_1}^2 \tag{5}$$

$$f_2(\mathbf{x}) = \kappa r|x_3|x_5 \tag{6}$$

$$f_3(\mathbf{x}) = \frac{|(x_1 - rx_3)|}{h(x_1, x_3)}\xi(t) \tag{7}$$

In the modeled system dynamics, the braking torque T_b is the control input for the system, denoted as $\mathbf{u}$ in (4). The unknown input for the system is $\mathbf{f}(\mathrm{t}) = f_3(\mathbf{x})$. Considering longitudinal velocity and angular velocity on the ring side as outputs, the output matrix can be given by

$$\mathbf{C} = \begin{bmatrix} 1\,0\,0\,0\,0 \\ 0\,0\,1\,0\,0 \end{bmatrix}$$

Now, the objective is to design an observer to estimate the states and unknown input ($f_3(\mathbf{x})$) in finite time.

4 HOSM Observer Design

Now, we consider the following class of system that is similar to (4) represented by

$$\begin{cases} \dot{\mathbf{x}} = \mathbf{A}\mathbf{x} + \mathbf{B}(\mathbf{x}, \mathbf{u}) + \mathbf{E}\mathbf{f}(t) \\ \mathbf{y} = \mathbf{C}\mathbf{x} \end{cases} \tag{8}$$

where, $\mathbf{A} \in \mathbb{R}^{n\times n}$, $\mathbf{C} \in \mathbb{R}^{p\times n}$, $\mathbf{x} \in M \subset \mathbb{R}^n$, $\mathbf{B} \in M \subset \mathbb{R}^n$ $\mathbf{f(t)} = [f_1(t).....f_m(t)]$ $\in \mathbb{R}^m$, with $m < p \leq n$, is the unknown function and $\mathbf{E} \in \mathbb{R}^{n\times m}$.
To facilitate the design of the observer, the following assumptions are required.
Assumption 1 :

- $rank(\mathbf{CE}) = rank(\mathbf{E})$.
- All invariant zeros of the triple **(A,E,C)** must lie in left half plane, such that for every complex number λ with non negative real part :

$$rank \begin{bmatrix} \lambda\mathbf{I} - \mathbf{A} & \mathbf{E} \\ \mathbf{C} & 0 \end{bmatrix} = n + rank(\mathbf{E})$$

Assumption 2 : The function $\mathbf{f}$(t) and its derivative are bounded.
Assumption 3 : The control input is bounded.
Assumption 4 : The nonlinear function satisfies the Lipschitz conditions.
From Assumption 1, without loss of generality, we can partition $\mathbf{E} = \begin{bmatrix} \mathbf{E}_1 \\ \mathbf{E}_2 \end{bmatrix}$ such that $\mathbf{E}_1 \in \mathbb{R}^{m\times m}$ with $rank(\mathbf{E}_1) = m$. With the Assumptions (1-4) satisfied, we introduce the following transformation:

$$\mathbf{T}_1 = \begin{bmatrix} \mathbf{I_m} & 0 \\ -\mathbf{E}_2\mathbf{E}_1^{-1} & \mathbf{I_{n-m}} \end{bmatrix} \tag{9}$$

Now we have, $\mathbf{CT}_1^{-1} = \begin{bmatrix} \mathbf{C}_1 & \mathbf{C}_2 \end{bmatrix}$, where $\mathbf{C}_1 = \begin{bmatrix} \mathbf{C}_{11} \\ \mathbf{C}_{12} \end{bmatrix}$ and $\mathbf{C}_2 = \begin{bmatrix} \mathbf{C}_{21} \\ \mathbf{C}_{22} \end{bmatrix}$ with rank($\mathbf{C}_{11}$) = m. Considering $\mathbf{T} = \mathbf{T}_1\mathbf{T}_2$ where $\mathbf{T}_2 = \begin{bmatrix} \mathbf{I_m} & \mathbf{C}_{11}^{-1}\mathbf{C}_{21} \\ 0 & \mathbf{I_{n-m}} \end{bmatrix}$, we have $\mathbf{TAT^{-1}} = \tilde{\mathbf{A}} = \begin{bmatrix} \mathbf{A}_{11} & \mathbf{A}_{12} \\ \mathbf{A}_{21} & \mathbf{A}_{22} \end{bmatrix}$, $\overline{\mathbf{x}} = \mathbf{Tx} = \begin{bmatrix} \overline{\mathbf{x}}_1 \\ \overline{\mathbf{x}}_2 \end{bmatrix}$, $\overline{\mathbf{y}} = \mathbf{Ty} = \begin{bmatrix} \overline{\mathbf{y}}_1 \\ \overline{\mathbf{y}}_2 \end{bmatrix}$, and $\mathbf{TB}(\mathbf{x}, \mathbf{u})$ $= \boldsymbol{\Gamma}(\mathbf{T^{-1}}\overline{\mathbf{x}}, \mathbf{u}) = \begin{bmatrix} \boldsymbol{\Gamma}_1(\mathbf{T^{-1}}\overline{\mathbf{x}}, \mathbf{u}) \\ \boldsymbol{\Gamma}_2(\mathbf{T^{-1}}\overline{\mathbf{x}}, \mathbf{u}) \end{bmatrix}$. For a system modeled in the form (8) and satisfying the above assumptions, we can design the observer of the following form:

$$\dot{\hat{\mathbf{x}}} = \mathbf{A}\hat{\mathbf{x}} + \mathbf{B}(\hat{\mathbf{x}}, \mathbf{u}) + \mathbf{L}(\mathbf{y} - \mathbf{C}\hat{\mathbf{x}}) + \mathbf{E}\mathbf{E}_1^{-1}\nu(t) \tag{10}$$

where $\mathbf{L}$ is the feedback gain matrix to be designed later and $\nu(t)$ is the robust term based on the generalized STA [12] defined as

$$\nu(\mathbf{t}) = -K_1\phi_1(\overline{\mathbf{e}}_1) - K_2\int_{\mathbf{0}}^{\mathbf{t}} \phi_2(\overline{\mathbf{e}}_1) - K_3\overline{\mathbf{e}}_1 \tag{11}$$

$$\phi_1 = |\overline{\mathbf{e}}_1|^{\frac{1}{2}} sign(\overline{\mathbf{e}}_1)$$

$$\phi_2 = sign(\overline{\mathbf{e}}_1)$$

where the error dynamics is defined as, $\mathbf{e} = \hat{\mathbf{x}} - \mathbf{x}$ and $\overline{\mathbf{e}} = \mathbf{Te} = \left[\overline{\mathbf{e}}_1\ \overline{\mathbf{e}}_2\right]^T$. The objective of the designed observer is to reconstruct the unknown input $\mathbf{f}(t)$ from the robust term (11) after the error dynamics converges to zero.
For ease of analysis, we transform the error dynamics, with the transformation (9) to the form:

$$\dot{\bar{\mathbf{e}}}_1 = (\tilde{\mathbf{A}}_{11} - \mathbf{H}_{11})\bar{\mathbf{e}}_1 + (\tilde{\mathbf{A}}_{12} - \mathbf{H}_{12})\bar{\mathbf{e}}_2 + \boldsymbol{\Gamma}_1(\hat{\mathbf{x}}, \mathbf{u}) - \boldsymbol{\Gamma}_1(\mathbf{x}, \mathbf{u}) - \mathbf{E}_1\mathbf{f}(t) + \nu(t) \tag{12}$$

$$\dot{\bar{\mathbf{e}}}_2 = (\tilde{\mathbf{A}}_{21} - \mathbf{H}_{21})\bar{\mathbf{e}}_1 + (\tilde{\mathbf{A}}_{22} - \mathbf{H}_{22})\bar{\mathbf{e}}_2 + \boldsymbol{\Gamma}_2(\hat{\mathbf{x}}, \mathbf{u}) - \boldsymbol{\Gamma}_2(\mathbf{x}, \mathbf{u}) \tag{13}$$

where $\mathbf{H}$ is the feedback gain matrix defined as

$$\mathbf{H} = \begin{bmatrix} \mathbf{H}_{11}\ \mathbf{H}_{12} \\ \mathbf{H}_{21}\ \mathbf{H}_{22} \end{bmatrix} = \mathbf{TLCT}^{-1}$$

The design of $\mathbf{H}$ will be discussed in the later part of the paper. The transformed error dynamics (12) can be written as

$$\dot{\bar{\mathbf{e}}}_1 = \nu(t) + \Omega(\bar{\mathbf{e}}, t) \tag{14}$$

where

$$\Omega(\bar{\mathbf{e}}, t) = (\tilde{\mathbf{A}}_{11} - \mathbf{H}_{11})\bar{\mathbf{e}}_1 + (\tilde{\mathbf{A}}_{12} - \mathbf{H}_{12})\bar{\mathbf{e}}_2 + \boldsymbol{\Gamma}_1(\hat{\mathbf{x}}, \mathbf{u}) - \boldsymbol{\Gamma}_1(\mathbf{x}, \mathbf{u}) - \mathbf{E}_1\mathbf{f}(t)$$

For the system error dynamics (14), $\Omega(\overline{\mathbf{e}}, t)$ can be viewed as the perturbation term that can be separated into two components as

$$\begin{cases} \Omega_1(\bar{\mathbf{e}}, t) = (\tilde{\mathbf{A}}_{11} - \mathbf{H}_{11})\bar{\mathbf{e}}_1 \\ \Omega_2(\bar{\mathbf{e}}, t) = (\tilde{\mathbf{A}}_{12} - \mathbf{H}_{12})\bar{\mathbf{e}}_2 + \boldsymbol{\Gamma}_1(\hat{\mathbf{x}}, \mathbf{u}) - \boldsymbol{\Gamma}_1(\mathbf{x}, \mathbf{u}) - \mathbf{E}_1\mathbf{f}(t) \end{cases} \tag{15}$$

The matrices $\tilde{\mathbf{A}}_{11}$, $\tilde{\mathbf{A}}_{12}$, $\mathbf{H}_{11}$, and $\mathbf{H}_{12}$ are known, and hence bounded. With the system satisfying the Assumptions 2 and 4, the nonlinear function $\boldsymbol{\Gamma}_1(\mathbf{x}, \mathbf{u})$ and the unknown input function $f_3(\mathbf{x})$ along with their derivatives are also bounded. From (13) it can be seen that for the reduced order dynamics to be stable, proper design of the feedback gain matrix $\mathbf{H}_{22}$ is necessary. With proper choice of the feedback gain matrix, and if the bounds of the nonlinear function $\boldsymbol{\Gamma}_2(\mathbf{x}, \mathbf{u})$ are defined, then the reduced order dynamics is stable. For the system satisfying Assumption 4, it can be concluded that the nonlinear function $\boldsymbol{\Gamma}_2(\mathbf{x}, \mathbf{u})$ has specified bounds. The approach by which the reduced order dynamics is determined to be stable is stated in the next section. Considering these arguments, the bounds of the perturbation terms can be defined as

$$\begin{cases} \Omega_1(\bar{\mathbf{e}}, t) \leq \zeta_1 \parallel \bar{\mathbf{e}}_1 \parallel \\ \dot{\Omega}_2(\bar{\mathbf{e}}, t) \leq \zeta_2 \end{cases} \tag{16}$$

where, ζ_1 and ζ_2 are the bounds to be calculated with respect to the system dynamics. It can be concluded from (16) that for the dynamical system whose transformed error dynamics are given as per (14) the perturbation terms consist of a bounded linear growing term, $\Omega_1(\overline{\mathbf{e}}, t)$.

Theorem 1. *For the system* (8) *satisfying the Assumptions* $1-4$*, the observer system* (10) *with the robust term* (11) *will ensure that error dynamics will converge to zero (*$\overline{\mathbf{e}}_1 = 0$ *) in finite time .*

Proof. To show the convergence of the error $\overline{e}_1$ when faced with the linear perturbation, the following Lyapunov candidate function is chosen

$$V(\overline{\mathbf{e}}_1) = \varsigma^T \mathbf{Q} \varsigma$$

where $\varsigma = \begin{bmatrix} \phi_1(\overline{\mathbf{e}}_1) \\ \overline{\mathbf{e}}_1 \\ \int_0^t \phi_2(\overline{\mathbf{e}}_1) \end{bmatrix}$ and $\mathbf{Q}$ is a positive definite matrix. The functions $\phi_1(\overline{\mathbf{e}}_1)$ and $\phi_2(\overline{\mathbf{e}}_1)$ are as defined in (15). It can be proved that by the proper design of the gains $K_1 > 0$, $K_2 > 0$ and $K_3 > 0$, $\dot{V}(\overline{\mathbf{e}})$ is negative definite and the error converges to zero. The proof is similar to the work in [12]. Thus the sliding surface can be reached in finite time and maintained thereafter. □

4.1 Design of the Gain H

For the obtained perturbation terms (16) to hold, it is necessary that the reduced order dynamics is stable. This relies on proper design of the gain $\mathbf{H}_{22}$. Using the method suggested in [13], the reduced order system is stable if the following Algebraic Riccati Equation (ARE) is satisfied:

$$\mathbf{P}_2(\tilde{\mathbf{A}}_{22} - \mathbf{H}_{22}) + (\tilde{\mathbf{A}}_{22} - \mathbf{H}_{22})^{\mathrm{T}}\mathbf{P}_2 + l_\Gamma^2 \mathbf{P}_2\mathbf{P}_2 + \mathbf{I} < 0 \tag{17}$$

where l_Γ is the Lipschitz constant for $\boldsymbol{\Gamma}_2(\mathbf{x}, \mathbf{u})$ and $\mathbf{P}_2$ is the positive definite matrix. If the above condition (17) is satisfied and if there exists a stable $(\tilde{\mathbf{A}}_{22} - \mathbf{H}_{22})$ matrix, then there exists a symmetric positive definite (SPD) solution $\mathbf{P}_2 = \mathbf{P}_2^T$ for Ricatti equation (17). Also, the following choice of gain

$$\mathbf{H}_{22} = \frac{1}{2l_\Gamma^2}\mathbf{P}_2^{-1}\mathbf{C}_2 \tag{18}$$

guarantees the stability of the system.

4.2 Unknown Input Reconstruction

From (12), with error converging to zero in finite time$(\dot{\bar{\mathbf{e}}}_1 = \bar{\mathbf{e}}_1 = 0)$ we have

$$v_{eq} = -\Omega(\bar{\mathbf{e}}, t) + \mathbf{E}_1\mathbf{f}(t)$$

where

$$\Omega(\bar{\mathbf{e}}, t) = (\tilde{\mathbf{A}}_{11} - \mathbf{H}_{11})\bar{\mathbf{e}}_1 + (\tilde{\mathbf{A}}_{12} - \mathbf{H}_{12})\bar{\mathbf{e}}_2 + \boldsymbol{\Gamma}_1(\hat{\mathbf{x}}, \mathbf{u}) - \boldsymbol{\Gamma}_1(\mathbf{x}, \mathbf{u})$$

Since the nonlinearities are Lipschitz bounded and (17) is satisfied we can have

$$\| \Omega(\bar{\mathbf{e}}, t) \| \leq (\| \tilde{\mathbf{A}}_{12} - \mathbf{H}_{12} \| + l_\Gamma) \| \bar{\mathbf{e}}(t) \| \to 0 (t \to \infty)$$

The equivalent output error injection signal can be obtained from the generalized STA as

$$v_{eq} = K_2 \int_0^t sign(\overline{\mathbf{e}}_1(t))dt$$

Hence, the unknown input when $t \to \infty$ can be estimated as :

$$\mathbf{f}(t) = \mathbf{E}_1^{-1} K_2 \int_0^t sign(\overline{\mathbf{e}}_1(t))dt$$

5 Sliding Mode Observer for the Vehicle system

For the dynamic vehicle system in (4), we have $rank(\mathbf{CE}) = rank(\mathbf{E})$=1. Therefore Assumption 1 is satisfied. The matrix $\mathbf{E}$ is thus partitioned as,

$$\mathbf{E} = \begin{bmatrix} \frac{\sigma_1 \sigma_0 g}{} \\ 0 \\ -\frac{rF_N \sigma_1 \sigma_0}{J_r} \\ 0 \\ -\sigma_0 \end{bmatrix} = \begin{bmatrix} \mathbf{E}_1 \\ \hline \\ \mathbf{E}_2 \end{bmatrix}.$$

The transformation matrix can be obtained as

$$\mathbf{T} = \begin{bmatrix} 1 & 0 & 0 & 0 & 0 \\ 0 & 1 & 0 & 0 & 0 \\ \frac{rm}{J_r} & 0 & 1 & 0 & 0 \\ 0 & 0 & 0 & 1 & 0 \\ \frac{1}{\sigma_1 g} & 0 & 0 & 0 & 1 \end{bmatrix}$$

where, $\mathbf{C}_{11} = 1$, $\mathbf{C_{22}} = \begin{bmatrix} 0 & 1 & 0 & 0 \end{bmatrix}$, $\boldsymbol{\Gamma}_1(\overline{\mathbf{x}}, \mathbf{u}) = \frac{f_2(\mathbf{x})}{g\sigma_1} + \frac{\sigma_1 r^2 F_N^2}{g J_r^2} f_2(\mathbf{x}) + \frac{[f_1(\mathbf{x}) - \sigma_1 F_N f_2(\mathbf{x})]}{m}$ and $\boldsymbol{\Gamma}_2(\overline{\mathbf{x}}, \mathbf{u}) = \begin{bmatrix} 0 \\ -\frac{rF_N\sigma_1}{J_r}\left[f_2(\hat{\mathbf{x}}) - f_2(\mathbf{x})\right] \\ 0 \\ -\left[f_2(\hat{\mathbf{x}}) - f_2(\mathbf{x})\right] \end{bmatrix}$.The transformed error dynamics of the system can thus be written as

$$\begin{bmatrix} \dot{\overline{\mathbf{e}}}_1 \\ \hline \\ \dot{\overline{\mathbf{e}}}_2 \end{bmatrix} = \begin{bmatrix} \dot{e}_1 \\ \hline \dot{e}_2 \\ \dot{e}_3 \\ \dot{e}_4 \\ \dot{e}_5 \end{bmatrix} = \left[\begin{array}{ccccc} e_{11} & 0 & a_{13} - l_{21} & 0 & -\sigma_0 g \\ \hline 0 & -\frac{C_t}{J_w} & \frac{C_t}{J_w} - l_{22} & \frac{K_t}{J_w} & 0 \\ 0 & \frac{C_t}{J_r} & e_{33} & -\frac{K_t}{J_r} & 0 \\ 0 & -1 & 1 - l_{24} & 0 & 0 \\ 0 & 0 & e_{35} & 0 & -\frac{\sigma_0}{\sigma_1} \end{array}\right] \begin{bmatrix} e_1 \\ \hline e_2 \\ e_3 \\ e_4 \\ e_5 \end{bmatrix} + \begin{bmatrix} f_{11} \\ \hline 0 \\ f_{31} \\ 0 \\ f_{51} \end{bmatrix} + \begin{bmatrix} \sigma_0 \sigma_1 g \\ \hline 0 \\ 0 \\ 0 \\ 0 \end{bmatrix} \left(\frac{\nu(t)}{\sigma_0 \sigma_1 g} - f_3(\mathbf{x})\right)$$

where where L is the feedback gain given as $\mathbf{L} = \begin{bmatrix} l_{11} & l_{12} & l_{13} & l_{14} & l_{15} \\ l_{21} & l_{22} & l_{23} & l_{24} & l_{25} \end{bmatrix}^T$ and $e_{11} = \frac{\sigma_0}{\sigma_1} - \frac{F_N r^2(\sigma_1 + \sigma_2)}{J_r} - l_{11} - g(\sigma_1 + \sigma_2 + \sigma_v) - \frac{mr}{J_r} l_{21}$, $e_{33} = -\frac{mr}{J_r} l_{21} - l_{23} - \frac{C_t}{J_r}$

, $e_{35} = \frac{r\sigma_2}{\sigma_1} - \frac{l_{21}}{g\sigma_1} - l_{25}$, $f_{11} = \frac{f_2(\mathbf{x})}{g\sigma_1} + \frac{\sigma_1 r^2 F_N^2}{gJ_r^2} f_2(\mathbf{x}) + \frac{[f_1(\mathbf{x}) - \sigma_1 F_N f_2(\mathbf{x})]}{m}$, $f_{31} = -\frac{rF_N\sigma_1}{J_r}[f_2(\hat{\mathbf{x}}) - f_2(\mathbf{x})]$ and $f_{51} = [f_2(\hat{\mathbf{x}}) - f_2(\mathbf{x})]$. From the transformed error dynamics (14), we can obtain for the above vehicular system

$$\Omega(\overline{\mathbf{e}}, t) = e_{11}\overline{\mathbf{e}}_{\mathbf{1}} + \begin{bmatrix} 0 & a_{13} - l_{12} & 0 & \sigma_0 g \end{bmatrix} \overline{\mathbf{e}}_{\mathbf{2}} + f_{11} \tag{19}$$

Finally, (19) can be expressed into the form of (16) and the bounded constants ζ_1 and ζ_2 can be obtained. The evaluated Lipschitz constants of the nonlinear functions $f_1(\mathbf{x})$, $f_2(\mathbf{x})$ and $f_3(\mathbf{x})$ are given as with $l_{\Gamma_1} = C_{av}|v|_{max}$, $l_{\Gamma_2} = \kappa r|\mathbf{y}|_{max}$ $l_{\Gamma_3} = [l_{\Gamma_z} + l_{\Gamma_\alpha}]$ respectively, where

$$\begin{cases} l_{\Gamma_z} = \frac{|v_r|_{max}}{\mu_c} \\ l_{\Gamma_\alpha} = \frac{|z|_{max}}{\mu_c}(1 + \frac{(\mu_s - \mu_c)|v_r|_{max}}{(\mu_c v_s)}) \end{cases}$$

For more details, see [1]. Thus assumptions 2 and 4 are also satisfied.

5.1 Reconstruction of the Road Adhesion Coefficient

Once the sliding mode is established, we can recover the unknown input as

$$v_{eq} = -\Omega(\bar{\mathbf{e}}, t) + g\sigma_0\sigma_1 f_3(\mathbf{x})$$

where, $\Omega(\mathbf{e}, t) = e_{11}\mathbf{e}_1 + \begin{bmatrix} 0 & a_{13} - l_{12} & 0 & -\sigma_0 g \end{bmatrix} \mathbf{e}_2 + f_{11}$. We have $\Omega(\mathbf{e}, t) \to 0$ as $t \to \infty$. The unknown input can be reconstructed from the sliding mode as,

$$\hat{f}_3(\hat{\mathbf{x}}) = \frac{K_2}{\sigma_0\sigma_1 g} \int_0^t \phi_2(\mathbf{e}_1, t)dt \tag{20}$$

As estimation states converge to the true states, the road adhesion coefficient can be approximated from $\hat{f}_3(\hat{\mathbf{x}})$

$$\hat{\xi}(t) \cong \frac{\hat{f}_3(\hat{\mathbf{x}})\mathrm{h}(\hat{x}_1, \hat{x}_3)}{\mid (\hat{x}_1 - r\hat{x}_3) \mid \hat{x}_5} \tag{21}$$

6 Simulation

The parameters for the quarter vehicle model are chosen according to [7,3] as follows:

m = 425 kg, r = $0.3m$, J_w =1Kgm^2, J_r = 0.093 Kgm^2, C_t= 2.5 Ns/m, K_t = $7616N/m$, $\sigma_v = 0.005$, $\sigma_0 = 100m^{-1}$, $\sigma_1 = 0.7$ s/m $\sigma_2 = 0.011$ s/m , $\mu_c = 0.35$, $\mu_s = 0.5$, $r = 0.315m$, and $\kappa = 5.833m^{-1}$. The sliding mode gains are selected as $K_1 = 0.5$, $K_2 = 2$ and $K_3 = 0.001$. The initial conditions for the plant and observer were chosen as $\mathbf{x}(0) = \begin{bmatrix} 30 & 10 & 10 & 0 & 0 \end{bmatrix}$ and $\hat{\mathbf{x}}(0) = \begin{bmatrix} 0 & 0 & 0 & 0 & 0 \end{bmatrix}$. For stability of the reduced order dynamics, the feedback gain matrix was selected as $\mathbf{L}$=$\begin{bmatrix} 1 & 2 & 1 & 2 & -3 \\ 1 & -0.0138 & 0.0054 & -0.7729 & 1.2502 \end{bmatrix}^T$. For the design of the gain matrix $\mathbf{H}_{22}$, the positive definite matrix that satisfies the ARE in (17) is obtained as

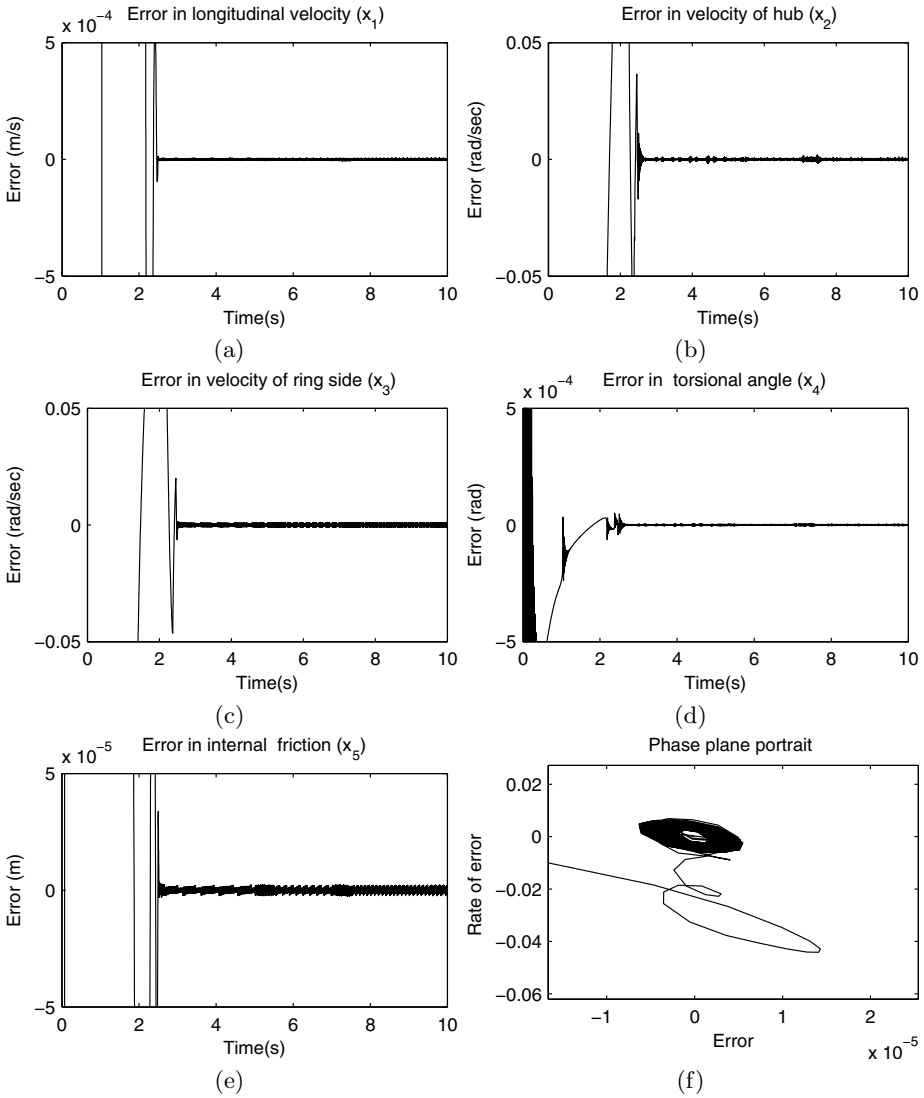

Fig. 1. (a) Estimation error for state x_1. (b) Estimation error for state x_2 (c)Estimation error for state x_3. (d) Estimation error for state x_4. (e) Estimation error for x_5. (f) The phase plane portrait for the error in state x_1.

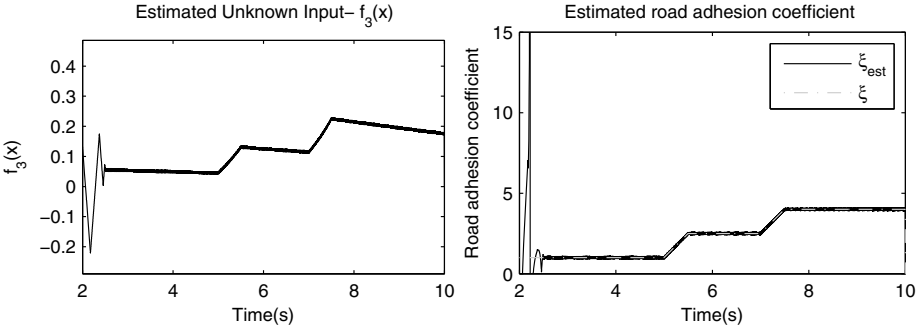

(a) (b)

Fig. 2. (a) Estimated unknown input $f_3(x)$. (b)Estimation of $\xi(t)$

$$\mathbf{P_2} = \begin{bmatrix} 650.2439 & 272.2172 & -9.4916 & 0.1294 \\ 272.2172 & 1443 & 1.5885 & -0.6296 \\ -9.4916 & 1.5885 & 0.1779 & -0.0017 \\ 0.1294 & -0.6296 & -0.0017 & 0.0031 \end{bmatrix}.$$

The simulation has been performed under low slip velocities. The different road conditions pertaining to various kinds of roads like snow, asphalt and wet have different values of ξ and μ. For simulation purpose the values of the ξ for different surfaces such as snow, wet and dry are chosen 4, 2.5 and 1 respectively [1]. The unknown input signal $f_3(\mathbf{x})$ and the road adhesion coefficient can be estimated from (20) and (21).

From the simulation results, Fig. 1 shows that the error in states converges to zero after some initial time taken by the observer. From the Fig. 2 it can be seen that the unknown input $f_3(\mathbf{x})$ has been estimated and ξ for different road conditions has been reconstructed.

7 Conclusion

In this work, a SMO based on STA was proposed to estimate the road adhesion coefficient for varying surface conditions of a quarter-vehicle. The torsional tyre model and the nonlinear LuGre model are integrated for modeling the quarter vehicle. The vehicle longitudinal velocity and ring velocity were considered as outputs for estimation. The employed observer estimates accurately the road adhesion coefficient in finite time after the error dynamics converge to zero. The accuracy of the designed observer is maintained with the changes in various surface conditions from asphalt to snow. The estimation of the road adhesion coefficient using the designed observer is achieved without use of any filtering procedure which is a necessity in case of first-order SMO.

Acknowledgements. This research was supported by the Basic Science Research Program through the National Research Foundation of Korea (NRF) funded by the Ministry of Education, Science and Technology (Grant No. 2011-0023999).

References

1. Canudas de Wit, C., Llnd, M.P., Shiralev, A.: A new nonlinear observer for tire/road distributed contact friction. In: Proceedings of the 42nd IEEE Conference on Decision and Control, pp. 2246–2251 (2003)
2. Alvarez, L., Yi, J., Horowitz, R., Olmos, L.: Dynamic Friction Model-Based Tire Road Friction Estimation and Emergency Braking Control. Journal of Dynamic Systems, Measurement and Control 127(1), 22–32 (2005)
3. Patel, N., Edwards, C., Spurgeon, S.: Comparative analysis of two non-linear observers for estimation of tyre/road contact in the presence of imperfect measurements. IET Control Theory & Applications 4(9), 1501–1510 (2010)
4. Magallan, G.: Maximization of the traction forces in a 2WD electric vehicle. IEEE Transactions on Vehicular Technology 60(2), 369–380 (2011)
5. Umeno, T., Ono, E., Asano, K., Ito, S.: Estimation of tire-road friction using tire vibration model. SAE technical Paper (2002)
6. Lee, D., Park, Y.: Sliding mode based parameter identification with application to tire pressure and tire-road friction. International Journal of Automotive Technology 12(4), 571–577 (2011)
7. Adcox, J., Ayalew, B., Tim Rhyne, S.C., Knauff, M.: Interaction of anti-lock braking systems with torsional tire dynamics. Tire and Science Technology 40(3), 171–185 (2012)
8. Wong, J.: Theory of Ground Vehicles. John Wiley & Sons (2008)
9. Pacejka, H., Sharp, R.: Shear force development by pneumatic tyres in steady state conditions: A reveiw of modelling aspects. Vehicle System Dynamics 20(3/4), 121–175 (1991)
10. Canudas de Wit, C., Tsiotras, P.: Dynamic tire friction models for vehicle traction control. In: Proceedings of the 38th IEEE Conference on Decision and Control, pp. 3746–3751 (1999)
11. Deur, J., Ivanovi, V., Pavkovi, D., Hrovat, D., Asgari, J., Troulis, M., Miano, C.: Experimental analysis and modelling of longitudinal tyre friction dynamics for abrupt transients. Vehicle System Dynamics 43(1), 525–539 (2005)
12. Moreno, J.A., Osorio, M.: A Lyapunov approach to second-order sliding mode controllers and observers. In: 47th IEEE Conference on Decision and Control, pp. 2856–2861 (2008)
13. Rajamani, R., Cho, Y.: Existence and design of observers for nonlinear systems: relation to distance to unobservability. International Journal of Control 69(5), 37–41 (1998)

Stability Domain Analysis for Input-Saturated Linear Systems Subject to Disturbance via Popov Criterion: An LMI Approach

S.T. Zhan[1], W.X. Yan[1], Z. Fu[1,2], and Yan-Zheng Zhao[1]

[1] Shanghai JiaoTong University, State Key Lab of Mechanical System and Vibration, Shanghai, 200240, P.R. China
[2] State Key Lab of Robotics and System (HIT), Harbin, 150001, P.R. China

Abstract. This paper addresses the problem of local stability analysis for linear systems subject to input saturation and persistent disturbance. The stability domain of a system under a saturated linear feedback and subject to persistent disturbance is determined by checking the invariance of a given ellipsoid via Popov criterion. The absolute stability with a finite domain is thus studied from the perspective of solving some inequalities under linear constraints. The estimation of stability domain under a known feedback controller is implemented via the use of Linear Matrix Inequalities (LMIs) and convex optimization.

Keywords: Popov criterion, input saturation, linear feedback, LMIs, convex optimization.

List of Notations and Symbols

$a \in A$	:	element a belongs to set A
$A \subset B$	:	set A is a proper subset of set B
$\mathbf{I}_n$	:	$n \times n$ identity matrix
$\mathbf{R}$, $\mathbf{R}^n$ and $\mathbf{R}^{m\times n}$	:	fields of real numbers, n-dimensional real vector and $m \times n$ real matrices
$\boldsymbol{x}^*$ and $\mathbf{X}^*$	:	optimal values of vector $\boldsymbol{x}$ and matrix $\mathbf{X}$
$\mathbf{X}^T$	:	transpose of matrix $\mathbf{X}$
$\mathbf{X}_i$	:	ith row of matrix $\mathbf{X}$
$\mathbf{X} > \mathbf{Y}$	:	matrix $\mathbf{X}$-$\mathbf{Y}$ is positive definite
□	:	end of proof

1 Introduction

In this paper, an approach is presented based on Popov criterion to address the problem of local stability analysis for linear systems subject to input saturation and

J. Lee et al. (Eds.): ICIRA 2013, Part II, LNAI 8103, pp. 214–225, 2013.

persistent disturbance. Such kind of linear systems are considered to be of the following representation:

$$\dot{\boldsymbol{x}}(t) = \mathbf{A}\boldsymbol{x}(t) + \mathbf{B}\boldsymbol{u}(t) + \mathbf{E}\boldsymbol{w}(t) \tag{1}$$

where $\boldsymbol{x}(t) \in \mathbf{R}^n$ is the state, $\boldsymbol{u}(t) \in \mathbf{R}^m$ is the control input, $\boldsymbol{w}(t) \in \mathbf{R}^q$ is the disturbance. $\mathbf{A}$, $\mathbf{B}$ and $\mathbf{E}$ are known real matrices of appropriate dimensions, with pair $(\mathbf{A}, \mathbf{B})$ controllable and $\mathbf{E}$ reflects the magnitude of disturbance. The vector $\boldsymbol{w}(t)$ is assumed to take values in the compact set $\mathfrak{V} = \{\boldsymbol{w} \subset \mathbf{R}^q; \boldsymbol{w}^T \boldsymbol{w} \le 1\}$. The vector $\boldsymbol{u}(t)$ is assumed to take values in the compact set $\Omega = \{\boldsymbol{u} \subset \mathbf{R}^m; -\boldsymbol{u}_0 \le \boldsymbol{u} \le \boldsymbol{u}_0\}$, with $\boldsymbol{u}_0$ component-wise positive vector of $\mathbf{R}^m$. The closed-loop local stability of system (1) under a given linear state feedback $\boldsymbol{u}(t) = -\mathbf{F}\boldsymbol{x}(t)$ when $\boldsymbol{w}(t) = 0$ has been explored in a lot of work [1]-[8]. Approaches of estimating the stability domain proposed in these work utilize the absolute stability analysis methods, e.g., the circle and Popov criteria in [3, 9], the quadratic Lyapunov function in [8]-[11]. The conditions for local stability and some other performance problems are expressed in terms of solvable linear matrix inequalities (LMIs).

However, in the presence of disturbance input $\boldsymbol{w}(t)$, which is introduced into system as in representation (1), the analysis of local stability becomes more complicated. Solutions to such kind of problems are provided in [2] and [10] for the cases that disturbances are of finite energy. This paper, however, from another perspective considers the case that the disturbance is magnitude-bounded and intends to propose for such cases a linear algorithm of estimating the stability domain via Popov criterion.

Although the conservatism in estimating the stability domain when applied to the saturation nonlinearity, the Popov criteria still occupies an important role in addressing general memoryless sector bounded nonlinearities due to its significant advantages in other aspects, e.g. the computation efficiency, the freedom of selecting Lyapunov functions, etc. The stability domain determined via Popov criterion, as was proved in [9], is larger than that determined via circle criterion. However, the synthesis of the stability domain via Popov criterion, which is still an open direction of research, cannot be realized by using the same LMIs algorithm designed for the realization via circle criterion.

The difficulty of synthesizing the stability domain via Popov criterion under given feedback controllers lies in that the derived constraints for stability domain determination are nonlinear inequalities, and the resulted domain is the union of three subsets. There exist two non convex sets in such a situation, which makes the estimation of via convex optimization impossible. To address this problem, this paper presents a solution which guarantees that all the constraints in a convex optimization problem are possible to be transformed to solvable LMIs.

This paper is organized as follows. Section 2 presents the background knowledge and states the problem to be addressed in detail. Section 3 presents the analysis of closed-loop stability of the input-saturated system, and addresses the issues related to the estimation of stability domain by an illustrative example. A brief concluding remark is given in Section 4.

2 Backgrounds

The saturation function $sat(\mathbf{F}\boldsymbol{x}(t))$ for system (1) is defined as:

$$sat(\mathbf{F}\boldsymbol{x}(t)) = [sat(\mathbf{F}\boldsymbol{x}(t))_1, sat(\mathbf{F}\boldsymbol{x}(t))_2, \cdots sat(\mathbf{F}\boldsymbol{x}(t))_m]^T$$

with for i=1,…,m:

$$sat(\mathbf{F}\boldsymbol{x}(t))_i = \begin{cases} -\boldsymbol{u}_{0i} & \text{if} \quad \mathbf{F}_i x < -\boldsymbol{u}_{0i} \\ \mathbf{F}_i x & \text{if} \quad -\boldsymbol{u}_{0i} \le \mathbf{F}_i x \le \boldsymbol{u}_{0i} \\ \boldsymbol{u}_{0i} & \text{if} \quad \mathbf{F}_i x > \boldsymbol{u}_{0i} \end{cases}$$

where the superscript i corresponds to the i-th row of a vector or the i-th row of a matrix. By implementing such a saturated state feedback control law $\boldsymbol{u}(t) = -sat(\mathbf{F}\boldsymbol{x}(t))$, the closed-loop system is

$$\dot{\boldsymbol{x}}(t) = \mathbf{A}\boldsymbol{x}(t) - \mathbf{B}sat(\mathbf{F}\boldsymbol{x}(t)) + \mathbf{E}\boldsymbol{w} \tag{2}$$

When the control inputs do not saturate, that is, for all $\boldsymbol{x}(t) \in L(\mathbf{F}, \boldsymbol{u}_0)$ defined as

$$L(\mathbf{F}, \boldsymbol{u}_0) = \{\boldsymbol{x} \in \mathbf{R}^n; -\boldsymbol{u}_0 \le \mathbf{F}\boldsymbol{x} \le \boldsymbol{u}_0\}$$

system (2) admits the linear model:

$$\dot{\boldsymbol{x}}(t) = (\mathbf{A} - \mathbf{BF})\boldsymbol{x}(t) + \mathbf{E}\boldsymbol{w}$$

Here the notation $L(\mathbf{F}, \boldsymbol{u}_0)$ denotes the region in the state space where the control is linear in $\boldsymbol{x}$.

2.1 Sector Condition

An equivalent form of the saturated system (2) is

$$\dot{\boldsymbol{x}}(t) = (\mathbf{A} - \mathbf{BK}_1\mathbf{F})\boldsymbol{x}(t) - \mathbf{B}\varphi(t, \mathbf{F}\boldsymbol{x}) + \mathbf{E}\boldsymbol{w} \tag{3}$$

where $\mathbf{K}_1 \in \mathbf{R}^{m \times m}$ is a diagonal positive matrix such that $\mathbf{A} - \mathbf{BK}_1\mathbf{F}$ is Hurwitz stable, $\varphi(t, \mathbf{F}\boldsymbol{x})$ is a decentralized nonlinear function described as

$$\varphi(t, \mathbf{F}\boldsymbol{x}) = sat(\mathbf{F}\boldsymbol{x}(t)) - \mathbf{K}_1\mathbf{F}\boldsymbol{x}(t)$$

Define the domain $L(\mathbf{F}, \boldsymbol{u}_0 / \mathbf{K}_1)$ as:

$$L(\mathbf{F}, \boldsymbol{u}_0 / \mathbf{K}_1) = \{\boldsymbol{x} \in \mathbf{R}^n; -\frac{\boldsymbol{u}_{0i}}{(k_1)_i} \le \mathbf{F}_i\boldsymbol{x} \le \frac{\boldsymbol{u}_{0i}}{(k_1)_i}, \\ i = 1, ..., m\}$$

where $(k_1)_i$ denotes the ith diagonal element of matrix $\mathbf{K}_1$. Note that $\varphi(t,\mathbf{F}\boldsymbol{x})$ satisfies the sector condition defined in [9], thus for $\forall t \geq 0$ and $\forall \boldsymbol{x} \in L(\mathbf{F},\boldsymbol{u}_0 / \mathbf{K}_1)$, there must exist another diagonal positive matrix $\mathbf{K}_2 (\geq \mathbf{K}_1 \in \mathbf{R}^{m\times m})$, such that

$$[sat(\mathbf{F}\boldsymbol{x}(t)) - \mathbf{K}_1\mathbf{F}\boldsymbol{x}(t)]^T [sat(\mathbf{F}\boldsymbol{x}(t)) - \mathbf{K}_2\mathbf{F}\boldsymbol{x}(t)] \leq 0$$

which equals to

$$\varphi(t,\mathbf{F}\boldsymbol{x})^T (\varphi(t,\mathbf{F}\boldsymbol{x}) - (\mathbf{K}_2 - \mathbf{K}_1)\mathbf{F}\boldsymbol{x}(t)) \leq 0 \tag{4}$$

Inequality (4) is said to be the sector condition for nonlinearity $sat(\mathbf{F}\boldsymbol{x}(t))$, and $sat(\mathbf{F}\boldsymbol{x}(t))$ is said to belong to the sector $[\mathbf{K}_1, \mathbf{K}_2]$.

2.2 Problem Statement

Since system (1) is not necessary to be stable before feedback stabilization, no open-loop stability properties are assumed in this paper for representation (1). As a result, the local stability of the closed-loop saturated system (2) must be investigated. Local stability is in the sense that there exists a bounded set M_0 in R^n such that for $\forall \boldsymbol{x}_0 = \boldsymbol{x}(t=0) \in M_0$, the resulting trajectories under $\boldsymbol{w} \in \mathfrak{V}$, denoted by $\boldsymbol{x}(t,\boldsymbol{x}_0,\boldsymbol{w})$, would asymptotically converge into a bounded invariant set M_1 determined by disturbance $\boldsymbol{w}$ (note that set M_1 is the origin if $\mathbf{E}\boldsymbol{w}(t) = 0$ holds for $\forall t > 0$).

Definition 1. *Let $\mathbf{P} \in \mathbf{R}^{n\times n}$ be a symmetric positive definite matrix, $\rho,\eta \in \mathbf{R}$ be non-negative real scalars and the convex set $D(S(\boldsymbol{x}),\rho)$ be given as*

$$D(S(\boldsymbol{x}),\rho) = \{\boldsymbol{x} \in \mathbf{R}^n : S(\boldsymbol{x}) \leq \rho\}$$

then the convex set $D(S(\boldsymbol{x}),\rho)$ is said to be (strictly) invariant if for all $\boldsymbol{x} \in \partial D(S(\boldsymbol{x}),\rho)$ and $\boldsymbol{w} \in \mathfrak{V}$, the time-derivative of the Lure- type Lyapunov function

$$V(\boldsymbol{x}(t)) = \boldsymbol{x}^T(t)\mathbf{P}\boldsymbol{x}(t) + 2\eta\int_0^{\mathbf{F}\boldsymbol{x}(t)} \varphi(\tau(t))\mathbf{K}d\tau$$

along the trajectories of system (2) is non-positive (negative), that is $\dot{V}(\boldsymbol{x}) \leq 0 (< 0)$. Here $\partial D(S(\boldsymbol{x}),\rho)$ denotes the boundary of the convex set $D(S(\boldsymbol{x}),\rho)$.

Definition 1 makes it possible to estimate the invariant set M_1 by a convex set of appropriate volume. Let the invariant convex set D_0 be an estimation of set M_1, with $D_0 \subset M_1$, then, as representation (1) is concerned, the problem related to the estimation of stability domain can be stated as: estimating invariant set D_0, such that

$$\begin{aligned} &\text{maximize} && D_0 \\ &\text{subject to} && D_0 \subset M_1 \end{aligned} \tag{5}$$

3 Stability Analysis

The local stability properties of system (2) under a given feedback controller $\mathbf{F}$ must be analyzed in order to address requirement (5). For this consideration, a set invariance condition, which can be used to determine whether a convex set is invariant in the state space, is proposed and thereafter proved in section 3.1 (see Theorem 1 and Corollary 1).

3.1 A Condition for Set Invariance

Based on the sector condition, the Popov criterion and the results proposed in [2], the following Theorem can be stated:

Theorem 1. *Assume that there exists a triplet* $(\mathbf{F},\mathbf{K}_1,\mathbf{K}_2)$ *with* $\mathbf{K}_1 < \mathbf{I}_m$, $\mathbf{K}_2 \geq \mathbf{I}_m$ *such that matrix* $\mathbf{A}-\mathbf{B}\mathbf{K}_1\mathbf{F}$ *is Hurwitz stable, pair* $(\mathbf{F},\mathbf{A})$ *is observable, and* $sat(\mathbf{F}\boldsymbol{x}(t))$ *satisfies the sector condition in sector* $[\mathbf{K}_1,\mathbf{K}_2]$. *Given a symmetric positive matrix* $\mathbf{P}$ *and a positive scalar* η, *such that* $-1/\eta$ *is not an eigenvalue of matrix* $\mathbf{A}$, *if there exist matrices* $\mathbf{L}\in\mathbf{R}^{q\times n}$ *and* $\mathbf{Z}\in\mathbf{R}^{q\times m}$, *positive scalars* μ *and* ρ, *and*

$$\begin{aligned} &(\mathbf{A}-\mathbf{B}\mathbf{K}_1\mathbf{F})^T\mathbf{P}+\mathbf{P}(\mathbf{A}-\mathbf{B}\mathbf{K}_1\mathbf{F})+\mathbf{L}^T\mathbf{L} \\ &+\frac{1}{\mu}\mathbf{P}\mathbf{E}\mathbf{E}^T\mathbf{P}+\frac{\mu}{\rho}\left(\mathbf{P}+\eta(\mathbf{I}_n-\mathbf{K}_1)(\mathbf{K}_1\mathbf{F})^T(\mathbf{K}_1\mathbf{F})\right)<0 \end{aligned} \tag{6}$$

$$\mathbf{P}\mathbf{B}=\mathbf{F}^T\mathbf{K}+\eta(\mathbf{A}-\mathbf{B}\mathbf{K}_1\mathbf{F})^T\mathbf{F}^T\mathbf{K}-\mathbf{L}^T\mathbf{Z} \tag{7}$$

$$2\mathbf{I}_m+\eta\mathbf{K}\mathbf{F}\mathbf{B}+\eta\mathbf{B}^T\mathbf{F}^T\mathbf{K}^T+\frac{\eta}{\mu}\mathbf{K}\mathbf{F}\mathbf{E}\mathbf{E}^T\mathbf{F}^T\mathbf{K}^T=\mathbf{Z}^T\mathbf{Z} \tag{8}$$

then the domain $D\left(S,(1+\eta)\rho\right)$ *is a strictly invariant set for system (2), with*

$$D\left(S,(1+\eta)\rho\right)=\{\boldsymbol{x}\in\mathbf{R}^n : S(\boldsymbol{x})=(1+\eta)\rho,\quad \rho>0\} \tag{9}$$

$$D\left(S,(1+\eta)\rho\right)\subset L(\mathbf{F},\boldsymbol{u}_0/\mathbf{K}_1) \tag{10}$$

$$S(\boldsymbol{x}(t))=\boldsymbol{x}^T(t)\mathbf{P}\boldsymbol{x}(t)+2\eta\int_0^{\mathbf{K}_1\mathbf{F}\boldsymbol{x}(t)}\varphi^T(t,\tau(t))\mathbf{K}d\tau \tag{11}$$

here, $\mathbf{K}=\mathbf{K}_2-\mathbf{K}_1$ *and* $\varphi(t,\tau(t))=sat(\tau(t))-\mathbf{K}_1\tau(t)$.

Proof. Consider the Lyr'e-type Lyapunov function

$$V(\boldsymbol{x}(t)) = \boldsymbol{x}^T(t)\mathbf{P}\boldsymbol{x}(t) + 2\eta\int_0^{\mathbf{F}\boldsymbol{x}(t)} \varphi(\tau(t))\mathbf{K}d\tau$$

Its time-derivative along the trajectories of system (2) is given by:

$$\begin{aligned}\dot{V}(\boldsymbol{x}) = \boldsymbol{x}^T\left((\mathbf{A}-\mathbf{B}\mathbf{K}_1\mathbf{F})^T\mathbf{P} + \mathbf{P}(\mathbf{A}-\mathbf{B}\mathbf{K}_1\mathbf{F})\right)\boldsymbol{x}\\ -2\boldsymbol{x}^T\mathbf{P}\mathbf{B}\varphi(t,\mathbf{F}\boldsymbol{x}) + 2\boldsymbol{x}^T\mathbf{P}\mathbf{E}\boldsymbol{w}\\ +2\eta\varphi^T(t,\mathbf{F}\boldsymbol{x})\mathbf{K}\mathbf{F}\left((\mathbf{A}-\mathbf{B}\mathbf{K}_1\mathbf{F})\boldsymbol{x} - \mathbf{B}\varphi(t,\mathbf{F}\boldsymbol{x}) + \mathbf{E}\boldsymbol{w}\right)\end{aligned}$$

The relationship (9) leads to the satisfaction of sector condition (5), thus there is

$$\begin{aligned}\dot{V}(\boldsymbol{x}) < \boldsymbol{x}^T\left((\mathbf{A}-\mathbf{B}\mathbf{K}_1\mathbf{F})^T\mathbf{P} + \mathbf{P}(\mathbf{A}-\mathbf{B}\mathbf{K}_1\mathbf{F})\right)\boldsymbol{x}\\ -2\boldsymbol{x}^T\mathbf{P}\mathbf{B}\varphi(t,\mathbf{F}\boldsymbol{x}) + 2\boldsymbol{x}^T\mathbf{P}\mathbf{E}\boldsymbol{w}\\ +2\eta\varphi^T(t,\mathbf{F}\boldsymbol{x})\mathbf{K}\mathbf{F}\left((\mathbf{A}-\mathbf{B}\mathbf{K}_1\mathbf{F})\boldsymbol{x} - \mathbf{B}\varphi(t,\mathbf{F}\boldsymbol{x}) + \mathbf{E}\boldsymbol{w}\right)\\ -2\varphi(t,\mathbf{F}\boldsymbol{x})^T\left(\varphi(t,\mathbf{F}\boldsymbol{x}) - \mathbf{K}\mathbf{F}\boldsymbol{x}(t)\right)\end{aligned}$$

Since it is assumed $\boldsymbol{w} \in \mathfrak{V}$, there is

$$\begin{aligned}2\boldsymbol{x}^T\mathbf{P}\mathbf{E}\boldsymbol{w} &\le \frac{1}{\mu}\boldsymbol{x}\mathbf{P}\mathbf{E}\mathbf{E}^T\mathbf{P}\boldsymbol{x} + \mu\boldsymbol{w}^T\boldsymbol{w}\\ &\le \frac{1}{\mu}\boldsymbol{x}\mathbf{P}\mathbf{E}\mathbf{E}^T\mathbf{P}\boldsymbol{x} + \mu\\ 2\varphi^T(t,\mathbf{F}\boldsymbol{x})\mathbf{K}\mathbf{F}\mathbf{E}\boldsymbol{w}&\\ &\le \frac{1}{\mu}\varphi^T(t,\mathbf{F}\boldsymbol{x})\left(\mathbf{K}\mathbf{F}\mathbf{E}\right)^T\mathbf{K}\mathbf{F}\mathbf{E}\varphi^T(t,\mathbf{F}\boldsymbol{x}) + \mu\boldsymbol{w}^T\boldsymbol{w}\\ &\le \frac{1}{\mu}\varphi^T(t,\mathbf{F}\boldsymbol{x})\left(\mathbf{K}\mathbf{F}\mathbf{E}\right)^T\mathbf{K}\mathbf{F}\mathbf{E}\varphi^T(t,\mathbf{F}\boldsymbol{x}) + \mu\end{aligned}$$

If conditions (6) to (8) are satisfied simultaneously, it follows

$$\begin{aligned}&\boldsymbol{x}^T\left((\mathbf{A}-\mathbf{B}\mathbf{K}_1\mathbf{F})^T\mathbf{P} + \mathbf{P}(\mathbf{A}-\mathbf{B}\mathbf{K}_1\mathbf{F})\right)\boldsymbol{x}\\ &\quad -2\varphi(t,\mathbf{F}\boldsymbol{x})^T(\varphi(t,\mathbf{F}\boldsymbol{x}) - \mathbf{K}\mathbf{F}\boldsymbol{x}(t))\\ &\quad -2\boldsymbol{x}^T\mathbf{P}\mathbf{B}\varphi(t,\mathbf{F}\boldsymbol{x})\\ &\quad +2\eta\varphi^T(t,\mathbf{F}\boldsymbol{x})\mathbf{K}\mathbf{F}\left((\mathbf{A}-\mathbf{B}\mathbf{K}_1\mathbf{F})\boldsymbol{x} - \mathbf{B}\varphi(t,\mathbf{F}\boldsymbol{x}) + \mathbf{E}\boldsymbol{w}\right)\\ &< -\boldsymbol{x}^T\left(\frac{1}{\mu}\mathbf{P}\mathbf{E}\mathbf{E}^T\mathbf{P} + \frac{\mu}{\rho}\left(\mathbf{P} + \eta(\mathbf{K}_1\mathbf{F})^T(\mathbf{I}_m - \mathbf{K}_1)(\mathbf{K}_1\mathbf{F})\right)\right)\boldsymbol{x}\\ &\quad -(\mathbf{L}\boldsymbol{x} - \mathbf{Z}\varphi)^T(\mathbf{L}\boldsymbol{x} - \mathbf{Z}\varphi)\\ &\le -\boldsymbol{x}^T\left(\frac{1}{\mu}\mathbf{P}\mathbf{E}\mathbf{E}^T\mathbf{P} + \frac{\mu}{\rho}\left(\mathbf{P} + \eta(\mathbf{K}_1\mathbf{F})^T(\mathbf{I}_m - \mathbf{K}_1)(\mathbf{K}_1\mathbf{F})\right)\right)\boldsymbol{x}\end{aligned}$$

Hence

$$\dot{V}(\boldsymbol{x}) < -\mu \boldsymbol{x}^T \left(\mathbf{P} + \eta (\mathbf{K}_1 \mathbf{F})^T (\mathbf{I}_m - \mathbf{K}_1)(\mathbf{K}_1 \mathbf{F}) \right) \boldsymbol{x} \,/\, \rho + (\eta + 1)\mu$$

Moreover, from constraint (10), equation (11) can be simplified to

$$\begin{aligned} S(\boldsymbol{x}(t)) &= \boldsymbol{x}^T(t) \mathbf{P} \boldsymbol{x}(t) + 2\eta \int_0^{\mathbf{K}_1 \mathbf{F} \boldsymbol{x}} \frac{1}{2} (\mathbf{I}_m - \mathbf{K}_1) \tau^T \mathbf{K} d\tau \\ &= \boldsymbol{x}^T(t) \left(\mathbf{P} + \eta (\mathbf{K}_1 \mathbf{F})^T (\mathbf{I}_m - \mathbf{K}_1) \mathbf{K}_1 \mathbf{F} \right) \boldsymbol{x}(t) \end{aligned}$$

Since for all $\boldsymbol{x} \in \partial D\left(S, (1+\eta)\rho\right)$, there is $S(\boldsymbol{x}) = (1+\eta)\rho$, it must follow that $\dot{V}(\boldsymbol{x}) < 0$. Therefore, the domain $D\left(S, (1+\eta)\rho\right)$ is a strictly invariant set for system (2). □

Assuming that $\mathbf{Z}^T \mathbf{Z}$ is positive definite, then conditions (6) to (8) can be combined into one inequality and the following corollary can be stated.

Corollary 1. *Assume that there exists a triplet* $(\mathbf{F}, \mathbf{K}_1, \mathbf{K}_2)$ *with* $\mathbf{K}_1 < \mathbf{I}_m$, $\mathbf{K}_2 \geq \mathbf{I}_m$ *such that matrix* $\mathbf{A} - \mathbf{B}\mathbf{K}_1\mathbf{F}$ *is Hurwitz stable, pair* $(\mathbf{F}, \mathbf{A})$ *is observable, and sat*$(\mathbf{F}\boldsymbol{x}(t))$ *satisfies the sector condition in sector* $[\mathbf{K}_1, \mathbf{K}_2]$. *Given a symmetric positive matrix* $\mathbf{P}$ *and a positive scalar* η, *such that* $-1/\eta$ *is not an eigen value of matrix* $\mathbf{A}$, *if there exist a matrix* $\mathbf{Z} \in \mathbf{R}^{q \times m}$, *positive scalars* μ *and* ρ, *and*

$$\begin{aligned} &\left(\mathbf{A} - \mathbf{B}\mathbf{K}_1\mathbf{F} - \mathbf{B}(\mathbf{Z}^T\mathbf{Z})^{-1}\mathbf{K}^T\mathbf{F}\left(\mathbf{I}_n + \eta(\mathbf{A} - \mathbf{B}\mathbf{K}_1\mathbf{F})\right) \right)^T \mathbf{P} \\ &+ \mathbf{P}\left(\mathbf{A} - \mathbf{B}\mathbf{K}_1\mathbf{F} - \mathbf{B}(\mathbf{Z}^T\mathbf{Z})^{-1}\mathbf{K}^T\mathbf{F}\left(\mathbf{I}_n + \eta(\mathbf{A} - \mathbf{B}\mathbf{K}_1\mathbf{F})\right) \right) \\ &+ \left(\mathbf{I}_n + \eta(\mathbf{A} - \mathbf{B}\mathbf{K}_1\mathbf{F})^T \right) \mathbf{F}^T \mathbf{K} (\mathbf{Z}^T\mathbf{Z})^{-1} \mathbf{K}^T \mathbf{F} \left(\mathbf{I}_n + \eta(\mathbf{A} - \mathbf{B}\mathbf{K}_1\mathbf{F}) \right) \\ &+ \frac{1}{\mu} \mathbf{P}\mathbf{E}\mathbf{E}^T\mathbf{P} + \frac{\mu}{\rho} \left(\mathbf{P} + \eta \mathbf{F}^T \mathbf{K}_1^T (\mathbf{I}_n - \mathbf{K}_1) \mathbf{K}_1 \mathbf{F} \right) < 0 \end{aligned} \tag{12}$$

$$2\mathbf{I}_m + \eta \mathbf{K}\mathbf{F}\mathbf{B} + \eta \mathbf{B}^T \mathbf{F}^T \mathbf{K}^T + \frac{\eta}{\mu} \mathbf{K}\mathbf{F}\mathbf{E}\mathbf{E}^T \mathbf{F}^T \mathbf{K}^T = \mathbf{Z}^T\mathbf{Z} > \mathbf{0} \tag{13}$$

then the domain $D\left(S, (1+\eta)\rho\right)$ *with definitions (9) to (11) is a strictly invariant set for system (2).*

Corollary 1 can be used to deal with problem (5). The largest invariant set in the stability domain can be estimated by solving the equivalent optimization problem (14) [13], where α is a positive scalar, $X_J \subset \mathbf{R}^n$ is a prescribed convex set.

$$\begin{aligned} &\underset{\mathbf{P}>0, \rho, \eta, \mu > 0}{\text{maximize}} \quad \alpha \\ &\text{subject to} \quad a) \quad \alpha X_J \subset D\left(S, (1+\eta)\rho\right) \\ &\qquad\qquad\quad b) \quad D\left(S, (1+\eta)\rho\right) \subset L(\mathbf{F}, \boldsymbol{u}_0 / \mathbf{K}_1) \\ &\qquad\qquad\quad c) \quad \text{inequality (12)} \end{aligned} \tag{14}$$

Let $\mathbf{G}=\mathbf{K}^T\mathbf{F}\left(\mathbf{I}_n+\eta(\mathbf{A}-\mathbf{B}\mathbf{K}_1\mathbf{F})\right)$, $\tilde{\mathbf{A}}=\mathbf{A}-\mathbf{B}\mathbf{K}_1\mathbf{F}-\mathbf{B}(\mathbf{Z}^T\mathbf{Z})^{-1}\mathbf{G}$, $\mathbf{U}=(\sqrt{\mu\eta}/\rho)$ $\sqrt{(\mathbf{I}_m-\mathbf{K}_1)}\mathbf{K}_1\mathbf{F}$ and $\mathbf{Q}=\left(\mathbf{P}/\rho\right)^{-1}$ (the notation $\sqrt{(\mathbf{I}_m-\mathbf{K}_1)}$ corresponds to the diagonal matrix derived from taking the square root of each diagonal element of diagonal matrix $\mathbf{I}_m-\mathbf{K}_1$), then inequality (12) can be written as

$$\begin{aligned}&\mathbf{Q}^T\tilde{\mathbf{A}}^T+\tilde{\mathbf{A}}\mathbf{Q}+\frac{\rho}{\mu}\mathbf{E}\mathbf{E}^T+\frac{\mu}{\rho}\mathbf{Q}+\frac{\mu\eta}{\rho^2}\mathbf{Q}^T\mathbf{U}^T\mathbf{U}\mathbf{Q}\\&+\frac{1}{\rho}\mathbf{Q}^T\mathbf{G}^T(\mathbf{Z}^T\mathbf{Z})^{-1}\mathbf{G}\mathbf{Q}<0\end{aligned}\tag{15}$$

The LMIs realization of inequality (15) is given as

$$\begin{bmatrix}\mathbf{W}&(\mathbf{U}\mathbf{Q})^T&(\mathbf{G}\mathbf{Q})^T\\\mathbf{U}\mathbf{Q}&\mathbf{I}_m&0\\\mathbf{G}\mathbf{Q}&0&\rho\mathbf{Z}^T\mathbf{Z}\end{bmatrix}>0\tag{16}$$

where

$$\mathbf{W}=-(\tilde{\mathbf{A}}\mathbf{Q})^T-\tilde{\mathbf{A}}\mathbf{Q}-\frac{\mu}{\rho}\mathbf{Q}-\frac{\rho}{\mu}\mathbf{E}\mathbf{E}^T$$

From Schur complement, if X_J is an ellipsoid $\delta(\mathbf{J},1)$ defined by

$$\delta\left(\mathbf{J},1\right)=\{\boldsymbol{x}\in\mathbf{R}^n:\boldsymbol{x}^T\mathbf{J}\boldsymbol{x}\le 1,\mathbf{J}=\mathbf{J}^T\in\mathbf{R}^{n\times n}>0\},$$

then constraints (14a) would be equivalent to the following inequality,

$$\mathbf{P}/\rho+(\eta/\rho)(\mathbf{K}_1\mathbf{F})^T(\mathbf{I}_m-\mathbf{K}_1)\mathbf{K}_1\mathbf{F}-(1+\eta)\mathbf{J}/\alpha^2<0$$

which is equivalent to

$$\begin{bmatrix}(1+\eta)\dfrac{\mathbf{J}}{\alpha^2}-\dfrac{\rho}{\mu}\mathbf{U}^T\mathbf{U}&\mathbf{I}_n\\\mathbf{I}_n&\mathbf{Q}\end{bmatrix}>0\tag{17}$$

If X_J is a convex polyhedron defined by its vertices $X_J=\{\boldsymbol{x}_1,\boldsymbol{x}_1,...,\boldsymbol{x}_l\}$, then constraints (14a) would be equivalent to the following inequality, for all $i\in[1,l]$.

$$\boldsymbol{x}_i^T\left(\mathbf{P}/\rho+(\eta/\rho)(\mathbf{K}_1\mathbf{F})^T(\mathbf{I}_m-\mathbf{K}_1)\mathbf{K}_1\mathbf{F}\right)\boldsymbol{x}_i-(1+\eta)1/\alpha^2<0$$

which is equivalent to

$$\begin{bmatrix}(1+\eta)\dfrac{1}{\alpha^2}-\dfrac{\rho}{\mu}\boldsymbol{x}_i^T\mathbf{U}^T\mathbf{U}\boldsymbol{x}_i&\boldsymbol{x}_i^T\\\boldsymbol{x}_i&\mathbf{Q}\end{bmatrix}>0,\quad i\in[1,l]\tag{18}$$

From [12], constraint (14b) is equivalent to the following inequality for all $i \in [1,m]$,

$$\mathbf{K}_{1i}\mathbf{F}_i\left(\mathbf{P}/\rho+\sqrt{\eta/\mu}\mathbf{U}_i^T\mathbf{U}_i\right)^{-1}\mathbf{F}_i^T\mathbf{K}_{1i}<\frac{\boldsymbol{u}_{0i}^2}{1+\eta} \tag{19}$$

The equivalent form of inequality (19) is given as LMI (20).

$$\begin{bmatrix} \dfrac{u_{0i}^2}{1+\eta}\mathbf{Q} & \left(\mathbf{U}_i\mathbf{Q}\right)^T \\ \mathbf{U}_i\mathbf{Q} & \left(\dfrac{\rho^2}{\mu\eta(1-\mathbf{K}_{1i})}-\dfrac{u_{0i}^2}{1+\eta}\sqrt{\dfrac{\eta}{\mu}}\right)^{-1} \end{bmatrix}>0\,,\quad i\in[1,m] \tag{20}$$

Therefore, the problems (14) can be rewritten as problems (21). All the constraints are given in LMIs if ρ and μ are fixed. The global maximum and minimum values of α would be obtained by running ρ from 0 to 1 and ρ/μ from 0 to $+\infty$.

$$\begin{aligned} &\underset{\mathbf{P}>0,\rho,\eta,\mu>0}{\text{maximize}} && \alpha \\ &\text{subject to} && a)\ \text{condition (18) or condition(19)} \\ &&& b)\ \text{condition (23)} \\ &&& c)\ \text{condition (17)} \end{aligned} \tag{21}$$

Remark 1: *Solving problem (21) under given $\boldsymbol{K}_1$, $\boldsymbol{K}_2$ and η would lead to a group of invariant sets in the stability domain. The volume of each invariant set depends on the selection value of η. Therefore, by varying the value of η, the stability domain which is the union of all the invariant sets can be finally estimated.*

Remark 2: *the Popov criterion would be equivalent to the circle criterion once the value of η is equal to zero, thus the estimation via the former would be offered more freedom than the latter, and the boundary of stability domain would be the envelope of all the derived invariant sets.*

3.2 Illustrative Example

Example 1 : The system to be considered has a representation as system (1), and there are

$$\mathbf{A}=\begin{bmatrix}0.6 & -0.8\\ 0.8 & 0.6\end{bmatrix},\ \mathbf{B}=\begin{bmatrix}2\\4\end{bmatrix},\ \mathbf{E}=\begin{bmatrix}0.1\\0.1\end{bmatrix},\ \mathbf{F}=\begin{bmatrix}-0.2844\\1.4430\end{bmatrix},\ \boldsymbol{u}_0=1$$

Solving problem (24) under the condition: $\mathbf{K}_1$=0.44, $\mathbf{K}_2$=1, $X_J = \delta$ ($\mathbf{I}_2$,1) to derive the largest invariant set in the stability domain (the selection values of η and the corresponding results α, μ, ρ, $\mathbf{P}$ are listed as in Table 1). This would lead to a group of invariant sets as shown in figure 1, where for the purpose of further illustration a state trajectory is also plotted, and for the purpose of comparison the boundaries of invariant sets derived via Popov criterion are plotted with solid lines, while the boundary of invariant set derived via Circle criterion is plotted with dash-dot line. The stability domain can be estimated by the enveloping outer the boundaries of these derived invariant sets. It is found that the trajectory starting from inside the envelope boundary is also bounded, and the stability domain is effectively extended via Popov criterion.

Table 1. A group of estimated invariant sets

η	α^*	μ^*	ρ^*	$\mathbf{P}^*$
0	1.3030	0.0073	0.8	$\begin{bmatrix} 0.1939 & -0.2000 \\ -0.2000 & 0.4911 \end{bmatrix}$
0.05	1.3721	0.0063	0.3	$\begin{bmatrix} 0.1788 & -0.1842 \\ -0.1842 & 0.4546 \end{bmatrix}$
0.3	1.3501	0.0034	0.6	$\begin{bmatrix} 0.2293 & -0.2305 \\ -0.2305 & 0.5092 \end{bmatrix}$
0.6	1.3523	0.0021	0.5	$\begin{bmatrix} 0.2757 & -0.2800 \\ -0.2800 & 0.5595 \end{bmatrix}$
0.8	1.3674	0.0151	0.6	$\begin{bmatrix} 0.3061 & -0.3178 \\ -0.3178 & 0.6853 \end{bmatrix}$
1.0	1.3726	0.0013	0.4	$\begin{bmatrix} 0.3169 & -0.3315 \\ -0.3315 & 0.6069 \end{bmatrix}$
1.2	1.4121	0.0011	0.3	$\begin{bmatrix} 0.3590 & -0.3708 \\ -0.3708 & 0.5856 \end{bmatrix}$
1.5	1.3910	0.0013	0.3	$\begin{bmatrix} 0.3435 & -0.3936 \\ -0.3936 & 0.6636 \end{bmatrix}$
2.0	1.3909	0.0007	0.3	$\begin{bmatrix} 1.8518 & -1.8581 \\ -1.8581 & 2.9825 \end{bmatrix}$

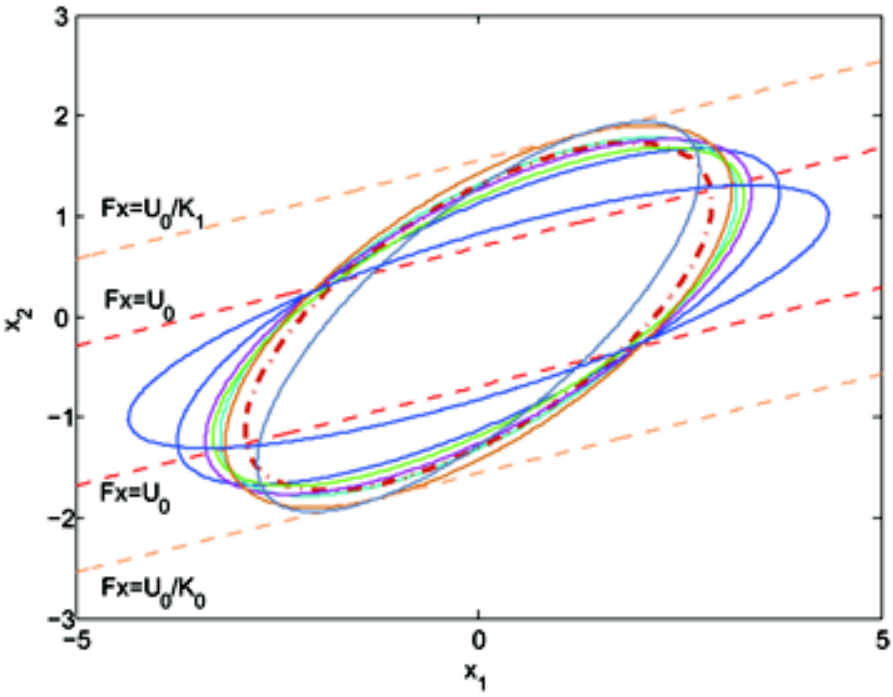

Fig. 1. Estimation of stability domain

4 Conclusions

In this paper, a method of local stability analysis via Popov criterion was presented for linear systems subject to input saturation and persistent disturbance. A set invariance condition was proposed to determine the invariance of convex sets in the stability domain. The largest invariant set was derived by means of solving LMIs in a convex optimization problem. Due to the freedom in selecting the Lyapunov functions, there would be more than one invariant sets derived, thus the domain of stability can be estimated by enveloping the outer boundaries of these derived sets. An illustrative example was presented to demonstrate the effectiveness of the proposed method.

Acknowledgments. This work was partially supported by the Research Fund of State-Key Lab of MSV (Grant No.MSV-MS-2010-03), the State-Key Laboratory of Robotics and System (HIT) (Grant No.SKLRS-2010-ZD-06), the Shanghai Aerospace Fund (Grant No.ZYJ-09052), the National Natural Science Foundation of China (Grant No.61075086, 61105101).

Reference

1. Delibasi, A., Kucukdemiral, I., Cansever, G.: L-2 control of LPV systems with saturating actuators: Polya approach. Journal of Optimal Control Applications & Method 34(1), 17–34 (2013), doi:10.1002/oca.1025
2. Hindi, H., Boyd, S.: Analysis of linear systems with saturation using convex optimization. In: Proceedings of IEEE Conference on Decision and Control, Tampa, US, pp. 903–908. IEEE, New York (1998)
3. Pittet, C., Tarbouriech, S., Burgat, C.: Stability regions for linear systems with saturating controls via circle and popov criteria. In: Proceedings of the 36th Conference on Decision & Control, San Diego, California, US, pp. 4518–4523 (December 1997)
4. Olalla, C., Queinnec, I., Leyva, R., et al.: Optimal State-Feedback Control of Bilinear DC-DC Converters With Guaranteed Regions of Stability. In: Proceedings of IEEE International Symposium on Industrial Electronics (ISIE), Bari, Italy, pp. 3868–3880. IEEE, New York (2010), doi:10.1109/TIE.2011.2162713
5. Oliveira, M.Z., Gomes da Silva Jr., J.M., Coutinho, D.: State Feedback Design for Rational Nonlinear Control Systems with Saturating Inputs. In: Proceedings of American Control Conference (ACC), Montreal, Canada, pp. 2331–2336. IEEE, New York (2012)
6. Kladis, G.P., Economou, J.T., Knowles, K., et al.: Energy conservation based fuzzy tracking for unmanned aerial vehicle missions under a priori known wind information. Engineering Applications of Artificial intelligence 24, 279–294 (2011)
7. Davison, E.J., Kurak, E.M.: A computational method for determining quadratic Lyapunov functions fro non-linear systems. Automatica 7, 627–636 (1971)
8. Hu, T.S., Lin, Z.L., Chen, B.M.: An analysis and design method for linear systems subject to actuator saturation and disturbance. Automatica 38(2), 351–359 (2002)
9. Khalil, H.K.: Nonlinear Systems, 3rd edn., p. 339. Prentice-Hall, New Jersey (2002)
10. Fang, H.J., Lin, Z.L., Hu, T.S.: Analysis of linear systems in the presence of actuator saturation and L2-disturbance. Automatica 40(7), 1229–1238 (2004)
11. Hu, T.S., Lin, Z.L.: Practical stabilization of exponentially unstable linear systems subject to actuator saturation nonlinearities and disturbance. International Journal of Robust and Nonlinear Control 11(6), 555–588 (2001)
12. Hindi, H.: A tutorial on convex optimization. In: Proceedings of American Control Conference, Boston, US, pp. 3252–3265 (June 2004)
13. Boyd, S., Ghaoui, L., Feron, E., Balakrishnan, V.: Linear matrix inequality in system and control theory. In: Proceedings of Studies in Applied Mathematics, PA, Philadelphia, pp. 555–588 (June 1994)

Synergetic Control Strategy for a Hybrid FES-Exoskeleton System: A Simulation Study

Yong Ren, Qing Zhang, and Dingguo Zhang*

State Key Laboratory of Mechanical System and Vibration,
School of Mechanical Engineering, Shanghai Jiao Tong University,
Shanghai 200240, P.R. China
dgzhang@sjtu.edu.cn

Abstract. This paper proposes a novel control strategy for a hybrid assistive system that combines functional electrical stimulation (FES) with a powered lower extremity exoskeleton to provide adaptive torque assistance for paraplegic patients. The control architecture is based on central pattern generator (CPG) that acts as a feature extractor, and a proportional-derivative (PD) controller that adaptively regulates the exoskeleton's assistive torque. Currently our work focuses on controlling the swing of shank, so two muscle groups (Vasti and Hamstrings) are stimulated to produce active torque for knee joint. However some drawbacks such as rapid muscle fatigue and uneven muscle response severely limit FES-aided systems. We use a powered extremity exoskeleton to adaptively compensate the torque loss. The CPG model keeps its output in phase with the measured angle trajectory to predict total torque with a torque estimator. The PD controller regulates the gain that determines how much of estimated total torque should feed back to the musculoskeletal system. The control system is implemented in MATLAB/SIMULINK.

Keywords: Synergetic control, functional electrical stimulation (FES), exoskeleton, central pattern generator (CPG), PD control.

1 Introduction

Functional electrical stimulation (FES) has been demonstrated as an effective way to help paralyzed patients such as spinal cord injured (SCI) restore legged mobility. However considering the musculoskeletal system's nonlinearity and time variability, controlling FES to assist SCI individuals to move in a natural manner is a complicated problem. There are two significant drawbacks that severely hindered the use of FES [1]. The first is rapid muscle fatigue caused by continuous stimulating muscles and the second is poor controllability resulting in inadequate joint torque to produce reliable limb movement and body support.

* Corresponding author.

J. Lee et al. (Eds.): ICIRA 2013, Part II, LNAI 8103, pp. 226–236, 2013.

Some hybrid systems have been developed to solve these problems. A controlled-brake orthosis combined with FES aids hip and knee flexion with a spring assist, and uses sensors and modulated friction brakes for the feedback control of joint angles [1-2, 4]. However this device can only provide passive torque for lower limb joints, and the control structure is based on finite state machine that cannot adaptively deal with the synergy between the orthosis and legs.

Exoskeletons, such as Lokomat (Hocoma, AG, Volketswil, Switzerland) [3], has been widely used in gait rehabilitation. However, the patients' muscles are not excited actively in such a pure exoskeleton system, i.e. the movement is generated passively. Therefore it is a natural idea to use a powered exoskeleton as a torque compensator for FES. Some previous work has been done so [5]. However in this work, the FES is merely a subsidiary approach to aid the hip extension with affecting the system when flexion torques are needed. The stimulator basically relies on an on-off controller. We hope the FES technique can be a main actuator to enhance SCI patients' active motion and the loss torque can be adaptively compensated by powered exoskeletons. Therefore we propose a synergetic control structure that can achieve this goal.

The idea originates from human-robot synchrony developed by Ronsse et al [6], which uses adaptive Hopf oscillators and a torque estimator to predict the torque during the elbow's rhythmic flexion-extension movement. Thus robot can detect the users' motion intention and provide realtime torque assistance needed by the user. The whole system in this work does not explicitly model the human and elbow dynamics and regulates the feedback gain by hand. In this paper we propose an alternative method for a hybrid FES-exoskeleton system with automatical movement assistance for the knee joint. For our purpose, the joint angle needs to be measured to entrain the artificial oscillator. A Matsuoka model [7] is used as adaptive oscillators. Besides, we use a model-based feedforward controller combined with PD to control FES-induced joint movements. Some research groups have investigated feedback and adaptive controllers for FES [8], from which our work draws useful ideas.

2 Methods

The simulation study in this paper is for the practical use of hybrid FES-exoskeleton systems. Multiple joints control deals with greater challenges than single joint control, such as motion coupling between joints. Our goal is to present a novel control strategy for the hybrid system so we take the knee joint movement for instance. Unlike the human-robot synchrony method, a reference trajectory is necessary for the simulation. Here we set a sinusoidal angle trajectory for the shank to move.

2.1 The Musculoskeletal Model

To control the movement of knee joint, we adopted a musculoskeletal model based on Hill-type muscle model [9-10] and generic dynamics functions. The Hill-type model describes the activation and contraction properties of muscles. The

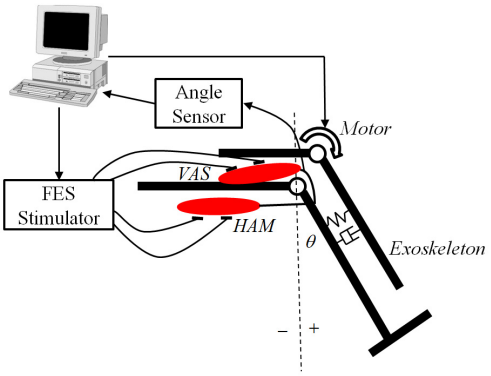

Fig. 1. Simplified model of the hybrid FES-exoskeleton system

muscles can be seen as biological actuators via FES. The whole model consists of three parts (Fig. 2): activation dynamics, contraction dynamics and segmental dynamics, in which muscle fatigue and passive characteristics (viscosity and elasticity) are modeled separately.

The activation dynamics relate FES input to muscle activation. Generally speaking, muscle force can be controlled by adjusting pulse width PW and pulse frequency f. To minimize the influence of muscle fatigue, we set the pulse frequency at 20Hz and modulate pulse width. The recruitment function is determined by three factors [10]: a threshold pulse width *Thres* [s], a saturation pulse width *Sat* [s], and a scaling factor *Sf* [Nm]. The muscle activation Act is given as follows:

$$Act = \begin{cases} 0 & PW \leqslant Thres \\ \frac{Sf \cdot (PW - Thres)}{Sat - Thres} & Thres < PW < Sat \\ Sf & PW \geqslant Sat \end{cases} \tag{1}$$

Muscle fatigue is one of the most important factors we should consider. We use a generic fitness function *fit(t)* to describe the effect of muscle fatigue:

$$\frac{dfit}{dt} = \frac{(fit_{min} - fit)a(t)\lambda}{T_{fat}} + \frac{(1 - fit)(1 - a\lambda)}{T_{rec}} \tag{2}$$

Where T_{fat} is the time constant for fatigue, and T_{rec} for recovery. λ stands for the effect of stimulation frequency on muscle fatigue. We set f at a certain value so λ is a constant here.

The moment-angle relation is given by [10]:

$$T_{ma} = exp[-(\frac{\theta + \pi/2 - K_1}{K_2})^2] \tag{3}$$

where K_1 and K_2 are two parameters that decide where the maximum and minimum angles locate.

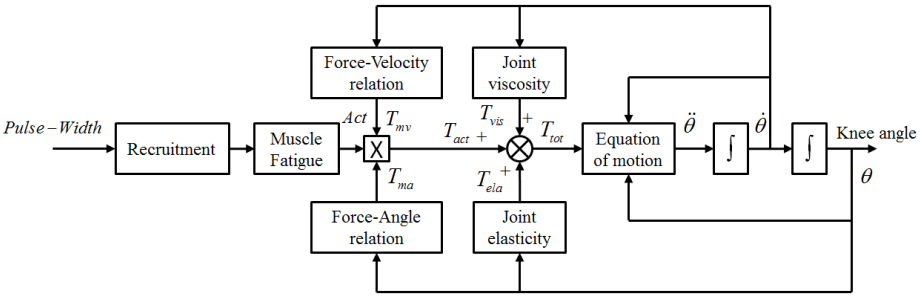

Fig. 2. The musculoskeletal model of the knee joint

The moment-angular velocity can be expressed as follows:

$$T_{mv} = 1 - K_3\dot{\theta}(t) \tag{4}$$

the parameter K_3 equals the knee-moment arm over the maximum contraction velocity. Then we can get the active muscle moment via multiplying activation by the moment-angle and moment-velocity parameters. The total moment exerting on the knee is obtained by adding active, passive and gravitational moments.

The passive viscous of the knee joint can be modeled proportional to the angular joint velocity [9]:

$$T_{vis} = k_{vis}\dot{\theta} \tag{5}$$

with the damping coefficient k_{vis}.

The passive elastic joint moment is related to three joint angles of lower limbs, but we assume that the knee joint oscillates like the scheme described in Fig. 1. Thus the angles of ankle and hip will be constants. The passive elastic joint moment is given by [9]:

$$T_{ela} = exp(3.2872{-}0.0494\theta){-}exp(-1.4261{+}0.0254\theta){+}exp(2.5{-}0.25\theta){+}1.0 \tag{6}$$

For our purpose, we merely consider one-segment skeletal dynamics. The Lagrange's equation is used to solve this problem. Thus the dynamics function is given by:

$$T_{tot} = (\frac{1}{8}ml^2 + \frac{1}{2}J)\ddot{\theta} + \frac{1}{2}mglsin\theta \tag{7}$$

where T_{tot} is the total torque exerting on the knee joint, m is the skeleton mass and J the moment of inertia, and g is the gravitational constant.

2.2 The Control Architecture

In this paper, we propose a synergetic control strategy for the hybrid FES-exoskeleton system based on initial work on human-robot synchrony, which uses adaptive oscillators to provide flexible torque assistance. However in our study,

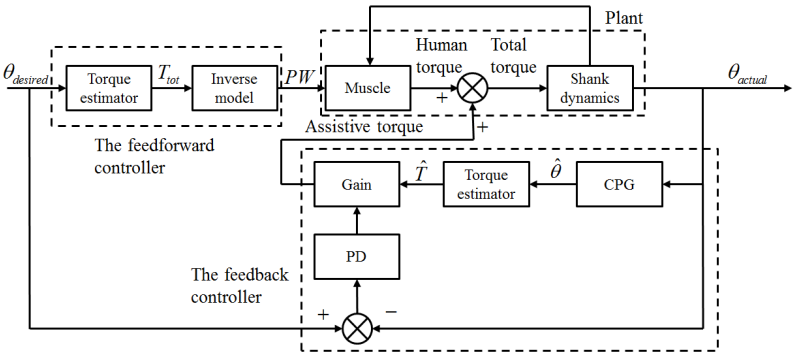

Fig. 3. Block diagram of the whole system. Each box is detailed in the paper

FES will replace healthy people's active motion and an inverse model is used as a feedforward controller to modulate stimulation intensity (pulse width) that muscles need. We choose the Matsuoka model as a feature extractor, which is a widely-used CPG algorithm. The estimated total torque can be predicted via a torque estimator and the assistive torque produced by exoskeletons is part of that. In the model the torque estimator is calculated by an inverse dynamical function of a single joint, which has been expressed in (7). A proportional-derivative (PD) controller is introduced to adaptively control the gain. Each part of the control architecture will be detailed in the paper.

The Feedforward Controller. To perform a desired joint angle trajectory, a feedforward controller based on the inversion of the direct model is an effective method. Firstly the total torque required can be computed by (7) and the passive torque is neglected in the inverse model to obtain an ideal pulse width output. The activation can be given by [10]:

$$Act = T_{tot} \cdot exp[(\frac{\theta + \pi/2 - K_1}{K_2})^2] \cdot (1 - K_3\theta(\dot{t}))^{-1} \tag{8}$$

Then the desired pulse width can be computed by the inverse recruitment function. We use the linear part to calculate:

$$PW = \frac{Act(Sat - Thres)}{Sf} + Thres \tag{9}$$

The CPG Model. A CPG has been demonstrated to exist in animals' central nervous system to regulate locomotion without sensory feedback or brain input. The most significant property of the CPG is entrainment that can synchronize the oscillation of feedback signals. The CPG can produce a robust pattern with appropriate feedback signals even in unpredictable situations. It has been widely

used in controlling the locomotion of humanoid robots. There are several mathematical tools to describe CPG and we choose a model proposed by Matsuoka based on mutual inhibiting neurons. It can be given by the following equations:

$$\begin{cases} \tau_1 \dot{x_1} + x_1 = -a_{12} y_2 + s_1 - b_1 x_1' - \theta^+_{actual} \\ \tau_2 \dot{x_2} + x_2 = -a_{21} y_1 + s_2 - b_2 x_2' - \theta^-_{actual} \\ T_1 \dot{x_1}' + x_1' = y_1 \\ T_2 \dot{x_2}' + x_2' = y_2 \\ y_i = max(x_i, 0), i = 1, 2 \\ \hat{\theta} = x_1 - x_2 \end{cases} \tag{10}$$

Where x_i represents the inner state of the ith neuron, x_i' represents the degree of the adaptation, and y_i is the output (i=1, 2). Here τ_i and T_i are time constants, s_i an impulse rate of the tonic input, b_i the parameter that determines the steady-state firing rate, a_{12} and a_{21} the weight of inhibitory connection between the neurons, θ_{actual} the actual angle, and $\hat{\theta}$ the estimated angle. We use a symmetric CPG model. The parameters are set as follows: τ_1=τ_2=0.224, a_{12}=a_{21}=2.0, s_1=s_2=2.0, b_1=b_2=2.5, T_1=T_2=0.280.

The Gain Regulation. The total torque needed for knee joint can be estimated via appropriately tuning the parameters of the CPG. The assistive torque produced by the exoskeleton is a fraction of the total estimated torque, which is determined by the gain. In the human-robot synchrony experiment [6], the equivalent gain is tuned artificially, reflecting the collaboration between the subject and the assistance device. However, it is not a convenient way for practical use in hybrid FES-exoskeleton systems and we hope the assistance device can automatically compensate torque loss for the subject. Therefore we introduce a regulation rule for the gain to achieve this goal. In the control rule, a PD controller is used to minimize the tracking error between the reference knee joint angle and the actual one, which makes the system become closed-loop architecture. The adaptive gain can be computed by the following rule:

$$\mathscr{G} = \kappa(1 + K_p e + K_d \dot{e}) \tag{11}$$

where κ represents how much effort the exoskeleton should perform, and e represents the tracking error, K_p and K_d are parameters of the PD controller. We set K_p at 2.0 and K_d at 0.12 by trial and error. If there is no muscle fatigue, the torque produced by FES will be stable and we can set κ as a constant, still resulting in a quite small error. Considering the effect of muscle fatigue, the active torque will drop with time, so the error will increase and can be used to adaptively tune the gain. For practical consideration, we set κ no higher than 0.5.

3 Results

In this paper, we mainly focus on controlling single joint movements. To test the synergetic control strategy we developed for hybrid FES-exoskeleton

Table 1. Muscle-Specific Parameters

Muscle group	λ	fit_{min}	T_{fat}[s]	T_{rec}[s]
Hamstrings	0.424	0.2	25	30
Vasti	0.424	0	18	30

Table 2. Parameters of the Musculoskeletal Model

Sf[Nm]	$Thres$[μs]	Sat[μs]	K_1[deg]	K_2[deg]	K_3[s/rad]	k_{vis}[Nms/rad]	m[kg]	l[m]	J[kgm^2]
15	100	500	50	65	0.04	1.0	3.5	0.45	0.0476

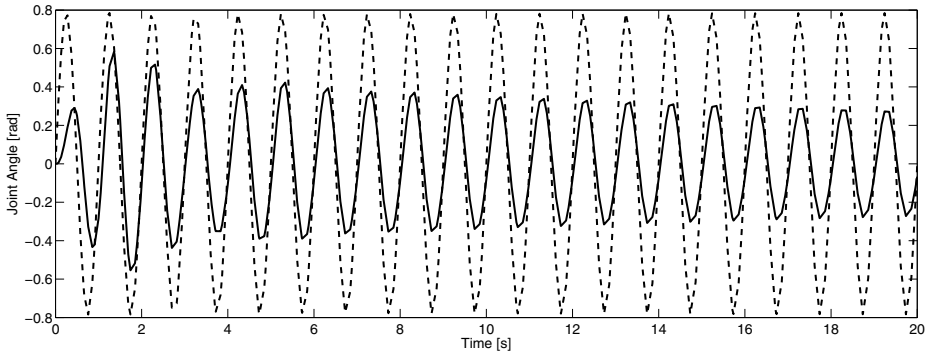

Fig. 4. Comparison between the actual joint trajectory (solid line) and the reference angle (dashed line) without any assistive torque

systems, a reference knee angle trajectory should be given in advance. For example, $\theta_{desired} = \frac{\pi}{4} sin(2\pi t)$, which means the shank oscillates at 1Hz and moves within a relatively large range. All data processing and modeling were realized in MATLAB/SIMULINK. The following tables show the relevant parameters of the musculoskeletal model. They correspond to real physiological parameters based on simplified models [9], [10].

For validating the effect of muscle fatigue, the κ should be zero at first. In the absence of exoskeletons' assistive torque, a comparison between the reference and actual knee joint angle is shown in Fig. 4. There is a significant attenuation with time because of muscle fatigue. The actual angle reached merely 50% of the originally desired trajectory after 10 seconds stimulation, which means assistive torque is highly necessary. Then we tuned κ respectively at 0.3 and 0.4 to make the assistance device work. The κ should not be tuned too high because the error in the beginning is large and then overshoot will be great. Actually even though κ is not very large, the overshoot is still unacceptable in some sense. For practical purposes, we should make the stimulation increase with time from a small value, so the hybrid system will transform to the stable state in a smooth and steady

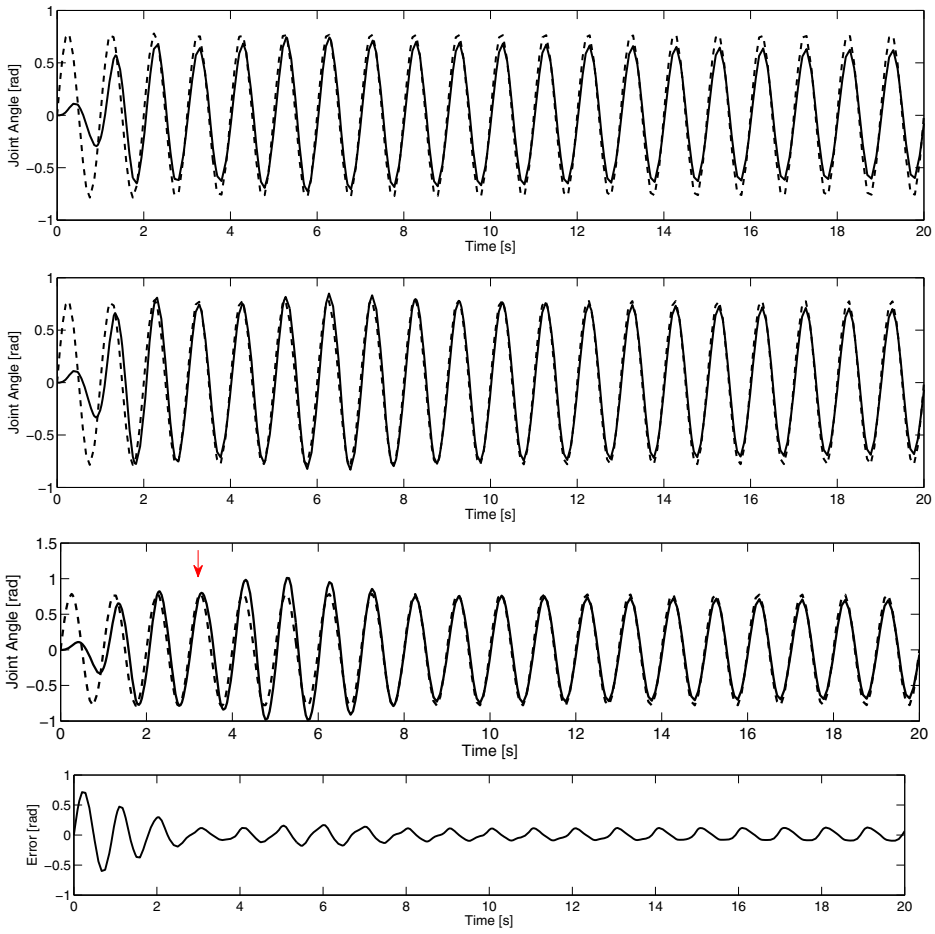

Fig. 5. Comparison between the actual joint trajectory (solid line) and the reference angle (dashed line) by using the synergetic control strategy. The κ is 0.3 for the top figure and 0.4 for the second and third. The third figure shows the joint angle after the whole system is interrupted by a torque pulse of 2Nm on the third second. The bottom figure shows the error when κ equals 0.4.

manner. Fig. 5 shows the results by using the synergetic control strategy for the hybrid system. When κ is 0.4, the exoskeleton can compensate the torque loss caused by muscle fatigue and make the knee joint move as a relatively ideal trajectory.

However if the torque loss caused by muscle fatigue is too large, there will be a slight reduction of the actual joint angle with time. The reason is that we limit the effort performed by the exoskeleton by κ. Thus in practical use, the subjects should have a rest after a relatively long time training. Besides, the CPG model extracts the pattern of joint angle with superior performance in

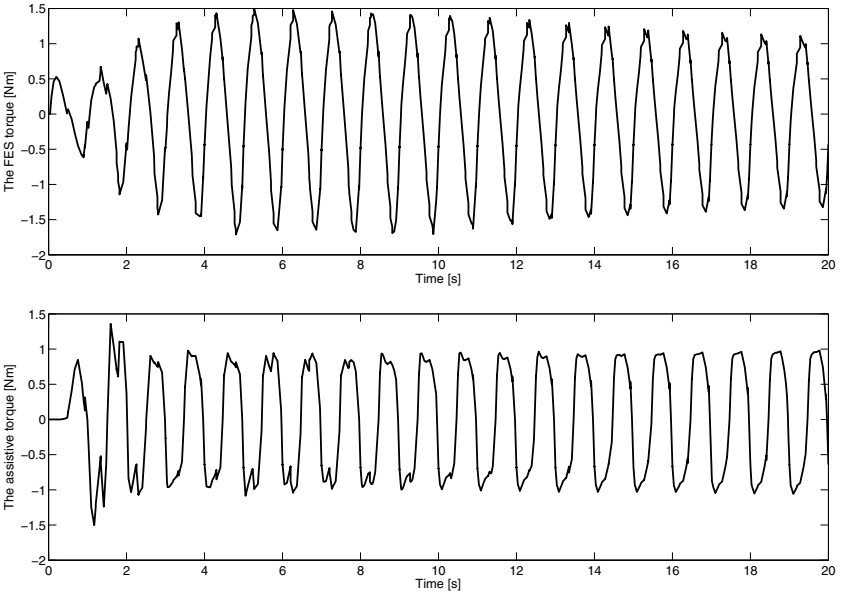

Fig. 6. The torque produced by FES (upper) and the exoskeleton (lower).

robustness. It has been testified that CPG can produce a robust motion pattern with proper feedback signals even in an unpredictable situation. Therefore, even though the real joint angle does not keep stable all the time, the output of the CPG model for torque estimator is nearly invariable owing to its entrainment property, so the relative stability of assistive torque provided by the exoskeleton can be guaranteed. We add a disturbance torque pulse into the hybrid system and the result shows basically little change for the actual angle. Fig. 6 shows the torque produced respectively by FES and the assistance device. We can see the torque generated by the exoskeleton increases to overcome the torque attenuation. The results show that the hybrid FES-exoskeleton system can be an effective way for SCI patients' rehabilitation.

We merely use a rhythmic signal to test the proposed method. Actually in daily life, the movements of lower limbs are usually rhythmical, so the control strategy presented in this paper will have practical use in rehabilitation engineering. A lot of previous work mainly focused on controlling FES to produce a desired trajectory for lower limb joints. The simulation results show that the exoskeleton as an assistance device can be used as an alternative way to make up some intrinsic drawbacks of FES.

4 Conclusion

In this paper, we have proposed a novel control strategy for hybrid FES-exoskeleton systems. A mathematical model of the Hill-type musculoskeletal

system is employed to test this method. The inverse model of the stimulated muscle is adopted as a feedforward controller to generate modulated pulse width signals for FES. The CPG based on Matsuoka model acts like a feature extractor to track actual motion patterns of knee joint. Finally a PD controller is used for dynamically regulating feedback torque. The simulation results show that the control structure is efficient to regulate rhythmic movements of the knee joint. This method will bring benefit to ameliorating FES-aided movements for SCI patients.

In the future, this method can be extended to control 2-DOF hybrid systems including the hip joint. However motion coupling between two joints will be a hard problem to deal with, which needs more complicated CPG networks and optimization algorithms to design the gain regulation rules. Besides, our work proposed in this paper implemented mathematical simulations based on simplified physiological models. For practical use, real experiments based on the control strategy need to be conducted to demonstrate its actual efficiency. Our future work will focus on experimental setup and execution of the swing of shank. A hybrid system that combines FES with a knee exoskeleton will be developed, and in the early stage, experiments for this will be done on healthy subjects. After that, we will consider clinical experiments and application involving paraplegic patients.

Acknowledgement. This work is support by National Natural Science Foundation of China (51075265) and HIT State Key Laboratory of Robotics and System (SKLRS-2012-ZD-04).

References

1. Farris, R.J., Quintero, H.A., Withrow, T.J., Goldfarb, M.: Design and Simulation of a Joint-Coupled Orthosis for Regulating FES-Aided Gait. In: IEEE International Conference on Robotics and Automation, pp. 1916–1922. IEEE (2009)
2. Goldfarb, M., Durfee, W.K.: Design of a Controlled-Brake Orthosis for FES-Aided Gait. IEEE Transactions on Rehabilitation Engineering 4(1) (1996)
3. Veneman, J.F., Kruidhof, R., Hekman, E.E.G., Ekkelenkamp, R., Van Asseldonk, E.H.F., van der Kooij, H.: Design and Evaluation of the LOPES Exoskeleton Robot for Interactive Gait Rehabilitation. IEEE Transactions on Neural Systems and Rehabilitation Engineering 15(3) (2007)
4. Stauffer, Y., Allemand, Y., Bouri, M., Fournier, J., Clavel, R., Metrailler, P., Brodard, R., Reynard, F.: The WalkTrainer–A New Generation of Walking Reeducation Device Combining Orthoses and Muscle Stimulation. IEEE Transactions on Neural Systems and Rehabilitation Engineering 17(1) (2009)
5. Ha, K.H., Quintero, H.A., Farris, R.J., Goldfarb, M.: Enhancing Stance Phase Propusion during Level Walking by Combining FES with a Powered Exoskeleton for Persons with Paraplegia. In: 34th Annual International Conference of the IEEE EMBS, San Diego, pp. 344–347. IEEE (2012)
6. Ronsse, R., Vitiello, N., Lenzi, T., van den Kieboom, J., Carrozza, M.C., Ijspeert, A.J.: Human-Robot Synchrony: Flexible Assistance Using Adaptive Oscillators. IEEE Transactions on Biomedical Engineering 58(4) (2011)

7. Matsuoka, K.: Sustained Oscillations Generated by Mutually Inhibiting Neurons with Adaptation. Biol. Cybern. 52, 367–376 (1985)
8. Riess, J., Abbas, J.J.: Adaptive Neural Network Control of Cyclic Movements Using Functional Neuromuscular Stimulation. IEEE Transactions on Rehabilitation Engineering 8(1) (2000)
9. Riener, R., Fuhr, T.: Patient-Driven Control of FES-Supported Standing Up: A Simulation Study. IEEE Transactions on Rehabilitation Engineering 6(2) (1998)
10. Ferrarin, M., Palazzo, F., Riener, R., Quintern, J.: Model-Based Control of FES-Induced Single Joint Movements. IEEE Transactions on Neural Systems and Rehabilitation Engineering 9(3) (2000)

A Balance Control Method of a Walking Biped Robot under a Continuous External Force

Yeoun-Jae Kim[1], Joon-Yong Lee[2], and Ju-Jang Lee[3]

[1] Robotics Program, Korea Advanced Institute of Science and Technology, Euseong-Gu Daehak-Ro 291 Daejeon, 305-701, Korea
lethkim@kaist.ac.kr
[2] Department of Genetics Development and Cell Biology, Iowa State University, Ames, Iowa, 50011, USA
junyoni@gmail.com
[3] Electrical Engineering Department, Korea Advanced Institute of Science and Technology, Euseong-Gu Daehak-Ro 291, Daejeon, 305-701, Korea
jjlee@ee.kaist.ac.kr

Abstract. In this paper, we present a force resisting balance control method of a walking biped robot under a continuous external force. The balance control method consists of two steps. The first step is to recognize the external force which is applied to the pelvis of the biped robot by ZMP position analysis. The second step is to move the joint angles of the biped robot by the pre-defined angle trajectory. The pre-defined angle trajectory is constructed by single objective optimization process and linear interpolation. We assumed that the biped robot which is used in this research has a position-controlled joint motor. And it has 12 degrees of freedom. The proposed balance control method is verified by numerical simulations.

Keywords: Biped robot, ZMP, Balance, External force, Optimization.

1 Introduction

The humanoid (biped) robot is a robot which has a human-like appearance. Its main ability is to use its arm and hand as if humans does, and walks with two legs like human walking. The study about biped walking has been a main theme in humanoid robotics society. Geng et.al.[1] made a planar biped walking gait with state machine. Sato et.al.[2] made a real-time biped walking trajectory which makes use of three mass robot model. Kajita et.al.[3] made a biped running trajectory using a ZMP based control method. These studies are just a glimpse of numerous biped walking researches performed worldwide in the past years.

In the meantime of biped walking research, some question raised about the dynamic stability of a standing humanoid robot under external disturbance. The external disturbance means that some external force is applied to the biped robot by accident either impulsively or continuously. With regard to this topic, the biped balance strategies against these kinds of external disturbances can be

J. Lee et al. (Eds.): ICIRA 2013, Part II, LNAI 8103, pp. 237–245, 2013.

categorized by three. These strategies are "ankle strategy", "hip strategy" and "step-out strategy". The ankle strategy is to control the ankle of the biped robot in a small disturbance. The hip strategy is also called the momentum strategy and makes use of the hip and ankle torque control to keep balance against an intermediate external disturbance. Asmar et.al.[4] use the mixture of ankle and hip strategy to avoid a fall of a humanoid robot. Stephens et.al.[5] used the two link model and integral (ankle plus hip) strategy to balance the standing robot. Stepping to avoid falling was studied by Goddard et.al.[6].

The balance control strategy of a walking humanoid robot under an external disturbance was studied recently. Yasin et.al.[7] used the capture point [8] to balance the walking biped robot by step out strategy. Yi et.al.[9] used the capture point and reinforcement learning to make the walking biped robot stabilized against an unknown external disturbance. Li.et.al.[10] made a dynamic balance control of a walking biped robot using sensor fusion, Kalman filtering and fuzzy logic. We presented a balance control strategy of a walking biped robot in an externally applied force [11]. This strategy has some advantages over previous researches such that it needs no external sensors except ZMP sensor, it can be applicable to any lateral direction disturbance, and it can be applicable to a continuous external disturbance. In [11], the balance control strategy makes use of the COG Jacobian and constrained linear quadratic programming technique. But in this paper we used the single objective optimization process and linear interpolation technique in the balance control method to make a more energy efficient balance control strategy.

The consequent chapters are as follows. In chapter 2, we present the biped model and walking gait. In chapter 3, we explain the two step balance control method. And the numerical simulation result is presented in chapter 4, and the conclusion is drawn in chapter 5.

2 The Biped Model and Predefined Walking Gait

We present the biped model and the predefined walking gait which is used in this research. The biped model has 12 degrees of freedom as depicted in Fig. 1. And the detailed inertia and geometric date is described in Table 1.

We assumed that the motors of the biped robot in each joint are position-controlled and the external force is applied in the pelvis of the biped robot. The sole of the biped model is depicted in Fig. 2. The ZMP stability region in Figure 2 will be explained later. The pre-defined walking gait which is used in this paper is represented and explained in our previous paper [12]. The main research of previous paper [12] is to construct the energy efficient optimal gait trajectory by Tchebyshev method. The gait is consists of SSP (Single Support Phase), DSP1 (Double Support Phase 1) and DSP2 (Double Support Phase 2). And in this paper, we only use the SSP walking gait for we assumed that the external force is applied in SSP. Overall SSP walking time is 1300msec.

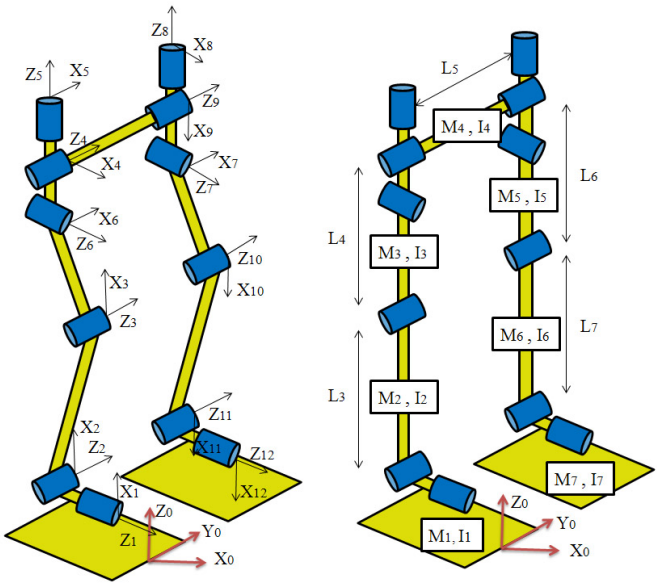

Fig. 1. The biped model

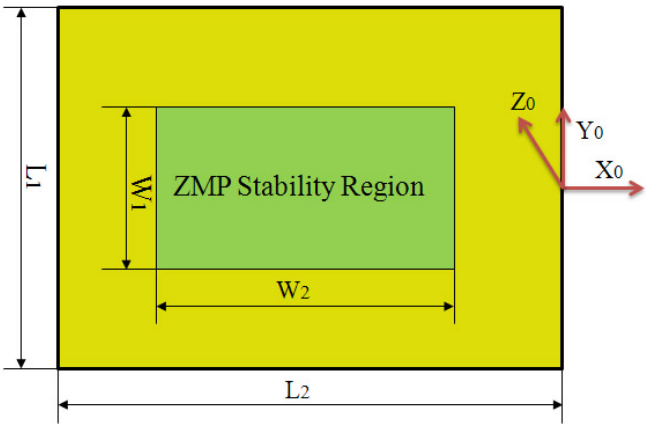

Fig. 2. The sole of the biped model

Table 1. Inertia and geometrical data

mass [kg]						
M_1	M_2	M_3	M_4	M_5	M_6	M_7
2.34	5.93	10.9	58.3	10.9	5.93	2.34

Inertia matrix component [m^2kg]							
	I_1	I_2	I_3	I_4	I_5	I_6	I_7
I_{xx}	0.07	0.02	0.06	5.86	0.06	0.02	0.07
I_{yy}	0.00	0.47	0.82	1.11	0.82	0.47	0.00
I_{zz}	0.07	0.47	0.8	6.75	0.8	0.47	0.07

Length [m]								
L_1	L_2	L_3	L_4	L_5	L_6	L_7	W_1	W_2
0.2	0.27	0.41	0.41	0.22	0.41	0.41	0.14	0.21

3 Proposed Balance Control Method

The proposed balance control method consists of two. Step 1 and step 2. Each step will be explained in subsequent chapters.

3.1 Step 1: Recognizing the Force Applying Situation (the Abnormal Situation)

To apply the proposed main balance control method, the biped robot must be able to recognize that some external force is applied to it. We used only the ZMP sensor to recognize this force applying situation. The applied external force will push the ZMP from the center of the sole to the outside of the sole. So, we defined the ZMP stability region which is depicted in Figure 2. When the biped robot walks normally without any external force application, the ZMP will remain inside the ZMP stability region. We make the SSP walking gait as such. But when the biped robot walks with some continuous external force application, the ZMP moves toward the boundary of the ZMP stability region. And it eventually goes out of the ZMP stability region. In summary, the robot recognizes the external force applying situation when the ZMP is outside of the ZMP stability region.

3.2 Step 2: Applying the Main Balance Control Method

After recognizing some external force application, the robot must activate the balance control method not to fall down. The main balance control method is explained below. The Figure 3 represents one step gait sequence of a biped robot.

There are 5 pictures of one step gait sequence in Figure 3. In this research we assumed that the external force is applied from picture 2 to picture 4 in Figure 3. The one step gait is 1300msec. So the external force is applied from 400msec to 800msec in time base calculation. And somewhere in gait sequence from 400msec

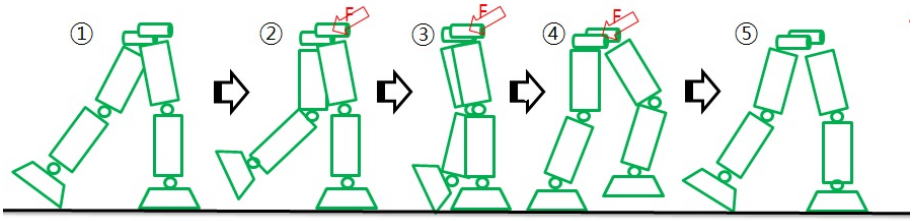

Fig. 3. One step gait sequence

to 800msec, by the applied external force, the +y direction ZMP is out of the ZMP stability region. I calculated the optimal gait sequence which makes the robot stabilized in this moment by single objective optimization procedure. The constraints in single objective optimization procedure are the same as in our previous paper [11]. The objective function is generated to make the stabilizing gait sequence energy efficient. The detailed formula is in (1).

$$
\begin{aligned}
&Minimize\\
&J = J_1 + J_2 + J_3\\
&J_1 = \tfrac{1}{2}(\Delta^{cmd}\theta_t - \Delta\theta_t)^T W(\Delta^{cmd}\theta_t - \Delta\theta_t)\\
&J_2 = \tfrac{1}{2}(\Delta\theta_t - \sqrt{\frac{\Delta{\theta_t}^T\Delta\theta_t}{13}}\begin{bmatrix}1\\1\\\vdots\\1\end{bmatrix})^T Q(\Delta\theta_t - \sqrt{\frac{\Delta{\theta_t}^T\Delta\theta_t}{13}}\begin{bmatrix}1\\1\\\vdots\\1\end{bmatrix})\\
&J_3 = \tfrac{1}{2}\tau^T R\tau, \tau = \begin{bmatrix}\tau_1\\\tau_2\\\vdots\\\tau_{13}\end{bmatrix}\\
&Subjectto\\
&J_{COG}\Delta\theta_t = \Delta COG\\
&-0.01^\circ < \Delta\theta_t < +0.01^\circ
\end{aligned}
$$

$$
W = \begin{bmatrix}1&0&\cdots&0\\0&1&\cdots&0\\\vdots&\vdots&\ddots&\vdots\\0&0&\cdots&500\end{bmatrix}, Q = R = \begin{bmatrix}1&0&\cdots&0\\0&2&\cdots&0\\\vdots&\vdots&\ddots&\vdots\\0&0&\cdots&1\end{bmatrix}, J_{COG} = \begin{bmatrix}\frac{\partial x_{COG}}{\partial\theta_1}&\frac{\partial x_{COG}}{\partial\theta_2}&\cdots&\frac{\partial x_{COG}}{\partial\theta_{13}}\\\frac{\partial y_{COG}}{\partial\theta_1}&\frac{\partial y_{COG}}{\partial\theta_2}&\cdots&\frac{\partial y_{COG}}{\partial\theta_{13}}\\\frac{\partial z_{COG}}{\partial\theta_1}&\frac{\partial z_{COG}}{\partial\theta_2}&\cdots&\frac{\partial z_{COG}}{\partial\theta_{13}}\end{bmatrix} \tag{1}
$$

J in (1) is the objective function and the remains are the constraints. The value which must be solved is θ_t, the joint angles. θ_{target} is the target motor angle. The target motor angles are determined by inverse kinematics in which the robot is in DSP in minimal angular displacement from current posture. The objective function has three sub-objective functions J1, J2, J3. J1 represents that the value must be as close as the target motor angle. J2 represents that the joint

angle value must not deviate significantly from its average value. J3 represents that the torques in motor angle must be as small as possible. The constraints represented in (1) are that the COG Jacobian times $\Delta\theta_t$ equals ΔCOG. The ΔCOG is set to 0.1mm in our simulation. If the applied external force is +y direction, the ΔCOG is -0.1mm and if the applied external force is -y direction, the ΔCOG is +0.1mm. The $\Delta\theta_t$ must be in the range of 0.01°. The sampling rate is 1ms and the θ_t is calculated at about 1000 sampling time.

The problem is that this optimization problem must be solved in each gait from 400msec to 800msec for there are cases when the ZMP is out of the ZMP stability region in any time from 400msec to 800msec by some arbitrary continuous external force application. The sampling time is 1msec, so the instances in which the biped robot undergoes the abnormal situation (recognizing the external force application) are 800-400=400instances and in each instances, the single objective optimization problem must be solved at about 1000 sampling time. Eventually we need to solve the optimization problem totally 400 instances * 1000sampling time = 400,000 times. This is not a reasonable number to solve the optimization problem. So, I solved the optimization problem with 400, 600, 800msec instances. And performed the linear interpolation at the time when the biped robot undergoes the abnormal situation is between 400 600msec or 600 800msec. The overall procedure in which the stabilizing gait sequences are generated is depicted in Figure 4.

The gait sequence which is made as described in Figure 4 will be used when the biped robot undergoes the abnormal situation. For example, if the abnormal situation is recognized by the biped robot in 467msec during SSP, the robot get the gait sequence which is made by linear interpolation, and performs the gait sequence until the +y direction ZMP is in the center of the sole.

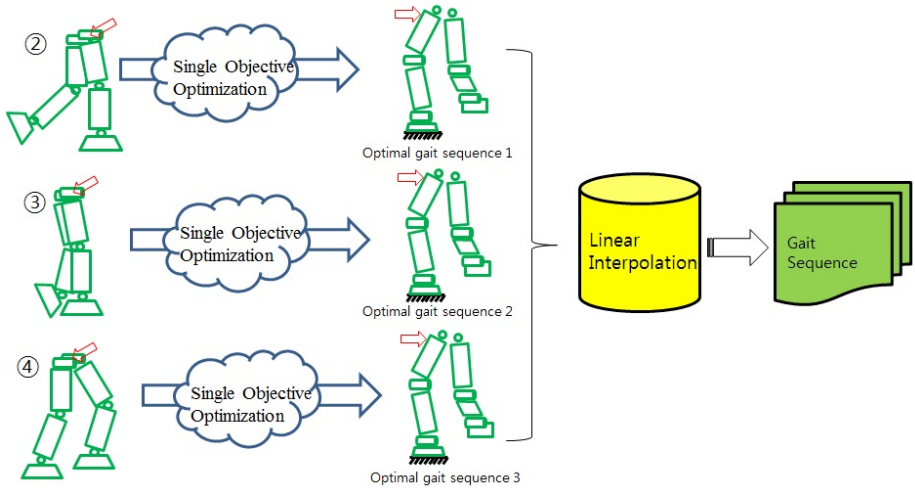

Fig. 4. Overall procedure of making stabilizing gait sequences

4 Numerical Simulation Result

The numerical simulation results are explained in this chapter. The result consists of ZMP result and Torque result. The simulation condition is that 130N +y direction force is applied to the pelvis of the biped robot at about 0.33sec and the ZMP goes out of the ZMP stability region at about 0.5sec.

4.1 ZMP Results

The ZMP results are depicted in Figure 5. The ZMP_y goes jump at 0.33 sec for +y direction constant +130N force is applied to the robot at 0.33 sec. The ZMP_x remains flat for the external force is applied in y direction only. At 0.5sec, the robot recognizes that some external force is applied and activates the step 2. The ZMP_y goes down to 0 gradually while ZMP_x remains constant. There are some noisy characteristics in step 2 phase for the gait sequence is calculated by single objective optimization process. Actually, the noisy characteristics were intense, so I inserted low-pass filter to the output of ZMP results.

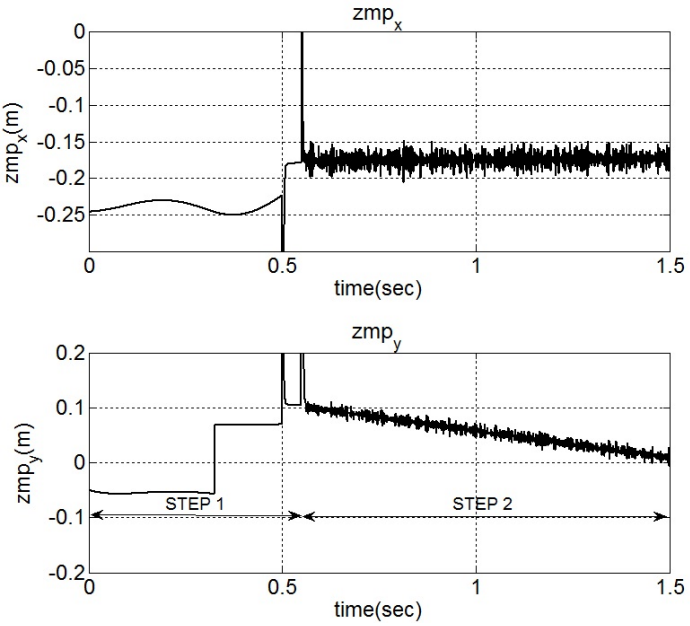

Fig. 5. ZMP results

4.2 Torque Results

There are three graphs in Figure 6. They are roll direction ankle torque graph, pitch direction knee torque graph and roll direction hip torque graph of the

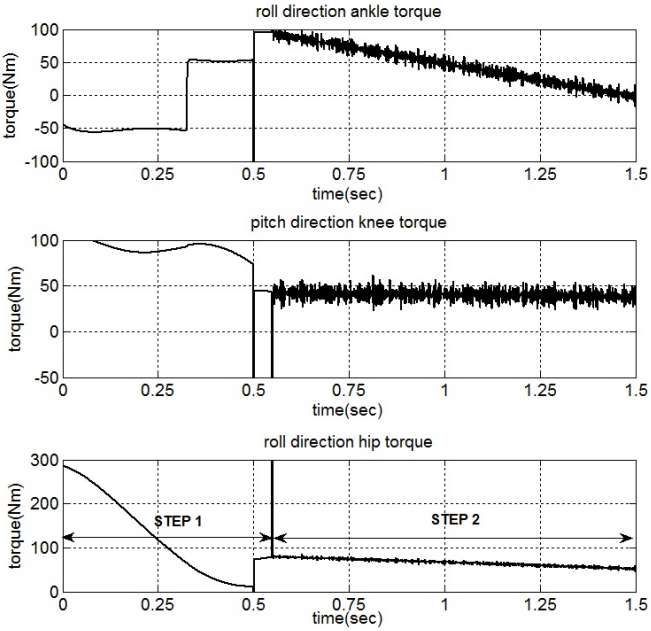

Fig. 6. Torque results

stance leg. These torques are the most important for the most of force and weight is applied to these joint motors. The roll direction ankle torque is quite resembles the ZMP_y graphs for it directly affects the ZMP_y value. When the ZMP_y reaches 0, So does the roll direction ankle torque. Pitch direction knee torque is almost flat in STEP 2 process and the value is about 50N. the roll direction hip torque is about 70N at the beginning of STEP 2 and gradually diminished to 50N during STEP 2 region.

5 Conclusion

In this study, we suggested a balance control method of a walking biped robot under an externally applied continuous force. Actually this research is upgrade version of previous research results [11]. With advantage of a suggested balance control strategy suggested by [11], this paper found an energy efficient optimal balancing control method with the aid of single objective optimization and linear interpolation technique. The proposed balance control method consists of step 1 and step 2. Step 1 is to recognize the abnormal situation by ZMP position. Step 2 is applying the energy efficient optimal balancing control method. The proposed method is verified by the numerical simulation and the numerical simulation result tells that the proposed method will balance the biped robot by moving the ZMP to the center of the sole. Further research will be demonstrating the proposed method by a real biped robot.

References

1. Geng, T., Gan, J.Q.: Planar Biped Walking With an Equilibrium Point Controller and State Machines. IEEE/ASME Transactions on Mechatronics 15(2), 253–260 (2010)
2. Sato, T., Sakaino, S., Ohnishi, K.: Real-Time Walking Trajectory Generation Method with Three-Mass Models at Constant Body Height for Three-Dimensional Biped Robots. IEEE Transactions on Industrial Electronics 58(2), 376–383 (2011)
3. Kajita, S., Nagasaki, T., Kaneko, K., Hirukawa, H.: ZMP-Based Biped Running Control. IEEE Robotics and Automation Magazine 14(2), 63–72 (2007)
4. Asmar, D.C., Jalgha, B., Fakih, A.: Humanoid Fall Avoidance Using A Mixture of Strategies. International Journal of Humanoid Robotics 9(1), 125002 (2012)
5. Stephens, B.: Integral Control of Humanoid Balance. In: IEEE/RSJ International Conference on Intelligent Robots and Systems, pp. 4020–4027 (2007)
6. Goddard, R., Hemami, H., Weimer, F.: Biped side step in the frontal plane. IEEE Transactions on Automatic Control 28(2), 179–187 (1983)
7. Yasin, A., Huang, Q., Xu, Q., Ahang, W.: Biped Robot Push Detection and Recovery. In: Proceedings of the IEEE International Conference on Information and Automation, pp. 993–998 (2012)
8. Pratt, J.E., Carff, J., Drakunov, S., Goswami, A.: Capture point: A step toward humanoid push recovery. In: Proceedings of the IEEE-RAS International Conference on Humanoid Robots, pp. 200–207 (2006)
9. Yi, S.J., Zhang, B.T., Hong, D., Lee, D.D.: Online Learning of a Full Body Push Recovery Controller for Omnidirectional Walking. In: 2011 11th IEEE-RAS International Conference on Humanoid Robots, pp. 1–6 (2011)
10. Li, T.S., Su, Y.T., Liu, S.H., Hu, J.J., Chen, C.C.: Dynamic Balance Control for Biped Robot Walking Using Sensor Fusion, Kalman Filter, and Fuzzy Logic. IEEE Transactions on Industrial Electronics 59(11), 4394–4408 (2012)
11. Kim, Y.J., Lee, J.Y., Lee, J.J.: A Balance Control Strategy of A Walking Biped Robot in an Externally Applied Force. In: Proceeding of the IEEE International Conference on Information and Automation, pp. 572–577 (2012)
12. Kim, Y.J., Lee, J.Y., Lee, J.J.: Bipedal Walking Trajectory Generation Using Tchebychev Method. In: International Conference on Mechatronics and Informatics (2011)

Design and Control of a Four-Link Mechanism for High Speed and Dynamic Locomotion*

Huiyang Yu, Ronglei Sun**, Hua Nie, and Guohua Qin

State Key Lab of Digital Manufacturing Equipment and Technology,
Huazhong University of Science & Technology
Wuhan 430074, China
ronglei@mail.hust.edu.cn

Abstract. With limited motor power, a good balance must be made between high speed and high torque to keep a robot run as fast as possible after meeting the torque demand for each joint. A quadruped robot with a novel leg mechanism is designed for high speed and dynamic locomotion. Two design principles are proposed in the design of a leg with low moment of inertia. A four-link transmission unit is proposed to change the motor's fixed-direction rotation into the leg's reciprocating swing. Optimization is carried out to acquire the biggest driving force. Kinematic analysis based on screw theory is made to help find out kinematic characteristics such as operating space and joint angular velocity.

Keywords: dynamic locomotion, low moment of inertia, optimization, screw theory.

1 Introduction

Research in the field of quadruped locomotion started in the fourth century when a four-legged wooden device was built [1]. Developed in the 1960s, walking robots have an advantage over wheeled robots in walking on uneven terrain [2]. Walking robot is divided into monopod robot, biped robot, quadruped robot and multi-legged robot [3].

Two of early representatives are the G.E. Quadruped and the Phoney Poney. Due to the state of development of control systems, they were both controlled with rather simple mechanisms [1]. In 1999 Martin Buehler presented Scout II, a dynamically stable running quadruped robot with a very simple mechanical design [4]. The KOLT robot was developed using electric actuation with mechanical springs for added compliance [5]. The Titan series are walking machines with reptile-like legs [6].

* This work was supported in part by the National Nature Science Foundation of China(Grant No. 50875100, 51205145) and National Basic Research Program of China (973 Program) granted No.2013CB035805.

** Corresponding author.

J. Lee et al. (Eds.): ICIRA 2013, Part II, LNAI 8103, pp. 246–256, 2013.

With good environment adaptability and anti-jamming capability, Bigdog robot is acknowledged as the most robust as well as versatile robot ever since and has a good prospect of applications in the military field [7, 8]. The cheetah robot developed by the Boston Dynamics has reached 18mph in a video posted on its website and becomes the fastest robot ever since. Using made-to-order motors, the MIT cheetah has a good performance in both stability and bio-mimics [9].

This paper introduces the design of a quadruped robot possessing a novel leg mechanism with low moment of inertia. Section 2 presents detailed design of the leg mechanism. In Section 3 the kinematics analysis is done with screw theory. Section 4 describes the set-up of the control system. Conclusions are drawn in Section 5.

2 Detailed Mechanism Design

2.1 Actuator Choosing

Compared with Hydraulic actuators and pneumatic actuators, electric motors are the most widely used actuators in robots. They are inexpensive and available in a big variety of sizes and specifications. Furthermore, they are popular because of their ease and accuracy of control. The battery is the most light power source compared with the oil compressor and the air compressor. That makes it possible to build a light-weight robot with high moving speed. Its biggest disadvantage is limited actuation power and low power density. When the power is set, increasing the motor's rotational speed will decrease the torque, and vice versa.

With comprehensive consideration, high-torque servo motor is chosen as the actuator of the light-weight robot with high moving speed. But a good balance must be made between high speed and high torque. As the overall body mass is limited, a light-weight mechanism is essential.

2.2 Design Principles

In order to solve the problems stated above, two design principles are proposed. One is to reduce the moment of inertia of each leg; the other is to design a proper leg mechanism which is good at fast swing.

To reduce the moment of inertia of the leg, lightweight materials such as aerolite and carbon fiber are selected as the part material and high power density servo motor is utilized. On the other hand, the driving motors should be arranged on the body instead of the leg.

Due to the time cost in each circle of acceleration and deceleration, it's hard to keep swift leg swing at a relatively high speed just by changing the motor's rotating direction. In mechanical design, crank-rocker mechanism and cam mechanism both can realize the swift leg swing at a high speed by changing the motor's fixed-direction rotation into the leg's reciprocating swing.

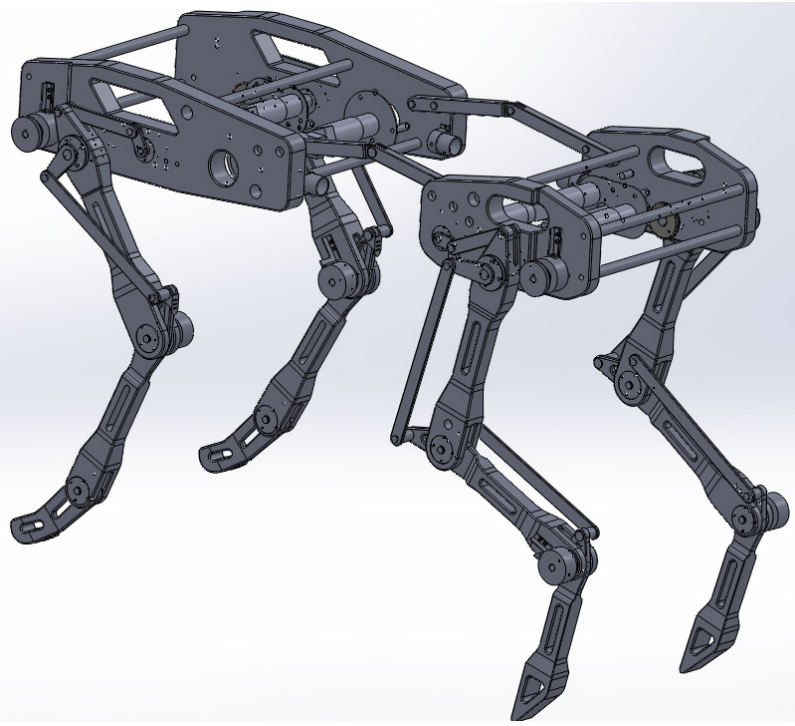

Fig. 1. The overall design of the robot

Based on the two design principles above, a novel mechanism using the crank-rocker mechanism as the transmission unit is developed, as *Fig. 1*. In order to reduce the shank's moment of inertia, the driving motor for the shank is coupled with the rotary shaft of the thigh by a clutch. That is to say, the driving shaft of the shank is also the rotary shaft of the thigh. Since the motor passes right the rotary shaft, zero moment of inertia is put on the thigh.

In order to achieve a better stress distribution, a connecting rod is laid between the thigh and the metatarsal forming a parallelogram to keep the thigh and the metatarsal parallel.

2.3 Setting the Dimension and Angle

Referring to the literature covering the bio-mimics of the cheetah, the dimension and diameter of all the bones is set. The swing angle range of the thigh and the shank is set by measuring the actual angle range of a running cheetah in the video-capture software, *Fig. 2*. Both the dimensions and swing angle ranges is given in *Table 1*.

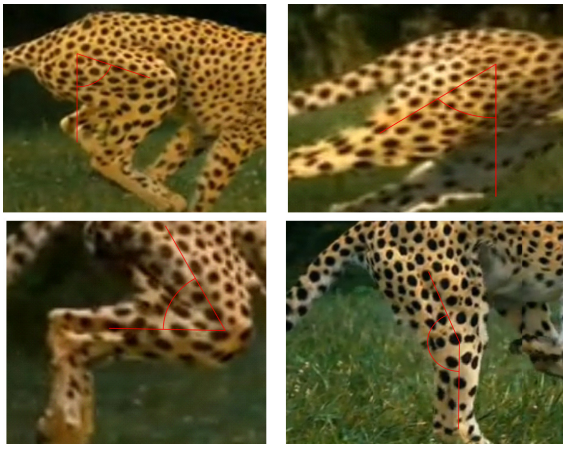

Fig. 2. Angle range of a running cheetah in the video-capture software

Table 1. Dimensions and swing angle ranges of the leg

Specification	Value
Shoulder swing range	130°
Knee swing range	100°
Thigh dimension	250mm
Shank dimension	230mm
Bone diameter	22mm

2.4 Transmission Unit Optimization

The four-link transmission unit can be simplified into the model depicted as *Fig. 3*. The four links are respectively the crank, the connecting rod, the rocker and the fixed link, and their length is the undetermined parameters a, b, c and d. Since the motor's motion is controlled, the angle between the crank and the fixed link θ_1 is known. The next is to find the relationship between θ_1 and the angle between the rocker (which stands for the thigh or the shank) and the fixed link θ_4. The folln be got, using the cosine theorem.

$$\begin{cases} e = \sqrt{a^2 + b^2 - 2ad\cos(\theta_1)} \\ \alpha = \arccos\left(\dfrac{d^2 + e^2 - a^2}{2ed}\right) \\ \beta = \arccos\left(\dfrac{c^2 + e^2 - b^2}{2ec}\right) \\ \theta_3 = \arccos\left(\dfrac{b^2 + c^2 - e^2}{2bc}\right) \end{cases} \tag{1}$$

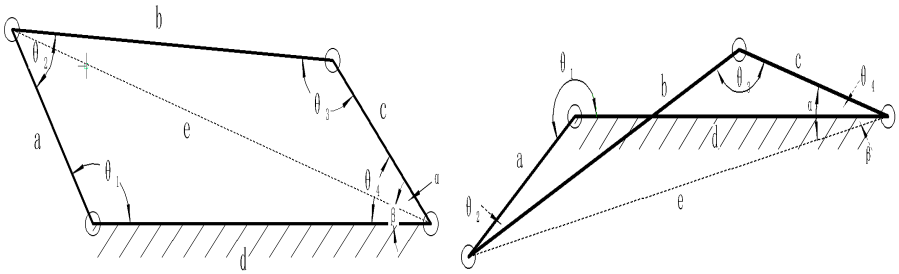

Fig. 3. (a) Configuration 1 of the four-link transmission unit (b) Configuration 2 of the four-link transmission unit

When the configuration is as the Fig. 2. (a),

$$\theta_2 = \arccos(\frac{a - d\cos\theta_1}{e}) + \arccos(\frac{b^2 + e^2 - c^2}{2be}) \tag{2}$$

$$\theta_4 = \alpha + \beta = \arccos(\frac{d^2 + e^2 - a^2}{2ed}) + \arccos(\frac{c^2 + e^2 - b^2}{2ec}) \tag{3}$$

When the configuration is like Fig. 2. (b),

$$\theta_4 = \beta - \alpha = \arccos(\frac{c^2 + e^2 - b^2}{2ec}) - \arccos(\frac{d^2 + e^2 - a^2}{2ed}) \tag{4}$$

The formulas (1)-(4) give the mapping from angle between the rocker (which stands for the thigh or the shank) and the fixed link θ_4 to θ_1.

According to the swing angle range got in the previous section, the following equations can be got for the two extreme positions.

$$\begin{cases} e = \sqrt{a^2 + b^2 - 2ad\cos(\theta_1)} \\ \alpha = \arccos(\dfrac{d^2 + e^2 - a^2}{2ed}) \\ \beta = \arccos(\dfrac{c^2 + e^2 - b^2}{2ec}) \\ \theta_3 = \arccos(\dfrac{b^2 + c^2 - e^2}{2bc}) \end{cases} \tag{5}$$

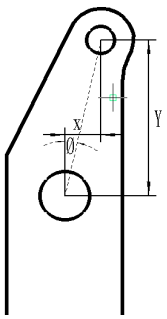

Fig. 4. The point of force application on the connecting rod

where φ is the angle between the center line of the rocker and the line from the center of rotation to the point of force application on the connecting rod. X and Y stand for the coordination of the point of force application on the connecting rod relative to the center of rotation. Using the simultaneous equations above, parameter *a* and *b* is set as follows.

$$a = \frac{\left[\sqrt{c^2 + d^2 - 2 \cdot c \cdot d \cdot \cos(150^\circ + \varphi)} - \sqrt{c^2 + d^2 - 2 \cdot c \cdot d \cdot \cos(20^\circ + \varphi)}\right]}{2}$$

$$b = \frac{\left[\sqrt{c^2 + d^2 - 2 \cdot c \cdot d \cdot \cos(150^\circ + \varphi)} + \sqrt{c^2 + d^2 - 2 \cdot c \cdot d \cdot \cos(20^\circ + \varphi)}\right]}{2}$$

At last the relationship between the driving torque M_1 and the equivalent torque M_2 transferred from the motor to the rocker can be calculated as follows. Ignoring the mass of all the rods, the connecting rod can be regarded as a two-force rod. The force applied on the two-force rod by the driving torque M_1 is

$$F = \frac{M_1}{l_1}$$

The equivalent torque M_2 on the rocker by the force F is $M_2 = F \cdot l_2$

Where $l_1 = a \cdot \sin\theta_2$, $l_2 = c \cdot \sin\theta_3$

Thus M_2 can be got, $M_2 = \frac{M_1}{a \cdot \sin\theta_2} \cdot c \cdot \sin\theta_3$

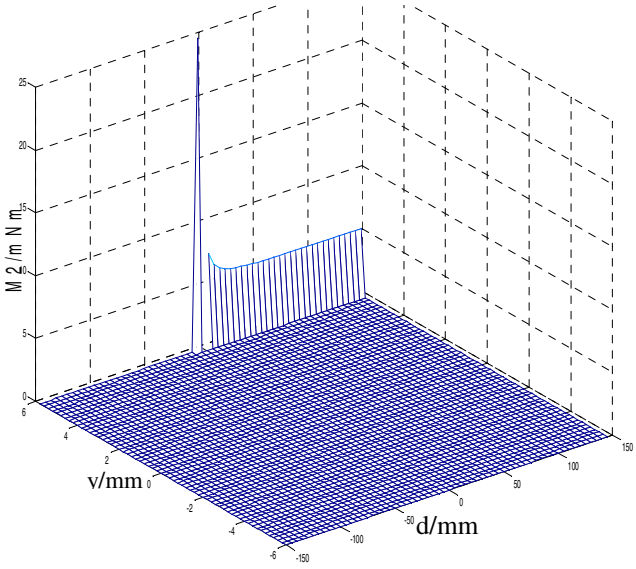

Fig. 5. MATLAB simulation of the equivalent torque M_2

Using the mathematic model proposed above, a curved surface standing for M_2 can be got with three variables x, y, d in the MATLAB as *Fig. 5*. By selecting the apogee of the curved surface, all the undetermined parameters a, b, c and d can be determined.

The point where most equivalent torque M_2 transferred from the driving torque M_1 is got(d=-100,y=6, x=10) in the MATLAB simulation. When x=10, y=6, d=-100, we can get a=29, b=171, c=51. The whole four-link crank-rocker mechanism is set.

3 Kinematics Analysis

Theories used to do kinematics analysis include the inverse transformation method, the geometric method, the Pieper method and so on. Compared to all the methods above, the screw theory has the following advantages.

（1） The position and orientation of the actuator can be described directly according to the pose of the joint axis. The solution is simplified by just finding out the rotational axis of the kinematic pair in each joint.

（2） Since a spinor represents a group of dual vector, it can be used to describe the position and orientation of a vector, the angular velocity and the linear velocity in kinematics, the force and torque in dynamics. Thus spinor is very simple in the description and clear in geometric concept.

（3） The kinematic model is more precise and efficient by using the screw theory compared to other theories.

The coordination of the leg is as *Fig. 6.*

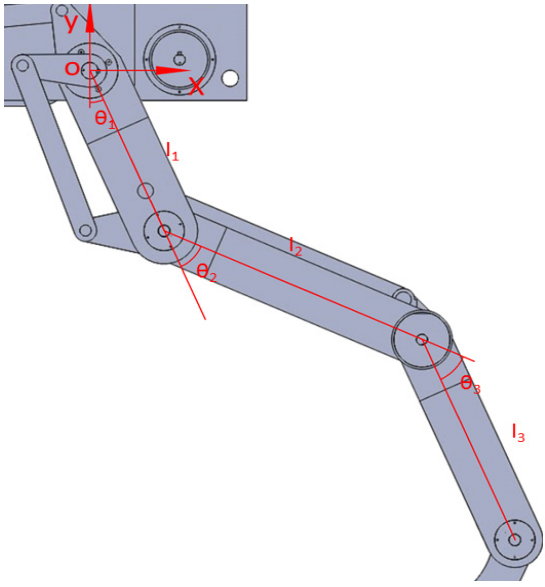

Fig. 6. The coordination of the leg

The initial pose matrix is $g_{ST}(\mathbf{0})$, according to the screw theory,

$$g_{ST}(\mathbf{0}) = \begin{bmatrix} & & 0 \\ & \mathbf{I}_{3\times3} & -(l_1+l_2) \\ & & 0 \\ 0 & & 1 \end{bmatrix}$$

All the angular velocity and position vector of each joint in the initial state are as follows,

$$\boldsymbol{\omega}_1=\boldsymbol{\omega}_2=\boldsymbol{\omega}_3=\begin{bmatrix}0\\0\\1\end{bmatrix},\quad \mathbf{r}_1=\begin{bmatrix}0\\0\\0\end{bmatrix},\quad \mathbf{r}_2=\begin{bmatrix}0\\-l_1\\0\end{bmatrix},\quad \mathbf{r}_3=\begin{bmatrix}0\\-l_1-l_2\\0\end{bmatrix}$$

Using screw theory, spinors of each joint $\boldsymbol{\xi}_1, \boldsymbol{\xi}_2, \boldsymbol{\xi}_3$ are as following,

$$\boldsymbol{\xi}_1=\begin{bmatrix}\boldsymbol{\omega}_1\\ \mathbf{r}_1\times\boldsymbol{\omega}_1\end{bmatrix}=\begin{bmatrix}0\\0\\1\\0\\0\\0\end{bmatrix},\quad \boldsymbol{\xi}_2=\begin{bmatrix}\boldsymbol{\omega}_2\\ \mathbf{r}_2\times\boldsymbol{\omega}_2\end{bmatrix}=\begin{bmatrix}0\\0\\1\\-l_1\\0\\0\end{bmatrix},\quad \boldsymbol{\xi}_3=\begin{bmatrix}\boldsymbol{\omega}_3\\ \mathbf{r}_3\times\boldsymbol{\omega}_3\end{bmatrix}=\begin{bmatrix}0\\0\\1\\-l_1-l_2\\0\\0\end{bmatrix}$$

The kinematic matrix of each joint $e^{\theta_1\hat{\xi}_1}, e^{\theta_2\hat{\xi}_2}, e^{\theta_3\hat{\xi}_3}$ are as follows,

$$e^{\theta_1\hat{\xi}_1}=\begin{bmatrix}c\theta_1 & -s\theta_1 & 0 & 0\\ s\theta_1 & c\theta_1 & 0 & 0\\ 0 & 0 & 1 & 0\\ 0 & 0 & 0 & 1\end{bmatrix}\quad e^{\theta_2\hat{\xi}_2}=\begin{bmatrix}c\theta_2 & -s\theta_2 & 0 & -l_1s\theta_2\\ s\theta_2 & c\theta_2 & 0 & -l_1(1-c\theta_2)\\ 0 & 0 & 1 & 0\\ 0 & 0 & 0 & 1\end{bmatrix}\quad e^{\theta_3\hat{\xi}_3}=\begin{bmatrix}c\theta_3 & -s\theta_3 & 0 & -(l_1+l_2)s\theta_3\\ s\theta_3 & c\theta_3 & 0 & -(l_1+l_2)(1-c\theta_3)\\ 0 & 0 & 1 & 0\\ 0 & 0 & 0 & 1\end{bmatrix}$$

So finally we get the kinematic matrix of the leg $g_{ST}(\mathbf{\theta})$ as following,

$$\begin{aligned} g_{ST}(\boldsymbol{\theta}) &= e^{\theta_1\hat{\xi}_1}e^{\theta_2\hat{\xi}_2}e^{\theta_3\hat{\xi}_3}g_{ST}(\mathbf{0}) \\ &= \begin{bmatrix} c\theta_{123} & -s\theta_{123} & 0 & l_1s\theta_1+l_2s\theta_{12} \\ s\theta_{123} & c\theta_{123} & 0 & -l_1c\theta_1-l_2c\theta_{12} \\ 0 & 0 & 1 & 0 \\ 0 & 0 & 0 & 1 \end{bmatrix} \end{aligned}$$

$$\begin{cases} x = l_1 s\theta_1 + l_2 s\theta_{12} \\ y = -l_1 c\theta_1 - l_2 c\theta_{12} \\ \varphi = \theta_{123} \end{cases}$$

Fig.7 and *Fig. 8* is the operating space of the leg and the angular of the thigh joint calculated in the MATLAB

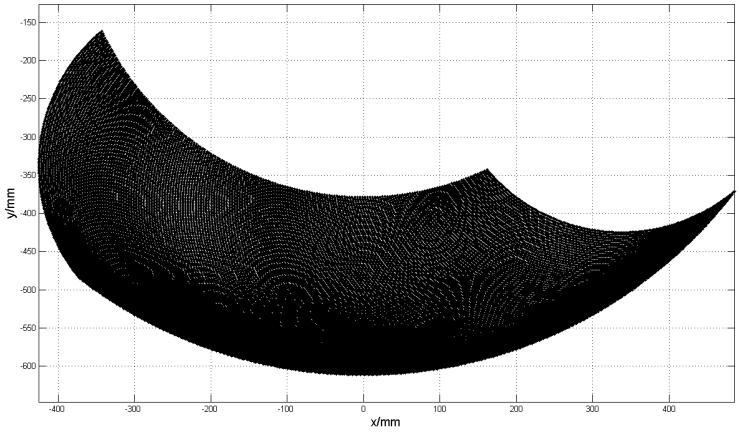

Fig. 7. The operating space of the leg

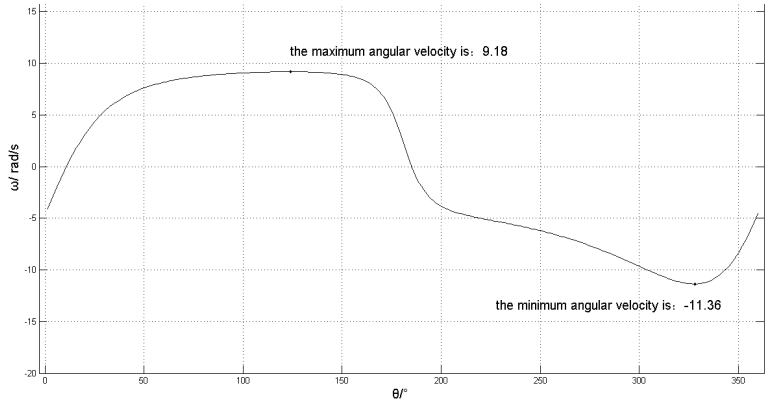

Fig. 8. The angular velocity of the thigh joint

4 Control System

The control system is based on a single centralized host-PC which is responsible for the entire high-level control part.The software system based on a multithread real-time operating system QNX is responsible for pose data acquisition, path planning,

algorithm scheduling as well as handling the internal messaging through PC/104 bus or RS-232.

The angular positions are messaured by potentiometers which send analog signals to the A/D convertor to get a digital signal. The pose of the robot is messured by the Inertial Measurement Unit(IMU). CANOPEN protocol is developed to transmit data between the motor controller and the host-PC via CAN bus to communicate with the actual robot.

The most outstanding advantage of this control system is the modularization of the system. All the cards composing the hardware system use the pc/104 standard, and is mass-produced by famous companies. In this way, A/D convertion, CAN communication and the host-PC is integrated into a robust and compact system easily. The framework of the control system is as *Fig. 9*.

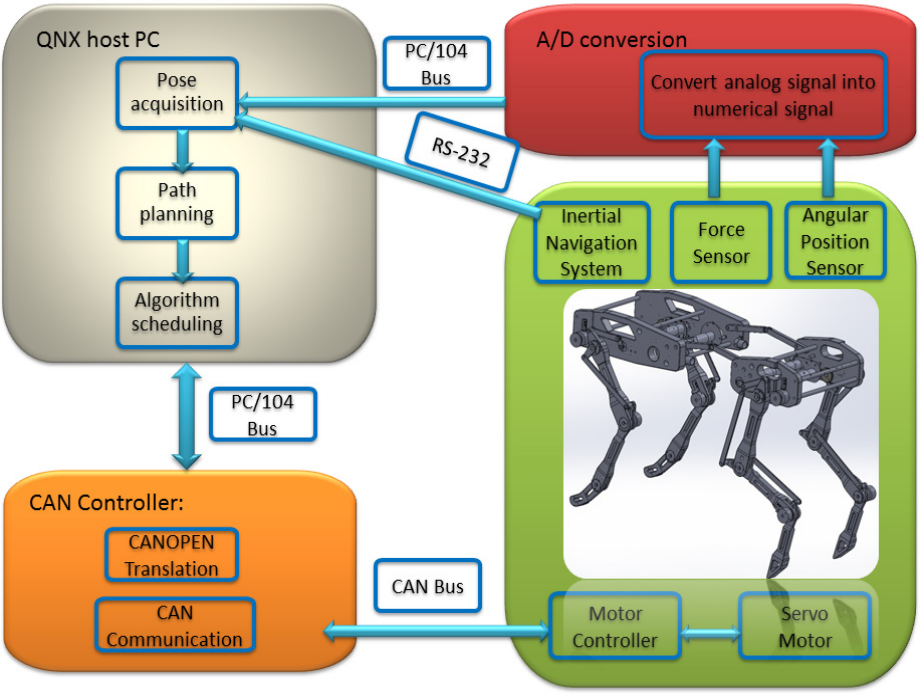

Fig. 9. The framework of the control system

5 Conclusion and Discuss

To achieve high speed and dynamic locomotion, two design principles are suggested to design a leg mechanism with low moment of inertia. A four-link transmission unit is proposed to change the motor's fixed-direction rotation into the leg's reciprocating

swing. Parameters optimization for the transmission unit is carried out to find out parameters to get the most driving force.

Currently, the prototype of the leg mechanism is confined to a planar model. In the following step, the abduction/adduction plane will be taken into account.

References

[1] Berns, K., Ilg, W., Deck, M., Albiez, J., Dillmann, R.: Mechanical Construction and Computer Architecture of the Four-Legged Walking Machine BISAM. IEEE/ASME Transactions on Mechatronics 4(1) (March 1999)

[2] Song, S.-M., Waldron, K.J.: Machines That Walk - The Adaptive Suspension Vehicle. The MIT Press (1989)

[3] Barai, R.K., Nonami, K.: Locomotion control of a hydraulically actuated hexapod robot by robust adaptive fuzzy control with self-tuned adaptation gain and dead zone fuzzy pre-compensation. Journal of Intelligent and Robotic Systems 53, 35–56 (2008)

[4] Buehler, M., Cocosco, A., Yamazaki, K., Battaglia, R.: Stable open loop walking in quadruped robots with stick legs. In: Proc. of the IEEE ICRA, Michigan (1999)

[5] Palmer, L., Orin, D.: Quadrupedal running at high speed over uneven terrain. In: Proc. of the IEEE IROS 2007, pp. 303–308 (2007)

[6] Hirose, S.: A study of design and control of a quadruped walking vehicle. International Journal of Robotics Research 3(2) (1984)

[7] Raibert, M., Blankespoor, K., Nelson, G., Playter, R., the BigDog Team: Bigdog, the rough-terrain quadraped robot. In: Proc. 17th World Congress of the International Federation of Automatic Control, pp. 10 822–10 825 (2008)

[8] Wooden, D., Malchano, M., Blankespoor, K., Howard, A., Rizzi, A., Raibert, M.: Autonomous Navigation for BigDog. In: Proc. of the IEEE ICRA, Alaska (2010)

[9] Ananthanarayanan, A., Azadi, M., Kim, S.: Towards a bio-inspired leg design for high-speed running. Bioinspir. & Biomim. 7, 46005 (2012)

A Six-Legged Walking Robot Inspired by Insect Locomotion

Yeongtae Jung and Joonbum Bae

Bio-Robotics and Control (BiRC) Lab.
School of Mechanical and Advanced Materials Engineering
UNIST, Korea
{ytjung,jbbae}@unist.ac.kr

Abstract. In this paper, a six-legged walking robot inspired by insect locomotion is discussed. To implement the walking pattern of insects, four-bar linkage based structure is proposed and its performance is analyzed by kinematic simulation. Two servomotors are applied to left and right sides of the robot, which allows smooth turns and a natural walking pattern by the phase difference between two motors. The main structure of the robot is manufactured by a rapid prototyping method with polypropylene material, and a micro camera is installed for real-time video transmission to show its potential applications.

Keywords: Bio-inspired robot, Legged robot, Insect locomotion.

1 Introduction

Small legged robots inspired by insect locomotion have been researched actively [1-6]. Legged robots provide advantages over the wheeled systems. For instance, they can walk over rough terrain with obstacles, and may have extreme abilities such as climbing vertical surfaces. To mimic such advantages to robot systems, the characteristics of insect locomotion were analyzed and applied to robots. The robot leg was designed by mimicking the morphology of the animal leg [2], and the outside surface of the robot was manufactured by mimicking the micro structure of the animal skin for specific purposes such as climbing [3]. The walking patterns of animal were also analyzed and applied for legged robots [4-6].

Small robots in millimeter scale also offer advantages over larger robots: the small size enables to be operated in environments where large robots would be impractical or impossible. The low cost allows them to be produced in large quantities, and large numbers of them can be networked to form highly mobile and robust sensor and communication networks.

Previously developed legged robots in millimeter scale have complicated structure with many actuators for improved degrees of freedom [2, 3, 5, 6]. However, since the functions of legged robots in millimeter scale are limited by its size, the complicated structure and many actuators may not be fully functioned. In this paper, a six-legged walking robot inspired by insect locomotion, which has only two motors, is proposed. To implement the walking pattern of six-legged insects, four-bar based linkage structure is applied and its performance is analyzed by kinematic simulation. Two

J. Lee et al. (Eds.): ICIRA 2013, Part II, LNAI 8103, pp. 257–264, 2013.

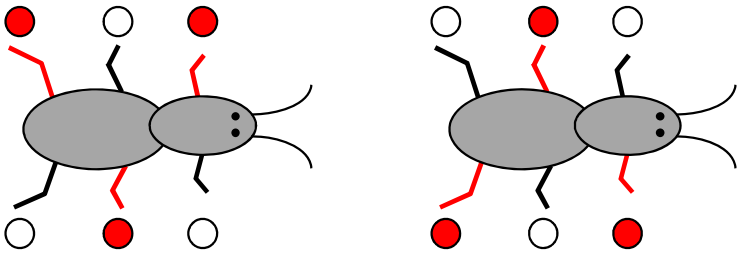

Fig. 1. Locomotion of six-leg insects for forward movement

servomotors are applied to left and right sides of the robot, which allows smooth turns and a natural walking pattern by the phase difference between the motors. The structure of the robot is manufactured by a rapid prototyping method with polypropylene material, and a micro camera for real-time video transmission is installed to show its potential applications.

2 Bio-Inspired Walking Pattern: Kinematic Analysis

2.1 Analysis of Six-Legged Insects Locomotion

Each leg of sig-legged insects such as ants or cockroaches can be moved independently for free motions, but a typical waking pattern for forward movement can be represented as shown in Fig. 1 [4, 6]. The red legs in the figure represent touching legs to the ground. The three legs in each side touch the ground sequentially; the front and rear legs touch the ground first, then the middle leg touches the ground. By repeating this sequence, a zigzag motion is generated, which enables stable forward movement.

2.2 Design of Linkage Structure for the Six Legs

To mimic the walking pattern of insects, four-bar linkage based structure is applied. Fig. 2 shows the leg structure by a four-bar linkage. The foot follows the red

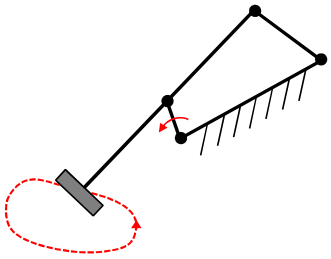

Fig. 2. Leg structure based on the four-bar linkage

trajectory with the rotation of the actuated link represented as a red arrow. With appropriate selection of lengths of each link, the trajectory of the foot can be changed.

In this paper, the four-bar based leg is installed to the middle leg of each side, and front and rear legs are linked with this leg. By actuating only the middle legs and linking the other legs with the middle leg, the number of required motors is minimized. The zigzag walking pattern in Fig. 1 can be generated by rotating the middle legs with phase difference.

2.3 Kinematic Analysis of the Linkage Structure

The trajectories of three feet of the proposed linkage structure are simulated by kinematic methods. The kinematics of the actuated middle leg is analyzed as a conventional four-bar linkage structure as shown in Fig. 3. Since a four-bar linkage has one degree of freedom, all kinematic information can be calculated by one input angle. The angles shown in Fig. 4 can be calculated with the input angle, θ, as follows:

$$\alpha = \arccos\left(\frac{g^2 + e^2 - a^2}{2ge}\right) \tag{1}$$

$$\beta = \arccos\left(\frac{e^2 + b^2 - h^2}{2eb}\right) \tag{2}$$

where $e = a^2 + g^2 - 2ag \cdot \cos\theta$. Then, the output angle is,

$$\psi = \pi - \alpha - \beta \tag{3}$$

Since all kinematic information of the actuated link can be determined by (1), (2) and (3), the positions of linked structures, which are front and rear legs, can be easily determined.

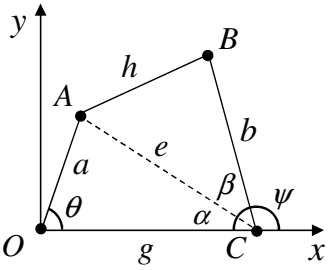

Fig. 3. Conventional four-bar linkage

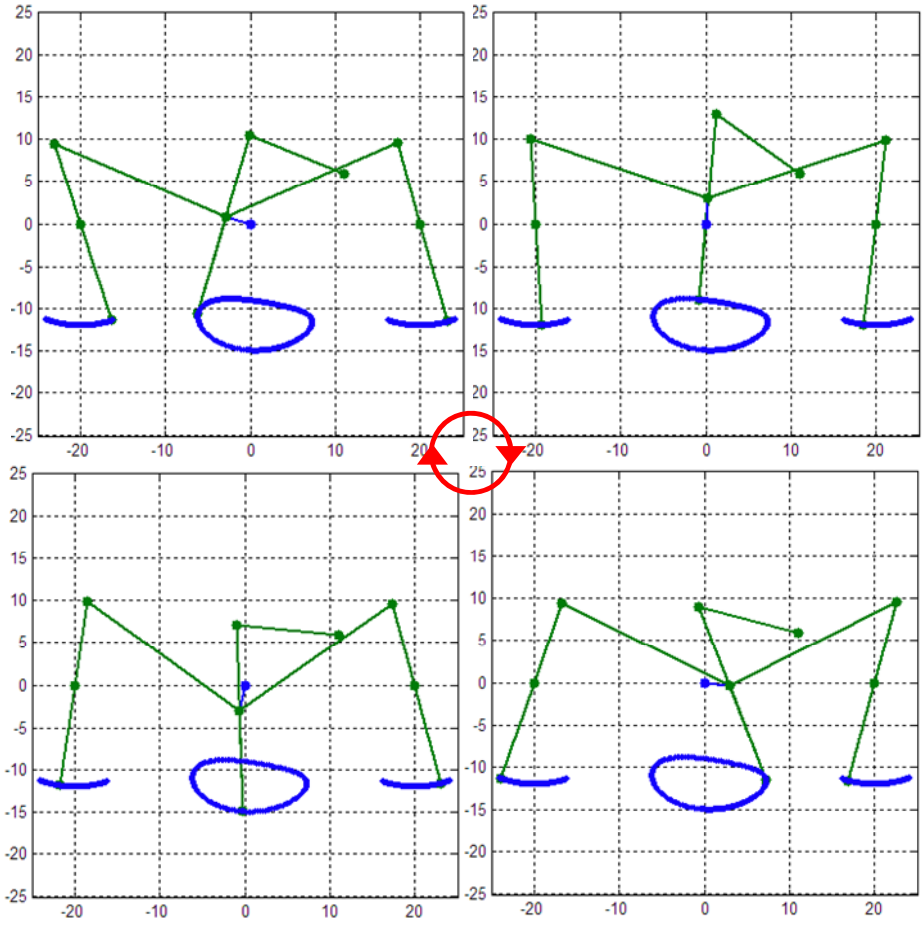

Fig. 4. Simulated trajectories of the feet

The simulated trajectories of the feet are shown in Fig. 5. The green lines and dots are the leg linkage structure, and the blue circle and arcs represent the trajectories of the feet. As shown in the figure, the actuated middle leg makes a circle-like trajectory, which mainly pushes the body forward, and the other feet act as supporting parts.

3 Design and Manufacturing

3.1 Mechanical Design and Manufacturing

Designing and manufacturing robots in millimeter size set unique challenges that result from size constraints. Especially, precise manufacturing small elements and assembling them into a robot take a lot of time and cost. Recent development in manufacturing technologies, however, enables quick and low-cost production. In this paper, a rapid prototyping method is applied to make the linkage structure.

Fig. 5(a) shows the Solidworks model of designed six-legged robot. The size of whole structure is about 25 × 50 × 15 mm. The body and legs of the robot were manufactured by rapid prototyping technology with polypropylene material. The links which connect the middle leg to the front or rear legs were made of carbon fiber composite considering the required stiffness for the robot weight and reliability. Fig. 5(b) verifies that the simulated trajectories in Fig. 4 can be realized by the proposed design.

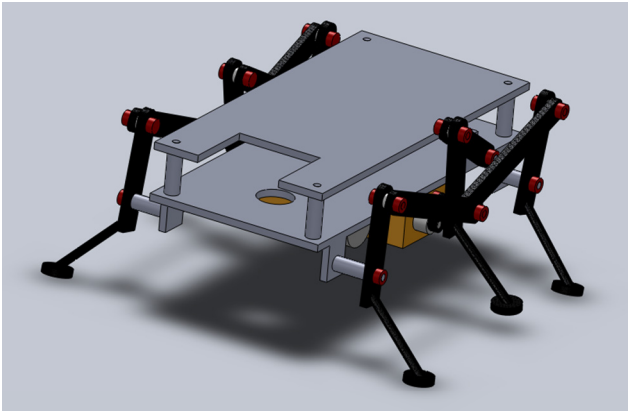

(a) Proposed design of the six-legged robot

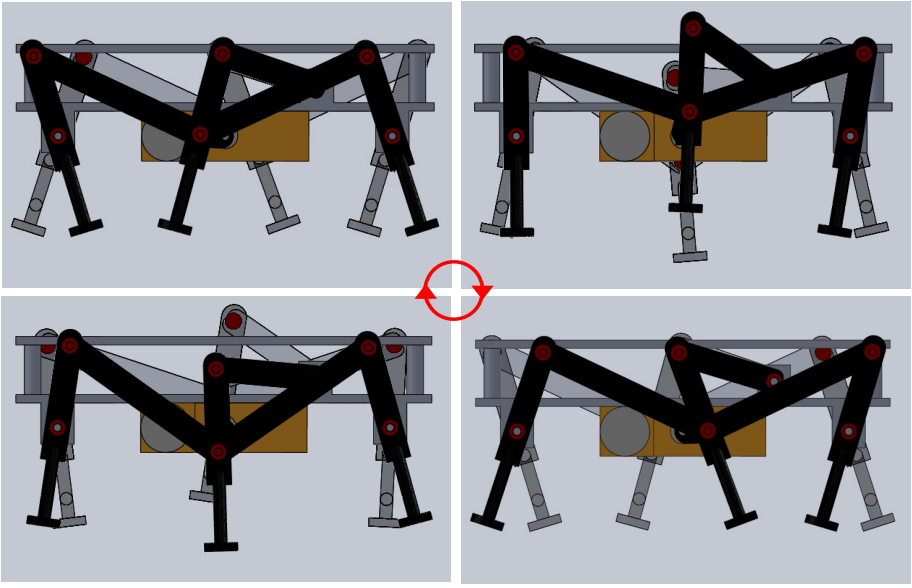

(b) Implementation of the insect locomotion

Fig. 5. Proposed design of the six-legged robot and performance verification

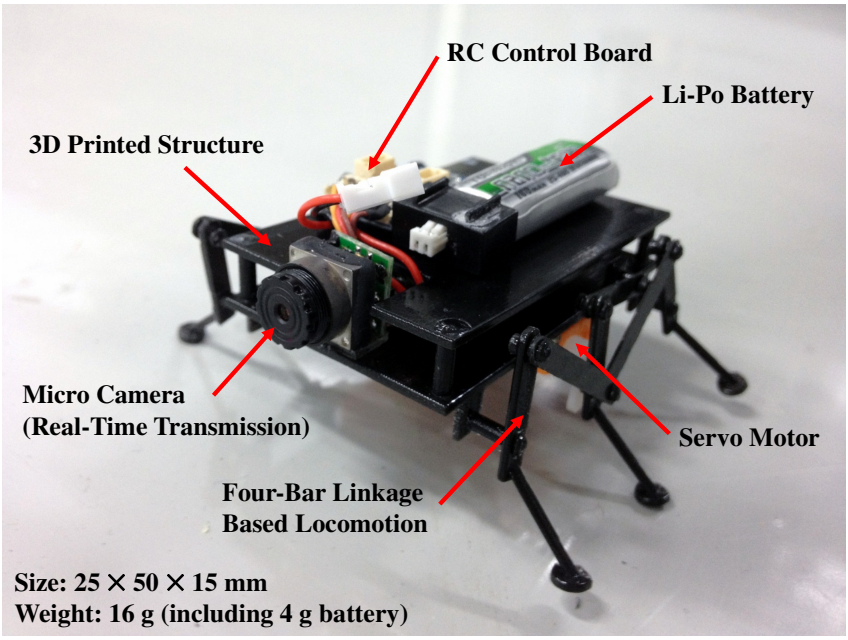

Fig. 6. Completed six-legged robot

3.2 Actuation and Electronics

At the millimeter scale, the size and number of actuators are limited by its small size. More actuators allow more degrees of freedom, but the increased weight and volume by the actuators decreases the mobility of the robot. In this paper, only two actuators are applied to implement the six-leg locomotion inspired by insect locomotion. The three legs in each side of the robot are moved by the actuated link in the middle which connected to a servomotor in each side. By putting 180° phase difference between two motors, the zigzag locomotion in Fig. 4 is implemented. Also, the robot turns left or right by rotating the actuators to different directions. For the potential application of the proposed robot, a micro camera is installed for video transmission in real-time. One cell Li-Po battery is used as a power source. The total weight of the robot is about 16 g including 4 g battery. The completed robot is shown in Fig. 6.

4 Experiments

The developed robot was tested in lab environment. The average walking speed was about 4 cm/sec, but it can be changed by the actuator speed or lengths of the linkage structure. The forward/backward walking and left/right turns were easily available as shown in Fig. 7. The screen in the right bottom side of Fig. 7(c) shows the transmitted video from the robot in real-time.

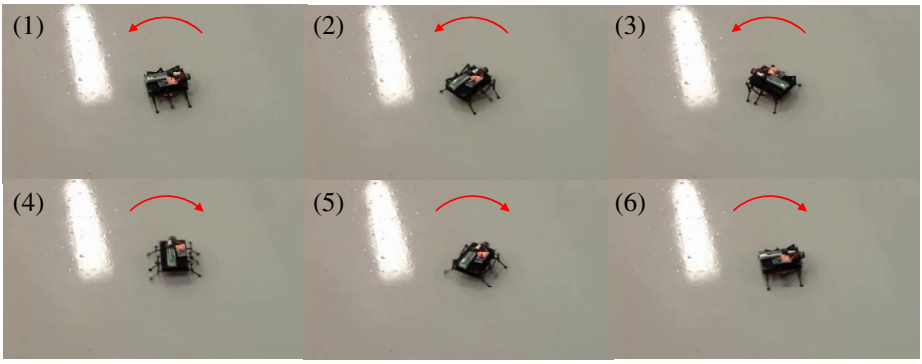

(a) Right/left turn

(b) Moving forward

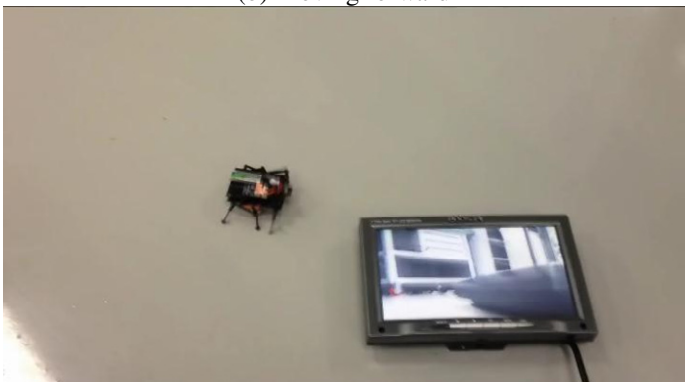

(c) Real-time video transmission

Fig. 7. Walking experiments and real-time video transmission

5 Conclusion and Future Work

In this paper, a six-legged walking robot inspired by insect locomotion was proposed. To implement the walking pattern of insects, four-bar based linkage structure was proposed and its performance was analyzed by kinematic simulation. Two servomotors were applied to left and right sides of the robot, which allows smooth turns and natural walking pattern by the phase difference between the motors. The structure of the robot was manufactured by a rapid prototyping method with polypropylene material, and a micro camera for real-time video transmission was installed to show its potential applications.

As a future work, the lengths of the leg structure will be optimized for fast and stable walking. Also, several legged-robots will be operated together with communicating each other with local wireless network.

Acknowledgments. This work was supported by the 2012 Creativity&Innovation Research Fund (Project No 1.120047.01) of UNIST(Ulsan National Institute of Science and Technology) and the Global Frontier R&D Program on <Human-centered Interaction for Coexistence> funded by the National Research Foundation of Korea grant funded by the Korean Government(MSIP) (NRF-2012M3A6A3056354).

References

1. Raibert, M.H.: Legged robots that balance. MIT Press, Cambridge (1986)
2. Nelson, G.M., Quinn, R.D., Bachmann, R.J., Flannigan, W.C., Ritzmann, R.E., Watson, J.T.: Design and Simulation of a Cockroach-like Hexapod Robot. In: IEEE ICRA Proceedings, pp. 1106–1111 (1997)
3. Cruse, H., Dean, J., Muller, U., Schmitz, J.: The stick insect as a walking robot. In: Proceeding of the 5th International Conference on Advanced Robotics, pp. 936–940 (1991)
4. Reinhardt, L., Weihmann, T., Blickhan, R.: Dynamics and kinematics of ant locomotion: do wood ants climb on level surfaces? J. Exp. Biol. 2426–2435 (2009)
5. Hoover, A.M., Steltz, E., Fearing, R.S.: RoACH: An autonomous 2.4g crawling hexapod robot. In: IEEE/RSJ International Conference on Intelligent Robots and Systems, pp. 26–33 (2008)
6. Kim, S., Clark, J.E., Cutkosky, M.R.: iSprawl: Autonomy, and the Effects of Power Transmission. In: Climbing and Walking Robots, pp. 859–867 (2005)

A Stable Walking Control of Two – Legs Biped Robot

Won Sung Ki[1,*], Byung Kyun Shim[1], Won Jun Hwang[2], Eun Uk Kang[3], Woo Song Lee[4], and Sung Hyun Han[5]

[1] Dept. of Advanced Eng., Graduate School, Kyungnam University
legna8588@naver.com
[2] Gyeongnam Technopark Industrial Co., Ltd.
[3] Ubtron Industrial Co., Ltd.
[4] SungsanarmDeco Industrial Co., Ltd.
[5] School of Mechanical System and Automation Eng., Kyungnam University

Abstract. The autonomous mobility for the biped robot M-HUMAN in the home environment is realized base on the development of a small stereo vision system, the recognition of floor and obstacles using plane extraction. The terrain is represented in a robot centric coordinate system without making any structural assumptions about the surrounding world. And the representation of a terrain map based on these observations, robot motion, and the generation of a walking path on the terrain map. We therefore believe, our approach is well suited for many different a home environment where no a priori information about the environment is given. The limitation of our system is that the terrain has to contain enough texture in order to obtain reliable stereo data.

Keywords: Humanoid Robot, Obstacle Avoidance, Factory and Home Environment.

1 Introduction

This paper describes our obstacle avoidance architecture allowing Walking Humanoid Robots to walk safely around in factory and home environment.

For a wheeled robot, many solutions on this subject have been presented in the literature using ultrasonic sensors or laser range finders and they mainly detect walls and relatively large obstacles around the robot. But solving the problem of obstacle avoidance for a humanoid robot in an unstructured environment is a big challenge, because the robot can easily lose its stability or fall down if it hits or steps on an obstacle.

Our strategy focuses on floor estimation, because in our view information about the floor is most important for a humanoid robot while walking. For this purpose, we developed a stereo-vision system and detect the floor plane using a randomized version of the Hough transform. The aim of this proposition is to establish a new industry involving autonomous robots and artificial intelligence.

* Corresponding author.

J. Lee et al. (Eds.): ICIRA 2013, Part II, LNAI 8103, pp. 265–273, 2013.

A main technological target of M-HUMAN is to autonomously explore and wander around in home environments as well as to communicate with humans.

2 Robot System Analysis

The M-HUMAN consists of 2 microphones for speech recognition and sound localization utilizing as well as speech synthesis play a big role in the communication capabilities of Robot. Audio and visual recognition results are memorized in a system that reflects the current environment. The stereo-vision system consists of 2 cameras as the robot's eyes and a module for stereo processing in the robot's head. Using its stereo camera M-HUMAN can compute distance to objects, extract a floor plane and generate a path for walking around obstacles.

M-HUMAN is able to communicate with network computers by utilizing its wireless LAN.

The M-HUMAN consist of 40 joints of the intelligent servo actuators. In real time, it enables M-HUMAN to walk adaptively on inclined and irregular terrain and allows the robot to re-stabilize immediately even when external forces affect its balance. Furthermore, a sub-system for real time step pattern generation realizes various walking patterns ranging from active and stable biped walking to moving flexibility.

Fig. 1. The image of the M-HUMAN

2.1 Structures

Base on the height of M-HUMAN, the Robot's structure and the main applications for the stereo system, the distant between 2 color CCD cameras is 4cm. This distant allows for reliable floor estimation up to a range of 3m and reliable distance estimation of other objects in the range of 20cm to 4m.

The system consists of an 8-bit micro processor with two 16Mbyte SDRAM units and a flash ROM. The stereo-vision module computes disparity between 2 CCD cameras by using block matching receives a pair of images from them. The main board of the CPU receives the resulting disparity image as a digital video signal. The stereo control parameters can be set between the main CPU and the 8bit CPU on board through a special serial communication link (see fig. 2).

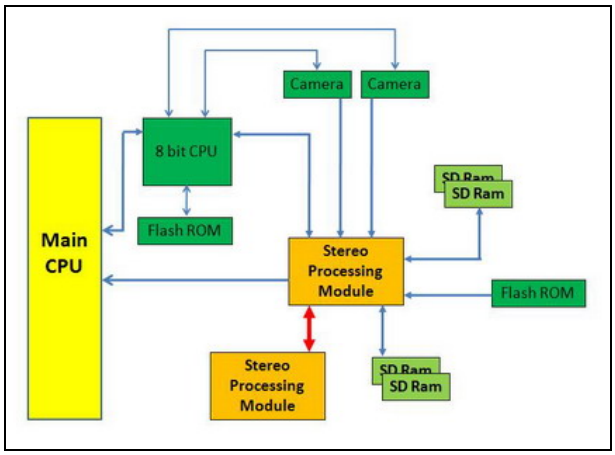

Fig. 2. System's hardware

The system's software briefly describes each module below (see Fig. 3)

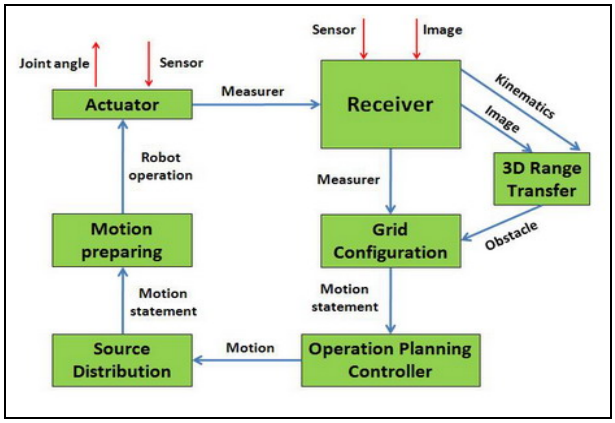

Fig. 3. The blocks function in system

(a) The Receiver module

The important point of this module is that to deliver disparity images with the corresponding kinematic transformations to the *3D Range Transfer* module. This module receives image data from the stereo-vision system and joint angle sensor data from each actuator.

(b) 3D Range Transfer module

This module aims at to convert all the 3D measurements to the floor coordinate system. The disparity image obtained from stereo-vision is first converted into 3D

range data using parameters from stereo calibration. Then a transformed data is applied for finding planes in the 3D data.

(c) The Grid Configuration module

It integrates information into a 2D grid configuration of size 3.5x3.5m around the robot. Image source: receiving either from the *3D Range Transfer* or odometer information from the Receiver module.

(d) The Operation Planning Controller module

Control mechanism where the behavior of the robot is determined autonomously according to internal states and external observations. A part of *Operation Planning Controller* is a *planning pioneer* that, given a goal point, computes a collision-free path leading to the destination. The *planning pioneer* system then generates walk and head motion commands which are sent to the *Source Distribution* which in turn send them to the *Motion preparing* and the *Actuator.*

The vision system (mentioned above) receives image from the two CCD cameras. These parameters are useful for computing 3D range data. The disparity is calculated for each pixel in the left image by searching for the corresponding pixel in the right image. An additional reliability image is calculated following criteria to reject results on above conditions. After block matching has been carried out, the matching score is calculated by interpolating scores near the highest peak. The sharpness of this peak corresponds to the available texture around this pixel and thus can be used as a reliability value for the disparity calculation. If there are other peaks with similar matching scores then the disparity computation is ambiguous and the reliability is set to a low value. (The matching score is compared with neighboring scores).

3 Operation

The method for estimating the parameters of a surface from a set of measured samples is called *Hough transformation.*

The *randomized Hough transformation* is the method to be applied if the number of sample points and parameters to be estimated is large, because apply the *Hough transformation* method is expensive in this case.

Firstly, the disparity is converted into 3D range data using the parameters from camera calibration and then a Hough transformation is applied to all data points. Apply the *randomized Hough transformation* selects sets of data points from which the surface parameters can be directly computed and records the result in a table. If many data sets yield the same parameters, a high score for these parameters is obtained.

The details of this method are showed in the flow chart in the Fig. 4 below.

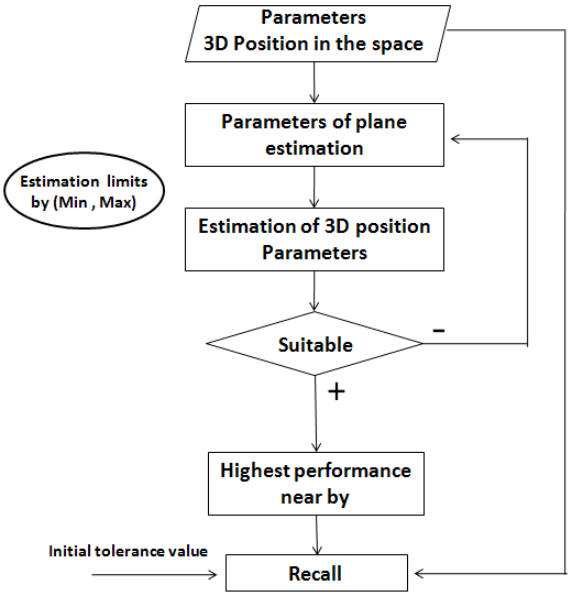

Fig. 4. Flow chart of plane extraction

The terrain map is a 2-dimensional occupancy grid centered on the current position of the robot (egocentric coordinate system). We maintain the (global) robot orientation and a small relative (x y) location of the robot within the cell at the center of the grid. Initially, all cells are set to a probability of 1.0 and time 0. Each grid cell contains the probability that an obstacle covers the cell and the time the cell was last updated.

The robot motion is defined as a coordinate transformation from one foot to the other whenever the robot performs a step. From this transformation a displacement and a change in orientation can be derived and applied to the position and orientation of the robot in the grid.

(a) If the robot stays within the cell at the center of the grid, no further actions have to be performed (see Fig. 5 (a)).

If the robot crosses the cell's boundary, we shift the grid by the number of cells the robot passed in each direction (Fig. 5 (b)).

In our implementation shifting the grid is actually performed by changing an offset into the grid data array so that no data has to be moved physically. After shifting the coordinate system of the occupancy grid, new cells at the border are initialized.

Define: the cell size Sc, the robot position (Rx, Ry) inside the grid, and the moving displacement (Mx, My), we obtain:

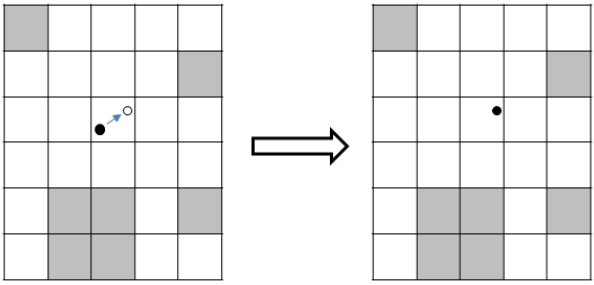

(a) Grid boundary moving limited

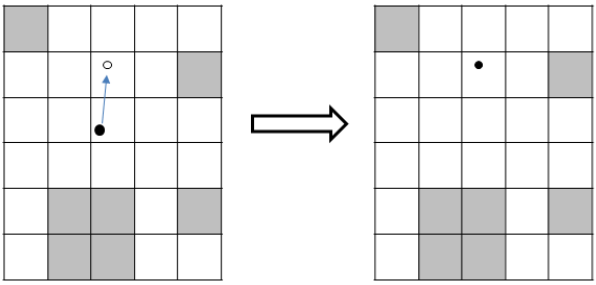

(b) Grid boundary moving passed

Fig. 5. Occupancy Grids update method

$$(Ax, Ay) = \left(\left(\frac{Rx + Mx}{Sc} \right), \left(\frac{Ry + My}{Sc} \right) \right), \tag{1}$$

The new robot position inside the grid becomes as follows:

$$(Mx - Sc \cdot Ax, My - Sc \cdot Ay) \rightarrow (Rx, Ry) . \tag{2}$$

The change in orientation $\_a$ is simply added to the global orientation of the robot (Fig. 6).

In an additional, searching for shortcuts along the found path, a smooth walking trajectory is realized.

The robot can find a path to a destination point by using the occupancy grid reflects the terrain around. The definition of each cell of the occupancy grid is a node connecting to neighboring cells and defines the path planning problem as a search problem on this graph.

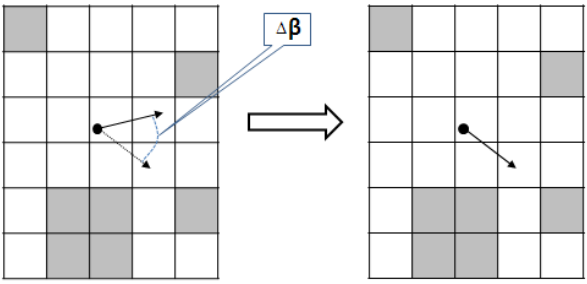

Fig. 6. Update method of Occupancy Grids
(Rotate operation)

Figure 6. Update method of Occupancy Grids (Rotate operation)

- The initial posture of the M-HUMAN is β (degree). The angular rotation is $\Delta\beta$.
- The posture after rotating is $\beta + \Delta\beta$

The potential $U(k,k')$ at node k to an obstacle k' is calculated as a repulsive potential from the obstacle probability $O(k')$:

$$U(k,k') = \frac{O(k')E_0}{\max(E_s, E(k,k'))}, \tag{3}$$

where

$E(k,k')$: Euclidean distance between k and k'
E_0 : A safety margin to ensure the robot does not steps on or hit any obstacle.
$U(k)$: The potential of a node k.

$$U(k) = \max_{k' \in K(k)} U(k,k') \tag{4}$$

(Chose the $U(k)$ as the maximum of $U(k,k')$ over all nodes k' close to node k)

Note that the $E(k)$ reflects the optimal estimated cost for passing through node k. By expanding nodes k with minimal $E(k)$ value, the optimal solution can be found.

The evaluation function is:

$$E(k) = D(n) + \beta \cdot C(n), \tag{5}$$

$$D(k) = \sum_{k_s}^{k} U(k) + L(k_{sta}, k), \tag{6}$$

$$C(k) = \hat{L}(k_{des}, k) = U(k_{des}, k), \tag{7}$$

where

$E(k)$: Resembles the path cost from start node k_{sta} to current node k

$C(k)$: Estimated path cost from the current node k to the destination node k_{des}

β : Weighting factor.

$L(k_{sta},k)$: Path distance between k_{sta} and k

$L(k_{des},k)$: Path distance between k and k_{des}.

4 Results and Conclusion

The autonomous mobility for the biped robot M-HUMAN in the home environment is realized base on the development of a small stereo vision system, the recognition of floor and obstacles using plane extraction.

The terrain is represented in a robot centric coordinate system without making any structural assumptions about the surrounding world. And the representation of a terrain map based on these observations, robot motion, and the generation of a walking path on the terrain map. We therefore believe, our approach is well suited for many different a home environment where no a priori information about the environment is given. The limitation of our system is that the terrain has to contain enough texture in order to obtain reliable stereo data.

References

1. Pagac, D., Nebot, E., Durrant-Whyte, H.: An evidential approach to map-building for autonomous vehicles. IEEE Transactions on Robotics and Automation 14(4), 623–629 (1998)
2. Wijk, O.: Triangulation Based Fusion of Sonar Data with Application in Mobile Robot Mapping and Localization. PhD thesis, Royal Institute of Technology, Stockholm, Sweden (2001)
3. Kuroki, Y., Ishida, T., Yamaguchi, J., Fujita, M., Doi, T.T.: A Small Biped Entertainment Robot. In: Proc. Int. Conf. on Humanoid Robots, pp. 181–186 (2001)

4. Fujita, M., Kageyama, K.: An Open Architecture for Robot Entertainment. In: Proc. Inernational Conference on Autonomous Agents, pp. 435–440 (1997)
5. Fujita, M., Kitano, H.: Development of an Quadruped Robot for Robot Entertainment. Autonomous Robots 5, 7–8 (1998)
6. Ishida, T., Kuroki, Y., Yamaguchi, J., Fujita, M., Doi, T.T.: Motion Entertainment by a Small Humanoid Robot Based on OPEN-R. In: Int. Conf. on Intelligent Robots and Systems (IROS 2001), pp. 1079–1086 (2001)

Design of a Time-Delayed Controller for Attitude Control of a Quadrotor System

Jeong Geun Lim and Seul Jung

Intelligent Systems and Emotional Engineering Laboratory
Department of Mechatronics Engineering, Chungnam National University
99 Daehak-Ro, Yuseong-Gu,
Dajeon, 305-764 Korea
jungs@cnu.ac.kr

Abstract. This paper presents the design of the time-delayed controller for the attitude control of a quadrotor system. Based on the measurement of acceleration data, the time-delayed control algorithm is implemented. Performances of the time-delayed control method are compared with the PD control method through empirical studies. Experimental results of the attitude control of a quadrotor system on the test platform verify that the performance of the time-delayed control method is better than that of the PD control method.

Keywords: quadrotor system, time-delayed control**,** attitude control.

1 Introduction

Recently research on unmanned aerial vehicles (UAVs) is enormously increasing due to interests of researchers in control and robotics communities. UAVs play an important role in dangerous areas like war zone for monitoring and surveillance. Long range UAVs have a conventional take-off and landing (CTOL) structure that requires large areas to take off while the vertical take-off and landing (VTOL) structure does not require long areas. Therefore, UAVs with VTOL structure have advantages over CTOL UAVs in terms of areas required for taking –off.

One of VTOL UAVs is a quadrotor system which has 4 rotors. Since quadrotor systems have 4 rotors, omni-directional movement is possible. Due to 4 rotors, a more stable hovering posture can be achieved. Therefore quadrotor systems can be used for surveillance or monitoring tasks in urban areas. Traffic accidents on the highway can be monitored and dangerous threat to special persons can be protected by monitoring vicinities.

These advantages lead to active research on quadrotor systems. Different designs of tilting mechanism of a quadrotor system for both driving and flying capabilities have been proposed [1,2]. Aggressive maneuvering control performances of quadrotor systems have been presented in the outdoor environment [3]. The precise position control performance of a quadrotor has been presented by University of Pennsylvania based on the accurate sensing of quadrotor position. The challenging passing control performance of an inverted pendulum between two quadrotor systems has been demonstrated by ETH Zurich.

J. Lee et al. (Eds.): ICIRA 2013, Part II, LNAI 8103, pp. 274–280, 2013.

The majority of research on quadrotor systems is about the attitude control that regulates three angles and an elevation. Neural network control methods have been applied to a quadrotor system [4]. The disturbance observer for the attitude control of quadrotor systems has been designed to reject disturbance [5].

In this paper, a time-delayed control method is used for the attitude control of a quadrotor system. The quadrotor system located on the test-bed is tested for the attitude control task by intentional disturbances. A weight is attached to the frame so that angles are disturbed. Experimental studies of attitude control are conducted to evaluate the control performance of the time-delayed control method.

2 Quadrotor System

A quadrotor system is one of under-actuated systems that have 4 rotors to represent the orientation of three angles, roll, pitch, and yaw($\phi\theta\psi$) and the position(xyz). A pair of two rotors rotates in the same direction to prevent from body rotation as shown in Fig. 1. Since quadrotor systems are an acceleration dominant system, simplified dynamic equations ignoring Coriolis force and other dynamic terms of a quadrotor system can be described as

$$\begin{aligned} m\ddot{x} &= f_{th}(\cos\phi\sin\theta\cos\psi + \sin\phi\sin\psi) \\ m\ddot{y} &= f_{th}(\cos\phi\sin\theta\sin\psi - \sin\phi\cos\psi) \\ m\ddot{z} &= f_{th}\cos\theta\cos\phi - mg \\ I_{xx}\ddot{\phi} &= \tau_{\phi} \\ I_{yy}\ddot{\theta} &= \tau_{\theta} \\ I_{zz}\ddot{\psi} &= \tau_{\psi} \end{aligned} \tag{1}$$

where m is the mass of the system, f_{th} is the total thrust force, g is the gravitational acceleration, I_{xx}, I_{yy}, I_{zz} are moments of inertia, and $\tau_{\phi}, \tau_{\theta}, \tau_{\psi}$ are torques about *x, y z* axis, respectively.

Dynamic equations for the attitude control of a quadrotor system can be further simplified to include elevation and orientation as

$$\begin{aligned} m\ddot{z} &= f_{th}\cos\theta\cos\phi - mg \\ I_{xx}\ddot{\phi} &= \tau_{\phi} \\ I_{yy}\ddot{\theta} &= \tau_{\theta} \\ I_{zz}\ddot{\psi} &= \tau_{\psi} \end{aligned} \tag{2}$$

Joint torques have the relationship with the thrust force of each rotor.

$$
\begin{aligned}
f_{th} &= F_F + F_B + F_R + F_L \\
\tau_\phi &= L(F_L - F_R) \\
\tau_\theta &= L(F_B - F_F) \\
\tau_\psi &= C(F_R + F_L - F_F - F_B)
\end{aligned} \tag{3}
$$

where L is the distance between the center of the mass and each rotor, and C is a constant factor.

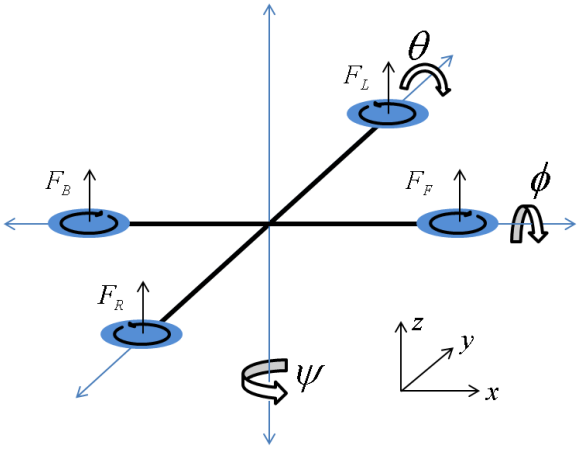

Fig. 1. Quadrotor system

3 Control Schemes

3.1 PD Control Method

A simple control method for the attitude control is proportional-derivative(PD) control. The reason for using the PD control method instead of the PID control method for the angle control is to avoid the accumulation error of integral action. Torques of roll and pitch directions are defined as

$$
\tau_{\phi,\theta}(t) = \hat{D}(K_P e_{\phi,\theta} - K_D \dot{q}_{\dot{\phi},\dot{\theta}}) - K_{D\psi}\dot{\psi} \tag{4}
$$

where $\hat{D}$ is the estimate of an inertia matrix, K_P, K_D are 2 x 2 PD gain matrices for the roll and pitch angles, $K_{D\psi}$ is the gain of yaw angle control. And the angle error is defined as

$$
e_{\phi,\theta} = q_d - q \tag{5}
$$

where $q_d = [\phi_d, \theta_d]^T, q = [\phi, \theta]^T$. The overall PD control block diagram is shown in Fig. 2.

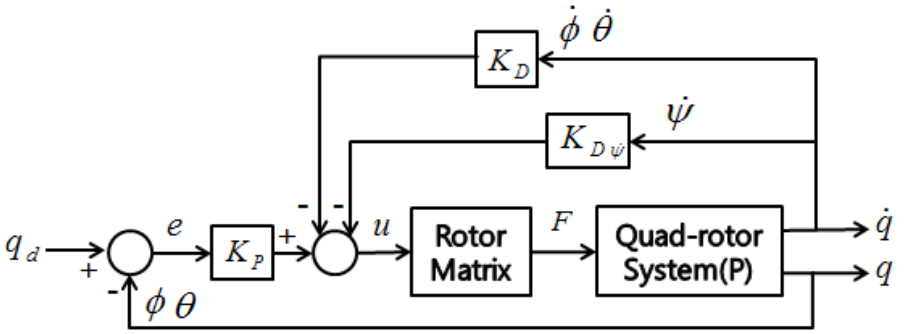

Fig. 2. PD control block diagram for the attitude control of a quadrotor system

3.2 Time-Delayed Control Method

The time-delayed control(TDC) method has been known as a robust controller to reject disturbance to the system. The TDC method has been effectively used in controlling robot manipulators. The idea of TDC is so simple that it uses the previous torque information to cancel out all the uncertainties in robot dynamics.

There are two major concerns for the effective TDC. One is the estimation of acceleration term and another is the estimation of inertia term. The estimation of an acceleration term from the position measurement is quite noisy that it would be better not to use the estimation if the estimation is noisy. Inertia estimation is a kind of gain adjustment so that it can be considered as a constant gain. Since the quadrotor system is assumed to be an acceleration dominant system, the estimation of acceleration signal plays a major role in the control law.

The time-delayed control law is given as

$$\tau_{\phi,\theta}(t) = \hat{D}(K_P e_{\phi,\theta} - K_D \dot{q}_{\phi,\dot{\theta}}) - K_{D\psi}\dot{\psi} + \left[\tau_{\phi,\theta}(t-\lambda)C_R - \hat{D}\ddot{q}(t-\lambda)\right]Q\frac{1}{C_R} \quad (5)$$

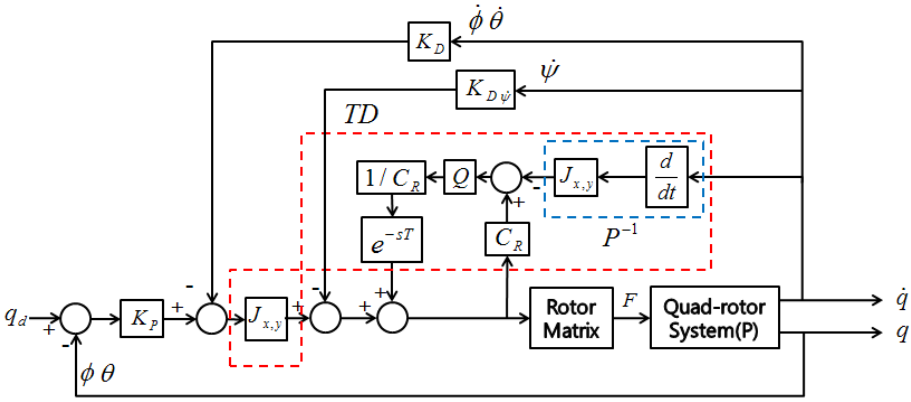

Fig. 3. Time-delayed control block diagram for the attitude control of a quadrotor system

where λ is the sampling time and Q is the filter and C_R is a constant. The control block diagram of the time-delayed control method is shown in Fig. 3

4 Experimental Studies

4.1 Experimental Setup

To test the performance of controllers, a test-bed is designed to hold the quadrotor system as shown in Fig. 4. Controllers make the quadrotor system balance on the testbed. Two angles, roll and pitch angles are required to be controlled. To test the robustness of the controller to the disturbance, a weight is intentionally installed between two frames so that the movement of a weight may affect both angles.

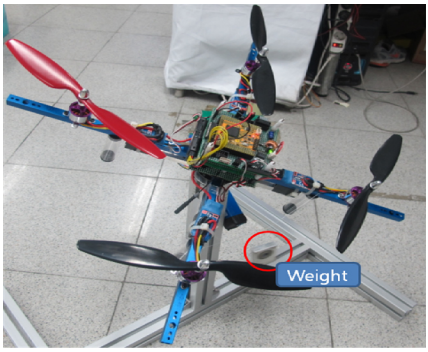

Fig. 4. Quadrotor system with a weight between two axes

4.2 Experimental Result

1) Attitude control without disturbance

Firstly, the performance of hovering control of a quadrotor system is tested. The PD control method is tested and its results are plotted in Fig. 5 (a). Roll and pitch angles are well controlled within ± 0.05 degrees. Better hovering performances by the time-delayed control method are observed from Fig. 5 (b). Roll and pitch angles are controlled within ± 0.01 degrees.

2) Attitude control with disturbance

Next experiment is to test the robustness of the controller. A weight is dropped intentionally to disturb the system. Fig. 6 shows the resultant attitude control performance by two control methods. Within 55 seconds, the weight is dropped 4 times. Each drop of the weight, the PD controller successfully maintains the balance as shown in Fig. 6(a). However, the recovery time and the error are larger than those of the time-delayed control method. The error is about 0.2 degrees, but the error for the time-delayed control is about 0.05 as shown in Fig. 6(b). The time-delayed control method makes the system recover faster so that disturbance effect is minimized.

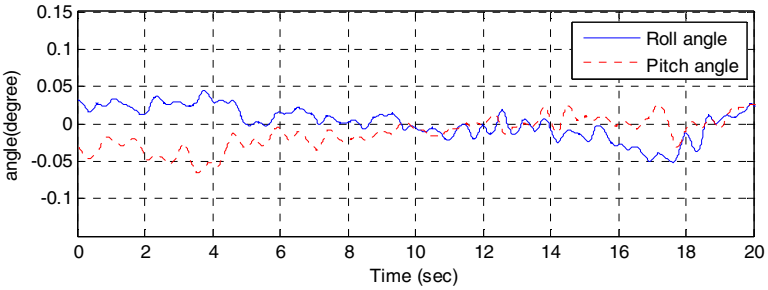

(a) PD control result

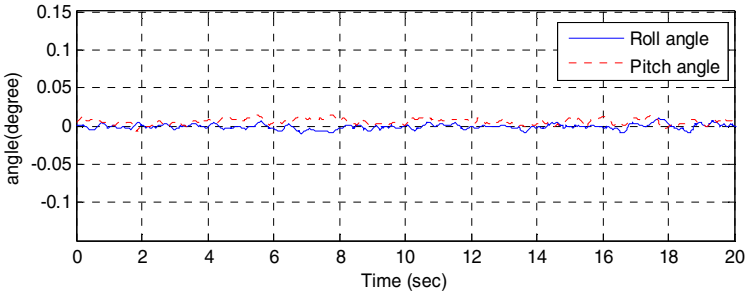

(b) Time-delayed control result

Fig. 5. Hovering control performance of a quadrotor system by two control methods

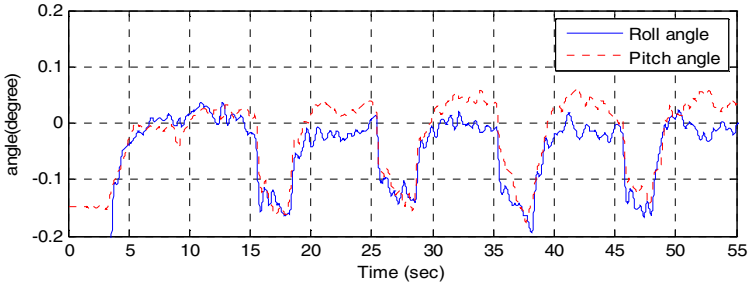

(a) PD control

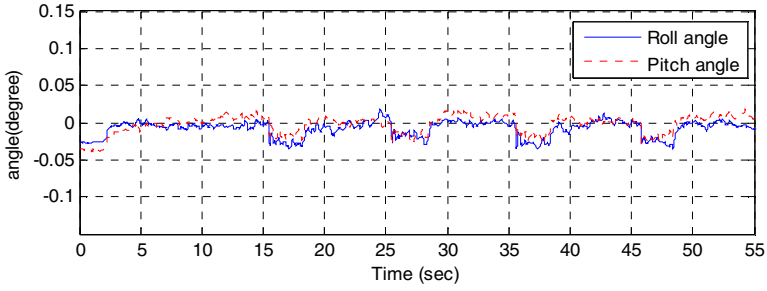

(b) Time-delayed control

Fig. 6. Hovering control performance of a quadrotor system by two control methods when disturbance is applied

5 Conclusion

In this paper, the attitude control of the quadrotor system is controlled. Roll and pitch angles are controlled by PD and time-delayed control methods. Their control performances are compared empirically. The time-delayed control method shows the outperformed control performance over the PD control method, especially when the disturbance is applied to the system. The time-delayed control method can be applied to the hovering control of the quadrotor system in the future.

Acknowledgments. The research has been supported by the 2013 Korea Research Foundation and the center for autonomous intelligent manipulation (AIM) for service robots of the MKE (The Ministry of Knowledge Economy), Korea, under the Human Resources Development Program for Convergence Robot Specialists support program supervised by the NIPA (National IT Industry Promotion Agency) under NIPA-2013-H1502-13-1001.

References

1. Oner, K.T., Cetinsoy, E., Unel, M., Aksit, M.F., Kandemir, I., Gulez, K.: Dynamic model and control of a new quad-rotor unmanned aerial vehicle with tilt-wing mechanism. World Academy of Science, Engineering and Technology 45, 58–63 (2008)
2. Jeong, S.H., Jung, S.: Novel design and position control of an omni-directional flying automobile (Omni-flymobile). In: ICCAS, pp. 2480–2484 (2010)
3. Huang, H., Hoffmann, G.M., Waslander, S.L., Tomlin, C.J.: Aerodynamics and control of autonomous quad-rotor helicopters in aggressive maneuvering. In: IEEE Conf. on Robotics and Automations, pp. 3277–3282 (2009)
4. Dierks, T., Jagannathan, S.: Output feedback control of a quad-rotor UAV using neural networks. IEEE Trans. on Neural Networks 21(1), 50–66 (2010)
5. Jeong, S.H., Jung, S., Tomizuka, M.: Attitude Control of a Quad-rotor System Using an Acceleration-based Disturbance Observer: An Empirical Approach. In: AIM, pp. 916–921 (2012)

Brain Flow in Application for SYNAP New Robotic Platform

Alberto Rovetta

Politecnico di Milano, Dept. Mechanics, Via Lamasa 1, 20156 Milan, Italy
alberto.rovetta@polimi.it

Abstract. This paper deals with SYNAP, a new robotic platform, able to interpret the actions of the persons operating in its environment. It uses not a deterministic logic, as usually in industrial and not industrial robotics. It adopts a structuralistic logic, where reality experience is executed with the personal structure, which is different from person to person.

SYNAP uses nodes structures, with a total participation of all sensors and actuators.

Application and realization is reported here, in its first phase.

Keywords: Robotics, brain, emotional robotics, interface, robotic special intelligence.

1 Special Intelligence

The POLIMI Platform has developed the new version, called SYNAP (Synaptic Neuronic Applicable Platform) , characterized by special intelligence. The structure of the platform is defined by many independent sensors connected to a central PC via software, which uses independent and interconnected nodes. Any information of each sensor reaches directly the central computer and, based on the data processing, controls the movement. The entire system is monitored on the screen of the Platform and can also be seen from the remote computer, from tablet, from cellphones, on the Internet. SYNAP goes a step further, and adapts to the new frontiers of bio robotics and modern neurology.

SYNAP acts in presence of human intellectual perception and logic, feelings and emotions. SYNAP uses a special node with logic, born from structuralism, which is pervading in recent years all the human sense, natural and theoretical sciences, philosophical and engineering disciplines, neurological and physical knowledge.

The logic of materialism considers as the only reality is external nature to man, who lives this reality as a passive protagonist. The idealist logic (especially by Plato and Aristotle [1] as many works in Thomas Aquinas and Kant to Hegel) considers instead the IDEAS as existing and reality must adapt to the ideas that encloses the whole. Today neither setting is accepted.

Today is born structuralism, where perception and intelligent understanding of things and reality are different from individual to individual. Everyone structures own life according to the experience of every moment.

J. Lee et al. (Eds.): ICIRA 2013, Part II, LNAI 8103, pp. 281–288, 2013.

Structuralism knows that reality is perceived and felt differently by each person, depending on his / her sensory system, nervous system, memory capacity and interpretation, conscious and unconscious experience. Materialism and idealism do not consider unconscious and instinctive, which instead have a great importance in human life. SYNAP wants to be the first robot (or robotic system) that works with structuralism. It uses the same hardware used by POLIMI PLATFORM, uses the same nodes, as if they were SYNAPses and the dendrites of the human brain, and uses them in a new way, by interpreting the patterns of structuralism.

SYNAP behaves differently depending on the reality surrounding human beings who interact.

The human person interprets reality, not with digital values, but with models created by each person through the senses, and the models are filtered and modified in each step by the sense organ. They transduce signals to the brain analysis, providing synthetic information, short and compact, so that the information is present in few elements.

SYNAP uses self-learning to grow and increase its basic statistical information and to become more and more safe and reliable

The perception of SYNAP can be changed according to the environment, to the people around, to the developed and expected events. SYNAP will have its own special intelligence, adaptive, not as a machine but as an object built by man for man, with a special intelligence gained from reality and life through restructuring.

The restructurism involves processing signals, derived from each sensor in order to provide the values of the models and the signals as indices of perception and communication. They are sent to all nodes of the computer to be processed by the network of nodes, passing through the nodes of the "special intelligence" that uses new logical models of interpretation.

The "new logic models" are nothing more than the recovery of some aspects of formal logic, ancient and ever born alive. They connect logic action, affection, emotion, without any distinction between quality and quantity, and application of brain control goes back to the basic principles of Aristotle, who first spoke.

2 Scientific Basis

Intelligent robotics exceeds mechanism theory and mechatronics of the years 1970 to 2000, and must use all the cultural bases. Scientific knowledge of the sensory, statistical methodologies that validate the results in an immediate time, developments in neurology and neuropsychology have revolutionized knowledge about the functions of the brain. They are bridging the gulf of ignorance that marked the years from 1980 up to about 1995. See bibliography [2,3,4,5,6,7]. The robotics applied to particular screens has exploded, adding large capacity computing, storage and flexible movement. Nothing that looked like some real intelligence out by man, however [8].

In the use of intelligent robots, with some really special symptom of intelligence, the robot must be the expression of knowledge. Human intelligence is not reproducible and appears to many as a divine gift. The next essential step for a new intelligent robotics is the application in daily life. Everyday life is the assessment factor of validation, and is effective for both aspects of utility, economy, respect for people, improving quality of life.

This raises the need for a different cultural setting, which we can call a MODERN RENAISSANCE for robotics. In the Middle Ages in the West have created immense knowledge bases in monasteries and royal palaces of kings, to open everyday culture. They have made great strides in the know, for design, and for quality of life (see Leonardo da Vinci). Today the robotics with special intelligence must be the most advanced expression of today's culture. Robotics must absorb the science and physics, economics and statistics, psychology and neurology, brain science and the study of degenerative conditions such as extreme. Robotics should offer a machine that lives with its some autonomy, perhaps strange perhaps unpredictable, but free and acceptable. Today the robotics with special intelligence must fit in homes, factories, theaters and nightclubs, supermarkets and hospitals, to give its contribution to the autonomous better quality of life. Intelligent robotics has to understand the wonderful quality of life today, foster its development, and not be content to ape tears, smiles and motions. Robotics with special intelligence must face the real world and be able to overcome every obstacle.

3 Objects

The object "intelligent robot" must also express the human tension towards the development of mind, brain. It will catch the reality towards humans happiness and well-being. An "intelligent robot" absolutely must be able to act as a support to the human when the shares are strenuous, difficult and extremely risky, dangerous in everyday life. It must not, however, constitute an element of anxiety and fear, and must not have a humanoid form, because very often the humanoid form is due to a subtle mental and behavioral uncertainty. Many times human shape causes anxiety in the human , much more if disabled.

What compels a robot to look like a man? Nothing.

Robot must therefore have its own operational personality with motion characteristics, behavior, perception, self-consciousness, although very limited.

Leonardo da Vinci in 1400 - 1500 with his technique has revolutionized the world, although very few people have been immediately aware of, and applied a new way of thinking, linked to free creativity, innovative, with the experimental verification of any theoretical result. His great philosophy has expanded over the centuries until the new millennium, and still his modernity amazes. Leonardo also drew robots, mostly automatic mechanisms, and with the intent to engage people, rather than astonish. It was the first example of intelligent robotics, because it explored a totally unexplored field, as a new planet. Now, in 2013, the new world explored is the BRAIN, which is mainly the human brain, and robotics first may offer active and cooperative tools for a new step forward in the cooperation between man and nature, the experience with life and new systems and creativity explosions built with the job. The concept developed in SYNAP is based on the use of logical interconnected rings, which contain the reality of the person, the nature of the environment and the reality, towards the construction of robots that interact continuously with special intelligence. SYNAP may be partially compared to traditional robotics, where the robot is a rigid entity in its behavior and not able to acquire cooperation and emotional behavior and experience, but only from programming assets. SYNAP builds step by step its reality,

as is the case for humans, gaining experience and processing all data with different perceptual models.

4 Description of SYNAP (Synaptic Neuronic Applicable Platform)

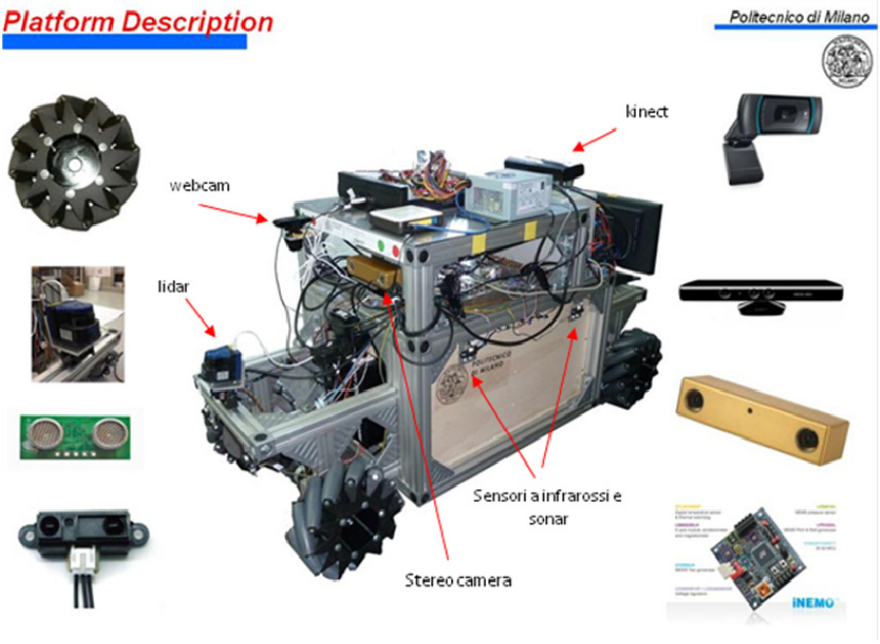

Fig. 1.

The Figure 1shows the Polimi Platform SYNAP, with the webcam, the lidar, the infrared sensors, the ultrasonic sensors, the Kinect, the stereo camera, the omnidirectional mecanum wheels. The safety is guaranteed.

The mental spaces that led to the design of SYNAP were born in the search for a robotic system that interprets the face, words, movements, and also the intentions and actions of human beings, adding a real active cooperation to the robotic machine. The concepts are spatial, in the sense that concepts are not running the traditional engineering method, the consequentiality after execution of the project, but working for cyclic rings linked together, as in a necklace. The strength of the series lies in its ability to add rings, and bring new systems, attached to the preferred or more suitable ring. SYNAP does not want to look like a humanoid robot, with face, legs, arms (see Author website, multipurpose hand 1979 Gilberto, 1981, prosthesis, 1984, etc.). Its genetic shape is to have a horizontal drooped body, that is linked to a movement parallel to the ground. The movement in the version examined here occurs with 4

wheels, and have been studied and developed versions with 6 legs, also at a stage of intelligence so far.

SYNAP has four omnidirectional wheels, such that the robot platform can move in any direction in the floor, with a control that allows the pure rotation or pure translation, and of course the rotation and translation motion.

4.1 Exploration and Automatic Navigation, with Perfect Understanding of the Environment and People

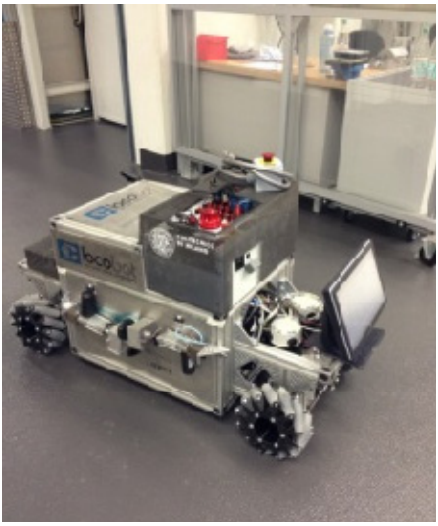

Fig. 2.

The Figure 2 shows SYNAP during its navigation, after exploration, with the action of all sensors and actuators.-

SYNAP explores by the radar 3D (and 2D) the whole environment, a webcam explores the ceiling and stores the main data; a stereo camera explores stores and analyzes all side walls and pulls out the main features. All results come in the memory of the PC board and are stored. A special tool widely used, called Kinect, is adopted to recognize people in their handling of arms, legs, and also to recognize the faces and expressions. These data are part of the exploration of the environment where SYNAP is chosen to operate. If the environment changes, SYNAP runs a new scan and stores all the obtainable data.

Simple algorithms traditional as well as new ones are applied, beyond the formal logic that is expressed with usual logical determinism, even with statistical forecasts.

Each received, read and interpreted data must pass through the filter of a logical structure non-formal and must obtain an index of validity and truth, which is now used in the application. In this way, it is like building a "mental space" for the robot with a "special intelligence" that must be filled, and must be made active and positive. The new "intelligent special robotics" can free the worker, the designer, the user, every person who interacts with the robot, from the bondage of the obligation of an asset.

4.2 Emotions in Action and Sharing

SYNAP presents a software connection to the sensors and actuators using the system ROS, applied with operating "nodes", so as each sensor runs independently of the other. In the same time SYNAP integrates data into an active and simple network, and each new sensory element can be added. SYNAP shall participate in personal,

emotional state of the person with whom it interacts, or with the emotional state of the group of people who interact, and also to the physical environment in which it operates. To perform these operations in an interactive way, it must be used a non-deterministic logic that has been designed and built in a "special node" of the network of data and commands in the computer. This node only performs with algorithms, which are enriched by the experience of SYNAP. The structure of the "intelligent node" can be expanded with the experience of SYNAP and all other similar robots in operation, which are networked via the Internet and via satellite with active tabs positioned in intelligent robot.

4.3 Expression of Emotion and Participation by SYNAP

SYNAP can express itself in relation to the input it receives from the outside world, consisting of the persons, from environment, from other SYNAP and other machines. The expression of SYNAP can be understood as a set of movements and gestures, voices and sounds issued, possibly with music, flashing and stained with led, by action of mechanical and mechatronic systems placed on the platform, and also from any external interfaces to the SYNAP platform placed in the environment of existence. It must therefore be build a reaction protocol of SYNAP that best shows its expressions and makes clear its reactions.

5 Applications

The man possible SYNAP applications for normal use are here reported.

1. Manufacturing industry for moving parts
2. Neurodegenerative cares
3. Cleaning of supermarkets
4. Cleaning of offices
5. In restaurants
6. In the stations
7. Robotics platform for space exploration
8. Building construction
9. Replacement of items in supermarkets
10. Industry: logistics
11. Mobility in hospitals
12. Transport in airports
13. Assembly in manufacturing industry
14. Buggy self-guided

6 General Specifications of SYNAP for Normal Applications

The INPUT may be endless, and yet the main categories are the following: type of person view, with levels of hierarchy and authority on the type of movement; type of voice command embossed, with level of significance on the function of SYNAP; type of emergency declared from zero to maximum, with action on the type of movement of SYNAP; kind of SAFETY imposed and verified, with management of the

movement of SYNAP. The outputs are therefore, for now, only 4 categories, in turn divided into sub-categories, which can be reported in a table attached for easy reading. Even this INPUT has different levels, between zero 0 and one 1, and the absolute value depends on the scale that SYNAP proposes for each application

MOTION

		OUTPUT	OUTPUT	OUTPUT	OUTPUT	OUTPUT
		trajectory	displacement	velocity	acceleration	jerk
INPUT	hierarchy	stable	small	0-1	0-1	0
INPUT	control	stable	regular	0-1	0-1	0
INPUT	emergency	stable	high	high	high	high
INPUT	safety	stable	low	low	low	low

SYNAP enters in a logical manner to obey commands, takes them into account and performs the necessary operations, not like a robot but as an object with its special intelligence. “Intelligence” is born from the embedded logic in the computer and experience growth is based on the actions carried out . The safety immediately reduces speed and acceleration, almost cancels the jerk, slows down and stops the movement, to assume a position of verification. The SAFETY engages an automatic trajectory, if necessary, even in extreme conditions of operation. The safety index ranges from 0, when the situation is critical and dangerous to the value 1 one when the system is always in the best possible safety.

For voice, SYNAP receives voice commands with a few keywords and executes the corresponding orders. The way to zero 0, is completely passive and the execution is not critical.

Level 1 is a budget higher and the software manages the voice as a manifestation of human phenomenon, to create a deep interaction between SYNAP, the human beings who speak, and the equipment which plays the sound. When the output is followed by a voice response system on SYNAP, the position of the source is identified by the system that calculates the GPS coordinates of the local source, and repeats in a loud voice, as well as write them on PC monitor process. The answer is vocally in the base language, which is English or other language according to the country chosen as the base of SYNAP. The vocal response of the position is clear and unambiguous. If the INPUT is a command word or phrase with words declaring control, SYNAP takes inputs and actuates links also to motion and to vision, sends the signal in the subsequent NODE OF SPECIAL INTELLIGENCE and executes orders in sequence, according to the rules in the node. Consequently, orders are executed by SYNAP in a way like an intelligent way.

If the INPUT is a phrase understandable, SYNAP voice confirms that the phrase has been understood, saves INPUT and proposes an answer. The operator who issued

the expressive phrase, accept the answer and answers "Yes" or suggests the correct answer, which SYNAP stores in the data base, and that he will use later on, if someone repeats the same question / phrase, also if part of an another operator. In fact, each response must exit the NODE OF SPECIAL INTELLIGENCE. SYNAP can also use a grid of LEDs in color, with 5 (or more) colored base. The grid is illuminated as a result of words and phrases which people pronounces, according to the sounds received and accepted. When the INPUT is a command word, when it is acknowledged and understood, LEDs light up green, the word order is sent to the NODE OF SPECIAL INTELLIGENCE. According to all other signs of movement and vision received, SYNAP decides the sequence to be executed, after having displayed the blue light of blue LEDs, as consent in the transactions. For vision, pattern recognition tools are SYNAP webcam, stereo cameras, lidar type radar, ultrasonic sensors and infrared sensors, sensor type kinect, and many others. The first objective is the recognition of the people, through the image of the face. The image appears from the camera and is stored in the data base. Each face is associated with an identifying name. The learning phase is about people who routinely interact with SYNAP, and the images will be used frequently. A new image and a new person is stored by the machine and requires a name to recognize it.

The second INPUT regards the facial expression of the person. The expression can be categorized on the basis of subdivisions which derive from the idea of the “emoticon” known everywhere for message telephone and email. The position of the eyebrows and mouth can help to fix the types of expression, which can be translated into suggestions for commands.

The parameters for face, expression and function come into NODE FOR SPECIAL INTELLIGENCE, and the output is a series of logical parameters that are joined with the other parameters of movement to define the behavior as intelligently as possible. For the EMERGENCY as OUTPUT, the face of the person and the person's expression can cause the stop of SYNAP. The position of the person may cause a RUN of Emergency, which is permitted by the position of the person recognized. For the OUTPUT of SAFETY, INPUT of face recognition and of face expression can induce a slow slowdown of the system, for the kinematics, and interfacing together with the other parameters of movement and voice. For safety, the recognition function makes it possible the system SYNAP organizing itself to follow a programmed cycle that guarantees maximum safety.

References

1. Aristotle, Metaphysics,1020 a33-b25 (330 b.C.)
2. Eccles, J.C.: Brain and Conscious Experience. Springer, Heidelberg (1966)
3. Levi-Montalcini, R.: Abbi il coraggio di conoscere, Milan (2004)
4. Eccles, J.C.: The Physiology of Synapses. Springer, Gottingen (1964)
5. Edelman, G.M.: Neural Darwinism, New York (1987)
6. Sherrington, C.S.: The Integrative Action of the Nervous System. Yale University Press, New Haven (1906)
7. Sperry, R.W.: Cerebral Dominance in Perception. In: Early Experience in Visual Information Processing. Nat. Acad. Sci., Washington (1970)
8. http://robotica.mecc.polimi.it

Design and Analysis on a New Underwater Robot

Ngoc-Huy Tran, Hyeung-Sik Choi*, Sang-Seob Lee, and Ba-Loc Mai

Division of Mechanical and Energy Systems Engineering, Korea Maritime University, Busan, Korea

Abstract. This paper describes the analysis of the architecture, and control system of a new underwater robot named underwater disk robot (UDR), which has six degrees of freedom (DOF) motion. With such thruster positions, the vehicle has omnidirectional manoeuvrability without heading motion. Also, the motion of the streamline disk-shaped UDR hull is less affected by side disturbances because the UDR can move robustly, swiftly along any direction, and the hull reduce the drag force on its body in the horizontal motion. Heave and pitch motion simulation studies of the UDR were carried out with the computational fluid dynamics (CFD) software. required format.

Keywords: Disk robot, autonomous underwater vehicle, CFD, PID, Extended Kalman Filter.

1 Introduction

Unmanned undersea vehicles (UUV) have become a main tool in undersea surveying for scientific, military and commercial applications, posing no risks to humans [1] [2]. Despite considerable improvements in the design and performance of UUVs, scientists and engineers still faced with the difficult tasks of designing the shapes for the UUV that will yield low hydrodynamic drag and of eliminating actuators for robust or swift motion along any direction [3] [4]. One of the shapes that have been proposed is the disk shape for the UUV hull. A disk-shaped vehicle hull is least affected by side disturbances during horizontal movement [5]. However, only few disk-shaped UUVs have been developed so far. The AQUA2 built at McGill University of Canada is flat-shaped [6].

To enhance the performance of UUVs, we have developed a new six DOF UDR with a streamline disk-shaped hull and 120-degree symmetrically disposed thrusters, as shown in Fig. 1. The horizontal thrusters are redundantly deployed so that the UDR can move in any direction with equal and robust thrust forces. In this paper, some of new features of the UDR are introduced, and its performance is presented through a theoretic analysis and experiments. In addition, pure heave motion and pure pitch motion studies were conducted to emulate the vertical planar motion mechanism (VPMM) test by CFD motion analysis.

* Corrsponding author.

J. Lee et al. (Eds.): ICIRA 2013, Part II, LNAI 8103, pp. 289–301, 2013.

The paper is organized as follows: in section 2, the design of mechanical and control system is presented; in section 3, a dynamics model; and in section 4, a motion analysis of the UDR using CFD software is presented.

2 Vehicle Design

2.1 Mechanical Design

The body of the UDR is designed as disk-shaped vehicle in order to minimize the effect of water resistance from side disturbances such as currents or wave effects. It is designed as flat as possible. However, this is difficult since various types of equipment such as thrusters, control system, sensors, camera, and lights needed to be included in the UDR. In this paper, an architectural design of the UDR including all the equipment is presented. The architecture design of the disk-shaped UDR is shown in Fig. 2 and the UDR's specifications are described in table 1.

Fig. 1. The disk-shaped UDR

Table 1. Architecture of UDR system

Hull structure specifications	Diameter: 1.9m Height: 0.45m Weight: 80kg Max. Speed: 5 Knots
Propulsion module	3 vertical thrusters 3 horizontal thrusters
Control system module	Embedded computer: Cuwin 5200 Processors:DSP28335,XMEGA128A1
Navigation sensors	GPS: AsteRx1 IMU sensor: MTi DVL: NavQuest 600 USBL: Tracklink 1500 Pressure sensor: Sensys
Observation module	1 camera, 2 lights

The propulsion system is composed of three vertical and three horizontal thrusters. The vertical thrusters inside the vertical channels are mounted upward on the perimeter of the circular chassis. Using the vertical thrusters, the UDR can perform heaving, rolling and pitching motions. The horizontal thrusters are mounted on the perimeter of the circular chassis. They are installed in the side direction for horizontal motion. The horizontal thrusters are disposed 120 degrees apart facing outward. The disposition of the horizontal thrusters yields a vector propulsion force in the horizontal direction. And an RC motor using a coupled belt and pulley arrangement is installed on each horizontal thruster to rotate the thrusting direction by $\delta \in \left[-\frac{\pi}{12}, \frac{\pi}{12}\right]$ (rad). Using the horizontal thrusters, the UDR can perform surging, swaying, and yawing motions. Hence, 6 DOF motion is possible and will be presented in the following section.

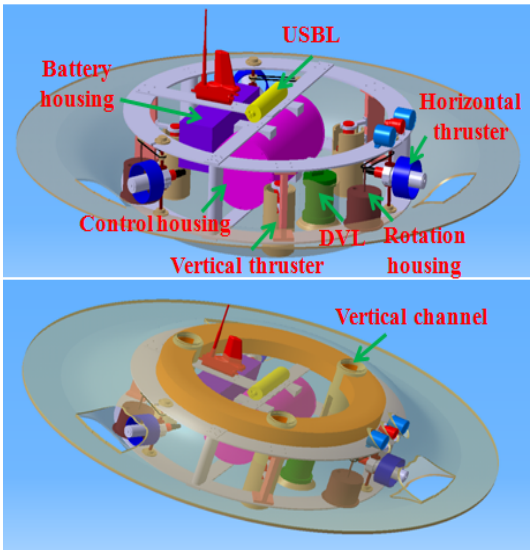

Fig. 2. The interior design of the UDR

2.2 Design of the Control System

As shown in Fig. 3, the UDR control system is composed of six parts which include the control system, navigation, power, propulsion, observation, and communication modules.

The power module is composed of a lithium battery pack and DC/DC converter board contained in the battery housing. This battery pack includes six 500W, 48V batteries parallel-connected to supply 3000W power to the UDR. The DC/DC converter module is used to lower the voltage for the sensor, light, and control subsystems.

The communication module is composed of a 24XStream RF module in the control housing. It transfers a standard asynchronous serial data stream over-the-air between devices at 2.4 GHz operating frequency up to 10 miles with a high gain antenna.

The observation module mainly contains one PHCS-C500 CCTV waterproof camera and two lights mounted on the UDR's fore. It records what is happening around the vehicle.

The propulsion control module shown in Fig. 3 is composed of three vertical 400HFS-L thrusters of 400W and three horizontal thrusters of 300W. The input power of the thrusters is fed using pulse width modulation (PWM) method. The thrusters are controlled by a RS-485 control signal according to a pre-defined protocol.

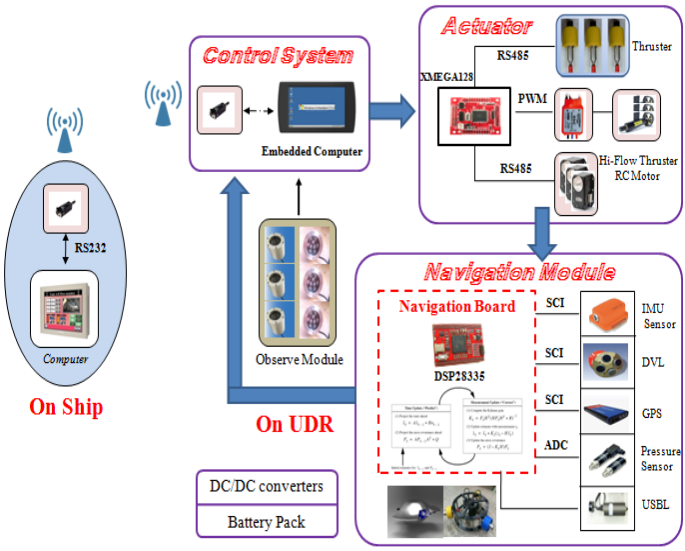

Fig. 3. Hardware architecture of UDR motion control system

The navigation module is composed of IMU, DVL, GPS, USBL and a pressure sensor. They are used to determine the position, velocity, acceleration, path, and distance traveled of the vehicle. The UDR is equipped with an inertial navigation system (INS), which calculates the position, velocity, and attitude of the vehicles from the data given by the IMU sensor. Since INS accumulates errors due to the inherent drift of dead-reckoning velocities and integration of acceleration, an Extended Kaman Filter (EKF) algorithm is implemented, which utilizes a wide range of navigation sensors, to compensate for the accumulation in position error [7].

The control system module contains the embedded computer Cuwin 5200 connected with two microprocessors TMS320F28335 (digital signal processors, DSP) and XMEGA128A1, which work together to perform all control tasks, as shown in Fig. 3.

3 Dynamic Modeling of the Vehicle

A coordinate system fixed at the body of the vehicle, called a body-fixed coordinate system, with its origin at the center of vehicle buoyancy, is used to build a dynamics model of the UDR. The motion of the body-fixed frame is described relative to an inertial or earth-fixed reference frame, as shown in Fig. 4.

In order to simplify the dynamics of the UDR model, the following assumptions are made:

- The vehicle is a rigid body of constant mass during operation.
- The effects of the vehicle's own wake are ignored.
- The vehicle is deeply submerged in a homogeneous fluid.

3.1 Vehicle Kinematics

As shown in Fig. 4, (x, y, z) and (ϕ, θ, ψ) are the position and orientation of the vehicle with respect to the inertial reference frame, respectively. The following coordinate transform relates the translational velocities between the body-fixed and inertial coordinates :

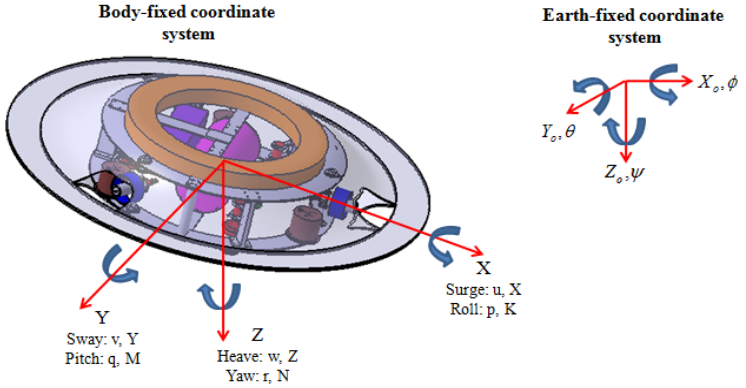

Fig. 4. Body-fixed and inertial coordinate systems

$$\begin{bmatrix} \dot{x} \\ \dot{y} \\ \dot{z} \end{bmatrix} = J_1(\eta_2) \begin{bmatrix} u \\ v \\ w \end{bmatrix}. \tag{1}$$

where

$$J_1(\eta_2) = \begin{bmatrix} c\psi c\theta & -s\psi c\phi + c\psi s\theta s\phi & s\psi s\phi + c\psi s\theta c\phi \\ s\psi c\theta & c\psi c\phi + s\psi s\theta s\phi & -c\psi s\phi + s\psi s\theta c\phi \\ -s\theta & c\theta s\phi & c\theta c\phi \end{bmatrix}.$$

The second coordinate transform relates the rotational velocities between the body-fixed and inertial coordinates:

$$\begin{bmatrix} \dot{\phi} \\ \dot{\theta} \\ \dot{\psi} \end{bmatrix} = J_2(\eta_2) \begin{bmatrix} p \\ q \\ r \end{bmatrix}. \tag{2}$$

where

$$J_2(\eta_2) = \begin{bmatrix} 1 & s\phi t\theta & c\phi t\theta \\ 0 & c\phi & -s\phi \\ 0 & s\phi / c\theta & c\phi / c\theta \end{bmatrix}.$$

Note that $J_2(\eta_2)$ is not defined for pitch angle $\theta = \pm 90^0$ as the vehicle motion does not ordinarily approach this singularity. If it becomes necessary to model the vehicle motion through extreme pitch angles, an alternate kinematic representation such as quaternions or Rodriguez parameters can be used.

3.2 Vehicle Dynamics

The In the following sections, the 6 DOF nonlinear dynamic equations of motion are conveniently expressed as:

$$M\dot{\upsilon} + C(\upsilon)\upsilon + D(\upsilon)\upsilon + g(\eta) = \tau. \tag{3}$$

where

M: Inertia matrix (including added mass)

$C(\upsilon)$: Matrix of Coriolis and centripetal terms (including added mass)

$D(\upsilon)$: Damping matrix

$g(\eta)$: Vectors of gravitational forces and moments

τ: Vectors of control inputs

Given that the origin of the body-fixed coordinate system is located at the center of buoyancy as noted, from equation (3), the 6-DOF equations of motion for a rigid body can be expressed in terms of body-fixed coordinates [8]:

$$
\begin{aligned}
&m[\dot{u}-vr+wq-x_g(q^2+r^2)+y_g(pq-\dot{r})+z_g(pr+\dot{q})]=\sum X\\
&m[\dot{v}-wp+ur-y_g(r^2+p^2)+z_g(pr-\dot{p})+x_g(qp+\dot{r})]=\sum Y\\
&m[\dot{w}-uq+vp-z_g(p^2+q^2)+x_g(rp-\dot{q})+y_g(rq+\dot{p})]=\sum Z\\
&I_{xx}\dot{p}+(I_{zz}-I_{yy})qr-(\dot{r}+pq)I_{xz}+(r^2-q^2)I_{yz}+(pr-\dot{q})I_{xy}\\
&\qquad+m[y_g(\dot{w}-uq+vp)-z_g(\dot{v}-wp+ur)]=\sum K\\
&I_{yy}\dot{q}+(I_{xx}-I_{zz})rp-(\dot{p}+qr)I_{xy}+(p^2-r^2)I_{xz}+(qp-\dot{r})I_{yz}\\
&\qquad+m[z_g(\dot{u}-vr+wq)-x_g(\dot{w}-uq+vp)]=\sum M\\
&I_{zz}\dot{r}+(I_{yy}-I_{xx})pq-(\dot{q}+rp)I_{yz}+(q^2-p^2)I_{xy}+(rq-\dot{p})I_{xz}\\
&\qquad+m[x_g(\dot{v}-wp+ur)-y_g(\dot{u}-vr+wq)]=\sum N
\end{aligned}
\tag{4}
$$

where

- u, v, w: Surge, sway, heave velocities respectively.
- p, q, r: Roll, pitch, yaw rates.
- X, Y, Z: External forces.
- K, M, N: External moments.
- x_g, y_g, z_g : Center of gravity with respect to the origin at the center of buoyancy.
- I_{ab} : Moments of inertia with respect to the origin at center of buoyancy (a, b symbolize x, y, z).

3.3 Mechanics of the Propulsion System

With the 120-degree symmetrical vector disposition of the horizontal and vertical thrusters, the UDR has 6 DOF and can carry out robust underwater motion under side disturbances. We analysed the propulsion system for two cases: horizontal propulsion and vertical propulsion.

1) Horizontal propulsion module

Each horizontal thruster can also rotate about their individual mounting point using a coupled belt and pulley arrangement within the bound $\delta \in \left[-\frac{\pi}{12}, \frac{\pi}{12}\right]$ (rad).

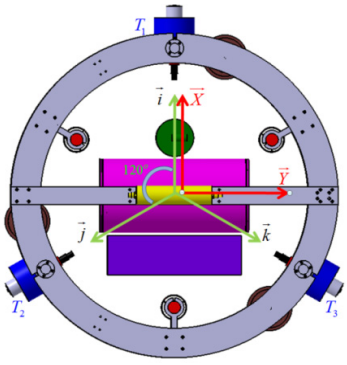

Fig. 5. Horizontal thrust forces with $\delta = 0$ (rad)

a) In case $\delta = 0$ (rad) shown in Fig. 5, the total force $\overrightarrow{F_T}$ from the three thrust forces $\overrightarrow{F_{T1}}, \overrightarrow{F_{T2}}, \overrightarrow{F_{T3}}$ on the plane XOY of the body-fixed coordinates O-XYZ can be expressed as:

$$\overrightarrow{F_T} = \overrightarrow{F_{T1}} + \overrightarrow{F_{T2}} + \overrightarrow{F_{T3}}. \tag{5}$$

$$X_T.\vec{X} + Y_T.\vec{Y} = F_{T1}.\vec{i} + F_{T2}.\vec{j} + F_{T3}.\vec{k} \tag{6}$$

$$\begin{aligned} X_T.\vec{X} + Y_T.\vec{Y} &= (F_{T1}.\sin\alpha + F_{T2}.\sin\beta + F_{T3}.\sin\theta)\vec{X} \\ &+ (F_{T1}.\cos\alpha + F_{T2}.\cos\beta + F_{T3}.\cos\theta)\vec{Y} \end{aligned} . \tag{7}$$

The total thrust forces along the X-axis and Y-axis, respectively:

$$\begin{bmatrix} X_T \\ Y_T \end{bmatrix} = \begin{bmatrix} \sin\alpha & \sin\beta & \sin\theta \\ \cos\alpha & \cos\beta & \cos\theta \end{bmatrix} \begin{bmatrix} F_{T1} \\ F_{T2} \\ F_{T3} \end{bmatrix}. \tag{8}$$

Rewriting this yields

$$\begin{bmatrix} X_T \\ Y_T \end{bmatrix} = \begin{bmatrix} 1 & -0.5 & -0.5 \\ 0 & -\frac{\sqrt{3}}{2} & \frac{\sqrt{3}}{2} \end{bmatrix} \begin{bmatrix} F_{T1} \\ F_{T2} \\ F_{T3} \end{bmatrix}. \tag{9}$$

where $\vec{i}, \vec{j}, \vec{k}$ are the unit vectors of the thrusters $\overrightarrow{F_{T1}}, \overrightarrow{F_{T2}}, \overrightarrow{F_{T3}}$, $\alpha = \frac{\pi}{2}$ is the angle of $\overrightarrow{OY}$ with $\vec{i}$, $\beta = \frac{7\pi}{6}$ is the angle of $\overrightarrow{OY}$ with $\vec{j}$ and $\theta = \frac{11\pi}{6}$ is the angle of $\overrightarrow{OY}$ with $\vec{k}$. Through Eq. (9), the maximum resultant force X_T is 2 F_{T1} along the X axis and the maximum resultant force Y_T is along the Y axis $\sqrt{3}F_{T1}$ when $F_{T1} = F_{T2} = F_{T3}$.

b) In case $\delta \neq 0$ (rad) described in Fig. 6, the thrust forces include the force along the UDR center $\overrightarrow{F_{TnP}}$ and the force $\overrightarrow{F_{TnR}}$ perpendicular to $\overrightarrow{F_{TnP}}$ for n=1, 2, 3. We have:

$$\overrightarrow{F_{T1}} = \overrightarrow{F_{T1P}} + \overrightarrow{F_{T1R}}. \tag{10a}$$

$$\overrightarrow{F_{T2}} = \overrightarrow{F_{T2P}} + \overrightarrow{F_{T2R}}. \tag{10b}$$

$$\overrightarrow{F_{T3}} = \overrightarrow{F_{T3P}} + \overrightarrow{F_{T3R}} . \tag{10c}$$

$$F_{Tn} = \left|\overrightarrow{F_{T1}}\right| = \left|\overrightarrow{F_{T2}}\right| = \left|\overrightarrow{F_{T3}}\right| . \tag{11}$$

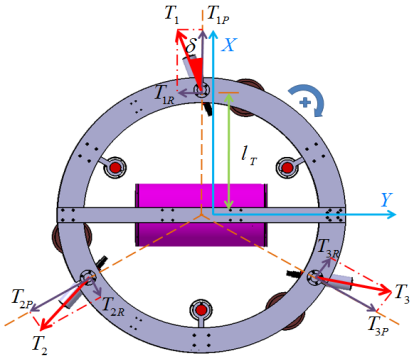

Fig. 6. Horizontal thrust forces with $\delta \neq 0$ (rad)

The total force $\overrightarrow{F_T}$ in this case is zero:

$$\overrightarrow{F_T} = \overrightarrow{F_{T1}} + \overrightarrow{F_{T2}} + \overrightarrow{F_{T3}} = \vec{0} \tag{12}$$

The moment N_T makes UDR rotate about the Z-axis:

$$N_T = 3F_{Tn} l_T \sin\delta \tag{13}$$

where L_T is the distance from the center to the thruster side.

2) The vertical propulsion module

A vertical thruster is placed at a distance l_H from the center of the vehicle. It produces the vertical forces in the UDR Z-axis direction, as shown in Fig. 7.

The total vertical force in the Z-axis direction:

$$Z_H = F_{H1} + F_{H2} + F_{H3} \tag{14}$$

The moment about the X-axis:

$$K_H = \frac{\sqrt{3}}{2} l_H (-F_{H2} + F_{H3}) \tag{15}$$

The moment about the Y-axis:

$$M_H = l_H (\frac{F_{H2} + F_{H3}}{2} - F_{H1}) \tag{16}$$

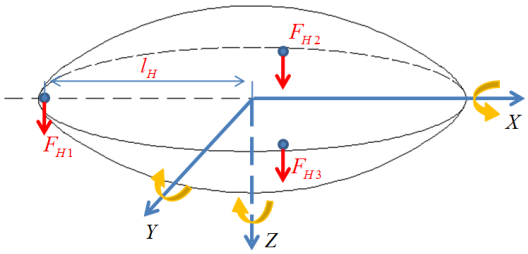

Fig. 7. The vertical forces on the UDR

In the equations of motion, the external forces and moments include hydrostatic forces and moments, hydrodynamic damping, added mass, body lift, and the propeller thrust and torque detailed in previous sections. According to the previous dynamic equation (4) and the propulsion mechanics equations (9), (12), (13), (14), (15), (16), the external forces and moments can be rewritten as follows:

$$\begin{aligned}
&\sum X = X_{HS} + X_{u|u|}u|u| + X_{\dot{u}}\dot{u} + X_{wq}wq + X_{qq}qq + X_{vr}vr \\
&+X_{rr}rr + X_T \\
&\sum Y = Y_{HS} + Y_{v|v|}v|v| + Y_{r|r|}r|r| + Y_{\dot{v}}\dot{v} + Y_{\dot{r}}\dot{r} + Y_{ur}ur + Y_{wp}wp \\
&+Y_{pq}pq + Y_{uv}uv + Y_T \\
&\sum Z = Z_{HS} + Z_{w|w|}w|w| + Z_{q|q|}q|q| + Z_{\dot{w}}\dot{w} + Z_{\dot{q}}\dot{q} + Z_{uq}uq \\
&+Z_{vp}vp + Z_{rp}rp + Z_{uw}uw + Z_H \\
&\sum K = K_{HS} + K_{p|p|}p|p| + K_{\dot{p}}\dot{p} + K_H \\
&\sum M = M_{HS} + M_{w|w|}w|w| + M_{q|q|}q|q| + M_{\dot{w}}\dot{w} + M_{\dot{q}}\dot{q} + M_{uq}uq \\
&+M_{vp}vp + M_{rp}rp + M_{uw}uw + M_H \\
&\sum N = N_{HS} + N_{v|v|}v|v| + N_{r|r|}r|r| + N_{\dot{v}}\dot{v} + N_{\dot{r}}\dot{r} + N_{ur}ur + N_{wp}wp \\
&+N_{pq}pq + N_{uv}uv + N_T
\end{aligned} \tag{17}$$

4 Motion Analysis of the UDR

A VPMM (Vertical Planar Motion Mechanism) test was carried out to find the hydrodynamic coefficients of the UDR for its control. That is, the VPMM test was carried out with the aim of measuring the hydrodynamic forces on the vehicle when changing the motion of the vehicle; e.g. Change of angle of attack, velocity, acceleration etc. The hydrodynamic forces for the VPMM test were obtained for the pure heave motion and the pure pitch motion of the vehicle.

For the case of pure heave motion, the vehicle moves in a sinusoidal fashion with amplitude (z_0), but no pitch angle (θ_0) as shown in Fig. 8 (A). Pure pitch motion, on the other hand, is such that the vehicle moves in a sinusoidal fashion, but this time with a pitch angle (θ_0) at the center of gravity of the vehicle body and the longitudinal body axis is oriented tangential to the path, as shown in Fig. 8 (B).

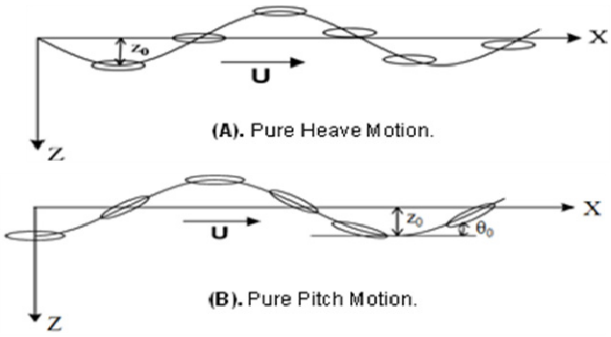

Fig. 8. Description of Pure Heave Motion (A) and Pure Pitch Motion (B)

Conventionally, the tests for the prediction of drag, and motion of an underwater robot are carried out in a large model basin equipped with a towing carriage, and dynamometer, making the test process expensive. The development of commercial codes for CFD analysis now make it possible to predict drag and propulsion performance of a ship or submersible vehicles such as an underwater robot without using a physical model test basin [9].

The position of the body should be defined and specified for motion analysis, which is the VPMM simulation. The motion of the UDR body is defined as shown in Fig. 9 (top) by using the ANSYS-CFX Command Language (CCL) to simulate the pure heave motion or pure pitch motion.

'Tetrahedral' and 'Prism' elements were employed for generating nodes and elements in the fluid domain. A hybrid mesh is created by merging the two mesh structures, and embodied for the CFD analysis by the "ANSYS-CFX-MESH" mesh generator as shown in Fig. 9 (bottom). The mesh properties for the UDR motion study are shown in table 2.

Table 2. Density of the model employed for the UDR motion analysis

Total no. of Nodes	523,899
No. of Faces	57,180
Total no. of elements	1,457,504
No. of Tetrahedrals	646,944
No. of Prisms (for B.C.)	810,560

The x-directional velocity of the vehicle is 1 m/s, and the pure heave motion was carried out with the period (Tt) of 8 seconds while the pure pitch motion has the period (Tt) of 12 seconds. Total computation time (T) is 24 seconds and time step (Δt) is 0.1 second for the CFD moving analysis.

The x-directional velocity of the vehicle is 1 m/s, but the boundary layer grows along the mid-body and the flow is accelerated as it reaches the stern so the velocity of the flow is higher than the x-directional velocity of the vehicle (1.917 m/s - Pure heave motion; 1.186 m/s - Pure pitch motion).

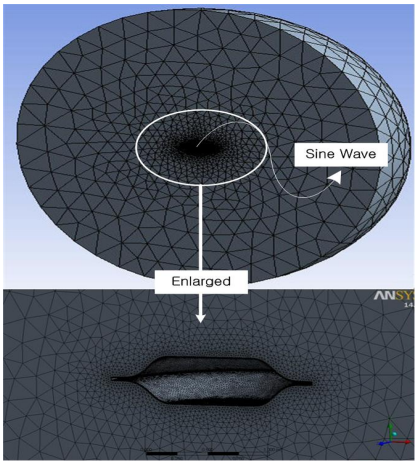

Fig. 9. General view of the mesh (top) and the hybrid mesh generated adjacent to the main body (bottom) of the UDR)

The x and z-axis directional forces of the pure heave motion and pure pitch motion obtained by the CFD analysis are shown in Fig. 10. The added mass and inertia of the vehicle are derived from these hydrodynamic forces .

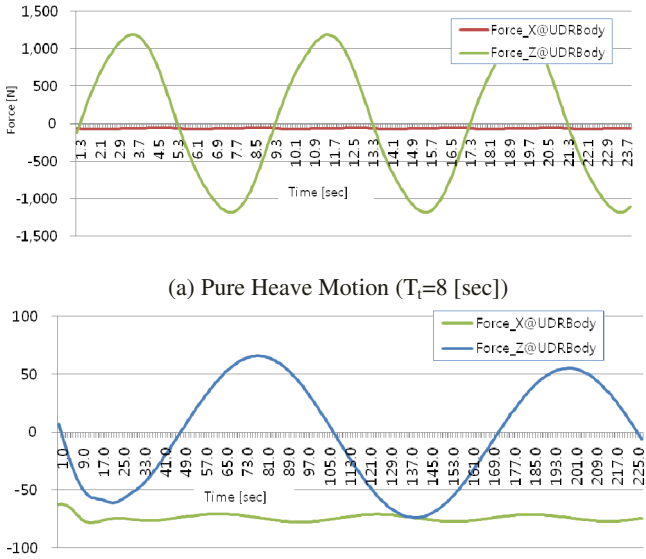

(a) Pure Heave Motion (T_t=8 [sec])

(b) Pure Pitch Motion (T_t=12 [sec])

Fig. 10. X and Z-directional forces on the UDR Body

5 Conclusion

An analysis on the architecture and control system of a new 6 DOF disk-shaped underwater disk robot (UDR) was presented. The streamline disk shape is chosen for the hull to allow the UDR to move flexibly with a low drag force in the horizontal direction.

The dynamics analysis of the UDR including that of the actuator mechanics were presented. And the heave and pitch motion simulation studies of the UDR were carried out with the computational fluid dynamics (CFD) software. We can use these results to estimate the hydrodynamic coefficients of the UDR for its control.

References

1. Manley, J.E.: Unmanned Surface Vehicles, 15 Years of Development. In: Proceedings of Oceans 2008, Quebec City, Canada (September 2008)
2. Wernli, R.L.: AUV'S - The Maturity of the Technology. In: Proceedings of Oceans 1999. MTS/IEEE, Seattle (1999)
3. Roman, C., Pizarro, O., Eustice, R., Singh, H.: A New Autonomous Underwater Vehicle for Imaging Research. In: Proceedings of Oceans 2000. MTS/IEEE, Providence (2000)
4. Gomes, R.M.F., Sousa, A., Fraga, S.L., et al.: A New ROV Design: Issues on Low Drag and Mechanical Symmetry. In: Proceedings of Oceans, Europe (June 2005)
5. Wang, T., Ye, X., Wang, L., Zhang, C.: Hydrodynamic Analysis and Optimization for Dish Shaped Underwater Robot. In: Proceedings of the 2011 IEEE International Conference on Mechatronics and Automation, Beijing, China, August 7-10 (2011)
6. Dudek, G., Giguere, P., Prahacs, C., et al.: AQUA: An Amphibious Autonomous Robot. Proceedings of the Computer Journal 40(1) (January 2007)
7. Titterton, D.H., Weston, J.L.: Strapdown Inertial Navigation Technology, 2nd edn. Americn Institute of Aeronautics and Astronautics (2004)
8. Fossen, T.I.: Guidance and Control of Ocean Vehicles. John Wiley & Son, New York (1994)
9. Joung, T.H., Sammut, K., He, F., Lee, S.K.: Shape Optimization of an Autonomous Underwater Vehicle with a Ducted Propeller using Computational Fluid Dynamics Analysis. International Journal of Naval Architecture & Ocean Engineering 4, 44–56 (2012)

Design and Manufacturing a Bio-inspired Variable Stiffness Mechanism in a Robotic Dolphin

Yong-Jai Park and Kyu-Jin Cho*

BioRobotics Laboratory, School of Mechanical and Aerospace Engineering/IAMD,
Seoul National University, 1 Gwanak-ro, Gwanak-gu, Seoul,
151-742, Republic of Korea
kjcho@snu.ac.kr

Abstract. To maximize the dynamic performance; especially swimming; of a robotic fish or an underwater vehicle, lots of research of mechanisms and actuators have been conducted. Among them, the compliance of the structure can help the robotic fish or the underwater robots to increase the thrust. Also, when oscillating frequency of a propulsion system increases, the stiffness of the caudal fin should increase to increase the thrust of the robotic fish. Therefore, the variable stiffness mechanism is needed to maximize the thrust of the robotic fish. In this paper, we present a design and manufacturing procedure using our bio-inspired variable stiffness mechanism which was developed before. We find the appropriate design of the bio-inspired variable stiffness mechanism for applying to a robotic dolphin. The novel variable stiffness mechanism was designed using the inspiration of anatomy of a fluke. Tendons which are used for changing the stiffness are arranged from dolphin's anatomy. This design and manufacturing procedure can be helpful to some researchers who try to apply the variable stiffness mechanism using flexible material.

Keywords: Robotic fish, Robotic dolphin, Underwater vehicle, Variable stiffness, Tendon driven, Manufacturing.

1 Introduction

As the importance of marine development is gradually increased, the research of unmanned underwater vehicles (UUVs) or autonomous underwater vehicles (AUVs) starts receiving attention from many researchers and people who are interested in this field. There are many issues to develop the performance of the UUVs or AUVs such as the maneuverability of the vehicle, navigation in the water, sensing, communication, hydrodynamics analysis, modeling, and maximizing thrust or efficiency [1]. Among them, we focused on the fundamental issues, the dynamic performance of the underwater vehicle. In order to increase the performance of the underwater vehicle, the thrust maximization should be considered with maintaining the efficiency of the underwater vehicle. To increase the thrust of the underwater

* Corresponding author.

J. Lee et al. (Eds.): ICIRA 2013, Part II, LNAI 8103, pp. 302–309, 2013.

vehicles, the concept of bio-inspiration is adapted and especially the motion of aquatic mammals and fish are focused.

Oscillating propulsion system is well-known as an effective way to swim in the water. Biomimetic propulsion system has better power efficiency and turning performance than that of screw propulsion [2]. Oscillating propulsion system was implemented using various mechanisms. Many smart actuators were used for making oscillatory motion and it is a simple way to generate the motion [3]. The smart actuators can be used as a structure of the underwater robot and also they can be actuated itself. However, even though the smart actuators have lots of advantage in terms of size, weight and flexibility of the structure, there are some limitations; relatively small force than conventional actuators and relatively low operating frequency. Therefore, if the researchers considered dynamic performance of a robotic fish, the conventional actuator; motor; is a reasonable solution. However, if we try to generate a travelling wave using motors, we need many motors to create smoother wave motion. To increase the efficiency and thrust of the robotic fish, various flexible materials have been concerned. It can be easily generated the travelling wave without linkages. As shown in Figure 1, the robotic fish with the compliant materials can be reduced the number of actuators.

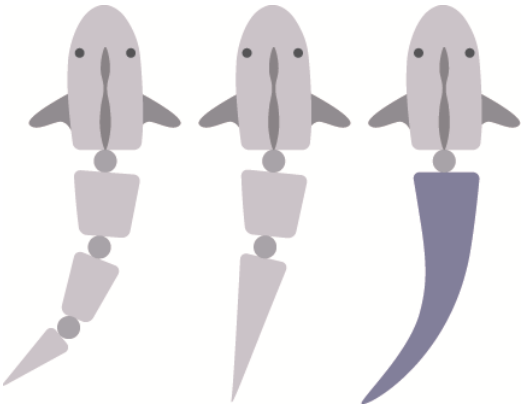

Fig. 1. Robotic fish with joints and rigid links and robotic fish with compliance

Several researchers have experimented using compliant material in their mechanisms. Lauder *et al.* studied the motion of the caudal fin and pectoral fins depending on a kinematic pattern and the stiffness of the fin [4]–[6]. Alvarado *et al.* designed a robotic fish which has a flexible tail made by silicone [7], [8]. Other researchers also studied the effect of the compliance which was applied to the fin [9]–[12]. The results showed that the flexibility of the caudal fin helps the robotic fish to generate more thrust than rigid fin. Park *et al*. introduced a kinematic condition of the caudal fin which can be used to maximize the thrust of the robotic fish [13]. Therefore, the flexible caudal fin is a key issue to increase the thrust of the robotic fish.

However, if we maintain the maximum thrust with varying the oscillating frequency, the stiffness of the caudal fin should be changed. If the oscillating frequency increases, the stiffness of the caudal fin must increase. Previous design of the robotic fish was used only one material in the caudal fin, so the stiffness of the fin cannot be actively changed. In general, the research of a variable stiffness mechanism has been conducted with changing the friction of the system [14], [15]. Kobayashi *et al.* have tried to develop a variable-stiffness fin with an effective-length spring [16]. Huh *et al.* researched a novel variable stiffness mechanism which was inspired by an endoskeleton [17].

In this paper, we propose a design and manufacturing process in order to apply a novel variable stiffness mechanism which was developed and was one of our previous developments. The proposed mechanism is modified for applying to the robotic fish which has the capability of the variable stiffness.

2 Concept of the Bio-inspired Variable Stiffness Mechanism

The novel variable stiffness mechanism was introduced by our previous paper [17]. The concept of this bio-inspired variable stiffness was inspired by endoskeleton. As shown in Figure 2, rigid segments and compliant segments are connected alternately and the segments are perfectly bonded. A tendon is located inside of the each segment. When the tendon is pulled, the compliant segments are compressed and the stiffness of the total system increases. It is because the property of the compliant material is nonlinear. Therefore, this nonlinear property induced the variation of the stiffness in the total system.

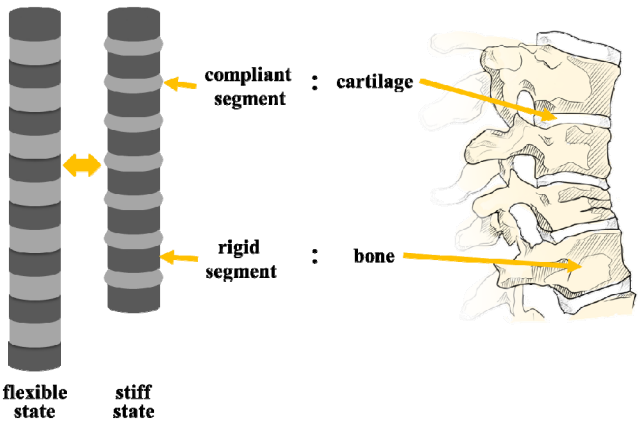

Fig. 2. Schematic drawing depicting the concept of a variable stiffness structure and it is similar to an endoskeleton, especially the vertebral column of mammals. The longer structure represents the flexible state and the shorter structure represents the stiff state due to compression of the compliant materials.

3 Design and Manufacturing

3.1 Design of the Variable Stiffness Mechanism

For designing the robotic fish, dolphins are considered. As described in a previous section, dolphins use only fluke to swim. One oscillation movement enables the dolphin to achieve swimming and jumping. The dolphin's peduncle and fluke is considered to design the driving device of the robotic fish. In general, dolphins swim by vertical oscillation of the fluke and the propulsive part of the dolphin consists of the vertebral column. Sun *et al.* investigated the fluke which was anatomized [18]. The fluke has three tendons; the epaxial tendon I, the epaxial tendon II, and the hypaxial tendon. The epaxial tendons Is inserted into each tail vertebra, the epaxial tendon IIs inserted into five tip tail vertebrae, and the hypaxial tendons inserted on the chevron bones and tail vertebrae. Inspired by the anatomy of the fluke, the driving device with variable stiffness is designed. The concept of the robotic dolphin is illustrated in Figure 3.

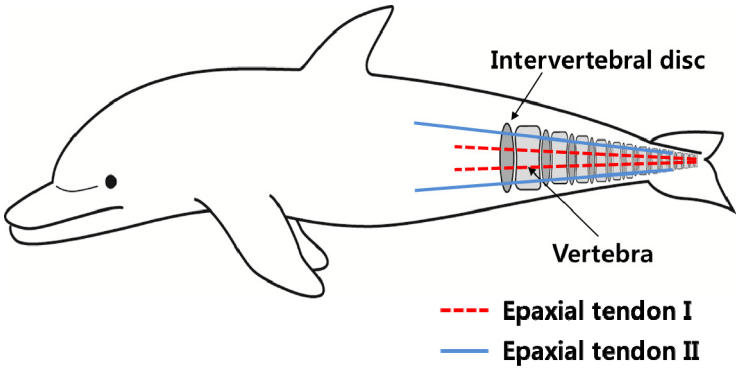

Fig. 3. Concept of the robotic dolphin adopted from the anatomy of the dolphin

The variable stiffness mechanism is implemented into the peduncle part as shown in Figure 4. The total shape of the peduncle is similar to that of the dolphin. Five rigid plates as back bones are placed with certain distance. Four tendons are installed; two tendons for driving, and two tendons for changing stiffness. In the Figure 4, a red dashed line shows the tendon for changing stiffness and two blue straight lines show the tendons for driving. As described earlier, the tendons for driving is set as the epaxial tendon II of the dolphin which is attached into five tip tail vertebrae. Furthermore, we consider a coupling effect between the tendons for driving and the tendons for changing stiffness. If the stiffness tendons are pulled, the structure of the peduncle is shrunk. Due to the shrinkage of the peduncle part, the driving tendons can be released. In order to solve this problem, we installed a spring which has zero pitch angle between the fifth rigid plate and the fourth rigid plate. This spring cannot be decreased its length due to the zero pitch angle but it can be easily bent. Therefore, the shrinkage effect of the stiffness tendons is decoupled with the driving tendons.

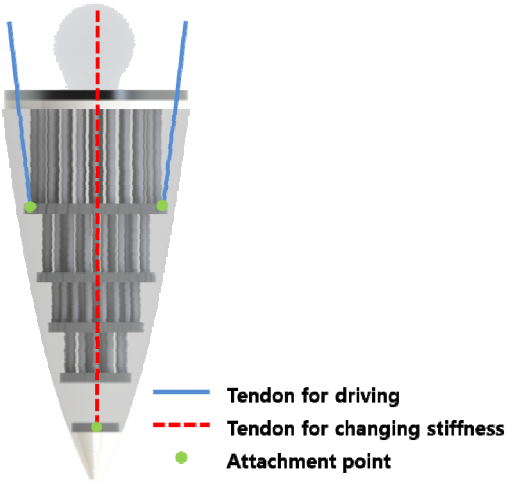

Fig. 4. Design of the driving part with variable stiffness structure and tendons

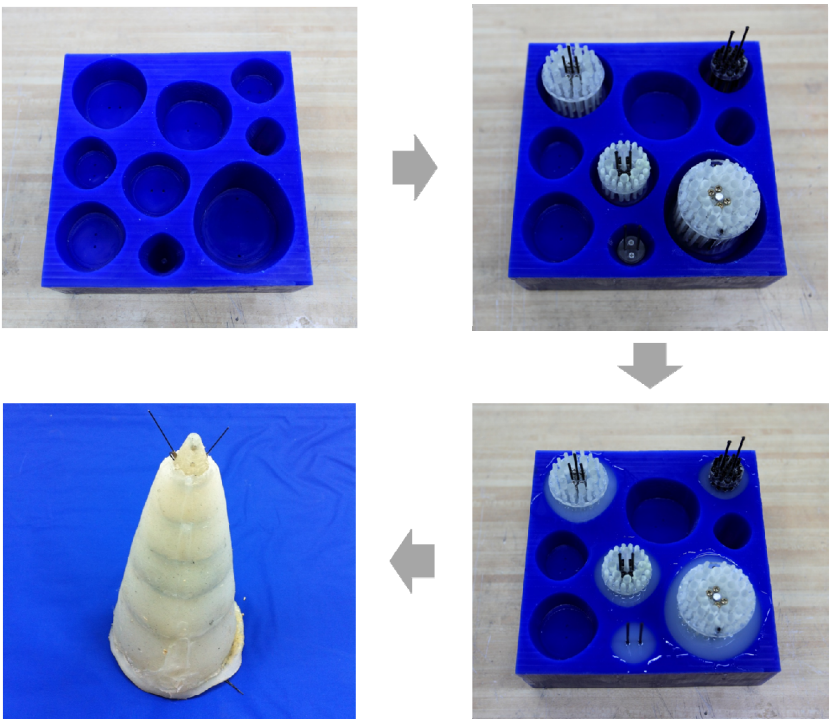

Fig. 5. Manufacturing process: Flexible component is poured over rigid component

3.2 Manufacturing of the Variable Stiffness Mechanism

Variable stiffness structure is manufactured with a mold. Figure 5 shows how the variable stiffness segments are made with a mold before assembling. Due to the weight balance of the robotic dolphin, air holes are needed inside of the peduncle so lots of rods are placed into the silicone (EcoFlex 0010: Smooth-On). These air holes also induce the reduction of the stiffness.

Figure 6 shows the total peduncle mold. Each component is aligned through the mold and the end part of the peduncle is connected with CFRP caudal fin. This end segment was made by Rapid Prototyping using 3D Systems ProJet HD 3000. Each rigid segment is made by CNC using a polycarbonate plate. Wacker Silicones E43 was used to bond the rigid segments and the compliant segments. The segments have a penetrating hole with a diameter of 1.5 mm at the center until 3rd segment and two holes after 3rd segment for the tendon to pass through. This tendon is attached to the rigid segment at the end segment and is actuated from the motor. Beadalon KINKFREE Ti (diameter: 0.53 mm) was used as a tendon wire. We control the amount of compression using a servo motor that pulls the tendon wire.

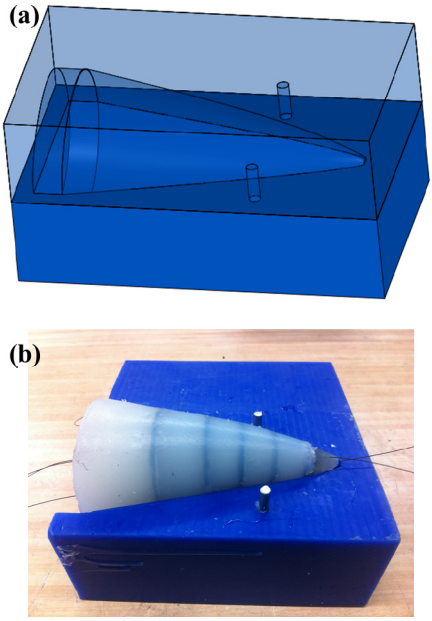

Fig. 6. (a) CAD of wax mold (b) Silicone is used to case the variable stiffness structure

4 Conclusion and Future Work

A bio-inspired variable stiffness mechanism for the robotic dolphin was presented. The characteristic of the variable stiffness is needed in order to maximize the thrust of the robotic dolphin using the compliant caudal fin. When the oscillating frequency of the propulsion device increases, the stiffness of the caudal fin should increases in order to maximize the performance.

Previous novel variable stiffness mechanism was considered to apply to the robotic dolphin. Tendons for changing the stiffness were arranged as considering the anatomy of the fluke of dolphin. Variable stiffness structure was manufactured with a mold and the final variable stiffness peduncle also made from the mold. This bio-inspired variable stiffness can be used for propulsion device to the robotic dolphin. The performance of the variable stiffness robotic dolphin should be verified with proper experimental setup.

Acknowledgments. This research was supported by the Converging Research Center Program and the Basic Science Research Program through the National Research Foundation of Korea (NRF) funded by the Ministry of Education, Science and Technology (2009-0082824 and 2009-0070058).

References

[1] United States. Naval Meteorology and Oceanography Command and Naval Research Laboratory (U.S.), Review of autonomous underwater vehicle (AUV) developments. Stennis Space Center, Miss.: Naval Oceanographic and Atmospheric Research Laboratory (2001)

[2] Liang, J., Wang, T., Wen, L.: Development of a two-joint robotic fish for real-world exploration. Journal of Field Robotics 28(1), 70–79 (2011)

[3] Chu, W.-S., Lee, K.-T., Song, S.-H., Han, M.-W., Lee, J.-Y., Kim, H.-S., Kim, M.-S., Park, Y.-J., Cho, K.-J., Ahn, S.-H.: Review of biomimetic underwater robots using smart actuators. Int. J. Precis. Eng. Manuf. 13(7), 1281–1292 (2012)

[4] Esposito, C.J., Tangorra, J.L., Flammang, B.E., Lauder, G.V.: A robotic fish caudal fin: effects of stiffness and motor program on locomotor performance. The Journal of Experimental Biology 215(1), 56–67 (2012)

[5] Tangorra, J., Phelan, C., Esposito, C., Lauder, G.: Use of Biorobotic Models of Highly Deformable Fins for Studying the Mechanics and Control of Fin Forces in Fishes. Integrative and Comparative Biology 51(1), 176–189 (2011)

[6] Lauder, G.V., Lim, J., Shelton, R., Witt, C., Anderson, E., Tangorra, J.L.: Robotic Models for Studying Undulatory Locomotion in Fishes. Marine Technology Society Journal 45(4), 41–55 (2011)

[7] Valdivia Y Alvarado, P., Youcef-Toumi, K.: Design of Machines With Compliant Bodies for Biomimetic Locomotion in Liquid Environments. J. Dyn. Sys., Meas., Control 128(1), 3–13 (2006)

[8] Valdivia Y Alvarado, P., Youcef-Toumi, K.: Performance of machines with flexible bodies designed for biomimetic locomotion in liquid environments, pp. 3324–3329 (2010)
[9] Daou, H.E., Salumae, T., Ristolainen, A., Toming, G., Listak, M., Kruusmaa, M.: A bio-mimetic design of a fish-like robot with compliant tail. Presented at the International Workshop on Bio-Inspired Robots (2011)
[10] Low, K.H., Chong, C.W.: Parametric study of the swimming performance of a fish robot propelled by a flexible caudal fin. Bioinspir. Biomim. 5(4), 046002 (2010)
[11] Yamamoto, I., Terada, Y., Nagamatu, T., Imaizumi, Y.: Propulsion system with flexible/rigid oscillating fin. IEEE J. Oceanic Eng. 20(1), 23–30 (1995)
[12] Ahlborn, B., Chapman, S., Stafford, R., Harper, R.: Experimental simulation of the thrust phases of fast-start swimming of fish. J. Exp. Biol. 200(17), 2301–2312 (1997)
[13] Park, Y.-J., Jeong, U., Lee, J., Kwon, S.-R., Kim, H.-Y., Cho, K.-J.: Kinematic Condition for Maximizing the Thrust of a Robotic Fish Using a Compliant Caudal Fin. IEEE Transactions on Robotics 28(6), 1216–1227 (2012)
[14] Kawamura, S., Yamamoto, T., Ishida, D., Ogata, T., Nakayama, Y., Tabata, O., Sugiyama, S.: Development of passive elements with variable mechanical impedance for wearable robots. In: Proceedings - IEEE International Conference on Robotics and Automation, vol. 1, pp. 248–253 (2002)
[15] Mitsuda, T., Kuge, S., Wakabayashi, M., Kawamura, S.: Haptic displays implemented by controllable passive elements. In: Proceedings - IEEE International Conference on Robotics and Automation, vol. 4, pp. 4223–4228 (2002)
[16] Nakabayashi, M., Kobayashi, R., Kobayashi, S., Morikawa, H.: Bioinspired propulsion mechanism using a fin with a dynamic variable-effective-length spring: Evaluation of thrust characteristics and flow around a fin in a uniform flow. Journal of Biomechanical Science and Engineering 4(1), 82–93 (2009)
[17] Huh, T.M., Park, Y.-J., Cho, K.-J.: Design and analysis of a stiffness adjustable structure using an endoskeleton. Int. J. Precis. Eng. Manuf. 13(7), 1255–1258 (2012)
[18] Sun, Q., Morikawa, H., Kobayashi, S., Ueda, K., Miyahara, H., Nakashima, M.: Structure and Bending Properties of Central Part of Tail Fin of Dolphin. Journal of Biomechanical Science and Engineering 5(4), 388–398 (2010)

Design and Control of 3-DOF Robotic Fish 'ICHTHUS V5.5'

Gi-Hun Yang, Kyung-Sik Kim, Sang-Hyo Lee, Chullhee Cho, and Youngsun Ryuh

Biomimetic Robot Research Group, KITECH, Ansan, Korea
{yanggh,kskim22,realwolf,ch.cho,ysryuh}@kitech.re.kr

Abstract. Recently, many kinds of biomimetic fish-like robots are being actively researched worldwide for practical use of them. However, there are still diverse problems about using of the robotic fish in the real environment such as in the river for monitoring water pollution. Therefore, this study mainly describes development of a robotic fish 'Ichthus V5.5' which can be used for water quality sensing system. The robotic fish 'Ichthus V5.5' has a 3-DOF serial link-mechanism for its propulsion, which is developed in KITECH. We added several sensors to navigate autonomously in the real environment like river. To measure the performance of the robotic fish, an experimental setup is developed for measuring the propulsion force of the robot. Also, we installed two kinds of sensor to detect temperature, electric conductivity, pH (hydrogen ion concentration) of water. Therefore, the developed robotic system can be applied to environmental monitoring system for detect pollution or quality of river.

Keywords: Robotic Fish, Environmental monitoring, Biomimetic, Navigation, Dynamic Analysis, Propulsion.

1 Introduction

Underwater vehicles have been widely used for the purpose of the marine exploration, surveillance, and environmental monitoring. In order to perform these goals, the propulsion of the high efficiency and the excellent dynamic property of the vehicles are needed [1]. However, when it comes to the efficiency and a moving ability, there are no positive advantages for the underwater vehicle that has pre-existing types of propeller to move forward. The driving efficiency of the vehicle does not exceed 70 % and this could lead to a short searching distance of the system. Also, the increasing capacity of the battery could cause its ability to carry the apparatuses to decrease. In place of conventional rotary propellers used in ships or other underwater vehicles, undulatory movement provides the most part of propulsion power for robotic fish. An observation of real fish shows that this kind of propulsion is less noisy, more effective, and more maneuverable than propeller-based propulsion [9]. Moreover, the turning radius is relatively big and evading speed is considerably slow. For these reasons, it is not appropriate for moving or exploring in the packed area [2]. As a

J. Lee et al. (Eds.): ICIRA 2013, Part II, LNAI 8103, pp. 310–319, 2013.

solution for this, there is a study underway and the study is related with the underwater mobile robots which mimic a fish's swimming movement.

At first, fishes usually have more excellent rapid turning movement rather than other underwater vehicles. So they can turn their way even though there is only 1/10 length of their body. However, submarines which developed by human require almost 10 times of the returning distance, because it needs a time to slow down and turning their body [4].

Second, the swimming mechanism of the fish is well known as more than a 20% efficient way rather that the way of propeller proceeding method which is more general one. For instance, MIT research team conducted an experiment about the comparing a performance between the fin which looks like a tuna's tail fin and a propeller in 1994 [5]. And they found that the fins are more efficient method to proceed in the water. The fins of fish could repulse the water more than the square of propeller's blade. And this makes more power to proceed forward. As a result the energy efficiency of the propeller became 70% but the robot tuna's fin recorded 87 % [3]. Several researchers developed various kinds of robot fish. In Japan, Nagoya University developed a micro robotic fish using ICPF actuators [7], while Tokai University produced a robot Blackbass [8] in order to research the propulsion characteristics of pectoral fins. North-western University applied shape memory alloy (SMA) to produce a robot lamprey [6] which aimed to provide mine countermeasures.

In this study, the development of novel robotic fish will be introduced from its design stage to the calculation of the Ichthus's dynamic equation which was executed to make more efficient swimming mechanism of the robot 'Ichthus V5.5'. The developed system has autonomous navigation ability and the water quality monitoring capability. An experimental setup for measuring propulsion force is developed. Sensors and related signal processing systems are integrated to the developed system for achieving its abilities. Navigation strategy was also developed and tested in real environment.

2 Design and Implementation of Robotic Fish

2.1 Mechanical Link Model

The target model as shown figure 1 of this paper is 'Ichthus V5.5' which has 3 Joints in the body and the tail. Also, it swims and moves its tail to the left and right side as like a real fish. A shape of a platform was designed to imitate the shape of aquatic creature to minimize resistance of platform received in the water. Several actuators were placed at specific points of the platform in order to do similar swimming with the aquatic creature. Each part and joint constituting the underwater robot was designed by using position of these actuators. Various components for drives, sensors, communications and control were placed in platform of the fish-like underwater robot. A total size and an interior design of the platform reflect these facts.

A length of the robotic platform is 500mm, the width is 146mm, the height is 170mm and the weight is about 4.7kg (Including buoyancy adjustment weights).

An external shape of the platform was designed to take a curved shape like a real aquatic creature by connecting longitudinal section of the aquatic creature. - The platform is easy to assemble and decompose by designing each part along top and bottom structure. Therefore, repair and replacement of an internal configuration module is easy when a malfunction occurs. The components placed in the platform consist of a drive part, a sensor part, a communication part, a control part. And a size of each part was determined in order to place an appropriate position. Also, we designed a buoyancy control device and a side fin part to control an up-and-down motion of the underwater robot.

On each joint, the servo motors are connected to the body frame of the robot. Therefore, by using the servo motors, we are able to control frequency and amplitude of the robot. Table 1 and Figure 2 show specifications of “Ichthus Ver. 5.5” and actual implementation of the robotic fish.

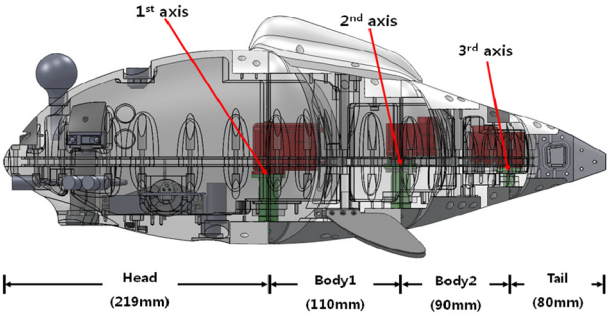

Fig. 1. Mechanical model of 'Ichthus'

Table 1. Specifications of 'Ichthus Ver. 5.5’

Specifications of 'Ichthus Ver. 5.5’	
Body size	500mm(L) x 146mm(W) x 170mm(H)
Weight	4.7 kg
DOF	5 (Tail 3, Side Fin 2)
Battery	14.8V Li-Io Battery

Fig. 2. Actual Implementation of Robotic Fish 'Ichthus V5.5'

2.2 Sensors

The developed robotic system has embedded several kinds of sensors for autonomous navigation and quality detection of water. Sensors to be used for autonomous navigation are IR sensors, ultrasound range sensors, GPS sensor, water pressure sensor, INS(Inertial Navigation System), USBL. Basically the developed robotic fish uses GPS sensor for localization when the robot is on the surface of water. In case that the robotic fish is located in the underwater environment, GPS data is not accessible. Therefore the robot needs to use water pressure sensor for depth detection and INS for localization. To compensate the error of INS, USBL location data is transmitted through an ultrasound modem. With these features, the robotic fish can move autonomously in the underwater environment as well as the surface of water. Since one of main purpose of the robotic fish is to prevent water pollution, the developed robotic fish has three kinds of sensors measuring temperature, EC(electric conductivity), pH(hydrogen ion concentration) of water. These features can be monitored anytime the operator wants to.

2.3 Simulation Design

The simulation was conducted through the Matlab™ and the acceleration of the robot was calculated from the equation (9), and the velocity of robot was derived by the equation of Runge-Kutta.

$$M\ddot{x}_G = F_F - F_D. \tag{1}$$

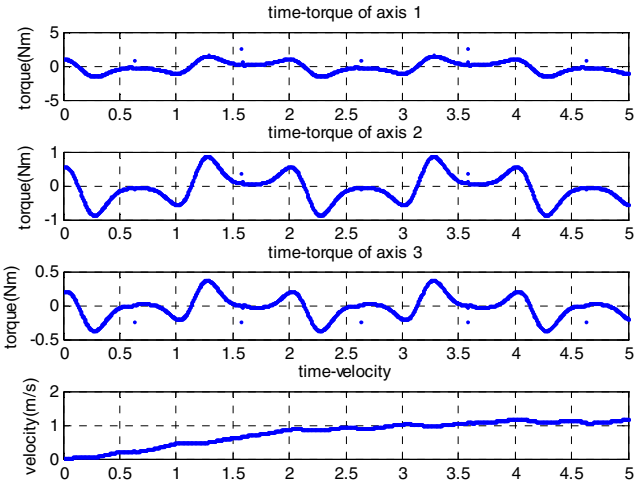

Fig. 3. Result of the simulation. In order joint 1 torque, joint 2 torque, joint 3 torque, velocity(Input : 0.8 Hz, Amplitude 20 deg Um 0.03m/s).

At this calculation, M means the total mass of the robotic fish, means position of the mass center, FF means the total thrust force, and FD means the total drag force. In the simulation, the amplitude and the frequency are input values; therefore, the swimming velocity along x-axis direction could be calculated. The figure 5 shows the simulation results. The superscript numeral used to refer to a footnote appears in the text either directly after the word to be discussed or – in relation to a phrase or a sentence – following the punctuation mark (comma, semicolon, or period). Footnotes should appear at the bottom of the normal text area, with a line of about 5cm set immediately above them.

3 Measurement of Thrust Force

Fish performs the major movement starting from tail to body in order to drive forwards. There is transformation of momentum between the fish and surrounding water during a fish swims. The propulsive wave of water which is generated by the movement of fish propels the fish forward. The reacting force by momentum of passing water could be divided into a thrust force component, which is the forward propulsion force of a fish, and a later force component [10]. Biologists and engineers have made considerable effort to examine the trust efficiencies of swimming robot, however, most works of the existing research have been conducted through computation with a lack of experimental validation [11, 12]. Recently, experimental studies examining the thrust force of fish were reported using flapping foils [13] or piezoelectric force transducer with servo towing system [11]. Nevertheless, the measurements could not fully deal with constructed robotic fish but only some parts of a fish especially the caudal fin or robotic fish without its mechanical system. Thus, a novel experimental setup that can measure thrust force of constructed robotic fish is proposed in this study.

3.1 A Novel Experimental Setup

A novel experimental setup was designed for gripping a pre-developed robotic fish 'Ichthus V5.5', which is developed in KITECH [14] and measuring its propulsion force. The experimental setup consists of two discrete parts: gripper and sensor rod. As shown in Figure 1 (a), there are two v-clamps on both sides with rubber pads to grab the front body segment of the robot fish without slip during experiments in the water. Head holder was attached considering the weight of Ichthus V5.5, which was about 5 kg, to prevent slip down of Ichthus V5.5 from gripper. 6-axis Torque/Force sensor (Delta SI-660-60) was attached on sensor rod with connecting rod that can be clamped with gripper as it is described in Figure 1 (b). Figure 2 shows actual clamping of Ichthus V5.5 by gripper. V-clamps and rubber pads only grab the front body segment of the robotic fish so as to measure the net thrust force from three actuators in tail segments.

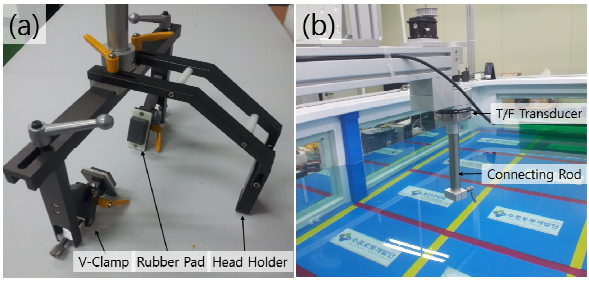

Fig. 4. Experimental setup: (a) Gripper, and (b) Sensor rod

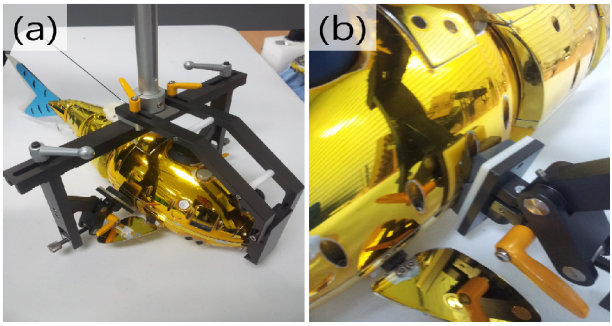

Fig. 5. Clamping of Ichthus V5.5 by gripper

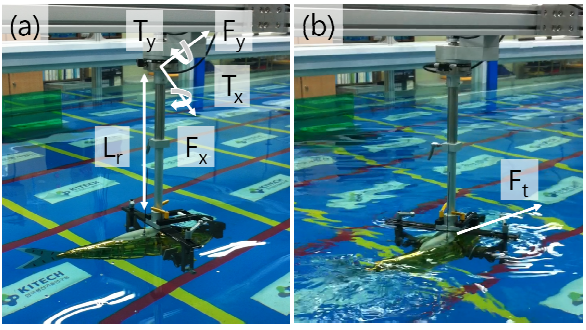

Fig. 6. Preparation of experiments: (a) Connecting gripper and sensor rod, and (b) propulsion test

3.2 Experimental Results

After the gripper is connected to the sensor rod with appropriate length to locate Ichthus V5.5 in the water tank to avoid the interference effect of the free surface, propulsion test could be conducted. Thrust force (F_t) could be calculated from experiment data measured at T/F transducer based on Eq. (1).

$$\overrightarrow{F_t} = \overrightarrow{F_x} + \frac{\overrightarrow{T_y}}{L_r} + \overrightarrow{F_y} + \frac{\overrightarrow{T_x}}{L_r} \tag{1}$$

Thrust force is calculated as vector combination of F_x, F_y, T_x and T_y with scalar component L_r. L_r is the perpendicular length between T/F transducer to mass center of robotic fish. However, head of the robotic fish also swing based on input frequency that was given at tail segments. Actual thrust force might be less than calculated thrust force from experiment data. In future work, force reduction that is occurred by head swing movement should be compensated.

4 Navigation of Robotic Fish

4.1 Localization

Localization of robotic fish is required to control the position of the robot whether it is floating on the surface of water or submerging underwater. The localization algorithm is proceeded through a combination of geomagnetic sensor, GPS, INS, USBL and ultrasonic wave. When the robotic fish is floating on the surface of water, GPS module enables to transfer data to INS so as to localize the position of the robotic fish as it is described in Fig. 6, with a heading direction that is determined by geomagnetic sensor. However, when the robot is submerged, USBL is used to replace the role of GPS module because GPS cannot transfer data to INS in underwater. A docking station recognizes a position of the robot through USBL and the robot conveys a current position of robot through an ultrasonic modem. Consequently, sonar modem transfers position data of the robotic fish to INS when the robotic fish is submerged in underwater. Additionally, water pressure sensor was implemented to the bottom surface of the robotic fish to get depth position of the robotic fish that is submerged in underwater like shown in Fig. 7. Resolution of water pressure sensor is 3 cm in underwater and waterproofed until 100 m depth.

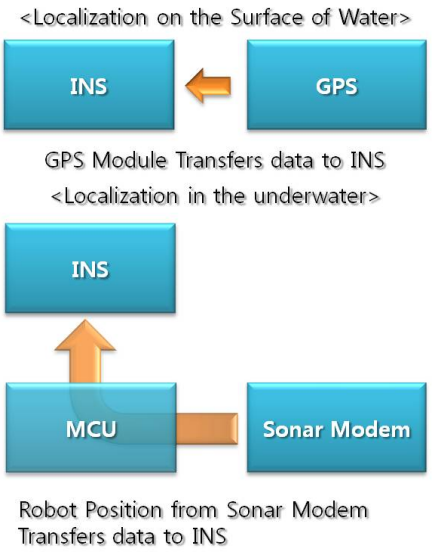

Fig. 7. Updating method of robot reference position

Fig. 8. Implementation of water pressure sensor to robotic fish

4.2 Navigation in the Field

We implemented a remote control and monitoring program of the robotic fish (WaveWork2). The docking station conveys path information about where the robot to navigate by using RF and the robot performs a command. Also, the docking station displays a navigation and environment information obtained from the robot on the map. The robot can be controlled directly by using RF or ultrasonic modem.

The docking station was linked with USBL, RF, ultrasonic modem, GPS module. The path points were obtained through Google Earth. Then, if target points enter into the program, it shows a position on the map as shown in Fig 7 and Fig 8. This is called point based navigation. The functions of the program include a goal point transfer, a search start and stop, swimming max-min velocity limit and an azimuth error control.

Point based navigating strategies can be divided into two different way: strategy for on the surface of water, and in underwater. First, if the entire given target points are on the surface of water, navigation path is determined by INS data that is transferred from GPS with heading direction from geomagnetic sensor. Then robotic fish could perform swimming path to next given point based on gathered position data. When any target point is given in underwater, robotic fish would have to submerge into water. As no longer GPS could transfer data to INS since the robotic fish start to sink into underwater, sonar modem and USBL that is linked with the docking station perform alternative role of GPS in order to transfer data to INS. Besides, heading direction of robotic fish to target point is determined by geomagnetic sensor and depth position data which is gathered from water pressure sensor assist to perform appropriate navigation path of swimming. Therefore, navigation in the field whether on the surface or under water could be performed by pointed based navigating strategies.

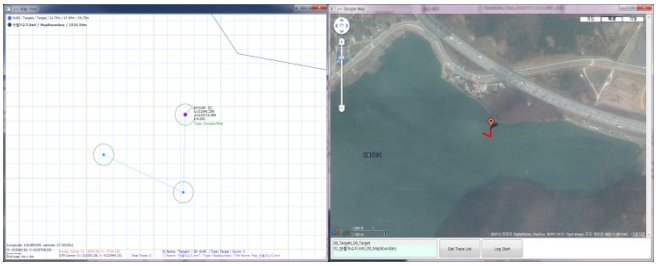

Fig. 9. Target point setting and its presentation over Google Map

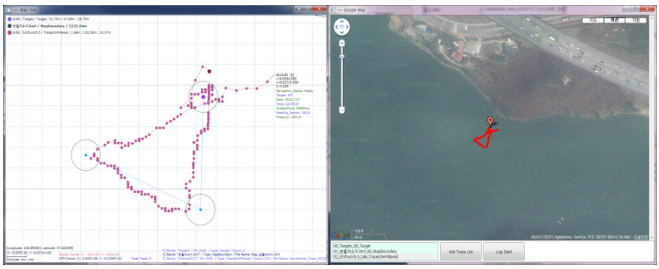

Fig. 10. Navigation path display and its presentation over Google Map

5 Conclusions

In this research, a robotic fish 'ICHTHUS V5.5' is introduced with its main components in the point of design and control. The developed robotic fish has many kinds of embedded sensors to navigate autonomously in the real environment like river. Also, additional three kinds of sensors are integrated to measure temperature, electric conductivity and pH of water for monitoring the quality of water in order to prevent water pollution. Since we already conducted parameter optimization in our previous research and confirmed that the optimized input value compared to the existing value that can produce faster velocity with smaller torque value, we can apply the input parameters which include the minimum RMS torque value. We are able to improve the energy efficiency and operating time of the robotic fish by applying this result. Also, the developed robotic fish is able to navigate in the real environment through field test. Localization and point-based autonomous navigation is successfully achieved while avoiding unknown obstacles in the real environment through those experimental results. In the future, the robotic fish should be improved for its performance. For example, it will be achieved high speed swimming like human. Also, we have a plan to apply the robotic fish to water pollution monitoring in the field.

Acknowledgments. This research was supported by Korea Research Council for Industrial Science and Technology, research grant B551179-10-02-00.

References

1. Hirata, K., Takimoto, T., Tamura, K.: Study on Turning Performance of a Fish Robot. In: Proc. 1st Int. Symp. Aqua Bio-Mech., pp. 287–287 (2000)
2. Cho, K., Park, H., Kim, S.-W., Yang, H., Park, Y.-P.: Development of Robot mimicking Propulsion of a Fish. In: Korean KSME, pp. 40–45 (2007)
3. Kim, Y.-H.: Robotic Fish, the prince of Ocean. Dong-A Science (Magazine in Korean) 8, 54–59 (2005)
4. Ryuh, Y.-S.: Development of Swimming mechanism and Algorithm of Fish-like Underwater Robot. In: KROS, pp. 43–48 (2009)
5. Streitlien, K., Triantafyllou, G.S., Triantafyllou, M.S.: Efficient foil propulsion through vortex control. AIAA Journal 34, 2315–2319 (1996)
6. `http://www.dac.neu.edu/msc/burp.html` (2004)
7. Guo, S., Fukuda, T., Kato, N., Oguro, K.: Development of underwater microrobot using ICPF actuator. In: Proceedings of the 1998 IEEE International Conference on Robotics & Automation, pp. 1829–1834 (1998)
8. Kato, N.: Control performance in the horizontal plane of a fish robot with mechanical pectoral fins. IEEE Journal of Oceanic Engineering 25(1), 121–129 (2000)
9. Hu, H.: Biologically Inspired Design of Autonomous Robotic Fish at Essex. In: Proceedings of the IEEE SMC UK-RI Chapter Conference 2006 on Advanced Cybernetics Systems, pp. 1–8 (2006)
10. Nilas, P., Suwanchit, N., Lumpuprakarn, R.: Prototypical robotic fish with swimming locomotive configuration in fluid environment. In: Proceedings of the International MultiConference of Engineers and Computer Scientists 2011, Hong Kong (March 2011)
11. Wen, L., Wang, T., Wu, G., Liang, J.: Quantitative trust efficiency of a self-propulsive robotic fish: Experimental method and hydrodynamic investigation. IEEE/ASME Trans. Mechatronics 18(3), 1027–1037 (2013)
12. Borazjani, I., Sotirropoulos, F.: Numerical investigation of the hydrodynamics of carangiform swimming in the transitional and inertial flow regimes. J. Exp. Biol. 211, 1541–1558 (2008)
13. Anderson, J.M., Streitlien, K., Barrrett, D.S.: Oscillating foils of high propulsive efficiency. J. Fluid Mech. 360, 41–72 (1998)
14. Yang, G.H., Lee, S.H., Lee, H.J., Ryuh, Y.S.: Implementation and Navigation of a 3-DOF fish robot 'Ichthus V5.5'. In: Proceedings of 2012 IEEE International Conference on Robotics and Biommimetics, Guangzhou, China, pp. 1045–1049 (December 2012)

High Efficiency Isolated Bidirectional AC-DC Power Converter

Ho-Sung Kim[1,2], Myung-Hyo Ryu[2,3], Ju-Won Baek[2], Jong-Hyun Kim[2], and Hee-Je Kim[1,*]

[1] Department of Electrical Engineering, Pusan National University, Busan, Korea
heeje@pusan.ac.kr
[2] Power Conversion Research Center, KERI, Chang-Won, Korea
[3] Department of Electrical Engineering, Kyungpook National University, Daegu , Korea

Abstract. In this paper, the high efficiency isolated bidirectional AC-DC converter system with several improved techniques will be discussed to improve the performance of a low voltage DC distribution system. In order to increase the efficiency of the non-isolated full-bridge AC-DC rectifier, the switching devices are designed by using IGBTs without an antiparallel diode, MOSFETs, and SiC diodes. Through the analysis of operational modes, each switch is selected by considering switch stresses. Finally, design guides and gain characteristics of the bidirectional full-bridge CLLC resonant converter with the symmetric structure of the primary inverting stage and secondary rectifying stage will be discussed for low voltage DC distribution system. Experimental results will verify the performance of the proposed methods using a 5kW prototype converter.

Keywords: AC-DC Converter, CLLC Resonant Converter, High Efficiency Converter.

1 Introduction

The DC distribution system is one of important future power systems to save energy and to reduce CO2 emission, because it can improve the efficiency of power consumption due to the reduction of the number of power conversion stages. In addition, the DC distribution system brings other many advantages such as easier interface of renewable energy sources to DC systems, easier expansion of power capacity, and less interference with AC grid. There are no issues of frequency stability and reactive power, and no skin effect losses [1-4].

DC distribution system for a residential house used DC home appliances can also allow the flexibility of merging many renewable energy sources because most of the output of renewable energy sources is DC. The overall system configuration of the proposed low voltage (DC 380V) DC distribution system is shown in Fig. 1. In order to balance the power flow and to regulate the DC-bus voltage, the DC distribution system requires a isolated bidirectional AC-DC converter. In particular, the

* Corresponding author.

J. Lee et al. (Eds.): ICIRA 2013, Part II, LNAI 8103, pp. 320–326, 2013.

bidirectional AC-DC converter has an important role for controlling the power flow between DC-bus and AC grid, which can optimize the utilization effectiveness of renewable and utility power.

In order to increase the power conversion efficiency of isolated bidirectional AC-DC converter, two power conversion topologies are proposed in this paper. In order to increase the efficiency of the non-isolated full-bridge AC-DC rectifier, the switching devices are designed by using IGBTs without an antiparallel diode, MOSFETs, and SiC diodes. Through the analysis of operational modes, each switch is selected by considering switch stresses. Finally, design guides and gain characteristics of the bidirectional full-bridge CLLC resonant converter with the symmetric structure of the primary inverting stage and secondary rectifying stage will be discussed for low voltage DC distribution system. Experimental results will verify the performance of the proposed methods using a 5 kW prototype converter. The detailed description of the proposed isolated bidirectional AC-DC converter for a residential house will be discussed.

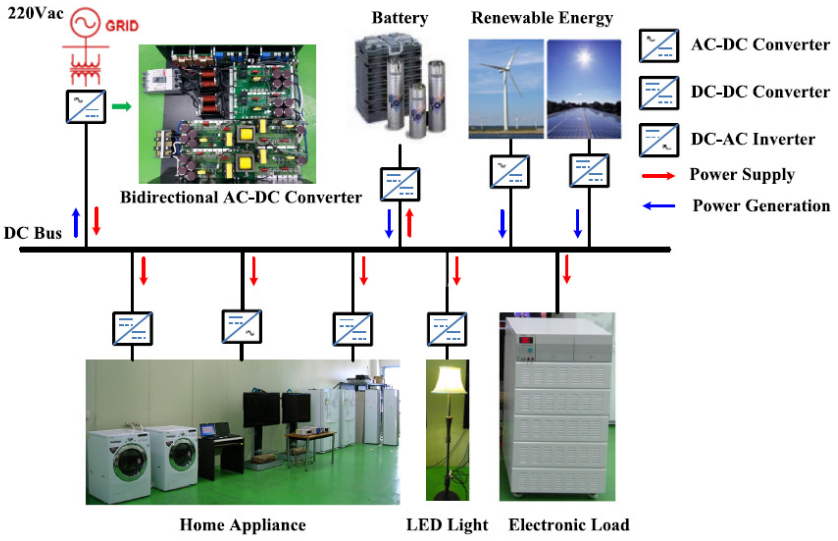

Fig. 1. The general system configuration of DC distribution for a residential house

2 Proposed Isolated Bidirectional AC-DC Rectifier

2.1 Circuit Configuration of Proposed Isolated Bidirectional AC-DC Rectifier

Fig. 2 shows the circuit configuration of the proposed isolated bidirectional AC-DC converter. It consists of the single-phase bidirectional rectifier for grid interface and the isolated bidirectional full-bridge CLLC resonant converter for galvanic isolation. To control the proposed converter, a single digital signal processor (DSP) controller

(TMS320F28335) was used. The power flow directions in the converter are defined as follows: rectification mode (forward direction of power flow) and generation mode (backward direction of power flow).

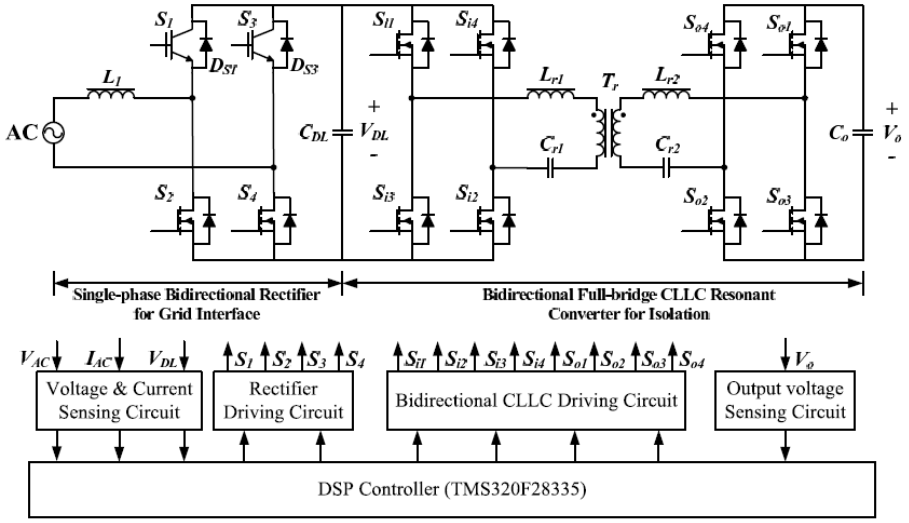

Fig. 2. Proposed isolated bidirectional AC-DC converter

2.2 Single Phase Non-isolated AC-DC Rectifier

The single-phase non-isolated bidirectional rectifier is typically consists of a conventional full-bridge structure. It has two sinusoidal pulse width modulation (SPWM) methods such as the bipolar and the unipolar switching modes. One of the disadvantages of the bipolar switching mode is the need of a large inductor to reduce the input current ripple because the peak-to-peak voltage of the inductor is more than twice the unipolar switching mode. If the full-bridge rectifier operates the unipolar switching mode, inductance for a continuous current mode (CCM) power factor correction (PFC) operation can be reduced. One of full-bridge rectifier legs in the unipolar switching mode is operated at a line frequency while the other one is modulated at switching frequency. However, the unipolar switching mode rectifier using conventional switching devices including a normal antiparallel diode causes high reverse recovery current and turn-on switching noise.

The switching method of the proposed single-phase bidirectional rectifier is unipolar SPWM. In order to reduce the switching losses caused by the reverse recovery current in the rectification mode, the high side switches of the proposed rectifier are composed of two IGBTs without antiparallel diodes (S_1 and S_3) and two SiC diodes (D_{S1} and D_{S3}). The low side switches are composed of two MOSFETs (S_2 and S_4) for reducing conduction loss and for using zero voltage switching (ZVS) operation in the generation mode.

2.3 CLLC Resonant Converter

The switching and the conduction losses in the bidirectional rectifier are the main cause of decreasing power conversion efficiency. Many electric power applications such as battery chargers, automobiles, renewable energy sources, uninterrupted power supplies (UPS), and smart grid power systems require bidirectional DC-DC converters (BDCs) to interface between dc voltage buses where energy generation and consumption devices are installed. Nowadays, plenty of soft switching BDCs focus on eliminating the switching loss, reducing the electromagnetic interference, and achieving an attainable high frequency operational ability. Therefore, power conversion techniques for high power density without leaking efficiency have been developed and extensively reported. In this paper, a bidirectional CLLC resonant converter is proposed with high frequency galvanic isolation.

The proposed bidirectional full-bridge CLLC resonant converter has the full-bridge symmetric structure of the primary inverting stage and secondary rectifying stage with a symmetric transformer. Using the high frequency transformer, the converter can achieve galvanic isolation between the primary side and the secondary side. The transformer T_r is modeled with the magnetizing inductance L_m and the transformer's turn ratio of 1:1. The leakage inductance of the transformer's primary and secondary windings is merged to the resonant inductor L_{r1} and L_{r2}, respectively. The resonant capacitors C_{r1} and C_{r2} make automatic flux balancing and high resonant frequency with L_{r1} and L_{r2}.

3 Experimental Results

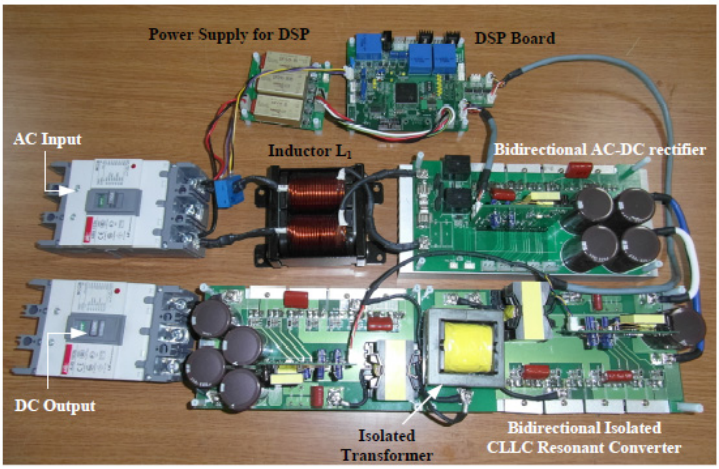

Fig. 3. Prototype of a 5kW bidirectional isolated AC-DC conveter

A 5 kW isolated bidirectional AC-DC converter has been designed and evaluated at 220 Vac input voltage. This prototype converter used a DSP of TI's TMS320F28335

as a digital controller to implement the proposed control algorithms: the unipolar SPWM control for the bidirectional AC-DC rectifier, the proposed SRF-PLL algorithm, the PFM control for the bidirectional CLLC resonant converter, and the dead-band and switch transition controls for the bidirectional power conversion. The switching frequency of the AC-DC rectifier is 13.8 kHz and the DC-DC converter operates within the range of 58 kHz and 65 kHz. The magnetizing inductance is selected as 130 uH in the prototype DC-DC converter which is the overload condition containing 10% margin from the rated load of 5 kW. Fig. 3 shows the configuration of the prototype converter.

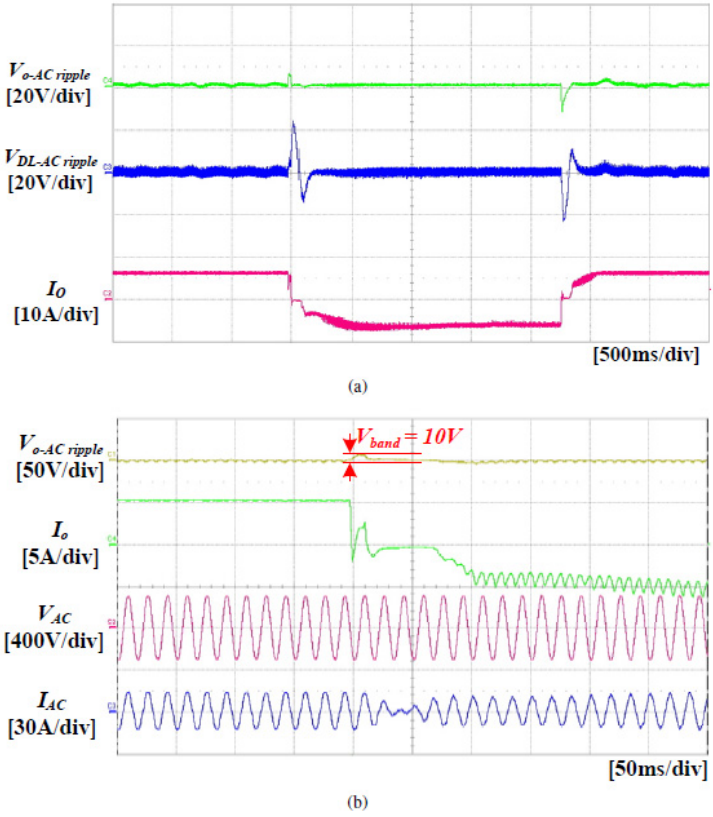

Fig. 4. Step load response of prototype converter

Fig. 4 (a) and (b) shows the experimental waveform of the step load response of the prototype DC-DC converter in the case of the bidirectional power conversion, respectively. In Fig. 4 (a), the distortion level of the output voltage is around 10 V during the mode transition of the power conversion way because the dead-band voltage V_{band} is set to 10 V in the prototype controller at the step load changes from 2.5 kW to -2.5 kW and vice versa. In Fig. 4 (b), when a bidirectional step load

changes from 2.5 kW to -2.5 kW, the AC input current is smoothly changed its phase angle within two cycles.

Fig. 5 shows efficiency curves of the prototype AC-DC rectifier, DC-DC converter, and overall converter system, respectively. They are measured at the input voltage of 220 Vac. The maximum efficiency of rectifier is 98.6% at 2 kW. In addition, the bidirectional CLLC resonant converter has a good efficiency characteristic under middle and high load conditions. The power conversion efficiency is higher than 97.5% at more than 50% (2.5 kW) of the full load. Finally, the power conversion efficiency of the overall converter system is 94.5% at the rated output power of 5 kW. The maximum efficiency is almost 96% at 2.5 kW.

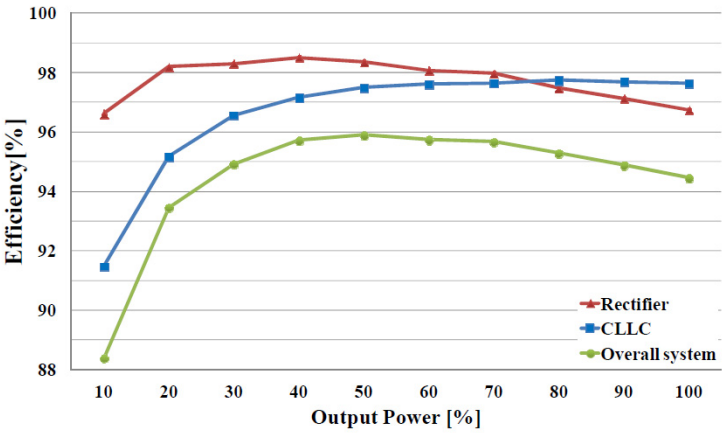

Fig. 5. Power conversion efficiency curves of the AC-DC rectifier, DC-DC converter, and overall converter system

4 Conclusions

In order to improve the reverse recovery problem, the high side switches of the AC-DC rectifier employ IGBTs without antiparallel diodes and SiC diodes. In addition, the low side switches are composed of two MOSFETs to reduce the conduction loss in the rectification mode. For comparison with the conventional IGBT switches, the total conduction losses of the rectifier's switches are calculated in the rectification mode. The proposed CLLC resonant converter can operate under the ZVS for the primary switches and the soft commutation for the output rectifiers. The soft switching condition of the converter is derived to obtain the design methodology of the resonant network. From light to full load, the overall power conversion efficiency of the 5 kW prototype converter was measured to almost 96% at 2.5 kW and 94.5% at the full load of 5 kW.

References

1. Seo, G.-S., Baek, J., Choi, K., Bae, H., Cho, B.: Modeling and analysis of DC distribution systems. In: Power Electronics and ECCE Asia (ICPE & ECCE), pp. 223–227 (May 2011)
2. Techakittiroj, K., Wongpaibool, V.: Co-existance between AC-distribution and DC-distribution: In the view of appliances. In: Computer and Electrical Engineering (ICCEE), vol. 1, pp. 421–425 (December 2009)
3. Stupar, A., Friedli, T., Minibock, J., Kolar, J.: Towards a 99% efficient three-phase buck-type PFC rectifier for 400-v DC distribution systems. IEEE Trans. Power Electronics 27(4), 1732–1744 (2012)
4. Dong, D., Cvetkovic, I., Boroyevich, D., Zhang, W., Wang, R., Mattavelli, P.: Grid-interface bidirectional converter for residential DC distribution systems part one: High-density two-stage topology. IEEE Trans. Power Electronics 28(4), 1655–1666 (2013)

Dynamic Analysis and Optimal Design of High Efficiency Full Bridge LLC Resonant Converter

Dong-Keun Jeong[1], Myung-Hyo Ryu[2], Joo-Won Baek[2,*], and Hee-Je Kim[3]

[1] Department of Interdisciplinary Program in Robotics, Pusan National University, Jangjeon-dong, Geumjung-gu, Korea
keunygajjang@nate.com
[2] Power Conversion Research Center, KERI, Changwon, Korea
{mhryu,jwbaek}@keri.re.kr
[3] Department of Electrical Enginneering, Pusan National University, Jangjeon-dong, Geumjung-gu, Korea
heeje@pusan.ac.kr

Abstract. In this paper, high efficiency full bridge LLCresonant converter for server power system is introduced. LLCresonant converter was reported in many papers recentlybecause of its simple structure, high efficiency and highswitching frequency ability. However, many SMPS designersand field engineers still encounter technical difficulties of powerstage design and control scheme due to environmentalregulations of power system. This paper clearly presentstheoretical and practical details involved with the dynamicanalysis and design procedures. The accuracy of dynamicanalysis and validity of optimal design are confirmed with bothcomputer simulations and experimental measurement.

Keywords: LLCresonant converter, high efficiency, optimal design.

1 Introduction

Nowadays, LLC resonant converters are widely used forfront-end DC/DC stage of distributed power system(DPS)because of high efficiency, small switching loss and notsensitive to load change. However, many power supplydesigners still encounter technical difficulties of power stagedesign and control scheme due to input variations andenvironmental regulations of power system. In particular, thepower system required low voltage and high current has adiversity of hardship. For example, engineers should considerefficiency, power density, reliability, and thermal problems.This paper presents practical issues and design procedures ofLLC resonant converter for server power system. Although itis well reported dynamic analysis and optimal design for LLCresonant converters, there are not papers which is dealt withspecific reference.

* Corresponding author.

J. Lee et al. (Eds.): ICIRA 2013, Part II, LNAI 8103, pp. 327–333, 2013.

This paper deals with a full bridge LLC resonant converteroperating at the presence of wide variations in both inputvoltage and load current for server power system. While anLLC converter for specific application will be used toillustrate technical contents of this paper, the results can beextended to most LLC converters intended for consumers andindustrial applications.

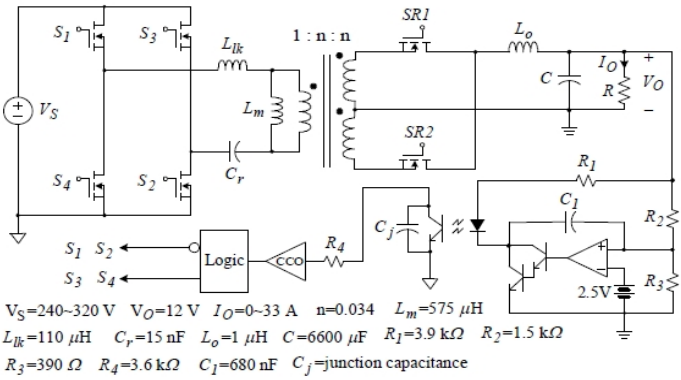

Fig. 1. Full bridge LLC resonant converter

2 Full Bridge LLC Resonant Converter

2.1 Circuit Configuration

Fig.1 shows a simplified circuit diagram of a full bridgeLLC resonant converter designed for server power system.The converter receives a 240~320 V input from a front-endpower unit and provides a 12 V output to CPUs and voltageregulator modules. While the maximum load current is 33 A,it can be reduced 0 A when a system is in standby mode. Afull-bridge converter is configured using MOSFET switches,three-winding transformer, and center-tapped rectifier. Thedistinctive part is a rectifier and used synchronous rectifiersinstead of diodes. This structure is more desirable than arectifier using diodes and recently adapted at SMPS in order toobtain high efficiency. An LLC resonant tank is formedby adding one resonant capacitor (Cr) to the leakageinductance (Llk) and magnetizing inductance (Lm) of thethree-winding transformer.The converter employs standard frequency control with anoutput voltage feedback. The optocoupler is combined with ashunt regulator-type error amplifier to implement an isolatedfeedback controller. The output of the voltage feedback is fedto the current controlled oscillator (CCO) to generate variablefrequency switch drive signals. A two-pole one-zerocompensation circuit, which offers good closed-loopperformance for resonant converters [1], is located around the error amplifier and optocoupler.

2.2 Design Procedures and Considerations

1) Minimize primary RMS current: To achieving highefficiency, the low primary current is better because ofswitching losses. In case of these operating conditions, output current is muchlarger than output voltage. Therefore, a full bridge-type isbetter than a half bridge-type because full bridge LLCconverter can reduce primary RMS current by 50% than halfbridge LLC converter.

2)Minimize secondary rectifiers loss under normaloperating condition: As we know the conduction loss insecondary rectifier is the greatest portion in total losses It is used synchronous rectifiers instead of diodes as asecondary rectification. A synchronous rectifier (SR) isrecently used for achieving high efficiency.

3)Determine operational region: Fig. 3 shows the voltagegain curve of the LLC resonant converter. The operationalmode is illustrated in Fig. 2, where a family of input-tooutputvoltage gain curves of the LLC resonant converterare shown, each with a different load condition. Based onthe location of the operating point, the operational mode ofthe LLC converter is divided into Mode 1 and Mode 2.

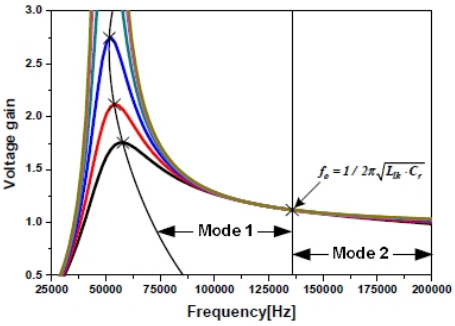

Fig. 2. Operational mode and operational region

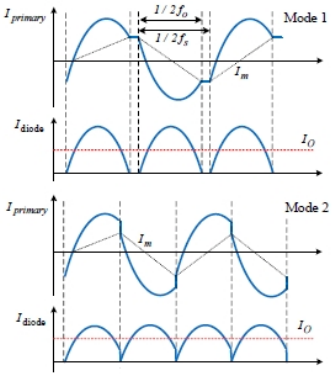

Fig. 3. Waveforms of each operation mode

It is well known that the LLC resonant converter should beoperated in Mode 1 and Mode 2 for ZVS in [3].In this application, the LLC resonantconverter operating in Mode 1 is more desirable than Mode 2.Fig. 3 presents waveforms in Mode 1 and Mode 2. Theoperation in Mode 1 allows the soft commutation of rectifiernetworks in secondary side, while the circulating current isrelatively large and peak current in rectifier networks isbigger than Mode 2. However, operation in Mode 1 issuitable for this application because output current isrelatively larger than output voltage.

3 Dynamic Analysis and Control Design

3.1 Frequency-to-Output Transfer Function

In general, high-order polynomials are necessary toaccurately describe the small-signal transfer functions ofresonant converters. However, for LC series resonantconverters and LLC resonant converters, some of theresonant poles appear at very high frequencies-far beyondthe control bandwidth. Thus, frequency-to-output transferfunction can be approximated by a third order polynomial[7].

3.2 Power Stage Dynamics

In this application, the operating region of designed LLCconverter covers Mode 1. The dynamics of Mode 1 is morecomplex than Mode 2, and it is illustrated in [1] in detail. Inbrief, the beat-frequency double pole splits into tworeal poles. As a result, this leads to phase delay in middlefrequency.However, designed LLC converter has a bigoutput capacitor because of output voltage ripple cancellation.

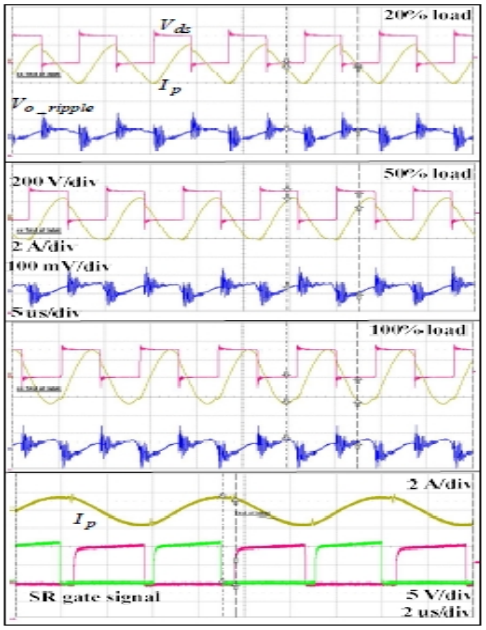

Fig. 4. Measured waveforms of LLC resonant converter prototype

3.3 Compensation Design Parameters

the voltage feedback compensation builtusing a shunt regulator-type error amplifier and optocoupler.The gain of compensator is 800, zero frequency is 40 Hz, andpole frequency is 30 kHz.With these compensation parameters, the loopgain wouldmaintain the desirable -20 dB/dec slope until theloop gain crossover frequency,thereby ensuring stability withsufficient phase margin.

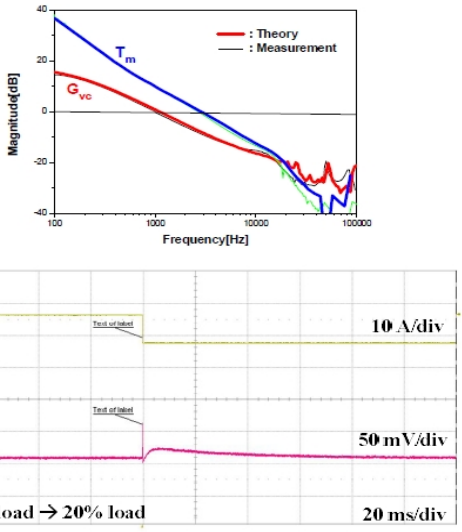

Fig. 5. Loop gain characteristic and step load response

4 Experimental Results

Fig. 4 shows operating waveforms of designed LLCresonant converter according to load conditions. Input voltageis 300 V, full load condition is 12 V/33 A. This converter issatisfied with ZVS in entire regions and synchronousrectification. Output voltage ripple is under 100 mV, Lineregulation and load regulation are very tight. Switchingfrequency variation of this converter is from 76 kHz to 117kHz. The primary switches are STP12NM50 from STMicro,FDP8400 MOSFET from Fairchild was employed for eachsynchronous rectifier SR1 and SR2. This MOSFET has lowerDS _ ON R . Transformer was built using PQ3230 ferrite cores.Turns ratio is 56:2:2, and Litz wire is used. Low-voltagealuminum capacitors were used for output capacitor.

Fig. 8 shows control-to-output transfer function, loop gainand step load response. The loop gain shows good correlationwith the design target, illustrated in Fig. 5.shows thewaveforms in response to the load change from 50% load(17A) to 20% load(6A) at VS300V.Designed converter isvery stable and well-controlled

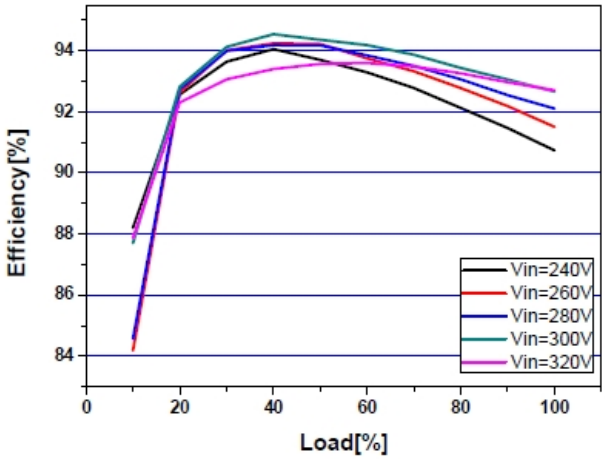

Fig. 6. Measured efficiencies of full bridge LLC resonant converter

behavior. The measured efficiencies of the full bridge LLC resonantconverter are shown in Fig. 6. It is confirmed the designedconverter has superior efficiencies in entire ranges. From 20%load condition to full load condition, it shows high efficiency.

5 Conclusions

This paper discussed all engineering issues involved withthe dynamic analysis and high efficiency design of the LLCresonant converter operating under large line andloadvariations. It has been demonstrated that the power stageproperly designed forthe entire range, offers stable operationwith satisfactory closed-loop performance for the operationalregion. Detailed design procedures to obtain a compensationdesignhave been presented.The proposed guideline is applicable to LLC resonantconvertersfor server power system without complex methods.This paper introduced a simpleand basic approach for obtainhigh efficiency. It will be perceived that this guidelinewouldhelp SMPS engineers to design high efficiency converter.

Acknowledgement. This research was supported by the MKE(The Ministry of Knowledge Economy), Korea, under the Human Resources Development Program for robotics support program supervised by the NIPA(National IT Industry Promotion Agency) (NIPA-2012-H1502-12-1002).

References

[1] Jang, J., Joung, M., Choi, B., Kim, H.-G.: Dynamic analysis and control designof optocoupler-isolated LLC resonant converters with wide input and load variations. In: Proc. ECCE 2009, San Jose, CA (September 2009)

[2] Lazar, J.F., Martinelli, R.: Steady-state analysis of the LLC series resonant converter. In: APEC 2001, pp. 728–735 (2001)

[3] Yang, B., Lee, F.C., Zhang, A.J., Huang, G.: LLC resonant converter for front end DC/DC conversion. In: APEC 2002, pp. 1108–1112 (2002)

[4] Lu, B., Liu, W., Liang, Y., Lee, F.C., Van Wyk, J.D.: Optimal design methodology for LLC resonant converter. In: APEC 2006, pp. 533–538 (2006)

[5] Choi, H.: Analysis and design of LLC resonant converterwith integrated transformer. In: APEC 2007, pp. 1630–1635 (2007)

[6] Yang, B., Lee, F.C.: Small-signal analysis for LLC resonant converter. CPES Seminar S7.3, 144–149 (2003)

[7] Yang, B.: Topology investigation for front end DC/DC Power Conversion for Distributed Power Systems. Dissertation, Virginia Polytechnic Institute and State University (2003)

[8] Yang, E.X.: Extended describing function method forsmall signal modeling of resonant and multi resonant converters. Dissertation, Virginia Polytechnic Institute and State University (1994)

A Boost PFC Rectifier with a Passive Lossless Snubber Circuit Using Coupled Inductors Methodes

Hyeok-Jin Yun[1], Jong-Hyun Kim[1], Myung-Hyo Ryu[1], and Hee-Je Kim[2,*]

[1] Power Conversion & Control Research Center, HVDC Research Division, KERI, Changwon, Korea
yhj3409@naver.com,
{kimjh,mhryu}@keri.re.kr
[2] Department of Electrical Enginneering, Pusan National University, Jangjeon-dong, Geumjung-gu, Korea
heeje@pusan.ac.kr

Abstract. In this paper, a boost PFC rectifier with a novel passive lossless snubber circuit is proposed to minimize switching loss in high power applications. A new turn-on mechanism of the lossless snubber using coupled inductor is applied to reduce the reverse recovery loss of the output diode rectifier. The turn-off operation of the lossless snubber is composed of a single capacitor and two diodes to reduce the voltage stress and the power loss at the turn-off of the switch. Due to the lossless clamping operation, the proposed PFC operates under soft switching conditions with high power conversion efficiency. The design and performance of the boost PFC rectifier using the proposed lossless snubber are verified by experimental results using a 3.3kW prototype rectifier.

Keywords: PFC, lossless snubber, boost.

1 Introduction

The conventional operation of the CCM boost converter causes high reverse recovery losses of the output diode as well as electromagnetic interference (EMI) noises. An alternative to minimize these drawbacks is the use of a silicon carbide (SiC) diode or a soft switching circuit instead of conventional diode rectifiers. The SiC diode can reduce a power loss caused by the reverse recovery current. However, this method still remains a hard switching problem of a main switch. Furthermore, the SiC diode has a higher forward voltage drop than the drop of a fast recovery diode (FRD). The soft switching circuit for the CCM boost rectifier can reduce the reverse recovery by reducing the variation rate of the output diode's turn-off current. Various soft switching techniques using active and passive snubber circuits have been proposed [1-7]. The power switch of the converter can be softly switched using the active snubber, however, it requires an additional control circuit to drive the auxiliary switch

* Corresponding author.

J. Lee et al. (Eds.): ICIRA 2013, Part II, LNAI 8103, pp. 334–337, 2013.

which operates under hard switching conditions. Using conventional method, in order to increase power conversion efficiency for high power applications, the expensive components with higher power rating are required. Generally, passive lossless snubbers are as effective as the active snubber without any additional auxiliary switches and control circuits. A passive snubber circuit using saturable inductors added to reduce reverse recovery current of the output diode has been proposed [5-6]. It causes extra voltage stress on main switches and increases extra cost. A turn off snubber of the main switch is composed of conventional RCD snubber so as to confine the rise of the switch voltage [7]. However, the loss of the snubber resistor reduces the overall power conversion efficiency.

In this paper, in order to improve the power conversion efficiency of a CCM boost PFC rectifier for high power applications, a novel passive lossless snubber circuit is proposed. The proposed turn-on snubber is composed of the coupled inductors merged to the boost inductor. The reverse recorvery current is alleviated using the proposed passive snubber circuit. In addition, the turn-off lossless snubber reduces the voltage overshoot of the main switch during a turn-off transition. The performance of the proposed lossless snubber was experimentally verified using a 3.3kW prototype PFC rectifier.

2 Introduction

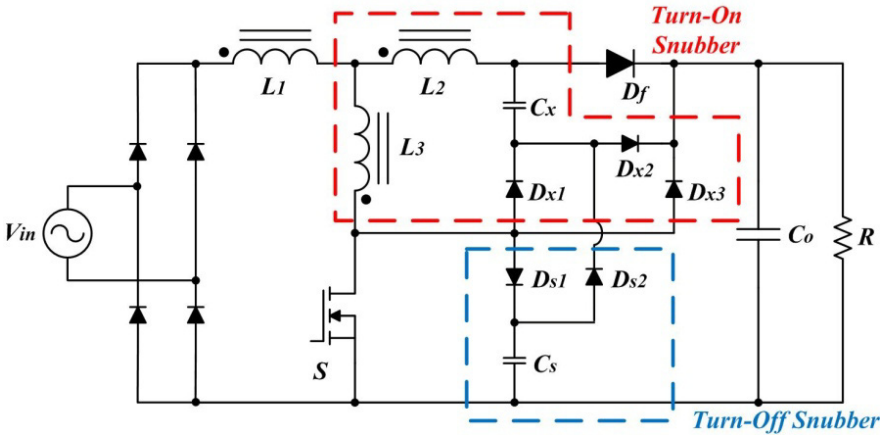

Fig. 1. Proposed PFC boost converter with lossless snubber

Fig. 1 shows the schematic of the PFC boost rectifier with the proposed lossless snubber circuit. The proposed turn-on passive snubber consists of two coupled inductors L_2 and L_3, three diode auxiliary D_{x1}, D_{x2}, and D_{x3}, and an additional capacitor C_x. L_1, L_2, and L_3 are coupled using a single core structure. The turn ratio of the coupled inductors isn:1:1 (n <<1).The turn-off snubber circuit consists of a capacitor C_s and two diodes D_{s1} and D_{s2}.

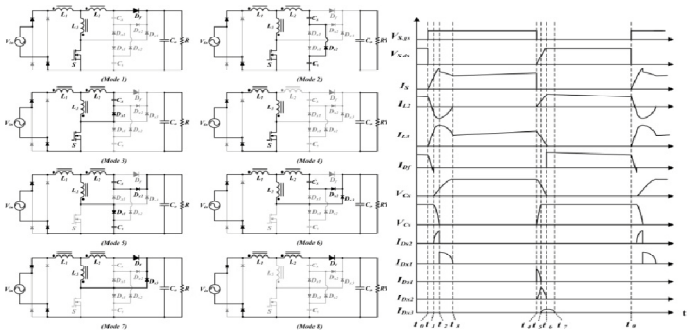

Fig. 2. Eight operating mode of the proposed rectifier and Theoretical waveforms of the converter

There are eight operating modes in a single switching cycle. The circuit operations in the positive half period of the input voltage are shown in Fig. 2. The theoretical waveforms of the proposed rectifier are given in Fig 3. of switching frequency is decided by resonant frequency. Gain is biggest at resonant frequency, but gain fluctuates by changing load. Fig.3

3 Experimental Results

Fig. 3 shows the voltage and current waveforms of the main switch during the turn-on-off transition. Experimental results are verifing that the variation of the output diode current is limited by the proposed lossless snubber using coupled inductors and lossless snubber(Cs, Ds1, and Ds2) can reduce the voltage stresses across the main switch. The proposed lossless snubber does not introduce extra voltage and current stress on the main switch during the turn-on and turn-off periods. It reduces the overlapped area between the switch voltage and current. Fig. 4 shows the measured curve of the power factor and efficiency according to the output power. It is measured at the input voltage of 220 Vac. At the rated load output of 3.3kW, the power conversion efficiency is 97.2%.

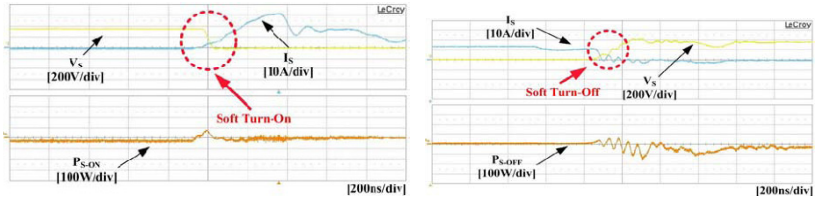

Fig. 3. Measured waveforms of the switch voltage and current during turn-on/off transition

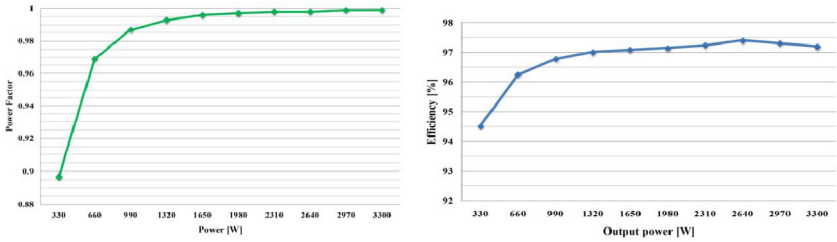

Fig. 4. Measured power factor and efficiency of the experimental rectifier

4 Conclusions

A novel passive lossless snubber for a CCM boost rectifier is proposed. The main switch of the boost PFC rectifier can operate under soft switching conditions with high power efficiency. The proposed passive losseles snubber has no energy consumption because it uses only inductive and capacitive components, which improves power conversion efficiency in CCM boost rectifier. The proposed passive lossless snubber circuit was verified using experimental results with a 3.3kW prototype PFC rectifier. Consequently, the power conversion efficiency was obtained to 97.2% at the rated load. In the final paper, detail analysis and additional experiment data will be presented with various experimental results.

Acknowledgement. This research was supported by the MKE(The Ministry of Knowledge Economy), Korea, under the Human Resources Development Program for robotics support program supervised by the NIPA(National IT Industry Promotion Agency) (NIPA-2012-H1502-12-1002).

References

1. Jovanovic, M.M., Jang, Y.: A novel active snubber for high power boost converter. IEEE Transactions on Power electronics 15(2), 278–284 (2000)
2. Li, R.T.H., Chung, H.S.-H., Sung, A.K.T.: Passive lossless snubber for boost PFC with minimum voltage and current stress. IEEE Transactions on Power Electronics 25(3), 602–613 (2010)
3. Jiang, S.-G., Liu, G.-H., Wang, W., Xu, D.-G.: Research on bridgeless boost PFC with soft-switching. In: 2009 IEEE Vehicle Power and Propulsion Conference, pp. 1461–1464 (2009)
4. Hwu, K.I., Tsai, C.-L., Lin, K.-F.: A simple passive ZCS circuit for PFC converter. In: IEEE 2008 Applied Power Electronics Conference, pp. 1022–1026 (2008)
5. Schenk, K.: Non dissipative snubber circuit with saturable reactor. U.S. Patent 7 233 507 (June 2007)
6. Joung, G., Ma, K., Kim, Y.: Battery discharger applications of high frequency boost converter with lossless snubber. In: Proc. 33th IEEE Power Electron. Spec. Conf. (PESC), pp. 938–942 (2002)
7. Hwu, K.I., Tsai, C.-L., Lin, K.-F.: A simple passive ZCS circuit for PFC converter. In: IEEE 2008 Applied Power Electronics Conference, pp. 1022–1026 (2008)

Experimental Investigation on the Hybrid Smart Green Ship

Kyoung-Jun Lee[1], Dongsul Shin[1], Jong-Pil Lee[2], Tae-Jin Kim[2], and Hee-Je Kim[1]

[1] Electrical Engineering Dept. Pusan National University, Korea, South
[2] Power Conversion Center, KERI, Korea, South

Abstract. The paper presents experimental results from the operation of a proto-type green ship in Geoje island, South Korea. After ground testing with a stand-alone PV generation system, this PV system was added to conventional diesel ship. Proto-type green ship is consisted of photovoltaic (PV) generation system, diesel engine, battery energy storage, hybrid control system, stand-alone and grid-connected inverter. The aim of the green ship is not only to minimize the fuel consumption but also to support the power grid as a distributed generation (DG) in the near future.

Keywords: Smart Green Ship, Hybrid PV/Diesel, Stand-alone mode, Grid-connected mode.

1 Introduction

Around the world, it has been a strong wish of governments to increase the share of renewable green energy in the power production. The main interest has mainly been energy security, rising prices of carbon based energy sources and the prospect of limiting global warming. Concerning the second, global shipping is a major contributor to Global Greenhouse Gas (GHG) emissions, responsible for approximately 3% of global CO_2 emissions [1-2]. The International Maritime Organization (IMO) is now working to start GHG regulations for global shipping, and is under pressure, e.g. from the EU and the United Nations Framework Convention on Climate Change (UNFCCC), to apply regulations with substantial impact on emissions [3]. Also, because the global shipping is normally powered by standalone diesel generator for electricity supply, the shipping industry is greatly affected by increase in global fuel prices. Therefore, the use of renewable energy resource in shipping industry would be of great advantage, especially in reducing CO_2 emissions and the dependence on such highly unpredictable diesel price [4]. There have been many researches world-widely on hybrid energy system [5-15]. Among renewable energies, the solar energy is most applicable to conventional ship at remote sea-shore, gifted with large amounts of solar radiation [16-17]. Therefore, a hybrid green ship (hybrid PV/diesel) will be one effective solution.

In this paper, a hybrid PV/Diesel green ship operating in stand-alone and grid-connected mode is proposed. PV is the primary power sources of the system to

J. Lee et al. (Eds.): ICIRA 2013, Part II, LNAI 8103, pp. 338–344, 2013.

electrical loads in ship, and the diesel engines are used at fluctuating electric power from PV system. A battery bank is also installed in the hybrid system to supply stable power [18]. Unlike the conventional PV hybrid system on land, a hybrid green ship utilized the free space on ship. Also, with the grid-connected inverters, an overall power flow is broadened from the smart grid in land to the off-grid on the island.

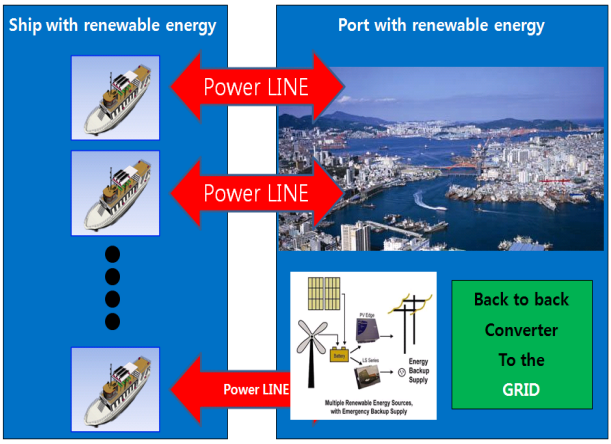

Fig. 1. Hybrid green ship connected with the smart grid

This paper presents experimental results from the operation of a proto-type green ship in Geoje island, South Korea. After ground testing with a stand-alone PV generation system, this PV system was adopted to conventional diesel ship. Proto-type green ship is consisted of photovoltaic (PV) generation system, diesel engine, battery energy storage, hybrid control system, stand-alone and grid-connected inverter. The aim of the green ship is only to minimize the fuel consumption but also to support the power grid through the smart grid in the near future, as shown in Fig. 1.

2 Hybrid PV/Diesel Experimental System

The Operation of Hybrid PV/Diesel green ship is mainly divided into the mode A (at sea) and mode B (in port). Power ratings of the hybrid PV/Diesel system is approximately 3.2 kW for electrical loads, such as lighting, GPS & Communication system and Video system, in cruise ship (80 ton).

2.1 Hybrid Smart Green Ship

After verification experiment of the hybrid PV/Diesel system in land in 2010, the proposed system was installed 80 ton level of cruise ship in 2011, in Geoje island. Unlike the PV plants in land, the total weight of PV generation system and the wind pressure on PV arrays are main concerns of safety of ship at sea. Approved by the

Korea Ship Safety Technology Authority (KST), PV systems were installed on conventional cruise ship and controlled by Hybrid control panel. 3.2 kW (200W / 16 EA) of PV arrays are installed on the back side of the ship. To consider the stability of the ship, battery bank was installed on the basement of ship.

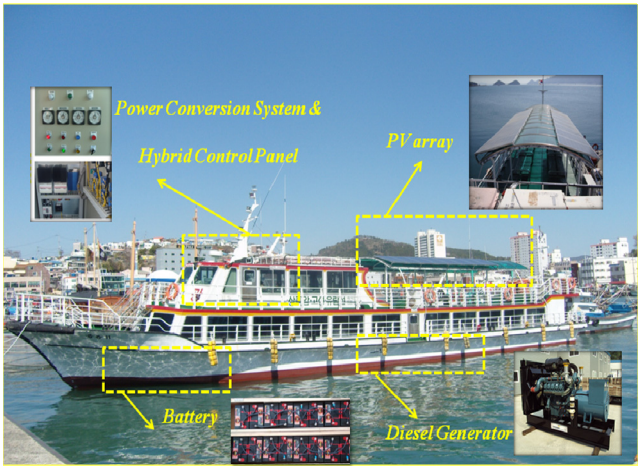

Fig. 2. Proto-type of Hybrid PV/Diesel Green ship (Geoje Island, South Korea)

The selected ship for the experiment is the normal passenger ship (84 ton, 263 Passengers). One of the greatest concerns for the passenger ship is the stability of the ship. The back side of the dock was renovated according to the design, as shown in Fig. 3, considering the average height of the passenger, wind pressure and maintenance.

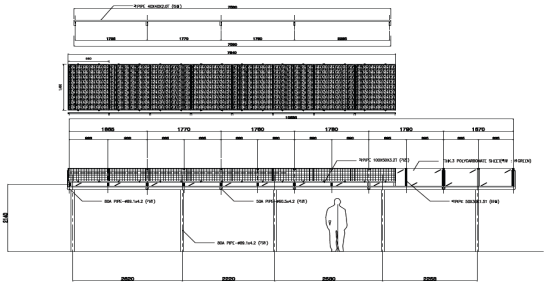

Fig. 3. Installation drawing of PV arrays

2.2 Power Conversion Unit in Smart Green Ship

As mentioned above, there are mainly two operation modes. Mode A (at sea) is like the stand-alone mode of PV systems in land, as shown in Fig. 4. According to the status of PV power, electrical loads in ship can be powered by either battery bank or

diesel generator. PV arrays on left and right side of the roof are connected separately to the solar controller (DC-DC Converter) due to the different maximum power point (MPP). Once the cruise ship is harbor and battery is full charged, extra PV power is utilized through the grid-connected inverter, as shown in Fig. 5. Monitoring system for hybrid green ship is established using LabVIEW^{TM} program. The proto-type hybrid green ship plied between Geojedo (island) and Somaemuldo (island). Through the experiment, validity of the hybrid green ship was approved.

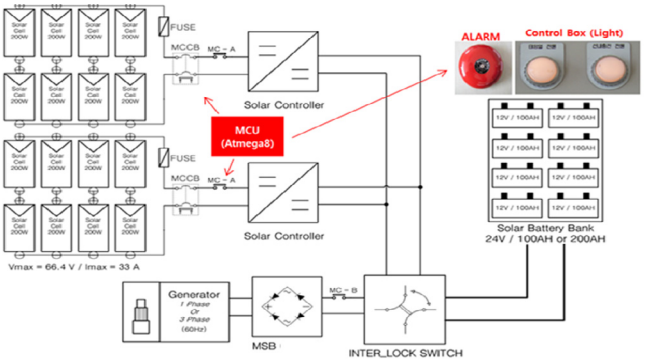

Fig. 4. Stand-alone mode of Hybrid PV/Diesel Green ship (Operation Mode A)

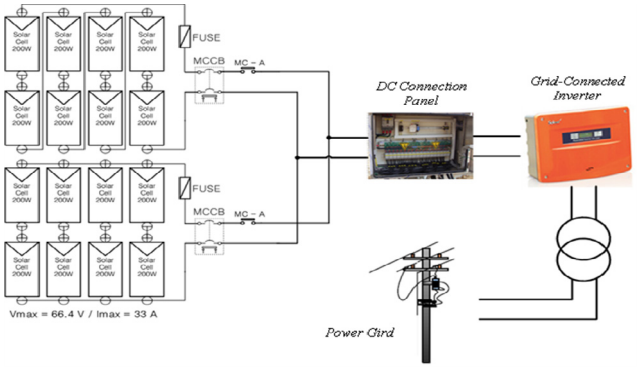

Fig. 5. Grid-connected mode of Hybrid PV/Diesel Green ship (Operation Mode B)

3 Experimental Results

In this study, a grid-connected mode is implemented when the ship at anchor in the harbor. By the simple change of magnet switches, the PV arrays are series connected, resulting in Ns (Number of series connections) = 8, Np (Number of parallel connections) = 2. An open-circuit voltage of PV arrays in grid-connected mode is 265.6 V, which satisfies the input voltage range of DC-AC inverter (Grid-connected). In the case of grid faults such as grid over/under voltage, grid over/under frequency, over current and ground fault, the grid-connected inverter will wait 5 minutes prior to

restarting. Fig. 6 illustrates the voltage of PV arrays (V_{PV}_Total), the current of PV arrays (I_{PV}_Total), the AC grid voltage (v_{Grid_INV}) and the AC grid current (i_{Grid_INV}) at Geojedo (island). The output voltage of PV arrays in the grid-connected mode is increased to 224 V, which is the voltage at maximum power (Vmp). The injected active power to the grid is about 600 W 3:20 PM (27 Sep, 2011) in Fig. 6. The injected grid current includes low-order harmonic components due to the effect of weak and distorted grid at Geojedo (island), requiring the improvement of power quality with such a shunt active power filter (SAPF) in the near future.

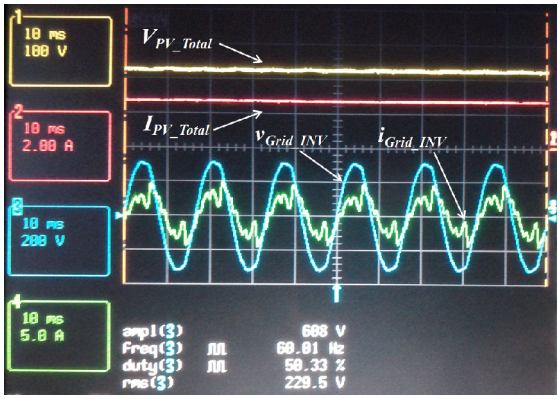

Fig. 6. Experimental waveforms in the grid-connected mode

4 Conclusion

In this paper, it has been proposed that the hybrid PV/diesel green ship operates not only in a stand-alone mode but also when connected to the smart grid. To commercialize the proposed green ship in the near future, the conventional passenger ship was renovated with 3.2 kW PV systems and operated during the project. The operating strategy of hybrid PV/diesel system, stability assessment and economic analysis were discussed and concluded as follows:

1. A 3.2 kW PV array is fixed on the top of the green ship with 15° tilted, considering cost of installation, maintenance cost and stability against wind.
2. Stand-alone mode and grid-connected mode is controlled automatically or manually by the captain of the ship.
3. Hybrid PV/diesel operation is stable with the battery bank during mode changes.
4. Hybrid PV/diesel green ship passed the stability assessment test by the authorized department (KST in this project)
5. Payback period of initial investment can be reduced due to decreasing PV module costs, increasing diesel fuel costs and CO_2 emission trade system.

6. Hybrid PV/diesel green ship will decrease the dependence of fossil fuels and be one solution for extending energy flow from land (smart grid) to island (remote areas).

Acknowledgement. This research was financially supported by the Ministry of TRADE INDUSTRY &Energy (MOTIE) Korea Institute for Advancement of Technology (KIAT) and Honam institute for Regional Program Evaluation.

References

1. Buhaug, Ø., Corbett, J.J., Endresen, Ø., Eyring, V., Faber, J., Hanayama, S., Lee, D.S., Lee, D., Lindstad, H., Markowska, A.Z., Mjelde, A., Nelissen, D., Nilsen, J., Palsson, C., Winebrake, J.J., Wu, W.-Q., Yoshida, K.: Second IMO GHG study 2009. International Maritime Organization (IMO), London (2009)
2. Endresen, Ø., Dalsøren, S., Eide, M., Isaksen, I.S., Sørgård, E.: The environmental impacts of increased international maritime shipping, past trends and future perspectives. OECD/ITF Global Forum on Transport and Environment in a Globalising World, Guadalajara, Mexico (2008), Also published in OECD 2010, Globalisation, Transport and the Environment (2010) ISBN 978926407919-9
3. Van Dender, K., Crist, P.: Policy instruments to limit negative environmental impacts from increased international transport: An economic perspective, Guadalajara, Mexico, November 10-12. Global Forum on Transport and Environment in a Globalising World (2008)
4. Lau, K.Y., et al.: Performance analysis of hybrid photovoltaic/diesel energy system under Malaysian conditions. Energy 35, 3245–3255 (2010)
5. Agbossou, K., Kolhe, M., Hamelin, J., Bose, T.K.: Performance of a stand-alone renewable energy system based on energy storage as hydrogen. IEEE Trans. Energy Convers. 19(3), 633–640 (2004)
6. Nelson, D.B., Nehrir, M.H., Wang, C.: Unit sizing and cost analysis of stand-alone hybrid Wind/PV/fuel cell systems. Renewable Energy 31(10), 1641–1656 (2006)
7. El-Shatter, T.F., Eskandar, M.N., El-Hagry, M.T.: Hybrid PV/fuel cell system design and simulation. Renewable Energy 27(3), 479–485 (2002)
8. Ulleberg, Ø., Mørner, S.O.: TRNSYS simulation models for solarhydrogen systems. Solar Energy 59(4-6), 271–279 (1997)
9. Iqbal, M.T.: Modeling and control of a wind fuel cell hybrid energy system. Renewable Energy 28(2), 223–237 (2003)
10. Sharma, H., Islam, S., Pryor, T.: Dynamic modeling and simulation of a hybrid wind diesel remote area power system. Int. J. Renewable Energy Eng. 2(1), 19–25 (2000)
11. Chedid, R., Akiki, H., Rahman, S.: A decision support technique for the design of hybrid solar-wind power systems. IEEE Trans. Energy Convers. 13(1), 76–83 (1998)
12. Kellogg, W.D., Nehrir, M.H., Venkataramanan, G., Gerez, V.: Generation unit sizing and cost analysis for stand-alone wind, photovoltaic, and hybrid wind/PV systems. IEEE Trans. Energy Convers. 13(1), 70–75 (1998)
13. Giraud, F., Salameh, Z.M.: Steady-state performance of a grid-connected rooftop hybrid wind-photovoltaic power system with battery storage. IEEE Trans. Energy Convers. 16(1), 1–7 (2001)

14. Abdin, E.S., Osheiba, A.M., Khater, M.M.: Modeling and optimal controllers design for a stand-alone photovoltaic-diesel generating unit. IEEE Trans. Energy Convers. 14(3), 560–565 (1999)
15. Bonanno, F., Consoli, A., Raciti, A., Morgana, B., Nocera, U.: Transient analysis of integrated diesel-wind-photovoltaic generation systems. IEEE Trans. Energy Convers. 14(2), 232–238 (1999)
16. Enslin, J.H.R., Snyman, D.B.: Combined low-cost, high-efficient inverter, peak power tracker and regulator for PV applications. IEEE Trans. Power Electron. 6(1), 73–82 (1991)
17. Jain, S., Agarwal, V.: A new algorithm for rapid tracking of approximate maximum power point in photovoltaic systems. IEEE Power Electron. Lett. 2(1), 16–19 (2004)
18. Wang, C., Nehrir, M.H.: Power management of a stand-alone wind photovoltaic fuel-cell energy system. IEEE Trans. Energy Convers. 23(3), 957–967 (2008)

Hybrid Control Scheme for a Half-Bridge LLC Resonant Converter with a Wide Input Range

Dongsul Shin[1], Kyoung-Jun Lee[1], Jong-Pil Lee[2], and Hee-Je Kim[1]

[1] Department of Electrical Engineering, Pusan National University, Busan, Koera
[2] Power Conversion & Control Research Center HVDC Research Division, Korea Electrotechnology Research Institute, Changwon, South Korea

Abstract. In this paper, the LLC resonant converter with hybrid PFM and PWM control scheme is proposed for the wide input range operation. In low input voltage range, the PFM control scheme is applied to LLC resonant converter for normal operation. In PFM mode, zero-voltage switching is achieved form no load to full load condition. In high voltage range, the PWM control scheme is applied to the converter to reduce the gain of resonant tank. In PWM mode, zero-voltage switching is not achieved because the current is not enough to discharge parasitic capacitor of power MOSFET for turning on the body diode. The proposed method is experimentally verified with 400W laboratory prototype.

Keywords: LLC resonant converter, Wide input range, PWM and PFM control scheme.

1 Introduction

Nowadays, Switched-Mode Power Supply (SMPS) plays an important role in the consumer power market. With its small size, it can be found everywhere from mobile phone chargers to LCD TVs in the consumer power market. Also, SMPS is used in robot applications for supplying high quality power to robots.

There are several control schemes in order to regulate an output voltage. Among them, Pulse-Width-Modulation (PWM) is most commonly used to control DC-DC converter. A switching frequency of these kinds of converters is far away from a resonant frequency of an output LC filter. A gain of output voltage to input voltage is determined by duty cycle of PWM. A gain decreased by means of increase of load is supplemented by increasing duty cycle. It is a merit that conduction loss is lower than resonant converters controlled by Pulse-Frequency-Modulation (PFM). The other control scheme is PFM used in resonant converter applications. Resonant converters have one resonant tank, sometimes two. The switching frequency is in the vicinity of resonant frequency. As the switching frequency is changed, the output voltage of resonant converter is changed because of the gain variation of resonant tank. It has a merit that soft switching technique is easily achieved by circulating energy of

J. Lee et al. (Eds.): ICIRA 2013, Part II, LNAI 8103, pp. 345–352, 2013.

resonant tank in all operation regions. However, conduction loss of the converter is higher than other kinds of converters controlled by PWM control scheme because of circulating energy. Furthermore, the variation of the switching frequency range for regulation of an output voltage is wide and the dependence of converter gain on load condition is high.

In this paper, hybrid control scheme of half-bridge LLC resonant converter is proposed for a wide input range application and the medium power applications. The full-bridge configuration could be applied to LLC resonant converter. However, that is not suitable for medium power application because of high cost of active switches. In order to compensate a weakness of LLC resonant converter abovementioned and for a wide input range in half-bridge configuration, PWM and PFM are simultaneously applied to regulate the output voltage. Therefore, the switching frequency range is reduced and circulating energy is also decreased. When proposed converter is controlled in PFM mode, the characteristics of the converter are the same as LLC resonant converter. When proposed converter is controlled in PWM mode, the characteristics of the converter are similar with asymmetric PWM half-bridge converter.

2 LLC Resonant Converter

High power density and high efficiency are the matter of the utmost concern. So, in many papers, the methods and strategies of control and topologies have been proposed. A half-bridge LLC resonant converter is widely used with great characteristic of LLC resonant tank in low and medium power application. The resonant tank is shown is Fig. 1.

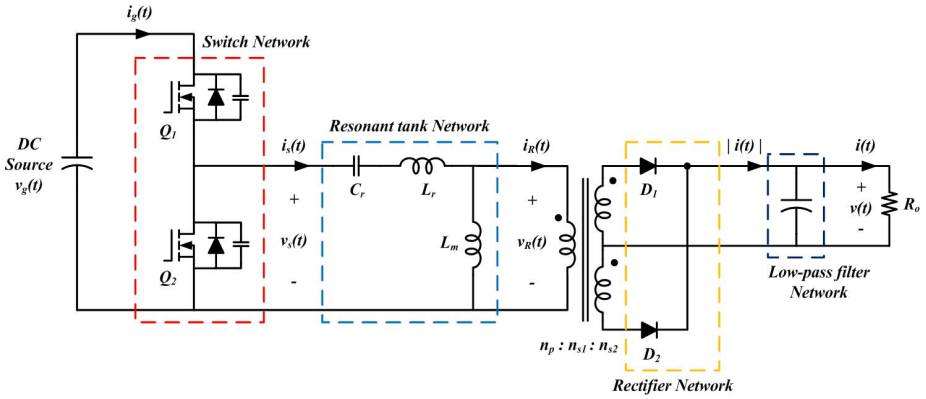

Fig. 1. The half-bridge LLC resonant converter

The resonant tank has both Series Resonant Converter (SRC) and Parallel Resonant Converter (PRC) characteristics. The resonant tank network is represented with fundamental output voltage of the switch network and an effective resistive load derived for rectifier network as shown in Fig. 2. From the resonant network in Fig. 2, the characteristics of LLC resonant converter can be derived. The transfer function of resonant network is

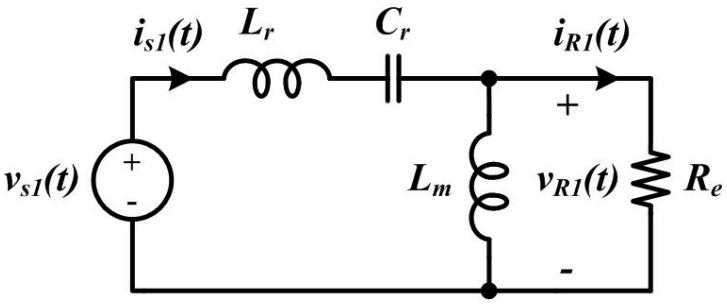

Fig. 2. LLC resonant tank with load

$$H(s) = \frac{sL_m \parallel \mathrm{Re}}{sL_r + \frac{1}{sC_r} + sL_m \parallel \mathrm{Re}} \tag{1}$$

As shown in above equation, there are two resonant frequencies. One resonant frequency is formed by L_r and C_r. The other resonant frequency is formed by L_r+L_m and C_r. The DC characteristic of LLC resonant tank is represented by above equation in Fig. 3.

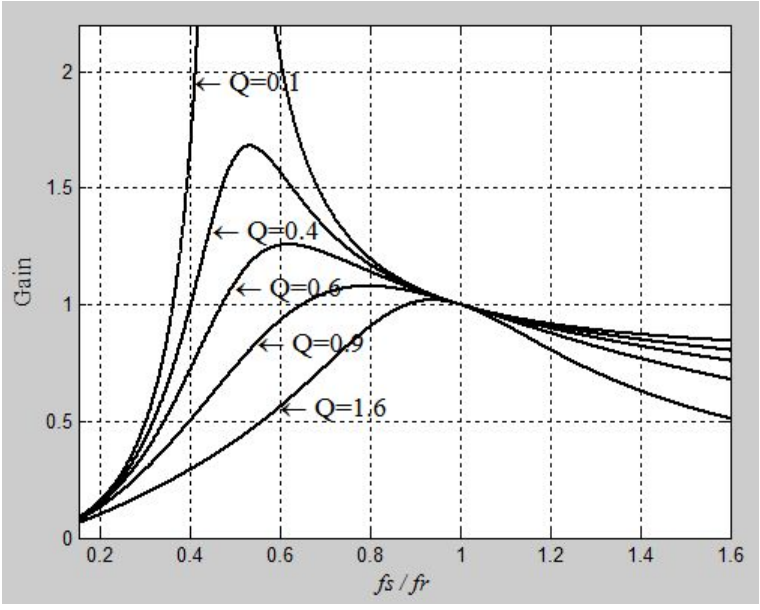

Fig. 3. DC characteristics of LLC resonant tank

3 Hybrid Control Scheme with Operation Region

In order to control the output voltage of resonant converter, the switching frequency control is mostly used to change the DC gain of resonant tank. This means that the impedance of resonant tank is varied by the change of switching frequency. LLC resonant converter also employ Pulse Frequency Modulation (PFM) control scheme to regulate the output voltage. When the input voltage of resonant converter is changed or the load variation happens, the switching frequency is changed to regulate the output voltage. The amount of switching frequency variation is changed according to the design of resonant tank which is concerned with the input voltage range and the load condition. However, in the wide input voltage application, there is the limitation of the switching frequency variation.

In this paper, a hybrid control scheme is proposed to make the range of switching frequency variation narrow. PWM and PFM are combined to minimize the variation of the switching frequency. In lower the input voltage range, PFM control method is employed. In higher input voltage range, PWM control method is employed. Because the voltage gain is not variable at the resonant frequency, the start point of PWM is chosen as resonant frequency. The other reason for the start point of PWM is to minimize the switching frequency variation. If the region of higher switching frequency than resonant frequency is chosen for the start point of PWM, switching frequency have to be reduced to take the maximum gain needed for PWM region. Fig. 4 shows the PFM and PWM operating region. This DC characteristics curve is

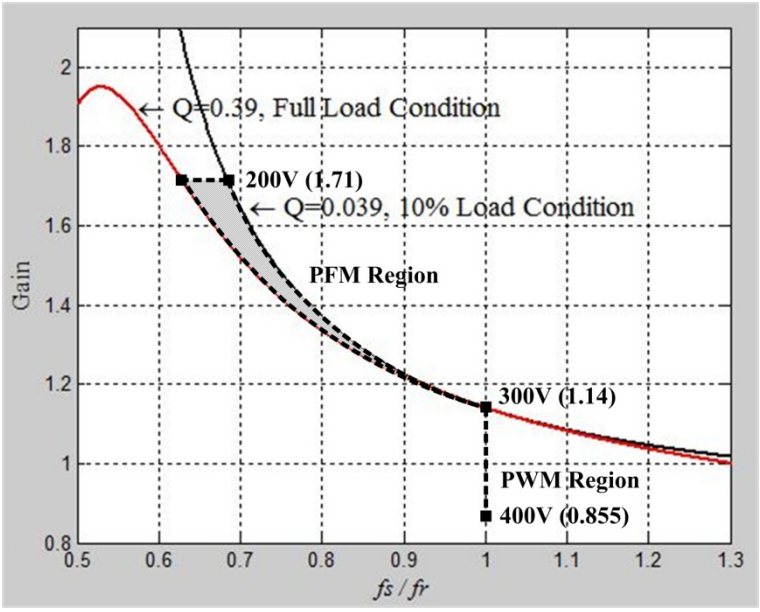

Fig. 4. PFM and PWM operating region from 200~400 V

used for the design of LLC resonant tank to be implemented. Upper line is gain curve at the 10% load condition and lower line is gain curve at the full load condition. When the input voltage becomes above 300 V, PWM control method is applied at that frequency. The critical value for determination of control scheme is 300 V. Fig. 4 PFM and PWM operating region from 200~400 V

4 Experimental Results

The 400 W experimental prototype is built. The input voltage range is from 200 V ~ 400 V and output voltage is 48 V. The specification of prototype forms the basis of LLC resonant tank. The LLC resonant converter is controlled by PFM control scheme at the input voltage range from 200 V to 300 V and by asymmetric PWM control scheme at input voltage range from 300 V to 400 V. So, the LLC resonant tank is designed with input voltage range from 200 V to 300 V. The specifications for the LLC resonant tank design are:

- Input voltage range: 200 ~ 300 V
- Output voltage: 48 V
- Maximum Load: 5.76 Ohm (P_o = 400 W)
- Resonant frequency: 100 kHz

With above information, the parameters below can be designed.

- Transformer turns ratio (N_P/N_S) : n = 3.4
- Resonant capacitance : Cr = 79.58 nF
- Series resonant inductance : Lr = 31.86 μH
- Resonant inductor ratio : Lp/Lr (Lp=Lm+Lr) = 4
- Parallel resonant inductance Lm = 127.45 μH

The designed LLC resonant tank has 1.68 voltage gain at input voltage 200 V and 1.12 voltage gain at input voltage 300 V. The switching frequency variation is from 50 kHz to 100 kHz.

Figure 5 shows the experimental waveforms of half-bridge LLC resonant converter with hybrid control scheme. Input voltages varies from 200 V to 400 V and output voltage is regulated to 48 V. Fig. 5 (a) represents a current of resonant inductor, a voltage of resonant voltage, a voltage of input voltage of LLC resonant tank and switching signal of Q_2 at input voltage 300 V. Figure 5. (b), (c), (d), (e), (f) and (g) also show the same experimental waveforms at each condition. As expected, the switching frequency is being decreased as the input voltage becomes larger to control output voltage in PFM operation region. Also, the peak value of resonant is increased because of increasing circulating current. In PWM operation region, duty cycle of switching signal is increased as input voltage is decreased.

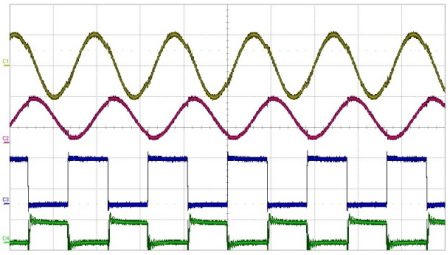

(a) V_{in}=300 V, f_s=109.23 kHz

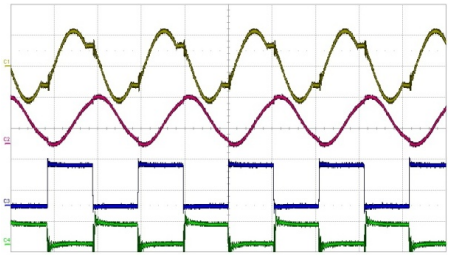

(b) V_{in}=270 V, f_s=96.36 kHz

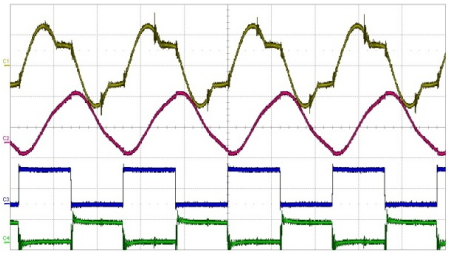

(c) V_{in}=230 V, f_s=83.31 kHz

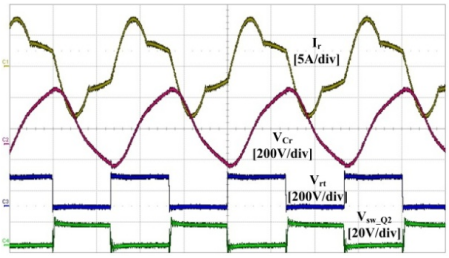

(d) V_{in}=200 V, f_s=74.67 kHz

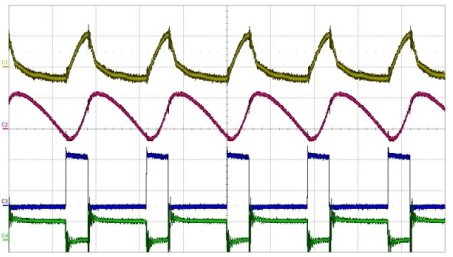

(e) V_{in}=330 V, f_s=109.23 kHz

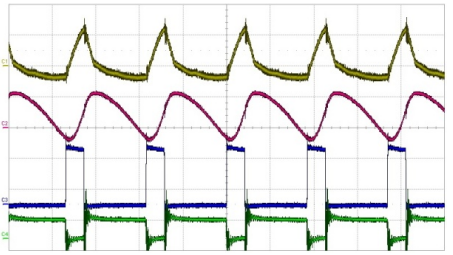

(f) V_{in}=370 V, f_s=109.23 kHz

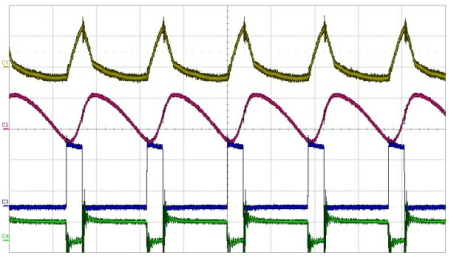

(g) V_{in}=400 V, f_s=109.23 kHz

Fig. 5. Experimental waveforms of half-bridge LLC resonant converter with hybrid control scheme (P_o=400 W)

5 Conclusion

A half-bridge LLC resonant converter with hybrid control schemes for wide input variation and medium power applications is proposed and verified by experiments with a 400W prototype. The hybrid control scheme is a hybrid combination of Pulse Frequency Modulation (PFM) and an asymmetric Pulse Width Modulation (PWM). In PFM operation region, ZVS of all switches is achieved along all load range. In a asymmetric PWM operation region, ZVS of high side switch and low side switch are also achieved along all load range. So, the higher switching frequency is possible with a wide input voltage range. Because of that, the power density could be higher by increasing switching frequency with reduced passive components.

References

[1] Sabate, J.A., Vlatkovic, V., Ridley, R.B., Lee, F.C., Cho, B.H.: Design considerations for high-voltage high-power full-bridge zero-voltage switched PWM converter. In: Applied Power Electronics Conference and Exposition, pp. 275–284 (March 1990)

[2] Redl, R., Balogh, L., Edwards, D.W.: Optimum ZVS full-bridge DC/DC converter with PWM phase-shift control: analysis, design considerations, and experimental results. In: Applied Power Electronics Conference and Exposition, vol. 1, pp. 159–165 (February 1994)

[3] Koo, G.-B., Moon, G.-W., Youn, M.-J.: Analysis and design of phase shift full bridge converter with series-connected two transformers. IEEE Transactions on Power Electronics 19(2), 411–419 (2004)

[4] Wu, X., Zhang, J.M., Qian, Z.: Optimum design considerations for a high efficiency ZVS full bridge DC-DC converter. In: Telecommunications Energy Conference, pp. 338–344 (September 2004)

[5] Wu, X., Zhang, J., Wu, G., Qian, Z.: High efficiency phase-shift controlled hybrid full bridge DC bus converter. In: Applied Power Electronics Conference and Exposition, pp. 1333–1338 (March 2006)

[6] Zhao, C., Wu, X., Qian, Z.: Optimum design considerations for Soft-switched Phase-shift Full-bridge converter with primary-side energy storage inductor. In: Power Electronics Specialists Conference, pp. 366–371 (June 2008)

[7] Chen, B.-Y., Lai, Y.-S.: Switching Control Technique of Phase-Shift-Controlled Full-Bridge Converter to Improve Efficiency Under Light-Load and Standby Conditions Without Additional Auxiliary Components. IEEE Transactions on Power Electronics 25(4), 1001–1012 (2010)

[8] Lin, B.-R., Chiang, H.-K., Tseng, C.-H., Chen, K.-C.: Analysis and Implementation of an asymmetrical half-bridge converter. In: Power Electronics and Drives Systems International Conference, vol. 1, pp. 407–412 (2005)

[9] Chen, W., Xu, P., Lee, F.C.: The Optimization of Asymmetric Half Bridge Converter. In: Applied Power Electronics Conference and Exposition, vol. 2, pp. 703–707 (March 2001)

[10] Liang, J.H., Wang, P.-C., Huang, K.-C., Chen, C.-L., Leu, Y.-H., Chen, T.-M.: Design Optimization for Asymmetrical Half-Bridge Converters. In: Applied Power Electronics Conference and Exposition, vol. 2, pp. 609–702 (March 2001)

[11] Lin, B.-R., Chiang, H.-K., Huang, C.-E., Wang, D., Chen, K.-C.: Analysis of an Active Clamp Forward Converter. In: Power Electronics and Drives Systems International Conference, vol. 1, pp. 140–145 (2005)
[12] Lin, B.-R., Chiang, H.-K., Huang, C.-E., Wang, D.: Analysis, Design and Implementation of an Active Clamp Forward Converter with Synchronous Rectifier. In: TENCON 2005 - 2005 IEEE Region 10 Conference, pp. 1–6 (November 2005)
[13] Han, S.-K., Kim, T.-S., Moon, G.-W., Youn, M.-J.: High Efficiency Active Clamp Forward Converter for Sustaining Power Module of Plasma Display Panel. IEEE Transactions on Power Electronics 55, 1874–1876 (2008)
[14] Adragna, C., De Simone, S., Spini, C.: A design methodology for LLC resonant converters based on inspection of resonant tank currents. In: Applied Power Electronics Conference and Exposition, pp. 1361–1367 (March 2008)
[15] Yang, B., Lee, F.C., Zhang, A.J., Huang, G.: LLC Resonant Converter for Front End DC/DC Conversion. In: Applied Power Electronics Conference and Exposition, vol. 2, pp. 1108–1112 (March 2002)
[16] Imbertson, P., Mohan, N.: Asymmetrical Duty Cycle Permits Zero Switching Loss in PWM Circuits with No Conduction Loss Penalty. IEEE Transactions on Industry Applications 29(1), 121–125 (1993)
[17] Steigerwal, R.L.: A Comparison of Half-Bridge Resonant Converter Topologies. IEEE Transactions on Power Electronics 3(2), 174–182 (1988)
[18] Choi, H.: Analysis and Design of LLC Resonant Converter with Integrated Transformer. In: Applied Power Electronics Conference and Exposition, pp. 1630–1635 (March 2007)
[19] Erickson, R.W., Maksimovic, D.: Fundamentals of Power Electronics, 2nd edn. (2001)

A Relay Shaping Method for Servo Mechanical System Identification

Chao Liu, Jia Liu, Jian-hua Wu, Hui Wang, and Zhenhua Xiong

State Key Laboratory of Mechanical System and Vibration, School of Mechanical Engineering, Shanghai Jiao Tong University, Shanghai 200240, China
{aalon,lamen,wujh,351582221,mexiong}@sjtu.edu.cn

Abstract. In this paper, a relay shaping method (RS) is proposed to identify the model of servo mechanical system. The conventional relay-based feedback technique utilizes the ideal relay (IR) for identification. However, the describing function (DF) of the ideal relay uses the main harmonic of the IR output to approximate the square wave and would lead to identification inaccuracy. The proposed relay shaping method regulates the shape of the ideal relay by bringing in a low-pass filter and hence make the response of the relay module more sin-wave-like. Simulations show that the identification error is reduced by using the RS method. Experimental studies are carried out through a permanent magnet linear synchronous motor (PMLSM) to show the effectiveness of the proposed method. Under the same condition of control algorithm and parameters, the RS method can obtain better identified model of servo mechanical system than the IR method by virtue of better tracking performances in all three cases: low-acceleration, mid-acceleration and high-acceleration.

Keywords: Ideal relay, Relay shaping, System identification, Servo mechanical system.

1 Introduction

With the development of manufacturing and control technology, precision motion control has been quickly developed and broadly applied in the modern industries [1,2]. In the last few years, many researchers dedicated to the servo mechanical controller design and proposed a vast amount of algorithms. Among the existing algorithms, model-based controllers are widely proposed to further improve the servo performance, such as H_∞-based robust control [3], adaptive robust control [4], iterative learning control [5] and so on. From the previous works, it is well known that model identification accuracy can greatly affect the performance of the controller. Supposing the identification parameters are relatively close to the ones of the employed plant, parameters of the advanced controllers can be tuned easily to achieve good performance. Otherwise, it could be time-consuming for parameters tuning. Therefore, the model identification techniques for advanced controllers need to be urgently explored.

J. Lee et al. (Eds.): ICIRA 2013, Part II, LNAI 8103, pp. 353–364, 2013.

One of the well known approaches for parameters tuning is the relay-based feedback technique (RFT), which is famous for simple and efficient. The basic idea of RFT is to identify the model parameters from the oscillations excited by the relay module. Relay-based feedback technique was first proposed by Astrom and Hagglund [6]. Since then, RFT is widely applied in large inertia systems such as process control and temperature control, in which the nonlinear factors are lumped into the linear model. Luyben proposed the auto tune variation method (ATV) which became a standard identification method from relay feedback test [7]. In recent years, the application of RFT appeared in identification of servo systems [8,9]. Liu [10] identified and compensated the asymmetric disturbances via a time-domain relay method. Liu [11] used a relay-based method to tune the controller of the PMLSM and achieve high acceleration positioning.

However, the relay modules of the above relay-based methods are almost ideal relay. The square wave of output from ideal relay is approximated to the sinusoidal input, which leads to erroneous results in the ultimate frequency and ultimate gain. Chiang et al. [12] point out that the truncation of the higher-order terms affects the ultimate gain and ultimate frequency of the oscillation. However, it is uneasy to mathematical analysis of the high-order terms. Shen [13] employs a saturation relay instead of the conventional ideal relay to improve the identification of the oscillation gain and frequency. Yu et al. [14,15] studied the shape factor of the relay feedback and analyzed its influence to identification accuracy. In this paper, we propose a relay feedback shaping method to transform the shape of the ideal relay for improving the identification accuracy.

The remainder of this paper is organized as follows: in Section 2, the PMLSMs driven X-Y table is firstly introduced and then dynamics model is given. In Section 3, the RS method is detailed and the identification algorithms are formulated. In Section 4, compared with the ideal relay method, simulations show that the validity of the proposed method. In Section 5, the experimental results are further presented to validate the effectiveness of the RS method. Section 6 gives the conclusion.

2 Model of Servo Mechanical System

2.1 Layout View of the X-Y Table

Fig.1 shows the mechanical structure of the PMLSMs driven X-Y positioning table, which has an effective stroke of $57mm \times 66mm$. The driving PMLSMS are composed of a base-mounted permanent magnet and two supporting carbon fiber brackets where the three-phase adjoining start-connection coils are embedded. By feeding appropriate three-phase current to the coils, the interaction between the permanent magnets and the coil brackets will generate thrust force to drive the bonding mechanical system through cross-roller linear guides, which are well lubricated and have little Coulomb friction. Each axis is equipped with a non-contact linear optical encoder (Heidenhain LIF 471) with the hardware resolution of 0.4 μm (0.1 μm after quadruplication).

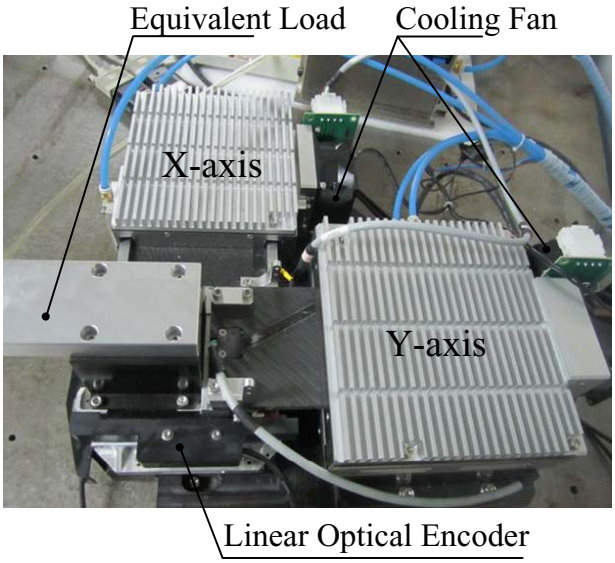

Fig. 1. Layout view of the X-Y table

2.2 Model of the PMLSM

In consideration of the above-mentioned PMLSMs-driven servo mechanical system with negligible Coulomb friction, the dynamics model of the above-mentioned PMLSM can be written as

$$m\ddot{x} + B\dot{x} = F_e - F_d, \tag{1}$$

where m, $\ddot{x}$, B and $\dot{x}$ are respectively the mass, acceleration, viscous coefficient and velocity of the slider, F_e is the generated thrust force $F_e = k_t u$, k_t denotes the thrust coefficient, u is the input voltage, F_d is the external disturbances.

Substitute $b = B/k_t$ and $\tau = m/B$ into the Eq.(1), the comprehensive model of PMLSMs-driven servo mechanical system can be expressed as

$$b\tau\ddot{x} + b\dot{x} = u, \tag{2}$$

The transfer functions from u to $\dot{x}$ is

$$G_v(s) = \frac{\dot{X}(s)}{U(s)} = \frac{1}{b(\tau s + 1)}, \tag{3}$$

where $\dot{X}(s)$ and $U(s)$ are the Laplace transformation of $\dot{x}$ and u respectively.

3 The Improved Relay Identification Method

3.1 Ideal Relay and Describing Function

Suppose the input signal $e(t)$ to the relay module is a sinusoidal wave, which is described as

$$e(t) = a\sin(\omega_u t), \tag{4}$$

where a and ω_u are the magnitude and frequency of the sinusoidal wave respectively. If the relay module has an ideal relay form, the output signal $u(t)$ of the module is a square wave. The input signal and output response of the IR are shown in Fig. 2.

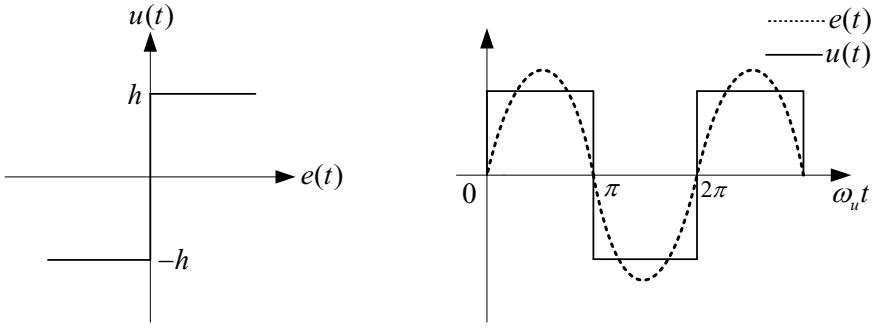

(a) Ideal relay (b) Input-Output responses

Fig. 2. Input-Output responses for ideal relay

The Fourier series of the output response of the IR can be expressed as

$$u(t) = A_0 + \sum_{k=1}^{+\infty} A_k \cos(k\omega_u t) + \sum_{k=1}^{+\infty} B_k \sin(k\omega_u t), \tag{5}$$

where,

$$A_0 = \tfrac{1}{2\pi}\int_0^{2\pi} u(t)d(\omega_u t)$$
$$A_k = \tfrac{1}{\pi}\int_0^{2\pi} u(t)\cos(k\omega_u t)d(\omega_u t)$$
$$B_k = \tfrac{1}{\pi}\int_0^{2\pi} u(t)\sin(k\omega_u t)d(\omega_u t)$$

Since the output signal is an odd-symmetric function, the coefficients A_0 and A_k are equal to zero, and thus the Eq.(5) becomes

$$u(t) = \sum_{k=1}^{+\infty} B_k \sin(k\omega_u t). \tag{6}$$

Only the first Fourier coefficient is used for the describing function analysis. Since $B_1 = 4h/\pi$, the describing function can be written as

$$N(a, \omega_u) = \frac{u(t)}{e(t)} = \frac{\frac{4h}{\pi}\sin(\omega_u t)}{a\sin(\omega_u t)} = \frac{4h}{\pi a}. \tag{7}$$

For the ideal relay module, the open-loop transfer function of a first order plus dead time model (FOPDT) is presented as

$$\frac{4h}{\pi a}\cos(D\omega_u) + \frac{4h}{\pi a}\sin(D\omega_u)j = -b + b\tau\omega_u j, \tag{8}$$

where D is the additional dead time, which is used to make up for the small dead time of the servo mechanical system. Compare the real part and imaginary part of the Eq.(8), the identified model values τ and b can be expressed as

$$\hat{\tau}_{IR} = \frac{\tan(\pi - D\omega_u)}{\omega_u}, \tag{9}$$

$$\hat{b}_{IR} = \frac{4h}{\pi a\sqrt{(\hat{\tau}_{IR}\omega_u)^2 + 1}}. \tag{10}$$

3.2 Relay Shaping Method

Obviously, the output of the ideal relay is a square wave instead of a sinusoidal wave. The describing function of the ideal relay utilizes the main harmonic to approximate the square wave. This leads to erroneous results in the oscillation amplitude a and frequency ω_u and hence influence the identification results. In this work, a relay shaping method is proposed to improve the output response of the relay module by making it more sin-wave-like.

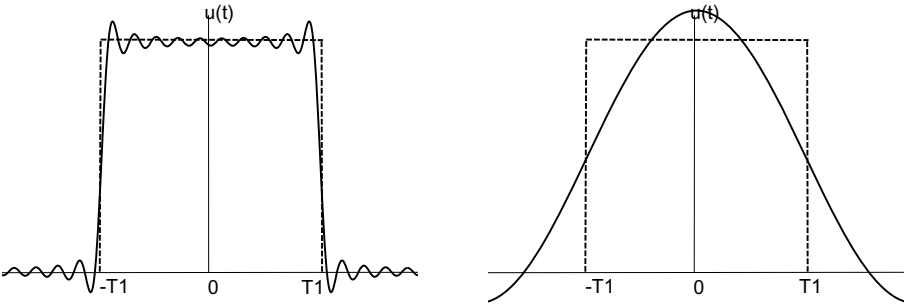

(a) k>>1 (b) k=1

Fig. 3. The Fourier transformation of the square wave

From the Eq. (6), it can be seen that the output signal $u(t)$ can be decomposed into sum of infinite sinusoidal waves. When the value of the order k is considerably larger than 1 (k>>1), the Fourier transformation of the square wave is shown in Fig.3a. The idea of the relay shaping is that, a low-pass filter (LPF) is connected after the ideal relay to filter out higher harmonic of Fourier series, retaining only the main harmonic (k=1), so that the square wave is more

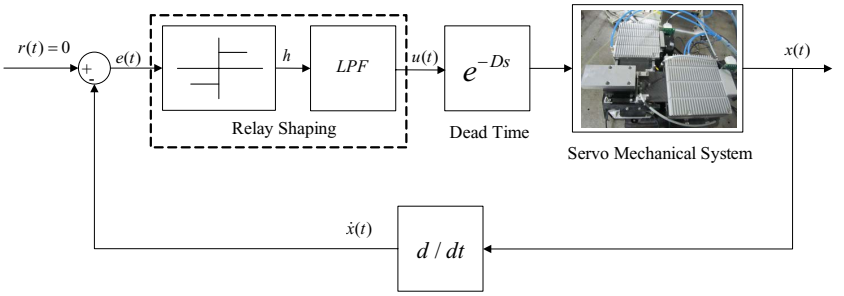

Fig. 4. Block diagram of relay shaping with artificial dead time

approximate to a sinusoidal wave. Fig.3b shows the output responses of the ideal relay shaping module.

By bringing a low-pass filter $H(s)$ into the employed system, as shown in 4, both of the gain $K_H = |H(j\omega_u)|$ and phase delay $\theta_H = \angle H(j\omega_u)$ are also introduced. In light of the frequency of the sustained oscillation generated from an RS feedback test corresponds to the limit of stability, the open-loop transfer function equals to -1. Therefore, the identified model values of τ and b from the RS method can be formulated as

$$\hat{\tau}_{RS} = \frac{\tan(\pi - D\omega'_u - \theta_H)}{\omega'_u}, \tag{11}$$

$$\hat{b}_{RS} = \frac{4hK_H}{\pi a' \sqrt{(\hat{\tau}_{RS}\omega'_u)^2 + 1}}. \tag{12}$$

where ω'_u and a' are the oscillation frequency and amplitude respectively. In this paper, a Butterworth filter is chosen for the low-pass filter. The higher order of the filter performs the better performance, but it requires the more complicated structure and calculation. By considering of the filter performance and the calculation ability, we choose a second order Butterworth filter to shape the ideal relay.

For unknown systems, it is difficult to set the cutoff frequency to filter out higher harmonics of Fourier series. Here, we perform the relay shaping with the following procedure:

1. Set the cutoff frequency of the low-pass filter to a very large value and perform the first relay feedback test(like ideal relay feedback);
2. Measure the ultimate frequency ω_u of the output response;
3. Set the cutoff frequency to the measured frequency ω_u and perform the second test(RS feedback);
4. Measure the new oscillation frequency $\omega_u{}'$ and amplitude a';
5. Calculate the identification values from the Eq.(11) and Eq.(12).

4 Simulations

Simulations are carried out to show the validity of the RS method. As described in the above-mentioned procedure, relay feedback tests are performed with ($h = 0.1, D = 0.06s$) to identify the four different sets of b and τ in the model.The identification results of $G_v(s)$ are listed in the Table 1.

Table 1. Identification results of $G_v(s)$

	Nominal value		Ideal relay				Relay shaping			
case	τ	b	$\hat{\tau}_{IR}$	error	$\hat{b}_{IR}$	error	$\hat{\tau}_{RS}$	error	$\hat{b}_{RS}$	error
1	0.15	0.2	0.1207	19.53%	0.2024	1.20%	0.1470	2%	0.1975	1.25%
2	0.15	1	0.1207	19.53%	1.0122	1.22%	0.1470	2%	0.9877	1.23%
3	1.5	0.2	1.2162	18.92%	0.2000	0%	1.4783	1.45%	0.1913	4.35%
4	1.5	1	1.2162	18.92%	0.9998	0.02%	1.4783	1.45%	0.9564	4.36%

From Table 1, it shows that using the ideal relay, the identification error of $\hat{\tau}_{IR}$ is about 20% and the identification error of $\hat{b}_{IR}$ is about 1%. Using the relay shaping method, the identification error of $\hat{\tau}_{RS}$ is reduced from about 20% to about 2% while the identification error of $\hat{b}_{RS}$ remains under 5%.

5 Experimental Studies

Experimental verification of the proposed method is implemented by the following servo mechanical system, as shown in Fig. 5, which consists of an X-Y positioning stage, a PC-based dSPACE control system, two amplifiers, power supplies and air cooling devices. The dSPACE DS1103 DSP board, which is used for computational intensive tasks associated with execution of the algorithms, together with MATLAB Real-Time Workshop.

5.1 Identifications

The block diagram of relay shaping test with artificial dead time is illustrated in Fig. 4. With an artificial dead time D, the relay shaping module excites a sin-wave-like waveform with the amplitude h. Using the exciting signal, the servo mechanical system oscillates with the amplitude a' and the oscillation frequency ω'_u.

According to the identification procedure, two relay feedback tests are implemented to identify the model parameters τ and b. The set of relay parameters (0.2V, 0.015s) is used to excite the controlled plant. The output signal and input signal of the IR module are shown in Fig. 6a and Fig. 6b respectively. Fig. 6c

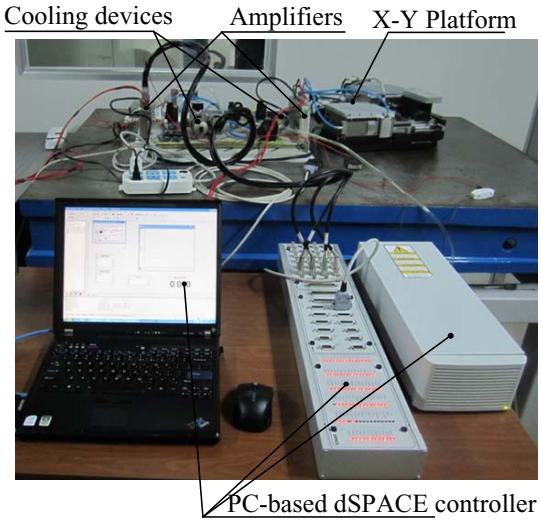

Fig. 5. Setup of the servo mechanical system

and Fig. 6d are the detailed informations about the output and input signals of the RS module.

The oscillation frequency ω_u (ω_u') is measured by averaging twenty stable cycles of the corresponding oscillation and the oscillation amplitude a (a') is taken as the mean value of the maximum and minimum amplitude. The model parameters of the PMLSM-driven servo mechanical system are then computed from Eq.(11) and Eq.(12). The oscillation characteristics and the identified parameters by using IR and RS method are listed in Table 2.

Table 2. Values of the oscillation characteristics and the identified parameters

	Ideal relay	Relay shaping
Relay parameters:		
	$h = 0.2(V)$	$h = 0.2(V)$
	$D = 0.015(s)$	$D = 0.015(s)$
Oscillation Characteristics:		
	$a = 43\,(\mathrm{mm/s})$	$a' = 70\,(\mathrm{mm/s})$
	$\omega_u = 105.67\,(\mathrm{rad/s})$	$\omega_u' = 105.6\,(\mathrm{rad/s})$
Model parameters:		
	$\hat{\tau}_{IR} = 0.7174\,(\mathrm{s})$	$\hat{\tau}_{RS} = 0.8281\,(\mathrm{s})$
	$\hat{b}_{IR} = 0.000078227\,(\mathrm{Vs/mm})$	$\hat{b}_{RS} = 0.000078169\,(\mathrm{Vs/mm})$

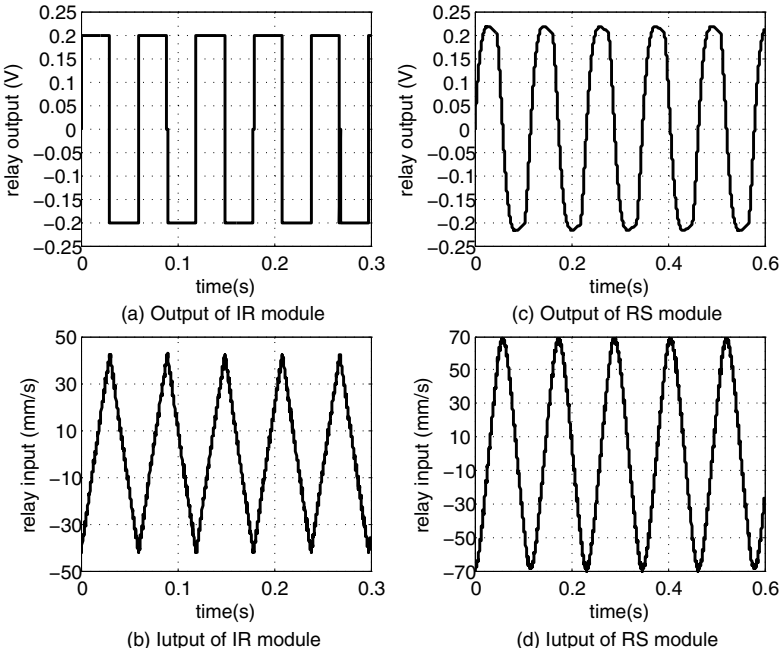

Fig. 6. The output and input of relay tests with (0.2V, 0.015s)

5.2 Sinusoidal Tracking

Fig. 7. With the identified model parameters of the servo mechanical system, a PD controller and a model based feedforward controller are designed as shown in The PD controller is designed by pole placement approach and the feedforward controller is designed by the inverse model.

Set the poles of the PD controller as -400 and two sinusoidal tracking experiments are conducted to verify the accuracy of the estimated results. The first motion profile is $x_1(t) = 5 - 5\cos(2\pi t)$ (unit in millimeter) as illustrated in Fig. 8a, whose acceleration is about 0.02 g ($1g = 9.806m/s^2$). The tracking performances with IR method and RS method are compared in Fig. 8b and-Fig. 8c. The tracking error by using RS method is reduced from 2.3 μm to 1.8 μm compared with the IR method,.

In the second sinusoidal tracking experiment, the motion profile is $x_2(t) = 5 - 5\cos(20\pi t)$ as shown in Fig. 8d. The acceleration is about 2 g. The tracking performance with IR method is illustrated in Fig. 8e and that with RS method is shown in Fig. 8f. The maximum tracking error with IR method and RS method are about 34.5 μm and 13.1 μm, respectively.

It is obviously seen that under the same condition of controller and parameters, the RS method performs better tracking performances than IR method in the low-acceleration case and mid-acceleration case. The high-acceleration case will be discussed in the next subsection.

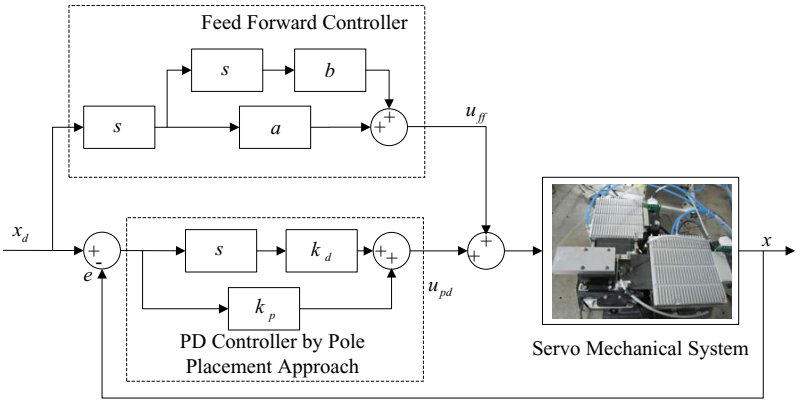

Fig. 7. Block diagram of PD with feedforward controller

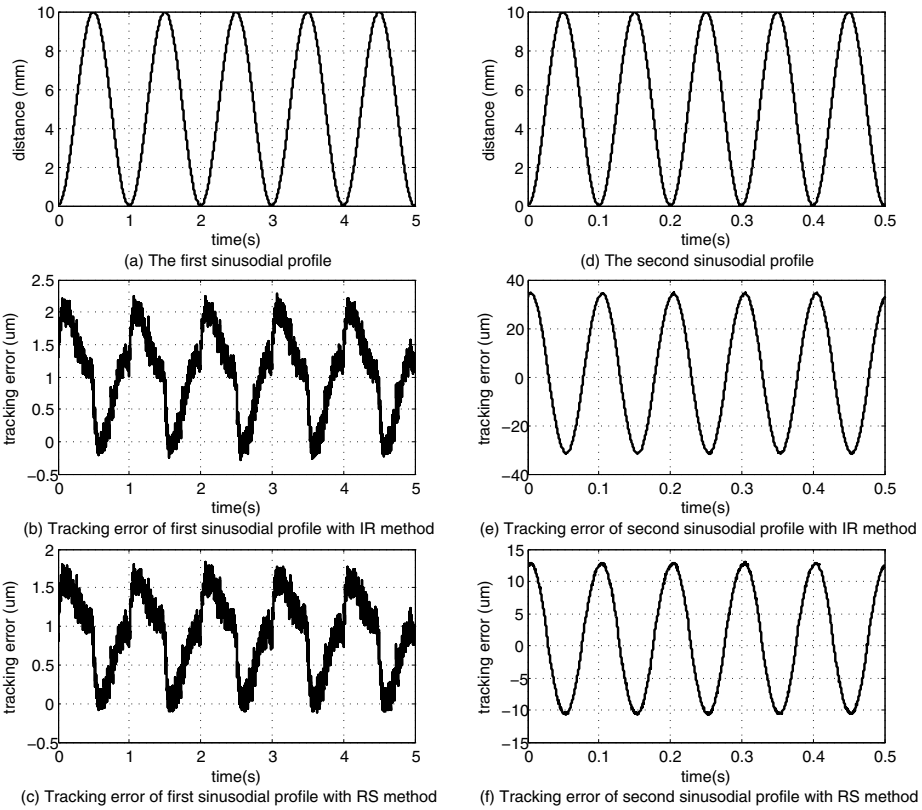

Fig. 8. Performance of the two sinusoidal experiments

5.3 Point to Point Motion

In this subsection, the effectiveness of the proposed method is verified through a high-acceleration point-to-point motion experiment. The reference position profile with a reciprocating stroke of 0.1 inch (2.54 mm) is generated by the asymmetric S-curve. The planned time of the reference position is 12 ms. The planned peak velocity is 0.392 m/s while the planned maximum acceleration and deceleration are 9.1 g and 7.2 g, respectively.

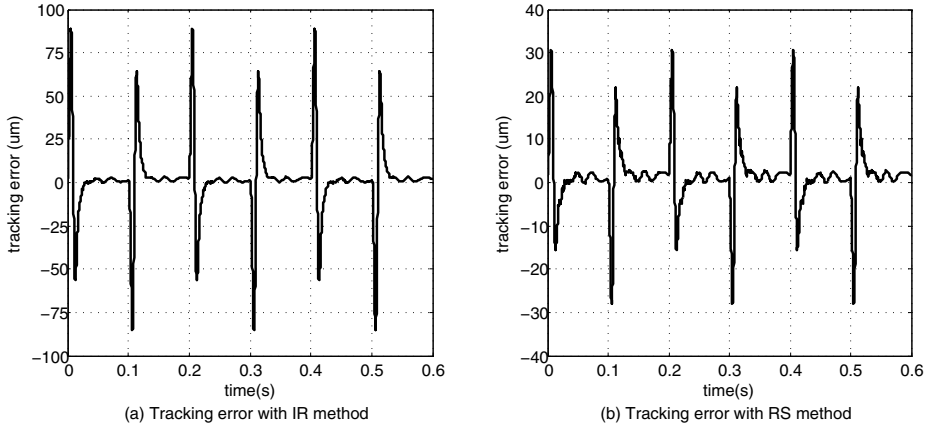

Fig. 9. Tracking performance of the high-acceleration point-to-point motion

The tracking performances under the IR method and RS method are compared in Fig. 9a and Fig. 9b. In point-to-point motions, the maximum tracking error with IR method is about 88.9 μm, while the maximum tracking error with RS method is about 30.8 μm. Both of Fig. 8 and Fig. 9 show that under the same structure and parameters of the controller, the proposed method is more effective and performs better tracking performances than the IR method in three different acceleration cases.

6 Conclusion

In this work, we proposed a relay shaping method to improve the identification accuracy of relay-based feedback technology. We discussed the principle of relay shaping and detailed the identification procedure.It is validated through simulations and experiments that the RS method shows better identification results comparing to the IR method.This method can obtain better identified model of servo mechanical system and hence provide good foundation for designing and tuning model based controllers.

Acknowledgements. This research was supported in part by National Key Basic Research Program of China under Grant 2013CB035804, National Natural Science Foundation of China under Grant 51120155001 and Program for New Century Excellent Talents in University under Grant NCET-11-0336.

Sincere thanks to Prof. Yanjie Liu of Harbin institute of technology for providing the experimental platform.

References

1. Tam, M.S., Cheung, N.C.: A high speed high precision linear drive system for manufacturing automation. In: Sixteenth Annual IEEE Applied Power Electronics Conference and Exposition, APEC 2001, vol. 1, pp. 440–444. IEEE (2001)
2. Ding, H., Xiong, Z.: Motion stages for electronic packaging design and control. IEEE Robotics & Automation Magazine 13(4), 51–61 (2006)
3. Lee, K.R., Kim, J.H., Jeung, E.T., Park, H.B.: Output feedback robust $H\infty$ control of uncertain fuzzy dynamic systems with time-varying delay. IEEE Transactions on Fuzzy Systems 8(6), 657–664 (2000)
4. Yao, B., Tomizuka, M.: Adaptive robust control of mimo nonlinear systems in semi-strict feedback forms. Automatica 37(9), 1305–1321 (2001)
5. Wu, J., Ding, H.: Iterative learning variable structure controller for high-speed and high-precision point-to-point motion. Robotics and Computer-Integrated Manufacturing 24(3), 384–391 (2008)
6. Åström, K.J., Hägglund, T.: Automatic tuning of simple regulators with specifications on phase and amplitude margins. Automatica 20(5), 645–651 (1984)
7. Luyben, W.L.: Derivation of transfer functions for highly nonlinear distillation columns. Industrial & Engineering Chemistry Research 26(12), 2490–2495 (1987)
8. Pu, D., Wu, J., Xiong, Z., Sheng, X., Ding, H.: Nonlinear analysis and parameters identification of servo mechanism with relay feedback. Assembly Automation 30(3), 221–227 (2010)
9. Jianhua, W., Jia, L., Zhenhua, X., Han, D.: A relay-based method for servo performance improvement. Mechatronics 21(6), 1076–1086 (2011)
10. Liu, J., Wu, J., Xiong, Z., Zhu, X.: Servo system identification using relay feedback: A time-domain approach. Transactions of the ASME-B-Journ Manufacturing Science Engineering 134(6), 061012 (2012)
11. Liu, C., Liu, J., Wu, J., Xiong, Z.: High precision embedded control of a high acceleration positioning system. In: Su, C.-Y., Rakheja, S., Liu, H. (eds.) ICIRA 2012, Part II. LNCS, vol. 7507, pp. 551–560. Springer, Heidelberg (2012)
12. Chang, R.C., Shen, S.H., Yu, C.C.: Derivation of transfer function from relay feedback systems. Industrial & Engineering Chemistry Research 31(3), 855–860 (1992)
13. Shen, S.H., Yu, C.C., et al.: Use of saturation-relay feedback for autotune identification. Chemical Engineering Science 51(8), 1187–1198 (1996)
14. Thyagarajan, T., Yu, C.C.: Improved autotuning using the shape factor from relay feedback. Industrial & Engineering Chemistry Research 42(20), 4425–4440 (2003)
15. Panda, R., Yu, C.C.: Shape factor of relay response curves and its use in autotuning. Journal of Process Control 15(8), 893–906 (2005)

Optimal Cross-Coupled Synchronization Control of a Precision Motion Stage Driven by Dual Linear Motors

Gang Zhang, Jian-hua Wu*, Pin-kuan Liu, and Han Ding

State Key Laboratory of Mechanical System and Vibration, School of Mechanical Engineering, Shanghai Jiao Tong University, Shanghai 200240, China
{zgrobot,wujh,pkliu,hding}@sjtu.edu.cn

Abstract. In this paper, the optimal cross-coupled synchronization control of a precision motion stage driven by dual linear motors is investigated. The single axis controller of linear motor is composed of a cascade PID/PI controller and a hybrid velocity and acceleration controller (VFC/AFC). The cross-coupled synchronization control scheme is incorporated with the hybrid trajectory tracking PID/PI+VFC/AFC controller to improve the tracking performance of single axis and reduce the synchronization error of dual linear motors simultaneously. The design of cross-coupled synchronization controller is formulated as an optimal control problem in which the performance index to be minimized weights the synchronization error explicitly. Experimental results show that the optimal cross-coupled synchronization control scheme has superior synchronization performance than the independent axis control scheme in synchronization error reduction.

Keywords: synchronization control, optimal cross-coupled control, linear motor, performance index.

1 Introduction

Precision trajectory tracking control is a fundamental requirement in modern industries, especially in high precision and high speed CNC machine tools [1] and semiconductor manufacturing equipments [2]. The application of linear motors [3] is a potential solution to displace the conventional ball-screw drives for the higher velocity and acceleration capacities and higher precision achievable. In recent years, the modeling, control and application of linear motors have been a focus of research in academy and industry [4-6].

Apart from the single axis control system, the multi-axis coordinated motion systems are used to improve the productivity of the manufacturing system, although the design of multi-axis coordinated controllers is a challenging task. Cross-coupled control (CCC) scheme is an effective approach to reduce contouring errors of multi–axis servomechanisms. It was first proposed by Koren [7] for the contouring control of bi-axis motion system. It has also been used for the dual-drive gantry system to reduce the synchronization error of gantry system. Iván Garcia-Herreros, etc [8] proposed a model-based decoupling control method for dual-drive gantry stage and implemented the control scheme via feedforward compensation. Min-Fu Hsieh, etc [9] proposed a position/thrust synchronization control scheme for a linear motor servo system applied to the vertical axis drive of a die-sinking electrical discharge machine.

* Corresponding author.

J. Lee et al. (Eds.): ICIRA 2013, Part II, LNAI 8103, pp. 365–374, 2013.

The performance of cross-coupled controller mainly depends on the tuning of controller parameters. Many controller tuning methods, such as the traditional PID control[10], the optimal control[11], robust control [12] and etc have been used to implement the cross-coupled controller. Giam T S, etc [13] presented the coordinated motion control of gantry stages and developed a robust control scheme to reduce both the tracking errors for the individual loops as well as the inner-axis offset. Xiao and Zhu [14] presented a generalized synchronization design for and formulated the LQG optimal control problem based on the synchronization error observer. Chu , etc[15] developed the optimal control algorithm for synchronizing the positions of dual axes gantry system for a SMD assembly machine.

The present paper describes the optimal cross-coupled synchronization control of a precision motion stage driven by dual linear motors. Firstly, the single axis controller of linear motor is presented in Section 2. The single axis controller is composed of a cascade PID/PI control plus a hybrid velocity and acceleration feedforward controller (VFC/AFC). Then, the cross-coupled synchronization control schemes are presented in section 3. The synchronization control schemes are incorporated with hybrid VFC/AFC compensator to improve the tracking performance of the dual linear motors. The optimal cross-coupled synchronization control problem is formulated with a performance index in section 4. The performance index to be minimized weights the synchronization error explicitly. The optimal cross-coupled synchronization control scheme is implemented using MATLAB/dSAPCE real time simulation platform and experimental results are presented in section 5. Conclusions are drawn in section 6.

2 Single Axis Controller Design

In this part, the hybrid trajectory tracking controller of single axis linear motor is presented. The single axis controller of linear motor is shown in Figure1, which is composed of a cascade PID/PI controller, a velocity feedforward controller (VFC) and acceleration feedforward controller (AFC). As is shown in Figure 1, K_{PP}, K_{PI} and K_{PD} are proportional, integral and derivative gains of PID controller in the outer position loop, K_{VP} and K_{VI} are proportional and integral gains of PI controller in the velocity loop, K_f is the force constant of linear motor and m_s is the moving mass of the slider, d(s) is the external disturbance applied at the linear motor. Notice that in Figure 1, the dynamics of linear motor, imperfection of sample/hold and the effects of feedback resolution and mechanical resonance are ignored since only low-frequency is concerned in the design of hybrid PID/PI+VFC/AFC controller.

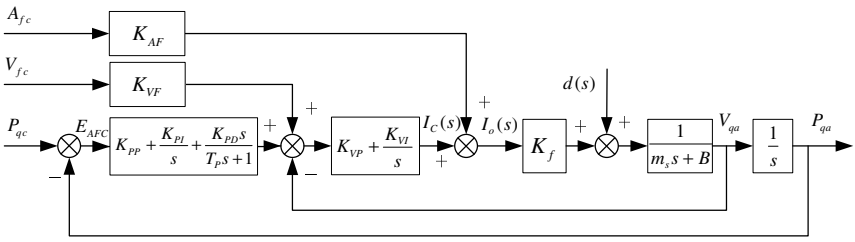

Fig. 1. Block diagram of hybrid PID/PI+VFC/AFC controller

With the PI controller, the closed-loop transfer function of the inner velocity loop, denoted as $G_{VL}(s)$, can be derived, i.e.,

$$G_{VL}(s)=\frac{K_{VP}s+K_{VI}}{\frac{m_s}{K_f}s^2+\left(K_{VP}+\frac{B}{K_f}\right)s+K_{VI}}, \tag{1}$$

Thus, the closed-loop transfer function of outer position loop, denoted as $G_{PL}(s)$, can be determined,

$$G_{PL}(s)=\frac{P_{qa}(s)}{P_{qc}(s)}=\frac{K_{PD}K_{VP}s^3+K_2s^2+K_1s+K_0}{\frac{m_s}{K_f}s^4+\left(K_{VP}+K_{VP}K_{PD}+\frac{B}{K_f}\right)s^3+(K_{VI}+K_2)s^2+K_1s+K_0}. \tag{2}$$

with $K_2=K_{PP}K_{VP}+K_{PD}K_{VI}$, $K_1=K_{PI}K_{VP}+K_{PP}K_{VI}$ and $K_0=K_{PI}K_{VI}$.

From the block diagram of hybrid controller, the tracking error of the hybrid PID/PI+VFC/AFC controller is

$$\Phi_A(s)=\frac{E_{AFC}(s)}{P_{qc}(s)}=\frac{(\frac{m_s}{K_f}-K_{AF})s^4+K_{VP}(1-K_{VF})s^3+K_{VI}(1-K_{VF})s^2}{\frac{m_s}{K_f}s^4+\left(K_{VP}+K_{VP}K_{PD}+\frac{B}{K_f}\right)s^3+(K_{VI}+K_2)s^2+K_1s+K_0}. \tag{3}$$

From Equation(3), it can be seen that the equivalent error transfer function of hybrid PID/PI+VFC/AFC controller is zero for all types of input signals when

$$K_{VF}=1, K_{AF}=\frac{m_s}{K_f}. \tag{4}$$

The control performance of cascade PID/PI controller largely depends on tuning of both inner velocity loop and outer position loop. Considering the cascade PID/PI controller as a whole system, the initial control parameters of cascade PID/PI controller are obtained by minimizing the integral of time-weighted absolute error (ITAE) [16] using a MATLAB/Simulink program. The final values of cascade PID/PI controller with VFC/AFC gains are tuned experimentally. The control parameters of VFC/AFC gains are calculated with Equation(4).

3 Cross-Coupled Synchronization Control Scheme

In this part, the cross-coupled control (CCC) scheme is presented for the synchronization control of dual linear motors. The cross-coupled synchronization control scheme is incorporated with hybrid PID/PI+VFC/AFC controller to improve the tracking performance of single axis linear motor and reduce the synchronization error of dual linear motors simultaneously.

The cross-coupled synchronization control scheme for the motion stage driven by dual linear motors is shown in Figure 2, in which $G_{p1}(s), G_{p2}(s)$ are the position loop PID controllers of q_1 and q_2 axis linear motors, $G_{v1}(s), G_{v2}(s)$ are the velocity loop PI controllers of q_1 and q_2 axis linear motors, $\triangle q_1, \triangle q_2$ are the tracking errors of q_1 and q_2 axis linear motors and ε_s is the synchronization errors of dual linear motors.

The synchronization error is defined as the subtraction of tracking errors of dual linear motors, that is

$$\varepsilon_s = \triangle q_1 - \triangle q_2. \tag{5}$$

The input of cross-coupled controller is the synchronization error of dual linear motors while the output of CCC is decoupled into two components, u_1 and u_2, which are injected into the velocity loop of each linear motor to compensate for the synchronization error of dual linear motors. From the control viewpoint, the synchronization error in both the master-slave control and independent axis control scheme[13] is open-looped while in the cross-coupled control scheme, closed-loop synchronization control is formulated.

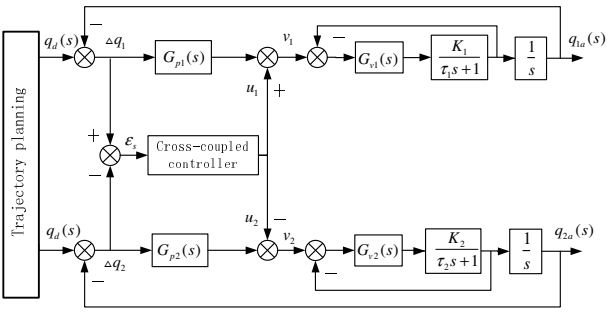

Fig. 2. Cross-coupled control scheme of dual linear motors

The block diagram of cross-coupled control scheme with hybrid VFC/AFC compensator is shown in Figure 3. Both the dual linear motors execute the desired trajectory directly. The hybrid velocity and acceleration feedforward controller is applied to dual linear motors improve the tracking performance of single axis linear motor and reduce the synchronization error of dual linear motors simultaneously.

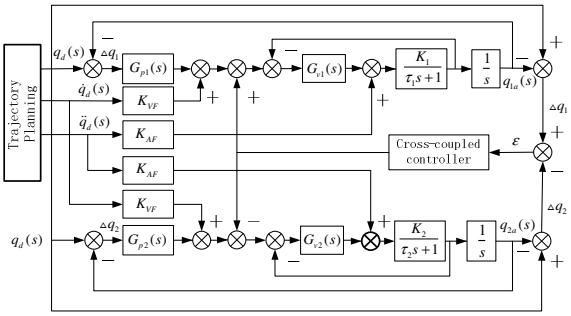

Fig. 3. Cross-coupled control scheme with hybrid feedforward controller

4 Design of Optimal Cross-Coupled Synchronization Controller

The performance of cross-coupled synchronization controller mainly depends on the tuning of control parameters. Based on the identified parameters of dual linear

motors, the design of cross-coupled synchronization controller is formulated as an optimal control problem. The performance index to be minimized contains the synchronization error and the output components of CCC explicitly.

4.1 Parameter Identification of Linear Motors

The first step in the design of cascade PID/PI controller and optimal cross-coupled synchronization controller is the parameter identification of dual linear motors. Time domain parameter identification was performed using system identification Toolbox™ of MATLAB. The input signal of parameter identification is Pseudorandom binary sequences (PRBS), which is generated using linear feedback shift registers.The results of parameter identification of linear motors are shown in Table 1, in which the transfer functions of P2IZ model is

$$G_{P2IZ} = \frac{K_p(T_Z s + 1)}{s(T_{p_1} s + 1)(T_{p_2} s + 1)}. \tag{6}$$

As is shown in Table 1, the simulated outputs of identified P2IZ model has higher fitness than the model of P1DI. This model will be used for the design of optimal cross-coupled synchronization controller in the next section.

Table 1. Identified results of P2IZ model transfer functions of dual linear motors

Linear motor	Identified results of P2IZ model				
	K_p	T_Z	T_{p1}	T_{p2}	Fitness (%)
q_1 axis	773.98	0.1739	0.0432	0.1592	87.75
q_2 axis	610.17	0.2668	0.0724	0.2139	89.33

4.2 Design of Optimal Cross-Coupled Controller

The identified models of dual linear motors are used to tune the optimal cross-couple synchronization controller, which is of PI type. The performance index used in the optimal cross-coupled synchronization controller is

$$J = \sum_{k=0}^{n} \left[r_1 \varepsilon_s^2(k) + u^T(k) R_2 u(k) \right]. \tag{7}$$

where $u(k) = [u_1(k) \quad u_2(k)]^T$, is the vector of output components of optimal cross-coupled controller, the related coefficient matrix is

$$R_2 = \begin{bmatrix} r_2 & 0 \\ 0 & r_2 \end{bmatrix}. \tag{8}$$

From Equation 7, it can be seen that the results of optimal cross-coupled synchronization mainly depend on the selection of coefficients r_1 and r_2. In the real implementation, r_1 is set to unity and the proportional gain of outer loop PID controller is chosen to equalize the synchronization error of dual linear motors, that is

$$r_1 = 1, r_2 = \frac{1}{K_{PP}}. \tag{9}$$

Based on the identified model of linear motor, a simulation program was developed with MATLAB/Simulink and the optimal cross-coupled synchronization control problem is solved by the Sequential Quadratic Programming (SQP) algorithm available in the MATLAB Optimization Toolbox™.

5 Experimental Results

5.1 Experimental Setup

The precision motion stage driven by dual linear motors, which is constructed in our laboratory, is a suitable platform for synchronization control scheme presented in this paper. The experimental setup of the motion stage is shown in Figure 5. The motion stage is driven by two Parker's 210-2T ironless linear motors, which are driven in current mode using 2-Axes GLENTEK SMB9715-2A-2 amplifiers. The synchronization tracking controllers are implemented in the dSPACE© DS1103 controller board, a single-board system with real-time processor and comprehensive I/O interfaces. An industrial PC is included in the control system, which is interfaced to the dSPACE DS1103 controller board via 16-bit ISA connector.

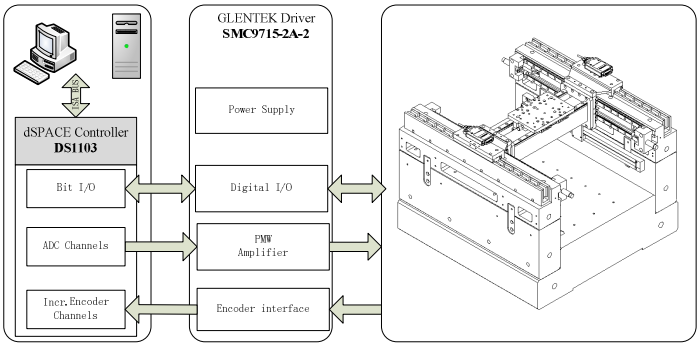

Fig. 4. Experimental setup of the motion stage driven by dual linear motors

Two synchronization control schemes are tested with the same trajectory specification and performance index, which are the independent axis control scheme and the optimal cross-coupled synchronization presented in this paper. With the independent axis control scheme, the two motors execute the desired trajectory directly. The hybrid VFC/AFC feedforward controller is also incorporated with traditional cascade PID/PI controller of each axis to improve the tracking performance of the dual linear motors.

Two trajectories are planned for the motion stage driven by dual linear motors. The input position commands and velocity feedforward signals of the planned trajectories are shown in Figure 6. Note that the double S trajectory planning methods have been applied to reduce the impacts and avoid saturation and commutation errors caused by large initial tracking errors. Experimental specifications of the planned trajectory are listed in Table 1.

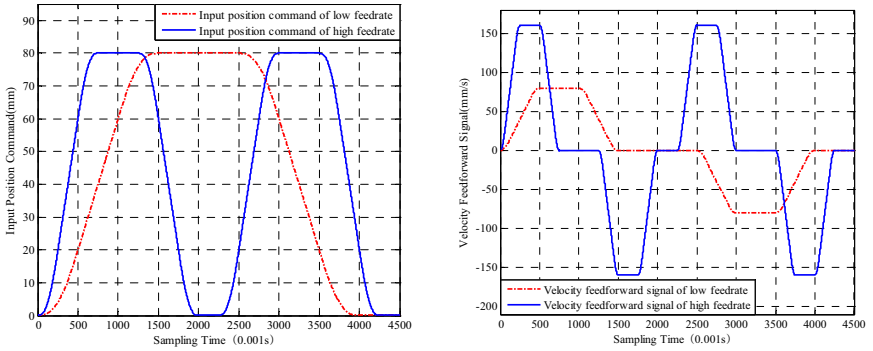

(a) Input position commands (b) Velocity feedforward signals

Fig. 5. Planned trajectory of dual linear motors

Table 2. Experimental specification of synchronization control of dual linear motors

Planned trajectory	Low feedrate		High feedrate	
	value	unit	value	unit
Traveling range	80	mm	80	mm
Traveling period	4	s	4	s
Maximum speed	80	mm/s	160	mm/s
Maximum acceleration	200	mm/s^2	800	mm/s^2

5.2 Experimental Results

In order to measure the performance of different synchronization control schemes, four performance indices are defined as following:

(1) $\|\varepsilon_T\|_{RMS} = \left(\frac{1}{T}\int_0^T |\varepsilon_T|^2 \, dt\right)^{1/2}$, the root mean square of tracking error;

(2) $\|\varepsilon_T\|_{MAX} = \max\{|\varepsilon_T|\}$, the maximum value of tracking error;

(3) $\|\varepsilon_S\|_{RMS} = \left(\frac{1}{T}\int_0^T |\varepsilon_S|^2 \, dt\right)^{1/2}$, the root mean square of synchronization error;

(4) $\|\varepsilon_S\|_{MAX} = \max\{|\varepsilon_S|\}$, the maximum value of synchronization error.

The experimental results of independent axis control scheme (IAC) and optimal cross-coupled control scheme in low feedrate conditions are depicted in Figure 7, in which Figure 7(a) and (c) depicts the tracking errors and synchronization errors independent axis control scheme, Figure 7(b) and (d) depicts the tracking errors and synchronization errors of cross-coupled control scheme. The independent axis control

scheme and optimal cross-coupled control scheme in high feedrate conditions are depicted in Figure 8. The tracking performance indices and synchronization errors of low and high feedrate are listed in Table 2.

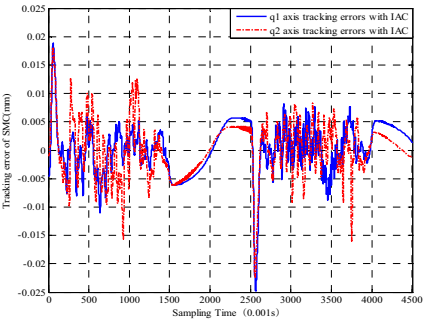

(a) Tracking errors of low feedrate with independent axis control scheme

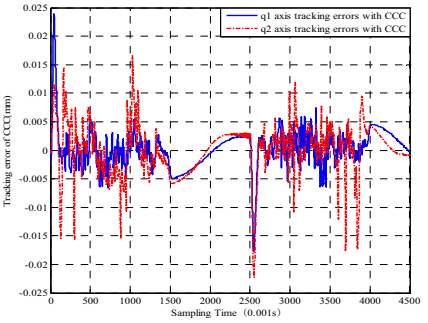

(b) Tracking errors of low feedrate with optimal cross-coupled control scheme

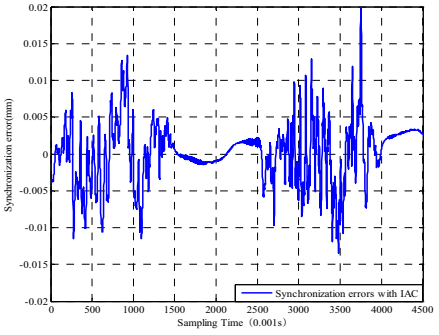

(c) Synchronization errors of low feedrate with independent axis control scheme

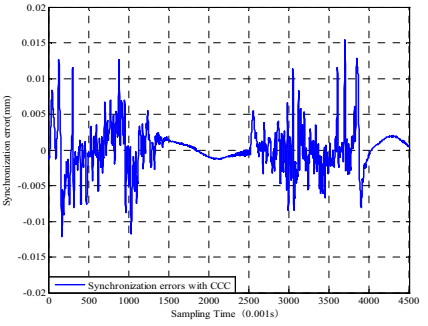

(d) Synchronization errors of low feedrate with cross-coupled control scheme

Fig. 6. Tracking results of synchronization control schemes under low feedrate condition

As is illustrated in Figure 7 and table 1, the two linear motors are tuned to perform similarly and the maximum values of synchronization errors are 0.0212mm and 0.0236mm in independent axis control scheme under the low and high feedrate conditions. Note that in Figure 8, although the maximum and root mean values of tracking errors are larger than those of the independent axis control scheme, the synchronization errors are relatively smaller. The maximum values of synchronization error are 0.0164mm and 0.0192mm in the low and high feedrate tracking experiments, which are at least 15% smaller than those of independent axis control scheme.

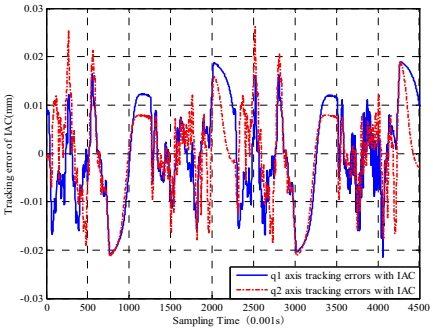

(a) Tracking errors of high feedrate with independent axis control scheme

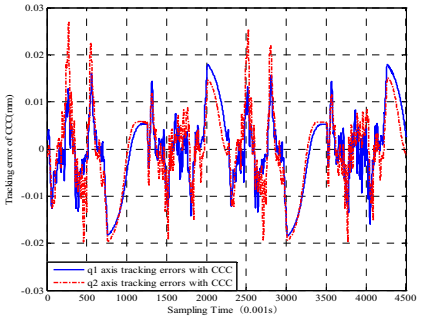

(b) Tracking errors of high feedrate with optimal cross-coupled control scheme

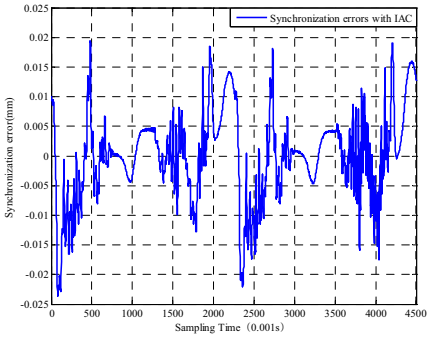

(c) Synchronization errors of dual linear motors with independent axis control scheme under high feedrate conditions

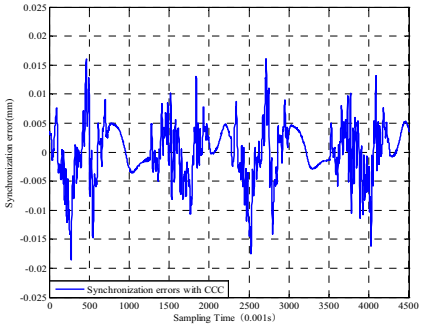

(d) Synchronization errors of dual linear motors with optimal cross-coupled control under high feedrate conditions

Fig. 7. Tracking results of synchronization control schemes under high feedrate condition

Table 3. Tracking performance index of synchronization control schemes

case	Control scheme	Tracking performance index(unit: mm)				Synchronization error (unit: mm)	
		q_1 axis		q_2 axis			
		$\|\varepsilon_T\|_{MAX}$	$\|\varepsilon_T\|_{RMS}$	$\|\varepsilon_T\|_{MAX}$	$\|\varepsilon_T\|_{RMS}$	$\|\varepsilon_S\|_{MAX}$	$\|\varepsilon_S\|_{RMS}$
Low feedrate	IAC	0.0258	0.0046	0.0235	0.0039	0.0212	0.0042
	CCC	0.0239	0.0035	0.0223	0.0030	0.0164	0.0031
High feedrate	IAC	0.0224	0.0096	0.0262	0.0085	0.0236	0.0072
	CCC	0.0286	0.0084	0.0269	0.0082	0.0192	0.0057

6 Conclusions

In this paper, the optimal cross-coupled synchronization control problem of a motion stage direct driven by dual linear motors is investigated. The optimal cross-coupled synchronization control problem is formulated as the minimization of a performance

index, in which the synchronization error and control effort of CCC are expressed explicitly. The optimal cross-coupled synchronization controller is incorporated with hybrid VFC/AFC feedforward controller to improve the tracking performance of individual axis and reduce the synchronization error of dual linear motors. Experimental results show that the optimal cross-coupled synchronization control scheme achieves better synchronization performance than the independent axis control scheme. At least 15% synchronization error reduction can be achieved with the proposed optimal cross-coupled synchronization control scheme.

Acknowledgement. This work is supported by the National Natural Science Foundation of China (NSFC) under Grant 51120155001.

References

1. Altintas, Y., et al.: Machine tool feed drives. CIRP Annals-Manufacturing Technology (2011)
2. Ding, H., Xiong, Z.: Motion stages for electronic packaging design and control. IEEE Robotics & Automation Magazine 13(4), 51–61 (2006)
3. Pritschow, G.: A comparison of linear and conventional electromechanical dives. CIRP Annals-Manufacturing Technology 47(2), 541–548 (1998)
4. Renton, D., Elbestawi, M.: Motion control for linear motor feed drives in advanced machine tools. International Journal of Machine Tools and Manufacture 41(4), 479–507 (2001)
5. Wu, J., Pu, D., Ding, H.: Adaptive robust motion control of SISO nonlinear systems with implementation on linear motors. Mechatronics 17(4), 263–270 (2007)
6. Bascetta, L., Rocco, P., Magnani, G.: Force ripple compensation in linear motors based on closed-loop position-dependent identification. IEEE/ASME Transactions on Mechatronics 15(3), 349–359 (2010)
7. Koren, Y.: Cross-coupled biaxial computer control for manufacturing systems. ASME Journal of Dynamic Systems, Measurement, and Control 102(4), 265–272 (1980)
8. García-Herreros, I., et al.: Model-based decoupling control method for dual-drive gantry stages: A case study with experimental validations. Control Engineering Practice (2012)
9. Hsieh, M.-F., et al.: Servo design of a vertical axis drive using dual linear motors for high speed electric discharge machining. International Journal of Machine Tools and Manufacture 47(3), 546–554 (2007)
10. Koren, Y., Lo, C.-C.: Variable-gain cross-coupling controller for contouring. CIRP Annals-Manufacturing Technology 40(1), 371–374 (1991)
11. Kulkarni, P., Srinivasan, K.: Optimal contouring control of multi-axial feed drive servomechanisms. ASME Journal of Engineering for Industry 111(2), 140–148 (1989)
12. Yeh, S.-S., Hsu, P.-L.: Theory and applications of the robust cross-coupled control design. In: Proceedings of the 1997 American Control Conference. IEEE (1997)
13. Giam, T., Tan, K., Huang, S.: Precision coordinated control of multi-axis gantry stages. ISA Transactions 46(3), 399–409 (2007)
14. Xiao, Y., Zhu, K., Choo Liaw, H.: Generalized synchronization control of multi-axis motion systems. Control Engineering Practice 13(7), 809–819 (2005)
15. Chu, B., et al.: Optimal cross-coupled synchronizing control of dual-drive gantry system for a SMD assembly machine. JSME International Journal Series C 47(3), 939–945 (2004)
16. Martins, F.G.: Tuning PID controllers using the ITAE criterion. International Journal of Engineering Education 21(5), 867 (2005)

Genetic-Based k-Nearest Neighbor for Chaff Echo Detection

Jonggeun Kim[1], HyeYoung Han[2], Jungwon Yu[1], Hansoo Lee[1], and Sungshin Kim[1,*]

[1] Department of Electrical and Computer Engineering, Pusan National University, Busan, Korea
[2] Weather Radar Center, Korea Meteorological Administration
hyhan98@korea.kr,
{wisekim,garden0312,hansoo,sskim}@pusan.ac.kr

Abstract. This paper proposes genetic-based k-nearest neighbor method for chaff echo identification. Weather radar provides various data: location, velocity, direction, and range of typhoon or precipitation, precipitation intensity, altitude and location of thunderstorm and rainfall. Above this data, topography echo, anomalous echo, second echo and chaff echo are observed from weather radar, and they are disrupt weather forecasting. They are called non-weather echo. In order to improve weather forecasting, we propose genetic-based k-nearest neighbor for chaff echo identification. Experimental result shows that chaff echoes are well removed, so performance weather forecasting will also be improved.

Keywords: k-nearest neighbor, Chaff echo, Identification, Genetic algorithms.

1 Introduction

Weather radar is essential to real time condition observation and forecast. Domestic weather radar is single polarization Doppler radar used in weather forecasting. This radar is located in Baekryeong island (BRI), Mt. Gwanak (KWK), Mt. Ohseong (KSN), Jin island (JNI), Mt. Go (GSN), Mt. Seong (SSP), Yeongjong island (IIA), Mt. Myoenbong (MYN), Gangreung (GNG), and Mt. Gwangdeok (GDK) in Korea. Doppler radar measures target's velocity that is extracted from frequency deviation between transmission wave of radar and reflected wave of target. Weather radar is excellent in observing reflecting material movement and change of convection system that become appear and disappear within short time, but it provide wrong observation data because it receive signal from all reflection object in atmosphere, including weather target such as snow and rain. We call it non-weather echo or weather target reflector. Ground echo, anomalous propagation echo, second echo, and chaff echo are included in non-weather echo. It is difficult for far sighted radar data to forecast weather because it has non-weather echo. Chaff is a matter spreading atmosphere with the purpose of preventing aircraft from detecting by radar. It is made of small steel piece, glass fiber, and synthetic resins. The chaff echo is detected from scattered radar wave from by

* Corresponding author.

J. Lee et al. (Eds.): ICIRA 2013, Part II, LNAI 8103, pp. 375–384, 2013.

sprayed chaff. The chaff echo disturbs weather forecasting because chaff echo has similar characteristic and appearance to precipitation echo. The inside red box area in Fig.1 shows chaff echo, and other area indicates precipitation echo. Initial research of chaff echo is conducted in USA related only to wind and warm current estimation.

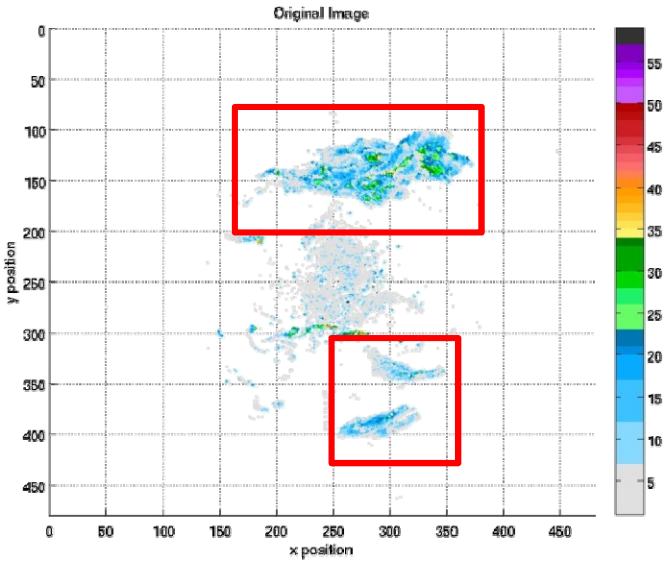

Fig. 1. Chaff echo and precipitation echo

Recent study deals with characteristic of chaff echo. In case of Korea, identification method of chaff echo using Doppler radar is discussed, and related about removal of non-weather echo is small in number. Related research is identification algorithm of chaff echo using infrared image and identification algorithm of chaff echo using fuzzy inference method. However, it is difficult for case of infrared image to identify chaff echo in cloudy weather, and performance time of algorithm is delayed as much as satellite data processing time (30~60 minutes), and it is essential to cooperate with satellite center. The rest of research shows identification method using dual-polarization radar, this can identify chaff echo to analyze differential reflection ratio and distribution of correlation through radar. However, this device is very expensive and difficult to install in short time. That's why it is essential to realize identification algorithm using Doppler radar [1][2].

This paper proposes chaff echo identification algorithm using genetic-based k-Nearest Neighbor (k-NN) from Universal Format type data generated by Doppler radar. There are some preceding researches that purpose identification method of chaff echo with fuzzy inference system and neural network [3]. Including the method which used the preceding, there are many classification methods. For example, k-NN, fuzzy c-means, GMMs etc. We research the identification method using k-NN because k-NN is simple nonparametric method [4]. In order to improve accuracy, we used scale extended method, and axis transformation parameters are optimized by Genetic algorithm (GA).

2 k-Nearest Neighbor Algorithm

Since its inception in 1951, the nearest neighbor method has been shown to be a powerful nonparametric technique for classification, density estimation, and regression estimation [5]. k-NN algorithm saves acquainted pattern at memory in advance. And when a new pattern enters as input, the algorithm identifies where the new pattern exists by similarity comparison between the new patterns and saved patterns. Distance function that compare new pattern with saved pattern must have following condition.

$$d(x, y) \geq 0 \tag{1}$$

$$d(x, y) = 0 \text{ if and only if } x = y \tag{2}$$

$$d(x, y) = d(y, x) \tag{3}$$

$$d(x, z) \leq d(x, y) + d(y, z) \tag{4}$$

Fig.2 (a) show result of classification at k equal 1. Instance data have been stored in the memory, a new pattern is coming in, and new pattern to compare the similarity between instance data. New pattern is identified in the class with the biggest similarity value.

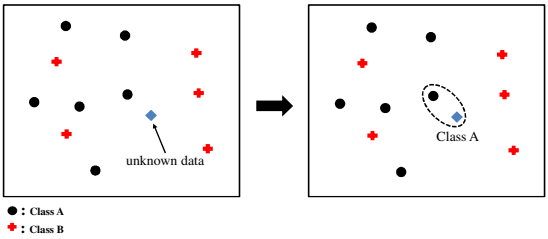

(a)

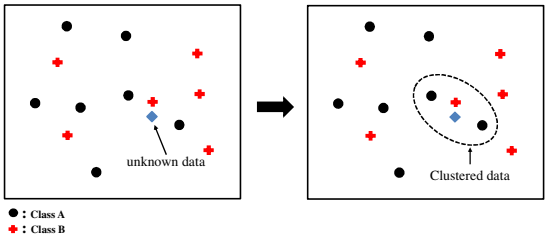

(b)

Fig. 2. Result if clustering: (a)k is 1 (b)k is 3

If k is larger than 1, k items from closest point are classified as same cluster, and then we add inverse number of similarity value among same things. Unknown point identified in the biggest value that is added similarity value. Fig.2 (b) show result of clustering at k = 3. There are four methods of distance function calculation for comparison to similarity value.

$$d(X,Y) = \sqrt{\sum_{i=1}^{m} \left(x_i - y_i\right)^2} \tag{5}$$

$$d(X,Y) = \sum_{i}^{m} \left|x_i - y_i\right| \tag{6}$$

$$d(X,Y) = 1 - \frac{\sum_{i=1}^{m} x_i y_i}{\sqrt{\sum_{i=1}^{m} x_i} \sqrt{\sum_{i=1}^{m} y_i}} \tag{7}$$

$$d(X,Y) = 1 - \frac{COV(X,Y)}{\partial X \partial Y} \tag{8}$$

$X = (x_1, x_2, \ldots, x_n)$, $Y = (y_1, y_2, \ldots, y_n)$. Above four equation called following (5) is called as Euclidean distance, (6) is called as Manhattan distance, (7) is called as Cosine distance, and (8) is called as Correlation distance. This paper used Euclidean distance for comparison to similarity value.

2.1 Stretching Axis Using Linear Transformation.

Each value, such as weather characteristic, do not equally influence result, when K-NN compares its similarity. Degree of that result values of radar site are influenced difference of each value in case of chaff echo identification using k-NN. Therefore, our research uses linear transformation in order to improve k-NN's algorithm performance. Fig.3 shows example against stretching the axis. Fig.3 (b) is the example of the axis stretching from Fig.3 (a) against x-axis component. Linear transformation function is expressed as equation (9).

$$\begin{bmatrix} x' \\ y' \end{bmatrix} = \begin{bmatrix} \alpha & 0 \\ 0 & \beta \end{bmatrix} \begin{bmatrix} x \\ y \end{bmatrix} \tag{9}$$

$$\begin{bmatrix} w' \\ x' \\ y' \\ z' \end{bmatrix} = \begin{bmatrix} \alpha & 0 & 0 & 0 \\ 0 & \beta & 0 & 0 \\ 0 & 0 & \gamma & 0 \\ 0 & 0 & 0 & \delta \end{bmatrix} \begin{bmatrix} w \\ x \\ y \\ z \end{bmatrix} \tag{10}$$

In this research, 4D vector linear transformation is conducted. It is expressed equation (10). This paper optimizes linear transformation parameter using GA. We get parameters $\alpha,\beta,\gamma,\delta$.

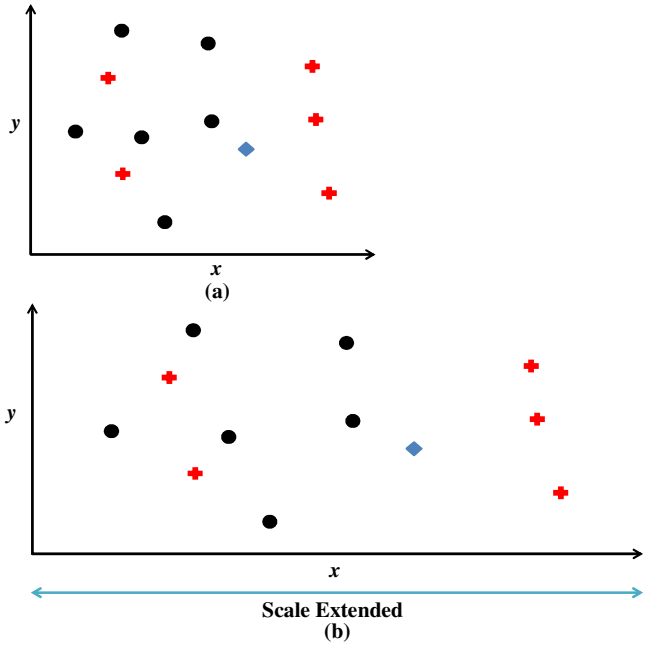

Fig. 3. Example of stretching axis (against x-axis component): (a)Non-stretched axis (b)stretched axis

3 Genetic Algorithm

GA is stochastic search mechanism [6]. Genetic mechanism is derived from Darwin's theory of natural selection. GA is widely used in engineering and business application. There are many examples: Parameter and system identification, Control, Robotics, Pattern recognition, Speech recognition, Engineering design, Planning and Scheduling, Classifier system [7]. GA is often used for the purpose of optimization method.

Encoding : Encoding is most important part in GA process. It transform input variable into binary type genes in order to enable genetic operation.
Fitness evaluation : Fitness function is used when GA compares with how optimal performance was against each chromosome. Used fitness variable in fitness function are decoded and calculated in fitness function. After this process, we arrange forward order.

Selection : The selection operation determines which parents participate in producing offspring for the next generation, and it is analogous to survival of the fittest in natural selection [8]. If some parent chromosomes have higher fitness value, it is easily selected than other parent chromosomes. Chromosomes excepted through elitism are not selected in this process.

Crossover : The crossover operation exchange genes between two chromosomes. Fig.4 shows two-point crossover. This method selects two points, and then exchanges the middle part genes.

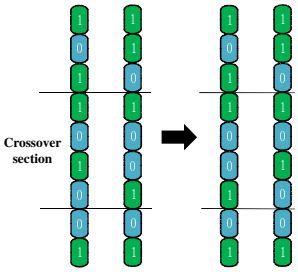

Fig. 4. Two-point crossover

Mutation : The mutation operation changes the selected genes that are randomly chosen. The mutation prevent locally minimum. However, if mutation ratio is big, result of GA will diverge.

4 Genetic-Based k-NN

In order to improve accuracy of k-NN's performance, there is the linear transformation method. Genetic-based k-NN optimizes stretching axis parameter using GA to improve performance accuracy. Fig.5 shows stretching axis parameter optimization process.

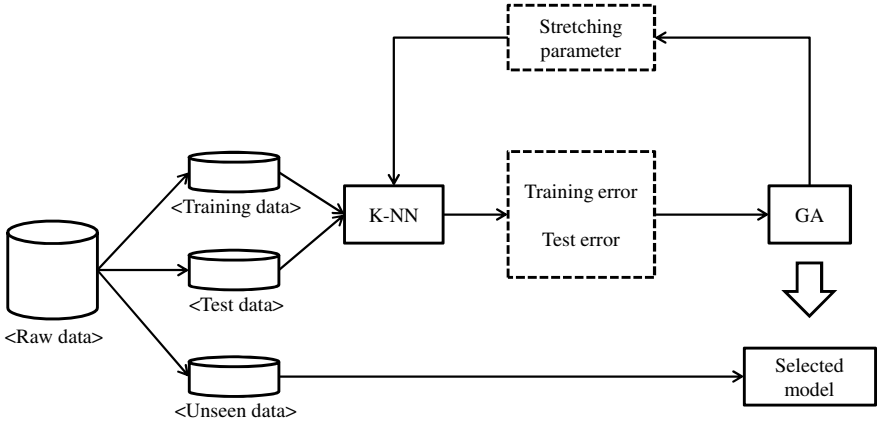

Fig. 5. Optimization process of stretching axis parameter

Initial stretching parameters are randomly created according to characteristic of each component within fixed range. We optimize stretching parameter utilizing training error and test error, and then applied model to identify chaff echo.

5 Experiment and Result

Experimental data was weather data that is used in weather forecasting. Weather data was composed of four characteristic for chaff echo identification. Followings show four characteristic for chaff echo identification.

1. X1(zdrop_freq): Observe how cluster's altitude(z-component of cluster's centroid) is changing over time [-1,1]
2. X2(expan_freq): Observe how cluster's volume or horizontal coverage area (projection area of orthogonal to z axis: altitude) is changing over time [-1,1]
3. X3(czmean_freq): Observe how cluster's mean reflectivity is changing over time [-1,1]
4. X4(lfact): Determine the degree in which the cluster's shape look ling and thin [-1,1]

In this experiment, we classify chaff echo using four characteristics with k-NN, and optimize Stretching axis parameter with GA. Table 1 shows initial parameter of GA, and k = 3 in k-NN.

Table 1. Setting of initial parameter

Initial Parameter	setting
Population	200
Initial Population	Randomly
Elitism	10%
Selection Function	Roulette Wheel
Crossover Operator	Two Point Crossover
Crossover rate	1
Mutation Operator	Uniform Mutation
Mutation rate	0.005

Fig.6 Show encoded chromosome, when we optimize stretching parameter using GA.

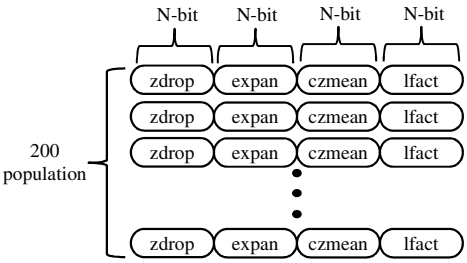

Fig. 6. Encoded chromosome

Table 2 shows result of stretching axis parameter optimization. Stretching axis parameters differ from location to location, and differ from characteristic of weather data to characteristic.

Table 2. Optimized stretching axis parameter

Site	α (zdrop)	β (czmean drop)	γ (expan)	δ (lfact)
BRI	0.3686	0.7843	0.4275	0.2235
GDK	0.8902	0.7255	0.5255	0.2157
GNG	0.9882	0.2784	0.6078	0.1216
GSN	0.3490	0.3608	0.0431	0.8039
IIA	0.1725	0.9020	0.7333	0.1882
JNI	0.2353	0.5490	0.0627	0.0824
KSN	0.0471	0.9647	0.3176	0.0471
KWK	0.8745	0.8824	0.6627	0.0784
MYN	0.1490	0.9725	0.6667	0.2235

The results of stretching axis parameter optimization are different for each site. This results are occurred because radar sites condition and characteristic of radar are different each other. Case of using same parameter occurs wrong identification. Fig.7 shows result of k-NN classification. Full echoes figures show before remove chaff echoes. Chaff echoes figures show identified chaff echo. Non-chaff echoes figures show after remove chaff echoes from full echoes. In full echoes figure, red box show section of chaff echo. Figure of result show five site result: GNG, GSN, KWK, MYN, and GDK.

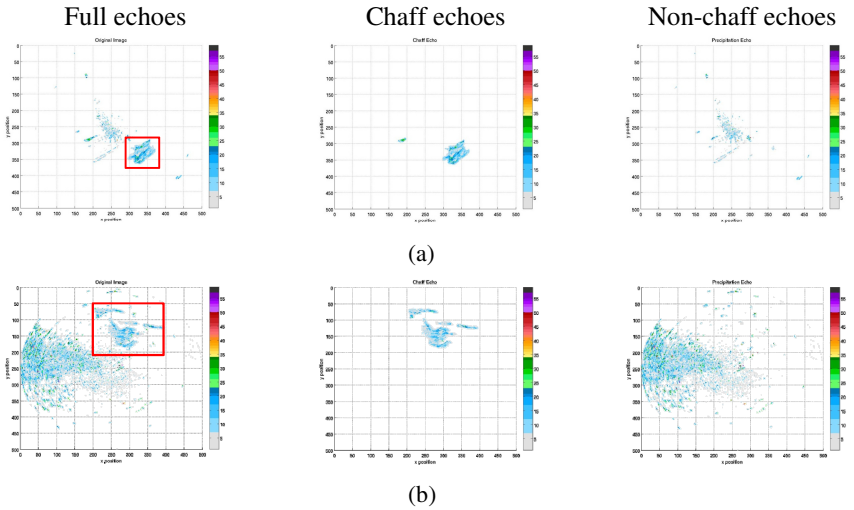

Fig. 7. Result of k-NN classification: (a) GNG 2011.11.02 13:00, (b) GSN 2012.05.03 16:01,(c) KWK 2011.11.09 13:00 (d) MYN 2011.11.04 16:01(e) GDK 2011.11.02 15:51

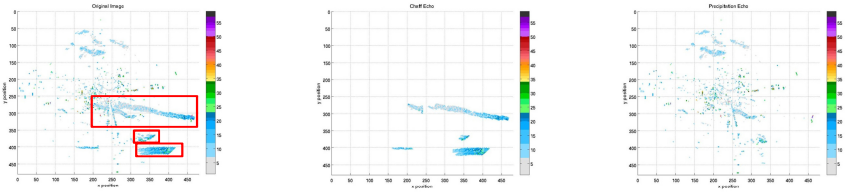

(c)

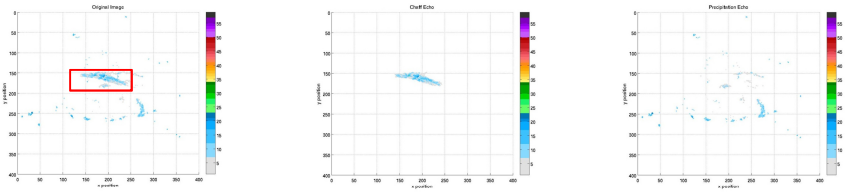

(d)

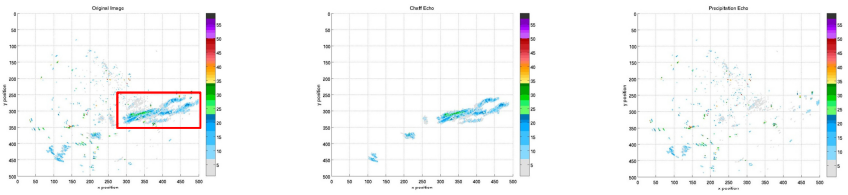

(e)

Fig. 7. (*continued*)

6 Conclusion

This paper proposed chaff echo and non-chaff echo classification utilizing genetic-based k-NN. In experimental result, it is possible to identify chaff echo although exist precipitation echo. However, it is difficult to identify in case of overlap chaff echo and precipitation echo. Next research, we study separation method chaff echo and precipitation echo, in order to solve overlap phenomenon.

Acknowledgement. "This research was supported by the MOTIE(The Ministry of Trade, Industry and Energy), Korea, under the Human Resources Development Program for Special Environment Navigation/Localization National Robotics Research Center support program supervised by the NIPA(National IT Industry Promotion Agency)." (H1502-13-1001).

References

1. Kim, S.: Single Frame Based Chaff Echo Detection Method using Fuzzy Inference System. Master's Thesis, Pusan National University, Korea (2012)

2. Kim, Y., et al.: Real-Time Detection and Filtering of Chaff Clutter from Single-Polarization Doppler Radar Data. J. Atmos. Ocean. Tech. 30(5), 873–895 (2013)
3. Lee, H., Yu, J., Jeong, Y., Kim, S.: Genetic based feed-forward neural network training for chaff cluster detection. In: International Conference of Fuzzy Theory and Its Application, pp. 215–219 (2012)
4. Choi, K., et al.: Novel classifier fusion approaches for fault diagnosis in automotive systems. IEEE Transactions on Instrumentation and Measurement 58(3), 602–611 (2009)
5. Wang, Q., Kulkarni, S.R.: Divergence Estimation for Multidimensional Densities Via k-Nearest-Neighbor Distances. IEEE Transactions on Information Theory 55(5), 2392–2405 (2009)
6. Ahn, C.W., Ramakrishna, R.S.: Elitism-Based Compact Genetic Algorithms. IEEE Transactions on Evolutionary Computation 7(4), 367–385 (2003)
7. Man, K.F., Tang, K.S., Kwong, S.: Genetic Algorithms: Concepts and Applications. IEEE Transactions on Industrial Electronics 43(5), 519–534 (1996)
8. Jang, J.S.R., Sun, C.T., Mizutani, E.: Neuro-fuzzy and Soft Computing: A Computational Approach to Learning and Machine Intelligence, vol. 23. Prentice Hall, Inc., Simon & Schuster/A Viacom Company, Upper Saddle River, NJ (1997)
9. Correa, R.C., Ferreira, A., Rebreyend, P.: Scheduling Multiprocessor Tasks with Genetic Algorithms. IEEE Transactions on Parallel and Distributed Systems 10(8), 825–837 (1999)
10. Jain, A.K., Duin, R.P.W., Mao, J.: Statistical Pattern Recognition: A Review. IEEE Transactions on pattern Analysis and Machine Intelligence 22(1), 4–37 (2000)
11. Han, H.-Y., Heo, B.-H., Jung, S.-H., Lee, G., You, C.-H., Lee, J.-H.: Elimination of Chaff Echoes in Reflectivity Composite from an Operational Weather Radar Network using Infrared Satellite Data. Atmosphere. korean Meteorological Society 21(3), 285–301 (2011)

Design and Analysis of a Spatial Remote Center of Compliance Mechanism

Lei-Jie Lai, Guo-Ying Gu, Hang Zhou, and Li-Min Zhu

State Key Laboratory of Mechanical System and Vibration, School of Mechanical Engineering, Shanghai Jiao Tong University, 200240, China
{lailj,guguoying,zhpeter,zhulm}@sjtu.edu.cn

Abstract. This paper presents a novel monolithic spatial remote center of compliant orientation-adjusting mechanism to resolve the parallelism alignment problem in the application of micro/nanofabrication. The mechanism is combined by two leaf-type isosceles-trapezoidal flexure pivots in a parallel manner to enable the spatial rotations around a fixed remote center. Based on the stiffness matrix method, the static model of the compliant mechanism is constructed to directly give the compliance factors that completely define the elastic response of the mechanism. The locations of remote center of compliance are also analyzed for the compliant mechanism in different loading cases. The finite element analysis results are then given to validate the analytical model and the remote center locations. The deviation of the analytical approach is less than 7% with respect to the finite element analysis method. Using the analytical model, the influences of the geometry parameters on the compliance factors and the remote center locations are graphically evaluated to provide theoretical guidelines for the practical design. The spatial remote center of compliant mechanism has the advantage of simple structure, balance, compactness, and can achieve high precision of rotation during the orientation motions.

Keywords: Compliant mechanism, Spatial remote center, Leaf-type isosceles-trapezoidal flexure, Stiffness matrix, Finite element analysis.

1 Introduction

Many micro/nanofabrication processes need precise parallelism alignment between two flat surfaces. In the nanoimprint lithography [1,2,3] and some electrochemical nanofabrication processes [4,5,6], the precise parallelism alignment between the template and substrate surfaces is a critical mechanical issue for pattern fidelity. A nonparallel surface between the template and substrate causes uneven transfer pattern [1]. The parallelism adjustment can be accomplished with two tilting motions around the X and Y axes located on template surface. If the tilting axis does not locate on the surface of the template, a coupled motion arises to cause a lateral shift of the imprint position [2]. Thus, in the parallelism adjustment, the motion of template can be considered as the two pure rotations

J. Lee et al. (Eds.): ICIRA 2013, Part II, LNAI 8103, pp. 385–396, 2013.

about the fixed intersection of the X and Y axes on the remote template surface, which can be achieved by the remote center of motion (RCM) mechanism.

To enable the precise orientation alignment motions of the template, the remote center of compliance (RCC) flexure mechanisms are increasingly adopted due to the advantages of no backlash, no friction, no wear, needless lubrication, compact structure and easy to manufacture [7]. Several RCC mechanisms have been proposed. Walsh [8] analyzed two Stewart platform remote center of compliance (SPRCC) devices that could be used to help guide a peg into a hole. Ahmed [6] designed a monolithic RCC orientation stage with the folded architecture using trapezoidal linkages. The remote center is found to lie at the intersection of the beam flexures. Choi et al. [2] developed an orientation stage for imprint machines by stacking two sets of notch isosceles-trapezoidal flexure pivots. Hiroshima et al. [9] designed an active orientation head that can be regarded as four-bar linkage mechanism. The four axes of the four bar intersect at a point as the rotation center. Shao et al. [10] proposed a monolithic design of a compliant template orientation stage for the step imprint lithography. Pei et al. [11,12] gave the detailed analysis of rotational precision for leaf-type isosceles-trapezoidal flexural (LITF) pivot. The LITF pivot can be of great use for practical designs, and has been used in remote center of compliance (RCC) mechanism in the micropositioning applications. Although the analytical model for the rotational precision of the planar LITF has been established, few efforts have been put into the design and analysis of the spatial remote center of compliant (SRCC) mechanism which is orthogonally combined by two sets of LITF pivots.

Therefore, this paper presents a novel SRCC mechanism for two rotations around X and Y axis in the remote plane. The SRCC mechanism is parallel combined by two LITF pivots which independently provide the tip and tilt motions of the end-effector. Therefore, the tip, tilt and Z linear motions of the end-effector are fully decoupled by this configuration of SRCC without cross-couplings in theory. Different from the serial structure that is formed by simply stacking the two 1-DOF RCC mechanisms [2], the parallel structure adopted in this kind of SRCC mechanism possesses the advantages of reduced weight, high load capacity, high stiffness, balance and compactness, and exhibits the same static and dynamic performances along the X and Y directions. The configuration of the SRCC mechanism is also much simpler than the Stewart platform RCC device described in the earlier publication [8]. It is ease of manufacturing and assembling from the economical point of view. Analytical model based on the compliance matrix method is first established for the SRCC mechanism to obtain the precision close-form equations for compliance factors in all directions and the SRCC locations, which provides the theoretical guidance for the design of other RCC mechanisms. The comparison between the analytical model and finite elements analysis (FEA) results demonstrates the high accuracy of the analytical model. The analysis results indicate that the proposed SRCC conforms to the principle of RCM device.

2 The SRCC Mechanism

Figure 1(a) shows a LITF structure with the upper rigid body fixed on the ground. The LITF pivot can be adopted in the one-dimensional RCC mechanism in the micropositioning applications [11] . In this configuration, the bottom rigid body can be forced to rotate around the virtual center Point O which is fixed at the intersection point of the two leaf flexures without any lateral shifts, as shown in Fig. 1(b).

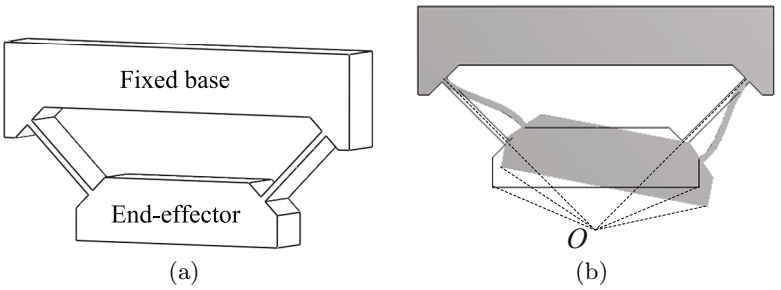

Fig. 1. The leaf-type isosceles-trapezoidal flexure mechanism.(a)Structure of the mechanism.(b)Working principle of the mechanism

To enable the rotations along two directions, two sets of LITF pivots are combined in a parallel manner to obtain a SRCC mechanism with four leaf flexures equally spaced at intervals of $\pi/2$, as shown in Fig. 2. Different from the orthodox manner by stacking the two LITF pivots, the parallel manner can achieve the desired movements without stacking to reduce the assemble errors and inter-couplings between the two LITF pivots. The two LITF pivots with orthogonal architecture independently provide the tip and tilt motions of the end-effector. Therefore, the tip, tilt and Z directional motions of the end-effector are fully decoupled, and are easy to control. This configuration also has the advantages of high stiffness, balance and compactness, and exhibits the same static and dynamic performances along the X and Y directions.

When the external loads are applied to the end-effector of this mechanism, the end-effector can be rotated around the fixed X and Y axes in a remote plane. The intersection of the X and Y axes which does not have any lateral shifts is considered as the remote center of compliance. Different from the conventional RCC mechanism used in task of inserting a peg into a hole, the SRCC mechanism proposed in this paper possesses much higher structure stiffness, which can work as the parallelism alignment stage in the micro/nanofabrication instruments, such as the nanoimprint lithography machines.

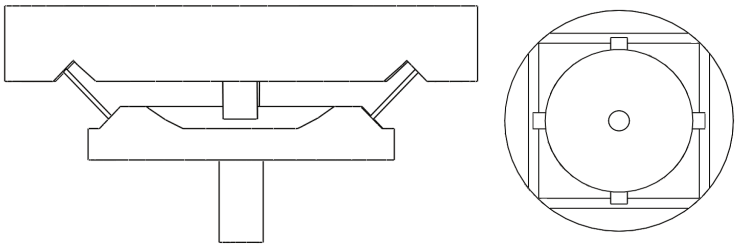

Fig. 2. The SRCC mechanism with four-leaf flexures

3 Analytical Model

The analytical model developed herein is based on the stiffness matrix method that enables formulating the load-displacement relationship for the compliant mechanism. By incorporating the stiffness that characterizes the elastic response of the single leaf flexure together with the other geometric and material properties that define the SRCC mechanism, close-form equations are generated to describe the system's response and enable further performances analysis and optimization.

3.1 Compliance Equation

The SRCC mechanism consists of four individual leaf flexures connected in parallel manners. In order to calculate the compliance model of the entire mechanism, the compliance characterization of a single leaf flexure should be obtained first. The compliance and stiffness matrices for a leaf flexure with the coordinate frame assigned in Fig. 3(a) can be described as [1]

$$\mathbf{C}^0 = \begin{bmatrix} \frac{l}{Ebt} & 0 & 0 & 0 & 0 & 0 \\ 0 & \frac{4l^3}{Eb^3t} + \frac{3l}{2Gbt} & 0 & 0 & 0 & \frac{6l^2}{Eb^3t} \\ 0 & 0 & \frac{4l^3}{Ebt^3} + \frac{3l}{2Gbt} & 0 & -\frac{6l^2}{Ebt^3} & 0 \\ 0 & 0 & 0 & \frac{3l}{Gbt^3} & 0 & 0 \\ 0 & 0 & -\frac{6l^2}{Ebt^3} & 0 & \frac{12l}{Ebt^3} & 0 \\ 0 & \frac{6l^2}{Eb^3t} & 0 & 0 & 0 & \frac{12l}{Eb^3t} \end{bmatrix} \tag{1}$$

$$\mathbf{K}^0 = \left(\mathbf{C}^0\right)^{-1}$$

where l, b and t are the dimensional parameters of the leaf flexure. E is the elastic modulus, and G is the shear modulus of the material. The $\mathbf{C}^0$ represents the compliance of free end O_i with respect to the other fixed end.

The coordinate systems of the SRCC mechanism are defined in Fig. 3(b). When the external force is applied to the end-effector of the stage, the displacement vector occurred at the Point O can be denoted as

$$\Delta\mathbf{q} = [\Delta x, \Delta y, \Delta z, \Delta\theta_x, \Delta\theta_y, \Delta\theta_z]^T \tag{2}$$

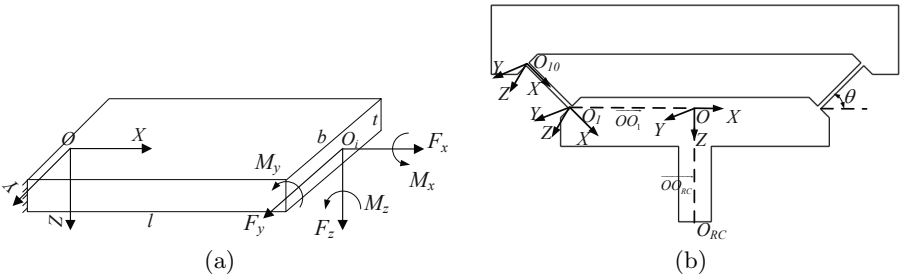

Fig. 3. (a) Model of a leaf flexure with coordinates.(b) Coordinate system of the SRCC mechanism

Transforming the displacement vector from $O - XYZ$ to $O_1 - XYZ$ yields

$$\Delta\mathbf{q}_1 = \mathbf{J}_1^T \Delta\mathbf{q} \tag{3}$$

where

$$\mathbf{J}_1 = \begin{bmatrix} \mathbf{I} & \mathbf{0} \\ \mathbf{R}_y(\angle O/O_1)\mathbf{C}(\overrightarrow{OO_1}) & \mathbf{R}_y(\angle O/O_1) \end{bmatrix} \tag{4}$$

$\mathbf{R}_y(\angle O/O_1)$ is the rotation matrix characterized by the rotating angle θ of the rotated $O_1 - XYZ$ with respect to $O - XYZ$ around the Y axis. $\mathbf{C}(\overrightarrow{OO_1})$ is the translation matrix characterized by the vector $\mathbf{r}(\overrightarrow{OO_1}) = [r_x, r_y, r_z]^T$,

According to the displacement vector $\Delta\mathbf{q}$ at Point O and the stiffness matrix of the leaf flexure, the 6×1 force vector $\mathbf{F}_1$ applied to O_1 is

$$\mathbf{F}_1 = \mathbf{K}^0 \Delta\mathbf{q}_1 = \mathbf{K}^0 \mathbf{J}_1^T \Delta\mathbf{q}. \tag{5}$$

Transforming the force vector $\mathbf{F}_1$ from $O_1 - XYZ$ to $O - XYZ$ yields the equivalent force vector $\mathbf{F}_{10}$ applied to O which can be represented as

$$\mathbf{F}_{10} = \mathbf{J}_1 \mathbf{F}_1 = \mathbf{J}_1 \mathbf{K}^0 \mathbf{J}_1^T \Delta\mathbf{q}. \tag{6}$$

There are four leaf flexures connecting to the end-effector with a radius of $|OO_1|$ and a interval angle of $\pi/2$. Hence, the relationship of the force and displacement with respect to the $O - XYZ$ is derived as

$$\mathbf{F} = \sum_{i=1}^{4} \mathbf{J}_i \mathbf{K}^0 \mathbf{J}_i^T \Delta\mathbf{q} \tag{7}$$

where

$$\begin{aligned} \mathbf{J}_2 &= diag(\mathbf{R}_z(-90°), \mathbf{R}_z(-90°))\mathbf{J}_1, \\ \mathbf{J}_3 &= diag(\mathbf{R}_z(180°), \mathbf{R}_z(180°))\mathbf{J}_1, \\ \mathbf{J}_4 &= diag(\mathbf{R}_z(90°), \mathbf{R}_z(90°))\mathbf{J}_1. \end{aligned} \tag{8}$$

$R_z(\theta_z)$ is the the rotation matrix around the Z axis of $O-XYZ$. The symmetric compliance matrix $\mathbf{C}$ of the SRCC mechanism is derived as

$$\mathbf{C} = \left(\sum_{i=1}^{4} \mathbf{J}_i \mathbf{K}^0 \mathbf{J}_i^T \right)^{-1} = \begin{bmatrix} C_{X,\,F_X} & 0 & 0 & 0 & C_{X,\,M_Y} & 0 \\ 0 & C_{Y,\,F_Y} & 0 & C_{Y,\,M_X} & 0 & 0 \\ 0 & 0 & C_{Z,\,F_Z} & 0 & 0 & 0 \\ 0 & C_{\theta_X,\,F_Y} & 0 & C_{\theta_X,\,M_X} & 0 & 0 \\ C_{\theta_Y,\,F_X} & 0 & 0 & 0 & C_{\theta_Y,\,M_Y} & 0 \\ 0 & 0 & 0 & 0 & 0 & C_{\theta_Z,\,M_Z} \end{bmatrix}. \tag{9}$$

3.2 SRCC Location

Assuming that the remote center O_{RC} is located at the vertical distance of $|OO_{RC}|$ from Point O, the displacement vector of Point O_{RC} can be obtained using translation matrix along Z axis from Point O. The relationship between the displacement vector of Point O_{RC} and the applied force $\mathbf{F}$ at O is then calculated as

$$\Delta \mathbf{q}_{RC} = \mathbf{J}_{RC}^T \Delta \mathbf{q} = \mathbf{J}_{RC}^T \mathbf{C} \mathbf{F} \tag{10}$$

where

$$\mathbf{J}_{RC} = \begin{bmatrix} \mathbf{I} & \mathbf{0} \\ \mathbf{C}(\overrightarrow{OO_{RC}}) & \mathbf{I} \end{bmatrix}. \tag{11}$$

According to the principle of the SRCC mechanism, the motion of the end-effector can rotate around the fixed SRCC without producing any lateral shifts. Hence, the SRCC location calculated based on the analytical model in different loading cases will be described later. Furthermore, the variations of the lateral shift at Point O_{RC} are plotted as a two-dimensional function of $|OO_{RC}|$ and external loads, while the other parameters are chosen as follows: $l = 15$ mm, $b = 8$ mm, $t = 1$ mm, $\theta = 45°$ and $|OO_1| = 30.5$ mm.

Case I: Pure Moment. In this loading case, a pure moment M_X is applied to the end-effector at Point O. For the analytical results from Eq. (10), the location of the SRCC can be calculated as

$$|OO_{RC}| = C_{Y,\,M_X} \Big/ C_{\theta_X,\,M_X} \tag{12}$$

The analytical lateral shift of Point O_{RC} is studied by means of three dimensional plot as function of the $|OO_{RC}|$ and the applied moment M_X, as shown in Fig. 4(a). As can be seen from this figure, the location of SRCC is found not to lie at the focus of the four leaf flexures, which is different from the 1-DOF isisceles-trapezoidal flexure pivot. It is also observed that the location of the SRCC is independent of the applied moment. The lateral shift of the SRCC is always zero regardless of how large the force is imposed, which conforms to the principle of SRCC mechanism.

Case II: Direction fixed Force. In this case, a force F_X is applied to the end-effector at Point O. The direction of the force is parallel to X axis and keeps orientation fixed to the space during deflection. The analytical location of the SRCC is

$$|OO_{RC}| = C_{X,\,F_X}/C_{\theta_Y,\,F_X} \tag{13}$$

Fig. 4(b) shows the plots of the lateral shift at Point O_{RC} in terms of the $|OO_{RC}|$ and the applied force F_X. Same conclusions as Case I can be formulated by analyzing the plots of Fig. 4(b).

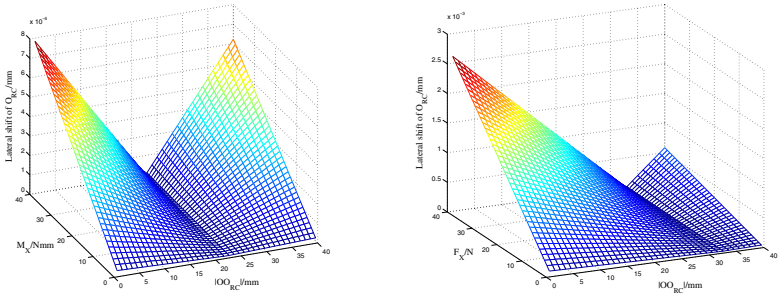

(a) (b)

Fig. 4. Lateral shift of O_{RC}.(a) Pure moment loading case.(b) Direction fixed force loading case.

Table 1. Comparison of the compliance factors

Compliance factors	Analytical results	FEA results	Error
$C_{X,\,F_X}$, $C_{Y,\,F_Y}$ (nm/N)	67.39	67.77	0.59%
$C_{X,\,M_Y}$, $C_{Y,\,M_X}$ (μm/Nm)	2.0489	2.0428	0.3%
$C_{Z,\,M_Z}$ (nm/N)	13.15	14.13	6.93%
$C_{\theta_X,\,F_Y}$, $C_{\theta_Y,\,F_X}$ (μrad/N)	2.0489	2.0135	1.76%
$C_{\theta_X,\,M_X}$, $C_{\theta_Y,\,M_Y}$ (μrad/Nm)	90.07	88.58	1.68%

4 Finite Element Analysis Validation

The finite element analysis is performed to validate the analytical model of the SRCC mechanism. The ANSYS Workbench finite element software is utilized to construct the FEA model of the mechanism. The mechanism is modeled as the material of Al7075 with a Young's Modulus of 71GPa and a Poisson's ratio of 0.33. The geometrical parameters of the SRCC mechanism are chosen as same as these in the above section. The Point O_{RC} is roughly specified as the focus of the four leaf flexures, hence $|OO_{RC}|$ also equals 30.5 mm.

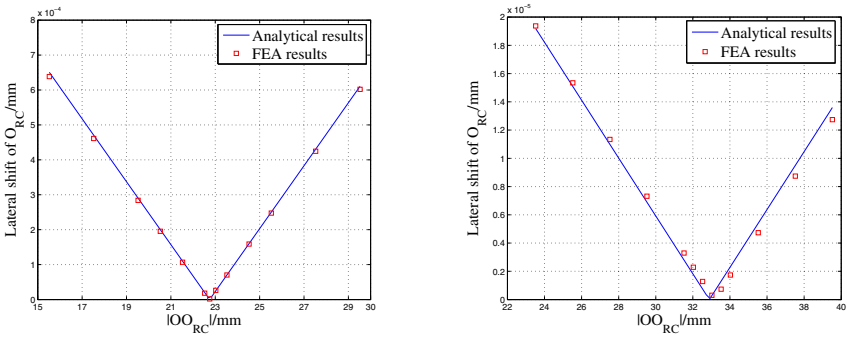

Fig. 5. Lateral shift of O_{RC}. (a) Pure moment loading case. (b) Direction fixed force loading case.

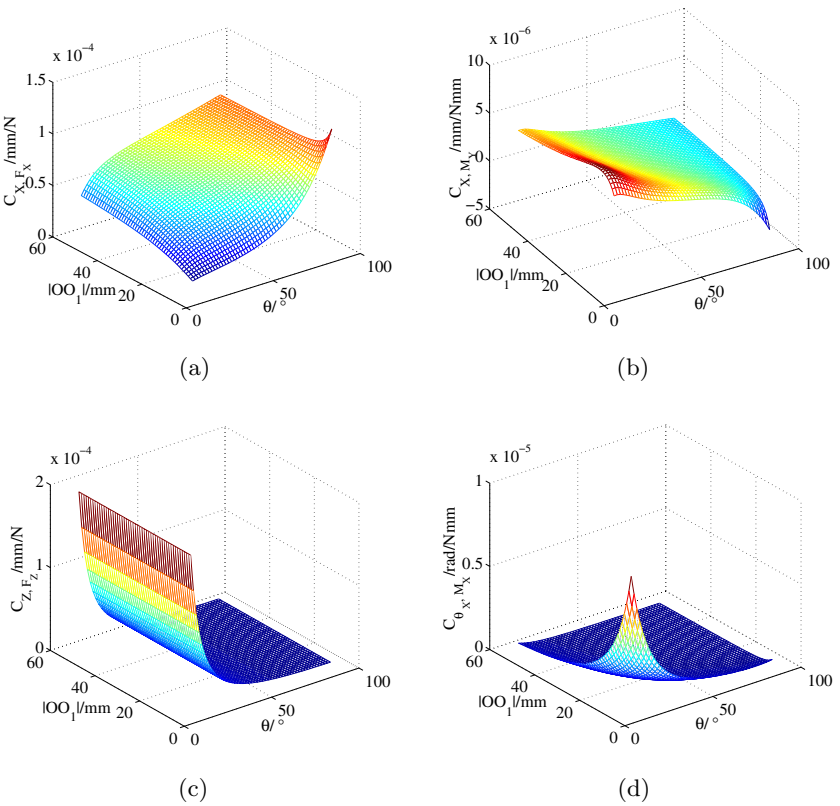

Fig. 6. Compliance factors plots in terms of mechanism geometry

The static analysis is performed to obtain the compliance factors in the compliance matrix of the mechanism, as Eq. (9) indicates. The compliance factors calculated from the analytical model and the FEA model are compared in Table 1. The analytical results and FEA results are in good agreement. The relative errors between the two results are less than 7%.

The lateral shifts of Point O_{RC} are also calculated by FEA with different length of $\overrightarrow{OO_{RC}}$ in two loading cases. As shown in Fig. 5, the lateral shifts obtained from FEA and the analytical model are both plotted for comparison. It is seen that the results from FEA match perfectly the results of the analytical model.

5 Performance Analysis

The analytical model is constructed to analyze the influences of the geometric parameters and the material properties on the compliance factors and SRCC location. The designed geometric parameters of the mechanism are chosen l, b, t, θ and $|OO_1|$. It can be obviously noticed that all compliance factors of the SRCC vary inversely proportional with the elastic Young's modulus E, and increase sensitively with the increase of l and the decrease of b and t .

To evaluate the influences of the other two parameters θ and $|OO_1|$ on the various compliance factors, three dimensional plots of the all compliance factors in terms of the two geometric parameters mentioned above are shown Fig. 6. Every time when the two parameters are varied, the other parameters are considered to be constant. These constant values are: $E = 71$ GPa, $l = 15$ mm, $b = 8$ mm and $t = 1$ mm. From the Fig. 6, it can be seen that the two geometric parameters of SRCC also have significant effects on the compliance factors at Point O, and several conclusions can be derived:

- The compliance factors $C_{X,\,F_X}$ increases when θ increases. The variation tendency of $C_{X,\,F_X}$ versus $|OO_1|$ is dependent on θ.
- The length of $\overrightarrow{OO_1}$ has no influence on the vertical compliance factor $C_{Z,\,F_Z}$, which increases sensitively with the decrease of θ. $C_{\theta_X,\,M_X}$ decreases when the two parameters increase.
- $C_{X,\,M_Y}$ varies slightly with $|OO_1|$, and presents a maximum in terms of $|OO_1|$, around 12 mm. The sign of $C_{X,\,M_Y}$ comes to change when the orientation angle of leaf flexure θ is larger than 80°.

The influences on the SRCC locations by different geometric parameters of the SRCC mechanism are also analyzed by the proposed compliance model, as shown in Fig. 7. The locations of SRCC are the ratio functions of the compliance factors, as calculated in Eqs. (12) and (13), hence, the influences of Young's modulus E of the material on the SRCC locations are removed. As can be seen from Figs. 7(a)-7(c), the dimensions of the leaf flexure have slight influences on the RCC locations. Moreover, all of the flexure dimensions have converse influences in the two loading cases. The SRCC locations in both loading cases vary quasi-linearly with $|OO_1|$, and increase sensitively with the increase of $|OO_1|$. In the

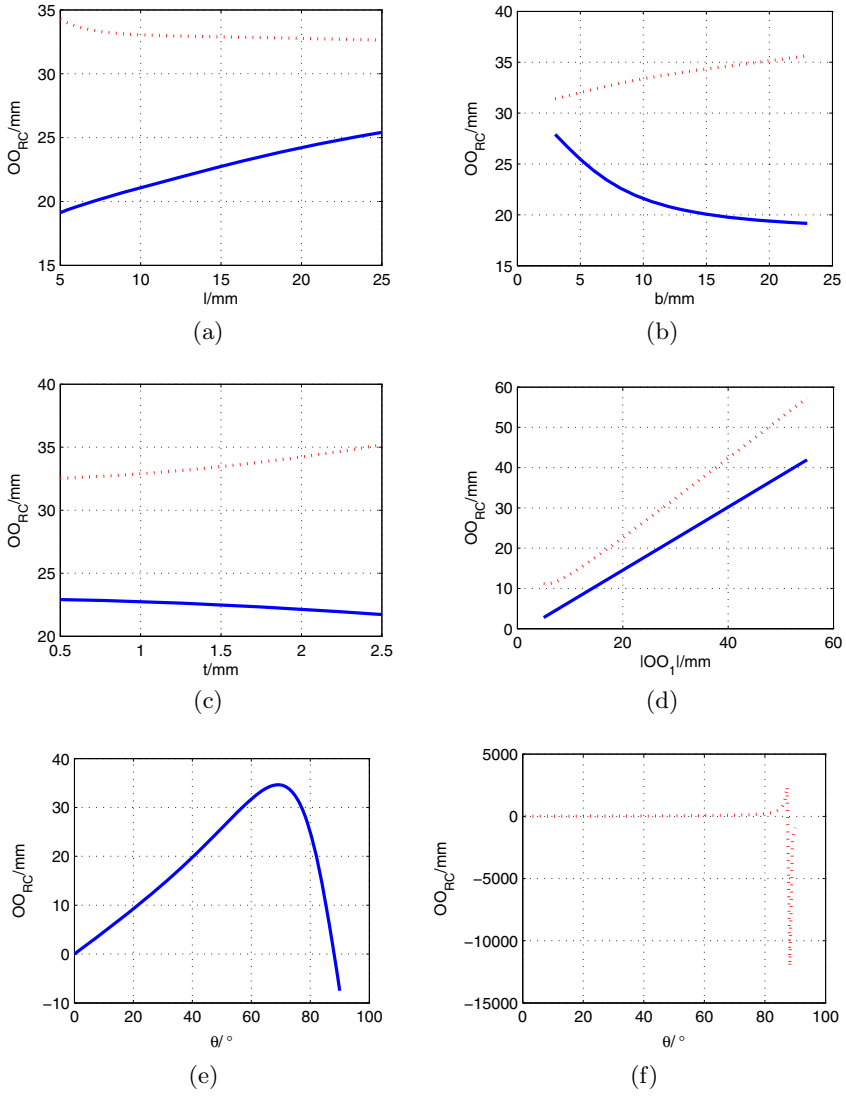

Fig. 7. The influence on the RCC location by different parameters of SRCC mechanism (solid-pure moment loading case, dot-direction fixed force loading case)

pure moment loading case, the SRCC location presents the maximum distance from Point O when θ is around 70°. When the four leaf flexures are horizontal orientation, namely, $\theta = 0°$, the SRCC coincides with the Point O (see Fig. 7(e)). As illustrated in Fig. 7(f), the end-effector can be considered to have nearly translational movement when θ approaches 90° in the loading case of direction fixed force, and the SRCC location is in the infinity position which can not be explicitly determined.

6 Conclusions

In this paper, a novel SRCC orientation mechanism is proposed to realize the 2-DOF rotations around the fixed X and Y axes in a remote plane. Two sets of isosceles-trapezoidal flexure pivots are combined in a parallel manner to obtain the advantages of simple structure, high stiffness, balance and compactness. The stiffness matrix approach is used to model the statics of the compliant mechanism, which provides the close-form equations of the compliance factors for the compliant mechanism. The SRCC locations in two different loading cases are also analyzed using the analytical model. In order to verify the analytical model, the FEA simulations of the SRCC mechanism are performed via the ANSYS Workbench. The comparison shows that the FEA and analytical results agree with each other with the deviation of less than 7%. Furthermore, the influences of geometric parameters on the compliance factors and the SRCC locations are presented graphically, which provide a theoretical basis for the practical design. The simulation results show that this kind of SRCC mechanism can realize the orientation movements with high precision of rotation, which has an great practical significance for the design of parallelism alignment stage in the micro/nanofabrication instruments. By comparing with the earlier publications, the advantages of the developed SRCC mechanism in this paper are summarized as follows:

- The tip, tilt and Z linear motions of the end-effector are fully decoupled by this configuration of SRCC without cross-couplings in theory, and are easy to control.
- The SRCC mechanism proposed in this paper possesses much higher structure stiffness, which can work as the parallelism alignment stage in the micro/nanofabrication instruments.

Acknowledgment. This work was supported by the National Natural Science Foundation of China under Grant No. 91023047, and the Science and Technology Commission of Shanghai Municipality under Grant No. 11520701500 and the Shu Guang Project of Shanghai Municipal Education Commission under Grant No. 10SG17, and Shanghai Postdoctoral Scientific Program under Grant No. 13R21414000.

References

1. Choi, K.B., Lee, J.J.: Passive compliant wafer stage for single-step nano-imprint lithography. Rev. Sci. Instrum 76(7), 075106.1 – 075106.6 (2005)
2. Choi, B.J., Sreenivasan, S.V., Johnson, S., Colburn, M., Wilson, C.G.: Design of orientation stages for step and flash imprint lithography. Precis. Eng. 25(3), 192–199 (2001)
3. Lan, H.B., Ding, Y.C., Lu, H.Z.L., Development, B.H.: of a step micro-imprint lithography tool. J. Micromech. Microeng. 17(10), 2039–2048 (2007)
4. Simeone, F.C., Albonetti, C., Cavallini, M.: Progress in micro- and nanopatterning via electrochemical lithography. J. Phys. Chem. C 113(44), 18987–18994 (2009)
5. Namatsu, H., Oda, M., Yokoo, A., Fukuda, M., Irisa, K., Tsurumi, S., Komatsu, K.: Chemical nanoimprint lithography for step-and-repeat si patterning. J. Vac. Sci. Technol. B 25(6), 2321–2324 (2007)
6. Ahmed, N.: Towards Active Monitoring Of The Micro Transfer Printing Process. MS Thesis, University of Illinois at Urbana-Champaign, Urbana, Illinois (2011)
7. Li, Y.M., Xu, Q.S.: Design and analysis of a totally decoupled flexure-based xy parallel micromanipulator. IEEE Trans. Rob. Autom. 25(3), 645–657 (2009)
8. Walsh, C.J.: Modelling Of Remote Centre of Compliance End-Efectors. MS Thesis, University of Dublin, Dublin (April 2003)
9. Hiroshima, H., Komuro, M., Kurashima, Y., Kim, S.H., Muneishi, T.: Step-and-repeat photo-nanoimprint system using active orientation head. Jpn. J. Appl. Phys. 43(6B), 4012–4016 (2004)
10. Shao, J.Y., Ding, Y.C., Liu, H.Z., Li, X.M., Tian, H.M., Xiao, B.H.: Monolithic design of a compliant template orientation stage for step imprint lithography. Proc. IMechE Part B: J. Engineering Manufacture 226(2), 221–228 (2012)
11. Pei, X., Yu, J.J., Zong, G.H., Bi, S.S., Yu, Z.W.: Analysis of rotational precision for an isosceles-trapezoidal flexural pivot. ASME J. Mech. Des. 130(5), 052302.1–052302.9 (2008)
12. Pei, X., Yu, J.J., Zong, G.H., Bi, S.S.: The stiffness model of leaf-type isosceles-trapezoidal flexural pivots. ASME J. Mech. Des. 130(8), 082303.1–082303.6 (2008)
13. Lai, L.J., Gu, G.Y., Zhu, L.M.: Design and control of a decoupled two degree of freedom translational parallel micro-positioning stage. Rev. Sci. Instrum 83(4), 045105.1–045105.17 (2012)
14. Lobontiu, N., Garcia, E., Hardau, M., Bal, N.: Stiffness characterization of corner-filleted flexure hinges. Rev. Sci. Instrum 75(11), 4896–4905 (2004)

A Novel Conductive Particle Dispersing Method via EHDA for POB-COG Packaging

Z. Ba, X. Yuan, L. Jia, X. Sheng, Zhenhua Xiong*, and Han Ding

State Key Laboratory of Mechanical System and Vibration, School of Mechanical Engineering, Shanghai Jiao Tong University, Shanghai 200240, China
{bazhengyu,kevinyuanxin,jerryjia,xjsheng,mexiong,hding}@sjtu.edu.cn

Abstract. With the continuous evolving of Liquid Crystal Display (LCD) panels and Integrate Circuits, conventional Anisotropic Conductive Film (ACF) has confronted with two paradoxical requirements: higher conductive particle density, while avoid serious aggregation. To solve this problem, a wafer level pretreatment technique, Particle on Bumps (POB), was proposed to renovate the usual Chip on Glass (COG) technology. Although we have demonstrated its feasibility and reliability, a fundamental route towards fully accomplishing the POB technique still needs to be paved out, that is the dispersing of conductive particles. Herein we introduced the method of Electrohydrodynamic Atomization (EHDA). EHDA is a technique which ultra-fine droplets can be induced due to electrical force. We build up a prototype apparatus for particle dispersing. With the help of high speed camera, we are able to verify certain behaviors and characteristics of different modes during the EHDA process. The deposition patterns generated under different spraying modes are observed and compared; the stable cone jet mode is therefore chosen as the operational state during our following deposition process. We investigate the connections between onset voltage and relevant spray parameters to optimize our EHDA configurations. By implementing the particle dispersing experiment via stable cone jet EHDA, we successfully obtained a pattern with high densely and uniformly distributed particles.

Keywords: COG, POB, Conductive particles, EHDA, Particle distribution, Pattern formation.

1 Introduction

As a prevailing interconnection material, anisotropic conductive film a.k.a. ACF has anchored itself in various microelectronic packaging and especially LCD manufacturing applications over the last decades [1]. The very characteristic which gains ACF such popularity is the unidirectional conductivity that enabled by the conductive particles dispersed within the ACF. When bonding an IC to the substrate through thermo-pressing, several particles are trapped by two connectors and thereupon forming an electrical path in Z-axis, meanwhile, the thermosetting resins will be cured to establish a mechanical connection [2]. Because of

* Corresponding author.

J. Lee et al. (Eds.): ICIRA 2013, Part II, LNAI 8103, pp. 397–408, 2013.

the natural resiliency provided by its polymer core, conductive particles may assist the bonding to be highly endurable under thermal load [3]. Nevertheless, with the continually evolving towards higher resolution and cost reduction, the bump pitch of driver IC is becoming smaller and denser [4]. Since the cross-section area of a bump and the gaps between them are both scaling down, two serious problems emerged with the conventional ACF based COG technology [5]. Fig.1illustrates those problems: The left happens when the IC bumps are too small to capture adequate conductive particles; while the right shows an aggregation of the conductive particles between adjacent bumps. The former can causes an electrical failure for high resistance, and the latter may lead to a short-circuiting. That is to say, the density and aggregation, which is a dilemma, of the conductive particle within the adhesive have prevented the COG technique from moving forward.

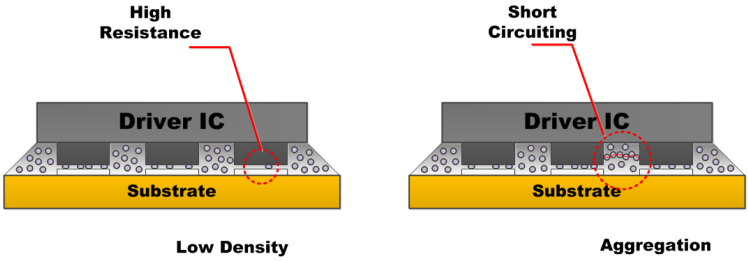

Fig. 1. Schematics of two typical ACF interconnection failures

To overcome this difficulty, our group had conceived a brand new technique named "Particle on Bump (POB)" to substitute for ACF in ultra-fine pitch COG bonding. We supposed the conductive particle can be somehow placed directly onto the entire IC surface, and then a wafer level pretreatment such as reflow will be employed to solder those particles onto the bump. Next, since a solder connector can only be built through an AU-SN intermetallic, the particles landed on a place other than the IC bumps can be easily wiped off. Finally, the IC chips diced from the processed wafer can be attached to the Indium Tin Oxide (ITO) glass simply by a Nonconductive Adhesives (NCA). Fig.2 shows a flow chart of the POB technique, and relevant works can be found in reference [6]. Within that paper, the AU-SN binary system has been demonstrated to be viable and reliable, whereas the particle placement which is also a critical step remains unsolved. Herein we introduced a new method based on EHDA to achieve a particle distribution pattern with both high density and good uniformity.

EHDA or Electrospray is the only technique known to atomize dielectric liquids into sub- micrometric droplets [7]. In electrospray, a high electric potential is exerted to a capillary. Liquid jet that flowing out of the capillary nozzle will be charged and disintegrate into fine droplets due to coulomb repulsion. These highly charged droplets are also controllable to some extent by means of the electric field. The droplet size can reach to a minimum of several tens of nanometers

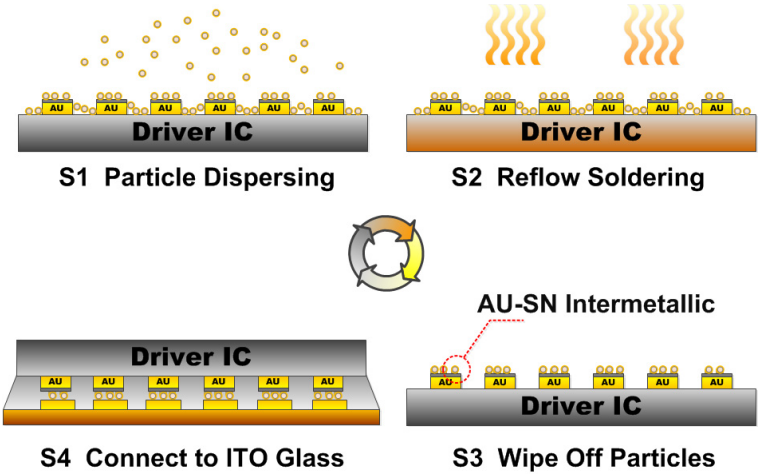

Fig. 2. Flow chart of the Particle on Bumps (POB) technique

and is nearly monodispersed distributed. Electrospray has found popularity in micro-pattern formation, thin film deposition, particle production, mass spectrometry and many other applications [8,9,10].

In this paper, a prototype experimental apparatus was designed to realize our purpose of utilizing EHDA as a dispersing method to generate particle patterns. Our attempts start up by studying the behaviors and characteristic of different electrospray modes. We analyzed the time-series photos captured within different EHDA modes; found the single cone-jet mode serves to be a highly stable mode out of the EHDA process. The liquid filament barely sways after issuing out of the nozzle tip, this stable behavior yields at least two advantages : the droplet size are much more monodispered and the geometry of the spray plume retains very symmetric, both features are helpful for us to get ideal particle patterns. Next, we implemented quite a few experiments to establish relationships between the stable cone jet mode and several critical EHDA parameters. By doing this, we are able to map out a preferred EHDA process that runs rightly in the stable cone jet mode. Lastly, particle dispersing experiments were operated under those combined parameters derived from former studies. The deposition patterns produced by stable cone jet EHDA process are shown and the properties are discussed.

2 Experimental Setup

2.1 Materials

Due to practical used conductive particles are gold-coated which render itself a highly expensive material, we take those non-coated epoxy microspheres (SEKISUI CHEM. CO.,LTD.), namely a semi-finished conductive particle, as a

replacement. We believe it is a good enough alternative for the diameter of particle narrowly range from 5 to 6 μm, approximately the same as those of the coated ones and both particles are sharing identical core material. Three liquids: Ethanol, Isopropanol, Acetone are chosen to be the carrier solution for concocting conductive particle suspension. Their physical properties which may have influence on our EHDA process are listed in Tab.1. Normally, the concentration of the particle suspension is 0.1 % (g/ml), each of the suspension mixture will go through ultrasonic treatment for 15 minutes before experiment. Two types of disc plate, one by stainless steel the other by silicon slice, both one side specular polished, are deployed as IC wafers for receiving conductive particles.

Table 1. Physical properties of the liquids used in the experiment

Liquid	Density $(kg \cdot m^{-3})$	Viscosity $(mPa \cdot S)$	Surface Tension $(N \cdot m^{-1})$	Conductivity $(S \cdot m^{-1})$	Relative Permittivity
Isopropanol	786	2.43	0.021	3.5	18.2
Ethanol	789	1.16	0.022	1.3×10^{-3}	24.3
Acetone	791	3.07	0.024	2×10^{-2}	20.7

2.2 Experimental Apparatus

A schematic of the EHDA dispersing system beside with an actual photo are illustrated in Fig.3. In order to be compatible with different wafer scales, an X-Y 2D planar moving stage is mounted to uphold the entire counter electrode and

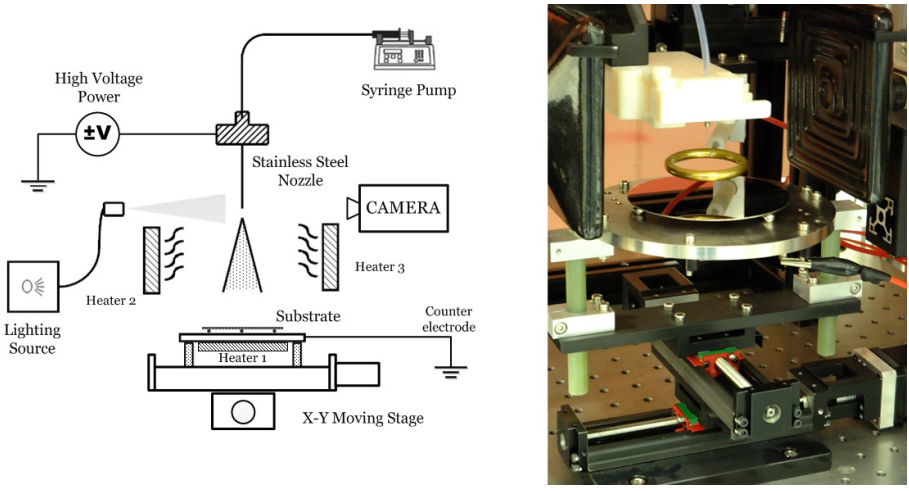

Fig. 3. Schematics of the Experimental Apparatus

the substrate. It covers an area by $100 \times 100mm$ which can satisfy an IC wafer no larger than 4 inches. We employed here a Capillary to Substrate configuration with stainless steel capillary nozzles of different inner $(0.18, 0.41, 0.6)mm$ and outer $(0.35, 0.71, 0.9)mm$ diameter. The nozzle is mounted vertically upon the substrate, distance from nozzle to substrate is adjustable which range from zero to several centimeters. The particle suspension is delivered to the capillary nozzle by a syringe pump (WZ-50C6, Smith Medical), and the feed rate of liquid is therefore regulated. As the electrode setting always plays an essential role in EHDA process, we use two glass fiber pillars to insulate the substrate from the moving stage beneath, together with a DC power supply (DW-SA303-1ACDE, Dongwen Inc.) which can generate positive and negative high voltages simultaneously, hence augment the possibility to obtain various electrode configurations.

As mentioned previously, liquid solvent within the particle suspension was regarded as carrier in our EHDA experiment. We have designed a stereo heating system, which consist of two vertical radiant ceramic heaters and a round contact metal heater, to help the evaporation of these liquid, so as to ensure those conductive particles won't become reaggregationed after their landing onto the disc plate. A high-speed digital camera (Phantom Miro M310, Vision Research Inc.), capable of 650000 (fps) at maximum, was utilized to observe the generation and fluctuation of the droplets during spray experiment. A zoom lens (Zoom 6000, Navitar Inc.) was connected to the camera to enlarge the spray observing space, so as to get clear time-series images, and facilitate our thorough analysis of the EHDA process. Other crucial accessory also includes a no stroboscopic Xenon light source (XD-300-250W, Yanan Lighting Inc), which is to provide illumination during the video shooting.

2.3 Experimental Methods

The main obstacle to further downscale the pitch size and pitch gaps of the driven IC lies in low density and nonuniformity of the conductive particles diffused within the ACF. Our experiment aims clearly at solve the problem by obtaining a densely laid particle patterns with good uniformity yet without agglomerate. We deployed various EHDA parameters, such as capillary diameter, nozzle tip to substrate distance, suspension feed rate, applying voltage, and test duration, etc. to determine the spray characteristic under different modes and the deposited patterns produced via the process. Under the help of high speed camera (the typical fps during test is set to 10000), we are capable of distinguishing detail difference among several sub spray modes, which helps us to optimize our experimental configurations. We also developed an optic inspection system based on image processing to calculate the density of the particles and make evaluations of its uniformity, all of which will be elaborated in the following sections.

3 Result and Discussion

The disruption of liquid jet into fine droplets during EHDA process is a result of the dynamic rebalances of the surface tension versus electric stress. The atomization phenomenon merely takes place when electric potential has surpassed certain level, and the feeding liquid maintains a proper flow rate[11]. Generally, EHDA process can be classified into several modes, which behaves quite different from one to another. This variation involves nearly all aspects of the EHDA technique, such as the onset voltage, spraying geometry, mean droplet sizes, etc. Despite numerous investigations have been made in comprehending such phenomenon, hardly can the very natural of EHDA, due to its complexity, be fully explained. Since it is a tough work to build connections between the operating parameters and the deposition patterns directly, we herein take the spraying mode as a bridge to mapping the relationships of EHDA process and particle distributions.

3.1 Spraying Modes of EHDA

As introduced by plenty of studying papers, the EHDA process can be grouped into four main spraying modes, Dripping, Spindle, Cone-jet, and Multi-jet, with the increasing of applied voltage [12]. If we take more details into consideration, some sub-modes (Microdripping, Multi-spindle, Oscillating-jet, and Precession mode, etc.) will be also categorized as the minor shift of the electric potential or flow rate. Under the help of high speed camera, we are able to observe the time-series images of three typical spraying modes: micro-spindle, single cone-jet, and multi-jet modes of the EHDA process, see Fig.4.

These photos are captured at intervals of 40 μs. We can see in Fig.4 (a), the liquid first elongate in the direction of the electric field. As the liquid continues to stretch out, a necking effect was then appeared at the middle of the emission cone jet. When the necking cuts off the liquid from the emission jet, the rest of the

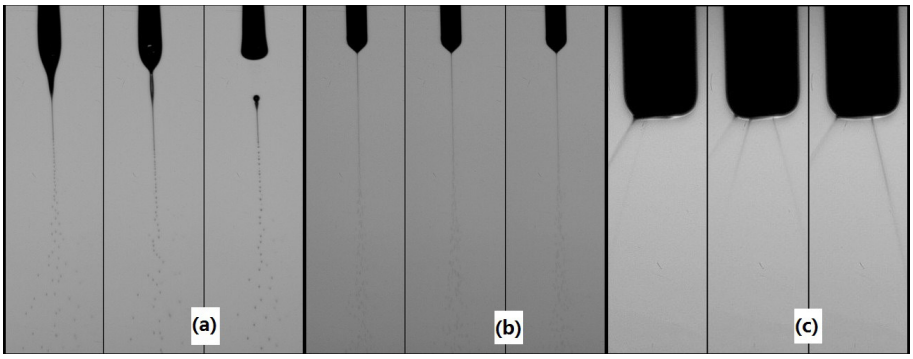

Fig. 4. Time-series images of different spraying modes, (a) micro-spindle mode,(b) single cone-jet mode,(c) multi-jet mode

emission tip will retract back to the capillary nozzle, a tiny liquid drop was then detached from the nozzle tip. Fine droplets are continually issuing out of both the tip of the liquid filament and the detached micro droplets, and moving separated from each other due to the coulomb repulsions. In Fig.4 (c), liquid ejections are not generated directly out of the nozzle tip, the Taylor cone can be recognized, nor will the ejection jets maintain stable here. Meanwhile the ejection jet will soon transfer to a different place or transform to some other ejections within very short intervals. Only the single cone jet mode (Fig.4 (b)) can maintain a relative stable spray plume, which are not time variable comparing to other two modes. It provides us a sufficiently good explanation for why only through stable cone-jet mode can we generate nearly monodispersed droplet, a conclusion that has been testified by many researches.

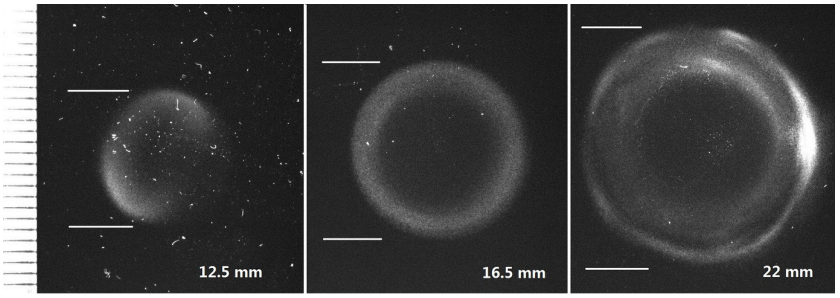

Fig. 5. Deposition patterns generated under different spraying modes, (a) Precession mode (4.58Kv), (b) Stable cone-jet mode (5.41Kv), (c) Multi-jet mode (8.01Kv)

Moving now to our main object of the present work, monodispersed droplet is likewise desired in our experiment to prevent aggregations during dispersing the conductive particles. More importantly, a uniformly distribution pattern we craved for is the logical subsequence since the spray plume of the single cone jet mode keeps stable and performs spatially symmetric. The deposition patterns obtained under three spraying modes are presented in Fig.5. The processing voltages are $4.58Kv$, $5.41Kv$, $8.01Kv$ and represent for Precession, Stable cone jet, and multi-jet mode respectively. Only the middle one remains the shape of a normal circle. The result indicates us that we share perform our distribution experiment via the stable cone jet mode, so as to ensure the acquisition of a uniformly scattering particle patterns.

3.2 Onset Configurations for Stable Cone Jet Mode

To induce a stable cone jet mode electrospray, an appropriate electric potential and befitting flow rate are required. Several studies indicates that when the liquid flow rates are larger than certain values, it is unlikely to achieve the stable cone-jet mode for the spray will evolve from the dripping mode directly into a higher

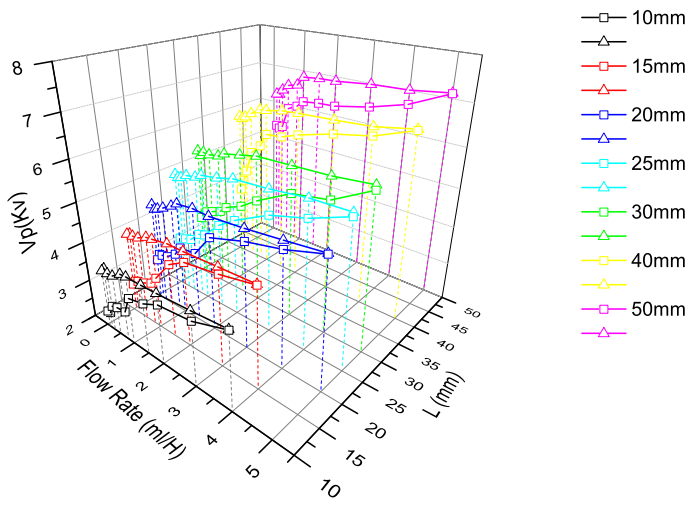

Fig. 6. Spraying onset voltage V.S. Flow rate and Nozzle to Substrate distance

mode (unstable cone jet, or multi-jet mode). The Nozzle to Substrate distance, a commonly fixed parameter as in many other investigations, also needs to be considered in our experiment for its influence of the sizes of deposition patterns.

The relationship between Flow rate and the apply voltage (Vp) under different Nozzle to Substrate distances are exhibited in Fig.6. Liquid used for spraying is pure ethanol, via a $0.18mm$ inner diameter capillary. The lower curves depicted by square bars are the bottom borders that divide the space into dripping modes and cone-jet modes; the upper lines denoted by triangle bars are the top borders that divide the space into multi-jet mods and cone-jet modes. In other words, the space among two groups of curve-sets constitutes a cone-jet mode space, while the other two spaces named by dripping mode space and multi-jet mode space. Besides, more facts can be inferred from this graph. Firstly, Nozzle to substrate distance and the onset voltage are in a near linear fashion; the gaps are slightly larger between two curves when nozzle is farther to the substrate. Second, the transition voltage from cone-jet-to-multi-jet is relatively stable with the change of liquid flow rate compare to the dripping-to-cone-jet transition voltage; we see a turning point near the flow rate of $1ml/H$, where the bottom curves will undergo a diminish of the slope. The last, flow rate larger the $5ml/H$ is unacceptable for a capillary of $0.18mm$ inner diameter in the EHDA process.

We also deployed some test to figure out the influence made by different diameter capillaries and different dielectric liquids, the results are shown in Fig.7. These legends show that a larger needle needs a higher electric potential. The solvent rarely affects the transition voltage from cone-jet to multi-jet, but the onset voltage of cone-jet mode for a liquid with lower conductivity is much higher.

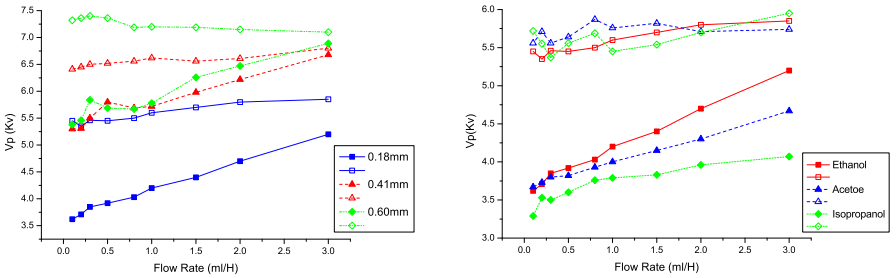

(a) Different Nozzle Diameter (b) Different solvent

Fig. 7. Nozzle and Solvent effect to Onset Voltage.

3.3 Final Result and Destabilization

We have discussed the relationship of maintaining the stable cone jet mode to obtain a uniformly distributed particle patterns, moreover, several onset parameters related to the stable cone jet EHDA have been investigated as well. Fig.8 demonstrated a group of photos of the deposition patterns with different diameters. The Nozzle to substrate distances are $15mm$, $20mm$, $25mm$, and $40mm$ in correspond to $7.5mm$, $13.5mm$, $16mm$, and $33mm$ pattern diameters respectively. Plenty test results demonstrate such a trend, As larger as the distance between nozzle and substrate, the diameter of the pattern also expanded. Once we have settled the hight of the nozzle, other parameters including nozzle size, solvent flow rate, applying voltage are adjusted for a stable cone-jet EHDA process.

But owing to the deposition via EHDA involves in a lot of complicated physical disciplines such as Electric fields, Atomization, Multiphase flow, Liquid characteristics and so on. The stable cone jet mode does not guaranty high yield rates of pattern deposition. Fig.9 shows the major flaws we encountered during our experiments. Fig.9 (a) represents a very pervasive flaws after the EHDA deposition, we call it circling effect, particles are lean to land on the outside edge of the patterns, such phenomenon occurs randomly and dense differently even under same EHDA parameters. This result has never been reported as far as we know, but we suppose the reason may relate to coulomb forces or the material the conductive particles are made of; Fig.9 (b) depicts the reaggregation of conductive particles since the carrier solvent can't evaporate completely during the spray process, when it falls down on to the surface, reunion of droplet may leads to such an effect (the lightspot scatter within the pattern). After we employed a stereo heating system, this defect has been greatly improved; Fig.9 (c) often appears when a low flow rate ($0.5ml/H$) and large nozzle to substrate distance ($50mm$) were used for deposition process. The end of the spray plume wandered to nearby place, thus ruined the pattern symmetry; Fig.9 (d) shows another frequently happened defect when large droplet burst out from the capillary

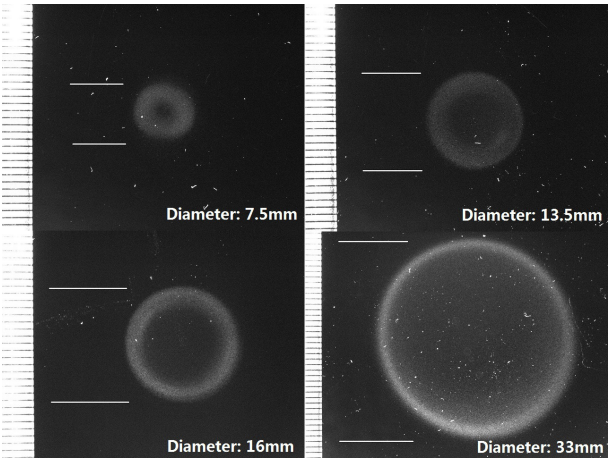

Fig. 8. Deposition patterns via stable cone-jet EHDA under different configurations

nozzles at the beginning and ending of the EHDA process, and bring about such damages to our experiment.

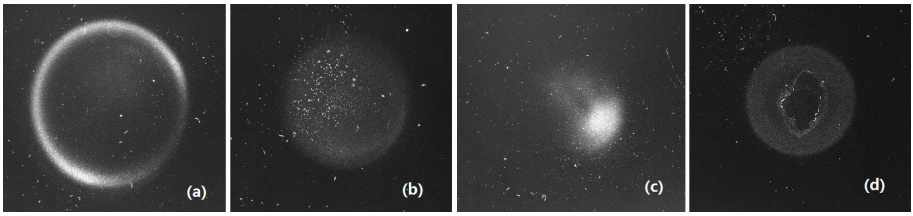

Fig. 9. Destabilized deposition patterns

3.4 Density Calculations of the Microscopy Images

In order to compare and assess our experiments quantitatively, an evaluation system based on image processing was developed. The original picture is initially handled by denoise and smooth treatment such as filtering and binarization , then it goes through an opening operation base on mathematical morphology to dispel physical contamination caused by solvent concocting and atomization. Finally, we do the counting jobs by calculate the areas of connected domain. The microscopy image and processed pictures are shown in Fig.10.

4 Conclusions and Future Works

We introduced a new method to dispersing conductive particles through EHDA technique so as to form a high density particle pattern without aggregation.

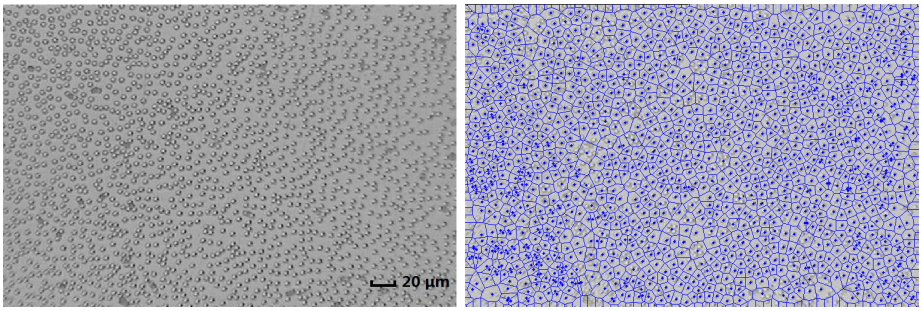

(a) Microscopy image of the pattern (b) Pictures by image processing

Fig. 10. Density calculations of the deposition patterns

Based on the investigation of EHDA process, we confirmed the stable cone-jet mode as the best EHDA mode to implement our dispersing experiment. Parameters and configurations evolved in maintaining a stable cone-jet electrospray are studied, other factors which may have affection on the deposition patterns are elaborated as well. We have achieved a preliminary result which verified EHDA technique to be a feasible way in particle dispersing. Meanwhile, several works need to be push forward in proving our method. More factors need to be considered to promote the stability of the spraying process, and a moving path strategy is also required to enable the coverage of the entire IC wafer. To sum up, we believe the EHDA is a very promising technology, and can be applied to the future COG packaging industry based on POB.

Acknowledgments. This work is supported jointly by National Natural Science Foundation of China under Grant 51175344, and the Shu Guang Program of Shanghai Municipal Education Commission and Shanghai Education Development Foundation under Grant 11SG14.

References

1. Kristiansen, H., Liu, J.: Overview of conductive adhesive interconnection technologies for lcds. IEEE Transactions on Components, Packaging, and Manufacturing Technology, Part A 21(2), 208–214 (1998)
2. Li, Y., Wong, C.: Recent advances of conductive adhesives as a lead-free alternative in electronic packaging: Materials, processing, reliability and applications. Materials Science and Engineering: R: Reports 51 (2006)
3. Lin, Y.C., Zhong, J.: A review of the influencing factors on anisotropic conductive adhesives joining technology in electrical applications. Journal of Materials Science 43 (2008)
4. Wang, Z.: Challenges in the reliability study of chip-on-glass (cog) technology for mobile display applications. In: 2003 5th Conference on Electronics Packaging Technology (EPTC 2003), pp. 595–599. IEEE (2003)

5. Jia, L., Ding, H., Sheng, X., Xie, B.: Evaluation of a double-layer anisotropic conductive film (acf) for fine pitch chip-on-glass (cog) interconnection. In: 2005 6th International Conference on Electronic Packaging Technology, pp. 344–347. IEEE (2005)
6. Jia, L., Wang, Z., Xiong, Z., Sheng, X., Ding, H.: Particle on bump (pob) technique for ultra-fine pitch chip on glass (cog) applications. In: 8th International Conference on Electronic Packaging Technology, ICEPT 2007, pp. 1–4. IEEE (2007)
7. Jaworek, A., Sobczyk, A.: Electrospraying route to nanotechnology: An overview. Journal of Electrostatics 66 (2008)
8. Jaworek, A.: Electrospray droplet sources for thin film deposition. Journal of Materials Science 42 (2006)
9. Hogan, C.J., Biswas, P.: Narrow size distribution nanoparticle production by electrospray processing of ferritin. Journal of Aerosol Science 39 (2008)
10. Park, J., Hardy, M., Kang, S., Barton, K., Adair, K., Mukhopadhyay, D., Lee, C., Strano, M., Alleyne, A., Georgiadis, J., Ferreira, P., Rogers, J.: High-resolution electrohydrodynamic jet printing. Nature Materials 6(10), 782–789 (2007)
11. Tang, K., Gomez, A.: Generation of monodisperse water droplets from electrosprays in a corona-assisted cone-jet mode. Journal of Colloid and Interface Science 175(2), 326–332 (1995)
12. Jaworek, A., Krupa, A.: Classification of the modes of EHD spraying. Journal of Aerosol Science 30(7), 975 (1999)

Performance Prediction of Hard Rock TBM Based on Extreme Learning Machine

Chengjun Shao, Xiuliang Li, and Hongye Su*

State Key Laboratory of Industrial Control Technology, Institute of Cyber-Systems and Control, Zhejiang University, Hangzhou, Zhejiang , 310027, China
scjwater@gmail.com

Abstract. Performance prediction of hard rock TBM is the key to the successful tunnel excavations. A series of TBM performance prediction models have been developed since 1970s. The empirical, semi-empirical models such as CSM, NTNU models have their limitations, because the models are unable to completely reflect the correlation between the parameters of the models and penetration rate (PR). Researchers propose some models based on data-driven, like neural network model, which have the over fitting problem generally. This paper proposes a new on-line prediction model with incremental learning method based on extreme learning machine (ELM). This algorithm randomly chooses hidden nodes and analytically determines the output weights of single-hidden layer feed forward neural networks (SLFNs). Unlike neural network model, over fitting does not need to be concerned and the iterative learning steps are not required in ELM. The database used to validate the model is collected from the Queens Water Tunnel #3, Stage 2, New York City, USA. Compared with other methods such as PLS, GP, LSSVM, ELM prediction model tends to provide precise prediction at extremely fast learning speed.

Keywords: TBM, Performance prediction, penetration rate, extreme learning machine

1 Introduction

Tunnel boring machine (TBM) is used for excavating tunnels through various types of rock masses. Compared to the conventional drill-blasting method, TBM has advantages in the high advance rate excavation, security and small impact on the surrounding environment. It is the most important method in boring of the tunnels in the past decades [1].

The reasonably accurate estimation of TBM performance parameters is the key component in a successful planning of tunnel excavations, especially the penetration rate (PR, the rate of TBM penetration during boring times) and the advance rate (AR, the rate of both mined and supported actual distance during a work time period) [2]. Most researchers take the penetration rate as the critical object of the studies. A series of TBM performance prediction models have been developed since 1970s, and

* This work was supported by Key Project of Chinese National Programs for Fundamental Research and Development(973 program), (No. 2013CB035406).

J. Lee et al. (Eds.): ICIRA 2013, Part II, LNAI 8103, pp. 409–416, 2013.

researchers are still trying to carry out studies to obtain more accurate and comprehensive prediction models.

The current TBM penetration rate prediction models can be divided into two groups: one is empirical models, the other is semi-empirical models [3], among them, Norwegian University of Science and Technology (NTNU) model and Colorado School of Mines (CSM) model are respectively the most recognized one. NTNU model takes both rock mass properties and machine parameters into considerations [4]. In this model, the penetration rate is estimated by the TBM machine specifications, rock fracture data, and laboratory measured indices which include drilling rate index, brittleness index, and cutter life index. The prediction of the empirical models is acceptable since the models are based on the data of the previous TBM constructions, but the limitation of this model cannot be ignored with the fast developing speed of TBM technique. CSM model is based on the measurement data and evaluation data of cutting forces on an individual cutter [5]. This semi-theoretical model is widely used in estimating the penetration rate. Since the engineering factors are not fully considered, it still has the limitation when the condition of the constructions is complicated. Rostami and Ozdemir improved this model by estimating cutting forces as a function of intact rock properties which including uniaxial compressive and tensile strength of rock and cutter geometry [3], [6]. However, rock mass properties are not quantitatively considered in this model, such as planes of weakness, fracture orientations, and rock brittleness. Yagiz modified the CSM model by adding intact rock brittleness and rock masses fracture properties as input parameters [7]. The prediction result shows that jointed rock mass is not being taken into consideration in the modified model.

Barton proposed a new model named QTBM based on Q rock mass classification system [8]. Many new parameters for practical application are added in model, then users can use the equation with some of the input parameters to estimate QTBM and penetration rate of TBM.

In addition to empirical and semi-empirical models, artificial intelligence has been applied to predict the penetration rate of TBM. Alvarez Grima utilized the fuzzy neural network [9] and Okubo took the expert system [10] to estimate the penetration rate. Monte Carlo-BP network model was proposed by Wen [11], which took the uncertainty of some important parameters into consideration. The artificial intelligence methods have a relatively long training and testing time, and over fitting is also a disadvantage for these methods to be successfully applied. This paper proposes a model based on extreme learning machine algorithm, it has an extremely fast learning speed and can train the model without iterative learning steps and over-fitting problems.

2 The Structure and Algorithm of ELM

ELMs proposed by Huang are originally developed for the SLFNs (SLFN shows in figure 1), then extend to the generalized SLFNs [12][13]. Unlike the traditional neural networks, the hidden layer of SLFN need not be tuned [13]. Applying the random computational nodes in the hidden layer is a typical implementation of ELM. Compared to the conventional learning algorithms for neural networks, the aim of ELM is not only the smallest training error but also tends to reach the smallest norm of output weights. According to Bartlett [14], the smaller the norm of weights is, the better generalization performance the networks have.

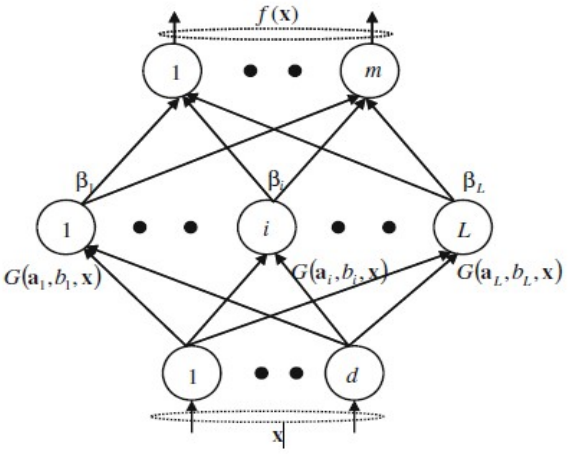

Fig. 1. Single-hidden layer feedforward network

For N different samples (x_i, y_i), where $x_i=[x_{i1}, x_{i2}, \cdots, x_{in}]^T \in R_n$, and $y_i=[y_{i1}, y_{i2}, \cdots, y_{im}]^T \in R_m$, ELMs with L hidden nodes are described as

$$\sum_{i=1}^{L} \beta_i g_i(x_j) = \sum_{i=1}^{L} \beta_i g(w_i \cdot x_j + b_i) = o_j, \quad j = 1, 2, ..., N \tag{1}$$

Where the weight vector $w_i=[w_{i1}, w_{i2}, \ldots, w_{in}]^T$ is connecting the input nodes and ith hidden node, weight vector $\beta_i=[\beta_{i1}, \beta_{i2}, \ldots, \beta_{im}]^T$ is connecting the ith hidden node and the output notes, constant b_i is the threshold of ith hidden node. $w_i \bullet x_j$ is the inner product of w_i and x_j, $g(x)$ is the activation function.

The aim of the ELM with L hidden nodes is approximating the N samples with zero error

$$\sum_{j=1}^{L} \left\| o_j - y_j \right\| = 0 \tag{2}$$

Described by β_i, w_i and b_i

$$\sum_{i=1}^{L} \beta_i g(w_i \cdot x_j + b_i) = y_j, \quad j = 1, ..., N. \tag{3}$$

Equation (3) can be written compactly as

$$H\beta = Y \tag{4}$$

where

$$H(w_1, ..., w_L, b_1, ..., b_L, x_1, ..., x_N) = \begin{bmatrix} g(w_1 \cdot x_1 + b_1) & \cdots & g(w_L \cdot x_1 + b_L) \\ \vdots & \cdots & \vdots \\ g(w_1 \cdot x_N + b_1) & \cdots & g(w_L \cdot x_N + b_L) \end{bmatrix}_{N \times m} \tag{5}$$

H is the hidden layer output matrix of ELM,

$$\beta = \begin{bmatrix} \beta_1^T \\ \vdots \\ \beta_L^T \end{bmatrix}_{L\times m} \quad \text{and} \quad Y = \begin{bmatrix} y_1^T \\ \vdots \\ y_N^T \end{bmatrix}_{N\times m} \tag{6}$$

The purpose of training the ELM is to obtain a least-squares solution $\overline{\beta}$ of the system $H\beta = Y$.

$$\left\| H\overline{\beta} - T \right\| = \min_{\beta} \left\| H\beta - T \right\| \tag{7}$$

According to Huang [15], if hidden node number L equals to the training samples number N, the error between ELM and the training samples can be zero. But in practical, the number of training samples is much more than hidden nodes, and a_i, b_i, β_i (i=1, 2, … , L) satisfying $H\beta$=T may not exist. The smallest norm least-squares solution is showing below:

$$\overline{\beta} = H^{+}Y \tag{8}$$

where H^+ is the Moore-Penrose generalized inverse of H.

3 Simulation Based on ELM

3.1 Input of The Model

The penetration rate of TBM is affected by various factors, such as rock parameters, construction parameters, TBM machine parameters. In this paper, uniaxial compressive strength (UCS) of intact rock, Brazilian tensile strength (BTS), peak slope index (PSI), distance between plane of weakness (DPW), angle between tunnel axis and the planes of weakness (α) are the input of the model. Generally, the data used to estimate the penetration rate are collected by the same type of TBMs, so the machine performance parameters need not to be considered.

3.2 Data Processing

In order to improve fresh water distribution throughout the City of New York, USA, the government designed the Queens Water Tunnel # 3, stage 2 [15]. A high power TBM was used to excavate the tunnel about 7.5 km long and 7 m in diameter beneath Brooklyn and Queens. The experiment data come from this project.

In this experiment, all the input attributes are normalized into the range [-1, 1] except penetration rate, using the equation below:

$$x'_{i,j} = \frac{x_{i,j} - \min(x_{1,j}, x_{2,j}, ..., x_{N,j})}{\max(x_{1,j}, x_{2,j}, ..., x_{N,j}) - \min(x_{1,j}, x_{2,j}, ..., x_{N,j})} \times 2 - 1 \tag{9}$$

3.3 Result of Penetration Rate Prediction

153 groups of Data are provided by paper [12], and this experiment divides the dataset into 2 parts, 133 data for training and other 20 for testing.

There are 20 hidden nodes assigned for the ELM algorithm. 10 trails have been conducted for it and the experiment takes the average outputs as results. The activation function in equation (1) is the sigmoid function:

$$g(x) = 1/(1+\exp(-x)) \tag{10}$$

The results of training and testing are respectively showing in Fig. 2, Fig. 3. It is apparent that the model is well-trained while the nodes in figure 2 are closely distributed in surrounding area of intermediate line. The RMSE in the training stage is 0.1738. In addition, the TBM penetration rate of the construction in Queens Water Tunnel # 3, stage 2 is mainly distributed in 1.5 to 2.5. The nodes of testing result also distribute tightly to the intermediate line, and the RMSE is 0.1426, which indicating the model with ELM algorithm predicting PR is workable.

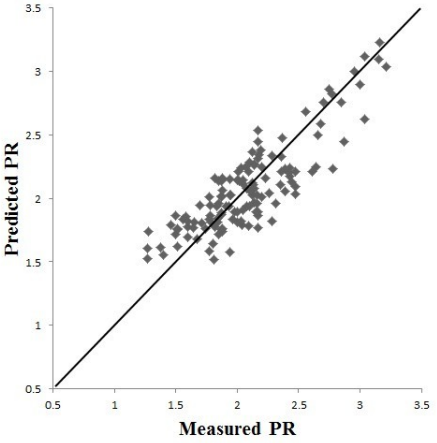

Fig. 2. Result of training data (Comparison between measured PR and predicted PR)

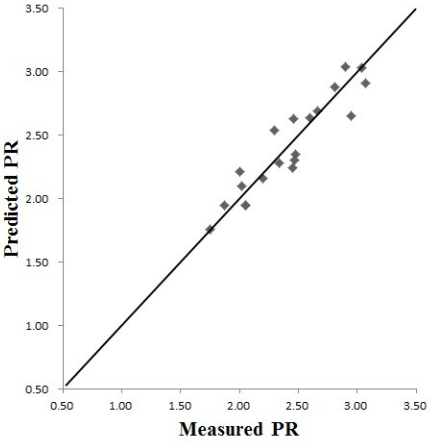

Fig. 3. Result of testing data (Comparison between measured PR and predicted PR)

3.4 Comparison between ELM and other Models

In order to compare the performance between ELM model and conventional models, this paper predicts PR with partial least square (PLS), least square support vector machine (LSSVM), Gaussian processes for machine learning (GP) in the meanwhile. PLS is commonly used in regression modeling, especially the internal variables have strong linear correlation. SVM has a more stringent theoretical and mathematical requirement than neural network. It is suitable for cases of limited samples since

SVM utilizes structural risk minimization method with no local minimum problems, and LSSVM is the most typical one in SVM. Gaussian process was proposed by William based on probabilistic kernel function, which is successfully applied in machine learning area.

20 groups of data are randomly chosen for training, the original data and the result of predicted PR by four different algorithms are shown in Table 1, and the comparison of prediction performance for 4 algorithms are shown in Table 2. From Table 1 and Fig. 4, the predicted PR of PLS and LSSVM algorithms are quite close. ELM has more precise prediction in the area of high PR compared to the others.

Table 1. Comparison between measured and predicted results

NO.	UCS	BTS	PSI	DP	α	PR/(m/h)				
	/MPa	/MPa	KN/mm	W/m	/(°)	Measured	PLS	GP	LSSVM	ELM
1	189.7	9.0	56	0.2	42	2.81	2.66	2.61	2.63	2.88
2	174.1	9.9	58	2.0	35	2.34	2.36	2.25	2.28	2.28
3	177.9	10.1	58	0.4	61	2.90	2.81	2.52	2.80	3.04
4	180.7	10.1	57	0.2	55	3.04	2.78	2.58	2.80	3.03
5	184.1	10.2	57	0.4	49	3.07	2.70	2.57	2.72	2.91
6	191.0	10.4	54	0.4	34	2.95	2.51	2.54	2.55	2.65
7	191.0	10.0	53	0.1	23	2.66	2.49	2.50	2.53	2.69
8	194.5	10.0	52	0.4	33	2.30	2.44	2.50	2.47	2.54
9	188.4	10.6	45	0.2	24	2.48	2.25	2.36	2.32	2.35
10	193.1	11.0	43	0.8	41	2.02	2.15	2.28	2.18	2.10
11	182.8	10.2	39	0.8	20	1.87	1.96	2.06	2.01	1.95
12	182.4	10.2	39	0.8	66	2.00	2.21	2.15	2.22	2.21
13	182.4	10.3	39	0.4	55	2.45	2.23	2.26	2.28	2.24
14	144.8	8.9	42	0.2	67	2.60	2.55	2.41	2.57	2.64
15	140.0	8.9	43	0.1	46	2.46	2.50	2.54	2.56	2.63
16	137.2	8.8	42	1.6	70	2.20	2.31	2.16	2.30	2.16
17	137.0	9.2	39	1.6	21	2.05	1.96	2.00	1.99	1.95
18	137.4	9.2	39	0.8	46	2.47	2.25	2.32	2.32	2.30
19	137.0	9.2	39	1.6	21	2.05	1.96	2.00	1.99	1.95
20	128.6	9.9	32	1.6	10	1.75	1.72	1.60	1.69	1.76

Table 2. Performance comparison for 4 algorithms

Method name	*Training time*	*Testing time*	Testing *RMS*E
ELM	0.0037	$<10^{-4}$	0.1426
LSSVM	0.4216	0.0304	0.1889
PLS	——	——	0.1919
GP	0.5012	$<10^{-4}$	0.2398

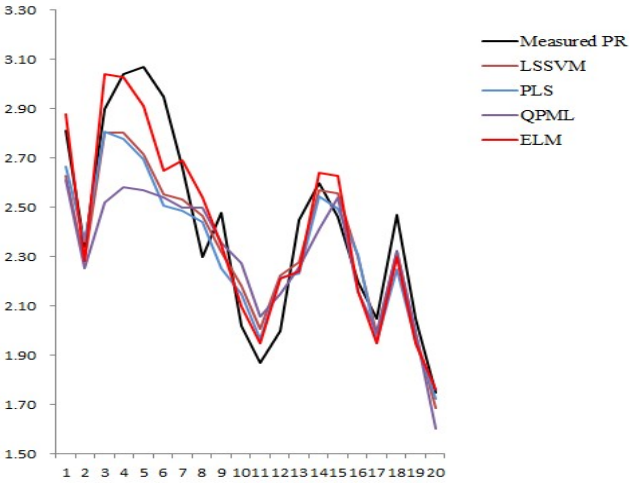

Fig. 4. PR Prediction with 4 methods

It can be seen from Table 2 that ELM learning algorithm spends 0.0037s CPU time training 133groups of data while GP takes 0.5012s. The ELM runs 135 times faster than GP algorithm. The training time of LSSVM is 0.4216s, 114 times longer than ELM. In addition, the testing time for the obtained LSSVM is 0.0304 which is less than 10^{-4}s of ELM, meaning that after training the ELM may response to new external unknown stimuli much faster than LSSVM in real deployment. The RMS of PLS almost equals to the RMS of LSSVM known from Table 2, that is well coincide with the result of Table 1 and Fig. 4. RMS of ELM is the smallest in proposed 4 algorithms, which means ELM model can provide the more precise prediction of TBM penetration rate.

What should be noticed is the data for training and testing are collected by the same TBM, and the experiment does not take the machine parameters into consideration. In practical, if different kinds of TBM are used in construction, the machine parameters should not be ignored. ELM model is still suitable, because the parameters can be regarded as input nodes of the algorithm.

4 Conclusions

This paper proposed a new model based on ELM algorithm to predict TBM performance. Compared with PLS, LSSVM, GP algorithms, ELM tends to provide better prediction performance at extremely fast learning speed, and over fitting is no more existed in the algorithm. However, the data in this experiment comes from the same TBM, this model cannot obtain the impact between PR and machine parameters. This may provide a direction for further research.

References

1. Hassanpour, J., Rostami, J., Zhao, J.: New Hard Rock TBM Performance Prediction Model for Project Planning. J. Tunnelling and Underground Space Technology 26, 595–603 (2011)
2. Ebrahim, F., Jamal, R., Chris, L.: Study of Various Models for Estimation of Penetration Rate of Hard Rock TBMs. J. Tunnelling and Underground Space Technology 30, 110–123 (2012)
3. Rostami, J., Ozdemir, L.: A New Model for Performance Prediction of Hard Rock TBM. In: Proceedings of Rapid Excavation and Tunnelling Conference, Society for Mining, Las Vegas, pp. 793–809 (1993)
4. Lislerud, A.: Hard Rock Tunnel Boring: Prognosis and Costs. J.: Tunnelling and Underground Space Technology 3, 9–17 (1988)
5. Ozdemir, L.: Development of Theoretical Equations for Predicting Tunnel Boreability. Colorado School of Mines, Golden (1997)
6. Rostami, J., Ozdemir, L.: Computer Modeling for Cutter Head Design and Layout of Mechanical Excavators. In: Proceedings of the Annual Technical Meeting of the Institute of Shaft Drilling Technology, Las Vegas, pp. 2–6 (1993)
7. Yagiz, S.: Development of Rock Fracture and Brittleness Indices to Quantify the Effects of Rock Mass Features and Toughness in The CSM Model Basic Penetration for Hard Rock Tunneling Machines. Colorado School of Mines, Golden (2002)
8. Barton, N.: TBM Performance Estimation in Rock Using QTBM. J. Tunnels and Tunneling International 31, 30–33 (1999)
9. Alvarez, G.M., Bruines, P.A., Verhoef, P.N.W.: Modeling Tunnel Boring Machine Performance by Neuro-Fuzzy Methods. J. Tunneling and Underground Space Technology 15, 259–269 (2000)
10. Okubo, S., Kfukui, K., Chen, W.: Expert System for Applicability of Tunnel Boring Machines in Japan. J. Rock Mechanics and Rock Engineering 36, 305–322 (2003)
11. Wen, S., Zhao, Y., Yang, S.Q.: Prediction on Penetration Rate of TBM Based on Monte Carlo-BP Neural Network. J. Rock and Soil Mechanics 30, 3127–3132 (2009)
12. Huang, G., Zhu, Q., Siew, C.: Extreme Learning Machine: A New Learning Scheme of Feedforward Neural Networks. In: Proceedings of International Joint Conference on Neural Networks (IJCNN 2004), vol. 2, pp. 985–990 (2004)
13. Huang, G., Zhu, Q., Siew, C.: Extreme Learning Machine: Theory and Applications. J. Neurocomputing 70, 489–501 (2006)
14. Huang, G., Wang, D.: Extreme Learning Machines: A Survey. J. Mach. Learn. & Cyber. 2, 107–122 (2011)
15. Saffet, Y.: Utilizing Rock Mass Properties for Predicting TBM Performance in Hard Rock Condition. J. Tunneling and Underground Space Technology 23, 326–339 (2008)

A Sensor for Large Strain Deformation Measurement with Automated Grid Method Based on Machine Vision

Yi Jin[1,⋆], Mingchi Feng[2], Tao Luo[2], and Chao Zhai[1]

[1] Experimental Center of Engineering and Material Sciences
[2] Department of Precision Machinery and Precision Instrumentation, University of Science and Technology of China, Hefei 230027, China

Abstract. The strain of the large deformation sample, such as rubber, can not be measured by the material testing machine because of the extensometer restriction for testing requirement. In order to solve this problem, a sensor for in-plane strain measurement of a large deformation sample based on machine vision was developed and verified for its application to rubber material characteristics testing. The system consists of a CMOS image sensor for image acquisition, a DaVinci DSP for image collection and processing, one S3C2440 chip for control function and improved automated grid method to achieve the desired efficiency and accuracy, which has been redesigned to be appropriate for embedded system. The calibration accuracy of this system is about 8 microns after decreasing distortion through camera calibration with the calibration board whose position precision is about 1.5 microns. The results of non-contact rubber tension test indicate that the system is reliable and stable,and the measurement range of strain exceeds 100%. This system has the potential in mechanical properties testing,industry measurement and other application areas.

Keywords: Automated Grid Method, Machine Vision, Large Strain Deformation, Real-Time.

1 Introduction

Strain is the important mechanical properties of the material,and it is often measured during a tension, compression or fatigue test. In normal strain measurement for different materials,two methods are often used. One is contacting strain method, including the strain gauge [1] and the fiber grating measurements [2][3], etc.. In this approach,the sensor is affixed to the sample and stretch with the sample deformation together. The strain information can be obtained from the variation of the resistance value or the modulation signal of external

⋆ Corresponding author, yjin@ustc.edu.cn. Funding Project: This work is supported by Equipment Function Development and Technology Innovation Project of The Chinese Academy of Sciences (CX2090000003).

J. Lee et al. (Eds.): ICIRA 2013, Part II, LNAI 8103, pp. 417–428, 2013.

physical parameters for the optical fiber wavelength. The method is simple in structure, easy to use and be suitable for hard materials. But large deformation measurements,such as the rubber tension test, can not be carried out. In order to overcome the shortcomings of the above method,another method is developed, that is non-contact measurement through the machine vision technique. The principle is digital image analysis through the correlation method [4][5][6] or automated grid method [7][8][9], and the strain can be calculated from the analysis results.

The rubber specimen strain should not be measured through the contact method, the range and accuracy is not enough, and the contact method will inevitably introduce some negative coupling effect. So non-contact method is applied to the mechanical performance test of some soft materia,instead of the traditional contact method. Compared to correlation method, automated grid method is more efficient and low-cost. In this method, grid matrix on the surface of the specimen during the process of the deformation is recorded through modern electronic image capture devices. The different grid images are automatically recognized and compared in order to obtain the specimen strain field.

In the current study, non-contact strain measurement is mostly achieved on PC-based platform, it is a way of relatively high cost, low integration and low intelligence degree. For in situ measurement and industrial application, embedded system, such as DSP and ARM, can be used to achieve highly integrated measurement system. In this paper, an embedded system is designed in detail, then the improved automated grid method is validated for strain measuring, at last, the application of an automated approach that combines the optimized automated grid method with embedded system to directly measure the large strain of rubber material is described.

2 The Sensor Structure

Non-contact strain measurement system is mainly composed of the CMOS image sensor, DaVinci digital signal processors TM320DM6437, ARM chip S3C2440 and some related external devices, including clock, power, CCDC interface, JTAG, etc.. In order to facilitate the control and display the results, the system configures a LCD touch screen. In addition, the system has a SD card and hard disk interface to storage and process images, the monitor is also equipped to display images.

The system is divided into three parts, data acquisition module, signal processing modules, and control software module. The data acquisition module, including CMOS image sensor, which is to realize data acquisition and delivery, collect digital images real time and then translate to the DSP. The signal processing module, containing a DSP processor, receives the data, processes the digital images to calculate the strain, then sends the result to the control software module. Control software modules, including ARM chip and a monitor, displays the measured strain after receive it in order to operate easily and detect real time.

CMOS image sensor is MT9V032, a 1/3 inch monochrome sensor. The power supply is 3.3V and the maximum power consumption is less than 320mW. The maximum resolution is 752 x 480 and in this resolution acquisition speed can reach 60fps. The control and transfer interface is I2C bus, 8-bit or 10-bit data can be transfered.

TMS320DM6437, which belongs to TI's DaVinci platform, is used to process the images.Its clock is up to 600MHz, and the peak processing capacity is up to 4800MIPS. The DM6437 video subsystem VPSS is mainly used, it consists of two parts: the front video processing for inputting digital data and the rear video processing for outputting digital data.

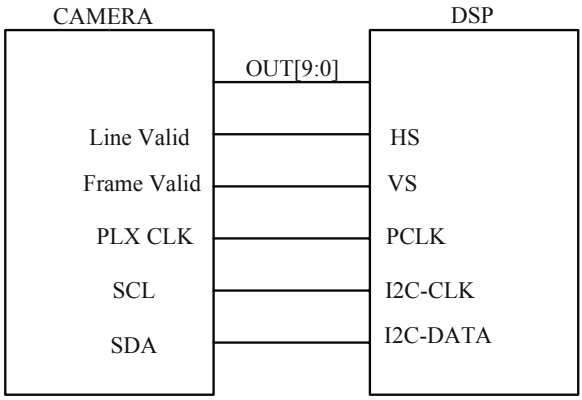

Fig. 1. The interface between DM6437 and CMOS image sensor

DM6437 digital video input interface provides data path and a synchronizing signal that is required for the input digital video stream. The interface contains a 16-bit video data bus and it can be directly connected to the CCD or CMOS image sensor. The DM6437 and CMOS image sensor connection diagram is shown as Fig. 1.

3 The Software Design

In this section,the software design of an embedded system is described in detail. It consists of driver development,DSP multi-processing and ARM programming. Through these designs the basic process structure can be established.

3.1 Driver Development

TI provides DSP/BIOS package for the development of DSP peripherals driver. The standard device driver model is defined and a series of API interface are provided. These API interface can be simply called for application development.

The peripheral driver model is divided into three categories: PIP/PIO model, SIO/DIO model and FVID/GIO model [10]. In our application FVID model is used, and it is an improved model specifically for video equipment from GIO model. *GIO_submit* function are packaged by the three specific function: *FVID_alloc* (allocated buffer), *FVID_exchange*(exchange buffer) and *FVID_free* (release buffer).

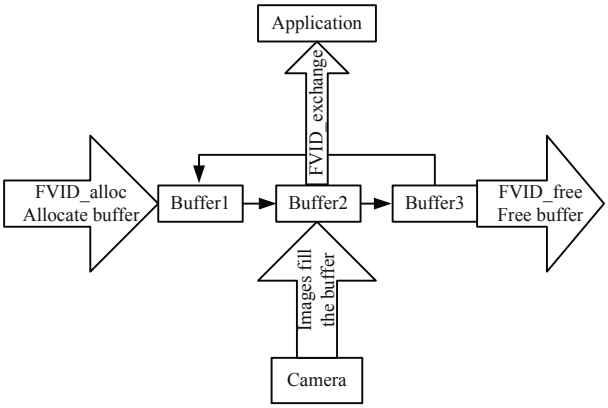

Fig. 2. Image acquisition flow

FVID_create first creates a CCDC video channel, mainly to create a device interface for the application and to complete the initialization of peripherals. *FVID_alloc* allocates image buffer for acquisition. In order to achieve high efficiency, in FVID model three buffers are assigned to each channel, they alternately exchange data with an external device, and each buffer corresponds to an image data capacity. The allocated buffer is set into the ready queue, so the image data will be populated to a ready buffer after peripherals finished collecting the data. *FVID_exchange* fills the ready buffer into the free queue, provides image data to the application, then return it to the ready queue after using. There are three buffers to be filled, so that the application can continuously capture images and the peripheral is in full use. After the end of the entire acquisition process, the allocated buffers are released and acquisition channels are deleted.

3.2 DSP Multi-processing

DSP function is divided into three relatively independent tasks in this system, namely image acquisition, image analysis and processing and the results transmission. DSP/BIOS kernel provides multitasking mechanism and multiple tasks run concurrently in the DSP/BIOS scheduler, according to the user's priority [11]. The various tasks can be set by users based on the priority.

The time for image acquisition is longest and it directly determines the system's efficiency, so this task has the highest priority, hardware interrupt (HWI). External image input is cyclical, so it is realized by the timer interrupt module (CLK). Images processing and results transmission are completed in the idle time. The priority of these two tasks are lower than the data acquisition task, so the task thread (TSK) is used. Improved Automated Grid Method described below is applied to process image data and results are stored in the storage area, The storage address of the data is returned to the ARM through the message queue.

3.3 ARM Programming

Wince5.0 operating system is used in ARM end and HPI interface driver is programmed according to DSP. The technique of interrupt driven mode and multithread are applied for data transfer and procedure controlling in this driver, including strain display and storage, measurement start and stop.

4 Algorithm Design for Strain Measurement

In this section,the algorithm for stain measurement is described in detail. firstly, Automated Grid Method is introduced, then algorithm improvement for high efficiency and accuracy is discussed.

4.1 Automated Grid Method

The first stage to achieve Automated Grid Method is to make good grids on the surface of a specimen, then installing the specimen on a material testing machine and shooting pictures continuously. After the equipment is running, the first digital image is set as the reference, the other images are compared to the reference, the grids positions on the specimen are calculated through Gray Gravity Method, then the strain can be obtained from the change of grids position between two images. The main process is divided into five sections, including the pretreatment, image segmentation, gravity center calculation,and node encoding.

Pretreatment. Original digital images from the CMOS camera will inevitably have porphyritic and punctate noise caused by irregular producing of specimens,the unevenness of the light source, the electronic hardware defects and other reasons, which will lead to uneven distribution of gray in the image. In order to avoid the impact of these noise pretreatment process is necessary before splitting the image to filter out these noise. In this system the median filter is preferred.

Image Segmentation. Image segmentation is to separate grids from the background in the image in order to process the follow-up calculation. A suitable threshold value is chosen. the gray value of the pixel less than the threshold is regarded as the background and is set to zero, the others maintain its original value as mesh nodes.

Gravity Center Calculation. In order to calculate the node distance and the distance change,the gravity center should be calculated. Make sure the area where the node is, then calculate the gravity center the nodes in this area with Gray Gravity Method. Set gravity center of one node as (m, n),then it can be calculated by the following formula.

$$m = \frac{\sum\sum xI\,(x, y)}{\sum\sum I\,(x, y)}\ . \tag{1}$$

$$n = \frac{\sum\sum yI\,(x, y)}{\sum\sum I\,(x, y)}\ . \tag{2}$$

Where (x, y) represents the pixel coordinates and $I(x, y)$ is the gray value of the pixel.

Node Encoding. Node encoding is to find the same node among different images,that is to say set a determined number for the same node in different images. After that calculating the displacement of the nodes' gravity center in the image, then a two-dimensional displacement can be obtained. In order to eliminate errors caused by the image random noise and improve accuracy, the image fitting method can be used.

4.2 Improved Automated Grids Method

Traditional Automated Grid Method is designed for complete computer architecture, it focused on user experience and multi-tasking rather than strict efficiency. Automated Grid Method can not meet the requirements of embedded system hardware and software structure, so the algorithm is improved and optimized for DSP system according to its efficiency and accuracy. To ensure accuracy, the first three steps can not be omitted, the main improvement is node encoding.

Node Region Segmentation Algorithm. The nodes on the grid image is regular and they are also regular during the stretching process because of the rectangular specimen. In order to draw the nodes location before encoding, the node area must be known before gravity center calculation. The system uses the following method to find all nodes computational domain.

Gray value of every pixel in one column should be summed for region search. In fig. 3 the abscissa represents the column number, and the ordinate is the gray value sum for one column. From the figure it can be seen that the node column

is at the peak position, similarly, the node row can also be obtained. The trough is the dividing line among nodes. When the row and column number around one node area are found out, the gravity center of this node can be calculated.

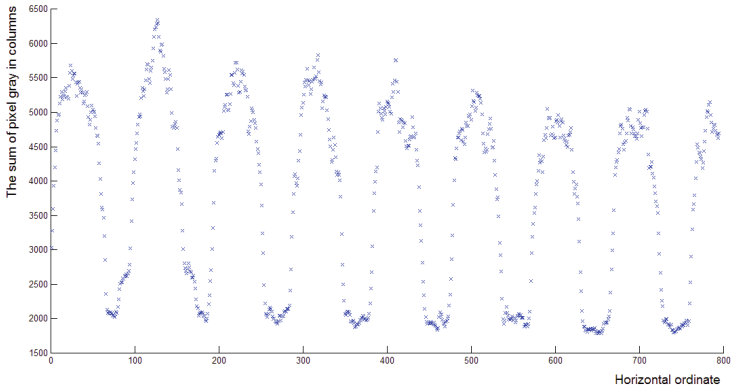

Fig. 3. vertical shadow casting

The nodes in the edge of the image sometimes is very small and not clear,or is not a complete circle due to the production reasons. These is no calculation value for these nodes, so the algorithm calculate from the second trough.

When the region of every node is obtained, the gravity center of every node can be calculated through Gray Gravity Method. Horizontal and vertical coordinates are stored in two arrays respectively.

Node Encoding Algorithm. The first image is set as the reference, and the nodes in two images must be encoding for matching in order to calculate the displacement of the same node during the stretching process because the nodes are moving. For matching easily, a mark node is selected which is in the center of grids and its diameter is bigger than others. So we can find out it from the position and the size quickly. Since the gravity center of the node are stored in order, as long as the mark point is matched successfully the other nodes can also be matched.

After node encoding,the strain can be calculated through the following formula:

$$E = \frac{\Delta L}{L} \ . \tag{3}$$

where E is the strain value, L is the image node distance and ΔL is its change value.

The whole algorithm flow is shown as Fig. 4.

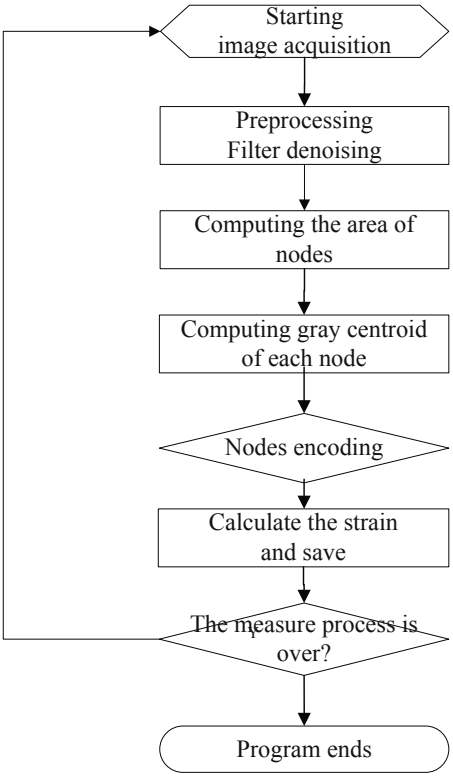

Fig. 4. software flow

5 Experiment Results

After this system is established, some experiments are made to test the algorithm practicality and the system performance. First, the whole system is calibrated with the calibration board to decrease the aberration effect. Then aluminum tensile test was done with vision measuring system and extensometer measuring to verify our system. At last, rubber tension results was described which indicates that this system is reliable and efficient.

5.1 The Calibration Process and Results

In general, an optical lens has the perspective distortion because of the lens inherent characteristics, it is also known as distortion. So it can only be improved but not eliminated. In our system it can reach several pixels in the edge of the image. To decrease the aberration effect of the CMOS chip an accurate

calibration board is necessary and its local sketch map is shown in Fig. 5. The distance between two adjoint points is 3±0.1%mm and the two directions are orthogonal. There are 784 points in all, they are illuminated by an area LED.

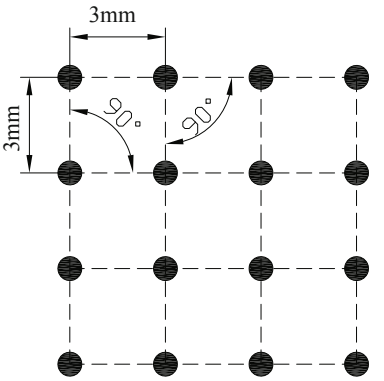

Fig. 5. vertical shadow casting

The radial distortion model is used to describe the aberration formation, as shown in the follow formula. From the Least Squares Method, $k = -1.9 \times 10^{-9}$.

$$\Delta x = (x_i - x_0)\left(k \times r^2\right) \ . \tag{4}$$

$$\Delta y = (y_i - y_0)\left(k \times r^2\right) \ . \tag{5}$$

where Δx and Δy are row residual error and column residual error respectively. x_i and y_i are row and column coordinates and x_0, y_0 are the projecting point. k is the aberration coefficient and r is the distance between points and the projecting point.

After aberration correction, the aberration affect is decreased greatly. The residual error is defined by the distance between actual coordinates and calculated ones. From Fig. 6 it can be seen that the residual error after correction is about 0.1pixel, that is about 8 microns.

5.2 Aluminum and Rubber Tension Results

In order to verify the reliability and accuracy of this system, aluminum tensile test was done with this system and extensometer measuring for small deformation respectively. Then the results from two systems can be analyzed comparatively. Fig. 7 is the stress-strain curve of the aluminum. From the figure it can be seen that there exits displacement response lag in the start position in extensometers measuring. While there is no such shortcoming in our system.

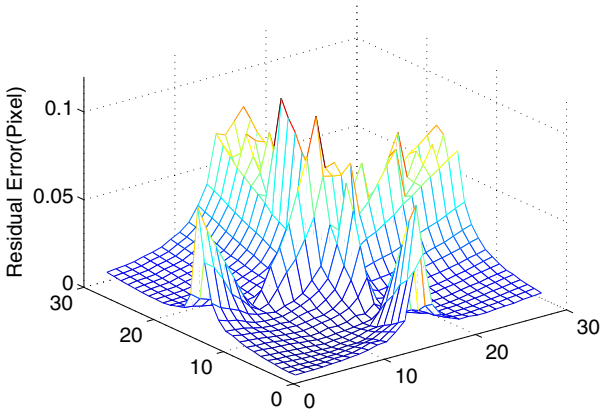

Fig. 6. Residual error after correcting aberration

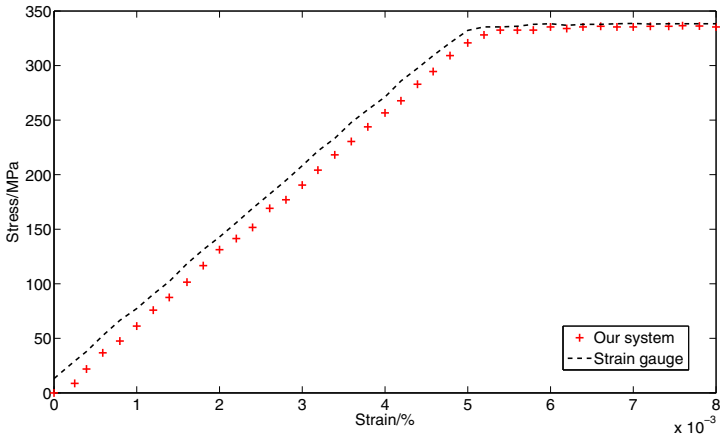

Fig. 7. stress-strain curve of AL

Fig. 8 is the stress-strain curve of the rubber specimen in the tensile test, it can be seen that the strain measuring range of this system is more than 100%. In the figure triangle points are measuring results by our system real time, while circle points are Matlab calculating results in computer after the test with the same original data. The two results agree well.

6 Conclusion

This paper proposed a real-time strain measurement sensor based on machine vision, the system uses image processing to measure the strain of the specimen.

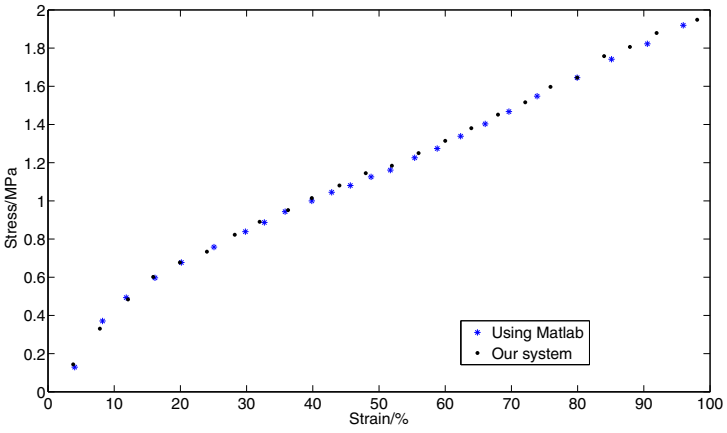

Fig. 8. stress-strain curve of rubber

The hardware design and the improvement on algorithm is described in detail. Besides,the whole system is calibrated with the calibration board to eliminate distortion which is important for high accuracy. The experiment results for rubber tension show that this equipment is intelligent, low-cost, real-time and high accuracy. The processing speed is up to 20 frames per second, and the strain measurement range is more than 100%.

This sensor is a compact one due to the application of CMOS chip and DSP processing, so it may have the potential in mechanical properties testing or industry measurement, in which the restricted size is required. In the real measurement, two points should be focused on:1. The accuracy depends greatly on grids in the specimen surface, so grids production is the key step for the measurement;2. The optical axis of the CMOS chip and the lens should be perpendicular to the specimen, otherwise the systematic error will be got.

References

1. Poussier, S., Rabah, H., Weber, S.: Smart adaptable strain gage conditioner: hardware/software implementation. IEEE Sensors Journal 2(4), 262–267 (2004)
2. Ball, G.A., Morey, W.W., Cheo, P.K.: Single and Multipoint Fiber-Laser Sensors. IEEE Photonics Technology Letters 5(2), 267–270 (1993)
3. Cranch, G.A., Flockhart, G., Kirkendall, C.K.: Distributed Feedback Fiber Laser Strain Sensors. Sensors Journal 8(7), 1161–1172 (2008)
4. Shi, X., Pang, H.L.J., Zhang, X.R., et al.: In-situ micro-digital image speckle correlation technique for characterization of materials' properties and verification of numerical models. Components and Packaging Technologies 27(4), 659–667 (2004)
5. Wang, C.C.-B., Deng, J.-M., Ateshian, G.A., Hung, C.T.: An Automated Approach for Direct Measurement of Two-Dimensional Strain Distributions Within Articular Cartilage Under Unconfined Compression. Journal of Biomechanical Engineering 124, 557–567 (2002)

6. Pan, B., Qian, K., Xie, H., Asundi, A.: Two-dimensional digital image correlation for in-plane displacement and strain measurement: a review. Meas. Sci. Technol. 20, 1–17 (2007)
7. Sirkis, J.S., Lim, J.T.: Displacement and Strain Measurem- ent with Automated Grid Method. Exp. Mech. 12, 382–388 (1991)
8. Goldrein, H.T., Palmer, S.J.P., Huntley, J.M.: Automated Fine Grid Technique for Measurement of Large-Strain Deformation Maps. Opfics and Lasers in Engineering 23, 305–318 (1995)
9. Xia, Y., Li, W., Xia, C.G., Xia, Y.M.: Application of Automated Grid Method in the Mechanical Behavior Testing of Tire Rubber. Journal of Experimental Mechanics 17(4), 412–418 (2002)
10. Texas Instruments. TMS320 DSP/BIOS v5.41 Users Guide (2009)
11. Yi, F., Xu, X.: Using DSP/BIOS in Data Acquisition Application Design[J]. Chinese Journal of Scientific Instrument 23(z2), 569–570 (2002)

A 6-Axis Sensor for Minimally Invasive Robotic Surgery

Jun Jiang[1], Le Xie[1,2,*], and Hailong Yu[1]

[1] National Digital Manufacturing Technology Center,
Shanghai Jiao Tong Univ., Shanghai, China
[2] Institute of Rehabilitation Engineering, Shanghai Jiao Tong Univ, Shanghai, China
0086-02162932119
lexie@sjtu.edu.cn

Abstract. In minimally invasive robotic surgery (MIRS), the force/torque which exists between instruments and organs can't be sensed by surgeon. The research present can't offer perfect solution for the disadvantage of minimally invasive robotic surgery. This paper presents development of a 6-Axis sensor based on double-hole parallel crossing beam, which can be integrated in instruments of MIRS. The size of sensor is 9.8(diameter)$\times$ 6(height)mm .The sensor can measure the force/torque set on the instrument and can be used in the area of the force feedback in teleportation surgery robot.

Keywords: minimally invasive robotic surgery, teleportation, 6-Axis sensor, force/torque, force feedback.

1 Introduction

Minimally invasive surgery (MIS) has caused a revolution in surgery since 1980s. Minimally Invasive Surgery (MIS) technology reduces trauma to alleviate the suffering of the patient, reduces scars, and helps to shorten the length of stay. Since 1980s, robotics has been introduced into surgery. The most successful surgery commercial robot is Da Vinci from Intuitive Surgical Inc. The robotic surgery features operation flexibility, stability, precision and so on. But the force/torque which exists between instruments and organs can't be sensed by surgeon. To solve the problem, there are generally three solutions.

Firstly, the strain gages are pasted on the instruments. The method is relatively simple. When the strain gages get outer force, the electric current of the strain gages is changed with the resistance quantity of strain gages changing. Therefore, the outer force can be measured by the method of measuring the electric current changing. The examples are surgery robot of UC Berkeley [1], surgery robot of UW [2], surgery robot of Iwate University [3], surgery robot of Tokyo University [4], surgery robot of M. Tavakoli[5] and so on. However, the instrument is not designed according to obtaining highest sensitivity strain region, the method is not available for application in force feedback for minimally invasive robotic surgery (MIRS).

* Corresponding author.

J. Lee et al. (Eds.): ICIRA 2013, Part II, LNAI 8103, pp. 429–435, 2013.

The second solution is to measure the driving force related quantity of the actuator of the device. When the force/torque exerted by the actuator change, the physical quantity will change, thus, the feedback force is obtained by the method of measuring changed quantity. The examples include the research of Tadano [6]. However, the method is also not suitable for MIRS because of its low precision.

In the third approach, the force / torque sensor is integrated in the instrument. The sensor can measure the force/ torque exerting on the instrument. Concordia University [7] manufactured a sensor which based on piezoelectric material, but the sensor only measure the force which set on the gripper, and is lack of the other force/torque set on the instrument. The other examples include the research of J. Peirs[8], the slave robot of Stanford University[9], the robot of Harvard University[10], the research of R. Brydges[11], the research of P. Puangmali[12] ,the sensor system of Hoseok Song[13] and so on. However, the size of the sensors is too large to apply in minimally invasive robotic surgery (MIRS). DLR manufactured a slave surgical robot which includes a 6-Axis sensor [14-15] based on the structure of Stewart. The sensor shown in Fig 1 is set between the gripper and the joint and can measure the force /torque set on the instrument directly. The diameter of the sensor is about 10mm.The research is still forward and has been not commercialized. It is convenient for the design to avoid the influence of the outer friction and realize precise measurement. The method is suitable for MIRS, but the structure is complex, and difficult for manufacturing.

This paper presents a 6-Axis sensor based on double-hole parallel crossing beam, which can be integrated in instruments of MIRS.

Fig. 1. DLR's sensor [14-15]

2 Structure of the 6-Axis Sensor

The 6-Axis force/torque sensor shown in Fig 2 is designed out. The sensor owns top lid (1), baffle (2), cross beam 1(3), cross beam 2(4), strain gages region (5).

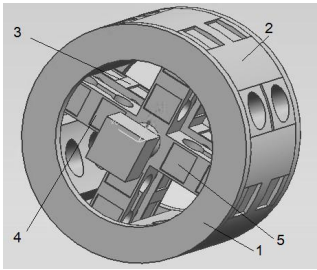

a

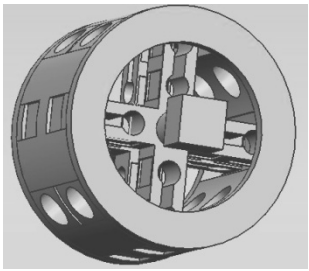

b

Fig. 2. 6-Axis force/torque sensor

Take the cross beam1 for example, which is shown in Fig 3. When the force F is applied on the centre of the cross beam, the strain of A, B, C and D is as follows,

$$\varepsilon_A = \frac{F\mathrm{b}}{2EW} \qquad \varepsilon_B = -\frac{F(\mathrm{b}+\mathrm{c})}{2EW}$$

$$\varepsilon_C = -\frac{F\mathrm{b}}{2EW} \qquad \varepsilon_D = \frac{F(\mathrm{b}+\mathrm{c})}{2EW}$$

The aluminum alloy LY12, whose $E = 72GPa$, is chosen to manufacture elastomer.

The size of the sensor is 9.8(diameter)× 6(height) mm ,

$$a = 9.6mm \text{ ,} b = 1.21mm \text{ ,} c = 2.2mm .$$

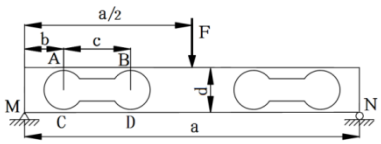

Fig. 3. Cross beam1

The FEA of the elastomer is shown in Fig 4.

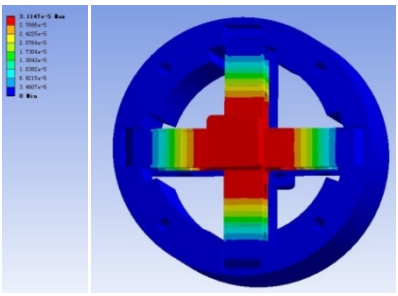

Fig. 4. FEA of the elastomer

According to FEA, the highest sensitivity strain region is on the tin wall of the beam, so the gage should be pasted on the thin wall symmetrically. KFRS-02-120-C1-13 L1M2R of KYOWA is chosen as strain gages which are pasted on the strain region.

In order to avoid the influence of the outer friction and realize precise measurement of the force/torque, the sensor is set between the gripper and the joint, shown as in Fig 5.

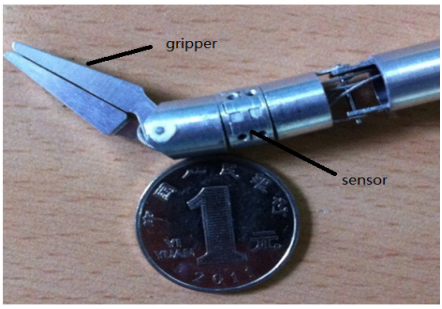

Fig. 5. End instrument

3 Analysis of the Sensor

The calibrations are conducted, the result is shown in Fig 6~Fig 9. It is unnecessary to get F_x and F_y in developed end instrument, because the force should be set on the gripper. The sensor was loaded at 1N increments to 10N in Z-direction. And the loaded torque is 5mNm increments to 50mNm in Z-direction, 15mNm increments to 150mNm in X-direction and Y-direction. The experiments prove the liner relation in all above directions.

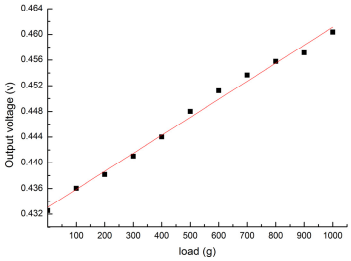

Fig. 6. Experiment result of F_z

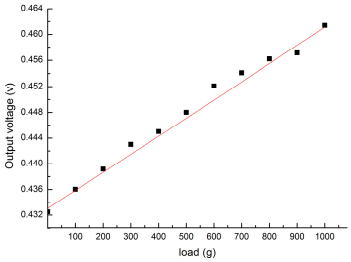

Fig. 7. Experiment result of M_z

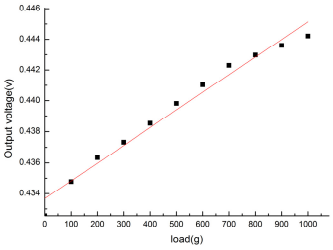

Fig. 8. Experiment result of M_x

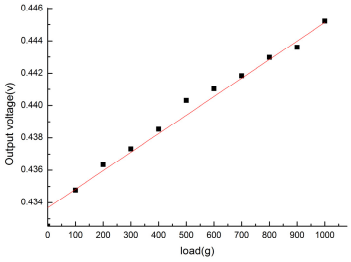

Fig. 9. Experiment result of M_y

4 Conclusion

Minimally invasive robotic surgery (MIRS) offers high precision and stability in the application of MIS. The lack of force feedback makes many operators not feel convenient to operate the surgery robot. It is necessary to design and manufacture micro size sensor to obtain the force/torque set on the instrument. The double-hole parallel cross beam sensor described above features simple geometry structure, thus it is easy for manufacture the sensor structure. Meanwhile, the structure of the sensor ensures the sensitivity. The outer force/ torque which make influence on force feedback can be avoided because of the position of sensor set. The experiments prove the linear relation of the force/ torque in X-direction, Y-direction and Z-direction. The preliminary work indicates that the sensor can meet the expectations.

Acknowledgement. The work described in this paper was supported by Key projects from the national science & technology pillar program of China (2009BAI71B06), the project of major program of national nature science foundation of china(61190124, 61190120), national nature science foundation of China (60873131), the project from national high technology research and development program of China (2006AA01Z310, 2009AA01Z313).

References

1. Cavusoglu, M.C., Cohn, M., Tendick, F., Sastry, S.: A Laparoscopic Telesurgical Workstation. IEEE Transactions on Robotics and Automation 15, 728–739 (1999)
2. Rosen, J., Hannaford, B., MacFarlane, M.P., Sinanan, M.N.: Force Controlled and Teleoperated Endoscopic Grasper for Minimally Invasive Surgery - Experimental Performance Evaluation. IEEE Transactions on Biomedical Engineering 46, 1212–1221 (1999)
3. Shimachi, S., Fujiwara, Y., Hakozaki, Y.: New Sensing Method of Force Acting on Instrument for Laparoscopic Robot Surgery. In: Computer Assisted Radiology and Surgery, Chicago, USA, pp. 775–780 (2004)
4. Takahashi, H., Warisawa, S., Mitsuishi, M., Arata, J., Hashizume, M.: Development of High Dexterity Minimally Invasive Surgical System with Augmented Force Feedback Capability. In: IEEE / RAS-EMBS International Conference on Biomedical Robotics and Biomechatronics (BIOROB), Pisa, Italy, pp. 284–289 (2006)
5. Tavakoli, M., Patel, R.V., Moallem, M.: Robotic Suturing Forces in the Presence of Haptic Feedback and Sensory Substitution. In: IEEE Conference on Control Applications, Toronto, Canada, pp. 1–6 (2006)
6. Tadano, K., Kawashima, K.: Development of 4-DOFs forceps with force sensing using pneumatic servo system. In: Proc. IEEE Int. Conf. Robot. Autom., pp. 2250–2255 (2006)
7. Sokhanvar, S., Packirisamy, M., Dargahi, J.: A Multifunctional PVDF-Based Tactile Sensor for Minimally Invasive Surgery. Smart Materials and Structures 16, 989–998 (2007)
8. Peirs, J., Clijnen, J., Reynaerts, D., van Brussel, H., Herijgers, P., Corteville, B., Boone, S.: A micro optical force sensor for force feedback during minimally invasive robotic surgery. Sens. Actuators A 115, 447–455 (2004)

9. Ottensmeyer, M.P., Salisbury Jr., J.K.: *in vivo* data acquisition instrument for solid organ mechanical property measurement. In: Niessen, W.J., Viergever, M.A. (eds.) MICCAI 2001. LNCS, vol. 2208, pp. 975–982. Springer, Heidelberg (2001)
10. Wagner, C.R., Stylopoulos, N., Howe, R.D.: The Role of Force Feedback in Surgery: Analysis of Blunt Dissection. In: Symposium on Haptic Interfaces for Virtual Environment and Teleoperator Systems (HAPTICS), Orlando, FL, USA, pp. 68–74 (2002)
11. Brydges, R., Carnahan, H., Dubrowski, A.: Surface Exploration Using Laparoscopic Surgical Instruments: The Perception of Surface Roughness. Ergonomics 48, 874–894 (2005)
12. Puangmali, P., Liu, H., Althoefer, K., Seneviratne, L.D.: Optical Fiber Sensor for Soft Tissue Investigation during Minimally Invasive Surgery. In: IEEE International Conference on Robotics and Automation (ICRA), Pasadena, CA, USA, pp. 2934–2939 (2008)
13. Song, H., Kim, H., Jeong, J., Lee, J.: Development of FBG sensor system for Force-feedback in Minimally Invasive Robotic Surgery. In: 5th International Conference on Sensing Technology, pp. 16–20 (2011)
14. Seibold, U., Kuebler, B., Hirzinger, G.: Prototype of Instrument for Minimally InvasiveSurgery with 6-Axis Force Sensing Capability. In: Proc. IEEE Int. Conf. Roboti. Autom., pp. 496–501 (2005)
15. Kuebler, B., Seibold, U., Hirzinger, G.: Development of actuated and sensor integrated forceps for minimally invasive robotic surgery. Int. J. Medical Robot. Computer Assisted Surgery 1, 96–107 (2005)

Mechanical Safety of Automatic Door by Using PFVA Based on 2-Stage Star Compound Gear

Min-Kyu Park[1] and Delbert Tesar[2]

[1] School of Mechanical and Automotive Engineering Technology,
Yeungnam College of Science and Technology, Daegu, Korea
mk_park@ync.ac.kr
[2] Robotics Research Group, School of Mechanical Engineering,
University of Texas at Austin, Austin, TX 78758, United State
tesar@mail.utexas.edu

Abstract. In this study, a new mechanism is proposed by using Parallel Force/ Velocity Actuator (PFVA) based on 2-stage star compound gear train. PFVA has two distinct actuators. One is force actuator (FA) with a low reduction gear train, the other is velocity actuator (VA) with a high reduction gear train. The combination of two independent and parallel inputs provides a mixing of control parameters such as position, velocity, and force in any kinds of combination. It means to enhance the dynamic range of the combination actuator. This study is carried out more focus on investigating mechanical safety characteristics of the proposed PFVA with 2-stage star compound gear. Mechanical safety can be achieved by limiting the torque on the FA and thus making it a backdriveable input. We present a numerical simulation to show that the proposed PFVA system can be mechanically safe under collision due to the back-driveability of the FA.

Keywords: Parallel Force/ Velocity Actuator, 2-stage star compound gear train, Force actuator, Velocity actuator, Mechanical safety, Back-driveability.

1 Introduction

There are increasing demands from industries to provide for both force and motion control in many applications (in a fixturing device, in cutting thin stock, in force-fit assembly, and so on). All these cases require independent pathways for distinct actuator properties that can be transformed at the system level to create greater flexibility for process control at the output. A Dual-Input-Single-Output (DISO) actuator is proposed here as a solution to the problem of achieving position control together with low stiffness and power assisting capability. DISO actuators have been studied in manipulation for implementing a dexterous task [1], [2]. PFVA which is one of DISO actuator combines a high reduction actuator, called a Velocity Actuator (VA), and Force Actuator (FA) using a planetary gear train [3], [4]. The high reduction VA input makes it a good candidate for velocity control. On the other hand, the low reduction FA input is suitable to manage a reference force [4].

It is dangerous to apply a high stiffness actuator to the velocity controlled automatic door which may require human intervention. In many cases, various sensors and observer

J. Lee et al. (Eds.): ICIRA 2013, Part II, LNAI 8103, pp. 436–441, 2013.

techniques are applied to the system for detecting and avoiding a human or an obstacle for safety. However, the ultimately best way is to design actuator system can be mechanically safe under collision.

This study proposes a PFVA actuator based on 2-stage star compound gear train and we address more focus on mechanical safety aspect of the actuator. To that end, we first briefly explained a PFVA structure and formulated a kinematic and a dynamic model for a door system driven by a PFVA. Numerical simulation using this model was then conducted in MATLAB/Simulink to evaluate the mechanical safety of a proposed PFVA system. We conclude with a summary of result and discussion.

2 Kinematics and Dynamics of Automatic Door with PFVA Based on 2-Stage Star Compound Gear

We will describe the kinematics and dynamics of an automatic door with PFVA as its actuator input. A graphical layout of the PFVA is shown in Fig. 1. The FA and VA are connected at ring gear (R) and sun gear (S), respectively. The output shaft is fixed at carrier (C) and it operates the door by a rack and pinion mechanism. We would like to design a PFVA with FA being a low gear ratio pathway to the output and VA being a high gear ratio pathway to the output.

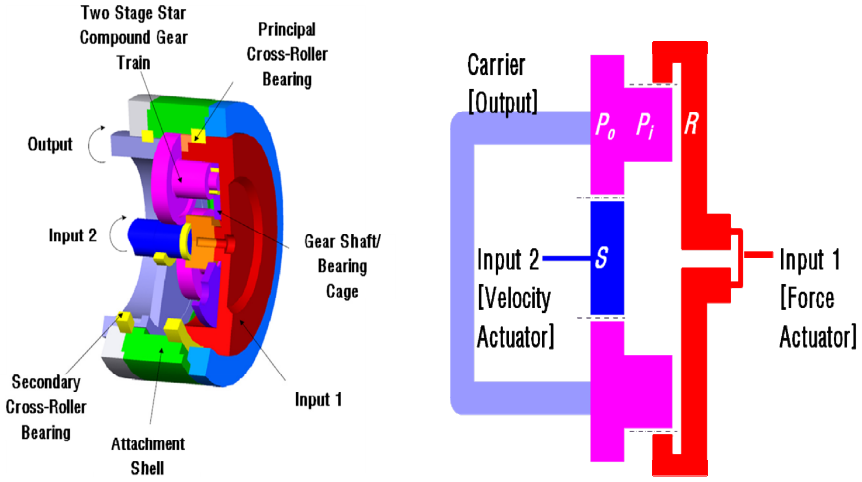

Fig. 1. Design and schematic diagram of PFVA based on 2-stage star compound gear train

It has two kinematic and two geometric constraints on the three connected axes (i.e., Sun, Ring, and Carrier) and planets as shown in Eq. 1.

$$r_C\omega_C = r_S\omega_S + r_{Po}\omega_{Po},\quad r_C = r_S + r_{Po},\ r_R\omega_R = r_C\omega_C + r_{Pi}\omega_{Pi},\ r_R = r_C + r_{Pi}, \tag{1}$$

where r_C, r_S, r_R, r_{Po} and r_{Pi} are radii of the carrier, sun, ring and two planetary gears,

respectively. $\omega_C, \omega_S, \omega_R, \omega_{Po}$ and ω_{Pi} are corresponding angular velocities. Gear ratios g_1 and g_2 are defined as

$$g_1 = r_{Po} / r_S, \; g_2 = r_R / r_{Pi} \tag{2}$$

A relation between angular velocities can be derived as in Eq. 3 by using Eq. 1 and Eq. 2.

$$(1 + g_1 g_2)\omega_C = \omega_S + g_1 g_2 \omega_R \tag{3}$$

If $\omega_C = \dot{\phi}_o$, $\omega_R = \dot{\phi}_f$, $\omega_S = \dot{\phi}_v$, $g_v = 1/(1+g_1 g_2)$, and $g_f = g_1 g_2 /(1+g_1 g_2)$, the equation of angular velocities can be rewritten as

$$\dot{\phi}_o = [G_a^o]\dot{\boldsymbol{\phi}} \tag{4}$$

where $[G_a^o] = \begin{bmatrix} g_v & g_f \end{bmatrix}$ and $\dot{\boldsymbol{\phi}} = \begin{bmatrix} \dot{\phi}_v & \dot{\phi}_f \end{bmatrix}^T$. In case of zero initial conditions, we also get the linear equation of angles as $\phi_o = [G_a^o]\boldsymbol{\phi}$.

Choosing numbers such as $r_S = r_{Pi} = 0.5$ and $r_{Po} = 1.15$ gives output ratios $g_v = 0.0918$ and $g_f = 0.9082$. In case of a single-stage star compound gear (i.e., $r_{Po} = r_{Pi} = 1.15$), the output ratios are calculated as $g_v = 0.1515$ and $g_f = 0.8485$. It means that 2-stage star compound gear can be designed as bigger gear ratio than single-stage star compound gear under same size of gear train.

Automatic door mechanism is composed of a PFVA, a modified checker, and rack and pinion gear [5]. First, a PFVA generates a driving torque, and then transfer to linear driving force (F) by using rack and pinion gear. A door can be opened or closed by the linear driving force. Fig. 2 shows a geometric definition which is referred to SAE conventional of coordinates and rotation angles [5]. The motion of vehicle' door is defined in a body fixed coordinate system (xyz) which is determined by roll (φ_x) and pitch (φ_y) motion of the vehicle. Gravity and position vectors of an automatic door with a PFVA are shown in Fig. 3.

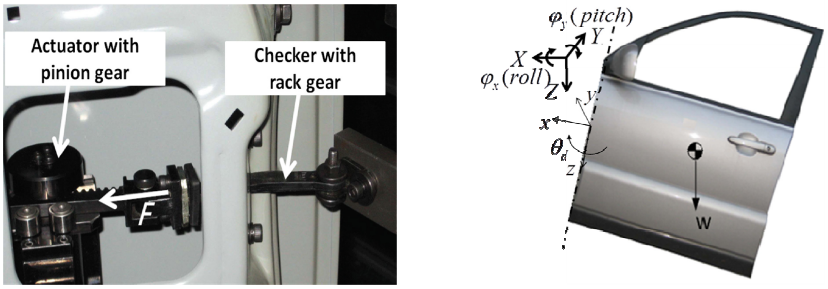

Fig. 2. Driving mechanism and Coordinates of automatic door driven by PFVA

In the previous study, the velocity relationship between PFVA's output and door was expressed as [5]

$$\dot{\theta}_d = r_p \frac{\sqrt{l_1^2 + l_2^2 - 2l_2(\varepsilon_x \cos\theta_d - \varepsilon_y \sin\theta_d)}}{l_2(\varepsilon_x \sin\theta_d + \varepsilon_y \cos\theta_d)} \phi_o \tag{5}$$

where r_p is radius of pinion gear.

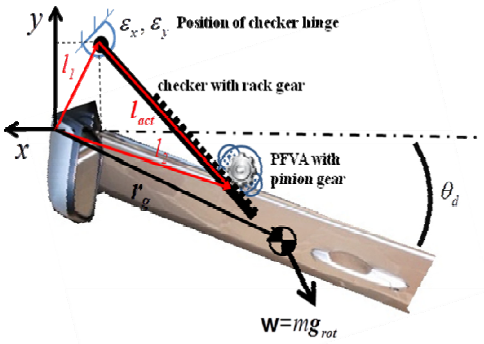

Fig. 3. Gravity and position vectors of automatic door driven by PFVA [5]

Considering control torques ($\tau_k = \begin{bmatrix} \tau_v & \tau_f \end{bmatrix}^T$) from the two actuators of the PFVA, the generalized dynamic equations was derived as [5]

$$\Gamma_k^I + \Gamma_k^G + \Gamma_k^S = \tau_k, \qquad k \in \{v \ f\} \tag{6}$$

where Γ_k^I, Γ_k^G, and Γ_k^S are inertial and centrifugal torque, gravity torque, and door stopper torque, respectively. For more details regarding the kinematics and dynamics of an automatic swing door, see Ref. [5]. For verifying the kinematics and dynamics

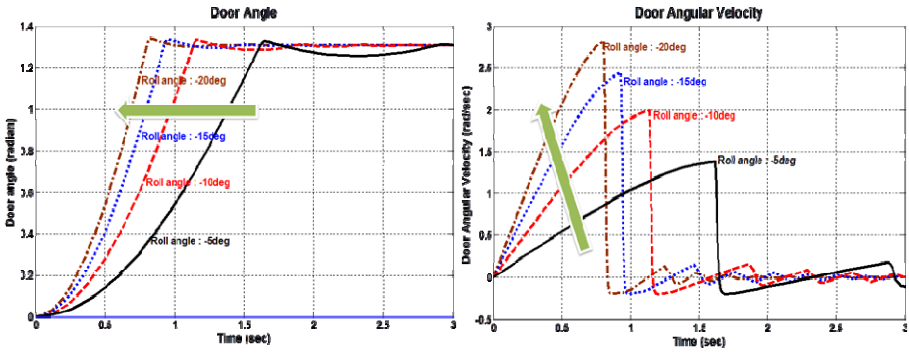

Fig. 4. Angle and angular velocity responses of vehicle door according to increasing a roll angle

of the system, numerical simulations are conducted. Fig. 4 shows the angle and angular velocity of door under no external and control inputs and increasing only roll angle of vehicle. Door opens faster as increasing a roll angle as shown in Fig. 4.

3 Simulation

In this section, we simulate the dynamic response of the proposed PFVA system to a collision scenario. In the general case, a collision is very dangerous for the velocity controlled door system. It could be unsafe and could cause severe damage. Therefore, it is necessary for an immediate response after impact in automatic operation. In previous study, the velocity controlled automatic door system was developed [5]. System parameters are listed in Table 1.

Table 1. System parameters of door with PFVA

Symbol	Quantity and description	Value(s)
g_v, g_f	Gear reduction ratio of velocity and force side	0.092, 0.908
φ_x, φ_y	Roll and pitch angle of vehicle [deg]	-20, 0
$\varepsilon_x, \varepsilon_y$	Installation coordinates of checker [m]	-0.05, 0.065
l_2, r_g	Length between origin to PFVA and COG [m]	0.4, 0.6
m, J_d	Mass and inertia of door [kg] [$kg \cdot m^2$]	40, 4.04
r_p	Radius of pinion gear [m]	0.01
J_{PFVA}	Inertia matrix of PFVA [$kg \cdot m^2$]	$\begin{bmatrix} 0.008 & 0.001 \\ 0.001 & 0.002 \end{bmatrix}$

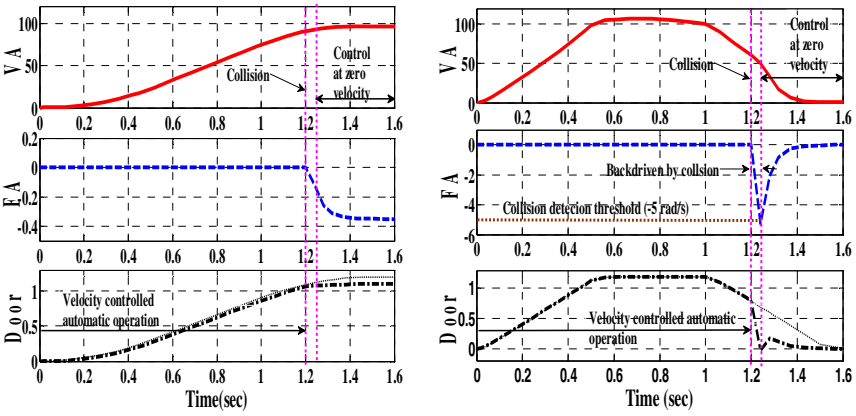

Fig. 5. Position and velocity responses of VA, FA, and Door to collision

Fig. 5 shows the dynamic response of a collision during velocity controlled automatic operation. The collision occurs at 1.2s during automatic operation. The contact force with the obstacle is 200N, FA is back-driven and the door moves backward because it is designed as near direct-drive. When the back-driving speed of the FA exceeds 5rad/s, the collision is detected and FA and VA is controlled as zero velocity command for stopping the door. The back-driveability of FA is big advantage in a human interaction application. This means that the proposed PFVA system inherently provides mechanical safety.

4 Conclusion

In this research, PFVA based on 2-stage star compound gear train has been proposed. PFVA composed of two distinct inputs: VA has a high gear ratio path for velocity control and FA has a low gear ratio path for compensating a torque or force. The PFVA has a wide spectrum of dynamic response as incorporating two distinct inputs. The main contributions of this paper are :

- The kinematics of the PFVA with 2-stage star compound gear train was derived.
- 2-stage star compound gear can be designed as bigger (≈ 1.6) gear ratio than single-stage star compound gear under same size of gear train
- In the automatic operation of door, the previous study showed that the VA was effective in tracking a velocity trajectory while the FA was able to compensate the gravity torque and the inertial coupling torque coming from the VA at the same time. In this study, we dealt with the safety issue in the velocity controlled door system. The results of simulation showed that the proposed PFVA system inherently provides mechanical safety.

Acknowledgments. We would like to thank Dr. Dinesh Rabindran for his valuable advices and sharing knowledge and experience on PFVA with us.

References

1. Lee, H.Y., Choi, Y.J.: A New Actuator System Using Dual-Motors and a Planetary Gear. IEEE/ASME Transactions on Mechatronics 17(1), 192–197 (2012)
2. Kim, B.S., Song, J.B., Park, J.J.: A serial-type dual actuator unit with planetary gear train: Basic design and applications. IEEE/ASME Transactions on Mechatronics 15(1), 108–116 (2010)
3. Rabindran, D., Tesar, D.: Parametric Design and Power-Flow Analysis of Parallel Force/Velocity Actuators. Journal of Mechanisms and Robotics 1(1), 1–10 (2009)
4. Rabindran, D.: A Differential-Based Parallel Force/Velocity Concept: Theory and Experiments. Ph.D. Dissertation, The University of Texas at Austin (2009)
5. Park, M.-K., Rabindran, D., Tesar, D., Lee, B., Sung, K.-G.: Automatic Swing Door For A Passenger Car By Using Parallel Force/Velocity Actuator (PFVA). Applied Mechanics and Materials 278-280, 641–646 (2013)

Development of Smart Actuator and Its Application

Seok-Jo Go[1], Min- Kyu Park[2], and Young-Jin Lee[3]

[1] Division of Mechanical Engineering, Dongeui Institute of Technology, Busan, 614-715, Korea
sjgo@dit.ac.kr
[2] School of Mechanical and Automotive Engineering Technology, Yeungnam College of Science and Technology, Daegu, Korea
mk_park@ync.ac.kr
[3] Autopower Co. Ltd, Obang-dong, Kimhae, Kyungnam 629-916, Korea
ceo@autopower.co.kr

Abstract. This study is dealing with an industrial robot with smart actuators for applying an industrial manufacturing process. A smart actuator is defined as the integrated actuator of all components such as motor, controller, sensors, and communication unit. The robot which is linked to a smart actuator can be assembled or disassembled and reconfigured. Therefore, there are increasing demands from industries for a smart actuator. We develop a smart actuator and an industrial robot with the developed smart actuator. We also introduce a robot control simulator for operating and monitoring the robot. Finally, trajectory tracking control is performed in experiment for evaluating a performance.

Keywords: Smart Actuator, Industrial Manufacturing Process, Integrated Actuator, Robot Control Simulator.

1 Introduction

Recently, a robotic system has been needed in various fields. However, the role of a robot is different according to a task. And, it is needed a lot of time to develop a robot. Therefore, there are increasing demands from industries for a smart actuator for easily developing a robot. A smart actuator is composed of a motor, gears, amplifier, servo controller, and communication module. It can be operated to plug-in and assemble. The robot which is linked to a smart actuator is also easily able to assemble/disassemble and reconfigure it. Due to these advantages, the studies on a smart actuator are very much on-going and have been reported [1-3]. In the previous studies, we developed the hollow shaft servo assembly and the dual arm robot with the servo assembly [4]. And a human-robot cooperative robot with smart actuator was presented [5].

The goal of this study is to develop an industrial robot with a smart actuator for applying an industrial manufacturing process. Firstly, a smart actuator for applying to the robot is described. Secondly, the monitoring software of the robot is developed. Finally, the 7-axis industrial robot with smart actuators is developed and the performance of trajectory control is evaluated.

J. Lee et al. (Eds.): ICIRA 2013, Part II, LNAI 8103, pp. 442–449, 2013.

2 Development of Smart Actuator

A smart actuator consists of a servo motor, a motor drive, gears, a brake, an encoder, a servo controller and a communication board as shown in Fig. 1 [1]. The specifications of the smart actuator are shown in Table 1. Fig. 2 shows manufacturing processes of servo motor assembly.

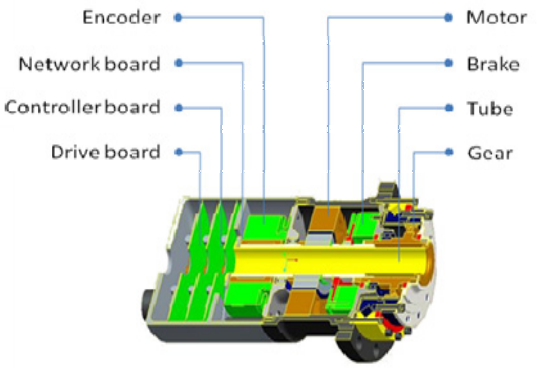

Fig. 1. Configuration of a smart actuator

Table 1. Specifications of the developed smart actuator

Item	Specification
Component	Motor/Drive/Brake/Encoder
Power of Motor(W)	200/400/750
Input Voltage (V)	DC 300V
Rated torque (Nm)	0.64 (200W) / 1.27 (400W) / 2.38 (750W)
CPU of controller	Drive : TMS320F2811 Slave : TMS320F2808
Sensors	Encoder : 17bit (Tamagawa) Current sensor : ACS712 Voltage sensor : HCPL788J Temperature sensor : ASM121
Communication	EtherCAT(Master - Slave) SPI (Slave - Drive)
Brake	DC24V (Autopower Co.)
Gear	Harmonic Drive

Material of The cores of stator and rotor is the Si-steel S18 and S30 respectively. And material of magnets is Nd-Fe-B and N-35SH. After assembling all sub components, encoder and brake are mounted at a servo motor. The controller generates PWM (pulse width modulation) signals. The signals are sent to the IPM (intelligent power module) for driving the smart actuator. Position/Velocity/Torque control functions are implemented by using PID control in the controller. The controller has two different type communication methods such as EtherCAT and CAN. The synchronous communications in EtherCAT is 100 Mbps between the master (main controller) and slave. And it is connected to SPI (14Mbps) between the slave and the drive.

Fig. 3 shows the developed controller. It can be mounted at the end of servo motor assembly. The smart actuator is developed as integrating a servo motor assembly and a controller as shown in Fig. 4.

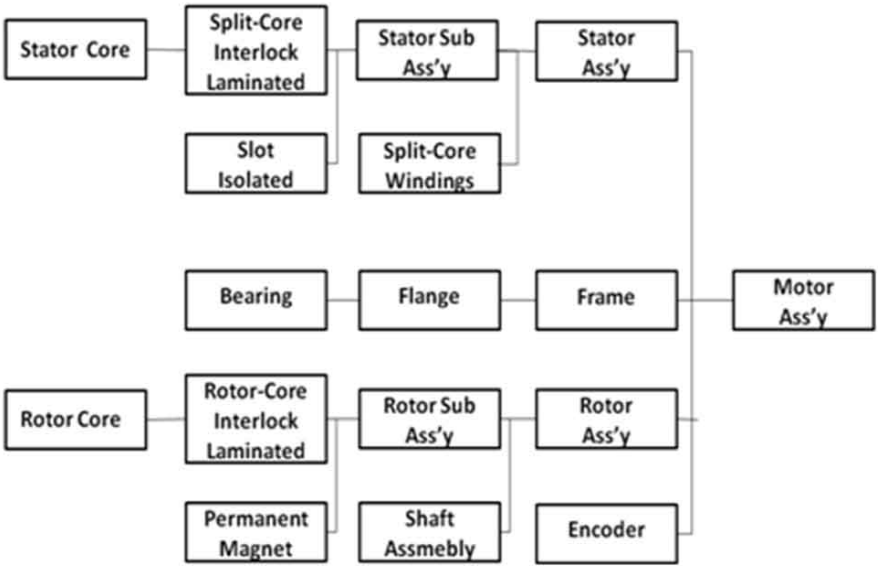

Fig. 2. Manufacturing process of servo motor assembly

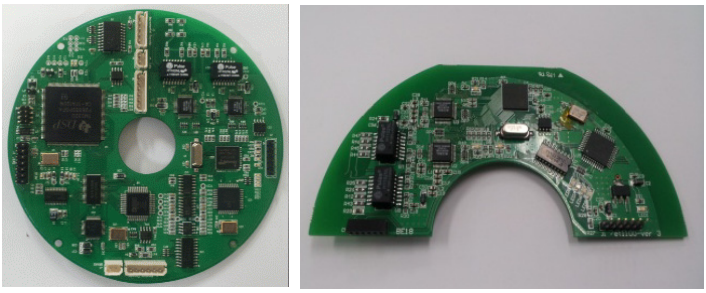

Fig. 3. The controller with drive and communication module

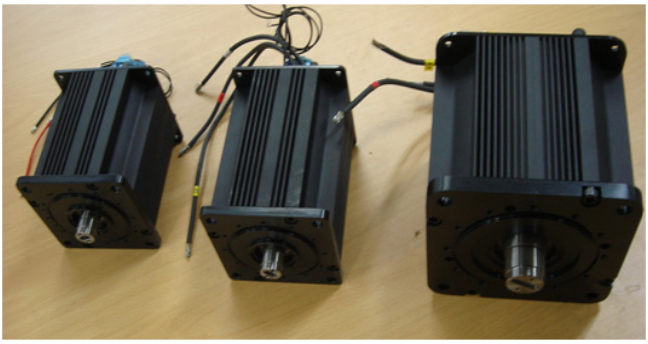

Fig. 4. The developed smart actuator

3 Industrial Robot with Smart Actuator

3.1 7-Axis Industrial Robot

The 7-axis industrial robot has been developed by using the developed smart actuators. The robot has a 6-axis articulated robot and a 1-axis linear driving unit for applying an industrial manufacturing process. Fig. 5 shows the virtual robot on a specific CAD interface and the fabricated the industrial robot.

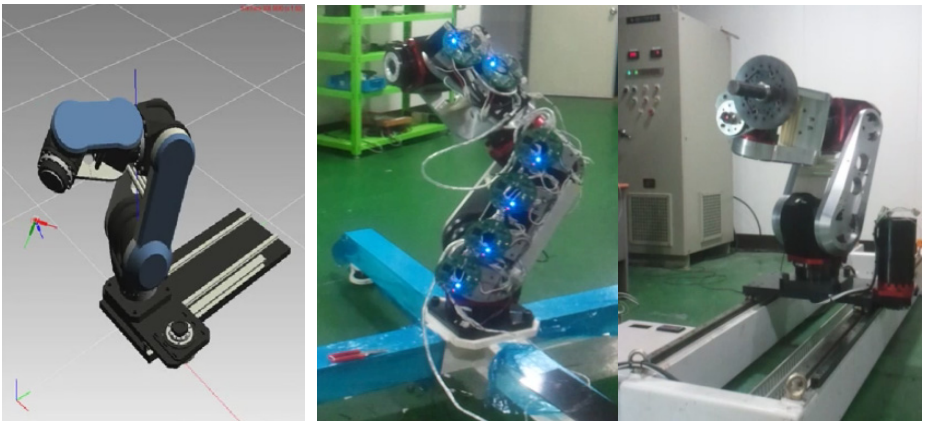

(a) Virtual robot (b) Fabrication of robot

Fig. 5. 7-axis industrial robot with smart actuators

3.2 Robot Control Simulator

Fig. 6 shows the overall scheme of a robot control simulator. It contains a dynamic analysis module, a real-time control module, and a communication module between

computer and the developed smart actuators. 'S/W MMC' of Fig. 6 is a module based on GUI. It can generate a command for trajectory control and monitor a tracking performance and a robot status.

The simulator is developed by using the RTX Real-Time Operating System. It includes a EtherCAT master module. The EtherCAT master module can be communicated with 32-axis EtherCAT slave modules at 1 kHz speed. Robot control algorithm can be programmed by using the 'Plug-In of User-Define Control Algorithm' module. The window and functions of 'S/W MMC' is shown in Fig. 7 and Table 2.

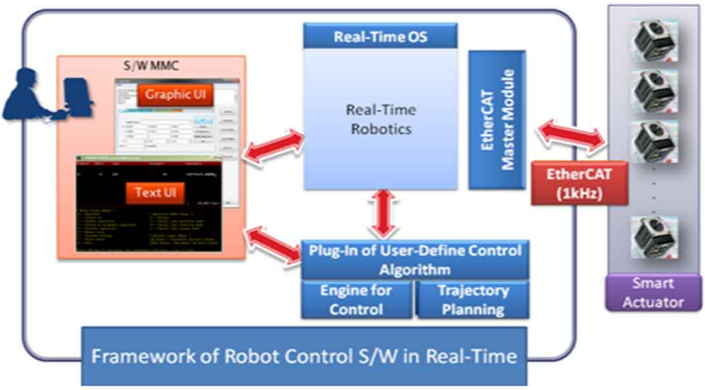

Fig. 6. Framework of robot control simulator

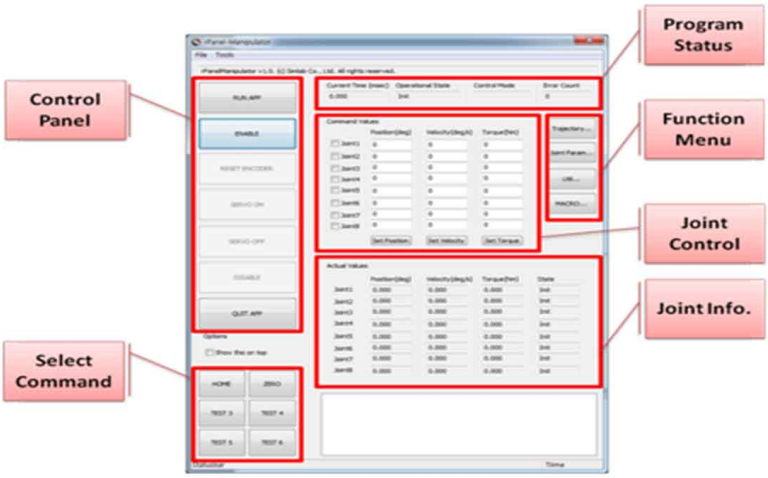

Fig. 7. Window of S/W MMC

Table 2. Functions of the S/W MMC

Item	Specification
Control Panel	Execute or terminate of S/W Enable or Disable of robot Servo On/Off Reset of encoder
Program Status	Current time Operational status Control mode Communication status
Select Command	Transfer robot command
Joint Control	Joint control (Position, Velocity, Torque mode)
Joint Info.	Monitoring of Position, Velocity, Torque and Status for all axes
Function Menu	Generate and modify of trajectory

3.3 Performance Evaluation of the Developed Robot System

A trajectory control experiment has been carried out for evaluating the performance of the robot. Fig. 8 shows the desired joint positions which are calculated by kinematics and a given reference trajectories in a task coordinate and the actual joint positions for each joint. The tracking position errors of joints are shown in Fig. 9.

As shown in Fig. 9, the maximum tracking position error is 0.002 rad and the steady-state error is 0.0001 rad. Fig. 10 shows the comparison between desired trajectories and actual trajectories in a task coordinate. The maximum trajectories tracking position error is 0.3 mm.

4 Conclusion

This study introduced a smart actuator which is integrated with a servo motor assembly and a controller. A smart actuator consists of a servo motor, a motor drive, gears, a brake, an encoder, a servo controller and a communication board. And then, 7-axis industrial robot with smart actuators and robot control simulator were developed. For verifying a robot performance, the trajectory tracking control was performed in experiment. The maximum trajectories tracking position error is 0.3 mm. In future work, the developed robot will be used in a mold and die manufacturing process.

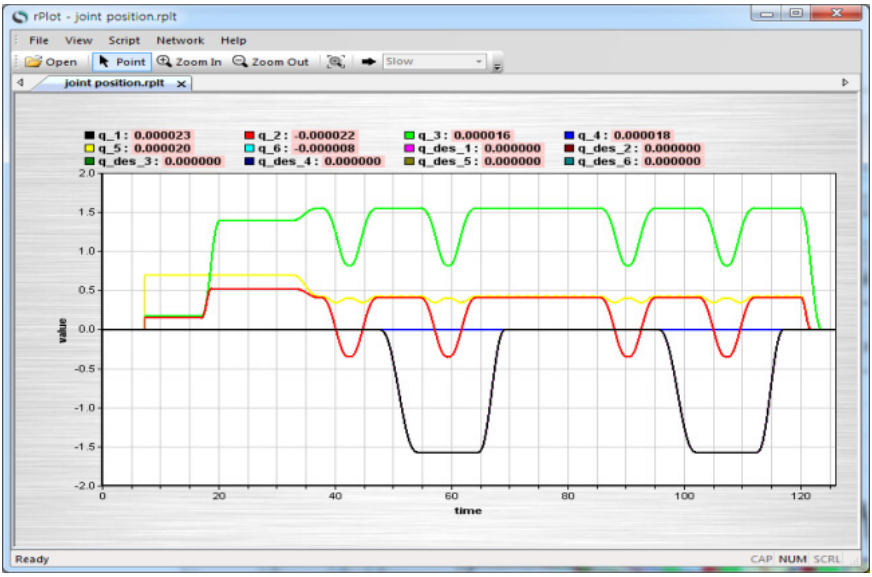

Fig. 8. Results of tracking control in each joint

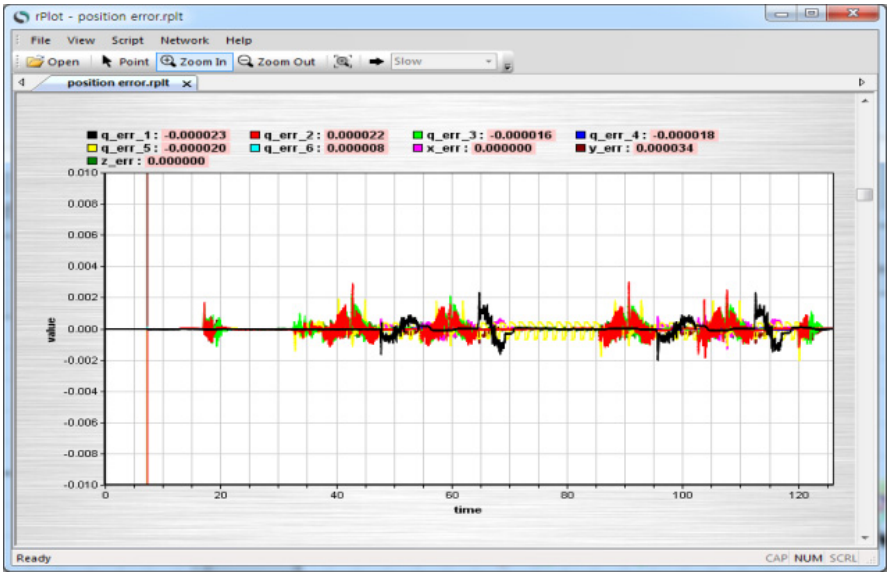

Fig. 9. Tracking errors of each joint

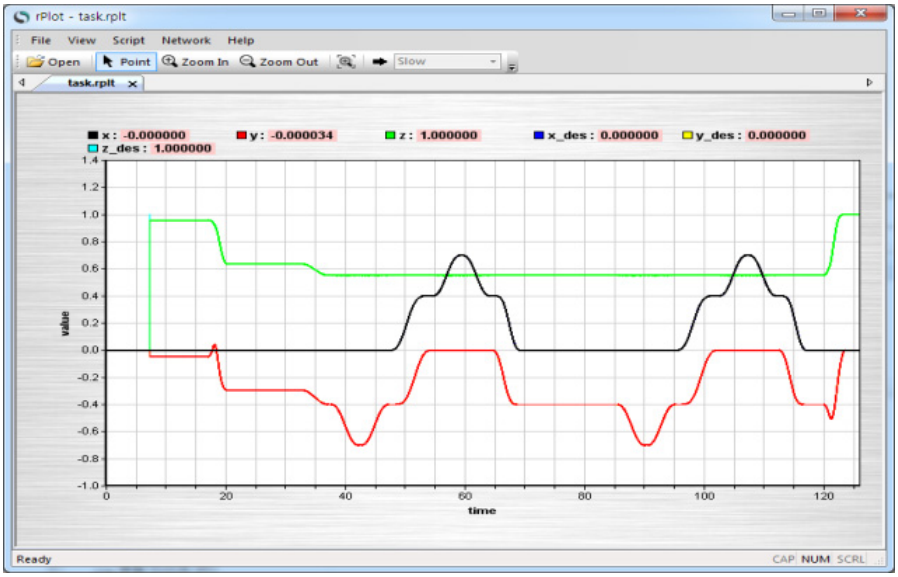

Fig. 10. Results of tracking control in a task coordinate

Acknowledgments. This research is supported the regional industry technology development project (research grant 70004909) of the Ministry of Knowledge Economy.

References

1. Lee, Y.J., Park, M.K., Go, S.J.: Development of Smart Actuator for Light-Weight Modular Arm. In: Proceedings of the 2010 International Conference on Control, Automation and Systems, pp. 674–677. ICROS (2010)
2. Choi, W.J., Yoon, M.K., Bang, Y.B., Cho, H.S.: Design and Fabrication of High-power Smart Actuator Module. In: Proceedings of the 2011 IEEE/SICE International Symposium on System Integration, pp. 434–439. SICE (2011)
3. Cao, P., Chen, W., Yu, S., Wang, J.: Development of Control Module in Small-Size Modular Actuator for Robotics. In: Proceedings of the 2011 IEEE Conference on Industrial Electronics and Application, pp. 1660–1665. IEEE (2011)
4. Park, M.K., Go, S.J., Lee, Y.J., Sung, K.G.: Design and Performance Evaluation of Lightweight Dual Arm Robot Featuring Hollow Shaft Servo Assembly. Advanced Science Letters 4, 1901–1907 (2011)
5. Park, C.H., Kyung, J.H., Choi, T.Y.: Design of a Human-Robot Cooperative Robot Manipulator using SMART Actuators. In: Proceedings of the 2011 International conference on Control, Automation and Systems, pp. 1868–1870. ICROS (2011)

Development of Single Channel Interrogator for Optical Sensors

Jang Sik Park, Jong Kwan Song, and Byung Woo Yoon

Department of Electronic Engineering, Kyungsung University,
Daeyeon 3-dong, 110 Nam-gu, Busan, 608-706- Korea
{jsipark,jsong,bwyoon}@ks.ac.kr

Abstract. A single channel FBG interrogator was designed and implemented in this paper. A developed interrogator consists of a laser source, optical grating, CCD sensor and controller. Especially, a CCD sensor controller is implemented with FBGA, controls the input and output. To verify the performance of developed interrogator, a simple deformation test is conducted.

Keywords: FBG sensor, Interrogator, FBGA, CCD sensor controller, Optical grating.

1 Introduction

A FBG(fiber Bragg grating) is a type of distributed bragged reflector constructed in a short segment of optical fiber that reflects particular wavelengths of light and transmit all others[1]. FBG sensors can measure strain and they also provide the superior advantages of the strain measuring principle, as metal foil strain gages do. Recently FBG has been accepted widely throughout the civil infra structures, especially for bridges[2-4], A new case study, FBG-based intelligent monitoring system of the Tiankin Yonghe bridge is introduced[5]. Recently, polymide patch type of FBG sensors are developed[6].

In this paper, a cost effective interrogator is developed to monitoring deformation s tructures such as hydroelectric power plants. Developed interrogator is composed wit h optical module such as optical grating and CCD controller. CCD controller impleme nted with FPGA is designed to capture deformation signal with 100Hz.

2 FBG Sensors and Interogator

Fiber optics sensors are light amplitude, phase, polarization of light such as the optical phenomena though the optical fiber using to detecting for physical quantity to be measured by detecting changes in the structure displacement, temperature, pressure, water level, sound and physical quantity. A FBG(fiber Bragg grating) by G. Meltz in 1989 has developed among fiber optic sensors that domestically and internationally widely using study in secure management of the structure. FBG sensor is achieved by

J. Lee et al. (Eds.): ICIRA 2013, Part II, LNAI 8103, pp. 450–453, 2013.

creating a periodic variation in the refractive index of the fiber core. Due to their low loss optical fiber sensor technology, most of the research is in progress technology.

It show change by linear Bragg wavelength with respect to stress and temperature by characteristic of the FBG, small size and the type of behavior have characteristics of wavelength encoding. It's real-time detection that deformation by environmental factor for installed in internal and external of structure etc. The phase mask proposed K. O. Hill and D. Z. Anderson et. al in 1993. It's method to make large quantity production more easily than the conventional method. This method is currently being studied in a wide range of worldwide[6]. Recently, FBG has been accepted widely throughout the civil infrastructures, especially for bridges. A new case study, FBG-based intelligent monitoring system of the Tianjin Yonghe Bridge is introduced[5].

A CCD type interrogator controller is developed for C-band wavelength range as measured at 1,520 nm to 1,560 nm. G11620-256DF-01 of Hamamatsu is used for CCD sensor of interrogator. Fig. 1 shows a timing diagram of the CCD image sensor.

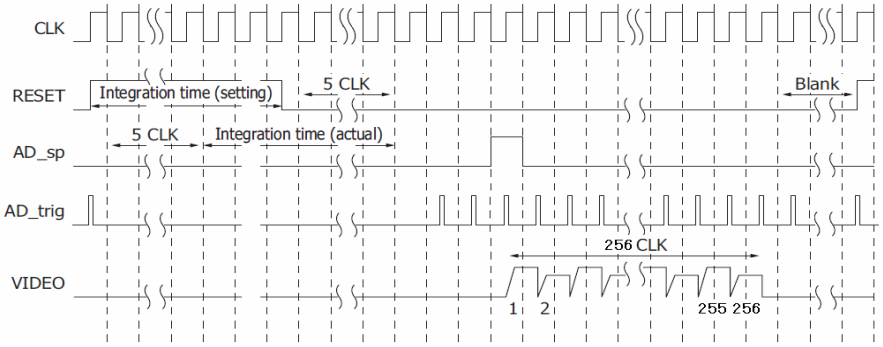

Fig. 1. Timing diagram of CCD image sensor of interrogator

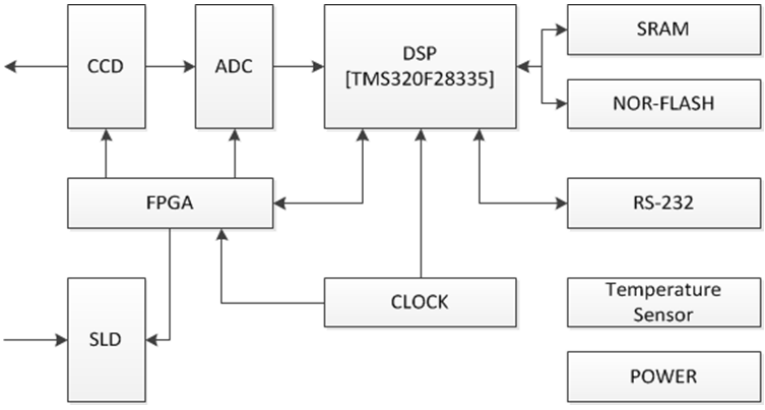

Fig. 2. Configuration of CCD image sensor

CLK is clock pulse for operating the shift register. RESET is a pulse for in itializing the feedback capacitance in the charge amplifier formed in the chip. I ntegration time is determined by the high period of this pulse. AD_sp is AD c onversion start pulse signal. AD_trig is a sampling synchronous signal for AD conversion. VIDEO is output analog signal of CCD image sensor. Configuration of CCD controller is shown in Fig. 2. CCD controller is composed with ADC, DSP, FBGA and peripheral devices. A signal sends to the CCD through A USB serial port to monitor FBG deformation.

3 Experimental Results and Considerations

A developed interrogator shown in Fig. 3 is composed with laser source, optical circulator, diffraction grating and CCD sensor controller. It estimates of error for stress by optical fiber with distance by optical fiber and phase mask. FBG fiber is formed by using a polyimide patch type FBG sensors were fabricated.

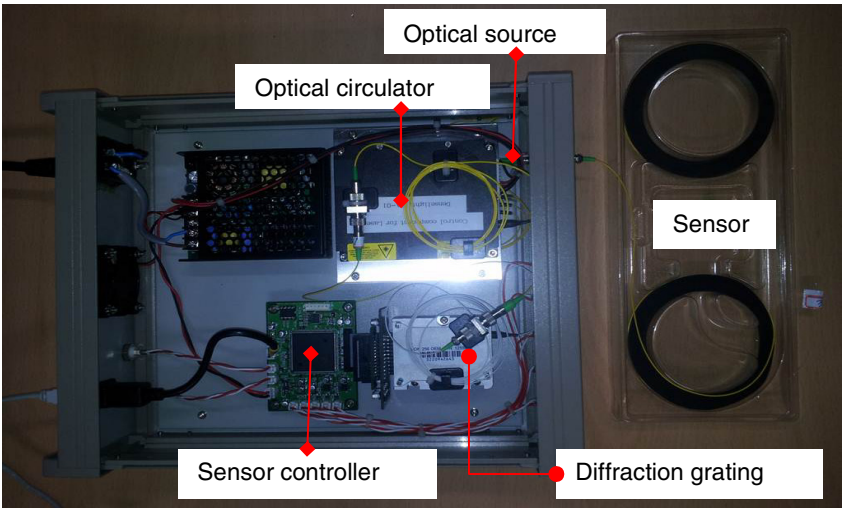

Fig. 3. Configuration of CCD type interrogator

Fig. 4 shows the signal that is sent from the interrogator. Frequency of capturing sensor is 100Hz. We used phase mask that FBG wavelength is 1,550nm. It is shown actual manufactured FBG Fig. 4 for center wavelength of 1549.710nm and reflection level of about 20 dBm. It estimates of error for stress by optical fiber with distance by optical fiber and phaser mask. FBG fiber is formed by using a polyimide patch type FBG sensors were fabricated.

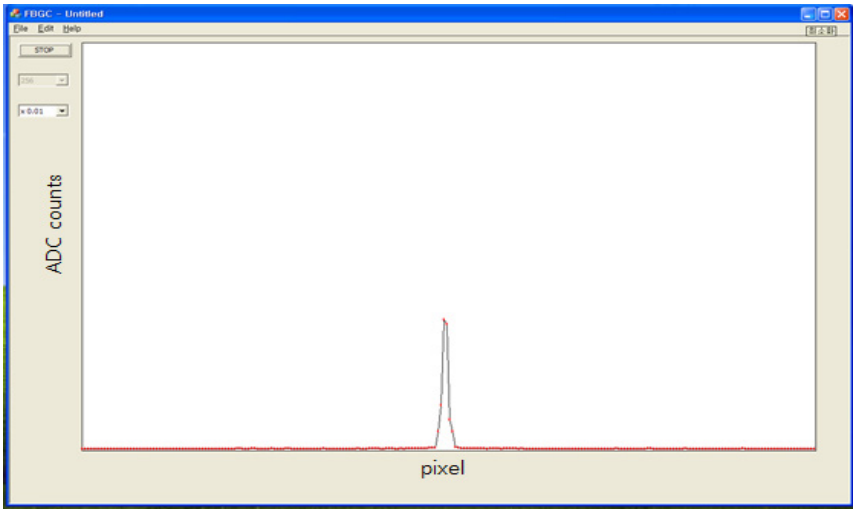

Fig. 4. Received signal from a CCD sensor and controller. When a FBG sensor is deformed by external forces, peak point is shifted.

4 Conclusions

In this paper, for more effective monitoring structure deformation, a single channel interrogator implemented by FBGA was developed. A simple experimental result is introduced.

Acknowledgments. This research was supported by Basic Science Research Program through the National Foundation of Korea(NRF) funded by the Ministry of Education, Science and Technology(2012M3C1A1048865).

References

1. http://en.wikipedia.org/wiki/Fiber_Bragg_grating
2. Lee, S.: Technique for Fiber Bragg Grid Sensor. Machines and Materials 14(4), 16–24 (2002) (in Korean)
3. Lee, S., Choi, S.: Interpretation for Dynamic Strain Signal using FBG Sensor. Institute of Electronics Engineers of Korea 247, 79–83 (1998)
4. Song, M., Lee, S., Choi, S., Lee, B.: Fiber Bragg Grid Sensor Using Mach-Zehnder Interferometer. Institute of Electronics Engineers of Korea, D d34, 105–113 (1997)
5. Lan, C., Zhou, Z., Sun, S., Ou, J.: FBG based intelligent monitoring system of the Tianjin Yonghe Bridge. In: Proc. of SPIE, vol. 6933 (2008)
6. Kim, H., Kim, Y., Do, J., Park, J., Yu, Y.: Development of FBG sensor for static stress. In: Proceedings of International Conference, IST 2012, Part 2, pp. 405–407 (2012)

In-network RFID Data Filtering Scheme in RFID-WSN for RFID Applications*

Ali Kashif Bashir[1,**], Myong-Soon Park[2], Sang-Il Lee[1], Jinseop Park[1], Wongryol Lee[1], and Sayed Chattan Shah[3]

[1] National Fusion Research Center, Daejeon, Korea
{ali12,leesi,linupark,wrlee}@nfri.re.kr
[2] Department of Computer Science and Engineering, Korea University, Seoul, Korea
myongsp86@korea.ac.kr
[3] Electronics and Telecommunications Research Institute, Daejeon, Korea
shah@etri.re.kr

Abstract. In the integration of wireless sensor networks (WSN) and radio frequency identification (RFID), RFID data can use WSN protocols for multi-hop communication. Due to readers overlapped regions in dense areas and due to readers multiple read cycles, a lot of duplicate data is produced. Transmitting such duplicates towards base station waste node energies. In-network filtering of these duplicates can save transmission overhead, but on the other hand it increases computation cost. Delay is an important parameter in RFID applications that has not been considered yet by existing approaches. Both communication overhead and computation overhead can affect the delay performance in terms of queuing delay and processing delay respectively. Therefore, it is required to tune the filtering algorithm. In this paper, our in-network filtering scheme tend to find this trade-off between these two costs for better delay performance. In simulation part, we showed the effect of these costs on delay performance.

Keywords: In-network processing in RFID-WSN integrated networks, In-network filtering, Duplicate data filtering, Delay in RFID, Communication and computation cost.

1 Introduction

The next revolution in computing technology is the widespread of small wireless computing and communication devices; they will integrate seamlessly into our daily life [1]. In the near future we can expect lots of devices to grow by multiple orders of magnitude such as tags, sensors, readers, etc. By technology perspective, RFID and sensor networks are important components of this paradigm since both technologies can be used for coupling physical and virtual world usually named as pervasive computing [2].

* This work is supported by Ministry of Education Science &Technology, South Korea.
** Corresponding author.

J. Lee et al. (Eds.): ICIRA 2013, Part II, LNAI 8103, pp. 454–465, 2013.

WSNs are networks of small, cost effective devices with ability of sensing, processing, and communication. On the other hand, RFID technology provides identification to tagged objects or humans. It consists of reader, tags, and the application. Readers read tags attached to objects, store data in its memory, and applications access it. RFID technology does not support multi-hop communication; however, by integrating it with WSN, we can route RFID data from readers to base station by using sensor network protocols. For this, nodes can have both functionalities: sensing and reading as shown in Fig. 1. RFID and WSN can be integrated in several other ways discussed in literature [2], [3], [4].

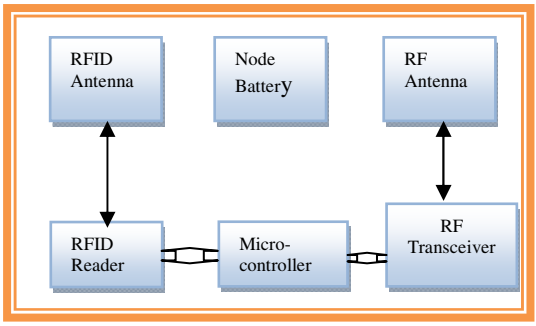

Fig. 1. Integrated WSN node and RFID Reader

RFID data is streaming in nature and usually contains an excessive amount of duplicate readings. In WSN, nodes are densely deployed usually and due to density they have overlapping regions with neighboring nodes. Tags that exist in overlapping areas are read by more than one reader and results in duplicate readings. Sending these duplicate data packets to the base station by multi-hop fashion consumes nodes energies, whereas, energy is a critical issue in WSN as nodes battery lifetime is limited.

By applying in-network processing we can filter these duplicates within the network to save extra transmissions. In-network processing reduces communication cost, but on the other hand increases computation cost. In the last few years, researchers found tradeoffs between computation and communication cost to increase energy efficiency [6], [7], [8]. WSN is tolerant to network delay since there is limited bandwidth [6, 9]. But, to provide better quality of service, improving network delay emerges as an important factor in WSNs. Delay can occur due to intensive communication on nodes or due to congestion [10].

In sensor networks, multiple packets can be aggregated into one due to the correlation of the sensed data. However, RFID data packets cannot be aggregated as every read data packet has its own identity, but due to duplications they can be filtered. In-network filtering drop RFID duplicate data packets to avoid redundant transmissions in the network. It reduces communication cost, but processing on nodes nodes result in computation overhead and in processing delays. RFID data contain real-time information and applications are interested in timely reports such as in a department store, managers would like to have the updated information about sales

and stocks. Therefore, a delay is an important metric to consider in RFID. In literature, several in-network filtering solutions [11], [12], [13], [14] are proposed, but they are focused on reducing communication overhead and do not consider delay.

In this paper, we propose IRDF :*In-network RFID Duplicate Data Filtering*, which is an extension of our previous work EIFS [14]. Topology and number of filtering points within network affect the performance of in-network filtering approaches. In IRDF, we choose clustering topology, as it helps in reducing energy consumption [15], whereas the filtering module runs only at cluster heads. Moreover, we vary the number of filtering points in the network and measure the communication cost, computational cost, and delay. On the base of these results, IRDF chooses the optimal filtering points that provide best delay performance.

The rest of this paper is organized as follows: Section 2 discusses related work. In section 3, we presented the assumptions and a preliminary algorithm. In section 4, we describe the proposed approach in detail. We analyze our idea and compare it with previous research by using simulations in section 5. Finally, in section 6, we conclude this paper.

2 Related Work

Data filtering is as an important issue in RFID applications. Several researchers provided solutions to filter RFID data to save communication cost. [5, 16] proposed their approaches to filter duplicate data using sliding-window. Sliding window keeps the history of the previous read cycles in buffer and output the data when it increases than a certain threshold. These solutions are proposed for server middleware. This middleware can be implemented in the readers, but due to the limited memory of readers this is not an appropriate solution. Moreover, the performance of this approach degrades with the smaller size of the window and filtering redundant data at base station do not decrease the transmission overhead on nodes.

In-network processing is widely researched in WSN in terms of data aggregation [10, 17]. In WSN data is highly correlated; therefore, parent nodes or cluster heads can aggregate multiple data packets into one. While RFID data is not correlated as each EPC tag represents one real world object. However, due to the enormous amount of duplication in RFID data, we need to perform in-network data filtering to avoid transmitting duplicate data within the network. Following are the duplication types that need to be filtered by in-network filtering solutions:

- *Data level:* Multiple tags with same EPC (Electronic Product Code) are attached to the same object in order to reduce missing rate and increase reliability [5].
- *Multiple Read Cycle:* Tags in the vicinity of a reader for a long time (in multiple reading cycles) are read by the reader multiple times [18]
- *Redundant Reader:* Multiple readers are installed to cover a larger area or distance, and tags in the overlapped areas are read by multiple readers [19] as shown in Fig. 2, where such as tag T3 is read by three readers R2, R3 and R4.

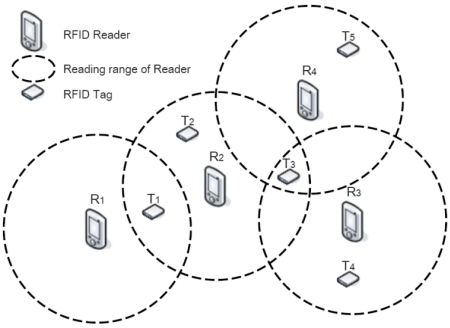

Fig. 2. Redundant Reader: Duplication due to overlapping of readers

Data level and multiple read cycle duplication can be eliminated by a simple filtering algorithm at the reader. To eliminate duplication generated due to overlapping, readers need to collaborate with each other. Such as [19] deals with the problem of redundant readers. This solution resolves the problem by temporarily deactivating the readers that have a maximum overlapped region with neighboring readers. This mechanism reduces the redundant transmission, but in large deployments finding which readers to be turned off is an NP-hard problem [21].

In-network processing also increases the computation overhead on nodes. An efficient solution should create a balance between communication and computation costs to meet the desired objectives of applications. Kadayif et al. [20] proposed a strategy to keep a balance between computation energy and communication energy in wireless sensor networks. In many streams-oriented WSN applications such as military scenarios, both link bandwidth and node energy are constraint resources. For such applications, in-network processing imposes non-negligible computational cost. In the last few years, researchers tried to tune the trade-offs among computation and communication cost to increase the network lifetime by increasing the lifetime of sensor nodes.

In RFID-WSN, routing RFID data in presence of duplicates waste nodes energies. Data should be filtered within the network ideally close to source to avoid redundant transmissions to save energy. Existing solutions [11], [12], [13], and [14] filter the data with less computation cost. These schemes mainly use two kinds of topologies: tree and clustering. Both of these technologies have their own pros and cons as explained below.

Tree based approaches: In the tree approaches [11], [13], node filters its own and children's data. Amount of data being filtered at one node is less. To filter the maximum amount of duplicate data, filtering algorithm need to run at every node for every incoming data packet which results in high computation cost and delay. INPFM [11] was the first in-network filtering approach in RFID-WSN. Dong-Hyun et al. [13] proposed in-network filtering scheme in object tracking applications. He assumed that data should meet within network, which is a strong assumption.

Cluster based approaches: To improve performance of filtering, CLIF [12] and EIFS [14] used clustering topology. They divided the redundancy into: intra-cluster

redundancy and inter-cluster redundancy. Intra-cluster redundancy is being filtered at local CH and inter-cluster redundancy at intermediate cluster heads. These schemes save computation overhead; on the other hand filters fewer amounts of data in comparison with [11]. EIFS [14] adopts a neighbor discovery algorithm for fast detection of duplicates. To filter inter-cluster data at neighboring cluster heads, they use feedback message. CHs update their routing tables to drop duplications on neighboring cluster heads.

The objective of these approaches was to filter the maximum amount of data to reduce communication overhead. On the other hand, huge traffic results in congestion and queuing delay. Therefore, it is important to choose an appropriate amount of data filtering at one node or number of nodes to filter data without increasing delay. None of the existing in-network filtering approaches have considered delay as a performance metric.

3 Preliminaries

In our scheme, duplication is divided into two: intra-cluster and inter-cluster duplication. Nodes that have overlapping with nodes of same cluster are called as intra-cluster nodes, whereas, nodes that have overlapping with neighboring nodes of another cluster are called inter-cluster nodes.

3.1 Assumptions

Following are the assumption of our model.

- Nodes are homogeneous in nature and static after deployment.
- Transmission range is double than the reading range and nodes can communicate with CH directly.
- Every sensor node contains a reader module.
- We assume a simple communication mechanism with a medium access control (MAC) protocol that ensures no collision and interference [10].
- Cluster heads will send data to the base station via intermediate cluster heads (multi-hop).
- Filtering process will run only at cluster heads.
- Clusters are static in nature, but the cluster head task can be rotated among member nodes.
- Data loss and possible contention are not considered.

3.2 Redundancy Definition

Check for duplication if following three conditions are true.

- The contents of tags (EPCs) are the same: In this research, we will only compare EPC serial numbers using BFF algorithm [22].

- The node IDs or cluster ID is the same in the intra-cluster phase. In an inter-cluster, if the data is from my neighboring cluster.
- The difference between the reading times of two data is less than a predefined time interval.

Cluster head will store a copy of tag data in a tag list for a certain time period for comparison with upcoming data to drop the duplications. In our research, we compare 32 bits of EPC Serial numbers. For that we used backward first search algorithm [22]. In our previous work EIFS; we compared 36 bits of EPC serial numbers. Therefore, to improve the performance of detection in IRDF, we compare 32 bits of Serial Number. The time interval can be defined as reporting time for cluster heads to send data.

3.3 ND Array

In our approach after cluster formation to distinguish among nodes, each node exchanges an *ND message* with neighboring nodes. The *ND message* contains *node ID* and *cluster ID*. A node that receives ND messages from its neighbors keeps the *cluster ID* in an *ND array*. From the *ND array* of a node, we can know whether it has the *ID* of any neighboring clusters or not. If the *IDs* of two or more than two clusters exist in a node *ND array*, it will be considered as an *inter - cluster node*. *ND message* helps in decreasing computation cost.

When an intra-cluster node, interrogates a tag x, after tag response, node generates an RFID data packet with the value of f (number of remaining filtering operations) as 1, shown in table 2. The node sends this data packet to its cluster head. If any other neighboring node also reports to the cluster head with tag x, the cluster head will filter it to avoid duplication. In case of inter-cluster nodes, the value of f is f_e. However, in this scheme we vary the f_e to monitor the network performance. Table 1 shows the structure of the RFID data packet in inter-cluster node. Every node sends their data to its cluster heads and they decide the type of the sender from the f field. If the value of f is 2 or more, the sender is considered an inter-cluster node. If the value of f is 1, the sender is intra-cluster node.

Table 1. The structure of the node generated data packet

	Tag *ID*	Node *ID*	Time Stamp	*f*
Intra-cluster Node	*x*	*N*	*T*	*1*
Inter-cluster Node	*x*	*N*	*T*	f_e

4 Proposed Algorithms

IRDF: In-network RFID data filtering scheme is an extension of our previous scheme named *EIFS: energy efficient in-network RFID data filtering scheme* [14] in terms of delay. Like EIFS, IRDF also adopts cluster topology. Process of intra-cluster duplication is similar like EIFS, however, in inter-cluster EIFS filter data at every

node and inform source cluster heads with feedback messages. In IRDF, we do not use any feedback mechanism and change routing paths. Feedback messages introduce heavy communication overhead that increase latency. Rather we find the optimal number of filtering points that provide best delay performance.

When a cluster head receives an RFID data packet, it decides the type of sender by the *f* field. If the value of *f* is 1, the sender is an intra-cluster node and local cluster head execute the duplicate detection algorithm to check for the duplication. After removing the duplication, it sets the *f* field as 0 and forwards the data to base station. Such packets will not be filtered at any intermediate cluster head which saves computation costs. At intermediate CH when the value of *f* of arrival packet is 0, it means the data is already filtered. This mechanism significantly reduces the number of comparisons. Detailed algorithm is given in fig. 3.

Intermediate CH's will check the value of *f,* if value of *f* is more than 0, they will perform duplicate detection mechanism for inter-cluster duplicates. The value of *f* decreases by 1 with each hop from source cluster head to intermediate cluster heads. Detailed inter-cluster duplicate data filtering algorithm is presented in fig. 4.

In EIFS, we filter data at every intermediate CH. Intermediate heads detects the duplication and inform source cluster heads that cause inter-cluster duplication with feedback messages. In the next rounds, they can change the routing path of that specific tags to drop duplications on neighboring cluster heads. IRDF filters inter-cluster duplicate data at neighboring cluster heads of a specific hop count. EIFS performance also degrades when tag mobility is high in the network.

```
Function Intra_cluster_duplicate_data filtering ()
Loop until I am cluster head
  If incoming data packet comes then
   If data.number_of_remaining filtering is 1
    // Intra-cluster duplication//
      Decrease data.number_of_remaining_filtering by 1.
      If it is not duplicated data then
          Update the tag_list.
          Send the data to the sink.
      Else
          Drop the data.
      End if
   End if
  Else if data.number_of_remaining_filtering is ∞ or 0 then
       // Inter-cluster duplication required to filtering//
       Call inter_cluster_duplicated_data filtering.
  Else if data.number_of_remaining_filtering is 0 then.
      Send the data to the next hop node.
   End if
  End if
  End loop
```

Fig. 3. Intra-cluster filtering algorithm

```
Function Inter_cluster_duplicate_data_filtering
  Seek the data.tag_id from the tag_list.
 If found then
  Decrease the value of f by 1
 If the data is duplicated then
Else
  Second the data to the next hop.
End if
Else
    Inset the data into tag_list.
     End if
Else
  Send the data to the next hop
    End if
End if
```

Fig. 4. Inter-cluster filtering algorithm

5 Simulation Results

In our previous work [14] we presented and compared our algorithms in detail with [11] and [12] in terms of communication cost and computation cost. However in this work, we will vary the number of detection points and measure the performance of the algorithm in terms of communication cost, computational cost, and delay. Computation cost and communication cost have a trade-off and delay is chosen as a decisive performance metric. We developed our simulator using C++. The detailed simulation environment is given in table 2.

Table 2. Simulation environment

Parameters	Value
Field Area	100 x 100 m^2
Number of nodes	361
Number of clusters	19
Members in a cluster	19 (including cluster head)
Reading Range	5 *m*
Transmission Range	10 *m*
Distance between nodes	7 *m*
Reading interval	2 *sec*
Duplication ratio	20 %
Number of tags	100 to 500
Limit of History Data	300

α is introduced as a variable representing number of intermediate cluster heads (detection points/filtering points) from source cluster heads to perform in-network filtering. We vary value of α and measure the computation cost, communication cost, and delay. Fig. 5 shows the computation cost of our algorithm in terms of number of computations. When we filters data at more intermediate CH, we require more comparisons to detect duplicates. Logic is very simple, if we filters data at every intermediate node for every arriving packet, it requires more comparisons to detect and hence increase computation cost.

Fig. 5. Computational cost

In fig. 6, we measured the communication cost in terms of number of relays required to send data from source to base station. It is visible that if value of α increases, number of relays decreases. Decreasing number of relays clearly means a reduction in the amount of packet transfer. In other words, if we filter data at more nodes, we can able to filter more duplicate data and can save more transmission overhead. In literature, approaches that filter data at more intermediate points have better performance in terms of communication cost [11], [13]. It is because, when α is 1, nodes have to transmit more packets to forward all read data to the base station in

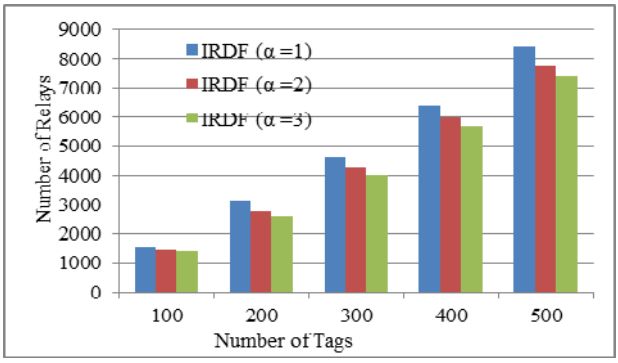

Fig. 6. Communication cost

the presence of duplicates. When α increases, the performance of in-network filtering algorithms improves in terms of communication cost.

From figure 5 and 6, it is clear that computation cost increase with increasing number of filtering points whereas computation cost decreases. Therefore, this tradeoff needs to be considered to use network resources efficiently. However, in IRDF we considered delay to be a deciding factor. In simulation, we assume the network delay the time it takes to reach the destination from source. The result of the delay parameter is quite different than computation and communication costs. When value α is 1 and 3, delay is high. When α is 1, communication cost is high as nodes have to forward a lot of packets which results in queuing delay at nodes. On the other hand, when α is 3, computation cost gets higher and that results in processing delay at nodes. Packets have to wait to be processed before being forward. However, in case of α as 2, delay is mediate as shown in fig. 7.

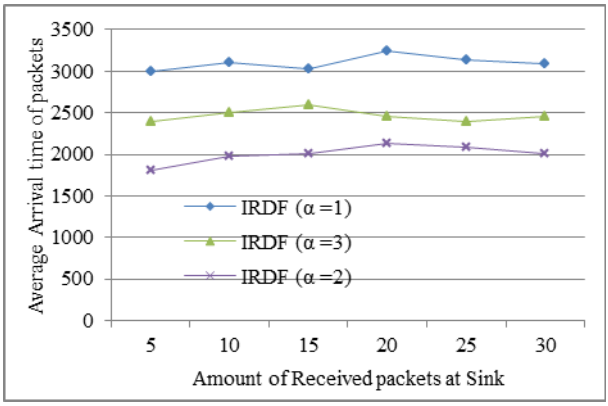

Fig. 7. Delay in terms of arrival time of packets at base station

6 Conclusions

In the integration of RFID-WSN, RFID data contain duplications which need to be filtered to avoid redundant transmissions hence to save node energies. Existing in-network filtering approaches tend to filter maximum duplicate data and results in increased computation cost and processing delay. Moreover they have not considered delay as a performance metric, whereas, a delay is an important factor in RFID applications. In this paper, our approach divides duplication into intra-cluster and inter-cluster. Intra-cluster duplication is being filtered at local CH and inter-cluster duplications at neighboring CHs. In simulation section, we monitored the trade-off between computation and communication costs. Moreover, considering delay as important parameter, we selected it to be deciding factor for selecting the appropriate number of filtering points within the network.

References

1. Sarma, S.E.: Towards the five-cent tag. Tech. Rep. MIT-AUTOID-WH-006, MIT Auto-ID Center (2001), http://www.autoidcenter.org/research/MIT-AUTOID-WH-006.pdf (accessed on January 2009)
2. Lopez, T.S., Kim, D., Canepa, G.H., Koumadi, K.: Integrating Wireless Sensors and RFID Tags into Energy-Efficient and Dynamic Context Networks. The Computer Journal 52, 240–267 (2008)
3. Ho, L., Moh, M., Walker, Z., Hamada, T., Su, C.F.: A Prototype on RFID and Sensor Networks for Elder Healthcare: Progress Report. In: Proceedings of the ACM SIGCOMM Workshop on Experimental Approaches to Wireless Network Design and Analysis, Philadelphia, PA, USA, pp. 70–75 (August 2005)
4. Smith, J.R., Fishkin, K.P., Jiang, B., Mamishev, A., Philipose, M., Rea, A.D., Roy, S., Rajan, K.S.: RFID-based techniques for human-activity detection. Commun. ACM 48, 39–44 (2005)
5. Jeffery, S.R., Garofalakis, M., Franklin, M.J.: Adaptive Cleaning for RFID Data Streams. In: Proceedings of the 32nd International Conference on Very Large Data Bases VLDB, Seoul, Korea, September 12-15, pp. 163–174 (2006)
6. Yang, Y., Krishnamachari, B., Prasana, V.K.: Data Gathering with Tunable Compression in Sensor Networks. IEEE Transactions on Parallel and Distributed Systems 19, 276–287 (2008)
7. Qinghai, W.: Traffic Analysis & Modeling in Wireless Sensor Networks and Their Applications on Network Optimization and Anomaly Detection. Network Protocols and Algorithms 2, 74–96 (2010)
8. Seung, J.B., Gustavo, D.V., Xun, S.: Minimizing Energy Consumption in Large-Scale Sensor Networks through Distributed Data Compression and Hierarchical Aggregation. IEEE Journal on Selected Areas in Communications 22, 1130–1140 (2004)
9. Jin, Y., Wei, D., Gluhak, A., Moessner, K.: Latency and Energy-Consumption Optimized Task Allocation in Wireless Sensor Networks. IEEE Wireless Communications and Networking Conference (WCNC), 1–6 (April 2010)
10. Krishnamachari, L., Estrin, D., Wicker, S.: The Impact of Data Aggregation In Wireless Sensor Networks. In: Distributed Computing Systems Workshops, pp. 575–578 (2002)
11. Choi, W., Park, M.S.: In-network Phased Filtering Mechanism for a Large-Scale RFID Inventory Application. In: Proceedings of the 4th International Conference on IT & Applications (ICITA), Harbin, China, pp. 401–405 (January 2007)
12. Kim, D.-S., Bashir, A.K., Ming, X., Kim, J.-H., Park, M.-S.: Energy Efficient In-Network Phase RFID Data Filtering Scheme. In: Sandnes, F.E., Zhang, Y., Rong, C., Yang, L.T., Ma, J. (eds.) UIC 2008. LNCS, vol. 5061, pp. 311–322. Springer, Heidelberg (2008)
13. Lee, D.H., Lee, E.-M., Bashir, A.K., Park, M.-S.: Efficient in-network redundancy filtering in RFID system integrated with wireless sensor networks. In: Networked Computing 6th International Conference, pp. 1–6 (May 2010)
14. Bashir, A.K., Lee, S.-J., Hussain, S.H., Park, M.-S.: Energy Efficient In-network RFID Data Filtering Scheme in Wireless Sensor Networks. In: Sensors MDPI 2011, vol. 11, pp. 7004–7021 (2011)
15. Kawadia, V., Kumar, P.R.: Power Control and Clustering in Ad Hoc Networks. In: Proceedings of IEEE INFOCOM, vol. 1, pp. 459–469 (April 2003)
16. Wang, F., Liu, P.: Temporal Management of RFID Data. In: Proceedings of the 31st International Conference on Very Large Data Bases, Trondheim, Norway, pp. 1128–1139 (August 2005)

17. Yujie, Z., Ramanuja, V., Seung-Jong, P., Raghupathy, S.: A Scalable correlation aware aggregation strategy for wireless sensor networks. Inform. Fusion 9, 354–369 (2008)
18. Carbunar, B., Ramanathan, M.K., Koyuturk, M., Hoffmann, C., Grama, A.: Redundant Reader Elimination in RFID Systems. In: Proceedings of the Second Annual IEEE Communications Society Conference on Sensor and Ad Hoc Communications and Networks, IEEE SECON 2005, Santa Clara, CA, USA, September 26-29, pp. 176–184 (2005)
19. Bai, Y., Wang, F., Peiya, L.: Efficiently Filtering RFID Data Streams. In: Proceedings of the First International VLDB Workshop on Clean Databases, Seoul, Korea (September 2006)
20. Kadayif, I., Kandemir, M.: Tuning In-Sensor Data Filtering to Reduce Energy Consumption in Wireless Sensor Networks. In: Proceedings of Design, Automation and Test in Europe Conference and Exhibition, Paris, France, pp. 1530–1539 (February 2004)
21. Chawathe, S.S., Krishnamurthy, V., Ramachandran, S., Sarma, S.: Managing RFID Data. In: Proceedings of the Thirtieth International Conference on Very Large Data Bases, Toronto, ON, Canada, pp. 1189–1195 (August 2004)
22. Boyer, R.S., Moore, J.S.: A Fast Searching Algorithm. In: CACM, pp. 762–772 (1997)
23. Bashir, A.K., Chauhdary, S.H., Shah, S.C., Myong-Soon, P.: Mobile RFID and its Design Security Issues. IEEE Potentials 30, 34–38 (2011)

Optimal Design of MR Shock Absorber for Passenger Vehicle

Kum-Gil Sung and Min-Kyu Park

School of Mechanical and Automotive Engineering Technology,
Yeungnam College of Science and Technology, Daegu, Korea
kgsung@ync.ac.kr

Abstract. This paper presents optimal design of a controllable magnetorheological (MR) shock absorber for a passenger vehicle. In order to achieve this goal, a cylindrical MR shock absorber, which satisfies design specifications for a mid-sized commercial passenger vehicle, is designed using an optimization methodology. The optimization problem is to find optimal geometric dimensions of the magnetic circuit for the MR shock absorber in order to maximize damping force. The first order optimization method using commercial finite element method (FEM) software is adopted for the constrained optimization algorithm.

Keywords: Optimal Design, Finite Element Method (FEM), Magneto-rheological (MR) Fluid, MR Shock Absorber.

1 Introduction

The vehicle dynamic characteristics such as ride comfort and steering stability can be normally improved by suspension systems. So far, passive oil shock absorber, which provides design simplicity and cost-effectiveness, is widely employed for conventional vehicles. However, the performance limitation is inevitable due to uncontrollable damping force. Recently, active shock absorber using a motor and electro-servo hydraulic valve is gradually used to achieve ride comfort as well as steering stability. However, design complication and high cost prevent the popularization of advanced active suspension systems. Therefore, alternative mechanisms for vehicle suspension systems have been studied to replace the passive and active shock absorbers.

When the MR fluid is employed in shock absorbers, the rheological change of the fluid causes a pressure drop in the control volume, which can be continuously tuned by controlling the intensity of the imposed magnetic field. This feature has triggered considerable research activities on modeling and design of MR devices. Numerous researches on the modeling and design of MR valves and shock absorbers have been performed in analytical manner [1~3]. The finite element method (FEM) has been also used in the modeling and design of MR valves and shock absorbers [4~5]. However, the researches on optimal design of MR valves and shock absorber are still considerably rare. Rosenfeld and Wereley [6] proposed an analytical optimization design method for MR valves and shock absorbers based on the assumption of constant magnetic flux

J. Lee et al. (Eds.): ICIRA 2013, Part II, LNAI 8103, pp. 466–469, 2013.

density throughout the magnetic circuit to ensure that one region of the magnetic circuit does not saturate prematurely and cause a bottleneck effect. Nevertheless, this assumption leads to a suboptimal result because the valve performance depends not only on magnetic circuit but also on the geometry of the ducts through which the MR fluid passes. Recently, Nguyen et al. [7] proposed a FEM based optimal design of MR valves constrained in a specific volume. In this prior work, the effects of geometric variables of MR valves are considered by minimizing the valve ratio as an objective function. However, the practical feasibility of the proposed optimal MR valve system in real field is not investigated. The research work about the effect of optimally designed MR shock absorber or valve on control performance is absolutely required.

Consequently, the main contribution of this work is to represent a general optimization design procedure of MR shock absorber for a passenger vehicle and show some effects of the optimized MR shock absorber on suspension control performance. The MR shock absorber, which can be applicable to a middle-sized commercial passenger vehicle, is designed using an optimization methodology. The optimization problem is to find optimal geometric dimensions of the magnetic circuit for the MR shock absorber in order to improve the damping performance.

2 MR Shock Absorber

The schematic configuration of the MR shock absorber proposed in this work is shown in Fig. 1. The MR shock absorber is composed of the cylinder, piston and gas chamber. The MR shock absorber is divided into the upper and lower chambers by the piston, and the MR fluid flows through the annular duct between inner and outer piston from one chamber to the other. The upper and lower magnetic poles in the annular duct are placed to control the yield stress of the MR fluid by supplying current to the coil. In order to effectively generate the magnetic field in the magnetic poles, the outer cylinder and both ends of inner piston are made of ferromagnetic substance, while the center of inner piston is paramagnetic substance. In the absence of the magnetic field, the MR shock absorber produces the damping force only caused by the fluid viscous resistance. However, if a certain level of the magnetic field is supplied to the MR shock absorber, the MR shock absorber produces additional damping force owing to the yield stress of the MR fluid. This damping force of the MR shock absorber can be continuously tuned by controlling the intensity of the magnetic field.

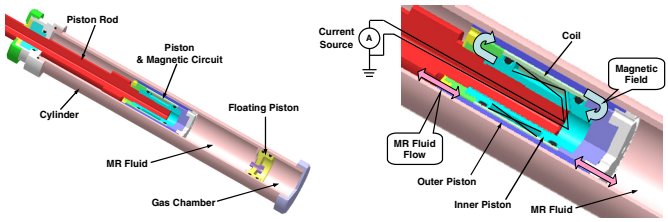

(a) MR shock absorber (b) piston

Fig. 1. Schematic configuration of the proposed MR shock absorber

3 Optimization

In this study, a commercial FEM software (ANSYS) is adopted to obtain optimal geometric dimensions of the proposed MR shock absorber. The objective function is to minimize the reciprocal value of the damping force. Magnetic properties of the piston components are given in Table 1. Low carbon steel is used for the ferromagnetic substance and the magnetic flux density of low carbon steel is saturated with 1.5Tesla at about 5A/mm.

Table 1. Magnetic properties of the MR shock absorber component

Component	Material	Relative Permeability	Saturation Flux Density
Ferromagnetic	Low Carbon Steel	2000	1.5 Tesla
Paramagnetic	Al Alloy	1	-
Coil	Copper	1	-
MR Fluid	MRF-132DG	B-H Curve	

The geometric dimensions of the MR shock absorber which significantly affect the performance, such as coil width (W_c), magnetic pole length (L_p) and armature width (W_a), are considered as design variables (DV). At first, a log-file for solving the magnetic circuit of the piston and calculating the damping force using the ANSYS parametric design language (APDL) is built. In this file, the DVs should be input as variables and initial values are assigned to them. Since the piston geometry of the MR shock absorber is axisymmetric, a 2D-axisymmetric coupled element (Plane 13) is used for electromagnetic analysis. The 4-node quadrilateral meshing is used for the finite element model. The geometric dimensions of the piston vary during the optimization process, so the meshing size should be specified by the number of elements per line rather than element size. After solving for the magnetic circuit of the piston, the average magnetic flux density through MR flows is calculated from the FE solution by integrating the flux density along the defined path then divided by the path length. The yield stress of the MR fluid caused by the magnetic field is calculated from the approximate curve

The shock absorber is constrained in design specifications for a commercial passenger vehicle. The size and the level of required damping force is determined so that the MR shock absorber can be applicable to the vehicle. Limits of DVs are assigned as follows: W_c=1~7mm, L_p=5~20mm and W_a=1~6mm. Initial values of W_c, L_p and W_a are 6, 10 and 3mm, respectively; and the damping force of the MR shock absorber at these initial values are 1256N. From the optimization results shown in Fig. 2, it is observed that the objective function of the MR shock absorber is converged from $796.2\text{x}10^{-6}$ to $655.5\text{x}10^{-6}$ after 6 iterations. At the optimum, the corresponding damping force is 1525.6N, which is increased about 21.5%. The DVs at the optimum are W_c=4.94mm, L_p=11.74mm and W_a=3.54mm. The optimization results show that the geometry of the MR shock absorber has a large effect on the shock absorber performance. Therefore, the damping force of the MR shock absorber can be much improved by choosing the optimal geometry.

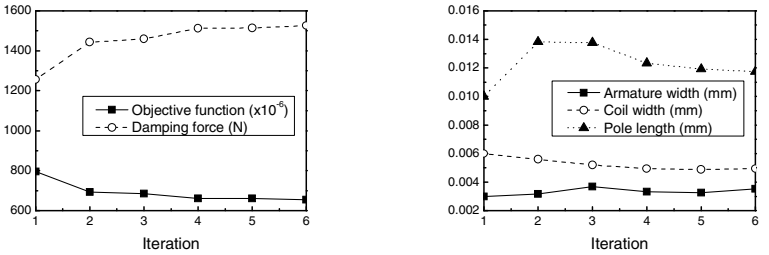

(a) objective function (b) design variables

Fig. 2. Optimization results of the MR shock absorber

4 Conclusion

In this work, optimal design of a controllable magnetorheological (MR) shock absorber for a passenger vehicle was undertaken and several advantages of the optimized MR shock absorber on vibration control performance were shown. The optimization tool was built by using the ANSYS parametric design language and optimal geometries of this MR shock absorber were determined to maximize the damping force. It is finally remarked that the experimental implementation of the quarter-vehicle equipped with optimal MR shock absorber will be undertaken soon as a second phase of this work.

References

1. Wereley, N.M., Pang, L.: Nondimensional analysis of semi-active electrorheological and magnetorheological dampers using approximate parallel plate models. Smart Materials and Structures 7, 732–743 (1997)
2. Wei, H., Wereley, N.M.: Nondimensional damping analysis of flow mode magnetorheological andelectrorheological dampers. In: Proc. of IMECE 2003, 43135 (2003)
3. Delivorias, R.P.: Application of ER and MR fluid in an automotive crash energy absorber. Report No. MT04.18 (2004)
4. Walid, H.E.A.: Finite element analysis based modeling of magnetorheological dampers. Master's thesis, Virginia Polytechnic Institute and State University, Blacksburg (2002)
5. Li, W.H., Du, H., Guo, N.Q.: Finite element analysis and simulation evaluation of a magnetorheological valve. Int. J. of Advanced Manufacturing Technology 21, 438–445 (2003)
6. Rosenfield, N.C., Wereley, N.M.: Volume-constrained optimization of magnetorheological and electrorheological valves and dampers. Smart Materials and Structures 13, 1303–1313 (2004)
7. Nguyen, Q.H., Han, Y.M., Choi, S.B., Wereley, N.M.: Geometry optimization of MR valves constrained in a specific volume using finite element method. Smart Materials and Structures 16, 2242–2252 (2007)

Fractional-Order PID Control of Hydraulic Thrust System for Tunneling Boring Machine*

Ling Fei[1], Jingcheng Wang[1,**], Langwen Zhang[1], Yang Ge[1], and Kang Li[2]

[1] Department of Automation, Shanghai Jiao Tong University and Key Laboratory of System Control and Information Processing, Ministry of Education of China, Shanghai, 200240, China
[2] School of Electronics, Electrical Engineering and Computer Science, Queen's University Belfast
{feeling,jcwang}@sjtu.edu.cn

Abstract. The hydraulic thrust system is a major system of tunneling boring machine (TBM). It is known that the flow rate is dramatically fluctuant under conventional PID pressure control. At the same time the pressure is fluctuant when applying conventional PID flow rate control. Considering the dynamic performance of the hydraulic thrust system, we make use of fractional calculus which results in more satisfactory results. The fractional-order PID controller is adopted to control the hydraulic thrust system in this paper. The simulation is carried out with the AMESim software and the MATLAB/Simulink tool. The result shows that flow and pressure control using fractional-order PID controllers can reduce the flow rate and pressure fluctuation and make the flow rate and pressure track the set value faster.

Keywords: Tunneling boring machine, hydraulic thrust system, AMESim, fractional-order control.

1 Introduction

Hard rock tunneling boring machines (TBMs) are used in the large construction for the complicated rock environment. The basic advantages of TBMs are high safety and rapid excavation speed with low overbreak and low manpower. Meanwhile, TBM tunneling has small effects on the surrounding rock mass and construction[1].

The hydraulic thrust system is the key part of the hard rock TBM. The characteristic of the hydraulic thrust system is varying load, high power and low flow [2]. In the process of the tunneling, the hydraulic system undertakes the driving task. The cutter head can go along the planned alignment by the thrust force supported by the hydraulic system[3]. The total thrust force, which has to be exerted axially, is

* This work was supported by National 973 Program of China (No. 2013CB035406), National Natural Science Foundation of China (No. 61174059, 60934007, 61233004),Research Project of Shanghai Municipal Economic and Informatization Commission.
** Corresponding author.

J. Lee et al. (Eds.): ICIRA 2013, Part II, LNAI 8103, pp. 470–480, 2013.

transferred by the clamping mechanism into the rock. To prevent the tunneling route from deviation and make the machine tunnel steadily, the gesture and position should be adjusted by the thrust control system. Monitor scan display the real-time status information of the boring machine, which is helpful for the decision of the operator.

In this paper, we make use of the AMESim software to build up the simple hydraulic thrust system to simulate the actual working principle of the system.In the simulation, the proportional flow control valve and proportional relief valve can meet the dynamic characteristicand the static characteristic of actual valves. We use fractional-order PID controller (FO-PID) to make compensate for the disadvantage of the conventional PID. The objective is to achieve the smoothly transient response of the thrust speed and the pressure of the hydraulic cylinders.

2 Thrust System

2.1 System Principle

Due to the complicated environment of the excavation and some unpredicted factors, the requirements for controlling the hydraulic system will be more rigorous. The goal of the hydraulic control system is to achieve straight forward, curve forward, attitude control by the coordinated actions of the hydraulic cylinders in the different areas. At present, hydraulic cylinders are divided into several groups and controlled by groups. It is greatly desirable that the thrust pressure and velocity can achieve smooth and step less regulation [4]. So some researchers are focusing on solving these problems. The double shield TBM has two tunneling modes, which are the double shield tunneling mode and the single shield tunneling mode. When the surrounding rock mass has an autostability and can withstand the pressure of the gripper system, the double shield tunneling mode can be applied. On the contrary, another mode can be used. In two modes, the hydraulic thrust system plays the key role.

In Fig.1, it describes that the hydraulic system for TBM works according to the proportional pressure and flow regulation principle. The whole hydraulic thrust systems are comprised of main thrust systems and auxiliary thrust systems. The hydraulic cylinders are divided into four groups such as A, B, C, D groups. The Fig.1 shows A group of the main thrust system and A group of the auxiliary thrust system. In Fig.1, The proportional flow control valve and proportional relief valve can adjust the flow rate and the pressure of the normal-working cylinders. So it is necessary to control the output signals of the two valves.

2.2 System Modeling

The structure of the hydraulic system is complicated. It is not easy to build up the models of the complete system. For we only research on the thrust process of the hydraulic system, we can simplify the basic structure of the system. The simplified system is shown in Fig.2. The thrust system contains one proportional relief valve, one proportional control flow valve, one direction-change over valve, hydraulic cylinders and dynamic loads.

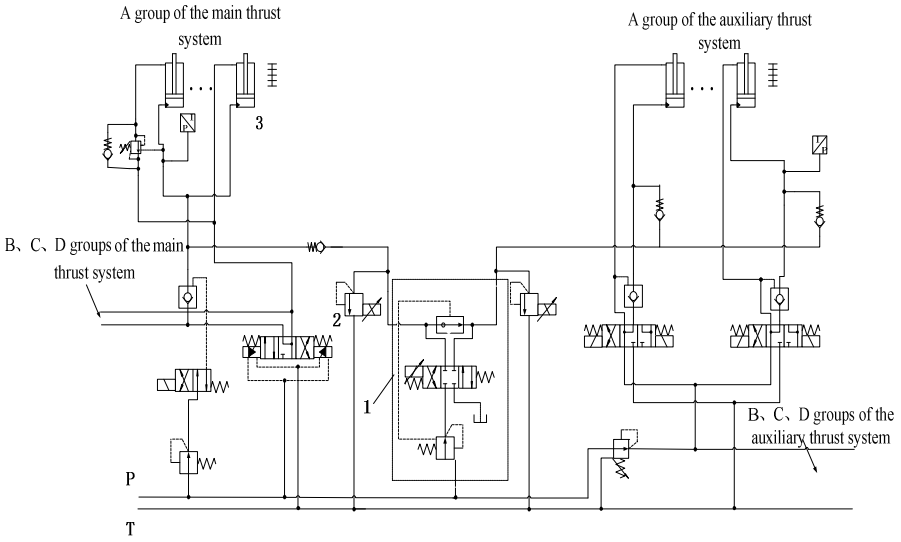

Fig. 1. Hydraulic circuit diagram of thrust system in the tunneling boring machine

(1、dual proportional control flow valve 2、proportional relief valve 3、hydraulic cylinders)

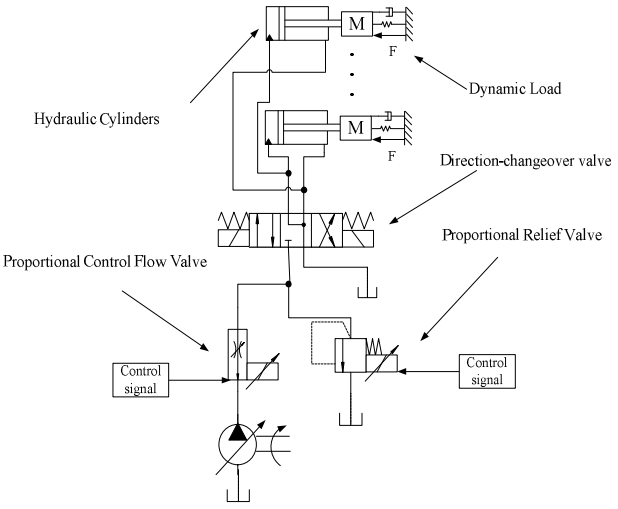

Fig. 2. Principle diagram for hydraulic cylinders of the hydraulic thrust system

In this paper, we take advantage of theAMESim software to simulate the simplified system.The output flow rate of the proportional flow control valve ranges from 0.1-25 $L/\min$ .And the maximum working pressure of the valve is 42 MPa . The maximum pressure controlled by the proportional relief valve is 31.5 MPa . The load of the

hydraulic cylinder is a linear viscoelastic model. The model that we build up can be seen in Fig.3.

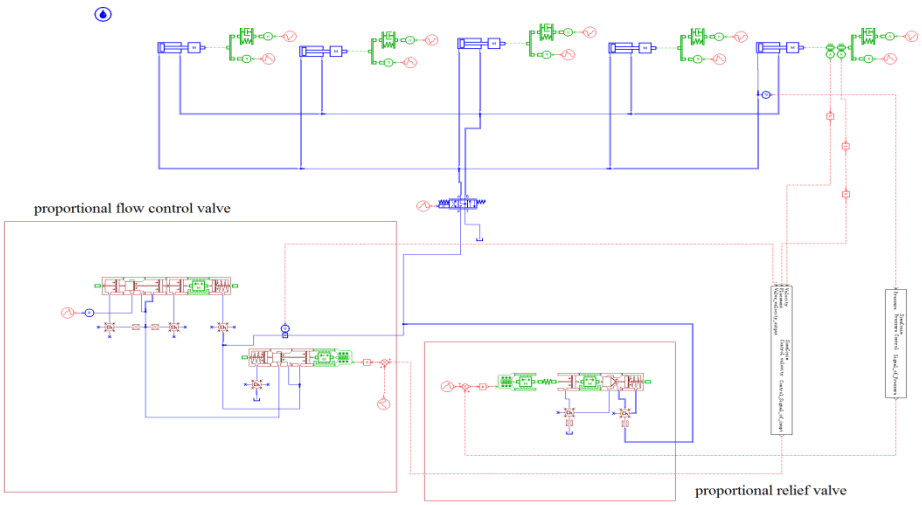

Fig. 3. The model of the hydraulic thrust system built up by the software AMESim

3 Control and Optimization Strategy

3.1 Fractional-Order PID Controller

Recently, in the field of control, the fractional-order theory and application have attracted increasing attention [5].Fractional-order control (FOC), which introduces the fractional calculus into the control field, has been used as an alternative strategy to solve robust control problems.

A fractional-order differentiator can be described by ageneral fundamental operator as a generalization of differential and integral operators, which is defined as follows[6].

$$ {}_aD_t^{\lambda} = \begin{cases} \dfrac{d^{\lambda}}{dt^{\lambda}} & ,R(\lambda) > 0 \\ 1 & ,R(\lambda) = 0 \\ \int_a^t (d\tau)^{-\lambda} & ,R(\lambda) < 0 \end{cases} \tag{1} $$

where λ is the fractional-order which can be a complex number, a and t are the limits of the operation (here $a = 0$).

The generally used definitions of fractional-order derivatives are the Riemann-Liouville (RL) definition, the Grünwald-Letnikov (GL) definition, and the Caputo

definition[7]. In this paper, we use the Caputo definition. The Caputo definition is described as follows:

$$D^q f(t) = \frac{1}{\Gamma(m-q)} \int_0^t \frac{f^{(m)}(\tau)}{(t-\tau)^{q-m+1}} d\tau \tag{2}$$

where q is the fractional-order, m is the integer that $m-1 < q < m$, and $\Gamma(\bullet)$ is the Euler Gamma function.

For the Caputo definition, the most general expression of the Laplace transform of the fractional-order derivative is given as:

$$L\{D^q f(t)\} = s^q F(s) - \sum_{k=0}^{m-1} s^{q-k-1} f^{(k)}(0) \tag{3}$$

where $\mathrm{F}(\mathrm{s}) = \mathrm{L}\{f(t)\}$. If the initial conditions are zero, then the fractional-order derivative can be shown as follows:

$$L\{D^q f(t)\} = s^q F(s) \tag{4}$$

In fact, the fractional-order PID controller is the spread of the integer-order PID controller. The integer-order PID is just the special case of the fractional-order PID. The detail description is shown in Fig.4.Except that four points belongs to integer-order controllers, other parts are the field of fractional-order controllers.

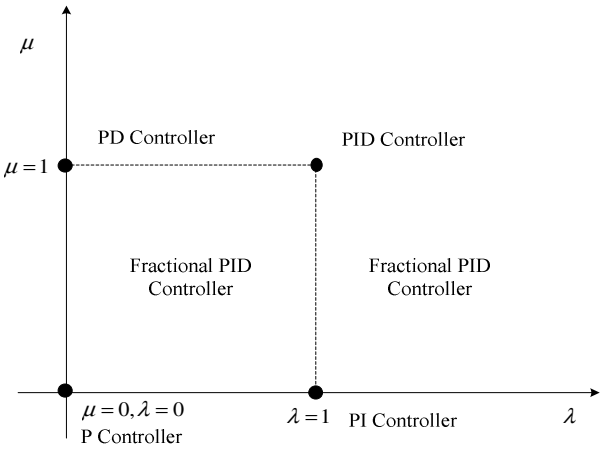

Fig. 4. The relationship between thefractional-order PID controller and the integer-order PID controller

3.2 Parameters Optimization

The fractional-order PID controller is shown as follows:

$$C_{fopi}(s) = fk_p + \frac{fk_i}{s^{f_r}} + fk_d s^{f_d} \tag{5}$$

The parameters fk_p, fk_i, fk_d, f_r, f_d of the fractional-order controller need to be calculated. In general speaking, the parameters of f_r, f_d range from 0 to 2. We can use the particle swarm optimization (PSO)algorithm to search the locally optimal solutions as the desirable values of the parameters [8].

The global version PSO algorithm converges fast, but it is easy to get caught in the local optimum. The local version PSO algorithm converges slowly, but relatively it is not easy to fall into the local optimum. In this paper, we make use of the improved PSO algorithm combined with the advantage of the global PSO algorithm, the local PSO algorithm and a dynamic inertia weight PSO algorithm. We consider the local impacts in the dynamic inertia weight PSO algorithm,make use of local mean values to avoid falling into the local optimum and use the global optimum to accelerate the convergent. We suppose the ith particle has n neighbors. Then the positions of $n+1$ particles can be represented as $(P_1, P_2, \ldots, P_{n+1})$. The average positionof the $n+1$ particles can be calculated as follows:

$$p_a = \sum_{i=1}^{n+1} \frac{P_i}{n+1} \tag{6}$$

where P_i is the position of the ith particle. The velocity updating equation of the improved PSO algorithm is represented[9]:

$$\begin{aligned} V_i(t+1) = {} & \omega_1(t)V_i(t) + c_1 r(P_i(t) - X_i(t)) \\ & + c_2 r(P_g(t) - X_i(t)) + c_3 r\omega_2(t)(P_a(t) - X_i(t)) \end{aligned} \tag{7}$$

$$\omega_1(t) = (0.5 + r/2.0) \tag{8}$$

$$\omega_2(t) = \omega_{2\max} - (\omega_{2\max} - \omega_{2\min})t / t_{\max} \tag{9}$$

And

$$X_i(t+1) = X_i(t) + V_i(t+1) \tag{10}$$

where $P_i(t)$ is the best position of the ith particle. $P_g(t)$ is the global best position of the particles. c_1, c_2, c_3 are the non-negative constants. r is the random number ranging from 0 to 1. In this paper, we put the ITAE index of the velocity and pressure deviation as the fitness function.

$$J_{ITAE} = \sum_{i}^{n} T \times |e(i)| \tag{11}$$

whereT is the sampling period. n is the number of the sampling.

4 Simulation

In the hydraulic control system, the main controlled variables are the thrust velocity and pressure of the hydraulic cylinders. The controlled object is built up based on the AMESim software. Using the simulink interface in AMESim software, the model can be applied in the MATLAB/Simulink environment. It is helpful for us to make use of the controller to control the object in the MATLAB/Simulink environment.

In the velocity/pressure control experiment, the structure of the control system is in Fig.5.The model built up by the AMESim software consists of a proportional flow control valve, a proportional relief valve, hydraulic cylinders and dynamic loads. The parameters of Lower_limit and Upper_limit are constrained by the characteristic of the valves.In this paper, we mainly analyze the control effect based on the PID controller and FO-PID controller. The parameters of the conventional PID controller can be got by the trial and error method. We can get the values of k_p, k_i, k_d successively according to the output effect. The values of fk_p, fk_i, fk_d, f_r, f_d can be calculated by the PSO optimum algorithm.

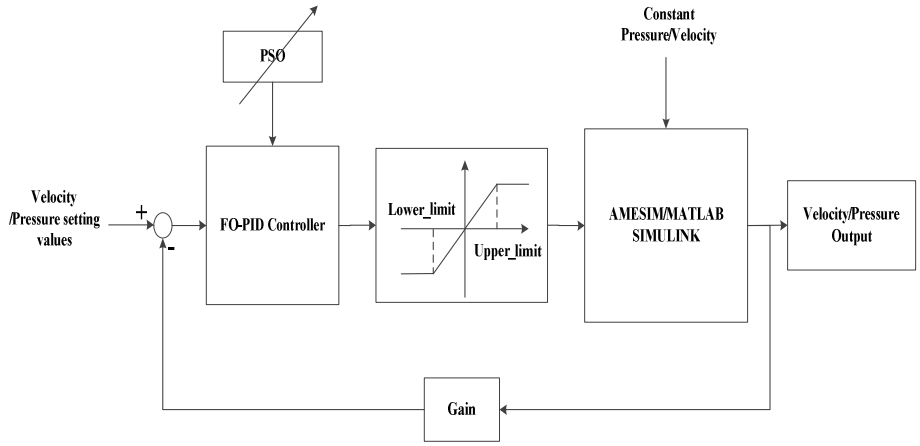

Fig. 5. The structure of the velocity/pressure control system with fractional-order PID controller

4.1 Velocity Control

The detail parameters for the PID controller and the fractional-order PID controller are shown in Table 1. The methods of getting the parameters are mentioned above. In Fig.6, the initial setting value of the thrust velocity is 40 $\mathrm{mm/min}$ when the simulation time ranges from 0 s to 10 s and 60 $\mathrm{mm/min}$ when the simulation time ranges from 10 s to 20 s. From the Fig.6, we can see that it is faster and more stable for using the fractional-order PID controller to track the setting velocity than the conventional PID controller. When the fractional-order PID controller is applied,

the stable time decreases, and the oscillation amplitude becomes small. The total performance index is better for the fractional-order PID controller. We can find that the output variable amplitudes for both the PID controller and the FO-PID controllerfrom $0\,s$ to $1\,s$ are large. One reason is that the proportional relief valve can generate large flow response instantly when starting and then it will achieve the stable flow rate rapidly. Another reason is that in order to make the control error close to zero, we need to change controllers' variables which will make an influence on the oscillation amplitudes.In Fig.7, pressure can be affected by the velocity control. Especially when the velocity step response happens, corresponding pressure will be changed. Because the change of the velocity can make the dynamic loads change. The constant load is set as $25\,MPa$. But in the control process, we need to consider the effect of the dynamic load. We can see that when the time is $0\,s$ and $10\,s$, thevelocity response happens. Using the fractional-order PID controller, the pressure oscillation is smaller.

Table 1. Parameters of conventional PID and fractional-order PID

Controller	Conventional PID	Fractional-order PID
k_p (fk_p)	0.02	0.0197
k_i (fk_i)	0.3	0.1953
k_d (fk_d)	0.0016	0.0011
f_r	—	1.2010
f_d	—	0.5136

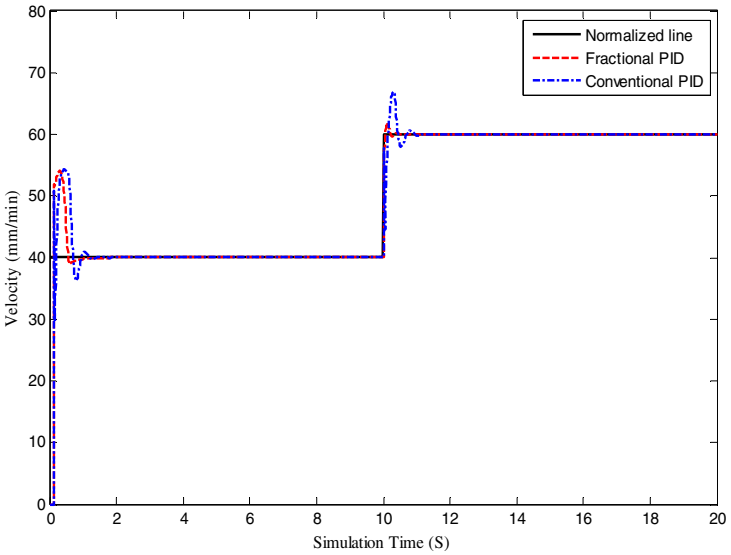

Fig. 6. Flow rate response in the PID controller and the fractional-order PID controller

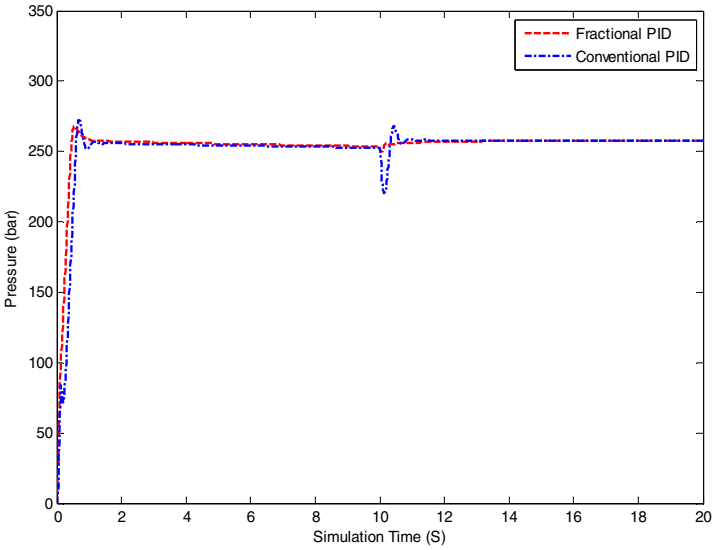

Fig. 7. Pressure changes in the velocity control for different controllers

4.2 Pressure Control

Certainly, in some conditions, we also need to control pressure to achieve different values. At the same time, the thrust velocity can be stable in the setting values. In this paper, we make use of the fractional-order PID controller built up in the velocity control to keep the thrust velocity stable. The parameters for the velocity controller can be seen in Table1. Then we try a PID controller and a fractional-order PID controller to control the pressure. The parameters for the pressure controllers are shown in Table2. In the pressure control, the velocity setting value is 60 mm/min . In Fig.8, the initial setting value of the pressure is 200 bar when the simulation time ranges from 0 s to 10 s and 250 bar when the simulation time ranges from 10 s to 20 s . In the pressure control, the oscillation amplitude when using the conventional PID controller is larger than using the fractional-order PID controller. And the fractional-order PID controller can make pressure track the setting value fast. The stable time is shorter. In Fig.9, when we make use of different pressure controllers, the thrust velocity controlled by the fractional-order PID controller can be affected. But in the mass, the velocity can be stable in the 60 mm/min .

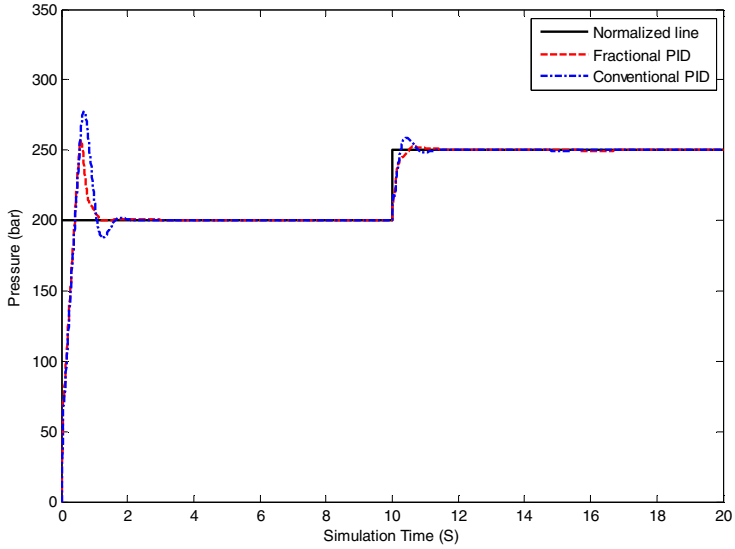

Fig. 8. Pressureresponse in the PID controller and the fractional-order PID controller

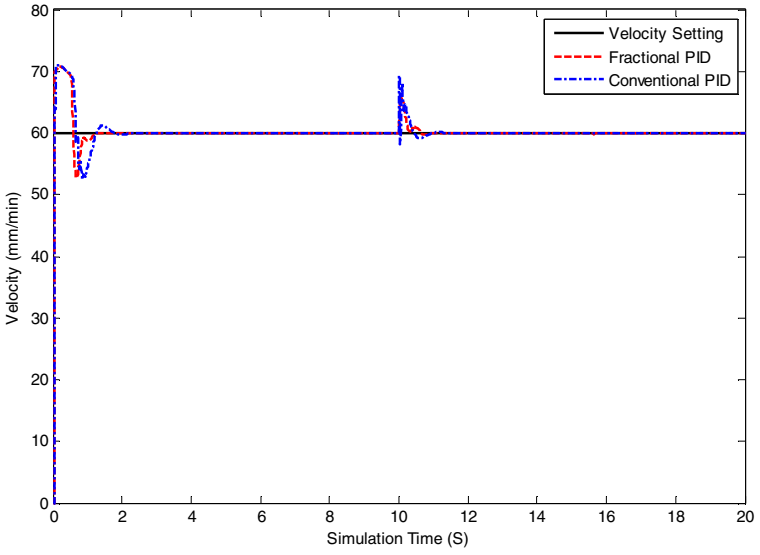

Fig. 9. Velocity changes in the pressure control for different controllers

Table 2. Parameters of conventional PID and fractional-order PID

Controller	Conventional PID	Fractional-order PID
k_p (fk_p)	0.05	0.0083
k_i (fk_i)	0.40	0.2715
k_d (fk_d)	0.01	0.0081
f_r	—	1.0987
f_d	—	0.4203

5 Conclusion

The hydraulic system has the characteristic of the nonlinearity, complexity and variable loads. In this paper, an electro-hydraulic control system with pressure and flow control for double shield TBM has been put forward. The model of the hydraulic thrust system is built up by the AMESim software. In the MATLAB/Simulink environment, the pressure and velocity can be controlled by a FO-PID controller and a PID controller. By analyzing the results of the co-simulation, we can find that the FO-PID controller can make the controlled parameters track the set value faster and more steadily and make lower oscillation amplitude than the PID controller.At the same time, the application of FO-PID controllers which are the spread of PID controllers can increase the adjustable dimensionality of parameters.Further research on this project needs to consider the uncertain of the geological condition and nonlinearity of load dynamics and electro-hydraulic system itself in the process of tunneling.

References

1. Okubo, S., Fukui, K., Chen, W.: Expert system for applicability of tunnel boring machines in Japan. Rock Mechanics and Rock Engineering 36(4), 305–322 (2003)
2. Kunzhou, H., Liping, X., Dezhi, R.: Hydraulic thrust system researchbased on single neuron adaptive PID controlfor double shield TBM. Fluid Power Transmission and Control (1), 39–41 (2010)
3. Maidl, B., Schmid, L., Ritz, W., et al.: Hardrock tunnel boring machines. Wiley-VCH (2008)
4. Huayong, Y., Hu, S., Guofang, G., et al.: Electro-hydraulic proportional control of thrust system for shield tunneling machine. Automation in Construction 18(7), 950–956 (2009)
5. Monje, C.A., Vinagre, B.M., Feliu, V., et al.: Tuning and auto-tuning of fractional order controllers for industry applications. Control Engineering Practice 16(7), 798–812 (2008)
6. Manabe, S.: Early development of fractional order control, pp. 2–6
7. Samko, S.G., Kilbas, A.A., Marichev, O.I.: Fractional Integrals and Derivatives: Theory and Applications, Gordon and Breach, Yverdon (1993)
8. Zhou, C., Gao, H.-B., Gao, L., et al.: Particle Swarm Optimization (PSO) Algorithm. Application Research of Computers 12, 7–11 (2003)
9. Hongqing, F., Zuyi, S.: Optimal hydraulic turbo generators PID governor tuning with an improved particle swarm optimization algorithm. Proceedings of the CSEE 25(22), 120–124 (2005)

Finite Element Research on Cutting Force and Temperature in Milling 300M Steel

Sen Lin[1], Fangyu Peng[2,*], Yizhi Liu[1], Sheng Yang[1], and Rong Yan[1]

[1] National Numerical Control System Engineering Research Center,
School of Mechanical Science and Engineering,
Huazhong University of Science and Technology, Wuhan 430074, China
{eversun1,101sunrise101}@163.com, yizhi_liu0623@126.com,
siqizaizai@yahoo.com.cn
[2] State Key Laboratory of Digital Manufacturing Equipment and Technology,
School of Mechanical Science and Engineering,
Huazhong University of Science and Technology, Wuhan 430074, China
zwm8917@263.net

Abstract. Cutting force and temperature are major concerns in the aircraft landing gear manufacture to implement milling for 300M steel. These two factors strongly influence the surface characteristics of a machined product that have close relation with functional performance of the product. This paper describes investigations realised to perform simulations of end milling operations on 300M steel via AdvantEdge FEM software. In the simulations, the geometry of cutting tool is measured by coordinate measuring machine and modeled in UG software. The material flow stress data are obtained from Split Hopkinson Bar experiment. The material behaviour is modelled with a classical Johnson–Cook law to accomplish the thermo-mechanical analysis. Good agreements between the numerical results and experimental data at various cutting velocities prove that the proposed model is capable of predicting the cutting forces and temperatures during milling of 300M steel accurately.

Keywords: Cutting force, Workpiece temperature, Finite element method (FEM), Constitutive model, End milling.

1 Introduction

300M steel possesses excellent comprehensive properties, such as high strength, good fatigue resistance performance, high stress corrosion resistance, low crack growth rate. Additionally, it is suitable for manufacturing integral forging. Owing to these advantages, 300M steel becomes a typical landing gear material and is extensively applied in aviation industry nowadays. Meanwhile, 300M steel belongs to difficult-to-machine material because its processability is impacted negatively by some material characteristics, such as high hardness and low thermal conductivity, etc.

* Corresponding author.

J. Lee et al. (Eds.): ICIRA 2013, Part II, LNAI 8103, pp. 481–490, 2013.

With the development of aviation industry, the requirements for the qualities and surface integrities of aeronautical components are increasing. The high cutting force and temperature during the process of 300M steel influence the tool life and the surface qualities of aviation parts heavily. Therefore, to better predict cutting force and temperature distribution has a great significance to control surface integrity, tool wear, size accuracy and machining efficiency.

Currently, there are many ways, which contains experimental methods, analytical approaches and numerical methods, to study cutting forces and temperatures. As for nonlinear problems caused by material properties, deformation states and boundary conditions, etc [1], numerical methods represented by FEM has become effective tool to reflect actual cutting process faithfully. But until now, numerical models have focused on orthogonal or oblique cutting. The success in developing quantitative finite element (FE) models for complicated metal machining processes like milling has not been widely reported.

Maurel-Pantel [2] conducted three-dimensional (3D) FEM simulations of shoulder milling operations on a 304L stainless steel using LS-Dyna software. Pittalà [3] used OXCUT software to obtain flow stress parameters and calibrated Johnson-Cook (JC) rheological model of Ti-6Al-4V from different milling tests. The workpiece thermal simulations for milling are performed by FEM software DEFORM-2D and DEFORM-3D. Man [4] presented a 3D explicit dynamic Lagrangian FE-based model to predict cutting force for end milling. Ding [5] undertook 3D hard turning simulations via AdvantEdge FEM software to investigate the surface microstructure alteration for AISI 52100 steel. Despite the relevance of the matter, very meager work has been dedicated to FEM analyses for super high strength steel in milling.

In order to optimize milling of the 300M super high strength steel, it is desirable to develop models capable to predict cutting forces and workpiece temperatures during the material removal processes. One of the most important issues is the identification of material constitutive law. In this paper, the material behaviour is modeled with a classical JC law [6]. The JC parameters are determined by using Split Hopkinson Bar (SHPB) technique which is a commonly used means. Milling tests on 300M steel are carried out in order to validate the proposed FE model. Reasonably close matches are obtained between the experimental and simulated results.

2 Thermo-Mechanical FE Model for End Milling

AdvantEdge FEM, which was published by Third Wave Systems Company in 1998, is a special modeling software for metal cutting. There are abundant standard cutting tool and workpiece material types in its material database. Moreover, it supports user-defined constitutive models. AdvantEdge FEM combines FE technology with a graphic interface designed for metal cutting simulations. Users only need to complete a few steps, such as defining tool geometries, material conditions, and machining parameters, to set up the entire simulation. FE analysis of cutting force and workpiece temperature in milling 300M steel based on coupled thermo-mechanical model is also performed by AdvantEdge FEM in this paper.

2.1 Geometric Modeling

Generally, the geometry of milling cutter is complex. Tool parameters are usually unknown. Therefore, tool geometric model can be obtained by reverse modeling methodology. A Hexagon articulated arm flexible coordinate measuring machine (CMM) shown in Fig. 1 is used to measure tool shape. The measurement result is shown in Fig. 2(a). These point clouds of cutting tool are edited and processed in imageware software. As shown in Fig. 2(b), Solid rebuilding of 3D tool model is accomplished with UG software.

Fig. 1. Hexagon articulated arm flexible CMM

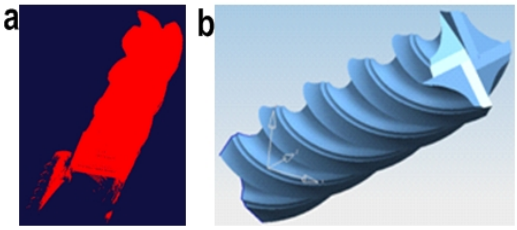

Fig. 2. Reverse modeling of cutting tool. (a) Tool point clouds; (b) Tool geometric model.

The tool model is intercepted in appropriate length to avoid unnecessary computing. The tool and workpiece 3D models are imported into AdvantEdge FEM. As shown in Fig. 3, the position relation and relevant movement relation between the tool and workpiece should be adjusted. In addition, boundary conditions should be set up.

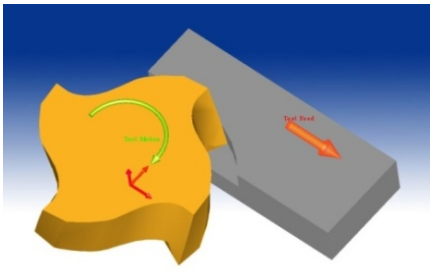

Fig. 3. Geometric modeling in AdvantEdge FEM

2.2 300M Steel Constitutive Model and SHPB Compression Experiment

In the cutting process, the material is removed under the condition of high temperature, high strain and high strain-rate. Considering this, to construct a material constitutive model including all these factors is important for guaranteeing the accuracy and reliability of FE analysis.

Recently, there are a lot of thermo-visco-plastic constitutive models, such as Johnson-Cook model [6], Zerrilli-Armstrong model [7] and Bodner-Paton model [8]. All of them can be used to describe material dynamic performance in mental cutting. JC model is widely accepted and has a simple form. It can reflect the thermal softening effect, strain-hardening effect and strain rate strengthening effect. It can be expressed as follows:

$$\sigma = (A + B\varepsilon^n)\left(1 + C\ln\frac{\dot{\varepsilon}}{\dot{\varepsilon}_0}\right)\left(1 - \left(\frac{T - T_r}{T_m - T_r}\right)^m\right) . \quad (1)$$

where ε is the equivalent plastic strain, $\dot{\varepsilon}$ is the equivalent plastic strain rate, $\dot{\varepsilon}_0$ is the reference plastic strain rate, T is instantaneous temperature of the workpiece material, Tr and Tm are room temperature and melting temperature, respectively. A, B, C, m, n are the material constants.

The 300M steel (52 HRC) studied in this paper is made in china. Its chemical composition is shown in Table 1. The 300M steel included in the workpiece material database of AdvantEdge FEM conforms to the American standard, which is a little different from the 300M steel in this research. So the constitutive model of 300M steel made in china should be established in the following discussion.

Table 1. Chemical composition of 300M steel

Composition	Ni	Si	Cr	Mn	Mo
Mass percentage %	1.65~2.00	1.50~1.80	0.70~0.95	0.65~0.90	0.35~0.50
Composition	Al	V	Sn	P	Ti
Mass percentage %	≤ 0.18	0.05~0.10	0.02	≤ 0.01	≤ 0.01
Composition	C	Cu	S	Fe	
Mass percentage %	0.38~0.43	≤ 0.35	≤ 0.008	Balance	

In the FE analysis, it is necessary to know the flow stress of the workpiece material under high strain, strain rate and temperature conditions that exist in practical cutting operations. SHPB compression experiment is adopted to obtain dynamic mechanical properties of 300M steel. The high temperature SPHB system consists of impact loading apparatus, striker bar, input bar, output bar, transmitter bar, heater installation and measuring instrument, as shown in Fig. 4(a). It is used to measure the true flow stress and true strain relationship for 300M steel from a strain rate of 500 to 3000 s^{-1} and from room temperature to 500 ℃. The test piece is designed as 10 mm in diameter and 15 mm in height as shown in Fig. 4(b). The roughness of the columnar surface is lower than Ra1.6 to reduce the friction between the test piece and bars.

The parameters in JC model can be obtained by fitting the flow stress curves. The curve segments for fitting should be selected very carefully, because values of parameters are likely to be inaccuracy if inappropriate curve segments are adopted. Additionally, the parameters in JC model can influence prediction accuracy greatly. After data processing, the material constitutive model parameters can be determined as follows: A = 1293.9, B = 1008.2, n = 0.0383, C = 0.014, m = 1.7362. The simulations are undertaken using this user-defined constitutive model.

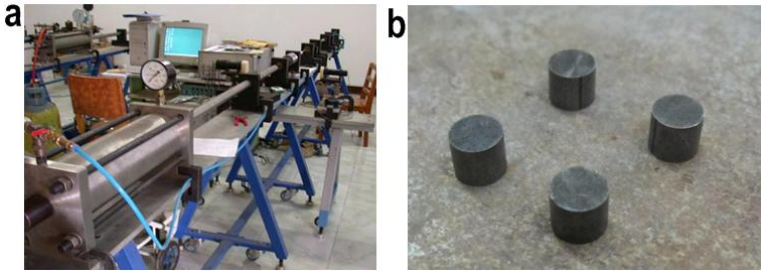

Fig. 4. SHPB experiment. (a) SPHB experimental system; (b) Experimental samples.

3 Milling Experiments

Milling experiments are conducted on Mikron five-axis machine center UCP800, as shown in Fig. 5(a). A SANDVIK monolithic carbide mill R216.34-20050-AK38H 1620 with 4 flutes is used in this research. The diameter is 20 mm. The workpiece material is 300M steel which is made in China. The hardness HRC = 52 after heat treatment. Up milling without cutting fluid is adopted. Piezoelectric dynamometer Kistler 9257B, Charge Amplifier 5070A and NI data acquisition system are applied to measure and record the three components of the cutting forces on the workpiece. The transient workpiece temperature profiles are measured by INOR fast response thermocouples whose diameters are 2 mm, as shown in Fig. 5(b). Thermocouples are inserted in blind holes of the workpiece. The thermocouples locate along the central line of the machined surface and keep a distance of 0.5 mm away from it. This arrangement can prevent them from being destroyed.

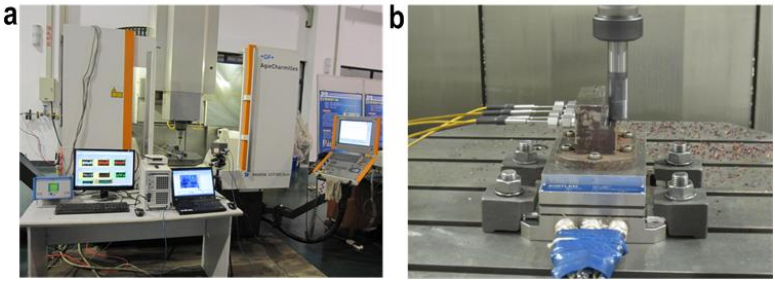

Fig. 5. Milling experiments setup. (a) Image of settings; (b) Detail view of test piece.

To assess the validity of the FE model, experiments is conducted under a set of machining parameters listed in Table 2.

Table 2. Machining parameters

axial depth of cut (mm)	radial depth of cut (mm)	feed rate (mm/tooth)	spindle speed (rev/min)
2	4	0.07	800, 1100, 1400

4 Results and Discussion

To verify the accuracy and effectiveness of this model, milling conditions as indicated in Table 2 are simulated via AdvantEdge FEM 3D. The comparisons of experimentally determined cutting forces and predicted values are presented in Fig. 6. Because of the long computing time, the process during a half of tool revolution period is simulated. The three-axis force predictions match well with the experimental data for various spindle speed amounts. The errors are controlled within 10% for average cutting forces. It is shown that the cutting forces have no increment and change slightly with the increasing cutting velocity.

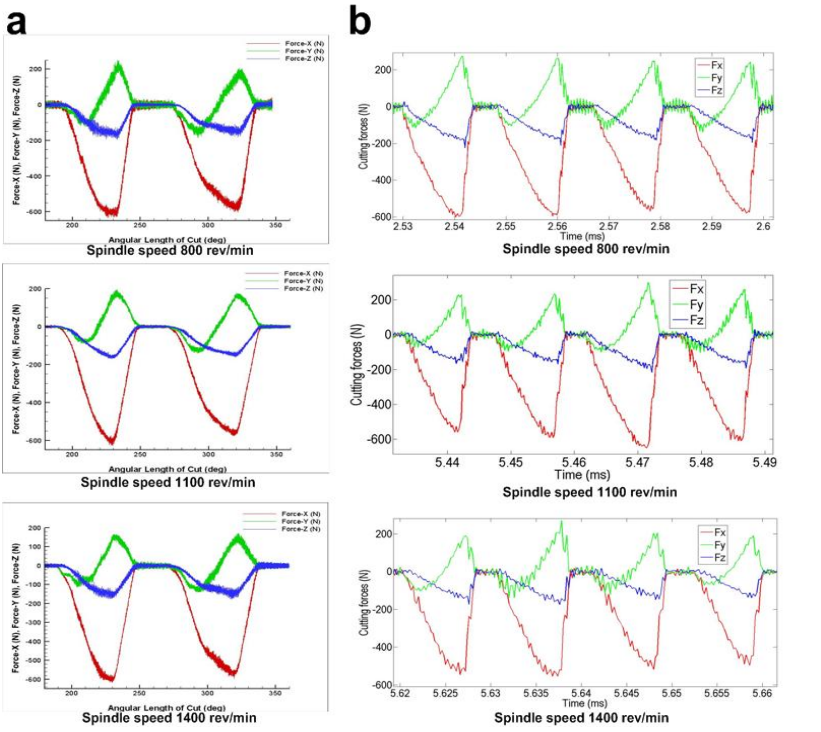

Fig. 6. Three components of the cutting forces at the varying of cutting velocities. (a) Predicted results; (b) Experimental results.

Temperature profiles recorded by three thermal couples in tests are shown in Fig. 7. It can be seen that temperatures of measuring points rise and fall with the tool getting close to and far away from them. The significant impact of cutting velocity on workpiece temperature can also be observed. The workpiece temperature increases rapidly with the increasing cutting velocity. Average peak temperatures of measuring points are about 72 ℃, 88 ℃ and 100 ℃ with spindle speed 800 rev/min, 1100 rev/min and 1400 rev/min.

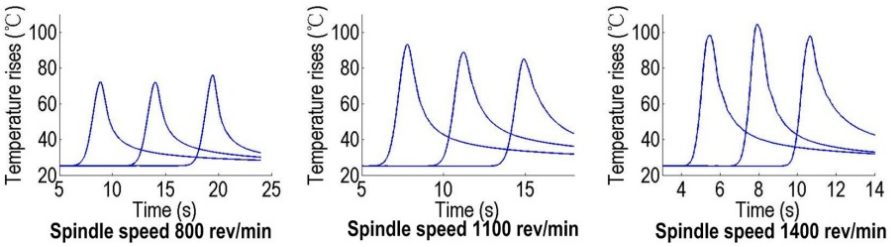

Fig. 7. Temperature histories of measuring points at the varying of cutting velocities

In order to compare the predicted workpiece temperatures and experimental results clearly, a slice is made on the workpiece in FE model, as shown in Fig. 8. Both the chip and tool are removed. To ensure the measuring points on the slice, the slice is set to be parallel to the machined surface and the distance between them is 0.5 mm. The temperature distributions of slices are shown in Fig. 9. The maximum temperatures are also in good agreement with the peak temperatures of measuring points shown in Fig. 7. The maximum temperatures of slices are about 63 ℃, 78 ℃ and 94 ℃ with spindle speed 800 rev/min, 1100 rev/min and 1400 rev/min. It can be concluded that errors are controlled within 15%.

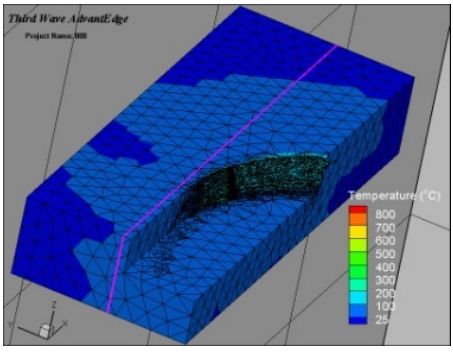

Fig. 8. Validated slice in workpiece

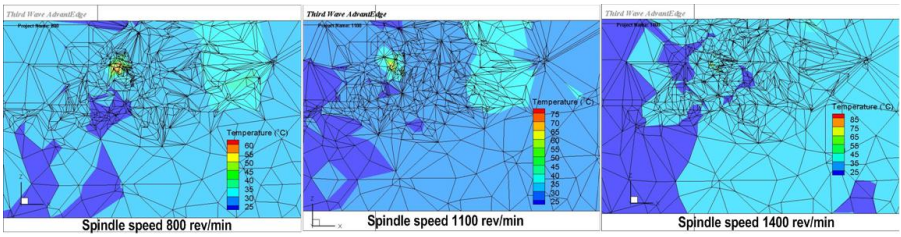

Fig. 9. Temperature distributions on slices with different spindle speed

It is obvious that both the amplitude of workpiece temperature and area of high temperature zone increase with the increasing immersion angle of cutting tool, as shown in Fig. 10. That is owing to the increasing instantaneous chip thickness. At the spindle speed of 1400 rev/min, the highest temperature of tool-workpiece contact area is about 970 ℃, which occurs in the pink circle as shown in Fig. 11. Under the condition of low cutting velocity, even at the spindle speed 800 rev/min, that is still higher than 890 ℃, which is also over austenitic temperature of 300M steel. In general, when the material temperature is raised above its austenitic temperature, combined with high pressure generated by the action of the tool, the tempered martensite transforms to austenite. And after the tool leaves, the austenite converts to un-tempered martensite as the temperature cools down quickly [5,9]. Therefore, if there is the corner feature in the workpiece, the thermal damage is likely to occur on the final machined surface of the corner feature.

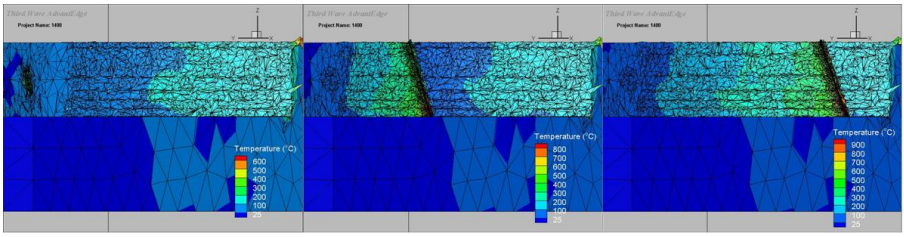

Fig. 10. Workpiece temperature varying with tool rotation angle

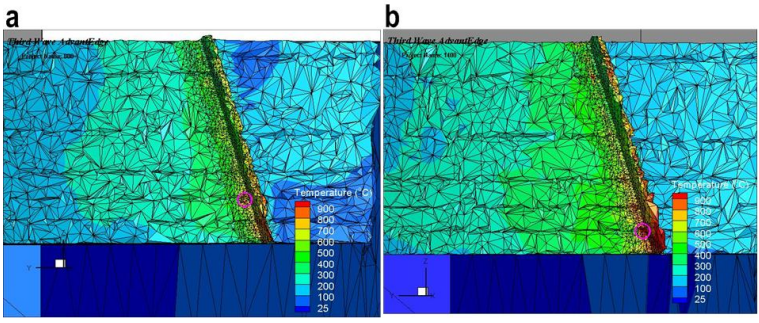

Fig. 11. Temperature of tool-workpiece contact area. (a) Spindle speed = 800 rev/min; (b) Spindle speed = 1400 rev/min.

5 Conclusion

The paper calibrates parameters in JC constitutive model of 300M steel and presents a FE model to investigate the cutting force and workpiece temperature in end milling of 300M steel. It is evident that the coupled thermo-mechanical simulations accurately predict the cutting forces and workpiece temperatures at the varying of cutting velocities. The good agreements obtained between the experimental and numerical results indicate that the proposed material model and the simulation strategy are suitable for studying the influence of cutting parameters on cutting force and workpiece temperature during milling of 300M steel.

The values of parameters in JC model influence the results of cutting force and cutting temperature heavily. In order to improve the accuracies of parameters in JC model, appropriate curve segments should be selected from the whole flow stress curve obtained by SPHB experiment. The precise parameters determined by fitting the curve segments can control the cutting force error and cutting temperature error.

For the simulation results it is found that the temperatures of tool-workpiece contact area increase with the increasing cutting velocity and immersion angle. It can reach 970 ℃ at a cutting velocity of 88 m/min, and all the maximum temperatures of tool-workpiece contact area for the whole range of cutting velocities in the experiments are over material austenitic temperature. Therefore, thermal damages may happen especially for corner features of aircraft landing gear components in the aviation industry.

The achievements obtained in this paper provide theoretical and experimental support on the future work of studying surface integrity on 300M steel. The method of developing the FE model adopted in this paper can also be applied to other materials.

Acknowledgements. This work was financially supported by the National Natural Science Foundation of China (51075168, 51275189) and 973 National Basic Research Program of China (2011CB706803).

References

1. Fang, G., Zeng, P.: Three-dimensional thermo–elastic–plastic coupled FEM simulations for metal oblique cutting processes. Journal of Materials Processing Technology 168, 42–48 (2005)
2. Maurel-Pantel, A., Fontaine, M., Thibaud, S., Gelin, J.C.: 3D FEM simulations of shoulder milling operations on a 304L stainless steel. Simulation Modelling Practice and Theory 22, 13–27 (2012)
3. Pittalà, G.M., Monno, M.: A new approach to the prediction of temperature of the workpiece of face milling operations of Ti-6Al-4V. Applied Thermal Engineering 31, 173–180 (2011)
4. Man, X.L., Ren, D.Y., Usui, S.J., Johnson, C., Marusich, T.D.: Validation of Finite Element Cutting Force Prediction for End Milling. In: 5th CIRP Conference on High Performance Cutting, pp. 663–668 (2012)
5. Ding, H.T., Shin, Y.C.: Multi-physics modeling and simulations of surface microstructure alteration inhard turning. Journal of Materials Processing Technology 213, 877–886 (2013)

6. Johnson, G.R., Cook, W.H.: Fracture characteristics of threemetals subjected to various strains, strains rates, temperatureand pressure. Engineering Fracture Mechanics 21(1), 31–48 (1985)
7. Zerilli, F.J., Armstrong, R.W.: Dislocation mechanics based constitutive relations for material dynamics calculations. Journal of Applied Physics 61(5), 1816–1825 (1987)
8. Bodner, S.R., Parton, Y.: Constitutive equations for elastic-viscoplastic strain hardening materials. ASME. J. Appl. Mech. 4-2, 385–389 (1975)
9. Umbrello, D., Jawahir, I.S.: Numerical modeling of the influence of process parameters and workpiece hardness on white layer formation in AISI 52100 steel. International Journal of Advanced Manufacturing Technology 44, 955–968 (2009)

Experimental Study of Surface Integrity of Aluminum Lithium Alloy by Face Milling

Haikuo Mou*, Xinda Huang, Xiaoming Zhang, and Han Ding

State Key Laoratory of Digital Manufacturing Equipment and Technology,
Huazhong University of Science and Technology, Wuhan 430074, China
haikuo.mou@gmail.com

Abstract. Aluminum lithium alloy will likely become the material of choice over composites as the fuselages of the next generation of narrow-body aircraft due to its high strength to weight ratio and excellent corrosion resistance. In this paper, aluminum lithium alloy samples are milled under air coolant condition and liquid nitrogen condition. Surface integrity factors including roughness and residual stress are measured. The results show that the angle between feed direction and rolling orientation dominates in the formation of surface finish, which is often neglected in previous study. The results also demonstrate the capacity of liquid nitrogen on improving the surface integrity followed by an increase of material removal rate in face milling of aluminum lithium alloy. Finally, the regression models for roughness and residual stress are established and the effectiveness of these models are validated.

Keywords: aluminum lithium alloy, surface integrity, cryogenic machining.

1 Introduction

Aluminum lithium alloy is demonstrating promising capacity as structural component material in aerospace industry for its high strength to weight ratio, excellent corrosion resistance, and good spectrum fatigue crack growth performance. It has been reported that the application of aluminum lithium alloy in aerospace can be tracked back to 1950's, while the limitation of property anisotropy and poor manufacturing issues prevent the widespread usage[1]. For the purpose of sustainable manufacturing, the mechanical milling process is gradually taking the place of chemical milling in the manufacturing process of airframe skins. What is the surface topography, residual stress state, micro-hardness, subsurface material alteration of third generation aluminum lithium alloy like after mechanical milling still remains not being well investigated in the open literature.

1.1 Surface Roughness

Surface roughness is a universal requirement for mechanical products which plays an important role in accuracy and service life of components [2]. Dewes[3] conducted a

* Corresponding author.

J. Lee et al. (Eds.): ICIRA 2013, Part II, LNAI 8103, pp. 491–502, 2013.

full experimental design to investigate the effect of cutting speed and feed rate on the surface roughness and formulated a response model to predict the surface roughness. Radhakrishnan[4] used graphite as a lubricating medium in the grinding of En-31 steel. The influence of process parameters such as speed, feed, infeed and mode of dressing on surface finish has been obtained. Ghani[5] adopted Taguchi method to achieve the optimal parameters in the machining of AISI H13 with TiN coated P10 carbide insert tool. The interaction among milling parameters were also taken into consideration.

1.2 Residual Stress

The residual stress introduced by material removal process has a significant influence on the fatigue behavior of component. Thus, the mechanism of residual stress has received a wide range of attention. The point that compressive residual stress contributes to the improvement of fatigue life and corrosion resistance is generally accepted. The relevant research can be divided into three catalogs: analytical method, numerical method, and semi-analytical method. Jacobus[6,7] investigated the residual stress in orthogonal cutting and oblique cutting with both analytical model and experiment model. Based on the contact mechanics and elasto-plastic theory, Johnson[8] established the predictive model of residual stress under coupled thermo-mechanical load. By taking the shear plane model presented by Oxley[9],the plough force model presented by Waldorf[10]and the analytical temperature field by Komanduri[11], Liang[12] presented a comprehensive model of residual stress prediction under orthogonal cutting.

1.3 Cryogenic Machining

Pu[13] conducted cryogenic machining experiment on AZ31B magnesium alloy with the assistance of liquid nitrogen. The results showed that the surface integrity of AZ31B is enhanced by reduced roughness, grain refinement from 12 μ m to 31nm, and compressive residual stress that is ten times larger compared to dry cutting. Umbrello[14] turned the AISI52100 steel by spraying the liquid nitrogen in the flank face. The experiment pointed out that the surface topography under liquid nitrogen reveals superior quality over the one in dry cutting condition. The average depth of white layer is around 1 μ m, compared to the average depth of 5 μ m~8 μ m in dry cutting condition. In addition, the residual stress at the surface, its maximum value and penetration depth are all smaller in cryogenic condition. Pusavec and Jawhir[15] also confirmed the effect of liquid nitrogen in increasing the depth of residual stress from 40 μ m to 70 μ m, as well as the increase of hardness at the surface.

1.4 Contribution of This Paper

Currently, the study of aluminum lithium alloy mainly focuses on the weldability [16]and issues on the fracture behavior[17], while the knowledge of the surface integrity after machining aluminum lithium alloy has not been well investigated.

The experimental work conducted in this paper is to observe the influence of cutting parameters and coolant on the surface integrity of aluminum lithium alloy, specifically, surface roughness and residual stress in face milling. In this study, the first phase of experimental work is accomplished with air coolant, and the second phase of work is performed with the assistance of liquid nitrogen as coolant. A comparison between both conditions is made and a possibility of using liquid nitrogen to improve surface finish and enhance compressive residual stress has been revealed. Finally, cutting parameters optimization and predictive model of surface roughness and residual stress are presented.

2 Experimental Work

2.1 Machine Tool Setup and Tool, Workpiece Material Property

The experimental study is conducted on a MikronUCP-800 five-axis CNC machining center with the maximum spindle speed of 20000rpm and positional accuracy of 0.006mm in X,Y,Z axis respectively. A face milling cutter with a diameter of 100mm is chosen. Uncoated PCD inserts produced by Sandvik(R590-1105H-PR5-NL) have been used as cutting tools with axis rake angle of 5°, radius rake angle of 10°and nose radius of 0.4mm. The workpiece used here has a form of 90mm x 90mm x 6mm. The work material is the aluminum lithium alloy provided by China Commercial Airplane. The details of its mechanical properties and chemical composition can be found in Tables 1 and 2. The down milling process was carried out under the cooling condition of air and liquid nitrogen respectively.

Table 1. Mechanical properties of 2060

Density($g \cdot cm^{-3}$)	Yield strength(MPa)	Tensile strength(MPa)	Hardness(HRWB)
2.57	472	518	81.8

Table 2. Chemical composition of 2060(wt%)

Li	Cu	Mg	Ag	Zr	Mn	Zn
0.7	3.7	0.7	0.34	0.11	0.29	0.32

In this study, the cutting experiment takes the four controllable parameters into account: spindle speed, feed rate, depth of axis cut, the angle between feed direction and rolling orientation. Radial cutting depth is kept constant of 15mm in all the cutting tests. The cutting tests setup and the schematic configuration of these variables are illustrated in Figs.1 and 2.

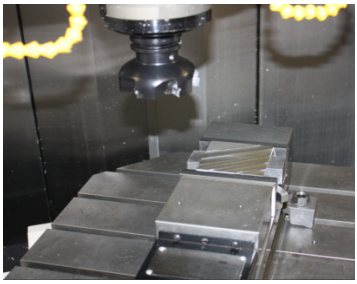

Fig. 1. Experiment Setup

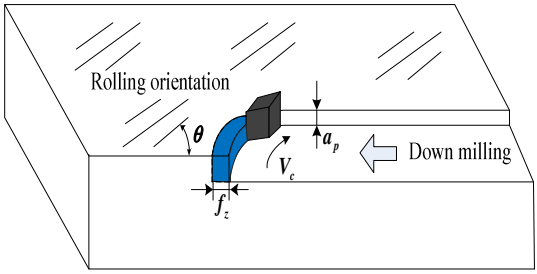

Fig. 2. Schematic configuration of variables

2.2 Roughness, Microstructure and Residual Stress Measurement

To ensure the accuracy of roughness and residual stress measurement, the evaluation of surface integrity is performed on three independent points located at half of the radial cutting depth along the feed direction as shown in Fig.3. In this paper, two characteristics of surface integrity, including surface roughness and residual stress are under investigation.

The surface roughness data is captured by Keyence 3D Laser Scanning Microscope which demonstrates a capacity of maximum magnification of 24000x. The line roughness is evaluated along diagonal in the view field illustrated in Fig.4. The surface roughness is characterized in the whole of view field. Here, the arithmetic average of the absolute values R_a and skewness values R_{sk} are taken into account

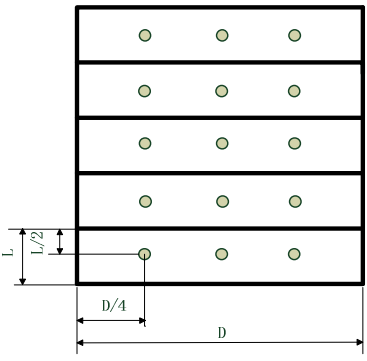

Fig. 3. Positions of measurement

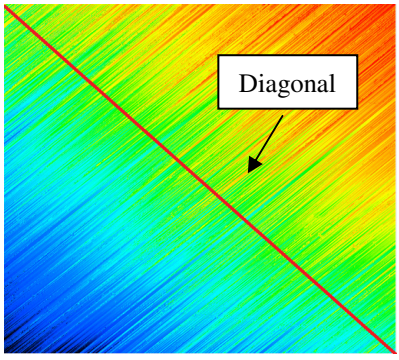

Fig. 4. Evaluation path of line roughness

The residual stress generated in the face milling of aluminum lithium alloy is measured by X-ray diffraction method. The parameters in XRD are shown in Table 3.

Table 3. Residual stress measurement setup

Tube voltage	Tube current	Target	Crystal face of diffraction	2θ range	scanning step	Stress constant
27KV	7mA	CrK_{α}	(311)	142°-136°	0.1°	-168

2.3 Orthogonal Array Experiment Design

Experimental design methods are used to conduct experiments with less number of observations [18]. In this study, the orthogonal array $L_{25}(5^6)$ with the 5th and 6th row left blank is used in the cutting test design. All the influential factors mentioned above and five levels are shown in Table 4. The $L_{25}(5^6)$ orthogonal experiment is repeated for both air coolant condition and liquid nitrogen as coolant. The results for these two cases are shown in Tables 5 and 6.

Table 4. Factors and levels for cutting test

Factor	Spindle speed(r/min)	Depth of cut(mm)	Feed rate(mm/z)	Angle
Label	s	d	f	θ
Level-1	5000	2	0.25	90°
Level-2	4500	1.5	0.2	60°
Level-3	4000	1	0.15	45°
Level-4	3000	0.7	0.12	30°
Level-5	2500	0.3	0.1	0°

Table 5. Cutting test results under air coolant condition

Trial No.	s (r/min)	d (mm)	f (mm/z)	θ	Line Roughness		Surface roughness		Residual stress(Mpa)
					R_a	R_{sk}	R_a	R_{sk}	
1	4500	2	0.15	0°	0.547	0.061	0.898	0.023	-47.5
2	3000	1.5	0.25	0°	0.429	0.277	0.816	0.186	-62.1
3	5000	1	0.12	0°	0.421	0.117	0.419	0.390	-58.7
4	4000	0.7	0.2	0°	0.425	0.046	0.409	0.393	-80.2
5	2500	0.3	0.1	0°	0.398	0.086	0.411	0.406	-150.2
6	3000	2	0.1	30°	0.635	-0.027	0.784	-0.094	-105.8
7	5000	1.5	0.15	30°	0.422	0.081	0.665	0.090	-135.2
8	4000	1	0.25	30°	0.339	0.432	0.551	0.269	-58.5
9	2500	0.7	0.12	30°	0.438	0.072	0.398	0.144	-61.2
10	4500	0.3	0.2	30°	0.388	0.031	0.386	0.338	-90.8
11	5000	2	0.2	45°	0.689	-0.101	1.080	-0.200	-98.6

Table 5. (*Continued*)

12	4000	1.5	0.1	45°	0.522	-0.105	0.749	-0.036	-235.5
13	2500	1	0.15	45°	0.360	0.166	0.531	0.015	-36.7
14	4500	0.7	0.25	45°	0.440	0.215	0.510	0.103	-179.3
15	3000	0.3	0.12	45°	0.308	0.231	0.314	0.406	-178.2
16	4000	2	0.12	60°	0.319	0.572	0.548	-0.066	-24.5
17	2500	1.5	0.2	60°	0.345	0.404	0.497	0.066	-245.1
18	4500	1	0.1	60°	0.416	0.197	0.490	0.253	-34.1
19	3000	0.7	0.15	60°	0.365	-0.110	0.365	0.229	-66.9
20	5000	0.3	0.25	60°	0.452	-0.039	0.405	0.104	-32.9
21	2500	2	0.25	90°	0.515	-0.156	0.558	0.117	-135.5
22	4500	1.5	0.12	90°	0.605	-0.206	0.558	0.031	-48.3
23	3000	1	0.2	90°	0.740	0.020	0.646	0.130	-138.7
24	5000	0.7	0.1	90°	0.668	-0.115	0.640	0.179	-47.5
25	4000	0.3	0.15	90°	0.567	-0.188	0.681	0.160	-59.8

Table 6. Cutting test results under liquid nitrogen condition

Trial No.	s （r/min）	d (mm)	f(mm/z)	θ	Line Roughness		Surface roughness		Residual stress(Mpa)
					R_a	R_{sk}	R_a	R_{sk}	
1	4500	2	0.15	0°	1.162	-0.126	1.294	-0.089	-145
2	3000	1.5	0.25	0°	0.689	-0.055	0.788	-0.007	-192
3	5000	1	0.12	0°	0.521	0.152	0.474	0.255	-130
4	4000	0.7	0.2	0°	1.236	0.002	1.099	-0.062	-164
5	2500	0.3	0.1	0°	1.312	-0.001	1.222	-0.071	-90.1
6	3000	2	0.1	30°	1.006	-0.124	0.721	-0.112	-171
7	5000	1.5	0.15	30°	0.352	0.430	0.577	0.124	-146.1
8	4000	1	0.25	30°	0.547	0.461	0.508	0.136	-121.2
9	2500	0.7	0.12	30°	0.497	0.002	0.429	0.111	-85
10	4500	0.3	0.2	30°	0.683	0.259	0.603	0.323	-231.5
11	5000	2	0.2	45°	1.280	-0.115	0.895	-0.092	-312
12	4000	1.5	0.1	45°	1.048	-0.154	0.765	-0.075	-202
13	2500	1	0.15	45°	0.926	0.073	0.711	0.012	-173

Table 6. (*Continued*)

14	4500	0.7	0.25	45°	0.769	0.031	0.624	0.081	-368
15	3000	0.3	0.12	45°	0.359	0.370	0.511	0.424	-148
16	4000	2	0.12	60°	0.894	-0.192	0.750	-0.022	-240
17	2500	1.5	0.2	60°	0.462	0.183	0.644	0.190	-264
18	4500	1	0.1	60°	0.451	0.352	0.552	0.308	-204
19	3000	0.7	0.15	60°	0.637	-0.154	0.508	0.036	-158
20	5000	0.3	0.25	60°	0.569	-0.196	0.469	0.012	-207
21	2500	2	0.25	90°	0.644	0.231	0.725	0.386	-228
22	4500	1.5	0.12	90°	1.636	-0.075	1.641	0.013	-110
23	3000	1	0.2	90°	1.988	-0.090	2.075	0.029	-259
24	5000	0.7	0.1	90°	1.431	-0.075	1.505	0.088	-173
25	4000	0.3	0.15	90°	0.663	0.209	0.678	0.213	-112

3 Results and Discussion

3.1 Level Average Response Analysis

The level average response analysis is performed by averaging the results data at each level of each factor. The trend of quality characteristics is obtained with the help of average response. The trend is shown in Fig.5~14.

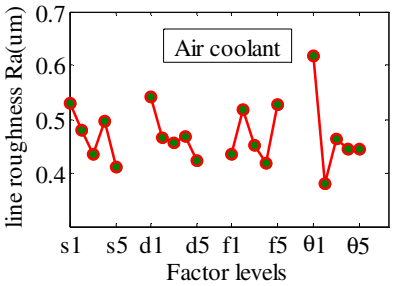

Fig. 5. Line R_a under air coolant

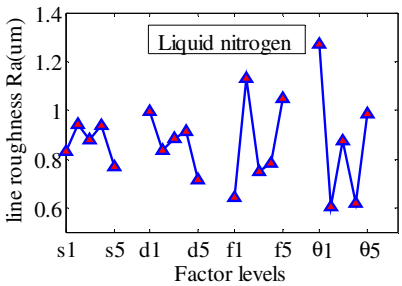

Fig. 6. Line R_a under LN

According to the effect of roughness and residual stress on the fatigue performance of structure, a smaller R_a, a larger R_{sk}, and a larger compressive residual stress are preferred. Base on the average response analysis, first, in air coolant machining condition, the following clues can be inferred: In the case of line roughness R_a, line roughness R_{sk}, the angle between the feed direction of rolling orientation, namely

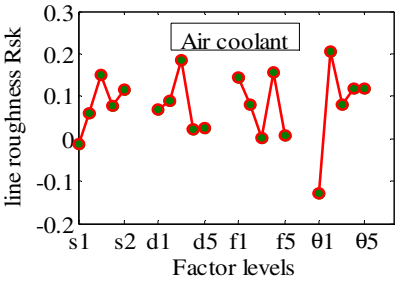

Fig. 7. Line R_{sk} under air coolant

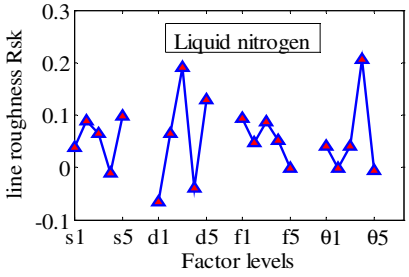

Fig. 8. Line R_{sk} under LN

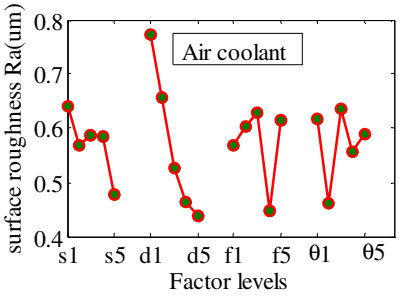

Fig. 9. Surface R_a under air coolant

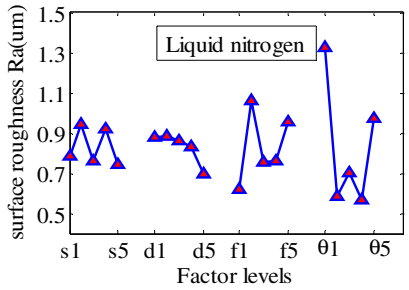

Fig. 10. Surface R_a under LN

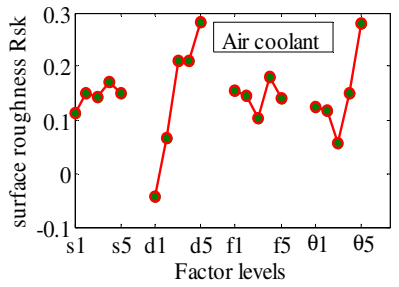

Fig. 11. Surface R_{sk} under air coolant

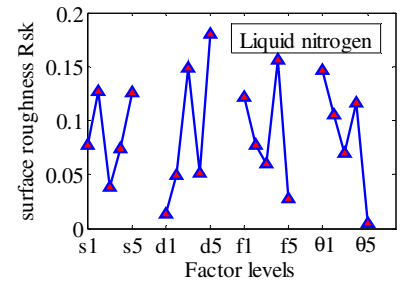

Fig. 12. Surface R_{sk} under LN

factor θ has a predominating influence over other three factors. The line roughness R_a decreases with the increase of spindle speed, which is in agreement with the cutting of titanium alloy in the work of Amin[19]. As for the line roughness of R_{sk}, it seems that the value of R_{sk} reaches its saturation with the increase of factor θ. The depth of cut, namely factor d, is the most significant effect in the determination of surface roughness R_a, factor of angle followed. It's noted that surface roughness

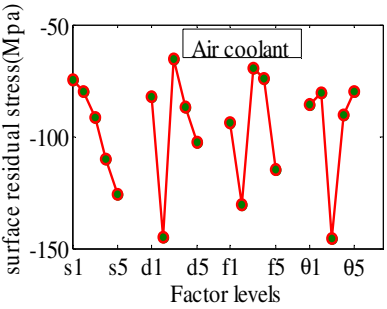

Fig. 13. Residual stress under air coolant

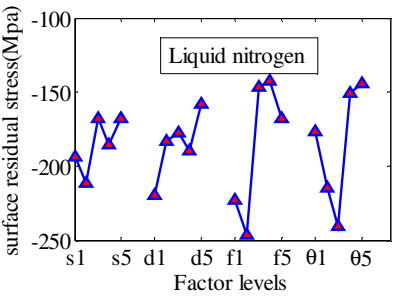

Fig. 14. Residual stress under LN

R_a is monotonously increase with the increase of cutting depth. Thus, smaller cutting depth is highly recommended for superior surface finish. In the case of residual stress, it indicates that the depth of cut bears the most important impact. Specifically, the compressive residual stress is decreasing all the way with the increase of spindle speed, which is consistent with Aspinwall[20] in the turning of gamma-titanium aluminide. In addition, factor θ ranks the second influential factor in the determination of residual stress. It can be concluded that the optimal compressive residual stress is obtained when θ equals 45°.Second, in liquid nitrogen condition, factor θ still dominates in the formation of line roughness R_a and surface roughness R_a. Factor θ should be 30°in both cases of air coolant condition and liquid nitrogen condition for the optimal line roughness R_a. The same situation applies to the optimal determination of surface roughness R_a. It's worthy to notice that surface roughness R_a decreases with the decrease of cutting depth, which is in line with the situation in air coolant condition. In the case of residual stress, a significant improvement by 150-200Mpa is achieved under liquid nitrogen as coolant. What's more, the compressive residual stress increases with the increase of spindle speed, which is contrary to that in air coolant case, and the compressive residual stress also increases with the increase of feed rate. The result has demonstrated the capacity of aluminum lithium alloy under cryogenic machining in large spindle speed and feed rate, thus resulting in high material removal rate followed by good residual stress state and surface finish.

3.2 Formation of the Regression Model

A regression model is developed using the four mentioned factors to model the cutting of aluminum lithium alloy process and then a correlation between the response and factors is obtained. A model consisting of main effects and quadratic effects is presented, and the coefficient in the model is identified by fitting the response data using the least square method. The expression is as following:

$$y = \sum_{i=1}^{4} a_{ii} x_i^{\,2} + \sum_{i=1}^{4} \sum_{j=1}^{4} a_{ij} x_i x_j + \sum_{i=1}^{4} a_i x_i + a_0 \tag{1}$$

Where x_1 - x_5 represent the spindle speed, depth of cut, feed rate and angle, the value of angle is unitized before regression analysis; x_i^2 represents the quadratic effects of these factors, respectively; $x_i x_j$ represents the interaction effects among the four factors. In order to obtain the most proper model for the prediction of roughness and residual stress, no all the mentioned terms above are used in the following identification process. For the purpose of simplicity, only the surface roughness R_{sk} in air coolant and residual stress in liquid nitrogen condition are presented. The R-square, adjusted R-square, and root MSE are shown in Table 7. The model for roughness R_{sk} is tested by variation analysis, as is shown in Table 8.

Table 7. Linear, interaction and second order model regression results for surface roughness R_{sk} in air coolant condition

Model type	Number of terms	R-square(%)	Adjusted R-square(%)	Root MSE
Linear	5	62.0	54.4	0.11
Linear+interaction	11	89.1	81.3	0.07
Second order	15	93.1	83.5	0.06

Table 8. Variation analysis for surface roughness R_{sk} in air coolant condition

Variance source	Degree of freedom	Sum of squares	Mean square	F value	P value
Model	14	0.5991	0.0428	9.6608	0.0005
Error	10	0.0443	0.0044		
total	24	0.6434			

Thus, the second order model is chose to describe the response of surface roughness R_{sk} . The final expression is followed:

$$\begin{aligned} Rsk &= 0.1131 + 0.002s - 0.7246d - 0.0759f + 0.6189 \times \left(\frac{\theta}{90}\right) \\ &+ 0.0001sd - 0.0014sf - 0.0002s \times \frac{\theta}{90} - 0.3084df + 0.1886d \times \frac{\theta}{90} \\ &- 2.1208f \times \frac{\theta}{90} + 0.0924d^2 + 18.7752f^2 + 0.1768\left(\frac{\theta}{90}\right)^2 \end{aligned} \tag{2}$$

Due to the low level of R-square value shown in Table 9, it indicates that the polynomial regression model may not be appropriate here. Instead, the exponential regression analysis is performed. The F-test is also performed here with results shown in Table 10.

Table 9. Linear, interaction and second order model regression results for residual stress in liquid nitrogen condition

Model type	Number of terms	R-square(%)	Adjusted R-square(%)	Root MSE
Linear	5	38.3	25.9	58.9
Linear+interaction	11	43.3	2.8	67.5
Second order	15	51.9	-15.2	73.5

Table 10. Variation analysis for residual stress in liquid nitrogen condition

Variance source	Degree of freedom	Sum of squares	Mean square	F value	P value
Model	4	1.3132	0.3283	3.3917	0.0284
Error	20	1.9359	0.0968		
total	24	3.2491			

The exponential regression model for residual stress is as following:

$$R.S = 55.67 \times s^{0.2340} \times d^{0.1558} \times f^{0.5021} \times \left(\frac{\theta}{90} + 1 \right)^{0.4413} \tag{3}$$

Where the value of angle is unitized and increased by one to avoid singularity. After the mathematical model is obtained here, the optimization procedure can be performed in the future work.

4 Conclusions

The functional performance of components manufactured by milling process heavily depends on the surface integrity factors. In this paper, an experimental study is conducted to investigate the effect of spindle speed, depth of cut, feed rate, angle between feed direction and rolling orientation on roughness and residual stress. Regression analysis is performed and a mathematical model is obtained. The optimal parameters in face milling of aluminum lithium alloy are presented, and measurement results show that the implement of liquid nitrogen benefits the surface topography and residual stress state.

Acknowledgments. This work was partially supported by the National Engineering and Research Center for Commercial Aircraft Manufacturing (SAMC12-JS-15-006) and the National Basic Research Program of China (2011CB706804).

References

1. Giummarra, C., Thomas, B., Rioja, R.J.: New aluminum lithium alloys for aerospace applications. In: Proceedings of the Light Metals Technology Conference, Bombardier Aerospace and Alcoa Trade Study (2007)

2. Jin, D., Liu, Z.: Effect of cutting speed on surface integrity and chip morphology in high-speed machining of PM nickel-based superalloy FGH95. Int. J. Adv. Manuf. Technol. 60, 893–899 (2012)
3. Axinte, D.A., Dewes, R.C.: Surface integrity of hot work tool steel after high speed milling-experimental data and empirical models. J. Mater. Process. Tech. 127, 325–335 (2002)
4. Shaji, S., Radhakrishnan, V.: Analysis of process parameters in surface grinding with graphite as lubricant based on the Taguchi method. J. Mater. Process. Tech. 141, 51–59 (2003)
5. Ghani, J.A., Choudhury, I.A., Hassan, H.H.: Application of Taguchi method in the optimization of end milling parameters. J. Mater Process. Tech. 145, 84–92 (2004)
6. Jacobus, K., DeVor, R.E., Kapoor, S.G., Peascoe, R.A.: Predictive model for the full biaxial surface and subsurface residual stress profiles from turning. J. Manuf. Sci. Eng. 123, 537–546 (2001)
7. Jacobus, K., DeVor, R.E., Kapoor, S.G.: Machining-induced residual stress: experimentation and modeling. J. Manuf. Sci. Eng. 122, 20–31 (2000)
8. Merwin, J.E., Johnson, K.L.: An analysis of plastic deformation in rolling contact. Proceedings of the Institution of Mechanical Engineers 177, 676–690 (1963)
9. Oxley P.L.B.: Mechanics of Machining: an Analytical Approach to Assessing Machinability (Retroactive Coverage) (1989)
10. Waldorf, D.J., DeVor, R.E., Kapoor, S.: A slip-line field for ploughing during orthogonal cutting. J. Manuf. Sci. Eng. 120, 693 (1998)
11. Komanduri, R., Hou, Z.B.: Thermal modeling of the metal cutting process—Part III: temperature rise distribution due to the combined effects of shear plane heat source and the tool–chip interface frictional heat source. Int. J. Mech. Sci. 43, 89–107 (2001)
12. Liang, S.Y., Su, J.: Residual stress modeling in orthogonal machining. CIRP Annals-Manufacturing Technology 56, 65–68 (2007)
13. Pu, Z., Outeiro, J.C., Batista, A.C., Dillon Jr., O.W., Puleo, D.A., Jawahir, I.S.: Enhanced surface integrity of AZ31B Mg alloy by cryogenic machining towards improved functional performance of machined components. Int. J. Mach. Tools Manuf. 56, 17–27 (2012)
14. Umbrello, D., Micari, F., Jawahir, I.S.: The effects of cryogenic cooling on surface integrity in hard machining: A comparison with dry machining. CIRP Annals - Manufacturing Technology 61, 103–106 (2012)
15. Pusavec, F., Hamdi, H., Kopac, J., Jawahir, I.S.: Surface integrity in cryogenic machining of nickel based alloy—Inconel 718. J. Mater. Process. Tech. 211, 773–783 (2011)
16. Moreira, P., de Jesus, A., de Figueiredo, M., Windisch, M., Sinnema, G., de Castro, P.: Fatigue and fracture behaviour of friction stir welded aluminium-lithium 2195. Theor. Appl. Fract. Mech. (2012)
17. Suresh, S., Vasudevan, A.K., Tosten, M., Howell, P.R.: Microscopic and macroscopic aspects of fracture in lithium-containing aluminum alloys. Acta Metall. 35, 25–46 (1987)
18. Ramesh, S., Karunamoorthy, L., Palanikumar, K.: Surface roughness analysis in machining of titanium alloy. Mater. Manuf. Process. 23, 174–181 (2008)
19. Amin, A., Ismail, A.F., Nor Khairusshima, M.K.: Effectiveness of uncoated WC–Co and PCD inserts in end milling of titanium alloy—Ti–6Al–4V. J. Mater. Process. Tech. 192, 147–158 (2007)
20. Mantle, A.L., Aspinwall, D.K.: Surface integrity of a high speed milled gamma titanium aluminide. J. Mater. Process. Tech. 118, 143–150 (2001)

Research on Active Vibration Control of Thin-Walled Workpiece in Milling Based on Voice Coil Motor

Puwei Chen, Jie Zhai, Xiaoming Zhang, Hai-Tao Zhang, and Han Ding

State Key Laboratory of Digital Manufacturing Equipment and Technology, Huazhong University of Science and Technology, Wuhan 430074, China

Abstract. Thin-walled workpieces are widely used in the industries of aerospace, national defense, petrochemistry and so on. Workpiece machining vibration induced by cutting tools greatly affects the milling efficiency and accuracy, and hence vibration alleviation has now become a bottleneck technique for the milling process of thin-walled workpieces. An active control method is developed here to attenuate the milling vibration by using voice coil motors and laser displacement detectors as actuators and sensors, respectively. The control algorithm is embedded in a FPGA module, and the closed-loop system is fulfilled by a FPGA card. Finally, this closed-loop control system is examined by vibration control experiments on a thin-walled aluminium alloy workpiece, where the vibration amplitudes have been decreased by 75% with cutting frequency bandwidth of 15Hz. The feasibility and superiority of the proposed active control method and the closed-loop system are thus verified.

Keywords: Active control, Vibration control, Thin-walled workpiece, FPGA.

1 Introduction

The thin-walled workpieces have been widely used in many industrials because of their excellent properties such as light weight and high strength. Vibration is an inextricable part of machining process which has detrimental effects on part quality,tool life,and productivity. In extreme situations, it may lead to chatter and destabilize the cutting system. The thin-walled workpiece is getting thinner and thinner during cutting process which leads to lower stiffness of the wall,so the cutting force can easily cause the forced vibration of the wall, which will cause bad effects such as deformation of the wall and chatter marks.

So far, there are two mainstream kinds of methods to tackle the control problems of attenuating unexpected vibrations, i.e., passive and active control approaches. The passive control method consists of mounting passive material on the structure in order to change its dynamic characteristics such as stiffness and damping coefficient. However, the passive control method usually leads to an increased weight of structure, which limits its further applications [1]. In special, this method is efficient at high frequencies but tend to be expensive and bulky

J. Lee et al. (Eds.): ICIRA 2013, Part II, LNAI 8103, pp. 503–512, 2013.

at low frequencies [1,2,3], and the effectiveness will be drastically reduced by operation frequency changes of the machining system[4]. Although some recent type of passive controller using piezoelectric connecting to resonant passive electric circuits [5] is light enough, it cannot be used for a sufficiently broad range of frequency control due to its internal dynamics limitations.

By contrast, a more prospective kind of control method is active vibration control (AVC), which uses intelligent actuators (like electro-strictive executors) to generate forces that absorb the energy caused by the unexpected vibrations in order to cancel or reduce their effect on the overall system [3]. The sensors and intelligent actuators form a closed-loop to facilitate controller design. By properly altering system dynamics, an active controller is able to further improve the stability of thin-walled piece machining systems and hence achieves a higher machining efficiency. These years have witnessed the increasing investigations on AVC for flexible thin-walled pieces [6,7]. As representative works, Zhang *et al.*[6] have used an active damping method to attenuate vibrations. Nagaya *et al.* [7] presented a method to drive the tool or workpiece move along the opposite direction of the cutting vibrations, which directly attenuates the vibrations especially in low frequency region. Jenifene *et al.* [1] proposed an AVC method for lightly damped dynamic systems, where a delayed position feedback signal was used to form a closed-loop controller. Kar *et al.* [8] and Xianmin *et al.* [9] applied H_∞ robust control approaches for flexible plate structures, which effectively suppress the low-frequency vibrations caused by external disturbances. Tokhi *et al.* [3] proposed active adaptive control approaches for a flexible beam and a square thin plate, respectively. In both methods, some feedforward control structures are included to enable a pre-cancelation of vibrations at operational points. Tavakolpour *et al.* [2] proposed an finite difference (FD) model based AVC approach, where an effective vibration suppression capability is achieved using piezoelectric actuator with the incorporated self-learning feedback controller. But most of the above-mentioned advanced control methods have not been applied into real machining processes yet but examined by numerical simulations. This paper proposes another active vibration control method. It compensates the milling vibration of thin-walled workpieces by using voice coil motors as actuators in a closed-loop control system. The experimental results show that the closed-loop control hardware platform works well and voice coil motors can efficiently control the vibration of thin-walled workpieces.

The paper is organized as follows. In Section 2, we give a detailed description of the hardware design of the active vibration closed-loop control platform. In Section 3, the PID control system based on LABVIEW FPGA module is designed to attenuate the vibration. In Section 4, the effectiveness of the proposed control method is examined by vibration control experiments on a thin-walled alloy workpiece. Finally, conclusions are drawn in Section 5.

2 Hardware Design

A photograph of the experimental installation of the active vibration is shown in Fig. 1.The vibration of the thin-walled workpiece excited by the milling cutter is

simulated using a voice coil actuator. A proper force is applied to the thin-walled aluminium alloy workpiece by the voice coil motor at the first beginning so that the voice coil motor can simulate the 'pull' behavior to compensate the vibration even though it does not stick to the workpiece.

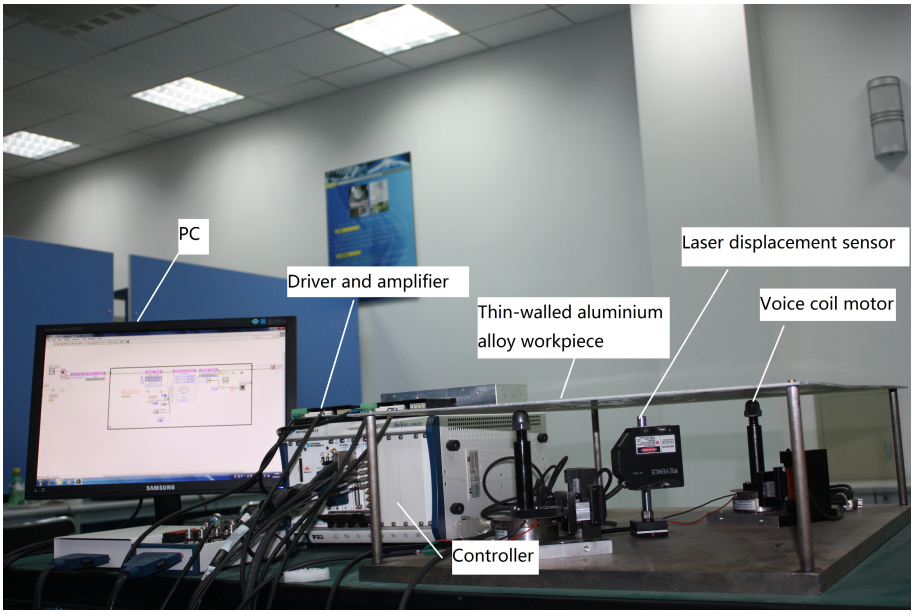

Fig. 1. Experiment platform

An illustration of the hardware designed and constructed to demonstrate the utility of active vibration control and the control system block diagram are shown in Fig. 2.The vibration of the thin-walled workpiece in milling is detected by the laser displacement sensors placed under the workpiece and sent to the FPGA analog input modules,the FPGA module processes the input signals using the control algorithm and outputs the control voltage signals to the drivers and amplifiers,which drive the voice coil motors to move up and down quickly to suppress the vibration of the workpiece.

2.1 Voice Coil Motor

In order to see the performance of voice coil motor to attenuate the vibration of thin-walled workpiece,we have to excite the thin-walled workpiece by vibration excitor,which is a good choice to simulate the vibration instead of milling cutter.The voice coil motor can also act as the vibration excitor for its excellent advantages mentioned above.The output voltage to control the voice coil excitor is given by the PXI-6733 card,which is a product produced by National Instruments(NI) and is a high-speed voltage output device that combines the latest

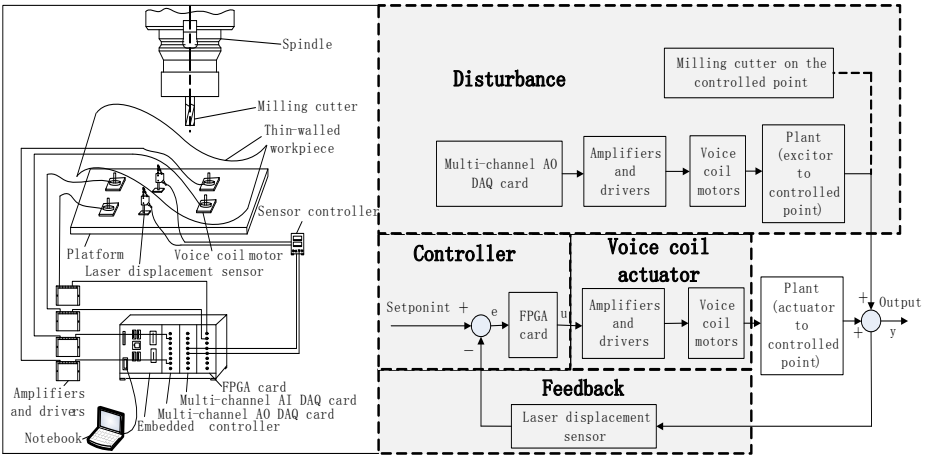

Fig. 2. Hardware configuration and control system block diagram

in PC technologies to deliver simultaneous,multichannel updates for control and waveform output applications.

Voice coil motor is a kind of direct drive device that converts electrical energy into a mechanical force[10].Its movement can be either linear or limited angle rotary motion.The advantages of voice coil motor are small size,non-commutated,quick response(within several milliseconds),high possible acceleration which is greatly suitable for fast oscillation movement(of course,the actual acceleration depends on the mass of the load being accelerated),simple control,non-backlash,good performance at low speed and long service life[11]. In our research,we apply the linear voice coil motor which utilizes a permanent magnetic field and coil winding to produce a force proportional to the current applied to the coil[12].The schematic of operating principle and structure of linear voice coil motor is shown in Fig. 3.The Lorentz force equation can be used to compute the thrust on the coil when it is electrified in the magnetic field.The thrust decides the direction of the coil's movement

$$\boldsymbol{F} = \alpha L \boldsymbol{I} \times \boldsymbol{B} \tag{1}$$

where $\boldsymbol{F}$ represents the thrust on the coil,α is the ratio of the effective length to the whole length L of the coil in the magnetic field,$\boldsymbol{I}$ is the current of the coil,and $\boldsymbol{B}$ is the magnetic flux density.When $\boldsymbol{B}$ and $\boldsymbol{I}$ are vertical to each other,the direction of $\boldsymbol{F}$ can be decided by Fleming's left-hand rule.Under this condition,(1)can be rewritten as

$$F = \alpha LIB = K_f I \tag{2}$$

where K_f is called the force constant($K_f = 21N/A$ for our voice coil motors). Thus, the thrust on the coil can be controlled by regulating the input current. Set the drivers and amplifiers at current mode so that the output current is

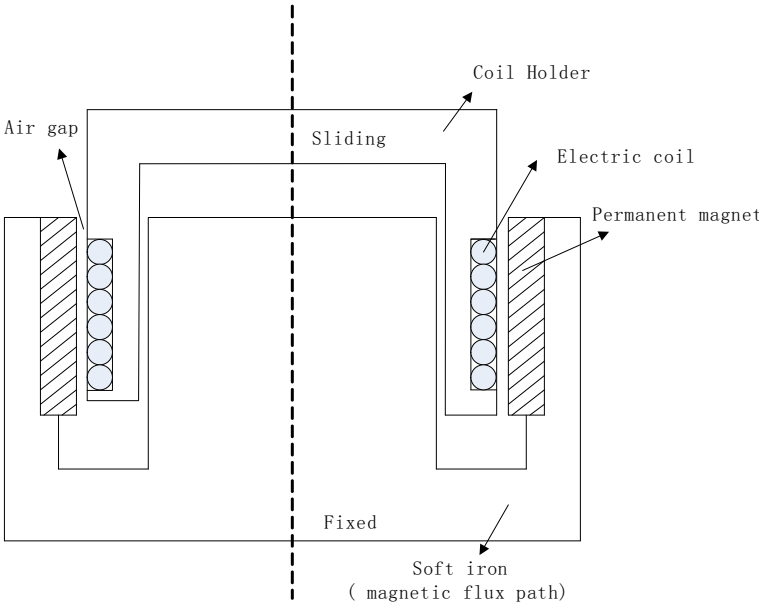

Fig. 3. Schematic of operating principle and structure of linear voice coil motor

proportional to the input voltage. And hence the current can be regulated by the control voltage signal $u(t)$. The relation between control force F(t) and control voltage signal $u(t)$ can be shown as

$$F = K_f K_a u(t) = K_c u(t) \tag{3}$$

where K_a is a constant between voltage and current($K_a = 1A/Volt$ for our voice coil motors), and K_c is a constant.

2.2 LABVIEW FPGA Module

The NI LabVIEW FPGA Module extends the LabVIEW graphical development platform to target field-programmable gate arrays (FPGAs) on NI reconfigurable I/O (RIO) hardware. LabVIEW is well suited for FPGA programming because it clearly represents parallelism and data flow, so users who are both experienced and inexperienced in traditional FPGA design can productively apply the power of reconfigurable hardware.

With the LabVIEW FPGA Module, users can:create custom hardware without VHDL coding or board design, Execute multiple tasks simultaneously and deterministically, and solve many applications, including unique timing and triggering routines, ultra high-speed control,digital signal processing (DSP), and any other application requiring high-speed hardware reliability and tight determinism.In contrast to the processors found in your PC, which run software application in predefined circuitry, programming an FPGA rewires the chip itself to

implement your functionality directly in hardware.For control systems, you can run advanced control algorithms directly in the FPGA fabric to minimize latency and maximize loop rates.

LabVIEW is a highly productive language for FPGAs because it abstracts complex details for quick design time, but it retains the ability to program every clock tick when necessary.[13]With the FPGA module like PXI-7854R card we use, you configure the behavior of the reconfigurable FPGA to match the requirements of a specific control system. The VI you create to run on an FPGA target is called the FPGA VI. Use the FPGA module to write FPGA VIs. When you download the FPGA VI to the FPGA, you are programming the functionality of the FPGA target.The PXI-7854R card has eight analog inputs and eight analog outputs which is suitable for us to acquire the vibration signals and output the control signals.

2.3 Data Acquisition

Data acquisition is an indispensable part of a control system,especially for a closed-loop control system.The vibration displacement signals are acquired not only by the PXI-7854R card but also by the PXI-4472 card at the same time, which has eight analog inputs with 24-bit resolution ADCs that are simultaneously sampled at a software-programmable rate.Thus we can observe the vibration displacement signals online while controlling the vibration.

3 Control Design

NI LABVIEW FPGA module is used to design the control system that includes analog input module to get the vibration displacement signals, PID controller module, and analog output module to drive the voice coil motors. PID (Proportional-Integral-Derivative) control is the most widely used in industrial control systems. The popularity of PID controller is mostly due to its appealing characteristics such as simple architecture, easy design and parameter tuning without complicated computation[14]. The general transfer function of the PID controller is shown as follows:

$$u = K_p e + K_i \int edt + K_d \frac{de}{dt} \tag{4}$$

- K_p=Proportional gain
- K_i=Integral gain
- K_d=Derivative gain

The control system block diagram is shown in Fig. 2.The setpoint is the displacement value of the controlled point which should be zero, the variable (e)represents the error which is used to compute the output voltage signal (u) in FPGA card,an embedded controller .The signal (u) is sent to the plant(actuator

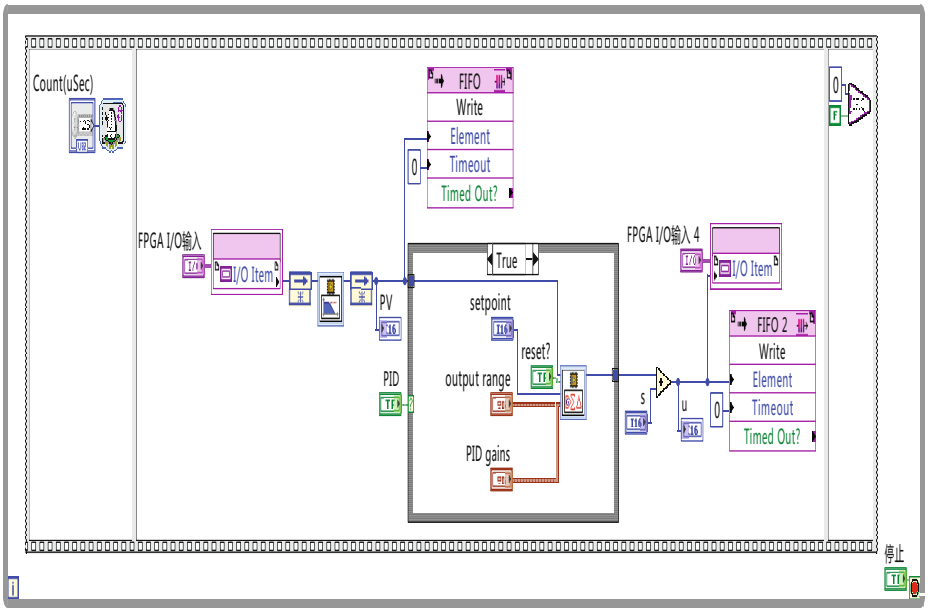

Fig. 4. The block diagram of FPGA VI

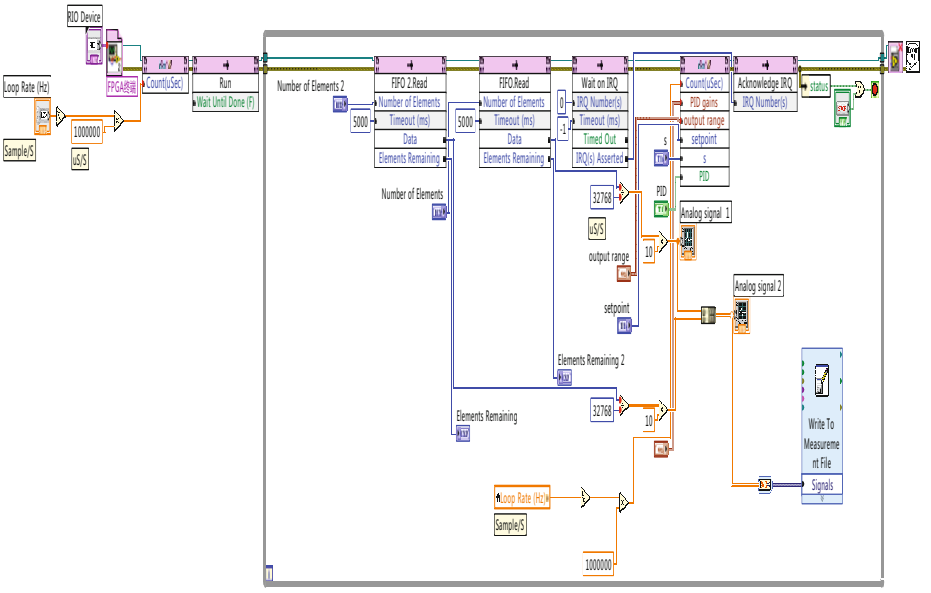

Fig. 5. The block diagram of host VI

to controlled point),and the new output (y) will be sent back to the sensor again to find the new error signal (e).The controller takes this new error signal and computes its output signal (u) again,this goes on and on until the error signal (e) equals zero[14].

On the LABVIEW FPGA platform, a LABVIEW project, a FPGA VI, and a host VI are created. The LABVIEW project is the file to manage all the VIs and the FPGA on the development computer. FPGA VI, as shown in Fig. 4, is compiled and downloaded onto the FPGA card to acquire the vibration displacement signals via the analog input modules, calculate the control signals according to the control algorithm and output the control signals via analog output modules. The host VI on PC, as shown in Fig. 5, is used to communicate with the FPGA VI and to convert the data from binary to decimal, so we can modify some important parameters such as PID parameters, loop rate and so on.

4 Experimental Test

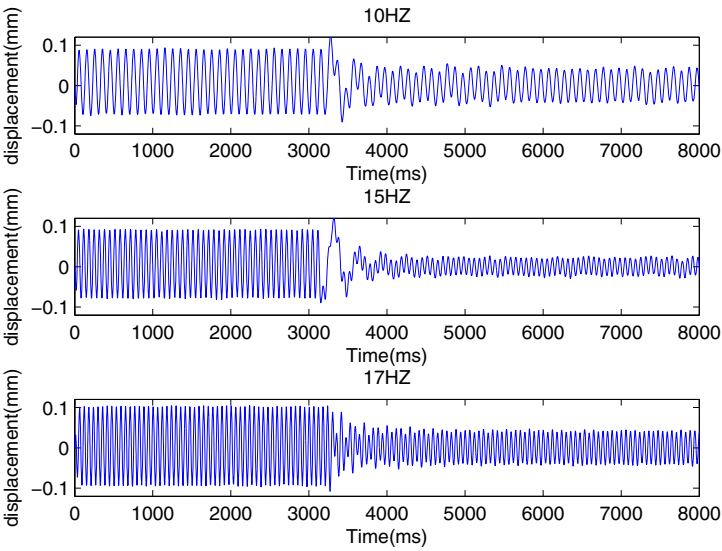

Fig. 6. Vibration signal

We choose a thin-walled aluminium alloy workpiece (3 mm of thickness) to conduct our active vibration control test. The output voltage signal to the driver and amplifier of the voice coil excitor given by PXI-6733 card is a sine wave whose amplitude and frequency can be modified via PC. The PID paraments can also be updated to control the vibration via the host VI on PC. We can see the vibration displacement via the chart whose data is acquired by the PXI-4472

card online. We carry out three tests to see the results of the active vibration control by different excited frequencies of 10Hz,15Hz,17Hz respectively. The results are shown in Fig. 6. The amplitude of the vibration can be decreased by 48%,75%,54% at excited frequency of 10Hz,15Hz,17Hz respectively.

5 Conclusion

In this paper,an active vibration control system is designed and build using NI control platform such as LABVIEW software and LABVIEW FPGA module.The experimental results presented verify that the closed-loop PID control implemented on NI FPGA module is an effective strategy to achieve the aim of active vibration control and using voice coil motor as the actuator to attenuate the vibration of thin-walled workpiece is feasible and effective.

Lacking of vacuum fixture to stick the voice coil motor to the thin-walled workpiece,we conduct the active vibration control by applying a proper force at the first beginning,which is not allowed at the actual machining.The model of thin-walled workpiece is a nonlinear system so that the PID control is limited and time-consuming.Therefore,the further work will focus on the fixture design and advanced algorithm such as predictive control,adaptive control,robust control and so on.And we can carry out the active vibration control in the practical milling even achieve the aim of chatter control in milling thin-walled workpiece.

References

1. Jenifene, A.: Active vibration control of flexible structures using delayed position feedback. J. Syst. Control Lett. 56, 215–222 (2007)
2. Tavakolpour, A.R., Mailah, M., Darus, I.Z.M., Tokhi, M.O.: Self-learning active vibration control of a flexible plate structure with piezoelectric actuator. Simulation Modelling Practice and Theory 18, 516–532 (2010)
3. Tokhi, M.O., Hossain, M.A.: A unified adaptive active control mechanism for noise cancellation and vibration suppression. Journal of Mech. Syst. Signal Process. 10, 667–682 (1996)
4. Long, X.H., Jiang, H., Meng, G.: Active vibration control for peripheral milling processes. Journal of Materials Processing Technology 213, 660–670 (2013)
5. Bisegna, P., Caruso, G., Maceri, F.: Optimized electric networks for vibration damping of piezoactuated beams. Journal of Sound and Vibration 289, 908–937 (2006)
6. Zhang, Y., Sims, N.D.: Milling workpiece chatter avoidance using piezoelectric active damping: A feasibility study. Smart Mater. Structures 14, 65–70 (2005)
7. Nagaya, K., Yamazaki, H.: Control of micro-vibration of a machine head by using piezoelectric actuators. Journal of Applied Electromagnetics and Mechanics 8, 315–326 (1997)
8. Kar, I.N., Miyakura, T., Seto, K.: Bending and torsional vibration control of a flexible plate structure using H_∞-based robust control law. IEEE Trans. Control Syst. Technol. 8, 545–553 (2000)
9. Xianmin, Z., Changjian, S., Erdman, A.G.: Active vibration controller design and comparison study of flexible linkage mechanism systems. J. Mech. Mach. Theory 37, 985–997 (2002)

10. Zhang, D.W., Feng, X.M.: The technical principle of voice coil actuator. The Journal of Zhongbei University 27(3), 224–228 (2006)
11. Chu, L.X., Lin, H.: The linear position tracking servo system using a linear voice-coil motor. Academic Journal of Xi'an Jiaotong University 20(3), 164–167 (2008)
12. Chen, Y.D., Fuh, C.C., Tung, P.C.: Application of voice coil motors in active dynamic vibration absorbers. IEEE Transactions on Magnetics 41(3), 1149–1154 (2005)
13. National Instruments for FPGA information, http://www.ni.com/labview/fpga/
14. Ali, F.H., Mahmood, H.M., Ismael, S.M.B.: LabVIEW FPGA implementation of a PID controller for D.C. motor speed control. In: 2010 1st International Conference on Energy, Power and Control (EPC-IQ), pp. 139–144. IEEE Press, Basrah (2010)

A Complete Methodology for Estimating Dynamics of the Heavy Machine Tool Structure

Hui Cai, Bin Li, Xinyong Mao*, Bo Luo, and Fangyu Peng

National Numerical Control System Engineering Research Center,
Huazhong University of Science and Technology, Wuhan 430074, China
maoxyhust@hust.edu.cn

Abstract. Dynamic properties of machine tool structure under machining operations are different from static results of impact or shaker tests. This paper proposes a complete methodology for applying operational modal analysis (OMA) in the case of heavy machine tool to estimate the dynamic modal parameters of the whole structure during machining. A random cutting technique is presented to meet the white noise excitation requirement of OMA. This technique is realized by interrupted cutting of a specially designed workpiece, of which the surface is modulated with pseudorandomly distributed teeth and channels. The resulting cutting force excites the structure in all three directions. Finally, Machine tool dynamic modal parameters are estimated and verified.

Keywords: Dynamics, Heavy machine tool, Random exciting technique, Operational modal analysis.

1 Introduction

The objective of high performance cutting (HPC) is to machine the parts in the shortest time, while respecting the physical constraints of the process, such as torque, power, vibrations, tool wear and failure, surface quality, and tolerances [1]. Although there has been a strong movement toward the high speed machining, HPC can also be achieved at low speeds by using higher depth of cut keeping the material removal rate high, which also results in longer tool life. One application of the strategy falls into heavy machine tool, the speed of which is often limited by its high inertia. This puts high demands on dynamic behavior of the machine tool in lower frequency range during machining. Thus an accurate estimation of the dynamic modal parameters in lower frequency bandwidth of the whole mechanical system is of great value in on line/real time monitoring, active maintenance and precise prediction of stability lobes diagrams in order to achieve high performance cutting.

Forced vibration tests (FVT), namely impact or shaker tests, are often employed to estimate the dynamics of machine tools with experimental modal analysis (EMA) approaches when the machine is under rest. However, heavy machine tool is quite difficult to excite in such tests. Impacting the tool tip during machining is not feasible

* Corresponding author.

J. Lee et al. (Eds.): ICIRA 2013, Part II, LNAI 8103, pp. 513–524, 2013.

because the operation presents high risk of injury both to machine tools and to the hammer, and thus violates health and safety regulations. Also, the slight nonlinearities of the machine structure appear regularly in impact testing resulting in less reliable results of the linear modal analysis. Shaker testing results in high cost and quite difficult set-up because the shaker stinger has to be in contact with the tool. Minis [2] developed a technique which provides a strong, broadband excitation by interrupted cutting of a specially designed workpiece, where the surface is modulated with pseudorandomly distributed teeth and channels. However, all the cutting forces must be measured by an expensive dynamometer in order to identify the dynamics of the structure in his case. This results in high cost in a factory background and is even impossible in heavy machine tools because of the high load. Also, significant changes in dynamic properties are expected to occur due to spindle rotation and changes of machine-tool-workpiece boundary conditions between the inactive state and the machining state [3]. Thus static results fail to characterize machine tool dynamics during machining accurately. All these lead to a failure of applying EMA to identify the dynamic modal parameters of machine tools during machining operation.

Operational modal analysis (OMA) or output-only modal analysis is a powerful tool for dynamic modal parameters identification in ambient vibration tests (AVT) in the case of Civil Engineering structures. Since the artificial excitation is replaced by freely available ambient forces, AVT are much more practical and economical. As structures are characterized under real operation conditions, in case of existence of non-linear behavior, the obtained results are associated with realistic levels of vibration and not with artificially generated vibrations, as it is the case when FVT are used [4, 5]. Zaghbani and Songmene [6] first developed a complete methodology to apply OMA in the case of machine tool structure under machining operations. They tried to estimate modal parameters during normal milling operations. However, the natural frequencies are quite difficult to distinguish from tooth-passing frequencies and their harmonics. Although some criteria were presented to get rid of these harmonics, the methods are complicated and rather experience-dependent. The reason for this problem is that the periodic cutting force does not fulfill the assumption of white noise excitation for OMA. Bin Li et al. [7, 8] developed two random exciting techniques to excite the machine structure by itself to do OMA. However, both two techniques only suit for middle or small size machine tools which can move promptly. Because of huge mass (or inertia), heavy machine tool is often not the case. So an effective random excitation is needed in order to apply OMA in the case of heavy machine tool structure.

This paper proposes a complete methodology for applying OMA in the case of heavy machine tool during machining operations through a random cutting technique based on the work of Minis. The background of OMA is first presented and then the technique to realize this signal with cutting force is proposed. The characteristics and feasibility of the proposed method are discussed and compared with impact tests employing a powerful customized hammer. Dynamic modal parameters are estimated by two OMA algorithms. The results are validated by modal assurance criterion (MAC).

2 Operational Modal Analysis Based on Random Cutting

2.1 Background of OMA

The relationship between the inputs $x(t)$ and the responses $y(t)$ can be expressed as:

$$G_{yy}(\omega) = H(\omega)G_{xx}(\omega)H(\omega)^H \tag{1}$$

where $G_{xx}(\omega)$ is the power spectral density (PSD) matrix of the input, $G_{yy}(\omega)$ is the PSD matrix of the responses, $H(\omega)$ is the frequency response function (FRF) matrix and superscript ^{H} denotes the hermitian of a matrix.

Operational modal analysis (OMA) is developed under an intrinsic assumption of white noise excitation, i.e. the $G_{xx}(\omega) = \text{const.}$, at least in the frequency band of interest. Then Eq. (1) can be written in the following well-known partial fraction form:

$$G_{yy}(\omega) = \sum_{r=1}^{N}\left(\frac{a_r\Psi_r\Psi_r^T}{j\omega-\lambda_r} + \frac{a_r^*\Psi_r^*\Psi_r^H}{j\omega-\lambda_r^*} + \frac{b_r\Psi_r\Psi_r^T}{-j\omega-\lambda_r} + \frac{b_r^*\Psi_r^*\Psi_r^H}{j\omega-\lambda_r^*}\right) \tag{2}$$

where a_r, a_r^*, b_r and b_r^* all are scalar constant coefficients and λ_r, Ψ_r are respectively, the pole, the unscaled mode shape vector of mode r. Superscript ^{T} and * denote the transpose and complex conjugate of a matrix, respectively. The goal of operational modal analysis is to identify the right hand side four terms of Eq. (2) only based on measured output data pre-processed into output spectral. However, it is obvious that this PSD model of outputs has four poles (λ_r, $-\lambda_r$, λ_r^*, and $-\lambda_r^*$) for each mode r, which means its order is twice the order of the FRF model. Fortunately, it is sufficient to compute the so-called half spectral, $G_{yy}^+(\omega)$, [9] which only consists of the first two terms in Eq. (2):

$$G_{yy}^+(\omega) = \sum_{r=1}^{N}\left(\frac{a_r\Psi_r\Psi_r^T}{j\omega-\lambda_r} + \frac{a_r^*\Psi_r^*\Psi_r^H}{j\omega-\lambda_r^*}\right) \tag{3}$$

The diagonal elements of the matrix $G_{yy}^+(\omega)$ are the so-called auto-power spectral density (Auto PSD) functions which are the magnitudes of the spectral densities between a response and itself. The off-diagonal elements are the cross-power spectral densities (CSD) between different responses. The Auto PSDs are all real-valued elements while the CSDs take complex values, carrying the phase information between the measured and the reference degree of freedom. The matrix is symmetric with complex conjugate elements around the diagonal, namely a Hermitian. Any column or row of the matrix carries enough information to extract the modal parameters like the $H(\omega)$ matrix. Then the natural frequency ω_r, damping ratio ξ_r and unscaled mode shape Ψ_r can be estimated based on $G_{yy}^+(\omega)$ with classical frequency domain identification methods based on FRF in EMA. Of course, there are some time domain OMA identification algorithms based on correlation function model similar to impulse response function (IRF) in EMA.

It should be noted that when OMA is applied in the estimation of machine-tool dynamics, there are two critical requirements for excitation. First, it needs white noise

excitation intrinsically, namely the PSD of the excitation should be reasonable flat over the frequency bandwidth of interests. Second, the corresponding frequency range and energy of the excitation should be adjustable according to different machine tools and actual situations so that all the structure modes in the frequency range of interest can be excited. The following section presents a random excitation technique based on cutting that meets the needs mentioned above.

2.2 Structure Excitation with Random Cutting Force

The white noise excitation needed in OMA is actually a pure random signal the PSD of which is a flat line over the entire frequency band. Ideal white noise excitation cannot be obtained in reality while the most common one has a reasonable flat PSD in a limited frequency range. Random excitation has the tendency to linearize the behavior of a structure even though it behaves nonlinearly. However, the fact that neither the force nor the response signal is periodic gives rise to an error called leakage.

Distributing many impulses randomly in time domain gives a new random excitation and the averaged PSD of this signal is yielded [8]:

$$\bar{G}(f) = N(A\tau)^2 \left(\frac{\sin \pi \tau f}{\pi \tau f} \right)^2 \tag{4}$$

Where N is the number of impulses the excitation contained, A is the average amplitude and τ is the average duration of all impulses. The first lobe BW_{1st} of the excitation is inversely proportional to τ, while the energy E_e is proportional to ρ (the number of impulses contained in unit time) and the square of both A and τ.

Minis's excitation method [2] generates a pseudorandom impulses force which excites the machine in all three directions. However, both the cutting force and corresponding response have to be measured to identify the modal parameters in his case leading to high cost. Fortunately, Minis's method can meet the white noise excitation requirement of OMA and the only information OMA needs is the responses. Employ Minis's exciting technique together with OMA results in a complete methodology to estimate the dynamic modal parameters of heavy machine tools. Fig. 1 shows the schematization of the excitation technique suit for a vertical lathe. The surface of the workpiece is modulated with randomly distributed steps and channels. The tool cuts the steps when the workpiece rotates. As cutting force is assumed to be proportional to the shear area (referred to as A_s). In this case, A_s consists of two faces, the flank and the button:

$$A_s = w_s a_f + w_s a_d = w_s (a_f + a_d) \tag{5}$$

where a_d is the axial depth, w_s is the width of the steps, and a_f is radial feed per revolution. The cutting speed v (mm/s) is:

$$v = \frac{\pi n \bar{D}_c}{60} \tag{6}$$

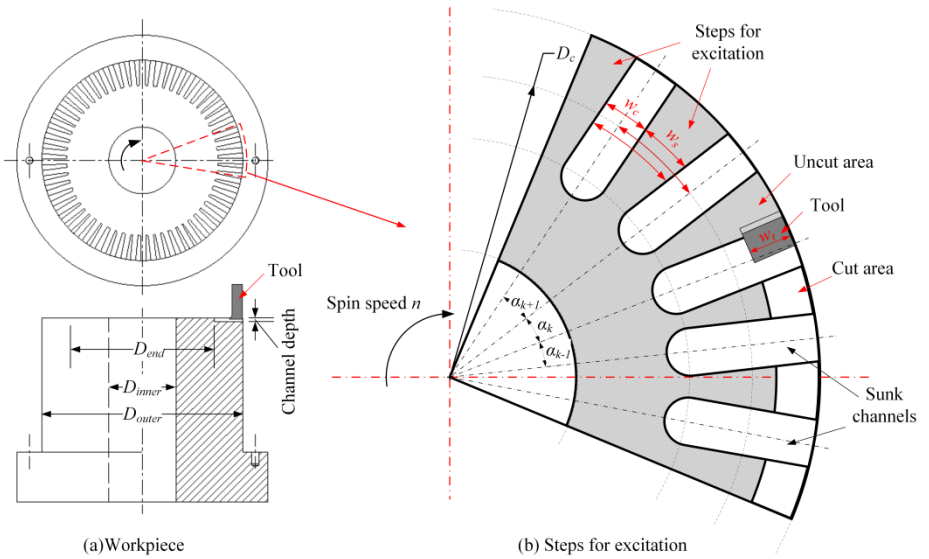

Fig. 1. Schematization of random impulses excitation technique suits for a vertical lathe

where n (rpm) is the revolution speed and $\bar{D}_c$ (mm) is the average diameter of the cutting trace. Random variable α_k is the angel between adjacent channels which determines the random characteristics of the cutting force. In order to meet the white noise excitation requirement of OMA, α_k is generated by Matlab having the Gaussian distribution over a range [α_{min}, α_{max}]. Then the average width $\bar{w}_s$ of all steps is:

$$\bar{w}_s = \frac{\pi \bar{D}_c \bar{\alpha}}{360} - w_c \tag{7}$$

where $\bar{\alpha}$ is the mean of α_k (k=1,2,…, i) and w_c is the width of the channels. Thus the average duration $\bar{\tau}$ of all pulses is:

$$\bar{\tau} = \frac{\bar{w}_s}{v} = \frac{60\bar{w}_s}{\pi n \bar{D}_c} \tag{8}$$

The first lobe BW_{1st} of the excitation is:

$$BW_{1st} = \frac{1}{\bar{\tau}} = \frac{\pi n \bar{D}_c}{60\bar{w}_s} \tag{9}$$

Finally the effective excitation bandwidth given by Minis is:

$$f_l = \frac{n}{4\pi} \le f \le \frac{BW_{1st}}{2} = \frac{\pi n \bar{D}_c}{120 \bar{w}_s} = f_h \tag{10}$$

Table 1. Summary of the relationships between cutting parameters and excitation signal

Energy E_e	*Bandwidth* BW_{1st}	*Impulse parameters*	*Cutting parameters*
$E_e \propto A^2$		$A \propto w_s$, (a_d+a_f)	w_s, a_d, a_f
$E_e \propto \tau^2$	$BW_{1st}=1/\tau$	$\tau \propto w_s$, $\propto^{-} n$	w_s, n
$E_e \propto \rho$		$\rho \propto n$	n

Where $\propto$ denotes proportional relationship and $\propto^{-}$ denotes inverse relationship.

Table 1 summarizes the relationships between BW_{1st} (and E_e) of the excitation and cutting parameters. The task of realizing random impulses excitation with cutting force is how to choose the cutting parameters according to actual needs. The complete steps to apply the random impulses excitation technique together with OMA in a heavy lathe machine tool are as follows:

- Prepare. Choose a workpiece according to the machine considered. Measure $\bar{D}_c$, set rotation speed n and BW_{1st} according to daily job the machine carries.
- Design the surface of the workpiece. Calculate the average width $\bar{w}_s$ of the teeth according to equation (9) and average angle $\bar{\alpha}$ (the mean of α_k) according to equation (7). Generate a number of values of α_k having Gaussian distribution within a certain limit $[\alpha_{min}, \alpha_{max}]$ by Matlab. The sum of these values should be 360 degree.
- Mill the channels according to parameters obtained in step ii. The depth and length of these channels should be chosen according to actual needs.
- Machine the surface of the workpiece to excite the structure and pick up vibrations of different points.
- Calculate PSD matrices and employ OMA algorithms to identify the modal parameters of the structure.

3 Experimental Verification

3.1 Realization of Random Cutting Excitation

The presented exciting technique was applied on a heavy vertical lathe C5250E shown in Fig. 2 from Wuhan heavy machine tools group Co., Ltd (WuChong) and the corresponding responses were collected to do OMA. The machine structure represents a very common type of machine tool design with a moving tool holder, a separate rotating worktable, two support columns, a fixed beam and a slide beam carrying the tool holder. The primary motion is the table rotation and the feed motion is completed by the slide beam moving along the z axis and the tool holder moving along the x axis. The total mass is about 100 t and the speed range of the worktable is 0.4 to 40 rpm.

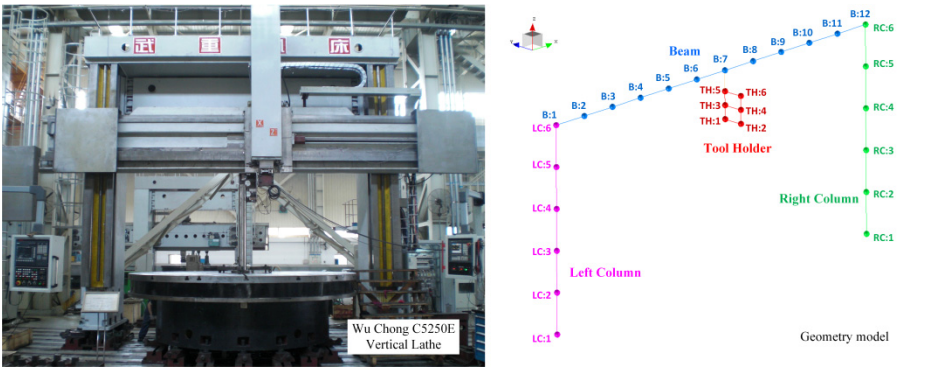

Fig. 2. The vertical lathe C5250E and its geometry model used in tests

Considering the cost, a standard workpiece for routine tests of machining performance check, a cast iron hollow cylinder (inner diameter D_{in} was 200 mm, outer diameter D_{out} was 600 mm, and the height h was 1000 mm), was used. The surface of the workpiece was designed and manufactured as Fig. 3 shows. Six parameters including n, a_f, a_d, D_c, w_c and α_k have to be chosen elaborately. An end milling tool with a diameter of 16 mm was chosen to machine the channels for convenience. So w_c was 16 mm. D_c was chosen varying from 400 to 600 mm, thus $\overline{D}_c$ was 500 mm. Because of the huge mass, the lower frequency range of the machine is critical. The bandwidth of interest was chosen to be 0~20 Hz. Thus f_h is 20 Hz and BW_{1st} is 40Hz. A rotation speed 10 rpm was originally chosen. The average width $\overline{w}_s$ is 6.542 mm according to equation (9) and then the average angle $\overline{\alpha}$ is 5.169° according to equation (7). $\overline{\alpha}$ was finally set to 6° and 60 values of α_k having Gaussian distribution over [5°, 7°] was generated by Matlab. The mean of these values is 6° and the sum is 360 degree. The channel depth was 10 mm. Finally, the workpiece was manufactured as Fig.3a shows.

3.2 Experimental Set-Up and Measurements

The experimental set up is shown in Fig. 3. The geometry model of the structure is shown in Fig. 2. Every round point in the model represents a measuring point and the total number of measuring points is 30. The distance between adjacent points is 0.6 m on the column, 0.55 m on the beam and 0.15 m on the tool holder. First, the specially designed surface was cut to excite the machine. Then, the inner smooth surface was cut in normal turning processes. Finally an impact test employing a powerful customized hammer of type DFC-1 (referred to as HDFC) which comes from China Orient Institute of Noise & Vibration (INV) was conducted. Table 2 summarizes all the tests.

Twenty-two signals can be collected simultaneously by the used acquisition system LMS SCADAS Mobile SCM05, and seven three-axis accelerometers of type PCB 356A15 were mounted every time to measure the vibrations of the machine structure. Each test was realized for all points, with each test repeated five times. The sampling rate of all tests was 1024 Hz. Test #3, #10 and #11 were used for analysis and extracting the modal parameters.

Table 2. Summary of the cutting conditions for the experimental tests. Case A is specially designed surface turning tests; Case B is normal turning tests; Case C is impact tests.

Case	*Test #*	*Feed (mm/r)*	*Axial depth (mm)*	*Spindle speeds (rpm)*
A	***1***	*1*	*0.3*	*6*
	2	*1*	*0.3*	*8*
	3	*1*	*0.3*	*10*
	4	*0.2*	*0.3*	*6*
	5	*0.8*	*0.3*	*10*
B	***6***	*0.66*	*0.3*	*6*
	7	*0.8*	*0.3*	*8*
	8	*1*	*0.3*	*10*
	9	*0.8*	*0.3*	*10*
C	***Test #***	***Tap point***		***Direction***
	10	*TH:2*		*X and Y*
	11	*B:12*		*X and Y*

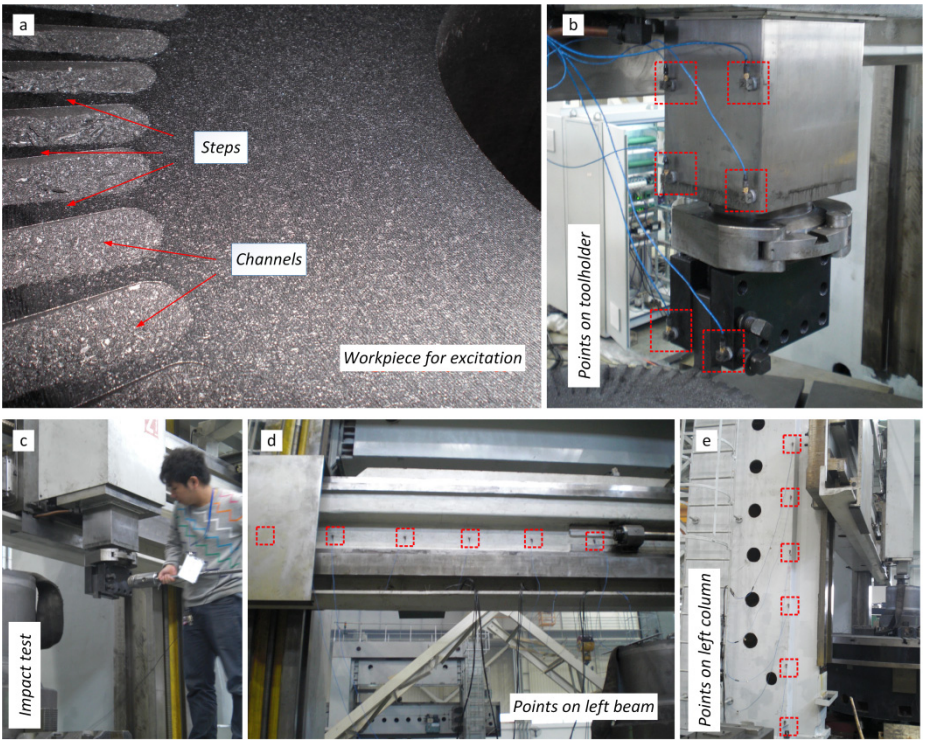

Fig. 3. Experimental setup: (a) Workpiece for excitation; (b) measuring points on tool holder; (c) impact test; (d) measuring points on left beam; (e) measuring points on left column

4 Results and Discussion

4.1 Spectral Analysis

As cutting force is not available in cutting tests, the responses are the only information to verify the effectiveness of the excitation technique. Fig. 4 shows the PSD comparison of responses of point TH:2 and LC:3 between test #3 and test #10 (#11). It is shown that the PSD of acceleration signals of cutting tests moves almost parallel to their impact test counterparts within the range 0~75 Hz which covers the range of interest 0~20 Hz. The former is at least 10 dB higher than the latter leading to a clearer presentation of the peaks and stronger ant-jam capability in a factory background. The modes in both directions are excited well in cutting tests compared with impact test. So it can be assumed that the modes in all three directions are excited well by cutting forces in the frequency range of interest.

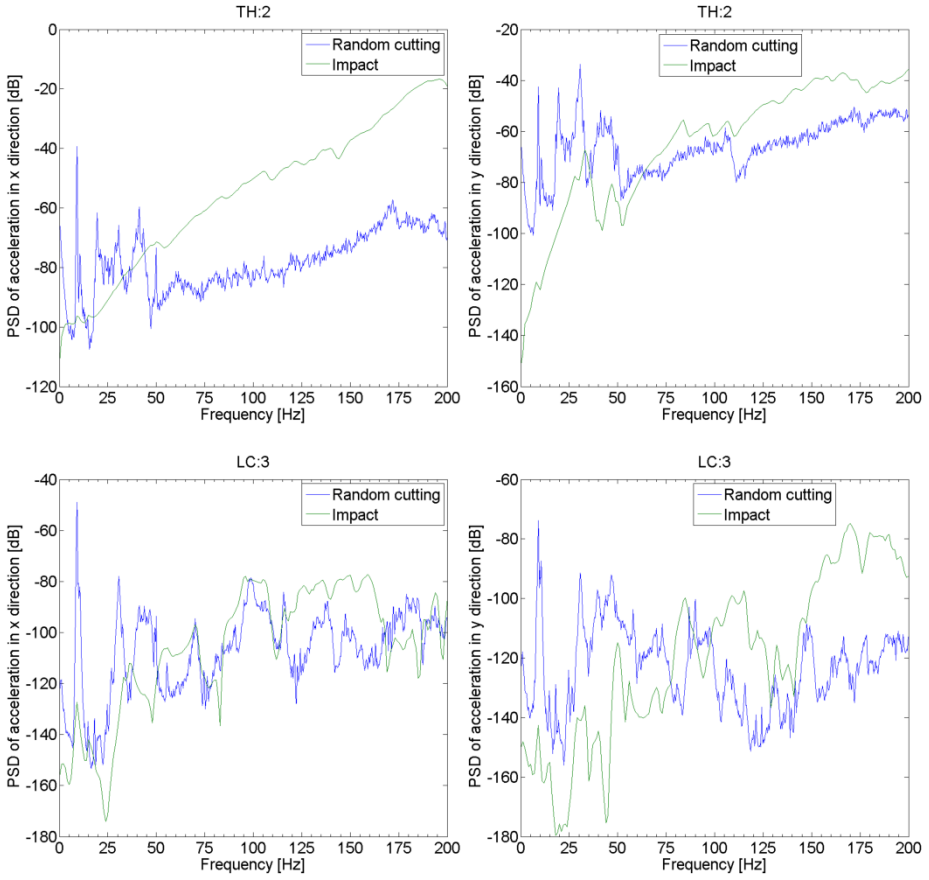

Fig. 4. PSD of acceleration signals of TH:2 and LC:3 under different excitations tests

4.2 Structure Identification

Three modes are dominant within the interest range 0~20 Hz as Fig. 4 shows. The dynamic modal parameters of the whole machine tool structure during machining were identified by OMA methods and compared with the results of conventional tap test. The employed EMA algorithm was the commercially well-known, poly-reference Least Square Complex Frequency domain method (pLSCF or PolyMAX) [10] and the OMA algorithms were numerically robust Stochastic Subspace Identification (SSI) method [11] and an operational version of PolyMAX method [9]. The results are compared in Fig. 5. It can be seen that the natural frequencies of the Op.PolyMAX method are quite similar to their SSI counterparts and there are obvious variations between OMA and EMA results. A 7.7 % relative variation ($[\omega_{\text{Op.PolyMAX}} - \omega_{tap}]/\omega_{tap}$) can be observed in mode 1. When it comes to damping, the results of the two OMA methods don't match well, however both are higher or lower than the EMA results. The results indicate that the dynamic properties of the machine tool structure under operations vary from the results of static impact tests.

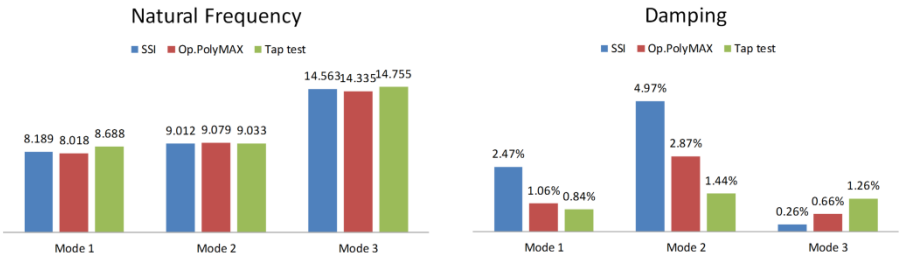

Fig. 5. Comparison of modal parameters generated by OMA methods and EMA method

A powerful tool, the modal assurance criterion (MAC), was used to evaluate the quality of mode shapes. MAC, which assesses the correlation between two mode shape vectors, is defined as the squared correlation coefficient between these two vectors [12]. If two vectors are estimates of the same physical mode shape, the MAC should approach unity (100%). Otherwise the MAC should be low. A high quality mode set normally contains diagonal elements which are 100% (by definition) and off-diagonal elements which have a low value (close to 0%). Fig. 6 shows the MAC evaluation of the mode shapes of different methods. Fig. 6a and b show that mode shapes of tap test and cutting test are rather good. And unscaled mode shapes estimated by two OMA methods are very similar, which is evidenced by Fig. 6c. Fig. 6d indicated that the mode shapes of cutting test are rather different from the shapes of tap test.

5 Conclusion and Future Research

This paper presents a complete methodology for applying operational modal analysis to estimate dynamic modal parameters in the case of heavy machine tool structure.

A random cutting excitation technique is presented to meet the white noise excitation requirements of OMA. Two OMA algorithms were employed to extract the modal parameters of the whole structure under machining operations. It can be observed that the dynamic properties of the structure under operations vary from the results of static impact tests. Because of no access to input information, the modal shapes from OMA are not mass normalized. A scaling factor (or modal mass) must be estimated to do it, which needs further investigation.

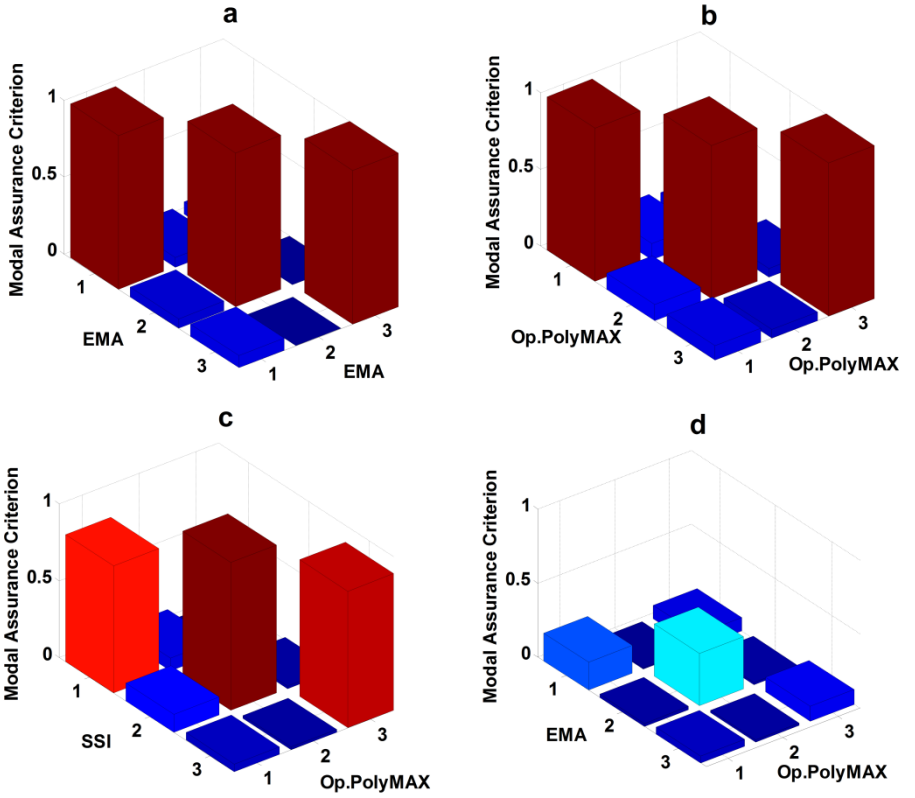

Fig. 6. MAC of mode shapes identified by different methods: (a) Auto MAC of scaled mode shapes by EMA. (b) Auto MAC of unscaled mode shapes by Op.PolyMAX. (c) MAC of unscaled mode shapes by SSI vs. Op.PolyMAX. (d) MAC of mode shapes by EMA vs. OMA.

Acknowledgements. This research is funded by the National Natural Science Foundation of China (NSFC) under Grant nos. 51275188 and 51121002, and the Science and Technology Major Special Project of China under Grant no. 2011CB706803.

References

1. Altintas, Y.: High Performance Cutting. Int. J. of Advanced Manufacturing Technology 33, 367–367 (2007)
2. Minis, I.E., Magrab, E.B., Pandelidis, I.O.: Improved Methods for the Prediction of Chatter in Turning, Part 1: Determination of Structural Response Parameters. Journal of Engineering for Industry 112, 12–20 (1990)
3. Gagnol, V., Le, T., Ray, P.: Modal identification of spindle-tool unit in high-speed machining. Mech. Syst. Signal Pr. 25, 2388–2398 (2011)
4. Reynders, E.: System Identification Methods for (Operational) Modal Analysis: Review and Comparison. Arch. Comput. Method. E. 19, 1–74 (2012)
5. Magalhães, F., Cunha, Á.: Explaining operational modal analysis with data from an arch bridge. Mech. Syst. Signal Pr. 25, 1431–1450 (2011)
6. Zaghbani, I., Songmene, V.: Estimation of machine-tool dynamic parameters during machining operation through operational modal analysis. Int. J. of Machine Tools & Manufacture 49, 947–957 (2009)
7. Li, B., Wei, Y.Q., Mao, X.Y., Mao, K.M., Liu, H.Q., Tian, H.L.: A Novel Vibration Exciting Method for NC Machine Tools. In: 1st International Conference on System Science, Engineering Design and Manufacturing Informatization, Yichang, pp. 45–48 (2010)
8. Li, B., Cai, H., Mao, X.Y., Huang, J.B.: Estimation of CNC machine-tool dynamic parameters based on random cutting excitation through operational modal analysis. Int. J. of Machine Tools & Manufacture (2013), http://dx.doi.org/10.1016/j.ijmachtools.2013.04.001
9. Peeters, B., Van der Auweraer, H.: POLYMAX: a revolution in operational modal analysis. In: 1st International Operational Modal Analysis Conference, Copenhagen, Denmark (2005)
10. Peeters, B., Van der Auweraer, H., Guillaume, P., Leuridan, J.: The PolyMAX frequency-domain method: a new standard for modal parameter estimation? Shock Vib. 11, 395–409 (2004)
11. Peeters, B., De Roeck, G.: Stochastic System Identification for Operational Modal Analysis: A Review. ASME Journal of Dynamic Systems, Measurement, and Control 123, 659–667 (2001)
12. Heylen, W., Lammens, S., Sas, P.: Modal analysis theory and testing. Katholieke Universteit Leuven, Belgium (1995)

Adaptive LQR Control to Attenuate Chatters in Milling Processes

Hai-Tao Zhang[1,2], Zhiyong Chen[3], and Han Ding[2]

[1] School of Automation, Huazhong University of Science and Technology, Wuhan 430074, China
[2] State Key Laboratory of Digital Manufacturing Equipment and Technology, Huazhong University of Science and Technology, Wuhan 430074, China
[3] School of Electrical Engineering and Computer Science, The University of Newcastle, Callaghan, NSW 2308, Australia

Abstract. Chatters are induced by rigidity-flexibility coupling between tools and workpieces, which cause cutting disturbances, over cut and quick tool wear and hence greatly limits the workpiece machining efficiency and quality. To attenuate the chatter dynamics, traditional passive control methods usually decrease the spin speed or cutting depth at the cost of reducing machining efficiency. In this work, we investigate deeply on the structure of the cutting force variation matrix and then design an online system identification method based on the Fourier series. In this way, a Linear Quadratic Regulator adaptive control method is developed to greatly enlarge the chatter stability region in the Lobe Diagram. Moreover, the receding horizon and output rectification mechanisms are applied to overcome the external disturbances as well. The feasibility and superiority of the method are verified by the benchmark examples, where closed-loop stable operation points are remarkably increased and a higher productivity rate is thus achieved.

Keywords: Active control, LQR control, Milling.

1 Introduction

High-speed milling is a key technology for machining high precision complex surfaces universally utilized in manufactory industries, e.g. aerospace, automotive, shipping, die and mold. In these years, many efforts have been devoted to improve the machining performance of the milling processes by enlarging the stable-region in the space composed of the cutting depth and the spindle speed [1,2,3,4]. These works aims at obtaining a large material removal rate, keeping relatively low cutting forces and maintaining a high quality level. In the milling process control system, however, chatter prohibition control is still a bottleneck technique, which could restrain the periodical instability and hence decrease the influence of the regenerative heavy vibrations on the workpiece surface quality.

Till now, most of the previous chatter prohibition control methods is called passive control, which alleviates the chattering effect by constraining the spindle speed or/and

J. Lee et al. (Eds.): ICIRA 2013, Part II, LNAI 8103, pp. 525–534, 2013.

the maximal cutting depth. Although it mitigates the machining instability, this conervative method will inevitably decreases the maximal metal removal rate (MMRR) and hence limits the productive capacity of a machine tool.

A second kind of methods is to disturb the regenerative effect by continuous spindle speed modulation [5,6]. Although the stability boundary is enhanced by spindle speed modulation, the spindle speed variation should be extremely fast in high-speed milling case, while the speed variation is constrained b the spindle power. Thereby, the practicability for high-speeding milling case is still limited.

A new kind of promising alternative approaches emerges to adopt an active structural control system to alter dynamics by installing some intelligent actuators (like electrostrictive ones) and vibrations sensors (like strain gages) onto the the spindle and rotation tools, respectively [7]. These sensors and intelligent actuators form an additional effective closed-loop to facilitate the controller design. By properly altering these dynamics, it expands the closed-loop stable region in the lobe diagram and therewith enables high MMRR. However, closed form stability conditions cannot be given for general milling cases. Thereby, the practically achievable amount of damping is rather limited. Moreover, vibration absorbers require accurate tuning of their natural frequencies and, consequently, lack robustness to changing machining conditions.

In brief, most of the existing active control methods seeks to mitigate chatter vibrations by applying damping to the spindle or the tool to alter the machining dynamics. In [3,7], the stability lobes of the machine and tool are actively raised by damping of a milling spindle with piezoelectric actuators and active magnetic bearing (AMB), respectively. In [8], stable machining region is expanded by minimization of the tooltip compliance using-synthesis. In [9], by mounting the piezoelectric actuators and sensors to the thin-walled workpiece, Zhang and Sims altered the workpiece flexibilities. In [10], by approximating the regenerate delay term by Pade series, Shiraishi *et al.* designs an optimal state feedback-observer controller for turning. Recently, in [11], Chen and Knospe designed chatter control approaches for speed-independent, speed-specified and speed-interval control, which show significant improvement in tailoring the stability lobes compared to conventional PID controllers.

Most of the existing active control methods enhance the stable boundary by adding damping to the spindle or the tool in an active way. However, the limitation of the existing active control methods are twofolds: 1) From theoretical point of view, a niched chatter control strategy tailored to the entire complexity of the high speed machining process is still lacked; 2) From engineering aspect, they are limited to low spindle speeds (i.e., below 5000 rpm).

From the control theory perspective, the active control for milling processes still requires deeper investigation. The main idea of this paper is not based on damping adjustment but on the fact that the chatter instability of a milling process is caused by regenerative effect, which is induced by the cutting force variation matrix. Therefore, by approximating the variation matrix in Fourier series, we developed an adaptive linear quadratic regulator (LQR) control scheme to compensate the regenerative effect. As a result, the chatter instability can be mitigated. Moreover, it is shown that the controller is adaptive to depths of cut, and robust with respect to some system parameters. Finally,

in numerical simulations, the feasibility and superiority of the proposed LQR controller is verified in terms of both SLD and SLE.

2 Chatter Instability in Milling Processes

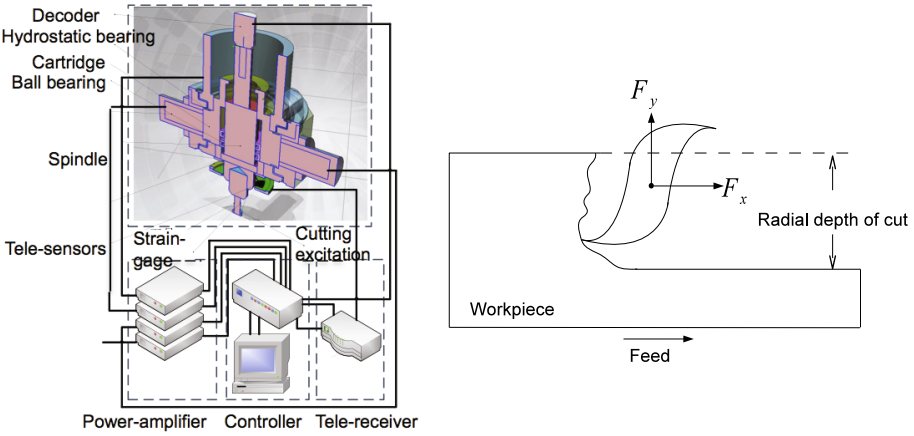

Fig. 1. Intelligent spindle (left) and illustration of the cutting force $F = [F_x, F_y]^\mathsf{T}$ for the cutting tool with two evenly spaced teeth (right))

As shown in the left panel of Fig. 1, the spindle with active controller is called intelligent spindle [4]. The "intelligence" lies in that the tele-receiver can detect the displacement of the tool and the electrostrictive actuators can produce motion in the tool. In this way, a closed-loop control system is established which can adaptively alter the rigidity of the whole system according to the operation situations.

With the aid of Fig. 2, the mechanism and hence the model of the cutting force are discussed as follows. We consider a 2 DOF model of a milling process where the tool with N evenly spaced teeth is assumed to be flexible relative to the rigid workpiece. The model is governed by the following time delay differential equation:

$$\mathbf{M}\ddot{\mathbf{x}}(t) + \mathbf{C}\dot{\mathbf{x}}(t) + \mathbf{K}\mathbf{x}(t) = b\mathbf{H}(t)[\mathbf{x}(t-\tau) - \mathbf{x}(t)] + \mathbf{G}(t) \tag{1}$$

where $\mathbf{M}, \mathbf{C}, \mathbf{K} \in \mathbb{R}^{2\times 2}$ are the mass, damping, and stiffness matrices, respectively. The vector $\mathbf{x} = [x, y]^\mathsf{T}$ represents the tool displacement in an orthogonal x-axis and y-axis. In the model, b is the axial depth of cut, $\mathbf{H} \in \mathbb{R}^{2\times 2}$ is called the cutting force variation matrix, and $\mathbf{G} \in \mathbb{R}^2$ the stationary cutting force vector. In particular, the matrix

$$\mathbf{H}(t) = \begin{bmatrix} H_{xx}(t) & H_{xy}(t) \\ H_{yx}(t) & H_{yy}(t) \end{bmatrix}$$

is specified as follows:

$$
\begin{aligned}
H_{xx}(t) &= \sum_{j=1}^{N} s[\varphi_j(t)][K_t \cos\varphi_j(t) + K_n \sin\varphi_j(t)] \sin\varphi_j(t) \\
H_{xy}(t) &= \sum_{j=1}^{N} s[\varphi_j(t)][K_t \cos\varphi_j(t) + K_n \sin\varphi_j(t)] \cos\varphi_j(t) \\
H_{yx}(t) &= \sum_{j=1}^{N} s[\varphi_j(t)][-K_t \sin\varphi_j(t) + K_n \cos\varphi_j(t)] \sin\varphi_j(t) \\
H_{yy}(t) &= \sum_{j=1}^{N} s[\varphi_j(t)][-K_t \sin\varphi_j(t) + K_n \cos\varphi_j(t)] \cos\varphi_j(t)
\end{aligned} \tag{2}
$$

where s is a screen function:

$$
s[\varphi_j(t)] = \begin{cases} 1 \text{ if } \varphi_e < \varphi_j(t) < \varphi_a \\ 0 \text{ otherwise} \end{cases} . \tag{3}
$$

More specifically, φ_e and φ_a are the angles where the j-th tooth enters and exist the cut, respectively. In particular, for an up-milling process, $\varphi_e = 0$ and $\varphi_a = \arccos(1-a/R)$ where a is the radial depth of cut and R the radius of cutter. The screen function equals 1 or 0 if the j-th tooth is cutting or not. In the definition (2),

$$
\varphi_j(t) = \frac{2\pi\Omega}{60} t + \frac{2\pi(j-1)}{N} \tag{4}
$$

is the angular position of the jth cutting edge where Ω is the spindle speed in revolutions per minute (rpm). The two parameters K_t and K_n are the linear tangential and the linear normal cutting coefficients, respectively. The stationary cutting force vector

$$
\mathbf{G}(t) = b f_z \begin{bmatrix} H_{xx}(t) \\ H_{yx}(t) \end{bmatrix}
$$

is a τ periodic excitation where f_z is the feed per tooth. The parameter

$$
\tau = \frac{60}{N\Omega} \tag{5}
$$

is the tooth passing period which is also the time delay appearing in the model (1).

Without the regenerative cutting force, represented by $\mathbf{H}(t)$ and $\mathbf{G}(t)$, the free process

$$
\mathbf{M}\ddot{\mathbf{x}}(t) + \mathbf{C}\dot{\mathbf{x}}(t) + \mathbf{K}\mathbf{x}(t) = 0
$$

in this paper is assumed stable. This assumption is certainly true in practice. However, the main research objective is to investigate the influence of the regenerative cutting force on the process stability. A typical analysis is to decompose the system (1) into two parts based on the linear property of the system with

$$
\mathbf{x}(t) = \mathbf{x}_o(t) + \boldsymbol{\xi}(t)
$$

where $\mathbf{x}_o(t)$ is the forced periodic chatter free motion and $\boldsymbol{\xi}(t) = [\xi_x(t)\ \xi_y(t)]^\intercal$ is perturbation corresponding to the self-excited vibrations (chatter). In particular, we have

$$\mathbf{M}\ddot{\mathbf{x}}_o(t) + \mathbf{C}\dot{\mathbf{x}}_o(t) + \mathbf{K}\mathbf{x}_o(t) = \mathbf{G}(t) \tag{6}$$

and

$$\mathbf{M}\ddot{\boldsymbol{\xi}}(t) + \mathbf{C}\dot{\boldsymbol{\xi}}(t) + \mathbf{K}\boldsymbol{\xi}(t) = b\mathbf{H}(t)[\boldsymbol{\xi}(t-\tau) - \boldsymbol{\xi}(t)]. \tag{7}$$

In particular, in (6), we use the assumption that the signal $\mathbf{x}_o(t)$ is τ periodic, i.e., $\mathbf{x}_o(t-\tau) - \mathbf{x}_o(t) = 0$, which is validated by the fact that it is excited by the τ periodic excitation $\mathbf{G}(t)$. Now, the investigation is left on the perturbation system (7). When the depth of cut b is small, the influence of $b\mathbf{H}(t)[\boldsymbol{\xi}(t-\tau) - \boldsymbol{\xi}(t)]$ does not destroy the stability of (7), or the milling process (1). However, with a significant increase of depth of cut, the system (7) becomes unstable and the perturbation $\boldsymbol{\xi}(t)$ increases exponentially. For a given spindle speed, the boundary of depth of cut for stable processes is given by a so-called stability lobes diagram (SLD). The main objective of this paper is to add an active control $\mathbf{u}$ to the perturbation system (7), i.e.,

$$\mathbf{M}\ddot{\boldsymbol{\xi}}(t) + \mathbf{C}\dot{\boldsymbol{\xi}}(t) + \mathbf{K}\boldsymbol{\xi}(t) = b\mathbf{H}(t)[\boldsymbol{\xi}(t-\tau) - \boldsymbol{\xi}(t)] + \mathbf{u}. \tag{8}$$

such that the closed-loop system is stable for larger depths of cut.

Now, we will propose a novel active adaptive LQR controller to stabilize the perturbation system (8). A trivial controller $\mathbf{u} = -b\mathbf{H}(t)[\boldsymbol{\xi}(t-\tau) - \boldsymbol{\xi}(t)]$ obviously exactly cancels the cutting force variation and hence stabilizes the system. However, this controller is not practically reasonable since $\varphi_j(t)$ and hence the matrix $\mathbf{H}(t)$ is not measurable. In particular, we set the reference time t_o as the time when the angular position of the first cutting edge is zero, i.e., $\varphi_1(t_o) = 0$. In the definition of (4), it is implicitly assumed that $t_o = 0$. However, in practice, this t_o is not measurable and hence neither is $\varphi_j(t)$.

The main idea of the new control algorithm is to investigate the structure of $\mathbf{H}(t)$ and then find the estimation of $\mathbf{H}(t)$ for the controller design. We note that, $\mathbf{H}(t)$ is obviously τ periodic and it can be approximated by its partial sum of the Fourier series, i.e., $\mathbf{H}(t) \approx \mathbf{H}_\ell(t)$ where

$$\begin{aligned} \mathbf{H}_\ell(t) &= \begin{bmatrix} \mathbf{w}_{xx}^\intercal \mathbf{h}(t)\ \mathbf{w}_{xy}^\intercal \mathbf{h}(t) \\ \mathbf{w}_{yx}^\intercal \mathbf{h}(t)\ \mathbf{w}_{yy}^\intercal \mathbf{h}(t) \end{bmatrix}, \\ \mathbf{h}(t) &:= [1, \cos(\omega t), \sin(\omega t), \cdots, \cos(\ell\omega t), \sin(\ell\omega t)]^\intercal \end{aligned} \tag{9}$$

and the vectors $\mathbf{w}_{xx}, \mathbf{w}_{xy}, \mathbf{w}_{yx}, \mathbf{w}_{yy} \in \mathbb{R}^{1+2\ell}$ with $\ell \geq 0$ are unknown constant vectors to be estimated.

Now, we will design an adaptive LQR controller with block diagram given in Fig. 2. To facilitate the design, we first discretize the system (7) by setting $t = k\epsilon$, where ϵ is the sampling period satisfying $\tau = \bar{\tau}\epsilon,\ k, \bar{\tau} \in \mathbb{N}$. Then, the system rewrites as

$$\begin{aligned} \mathbf{M}\boldsymbol{\xi}(k+1) - (2\mathbf{M} - \epsilon\mathbf{C})\boldsymbol{\xi}(k) + (\mathbf{M} - \mathbf{C} + \epsilon^2\mathbf{K})\boldsymbol{\xi}(k-1) \\ = b\epsilon^2\mathbf{H}_\ell(k)(\boldsymbol{\xi}(k-\bar{\tau}) - \boldsymbol{\xi}(k)) + \epsilon^2\mathbf{u}(k) \end{aligned} \tag{10}$$

where $\mathbf{H}_\ell(k)$ is a periodical matrix with period being $2\pi/\omega$, and for conciseness. Note that the vectors $\mathbf{w}_{xx}, \mathbf{w}_{xy}, \mathbf{w}_{yx}, \mathbf{w}_{yy} \in \mathbb{R}^{1+2\ell}$ with $\ell \geq 0$ are unknown constant vectors, we use the estimation of $\mathbf{H}_\ell(k)$, i.e., $\hat{\mathbf{H}}_\ell(k)$ in the following LQR algorithm derivation, and the vectors $\mathbf{w}_{xx}, \mathbf{w}_{xy}, \mathbf{w}_{yx}, \mathbf{w}_{yy}$ will be identified by recursive least square estimation (RLSE) online afterwards.

For conciseness, let $f(k\epsilon) := f(k)$ and $\mathbf{z}(k) = [\boldsymbol{\xi}^\mathsf{T}(k), \boldsymbol{\xi}^\mathsf{T}(k-1), \cdots, \boldsymbol{\xi}^\mathsf{T}(k-\bar{\tau})]^\mathsf{T}$, then the system rewrites in a compact form as

$$\mathbf{z}(k+1) = \mathbf{A}(k)\mathbf{z}(k) + \mathbf{B}\mathbf{u}(k)$$

with

$$\mathbf{A}(k) := \begin{bmatrix} 2\mathbf{I} - \epsilon\mathbf{M}^{-1}\mathbf{C} - b\epsilon^2\mathbf{M}^{-1}\hat{\mathbf{H}}_\ell(k) & -(\mathbf{I} - \epsilon\mathbf{M}^{-1}\mathbf{C} + \epsilon^2\mathbf{M}^{-1}\mathbf{K})) & \mathbf{0} \cdots \mathbf{0} & b\epsilon^2\mathbf{M}^{-1}\hat{\mathbf{H}}_\ell(k) \\ \mathbf{I} & \mathbf{0} & \mathbf{0} \cdots \mathbf{0} & \mathbf{0} \\ \mathbf{0} & \mathbf{I} & \mathbf{0} \cdots \mathbf{0} & \mathbf{0} \\ \vdots & \vdots & \ddots \quad \vdots & \vdots \\ \mathbf{0} & \mathbf{0} & \mathbf{0} \cdots \mathbf{I} & \mathbf{0} \end{bmatrix},$$

$$\mathbf{B} := [\epsilon^2(\mathbf{M}^{-1})^\mathsf{T}, \mathbf{0}, \cdots, \mathbf{0}]^\mathsf{T}.$$

An extended state-feedback LQR control law can be developed as

$$\mathbf{u}(k) = -K(k)\mathbf{z}(k). \tag{11}$$

If the performance index is set as $J = \Sigma_{k=0}^{\infty}(\mathbf{z}(k)^\mathsf{T}\mathbf{Q}\mathbf{z}(k) + \mathbf{u}(k)^\mathsf{T}\mathbf{R}\mathbf{u}(k))$, then the optimal control sequence minimizing the performance index is given by

$$K(k) = (\mathbf{R} + \mathbf{B}^\mathsf{T}\mathbf{P}(k)\mathbf{B})^{-1}\mathbf{B}\mathbf{P}(k)\mathbf{A}(k),$$

with $\mathbf{P}(k)$ being the solution of the Riccati equation

$$\mathbf{A}(k)^\mathsf{T}\mathbf{P}(k)\mathbf{A}(k) - \mathbf{P}(k) - \mathbf{A}(k)^\mathsf{T}\mathbf{P}(k)\mathbf{B}(\mathbf{B}^\mathsf{T}\mathbf{P}(k)\mathbf{B} + \mathbf{R})^{-1}\mathbf{B}^\mathsf{T}\mathbf{P}(k)\mathbf{A}(k) + \mathbf{Q} = 0.$$

Here, $\mathbf{Q}$ and $\mathbf{R}$ are both positive definite symmetric weighting matices.

To identify the cutting force variation matrix $\mathbf{H}_\ell(t)$, we derive from Eq. (10) that

$$\mathbf{w}(k)L(k) = Y(k) \tag{12}$$

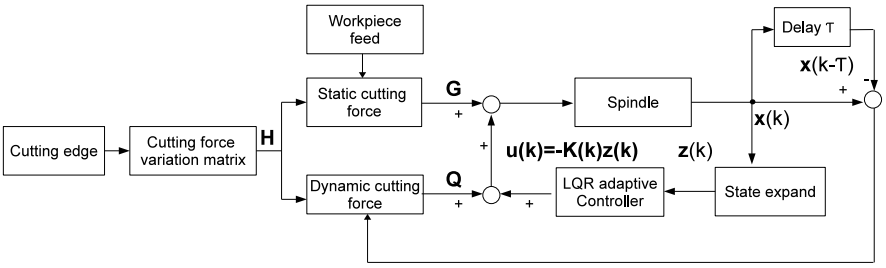

Fig. 2. Block diagram of the closed-loop control system embedded in the intelligent spindle

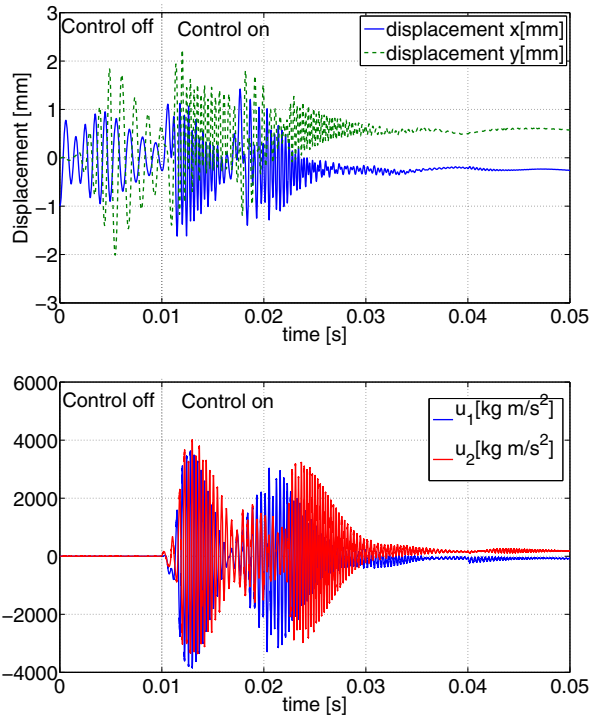

Fig. 3. Chatters are attenuated by the proposed LQR controller (11) with $\Omega = 3000$ RPM and $b = 1$ mm

and hence

$$\hat{\mathbf{w}}(k) = \hat{\mathbf{w}}(k-1) + \frac{\mathbf{\Gamma}(k-1)L(k)}{1 + L^{\mathsf{T}}(k)\mathbf{\Gamma}(k-1)L(k)}(Y(k) - \hat{\mathbf{w}}(k-1)L(k-1)),$$

$$\mathbf{\Gamma}(k) = \frac{1}{\lambda}\left[\mathbf{\Gamma}(k-1) - \frac{\mathbf{\Gamma}^{\mathsf{T}}(k-1)L(k)L^{\mathsf{T}}(k)\mathbf{\Gamma}(k-1)}{\lambda + L^{\mathsf{T}}(k)\mathbf{\Gamma}(k-1)L(k)}\right],$$

with $\hat{\mathbf{w}}(k) := \begin{bmatrix} \hat{\mathbf{w}}_{xx}^{\mathsf{T}} & \hat{\mathbf{w}}_{xy}^{\mathsf{T}} \\ \hat{\mathbf{w}}_{yx}^{\mathsf{T}} & \hat{\mathbf{w}}_{yy}^{\mathsf{T}} \end{bmatrix}$, $L(k) := \begin{bmatrix} \mathbf{h}(k)(\xi_x(k-\bar{\tau}) - \xi_x(k)) \\ \mathbf{h}(k)(\xi_y(k-\bar{\tau}) - \xi_y(k)) \end{bmatrix}$, $Y(k) := 1/b\epsilon^2$ $(\mathbf{M}\boldsymbol{\xi}(k) - (2\mathbf{M} - \epsilon\mathbf{C})\boldsymbol{\xi}(k-1) + (\mathbf{M} - \mathbf{C} + \epsilon^2\mathbf{K})\boldsymbol{\xi}(k-2) - \epsilon^2\mathbf{u}(k-1))$, and λ being a forgetting factor. $\mathbf{\Gamma}$ is an intermediate matrix which can be set as a unit matrix $\mathbf{I}$ from the beginning. Note that we use the currently available displacements $\boldsymbol{\xi}(k-i),\ (i = 0, \cdots, \bar{\tau})$ and $u(k-1)$ to identify $\mathbf{w}(k)$.

3 Numerical Simulation

In this section, we consider the model (1) whose parameters are summarized in Table 1. Moreover, we have used two typical parameter combinations of $b = 5$mm,

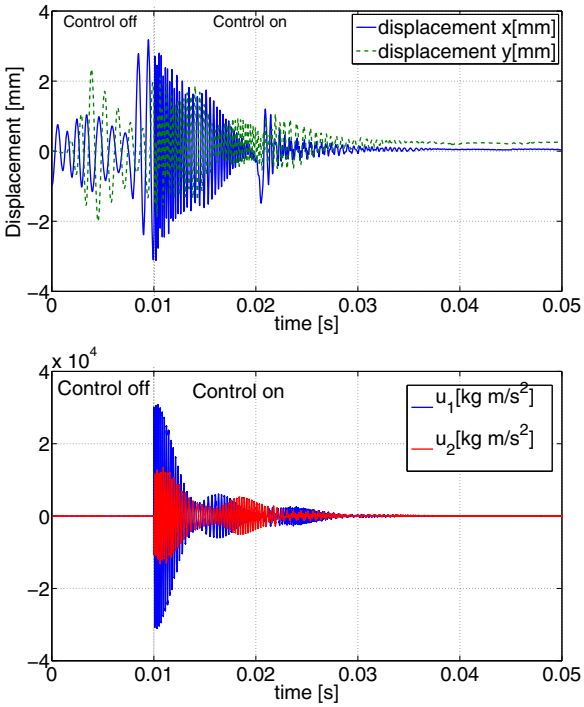

Fig. 4. Chatters are attenuated by the proposed LQR controller (11) with $\Omega = 4000$ RPM and $b = 1$ mm

Table 1. Model parameters

N	number of teeth	2
m	mass	0.013kg
K_t	linear tangential cutting coefficients	$6 \times 10^7 \text{kg}/(\text{ms}^2)$
K_n	linear normal cutting coefficients	$2 \times 10^7 \text{kg}/(\text{ms}^2)$
ζ	damping ratio	0.05
ω_n	natural frequency	$2\pi \times 778$rad/s
a	radial depth of cut	3mm
R	radius of cutter	3mm
f_z	feed per tooth	0.1mm
b	axial depth of cut	variable
Ω	spindle speed in rpm	variable

$\Omega = 4000$rpm and $b = 5$mm, $\Omega = 3000$rpm, respectively. Besides, we set the sampling time $T_s = 0.002s$ and hence $\bar{\tau} = \tau/T_s = 5$. The weighting matrices are set as $\mathbf{Q} = \mathbf{I}$ and $\mathbf{R} = 2\mathbf{I}$. As shown in Fig. 3, we initially set the active control law $u = 0$, i.e. the system is initially open-loop, then x-axis and y-axis displacements diverge shortly and hence the chatters happen as the combination of Ω and b is unstable from SLD.

To examine the proposed controller 11, from the 100-th ms, we implement the active LQR control law on the system, then x-axis and y-axis displacements of the closed-loop system quickly settle down, and hence the chatters are substantially attenuated. Analogously, we also carry our the active LQR control law for $\Omega = 4000$rpm in Fig. 4, and the chatters are effectively alleviated as well. The feasibility and superiority of the LQR control method are thus verified.

4 Conclusion

In this paper, a novel active LQR control method is proposed to attenuate the chatters of milling processes. Fourier series are use to approximate the periodical excitations of the cutting tools, and hence the system has been represented by an extended state-space form. Thereby, we have developed an LQR method to stabilize the self-excited vibrations or chatters. As the cutting angle is not measurable, we have used RLSE method to online identify the cutting force variation matrix. In this way, an active adaptive controller is developed, which stabilizes the chatter dynamics with adaptivity to the axial depth of cut. Intensive numerical simulation on a two DOF milling model has shown that the chatter effect can be substantially attenuated and the stable SLD region can be significantly expended. As a result, larger depths of cut and hence higher MMRRs are expected.

Acknowledge. H.-T. Zhang would like to acknowledge the support of the National Natural Science Foundation of China under Grant Nos. 5112015500 and 91023034, and the Program for New Century Excellent Talents in University of China under Grant No. NCET-09-0343. Z. Chen would like to acknowledge the support of the Australian Research Council under Grant DP0878724.

References

1. Ding, Y., Zhu, L.M., Zhang, X.J., Ding, H.: Milling stability analysis using the spectral method. Science China Technological Sciences 54(12), 3130–3136 (2011)
2. Ding, Y., Zhu, L.M., Zhang, X.J., Ding, H.: Numerical integration method for prediction of milling stability. J. Manuf. Sci. Eng. 133(3), 031005 (2011)
3. Kern, S., Ehmann, C., Nordmann, R., Roth, M., Schiffler, A., Abele, E.: Active damping of chatter vibrations with an active magnetic bearing in a motor spindle using μ-synthesis and an adaptive filter. In: Proc. 8th Int. Conf. Motion Vibr. Control, Daejeon, Korea (2006)
4. Insperger, T., Grandisek, J., Kalveram, M., Stépán, G., Winert, K., Govekar, E.: Machine tool chatter and surface location error in milling processes. J. Manuf. Sci. Eng. 128, 913–920 (2006)
5. Insperger, T., Stépán, G.: Stability analysis of turning with periodic spindle speed modulation via semi-discretisation. J. Vibr. Control 10, 1835–1855 (2004)
6. Yilmaz, A., AL-Regib, E., Ni, J.: Machine tool chatter suppression by multi-level random spindle speed variation. J. Manuf. Sci. Eng. 124(2), 208–216 (2002)
7. Dohner, J.L., Lauffer, J.P., Hinnerichs, T.D., Shankar, N., Regelbrugge, M., Kwan, C.-M., Xu, R., Winterbauere, B., Bridgerf, K.: Mitigation of chatter instabilities in milling by active structural control. J. Sound and Vibr. 269(1-2), 197–211 (2004)

8. Fittro, R.L., Knospe, C.R., Stephens, L.S.: μ-synthesis applied to the compliance minimization of an active magnetic bearing hsm spindle's thrust axis. Machin. Sci. Technol. 7(1), 19–51 (2003)
9. Zhang, Y., Sims, N.D.: Milling workpiece chatter avoidance using piezoelectric active damping: A feasibility study. Smart Mater. Structures 14(6), N65–N70 (2005)
10. Shiraishi, M., Yamanaka, K., Fujita, H.: Optimal control of chatter in turning. Int. J. Mach. Tools Manuf. 31(1), 31–43 (1991)
11. Chen, M., Knospe, C.R.: Control approaches to the suppression of machining chatter using active magnetic bearings. IEEE Trans. Control Syst. Technol. 15(2), 220–232 (2007)

Robot Surgery Simulation System for Soft Tissue Cutting

Hesheng Wang[1,2], Maojiao Cai[1], Weidong Chen[1,2], Meng Li[1], and Kang Li[3]

[1] Department of Automation, Shanghai Jiao Tong University, 200240 Shanghai, China
[2] Key Laboratory of System Control and Information Processing,
Ministry of Education of China, 200240 Shanghai, China
[3] Electrical Engineering and Computer Science, Queen's University Belfast,
Belfast BT9 5AH, UK
{wanghesheng,wdchen}@sjtu.edu.cn

Abstract. This paper presents a robot surgery simulation system for soft tissue cutting. Tetrahedron is used to construct the geometric model of soft tissue. An improved cutting algorithm based on minimal subset method is proposed. Splitting divisive issue in the minimal subset method is solved. By amending the relative position between the edge/surface intersection and the vertex during cutting, the emergence of small and narrow triangular surface and tetrahedral could be prevented. Hence enhance the stability of tetrahedral. GPU technology is implied for real time simulation. The performances of the computer simulation system are demonstrated with haptic device.

Keywords: Robot Surgery, Soft Tissue, Tetrahedral Cutting, Simulation.

1 Introduction

The virtual surgery system is an important application of virtual reality technology in the medical field. Virtual surgery system integrates computer graphics, control theory, robotics, biomechanics and medical fields. The major concern includes the interaction and visualization of medical image data, the simulation and feedback of the objects movement, surgical procedures such as cutting algorithm and so on. To achieve the purpose of training, the 3D models built in surgical simulation system must be truthful and reliable, the feedback must be timely, and data transmission must be accurate. Therefore, how to find an appropriate model structure and the cutting algorithm are important issues in surgical simulation system.

Soft tissue cutting simulation has been studied by many researchers in recent years. The research topic is focus on how to realize model cutting technology. Most methods are established based on the classic grid model. For model cutting with grids, grids of objects are formed by finite element, usually by tetrahedral. Thus the mesh is disassembled and calculated during cutting and visual effects and force feedback are provided. Modeling with tetrahedral mesh is effectiveness and accurate. However, it is time consuming and costly. Bro-Nielsen et al. [1] proposed removal method. In this method, the model is built by tetrahedral or polyhedral mesh, while the tool as the

J. Lee et al. (Eds.): ICIRA 2013, Part II, LNAI 8103, pp. 535–544, 2013.

eraser, those polyhedral who come into contact with it is immediately be got rid of. However, the realistic is poor since many jagged edges exist. It is also difficult for other calculation due to the quality of the model is lost. Bielser et al. [2][3] proposed segmentation method. This method greatly improves the true extent of the model simulation. However these methods led to the model number is growing exponentially large, resulting in real-time problems. More et al. [4][5] proposed minimal subset method. Topology is divided into five categories after tetrahedron cutting. The minimum number of tetrahedral element is achieved after tetrahedron splitting. Real time calculation is ensured. However, splitting divisive issues exist. Bielser [6] proposed an improved state machine method. This method produces a lot of cutting status information, also makes real-time is difficult to achieve. Wicke et al. [7] proposed an advanced algorithm which can be applied to the grid of the convex polyhedron. Denis Steinemann et al. [8] proposed mixed-cutting model for deformable objects. The intersection between the cutting plane and the tetrahedron vertices are divided into three kinds by this algorithm. The cutting point will be moved to the vertex if there distance is too close. All points which have been moved will be re-moved back to the tangent plane after cutting. Nienhuys et al. [9][10] proposed a cutting algorithm which gives a precise incision but does not increase the tetrahedrons number. However, there is inherent delay between the surgical instruments and actually cutting in this method. It is also easy to produce the degradation of the tetrahedron. Most of model cutting described in previously literature are classic grid cutting. It is hard to guarantee real time performance for some classic cutting methods such as removal method, subdivision method and minimal subset method.

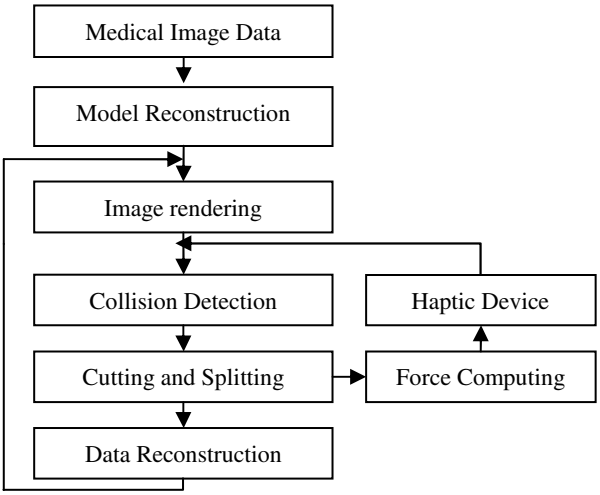

Fig. 1. Framework of soft tissue cutting simulation system

This paper presents a robot surgery simulation system for soft tissue cutting. Tetrahedron is used to construct the geometric model of soft tissue. An improved cutting algorithm based on minimal subset method is proposed. Splitting divisive issue in the minimal subset method is solved. The stability of triangle or tetrahedron has great impact on the stability of the entire system. Special circumstances during cutting or the appearance of abnormal polyhedron will result in the failure of the algorithm and the error occurred. By amending the relative position between the edge/surface intersection and the vertex during cutting, the emergence of small and narrow triangular surface and tetrahedral could be prevented. Hence enhance the stability of tetrahedral. GPU technology is implied for real time simulation. The performances of the computer simulation system are demonstrated with haptic device.

2 System Overview

The framework of soft tissue cutting simulation system is shown in Fig. 1. In this system, data is extracted from medical images or video. The soft tissue models, surgical instruments and scenes are drawn. In human-computer interaction phase, a haptic device is operated by a surgeon. A cycle of calculation including cutting and feedback will start when the collision between surgical instruments and soft tissue is detected. Then the tetrahedral model is reconstructed and split. The new model is drawn and refreshed in the final stage.

The whole system can be divided into four modules: data preprocessing module, the main processing module, human machine interaction module, graphics operator display module. The five most important parts including model reconstruction, image rendering, collision detection, cutting and splitting, and force computing will be introduced in the following.

Models are generally divided into two types: surface models and volume models. There are many modeling methods for soft tissue. Among them, triangle and tetrahedron are the most widely used surface and volume models. The volume model used to build bone and soft tissue structures. The surface model is for representing surface structure of the soft tissue and mucous membranes. The volume model is used to build bone and soft tissue structures.

In image rendering stage, GPU is implied for fast graphics computation to achieve real-time display performance. To display 3D model, perspective transformation, lighting, rendering and texture mapping are needed. These are realized by OpenGL interface.

AABB bounding box method is used for collision detection.When a collision occurs between surgical instruments and soft tissue model, a threshold judgment will start based on the intensity generated by the collision. If the value is larger than this threshold, it can be concluded that the cutting has begun. The tetrahedron encountered by the surgical instrument during collision is marked for cutting and splitting.

Cutting and splitting is a core part of the simulation system. Almost all surgical simulation systems consider whether the cutting is easy to implement or not,

otherwise this set of surgical simulation system will lose its most important meaning of the "operation". The main purpose is how to cut and split the tetrahedral mesh after the surgical instruments contact with the model in order to achieve the visual and tactile effect. The quality of the mesh cutting algorithm is the key to cutting and splitting. This part will be discussed in detail in next section.

For force computing, several methods have been proposed, which include spring-mass models, linear elasticity with finite volume method, and various finite element methods (FEM). Although FEM is sufficiently accurate, it is time-consuming and hence not suitable for real-time applications. One possible approach is the mass-spring model. In this model, tissue is represented by a mesh of springs, with point masses placed at the connecting nodes and elastic interactions among the nodes. Due to their computational simplicity, they can be rapidly updated to represent the dynamic behavior of the tissues.

3 Soft Tissue Cutting Algorithm

3.1 Minimal Subset Method

The major concern for soft tissue cutting is how to cut and split the tetrahedral mesh after the surgical instruments contact with the model. The cutting trajectory of curve formed by the tip and the tail of a knife is a plane. The problem can be simplified as, cutting the tetrahedron by a plane. It is proved by mathematics that there are total five topologies for a plane cutting the tetrahedron. These topologies are shown in Fig.2. The topological type could be estimated uniquely according to the number of edge intersection point and the number of plane intersection point. Then split schematic in the five topologies is confirmed as shown in Fig.3.

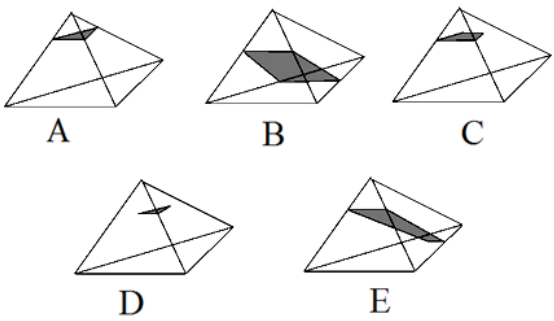

Fig. 2. The five topologies in tetrahedral cutting

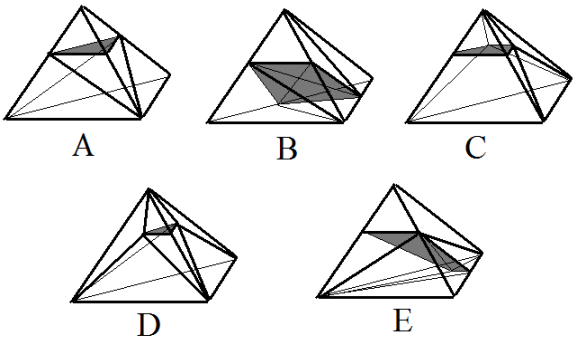

Fig. 3. Split schematic in the five topologies

Table 1. The relationship between the topological type and the plane/edge intersection

Topological type	The number of new tetrahedral	The number of plane intersection point	The number of edge intersection point
A	4	0	3
B	6	0	4
C	8	2	2
D	6	2	1
E	9	1	3

3.2 Revised Minimal Subset Method

The minimal subset method can solve a lot of cutting problems. But it can be known from Fig. 4, if the plane is cutting edge or point of the tetrahedron, minimal subset method is powerless. Although this probability is small, the optimization cannot be carried out during tetrahedral stability optimization if this type of cutting problem was not solved. In addition, the minimal subset method classify the topology of tetrahedral cutting first, and directly copy the split part into the corresponding new tetrahedron, this algorithm is more cumbersome to implement, there is room for improvement.

In general, if the cutting plane is coincided with one point, one edge or one plane of the tetrahedron, it will lead to the failure of the minimal subset method. The solution is to copy the split of the intersecting points, edges or planes.

The revised minimal subset method is as follows:

1) After collision detection, go through all the tetrahedral being cutting. Calculate the number of points, edges, and surface in these tetrahedrons.

2) According to the number of the plane intersection point and the edge intersection point, determine the topological type as Table 1. Classified according to the minimal subset method, A and B are completely cutting. It can be split into a minimal subset as Fig. 3. C, D and E belong to incomplete cutting. Perform fine operation for the

plane intersection point and the edge intersection point during cutting as shown in Fig. 5. The original tetrahedron is divided into three new tetrahedral by the plane intersection point; the original tetrahedron is divided into two new tetrahedral by the edge intersection point. C, D and E are split first according the above method. The new generated tetrahedron must belong to type A or B. Then follow A or B cutting method for complete cutting. Table 2 lists the detail types which C, D and E can be divided into.

3) Count the number of the point, edge or plane intersection point, if it belong to a special cutting situation, copy and split the corresponding points, edges or planes.

4) Refine the new generation of tetrahedral. Delete these split tetrahedron.

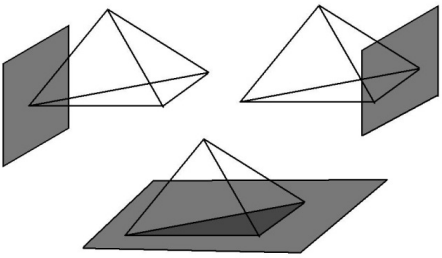

Fig. 4. Three special cutting circumstances

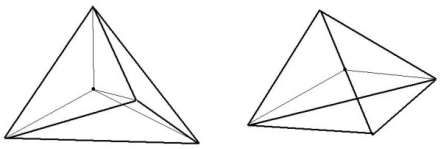

Fig. 5. Fine operation for the plane intersection point and the edge intersection point

Table 2. The cutting types for the five cutting topologies

Topological type	Cutting type	Subdivision species
A	Complete cutting	None
B	Complete cutting	None
C	Incomplete cutting	A+A
D	Incomplete cutting	A
E	Incomplete cutting	A+B

3.3 Stability Improvement

Some irregular polyhedron or abnormal cutting may happened during actual cutting. The reason is that there will be very small tetrahedral or narrow tetrahedron appears if

some cutting interaction points are particularly close to the tetrahedral vertices. These situations may lead to system instable or algorithm failure.

Abnormal cutting could be judged by the stability criterion. The general approach is to define the stability of the tetrahedral element by the radius ratio of the inscribed sphere and the circumscribed sphere of the tetrahedron unit. i.e.

$$Q=r/R \tag{1}$$

where r is the radius of the inscribed sphere of the tetrahedron unit, R is the radius of the circumscribed sphere of the tetrahedron unit. When Q is close to 0, the quality of this tetrahedron grows worse.

This method may achieve very good results for elimination of the narrow flat tetrahedron, but could do nothing for very small tetrahedron. The size of the tetrahedron cannot be characterized by the radius ratio of the inscribed sphere and the circumscribed sphere of the tetrahedron.

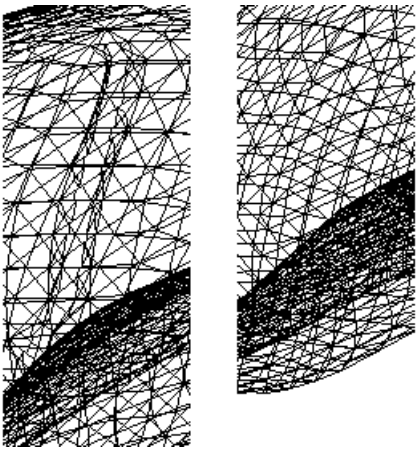

Fig. 6. Volume model cutting

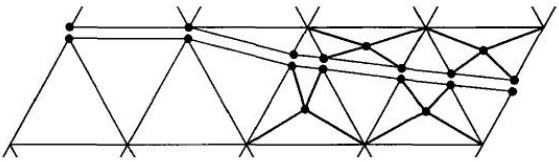

Fig. 7. Surface model cutting

In this paper, cutting translation method is adopted. Those edge/plane interaction point which are close to the vertex will be relocated. Whether the interaction point should be shift to the vertex is based on the relative distance between the edge/plane

interaction point and the vertex of the tetrahedron. Those edge/plane interaction point meet the conditions will be shift to the vertex, others remain in the same location.

The left part in Fig. 6 illustrates the real effect of cutting after application of the improved algorithm (wireframe display mode). Surface model simulation result is shown in Fig. 7. The cutting trajectory is significantly changed. It should be a straight line, but the cutting traces are changed due to the shift operation on the edge/plane interaction point. The cutting trajectory is no longer in strict accordance with the tool cutting path (of course, the elastic model may has impact on the cutting trajectory too). However, the stability of the tetrahedron would be enhanced to prevent the probability of cutting error in system operation.

4 Experimental Results

We have implemented the proposed method in a surgery simulation system (Fig. 8) at our laboratory. This system constitutes a haptic device, a computer and a display monitor. To increase the authenticity and real-time property of the 3D model simulation, GPU technology is adopted here. Falcon, a haptic device, is provided to the user for operating surgical instruments. This device will also bring real-time force feedback to the user. Schematic diagram of the system hardware is shown in Fig. 9.

Fig. 8. Simulation system setup

To demonstrate the performance of this system, we created a liver model. In the surface model, there are 4384 surfaces, which are constituted by 2193 points. In the volume model, 597 tetrahedral are selected. OpenGL is involved in the model rendering part. Two threads are created in system operation, one thread for computing, GPU and CPU data exchange, another thread for real-time monitoring of haptic devices.

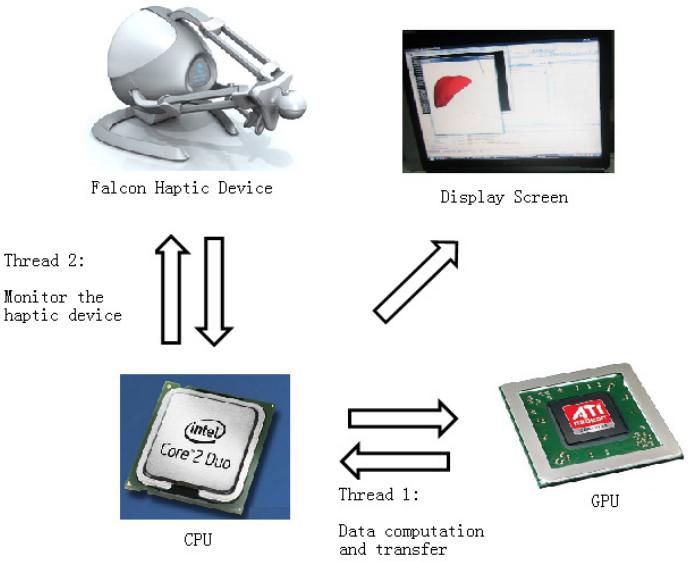

Fig. 9. Schematic diagram of the system hardware

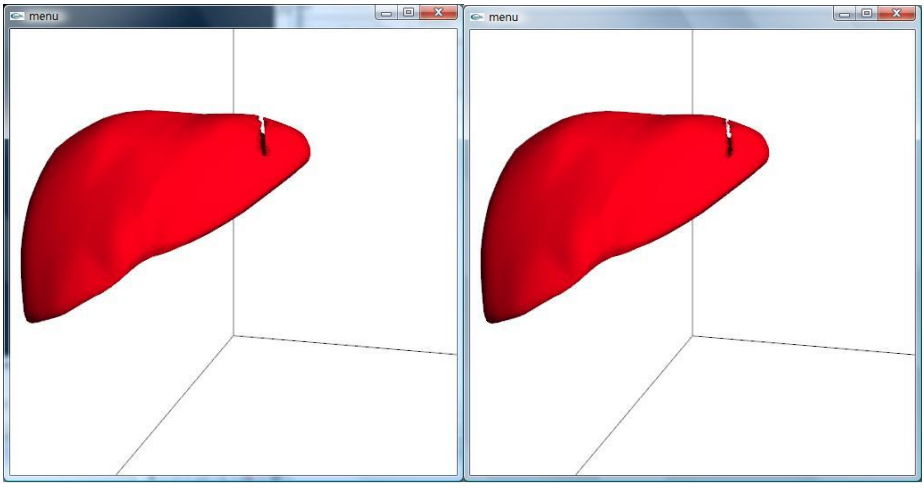

(a) (b)

Fig. 10. Simulation results: (a) minimal subset method; (b) improved minimal subset method

Fig 10(a) is the experimental result by minimal subset method. Some incomplete tetrahedral happened which was caused by edge or surface cutting. Therefore, as shown in the figure, some irregular situations appear in the gap. It is also difficult to deal with cutting of the next part. Fig.10(b) illustrate the performance of the proposed improved minimal subset method.

5 Conclusion

In this paper, we proposed a robot surgery simulation system for soft tissue cutting. Triangle and tetrahedron are used in surface and volume models. An improved minimal subset method is proposed for cutting algorithm. This method starts from the determination and classification of the number of edge intersection point, plane and volume intersection point. The topologies in minimal subset method are reclassified. These results by wrong cutting and unable to handle are disappear. It can also determine and solve the tetrahedron stability. To increase the real time performance, GPU is implied for parallel calculation. Simulations have been performed to verify the performance of the proposed method.

Acknowledgments. Manuscript received April 22, 2013. This work was supported in part by Specialized Research Fund for the Doctoral Program of Higher Education of China (20100073120020, 20100073110018), in part by Shanghai Municipal Natural Science Foundation (11ZR1418400), in part by the Natural Science Foundation of China (61105095, 60334010, 60475029), in part by International Cooperation Project of Science and Technology Department, China (2011DFA11780) and in part by Medical Engineering Project of Shanghai Jiao Tong University (YG2011ZD08).

References

1. Bro-Nielsen, M.: Finite element modeling in surgery simulation. Proceedings of the IEEE 86(3), 490–503 (1998)
2. Bielser, D., Gross, M H.: Interactive simulation of surgical cuts. In: Eighth Pacific Conference on Computer Graphics and Applications, pp. 116–125 (2000)
3. Bielser, D., Gross, M.H.: Open surgery simulation. In: Proceedings of Medicine Meets Virtual Reality, pp. 57–62 (2002)
4. Mor, A.B.: Progressive Cutting with Minimal New Element Creation of Soft Tissue Models for Interactive Surgical Simulation. Ph.D. dissertation, The Robotics Institute, Carnegie Mellon University, USA (2001)
5. Mor, A.B., Kanade, T.: Modifying soft tissue models: Progressive cutting with minimal new element creation. In: Delp, S.L., DiGoia, A.M., Jaramaz, B. (eds.) MICCAI 2000. LNCS, vol. 1935, pp. 598–608. Springer, Heidelberg (2000)
6. Daniel, B., Glardon, P., Teschner, M.: A state machine for real-time cutting of tetrahedral meshes. Graphical Models 66(6), 398–417 (2004)
7. Martin, W., Mario, B., Markus, G.: A finite element method on convex polyhedra. Computer Graphics Forum 26(3), 355–364 (2007)
8. Denis, S., Matthias, H., Markus, G.: Hybrid cutting of deformable solids. In: IEEE Virtual Reality Conference, pp. 35–42 (2006)
9. Nienhuys, H.-W., van der Stappen, A.F.: Combining finite element deformation with cutting for surgery simulations. In: EUROGRAPHICS 2000, pp. 274–277 (2000)
10. Nienhuys, H.-W., van der Stappen, A.F.: A Surgery Simulation Supporting Cuts and Finite Element Deformation. In: Niessen, W.J., Viergever, M.A. (eds.) MICCAI 2001. LNCS, vol. 2208, pp. 145–152. Springer, Heidelberg (2001)
11. Shewchuk, J.: Delaunay Refinement Mesh Generation: Ph.D. Dissertation. Carnegie Mellon University, Pittsburgh, Pennsylvania (1997)

A Novel PWM Scheme for Position Sensorless Control of BLDC Motor Drives Based on Back EMF

Zicheng Li, Zhouping Yin, and You-lun Xiong

State Key Lab of Digital Manufacturing Equipment and Technology,
Huazhong University of Science and Technology,
430074, Wuhan, China
lizich@sohu.com

Abstract. The method based on back electromotive force (EMF) of brushless direct current (BLDC) motor is one of the major approaches for rotor position estimation because of the advantages of simple and reliable detection. However, the position estimation precision is affected by different pulse width modulation (PWM) strategies. This paper presents a novel PWM strategy for position detection based on the zero-crossing of back EMF. Five traditional kinds of PWM strategies for BLDC motor are analyzed and compared. Through the analysis to the diode freewheeling currents in the unexcited phase on non-commutation period, the applicable PWM strategies are obtained corresponding to above rotor position identification methods. On the basis, a novel PWM scheme is proposed for position sensorless control of BLDC motor drives and it can reduce the diode freewheeling current. Simulation and experimental results show the good performance for the proposed PWM scheme in position estimation for sensorless BLDC motor drives.

Keywords: Brushless direct current motor, Position sensorless, Pulse width modulation, Rotor position estimation.

1 Introduction

BLDC motor is widely used in various applications of electromechanical systems such as computer, aerospace position and speed control, industrial and household products [1-3]. For three phase motors with six-step commutation, position information is indispensable and the BLDC motor requires rotor position sensor, such as resolver or three hall sensors. However, the sensors increase the cost and size of the motor drive system. Because of above reasons, sensorless algorithms have been widely developed in order to energize the correct phase of windings at the exact commutation position [4,5].

Sensorless position control strategies for BLDC motor have been proposed for obtaining the rotor position and speed [6-8]. The method based on back EMF of the motor is one of the major approaches for sensorless BLDC motor drives. For this method, estimating the rotor position is indirectly obtained by using the zero-crossing point detection from the terminal voltage of the unenergized phase winging. Some researchers have proposed several methods to detect the exact rotor position based on

J. Lee et al. (Eds.): ICIRA 2013, Part II, LNAI 8103, pp. 545–554, 2013.

the zero-crossing of back EMF [9]. Shao originally proposed the method of sensing back EMF to build a virtual neutral point, and then the voltage difference between the virtual neutral and the voltage at the floating terminal is sensed [10]. A new rotor position estimation method based on the zero-crossing of line back EMF of the motor is also presented in [11]. These methods have disadvantages to monitor both current and voltage.

For sensorless control of BDLC motor drives, different PWM schemes may involve the detection error of a rotor position due to the switching noise, and results in the reduction of maximum electromagnetic torque and efficiency of the BLDC motor.

This paper presents a novel PWM strategy for position estimation based on the zero-crossing detection of back EMF. Five traditional kinds of PWM strategies for BLDC motor with six-step commutation are analyzed and compared. Through the analysis to the diode freewheeling currents in the unexcited phase on non-commutation period, the applicable PWM strategies are obtained corresponding to above rotor position identification methods. On the basis, a novel PWM scheme is proposed for position sensorless control of BLDC motor drives. It can reduce the diode freewheeling current and the zero-crossing of back EMF can be detected accurately. Simulation results show the good performance for the proposed PWM scheme in position estimation for sensorless control for BLDC motor drives. It also develops a sensorless BLDC motor driver to implement the proposed method based on DSP and the experimental results verified its effectiveness.

This paper is organized as follows: Section 2: Zero-crossing of back-EMF model, Section 3: The optical PWM scheme for back-EMF sensing technique, Section 4: Simulation results, Section 5: Experimental results, and section 6: Conclusion.

2 Zero-Crossing Detection Method of Back EMF

2.1 Model of BLDC Motor

Generally, BLDC motor is driven by a three-phase inverter with six-step commutation as Fig. 1.

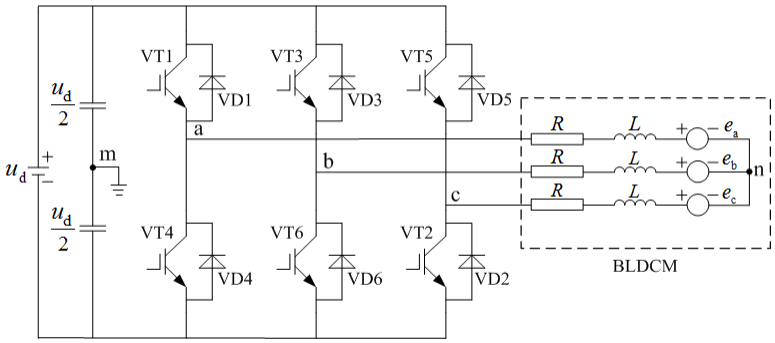

Fig. 1. Inverter configuration for BLDC motor

Assume the BLDC motor is in an electric balance condition and the back EMF of the three phase windings are symmetrical, each phase of BLDC motor can be described by a first order different equation. The general equations of the phase voltages for the BLDC motor can be derived in the matrix form as follows.

$$\begin{bmatrix} u_a \\ u_b \\ u_c \end{bmatrix} = \begin{bmatrix} R & 0 & 0 \\ 0 & R & 0 \\ 0 & 0 & R \end{bmatrix} \begin{bmatrix} i_a \\ i_b \\ i_c \end{bmatrix} + \begin{bmatrix} L & 0 & 0 \\ 0 & L & 0 \\ 0 & 0 & L \end{bmatrix} \frac{d}{dt} \begin{bmatrix} i_a \\ i_b \\ i_c \end{bmatrix} + \begin{bmatrix} e_a \\ e_b \\ e_c \end{bmatrix} \tag{1}$$

Where, u, i, e, R, L_s and L_m represent the phase voltage, phase current, phase back EMF, stator resistor, stator inductor and mutual inductor respectively. $L=L_s-L_m$, a,b and c represent different phase respectively.

Every phase back EMF is expressed as follows

$$\begin{cases} e_a = u_a - Ri_a - L\dfrac{di_a}{dt} \\ e_b = u_b - Ri_b - L\dfrac{di_b}{dt} \\ e_c = u_c - Ri_c - L\dfrac{di_c}{dt} \end{cases} \tag{2}$$

2.2 Detection Method Based on Zero-Crossing of Back EMF

To a BLDC motor, ideal back EMF is sinusoidal or trapezoidal waveform as in fig. 2. So the zero-crossing of phase back EMF shifted by 30° is commutation point.

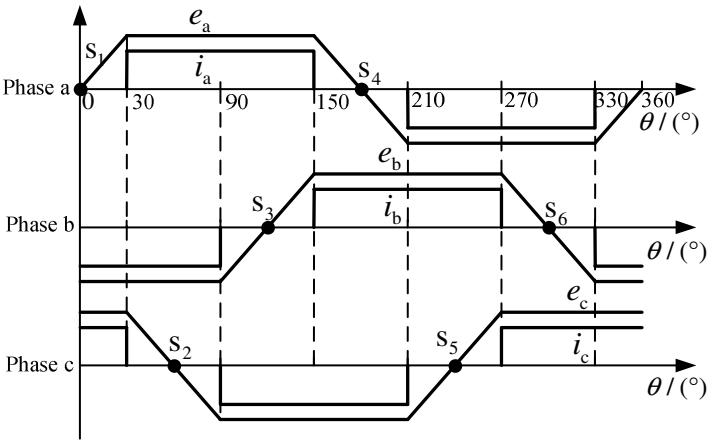

Fig. 2. Ideal back EMF and current waveforms

In fig. 2, there are six zero-crossing points of back EMF: S_1-S_6, which shifted by 30° respectively are rotor position commutation points. According to (2), back EMFs are

related with phase voltages. However, phase voltages are directly measured because the motor neutral point is not provided for Y type connection of stator windings. So every line-to-line voltage can be expressed as follows by phase currents and back EMFs.

$$\begin{cases} u_{ab} = R(i_a - i_b) + L\dfrac{d(i_a - i_b)}{dt} + e_a - e_b \\ u_{bc} = R(i_b - i_c) + L\dfrac{d(i_b - i_c)}{dt} + e_b - e_c \\ u_{ca} = R(i_c - i_a) + L\dfrac{d(i_c - i_a)}{dt} + e_c - e_a \end{cases} \tag{3}$$

According to (3), one line voltage is subtracted from another line voltage and it can be simplified as:

$$2e_b = (u_{bc} - u_{ab}) - 3Ri_b - 3L\frac{di_b}{dt} \tag{4}$$

So three back EMFs can be calculated by line voltages and phase currents and be used to estimate rotor position.

3 The Optimal PWM Strategy for Phase Back EMF

3.1 PWM Modes for BLDC Motor

BLDC motor speed is usually adjusted by the magnitude of phase voltage, which is changed by different PWM schemes. There are five PWM modes as table 1.

Table 1. PWM modes for BLDC motor driving

PWM mode	Meaning
Hpwm_Lon	Upper transistor PWM and lower transistor on
Hon_Lpwm	Upper transistor on and lower transistor PWM
PWM_ON	Last 60° PWM and next 60° on
ON_PWM	Last 60° on and next 60° PWM
Hpwm_Lpwm	Two transistors all PWM

3.2 Non-commutation Current Analysis of PWM Modes

Here, the diode freewheeling current in the unexcited phase on non-commutation is analyzed as example of phase b. Assume commutation is finished during 10 electric degree from figure 2, it shows that phase b commutation period can be divided into four periods: 100° -120° , 120° -150° , 280° -300° and 300° -330° . As a result, phase currents and back EMFs can be expressed during different non-commutation interval as follows

$$\begin{cases} i_a = -i_c = I, e_a = -e_c = E & 100° < \theta < 150° \\ i_c = -i_a = I, e_c = -e_a = E & 280° < \theta < 330° \end{cases} \tag{5}$$

There, I and E are amplitude of current and back EMF respectively in stable state. According to (1), phase voltage can be expressed as follows

$$\begin{cases} u_a = u_d s_a = Ri_a + Ldi_a / dt + e_a + u_n \\ u_b = e_b + u_n \\ u_c = u_d s_c = Ri_c + Ldi_a / dt + e_c + u_n \end{cases} \tag{6}$$

Where, s_a and s_c are voltage level state function of phase a and c. If s_a=1, it means that power transistor VT1 or diode VD1 is switched on. But on the contrary if s_a=0, it means that power transistor VT1 or diode VD1 is turn-off. It can be simplified further as follows

$$e_a = \frac{1}{2} u_d (s_a - s_c) - (Ri_a + Ldi_a / dt) \tag{7}$$

When 100° <θ<150° , i_a>0, then

$$E = e_a < \frac{1}{2} u_d - (Ri_a + Ldi_a / dt) < \frac{1}{2} u_d \tag{8}$$

When100° <θ<150° , i_a >0, then

$$-E = e_a > -\frac{1}{2} u_d - (Ri_a + Ldi_a / dt) > -\frac{1}{2} u_d \tag{9}$$

According to (8) and (9) , it can show that

$$E < \frac{1}{2} u_d$$

Terminal voltage and back EMF of the phase b are related to motor mid-point voltage. Table 2 shows current freewheeling states on condition of commutation period.

Table 2. Relation between PWM modes and freewheeling current

PWM mode	100° -120°	120° -150°	280° -300°	300° -330°
Hpwm_Lon	i>0	No current	No current	i>0
Hon_Lpwm	No current	i<0	i<0	No current
PWM_ON	No current	i<0	No current	i>0
ON_PWM	i>0	No current	i<0	No current
Hpwm_Lpwm	No current	No current	No current	No current

3.3 Influence on Detection for Back EMF Due to PWM Modes

According to fig. 1 and table 2, we can know which PWM mode satisfies the condition of calculation for improved back EMF.

When zero crossing of S_3 is calculated, the current of phase b must be zero. According to table 2, current freewheeling in 100° -120° period does not happen, which includes three PWM modes of Hon_Lpwm, PWM_ON and Hpwm_Lpwm.

In the same way, when zero crossing s6 is calculated, the current of phase b must be zero. According to table 2, current freewheeling in 280° -300° period does not happen, which includes three PWM modes of Hpwm_Lon, PWM_ON and Hpwm_Lpwm.

Obviously, PWM modes which fit for all above calculation conditions are PWM_ON and Hpwm_Lpwm. In consideration of consistence of up and down transistor, PWM mode of Hpwm_Lpwm is more suitable for estimation of rotor position.

4 Simulation Results

The proposed sensorless control algorithm for BLDC motor drives has been applied to current loop control. The simulation is performed for the verification of the above control scheme. It is simulated for one current loop by a sampling period of 100μs. The rated power and speed of the BLDC motor are 370W and 3000rpm, the rated voltage and frequency are 380V and 50Hz, number of pole is 4, and the motor parameters are as follows. *R*s=2.875Ω, *L*s=8.5mH, *L*m=1.60H.

Fig. 3 show the phase current waveforms by different PWM modes in close loop control at 300rpm respectively. In five PWM modes, the phase current is constant in un-excited for Hpwm_Lpwm mode and detection of back EMF is more precise.

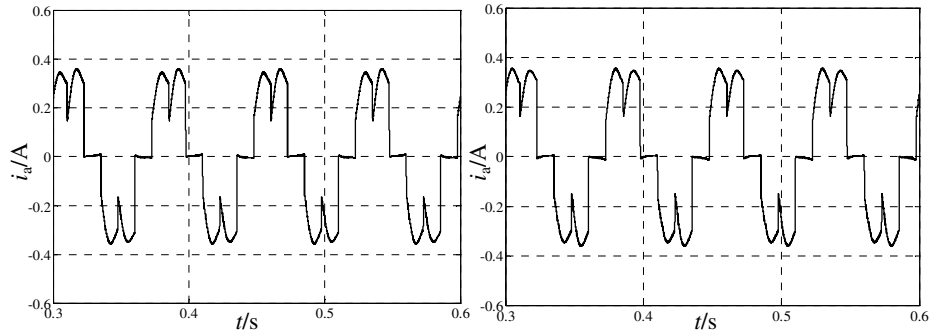

(a) Hpwm_Lon scheme (b) Hon_Lpwm scheme

Fig. 3. Current wavefroms by different PWM moedes

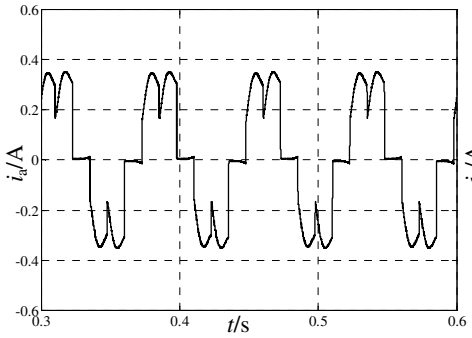

(c) PWM_ON scheme

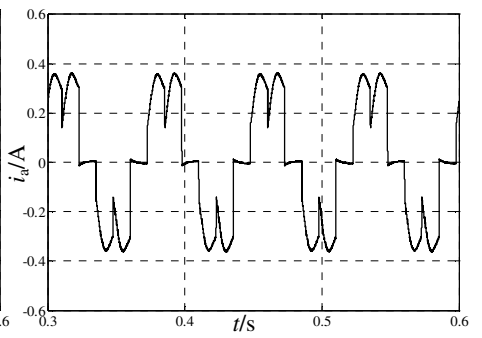

(d) ON_PWM scheme

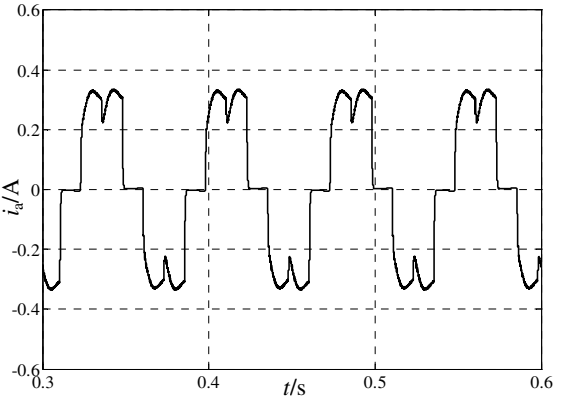

(e)Hpwm_Lpwm scheme

Fig. 3. (*Continued*)

5 Experimental Results

Hardware implementation for the proposed scheme has been configurated by sensorless BLDC motor drivers based dsPIC30F6010 DSP processor. The currents are measured by current sensors. The voltage and current signals are adjusted and sampled simultaneously with 12-bit A/D converters in DSP. The configuration of the proposed position phase correction system built for experimental research is shown in Fig. 4.

Phase current waveforms with different PWM modes based on proposed control method are shown in fig. 5. It can be seen from the figure, the waveform of estimated rotor speed and stator current waveforms have been significantly improved adding stator resistance error compensation. Experimental results verified that the proposed PWM mode can achieve good performance in current constant and position estimation.

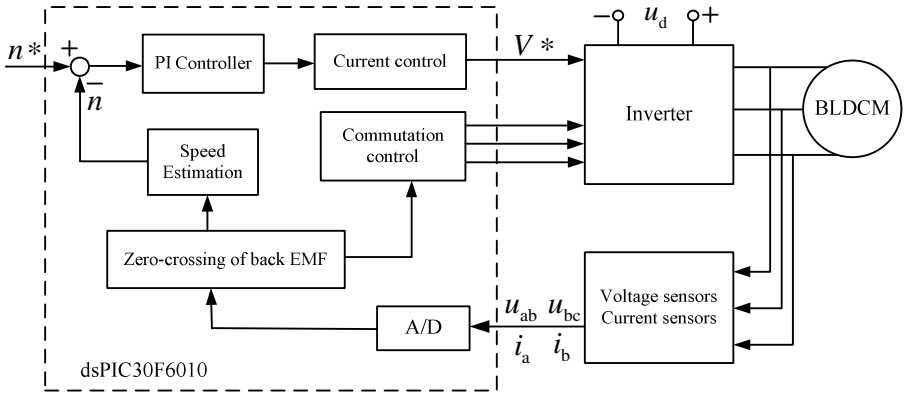

Fig. 4. The configuration of experimental system for BLDC motor based on DSP

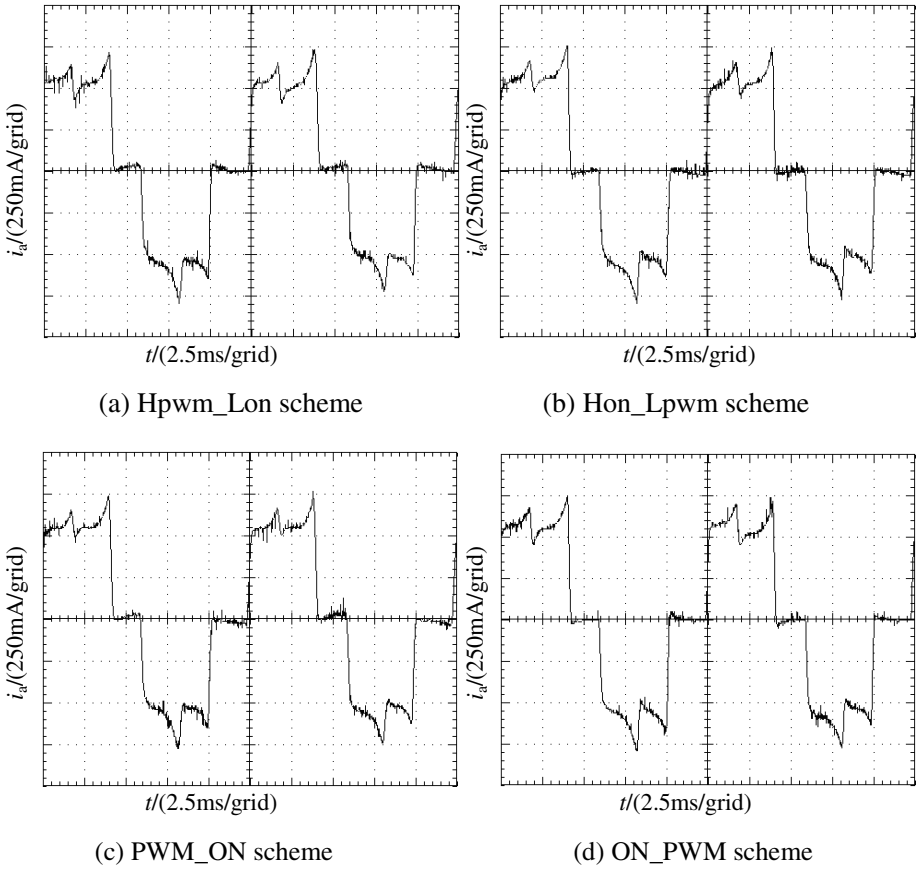

Fig. 5. Current wavefroms by different PWM moedes

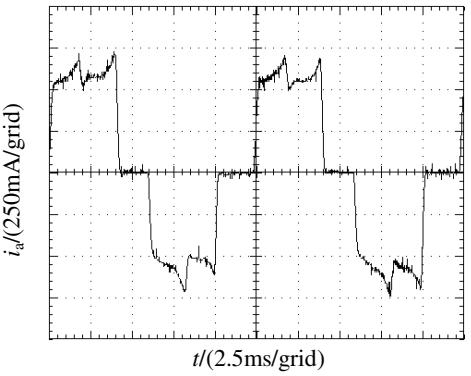

(e)Hpwm_Lpwm scheme

Fig. 5. (*Continued*)

6 Conclusion

This paper presents a back EMF sensing technique for sensorless BLDC motor drive. Five kinds of PWM strategies are analyzed and compared for detection of zero-crossing of back EMF. Through the analysis to the diode freewheeling currents in the unexcited phase on non-commutation period, PWM strategies are obtained corresponding to above rotor position identification methods. Compared to other PWM modes, PWM scheme of Hpwm_Lpwm is suitable for improved phase back EMF calculation. The validity of the proposed sensorless drive strategy using Hpwm_Lpwm is successfully verified from the simulation and experimental results.

Acknowledgements. This research is supported in part by National Basic Research Program of China(973)(No.2013CB035405) and China Postdoctoral Science Foundation(No.2012M511607).

References

1. Wu, H.X., Cheng, S.K., Cui, S.M.: A controller of brushless dc motor for electric vehicle. IEEE Transactions on Magnetics 41, 509–513 (2005)
2. Moreira, J.C.: Indirect sensing for rotor flux position of permanent magnet AC motors operating over a wide speed range. IEEE Transactions on Industry Applications 32, 1394–1401 (1996)
3. Wu, H.X., Cheng, S.K., Cui, S.M.: A controller of brushless dc motor for electric vehicle. IEEE Transactions on Magnetics 41, 509–513 (2005)
4. Li, Z., Cheng, S., Qin, Y., Cai, K.: A novel line-to-line back EMF calculation for sensorless brushless DC motor drivers. In: The 11th International Conference on Electrical Machines and Systems, pp. 1406–1411 (2008)

5. Zhou, G.F., Wu, Z.G., Ying, J.P.: Unattenuated BEMF detection for sensorless brushless DC motor drives. In: Proceedings of 4th International Power Electronics and Motion Control Conference, pp. 1899–1902 (2005)
6. Lai, Y.S., Lin, Y.K.: A unified approach to back-EMF detection for brushless DC motor drives without current and hall sensors. IEEE Transactions on Power Electronics 18, 1293–1298 (2003)
7. Chen, C.H., Cheng, M.Y.: A new cost effective sensorless commutation method for brushless DC motors without phase shift circuit and neutral voltage. IEEE Transactions on Power Electronics 22, 644–653 (2007)
8. Wu, Y., Deng, Z., Wang, X., Ling, X., Cao, X.: Position sensorless control based on coordinate transformation for brushless DC motor drives. IEEE Transactions on Power Electronics 25, 2365–2371 (2010)
9. Lee, D.-M., Lee, W.-C.: Analysis of relationship between abnormal current and position detection error in sensorless controller for interior permanent-magnet brushless DC motors. IEEE Transactions on Magnetics 44, 2074–2081 (2008)
10. Shao, J.W., Nolan, D., Teisier, M., et al.: A novel microcontroller-based sensorless brushless DC motor drive for automotive fuel pumps. IEEE Transactions on Industry Applications 39, 1734–1740 (2003)
11. Damodharan, P., Vasudevan, K.: Indirect back-EMF zero crossing detection for sensorless BLDC motor operation. In: Proceedings of International Conference on Power Electronics and Drives Systems, pp. 1107–1111 (2005)

Aviation Blade Inspection Based on Optical Measurement

Wen-long Li*, Li-ping Zhou, and You-lun Xiong

State Key Laboratory of Digital Manufacturing Equipment and Technology,
Huazhong University of Science and Technology, Wuhan, 430074, P.R. China
{wlli,zhoulp,famt}@mail.hust.edu.cn

Abstract. Inspecting the blade by optical method is a meaningful work in manufacturing industry. One common problem encountered is that the scanned point cloud is large-scale and noisy. In this paper, we present a systematic introduction of simplification, smoothing and feature extraction. The moving least square surface is applied to create a geometric deviation, which is used to identify sparse points or excessive deviation points, in order to subdivide and cluster the point cloud. Then, the information entropy in k-neighbourhood is defined to distinguish density difference of blade point cloud. The objective is to smooth point-sampling surface meanwhile preserving high curvature feature. Furthermore, the computation method of single/multi section parameters is presented. Finally, two cases are carried out to demonstrate the feasibility and effectiveness.

Keywords: blade inspection, point cloud, simplification, smoothing, feature extraction.

1 Introduction

Blade plays an important role in aviation engine and its assembly components. It works under high temperature, pressure and impact load. To meet the requirement of aerodynamic/thermodynamic performance, a turbine blade is designed with tortile, thin-walled and complex surface. A small change in geometric outlier may lead to a large change in engine performance. Therefore, inspection and control of blade shape is critical to design and manufacture. Traditional CMM inspection is slow, and may bring in cosine error especially in the leading/exhaust edges of the blade. Over the past decade, the development of optical measurement technology improves the optical measurement accuracy. For example, the measurement accuracy of Breuckmann StereoSCAN reaches up to 10um. Recently, Gao and Yilmaz [1-2] launched a meaningful work for blade repairing and on-line inspection, where a GOM-ATOS equipment is used to scan the blade.

One common problem encountered during optical inspection is that the scanned point cloud is large-scale and noisy. The processing steps of simplification, smoothing and feature extraction is limited to the point cloud dimension and potential noise. In recent

* Corresponding author.

J. Lee et al. (Eds.): ICIRA 2013, Part II, LNAI 8103, pp. 555–568, 2013.

years, many efforts have been devoted to large-scale point cloud processing. Pauly [3] proposed a hierarchical clustering method, where the surface variation is defined and used to identify surface feature and perform simplification. Shi [4] applied K-means clustering algorithm to gather similar points in the spatial domain and uses the normal deviation as a measure of cluster scatter to partition the point cloud. The problem is that it needs adding constraint condition for keeping high curvature feature, and sparse point cloud tends to intensive point cloud due to uneven sampling. Wang [5] proposed a robust mesh denoising method with preserving feature, Fleishman [6] and Zheng [7] serves image filtering as a foundation for surface smoothing. The results prove that bilateral filtering is a good idea to smooth surface noise but keep sharp feature. However, these methods are performed on image or mesh surface, not suitable for point-sampled blade surface. In addition, they inevitably give rises to volume shrinkage. Hsu [8] introduced the measurement and analysis of airfoil section parameters and geometric tolerance, Ravishankar [9] presented automated inspection method based on ICP registration [10], where laser scanner and coordinate measuring machine are used. Jonathan [11] presented a virtual inspection system, where 3-2-1 registration is used to evaluate profile error. However, registration methods based ICP are usually slow.

In this paper, we will introduce a systematic analysis of implementing blade inspection based on optical measurement. 1) A surface feature-preserving simplification and smoothing method is presented. The clustering regions of sparse points or excessive deviation points are subdivided, and the information entropy in - neighbourhood is applied to distinguish density difference of point cloud, and achieve the objective of smoothing blade surface meanwhile preserving high curvature feature. 2) The computation of single section parameter (mean camber line, section centroid) and multi section parameters (tortuosity, torsion, skewness) is presented. Its feasibility and effectiveness is verified by experiments.

2 Point Cloud Simplification and Smoothing

2.1 Construct Local Surface

Define initial point cloud and simplified point cloud as $\mathbf{P},\mathbf{Q}$ respectively. For each point $\mathbf{x}\in\mathbf{P}$, there exists neighbourhood point sets $\mathbf{U}(\mathbf{U}\subset\mathbf{Q},\mathbf{u}_i\in\mathbf{U})$, whose local surface is $S(\mathbf{U})$. Define the moving least square surface $f(\mathbf{x}):R^3\to R$, which denotes the vertical distance between point $\mathbf{x}$ and local surface $S(\mathbf{U})$. Explict equation of $f(\mathbf{x})$ is:

$$f(\mathbf{x})=(\mathbf{x}-\mathbf{a}(\mathbf{x}))\cdot\mathbf{v}(\mathbf{x}) \tag{1}$$

where $\mathbf{a}(\mathbf{x})=\sum_{i=1}^{n_i}w_i\mathbf{u}_i/\sum_{i=1}^{n_i}w_i$ denotes weighted avarage position of $\mathbf{x}$, and $\mathbf{v}(\mathbf{x})$ denotes the normal. Note that weight w_i should responses the curvature feature (suction surface, pressure surface and leading/trailing edge surfaces), and its definition can refer to [6]. The projecting position of $\mathbf{x}$ onto $S(\mathbf{U})$ is:

$$\mathbf{x}^{\perp} = \mathbf{x}_0 - f(\mathbf{x})\mathbf{v}(\mathbf{x}) \tag{2}$$

Then, the geometric deviation between $\mathbf{x}$ and $S(\mathbf{U})$ is:

$$d(\mathbf{x}, S(\mathbf{U})) = \left\|\mathbf{x} - \mathbf{x}^{\perp}\right\|_2 = \left\|f(\mathbf{x})\mathbf{v}(\mathbf{x})\right\|_2 = \left|f(\mathbf{x})\right| = \frac{\sum_{i=1}^{n_i} w_i[(\mathbf{x} - \mathbf{u}_i)\cdot\mathbf{v}(\mathbf{x})]}{\sum_{i=1}^{n_i} w_i} \tag{3}$$

2.2 Cluster-Based Simplification

Both simplification methods create a cluster cell $\mathbf{C}_i$ with a centre $\overline{\mathbf{c}}_i$ and three eigenvectors $\mathbf{v}_i$, where $\mathbf{v}_2$ is used to obtain the split plane. There exist two defects in traditional methods: 1) In each $\mathbf{C}_i$, key points in high curvature regions may lose, but just keeping selected point (Fig. 1. (b))); 2) It may bring in insufficient points in flat region (Fig. 1. (c)). It can be seen that it requires keeping key points in high curvature regions and creating enough selected points in flat regions.

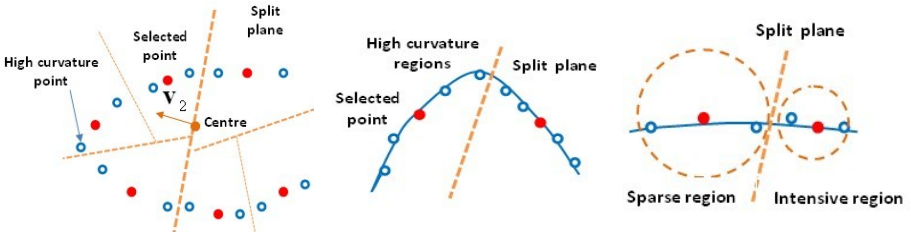

(a) cluster processing (b) lose high-curvature feature (c) sparse points in flat region

Fig. 1. Potential defect of traditional methods

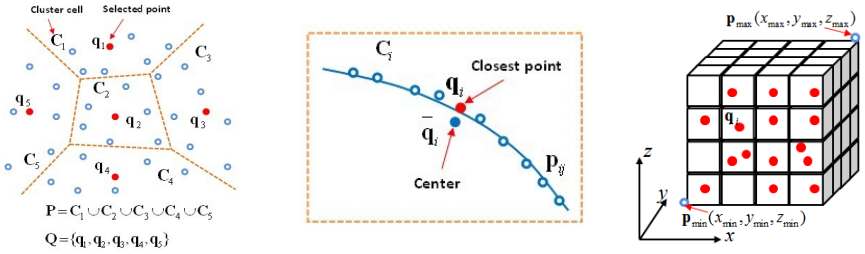

(a) cluster partition (b) select $\mathbf{q}_i$ in $\mathbf{C}_i$ (c) space grid

Fig. 2. Cluster analysis

In Fig. 2, assume initial point $\mathbf{P}$ is divided into $N_{\mathbf{P}}$ cluster cell $\mathbf{C}_i = \{\mathbf{p}_{ij} \mid j = 1, 2, \cdots, n_i\}$, and define the closed point $\mathbf{q}_i$ of $\bar{\mathbf{q}}_i$ as selected point:

$$\mathbf{q}_i = \{\mathbf{p}_{ij} \mid \min_{\mathbf{p}_{ij} \in \mathbf{C}_i} \left\| \mathbf{p}_{ij} - \bar{\mathbf{q}}_i \right\|_2\}, \ \bar{\mathbf{q}}_i = \frac{1}{n_i} \sum_{j=1}^{n_i} \mathbf{p}_{ij} (\mathbf{p}_{ij} \in \mathbf{C}_i) \tag{4}$$

Then, the simplified point cloud is $\mathbf{Q} = \{\mathbf{q}_1, \mathbf{q}_2, \cdots, \mathbf{q}_{N_{\mathbf{Q}}}\}$. For each cluster cell, define the geometric deviation $f_i(\mathbf{C}_i, \mathbf{Q})$:

$$f_i(\mathbf{C}_i, \mathbf{Q}) = \sum_{j=1}^{n_i} d(\mathbf{p}_{ij}, S(\mathbf{Q})) \tag{5}$$

where $d(\mathbf{p}_{ij}, S(\mathbf{Q}))(j = 1, 2, \cdots, n_i)$ denotes the vertical distance between point $\mathbf{p}_{ij}$ and local surface $S(\mathbf{Q})$, then define an avarage geometric deviation ε_i:

$$\varepsilon_i = \varepsilon_i(\mathbf{C}_i, \mathbf{Q}) = \frac{1}{n_i} f_i(\mathbf{C}_i, \mathbf{Q}) \tag{6}$$

Effective cluster should improve the number of cells in high curvature regions and flat regions. Therefore, let us define a space grid of $\mathbf{Q}$ as $List(\mathbf{Q})$ with k cells ($8 \le k \le 25$) in Fig. 2 (c), and the index of selected point $\mathbf{q}_i(x_i, y_i, z_i)$ is $List(\mathbf{q}_i)$. Search for the neighbourhold $\mathbf{\Omega}_i^l$ (k_i^l points) of selected point $\mathbf{q}_i^l$, then

- If $k_i^l < (k/2)$, cluster cell $\mathbf{C}_i^l$ is sparse, and it should further implement cluster (Fig. 3);
- If $k_i^l \ge (k/2)$ and $\varepsilon_i^l > \varepsilon_{C\max}$, cluster cell $\mathbf{C}_i^l$ is excessive deviation, and it should further implement cluster (Fig. 4);
- If $k_i^l \ge (k/2)$ and $\varepsilon_i^l \le \varepsilon_{C\max}$, cluster cell $\mathbf{C}_i^l$ is satified, and it should stop cluster.

Effective cluster should improve the number of cells in high curvature regions and flat regions. Therefore, let us define a space grid of $\mathbf{Q}$ as $List(\mathbf{Q})$ with k cells ($8 \le k \le 25$) in Fig. 2 (c), and the index of selected point $\mathbf{q}_i(x_i, y_i, z_i)$ is $List(\mathbf{q}_i)$. Search for the neighbourhold $\mathbf{\Omega}_i^l$ (k_i^l points) of selected point $\mathbf{q}_i^l$, then

- If $k_i^l < (k/2)$, cluster cell $\mathbf{C}_i^l$ is sparse, and it should further implement cluster (Fig. 3);

- If $k_i^l \geq (k/2)$ and $\varepsilon_i^l > \varepsilon_{C\max}$, cluster cell $\mathbf{C}_i^l$ is excessive deviation, and it should further implement cluster (Fig. 4);

If $k_i^l \geq (k/2)$ and $\varepsilon_i^l \leq \varepsilon_{C\max}$, cluster cell $\mathbf{C}_i^l$ is satified, and it should stop cluster.

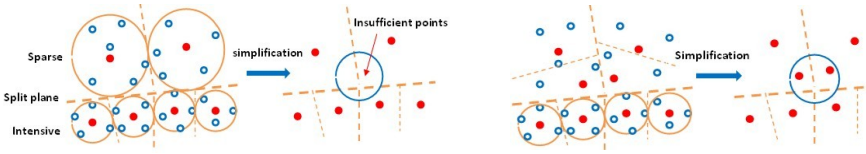

(a) insufficient points due to uneven sampling

(b) further cluster of sparse point cloud

Fig. 3. Improve the first defect

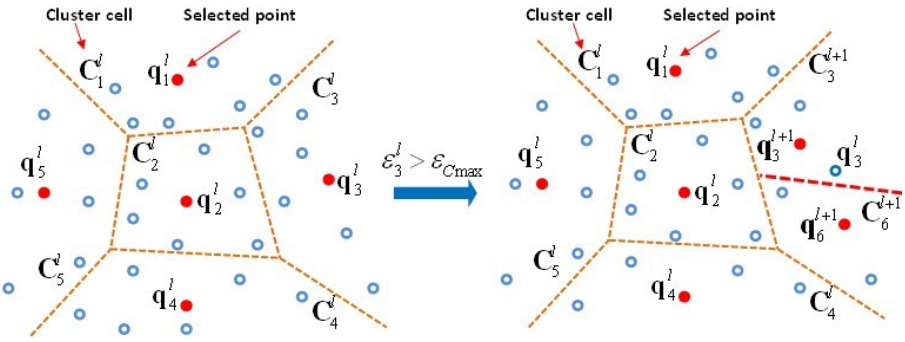

Fig. 4. Improve the second defect

2.3 Entropy-Based Smoothing

The objective of smoothing is to move point $\mathbf{x}$ for smoothing blade point cloud. Define renewed position $\mathbf{x}'$ as:

$$\mathbf{x}' = \mathbf{x} + \alpha \mathbf{v}(\mathbf{x}) \tag{7}$$

where the step size α is:

$$\alpha(\mathbf{x}) = \frac{\sum_{\mathbf{u}_i \in \mathbf{U}} \exp[-\frac{(\|\mathbf{x}-\mathbf{u}_i\|)^2}{2\cdot\delta_c^2}]\cdot\exp[-\frac{(<\mathbf{x}-\mathbf{u}_i,\mathbf{v}(\mathbf{x})>)^2}{2\cdot\delta_s^2}]\cdot<\mathbf{x}-\mathbf{u}_i,\mathbf{v}(\mathbf{x})>}{\sum_{\mathbf{u}_i \in \mathbf{U}} \exp[-\frac{(\|\mathbf{x}-\mathbf{u}_i\|)^2}{2\cdot\delta_c^2}]\cdot\exp[-\frac{(<\mathbf{x}-\mathbf{u}_i,\mathbf{v}(\mathbf{x})>)^2}{2\cdot\delta_s^2}]} \tag{8}$$

where δ_c, δ_s are referred as surface-smoothing factor and feature-preserving factor, respectively. Define a smoothing probability density $f_c(\mathbf{x})$ based on kernel estimation:

$$f_c(\mathbf{x}) = \frac{1}{n_i}\sum_{i=1}^{n_i} \exp[-\frac{(\| \mathbf{x} - \mathbf{u}_i \|)^2}{2 \cdot \delta_c^{\,2}}] \tag{9}$$

The objective of defining $f_c(\mathbf{x})$ is to distinguish that $\mathbf{x}$ belongs to an intensive region or a sparse region. According to information theory, entropy is an uncertainty measure of system. If the value of smoothness probability density $f_c(\mathbf{x})$ is quite asymmetric, the uncertainty distribution is the minimum, which stands for the minimum entropy. Then, we can define following smoothing density entropy $E(\delta_c)$:

$$E_c(\delta_c) = -\sum \frac{f_c(\mathbf{q}_i)}{G_c} \ln \frac{f_c(\mathbf{q}_i)}{G_c} \tag{10}$$

There is an optimal δ_c^* corresponding to the minimum entropy $E_{c-\min} = E_c(\delta_c^*)$, and δ_c^* is the optimal selection of $f_c(\mathbf{x})$ when identifying the attribute of $\mathbf{x}$. In (10), it is a minimization problem of entropy E_c with respect to δ_c^*. According to the optimization theory [12], there are mature methods for calculating δ_c^*. According to (9) and (10), δ_s^* is also calculated. With calculated δ_c^*, δ_s^*, the step size α in (8) is obtained.

3 Blade Feature Extraction

3.1 Mean Camber Line

Mean camber line is a continuous curve passing incircle centers of section surface, and plays a key role in engine aerodynamic performance. How to extract the parameter from point cloud and compare its error is an important task in blade inspection.

- Compute cubic B-spline curve of suction/pressure surfaces

The circle or ellipsoid of leading/trailing edges is first approximated, and four contact points in single section are computed. Then, two cubic B-spline curves are created in suction surface and pressure surfaces (shown in Fig. 5 (a)), respectively.

- Compute the intersection between suction normal and pressure surface

Discrete point $\mathbf{A}_i(x_i, y_i)$ is orderly selected from suction surface, whose normal is defined as $\mathbf{n}_i(x_i, y_i)$. The intersection between normal $\mathbf{n}_i(x_i, y_i)$ and the pressure surface is defined as $\mathbf{B}_i(x_i, y_i)$ (shown in Fig. 5 (b)).

- Compute contact point

If gradient $K_A = K_B$, the midpoint of **AB** is located on mean camber line. Otherwise, a circle with diameter **AB** is created, and intersection **C** in pressure surface is got (Fig. 6 (a)). Then, iteratively search point **D**, satisfying line **AD** is vertical to the pressure surface. Assume the intersection between **AD** and pressure surface is **D'**, the midpoint of **AD'** is located on mean camber line. The obtained mean camber line (black) is shown in Fig. 6 (b).

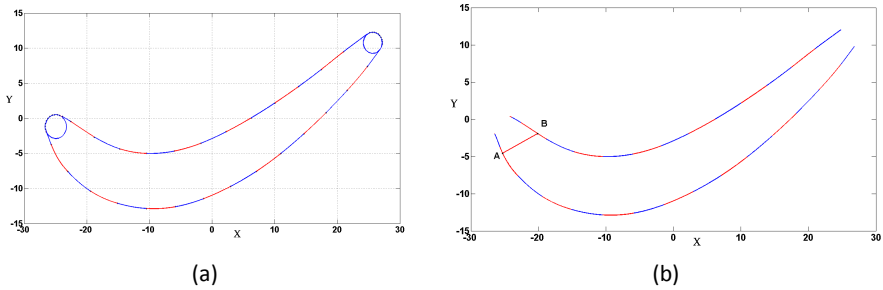

Fig. 5. Compute the intersection in suction/pressure surfaces

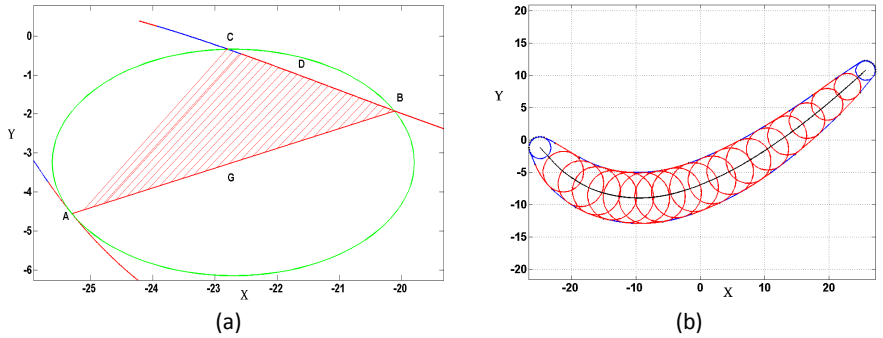

Fig. 6. Search for contact point and create mean camber line

3.2 Section Centroid

- Create 2D convex hull

In Fig. 7 (a), a 2D convex hull is first created, and some triangles with anti-clockwise arrange are obtained.

- Compute the centroid of convex hull/concave arc

In Fig. 7 (a), compute the area and the centre of the i th triangle in convex hull: $A_i, O_{Ai}(\mathbf{X}_{Ai}, \mathbf{Y}_{Ai})$; In Fig. 7 (b), compute the area and the centre of the i th triangle in concave arc: $B_i, O_{Bi}(\mathbf{X}_{Bi}, \mathbf{Y}_{Bi})$.

- Compute the section centroid $O_c(\mathbf{X}_c, \mathbf{Y}_c)$

$$\mathbf{X_c} = A\frac{\sum A_i \mathbf{X}_{Ai}}{A} - B\frac{\sum B_i \mathbf{X}_{Bi}}{B}, \mathbf{Y_c} = A\frac{\sum A_i \mathbf{Y}_{Ai}}{A} - B\frac{\sum B_i \mathbf{Y}_{Bi}}{B}.$$

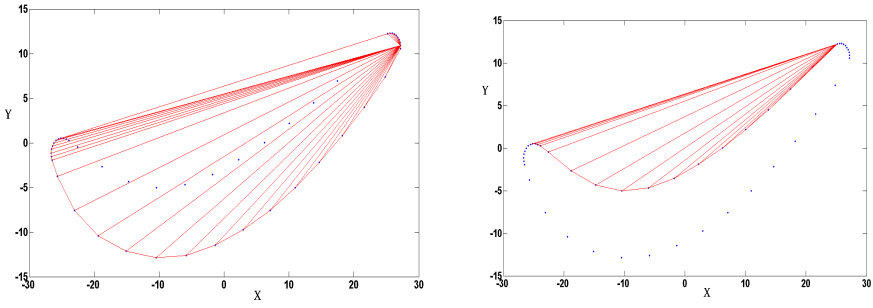

Fig. 7. Search for contact point and create mean camber line

3.3 Tortuosity/Torsion/Skewness

Blade is designed with variable cross-section, tortile and free-form surface. The machining accuracy can be reflected by multi-section parameters: tortuosity, torsion and skewness. Since the computation is complex, we just give the extraction result in Fig. 8.

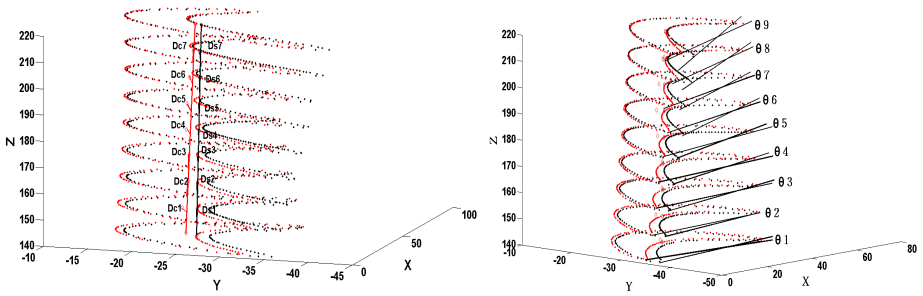

Fig. 8. Compute tortuosity and torsion

4 Verification

4.1 Case 1: Simplification and Smoothing

In the first experiment, the blade point cloud with 301,238 points is used to implement three simplification methods. The experimental results are shown in Fig. 9-11. It can be

seen that our method keeps the sharp feature, but other two methods show wrinkle in Fig. 10. In order to evaluate the smoothing effect, laplacian smoothing are implement and compared. The comparison results are shown in Fig. 12 and Fig. 13. The average error of laplacian smoothing is higher (0.0797mm) than our method (0.0108mm). It observes that an extensive unfairness and mismatch is found in Fig. 12(b-d). The main reason is that the idea of laplacian smoothing is just to move vertex to its k -neiborhood centroid, but pay little attention to keeping the surface feature in high curvature regions.

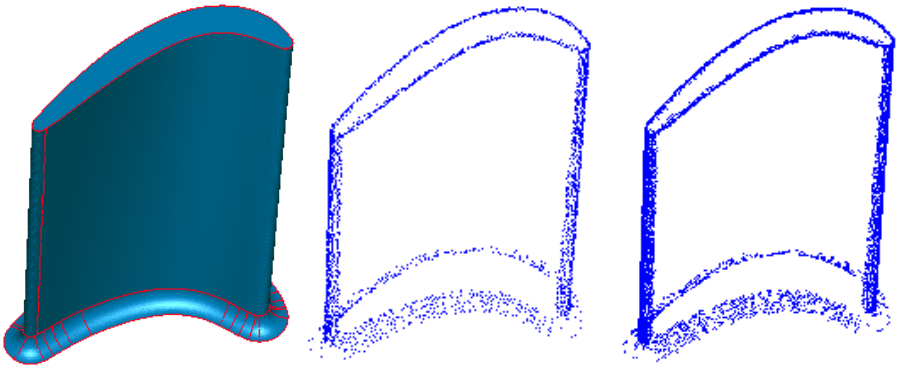

(a) blade model (301,238 points)

(b) the first cluster (2,390 points)

(c) the second cluster (6,869 points)

Fig. 9. Point cloud cluster where $\varepsilon_{C\max} = 0.02mm$

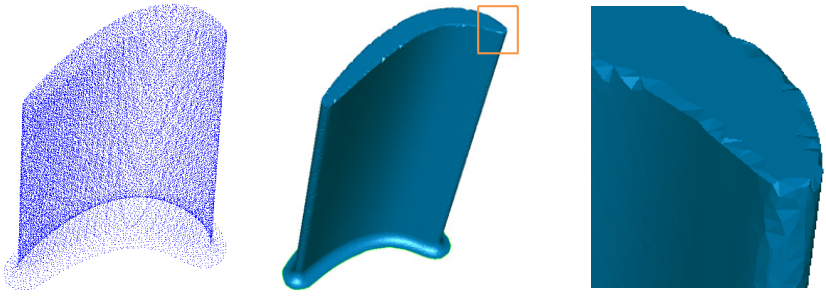

(a) uniform sampling (27,276 points)

Fig. 10. Simplification results for different methods

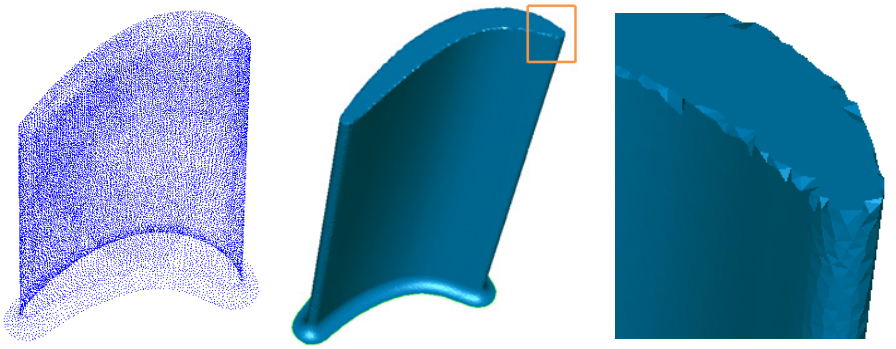

(b) hierarchical clustering (27,373 points)

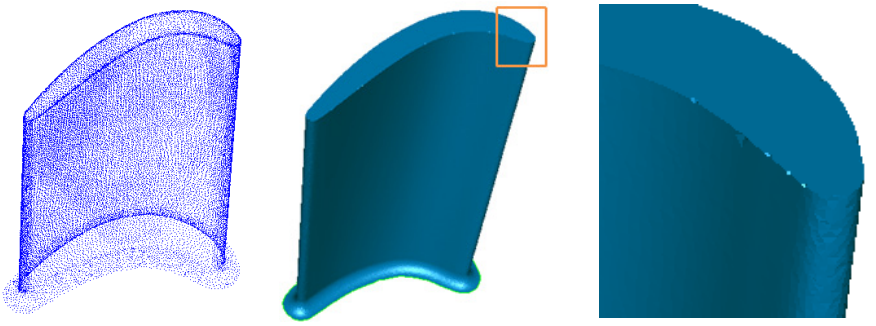

(c) our method (26,639 points)

Fig, 10. (*Continued*)

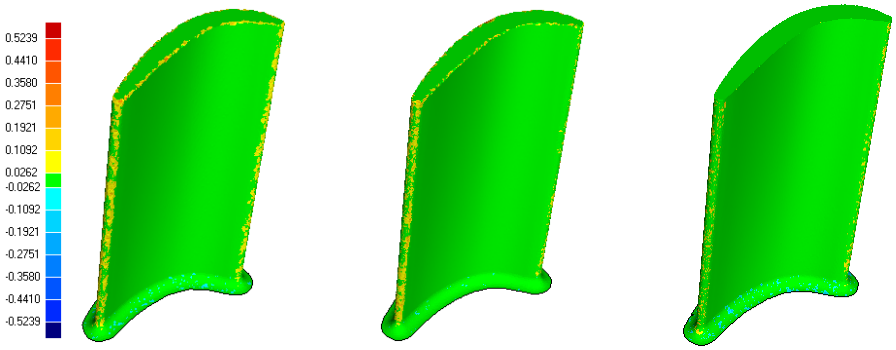

(a) uniform sampling: average error 0.0040, standard deviation: 0.0123

(a) hierarchical clustering: average error 0.0031, standard deviation: 0.0092

(a) our method: average error 0.0026, standard deviation: 0.0051

Fig. 11. Simplification errors for different methods

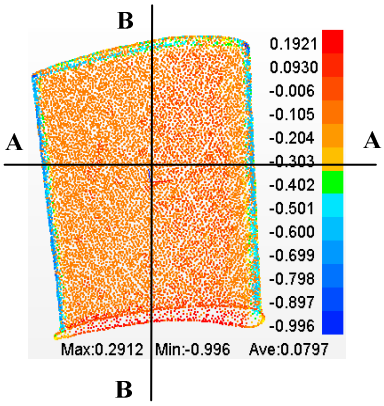

(a) error distribution

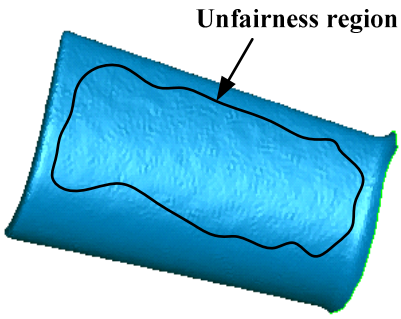

(b) triangular mesh after smoothing

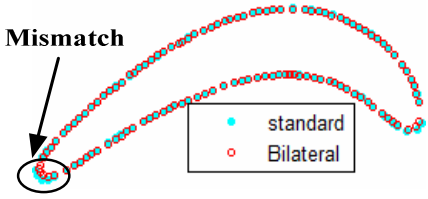

(c) comparing cross section A– A

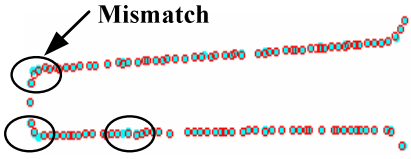

(d) comparing longitudinal section B– B

Fig. 12. The results of laplacian smoothing (2 iterations)

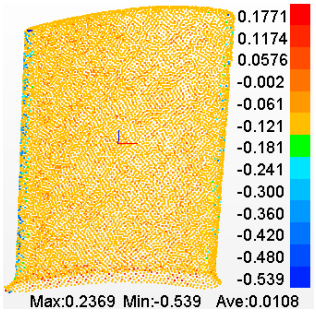

(a) error distribution

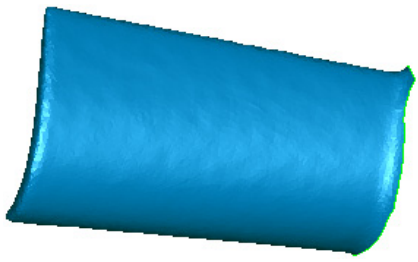

(b) triangular mesh after smoothing

Fig. 13. The results of our smoothing method (2 iterations)

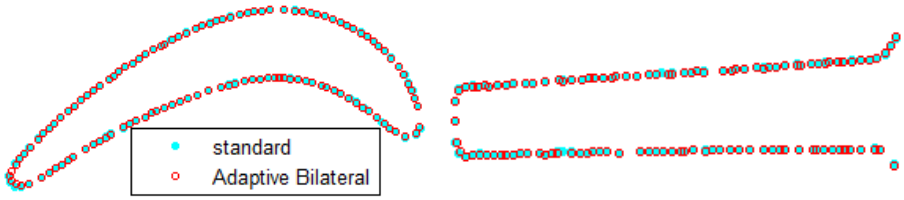

(c) comparing cross section A– A (d) comparing longitudinal section B– B

Fig. 13. (*Continued*)

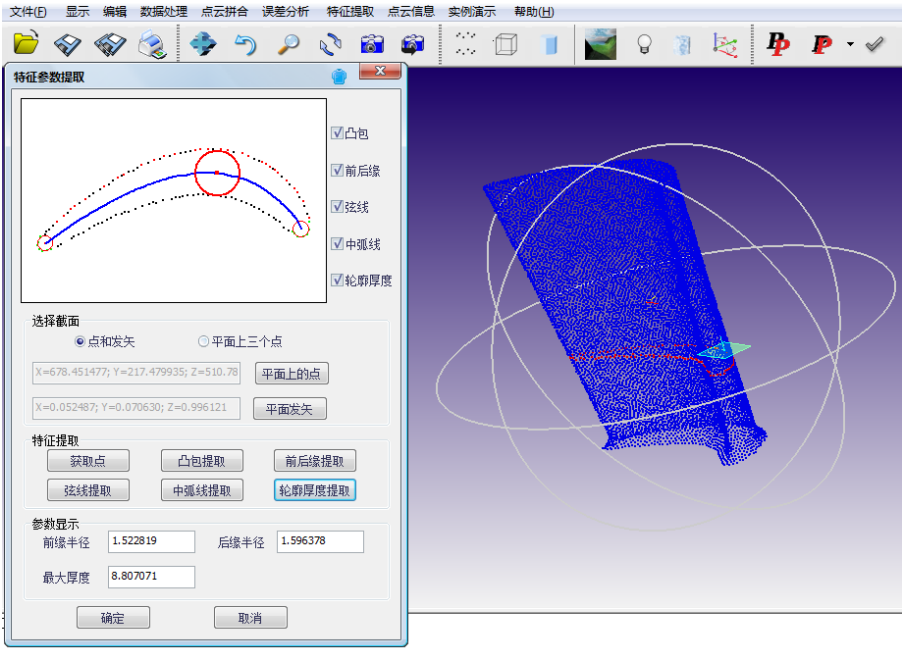

Fig. 14. Single section parameters

4.2 Case 2: Feature Extraction

After an implementation of simplification, smoothing and registration, feature extraction is carried out to evaluate the profile error. Fig. 14 gives the extraction results of single section parameters, where the mean camber line (blue) is successively extracted. The radiuses of leading/exhaust edges are 1.5228mm and 1.5963mm respectively, and the maximum gauge (red circle) is 8.8071mm. Further, the multi section parameters (tortuosity and skewness) are extracted and compared in Fig. 15. From section 2 to section 6, the tortuosity error is -0.5345mm, -0.8290mm, 2.7802mm, -4.0893mm, -0.7364mm, and the skewness error is 1.2470 degree.

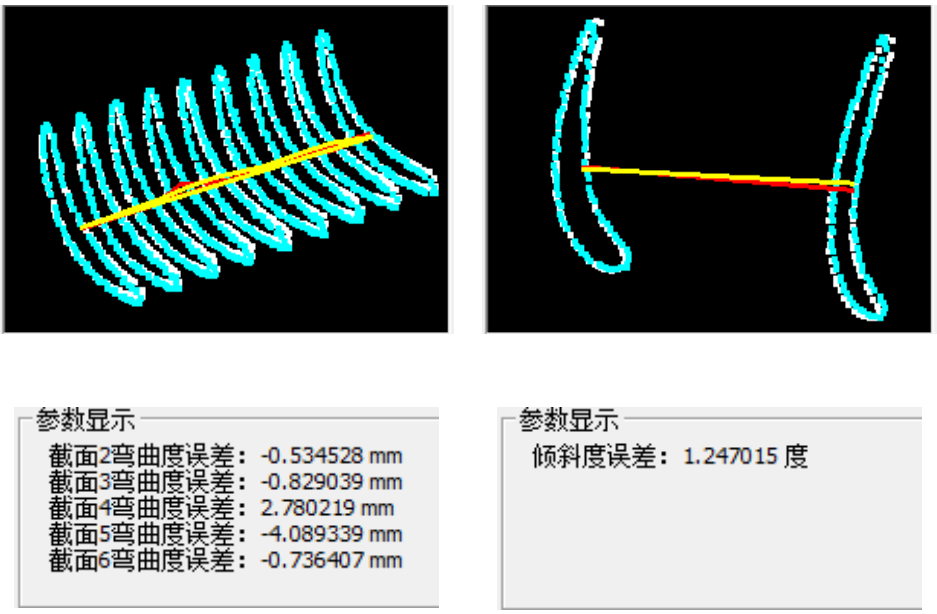

(a) tortuosity error (b) skewness error

Fig. 15. Multi section parameters

5 Conclusion

In this work, we present a systematic introduction of blade inspection based on optical method. The moving least square surface is used to identify sparse points or excessive deviation points for further cluster, and entropy theory is applied to distinguish point density difference, in order to smooth point-sampled surface meanwhile preserving sharp feature. Moreover, the computation of single/multi section parameter is introduced in detail. Finally, two cases are implemented. The experimental results demonstrate that the proposed methods of simplification, smoothing and feature extraction is effective and efficient.

Acknowledgments. This work is supported by the National Natural Science Foundation of China (Grant No. 51105155, 51275192). We would like to express our sincere thanks to the anonymous reviewers for constructive comments and helpful suggestions.

References

1. Gao, J., Gindy, N., Chen, X.: An automated GD&T inspection system based on non-contact 3D digitization. International Journal of Production Research 44(1), 117–134 (2006)

2. Yilmaz, O., Gindy, N., Gao, J.: A repair and overhaul methodology for aeroengine components. Robotic Computer-Integrated Manufacture 26(2), 190–201 (2010)
3. Pauly, M., Gross, M., Kobbelt, L.P.: Efficient simplification of point-sampled surfaces. In: Proceedings of Visualization, Boston, USA, pp. 163–170 (2002)
4. Shi, B., Liang, J., Liu, Q.: Adaptive simplification of point cloud using K-means clustering. Computer-Aided Design 43(8), 910–922 (2011)
5. Wang, J., Zhang, X., Yu, Z.: A cascaded approach for feature-preserving surface mesh denoising. Computer-Aided Design 44(7), 597–610 (2012)
6. Fleishman, S., Drori, I., Cohen-or, D.: Bilateral mesh denoising. ACM Transaction Graphics 22(3), 950–953 (2003)
7. Zheng, Y., Fu, H., Au, O., Tai, C.: Bilateral normal filtering for mesh denoising. IEEE Transaction on Visualization and Computer Graphics 17(10), 1521–1530 (2011)
8. Hsu, T.H., Lai, J.Y., Ueng, W.D.: On the development of airfoil section inspection and analysis technique. International Journal of Advanced Manufacturing Technology 17(10), 1521–1530 (2006)
9. Ravishankar, S., Dutt, H., Gurumoorthy, B.: Automated inspection of aircraft parts using a modified ICP algorithm. International Journal of Advanced Manufacturing Technology 46(1-4), 227–236 (2010)
10. Besl, P., McKay, H.: A method for registration of 3-D shapes. IEEE Transactions on Pattern Analysis and Machine Intelligence 14(2), 239–256 (1992)
11. Jonathan, E., Ou, H., Cecil, A.: A virtual inspection framework for precision manufacturing of aerofoil components. Computer-Aided Design 44(9), 858–874 (2012)
12. Nocedal, J., Wright, S.: Numerical optimization. Springer Press (1999)

Programmable Automation of Soccer Ball Stiching through Open Loop Control of a Path Tracing Gripper

Majid Munawar, Khurram Butt, Waseem Shahzad,
Mehran Ahmad, and Kamal Yousaf

Department of Electrical Engineering, GC University,
Lahore, Pakistan
{saytomajid,ws34pk,mehran.ahmad124}@gmail.com,
khurrambutt@gcu.edu.pk, yupsy_nupsy@hotmail.com

Abstract. With the increase in popularity and demand of soccer, more advance techniques are required to be used in the production of soccer balls. In this paper we have presented a stitching mechanism that can be programmed to stitch the panels of soccer ball according to the sequence given by the user. The system consists of a hinged gripper that can move the panels in a straight line and at any angle within the xy-plane, under the stitching needle. A system mounted control panel and computer can be used as interface for programming. Robot control functions with self explanatory syntax are developed. The option of programming both off-line and on-line increases the flexibility and operability of the system. The system was checked in industrial mass production environment and the results indicate that even the untrained workers were able to operate the system ambidextrously, showing good learning rates. The primary target of this effort is to assist the cottage industry of Sialkot.

Keywords: Robot control functions, Graphical user interface, Slope rate, Hard automation, Mathee.

1 Introduction

Since the inception of the game of soccer, the acrobatic techniques involved in its execution during the contest are improved. The result is an increment in number of balls produced each year and the demand for repeatability in the behavior of the ball, traveling through the air.

The soccer balls are produced mainly by three methods: hand stitching, machine stitching, and thermo bonding. The type of stitch is the difference between the first two methods. The third method involves the bonding of panels over the bladder. This paper is focused on second technique which involves lock type stitches.

The most important parameter that must be controlled is the proper alignment of seem lines, during stitching. For a typical soccer ball, total of 90 mathees of 32 panels are to be stitched together in a defined pattern to get the true shape. It is the straight line stitching that assures the spherical shape of the ball. The target of our work is to perform straight line stitching, between the coplanar points given by the user, with

J. Lee et al. (Eds.): ICIRA 2013, Part II, LNAI 8103, pp. 569–579, 2013.

good repeatability and accuracy. The production of discrete products in small batches is labor intensive and hard automation cannot be justified for it [1]. Programmable automation is introduced to reconfigure the manufacturing environment according to the requirement. Robot programming languages is one of the interesting topics, which are evolving continuously. The development of large number of robot programming languages, at times, is a reason for reducing the organizational efficiency through increased difficulty level and non standardized programming architectures.

The difficulty level might increase the time for training and the non standardization increases the cost of developing new language in terms of resources as well. Efforts are made towards the standardization of robot architectures whose aim is to allow code reuse and encapsulation of software parts which are formed by using conceptual boundaries [2]. Topic of code reuse and its standardization is beyond the discussion for this paper. The primary target of this paper is to develop an easy to adopt language which can be implemented through user friendly interface.

Groover in [3], has provided an explanation by distinguishing three methods for the programming of industrial robots: lead through programming, computer like robot programming languages, and off-line programming. Powered lead through is used for point to point control of manipulators. The buttons of the control box are used to move the manipulator through the required sequence of motion and the coordinates are stored for each desired position. These points are later used in the commands of programming language, during on-line and off-line programming. The standard languages like Pascal and C are successfully used [4], [5], [6] to develop and implement the robot programming languages. In our work, we have used the C language to develop the robot programming functions. These functions are easy to understand and have self explanatory syntax.

We have used a system mounted, portable control panel to allow online operation. It consists of 4 line 16 character LCD. A key pad having 16 keys in 4×4 matrix, is used to insert the commands. We have used the EEPROM of PIC16F877A microcontroller to save the two dimensional coordinates of the points, teached by the user. This memory is divided into sections, separable through the programmed logical boundaries. These Sections are further used to store, update and transmit the information related to the programs. This will be explained in the later sections.

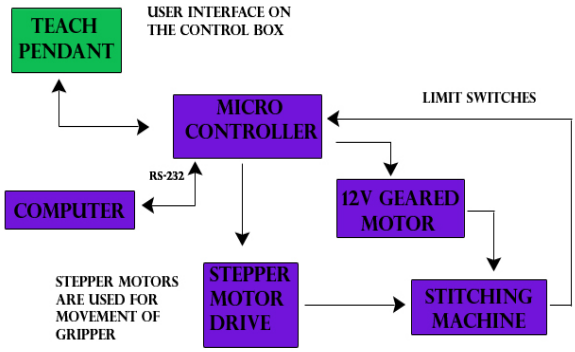

Fig. 1. Flow path of the control signals for complete system

The soccer ball panels are moved under the stitching needle by placing them in a hinged gripper that can move in the plane, whose boundaries are specified by the limit switches. They indicate the home position and the adjustable design allows relocation of the limit switches, so that work space of the gripper can be changed without making any change in the programming. Stepper motors are used to control the precise movement of the gripper. A stepper motor [7] is a device that converts a voltage pulse train into a proportional mechanical rotation of its shaft. Geared pulleys are mounted on the shafts of the stepper motors, and timing belts are used to drag the axes on the sliding bar mechanism. Path tracing stitching machines with open loop control, provided by companies like JUKI and Tajima, are successfully used in the sports apparel manufacturing industry. In this type of open loop control [7], the setting of actuator is based on initial evaluation and understanding of the variables that are or can be disturbing for the system under consideration.

A 220 volts AC clutch control motor is used to move the stitching head. We have used cam and rod mechanism to connect or disconnect the clutch. A 12 volt DC geared motor is used to ensure the self locking through the worm gear.

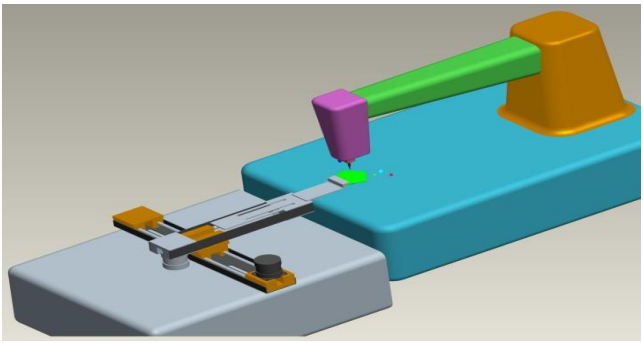

Fig. 2. View of 3D CAD model of machine

The structure of panel movement mechanism is so designed that different end effectors can be interchanged. Because of the wide variety of tasks performed by industrial robots, the end effectors must be custom engineered and fabricated for each different application [3]. We have used a spring loaded hinged gripper which can grasp the panels to be stitched in such a fashion that they do not change there position while exposing there edges to the stitching needle.

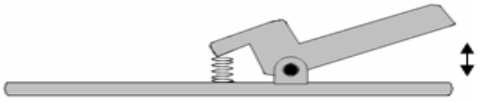

Fig. 3. Spring loaded hinged gripper

A spring is also added at the end of both axes, inside a casing. If accidentally, the motor moves the belt beyond the limit switches then the pull of motor will cause the spring to be compressed. This ensures the safety of the belt that is used to drag the

mechanism. Since the artificial leather to be clamped is soft material, so the gripper is also made from aluminium which is light and soft material. The hinged gripper is particularly useful in fast production lines. The edge of the panel is kept outside the gripper, on the table, to perform stitching. The area of the panel, exposed to the needle is defined by the dimensions of the gripper. The sewing area is 210×120 mm, which is good enough for the application. The mechanism is designed and simulated in related softwares. Geared pulleys are used to prevent any slipping of the belt, during operation.

2 Microcontroller as Storage Medium

The PIC16F877A is a low cost microcontroller which offers a 256 byte of EEPROM with data retention and in-circuit serial programming [8].

This memory is further divided into sections to store the coordinate values of the points and the instructions. The program instructions tell the system that what to do with the points. The second section is further sub divided and each division is reserved for individual programs. Each sub section contains the serial number of the program, the number of lines in the program, and the commands to be executed. All these values are continuously changed by the end user. These values are used to move the gripper in a specific path and also to display the information related to the program being executed.

Once the number of program to be executed is entered by the user, the control will be shifted to the starting point of that program, reserved in the memory. The instructions will be performed according to the sequence of their appearance.

3 Online Programming through Control Panel

The control panel is provided with the system for online programming. Most of the control panels provided with the path tracing machines have such arrangement and headings of the keys, which makes the process of programming as convincing as possible. In present case, the control panel has a keypad with its 16 keys arranged in four rows and four columns. These keys are used to enter the numeric digits, program instructions and also to jog the gripper. Multiple purpose keys are present but each key has one value for any mode of operation. A four line 16 character LCD is attached to make the interface more illustrative. The main menu offers four selection choices:

3.1 Teach Mode

This mode allows jogging of gripper by pressing the push buttons. This is used to locate and store the exact points. The last two lines of the LCD are used to display the current position of the gripper in the stitching plane.

Values of both x and y coordinates are updated and displayed continuously after every step of the motor.

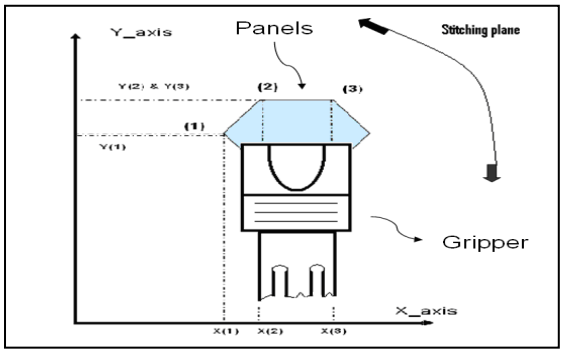

Fig. 4. Identification of Points

As shown in figure, the points in between stitching is to be performed, are brought under the needle. On pressing the save button, each point is saved in terms of the number of steps moved by the two motors.

3.2 Instruction Mode

The points that we have saved in the previous mode are used along with the robot specific commands, during the instruction mode.

On start of this mode, user is asked to enter the number of program location that he wants to use. On entering any command, the command itself and its line number in the program are displayed.

3.3 Execution Mode

Command Execution. Here the system will perform the commands of the program one by one. Each command is executed when the step button is pressed. After performing each command, the motors are stopped and wait for the user to press the step button again to perform the next instruction. This mode is helpful to illustrate the results of individual instruction.

Program Execution. Here the system will perform the commands of the program one by one. After entering the program number to be executed, the complete program is executed. At the end of program, system exits from the execution mode and main menu is displayed.

Cycle Execution. In this execution mode**,** the user enters the number of program to be executed. A foot-pedal is attached to the system. After pressing the pedal once, the system performs the complete program and comes back to the home position. After pressing the foot-pedal again, the complete program is again executed. This process continues unless the mode selection button is pressed, which causes the system to exit the execution mode.

3.4 Refresh Mode

This mode has proved to be very useful during the training of workers through simulation. The user is asked to enter the choice of refreshing either the saved points or the entered programs. The data stored in the identified memory location is permanently erased. In eeprom, the total number of lines in each program are known and the new commands are written over the previous one. Introduction of a separate mode for editing or deleting the instructions would be unnecessary.

3.5 Main Menu

By using the menu selection button, we can display the main menu of machine. At any stage of operation we can exit the running mode by pressing this button and the system will return to its home position. This would not work during the execution of a line of program but only after completion of that particular command.

4 Offline Programming

In on-line programming we have to stop the production sequences to enter the new commands. In our off-line programming module, we can write program and visualize its simulated outcome before actual execution.

4.1 Programming Commands

The variety in the tasks to be performed by the robotic systems calls for developing such textual and computer like robot programming languages which are effective and easy to understand at the same time.

Table 1. Programming language commands

Instruction	Purpose
Stitch from()	Gives starting point of stitching.
Stitch to()	End point of stitching.
Home	Moves gripper to the origin.
Stay()	Time in seconds for which the system has to wait.
Trace()	Number of times the defined path is to be traced.
End tracing	Last line of code to be traced.

The commands established for our system are partially dependent upon the information stored as points, in the memory. The difference in the current and target points is the most important input for our algorithm. Consider the following program with reference to the fig.4:

Trace (3)
Stitch from (1)
Stitch to (2)
Stitch from (2)
Stitch to (3)
Stay (3)
Home
End tracing
The path defined by the code written in between first and last line will be traced three times. The gripper will move through the point 1 to point 3 after which delay of three seconds is taken for cutting the thread and feeding new panels. After each cycle, the gripper will move to the home position.

4.2 Gripper Direction Control

For moving from one point to other, the present and future positions of motors are used to calculate the magnitude and direction of change.

Slope Rate. Let us suppose that present and future positions of gripper in x and y axes are represented by subscripts 1 and 2 respectively. The change in the rotor position for both motors, in terms of steps moved, is represented as:

$$x\_change=(x_{(2)} - x_{(1)}) \tag{1}$$

$$y\_change=(y_{(2)} - y_{(1)}) \tag{2}$$

Also if, x_change<y_change then

$$\text{Slope Rate}= (y_{(2)} - y_{(1)}) / (x_{(2)} - x_{(1)}) \tag{3}$$

If, x_change>y_change then

$$\text{Slope Rate}= (x_{(2)} - x_{(1)}) / (y_{(2)} - y_{(1)}) \tag{4}$$

The gripper at start of every stitching point considers itself to be standing at the origin and position of target point is identified by its quadrant.

In fig.4, the point2 is in the first quadrant for the gripper at point 1. For the gripper at point 2, point 1 is in the third quadrant. The motor which has to move maximum distance moves with fixed calculated maximum speed. The other motor has to move

slowly in such a way that both motors start their movement and reach their target positions simultaneously.

Algorithm Sequence. For the example code given in the section 5.1, the flow of the algorithm will be as given:

: MAIN
BEGIN
Teach coordinates of stitching points
Write instructions about usage of points
Execute instructions
END
: EXECUTE INSTRUCTIONS
BEGIN
Initialize Cycle number
WHILE (cycle number < target)
Increment in cycle number
Call STITCH (motor positions)
Stop motors (Delay in seconds)
Move motors until they hit the limits
END while loop
END

: STITCH (I: positions O: speeds, directions)
BEGIN
Identify motor directions for target positions
Relative slope gives speed of motors
Start all motors
WHILE (current positions ≠target positions)
Move stepper motors through one step
Update and display motor positions
IF current positions=target positions
Stop all motors
Reverse cam motor
END while loop
END

4.3 Simulation

The purpose of offline programming is only fulfilled if we can program the system without interrupting its operation. In on-line programming we can move the system through the entire sequence of the program to confirm its usefulness.

For off-line programming, we have accomplished this confirmatory process through the simulated visualization of the instructions. We have used graphical user interface development environment (GUIDE) of MATLAB 7.0 for this purpose. It provides rich set of tools for incorporating the designing and programming of GUIs [9].

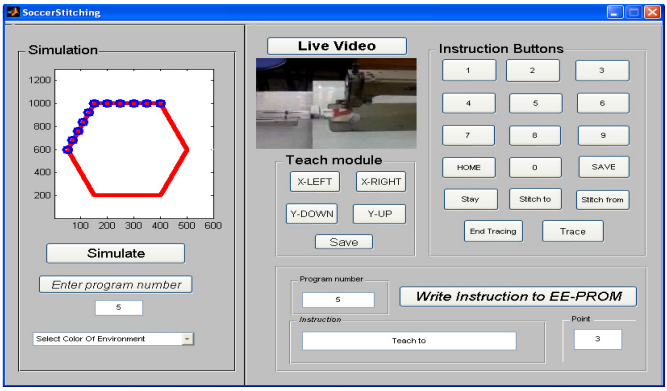

Fig. 5. GUI for offline programming

It may not be sufficient for very complex applications but still it can do the bulk of the GUI work [10]. The orientation of the panels and there edges that are being stitched, can be displayed by identifying a minimum of 3 points. The simulation window along with the live feed of the process makes it very useful for both training and operation.

5 Summary and Results

In our discussion we have successfully used the methods explained in [3] for the development and working of such a stitching mechanism which is low cost and easy to operate. Slope rate algorithm is applied through control panel and graphical user interface to program, execute and, visualize the stitching path of the machine. The design of the GUI and the control panel were developed according to the suggestions of the experienced workers and managers of soccer ball production industry.

Learning rates of 53 to 78 percent were recorded for different workers. The sequences of stitching the panels together, can be followed efficiently even by using only 9 memory locations of each program.

We, through this effort, have tried to make the stitching process enjoyable for the workers with low literacy rate. Balls of sizes 1 to 5 are covered in this design. The speed of stitching and number of stitches per unit length are adjustable. The deviation from the target point was observed to be between 0 to 3 percent. Such machines are useful for the industries that are producing related apparels as well.

6 Conclusion and Future Work

Pakistan is among the leading soccer ball manufacturing countries. Stitchers are changing their profession due to unsupportive economic and working environment. Because of cyclic application of the compressive load on hands, during stitching, the women have complained that they are facing problems in their marriages. It is required to design and introduce such machines and gadgets which might help the

soccer industry. Out of approximately 1260 stitches of a machine stitched ball, we have tried to automate the first 1176 stitches.

To get the strong feet hold in market, direct control of the stitching head movement shall be introduced. Stitching needle should be raised automatically at the end of stitching. The touch screen can be added on the control panel to add more functions to the system.

Process quality control parameters, like number of stitches per unit length of the panel can be observed and controlled by using the image processing techniques. In past years, significant work is done to add some intelligence level to the system which is imitating the teached action [13]. Image acquisition can be used to identify the orientation of the panel and to take the decision about the sequence of stitching path. This would change the current programming language with more generalized commands. Our future target will be the development of such robot programming language which contains the fundamental elements of a high level language along with the robot specific commands [11].

Acknowledgments. The authors are thankful to Doctor Khurram Anwar Khawaja of anwar khawaja industries (pvt) Ltd, Sialkot for providing necessary technical and logistic support.

References

1. Kinnunen, S., Nitzan, D., Rosen, C.A.: Programmable Industrial Automation. IEEE Transactions on Computers (December 1976)
2. Du Casse, K.M., Koay, K.L., Ho, W.C., Dautenhahn, K.: Reducing the cost of robotics software: SAMGAR, A generic modular robotic software communication architecture. IEEE Transactions on Advanced Robotics (ICAR) (2009)
3. Groover, M.P.: Automation, production systems, and Computer integrated manufacturing, 2nd edn. Pearson Education (2007)
4. Hayward, V., Paul, R.P.: Robot Manipulator Control under UNIX - RCCL: A Robot Control C Library. International Journal of Robotics Research 6(4), 94–111 (1986)
5. Corke, P.I., Kirkham, R.J.: The ARCL Robot Programming System. In: Proceedings of International Conference of Australian Robot Association, Brisbane, pp. 484–493 (July 1993)
6. Blume, C., Jakob, W.: PasRo-PASCAL for Robot. Springer (1985)
7. Onwubolu, G.: Mechatronics Principles and Applications. Elsevier Butter Worth Heinemann (2005)
8. `http://www.microchip.com` (accessed on March 9, 2013)
9. Gonzalez, R.C., Woods, R.E., Eddins, S.L.: Digital Image Processing Using MATLAB. Pearson Education (2007)
10. DeMoyer, R., Mitchell, E.E.: Use of the MATLAB Graphical User Interface Development Environment for Some Control System Applications. In: 29th ASEE/IEEE Frontiers In Education Conference, San Juan, Puerto Rico (1999)

11. Ghuffar, S., Iqbal, J., Mehmood, U., Zubair, M.: Design and Fabrication of a Programmable Autonomous Robotic Arm. WSEAS Transactions on Systems 5(11) (November 2006)
12. Giurgiutiu, V., Lyshevski, S.E.: Micromechatronics, Modeling, Analysis, and Design with MATLAB. CRC Press (2009)
13. Biggs, G., MacDonald, B.: A Survey of Robot Programming Systems. In: Proceedings of the Australasian Conference on Robotics and Automation, Brisbane, Australia (2003)

A Design and Development of Robotics Integrated Curriculum Based on Storytelling for Elementary School Student

Ji-Hun Sung[1], Young-Hoon Sung[2], and Wae-Shik Moon[1]

[1] Dept. Of Robot Education, Jinju National University of Education, Shinandong 380, Jinju, Gyeongsangnamdo, Korea
[2] NEIS Center, Korea Education and Research Information Service, KERIS building, Toegyero 299, Junggu, Seoul, Korea
{mywiez,pdzion}@naver.com, wsmoon@cue.ac.kr

Abstract. Most of robotics in education consists mainly of learning basic robot programming, these curriculums impose a burden on children's learning. Storytelling offers opportunities for continuation of children's' positive learning motivation to practice symbolic manipulations, hold multiple abstract concepts in their heads, and create meaning between these ideas. In this paper, we investigate a storytelling-based robotics curriculum and implement its support system, which allows students can enjoy their robot programming experience and education through the use of programmable robots with seven scenes of Cinderella story based on storytelling.

Keywords: Robotics integrated curriculum, Mechatronics education, Storytelling.

1 Introduction

It is an important method to improve individual logical thinking and creative problem solving skills to solve the new problems [1]. The creative problem-solving ability based on the creativity is required a learning process which develops abilities like gathering personal information, processing, production, and new problem solving skills [2]. Robotics curriculum is an integrated instructional tool which consists designing, assembling and processing programming and it has been shown that it has positive effects on improving creativity and promoting academic achievement for learners [3][4][5][6].

However, Current robotics curriculum has remained a simple learning process of basic programming and assembly of robot by formal template so, learners tend to decline a concentration and participation significantly during learning robot programming based on project or logical thinking [7].

Therefore, in this paper, to solve these problems, we are designing robotics curriculum and mobile/web learning application system by storytelling to develop logical thinking of learners.

J. Lee et al. (Eds.): ICIRA 2013, Part II, LNAI 8103, pp. 580–591, 2013.

Robotics curriculum based storytelling consists of making a story by learner's individual experience and logical expression activities to deliver the story effectively. The application system allows users to learn seven scenes which the theme of storytelling have based on the story of the world's fairy tales, design robot, and share with users idea based on mobile.

We present robotics curriculum based on storytelling in elementary school for improving learners' immersion and logical representation ability.

By applying this curriculum and support system, we expect that it makes easy to express logically through learner's experiences and offers the pivotal role which makes learners be absorbed in their study.

2 Related Works

2.1 Robotics in Education

Robot is the educational tool to produce something that is motivation of learning and achievement and has been shown several studies [8][9][10]. According to the study of Lee, E.G., et al., (2008), the control group who performed utilizing the learning of programming the robot was significantly higher levels than the general programming group in terms of immersion experiments [11].

Robotics in education requires a systematic and logical approach for problem-solving and especially it was an effective learning tool to educate the creativity to stimulate the ability of curiosity and imagination [12].

Robotics is not included in the official curriculum of school education in Korea. Some occasional implications are mentioned in literature mainly for research reasons. There have also been several examples of use of Robotics activities in private schools and gifted schools as extra curriculum activities.

Nevertheless, educational robotics seem to be very popular in higher education and especially in Engineering and Computer Science departments, as part of curriculum or as a subject for extended coursework e.g. at university and several research projects in this field have been developed focusing on the use of educational robotics in primary and secondary education in Korea.

Utilizing robot programming has highly effects on improving academic achievement because learners are exposed the elements to solve problems during the learning process. Nevertheless, it can be a meaningful educational method to raise the higher thinking skill from the experience through designing the robot, assembling and programing to solve the problem [13].

Integration of robotics research with undergraduate courses was demonstrated by developing a robot called Rusty. Lego-based robots have been used in lab exercises and projects, in basic to advanced courses covering operating system, networks, and artificial intelligence [14].

Thus, we investigate a storytelling-based robotics curriculum, which allows students can enjoy their robot programming experience and education through the use of programmable robots with seven scenes of Cinderella story based on storytelling.

Table 1. Robotics courses

Robotics courses	Features
Group organization - Insects observed - Robot design and assembly - Programming and test - Robot competition[15]	Insects-robot assembly and competition
Robot behavior initiative - Robot assembly - Programming - Evaluation[16]	Improving of logical thinking ability
General exploration activities - Group training activities(Problem solving through programming) - Actual research of individuals or small group[17]	The various learning form: attendance, distance, and intensive study
Problem determination - Research - Brainstorming - Select the best solution - Production - Test - Redesign - Demonstration[18]	STEM(Science-Technology-Engineering-Mathematics)
Brainstorming and surveys - Design of topography - the production of the rovers - Creating programs - drawing - test and re-design - Data collection and processing[19]	Mars Explorer rover

As shown in Table 1, most robotics curriculum is run by group learning process which is based on the engineering design process. Learners is master the name of the robot parts and making the robot to solve the problem, its operating system is contained the programming process and testing process.

2.2 Robotics and Storytelling in Education

What is storytelling? Storytelling, combination words of story and telling, is making a representation story with characters, events, and in the background.

Storytelling is a means for sharing and interpreting experiences. Stories are universal in that they can bridge cultural, linguistic, and age-related divides. Storytelling has the characters, events, and background and can be used as a method to teach ethics, values. Storytelling combined with a variety of digital media and methods is an effective education tools to develop of cognitive ability and creativity [20].

According to the study of Kim, K.Y., et al., (2009), Adaption of programming writing skills based on storytelling is an effective method to improve problem solving and achievement of learning [7].

To understand the concept of robot design and programming requires students' high level abstraction ability. In order to solve the problem easily, We investigate the robotics convergence curriculum for elementary school students -Robotics, Mechanism, Art, Music, Science based on storytelling(RMAMS)-, and formally introduce the key ideas of this as follows:

- Use of well-known fairy tale divided into 7~8 concepts
- Each concept has a mission to learning the robotic conception related story
- Each mission is included integrating subjects: Science, Art, and Music in elementary school
- Sharing robot ideas and story with friends on the Web and Mobile

2.3 Robotic Platform and Framework

1) LEGO® MINDSTORMS® NXT: The current robotic platform in use is The LEGO® MINDSTORMS® NXT. LEGO NXT robot appears as a simple, flexible and attractive educational platform to achieve the creative programming ability. The LEGO MINDSTORMS NXT design is based on the advanced 32-bit ARM7 microcontroller, which can be programmed with the LabView based block-oriented language.

Working with communication algorithms the LEGO MINDSTORMS built-in Bluetooth media or IEEE 802.11 extension can be explored. The NXT has three output ports for attaching motors and four input ports for attaching sensors as shown in Figure 1.

Fig. 1. LEGO MINDSTORMS NXT

2) Adobe Flex: Adobe Flex is free open source framework for building and maintaining expressive web applications that deploy consistently on all major browsers, desktops, and operating systems. Also Flex is a solution for building RIA (Rich Internet Application). It is a script language to easily make an open and dynamic application based on Web 2.0.

Adobe Flex provides an interactive development environment between server and clients. Under the opening and sharing platform, Web 2.0, Adobe Flex makes it easy to share experiences and knowledge.

3 RMAMS (Robot-Mechanism-Art-Music-Science) Curriculum

To strengthen learner's academic achievement and studying immersion, RMAMS (Robot-Mechanism-Art-Music-Science based on storytelling) is designed which is based on reconstructed storytelling through combining the events from the fairy tale, Cinderella with Robotics curriculum.

In summary, Robotic concepts are introduced each week during lectures. Topics with story include motor control, sensors (sonars, sound, and light), design, sharing with friends. The topics of RMAMS are designed an integrated education process through the immersion of some subjects during 1 semester.

In this paper, we utilized NXT that were jointly developed by LEGO and M.I.T.

NXT consist of intelligent brick equipped with ARM7 processor, input sensors (touch sensor, sound sensor, light sensor, ultra sonic sensor), and interactive servo motor and various block components.

Learners can design and assemble the robot by using Mindstorms NXT and they can control the robot easily by using the provided program, NXT-G.

Furthermore, there's programming software based on a form of the text RobotC, NQC and a form of GUI programming software, NXT-G which can control intelligent brick.

Table 2. RMAMS Curriculum Outline

Lecture	Scene	Topic	Week
Introduction	encounter with two stepdaughters and stepmother	Greeting with Cinderella	1
Speed and Motor Control	stepmother's abuse	Lifting heavy objects	2
		Movement heavy objects	3
		Movement of objects in place	4
Electronic and Light Sensor	Prince live in Castles	To think of how to decorate the castle of the prince lived	5
		Installation of street lights	6
Environment and Carriage action	That Cinderella's pumpkin carriage ride production	Carriage forward	7
		Carriage backward	8
		Proceeding carriage	9
Remake a story and Line trace	Pumpkin carriage ride to the castle.	Cinderella visit castle at home	10~11
Dancing with LCD display	The Ballroom To choose bride	Create a bulletin board lightning in the ballroom	12
		Installation a lightning in the ballroom	13
		Dancing	14
Final contest	A happy life with princess	Production of the "good triumphing over the evil" campaign	15
		Creative song of the campaign	16

As shown in Table 2, Appearing in the Cinderella fairy tale, Main story is divided into seven lecture, seven scenes and 15 topics. Learners need to learn to solve each topic consists of the integrated elements of the robotic and subjects.

Learners will design the robot, assemble, make a program to solve the problems which is from each subtitles and develop the story with the robot they made.

Table 3. Integrated Subjects accorded to the Topic in RMAMS Curriculum

Topic	**Robotics & Mechatronics**	**5, 6th Grade Subjects for elementary school in Korea**		
		Science	**Art**	**Music**
Greeting with Cinderella	Using of the sound sensor	Chapter 6.(1/10) Electrical and electronic in life	Chapter 4.(1/4) Observation	Chapter 1. Create a rhythm accompaniment
Lifting heavy objects	Design of Robot movement	Chapter 3.(6/9) Energy and tool: Understanding concept of pulley &	Chapter 12.(2/4) Photo and video	Chapter 5. Similar rhythm and different rhythm
Movement heavy objects	Motor control	Chapter 5.(8/8) Magnetic field		
Movement of objects in place	Using of the Touch sensor and the Ultrasonic sensor	Chapter 3.(2/10)(5 grade) Speed of an object		
To think of how to decorate the castle of the prince lived	Electronic and Light Sensor	Chapter 2.(10/10) Electrical circuits	Chapter 3.(1-2/4) Life and space	Chapter 13. Create a musical play
Installation of street lights	Make electric-test-board			
Carriage forward	Motor movement	Chapter 3.(6/9) Energy and tool: moving a cay-toy Chapter 6.(6-8/10) Design of electrical circuits with electronic test blocks	Chapter 9.(5-6/6) Imagination and Expression	Chapter 7. Rhythm play
Carriage backward				
Proceeding carriage				
Cinderella visit castle at home	Line trace	Chapter 6.(6-8/10) Design of electrical circuits with electronic test blocks	Chapter 10.(2/4) Design and living	Chapter 8. Variations

Table 3. (*Continued*)

Create a bulletin board lightning in the ballroom	LCD display	Chapter 5.(6/10)(5 grade) Simple electrical circuits design	Chapter 3.(1/4) Visual culture environment and art	Chapter 12. Opera
Installation a lightning in the ballroom	Electric light			
Dancing	Motor swing-turn			
Production of the "good triumphing over the evil" campaign	Champaign	Chapter 6.(9-10/10) Problem solving of electric design in life	Chapter 10.(3-4/4) Design and living	Chapter 13. Simple composition
Creative song of the campaign	Using LCD display and sound sensor			

Learners are designing, assembling, and programing a robot to solve the offered problems to help Cinderella based on the previously set topic by the story "Cinderella". Therefore, they are making a new story with the robot they made.

Each topic which is suggested weekly from the RMAMS was extracted by the story of Cinderella. The extracted topic was connected with the learning elements from the relevant curriculum and we reorganized into the robotic learning elements to solve the offered problems in the topic.

As shown in Table 3, each topic is comprised of the robotics principles which learners should be learned to succeed the mission. Through combining the curriculum at the elementary school (Science, Art, and Music) with each topic, it can make learners learn something fun and interesting. The basic learning elements of the robot are integrated robotics and science curriculum of electrical and electronic components. Learning elements which is to support the learners is extracted by the expression parts of art curriculum. Learners made use of music curriculum to make enriched expression and reconstruct the story.

We made a system which is based on the Web and Mobile to help learners learn about robot, so we are going to give a detailed account in Section 4.

RMAMS curriculum is composed 4 stage; Story-Learning-Design-Share teaching-learning model to learn the each topic.

In the story stage, Learners listen to one story which is suggested by the topic. After listening they think about a robot which is able to help Cinderella in the story.

In the Learning stage, Learners learn basic learning elements to solve the problem in the topic and design the robot. To reconstruct the story, Cinderella they need to design the robot to understand the concept easily by using four frame cartoons.

In the Design stage, after expression activities of the abstracted concept, Learners are able to understand how to move and control the robot by expressing with the story included Robot algorism. After finishing the final trial performance and the

programming, Learning is completed by sharing the programming code, robot design date and the own story to make a robot through shared module in the support system with other learners.

4 System Implementation

That can easily be accessible in a mobile environment to help learners of storytelling-based robot programming learning system - RMAMS was implemented.

In this section we will address the following challenges:

- The ease of learning and enjoying variety properties of Robotics with integrated subjects based on storytelling
- Providing flexible studying tools for improving learners creativity by web and mobile
- Sharing idea and own story with friends about robot programming

4.1 Overview of RMAMS Support System

As shown in Figure 2, Support system for robotics curriculum which is based on learner's story telling is made up of three parts that is the robot storytelling web services, mobile services, and content DB.

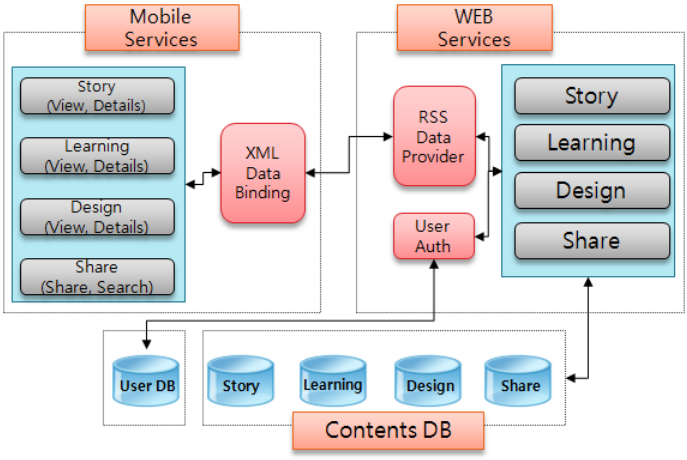

Fig. 2. Mobile, WEB Services, and Contents DB Structure of RMAMS support system

Robot storytelling web services consist of story, learning, designing, sharing module to learn to fit the step of storytelling based on robotics curriculum. So that learners can easily access anywhere at any time easily, providing us with a mobile learning environment is a mobile service.

Mobile services provide learners with contents through the linkage of web services and RSS Data provider module.

Content shared server is a database that can store story topics, code files, storytelling educational robotics file and can share.

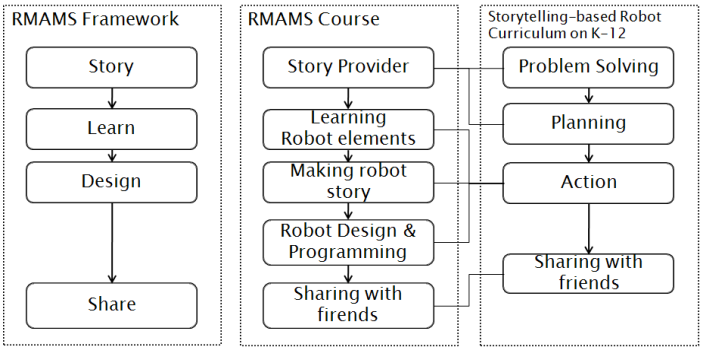

Fig. 3. RMAMS Framework and Robotics integrated Curriculum

As shown in Figure 3, Story module is equivalent to the problem solving and the planning stage, Learn and Design module corresponds to the action of the planning. And Share module corresponds to the stage to share with friends.

4.2 Experimental Results

The software environment to develop the RMAMS support system is composed of Window XP, PHP5, MySQL 5, Adobe Flex 4.6 SDK, and JDK 1.6.

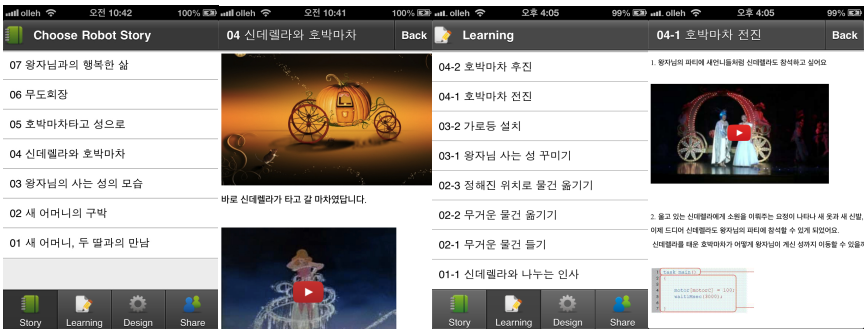

Fig. 4. Story Module and Learn Module

As shown in Figure 4(Left Side), Story module is an understanding and planning stage which has 7 sub-stories of the storytelling according to the story development and it is designed to learn the story that fits on the selected story by learners.

Students can be provided idea about the robot to learn in the story. As shown in Figure 4(Right side), Learn module provides learning contents which is composed with elements from the variety of subjects to design the suitable robot on the proposed sub-stories. The elements on the Learn contents which is also contained RMAMS support system elements provide the function to learn easily and interestingly.

Fig. 5. Design Module and Share Module

Share module is collaborative supporting system which can provide a function to share the made up story and the robot with friends. RoboLab is covered the advanced robotics educational contents, searching and collaboration function.

All these modules are organized a form of a class to help the learners when they want to need because it is running independent in the RMAMS support system framework.

5 Conclusion and Future Work

In this paper, we have designed and implemented robotics curriculum, RMAMS support system which is based on storytelling to improve learner's logical thinking and studying immersion.

RMAMS consists of seven scenes which are learning elements according to the development of the story from a variety of subjects based on the fairy tales. Each scene has a topic that includes 2-3 learning elements, Learners will design and make a programming to solve the given mission through the idea which is obtained from the story. A robot who designed by the learner will improve the logical thinking through the processing to collaborate and share the idea with friends.

Learners can access from not only web but also mobile environment easily with RMAMS support system framework so as to improve learner's participation and studying immersion. It is necessary to verify Based robot programming system which is designed RMAMS curriculum and support system by applying the academic achievement of learners and learning interest in development and how it influences.

References

1. Park, J.H., Kim, C.: A Study in Program Development of Course Incorporated Education by Utilizing Robots in Elementary Schools. Journal of Korea Association of Information Education 14(1), 35–44 (2010)
2. Sung, Y.H., Ha, S.W.: Development of an online robot programming education system based on Web 2.0. Journal of Korea Association of Information Education 14(1), 13–23 (2010)
3. Hong, K.C.: A Study of Programming Language Class with Lego NXT Robot for University of Education Students. Journal of the Korea Association of Information Education 13(1), 71–78 (2009)
4. Hong, S.H., Jeon, J.W.: A Web-based Distance Learning System for Robotics. Korea Journal of the Information Processing Society 11-A(7) (2004)
5. Lee, J.T., Yi, S.B.: A Study on the Development and Verification of a Logical Thinking Ability Measuring Tool in Computer Programming Learning. Journal of the Korea Association of Computer Education 7(4), 15–25 (2004)
6. Hong, K.C.: A Study of Programming Language Class with Lego NXT Robot for University of Education Students - Centered on Maze Problem. Journal of Korea Association of Information Education 13(1), 71–78 (2009)
7. Kim, K.Y., Song, J.B., Lee, T.W.: Effect of Digital Storytelling based Programming Education on Motivation and Achievement of Students in Elementary school. Journal of the Korea Society of Computer and Information 14(1), 47–55 (2009)
8. Fagin, B.S., Merkle, L.D., Eggers, T.W.: Teaching computer science with robotics using Ada/Mindstorms 2.0. In: Proceedings of the 2001 Annual ACM SIGAda International Conference on Ada, vol. 21(4), pp. 73–78. ACM SIGAda Ada Letters (2001)
9. Fagin, B.S., Merkle, L.D.: Measuring the effectiveness of robots in teaching computer science. In: Proceedings of the 34th SIGCSE Technical Symposium on Computer Science Education, vol. 35(1), pp. 307–311. ACM SIGCSE Bulletin (2003)
10. Flowers, T.R., Gossett, K.A.: Teaching problem solving, computing, and information technology with robots. Journal of Computing Sciences in Colleges 17(6), 45–55 (2002)
11. Lee, E.K., Lee, Y.J.: The Effects of 4CID Model based Robot Programming Learning on Learners‘ Flow Level. The Journal of Korean Association of Computer Education 11(4), 37–46 (2008)
12. Kang, H., Lee, J.H.: Design of Robot Instruction Program for Lower Classes of Elementary School. Korea Association of Information Education, 129–134 (2006)
13. Moon, W.S.: Influential Error Factors of Robot Programming Learning on the Problem Solving Skill. Journal of the Korea Association of Information Education 12(2), 195–202 (2008)
14. Seul, J.: Experiences in Developing an Experimental Robotics Course Program for Undergraduate Education. IEEE Transactions on Education 56(1), 129–136 (2013)
15. Moon, W.S., Yoo, S.H.: Development and Application of Robot Curriculum Based education in Insects Robot. Journal of the Korean Association of Information Education 14(2), 209–218 (2010)
16. Park, E.S., Moon, S.H.: Development and Application of a Robot Education Program for Logical Thinking Ability in Elementary Students. Journal of the Korean Association of Practical Arts Education 22(1), 175–198 (2009)

17. Kim, S.Y., Yoo, I.H.: Development of the Robot Programming Curriculum for Elementary Gifted Children. Proceeding of the Korean Association of Information Education, pp. 173–178 (2007)
18. STEAM: A Framework for Teaching across the Disciplines, http://www.steamedu.com
19. NASA: Mars Exploration Program, http://mars.jpl.nasa.gov/participate/marsforeducators/
20. Ryokai, K., Lee, M.J., Breitbart, J.M.: Children's storytelling and programming with robotic characters. In: Proceeding of the Seventh ACM Conference on Creativity and Cognition, pp. 19–28 (2009)

Cutting Force Prediction of Plunge Milling Based on Precise Cutting Geometry

Kejia Zhuang, Xiaoming Zhang, and Han Ding

State Key Laboratory of Digital Manufacturing Equipment and Technology,
Huazhong University of Science and Technology,
Wuhan 430074, China

Abstract. As one of the most effective methods, Plunge milling is widely used for mass material removal in rough and semi-rough machining of heat-resistant-super-alloys in metal cutting. The cutting force in plunge milling operation differs from that in side milling or end milling for the cutting geometry is more complex in plunge milling. In this paper, a new cutting force model is developed based on the more precise cutting geometry in plunge milling process. The cutting step is taken into account for real-time uncut chip thickness calculation as well as radial cutting width in the proposed cutting model. In the last, the sample cutting tests are carried out to indicate the correctness of the proposed cutting force model.

Keywords: Cutting force, plunge milling, cutting geometry, real-time uncut chips.

NOMENCLATURE			
N	number of flutes	R	radius of the tool
ϕ_{ji}	immersion angle of tooth *j*	K_t, K_r, K_f	cutting coefficients
Ω	spindle speed	φ_p	cutter pith angle
a_e	radial depth of cut	a_s	step of cut
F_x, F_y, F_z	cutting force in Cartesian coordinate	$a(\phi_{ji})$	real-time uncut width thickness
f_z	feed per tooth	ϕ_{st}	cutting in angle
ϕ_{stn}	changeable cutting angle	ϕ_{ex}	cutting out angle
$S(\phi_{ji})$	real-time dynamic cutting area(tooth *j* at time *i*)	$h(\phi_i)$	dynamic uncut chip thickness
F_{qd}	dynamic cutting force	HRSA	Heat-resistant-super-alloys

J. Lee et al. (Eds.): ICIRA 2013, Part II, LNAI 8103, pp. 592–601, 2013.

1 Introduction

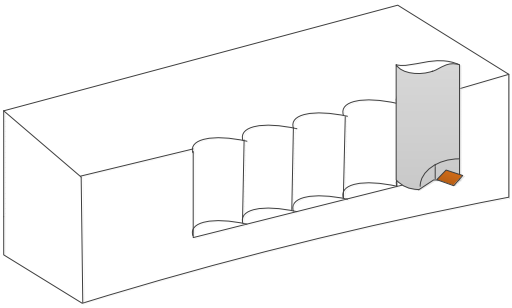

Fig. 1. Plunge milling operation

Since the strategy is more vibration free than in plane milling and side milling operations, plunge milling operation has gained more attention as a promising roughing and semi-roughing process. This operation is often used for roughing cavities and walls in moulds and dies, also used in machining of hard material such as Inconel 718 for remove excess material rapidly. Sample plunge milling operation is illustrated in Fig. 1, the feed direction is along to the spindle axis z where axes x, y are the horizontal coordinates. This strategy is more stable than conventional cutting for the spindle in the axial direction has the highest rigidity in plunge milling. Also there are many difficulties in plunge milling operations that limits the use of this strategy. Most of the previous works concentrated on the design of cutter geometry and the chatter stability of the plunge milling. Wakaoka et al. [1] studied the intermittent plunge milling process to make vertical walls by focusing on the tool geometry and motion. Li et al. [2] presented a plunge milling method to create complex chamfer patterns and estimated cutting forces while neglecting the structural dynamics of the system. There are many literatures belonging to the commercial tool catalogs, which present only the dimensions and shape of the plunge milling cutters. Ahmed et al. has done some work in cutting Inconel 718 and the modeling of plunge milling operation. Ahmed and Mohamed Elbestawi et al. [3] proposed a horizontal approach to compute the chip area to consider the contribution of the main and side edge in the cutting zone and to deal with any geometric shape of the insert. M. Al-Ahmad et al. [4] proposed a cutting model that included the determination of tool geometry (radial engagement, chip thickness) and the evaluation of the cutting forces. Recently, some researches focused on the dynamics of the cutting system of plunge milling operation, the dynamic uncut chip was computed along the cutting width as a function of the cutter vibrations. Y. Altintas et al. [5] have proposed a comprehensive model of plunge milling process by considering rigid body motion of the cutter, and three translational and torsional vibrations of the structure, also he and his colleagues [6] presented a frequency domain, chatter stability prediction theory for plunge

milling by regenerative the chip thickness. But the previous work did not take the cutting step to analysis the mechanical model as well as the radial cutting width, and the cutting force model in plunge milling previous was similar to the side milling.

In the field of metal cutting, the study of the cutting forces and its modeling is one of the classic research areas of machining processes for its importance in milling operation. There have been many establishing process mechanics models in metal cutting field, i.e. empirical formula models, finite element models, numerical models. A cutting force model to predict the milling forces based on the chip load was proposed by Kline et al. [7] in 1982. Also Y. Altintas et al. [8] modeled the cutting forces as a function of uncut chip area with the empirically cutting force coefficients, which are calibrated from various feed rate cutting tests. Then, Lee and Altintas [9] used the orthogonal cutting tests with oblique cutting analysis and transformation to determine the cutting coefficients. A cutting force model with the analysis of the cutter run-out studied by Feng and Menq [10]. The relationship of the derived cutting force coefficients with the relevant cutting condition parameters from the measured cutting forces was proposed by Cheng et al. [11] though a series of cutting tests. But there are limited literatures focused on the cutting force model in plunge milling operation for the cutting geometry of that is more complex than conventional milling.

In this paper, a new cutting force model is proposed based on the precise cutting geometry in machining of Heat-resistant-super-alloys with plunge milling method. The precise cutting geometry reflects the nature of plunge milling with different cutting situations. With the radial cutting width various, the cutting geometry is different and the precious cutting geometry are analyzed in the proposed cutting force model. In the last, the correctness of the proposed model are indicated by analysis of the results of the simulations and cutting tests.

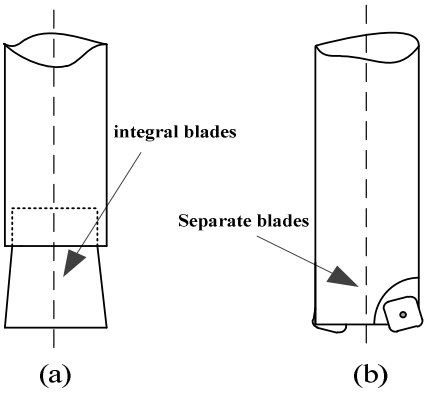

Fig. 2. Two types of plunge milling cutter (integral blades and separate blades)

2 Cutting Model of Plunge Milling

The tool manufactures developed the plunge milling cutter consist of the cutter body and the inserts from the consideration on the economy. As shown in Fig. 2, there are two types of cutters in plunge milling operation, i.e., separate ones (Fig.2(a)) and integral ones (Fig.2(b)). The separate plunge milling cutter can be used in roughing or semi-roughing, enlarging small holes while the integral cutter used for makeing big holes. The cutting force model proposed in this paper analysis the precious cutting geometry independently with different radial cutting width.

2.1 Cutting Geometry with Small Radial Cutting Width

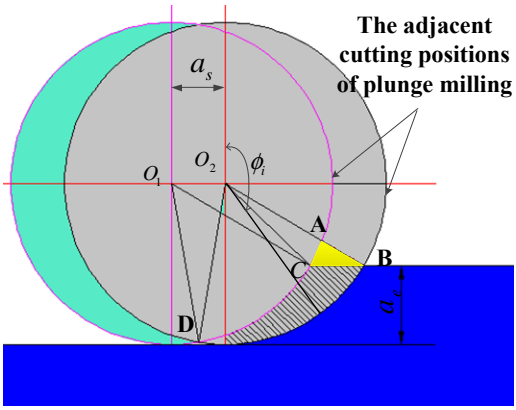

Fig. 3. Cutting geometry of plunge milling with small radial cutting width

When the plunge milling operation is used for roughing of semi-roughing with small radial cutting width, as the cutting geometry is shown in Fig. 3, i.e. $a_e < R$, then the cutting geometry can be describe as

$$a(\phi_{ji}) = \begin{cases} 0 & \phi_{ji} < \phi_{st}, \phi_{ji} > \phi_{ex} \\ R - \dfrac{a_e - R}{\cos\phi_{ji}} & \phi_{st} \le \phi_{ji} \le \phi_{stn} \\ R - \sqrt{R^2 - a_s{}^2 \cdot \cos^2\phi_{ji}} + a_s \cdot sin\phi_{ji} & \phi_{stn} \le \phi_{ji} \le \phi_{ex} \end{cases} \quad (1)$$

In Eq. (1), the boundary of the cutting angle ϕ_{st}, ϕ_{stn}, ϕ_{ex} with small radial cutting width in plunge milling process can be stated as

$$\begin{aligned}\phi_{st} &= \pi - \text{acos}(1-\frac{a_e}{R}) \\ \phi_{stn} &= \pi - \text{atan}(\frac{\sqrt{2Ra_e - a_e^{\,2}} - a_s}{R-a_e}) \\ \phi_{ex} &= \pi + \text{atan}(\frac{a_s}{2\text{R}})\end{aligned} \tag{2}$$

2.2 Cutting Geometry with Large Radial Cutting Width

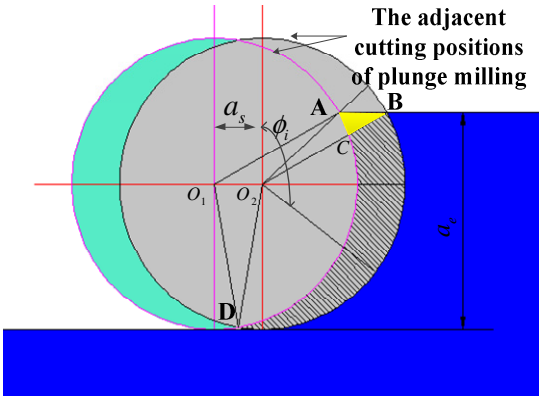

Fig. 4. Cutting geometry of plunge milling with large radial cutting width

When the radial cutting width is larger than the radius of the plunge milling cutter, i.e. $a_e > R$, as shown in Fig. 4, the cutting geometry can be described as

$$a(\phi_{ji}) = \begin{cases} 0 & \phi_{ji} < \phi_{st}, \phi_{ji} > \phi_{ex} \\ \dfrac{a_e - R}{\cos\phi_{ji}} - \sqrt{R^2 - a_s^{\,2}\cdot\cos^2\phi_{ji}} + a_s \cdot sin\phi_{ji} & \phi_{st} \le \phi_{ji} \le \phi_{stn} \\ R - \sqrt{R^2 - a_s^{\,2}\cdot\cos^2\phi_{ji}} + a_s \cdot sin\phi_{ji} & \phi_{stn} \le \phi_{ji} \le \phi_{ex} \end{cases} \tag{3}$$

In Eqs. (3), the boundary of the cutting angle ϕ_{st}, ϕ_{stn}, ϕ_{ex} with large radial cutting width in plunge milling process can be stated as

$$\begin{aligned}\phi_{st} &= \pi - \text{atan}\left(\frac{a_e - R}{\sqrt{2Ra_e - a_e^{\,2}} - a_s}\right)\\ \phi_{stn} &= \pi - \text{acos}\left(1 - \frac{a_e}{R}\right)\\ \phi_{ex} &= \pi + \text{atan}\left(\frac{a_s}{2\text{R}}\right)\end{aligned} \tag{4}$$

2.3 Cutting Force Model

With the cutting geometry proposed previously, the cutting forces in tangential, radial, feed directions of the tooth j at the cutting angle ϕ_{ji} are given by

$$\begin{aligned}F_{tj}(\phi_{ji}) &= K_t S(\phi_{ji})\\ F_{rj}(\phi_{ji}) &= K_r S(\phi_{ji})\\ F_{fj}(\phi_{ji}) &= K_f S(\phi_{ji})\end{aligned} \tag{5}$$

where $S(\phi_{ji})$ is the real-time dynamic uncut chip area by cutter tooth j.

The predicted cutting force above can be transformed into three orthogonal components in Cartesian coordinates of the cutter axes as follows

$$\begin{bmatrix}F_{xj}(\phi_{ji})\\ F_{yj}(\phi_{ji})\\ F_{zj}(\phi_{ji})\end{bmatrix} = \begin{bmatrix}-\cos\phi_{ji} & -\sin\phi_{ji} & 0\\ \sin\phi_{ji} & -\cos\phi_{ji} & 0\\ 0 & 0 & 1\end{bmatrix}\begin{bmatrix}F_{tj}(\phi_{ji})\\ F_{rj}(\phi_{ji})\\ F_{fj}(\phi_{ji})\end{bmatrix} \tag{6}$$

The total instantaneous cutting forces on the cutter can be evaluated by

$$\begin{bmatrix}F_x(\phi_i)\\ F_y(\phi_i)\\ F_z(\phi_i)\end{bmatrix} = \sum_{j=1}^{N}\begin{bmatrix}F_{xj}(\phi_{ji})\\ F_{yj}(\phi_{ji})\\ F_{zj}(\phi_{ji})\end{bmatrix} = \sum_{j=1}^{N}\begin{bmatrix}K_t\\ K_r\\ K_f\end{bmatrix}\begin{bmatrix}-\cos\phi_{ji} & -\sin\phi_{ji} & 0\\ \sin\phi_{ji} & -\cos\phi_{ji} & 0\\ 0 & 0 & 1\end{bmatrix}S(\phi_{ji}) \tag{7}$$

where N is the teeth number and K_t, K_r and K_f are the cutting coefficients fitted by the various feed rate in plunge milling with the same conditions.

3 Simulation and Experiment

In this section, simulations and cutting tests are carried out to validate the proposed cutting force model. The schematic diagram of the experiment setup of plunge milling operation is shown in Fig. 5. Fig. 6 shows the setting of the cutting tests of plunge

milling HRSA. First, a series cutting tests are conducted to calibrated the cutting coefficients of the workpiece-tool system. Then, sample cutting tests are used to comparative analysis with the simulation results.

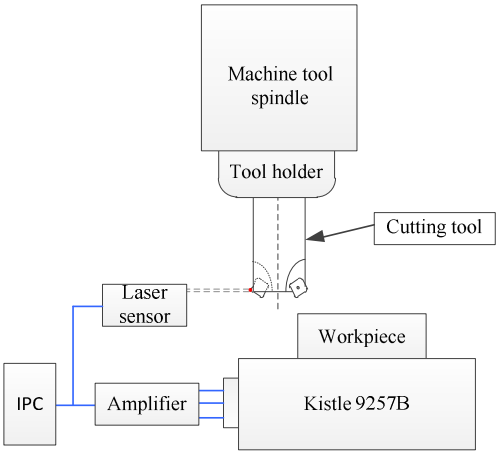

Fig. 5. The schematic diagram of cutting tests

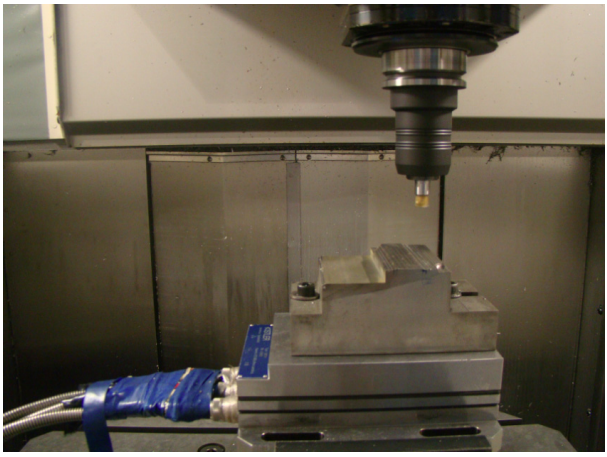

Fig. 6. The experiment setting of plunge milling

Table 1. The mechanical composition of the workpiece

C	Mn	Si	P	Ni	Cr	Mo	Ti	Nb	Co	Al	Fe
0.03	0.02	0.09	0.003	52.48	18.94	3.03	0.98	5.13	0.02	0.51	other

The material tested in this study is HRSA with the size of rectangle block 85mm×70mm×30mm, the hardness of this material is HRC 42 and the mechanical composition of this material is shown in Table 1. The experiments of plunge milling

are performed in MIKRON DURO UCP 800, a 5-axis milling center with a Heidenhain numerical control system. The test cutter is a 12mm SECO plunge milling cutter, and the appearance of the plunge milling cutting test is shown in Fig. 6.

Table 2. Identified cutting coefficients in plunge milling of HRSA

K_t (N/mm^2)	K_r (N/mm^2)	K_f (N/mm^2)
1010	1880	1235

The cutting forces in plunge milling are predicted by the method proposed previously with the cutting coefficients shown in Table 2 which are fitted by a series cutting tests. The dynamic uncut chips are shown in Fig. 7 and 8 with the cutting parameters shown in Table 3. Fig. 9 and 10 show the predicted and measured cutting forces with the cutting parameters given in Table 3. From the figures, the correctness of the proposed model in this paper is indicated with the good quantitative agreement of the predicted and measured cutting forces in plunge milling.

Table 3. Cutting parameters in plunge milling

No	Spindle speed(Ω)	Feed rate(f_z)	Cutting width(a_e)	Cutting step(a_s)
1	1000rpm	0.05mm	8mm	3mm
2	1000rpm	0.05mm	3mm	2.5mm

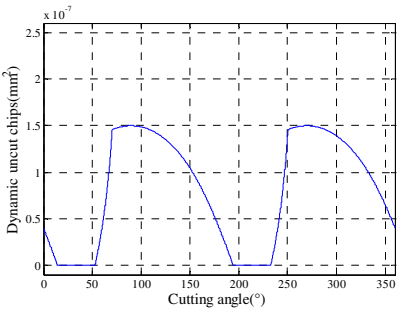

Fig. 7. Dynamic uncut chips with large radial cutting width (No.1 in Table 3).

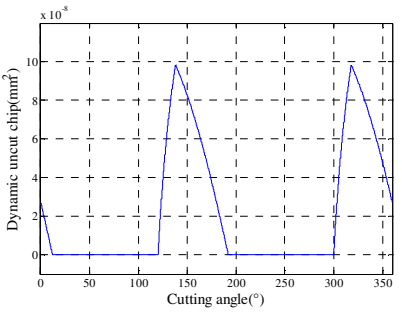

Fig. 8. Dynamic uncut chips with small radial cutting width (No.2 in Table 2).

4 Conclusions

In milling operation, predicting the cutting force is a critical work for that greatly affects the machine situations. In this paper, a new cutting force model with different cutting width of plunge milling is proposed. The cutting step is used to predict the

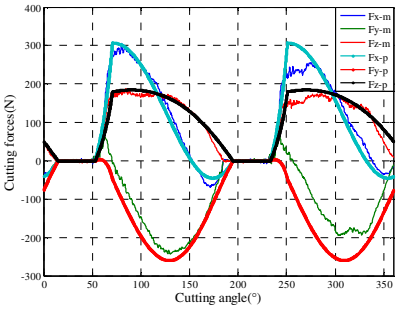

Fig. 9. The predicted and measured cutting forces (*F-m* and *F-p* indicate the predicted and measured ones, respectively). (No.1 in Table 3)

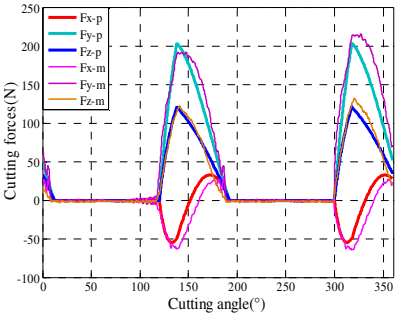

Fig. 10. The predicted and measured cutting forces (*F-m* and *F-p* indicate the predicted and measured ones, respectively). (No.1 in Table 3)

real-time dynamic cutting width as well as cutting width in the operation. The proposed cutting force model is generally application to the plunge milling operation with different cutting situations. In the last, the results of two samples cutting test shows the correctness of the proposed cutting model.

Acknowledgments. This work was partially supported by the National Basic Research Program of China (2011CB706804), the National Natural Science Foundation of China (51005087) and the National Science & Technology Pillar Program (2012BAF08B01).

References

1. Wakaoka, S., Yamane, Y., Sekiya, K., Narutaki, N.: High-speed and high-accuracy plunge cutting for vertical walls. Journal of Materials Processing Technology 127, 246–250 (2002)
2. Li, Y., Liang, S., Petrof, R., Seth, B.: Force modelling for cylindrical plunge cutting. The International Journal of Advanced Manufacturing Technology 16, 863–870 (2000)
3. Damir, A., Ng, E.G., Elbestawi, M.: Force prediction and stability analysis of plunge milling of systems with rigid and flexible workpiece. The International Journal of Advanced Manufacturing Technology 54, 853–877 (2011)
4. Damir, A.: Modelling the dynamics of plunge milling with workpiece vibrations consideration. ETD Collection for McMaster University (2011)
5. Ko, J.H., Altintas, Y.: Time domain model of plunge milling operation. International Journal of Machine Tools and Manufacture 47, 1351–1361 (2007)
6. Ko, J.H., Altintas, Y.: Dynamics and stability of plunge milling operations. Journal of Manufacturing Science and Engineering 129, 32 (2007)
7. Kline, W., Devor, R., Lindberg, J.: The prediction of cutting forces in end milling with application to cornering cuts. International Journal of Machine Tool Design and Research 22, 7–22 (1982)

8. Budak, E., Altintas, Y., Armarego, E.: Prediction of milling force coefficients from orthogonal cutting data. Journal of Engineering for Industry 118, 216–224 (1996)
9. Lee, P., Altintaş, Y.: Prediction of ball-end milling forces from orthogonal cutting data. International Journal of Machine Tools and Manufacture 36, 1059–1072 (1996)
10. Feng, H.Y., Menq, C.H.: The prediction of cutting forces in the ball-end milling process—I. Model formulation and model building procedure. International Journal of Machine Tools and Manufacture 34, 697–710 (1994)
11. Feng, H.Y., Ning, S.: A mechanistic cutting force model for 3D ball-end milling. Journal of Manufacturing Science and Engineering 123, 23–29 (2001)

Distributed Coordination of Multiple Robot Systems Based on Hierarchical Petri Net Models

Gen'ichi Yasuda

Nagasaki Institute of Applied Science
536 Aba-machi, Nagasaki 851-0193, Japan
yasuda_genichi@pilot.nias.ac.jp

Abstract. The paper presents a systematic methodology for modeling multi-robot production tasks based on extended Petri nets. To overcome some difficulties in the modeling of complex discrete event systems with a large number of elements in basic Petri nets, extended high-level Petri nets are introduced based on condition-event Petri nets. The high-level net representation of the conceptual task flows and detailed control functions with a top-down refinement methodology can provide more synthetic specifications for consistent management and distributed coordination of multi-robot systems.

Keywords: Multiple robot systems, hierarchical modeling, discrete event nets, distributed coordination.

1 Introduction

One of the key issues in the research on intelligent robotics is the control system design problem; their controllers must be realized with parallel and distributed architecture, because large and complex robotic systems such as multi-robot flexible manufacturing cells have operation features of parallelism and concurrency according to the physically distributed structure of the control system. The author originated the researches on non–centralized systems since 1971 [1], [2], especially center-less robot groups and self-coordinating motion control systems with non-centralized modular neural nets. Non-centralized systems are composed of several autonomous subsystems and their behaviors are asynchronous and parallel in nature. Distributed autonomous control must be accomplished through local and mutual interaction among subsystems. The non-centralized systems have been classified into the following three systems with respect to the emergence of the master function in the system: variable master (leader) and slave (follower) systems without any fixed master-slave relationship or hierarchical structure, emergent hierarchical systems, and ideally perfect cooperating systems. Conventional computer-controlled systems for present autonomous intelligent robots and manufacturing systems are centralized systems with fixed master-slave relationship or hierarchical structure. Animal groups and human organizations are non-centralized systems, where each member in the group or organization has the potentiality of the master (leader). Self-coordinating motion control systems with non-centralized modular neural nets, including turnover motion of starfishes and

J. Lee et al. (Eds.): ICIRA 2013, Part II, LNAI 8103, pp. 602–613, 2013.

human manipulation with both arms and/or hands, are considered as ideally perfect cooperating systems. Biological production processes such as cellular tissues and plants are non-centralized, emergent hierarchical systems composed of self-reproducing cells with DNA-based information structures. Each cell produces proteins and other biochemical components directed by the genetic information and forms cellular tissue structures, communicating and cooperating with other neighboring cells. Resultant biological products and tissue fields are used as feedback signals to regulate, that is, excite or inhibit the activities of the genetic components in each cell.

Inspired by biological non-centralized control systems, this paper focuses on control system design for multi-robot coordination. To implement the controllers it is necessary to provide effective tools for modeling and control algorithms development of coordinated tasks of multiple robots. In many modeling techniques which effectively represent and analyze discrete parallel systems, modeling with finite state machines brings about difficulties when a system becomes sufficiently complex, because the state of the whole system must be known. On the other hand Petri nets use local state without requiring the remainder of the system to be known. Thus, Petri nets can be easily expanded and they can efficiently model multiple robot systems. Due to the distributed and non-deterministic nature, Petri nets have the possibility of modeling non-centralized control systems. Petri nets were used as an effective tool for describing control specifications for robotic tasks [3], [4], [5]. However, the implementation method for hierarchical and distributed control of complex multiple robot systems has not been established sufficiently so far. This paper presents a systematic method of the design of Petri net based hierarchical and distributed controllers for coordinated tasks of multiple robot systems. Based on hierarchical representation of Petri nets, the architecture of the controllers and its main capabilities for multi-robot system coordination are provided.

2 Hierarchical Approach for Modeling Robotic Tasks

In actual production systems, production processing controllers are structured in a hierarchy, so there is a close relationship between the conceptual simulation objects and the actual objects. The hierarchical approach offers a simple model building and provides possibilities to reduce the size of the specifications. In this context, a hierarchical formalism should be adopted, which allows some structural and behavioral properties of a model to be formally proved. A production system is composed of generic objects having all structural and functional characteristics of the relevant production resources [6], [7]. Each object is a recursive structure able to develop models of production flows and corresponding activities at different levels of abstraction and hierarchy, according to the level of detail needed in the model. At the same time it is a function of lower-level objects. The main advantages of modeling and simulation using the conceptual object in hierarchical production systems can be summarized in the following points: the reusability of the generic objects by the systematic refinement over the different levels of abstraction, and the modular modeling property considering the use of recursive structures of the overall system.

Petri nets are a modeling technique that captures the causal relationships between conditions and events [8]. They are commonly used to model concurrent processes, such as the flows of information and control in programmable systems. A Petri net comprises two types of nodes, places representing conditions or states and transitions representing events, which are interconnected by directed arcs. Tokens, which reside at the places, are used to indicate the instantiation of a state. The current state of a net is represented by the distribution of tokens in the net, which is called the marking which maps places to the number of tokens in each place. In a Petri net, the places, transitions and tokens are represented by the circles, bars and dots, respectively. In basic Petri nets, a transition is enabled if each of its input places contains the specified number of tokens according to the input arc weight. When a transition is enabled, it can possibly fire. If it fires, tokens are removed, from each of its input places and placed in each of its output places according to input and output arc weights, respectively. The marking of a Petri net changes when a transition, which is enabled, eventually fires.

Condition-event nets, where each place can contain not more than one token, are very useful in the analysis of the qualitative behavior of multi-sequence control systems, because this allows a one-to-one semantic correspondence between places and conditions. Thus, a Petri net representation of a system can be used as a design schema as well as a supervising framework [9], [10], a lowest-level real-time control algorithm [11], [12] etc. The drawback in applying this technique to the modeling and analysis of production systems is its expressiveness, principally when a big number of conditions are involved. Unfortunately, modeling real production systems frequently implies the representation of a great number of conditions, and leads to complex net structures.

From an abstract viewpoint, a discrete production system is characterized by the flow of discrete items such as workpieces, parts, tools, palettes, information, etc. which pass in ordered form through subsystems and receive appropriate operations to achieve the purpose of the production system. Concepts such as non-determinism, concurrence, parallelism and synchronism are the basis on which real models of production systems are depicted. Such a system is composed of a set of resources for dedicated production purposes, that is, physical transformations such as machining, assembling, transfer operations such as loading and unloading, or buffering. These resources are classified into two categories: active resources such as robots and machine tools and passive resources such as buffers and workplaces. Various resources are interconnected in a production system and controlled so that some items are passed and others are circulated to achieve the production purpose. The functions of active resources can be viewed abstractly as activities. An activity starts when all the specified items are arrived, and after the working time it ends and as a result produces particular items at the same time. A sub-flow of items may intervene into an activity in a main flow. Sub-flows can be seen as involved with an activity in a lower level. After an item exits from an activity and then it enters the next activity, passing through a passive resource such as a buffer. Thus, the functions of passive resources can be viewed abstractly as distributions. An item can not change its physical characteristics in a distribution. Thus an activity is distinguished from a distribution. From the viewpoint of discrete event process control, an overall production process can be

decomposed into a set of distinct activities or events and distributions or conditions mutually interrelated in a complex form.

The abstract concepts of activities and distributions are combined with the pure objects of conditions and events in the condition-event net. Thus, a high-level Petri net is defined to extend the condition-event formalism to the modeling and design phases. The extended high-level Petri net is represented as a bipartite graph, similarly to conventional condition-event nets. Fig. 1 indicates the elements of the extended high-level Petri net.

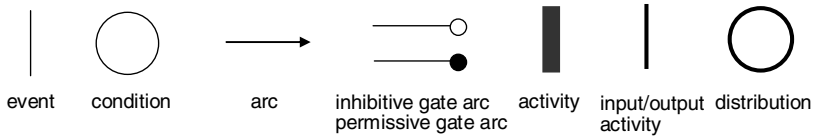

Fig. 1. Elements of the extended high-level Petri net

The class 'activity' is defined as the abstract active resource. Each activity is represented by an object characterized by a set of attributes. A simple activity is an object instance of the class and an alternative definition of an event. An activity is defined by two primitive activities called start and end activities respectively, an active place which stores estimated time of processing and a pointer to another net representing the model of the specified process. Every activity can have its own state and perform planning and execution phases. These activities may coexist with stateless reactive processes in order to add robustness and smart response to the planned control activities. Once an estimated time argument is provided, the model of an activity could be simulated as a basic Petri net including input and output events separated by an active place.

The abstract activity is classified into the following levels: action, operation, and task. At the action level, actions executed by machines and devices are considered, such as forward and backward, up and down, start and stop, etc. At the operation level, operations executed one or several devices are considered, such as insertion, mating, screwing, opening and closing of a door, etc. At the task level, integrated activities as productive behaviors are considered, such as processing, assembly, disassembly, treatment, packaging, etc.

The class 'distribution' is defined as the abstract passive resource. A condition in a conventional condition-event net is a simple object instance of the class. A passive resource is generally defined as the system workplace where parts can be temporary held or stored in a stable position. In extended high-level Petri nets, each passive resource may be single or composed, held one part or subassembly. Composed resources manage the information attached to a set of single resources closely located and functionally equivalent. A resource contains information about the work zone if it can be used as mutual exclusion resource. Thus specific ways to store items, such as FIFO, LIFO, etc., can be represented in the subnet of the resource. Assembling and disassembling processes which only affect the item flow are abstracted in the subclasses of the class 'distribution'. Thus, assembling stations and storage mechanisms such as intermediary buffers are considered static compound resources as macro-places and can be reduced to conditions in the condition-event net.

There are some subclasses of the class ‘distribution’. A ‘timer’ inherits all the attributes of ‘distribution’ and has an extra parameter with the estimated time to enable the firing. Similarly subclass ‘capacity’ is the maximum number of marks it could accept. There are also other subclasses for capacity; assembling and disassembly capacity according to input-output relation values. The attribute of the subnet is a pointer to a subnet. By defining subclass with other input-output relation values, the relationship between conceptual distribution and extended ones can be established. Fig. 2 depicts an example net representation of a production task flow.

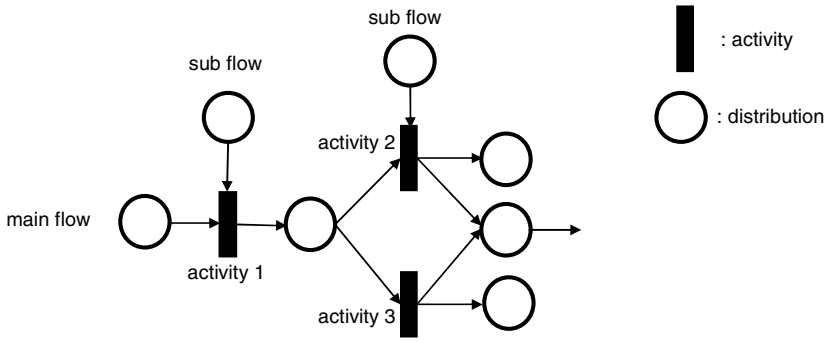

Fig. 2. Net representation of a production task flow

Similar to conventional nets, a gate is introduced to control the firing of an activity as a relation between the activity and an internal or external condition, whether the condition belongs or not to the system being modeled respectively, which is represented as another class of objects. An internal gate can be used to connect and synchronize the aggregated subnets. An external condition is a rule that is not part of the system in the sense that its satisfaction is not controlled by the target system. Anthropomorphic control actuators such as buttons and switches are examples of external conditions. Internal and external gates can still be classified as permissive or inhibitive according to whether it can enable an activity when it is marked or when it is unmarked. An external permissive condition can be interpreted as a relation between an external precondition and an activity element in the system. On the other hand, an external inhibitive condition would stand for a relation between an activity element in the system and an external post-condition. In situations such as conflicts, the permissive or inhibitive arc is used effectively to enforce priorities.

3 Description of Multi-robot Tasks Using High-Level Petri Nets

Net models of multi-robot tasks are described in a compact form using the extended high-level Petri nets. One of the features of the extended high-level Petri nets is the capability of representing numerable items or conditions. The capacity element is the basic element capable to hold multiple tokens. Any other places can be represented by a subnet composed of the basic elements, starting and ending with a condition. Activities in multi-robot systems are redefined using input and output transitions and

the extended conditions, or distributions with capacity, as shown in Fig. 3. In single activities, only one activity element or a robot acts. In concurrent activities, up to N elements act independently and concurrently by starting separately at the common input transition and ending separately at the common output transition. In assembling activities, each of N elements starts separately at the common input transition and ending simultaneously at the common output transition. For example, in case several robots transport a large and heavy part cooperatively, they must separately take the part and then start to move simultaneously. In disassembling activities, N elements start simultaneously at the common input transition and end separately at the common output transition. The hierarchical net representation of an activity composed of concurrent sub-activities is illustrated in Fig. 4.

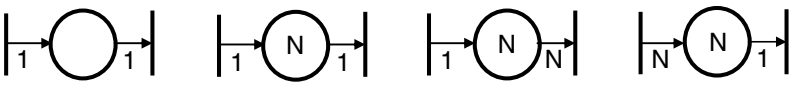

Fig. 3. Activity elements: (a) single. (b) concurrent, (c) assembling, (d) disassembling

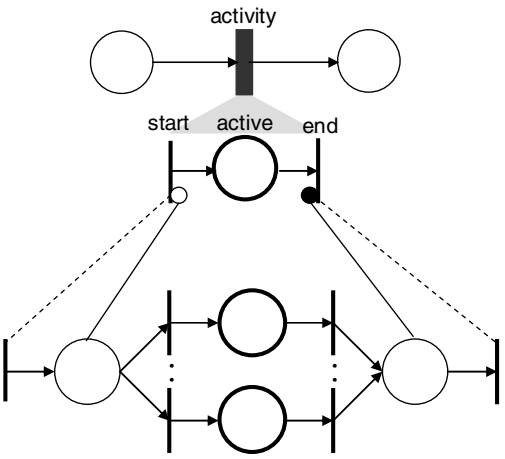

Fig. 4. Hierarchical net representation of concurrent activities

Activities and distributions are hierarchically structured and approached at different levels of abstraction. Each activity can be substituted by a subnet starting and ending with an event, while each distribution element can be substituted by a subnet starting and ending with conditions. Hierarchy of activity, such as action, operation, and task, is defined by introduction of substitution transitions. A substitution transition is a transition which is refined by another Petri net. All the input and output places of the transition at the higher level are mapped into associated places in the lower level subnet. For simulation, these corresponding places are glued together, since physically different but logical same places have always the same marking as a fusion set.

In a functional net representation, an activity at a higher-level is decomposed into some sub-activities, which are interconnected with distributions by directed arcs, such that a distribution intervenes between two activities. Fig. 5 shows a hierarchical description of an activity, where the activity at the higher level constitutes a parallel construct with an activity path composed of several sub-activities at the lower level, since the net of the activity must be safe. If the start of an activity occurs at the same time with the end of the preceding activity, then the distribution between them can be omitted in the net model. In this case, two activities are directly connected through a simple transition.

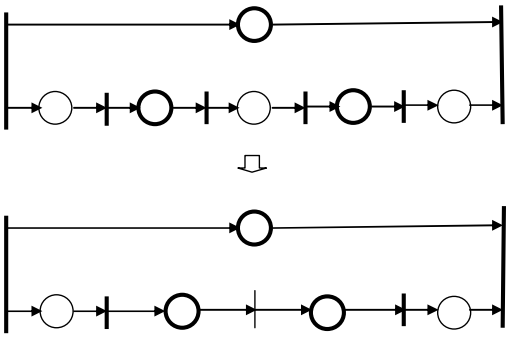

Fig. 5. Representation of hierarchy of activity in a net

The subnet model that represents the contents of an activity at the upper level must be structurally live such that when the activity is finished, the state of the net returns to the initial state. If it can not return to the initial state, the behavior of the net is in an abnormal state and the evolution of the net is not possible. In the hierarchical refinement procedure, net structures such as trap and siphon are prohibited so that the net does not enter into a state that is not live. The overall net model of task specification is composed of the subnet models of the activities. So the conditions that all the subnets are live are not sufficient for the overall net to be live. The liveness is determined by the connection structure among the subnets.

Tokens in extended high-level Petri nets are classified into flow and control tokens. Flow tokens describe the flow of system resources in a dynamic system operation or task flow. They are useful in representing input and output conditions for subnets. Control tokens are used in representing actual system resources. The presence or absence of these tokens denotes resource availability. Communication messages with synchronous or asynchronous communication are also indicated using control tokens to control simultaneous or interlocked activities among associated robots. For real-time control, the net models should be live such that their initial states are reachable repeatedly. A direct algorithm to find all the enabled events and any knowledge based approach as an arbiter to choose a configuration for the enabling vector can be used. Normally only independent events are allowed to be enabled simultaneously. Conflicting situations can be solved trivially by concurrent firing if they are in the concurrent list of each other, or by a firing policy deduced from the application or with the inclusion of an arbiter to solve conflicting situations.

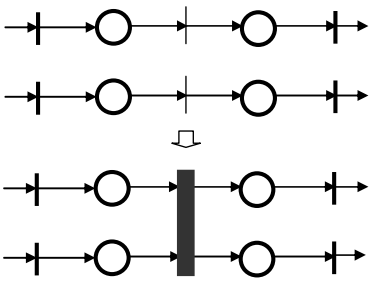

Fig. 6. Representation of synchronization between sub-activities using high-level transition

In multi-robot systems, there are some sub-activities interrelated with each other during the execution of concurrent activities. In case that synchronization of start or end of some sub-activities is included, it is modeled through the fusion of the transitions that represent the start or end of the corresponding sub-activities as shown in Fig. 6. The fused transition represents cooperative activities for synchronous or asynchronous communication between associated activity elements as a high-level transition [13]. By modeling the communication activities using Petri nets with shared places, a distributed simulation and control of the overall net can be performed.

Active resources, such as robots, return to their initial states when the assigned activities end. In this way, at the start of an activity, the required resources must be available. Each active resource is represented as a unique distribution, where the number of tokens corresponds to the number of resources which can be assigned. The arc from the distribution to the input transition of the activity represents the request for the use of the resource when the activity starts, while the arc from the output transition of the activity to the distribution represents the release of the resource when the activity ends. Thus, such a distribution element represents the function of assignment of a resource involved with an activity, which is called semaphore. Fig. 7(a) shows a case where two sequential activities share a same resource, while Fig. 7(b) shows a case where two concurrent activities share a same resource. Dummy capacity place is connected between the start and end transitions of the section, where maximum number of items processed is specified because of physical constraints.

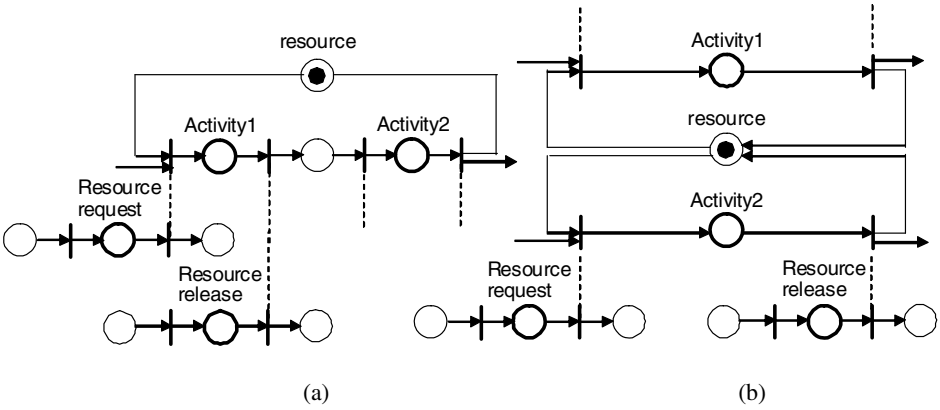

Fig. 7. Example of resource assignment; (a) sequential, (b) parallel mutual exclusion

4 Net Based Control System Design and Implementation

A particular implementation of the proposed procedure to define a production service is presented through a simple example. In the example, the objective is to automate and coordinate different activities and services executed in a distributed production system composed of the following subsystems: part supply, palletizing, pallet transportation, parts processing, product transportation, unpalletizing, and product carrying out. These subsystems are interconnected through a communication network to produce the customers' requested products. The part supply subsystem executes the service that carrying parts from a storage system into a buffer. The palletizing subsystem puts them in order in a pallet. Then, the transportation subsystem moves the pallet to the assembly subsystem. When the pallet reaches the assembly subsystem, two robots R1, R2 execute assembly activities cooperatively to produce the final product. The assembly service is carried out in three stages. Initially, parts are located in an appropriate base. Then, according with parts physical characteristics inspected using a camera, some identified parts, part A and part B, are moved to buffer 1 and buffer 2, respectively, and assembled in buffer 1. The assembled product is put on a free pallet of the transportation subsystem to leave the system. Finally, products are carried out by the discharge conveyor. The type and quantity of products are defined and requested by a customer. The production task flow net with a hierarchical description of the activity 'Processing' is shown in Fig. 8. By refinement of activities 'Supply', 'Carrying out', the overall functional net model is shown in Fig. 9.

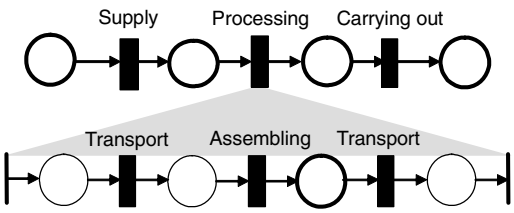

Fig. 8. Example of specification of production task flow

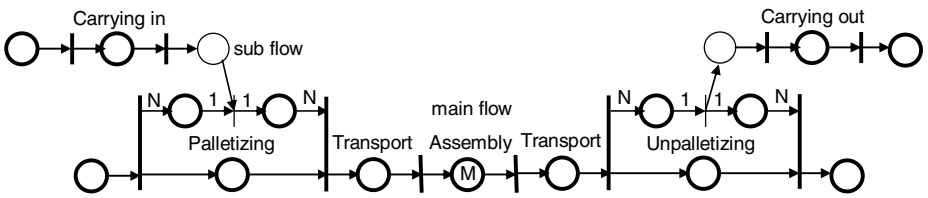

Fig. 9. Functional net model of example system

Fig. 10 shows the subnet of the part picking operation by the robot. During the movement toward the part, if the part is reachable and it can be grasped, the robot picks up the part. Fig. 11 shows the subnet of the part placing operation, responsible for the two robots, R1 and R2, moving a part from a conveyor to a buffer and from a buffer to a conveyor, respectively. During the movement, the robot checks if the part was dropped. If it was dropped, the robot locates it and picks up it. If the part is at the destination, the part is placed on it. Fig. 12 shows the subnet for the assembly operation of two parts A, B by the two robots. If part A is identified, it is moved to buffer 1 by robot R1. If part B is identified, and if part A is not in buffer 1, part B is temporarily moved to buffer 2, otherwise moved to buffer 1 to form the assembly. When part B is in buffer 2, if part A is moved to buffer 1, then part B is moved to buffer 1 by robot R2 and mated with part A to form the assembly. The assembly is shifted from buffer 1 to the transportation subsystem by robot R2.

Net based control is achieved by starting or ending activity elements or transitions according to the rules of transition firing with respect to system conditions of required subtasks and resources. For example, when part B is in buffer 2, if part A is moved to buffer 1 then robot R2 is requested to move the part B to buffer 1. When the operation is finished, robot R2 is released. Events of system conditions are sent from low-level subsystem controllers to the system controller using interrupts in order to report the current status and to notify termination of an activity or an unexpected condition. The system controller coordinates the overall behavior by sending the activity start events and waiting for the incoming events and clock events. The subsystem controllers give timely response to the events as an activity start, activity stop, or synchronization point acknowledgment.

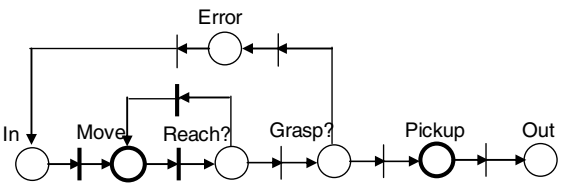

Fig. 10. Detailed net model of picking operation

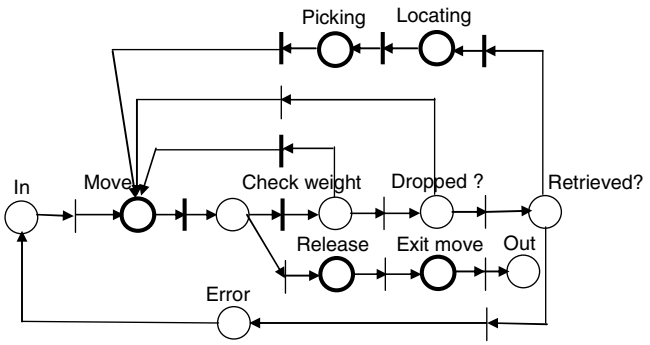

Fig. 11. Detailed net model of placing operation

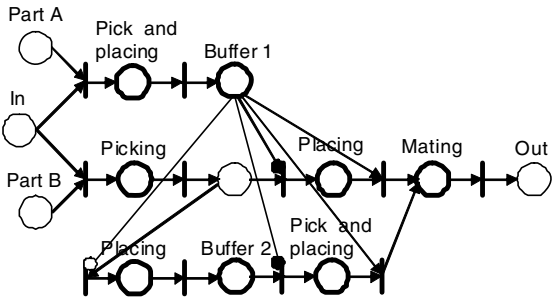

Fig. 12. Detailed net model of assembly operation

The proposed specification procedure for distributed multi-robot control systems is summarized as follows.

1) Specify task flows using activity elements and distribution elements.
2) Represent net models of the activity elements and distribution elements using extended high-level Petri nets.
3) Transform the task flows into the detailed net models needed for simulation and control.
4) Add the control places and net models that represent availability and exclusive assignment control (request and release) of the associated resources.
5) Add control places required for liveness and safeness of the overall net model.
6) Divide the resultant overall net model and distribute into the system controller and the subsystem controllers.

Due to the complementary definition between the extended high-level Petri nets and conventional Petri nets, different abstraction levels of composed resources of activities and distributions can be connected with simple events and conditions in the same representation. The specification of a production task using abstract resources is supposed to be filled later with proper detailed subnets in a top-down refinement methodology until it reaches a condition-event net form as the final representation. The verification of correctness of the functional net model, the validation of the functional requirements of the system, and structural and dynamic behavior analysis are done using the plain condition-event net form in the final design step, based on Petri net properties such as liveness, reversibility, existence of unreachable states, where the formal analysis techniques are combined with simulation.

5 Conclusions

The Petri net approach was extended for hierarchical description, analysis and control of discrete event systems to fit the high-level representation of task flows in multi-robot production systems; the concept of event is extended to enclose the idea of production activity elements, while the concept of condition to enclose several kinds of distribution elements. The global control of the system is hierarchical, but the

internal modular implementation is layered. Production task flows at the highest level are directly obtained from the system requirements using activity and distribution elements, and functional models for robot control are developed in conditional-event Petri nets through a top-down refinement technique. Thus, the remaining levels of the control structure are common to a wide range of industrial applications. The user can specify the production task by means of process description tables or the common UML Use Case Diagram. The extended transition firing and state change rules are very similar to the conventional condition-event nets, and it preserves most of the formalism and properties of Petri nets and also improves their expressiveness. The current approach is more suitable to applications in robotic production systems where models are revised several times and improve reusability. Also, separating a large net in several subnets can produce a representation amenable to a distributed implementation of a high-level Petri net simulator.

References

1. Yasuda, G., Mori, M.: Application of Graph Theory to Self-Reproducing Processes. In: Proc. of the 10th SICE Annual Conference, pp. 271–272 (1971)
2. Yasuda, G., Mori, M.: Construction of an Artificial Multi-Molecular Self-Reproducing Mechanism. In: Proc. of the 14th Joint Automatic Control Conference of Japan, pp. 65–66 (1971)
3. Cao, T., Sanderson, A.C.: Task Decomposition and Analysis of Robotic Task Plans using Petri Nets. IEEE Trans. on Industrial Electronics 41(6), 620–630 (1994)
4. Ramaswamy, S., Valavanis, K.P.: Modeling, Analysis and Simulation of Failures in a Material Handling System with Extended Petri Nets. IEEE Trans. on Systems, Man, and Cybernetics 24(9), 1358–1373 (1994)
5. Lee, J.-S., Hsu, P.-L.: Implementation of a Remote Hierarchical Supervision System Using Petri Nets and Agent Technology. IEEE Trans. on Systems, Man, and Cybernetics 37(1), 77–85 (2007)
6. Duffee, N.A., Prabhu, V.V.: Heterarchical Control of Highly Distributed Manufacturing Systems. Int. Journal of Computer Integrated Manufacturing 9(4), 270–281 (1996)
7. Cho, K., Lim, J.: Mixed Centralized/Decentralized Supervisory Control of Discrete Events Dynamic Systems. Automatica 35, 121–128 (1999)
8. Peterson, J.: Petri Net Theory and the Modeling of Systems. Prentice-Hall International, Englewood Cliffs (1981)
9. Villani, E., Miyagi, P.E., Valette, R.: Modeling and Analysis of Hybrid Supervisory System: A Petri Net Approach. Springer, London (2006)
10. Villarroel, J.L., Martinez, J., Silva, M.: GRAMAN: A Graphic System for Manufacturing System Design. In: Proc. IMACS Int. Symposium on System Modeling & Simulation (SMS'SS), pp. 311–316 (1988)
11. Yasuda, G., Takai, H., Tachibana, K.: Performance Evaluation of a Multimicro computer Based Software Servo System for Real-Time Distributed Robot Control. In: Proc. of 12th Triennial World Congress of IFAC, Pergamon, Oxford, vol. 2, pp. 673–678 (1993)
12. Yasuda, G., Takai, H., Tachibana, K.: Implementation and Performance Evaluation of Parallel Processing Architectures for Distributed Autonomous Motion Control Systems. In: Proc. of the 2nd Asian Control Conference, vol. 2, pp. 823–826 (1997)
13. Yasuda, G.: Implementation of Hierarchical and Distributed Control for Discrete Event Robotic Manufacturing Systems. In: Proc. of the 38th International Conference on Computers and Industrial Engineering, pp. 2580–2589 (2008)

Study on Collaborative Simulation of Excavation System of the Shield Machine in Composite Strata

Yanmin Zhao, Jianfu Zhang, and Pingfa Feng

State Key Laboratory of Tribology, Department of Mechanical Engineering,
Tsinghua University, Beijing, 100084, China
plont.zhao@163.com, {zhjf,fengpf}@mail.tsinghua.edu.cn

Abstract. Based on the characteristics of variable loads during the shield machine tunneling in composite strata, a collaborative simulation method was proposed to establish the mechanical control model of the excavation system. Working conditions including the angle of strata, the aperture ratio of the cutter head and the thickness of covering soil were defined to analyze the situation that the shield machine was tunneling in composite strata. The rotating speed of the cutter head was determined by the dynamics model of the mechanical system, and the required driving torque was calculated by the control system model. Through the real-time data exchange between the mechanical system and the control system, the dynamic control of the rotating speed of cutter head was implemented when the resistance moment varied. The established collaborative simulation model of the excavation system has good adaptability to the composite strata, and could provide reference for further study on the design of cutter head with geology adaptability, and also for the optimization of coordination control of the excavation system.

Keywords: excavation system, collaborative simulation, mechanical control model, composite strata.

1 Introduction

Shield machine has been widely used in tunneling engineering, such as the subway, municipal engineering, where the excavation environment especially in composite strata is relatively bad [1, 2]. One of the characteristics in tunneling composite strata is that the external load acting on the excavation system varies with strata and rotating angle of the cutter head [3-5]. It will cause fluctuation of rotating speed of the cutter head, and aggravate the wear-out failure of cutter head and other key components. Therefore, one of the most important research topics in the design of cutter head with geology adaptability is how to maintain the stability of the rotating speed of excavation system. It need that the control system could adjust the rotating speed of the cutter head in real time according to the feedback from the mechanical system, so that the shield machine could adapt to the variation of the external loading and tunnel smoothly.

J. Lee et al. (Eds.): ICIRA 2013, Part II, LNAI 8103, pp. 614–622, 2013.

As is known to all, the actual excavation cost is too high, so simulation is a good method to study the optimal response. There are some papers about simulation of hydraulic system of the shield machine [6, 7], but research about simulation between mechanical system and control system is little reported.

In order to achieve the above functions, it needs to establish the collaborative simulation model between the mechanical system and the control system. According to the characteristics of variable resistance moment in composite strata, several typical working conditions were chosen as the research background in this paper. The collaborative simulation model for mechanical dynamics and control of excavation system has been established by adopting collaborative simulation technique [8-12]. The optimal control of rotating speed was implemented when the shield machine tunneling at the condition of variable resistance moment.

2 Characteristics of the Resistance Moment in Composite Strata

The cutter head is subjected to resistance and resistance moment during the shield machine tunneling in composite strata, which varies with strata and cutting position of the cutter head [13, 14]. The resistance moment acting on excavation system can be calculated by adopting external load model in composite strata as follows.

$$T = T_1 + T_2 + T_3 \tag{1}$$

Where T_1, T_2, T_3 is the front frictional resistance moment of the cutter head, the lateral frictional resistance moment of the cutter head and the cutting resistance moment of the cutting tools respectively. The results according to the resistance moment model are shown in Fig.1. It can be seen from Fig.1 that the resistance moment varies not only with the strata, but also with the rotating angle of the cutter head. The variation of external load will make the rotating speed of the cutter head unstable in tunneling.

3 Establishment of Collaborative Simulation Model

In order to reduce the vibration and impact on the shield machine caused by external load varying during tunneling, it needs to keep rotating speed of the cutter head relatively stable. So it is necessary to control the hydraulic motor of the excavation system properly. The rotating speed of the cutter head was solved in ADAMS under the condition of variable resistance moment. Then the result was sent to the control system model established in MATLAB/Simulink as a variable, and the rotating speed would be adjusted to an appropriate value by a PID controller. The driving torque obtained in MATLAB/Simulink would be sent back to the mechanical dynamics system at last. Thus a closed-loop system has been formed, and the collaborative simulation between mechanical system and control system could be realized, which can be seen from Fig.2.

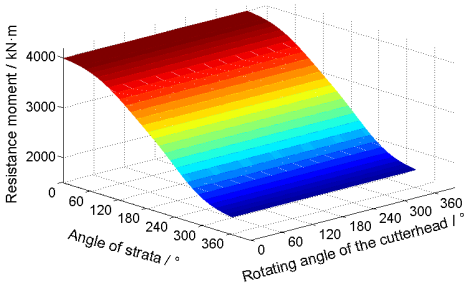

Fig. 1. Resistance moment acting on the excavation system

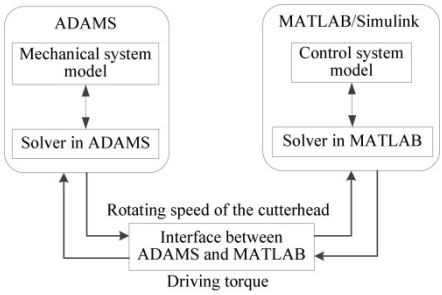

Fig. 2. Schematic design of collaborative simulation

3.1 Establishment of the Mechanical Dynamics Model

The transmission path of the external load should be confirmed at first. The propulsion system mainly bears the resistance, and the excavation system mainly bears the resistance moment , as shown in Fig.3.

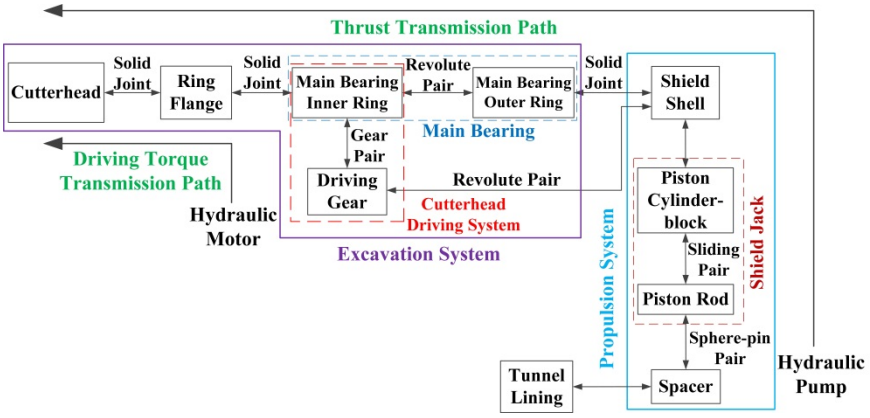

Fig. 3. Transmission path of the external load

Then the 3D model of the excavation system could be imported into ADAMS, and the rigid bodies, kinematic pairs and motions could be set. The resistance moment was applied on the cutter head by using STEP function, which takes the average value at a rotation period, as shown in Fig.4.

Driving torque was applied on the driving gear. The rotating speed of the cutter head and driving torque were variables to be solved. The final mechanical dynamics model of the excavation system is shown in Fig.5.

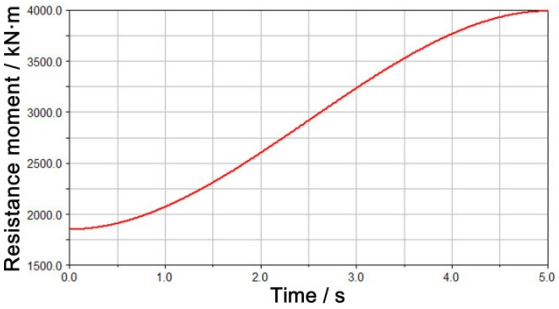

Fig. 4. Loading curve of the resistance moment

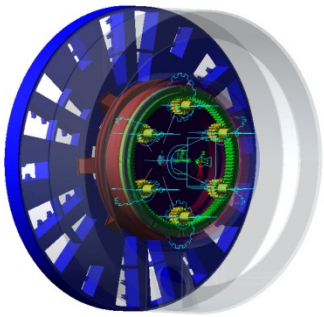

Fig. 5. Mechanical dynamics model of the excavation system

The contact force of driving gears of the excavation system is shown in Fig.6. As can be seen from the simulation results, that the contact force of driving gears vibrates periodically while the rotating speed of the cutter head is stable, and the contact force of the driving gears will oscillates strongly when the rotating speed of the cutter head is not stable. In addition, the contact force of driving gears is different from each other. This will affect the stability of the shield machine in tunneling seriously and shorten the life of cutter head. Therefore, it is necessary to control the rotating speed of the cutter head effectively.

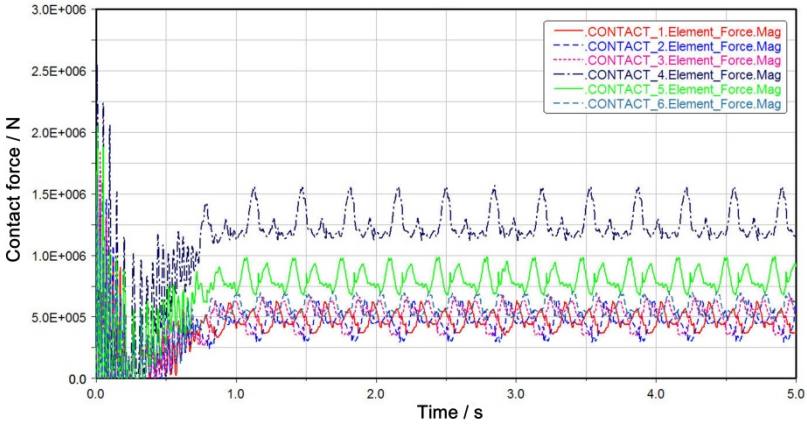

Fig. 6. Curves of contact force of driving gears

The driving torque was defined as input variable, and the rotating speed of the cutter head was defined as output variable. So the rotating speed of the cutter head could be controlled by adjusting the driving torque dynamically. The interface between mechanical system and control system has been set up.

3.2 Establishment of the Control System Model

It is assumed that there is no power loss in the power transmission process of the excavation system. The transfer function of the excavation system can be derived according to the power equality of input and output.

$$G_i(z) = \frac{R_c(z)}{M_i(z)} = \frac{6i_{12}z}{(J_2 + 6i_{12}^2 J_1)(z-1)} \tag{2}$$

$$G_o(z) = \frac{R_c(z)}{M_o(z)} = \frac{-z}{(J_2 + 6i_{12}^2 J_1)(z-1)} \tag{3}$$

The equations above are both the transfer function after discrete transform. $G_i(z)$ is the pulse transfer function between driving torque and rotating speed of the cutter head, while $G_o(z)$ is the pulse transfer function between resistance moment and rotating speed of the cutter head, and $R_c(z)$, $M_i(z)$, $M_o(z)$ is Z-transform for rotating speed of the cutter head, driving torque and resistance moment respectively, and i_{12} is the transmission ratio of excavation system, and J_1, J_2 is the rotational inertia of the driving gear and the load respectively.

The control model of the excavation system was built in Simulink according to the transfer function above. The resistance moment was treated as disturbance, and the rotating speed of the cutter head was the control target. The rotating speed of the cutter head was debugged by the PID controller. Then input and output variables and the dynamics model of the excavation system were added into the control model through the interface module. The established collaborative simulation model is shown in Fig.7. The collaborative simulation between mechanical and control system could be implemented by tuning the parameters of the PID controller according to the target rpm.

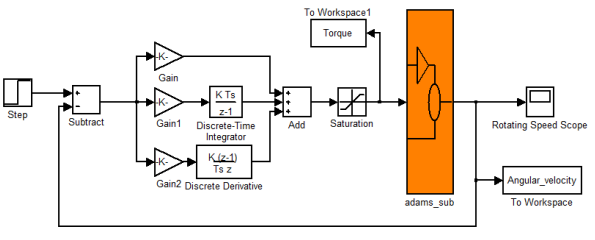

Fig. 7. Collaborative simulation model of the excavation system

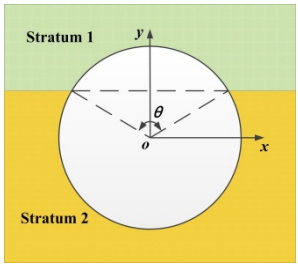

Fig. 8. Schematic diagram of strata angle

4 Case Analysis and Discussion

As an application example of the established collaborative simulation model, two typical working conditions are chosen to analyze the response of the excavation system during the shield machine tunneling. One is the shield machine tunneling at the angle of strata from 360° into 0°, and the other is the shield machine tunneling at the angle of strata from 240° into 120° and its reverse process. As can be seen from Fig.8, the strata angle θ is the central angle between the cross section center of the shield machine and the boundary of the two strata. The first working condition represents tunneling from soft soil stratum into hard soil stratum, and the second working condition represents tunneling from one composite strata into another. The aperture ratio of the cutter head and the thickness of covering soil in the two working conditions are the same.

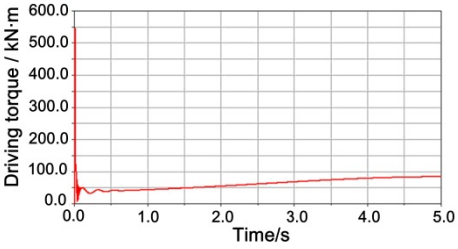

a. Curve of the driving torque

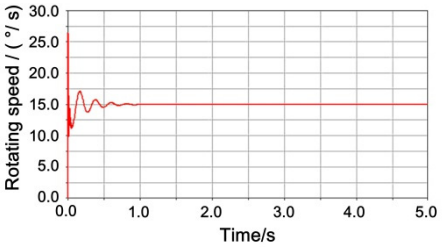

b. Curve of the rotating speed of the cutter head

Fig. 9. Simulation results in ADAMS

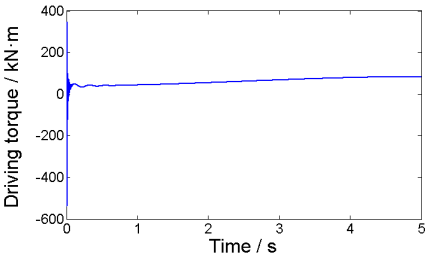

a. Curve of the driving torque

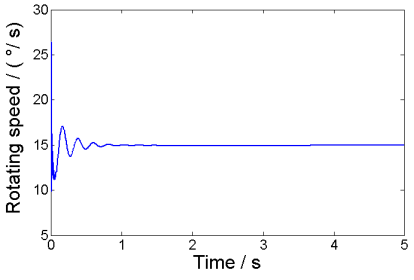

b. Curve of the rotating speed of the cutter head

Fig. 10. Simulation results in Simulink

When the shield machine tunnels at the angle of strata from 360° into 0°, the curves of driving torque and rotating speed of the cutter head are shown in Fig.9a and Fig.9b, which were drawn in ADAMS. And the curves shown in Fig.10a and Fig.10b were drawn in Simulink. The results of the collaborative simulation coincide with each other very well. It can be seen from the simulation results that the rotating speed of the cutter head could be adjusted by the established collaborative simulation model according to the variation of the resistance moment. The maximum overshoot is about 65.7%, and the transient time is about 0.72s. The rotating speed of the cutter head will achieve steady quickly. The fluctuation of the rotating speed of the cutter head has been reduced, and the excavation system has been protected effectively.

When the shield machine tunnels at the angle of strata from 240° to 120° and its reverse process, the curves of rotating speed of the cutter head are shown in Fig.11a and Fig.11b, which were obtained by the collaborative simulation model.

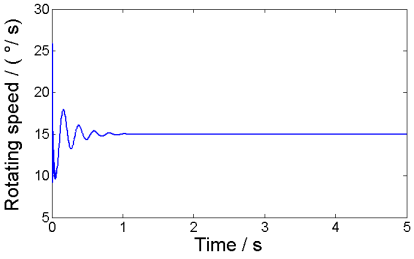

a. Curve of the rotating speed from 240° to 120°

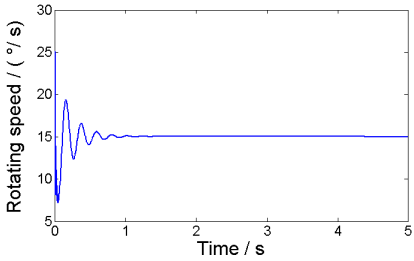

b. Curve of the rotating speed from 120° to 240°

Fig. 11. Simulation results of the rotating speed of the cutter head

As can be seen from the simulation results, the shield machine could overcome the fluctuations of the resistance moment during tunneling in composite strata, and the rotating speed of the cutter head could be adjusted to the setting value quickly. The established collaborative simulation model of the mechanical control system for the excavation system has good adaptability to strata.

5 Conclusions

1. The collaborative simulation model between mechanical and control system has been established. And collaborative simulation is an effective method to study the optimal response during tunneling in composite strata. The mechanical dynamics model of the excavation system was built in ADAMS, and the control model of the excavation system was built in Simulink according to the transfer function.

The rotating speed of the cutter head was solved in ADAMS, and the driving torque was solved in Simulink. The data transmission and communication between mechanical system and control system was realized by the interface module.

2. The rotating speed of the cutter head was sent to the control system model as a variable, and it would be adjusted to an appropriate value by a PID controller. Then the driving torque would be sent back to the mechanical dynamics system. Thus the collaborative simulation between mechanical and control system has been implemented. So the driving torque could be adjusted to the variation of the resistance moment effectively, and the rotating speed of the cutter head could maintain stable by adjusting the driving torque dynamically. The simulation results could provide guidance for the selection of excavation parameters.
3. As there are lots of extremely complex factors affecting the external load while the shield machine is tunneling in composite strata, the in-depth study need to combine a large number of experimental and engineering data for validation. In order to reflect the situation of the shield machine tunneling in composite strata better, the collaborative simulation model for the propulsion system still need to be established.

Acknowledgements. This research was financially supported by the National Basic Research Program of China (2013CB035400), the State Key Laboratory of Tribology Foundation (Grant No. SKLT11C7) and the Key National Science and Technology Projects of China (Grant No. 2012ZX04002-061).

References

1. Clough, G.W., Leca, E.: EPB shield tunneling inmixed face conditions. J. Geo. Engin. 119(10), 1640–1656 (1993)
2. Zhao, J., Gong, Q.M., Eisensten, Z.: Tunnelling through a frequentlychanging and mixed ground: A case history in Singapore. Tun. & Und. Space Tech. 22(4), 388–400 (2007)
3. Lu, Q., Fu, D.M.: Research on torque of cutterhead for earth pressure balance shield with simulating experimental. Ch. J. Rock Mech. and Engin. 25(S1), 3137–3143 (2006)
4. Song, K.Z.: Calculation on thrust and cutter disc torque of shield in sandy cobble with no water. Cons. Mach. 10, 58–60 (2004)
5. Wen, W., Feng, P., Wu, Z., Liu, J.: Study on external load domain of shield machine cutterhead. In: Xie, M., Xiong, Y., Xiong, C., Liu, H., Hu, Z. (eds.) ICIRA 2009. LNCS, vol. 5928, pp. 1176–1182. Springer, Heidelberg (2009)
6. Ma, C.L., Huang, X., Hao, L.: Simulation and optimization studies of electro-hydraulic servo system based on AMESim. Hydra. Pneu. & Seals 1, 32–34 (2006)
7. Yang, Y., Gong, G.F., Hu, G.L., Yang, H.Y.: Simulation of Shield's Thrust Hydraulic System Based on AMESim and MATLAB. Mach. Tool & Hydra. 6, 119–120 (2006)
8. Wang, K.M., Xiong, G.L.: Cooperative design and simulation for complex product. CIMS (S1), 15–19 (2003)
9. Feng, H.S., Wang, R.X.: The method of stabilityanalysis for quadruped robot based on collaborative simulation.Mod. Mach. Tool & Auto. Manuf. Tech. (11), 13–18 (2008)
10. Liu, G.C.: Method and utilization of disciplinary collaborative simulation. Modern Manuf. Engin. (7), 135–137 (2009)

11. Xia, M.C., Jiang, Y.Y., Li, J.: Research on complex product cooperative simulation and design technology. Com. Tech. & Dev. 19(3), 70–73 (2009)
12. Meng, X.D., Li, L.S., Wang, B., et al.: The study of collaborative simulation based on CAD/CAE. Mach. Design & Manuf. (9), 213–215 (2007)
13. Cui, G.H., Wang, G.Q., Wang, J.X., et al.: Cutting dynamic model for cutters of shield machine under soft soil. J. JLU (Engin. and Tech. Ed.) 38(S2), 139–143 (2008)
14. Sugimoto, M., Sramoon, A.: Theoretical model of shield behavior during excavation I: Theory. J. Geo. and Geoen. Engin. 128(2), 138–155 (2002)

Robust Adaptive Control of a Class of Nonlinear Systems with Unknown Hysteresis Nonlinearity

Yong-Hua Liu*, Ying Feng, and Chun-Yi Su

College of Automation Science and Engineering,
South China University of Technology,
Guangzhou, Guangdong, 510640 P.R. China
{scutliux,zhdfengying,chunyi.su}@gmail.com

Abstract. In this paper, the tracking problem for a class of uncertain nonlinear systems preceded by unknown Coleman-Hodgdon hysteresis is investigated. By analysing the hysteresis conditions, an important property is given, and hence Coleman-Hodgdon hysteresis can be decomposed as a nonlinear smooth term and a nonlinear bounded distrubance-like term. In order to remove the difficulty arising from the nonlinear smooth term, mean value theorem and a Nussbaum function lemma are introduced. Then following backstepping design procedure, a novel adaptive controller is developed without constructing a hysteresis inverse. The proposed controller not only doesn't need any assumptions on the uncertain system parameters within a known compact and a priori knowledge on the bound of the external disturbance, but also can guarantee global uniformly ultimately boundedness of all signals in the closed-loop system. Simulations performed on a nonlinear system illustrate and clarify the proposed scheme.

Keywords: robust adaptive control, nonlinear systems, Coleman-Hodgdon hysteresis, Nussbaum function.

1 Introduction

The hysteresis phenomenon exists in wide range of physical systems and devices, such as mechanical systems [1], electromagnetism [2], smart material-based actuators [3] etc. Multi-valued and non-smoothness, the main feature of hysteresis, which usually causes undesirable inaccuracies or oscillations, and even instability in controlling a system with hysteresis [4]. To mitigate the effects of hysteresis, modeling of hysteresis nonlinearities is the principal step. From nowadays, several mathematical models have been developed, Such as lines-segments hysteresis model [5], Preisach model [6], Prandtl-Ishlinskii model [7], Krasnosel'skii-Pokrovskii hysteron [8], Dahl model [9], Lugre model [10], Jiles-Atherton model [11], Bouc-Wen model [12, 13], Backlash-like model [14] and Duhem model [15] etc.

* Corresponding author.

J. Lee et al. (Eds.): ICIRA 2013, Part II, LNAI 8103, pp. 623–634, 2013.

Recently, control problem of system with unknown hysteresis have been received much attention [4, 14, 16–22]. In the literature, inverse control and robust adaptive control are two main approaches to be applied to mitigate the effects of hysteresis. Inverse control, which was pioneered by Tao and Kokotovic [4], can exactly or approximately cancel the adverse effects of hysteresis nonlinearities. In [16], Krejči and Kuhnen presented an exact analytical inverse of Prandtl-Ishlinskii model and applied it to compensate hysteresis nonlinearities of a piezoceramic actuator. In [17], an approximate smooth inverse model of the backlash was constructed, and was employed to develop an adaptive controller for a class of uncertain nonlinear systems preceded by unknown backlash nonlinearity. In [18], for Prandtl-Ishlinskii model, an approximate implicit inversion was developed by searching an optimal value of the inversion based on a performance index, an adaptive controller based on this inversion was derived for uncertain continuous-time systems preceded by Prandtl-Ishlinskii hysteresis. Further more, in [19], an perfect inversion of Prandtl-Ishlinskii hysteresis was developed without any approximation and an adaptive controller was formulated. However, constructing inverse model depends on the modeling of hysteresis, and the inversion always generates certain errors and possesses strong sensitivity to the model parameters, which influence strongly the practical application in control deign. Another approach, robust adaptive control, instead of constructing the inverse model from the hysteresis model, which was developed by Su, Stepanenko, Svoboda and Leung [14]. The main idea of this approach is to decompose the hysteresis model as a linear term and a nonlinear bounded "disturbance-like" term. For the same system as [14], in [20], an adaptive backstepping controller was developed, which did not need any assumptions on the uncertain system parameters within a known compact and a priori knowledge on the bound of the "disturbance-like" term. In [21], an adaptive controller was designed for a second structural systems with unknown Bouc-Wen hysteresis. In [22] and [**?**], adaptive variable structure control and adaptive backstepping methods were designed for a class of uncertain nonlinear systems with unknown Prandtl-Ishlinskii hysteresis.

Coleman-Hodgdon model in [23–25] is one of the widely accepted phenomenological models of the hysteresis in ferromagnetic materials, which is a typically special case of the Duhem model [26]. However, to the best of author's knowledge, control problem of system involving Coleman-Hodgdon hysteresis has few consideration in the literature. In this paper, we try to investigate this problem. Following the idea of robust adaptive control approach, the Coleman-Hodgdon model is decomposed as a smooth nonlinear function and a bounded disturbance-like term. Combining a useful property of Coleman-Hodgdon model, mean value theorem and a Nussbaum function lemma are introduced to overcome the difficulty of the nonlinear term arising from the unknown hysteresis. By using backstepping technique, a novel adaptive controller for uncertain nonlinear systems with Coleman-Hodgdon hysteresis is developed without constructing a hysteresis inverse. The developed controller does not need any assumptions on the uncertain system parameters within a known compact and a priori knowledge on the

bound of the external disturbance. The novel control algorithm can also be able to guarantee global uniformly ultimately boundedness of all signals in the closed-loop system. Simulations performed on a nonlinear system illustrate and clarify the proposed scheme.

2 Problem Formulation and Preliminaries

Consider the following nonlinear systems

$$\begin{aligned} \dot{x}_i(t) &= x_{i+1}(t) + \theta^T f_i(\bar{x}_i(t)), 1 \le i \le n-1 \\ \dot{x}_n(t) &= au(v) + \theta^T f_n(x(t)) + \bar{d}(t) \\ y(t) &= x_1(t) \end{aligned} \tag{1}$$

where $\bar{x}_i(t) = [x_1(t), ..., x_i(t)] \in R^i$, $x(t) = [x_1(t), ..., x_n(t)]^T \in R^n$ are state variables, $\theta \in R^r$ is an unknown constant parameter vector, a is the unknown control gain, $f_i(\bar{x}_i(t)) \in R^r, i = 1, ..., n$ are known smooth functions, $\bar{d}(t)$ denotes a bounded external disturbance by unknown constant, v is the controller to be designed, $u(v)$ denotes the plant input subject to hysteresis nonlinearity. The control objective is to make the system output y track the desired trajectory y_d.

In this paper, $u(v)$ is described as [24]

$$\frac{du}{dt} = \alpha|\frac{dv}{dt}|[m(v) - u] + \frac{dv}{dt}n(v) \tag{2}$$

with constant $\alpha > 0$, and satisfying the following three conditions.

Condition 1. *$m(\cdot)$ is a piecewise smooth, monotone increasing, odd function of v, with a derivative $\dot{m}(v)$, that obtains a finite limit $\lim_{v\to\infty} \dot{m}(v)$.*

Condition 2. *$n(\cdot)$ is a piecewise continuous, even function of v, with a finite limit satisfying*

$$\lim_{v\to\infty} n(v) = \lim_{v\to\infty} \dot{m}(v)$$

Condition 3. *$\dot{m}(v) \ge n(v) \ge \alpha e^{\alpha v} \int_v^\infty |\dot{m}(\xi) - n(\xi)|e^{-\alpha\xi}d\xi$ for all finite v.*

Remark 1. *The hysteresis model (2) is called Coleman-Hodgdon hysteresis, which is extensively used in ferromagnetically soft, isoperm materials [23–25]. An example is illustrated in Fig.1, where $\alpha = 5$, $m(v) = 2\tanh 1.3v$, and $n(v) = \dot{m}(v)(1 - 0.85e^{(-0.1|v|)})$.*

Remark 2. *It should be pointed out that the backlash-like hysteresis discussed in [14] is not an special case of Coleman-Hodgdon hysteresis, i.e., $\dot{m}(v) = c > n(v) = B$, which can't satisfy the Condition 2 in Coleman-Hodgdon hysteresis.*

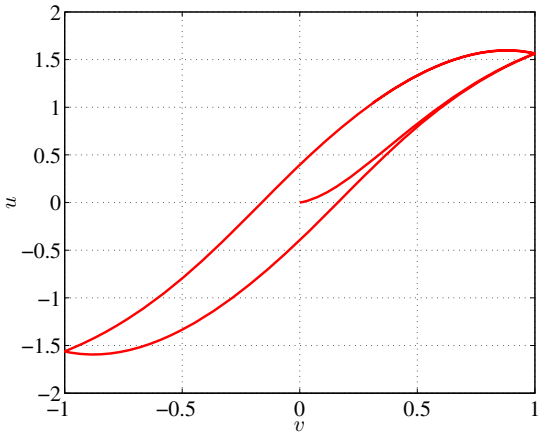

Fig. 1. Hysteresis curve for chirp signal input v

The equation (2) can be solved explicitly for v piecewise monotone as follows

$$u(v) = m(v) + d_1(v) \tag{3}$$

with

$$d_1(v) = [u_0 - m(v_0)]e^{-\alpha(v-v_0)sgn(\dot{v})} + e^{-\alpha sgn(\dot{v})} \int_{v_0}^{v} [n(\xi) - \dot{m}(\xi)]e^{\alpha\xi sgn(\dot{v})} d\xi$$

for $\dot{v}$ constant and $u(v_0) = u_0$. For $d_1(v)$, it can be easily shown that if $u(v; v_0, u_0)$ is the solution of (3) with initial values (u_0, v_0), then, if $\dot{v} > 0 (\dot{v} < 0)$ and $v \to +\infty(-\infty)$, one has

$$\lim_{v\to+\infty} d_1(v) = \lim_{v\to+\infty} [u(v; v_0, u_0) - m(v)] = 0 \tag{4}$$

$$(\lim_{v\to-\infty} d_1(v) = \lim_{v\to-\infty} [u(v; v_0, u_0) - m(v)] = 0.) \tag{5}$$

It can be concluded that there exists a uniform bound D_1 satisfying

$$|d_1(v)| \le D_1 \tag{6}$$

The following lemma and assumptions are made.

Lemma 1. *[27] Let $V(\cdot)$ and $\zeta(\cdot)$ be smooth functions defined on $[0, t_f)$ with $V(t) \ge 0$, $\forall t \in [0, t_f)$, and $N(\zeta)$ be an even smooth Nussbaum-type function. If the following inequality holds:*

$$V(t) \le c_0 + e^{-c_1 t} \int_0^t g(\tau)N(\zeta)\dot{\zeta}e^{c_1\tau} d\tau + e^{-c_1 t} \int_0^t \dot{\zeta}e^{c_1\tau} d\tau, \ \forall t \in [0, t_f) \tag{7}$$

where constant $c_1 > 0$, $g(t)$ is a time-varying parameter which takes values in the unknown closed intervals $I := [l^-, l^+]$ which $0 \notin I$, and c_0 represents some suitable constant, then $V(t)$, $\zeta(t)$ and $\int_0^t g(\tau)N(\zeta)\dot{\zeta}d\tau$ must be bounded on $[0, t_f)$.

Assumption 1. *The function $m(v)$ of Coleman-Hodgdon hysteresis (2) is a smooth and strictly increasing function.*

Remark 3. *From the definition of Coleman-Hodgdon model, the function $m(v)$ is a piecewise smooth function, which implies $\dot{m}(v)$ maybe not exist in a finite set of points. In order to satisfy the basic requirements of latter controller design, Assumption 1 is a necessary condition.*

Assumption 2. *The desired trajectory y_d and its nth order derivatives are known and bounded.*

Assumption 3. *The unknown control gain a is nonzero constant.*

From the definition of Coleman-Hodgdon model and Assumption 1, a useful property is given.

Property 1. *$m(0) = 0$, $\dot{m}(v) > 0$, and $\dot{m}(v)$ is a bounded smooth even function of v.*

3 Control Design

In this section, we will develop a smooth adaptive control employing σ-modification.

Following backstepping design procedure as general, a tremendous obstacle will be occurred, the control input v is implicit in $m(v)$ of the *step* n, which cannot be directly obtained. To remove this difficulty, the derivative form of mean value theorem are used, and hence there exists a point $\epsilon(\epsilon \in (\min(0, v), \max(0, v)))$ satisfying

$$m(v) - m(0) = \frac{dm(v)}{dv}\Big|_{v=\epsilon}(v - 0) \tag{8}$$

According to Property 1, $m(0) = 0$, it can be obtained that

$$m(v) = \dot{m}(\epsilon)v \tag{9}$$

Consequently, $u(v(t))$ can rewritten as

$$u(v) = \dot{m}(\epsilon)v + d_1(v) \tag{10}$$

The system (1) can be rewritten as follow

$$\begin{aligned} \dot{x}_i(t) &= x_{i+1}(t) + \theta^T f_i(\bar{x}_i(t)), 1 \le i \le n-1 \\ \dot{x}_n(t) &= a\dot{m}(\epsilon)v + \theta^T f_n(x(t)) + d(t) \end{aligned} \tag{11}$$

where $d(t) = \bar{d}(t) + ad_1(t)$. The effect of $d(t)$ is due to the external disturbance and $ad_1(t)$ and thus it is called as a disturbance-like term. Due to $\bar{d}(t)$ and $d_1(t)$ are bounded, thus, $d(t)$ is bounded, it can be denoted as $d(t) \le D$, where D is a unknown positive constant.

Remark 4. *From Property 1, it is easy concluded that* $a\dot{m}(\epsilon)$ *is a bounded nonzero time-varying function.*

As in the usual tracking problem with backstepping approaches, the following coordinate transformation is made:

$$z_1 = x_1 - y_d \tag{12}$$

$$z_i = x_i - y_d^{(i-1)} - \alpha_{i-1},\ i = 2, ..., n \tag{13}$$

where α_i is the virtual control at the *ith step* to be determined.

Step $i(i = 1, ..., n-1)$: As the design procedure in [28], the virtual control law α_i and tuning function τ_i are chosen as

$$\alpha_1 = -c_1 z_1 - \hat{\theta}^T f_1 \tag{14}$$

$$\alpha_2 = -c_2 z_2 - z_1 + \frac{\partial \alpha_1}{\partial x_1} x_2 - \hat{\theta}^T \Big(f_2 - \frac{\partial \alpha_1}{\partial x_1} f_1 \Big) + \frac{\partial \alpha_1}{\partial \hat{\theta}} \Gamma \tau_2 \tag{15}$$

$$\begin{aligned} \alpha_i = & -c_i z_i - z_{i-1} + \frac{\partial \alpha_{i-1}}{\partial \hat{\theta}} \Gamma \tau_i + \sum_{j=1}^{i-1} \Big(\frac{\partial \alpha_{i-1}}{\partial x_j} x_{j+1} + \frac{\partial \alpha_{i-1}}{\partial y_d^{(j-1)}} y_d^{(j)} \Big) \\ & + \Big(\sum_{j=1}^{i-2} z_{j+1} \frac{\partial \alpha_j}{\partial \hat{\theta}} \Gamma - \hat{\theta}^T \Big) \Big(f_i - \sum_{j=1}^{i-1} \frac{\partial \alpha_{i-1}}{\partial x_j} f_j \Big) \end{aligned} \tag{16}$$

$$\tau_1 = z_1 f_1 \tag{17}$$

$$\tau_2 = \tau_1 + \Big(f_2 - \frac{\partial \alpha_1}{\partial x_1} f_1 \Big) z_2 \tag{18}$$

$$\tau_i = \tau_{i-1} + \Big(f_i - \sum_{j=1}^{i-1} \frac{\partial \alpha_{i-1}}{\partial x_j} f_j \Big) z_i \tag{19}$$

where $\hat{\theta}$ is the estimation of θ, $\tilde{\theta} = \theta - \hat{\theta}$. c_i are the design positive constants, $\Gamma = \Gamma^T$ is a design constant matrix.

Step n: In the last step, the derivative of z_n can be expressed as

$$\dot{z}_n = a\dot{m}(\cdot) v + d(t) + \theta^T f_n - y_d^n - \dot{\alpha}_{n-1} \tag{20}$$

The actual control v is designed as

$$v = N(\zeta) w \tag{21}$$

$$\begin{aligned} w = & c_n z_n - \sum_{j=1}^{n-1} \Big(\frac{\partial \alpha_{n-1}}{\partial x_j} x_{j+1} + \frac{\partial \alpha_{n-1}}{\partial y_d^{(j-1)}} y_d^{(j)} \Big) \\ & - \Big(\sum_{j=1}^{n-2} z_{j+1} \frac{\partial \alpha_j}{\partial \hat{\theta}} \Gamma - \hat{\theta}^T \Big) \Big(f_n - \sum_{j=1}^{n-1} \frac{\partial \alpha_{n-1}}{\partial x_j} f_j \Big) \\ & - \frac{\partial \alpha_{n-1}}{\partial \hat{\theta}} \Gamma [\tau_n - \eta_\theta (\hat{\theta} - \theta_0)] + \tanh(\frac{z_n}{\varepsilon}) \hat{D} + z_{n-1} - y_d^{(n)} \end{aligned} \tag{22}$$

$$\tau_n = \tau_{n-1} + \Big(f_n - \sum_{j=1}^{n-1} \frac{\partial \alpha_{n-1}}{\partial x_j} f_j\Big) z_n \tag{23}$$

$$\dot{\hat{\theta}} = \Gamma[\tau_n - \eta_\theta(\hat{\theta} - \theta_0)] \tag{24}$$

$$\dot{\hat{D}} = \chi_D[z_n \tanh(\frac{z_n}{\varepsilon}) - \eta_D(\hat{D} - D_0)] \tag{25}$$

$$\dot{\zeta} = \mu w z_n \tag{26}$$

where $\hat{D}$ is the estimation of D, $\tilde{D} = D - \hat{D}$. $\eta_\theta > 0, \chi_D > 0, \eta_D > 0$, $\mu > 0$ and D_0 are design constants, θ_0 are design constant vector.

To establish global boundedness, the following Lyapunov function candidate can be defined as:

$$V = \frac{1}{2}\sum_{i=1}^{n} z_i^2 + \frac{1}{2}\tilde{\theta}\Gamma^{-1}\tilde{\theta} + \frac{1}{2\chi_D}\tilde{D}^2 \tag{27}$$

The time derivative $\dot{V}$ is obtained

$$\begin{aligned}
\dot{V} &= \sum_{i=1}^{n} z_i \dot{z}_i + \tilde{\theta}\Gamma^{-1}\dot{\tilde{\theta}} + \frac{1}{\chi_D}\tilde{D}\dot{\tilde{D}} \\
&\le (a\dot{m}(\cdot)N(\zeta) + 1) w z_n + \frac{1}{\chi_D}\tilde{D}(\chi_D z_n \tanh(\frac{z_n}{\varepsilon}) - \dot{\hat{D}}) \\
&\quad - \sum_{i=1}^{n} c_i z_i^2 + +0.2785\varepsilon D + \eta_\theta \tilde{\theta}(\hat{\theta} - \theta_0) + \eta_D \tilde{D}(\hat{D} - D_0) \\
&\le -\sum_{i=1}^{n} c_i z_i^2 + \frac{1}{\mu}(a\dot{m}(\cdot)N(\zeta) + 1)\dot{\zeta} - \frac{1}{2\eta_\theta}||\tilde{\theta}||^2 - \frac{1}{\eta_D}\tilde{D}^2 \\
&\quad + 0.2785\varepsilon D + \frac{1}{2\eta_\theta}(\theta - \theta_0)^2 + \frac{1}{2\eta_D}(D - D_0)^2
\end{aligned} \tag{28}$$

where the following important inequality [29] are used.

$$|z_n| \le z_n \tanh(\frac{z_n}{\varepsilon}) + 0.2785\varepsilon,\ \varepsilon > 0.$$

Theorem 1. *Consider the uncertain nonlinear systems (1) satisfying Assumptions 1-3. With the application of the controller (20) and the parameters update laws (24)-(26), all signals of the resulting closed-loop system is globally uniformly ultimately bounded.*

Proof. From (28), it can be obtained that

$$\dot{V} \le -\rho V + M + \frac{1}{\mu}(a\dot{m}(\cdot)N(\zeta) + 1)\dot{\zeta} \tag{29}$$

where

$$M = 0.2785\varepsilon D + \frac{1}{2\eta_\theta}(\theta - \theta_0)^2 + \frac{1}{2\eta_D}(D - D_0)^2$$
$$\rho = \min\{2c_i, \chi_D\eta_D, \eta_\theta\lambda_{max}(\Gamma)\}$$

where $\lambda_{max}(\Gamma)$ is the maximum eigenvalue of Γ.

By integrating the differential inequality (29) on $[0, t]$, it has

$$\begin{aligned} V &\le V(0)e^{-\rho t} + \frac{M}{\rho}(1 - e^{-\rho t}) + \frac{e^{-\rho t}}{\mu}\int_0^t (a\dot{m}(\cdot)N(\zeta) + 1)\dot{\zeta}e^{\rho\tau}d\tau \\ &\le \pi + \frac{e^{-\rho t}}{\mu}\int_0^t (a\dot{m}(\cdot)N(\zeta) + 1)\dot{\zeta}e^{\rho\tau}d\tau \end{aligned} \tag{30}$$

where $e^{-\rho t} \le 1$ and $(1 - e^{-\rho t}) < 1$ are used, $\pi = V(0) + \frac{M}{\rho}$.

From Remark 4, $a\dot{m}(\cdot)$ is a bounded nonzero time-varying function. By using Lemma 1, it can be concluded that $V, \zeta, \int_0^t \frac{a\dot{m}(\cdot)}{\mu}N(\zeta)\dot{\zeta}d\tau$ are bounded on $[0, t_f)$. So $z_i, i = 1, ..., n, \hat{\theta}, \hat{D}$ are also bounded on $[0, t_f)$, and hence x_i are bounded on $[0, t_f)$. Therefore, no finite-time escape phenomenon may occur and hence $t_f = \infty$ [30].

4 Simulation Studies

In this section, we illustrate the methodology presented in the previous sections using a simple nonlinear system described by

$$\begin{aligned} \dot{x}_1 &= x_2 \\ \dot{x}_2 &= \theta(-8x_1 - 2x_2) + au(v) + \bar{d}(t) \end{aligned} \tag{31}$$

where $y = x_1$, the external disturbance $\bar{d}(t) = 0.3\sin(2\pi t)$, the actual parameter values are $\theta = 1$ and $a = 1$. $u(v)$ represents the output of the Coleman-Hodgdon hysteresis (2), and $\alpha = 1$, $m(v) = 5\tanh 1.3v + 2.5v$, $n(v) = \dot{m}(v)(1 - e^{(-2.3|v|)})$. The objective is make the output y of system (31) to track the desired trajectory $y_d = 2\sin 2t - 0.3\cos(t)$.

In this simulation, the initial conditions are $x_1(0) = 1$, $x_2(0) = 0$. The Nussbaum function $N(\zeta) = \zeta^2\cos(\frac{\pi}{2}\zeta)$. The initial parameters for undate laws are $\theta_0 = -0.5$, $D_0 = 0.25$, $\zeta(0) = 0$. In addition, the control gains are chosen as $c_1 = 3$, $c_2 = 1$, and the designed parameters $\omega = 0.1$, $\Gamma = \chi_D = 5$, $\eta_\theta = \eta_D = 0.001$, $\mu = 1$.

The simulation results are shown in Figs 2-5. From Fig. 2, it can be shown that good tracking performance is achieved. Fig. 3 shows the control input signal v. Figs. 4 and 5 show the response curves of adaptive parameters $\hat{\theta}$, $\hat{D}$ and ζ. These results verify the effectiveness of the proposed adaptive backstepping control scheme.

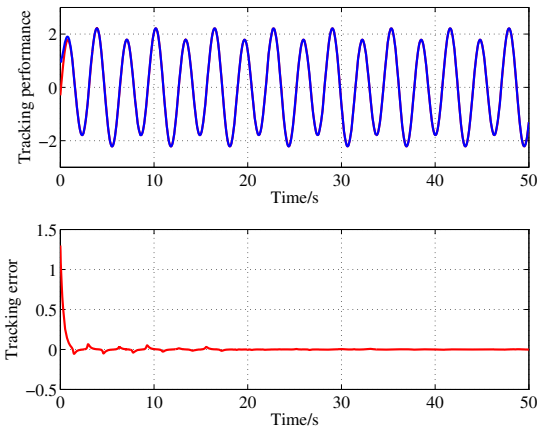

Fig. 2. Output tracking performance

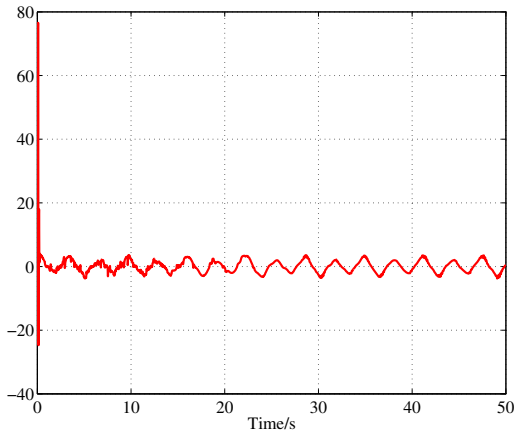

Fig. 3. Control input v

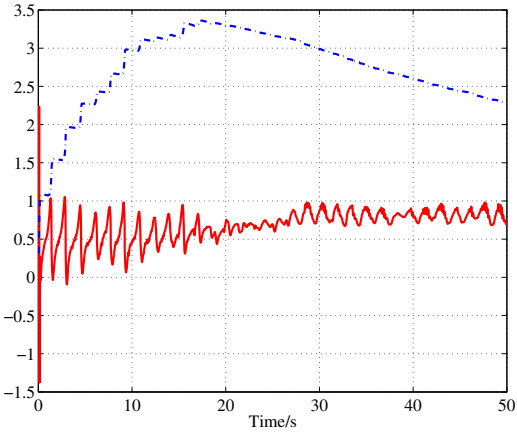

Fig. 4. Adaptive parameters $\hat{\theta}$ (real line) and $\hat{D}$ (dotted line)

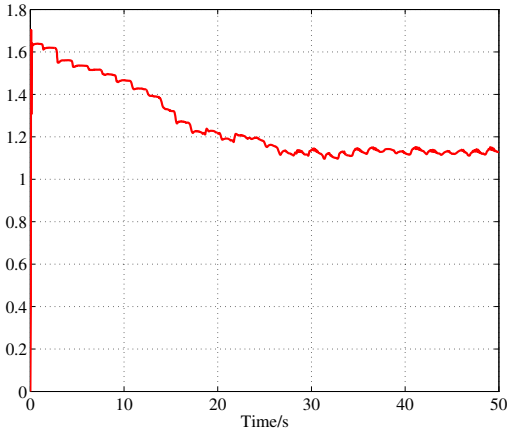

Fig. 5. Variable ζ

5 Conclusion

In this paper, the output tracking problem for a class of uncertain nonlinear systems with unknown Coleman-Hodgdon hysteresis is discussed. By combining a useful property of Coleman-Hodgdon hysteresis, mean value theorem and a Nussbaum function lemma are introduced to mitigate the difficulty of the nonlinear term arising from the hysteresis nonlinearity. Then following the backstepping design procedure, a novel adaptive control algorithm is developed without constructing hysteresis inverse. The proposed controller not only mitigates the

adverse effects of unknown hysteresis, but also ensures global uniformly ultimately boundedness of all signals in the closed-loop system. Simulation results performed on a nonlinear system illustrate and clarify the proposed scheme.

Acknowledgment. This work was supported by the Funds for National Natural Science Foundation of China under grants (61020106003, 61074097, U1201244), and the 111 project (B08015).

References

1. Nordin, M., Gutman, P.-O.: Controlling mechanical systems with backlash a survey. Automatica 38(10), 1633–1649 (2002)
2. Mayergoyz, I.D.: Mathematical Models of Hysteresis and their Applications. Elsevier Science, New York (2003)
3. Smith, R.: Smart Material Systems: Model Development. SIAM, Philadelphia (2005)
4. Tao, G., Kokotovic, P.V.: Adaptive control of plants with unknown hystereses. IEEE Trans. Autom. Control 40(2), 200–212 (1995)
5. Tao, G., Kokotovic, P.V.: Adaptive Control of Systems with Actuator and Sensor Nonlinearities. John Wiley & Sons, New York (1996)
6. Preisach, F.: *Ü*ber die magnetische Nachwirkung. Zeitschrift *für* Physik 94, 277–302 (1935)
7. Visintin, A.: Differential Models of Hysteresis. Springer, New York (1994)
8. Krasnosel'skii, M.A., Pokrovskii, A.V.: Systems wirh Hysreresis. Springer, Berlin (1983)
9. Dahl, P.R.: Solid friction damping of mechanical vibrations. AIAA J. 14(12), 1675–1682 (1976)
10. Canudas, C., Olsson, H., *Ă*strom, K.J., Lischinsky, P.: A new model for control of systems with friction. IEEE Trans. Autom. Control 40(3), 419–425 (1995)
11. Jiles, D.C., Atherton, D.L.: Theory of ferromagnetic hysteresis. Journal of Magnetism and Magnetic Materials 61, 48–60 (1986)
12. Bouc, R.: Forced vibrations of mechanical systems with hysteresis. In: Fourth Conference on Nonlinear Oscilation. Prague, Czechoslovakia (1967)
13. Wen, Y.K.: Method for random vibration of hysteretic systems. Journal of Engineering Mechanics. ASCE 102(2), 249–263 (1976)
14. Su, C.-Y., Stepanenko, Y., Svoboda, J., Leung, T.P.: Robust adaptive control of a class of nonlinear systems with unknown backlash-like hysteresis. IEEE Trans. Autom. Control 45(12), 2427–2432 (2000)
15. Duhem, P.: Die dauernden Aenderungen und die Thermodynamik. I, Z. Phys. Chem. 33, 543–589 (1897)
16. Krejči, P., Kuhnen, K.: Inverse control of systems with hysteresis and creep. IEE Proceedings Control Theory and Applications 148(3), 185–192 (2001)
17. Zhou, J., Zhang, Y., Wen, C.: Robust Adaptive Output Control of Uncertain Nonlinear Plants With Unknown Backlash Nonlinearity. IEEE Trans. Autom. Control 52(3), 503–509 (2007)
18. Chen, X., Su, C.-Y., Fukuda, T.: Adaptive Control for the Systems Preceded by Hysteresis. IEEE Trans. Autom. Control 53(4), 1019–1025 (2008)

19. Chen, X., Hisayama, T., Su, C.-Y.: Adaptive Control for Uncertain Continuous-Time Systems Using Implicit Inverse of Prandtl-Ishlinskii Hysteresis Representation. IEEE Trans. Autom. Control 55(10), 2357–2363 (2010)
20. Zhou, J., Wen, C., Zhang, Y.: Adaptive backstepping control of a class of uncertain nonlinear systems with unknown backlash-like hysteresis. IEEE Trans. Autom. Control 49(10), 1751–1759 (2004)
21. Ikhouane, F., Mañosa, V., Rodellar, J.: Adaptive control of a hysteretic structural system. Automatica 41(2), 225–231 (2005)
22. Su, C.-Y., Wang, Q., Chen, X., Rakheja, S.: Adaptive variable structure control of a class of nonlinear systems with unknown Prandtl-Ishlinskii hysteresis. IEEE Trans. Autom. Control 50(12), 2069–2074 (2005)
23. Coleman, B.D., Hodgdon, M.L.: A constitutive relation for rateindependent hysteresis in ferromagnetically soft materials. Int. J. Eng. Sci. 24, 897–919 (1986)
24. Hodgdon, M.L.: Applications of a theory of ferromagnetic hysteresis. IEEE Trans. Magn. 24(1), 218–221 (1988)
25. Hodgdon, M.L.: Mathematical theory and calculations of magnetic hysteresis curves. IEEE Trans. Magn. 24(6), 3120–3122 (1988)
26. Macki, J.W., Nistri, P., Zecca, P.: Mathematical models for hysteresis. SIAM Rev. 35, 94–123 (1993)
27. Ge, S.S., Wang, J.: Robust adaptive tracking for time-varying uncertain nonlinear systems with unknown control coefficients. IEEE Trans. Autom. Control 48(8), 1462–1469 (2003)
28. Krstic, M., Kanellakopoulos, I., Kokotovic, V.: Nonlinear and adaptive control design. John Wiley & Sons, New York (1995)
29. Plycarpou, M.M., Ioannou, P.A.: A robust adaptive nonlinear control design. Automatica 31, 423–427 (1995)
30. Ryan, E.P.: A universal adaptive stabilizer for a class of nonlinear systems. Syst. Control Lett. 16, 209–218 (1991)

A Prandtl-Ishlinskii Model for Characterizing Asymmetric and Saturated Hysteresis of Smart Material Actuators

Omar Aljanaideh*, Subhash Rakheja, and Chun-Yi Su

Department of Mechanical and Industrial Engineering
Concordia University, 1455 de Maisonneuve Blvd. W.
Montreal, Quebec, H3G 1M8, Canada
omaryanni@gmail.com, {cysu,rakheja}@alcor.concordia.ca

Abstract. Laboratory measurements were performed to characterize output-input characteristics of a magnetostrictive actuator under a wide range of input current amplitudes in the 10-200 Hz frequency range. The measurements revealed asymmetry in the output and output saturation under moderate and high amplitude current, and increasing hysteresis effects with the input frequency. A Prandtl-Ishlinskii model integrating a memoryless function was formulated to characterize the asymmetric nonlinear hysteresis and output saturation properties of the actuator as a function of input current amplitude and frequency. Through comparisons of the integrated Prandtl-Ishlinskii model results with the measured data, it is shown that the proposed model can accurately characterize the asymmetric and saturated hysteresis nonlinearities of smart material actuators under a wide range of excitation amplitudes and frequencies.

Keywords: Magnetostrictive actuator, Asymmetric output-input, Output saturation, Rate-dependent Hysteresis model, Memoryless function, Dead-band operators.

1 Introduction

Compared to other smart material actuators, magnetostrictive Terfenol-D actuators are known to deliver large strain with high force capacity over a broad range of frequencies. The magnetostrictive actuators are known to provide rapid and high resolution actuations attributed to deformations of the Terfenol-D material under an external magnetic field [1]. Such actuators are thus increasingly being explored for applications as high speed precision milling machines, vibrations control [2], and hydraulic valves [3]. The output-input characteristics of such smart material actuators, however, exhibit strong hysteresis nonlinearities and output saturation, which could cause oscillations in the response and greater positioning errors, instability in the closed-loop system response [4]. Furthermore, the hysteresis tends to be far more

* Corresponding author.

J. Lee et al. (Eds.): ICIRA 2013, Part II, LNAI 8103, pp. 635–643, 2013.

significant under high amplitude and rate of input, as observed in all smart material actuators.

An accurate characterization of asymmetric output-input characteristics with saturation and hysteresis over a wide range excitation magnitudes and frequencies has been considered vital for developing effective methods for compensating the hysteresis effects. Consequently, considerable efforts have been made towards developing models that can effectively describe the hysteresis nonlinearities of a class of smart material actuators including the magnetostrictive actuators. Although a few physics-based models have been reported [5], the phenomenological models, particularly those based on operator functions, have proven to be effective in describing nonlinear hysteresis effects in an efficient manner [4,12]. The operator based models such as Preisach and Prandtl-Ishlinskii models have been widely used not only for characterization but also for compensation of hysteresis nonlinearities of smart actuators. Compared with the other phenomenological models, the Prandtl-Ishlinskii model, owing to continuous nature of the play operators, offers a unique advantage in formulating its exact analytical inverse, which facilitates real-time hysteresis compensation [6].

Prandtl-Ishlinskii models with either rate-dependent threshold function of the play operators or rate-dependent density function have been reported to characterize input rate-dependent symmetric hysteresis nonlinearities of piezo-ceramic actuators [7]. A generalized play operator with dissimilar hyperbolic tangent envelop functions corresponding to loading and unloading inputs has been applied to obtain asymmetric hysteresis loops, as observed for the magnetostrictive actuators [8,10,11]. This approach, however, could cause an instability due to lack of convergence of the envelop functions near the extreme inputs, particularly at higher frequency inputs. This study presents an alternate Prandtl-Ishlinskii model to fully describe asymmetric hysteresis characteristics of smart material actuators with output saturation. The proposed alternate model is formulated as a cascade of the reported rate-dependent Prandtl-Ishlinskii model with a memoryless function of dead-band operators.

2 Measurements of Output-Input Characteristics

The output-input characteristics of a 100 μm stroke magnetostrictive actuator (Etrema Inc; model MFR OTY77) were measured in the laboratory under harmonic currents of different magnitudes (1 to 9 A) and frequencies (10 to 200 Hz). The measurement setup included the input signal generation using ControlDesk platform, a power amplifier and a capacitive displacement sensor (Lion Precision; model $C23-C250$) with a resolution of 35.53 nm. The actuator was designed with a magnetic bias of 44.1 kA/m and peak current of 7.07 A. The experiments were conducted under relatively higher current so as to investigate the nonlinearity under extreme inputs. The displacement and the current signals were acquired using a dSpace control board (DS 1104) and analyzed to determine the output-input and hysteresis characteristics.

The output-input properties under different excitation current amplitudes at 10 Hz (Fig. 1) show increase in output displacement with increasing current amplitude and

substantial hysteresis. The output displacement response is symmetric about the input, when subjected to input current below 3A. The output saturation is clearly evident under moderate to high input currents. Fig. 2 illustrates variations in peak-peak displacement and the area bounded by the hysteresis loop as a function of input current. The results suggest nonlinear increase in actuator displacement and hysteresis with increasing input.

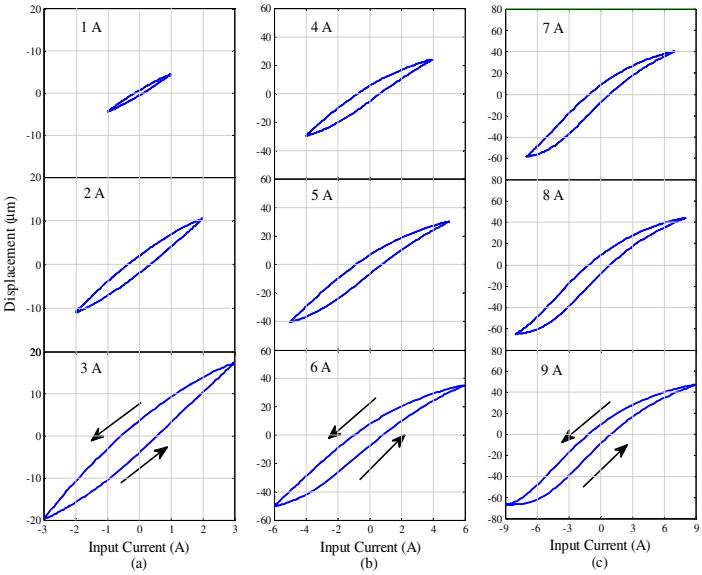

Fig. 1. Hysteresis nonlinearities of the magnetostrictive actuator under different input currents

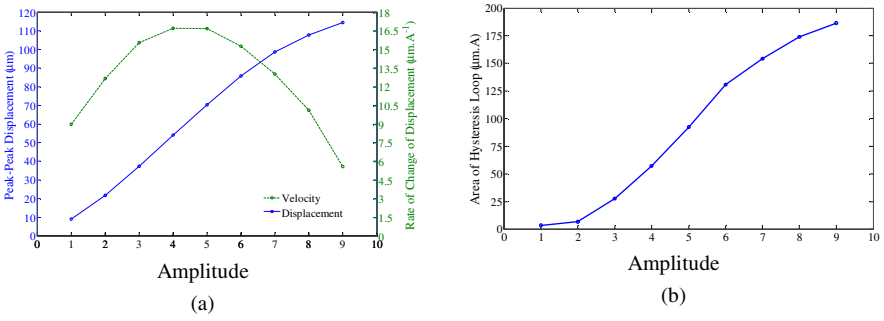

Fig. 2. Effects of applied current: (a) peak-peak displacement and its rate of change; and (b) the area bounded by the hysteresis loop (f=10 Hz)

Fig. 3 illustrates output-input characteristics under 3A and 7A currents at different frequencies in the 10 to 200 Hz range. An increase in width of the hysteresis loop with increasing excitation frequency, irrespective of the input current, is clearly evident suggesting rate dependence of the actuator hysteresis. The peak-peak output displacement and the area bounded by the hysteresis loop are also presented in

Figs. 4(a) and (b), respectively, as a function of excitation frequency. It can be seen that the lower current input (3A) yields relatively smaller output asymmetry while the effects are significant under 7A input. The results also show linear increase in hysteresis with input frequency.

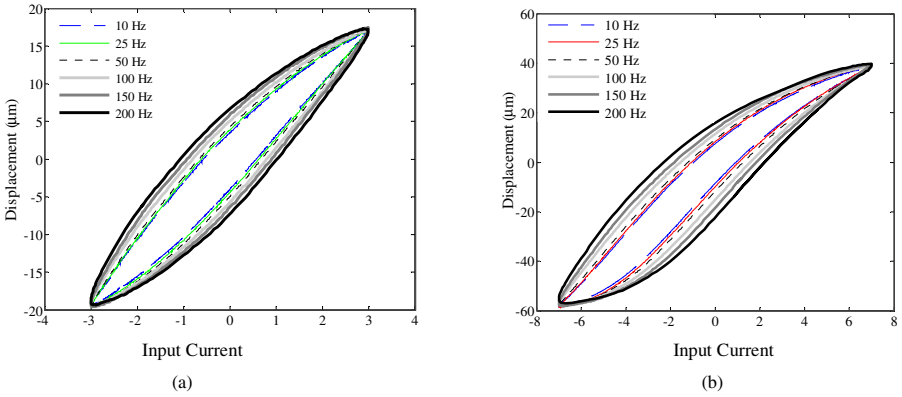

Fig. 3. Influence of excitation frequency on actuator displacement response: (a) 3 A, and (b) 7 A

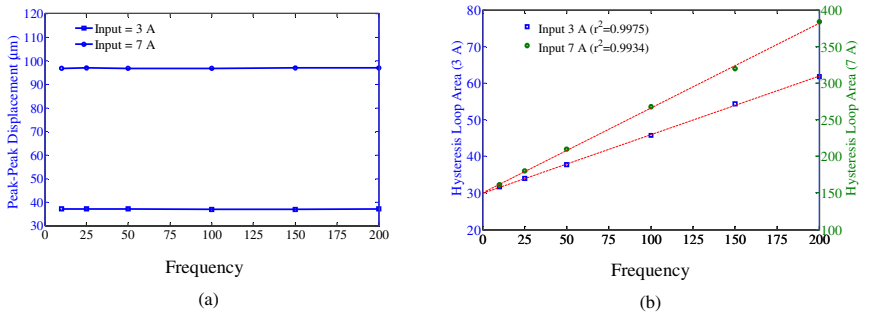

Fig. 4. Influence of excitation frequency on: (a) the peak-peak displacement response; and (b) the area covered by the hysteresis loop

3 Modeling Asymmetric and Saturated Rate-Dependent Hysteresis

It has been shown that a Prandtl-Ishlinskii model comprising dynamic thresholds of the play operators as a linear function of the rate of input could effectively characterize the rate-dependence of smart material actuator hysteresis [6]. This model, however, could describe only symmetric output-input properties. The asymmetry of the actuator output has been attempted by a rate-dependent Prandtl-Ishlinskii model with generalized play operators of dissimilar hyperbolic tangent envelop functions corresponding to loading and unloading inputs [8]. The lack of convergence of the

envelop functions, particularly under inputs at high rates, however, could make the model discontinuous. Alternatively, a memoryless function, proposed in [9], could be applied in conjunction with rate-dependent Prandtl-Ishlinskii model for characterizing asymmetric and saturated hysteresis nonlinearities of smart material actuators. In this study, a rate-dependent Prandtl-Ishlinskii model Π is cascaded with a memoryless function Γ_d, so as to describe asymmetric and saturated hysteresis nonlinearities. The output $y(t)$ of the integrated Prandtl-Ishlinskii model Φ is a represented as a composition of Π and Γ_d, as:

$$y(t) = \Phi[v](t) = (\Gamma_d \circ \Pi)[v](t) = (\Gamma_d(\Pi))[v](t) \tag{1}$$

In the above, the rate-dependent Prandtl-Ishlinskii model Π is formulated as a summation of weighted rate-dependent play operators $\Delta_{\rho_i(\dot{v}(t))}$. For an input $v(t) \in AC(0,T)$, where AC represents a space of real absolute continuous functions, the symmetric output $p(t)$ of Π can be expressed as:

$$p(t) = \Pi[v](t) = \sum_{i=0}^{n} q_i \Delta_{\rho_i(\dot{v}(t))} \tag{2}$$

where q_i are weighting constants, n is the number of play operators and $\rho_i(\dot{v}(t))$ are rate-dependent thresholds of the play operators, which are defined such that $0 \le \rho_0(\dot{v}(t)) \le \rho_1(\dot{v}(t)) \le ... \le \rho_n(\dot{v}(t))$. The input function $v(t)$ is considered monotone over each sub-interval $[t_{j-1}, t_j]$, where $0 = t_0 < t_1 < ... < t_l = T$ define the intervals. The rate-dependent play operator over the interval $t \in [t_{j-1}, t_j]$ is expressed as [6]:

$$\Delta[v](t_j) = \max(v(t_j) - \rho_i(\dot{v}(t_j)), \min(v(t_j) + \rho_i(\dot{v}(t_j)), \Delta_{j-1}) \tag{3}$$

The memoryless function Γ_d in cascaded Prandtl-Ishlinskii model in (1), comprises a superposition of weighted deadband operators S_{di} of thresholds d_i and weights b_i that relate to asymmetry and saturation the symmetric output $p(t)$ of Π, described in (2):

$$y(t) = \Gamma_d[p](t) = \sum_{i=-m}^{m} b_i S_{d_i}[p](t) \tag{4}$$

where the deadband operator, S_{di}, i=(-m, …, 0, …, m), m is an integer, expressed as [9]:

$$S_{d_i}[p](t) = \begin{cases} \max\{p(t) - d_i, 0\} & for \quad d_i > 0, \\ p(t) & for \quad d_i = 0, \\ \min\{p(t) - d_i, 0\} & for \quad d_i < 0. \end{cases} \tag{5}$$

The measured characteristics revealed linear increase in hysteresis with input frequency, as seen in Fig. 4(b). Thus, the threshold is formulated as a linear function of the rate of input:

$$\rho_i(\dot{v}(t)) = \eta|\dot{v}(t)| + ci \tag{6}$$

where η and c are positive constants. This formulation ensures the analytical inevitability of the rate-dependent Prandtl-Ishlinskii model, described in (2).

The parameters vector, $X=\{q_i, \eta, c, b_i, d_i\}$, of the cascaded model Φ is subsequently identified through minimizing the error sum-squared function, $\Theta(X)$:

$$\Theta(X)=\sum_{a=1}^{A}\sum_{r=1}^{R}\sum_{k=1}^{K}W_a(y(t,k,f_r,I_a)-g(t,k,f_r,I_a))^2 \tag{7}$$

where $y(t, k, f_r, I_a)$ is response of the model Φ corresponding to an input current I_a (a=1,…, A) at an excitation frequency f_r (r=1,…, R), and $g(t, k, f_r, I_a)$ is the measured response under same excitation. The indices $A=2$ and $R=6$ denote the number of amplitudes and frequencies considered for solving the minimization problem. The above minimization problem was solved considering K = 200 data points for each measured hysteresis loop, 17 dead-band operators, and considering different number of rate-dependent play operators ranging from 2 to 15. The sum-squared error between the model responses and the measured data was calculated over the entire range of frequencies and amplitudes considered for each value of n. The error was observed to decrease with increasing number of operators but the decrease in error was minimal for $n \geq 8$. Consequently, the rate-dependent model was formulated considering 8 rate-dependent play operators.

4 Results

Validity of the proposed cascaded model was examined by comparing model responses with the measured data under 3A and 7A current inputs at different frequencies (Fig. 5). The comparisons show very good agreements between model and measured responses over the entire range of inputs considered in the study. The model results particularly show that the output asymmetry and saturation together with rate-dependent hysteresis, as observed from the measured data, can be effectively characterized by the proposed cascade of rate-dependent Prandtl-Ishlinskii model Π with the memoryless function Γ_d.

The output-input characteristics obtained from the proposed cascaded model are also compared with those attained from a rate-dependent Prandtl-Ishlinskii model, reported in [6], and a rate-independent Prandtl-Ishlinskii model integrating a memoryless function Γ_d, as reported in [9]. The responses of these two models, obtained under a current of 7 A at 10 and 200 Hz range are compared with measured responses in Fig. 6. Comparisons show substantial errors in both the models. The rate-dependent Prandtl-Ishlinskii model yields only symmetric hysteresis loops, while the rate-independent model with a memoryless function [9] yields asymmetric and saturated hysteresis. This model yields good agreement with the measured data at 10 Hz but substantially large error at 200 Hz.

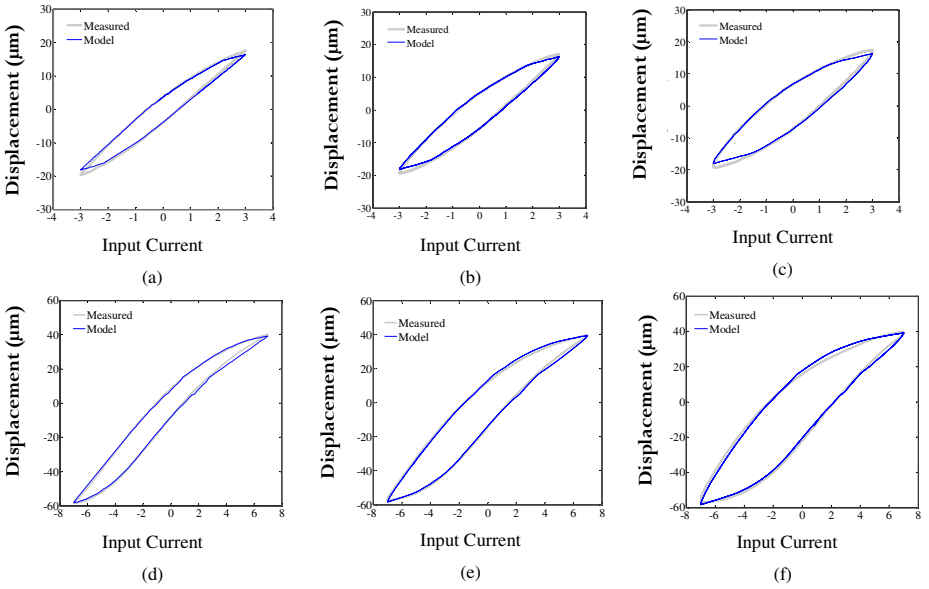

Fig. 5. Output-input properties of the magnetostrictive actuator obtained from the measured data and the cascaded rate-dependent Prandtl-Ishlinskii model: (a) I_a=3A at 10 Hz; (b) I_a=3A at 100 Hz; (c) I_a=3A at 200 Hz; (d) I_a=7A at 10 Hz; (e) I_a=7A at 100 Hz; and (f) I_a=7A at 200 Hz

The results thus suggest that output-input characteristics of the magnetostrictive actuators can be accurately described through consideration of both the rate-dependence of output hysteresis, and output asymmetry and saturation, as in the proposed cascaded Prandtl-Ishlinskii model. Neglecting the rate effect, described by the rate-dependent Prandtl-Ishlinskii model, or the asymmetry, attributed to the memoryless function, would yield significant errors in the actuator displacement response (Fig. 6).

5 Conclusions

The magnetostrictive actuator revealed asymmetry in displacement response about the input current and output saturation under moderate to high input currents, which is attributable to hysteresis of the Terfenol-D material rods. Furthermore, the hysteresis increased linearly with rate of applied input. The proposed cascade of a rate-dependent Prandtl-Ishlinskii model and a memoryless function could accurately describe the output-input characteristics of the actuator, particularly the output asymmetry, hysteresis and saturation over a wide range of input amplitudes and frequencies considered. It is further shown that neglecting either the rate dependence of hysteresis or output saturation would yield substantial errors in model responses when compared with the measured data.

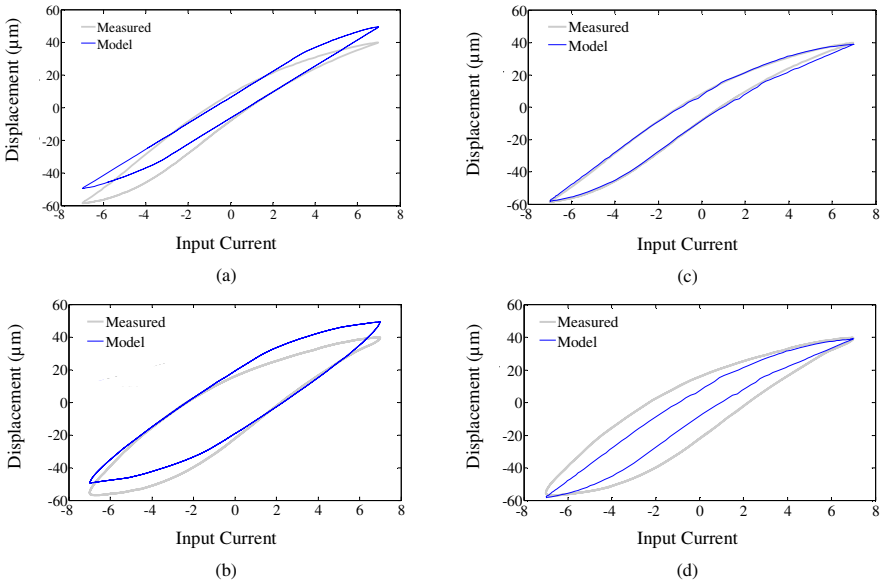

Fig. 6. Comparison of measured responses under 7 A current with the rate-dependent Prandtl-Ishlinskii model [6], under: (a) 10 Hz; (b) 200 Hz; and with the rate-independent Prandtl-Ishlinskii model with a memoryless function [9], under: (c) 10 Hz; (d) 200 Hz

References

1. Engdahl, G.: Handbook of Giant Magnetostrictive Materials. Morgan Kaufmann, Academic Press, New York (1999)
2. José Pons, L.: Emerging Actuator Technologies. Wiley, New York (2005)
3. Karunanidhi, S., Singaperumal, M.: Design, Analysis and Simulation of Magnetostrictive Actuator and its Application to High Dynamic Servo Valve. Sens. & Actu. A. Phy. 157, 185–197 (2010)
4. Visone, C.: Hysteresis Modelling and Compensation for Smart Sensors and Actuators. J. Phy.: Conference Series 138, 1–25 (2008)
5. Jiles, D., Atherton, D.: Theory of Ferromagnetic Hysteresis. J. Mag. & Mag. Mat. 61, 48–60 (1986)
6. Aljanaideh, O., Al Janaideh, M., Rakheja, S., Su, C.-Y.: Compensation of Rate-Dependent Hysteresis Nonlinearities in a Magnetostrictive Actuator Using an Inverse Prandtl-Ishlinskii Model. Sma. Mate. & Str. 22, 1–10 (2013)
7. Al Janaideh, M., Rakheja, S., Su, C.-Y.: Experimental Characterization and Modeling of Rate-Dependent Hysteresis of a Piezoceramic Actuator. Mech. 19, 656–670 (2009)
8. Al Janaideh, M., Rakheja, S., Su, C.-Y.: Modelling Rate-Dependent Symmetric and Asymmetric Hysteresis Loops of Smart Actuators. Int. J. Adv. Mech Sys. 1, 32–43 (2008)
9. Kuhnen, K.: Modeling, Identification and Compensation of Complex Hysteretic Nonlinearities - A Modified Prandtl-Ishlinskii Approach. Euro. J. Con. 9, 407–418 (2003)
10. Al Janaideh, M., Rakheja, S., Su, C.-Y.: A generalized Prandtl-Ishlinskii model for characterizing the hysteresis and saturation nonlinearities of smart actuators. Smart Mater. Struct. 18, 045001 (2009)

11. Al Janaideh, M., Feng, Y., Rakheja, S., Su, C.-Y., Rabbath, C.: Hysteresis compensation for smart actuators using inverse generalized Prandtl-Ishlinskii model. In: American Control Conference Series, St. Louis, pp. 307–312. IEEE Press (2009)
12. Gu, G.-Y., Yang, M.-J., Zhu, L.-M.: Real-time inverse hysteresis compensation of piezoelectric actuators with a modified Prandtl-Ishlinskii model. Rev. Sci. Instrum. 83, 065106 (2012)

Improving Tracking Precision of Piezoceramic Actuators Using Feedforward-Feedback Control

Guo-Ying Gu, Chun-Xia Li, Lei-Jie Lai, and Li-Min Zhu

State Key Laboratory of Mechanical System and Vibration,
Shanghai Jiao Tong University, Shanghai 200240, China
{guguoying,chunxia19881226,lailj,zhulm}@sjtu.edu.cn

Abstract. This paper presents a feedforward-feedback controller to improve tracking precision of piezoceramic actuators with hysteresis and creep nonlinearities. Rather than the commonly used approach to construct an inverse of the hysteresis model in the feedforward path, a direct inverse hysteresis compensation method is used to linearize the asymmetric hysteresis nonlinearity with a modified Prandtl-Ishlinskii model. Considering the limitation of the robustness of the feedforward controller, a proportional integral derivative controller is integrated in the feedback loop to mitigate the modeling uncertainty and creep nonlinearity. To demonstrate the performance improvement of the feedforward-feedback control strategy, a piezoceramic actuated platform is built, and comparative tests are conducted on the experimental platform. In comparison with the open-loop operation, the maximum tracking error of the feedforward-feedback controller is reduced from 6.47 μm to 30 nm, and the maximum hysteresis caused error is reduced from 13.19% to less than 0.1% with respect to the desired displacement range. The experimental results clearly demonstrate the feasibility and effectiveness of the developed feedforward-feedback controller using the modified Prandtl-Ishlinskii model.

Keywords: Hysteresis, piezoceramic actuator, modified Prandtl-Ishlinskii model, feedforward control, feedback control.

1 Introduction

Piezoceramic actuators (PCAs) have been recognized as the most popular actuation devices for micro/nano manipulations to achieve high-precision motion control tasks [2,9]. However, due to the presence of hysteresis and creep nonlinearity in the piezoceramic material, it is quite challenging to design a high-precision motion controller for PCAs.

Hysteresis is a multi-valued nonlinear phenomenon between the applied voltage and the output displacement, which is a consequence of the effects of domain switching in the piezoceramic materials due to the action of the applied electric

J. Lee et al. (Eds.): ICIRA 2013, Part II, LNAI 8103, pp. 644–655, 2013.

field. Creep is the drift of the output displacement for a constant applied voltage under low-speed operations, which is caused by the follow-up polarization of the piezoceramic materials.

In order to remedy the nonlinearities in PCAs, various control techniques have been developed in the literature, which can be roughly classified into three categories: i) charge control, ii) feedforward control, and iii) feedback control. In comparison with voltage control, charge control [3] is an effective method to mitigate the hysteresis based on the fact that there is a less hysteresis between the displacement of a PCA and the applied charge than that between displacement and applied voltage. However, charge control has not been widely applied due to the implementation complexity and cost. Feedforward control is a common control technique to mitigate the nonlinear effects of PCAs in the voltage control case. The key of the feedforward control technique is to construct an inverse hysteresis model, cascaded with the PCA to linearize the actuator response. Various models have been developed for this purpose, for example, the Jiles-Atherton model [16], the Preisach model [18,10], the Prandtl-Ishlinskii (P-I) model [12,1], and the ellipse-based model [7], and so on. With the hysteresis model based compensators, the inverse creep models [11,14] have been designed to compensate for the creep nonlinearity. Rather than using the inverse creep compensation, feedback control is an alternative effective choice. To further improve the tracking precision, feedback controllers are generally integrated with the feedforward controller to eliminate the positioning error caused by the modeling uncertainties of the developed models, which was pioneered by Ge and Jouaneh [4]. The reader may refer to [17,13,6,15] for a recent review on feedforward-feedback control progresses of PCAs.

Following this line, the feedforward-feedback control strategy is implemented in this work to improve the tracking performance of the PCA. Different from the commonly used approach on feedforward control of hysteresis that constructs an inverse of the hysteresis model as the compensator, a direct inverse hysteresis compensation method with the modified Prandtl-Ishlinskii (MPI) model [5] is utilized to mitigate the asymmetric hysteresis nonlinearity of the PCA. Considering the limitation of the robustness of the feedforward controller, a feedback controller is integrated to handle the modeling uncertainty and creep nonlinearity. The main contribution of this paper is to design a novel real-time feedforward-feedback controller with a direct inverse hysteresis compensator, that utilizes the asymmetric MPI model in the feedforward path, to improve the tracking precision of the PCA. To demonstrate the precision enhancement of the developed feedforward-feedback control strategy, we establish a PCA actuated platform and comparative tests are conducted for verification.

The remainder of this paper is organized as follows. In the next section, the MPI model is introduced. In Section 3, several tracking control schemes are presented. The experimental platform and comparative experiments to verify the different control schemes are presented in Section 4, followed by the conclusion in Section 5.

2 MPI Model

The MPI model [8] is defined in terms of weighted play operators and a polynomial input function to describe the asymmetric hysteresis effect of the PCA. In this section, a brief introduction of the MPI model is given.

The play operator is the basic hysteresis operator with symmetric and rate-independent properties. Generally, the one-dimensional play operator can be recognized as a piston with plunger of length $2r$. The output $F_r[x](t)$ is the position of the center of the piston, and the input x is the plunger position. Considering the positive excitation nature of the used PCA, an one-side play (OSP) operator with $r \geq 0$ is adopted as follows [8]

$$\begin{aligned} F_r[x](0) &= f_r(x(0), 0) \\ F_r[x](t) &= f_r(x(t), F_r[x](t_i)) \end{aligned} \tag{1}$$

for $t_i < t \leq t_{i+1}, 0 \leq i \leq N-1$ with

$$f_r(v, w) = \max(v - r, \min(v, w)) \tag{2}$$

where $0 = t_0 < t_1 < \ldots < t_N = t_E$ is a partition of $[0, t_E]$, such that the function $x(t)$ is monotone on each of the subintervals $[t_i, t_{i+1}]$. The argument of the operator $F_r[x]$ is written in square brackets to indicate the functional dependence, since it maps a function to another function.

On the basis of the OSP operator (1), the MPI model is, for asymmetric hysteresis description, expressed as [8]

$$y(t) = g(x(t)) + \int_0^R p(r) F_r[x](t) dr \tag{3}$$

where $g(x(t)) = a_1 x^3(t) + a_2 x(t)$ is a polynomial input function with constant a_1 and a_2, and $p(r)$ is a density function that is generally calculated from the experimental data. The density function $p(r)$ usually vanishes for large values of r , while the choice of $R = \infty$ as the upper limit of integration is widely used in the literature for the sake of convenience [12]. It should be noted that the difference between the MPI model (3) and the classical P-I model is the selection of the input function $g(x(t))$. If $g(x(t))$ is selected as $g(x(t)) = p_0 x(t)$, the MPI model can be reduced to a classical case. The advantage for choosing such an nonlinear input function $g(x(t))$ is that the MPI model can describe a more general class of hysteresis shapes in the piezoelectric actuator with the asymmetric behavior. The reader may refer to [8] for a detailed discussion. In the following development, a real-time direct hysteresis compensation method with the MPI model (3) will be used for asymmetric hysteresis reduction.

3 Feedforward-Feedback Controller Design

In this section, a feedforward-feedback controller is designed to improve trajectory-tracking precision of PCAs. Firstly, the MPI model with the identified parameters is directly adopted to develop the feedforward controller for

hysteresis cancelation. Then, a proportional-integral-derivative (PID) feedback controller is developed to compensate for the modeling uncertainty and creep nonlinearity. Finally, we integrate the feedforward controller in conjunction with the PID feedback loop for tracking control of the PCA. It is worthy of mentioning that such feedforward-feedback integration does not limit the choice of the feedback controller, that is, the model-based feedforward technique can be utilized with other feedback approaches, for instance, sliding model control, disturbance-observer control, and robust adaptive control. Without losing generality, the PID feedback control is selected in this work due to its simple implementation and structure. Moreover, the integrated approach provides robustness to parameter variation and simplifies the computation of the feedforward input because modeling of the creep behavior is not required in the combined feedforward-feedback controller.

3.1 Feedforward Controller

The feedforward controller is used to predict and linearize the hysteresis nonlinearity using the MPI hysteresis model. As addressed in our early research without constructing an inverse of the hysteresis model [5], the feedforward controller is based on the direct hysteresis compensation method, which directly applies the MPI model to characterize the inverse hysteresis loops. According to the experimental data, an identification algorithm is adopted to identify the parameters of the MPI model for feedforward controller design.

In order to implement the feedforward controller in a digital signal processor, the compensation signal $v_{ff}(t)$ is obtained by a discrete form of the MPI model (3)

$$v_{ff}(t) = g(y_d(t)) + \sum_{i=1}^{n} b(r_i) F_{r_i}[y_d](t) \tag{4}$$

where $y_d(t)$ is the desired trajectory, $g(y_d(t)) = p_1 y_d^3(t) + p_2 y_d(t)$, n is the number of the adopted play operators for modeling, and $b(r_i)$ is the weighted constant for the threshold r_i.

3.2 Feedback Controller

In the absence of the analytical dynamic model on the plant, the PID algorithm is a good choice for controller design [4,13,6]. The PID controller in the continuous time domain can be described by the following

$$v_{fb}(t) = k_p(e(t) + k_i \int_0^t e(\tau)d\tau + k_d \dot{e}(t) \tag{5}$$

where k_p, k_i and k_d are the proportional gain, integral gain and derivative gain respectively, $e(t)$ is the tracking error between the actual position and desired position. Genarally, the trail and error method can be adopted to tune PID parameters [4].

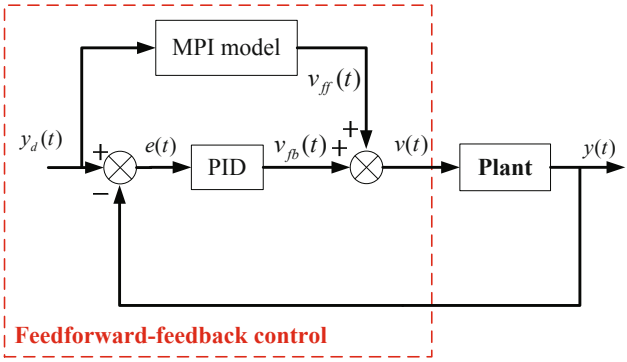

Fig. 1. Block diagram of feedforward-feedback control for the PCA

3.3 Feedforward-Feedback Controller

Fig. 1 shows the block diagram of the feedforward-feedback tracking control system that is composed of a feedforward control loop and a PID feedback loop. In the feedforward loop, the control voltage $v_{ff}(t)$ corresponding to the desired displacement $y_d(t)$ is real-time obtained through (4), whose parameters are identified based on the prior experimental data. In the feedback loop, the desired displacement $y_d(t)$ is compared with the real-time displacement $y(t)$ of the PCA, and the error signal $e(t)$ is transferred to the PID controller (5) to calculate the feedback control voltage v_{fb}. Therefore, the control voltage $v(t)$ of this feedforward-feedback controller for the plant is expressed as

$$v(t) = p_1 y_d^3(t) + p_2 y_d(t) + \sum_{i=1}^{n} b(r_i) F_{r_i}[y_d](t) + k_p(e(t) + k_i \int e(\tau)d\tau + k_d \dot{e}(t). \quad (6)$$

4 Experiments

In this section, an experimental platform with a PCA shall be established and experimental tests are conducted to verify the effectiveness of the developed feedforward-feedback controller for high-precision tracking control of the PCA.

4.1 Experimental Setup

For tracking control of a PCA, the experimental setup is shown in Fig. 2, which consists of a dSPACE DS1103 controller board, a PCA, a piezo amplifier, a strain gauge sensor (SGS) and a signal conditioner. The dSPACE DS1103 (from dSPACE in Germany) rapid prototyping system equipped with 16-bit DAC and 16-bit ADC modular boards are employed to implement the developed controller with the help of the Matlab/Simulink environment. The DAC board produces an analog voltage output for the piezo amplifier, which is then amplified by

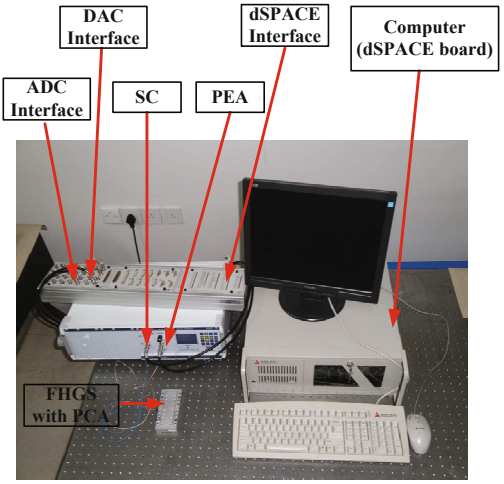

Fig. 2. Experimental setup

15 times to drive the PCA with excitation voltage ranging from 0 to 150 V. The PCA is a preloaded piezoelectric stack actuator (PSt 150/7/100 VS12 from Piezomechanik in Germany), which is used to drive the one-dimensional flexure hinge guiding stage (FHGS) with the nominal 75 μm displacement. The high-resolution SGS integrated with the PCA is adopted to measure the real-time position. The output signals of the SGS pass through the signal conditioner, which are simultaneously sampled by the 16-bit ADC for the feedback controller.

4.2 Open-Loop Control without Compensation

In order to compare the tracking performance of each control scheme, an open-loop test without compensation was firstly conducted on the piezoceramic actuated platform. It is necessary to serve as a reference for the following comparative tests. In this test, the desired trajectory is shown in Fig. 3(a), which is indicated by the solid blue line. In this figure, it can also be seen that the actual trajectory deviates from the desired trajectory, exhibiting considerable errors. The maximum error of the open-loop system is about 6.47 μm. Fig. 3(b) shows the experimental output-input relationship, which is asymmetric hysteresis loops. From Fig. 3(b), we obtain that the maximum hysteresis caused error is about $e_{mhe} = 13.19\%$, defined as

$$e_{mhe} = \max \left| \frac{MHE}{\max(y_d) - \min(y_d)} \right| \times 100\%. \tag{7}$$

Therefore, we can see that the tracking precision of the PCA is unacceptable in open-loop operation. It is why the following feedforward-feedback controller is presented in this paper to improve the tracking precision.

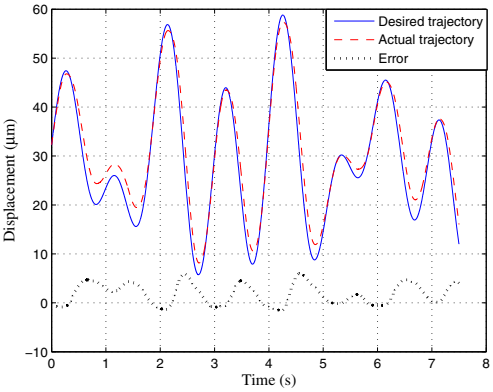

(a) Trajectory following

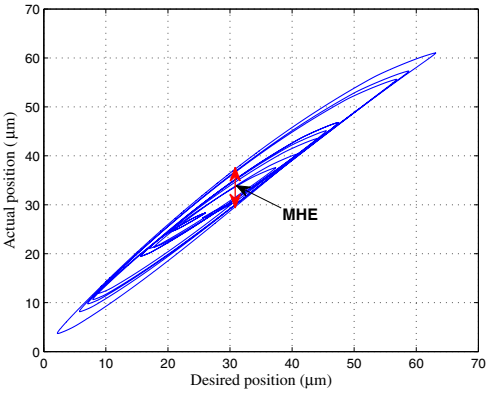

(b) Output-input relationship

Fig. 3. Open-loop tracking control response without compensation

4.3 Feedforward Control with the MPI Model

This set of experiments was conducted by only using the feedforward control when $v_{fb}(t) = 0$ as shown in Fig. 1. The feedforward controller (4) was designed based on the MPI model to cancel the hysteresis nonlinearity. Before implementing the controller, the parameters n, r_i, p_1, p_2 and $b(r_i)$ should be identified firstly. In general, it may be more accurate to describe the inverse hysteresis loops if a larger n is selected. However, more efforts should be made in the real-time calculation of compensation signals. In this work, ten play operators (i.e. $n = 10$) were chosen for identification and compensation with fixed threshold values r_i defined as

$$r_i = \frac{i}{n}||y_d(t)||_\infty,\ i = 0, 1, 2, ..., n-1 \tag{8}$$

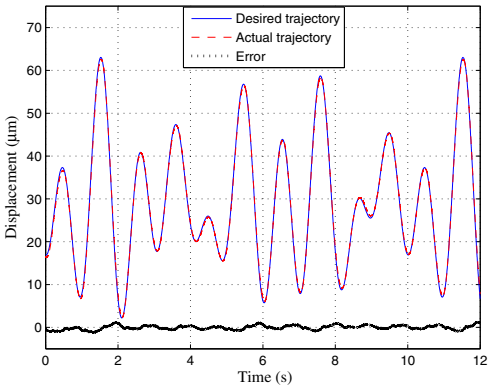

(a) Trajectory following

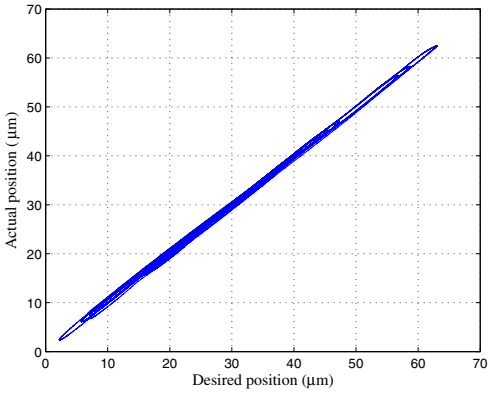

(b) Output-input relationship

Fig. 4. Feedforward tracking control response

with $||y_d(t)||_\infty = 1$ in the normalized case. Then, the other parameters p_1, p_2 and $b(r_i)$ were identified by a particle swarm optimization algorithm [5].

The multi-amplitude sine signal was also used to evaluate the performance of the feedforward controller that utilized the direct hysteresis compensation method. Fig. 4 shows the feedforward tracking control results with the multi-amplitude sine signal. The maximum error of the feedforward system is about 1.24 μm. As described in Fig. 4(b), the maximum hysteresis caused error is about $e_{mhe} = 2.46\%$, which is reduced by up to 81.35% comparing with the open-loop response as illustrated in Fig. 3(b). From Fig. 4(b), it can also be observed that the hysteresis nonlinearity is greatly mitigated and the resulted relationship between the desired position and the actual position is almost symmetric. Therefore, the results of feedforward control demonstrate the effectiveness of the MPI model for asymmetric hysteresis compensation. However, due to the existence of modeling uncertainty and creep nonlinearity, the tracking errors

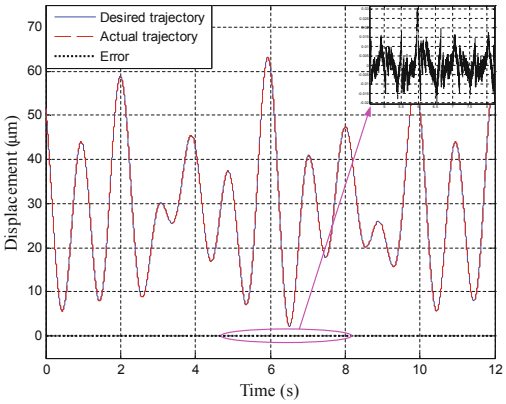

(a) Trajectory following

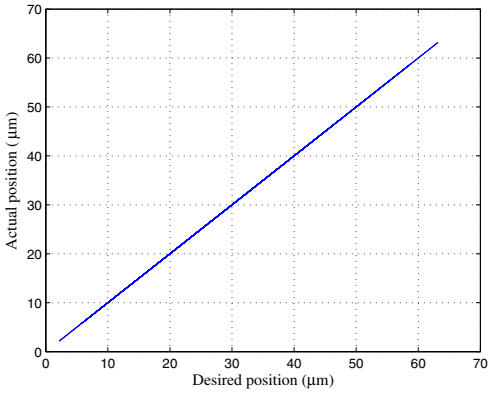

(b) Output-input relationship

Fig. 5. Feedforward-feedback tracking control response

cannot converge to zero. In the following development, the feedback control will be combined to eliminate these errors by using the actual position deviations from the desired position.

4.4 Feedforward-Feedback Control

Finally, the combined feedforward-feedback control strategy (6) was tested. Before implementing the PID controller, the control parameters k_p, k_i and k_d were tuned as $k_p = 0.8$, $k_i = 1000$ and $k_d = 0.00001$ by the trail and error method [4]. With these tuned parameters of the PID control law and the feedforward compensator, Fig. 5 shows the feedforward-feedback tracking control response of the PCA. It can be observed, from Fig. 5(a), that the actual trajectory well follows the desired trajectory. The maximum error of the feedforward-feedback

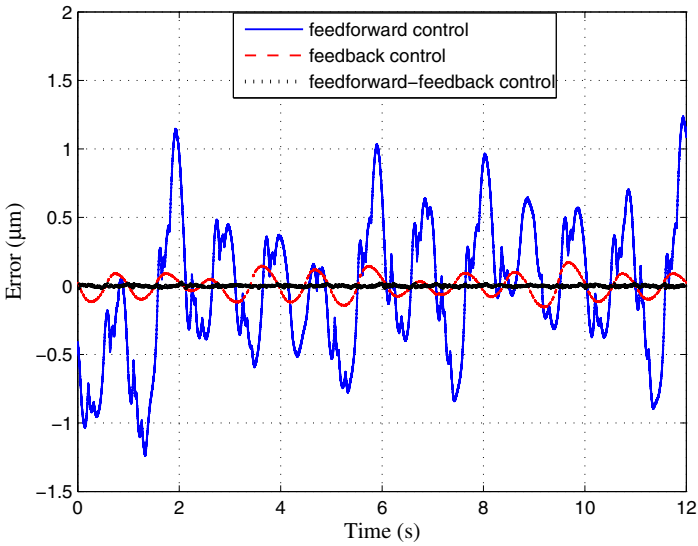

Fig. 6. Comparisons of tracking errors with different control strategies

control system is about 30 nm. Fig. 5(b) shows the resulted output-input relationship between the desired position and actual position, where the hysteresis nonlinearity is exactly mitigated. From Fig. 5, we can see that the maximum hysteresis caused error e_{mhe} is less than 0.1%. To further elucidate the advantage of feedforward-feedback control, Fig. 6 gives the comparisons of tracking errors with three kinds of control strategies. It can be concluded that by compensating for hysteresis, the performance of the feedback system designed is enhanced. In summary, the comparative experimental results demonstrate that the developed feedforward-feedback controller with the MPI model is quite feasible and effective to improve the tracking performance of the PCA with asymmetric hysteresis and creep nonlinearities.

5 Conclusion

In this paper, a MPI model is adopted to characterize the asymmetric hysteresis of the PCA. Based on the model, a direct inverse hysteresis controller is utilized in the feedforward path to cancel the asymmetric hysteresis nonlinearity. In order to further improve the tracking precision, a PID controller is combined to mitigate the modeling uncertainty and creep nonlinearity. In comparison with the open-loop operation, the maximum tracking error is reduced from 6.47 μm to 30 nm, and the maximum hysteresis caused error is reduced from 13.19% to less than 0.1% with respect to the desired displacement range. In the future, advanced model-based feedback control approaches will be used to replace the PID control law for further enhancement of the tracking performance.

Acknowledgements. This work was partially supported by the National Natural Science Foundation of China under grant No. 91023047, China Postdoctoral Science Foundation under Grant 2013M530193, and Shanghai Postdoctoral Scientific Program under Grant No. 13R21414000.

References

1. Al Janaideh, M., Rakheja, S., Su, C.Y.: A generalized Prandtl-Ishlinskii model for characterizing the hysteresis and saturation nonlinearities of smart actuators. Smart Materials and Structures 18(4), 0450011–0450019 (2009)
2. Devasia, S., Eleftheriou, E., Moheimani, S.O.R.: A survey of control issues in nanopositioning. IEEE Transactions on Control Systems Technology 15(5), 802–823 (2007)
3. Fleming, A.J., Leang, K.K.: Charge drives for scanning probe microscope positioning stages. Ultramicroscopy 108(12), 1551–1557 (2008)
4. Ge, P., Jouaneh, M.: Tracking control of a piezoceramic actuator. IEEE Transactions on Control Systems Technology 4(3), 209–216 (1996)
5. Gu, G.Y., Yang, M.J., Zhu, L.M.: Real-time inverse hysteresis compensation of piezoelectric actuators with a modified Prandtl-Ishlinskii model. Review of Scientific Instruments 83(6), 065106 (2012)
6. Gu, G.Y., Zhu, L.M.: High-speed tracking control of piezoelectric actuators using an ellipse-based hysteresis model. Review of Scientific Instruments 81(8), 085104 (2010)
7. Gu, G.Y., Zhu, L.M.: Modeling of rate-dependent hysteresis in piezoelectric actuators using a family of ellipses. Sensors and Actuators A: Physical 165(2), 202–209 (2011)
8. Gu, G.Y., Zhu, L.M., Su, C.Y.: Modeling and compensation of asymmetric hysteresis nonlinearity for piezoceramic actuators with a modified Prandtl-Ishlinskii model. IEEE Transactions on Industrial Electronics (2013), http://dx.doi.org/10.1109/TIE.2013.2257153
9. Gu, G.Y., Zhu, L.M., Su, C.Y., Ding, H.: Motion control of piezoelectric positioning stages: modeling, controller design and experimental evaluation. IEEE/ASME Transactions on Mechatronics (2012), doi:10.1109/TMECH.2012.2203315
10. Iyer, R.V., Tan, X.: Control of hysteretic systems through inverse compensation. IEEE Controls Systems Magazine 29(1), 83–99 (2009)
11. Janocha, H., Kuhnen, K.: Real-time compensation of hysteresis and creep in piezoelectric actuators. Sensors and Actuators A: Physical 79(2), 83–89 (2000)
12. Krejci, P., Kuhnen, K.: Inverse control of systems with hysteresis and creep. IEE Proceedings of Control Theory and Applications 148(3), 185–192 (2001)
13. Leang, K.K., Devasia, S.: Feedback-linearized inverse feedforward for creep, hysteresis, and vibration compensation in AFM piezoactuators. IEEE Transactions on Control Systems Technology 15(5), 927–935 (2007)
14. Rakotondrabe, M.: Complete open loop control of hysteretic, creeped, and oscillating piezoelectric cantilevers. IEEE Transactions on Automation Science and Engineering 7(2), 428–431 (2010)
15. Rakotondrabe, M., Rabenorosoa, K., Agnus, J., Chaillet, N.: Robust feedforward-feedback control of a nonlinear and oscillating 2-DOF piezocantilever. IEEE Transactions on Automation Science and Engineering 8(3), 440–450 (2011)

16. Rosenbaum, S., Ruderman, M., Strohla, T., Bertram, T.: Use of Jiles-Atherton and Preisach hysteresis models for inverse feed-forward control. IEEE Transactions on Magnetics 46(12), 3984–3989 (2010)
17. Song, G., Zhao, J.Q., Zhou, X.Q., de Abreu-Garcia, J.A.: Tracking control of a piezoceramic actuator with hysteresis compensation using inverse Preisach model. IEEE/ASME Transactions on Mechatronics 10(2), 198–209 (2005)
18. Visone, C.: Hysteresis modelling and compensation for smart sensors and actuators. Journal of Physics: Conference Series 138(1), 012028 (2008)

A Novel Analytical Inverse Compensation Approach for Preisach Model

Zhi Li*, Sining Liu, and Chun-Yi Su

Department of Mechanical Engineering, Concordia University
1455 De Maisonneuve Blvd. W., Montreal, Quebec, Canada H3G 1M8
gavinlizhi@gmail.com, siningliu@live.ca, cysu@alcor.concordia.ca

Abstract. Hysteresis a non-smooth and non-differential phenomena. The inverse compensation for the purpose of removing the hysteresis effect is the most popular approach. Because the Preisach model is the widespread used hysteresis model, research on inverse compensation based on Preisach model attracts much attention. In this paper, we develop a novel analytical inverse compensation method for the Preisach model, in which we divided the Preisach model into two parts: non-memory part and memory part. Due to this division, we only need to construct the inverse of the non-memory part, which is invertible through selection of the suitable density function, instead of the whole Preisach model, which avoids to solve the inverse of the complex dual integral formulation of the Preisach model. The simulation and experimental results demonstrate the effectiveness of the proposed method.

Keywords: Hysteresis, Preisach model, inverse compensation, magnetostrictive actuator.

1 Introduction

Hysteresis is a nonlinear phenomenon that appears in many different areas. Ferromagnetic hysteresis [1] and plastic hysteresis [2] are two typical examples. Hysteresis exhibited in the smart material-based actuators, such as magnetostrictive actuators, reveals a looped and branched nonlinear relation between the input excitation and the output displacement. Hysteretic behaviors also arise in aerodynamics, where the aerodynamic forces and moments show hysteresis when the attack angle of the airplane varies. Others are encountered in mechanical systems, economics, ecohydrology and neuroscience, etc. For most cases, the hysteresis is regarded as an undesired and detrimental effect, which will deteriorate the system performance and cause inaccuracy or oscillations. The common approach for remedying hysteresis effect is to construct a hysteresis inverse. Therefore, mathematical models should be first developed.

There are several models available for representing hysteretic behaviors, such as Preisach model [3], Prandtl-Ishlinskii (PI) model [4], Bouc-Wen model [5],

* Corresponding author.

J. Lee et al. (Eds.): ICIRA 2013, Part II, LNAI 8103, pp. 656–665, 2013.

and Duhem model [6]. Among them, Preisach model is the most common and accepted hysteresis model. Unlike the PI model, which can only describe the symmetric hysteretic behaviors, the Preisach model can represent symmetric, asymmetric as well as saturated hysteresis effect. Although the construction of the Preisach model is complex, from the modeling accuracy point of view, the Preisach model shows its superiority over the other hysteresis models.

Inverse compensation is a common method to cancel the hysteresis effect. However, for the Preisach model its analytical inverse construction is still not available. In [4], an analytical inverse compensation approach for PI model which is the subset of Preisach model was developed by P. Krejci by utilizing the initial loading curve to construct the inverse density function for the PI model. However, for the Preisach model it is difficult to analytically construct such an inverse density function as represented in [4]. In the literature, most existing inverse compensation approaches for the Preisach model are numerical inversion algorithms [7] [8], which usually rely on the information of the output of the Preisach model (actuator) in real time. However, when a system is preceded by actuators containing the hysteresis nonlinearity, real time information of the output of the actuator is unavailable. Therefore, we attempt to seek new ways to develop the analytical inverse compensator.

In this paper, a novel analytical inverse compensator is developed. We firstly divided the Preisach model into two parts: non-memory part and memory part, and then we solve the analytical inverse solution of the non-memory part, which avoids to construct the inverse compensator based on the complex dual integral formulation of the Preisach model. Experimental tests were then conducted on the magnetostrictive actuator. The experimental results demonstrated the modeling accuracy of the Preisach model and the effectiveness of the proposed inverse compensation method.

2 Preisach Model

Preisach model is the most common and accepted hysteresis model which was first presented in 1935 by F. Preisach [3] for the purpose of describing the hysteresis effect in ferromagnetic materials. The classical Preisach model constructed by accumulating a series of relay operators is defined as

$$\begin{aligned} f(t) &= \Gamma[\psi(u_1, u_2, ..., u_N), u](t) \\ &= \int_0^{+\infty} \int_{-\infty}^{+\infty} \mu(r, s) \hat{\gamma}_{s-r, s+r}[u](t) ds dr \end{aligned} \tag{1}$$

where $\psi(u_1, u_2, ..., u_N) \in \Lambda$, $\Lambda := \{\psi \in C[0, T]; |\frac{d\psi}{dr} = 1|, a.e.\}$, $u_1, u_2, ..., u_N$ denote previous input extrema. $\hat{\gamma}_{s-r,s+r}$ is the relay operator as

$$\hat{\gamma}_{s-r,s+r} = \begin{cases} +1 & \text{if } u(t) > s + r \\ -1 & \text{if } u(t) < s - r \\ \textit{remains unchanged} & \text{if } v - r \leq u(t) \leq v + r \end{cases}$$

$\mu(r,s)$ is the density function of Preisach model, s and r are two parameters that determine switching values +1 (the switch is "on") and -1 (the switch is "off") of input. Fig. 1 demonstrates the geometric interpretation of the Preisach model when $u(t)$ is increasing and decreasing separately. $S^+(t)$ denotes region where all switches $\hat{\gamma}_{s-r,s+r}[u](t)$ are on, $S^-(t)$ denotes region where all switches $\hat{\gamma}_{s-r,s+r}[u](t)$ are off.

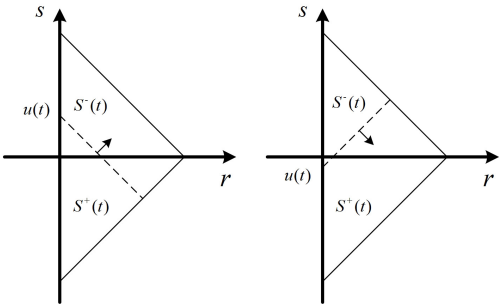

Fig. 1. The geometric interpretation of the Preisach model

3 The Novel Analytical Inverse Compensator for the Preisach Model

3.1 The Analytical Inverse Compensator for the Preisach Model

In this section, we seek novel approach to develop the analytical inverse compensator for the Preisach model. The geometric interpretation of the Preisach model shows that the Preisach plane is divided into two parts $S^+(t)$ and $S^-(t)$, which are related to the input history and represent the memory characteristics of the Preisach model. However, it is difficult to construct the inverse compensator based on this division, and there is no perfect analytical compensator to compensate the Preisach model in the literature review.

We found that the Preisach plane can also be divided into non-memory part $\Delta_{r=0}$ and memory part $\Delta_{r>0}$, see Fig.2. The non-memory part is only related to the current input value with

$$\hat{\gamma}_{s-r,s+r}u(t) = \{\pm 1 | (r,s) \in IR_0 \times IR\} \tag{2}$$

Therefore, the Preisach model can be rewritten as

$$\begin{aligned} \Gamma[u](t) &= \Gamma_{r=0}[u](t) + \Gamma_{r>0}[u](t) \\ &= 2\iint_{\Delta_{r=0}} \mu(r,s)drds - C_{\Delta_{r=0}} + \iint_{\Delta_{r>0}} \mu(r,s)\hat{\gamma}_{s-r,s+r}u(t)drds \\ &= 2\int_{-R}^{u} \mu(s)ds - C_{\Delta_{r=0}} + \iint_{\Delta_{r>0}} \mu(r,s)\hat{\gamma}_{s-r,s+r}u(t)drds \end{aligned} \tag{3}$$

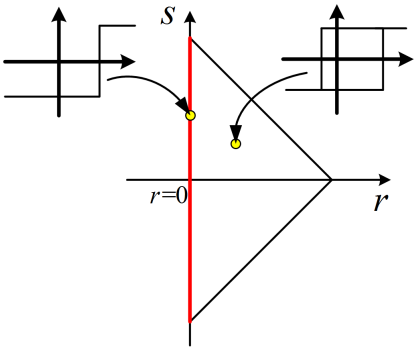

Fig. 2. The triangle area

where

$$C_{\Delta_{r=0}} = \int_{-R}^{+R} \mu s ds \tag{4}$$

Define $\lambda'(\alpha) = \mu(\alpha)$,

$$\begin{aligned} \int_{-S}^{u} \mu(s) ds &= \int_{-S}^{u} d\lambda \\ &= \lambda(u) - \lambda(-R) \end{aligned} \tag{5}$$

Therefore, we have

$$\begin{aligned} &\Gamma_{r=0}[\cdot] = 2\lambda(\cdot) - 2\lambda(-R) - C_{\Delta_{r=0}} \\ &\Gamma_{r=0}^{-1}[\cdot] = \lambda^{-1}(\frac{1}{2}(\Gamma_{r=0}[\cdot] + C_{\Delta_{r=0}} + 2\lambda(-R))) \end{aligned} \tag{6}$$

According to (3), the inverse compensator can be expressed as

$$u = \Gamma^{-1}[u] = \Gamma_{r=0}^{-1}[\Gamma[u] - \Gamma_{r>0}[u]] \tag{7}$$

Fig. 3 shows the scheme of the inverse compensator.

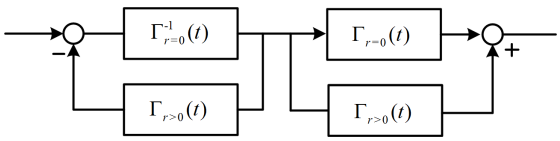

Fig. 3. The scheme of the inverse compensator

4 Experimental Tests

4.1 Experimental Platform

In this paper, experimental tests were conducted on a magnetostrictive actuator MFR OTY77, manufactured by Etrema Products, Inc. The actuator consists of a wound wire solenoid surrounding two Terfenol-D rods, which are preloaded by a compression bolt and a spring washer. Three permanent magnets are installed along the Terfenol-D rods to provide a magnetic field with a bias. Fig. 4 shows main components of the actuator. The actuator provides a peak-to-peak output displacement of 100 μ m under excitations at frequencies up to 1250 Hz. A capacitive sensor (Lion Precision, model C23-C) with a capacitive sensor driver(Lion Precision, Elite Series CPL190) is used for measurement of the actuator displacement response with a sensitivity of 80 mV/μm, bandwidth of 15 kHz and a resolution of 35.53 nm. The excitation current to the actuator is applied through the power amplifier LVC2016 produced by AE Techron Inc. The displacement response of the actuator, measured by an integrated capacitive sensor, is obtained via the dSPACE control board equipped with 16-bit analog-to-digital converters (ADC) and 16-bit digital-to-analog converters (DAC). Fig. 5 illustrates the entire experimental platform.

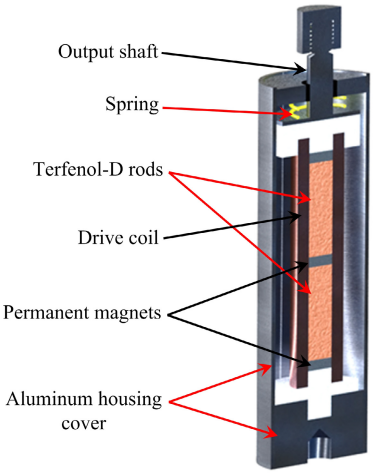

Fig. 4. Magnetostrictive actuator [9]

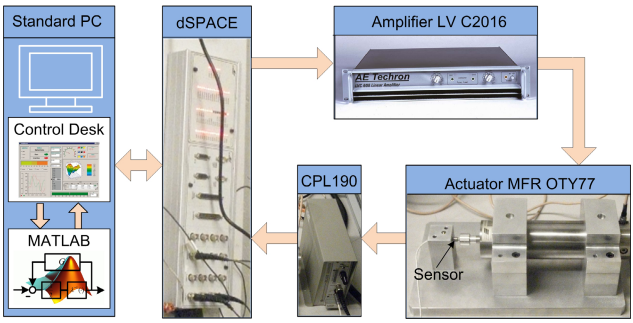

Fig. 5. The experimental platform

4.2 Hysteresis Identification

For the real applications, we usually use the discrete form of the Preisach model as

$$\begin{aligned} \Gamma[n] &= \Gamma_{r=0}[n] + \Gamma_{r>0}[n] \\ &= 2\lambda(u) - 2\lambda(-R) - C_{\Delta_{r=0}} + \sum_{i=1}^{M} \upsilon_i[n] w_i[n] \end{aligned} \tag{8}$$

where υ_i denotes the state of the relay operator, w_i denotes the weights of Preisach model with $r > 0$. In this paper, we select

$$\lambda(s) = ae^{-s} \tag{9}$$

Substitute (9) into (10),

$$\begin{aligned} \Gamma[n] &= 2ae^{-u} - a(e^{R} + e^{-R}) + \sum_{i=1}^{M} \upsilon_i[n] w_i[n] \\ &= \upsilon^{T}[n]\mathbf{w}[n] \end{aligned} \tag{10}$$

where $\boldsymbol{\upsilon}[n] = [2e^{-u} - (e^{R} + e^{-R}), \upsilon_1, \upsilon_2, ...\upsilon_M]^T$, $\mathbf{w}[n] = [a, w_1, w_2, ..., w_M]^T$, M denotes the total numbers of the discrete components for $r > 0$ in the triangle plane, and the discretization scheme is shown in Fig. 6 We employ the gradient algorithm [10] to identify the weights $\mathbf{w}[n]$ as

$$\mathbf{w}[n+1] = \mathbf{w}[n] - \delta \frac{(\Gamma[n] - \Gamma_d[n])\upsilon[n]}{\upsilon[n]^T \upsilon[n]} \tag{11}$$

where $0 < \delta < 1$ is the constant, $\Gamma_d[n]$ denotes the desired input. To guarantee that the weights are nonnegative, define $w_i[n+1] = 0$ if $w_i[n+1] < 0$. Fig.7 demonstrates the identified weights $\boldsymbol{\upsilon}[n]$, where $\boldsymbol{\upsilon}_1 = a = 0.01$.

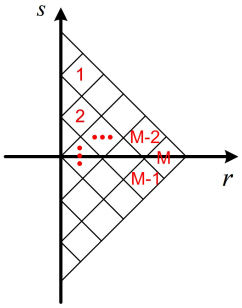

Fig. 6. The discretization scheme

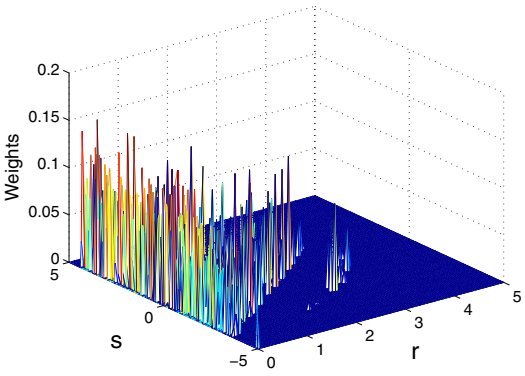

Fig. 7. The identified weights

Fig. 8 shows the comparison of output of the magnetostrictive actuator and the Preisach model. The modeling error is defined as

$$e_m(t) = \frac{100(y(t) - \Gamma(t))}{max(y(t))} \tag{12}$$

where $y(t)$ and $\Gamma(t)$ are the output of the magnetostrictive actuator and the Preisach model. The hysteresis loops are shown in Fig. 8(b). From comparisons in Fig. 8(a), the output of the Preisach model corresponds well with the experimental data and the maximum error is less than 0.6% of the total range.

4.3 Analytical Inverse Compensator

The identified non-memory part can be written as

$$\Gamma_{r=0}[u] = 0.02e^{-u} - 0.02(e^5 + e^{-5}) \tag{13}$$

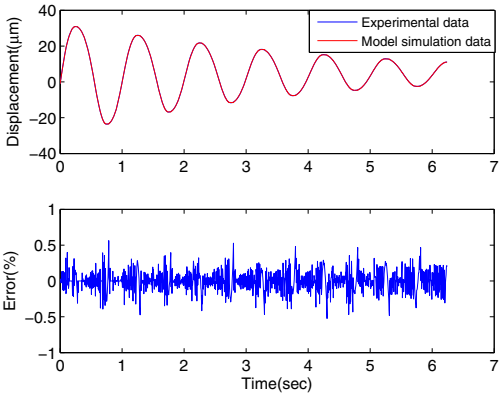

(a) Displacement vs time.

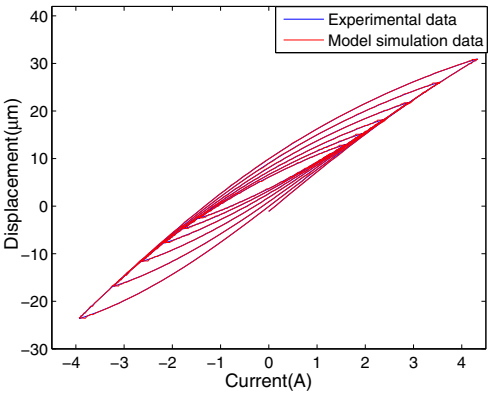

(b) Hysteresis loop.

Fig. 8. Comparisons of experimental data and ASPI model output

where $\pm R = \pm 5$. The inverse formulation of (13) can be expressed as

$$\Gamma_{r=0}^{-1}[\cdot] = \ln \frac{0.02}{\Gamma_{r=0}[\cdot] + 0.02(e^5 + e^{-5})}$$
$$u = \Gamma_{r=0}^{-1}[\Gamma[u] - \sum_{i=1}^{M} \upsilon_i[n] w_i[n]] \tag{14}$$

Fig. 9 shows input-output relationship of the magnetostrictive actuator with the inverse compensation. The desired tracking signal is $w_d(t) = 30sin(t)$. The experimental results demonstrate that the proposed analytical inverse compensator can effectively mitigate the hysteretic behavior in the magnetostrictive actuators.

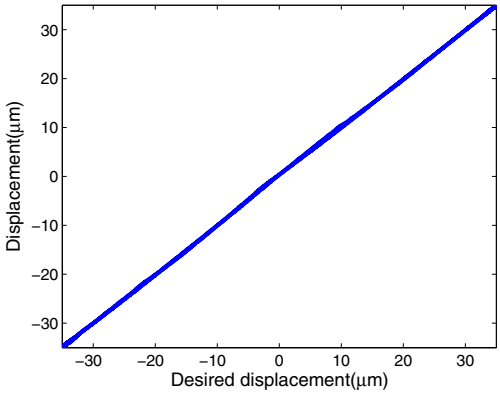

Fig. 9. The input-output relation with the proposed inverse compensator

5 Conclusion

In this paper, a novel analytical inverse compensator is developed. The Preisach model is firstly divided into two parts: non-memory part and memory part, then an inverse scheme is proposed based on this division. The advantage of this method is to avoid to construct the complex inverse density function. The attached simulation and experimental results demonstrate the effectiveness of the proposed method. The future work will focus on developing the analytical inverse compensation error of the Preisach model and fused this analytical compensator with adaptive controller design.

Acknowledgment. The work was supported by the Funds for Natural Science Foundation of China under Grants (61020106003, 61074097 and U1201244), the 111 project (B08015), and by the Key Laboratory of Autonomous Systems and Network Control, Ministry of Education.

References

1. Brokate, M., Sprekels, J.: Hysteresis and Phase Transitions. Springer, New York (1996)
2. Jiles, D.C., Atherton, D.L.: Theory of ferromagnetic hysteresis. Journal of Magnetism and Magnetic Materials 61(1-2), 48–60 (1986)
3. Preisach, F.: Über die magnetische nachwirkung. Zeitschrift für Physik 94, 277–302 (1935)
4. Krejci, P., Kuhnen, K.: Inverse control of systems with hysteresis and creep. IEE Proceedings Control Theory and Applications 148(3), 185–192 (2001)
5. Wen, Y.-K.: Method for random vibration of hysteretic systems. Journal of the Engineering Mechanics Division 102(2), 249–263 (1976)

6. Oh, J., Bernstein, D.S.: Identification of rate-dependent hysteresis using the semilinear duhem model. In: Proceedings of the 2004 American Control Conference, vol. 5, pp. 4776–4781 (2004)
7. Visone, C.: Hysteresis modelling and compensation for smart sensors and actuators. Journal of Physics: Conference Series 138(1), 012028 (2008)
8. Tan, X.B., Bennani, O.: Fast inverse compensation of preisach-type hysteresis operators using field-programmable gate arrays. In: 2008 American Control Conference, vol. 1-12, pp. 2365–2370, 5286 (2008)
9. Aljanaideh, O., Al Janaideh, M., Rakheja, S., Su, C.-Y.: Compensation of rate-dependent hysteresis nonlinearities in a magnetostrictive actuator using an inverse prandtl–ishlinskii model. Smart Materials and Structures 22(2), 025027 (2013)
10. Tan, X.B., Baras, J.S.: Recursive identification of hysteresis in smart materials. In: Proceedings of the 2004 American Control Conference, vol. 1-6, pp. 3857–3862, 5828 (2004)

High Precision Control for Nano-stage Driven by Magnetostrictive Actuator

Xinkai Chen* and Chun-Yi Su

[1] Department of Electronic and Information Systems
Shibaura Institute of Technology
Minuma-ku, Saitama-city, Saitama 337-8570, Japan
[2] School of Automation Science and Engineering,
South China University of Technology
Tianhe District, Guangzhou, 510641, P.R. China

Abstract. The nano-stage driven by magnetostrictive actuator is composed of a magnetostrictive actuator and a positioning mechanism (PM). Due to the existence of hysteretic nonlinearity in the magnetostrictive actuator and the friction behavior in the PM, the accurate position control of the nano-stage is a challenging task. This paper discusses the high precision control for the magnetostrictive nano-stage, where the hysteresis is described by Preisach model. The proposed control law ensures the zero output tracking of the controlled stage. Experimental results show the effectiveness of the proposed method.

Keywords: Nano-stage, magnetostrictive actuator, hysteresis, Preisach model.

1 Introduction

Smart material based actuators have many potential applications in scanning probe microscopy, optical alignments, diamond turning machines, active vibration control, bio-operation devices [2,5,8,12-14,16,20,22]. These kind of actuators are used to meet the requirement of nanometer resolution in displacement, high stiffness and rapid response. However, the main disadvantage is the hysteresis phenomenon between the applied voltage/current and the displacement. Due to the undifferentiable and nonmemoryless character of the hysteresis, it causes position errors which limit the operating speed and precision of the smart material based actuators. The development of control techniques to mitigate the effects of hysteresis has been studied for decades and has recently re-attracted significant attention. Interest in studying dynamic systems with actuator hysteresis is motivated by the fact that they are nonlinear system with non-smooth nonlinearities for which traditional control methods are insufficient and thus require development of alternate effective approaches. It should be noted that the control of magnetostrictive actuator is much more difficult than that of other kind of smart material based actuators [14,20].

* This work is partially supported by JSPS Grants-in-Aid for Scientific Research C-24560553, Funds for Natural Science Foundation of China under Grant 61074097 and 61228301, and Key Laboratory of Integrated Automation for the Process Industry (Northeastern University), China.

J. Lee et al. (Eds.): ICIRA 2013, Part II, LNAI 8103, pp. 666–677, 2013.

About the challenge of the problem, the thorough characterization of the hysteresis forms the foremost task [1,15]. Appropriate hysteresis models may then be applied to describe the nonsmooth nonlinearities for their potential usage in formulating the control algorithms. The basic idea consists of the modeling of the real complex hysteresis nonlinearities by the weighted aggregate effect of all possible so-called elementary hysteresis operators. Elementary hysteresis operators are noncomplex hysteretic nonlinearities with a simple mathematical structure. The popular models are Preisach model [14,15,20], Prandtl-Ishlinskii model [3,21], and Krasnosel'skii-Pokrovskii model [8,21]. The Preisach model and Krasnosel'skii-Pokrovskii (KP) model are parameterized by a pair of threshold variables [3,21], whereas the Prandtl-Ishlinskii (PI) model is a superposition of elementary stop operators which are parameterized by a single threshold variable [21].

Upon the developments in various hysteresis models, it is by nature to seek means to fuse these hysteresis models with the available control techniques to mitigate the effects of hysteresis, especially when the hysteresis is unknown, which is a typical case in many practical applications. However, the results on the fusion of the available hysteresis models with the available control techniques is surprisingly spare in the literature [4,17,18,20]. The most common approach in coping with hysteresis in the literature is to construct an inverse operator, which is pioneered by Tao and Kokotovic [18], and the reader may refer to, for instance, [9] and [20] and the references therein. Essentially, the inverse problem depends on the phenomenological modeling methods (for example, using Preisach models). Due to multi-valued and non-smooth features of hysteresis, the inverse always generates certain errors and possesses strong sensitivity to the model parameters. Furthermore, for the dynamical systems with hysteresis, the inverse errors directly make the stability analysis of the closed-loop system very difficult.

This paper considers the high precision control for the nano-stage driven by magnetostrictive actuator. The considered system can be regarded as the control problem for a linear dynamical system preceded by Preisach hysteresis. First, an implicit inverse of the Preisach hysteresis is introduced, Then, a new approach for fusion of the adaptive control techniques with the Preisach hysteresis model is proposed. The advantage is that only the parameters in the formulation of the controller need to be adaptively estimated, and the real value of the parameters of the stage need to be neither identified nor measured. The proposed control law ensures the global stability of the adaptive system, and the position error of the stage can be controlled by choosing the design parameters. Experimental results confirm the effectiveness of the proposed method.

2 Problem Statement

2.1 System Description

In this paper, the position control of the nano-stage diven by magnetostrictive actuator is considered. The nano-stage used in the experiment is shown in Fig. 1. The dynamic equation of the nano-stage can be formulated as follows

$$m\ddot{y}(t) + \mu_1 \dot{y}(t) + ky(t) = u(t) \tag{1}$$

where $y(t)$ represents the displacement of the stage, $u(t)$ is the force generated by the magnetostrictive actuator, m is the mass of the stage, μ_1 is kinetic coefficient of friction at the installation side of the stage which is very small, k is spring constant which is very large.

Suppose $u(t)$ is constant during the sampling instants. By discretizing system (1) based on zero-order-hold (ZOH) input, the input-output discrete-time expression of system (1) can be given by

$$A(q^{-1})y(k) = q^{-1}B(q^{-1})u(k), \tag{2}$$

where q^{-1} is the delay operator, $A(q^{-1})$ and $B(q^{-1})$ are polynomials defined by

$$A(q^{-1}) = 1 + a_1 q^{-1} + a_2 q^{-2}, \tag{3}$$
$$B(q^{-1}) = b_0 + b_1 q^{-1}. \tag{4}$$

If the sampling time is small enough, then, by some elementary calculations, it can be easily shown that $A(q^{-1})$ and $B(q^{-1})$ are coprime, and $B(q^{-1})$ is a Hurwitz polynomial. Let $v(k)$ be the current applied to the actuator. The relation between $v(k)$ and $u(k)$ is expressed by

$$u(k) = H[v](k) \tag{5}$$

where $H[*](k)$ is the Preisach hysteresis operator.

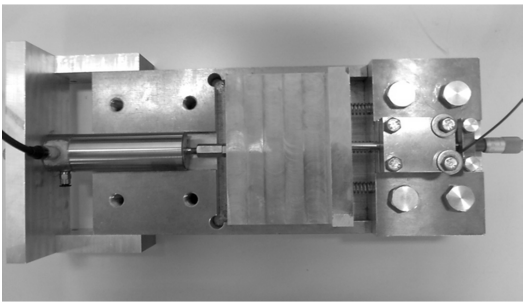

Fig. 1. The stage driven by magnetstrictive actuator

The control purpose is to drive the stage to track a uniformly bounded signal $y_m(k)$. It should be noted that the signal $u(k)$ which is the force generated by the actuator is not available in the control design.

2.2 Preisach Hysteresis Model

Detailed definition on Preisach model can be found in [3] [15] [20]. The basic element of the Preisach operator is the so-called relay operator. For a pair of threshold (β, α) with $\beta < \alpha$, consider a simple hysteretic element $\gamma_{\beta,\alpha}[\cdot]$, as illustrated in Fig. 2. For

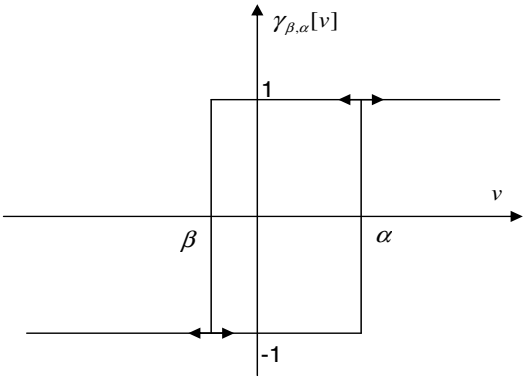

Fig. 2. Relay operator $\gamma_{\beta,\alpha}[v]$

arbitrary piece-wise monotone function $v(k)$ and an initial configuration $w_{-1} \in \{-1,1\}$, define $w(k) = \gamma_{\beta,\alpha}[v](k)$ as

$$w(k) = \begin{cases} -1 & if\ v(k) < \beta \\ 1 & if\ v(k) > \alpha \\ w(k-1) & if\ \beta \le v(k) \le \alpha \end{cases} \tag{6}$$

Define

$$P_0 = \left\{(\beta,\alpha) \in R^2 : \beta \le \alpha\right\}.$$

P_0 is called the Preisach plane, and each $(\beta,\alpha) \in P_0$ is identified with the relay operator $\gamma_{\beta,\alpha}$. The Preisach operator is defined as

$$u(k) = H[v](k) = \int_{P_0} \mu(\beta,\alpha)\gamma_{\beta,\alpha}[v](k)d\beta d\alpha, \tag{7}$$

where the weighting function $\mu(\beta,\alpha)$ is often referred to as the Preisach function or density function. In this paper, it is assumed $\mu(\beta,\alpha) \ge 0$ for all $(\beta,\alpha) \in P_0$. Furthermore, assume that $\mu(\beta,\alpha) = 0$ if $\beta < \beta_0$ or $\alpha > \alpha_0$ for some β_0 and α_0 (see Fig. 3. (a)). Thus, it is sufficient to consider a finite triangular area in the Preisach plane $P = \{(\beta,\alpha) \in P_0 \mid \beta \ge \beta_0, \alpha \le \alpha_0\}$.

The memory effect of the Preisach operator can be captured by the memory curves in P. At step k, P can be divided into two regions

$$P_+(k) = \left\{(\beta,\alpha) \in P : output\ of\ \gamma_{\beta,\alpha}\ at\ k\ is\ +1\right\},$$
$$P_-(k) = \left\{(\beta,\alpha) \in P : output\ of\ \gamma_{\beta,\alpha}\ at\ k\ is\ -1\right\}.$$

Now, assume that at the initial time instant $k = k_0$, the input $v(k_0) = v_0 < \beta_0$. Then, the output of every relay operator is -1. Thus, $P_+(k_0) = P$, $P_-(k_0) = \Phi$ and this corresponds to the negative saturation (see Fig. 3. (b)), where Φ denotes empty set. Next, assume that the input is monotonically increased to some maximum value at k_1 with

$v(k_1) = v_1 > \beta_0$. The output of $\gamma_{\beta,\alpha}$ for $\alpha < v_1$ is switched to $+1$ as the input $v(k)$ increases past α. Thus, at time instant k_1, the boundary between $P_+(k_1)$ and $P_-(k_1)$ is the horizontal line $\alpha = v_1$ (see Fig. 3. (c)). Next assume that the input $v(k)$ starts to decrease monotonically until it stops at instant k_2 with $v(k_2) = v_2$. It is obvious that the output of $\gamma_{\beta,\alpha}$ becomes -1 as $v(k)$ sweeps past β, and correspondingly, a vertical line segment $\beta = v_2$ is generated and a part of $P_+(k_1)$ is changed into $P_-(k_2)$ (see Fig. 3. (d)).

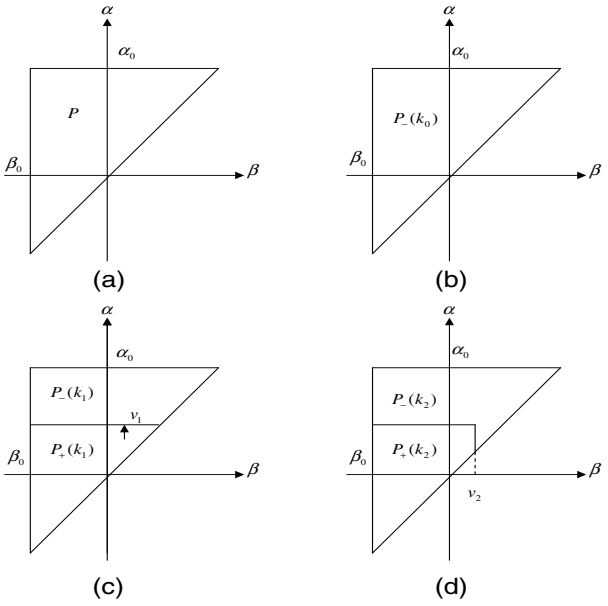

Fig. 3. Occurence of memory curves on the Preisach plane

It can be seen that each P_+ and P_- is a connected set [3][15], and the output of $H[\cdot]$ is determined by the boundry between P_+ and P_-. This boundary is called *the memory curve* since it characterizes the states of all relay operators. The memory curve has a staircase structure and its intersection with the line $\alpha = \beta$ gives the current input value. The memory curve at $k = 0$ is called the initial memory curve and it represents the initial condition of the Preisach operator. Two examples of the staircase structures are shown in Fig. 4.

Remark 1. *It should be noted that the Preisach operator is rate − independent and have the well-known wiping − out property.*

3 Implicit Inverse of Hysteresis

In this subsection, an input $v(k)$ is tried to calculate for a given output $u(k)$ for the operator described in (7). For this purpose, suppose the density function $\mu(\beta, \alpha)$ is

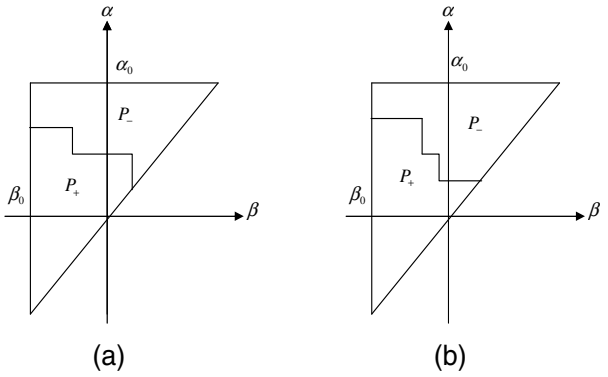

Fig. 4. Two types of memory curves on the Preisach plane

known in this subsection. Without loss of generality, suppose $u(k)$ is monotonically increasing on the interval $k_i \le k \le k_{i+1}$. For each $k \in (k_i, k_{i+1}]$, define a new variable $\bar{v}_\eta(k)$ with $\bar{v}_0(k) = v(k-1))$ and another new variable $u_\eta(k)$, where η is a parameter varying in the range $\eta \in [0, \alpha_0 - \beta_0]$

$$\bar{v}_\eta(k) = \bar{v}_0(k) + \eta, \tag{8}$$

$$u_\eta(k) = \int_P \mu(\beta,\alpha)\gamma_{\beta,\alpha}[\bar{v}_\eta](k)d\beta d\alpha. \tag{9}$$

Let $[v_{min}, v_{max}]$ be the practical input range, which is a subset of $[\beta_0, \alpha_0]$, to the hysteresis operator, and

$$\int_P \mu(\beta,\alpha)\gamma_{\beta,\alpha}[v_{max}](k)dr = \bar{U}, \tag{10}$$

$$\int_P \mu(\beta,\alpha)\gamma_{\beta,\alpha}[v_{min}](k)dr = \underline{U}. \tag{11}$$

If $u(k) > \bar{U}$, let $v(k) = v_{max}$
If $u(k) < \underline{U}$, let $v(k) = v_{min}$
If $\underline{U} \le u(k) \le \bar{U}$, the value of $v(k)$ is derived from the following algorithm.

Step 1: Let η increase from 0.
Step 2: Calculate $\bar{v}_\eta(k)$ and $u_\eta(k)$. If $u_\eta(k) < u(k)$, then let η increase continuously and go to Step 2;
Otherwise, go to Step 3.
Step 3: Stop the increasing of η, memorize it as η_0 and define $v(k) = \bar{v}_{\eta_0}(k)$.

Remark 2. *For $k = 0$, $\bar{v}_0(0)$ can be defined as $\bar{v}_0(0) = v_{min}$.*

Remark 3. *The value of $v(k)$ is sought by beginning from $v(k-1)$. The algorithm is based on the property that, if $\eta_1 < \eta_2$, then $u_{\eta_1}(k) \le u_{\eta_2}(k)$.*

4 Adaptive Control for Nano-stage Driven by Magnetostrictive Actuator

In this section, the control design for the nano-stage driven by magnetostrictive actuator which is modelled by (2) and (7) will be given. In the proposed approach, the parameters in $A(q^{-1})$ and $B(q^{-1})$ and the density function $\mu(\beta,\alpha)$ are assumed to be unknown and need not to be identified. The adaptive control method will be employed.

4.1 Some Preliminaries

Define the new variable

$$s(k) = C(q^{-1})(y(k) - y_d(k)), \tag{12}$$

where $C(q^{-1})$ is a Schur polynomial defined by

$$C(q^{-1}) = 1 + c_1 q^{-1} + c_n q^{-2}. \tag{13}$$

It is obvious that $lim_{k\to\infty} s(k) = 0$ implies $lim_{k\to\infty}(y(k) - y_d(k)) = 0$.

Now, consider the polynomial equation

$$C(q^{-1}) = A(q^{-1}) + q^{-1}F(q^{-1}), \tag{14}$$

where $F(q^{-1})$ is in the following form

$$F(q^{-1}) = f_0 + f_1 q^{-1}. \tag{15}$$

Thus, the parameters in $F(q^{-1})$ can be uniquely determined.

By operating the both sides of (14) on $y(k)$ and employing (2), it gives

$$C(q^{-1})y(k+1) = B(q^{-1})u(k) + F(q^{-1})y(k). \tag{16}$$

Substituting the Preisach model into (16) yields

$$C(q^{-1})y(k+1) = \phi^T(k)\theta + \sum_{i=0}^{1}\int_P b_i\mu(\beta,\alpha)\gamma_{\beta,\alpha}[v](k-i)d\beta d\alpha \tag{17}$$

with

$$\phi(k) = [y(k), y(k-1)], \tag{18}$$

$$\theta = [f_0, f_1]. \tag{19}$$

When the parameters are all known, it is obvious that, if the input $v(k)$ is chosen such that

$$\begin{aligned}&\int_P b_0\mu(\beta,\alpha)\gamma_{\beta,\alpha}[v](k)d\beta d\alpha\\ &= -\int_P b_1\mu(\beta,\alpha)\gamma_{\beta,\alpha}[v](k-i)d\beta d\alpha - \phi^T(k)\theta + C(q^{-1})y_d(k+1) + \varepsilon s(k),\end{aligned} \tag{20}$$

where ε is the weighting factor in the range $0 < \varepsilon < 1$, then the output tracking can be asymptotically achieved.

4.2 Adaptive Control Design

Since the parameters of the polynomials $A(q^{-1})$ and $B(q^{-1})$ are unknown, the parameters in $F(q^{-1})$ can not be obtained. Furthermore, since the density function $\mu(\beta,\alpha)$ is unknown in practice, the control law in (20) can not be derived.

In the following, we try to estimate the parameters f_i and the unknown functions $b_i\mu(\beta,\alpha)$. Let

$$\hat{\theta}(k) = \left[\hat{f}_0(k), \hat{f}_1(k)\right]^T \tag{21}$$

denote the estimate of θ at the $k-th$ step, and $\hat{\mu}_i(\beta,\alpha,k)$ denote the estimate of $b_i\mu(\beta,\alpha)$ at the $k-th$ step for fixed β and α.

Define

$$\tilde{\theta}(k) = \hat{\theta}(k) - \theta, \;\; \tilde{\mu}_i(\beta,\alpha,k) = \hat{\mu}_i(\beta,\alpha,k) - b_i\mu(\beta,\alpha) \tag{22}$$

and the estimation error as

$$\begin{aligned} e(k) &= C(q^{-1})y(k) - \phi^T(k-1)\hat{\theta}(k-1) \\ &\quad + \sum_{i=0}^{1}\int_P \hat{\mu}(\beta,\alpha,k-1)\gamma_{\beta,\alpha}[v](k-1-i)d\beta d\alpha. \end{aligned} \tag{23}$$

Now, substituting (17) into (23) yields

$$e(k) = -\phi^T(k-1)\tilde{\theta}(k-1) - \sum_{i=0}^{1}\int_P \tilde{\mu}(\beta,\alpha,k-1)\gamma_{\beta,\alpha}[v](k-1-i)d\beta d\alpha. \tag{24}$$

For simplicity, define

$$D(k-1) = \phi^T(k-1)\phi(k-1) + 2S, \tag{25}$$

where S is the area of region P. The estimates $\hat{\theta}(k)$ and $\hat{\mu}_i(\beta,\alpha,k)$ are updated by the following adaptive laws with constraints

$$\hat{\theta}(k) = \hat{\theta}(k-1) + \rho\frac{e(k)\phi(k-1)}{1+D(k-1)}, \tag{26}$$

$$\hat{\mu}_0(\beta,\alpha,k) = \mid \hat{\mu}_0(\beta,\alpha,k-1) + \rho\frac{e(k)\gamma_{\beta,\alpha}[v](k-1)}{1+D(k-1)} \mid, \tag{27}$$

$$\hat{\mu}_1(\beta,\alpha,k) = \hat{\mu}_1(\beta,\alpha,k-1) + \rho\frac{e(k)\gamma_{\beta,\alpha}[v](k-2)}{1+D(k-1)}, \tag{28}$$

where ρ is the adaptation gain satisfying $0 < \rho < 2$, the initial condition $\hat{\mu}_0(\beta,\alpha,0)$ should be chosen such that $\hat{\mu}_0(\beta,\alpha,0) > 0$ and $\int_P \hat{\mu}_0(\beta,\alpha,0)d\beta d\alpha < \infty$.

Lemma 1. *For the estimated parameters, the following properties are valid.*

(1). $\hat{\theta}(k)$ and $\int_P \hat{\mu}_i^2(\beta,\alpha,k)d\beta d\alpha$ are uniformly bounded.

(2). $\sum_{k=1}^{\infty} \frac{e^2(k+1)}{1+D(k)} < \infty$.

(3). $lim_{k\to\infty} \frac{e^2(k+1)}{1+D(k)} = 0$.

(4). For any positive finite integer υ,

$\sum_{k=\upsilon}^{\infty} \|\hat{\theta}(k) - \hat{\theta}(k-\upsilon)\|_2^2 < \infty$,

$\sum_{k=\upsilon}^{\infty} \int_P \left(\hat{\mu}_i^2(\beta,\alpha,k) - \hat{\mu}_i^2(\beta,\alpha,k-\upsilon)\right)^2 d\beta d\alpha < \infty$.

Proof: The lemma can be proved by taking the difference of the Lyapunov function defined by

$$\Gamma(k) = \tilde{\theta}^T(k)\tilde{\theta}(k) + \sum_{i=0}^{1} \int_P \tilde{\mu}_i^2(\beta,\alpha,k) d\beta d\alpha.$$

For the input range $[v_{min}, v_{max}]$, suppose the saturation output of the integral

$$\int_P \hat{\mu}_0(\beta,\alpha,k)\gamma_{\beta,\alpha}[v](k) d\beta d\alpha \tag{29}$$

be $\underline{W}_{sat}$ and $\bar{W}_{sat}$, which can be calculated as in (10) and (11). For simplicity, define

$$\begin{aligned} W(k) = &- \int_P \hat{\mu}_1(\beta,\alpha,k)\gamma_{\beta,\alpha}[v](k-1) d\beta d\alpha \\ &- \phi^T(k)\hat{\theta}(k) + C(q^{-1})y_d(k+1) + \varepsilon s(k), \end{aligned} \tag{30}$$

which is an avaiable signal at step k. Based on the method proposed in Section III, a signal $v^*(k)$ can be derived such that

$$\int_P \hat{\mu}_0(\beta,\alpha,k)\gamma_{\beta,\alpha}[v^*](k) d\beta d\alpha = W(k). \tag{31}$$

The control input is determined as

$$v(k) = v^*(k). \tag{32}$$

4.3 Stability Analysis

In this subsection, the discussion is based on the assumption $\underline{W}_{sat}(k) \le W(k) \le \bar{W}_{sat}(k)$.

By (30)-(32), it gives

$$\phi^T(k)\hat{\theta}(k) + \sum_{i=0}^{1} \int_P \hat{\mu}_i(\beta,\alpha,k)\gamma_{\beta,\alpha}[v](k-i) d\beta d\alpha = C(q^{-1})y_d(k+1) + \varepsilon s(k). \tag{33}$$

From (24) and (33), it yields

$$\begin{aligned} &\phi^T(k)\theta + \sum_{i=0}^{1} \int_P b_i \mu(\beta,\alpha)\gamma_{\beta,\alpha}[v](k-i) d\beta d\alpha \\ &= C(q^{-1})y_d(k+1) + \varepsilon s(k) + e(k+1). \end{aligned} \tag{34}$$

By substituting (34) into (17) and using (12), the variable $s(k+1)$ can be expressed as

$$s(k+1) = \varepsilon s(k) + e(k+1) + \xi(k). \tag{35}$$

By combining (2), (34) and (35), the closed-loop system can be described by

$$\begin{bmatrix} A(q^{-1}) & -q^{-1}B(q^{-1}) & 0 \\ F(q^{-1}) & B(q^{-1}) & -\varepsilon \\ 0 & 0 & q-\varepsilon \end{bmatrix} \begin{bmatrix} y(k) \\ u(k) \\ s(k) \end{bmatrix} = \begin{bmatrix} 0 \\ 1 \\ 1 \end{bmatrix} (e(k+1)+\xi(k)) + \begin{bmatrix} 0 \\ 1 \\ 0 \end{bmatrix} C(q^{-1}) y_d(k+1). \tag{36}$$

Based on the equation (36), the stability of the closed loop system can be analyzed.

Theorem 1. *Consider the system (2) and (7) controlled by input (32). If there exists an integer $K > 0$ such that $\underline{W}_{sat}(k) \le W(k) \le \bar{W}_{sat}(k)$ for all $k > K$, then all the signals in the closed loop are uniformly bounded and $lim_{k\to\infty} e(k) = 0$. Furthermore, $lim_{k\to\infty}(y(k) - y_d(k)) = 0$*

Proof: The proof is omitted.

4.4 Experimental Results

In the experiment, the sampling period is chosen as 0.001 second, the control purpose is to drive the stage to track the signal $y_m(k) = 8sin(2\pi \times 0.001k)\mu m$. By using the fact that μ_1 is very small and k is very large, it can be shown that $b_0 + b_1 q^{-1}$ is a Hurwitz polynomial. Thus, the control algorithm proposed in Subsection C of this section can be applied.

The control input is shown in Figure 5. The position tracking error is shown in Figure 6, where the error in the steady state is within $0.08\mu m$. It can be seen that good tracking of the nano-stage is achieved.

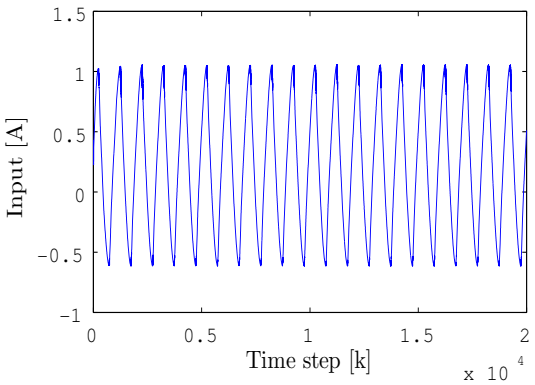

Fig. 5. The adaptive control input

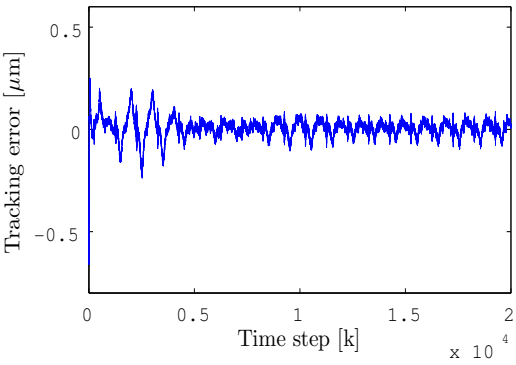

Fig. 6. The output tracking error

5 Conclusions

This paper has discussed the high precision control for the nano-stage driven by megnetostrictive actuator. The hysteresis relation between the input current and the generated force in the megnetostrictive actuator is described by Preisach model. For the derivation of the control input, an implicit inverse of the Preisach hysteresis model is given. In the control design, only the parameters (which are generated from the parameters of the stage and the density function of the Preisach hysteresis model) directly needed in the formulation of the controller have been adaptively estimated online. The control input has been derived by using the estimated parameters and the implicit inverse of the Preisach hysteresis model. The proposed controller assures the stability and zero position tracking error of the nano-stage. Experimental results show the effectiveness of the proposed algorithm.

References

1. Adly, A.A., Mayergoyz, I.D., Bergqvist, A.: Preisach modeling of magnetostrictive hysteresis. J. Appl. Phys. 69(8), 5777–5779 (1991)
2. Banks, H.T., Smith, R.C.: Hysteresis modeling in smart material systems. J. Appl. Mech. Eng. 5, 31–45 (2000)
3. Brokate, M., Sprekels, J.: Hysteresis and Phase Transitions. Springer, New York (1996)
4. Chen, X., Su, C.Y., Fukuda, T.: Adaptive control for the systems preceded by hysteresis. IEEE Transactions on Automatic Control 53(4), 1019–1025 (2008)
5. Croft, D., Shed, G., Devasia, S.: Creep, hysteresis, and vibration compensation for piezoactuators: atomic force microscopy application. ASME J. Dyn. Syst., Meas., and Contr. 123, 35–43 (2001)
6. Cross, R., Krasnosel'skii, A.M., Pokrovskii, A.V.: A time-dependent Preisach model. Physica B 306, 206–210 (2001)
7. Guyer, R.A., McCall, K.R., Boitnott, G.N.: Hysteresis, discrete memory and nonlinear wave propagation in rock. Physica Review Letters 74, 3491–3494 (1994)
8. Gorbet, R.B., Morris, K., Wang, D.W.L.: Passivity-based stability and control of hysteresis in smart actuators. IEEE Trans. on Control Systems Technology 9(1), 5–16 (2001)

9. Iyer, R.V., Shirley, M.: Hysteresis parameter identification with limited experimental data. IEEE Transactions on Magnetics 40(5), 3227–3239 (2004)
10. Krasnosel'skii, M.A., Pokrovskii, A.V.: Systems with Hysteresis. Springer, New York (1989)
11. Krejci, P., Kuhnen, K.: Inverse control of systems with hysteresis and creap. Proc. Inst. Elect. Eng. Control Theory Appl. 148, 185–192 (2001)
12. Kuhnen, K., Krejci, P.: Compensation of complex hysteresis and creep effects in piezoelectrically actuated systems - A new Preisach modeling approach. IEEE Transactions on Automatic Control 54(3), 537–550 (2009)
13. Moheimani, S.O.R., Goodwin, G.C.: Guest editorial introduction to the special issue on dynamics and control of smart structures. IEEE Trans. on Control Systems Technology 9, 3–4 (2001)
14. Natale, C., Velardi, F., Visone, C.: Identification and compensation of preisach hysteresis models for magnetostrictive actuators. Physica B 306, 161–165 (2001)
15. Mayergoyz, I.D.: Mathematical Models of Hysteresis. Springer, New York (1991)
16. Smith, R.: Smart Material Systems: Model Development. SIAM, Philadelphia (2005)
17. Su, C.Y., Wang, Q., Chen, X., Rakheja, S.: Adaptive variable structure control of a class of nonlinear systems with unknown Prandtl-Ishlinskii hysteresis. IEEE Trans. on Automatic Control 50(12), 2069–2074 (2005)
18. Tao, G., Kokotovic, P.V.: Adaptive control of plants with unknown hysteresis. IEEE Trans. on Aut. Contr. 40, 200–212 (1995)
19. Tao, G.: Adaptive Design and Analysis. Wiley-Interscience (2003)
20. Tan, X., Baras, J.S.: Modeling and control of hysteresis in magnetostrictive actuators. Automatica 40(9), 1469–1480 (2004)
21. Visintin, A.: Differential Models of Hysteresis. Springer, New York (1994)
22. Webb, G.V., Lagoudas, D.C., Kurdila, A.J.: Hysteresis modeling of SMA actuators for control applications. J. Intell. Mater. Syst. Struct. 9(6), 432–448 (1998)

Development of a Parallel-Kinematic High-Speed XY Nanopositioning Stage

Chun-Xia Li, Guo-Ying Gu, Mei-Ju Yang, and Li-Min Zhu

State Key Laboratory of Mechanical System and Vibration, School of Mechanical Engineering, Shanghai Jiao Tong University, 200240, China
{chunxia19881226,guguoying,yangmeixianglian,zhulm}@sjtu.edu.cn

Abstract. This paper presents a parallel-kinematic high-speed XY nano-positioning stage driven by piezoelectric stack actuators. With the purpose to achieve high resonance frequencies and a relatively large travel range, four special flexure modules are used to provide large stiffness. A symmetric configuration is adopted for the designed stage to reduce the cross-coupling between two axes and restrict parasitic motions as well. Static and dynamic analysis of the stage is performed respectively, and the dimensional optimization is carried out on the basis of static and dynamic models to maximize the first resonance frequency of the stage. Finite-element analysis (FEA) is utilized to confirm the effectiveness of the design. The FEA results show that the stage has good static and dynamic performances, which are well validated by the experiments. According to the experimental results, the stage is capable of a workspace of $11.2\mu m \times 11.6\mu m$ with positioning resolution of 3 nm. Besides, the resonance frequencies of the stage are over 13.6 kHz with the cross-coupling between two axes lower than -44 dB. It is clearly demonstrated that the stage has high resonance frequencies, relatively large travel range and nearly decoupled performance in two axes.

Keywords: Compliant mechanism, parallel-kinematic positioner, nanopositioning, piezoelectric stack actuator, finite-element analysis.

1 Introduction

With the capabilities of nanometer positioning accuracy, nanoposioning stages are widely used in many industrial applications, such as scanning probe microscopy (SPM) [1], [2], lithography [3], [4], nano-manipulation and manufacturing [5], [6], and biological science [7], [8]. Flexure mechanisms, which have advantages of no friction, no backlash, compact and monolithic structure, and ease of fabrication, are usually employed in nanopositioning stages to provide smooth motions by their elastic deformation. The piezoelectric actuators (PZTs) are widely used to drive flexure mechanisms due to their advantages of ultra-high resolution, fast response and large stiffness.

Recently, high-speed nanopositioning stages is increasingly required [9], [10], [11], especially in the fields of high-throughput nano-manufacturing and biological molecules studying. Many high-speed nanopositioning stages have been

J. Lee et al. (Eds.): ICIRA 2013, Part II, LNAI 8103, pp. 678–689, 2013.

developed during the past several years [1], [2], [9], [12], [13]. These stages can be classified into two categories: the serial-kinematic positioners (SKPs) and the parallel-kinematic positioners (PKPs). SKPs usually adopt a structure with one-degree-of-freedom nanopositioner nested in another one [2]. However, the high resonance frequency can be only achieved in one axis and the SKPs generally have disadvantages of cumulative error and parasitic motion. Compared with SKPs, PKPs can achieve high resonance frequencies for both axes. Furthermore, there is no cumulative error for PKPs and it is easy to measure and correct for the parasitic motion. PKPs can also be developed with low-coupling or decoupling performance when appropriately designed [14], [15]. Recently, the PKPs are widely applied in high-speed nanopositioning stages [1], [9], [13]. To improve the mechanical resonance frequency, most of the stages are made compact and rigid. However, the increase in stiffness results in the reduction of the stage's maximum travel range, as they are contradictive. As reported in [13], the stage has a relatively large resonance frequency of 8.9 kHz for X- and Y-axis, with a small travel range of $6.5\mu m \times 6.6\ \mu m$. There is a PKP with both high resonance frequency (22 kHz) and large scanning range ($13\mu m \times 13\mu m$) [1]. However, there are 8 PZTs used in X- and Y-axis arranged in a push-pull configuration, which would cost high-power voltage amplifiers to drive these PZTs. Thus, trade-off between stiffness and scanning range has to be made during PKPs' design. Besides, the mechanical structure also needs to be designed carefully as the scaling up of flexures' dimensions brings in undesired parasitic motion and cross-coupling. The low cross-coupling or decoupling PKPs tend to own low mechanical resonance frequency. An example was presented in [9]. This positioner has decoupled performance in X- and Y-axis and restricted parasitic rotations in XY plane, but the first resonance frequency is relatively low (approximately 8 kHz).

This paper presents a parallel-kinematic piezo-actuated XY nanopositioning stage for high-speed and high-precision positioning and tracking. The development of the stage is intended to achieve high resonance frequencies while keeping a relatively large travel range, low parasitic motion, and low cross-coupling. To obtain the objective, four special flexure modules are adopted to provide large stiffness. They are arranged symmetrically around the end-effector to restrict the parasitic motion and cross-coupling. Finite-element analysis (FEA) and experimental results are also presented to verify the effectiveness of the development. The remainder of the paper is organized as follows. Section 2 presents the detailed mechanical design and analysis of the stage. The dimensional optimization is presented in section 3 with the purpose to maximize the first resonance frequency of the stage. FEA and experiments are respectively carried out to evaluate the performance of the stage in Section 4 and Section 5. Finally, Section 6 concludes this paper.

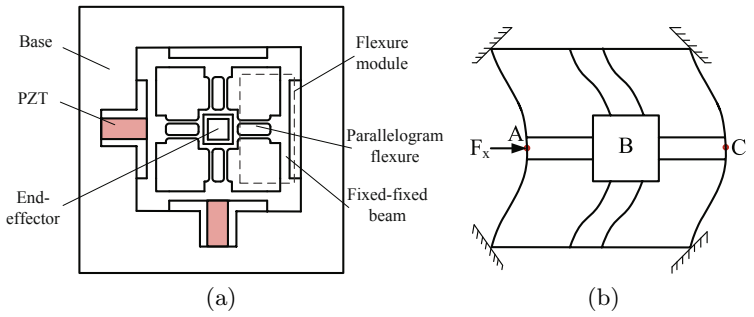

Fig. 1. The XY nanopositioning Stage. (a) Mechanical structure of the stage. (b) Simplified schematic representation of the deformed stage when X-axis is actuated.

2 Mechanical Design and Analysis of the Stage

2.1 Mechanical Design

Fig. 1(a) illustrates the monolithic compliant mechanical structure of the developed parallel-kinematic stage. The compliant mechanical structure consists of an end-effector and four flexure modules. The four flexure modules array symmetrically around the end-effector and connect it to the base. Each flexure module comprises a fixed-fixed beam and a parallelogram flexure. When the stage is actuated in the X-axis as shown in Fig. 1(b), the translational motion of the end-effector is provided by the deformation of fixed-fixed beams in X-axis, and accommodated by the parallelogram flexures in Y-axis. The parallelogram flexures in X-axis undergo pure translational motion with the end-effector. The process is similar when the stage is actuated in Y-axis. Due to the symmetric mechanical structure, the stiffness and dynamic performances in X- and Y-axis of the stage are the same. The symmetric structure also restrict parasitic motion and reduce cross-coupling between two axes, which would be verified in the following development.

In order to ensure that the stage has good performance, a center-thickened beam (CT beam, see Fig. 2(a)) is utilized to act as the fixed-fixed beam in the stage. Compared with the commonly used constant rectangular cross section beam (CRCS beam, see Fig. 2(b)), the CT beam has several advantages. When the stage is actuated in one direction (e.g. in the X-axis), a CRCS beam would cause the undesired bend of parallelogram flexure besides translational motion (as depicted in rectangular d1 in Fig. 2(d)). In addition, the parallelogram flexures in Y-axis apply bending moment on the fixed-fixed beams in the same flexure module, leading to the twisting of fixed-fixed beams (as shown in rectangular d2 in Fig. 2(d)). The phenomenon above may result in unexpected cross-coupling when the other axis is actuated at the same time. As a CT beam has larger stiffness than the CRCS beam when the dimensional parameters are the same, the disadvantages caused by CRCS beam can be avoided (as shown in rectangular c1 and c2 in Fig. 2(c)).

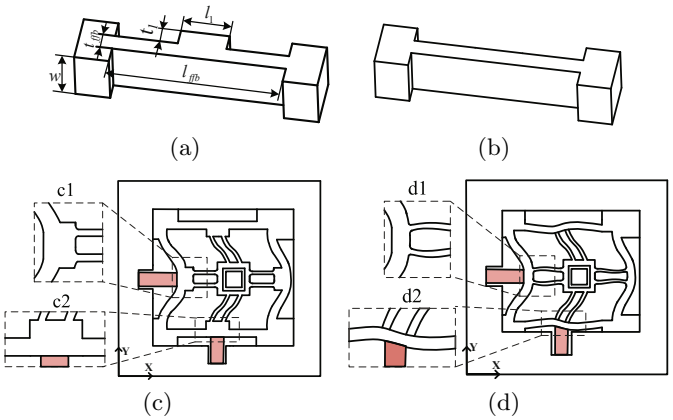

Fig. 2. Fixed-fixed beam design. (a) CT beam. (b) CRCS beam. (c) Flexure deformation using CT beam. (d) Flexure deformation using CRCS beam.

Considering the achievable stiffness, structural frequency and tolerance to manufacturing error, two corner-filleted beams are adopted to compose the parallelogram flexure.

2.2 Static Analysis

When the stage is actuated in the X-axis by force F_x at Point A as shown in Fig. 1(b), the axial deformation of parallelogram flexures in X-axis can be ignored as the flexures are rigid in axial direction. Then, we can obtain that displacement Δx_A of point A, displacement Δx of the end-effector, and displacement Δx_C of point C are equal, i.e.$\Delta x_A = \Delta x_C = \Delta x$. Based on the work-energy theorem, the work done by the actuated force is equal to the strain energy stored in the fixed-fixed beams and parallelogram flexures. Suppose that the stiffness of fixed-fixed beam is K_{ffb}, and the stiffness of parallelogram flexure is K_{pf}. The following equation can be derived

$$\frac{1}{2}F_x\Delta x_A = \frac{1}{2}K_{ffb}{\Delta x_A}^2 + \frac{1}{2}K_{pf}\Delta x^2 \cdot 2 + \frac{1}{2}K_{ffb}{\Delta x_C}^2 \tag{1}$$

If K_x is used to represent the stiffness of the stage in X-axis, it can be defined as the ratio of a load F_x and the resulting displacement of the end-effector Δx. Considering Eq. (1), K_x can be expressed as

$$K_x = 2(K_{ffb} + K_{pf}) \tag{2}$$

Similarly, the stiffness in Y-axis K_y can be obtained, which is equal to K_x.

The stiffness of the fixed-fixed beam and parallelogram flexure can be derived by using Castigliano's second theorem. For a fixed-fixed beam with force F_{ffb} applied at the middle of the beam as shown in Fig. 3(a), the deformation along

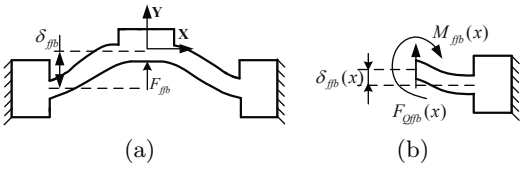

Fig. 3. Fixed-fixed beams. (a) Fixed-fixed beam shown with load and displacement. (b) Detailed loads at cross section x.

X-axis is so small that the axial force along X-axis is ignored to simplify the analysis. Hence, the strain energy is

$$U_{ffb} = U_{bending} + U_{shear} = \int_{-l_{ffb}/2}^{l_{ffb}/2} [\frac{M_{ffb}(x)^2}{2EI_{ffb}(x)} + k\frac{F_{Q\,ffb}(x)^2}{2GA_{ffb}(x)}]\, dx \quad (3)$$

where $M_{ffb}(x)$ and $F_{Q\,ffb}(x)$ (as shown in Fig. 3(b)) are the bending moment and shear force applied at the cross section (coordinated by x), l_{ffb} is the length of the fixed-fixed beam, $t_{ffb}(x)$ is the thickness, w is the height (see Fig. 2(a)), $A_{ffb}(x) = wt_{ffb}(x)$ is the cross-sectional area of the fixed-fixed beam, $I_{ffb}(x) = \frac{1}{12}wt_{ffb}(x)^3$ is the second moment of inertia about Z-axis, E is Young's modulus of beam material, G is the shear modulus, and k is a coefficient related to the shape of cross section(for a rectangular cross section $k = 1.2$).

Applying Castigliano's second theorem, the displacement of the fixed-fixed beam's center δ_{ffb} can be obtained, and the the stiffness of fixed-fixed beam k_{ffb} is achieved afterwards, as follows

$$\delta_{ffb} = \frac{\partial U_{ffb}}{\partial F_{ffb}}; \quad K_{ffb} = \frac{F_{ffb}}{\delta_{ffb}}\ . \quad (4)$$

For a parallelogram flexure, it is composed of two corner-filleted beams. The stiffness of the parallelogram flexure K_{pf} is the sum of each single corner-filleted beam's stiffness K_{spf}, i.e. $K_{pf} = 2K_{spf}$. For K_{spf}, it is also obtained by using Castigliano's second theorem, as addressed for K_{ffb}.

2.3 Dynamic Analysis

In this work, Lagrange's equation is used for the dynamics modeling of the stage. The displacements of the end-effector in X-axis and Y-axis are chosen as the generalized coordinates of the stage, i.e. $q = [\Delta x,\ \Delta y]^T$.

The kinetic energy of the stage is the summation of the energy of fixed-fixed beams, parallelogram flexures, and the end-effector, expressed as

$$T = T_{ffb} + T_{eft} + T_{pf} = \frac{1}{2}M_{ex}\Delta\dot{x}^2 + \frac{1}{2}M_{ey}\Delta\dot{y}^2 \quad (5)$$

where M_{ex} and M_{ey} are the total equivalent mass of the stage in X- and Y-axis with $M_{ex} = M_{ey} = 2m_{e-ffb} + m_{eft} + 2m_{pf} + 2m_{e-pf}$.

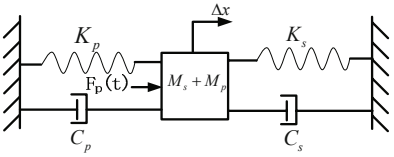

Fig. 4. Dynamic model of the system

The total potential energy of the stage is

$$V = V_{ffb} + V_{pf} \ = \frac{1}{2}K_x \Delta x^2 + \frac{1}{2}K_y \Delta y^2 \tag{6}$$

Using the Lagrange's equation for the undamped free vibration of the developed stage

$$\frac{d}{dt}\frac{\partial T}{\partial \dot{q}_i} - \frac{\partial (T - V)}{\partial q_i} = 0 \tag{7}$$

the dynamics equation of the XY stage can be derived as

$$\begin{bmatrix} M_{ex} & 0 \\ 0 & M_{ey} \end{bmatrix} \begin{pmatrix} \Delta \ddot{x} \\ \Delta \ddot{y} \end{pmatrix} + \begin{bmatrix} K_x & 0 \\ 0 & K_y \end{bmatrix} \begin{pmatrix} \Delta x \\ \Delta y \end{pmatrix} = 0 \tag{8}$$

Since $\mathbf{K} = diag(K_x,\ K_y)$ and $\mathbf{M} = diag(M_x,\ M_y)$ are diagonal matrixes, it can be demonstrated that the two axes of the stage are decoupled. Solve the characteristic equation, and then the natural frequencies of the mechanical structure can be calculated out, i.e.

$$|\mathbf{K} - \mathbf{M}\lambda_i| = 0; \quad f_i = (1/2\pi)\sqrt{\lambda_i} \tag{9}$$

In the above analysis, the dynamics behavior of PZTs is not considered. When the PZT is taken into account, a lumped mass-spring model can be used to describe the dynamic performance for one axis of the stage, as shown in Fig. 4. The dynamics equation of each axis is

$$(M_s + M_p)\Delta \ddot{x} + (C_s + C_p)\Delta \dot{x} + (K_s + K_p)\Delta x = F_p(t) \tag{10}$$

where $M_s (M_s = M_{ex} = M_{ey})$, M_p, C_s, C_p, $K_s (K_s = K_x = K_y)$, and K_p are, respectively, the equivalent mass, damping and stiffness of the stage and PZT. $F_p(t)$ is the actuating force of the PZT. As the damping of the system is negligible, the fundamental natural frequency of the whole system in X-axis and Y-axis is approximately calculated by

$$\bar{f}_i = \frac{1}{2\pi}\sqrt{\frac{K_s + K_p}{M_s + M_p}} \tag{11}$$

3 Dimensional Optimization

The objective is to design a stage with high resonance frequencies (no less than 8 kHz without PZTs), large workspace (over $10\mu m \times 10\ \mu m$) and decoupled performance. The first two vibration modes should occur in the two actuation directions and they are expected to be as high as possible since they are directly related to the dynamic performance of the stage. To achieve the desired workspace, two Noliac NAC 2021-H12 piezoelectric stack actuators ($7\text{mm} \times 7mm \times 12mm$, 1050 nF) are chosen for the stage. The free stroke, stiffness and blocking force of the actuator are 14.7 μm, 140 N/μm, and 2060 N, respectively. To ensure high resonance frequencies, aluminum 7075 is chosen as body material.

The dimensions are optimized to maximize the first resonance frequency f of the mechanical structure, and the dimensions to be optimized are l_{ffb}, t_{ffb}, l_{spf}, and t_{spf}. The constraints of the optimization are described as follows.

1) Workspace of the stage: The designed maximum workspace of the stage $\Delta L_s \times \Delta L_s$ should be larger than the objective value, i.e.

$$\Delta L_s = \frac{K_p \Delta L_{nom} - F_{pre}}{K_s + K_p} > 10.5\mu m \tag{12}$$

where ΔL_{nom} is the maximum nominal displacement of the PZT, F_{pre} is the preload applied on the PZT chosen as 200N (recommended by the manufacturer), and the designed displacement threshold is conservatively chosen as $10.5\mu m$.

2) Maximum stress: The maximum stress generated inside the compliant mechanical structure should always be kept within the maximum allowable stress of the material.

$$\sigma_{\max -ffb} = \alpha \frac{12\Delta d_{\max -ffb} E t_{ffb}}{l_{ffb}^2} \leq [\sigma] = \frac{\sigma_y}{n} \tag{13}$$

$$\sigma_{\max -spf} = \alpha \frac{3\Delta d_{\max -spf} E t_{spf}}{l_{spf}^2} \leq [\sigma] \tag{14}$$

where α is the stress concentration factor chosen as 2, $\Delta d_{\max -ffb}$ and $\Delta d_{\max -spf}$ are the maximum displacement of the fixed-fixed beam and single parallelogram flexure ($\Delta d_{\max -ffb} = \Delta d_{\max -spf} = \Delta L_s$), σ_y is the yield stress of the material, and n is the safety factor chosen as 2.

3) Stiffness of the fixed-fixed beam and parallelogram flexure: The stiffness of the fixed-fixed beam has to be much larger than the stiffness of parallelogram flexure to ensure the decoupled performance. Meanwhile, the stiffness of the parallelogram flexure shouldn't be too small, i.e.

$$20K_{pf} > K_{ffb} > 10K_{pf} \tag{15}$$

4) Ranges of parameters: The thickness (w) of the stage is chosen as $10mm$ to guarantee the stage's stiffness in Z-axis. After finite element analysis over a wide range of parameters, the size of rectangular lump in the fixed-fixed beam is chosen as $8.42mm \times 3mm$ and the corner radius of parallelogram flexure

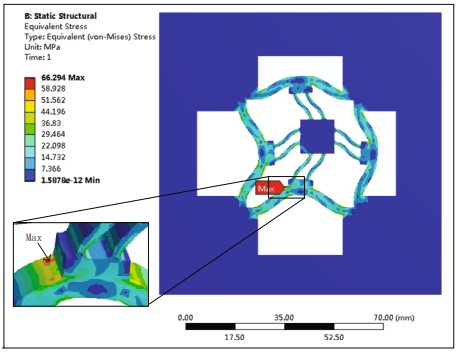

Fig. 5. Von Mises stress distribution under maximum axtuating force

is chosen as $1mm$. Other dimensions are chosen as: $30mm \leq l_{ffb} \leq 45mm$, $1.5mm \leq t_{ffb} \leq 5mm$, $10mm \leq l_{spf} \leq 15mm$, $0.8mm \leq t_{spf} \leq 1.5mm$.

The optimization is carried out with the "fmincon" function in MATLAB, and the optimal results are $l_{ffb} = 30mm$, $t_{ffb} = 2.76mm$, $l_{spf} = 10mm$, $t_{spf} = 1mm$. Based on the optimized dimensions, the output parameters of the stage are calculated out by (2), (9), (11) and (12). The results show that the stage has a travel range of 10.7 $\mu m \times 10.7$ μm and stiffness of 33.5 $N/\mu m$ in both X and Y-axis. Besides, the first resonance frequencies without and with PZTs are 8844 Hz and 15691 Hz, respectively.

4 Finite-Element Analysis (FEA)

FEA is generally used to analyze the static and dynamic performance of flexure-guided stages during the design process [4], [13], [14], [15]. In this work, FEA is carried out using ANSYS WorkBench software to evaluate the performance of the optimized stage. The output stiffness, workspace, stress distribution, and dynamic behavior of the stage are studied.

The FEA results show that the displacement of the end-effector increases linearly with the increasing actuating force. The stiffness is obtained by the slope of the force-displacement line and it is 31.4 $N/\mu m$ for both axes. There is an error of between 6.69 % between the theoretical value and FEA results. The reason lies in that the stiffness is overestimated in the theoretical analysis. Considering (12), the maximum displacement of the stage along one axis is 10.8 μm.

To test the stress distribution, an input force $F = [600N, 600N]$ is applied to the stage. The maximum von Mises stress is 66.3 MPa occurring near the rectangular lump in the PZT-actuated fixed-fixed beam as shown in Fig. 5, which is much lower than the allowable stress ($250MPa$) of the body material.

The first six modal shapes of the stage by FEA are shown in Fig. 6. the first two modes are the translational modes. Besides, the resonance frequencies of the

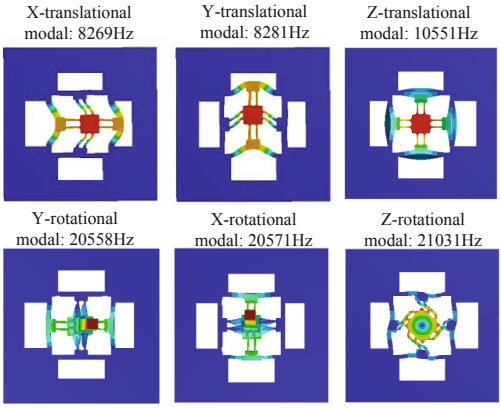

Fig. 6. Modal analysis results by FEA

first two modes are almost the same because of the symmetric structure of the stage. The corresponding theoretical values are both 8844 Hz. It can be seen that there is approximately 6.95% difference between the theoretical values and the FEA results. It may be caused by the overestimated stiffness of the structure in theoretical analysis. This problem can also be found in other reported works such as [4], [14].

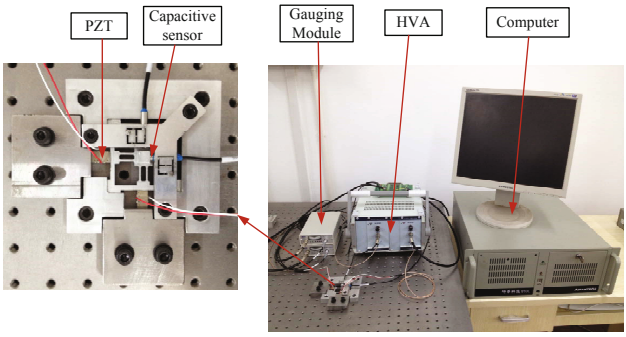

Fig. 7. Experimental setup of the XY stage

5 Experiments

5.1 Experimental Setup

A prototype of the XY stage is fabricated using WEDM technique with aluminum 7075, and an experimental platform as shown in Fig. 7 is established to verify the development. The two pre-selected PZTs are mounted to drive the

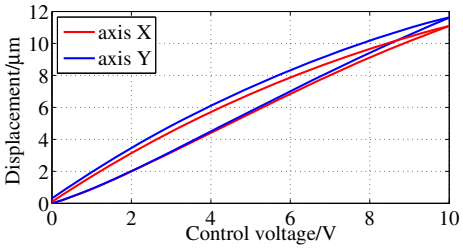

Fig. 8. Experimental results of the maximum travel range

stage, and a dual-channel high-voltage amplifier (HVA) is used to provide excitation voltage for the PZTs. Two capacitive sensors (Probe 2823 and Gauging Module 8810 from MicroSense) are adopted to measure the displacements of the end-effector in X- and Y-axis. A dSPACE-DS1103 board equipped with the 16-bit analog to digital converters (ADCs) and 16-bit digital to analog converters (ADCs) is utilized to output the excitation voltage for the HVA and capture the real-time displacement information from the Gauging Module.

5.2 Static and Dynamic Tests

The static displacements of the stage in X-axis and Y-axis under different driving voltage are tested, as shown in Fig. 8. The maximum travel range is $11.2\mu m \times 11.6\mu m$, which agrees with the FEA result. Besides, a 5nm stepwise response is performed with proportional-integral controller to test the positioning resolution of the stage and the results are shown in Fig. 9. Obviously the positioning resolution of the stage is 3 nm, which demonstrate that the stage achieves nm-level positioning.

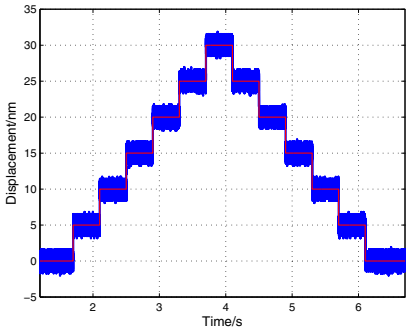

Fig. 9. 5nm stepwise response of Y axis

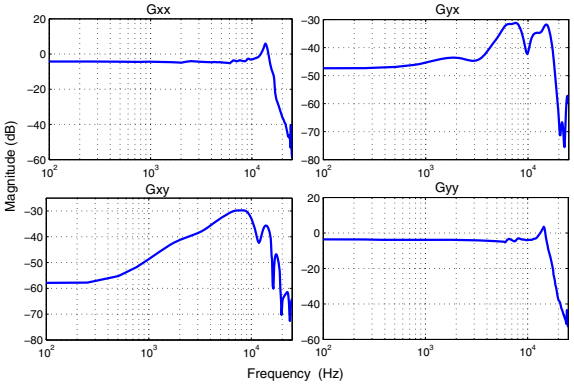

Fig. 10. Measured frequency responses of the nanopositioning stage

To obtain the dynamic characteristic of the stage, a band-limited white noise signal with amplitude of 100 mV and frequency range of 1 $Hz - 20\ kHz$ is used to excite the stage. The inputs are in volts, and the outputs are in micrometers. Fig. 10 plots the frequency responses of the system. The first resonant peak of the stage in two axes occurs at 13.6 kHz and 14.4 kHz respectively, while the theoretical value is calculated out as 15.7 kHz. This may be caused by machining imperfections, PZTs assembling error and manufacturing tolerances. The magnitudes of the cross-coupling terms G_{yx} and G_{xy} are only about -44 dB and -55 dB less than that of G_{xx} and G_{yy} respectively, which indicates that the cross-coupling between two axes of the developed stage is tiny.

6 Conclusions

In this paper, a piezo-driven high-speed XY nanopositioning stage with parallel kinematic mechanisms is developed. The stage is designed to achieve a high resonance frequencies and a relatively large travel range while keeping low cross-coupling and low parasitic motion. To obtain the goal, four special flexure modules and a symmetric structure are used. Theoretical analysis are adopted to model the developed stage and dimensional optimization is utilized to optimize the stage. FEA and experiments are carried out to validate the stage. The results show that the stage has high resonance frequencies, a relatively large travel range and decoupled motion. In the future, advanced control algorithms will be implemented to realize the high-bandwidth nanopositioning control.

Acknowledgment. This work was supported in part by the National Natural Science Foundation of China under Grant 91023047, the Science and Technology Commission of Shanghai Municipality under Grant 11520701500, the Shu Guang Project supported by Shanghai Municipal Education Commission under Grant 10SG17, and China Postdoctoral Science Foundation under Grant 2013M530193.

References

1. Schitter, G., Astrom, K.J., DeMartini, B.E., Thurner, P.J., Turner, K.L., Hansma, P.K.: Design and modeling of a high-speed AFM-scanner. IEEE Transaction of Control System Technology 15(5), 906–915 (2007)
2. Leang, K.K., Fleming, A.J.: High-speed serial-kinematic AFM scanner: Design and drive considerations. Asian Journal of Control 11(2), 144–153 (2009)
3. Choi, B.J., Sreenivasan, S.V., Johnson, S., Colburn, M., Wilson, C.G.: Design of orientation stages for step and flash imprint lithography. Precision Engineering 25, 192–199 (2001)
4. Choi, K.B., Lee, J.J.: Passive compliant wafer stage for single-step nano-imprint lithography. Review of Scientific Instruments 76, 075106.1–075106.6 (2005)
5. Culpepper, M.L., Anderson, G.: Design of a low-cost nano-manipulator which utilizes a monolithic, spatial compliant mechanism. Precision Engineering 28, 469–482 (2004)
6. Verma, S., Kim, W.J., Shakir, H.: Multi-axis maglev nanopositioner forprecision manufacturing and manipulation applications. IEEE Transactions on Industrial Applications 41(5), 1159–1167 (2005)
7. Ando, T., Kodera, N., Maruyama, D., Takai, E., Saito, K., Toda, A.: A high-Speed atomic force microscope for studying biological macromolecules in action. The Japan Society of Applied Physics 41(7B), 4851–4856 (2002)
8. Kim, H.Y., Ahn, D.H., Gweon, D.G.: Development of a novel 3-degrees of freedom flexure based positioning system. Review of Scientific Instruments 83, 055114.1–055114.11 (2012)
9. Polit, S., Dong, J.Y.: Development of a High-Bandwidth XY Nanopositioning Stage for High-Rate Micro/Nano Manufacturing. IEEE/ASME Transactions on Mechatronics 16(4), 722–724 (2011)
10. Ando, T.: High-speed atomic force microscopy coming of age. Nanotechnology 23, 062001.1–062001.27 (2012)
11. Yong, Y.K., Moheimani, S.O.R., Kenton, B.J., Leang, K.K.: Invited Review Article: High-speed flexure-guided nanopositioning: Mechanical design and control issues. Review of Scientific Instruments 83, 121101.1–121101.22 (2012)
12. Kenton, B.J., Leang, K.K.: Design and control of a three-axis serial-kinematic high-bandwidth nanopositoner. IEEE/ASME Transactions on Mechatronics 17(2), 356–369 (2012)
13. Yong, Y.K., Bhikkaji, B., Moheimani, S.O.R.: Design, Modeling and FPAA-based Control of a High-speed Atomic Force Microscope Nanopositioner. IEEE/ASME Transactions on Mechatronics 18(3), 1060–1071 (2013)
14. Lai, L.J., Gu, G.Y., Zhu, L.M.: Design and control of a decoupled two degree of freedom translational parallel micro-positioning stage. Review of Scientific Instruments 83(4), 045105.1–045105.17 (2012)
15. Li, Y.M., Huang, J.M., Tang, H.: A Compliant Parallel XY Micromotion Stage With Complete Kinematic Decoupling. IEEE Transactions on Automation Science and Engineering 9(3), 538–553 (2012)

Dynamical Behavior of Redundant Thrusting Mechanical System in Shield Machines with Various Grouping Strategies

Chunzhang Zhao, Haidong Yu, and Yong Zhao

Shanghai Key Laboratory of Digital Manufacture for Thin-walled Structures, Shanghai Jiao Tong University, 200240 Shanghai, China

Abstract. The thrusting system of shield machines is consisted of multiple hydraulic cylinders which are usually divided into four groups. The dynamical behavior of shield is closely dependent on the grouping strategies. In this context, the thrusting system is equivalent as a redundant actuating parallel mechanism. Two grouping strategies are used as 4147 and 4345 for sixteen hydraulic cylinders. The dynamical model of shield was established by using Newton-Euler method. The dynamical behavior is investigated considering the two grouping methods. The results show that the fluctuations of velocities and displacements of shied are obviously different for the two grouping strategies when the fraction of soft soil on the excavating face is changed. The grouping strategies should be determined based on the complex geological structures in order to reduce the blockage accidents

Keywords: redundant parallel mechanism, grouping strategies, dynamic behavior, complex geological structures.

1 Introduction

Shield machine is widely used in the infrastructure construction projects, which is a kind of technology-intensive equipment including mechanical, electrical, hydraulic facilities, measurement, manipulation system and other functions. The thrusting system is one of the most important parts in shield machines. It takes on the promoting mission. The thrusting system is a redundant parallel driving mechanism composed of the multiple propulsion hydraulic cylinders. Packet control is now used to reduce the complexity of the equipment operation. Different grouping strategies have great influences on the dynamical behavior of thrusting system. The thrusting system could offer strong propulsive force and bending moment[1]. Abnormal internal forces caused by motion error [5] sometimes cause the instability of the propulsive force and bending moment, which easily causes some accidents such as locked-rotor, block stop, snake-like tunneling. Therefore, it is significant to analyze the dynamical behavior of the thrusting system with different grouping strategies.

During cutting process, the cutting load is transferred to the thrusting system through cutterhead and affects its dynamical performance. Different factors, such as cutters, geology conditions, cutting parameters, cutter arrangement positions, could

J. Lee et al. (Eds.): ICIRA 2013, Part II, LNAI 8103, pp. 690–699, 2013.

impact cutting load and cutting performance[2,3]. So it is necessary to build the load equivalent model for different cutters in compound geology to reduce the complexity of dynamical model of the thrusting system.

In this paper, a dynamical model of the redundant thrusting system in shield machine is proposed. The force transmission behavior of the thrusting system with different grouping strategiesis analyzed. A load equivalent model for cutterhead which contains different kinds of cutters is given. Based on above analysis, a simulation model is built by using MATLAB/SIMULINK. The dynamical behavior of the thrusting system with different grouping strategies is investigated numerically.

2 Dynamical Model of the Thrusting System with Various Grouping Strategies

In this section, the dynamics model of redundant thrusting system in shield machine is proposed by the Newton-Euler method. Then grouping strategy is introduced to form a new dynamics formulation.

2.1 Dynamical Model of the Redundant Thrusting System

Figure 2.1 shows the lumped parameter model of the thrusting system. Origin O of fixed coordinate system $O-xyz$ is located at the geometric center of fixed platform and its x axis is vertical to the platform. The float coordinate system $O'-x'y'z'$ and the fixed coordinate system $O-xyz$ are connected by hydraulic cylinders. Axes of fixed coordinate system and float coordinate system are parallel at the initial moment, respectively. When the thrusting system works in the tunnel, the thrusting system only has three degrees of freedom: translation along tunneling direction x axis, rotations around the y axis and the z axis in the excavated section.

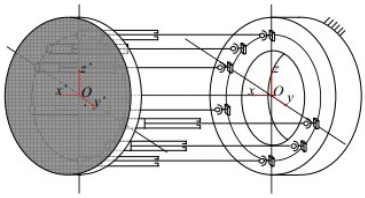

Fig. 2.1. The lumped parameter model of the thrusting system

Based on Newton formulation[4], a general dynamics equation for the thrusting system moving along x axis is given by:

$$\boldsymbol{m}\ddot{\boldsymbol{x}} = \mathbf{e}_1 \cdot \left(\mathbf{F}_e + \sum_{i=1}^{16} \mathbf{F}_d^i \right) \tag{1}$$

Where $\mathbf{e_1} = [1 \quad 0 \quad 0]$ is the basis vector, $\mathbf{F}_e$ is the external force acting on cutters, $\mathbf{F}_d^i$ is the driving force provided by thrusting hydraulic cylinders.

For rotations around y axis and z axis, if the moment of inertia of shield machine is assumed to be centrosymmetric, which means x, y, z are the principal axes of inertia, the inertia matrix in fixed coordinate system is defined as:

$$\mathbf{I}_p = \mathbf{A}_{bp}^T \mathbf{I}_p^{'} \mathbf{A}_{bp} = \mathbf{A}_{bp}^T \begin{bmatrix} I_{xx} & & \\ & I_{yy} & \\ & & I_{zz} \end{bmatrix} \mathbf{A}_{bp} \tag{2}$$

Using Euler formulation, one has the thrusting system rotation formulation[4].

$$\mathbf{I}_p \dot{\boldsymbol{\omega}}_p + \boldsymbol{\omega}_p \times \left(\mathbf{I}_p \boldsymbol{\omega}_p \right) = \mathbf{M}_e + \sum_{i=1}^{16} \mathbf{F}_d^i \times \mathbf{r}_p^i \tag{3}$$

Here $\mathbf{M}_e$ is the external torque on cutterhead, $\mathbf{F}_d^i \times \mathbf{r}_p^i$ is the driven torque of every thrusting hydraulic cylinder. $\mathbf{A}_{bp}$ is the direction cosine matrix between the float coordinate system $O'-x'y'z'$ and the fixed coordinate system $O-xyz$. When $O'-x'y'z'$ revolves θ_y and θ_z degree around y axis and z axis with respect to $O-xyz$, $\mathbf{A}_{bp}$ can be written as:

$$\mathbf{A}_{bp} = \begin{bmatrix} \cos\theta_y \cos\theta_z & -\cos\theta_y \cos\theta_z & \sin\theta_y \\ \sin\theta_z & \cos\theta_z & 0 \\ -\sin\theta_y \cos\theta_z & \sin\theta_y \sin\theta_z & \cos\theta_y \end{bmatrix} \tag{4}$$

The angular velocity of cutterhead in fixed coordinate system $O-xyz$ is given by:

$$\boldsymbol{\omega}_p = \mathbf{A}_{bp} \mathbf{L} \begin{bmatrix} 0 & \dot{\theta}_y & \dot{\theta}_z \end{bmatrix}^T \tag{5}$$

Where $\mathbf{L} = \begin{bmatrix} \cos\theta_y \cos\theta_z & \sin\theta_z & 0 \\ -\cos\theta_y \sin\theta_z & \cos\theta_z & 0 \\ \sin\theta_y & 0 & 1 \end{bmatrix}$. Substitute $\mathbf{L}$ and $\mathbf{A}_{bp}$ into Eq. 5, the angular velocity of cutterhead can be rewritten as:

$$\boldsymbol{\omega}_p = \begin{bmatrix} 1 & 0 & \sin\theta_y \\ 0 & 1 & 0 \\ 0 & 0 & \cos\theta_y \end{bmatrix} \begin{bmatrix} 0 \\ \dot{\theta}_y \\ \dot{\theta}_z \end{bmatrix} \tag{6}$$

By differentiating $\boldsymbol{\omega}_p$ with respect to time, the angular acceleration is given by:

$$\dot{\boldsymbol{\omega}}_p = \begin{bmatrix} 1 & 0 & \sin\theta_y \\ 0 & 1 & 0 \\ 0 & 0 & \cos\theta_y \end{bmatrix} \begin{bmatrix} 0 \\ \ddot{\theta}_y \\ \ddot{\theta}_z \end{bmatrix} + \begin{bmatrix} \cos\theta_y \cdot \dot{\theta}_y \cdot \dot{\theta}_z \\ 0 \\ -\sin\theta_y \cdot \dot{\theta}_y \cdot \dot{\theta}_z \end{bmatrix} \tag{7}$$

Substitute Eq.4, 6, 7 into Eq. 3, and use the basis vector $\mathbf{e}_{2,3} = \begin{bmatrix} 0 & 1 & 0 \\ 0 & 0 & 1 \end{bmatrix}$, the system Euler formulation can be rewritten as:

$$\begin{aligned} &\mathbf{e}_{2,3} \begin{bmatrix} 1 & 0 & \sin\theta_y \\ 0 & 1 & 0 \\ 0 & 0 & \cos\theta_y \end{bmatrix} \begin{bmatrix} 0 \\ \ddot{\theta}_y \\ \ddot{\theta}_z \end{bmatrix} + \mathbf{e}_{2,3} \begin{bmatrix} \cos\theta_y \cdot \dot{\theta}_y \cdot \dot{\theta}_z \\ 0 \\ -\sin\theta_y \cdot \dot{\theta}_y \cdot \dot{\theta}_z \end{bmatrix} + \mathbf{e}_{2,3} \boldsymbol{\omega}_p \times \left(\mathbf{I}_p \boldsymbol{\omega}_p \right) \\ &= \mathbf{e}_{2,3} \left(\mathbf{M}_e + \sum_{i=1}^{16} \mathbf{F}_d^i \times \mathbf{r}_p^i \right) \end{aligned} \tag{8}$$

Combine Eq. 1 and Eq. 8, the dynamics formulation of the thrusting system can be written as:

$$\hat{\mathbf{I}} \begin{bmatrix} \ddot{x} \\ \ddot{\theta}_y \\ \ddot{\theta}_z \end{bmatrix} + \hat{\mathbf{K}}(\dot{\mathbf{q}}) - \hat{\mathbf{M}}(\mathbf{q}) - \mathbf{F} = 0 \tag{9}$$

Where $\mathbf{q} = \begin{bmatrix} x & \theta_y & \theta_z \end{bmatrix}^T$ is the general coordinates of the system.

2.2 Grouping Strategies of the Thrusting System in Shield Machine

The thrusting system is commonly composed of multiple hydraulic cylinders, which can be regarded as a redundant parallel mechanism according to its working principle. As Fig. 2.2 shows:

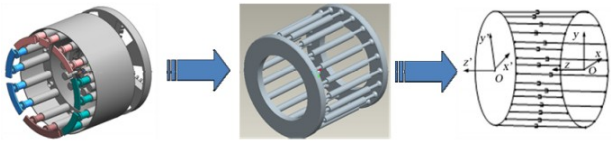

Fig. 2.2. Equivalent model of thrusting system of shield machine

The mapping features between the load in each chain and the load on cutterhead is given by[6]:

$$\mathbf{G} \cdot \mathbf{f} = \mathbf{F}_e = \begin{bmatrix} \mathbf{F} \\ \mathbf{M} \end{bmatrix} \tag{10}$$

$$\mathbf{G} = \begin{bmatrix} \boldsymbol{n}_1 & \cdots & \boldsymbol{n}_{16} \\ \boldsymbol{r}_1 \times \boldsymbol{n}_1 & \cdots & \boldsymbol{r}_{16} \times \boldsymbol{n}_{16} \end{bmatrix} \tag{11}$$

Where $\mathbf{F}_e$ is the resistance load on cutterhead, $\mathbf{F}$ and $\mathbf{M}$ are the external force and bending moment respectively, $\mathbf{f}$ is the load in each chain. $\mathbf{G}$ is the force transmission matrix between cutterhead and drive cylinders, known as the force Jacobi matrix. Using the relationship between force and velocity Jacobi matrix, Eq. 10 can be rewritten as:

$$\mathbf{J}^T \mathbf{f} = \mathbf{F}_e \tag{12}$$

The thrusting system achieves movements such as traveling in straight, pitching, turning left and right during tunneling process. So cutterhead mainly suffers from bending momentsin up-down and left-right directions. Because the effect of gravity, a common hydraulic cylinder grouping strategy is left-right symmetrical and upper-lower unsymmetrical, and lower group has more hydraulic cylinders than upper group. Figure 2.3 shows two typical group strategies (4-1-4-7 group strategy and 4-3-4-5 group strategy) of 16 hydraulic cylinders. For 4-1-4-7 group strategy, hydraulic cylinders are evenly distributed, and the angle between two hydraulic cylinders is 22.5°. While 4-3-4-5 group strategy is unevenly distributed, the angle between hydraulic cylinders is 27°in F_2, and is 18°between others.

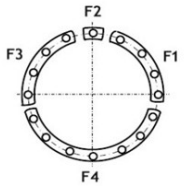

(a)4-1-4-7 Group strategy

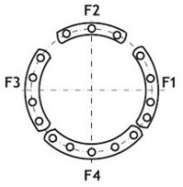

(b)4-3-4-5 Group strategy

Fig. 2.3. Two different group strategies for 16 hydraulic cylinders

Since all hydraulic cylinders in one group have the same oil pressure, a matrix $\mathbf{Q}$ is introduced, which describes grouping strategies. For the two groups in figure 2.3, $\mathbf{Q}$ is defined as:

$$\mathbf{Q}_{4147} = \begin{bmatrix} 1 & 1 & 1 & 1 & 0 & 0 & 0 & 0 & 0 & 0 & 0 & 0 & 0 & 0 & 0 & 0 \\ 0 & 0 & 0 & 0 & 1 & 0 & 0 & 0 & 0 & 0 & 0 & 0 & 0 & 0 & 0 & 0 \\ 0 & 0 & 0 & 0 & 0 & 1 & 1 & 1 & 1 & 0 & 0 & 0 & 0 & 0 & 0 & 0 \\ 0 & 0 & 0 & 0 & 0 & 0 & 0 & 0 & 0 & 1 & 1 & 1 & 1 & 1 & 1 & 1 \end{bmatrix}^T \tag{13}$$

$$\mathbf{Q}_{4345}=\begin{bmatrix}1&1&0&0&0&0&0&0&0&0&0&0&0&0&1&1\\0&0&1&1&1&0&0&0&0&0&0&0&0&0&0&0\\0&0&0&0&0&1&1&1&1&0&0&0&0&0&0&0\\0&0&0&0&0&0&0&0&0&1&1&1&1&1&0&0\end{bmatrix}^{T} \tag{14}$$

So the force mapping feature for redundant mechanism with grouping strategies can be written as:

$$\mathbf{J}^{T}\mathbf{Q}\mathbf{f}=\mathbf{F}_{e} \tag{15}$$

Where $\mathbf{f}=[f_1 \quad f_2 \quad f_3 \quad f_4]^T$ is the load on hydraulic cylinders in each group. The equivalent Jacobi matrix is:

$$\hat{\mathbf{J}}^{T}=\mathbf{J}^{T}\mathbf{Q} \tag{16}$$

Therefore the load on single hydraulic cylinder in each branched chain is:

$$\mathbf{f}=\left(\hat{\mathbf{J}}^{T}\right)^{-1}\mathbf{F}_{e} \tag{17}$$

Substitute Eq. 17 into dynamic Eq.9, dynamical model with different grouping strategies of the thrusting system can be obtained. With certain initial condition, one can get the dynamic response of the thrusting system by solving the differential equations.

3 Resistance Load Model of Cutterhead Excavating in Compound Geologic Conditions

According to load characteristics of single dick cutter and drag bit, the calculating model of total bending moment and torque on composite cutterhead is given by [7]:

$$\begin{cases}\boldsymbol{M}_{x}=\sum_{0}^{n}\boldsymbol{F}_{Ti}\cdot l_{ix}+\sum_{0}^{m}\boldsymbol{F}_{Rj}\cdot l_{jx}\\ \boldsymbol{M}_{y}=\sum_{0}^{n}\boldsymbol{F}_{Ti}\cdot l_{iy}+\sum_{0}^{m}\boldsymbol{F}_{Rj}\cdot l_{jy}\\ \boldsymbol{T}_{\text{total}}=\sum_{i=1}^{n_D}\boldsymbol{F}_{Ni}\cdot r_{i}+\sum_{j=1}^{n_R}\boldsymbol{F}_{Vj}\cdot r_{j}\end{cases} \tag{18}$$

Where r_i and r_j are distance between positions of the $i^{\text{-th}}$cutter and the $j^{\text{-th}}$hob and the center of cutter head. l_{ix} and l_{iy} are distance between the $i^{\text{-th}}$ cutter and x, y axes. l_{jx} and l_{jy} are distance between the $j^{\text{-th}}$disc cutter and x, y axes. n and m are numbers of drag bits and disc cutters in soil and rock, and they vary with the rotation position of cutterhead. For typical drag bits and disc cutters, the normal and the tangential force can be calculated as:
For disc cutters:

$$\boldsymbol{F}_V = TR\cos^{-1}\left(\frac{R-P}{R}\right)C\sqrt{\frac{\sigma_c^2\sigma_t S}{\sqrt{RT}}}\cos\frac{\phi}{2} \tag{19}$$

$$\boldsymbol{F}_R = \boldsymbol{F}_V\tan\left(\frac{\phi}{2}\right) \tag{20}$$

Where $\boldsymbol{F}_V$ is the normal force, $\boldsymbol{F}_R$ is the tangential force, P is the penetration depth, R is the radius of disc cutter, σ_c is the uniaxial compressive strength of rock, σ_t is the tensile strength of rock, S is the distance between hobs, C is the cohesion factor of rock in shear fracture surface, T is the width of the blade.
For drag bits:

$$\boldsymbol{F}_T = \frac{\mathbf{C}_1 S_1}{A(\sin\theta + \mu_1\cos\theta)} \tag{21}$$

$$\boldsymbol{F}_N = \frac{\mathbf{C}_1 S_1(\cos\alpha - \mu_0\sin\alpha)}{B} \tag{22}$$

$$A = \frac{\cos\alpha - \mu_1\sin\theta}{\sin\alpha + \mu_1\cos\theta} + \frac{\cos\alpha - \mu_0\sin\theta}{\sin\alpha + \mu_0\cos\theta} \tag{23}$$

$$B = (\cos\alpha - \mu_1\sin\theta)(\sin\alpha + \mu_0\cos\theta) + (\cos\alpha - \mu_0\sin\theta)(\sin\alpha + \mu_1\cos\theta) \tag{24}$$

Where $\boldsymbol{F}_T$ is the normal force, $\boldsymbol{F}_N$ is the tangential force, μ_0 is the friction coefficient between cutter and soil contact surface, μ_1 is the friction coefficient of shear surface, $\mathbf{C}_1$ is the soil cohesion, α is the angle between shear fracture surface and cutting surface, θ is the rake angle of cutter, S_1 is the contact area between cutters and shear fracture surface.

4 Dynamical Simulation of Redundant Thrusting Mechanical System

A simulation model is built by using Matlab/Simulink[8]. The initial position of cutterhead is $(x,\theta_y,\theta_z)^T=(0,0,0)^T$, the initial rotation speed is $3\mathrm{r/min}$ and the simulation time is $200\mathrm{s}$.

4.1 Dynamical Performance of Shield Machine with Various Grouping Strategies

The excavating velocity characteristic of shield machine with two different group strategies (4345 and 4147) is shown in Fig. 4.1. The fluctuation of velocity with 4345 is bigger than that with 4147. The average fluctuationis smaller and the fluctuation frequency is more stable with 4345 than that with 4147 group strategy. Integrating two curves over time, tunneling distances under different group strategies can be calculated. The distance is $598.03\mathrm{m}$ with 4147 group strategy while it is $579.4\mathrm{m}$ with 4345. That means in $200\mathrm{s}$, shield machine can advance father with 4147 group strategy.

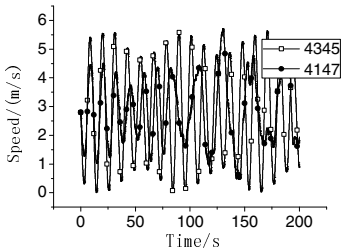

Fig. 4.1. Velocities of shield machine with different group strategies

The penetration depth of cutterhead with two group strategiesis shown in Fig. 4.2. The fluctuation of penetration depth with 4345 group strategy is stable. While with 4147 group strategy, the fluctuation is unstable and diffuse. In addition, the average fluctuation and amplitude increase with time and the fluctuation frequency decrease with time with 4147. This unstable status should be paid more attention in actual work.

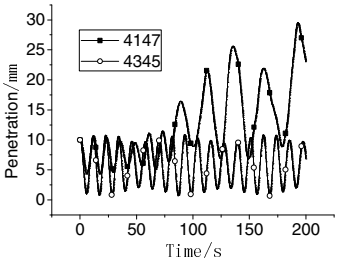

Fig. 4.2. Penetration of cutterhead in different group strategies

4.2 Dynamical Performance of Shield Machine in Compound Geology

The excavating velocity of shield machine with 4345 group strategy in various composite geologic structures (the ratio of soil is 20%, 40% and 60%) is shown in Fig. 4.3. When the ratio is 20%, the fluctuation behavior is stable. When the ratio is 40%, the amplitude of fluctuation becomes diffuse in the late and is bigger than that at 60%. When the ratio increases to 60%, the amplitude fluctuation comes back to stable.

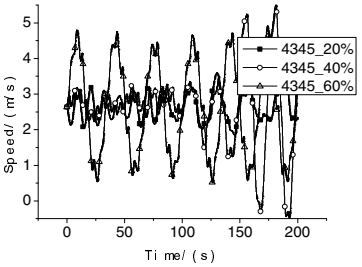

Fig. 4.3. Velocities of shield machine in different soil percentage

Figure 4.4 shows that when the ratio of soft soil is 20%, the penetration of cutter head is stable. When the ratio is up to 40%, the penetration is abnormal and has no fixed period. When the ratio is 60%, the penetration returns to periodic fluctuations and the period is about 3 times that of 60%.

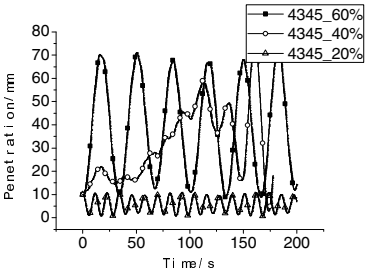

Fig. 4.4. Penetration of cutterhead in different soil percentage

5 Conclusions

In this context, an equivalent load model is developed. A dynamic model which contains different grouping strategies is built for the redundant thrusting system. By using MATLAB/SIMULINK software, dynamical behavior of shield machine is investigated.The conclusions are listed as follows:

1) In geological condition which contains 20% soft soil, the velocityis more stable with 4345 group strategy. While with 4147 group strategy, tunneling is more efficient at the beginning, and the fluctuation amplitude of velocity increase with time, fluctuations of penetration of cutter head is diffuse.

2) In geological condition which contains less soft soil, fluctuations of velocity and penetration of cutter head are stable. With the ratio of soft soil increases, fluctuations become abnormal and have no fixed period. When the percentage is bigger than 60%, fluctuations again has a stable periods, average fluctuations and amplitude get bigger.

Acknowledgements. The authors appreciate the financial support by the National Natural Science Foundation of China (51275292) and State Key Development Program of Basic Research of China (2013CB035403).

References

1. Cheng, H., Liu, G.F.: Advantages and dynamics of parallel manipulators with redundant actuation. Intelligent Robots and Systems 1, 171–176 (2001)
2. Innaurato, N., Oggeri, C., Oreste, P.P., Vinai, R.: Problems concerning cutting tool performance during TBM work: modelisation and testing of the rock underthe action of the tool. In: 29th ITA World Tunneling Congress, Amsterdam, pp. 12–17 (2003)
3. Bruland, A.: Hard rock tunnel boring. Doctoral thesis, Norwegian University of Science and Technology, Trondheim (1998)
4. Dasgupta, B., Choudhury, P.: A general strategy based on the Newton–Euler approach for the dynamic formulation of parallel manipulators. Mechanism and Machine Theory 34(6), 801–824 (1999)
5. Zhao, Y., Gao, F.: Dynamic formulation and performance evaluation of the redundant parallel manipulator. Robotics and Computer-Integrated Manufacturing 25(4-5), 770–781 (2009)
6. Gosselin, C.M.: Stiffness mapping for parallel manipulators. IEEE Transactions on Robotics and Automation 6(3), 377–382 (1990)
7. Zeng, X.X., Yu, H.D., Wang, H.: Equivalent load model on the cutterheadsof TBM excavating in heterogeneous geologic strata. Rock and Soil Mechanics 31(4), 1199–1203 (2010) (in Chinese)
8. Chen, J.: MATLAB Collection. Publishing House of Electronics Industry (2007) (in Chinese)

Cutters Layout Design of the Full-Face Rock Tunnel Boring Machine Based on Physical Programming

Xu Zhang*, Wei Sun, Junzhou Huo, and Jingxiu Ling

School of Mechanical Engineering, Dalian University of Technology,
116023 Dalian, China

Abstract. A cutters layout method of the full-face rock TBM is proposed in this paper, in which the technology requirements of the cutters layout are summarized, then the rock-broken volume estimation method for the non-equality cutters space is given and a nonlinear multi-objective cutters layout mathematical model with complex constraints is established, further, based on the coupling analysis of the multi-objectives and constraints of the mathematical model, a hierarchy solving strategy of polar radius and polar angle is given and physical programming is used to solve cutters layout design of the full-face rock TBM. Finally taking the some imported full-face rock TBM cutters layout design as an experimental example, compared with the computational results of the original layout design, the experimental results show that the proposed cutters layout mathematical model and corresponding solution strategy are feasible and effective.

Keywords: Full-face tunnel boring machine, Cutters layout, Cutters space, Design method, Physical programming.

1 Introduction

The full face rock tunnel boring machine (TBM) is a large and special engineering machine for tunnel boring that has been widely applied to subway projects, railway projects, highway projects and water-electricity projects. It is a very high cost machine. Disc cutters' layout design of the TBM is one of the key technologies to improve the global performance of a TBM [1], and it directly affects the boring performance, the service life, the main bearing of the cutter head, the vibration and the noise of the TBM. The main difficulties of disc cutters' layout design of the TBM lie in the combinational explosion of computational complexity, the engineering complexity, and the pragmatic approaches of engineering practices, and belongs to a multi-objective optimization problem with nonlinear constraints.

Three cutting forces are exerted on the tip of the disc cutter during excavation: the normal force, the rolling force and the side force. Many investigators have studied the cutting force models that can be used to calculate the the normal force and the rolling

* Corresponding Author: Zhang Xu, Ph.D., School of Mechanical Engineering, Dalian Univ. of Technology, Dalian 116024, P.R. China. E-mail: zhangxu_dlut@163.com

J. Lee et al. (Eds.): ICIRA 2013, Part II, LNAI 8103, pp. 700–709, 2013.

force. These models can be divided into two categories: the semi-theoretical model, based on tests and the theoretical analysis of the linear cutting machine (LCM), for example the Colorado School of Mines (CSM) model [1]; and the empirical model, which is based on the historical field performance of machines, for example the Norwegian Institute of Technology (NTH) model [2]. Gertsch [3] and Song [4] have systematically reviewed the present cutting force models. Rostami [5] adopted the regression analysis method and built the cutting force model based on the experimental data. In the above-mentioned models, the multi-factor cutting force models (e.g. CSM and NTH) are more widely accepted and applied in industry because all the effects of their ground conditions, rock properties, machine parameters, and operational and practical constraints can be accounted for.

The layout of the buckets, the blowholes and the manholes should be considered properly in the layout design of the disc cutters of the cutter head. The layout design of the disc cutters correlates with the forces exerted on the cutter head, the crushed rock mobility and the manufactural process of the cutter head, and it is a technically effective way to improve the boring performance of the TBM [6]. With the increasing complexity of the ground conditions and the practical constraints, the layout design of disc cutters is more difficult and more important, and has become an essential part of the design of a TBM. All successfully designed TBMs, with no exception, have successfully designed the disc cutters' layout. A typical case is the excavation of the Kranji tunnel in Singapore. During the excavation, it was found that the frequency of the ground change between the hard rocks and the residual soil was much higher than what had been expected. The highly abrasive and frequently changing mixed face ground caused high cutter wear, especially flat cutter wear. After reducing the number of disc cutters from 35 to 33 and increasing the cutter spacing of the normal cutter from 90mm to 100mm, it could be seen that the overall progress of the TBM utilization and the abrasion of cutters was clearly better than before[7].

The layout design of the disc cutters includes the disc cutters' spacing design and the disc cutters' plane (circumferential) layout design. Considersing the researches of the disc cutters' spacing design, many investigators adopted the numerical simulation method and the linear cutting machine (LCM) experimental method. Ozdemir[8] and Snowdon[9] used a V-profile disc cutter to do the cutting tests based on the LCM and found that when the cutting spacing was small, the resultant chip size was small too and the specific energy (SE) of the disc cutters was high. When the cutting spacing increased, the resultant chip size became larger and the SE of the disc cutters decreased to the minimum. As the cutting spacing continued to increase, the SE of the disc cutters also increased because the interaction among the disc cutters decreased. Based on the LCM test, CSM [6] systematically analyzed the cutting forces from the LCM testing with intact rock properties, cutting geometry, and cutter geometry and proposed a semi-theoretical computer model that could formulate the cutting forces exerted on tip of the disc cutter. This makes penetration rate prediction possible for a TBM in given rock conditions by using the formulation from the LCM testing. Gertsch [1] conducted a series of full-scale laboratory cutting tests by using a single disc cutter (with 432mm diameter and a constant cross-section profile) and a single rock type (a coarse-grained red granite). Specific energy (SE) considerations indicate

that a spacing of 76mm is close to the optimum in this hard, brittle crystalline rock. At this spacing, penetration has very little effect on SE. These results show why spacing near 76mm is commonly found on tunnel boring machines operating in hard rock. Although a great deal of preparation work needs to be done, this kind of physical experiment based on the LCM testing is very practical and can be used to determine the optimal cutting parameters, since it can improve the boring performance and reduce the costs. From 2005 to 2007, Gong Q M [10] adopted the discrete element method (DEM) to simulate the rock chipping process induced by two disc cutters and analyzed the influence of the difference of cutters' spacing on the penetration process by setting up a series of two dimensional UDEC models. Many significant conclusions were drawn from analyzing the simulation results. Moon [11] studied the rock cutting parameters by optimizing the ratio of spacing to penetration (S/P) and proposed that the optimal S/P was a linear function of the rock's brittleness and the width of the disc cutters.

After cutting spacing has been determined, the disc cutters are to be placed circumferentially on the plane of the cutter head. There are few published papers on the study of the disc cutters' circumferential layout in the literature. The CSM computing model can be used to design the circumferential layout and calculate the individual loads. Rostami [12] studied the methods of cutter head modeling for the hard rock TBM that had been a successful tool used by the industry at various levels of sophistication relative to the end use. These models are based on the estimation of the cutting forces and can be used for the cutter head design optimization as well as for the performance estimation. Zhang [13] studied the spiral layout rule of the disc cutters and gave out computational equations of the simplified cutter head force distribution. The disc cutters' layout design should meet the geometrical constraints and other performance constraints like the balance constraints and the assembly manufacturing requirements, etc. It is a complex engineering design problem that involves multidisciplinary knowledge. There is a need to establish a practical computational model for the disc cutters' layout, considering factors of the rock properties, the cutting parameters, the performance constraints and the cutting force model. And it is necessary that advanced computational methods should be studied and applied to solve the problem more efficiently.

Theories of the cutters' penetration into rocks, the disc cutters' force models and the cutting spacing have been widely studied, but there are only a few published researches on the disc cutters' layout design. In this study, according to the complex engineering technical requirements and the corresponding cutter head structure design requirements, a nonlinear multi-objective disc cutters' layout mathematical model with complex constraints and the corresponding multi-stage solution strategy is presented, and a numerical simulation method and a cooperative coevolutionary algorithm are utilized to solve the disc cutters' layout design problem. Finally, using the above-metioned proposed method, an instance of the disc cutters' layout design of a TBM is presented.

2 Problem Model of Cutters Layout Design of the TBM

As shown in Fig. 1 and Fig. 2, the discs are so arranged that they contact the entire cutting face in the concentric tracks when the cutter head turns. The distance of the cutting tracks and the discs are chosen depending on the rock type and the difficult level of cutting. The rotating cutter head presses the discs with high pressure against the rock face. The discs therefore make a slicing movement across the rock face. The pressure at the cutting edge of the disc cutters exceeds the compressive strength of the rock and locally grinds it. So the cutting edge of the disc pushes the rolling into the rock, until the advance force and the hardness of the rock are in balance. Through this displacement, described as net penetration, the cutter disc creates a high stress locally, which leads to long flat pieces of rock breaking off. The cutting forces mainly contain the normal force, the rolling force and the side force. Fig. 2 illustrates these three cutting forces that are exerted on the tip of the disc cutter during excavation. According to the related literature [12] and the practical engineers' experiences, the technical requirements of disc cutters' layout design can be summarized as follows[14]:

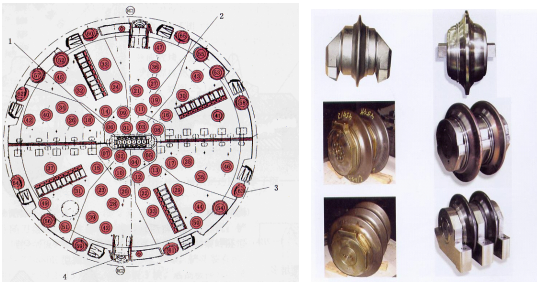

1-Center cutters; 2-Normal cutters; 3-Gauge cutters; 4-Reaming cutters.

Cutting tools

Fig. 1. The disc cutters' layout scheme and the cutting tools

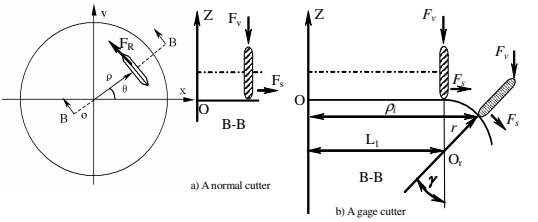

Fig. 2. Individual forces acting on a normal cutter and a gage cutter

① The amount of the eccentric forces of the whole system is expected to be as small as possible;

② The amount of the eccentric moments of the whole system is expected to be as small as possible;

③ The spacing of the disc cutters needs to be optimized, which means that the specific energy needed to cut off unit volume of rock is expected to be as small as possible;

④ Two adjacent disc cutters should crush the rock successively to maintain high cutting efficiency;

⑤ All the disc cutters should be contained within the cutter head, with no overlapping among the disc cutters;

⑥ The position error of the centroid of the whole system should not exceed an allowable value, and the smaller the better;

⑦ All the disc cutters should not interfere with manholes and buckets, respectively.

Suppose that the set of disc cutters to be located on the cutter head with radius equals to R is $\boldsymbol{CUTs} = \{ Cut_1, Cut_2, \ldots, Cut_n \}$, where n = total number of cutters. As shown in Fig. 1, all the disc cutters are simplified as circles in this study and are regarded as rigid bodies with uniform mass distribution. So the ith cutter can be denoted as $Cut_i\ (p_i, r_i)$, where $p_i = (r_i, \rho_i, \theta_i)^T \in R^3$ is the position of a reference point (the centroid of the object) of Cut_i in the coordinate system $oxyz$; $\rho_i \in (0, R)$ is the radius of the ith cutter from the center of the cutter head; $\theta_i \in [0, 2\pi)$ is the position angle of the ith cutter; $\gamma_i \in [0, \frac{\pi}{2})$ is the tilt angle of the ith cutter; r_i is the radius of the ith cutter. The masses and dimensions of all the disc cutters are given in advance, so p_i is the variable to be manipulated in the following procedure. Thus, a general disc cutters' layout scheme of a cutter head can be formulated as:

$$\mathrm{X} = \{x_1, x_2, \cdots, x_i, \cdots, x_n\},\ x_i = \{\rho_i, \theta_i, \gamma_i\} \tag{1}$$

Then based on the technical requirements, the mathematical model of the disc cutters' layout problem can be formulated as follows[14]:

$$\begin{aligned}
&\min_{\mathrm{X}\in\mathrm{D}} \mathrm{Y}=\mathrm{f}(\mathrm{X})=(\mathrm{f}_1(\mathrm{X}),\mathrm{f}_2(\mathrm{X}),\mathrm{f}_3(\mathrm{X})) \\
&s.t.\quad g_1(\mathrm{X}) = \sum_{i=0}^{n-1}\sum_{j=i+1}^{n} \Delta V_{ij} \le 0 \\
&\qquad g_2(\mathrm{X}) = \sum_{i=0,\,j=i+1}^{n-1} (S_{ij} - [S]) \le 0 \\
&\qquad g_3(\mathrm{X}) = \sum_{i=0}^{n-1} (\theta_{i+1} - \theta_i) \ge \Delta\theta \\
&\qquad g_4(\mathrm{X}) = \left| x_m - x_e \right| - \delta x_e \le 0 \\
&\qquad g_5(\mathrm{X}) = \left| y_m - y_e \right| - \delta y_e \le 0 \\
&\qquad g_6(\mathrm{X}) = \{\forall i \in \{1, \cdots, n\} : cut_i \cap OP \in \varnothing\}
\end{aligned} \tag{2}$$

3 Physical Programming Method for Cutters Layout Design

Linear physical programming is a simplified form of physical programming, in order to facilitate the practical application and burden reduce the computational intensity. Linear physical programming model is shown in fig. 3, the horizontal axis represents the value of the i-th(i=1~n_s) design target f_i, the vertical axis represents the value of preference function u_i, t_{is}^+ and t_{is}^- (s=1,2,…5) represent the boundary values of region limits of the i-th design target. t_{is}^+, t_{is}^- are constant of practical physical significance, the value of which is evaluated by the designer. There are four types of preference function for decision-makers to select in linear physical programming model and the physical meanings of them are: minimization (1S), maximization (1S), assessing point (3S), and assessing interval (4S). Decision-makers can express the internal criterion for certain design target by specifying ranges of different degrees of desirability. In the case of 1S, there are six preference ranges for 1S design metrics: highly desirable ($f_i \le t_{i1}^+$), desirable ($t_{i1}^+ \le f_i \le t_{i2}^+$), tolerable ($t_{i2}^+ \le f_i \le t_{i3}^+$), undesirable ($t_{i3}^+ \le f_i \le t_{i4}^+$), highly undesirable ($t_{i4}^+ \le f_i \le t_{i5}^+$), and unacceptable ($f_i > t_{i5}^+$).

The aggregate objective function is formed by combining the preference functions of all the soft metrics. The physical programming model takes the following form[15]

$$
\begin{aligned}
&\min_x \ U = \log_{10}\left\{\frac{1}{n_{sc}}\sum_{i=1}^{n_{sc}} u_i(f_i(x))\right\} \\
&\text{s.t.} \quad f_i(x) \le f_{i5} \qquad \text{(for class1-S)} \\
&\qquad\ f_i(x) \ge f_{i5} \qquad \text{(for class2-S)} \\
&\qquad\ f_{i5L} \le f_i(x) \le f_{i5R} \qquad \text{(for class 3-S and 4-S)} \\
&\qquad\ f_i(x) \le f_{iM} \qquad \text{(for class1-H)} \\
&\qquad\ f_i(x) \ge f_{im} \qquad \text{(for class2-H)} \\
&\qquad\ f_{im} \le f_i(x) \le f_{iM} \qquad \text{(for class 3-H and 4-H)} \\
&\qquad\ x_{jm} \le x_j \le x_{jM}
\end{aligned}
\tag{3}
$$

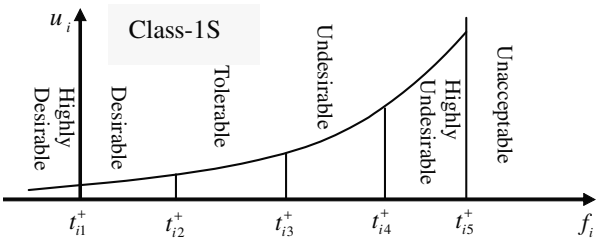

Fig. 3. Preference functions of the *i*-th design objective

The mathematical model of the cutters' plane layout problem based on physical Programming can be formulated as follows:

$$\begin{aligned} &\min_x \ f(x) = \log_{10}[\frac{1}{3}(u_1(f_1)+u_2(f_2)+u_3(f_3))] \\ &\text{s.t.} \qquad f_1(x) \le f_{15} \\ &\qquad\quad f_2(x) \le f_{25} \\ &\qquad\quad f_3(x) \le f_{35} \end{aligned} \tag{4}$$

4 Example

Taking the disc cutters' layout design of the full face rock TBM of a water tunnel project as a background[14], an application instance is presented. Forty-one disc cutters are needed to be located on the cutter head surface shown in Fig. 1. The relative parameters are as follows: (1) Rock physical properties: the rock is mainly in granite-based geology，the punch shear strength of rock τ =7~13(MPa)，the uniaxial compressive strength of rock σ_c =50~93.6 (MPa)，and the Brazilian tensile strength σ_t =2.14~4.0 (MPa). (2) Cutter head geometry: the cutter head radius R=4.015m，the rotational speed of cutter head ω=6(r/min)= 0.6283 rad/s，the mass of each cutter M=200kg，the diameter of each cutter D=483mm，the cutter tip width *T*=10mm, the cutter penetration *P*=7mm，and the cutter edge angle α = 1.5708 rad. The center cutter number n_1=8, the gage cutter number n_2=10, and the normal cutter number n_3=33. As mentioned earlier, locations of the eight center cutters are pre-determined by human experience. So in the optimization process, there are totally 43 cutters whose locations need to be decided. The technical requirements of the disc cutters' layout design are as follows：the expected centroid position of the cutter head x_e=0 mm, y_e=0 mm; the allowable centroid error of the whole system δx_e =5mm, δy_e =5mm; and the allowable angle difference $\Delta\theta$ =45°.

The types of preference function of each attribute are defined in Tab. 1. Performance indexes of the cutter head of the scheme obtained by physical programming are shown in Tab. 2. Overturning moment of the cutter head, M_v, was reduced dramatically. The stress distribution and the deformation distribution of the cutter head of the scheme obtained by physical programming are shown in Fig. 4. After optimization, the stress was reduced by 12%, and the stress was reduced by 25%.

Table 1. The region limits of designer's preference

	Class type	t_{i5}	t_{i4}	t_{i3}	t_{i2}	t_{i1}
$f_1(x)$	1-S	120	80	50	20	0
$f_2(x)$	1-S	120	80	50	20	0
$f_3(x)$	1-S	250	180	130	60	0

Table 2. Performance indexes of the optimal design by physical programming method

	M_v / *KN.m*	F_s /*KN*	x_m /*mm*	y_m /*mm*
Original design	154.840	11.558	-2.135	-0.221
PP design	0.852	5.369	-0.478	0.149

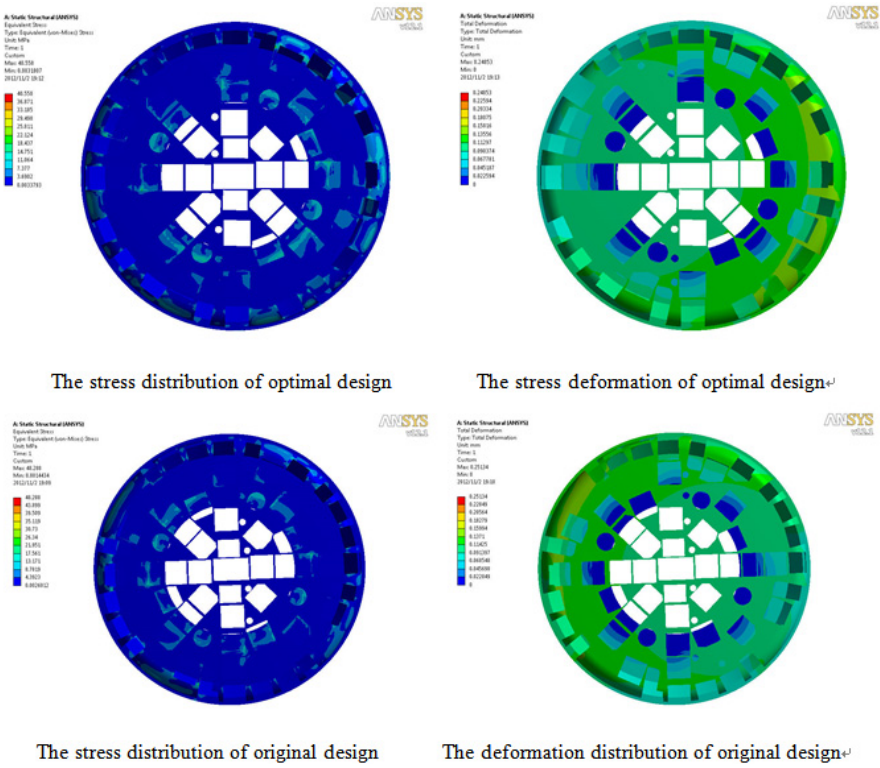

Fig. 4. The stress distribution and the deformation distribution of the cutter head of the scheme

5 Conclusions

Based on the complex technical requirements and the cutter head's geometry design requirements, this study formulates a multi-objective disc cutters' layout design model with multiple nonlinear constraints and presents a corresponding two-stage solution strategy that includes the disc cutters' spacing design and the disc cutters' plane layout design. A numerical simulation method based on the FEM theory is adopted to simulate the rock chipping process induced by three TBM disc cutters to determine the optimal cutter spacing. And the physical programming model is adopted to solve the disc cutters' plane layout problem. The application instance demonstrates the feasibility and effectiveness of the proposed method. The computational results show that the proposed method is quick in providing Pareto-optimal disc cutters' layout designs for engineers to choose from. The optimal design has been tested to be superior to the human experience design in some aspects.

Acknowledgments. This research was partially supported by National Natural Science Foundation of China under Grant No. 51005033, the Major State Basic Research Development Program of China (973 Program) under Granted No. 2013CB035402 and National Key Technologies R & D Program of Liaoning Province under Grant No. 2012220038.

References

1. Gertsch, R., Gertsch, L.: Disc Cutting Tests in Colorado Red Granite: Implications for TBM Performance Prediction. International Journal of Rock Mechanics and Mining Sciences 44, 238–246 (2007)
2. Rostami, J., Ozdemir, L.: Comparison between CSM and NTH Hard Rock TBM Performance Prediction Models. In: Proceedings of Institute of Shaft Drilling Technology (ISDT) Annual Technical Conference 1996, Las Vegas (1996)
3. Gertsch, R.E.: Rock Toughness and Disc Cutting. University of Missouri, Missouri (2000)
4. Song, K.Z., Yan, D.J.: Study Review on the Interaction between Disk Cutter and Rock. Journal of Railway Engineering Society 6, 66–69 (2005)
5. Rostami, J.: Development of a Force Estimation Model for Rock Fragmentation with Disc Cutters through Theoretical Modeling and Physical Measurement of Crushed Zone Pressure. Golden, Colorado (1997)
6. Rostami, J., Ozdemir, L.: Computer Modeling of Mechanical Excavators Cutterhead. In: Proceedings of the World Rock Boring Association Conference, Ontario (1996)
7. Zhao, J., Gong, Q.M.: Tunneling through A Frequency Changing and Mixed Ground: A Case History in Singapore. Tunneling and Underground Space Technology 22, 388–400 (2007)
8. Ozdemir, L., Wang, F.D.: Mechanical Tunnel Boring Prediction and Machine Design, Washington (1979)
9. Snowdon, R.A., Ryley, M.D.: A Study of Disc Cutting in Selected British Rocks. Journal of Rock Mechanics and Mining Sciences and Geomechanics Abstracts 19, 107–121 (1982)

10. Gong, Q.M., Zhao, J.: Numerical Simulation of Rock Fragmentation Process Induced by two TBM Cutters and Cutter Spacing Optimization. In: AITES-ITA 2006 Congress, Seoul, South Korea (2006)
11. Moon, T.: A Computational Methodology for Modeling Rock Cutting with A Discrete Element Method: Prediction of TBM Rock Cutting Performance. Colorado School of Mines (2006)
12. Qiao, S.S., Mao, C.J.: Full-face Rock Tunnel Boring Machine. Petroleum Industry Press, Beijing (2005)
13. Zhang, Z.H.: An Investigation in the Cutter Arrangement Rules for Tunneler Disk. Construction Machinery and Equipment 7, 24–25 (1996)
14. Huo, J.Z., Sun, W.: Optimal Disc Cutters Plane Layout Design of the Full-face Rock Tunnel Boring Machine (TBM) based on a Multi-objective Genetic Algorithm. Journal of Mechanical Science and Technology 24, 521–528 (2010)
15. Zhang, X., Sun, W.: Interval Multi-objective Optimization Design based on Physical Programming. Przeglad Elektrotechiczhy 88, 379–381 (2012)

Analysis of Multi-sensor Attitude Measurement System on TBM

Chuncao Zhang, Guoli Zhu, Jianbo Zhang, and Minghua Pan

School of Mechanical Science & Engineering,
Huazhong University of Science & Technology, Wuhan, China
{Chuncaozhang,pmh24}@163.com, glzhu@mail.hust.edu.cn,
zhangjianbo@hust.edu.cn

Abstract. It is well known that the real-time high accuracy attitude measurement is required during the tunnel construction. The vibration is caused by hard rock tunneling, which makes the inclinometer fail to work, and then the current system can not meet the demand of auto-guide control. In this paper, we describe the fusion and test of an optic fiber gyroscope and inclinometer based on multi-sensor fusion algorithm. The proposed multi-sensor is used for measuring the attitude of TBM(Tunnel Boring Machine),which can solve those problems. Inclinometer has the advantage of high accuracy output and gyro is not sensitive to vibrations. The system discusses fuse information from two sensors and develops the fusion algorithms. Firstly, stochastic error model of gyro is built on the basis of ARMA(auto regressive moving average) modeling. Secondly, the detail modeling of fuse information for multi-sensor is made by using Kalman filter, which estimates and compensates zero drift of gyro with the high accurate output of inclinometer. The attitude under the strong vibration is calculated by compensated gyro. Finally, using test results, it is shown that the multi-sensor information fusion algorithm is effective and improves the accuracy of attitude measurement. It ensures that the error of multi-sensor attitude measurement system is less than 2 milliradian under the static and dynamic state.

Keywords: Multi-sensor fusion, Inclinometer, Fiber optic gyroscope, Kalman filtering, TBM.

1 Introduction

The attitude measurement system, which can control the TBM and can directly affect the construction precision of the tunnel is an important part of the TBM. During the hard-rock tunneling, the strong vibration makes the sensor lose effectiveness, for example, the inclinometer sensor of laser target system is not able to work reliably under strong vibration. To ensure the TBM going along the designed tunnel path and get high-accuracy measurement of the attitude, it becomes an essential problem that we need to recognize and collect the attitude information of the tunneling process. Aiming at the above-mentioned issue, this paper integrated the characteristic of inclinometer and optic fiber gyroscope, proposed the multiple-sensor information fusion attitude measurement method.

J. Lee et al. (Eds.): ICIRA 2013, Part II, LNAI 8103, pp. 710–719, 2013.

The multiple-sensor fusion technology has developed rapidly and is applied widely in recent years. The available fusion algorithm includes: Kalman filtering,ARMA,multiple Bayesian estimation, neural network and fuzzy logic. In time domain the Kalman filtering algorithm has small quantity of data storage and calculation, good real-time performance etc, so it fits the automatic guide system which requests good real-time performance. Compared with neural network algorithm, Kalman filtering is more mature and is proper for managing the non-stationary random signals. Under the strong vibration condition, the TBM attitude process data is time-variant and non-stationary. This paper designs the multiple-sensor fusion attitude measurement system basing on Kalman filtering algorithm. Generally, multiple-sensor fusion Kalman filtering technology is applied in satellite navigation system, this is the first example to apply in the hard-rock tunneling automatic guide system.

The bi-axis inclinometer which is often used for measuring the pitching angle and roll angle has the advantages of small-volume, high-accuracy and high-reliability etc, but under the strong vibration condition, the effectiveness will reduce drastically and the accuracy of attitude measurement will be seriously affected. The optic fiber gyroscope has the advantages of small-volume, low cost and good anti-vibration ability, but its zero drift affects the measurement accuracy. In this paper, it researches the information fusion of the inclinometer's high-accuracy output and the optic fiber gyroscope's output in the condition of non-vibration. We use the inclinometer information to estimate the gyroscope's random error and effectively corrected the gyroscope's output. And then under the strong vibration condition we used the compensated gyroscope data to calculate the TBM attitude angle.

Firstly, we built an optic fiber gyroscope's random error model based on the analysis of time series. Generally, the identification methods of optic fiber gyroscope's error and noise includes time series analysis method,power spectral density(PSD) and Allan method etc. Time series analysis method has very widespread use in random error analysis.

Secondly, we proposed the multiple-sensor fusion algorithm. Basing on the optic fiber gyroscope's random error model, we designed the Kalman filtering algorithm. The inclinometer's information as a part of measurement information estimates the system status and improve the gyroscope's accuracy. The TBM attitude angle is calculated using the compensated gyroscope data under strong vibration.

Experiment shows that multiple-sensor information fusion algorithm can well estimate the gyroscope's zero drift and the convergence speed of the method is fast. It ensures that the error of multi-sensor attitude measurement system is less than 2 milliradian under the static and dynamic state.

2 The Measurement of Attitude

The roll angle αrotates around the TBM's own axis during tunneling and its variation range is generally not more than$\pm 5^\circ$. The pitching angle$\beta$is between the horizontal plane and the center axis of TBM and its variation range is generally not more than$\pm 3^\circ$.

2.1 The Attitude Calculation of Bi-axis Inclinometer

The inclinometer can measure the roll and pitch angle. If X and Y is respectively as the measurement axis of roll and pitch angle. Ja and Jb are the output of two axis.Jb can be a real pitch angle and Ja cannot be directly defined as the roll angle.According to the corresponding geometric relationships, rolling Angle is given as follows:

$$\alpha = \sin^{-1}\left(\frac{\sin(Ja)}{\cos(Jb)}\right) \tag{1}$$

2.2 The Attitude Calculation of Optic Fiber Gyroscope

Using two gyroscope measure roll and pitch angle.The sensitive axis of gyroscope to measure roll angle parallels the axis of TBM, which measured value can be directly converted to the roll angle of TBM. Roll angle can be expressed as following:

$$\alpha = \alpha_0 + \int \omega_\alpha dt \tag{2}$$

where α_0 is the initial roll angle. ω_α represents the angular velocity of roll angle gyro.The pitch angle is not the integration of ω_β ,which can be expressed

$$\beta = \beta_0 + \int \frac{\omega_\beta}{\cos\alpha} dt \tag{3}$$

where β_0 is the initial roll angle. ω_β stands for the angular velocity of pitch angle gyroscope.

3 The Error Modeling of Optic Fiber Gyroscope

Time series analysis model includes: data collection, data statistical analysis and pre-treatment, modeling. Eviews is a soft to analysis time series.

It ensures that the random drift signal of gyro is time series with zero mean, stable, normal, not the white noise.

Zero mean processing. The original signal of gyro includes constant component and random component. The constant can be extracted by mean of signal, and then the random component is zero drift of gyro.

Data stability testing. The line chart method and unit root test are used for testing stability. ADF (Augmented Dickey Fuller) test is generally adopted as an important index. According to the value of ADF statistic (less than 1%, 5% or 10% level of statistical quantity), the original series is stable under the condition of the confidence level P is less than 0.05.

Normality test. Jarque-Bera statistics is used to test whether the sample is normal distribution. If JB statistics and the value of P is very small, or the value of P greater than 0.05,the series depends on normal distribution.

The different order of AR model and ARMA model are generally built to estimate the zero drift of gyro. The residual error is smaller and the accuracy of error model is higher.

ARMA(p,q) can be expressed by equation(4):

$$x(k) = a_1 x(k-1) + \cdots + a_p x(k-p) + e(k) + b_1 e(k-1) + \cdots + b_q e(k-q) \quad (4)$$

where e(k) stands for state white noise with zero mean and its variance is σ_e^2. $x(k)$ is time series. In this paper, Eviews analysis result shows that the ARMA(2,1) is a good model. We consider that the below formula is the error model of gyro.

$$x(k) = a_1 x(k-1) + a_2 x(k-2) + e(k) + b_1 e(k-1) \quad (5)$$

4 Multi-sensor Fusion Model

The output of inclinometer is stable and accurate under weak vibration. Moreover it has a big error under strong vibration and can't be restored. At the same time, the optic fiber gyro's zero drift performed an evolution of slowly changing under the influence of the system noise. Under strong vibration, the variance around the zero drift is increasing and the error is on a manageable level. Basing on inclinometer and gyro, we built the fusion attitude measurement method, the process is as follows:

Multiple sensor information fusion system firstly pre-treats the inclinometer's output and gyroscope's data. Then it fuses two sensors information, estimates the gyroscope's zero drift and compensates it.

Basing on the gyro's error model, the state equation is built. The status equation and measurement equation are given.

$$\begin{cases} X(k) = AX(k-1) + BV(k) \\ Y(k) = CX(k) + W(k) \end{cases} \quad (6)$$

where $X(k) = [x(k), x(k-1)]^T$ stands for a status vector. $V(k) = [e(k), 0]^T$ for a random variable. $Y(k) = [\omega(k), \Delta\theta(k)]^T$ is a measurement vector. $\omega(k)$ represents the output of gyro. $C = \begin{pmatrix} 1 & 0 \\ 1 & 0 \end{pmatrix}$, $W(k) = [n_{ak}, n_k]^T$. n_{ak} and n_k are the measurement noise of gyro and inclinometer. $\Delta\theta(k)$ indicates the inclinometer's angular displacement during a sampling period and its difference expressions can enlarge the inclinometer's measurement noise error.

The Kalman filtering fusion algorithm basing on inclinometer and gyroscope is showed as follows:

Step1 time update

The symbol "∧" represents estimated value. We can estimate error covariance $P_{k|k-1}$ at time k-1 on the basis of mean square error P_k and process noise covariance Q_k.

$$P_{k|k-1} = A_{k|k-1} P_{k-1} A_{k|k-1}^T + Q_k \tag{7}$$

Step 2 measurement update .

The Kalman gain is calculated at time k with the measurement of inclinometer and gyro as follows:

$$K_k = P_{k|k-1} C_k^T (C_k P_{k|k-1} C_k{}^T + R_k)^{-1} \tag{8}$$

The status at time k is forecasted by the state estimate at time k-1.

$$\hat{X}_{k|k-1} = A_{k|k-1} \hat{X}_{k-1} \tag{9}$$

And then the optimal estimator at time k is expressed by equation(10):

$$\hat{X}_k = \hat{X}_{k|k-1} + K_k (Y_k - C_k \hat{X}_{k|k-1}) \tag{10}$$

The error covariance of $\hat{X}_k$ is updated as following;

$$P_k = P_{k|k-1} - K_k C_k P_{k|k-1} \tag{11}$$

Step3 status correction.

The zero drift can be corrected by the $\hat{X}_k$.

Process noise covariance is $Q_k = \begin{pmatrix} \sigma_e^2 & \\ & \sigma_e^2 \end{pmatrix}$, R_a stands for the covariance of n_{ak}. δ_k is the measurement noise of inclinometer and then $n_k = \delta_k - \delta_{k-1}$. The covariance of n_k is $4R_\delta$. Measurement noise covariance is $R_k = \begin{pmatrix} R_a & \\ & 4R_\delta \end{pmatrix}$.

5 Experiment

Two experiments were made to verify the validity and reliability of multi-sensor fusion algorithm. Sensor combined system used biaxial inclinometer (SST260) and fiber optic gyro(VG951). Servo motor(SGMCS-05B3B11) and the vibration platform were experimental auxiliary equipments, which can simulate the vibration environment state of TBM. The hardware system is shown in Fig. 1:

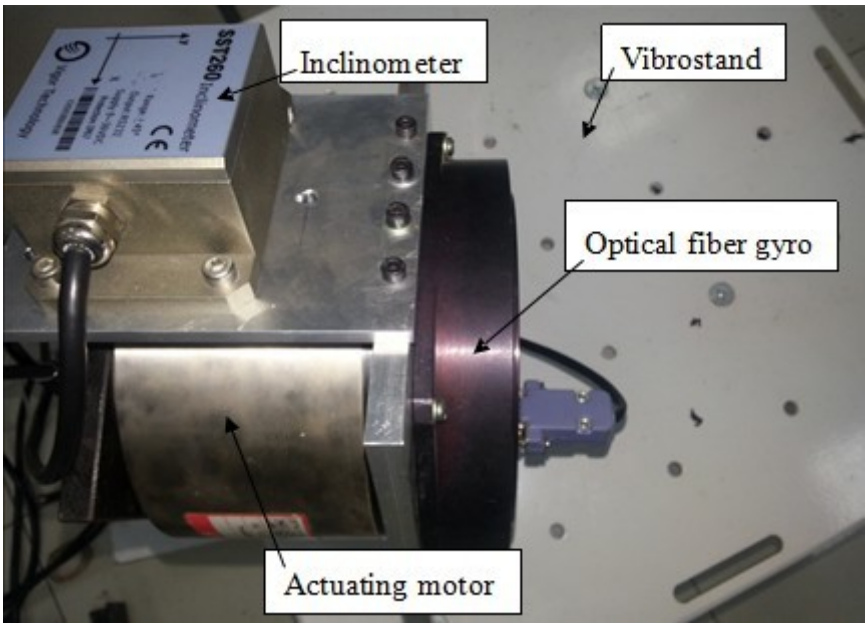

Fig. 1. The hardware system of multi-sensor

The vibration table simulates the vibration environment of TBM. Servo motor simulates the change of attitude. The system makes sure that rotor axis of gyro parallels sensitivity axis of inclinometer.

Now the inclinometer and gyroscope are tested under the same attitude between 0-320 s tests and the strong vibration is given during the period from 100s to 200s.The following Fig.2 shows that the inclinometer has a big distortion under the strong vibration and its error reaches 1 ° . The variance around zero bias of gyro increases a lot, but it can be restored with the filter and integral.

Zero drift is contained in the output of the gyro, it will produce larger cumulative error after long time integral. The zero bias compensated before integral can avoid the bigger error and improve the accuracy of gyro. In Fig.3, a image shows that the error of gyro reaches about 20 ° and the measurement result is seriously distorted. The estimation and compensation of zero drift meet the demand of multi-sensor accuracy before the integral of angular rate for gyro.

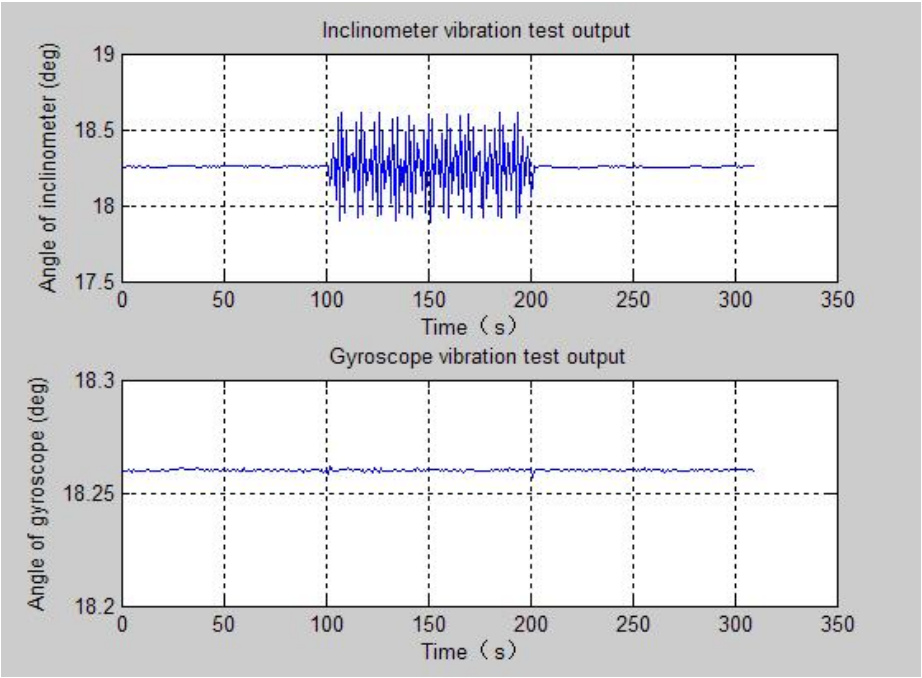

Fig. 2. The output of inclinometer and gyro under the vibration

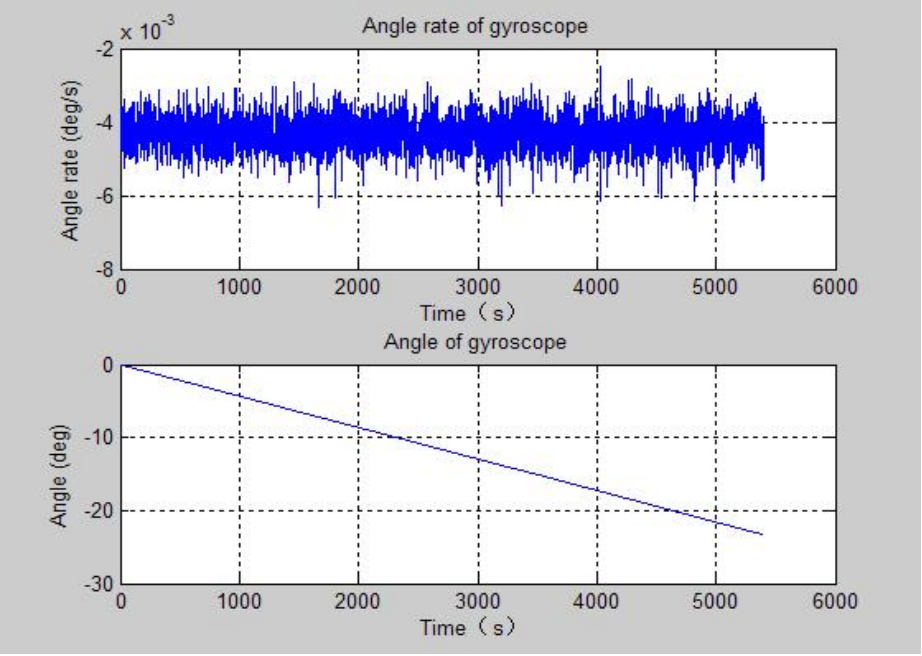

Fig. 3. Output and integral of angular rate for gyro

As long as the error of inclinometer is controlled in 0.03 ° , and the error variance reaches 10 e -5 orders of magnitude. The output of the inclinometer can be restored using the wavelet filter method. We choose the strong vibration time in 1 hour because the time which can cause inclinometer failure under strong vibration is short.

Eviews analysis the error model of gyro as following:

$$x(k) = 0.7143x(k-1) + 0.0793x(k-2) + e(k) - 0.7739e(k-1) \quad (12)$$

We can establish the status equation on the basis of the above model.

5.1 Multi-sensor Fusion Algorithm Test under the Fixed Attitude

Motor simulates the fixed attitude of TBM and then we collect data of inclinometer and gyro 1800s under weak vibration and collect data of 3600s under strong vibration. First of all, the data is pretreated using 3 sigma criteria, it can get rid of the abnormal data which is caused by disturbance of the external environment and noise. Using the fusion algorithm, the effect is shown as following Fig.4.

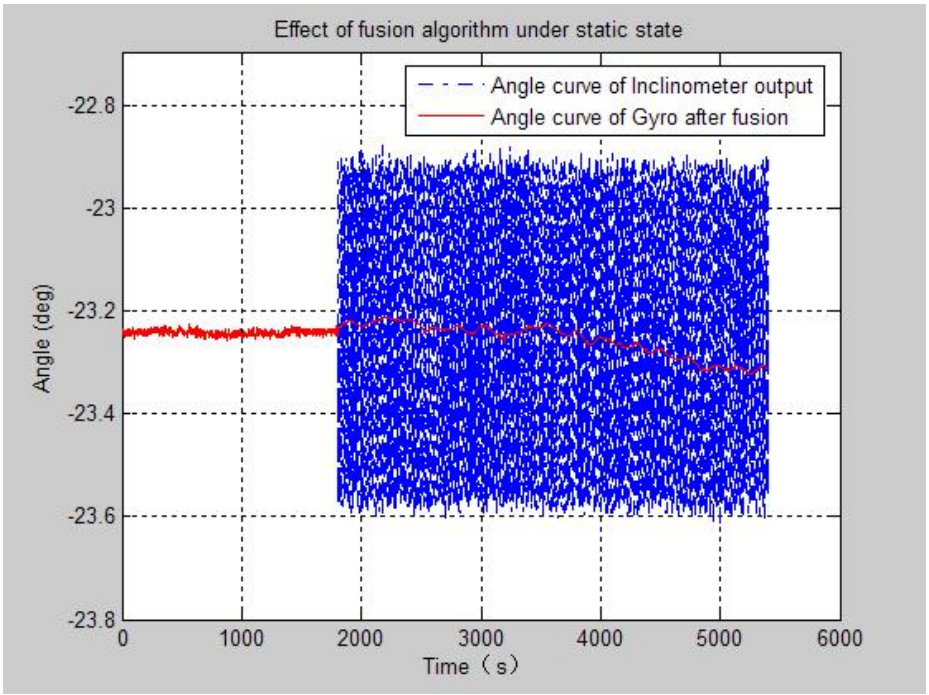

Fig. 4. Comparison figure in before and after fusion with fixed attitude

In Fig.4, it shows that the inclinometer estimates the zero drift of gyro before 1800 s and then fails to work during the period of 1800s – 5400s.The compensated output of gyro can calculate the attitude of TBM under the strong vibration and ensures the error range in 2 milliradian.

5.2 Multi-sensor Fusion Algorithm Test under the Dynamic Attitude

Servo motor simulates the dynamic change of attitude. The speed of motor is 6.866×10^{-3} deg/ s .The rotation angle of motor is reference of the true attitude.

The collected data of inclinometer and the gyro data is pretreated and fused. The zero drift is estimated in real time and the integral of compensated output of gyro is given. The error of inclinometer and gyro in fusion system is shown in Fig.5.

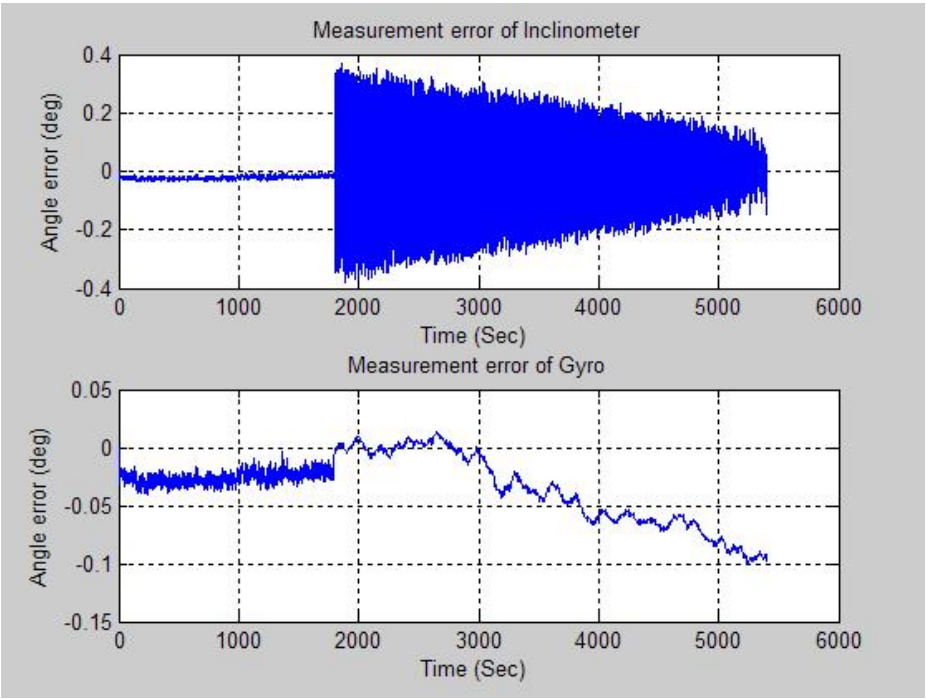

Fig. 5. Comparison figure in before and after fusion under dynamic attitude

According to the experimental data, it shows that the maximum deviation of attitude is controlled in 2 milliradian. The multi-sensor ensures reliability and effective in strong vibration envrioment.

6 Conclusion

We have described and analysis the multi-sensor attitude measurement method on TBM. The method discussed fuse information from inclinometer and optical fiber gyroscope. At the design phase of the multi-sensor, before strong vibration, the zero drift of gyro was estimated and compensated. The managed output of gyro can calculate the attitude of TBM with high accuracy. The problem occurs in inclinometer under the strong vibration and zero drifts exists in the output of gyro, the proposed

method is needed in the problem resolution process. Time series modeling is used to build error model of optical fiber gyro. The fusion algorithm is presented using Kalman filtering, which estimates zero bias of gyro with the high accurate output of inclinometer . Experimental results are presented to verify the effectiveness and reliability of fusion algorithm. The method ensures that the error of multi-sensor attitude measurement system is less than 2 milliradian with the fixed attitude and dynamic attitude. The algorithm is not perfect and needed to improve next step.

References

[1] Duslman, A.: On Gyro Drift Models and Their Evaluation. IEEE Transactions on Aerospace and Navigation Electronic 5(2), 230–234 (1962)
[2] Akiyama, A., Namiki, et al.: Development of Flexible Section Shield Tunneling Machine. Research and Development, 125–128 (January 1993)
[3] Gebre-Egziabher, D., Hayward, R.C., Powell, J.D.: Design of Multi-Sensor Attitude Determination System. IEEE Transaction on Aerospace and Electronic Systems 40(2), 901–917 (2004)
[4] Philip, L.B.: Shafer-Dempster Reasoning with Application to Multisensory Target Identification System. IEEE Trans. SMC 17(6), 968–977 (1987)
[5] Ren, C.L., Michael, G.K.: Multisensor Integration and Fusion Intelligent System. IEEE Trans. SMC 19(5), 901–931 (1989)
[6] Kalman, R.E.: A New Approach to Linear Filtering and Prediction Problems. Journal of Basic Engineering 82(1), 35–45 (1960)
[7] EI-Sheimy, N., Hou, H., Niu, X.: Analysis and Moldeling of Inertial Sensors Using Allan Variance. IEEE Transactions on Instrumentation and Measurement 57(1), 140–149 (2008)
[8] Bayard, D.S.: High Accuracy Inertial Sensors from Inexpensive Components. United States Patent US6882964 (July 26, 2005)
[9] Possetti, G.R.C., Kamikawachi, R.C., et al.: Metrological Evaluation of Optical Fiber Grating-Based Sensors: An Approach towards the Standardization. Journal of Lightwave Technology 30(8), 1042–1052 (2012)
[10] Riewe, F.: Low-cost Multiple Sensor Inertial Measurement System for Locomotive Navigation. Transportation Research Board National Research Council (2000)
[11] Azmi, A.I.: Development of Fiber Grating-Base Sensing Techniques and Application in Mechanical Engineering. UNSW, Austrilia (2012)
[12] Antunes, P.F.C., et al.: Biaxial Optical Accelerometer and High-Angle Inclinometer with Temperature and Cross-axis Insensitivity. IEEE Sensors Journal 12(7), 2399–2406 (2012)

Endocrine Intelligent Control of Thrust Hydraulic System for TBM

Jin Yao[1,2], Xia Yimin[1,*], Cheng Yongliang[1], and Zhang Huan[1]

[1] The State key Laboratory of High Performance and Complex Manufacturing, Changsha 410083, China
[2] College of Engineering and Design, Hunan Normal University, Changsha 410081, China
xiaymj@csu.edu.cn

Abstract. An electro-hydraulic control system for the thrust speed control in TBM was introduced and its dynamics model was established. An endocrine intelligent controller was then designed based on the endocrine hormone regulation principles for improving effects in thurst speed control. And on this basis the co-simulation of thrust hydraulic system was conducted in AMESim and MATLAB/Simulink software environments. Simulation results demonstrate that the proposed endocrine control has better control performance and adaptability compared with conventional PID control. The proposed endocrine strategy provides a possible new way for thrust hydraulic system of TBM, and also extend the applications for endocrine intelligent control.

Keywords: TBM, thrust hydraulic system, endocrine, intelligent control.

1 Introduction

It is well known that the tunnel boring machine (TBM) is a large-scale modern construction machine, and nowsday has become the primary choice for excavating the subways or tunnels in nearly all type rock masses and geological conditions [1,2]. As a key part of TBM, the thrust system driven by hydraulic system not only performs the task of driving TBM ahead while tunneling, but also controls the posture adjusting [3]. [1]And the thrust speed of thrust hydraulic system for TBM plays an important role, which is directly related to the rapidity, safety and construction quality during excavation. Due to the complicated geological conditions and other unpredictable factors during excavation, the thrust speed easily gets out of control, such as deviation from the set value and oscillation while speed adjustment. Therefore the thrust speed control which can adapt to the varying geological conditions is greatly desirable. The conventional PID control strategy, which has advantages of simple structure and high reliability, etc., is one of the choices in thrust speed controlling. Due to the drawback of poorly adjusting the parameter online, PID is still difficult to meet the thrust requirements for TBM under nonlinear complex thrust working conditions. So it is

* Corresponding author.

[1] This work is supported by National 863 Plan of China (No. 2012AA041801) and Postdoctoral Fund Project of Central South University (No. 89340).

J. Lee et al. (Eds.): ICIRA 2013, Part II, LNAI 8103, pp. 720–726, 2013.

natural to turn to the intelligent control such as fuzzy control and neural network algorithm. As we know, the intelligent control can promote control quality remarkably under nonlinear complex conditions for its ability to simulate human intelligence, self-learning and self-adaptive ability.

As a new bionic intelligent strategy, the artificial endocrine system starts to obtain attention in recent years [4,5]. Neural networks, immune system and endocrine system are the three physiological regulation systems of the human body. And the research on their bioinformatics mechanism is the core of biological intelligent control. Nowsday, artificial neural network and artificial immune system have been deeply studied and widely applied. However, as another important physiological adjustment mechanism, artificial endocrine system needs urgently further development, whose theory study has just started and application scope is relatively narrow.

Recently there have been few reports on artificial endocrine control. An intelligent cooperative decoupling controller based on the neuroendocrine regulation principle of human body is proposed and applied to the coagulation bath in the polycarylonitrile carbon fiber production [6]. Inspired by the distributed and collaborative features of hormones regulating system, the task assignment adaptability of the autonomous robots system is studied when changing in internal and external environment [7]. A double level controller cascaded by two controllers based on the modulation principle of testosterone release is presented and applied to the liquid-level control of a second-order liquid-level flow system [8]. These cases indicate that one of the important functions of endocrine system, which acts as the regulation center of all sorts of hormones in the body, is to modulate the body's various hormones, regulate the growth, development, metabolism and reproduction of the whole organism, and then improve human's perception and the ability to adapt the complex environment. Furthermore, the hormone regulation mechanism has such advantages as better self-learning ability, adaptability and stability, etc [9,10]. Therefore the hormone regulation mechanism of endocrine system can help to improve the control performance and adaptability of thrust hydraulic system for TBM working under the varying complex geological conditions, and it also accords with the intelligent development direction of TBM electro-hydraulic control technology.

In this paper, an endocrine intelligent controller and its control scheme are presented based on hormone regulation mechanism of endocrine system, and applied to the thrust speed control of thrust hydraulic system for TBM. Simulation results show that the proposed endocrine control can provide better control quality and adaptability than that of conventional PID control.

2 Thrust Hydraulic System for TBM

The task of pushing TBM forward while tunneling is performed by multiple thrust hydraulic cylinders distributed in the circular direction of shield section. In practice, these thrust hydraulic cylinders are usually divided into several groups and in tunneling each group can be controlled individually through adjusting pressure and displacement/speed of each group. And the cylinders of the thrust system in each group are controlled by the same way, which can be simplified as shown in Fig.1.

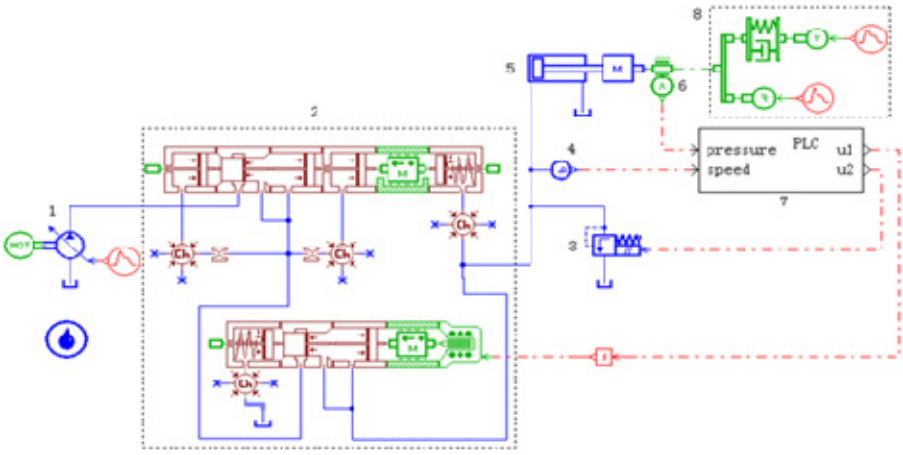

Fig. 1. Simplified thrust hydraulic system

As shown in Fig. 1, the electro-hydraulic proportional control system of the thrust cylinder comprises a proportional flow control valve 2 and a proportional pressure relief valve 3, in which the thrusting pressure and speed can be regulated [3]. When thrust, the variable displacement pump 1 provides the fluid flow, and the solenoid of proportional flow control valve 2 is energized, shifting the spool to its left position to make the cylinder piston rod move forward driving load 8. Pressure sensor 4 and speed sensor 6 realtimely measure the pressure and velocity of the hydraulic cylinder 5. The measured signals are delivered to the central control unit PLC 7 so as to be compared with reference input signals, then output control signals u1 and u2 adjust the openings of the proportional valves, and pressure and flow/speed control are implemented respectively to meet the thrust requirements.

This paper mainly focuses on the speed control of the thrust hydraulic system. The control block diagram of one group in the thrust system is shown in Fig.2, which represents the thrust speed adjustment in forward direction. In the speed closed-loop control system, by comparing the reference speed signal r_v and the feedback signal v from speed sensor, the speed error is produced then transferred to the controller, and then the openings of the proportional flow valve is adjusted, the flow entering the hydraulic cylinder is regulated indirectly, thus the speed regulation is implemented.

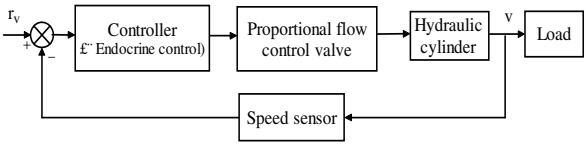

Fig. 2. Principle of the thrust speed control

3 Design of Endocrine Controller

3. 1 Hormone Regulation Mechanism of Endocrine System

The endocrine system secretes relevant hormone H3 (such as thyroxin, adrenalin and testosterone, etc) through target glands (such as thyroid gland, adrenal gland and sexual gland, etc), and thus regulates the growth, development, metabolism and reproduction of organism. The secretion of each hormone is coordinated and controlled by hypothalamus and pituitary in nervous system. Fig.3 illustrates the regulation loop of endocrine hormones [9,10]. As shown in Fig. 3, hypothalamus secretes hormone H1 which stimulate pituitary to secrete hormone H2 during the process of hormone regulation. These hormones do work on target glands, and thus the target glands can be promoted to secrete its relevant hormone H3 to play a role of physiological regulation. This process is called positive feedback ("+") enhancing the concentration of hormone H3. It is noted that H1,H2,H3 are the general terms for a variety of hormones. While if a certain hormone H3 level is too much, the level will feed back to pituitary and hypothalamus through transmission factor or receptor negatively, the secreting of pituitary and hypothalamus (H1 and H2) will reduce, thus the concentration of hormone H3 secreted by endocrine glands keeps down. This is negative feedback ("-") inhibiting the concentration of hormone H3. With the two kinds of feedback hormone H3 finally come to a certain state of equilibrium and stability. The above hormone regulation mechanism of endocrine system is similar to the closed-loop feedback regulation mechanism in control theory, and provides knowledge that could be utilized in the following controller design.

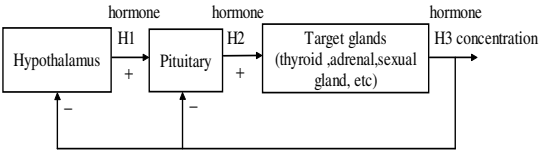

Fig. 3. Regulation loop of endocrine hormone

3.2 Structure of Endocrine Controller

As shown in Fig.4, the structure of endocrine controller in this paper is based on the hormone regulation loop of endocrine system in Fig.3, and is a two-level controller cascaded by two controllers. In this structure, the first controller (master controller) corresponds to hypothalamus, the secondary controller (slave controller) corresponds to pituitary, actuator corresponds to glands, the plant output y corresponds to hormone H3 concentration, and the given value r corresponds to the normal value of gland hormone in the body. e_1, u_1 and e_2, u_2 are the control error and control output of the first and secondary controller respectively. Thus, endocrine controller follows endocrine hormone modulation mechanism in structure, and it should work according to endocrine hormone modulation principle, so it has good adaptability and stability naturally. Furthermore, endocrine control system shown in Fig.4 differs from

traditional cascade control system in that its first and secondary control loops use plant output simultaneously as feedback signal, while in conventional cascade control system the first and secondary control loops take primary controlled variable and secondary controlled variable separately as feedback signal.

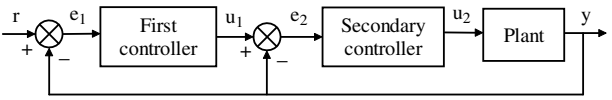

Fig. 4. Structure of endocrine controller

3.3 Control Law

The main function of the first controller is that it can change dynamically the control error of secondary controller, thus eliminate its own control error quickly and steadily. Proportional control law is used in the first controller, the control output u1 is as follows:

$$u_1 = r + K_1 e_1 = r + K_1(r - y) \tag{1}$$

where $K_1>0$ is the scale factor of the first controller.

The secondary controller is regulated by the first controller, and its given value is the output u1 of the first controller. In this paper the secondary controller takes the conventional PID control, the control output u2 is as follows:

$$u_2 = K_2 e_2 + K_3 \int e_2 + K_4 de_2 / dt \tag{2}$$

where K_2, K_3, K_4 are the coefficients of proportion, integrator and derivativel, and the control error e_2 is:

$$e_2 = u_1 - y \tag{3}$$

4 Simulation and Results

In order to investigate the effectiveness of the endocrine controller above for thrust hydraulic system, the cosimulation is conducted in AMESim software and MATLAB/Simulink software. The AMESim co-simulation model of thrust hydraulic system is shown in Fig.5. Here, the mechanical models of the proportional flow control valve are established using the tool of HCD in AMESim software. And hydraulic system is simplified, some components which have relatively less relation to the normal thrust process are neglected in the model. During the cosimulation, the system pressure keeps 25 MPa by means of the constant pressure oil source, the thrust load with load force of 1000 kN is regarded as a moving viscous-elastic model according to the soil mechanics. The desired thrust speed is 0.5 mm/s for the first 5 s, 1 mm/s for the latter 5 s. Considering the thrust cylinders in each group are controlled by the same way, we just take one group of thrust cylinders into account.

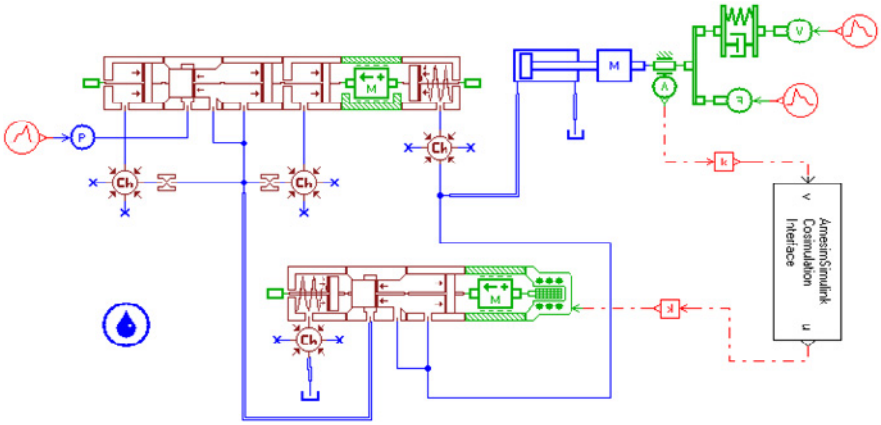

Fig. 5. AMESim co-simulation model for thrust speed control

With the endocrine control strategy described above, the simulation results of thrust speed control are illustrated in Fig.6. It is clear that the overshoot and adjustment time of the endocrine control at the beginning of the first 5s is superior to those of conventional PID control. When the thrust speed of the cylinder is adjusted to 1 mm/s from 0.5 mm/s at the fifth second, the endocrine control still obtain less overshoot and adjustment time. It means that the endocrine controller can obtain better control performance and rapid adaptability to varying conditions. Such phenomenon should be due to the advantages of the endocrine intelligent control.

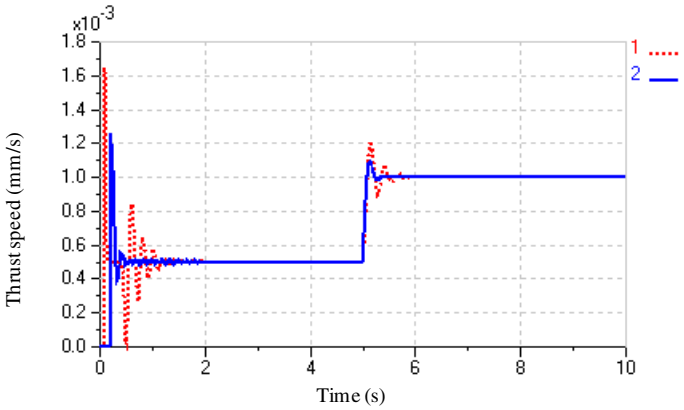

1 PID control 2 Endocrine control

Fig. 6. Thrust speed of TBM

5 Conclusion

This paper introduced an electro-hydraulic control system of thrust speed control for TBM. In order to obtain better control performance in thurst speed control, an endocrine intelligent controller was proposed based on the endocrine hormone regulation principles. The cosimulation was then performed in AMESim and MATLAB/Simulink software environments. Simulation results demonstrate that the proposed endocrine control is superior to conventional PID control and can achieve a desired tunneling performance. The proposed control strategy provides a possible new way for thrust hydraulic system of TBM.

References

[1] Acaroglu, O.: Prediction of thrust and torque requirements of TBMs with fuzzy logic models. Tunnelling and Underground Space Technology 26(2), 267–275 (2011)
[2] Li, X.H., Yu, H.B., Yuan, M.Z., et al.: Dynamic Modeling and Analysis of Shield TBM Cutterhead Driving System. Transactions of the ASME: Journal of Dynamic Systems Measurement and Control 132(4), 1–14 (2010)
[3] Yang, H.Y., Shi, H., Gong, G.F., et al.: Electro-hydraulic proportional control of thrust system for shield tunneling machine. Automation in Construction 18(7), 950–956 (2009)
[4] Xu, Q., Wang, L.: Recent advances in the artificial endocrine system. Journal of Zhejiang University-Science C 12(3), 171–183 (2011)
[5] Mendao, M.: A neuro-endocrine control architecture applied to mobile robotics, Canterbury, UK, University of Kent (2007)
[6] Ding, Y., Xiao, L., Hao, K., et al.: An intelligent cooperative decoupling controller for coagulation bath in polyacrylonitrile carbon fiber production. IEEE Transactions on Control Systems Technology 21(2), 467–479 (2013)
[7] Walker, J., Wilson, M.: A performance sensitive hormone-inspired system for task distribution amongst evolving robots. In: IEEE/RSJ International Conference on Intelligent Robots and Systems, Nice, France, pp. 1293–1298 (2008)
[8] Liu, B., Ding, Y.: A two-level controller based on the modulation principle of testosterone release. Journal of Shanghai Jiaotong University 40(5), 822–824 (2006)
[9] Tilbrook, A.J., Clarke, I.J.: Neuroendocrine mechanisms of innate states of attenuated responsiveness of the hypothalamo-pituitary adrenal axis to stress. Frontiers in Neuroendocrinology 27(3), 285–307 (2006)
[10] Chen, D., Zou, F., Wang, J.: A multi-objective endocrine PSO algorithm and application. Applied Soft Computing 11(8), 4508–4520 (2011)

A Cutter Layout Optimization Method for Full-Face Rock Tunnel Boring Machine

Geng Qi, Wei Zhengying, Du Jun, and Tang Yiping

State key Laboratory of Manufacturing System Engineering, Xi'an Jiaotong University, Xi'an 710049, China
gengqi8902@gmail.com, zywei@mail.xjtu.edu.cn

Abstract. A cutter layout optimization strategy for full-face rock tunnel boring machine (TBM) is proposed, to overcome the drawback that the original design usually can not meet the balance requirements for cutter head forces and the rock breaking amount of each cutter. The layout schemes are designed by grouping the cutters and exerting micro-adjustment for the position angle and radius. The best layout is achieved by selecting the layout schemes using grey relational analysis and the TB880E TBM cutter layout are optimized. Compared with the computational results of the original layout design, the eccentric moment decreases by 65%. It is concluded that the position angle plays a main role in cutter layout optimization, and the cutter layout exerts obvious influence on cutter head performance. The optimization strategy can avoid stress concentration without doing harm to structural stiffness.

Keywords: Full-face rock tunnel boring machine; Cutter layout optimization; Grey relational analysis.

1 Introduction

The full-face rock tunnel boring machine (TBM) is a large special engineering machine for tunnel boring. TBM has been widely applied to the subway, railway and water-electricity projects. The layout design of the cutters is a key technology in cutter head design[1], which directly affects TBM's boring performance, service life of cutterhead bearing as well as cutterhead's vibration and noise.

The CSM computer model for hard rock TBM utilizes semi-theoretical formulas to estimate the cutting forces, and work out the cutterhead's geometry and profile[2]. Zhang[3] presented a model of single-spiral layout and its solving method in view of cutter head force balance and cutting efficiency. Zhang[4] presented a method to optimize the spacing of the cutters without changing the cutter amount and polar angle. Using this method, the cutter forces of the cutter head crown can be reduced obviously, and amount of muck cut by each cutter can be more uniform. Huo[5] studied the factors influencing the cutter head force balance, and presented a cutter layout design method using genetic algorithm. The cutter layout is a kind of multiple-objective decision-making problem. The grey relational analysis is an effective method in solving multiple-objective decision-making problem, it has been adopted in system

J. Lee et al. (Eds.): ICIRA 2013, Part II, LNAI 8103, pp. 727–737, 2013.

assessment of weapons and electricity[6-8]. However, applications of grey relational analysis on cutter layout optimization has not been found yet.

This paper presents a cutter layout optimization method based on grey relational analysis. In this method, micro-adjustment is exerted for the position angle and radius of each cutter, we hope to reduce the cutter head eccentric force, the cutter head eccentric moment, the error of the centroid of the cutters and the variance of the muck amount by each cutters, in order to get better cutter head performance.

2 The Optimization Method

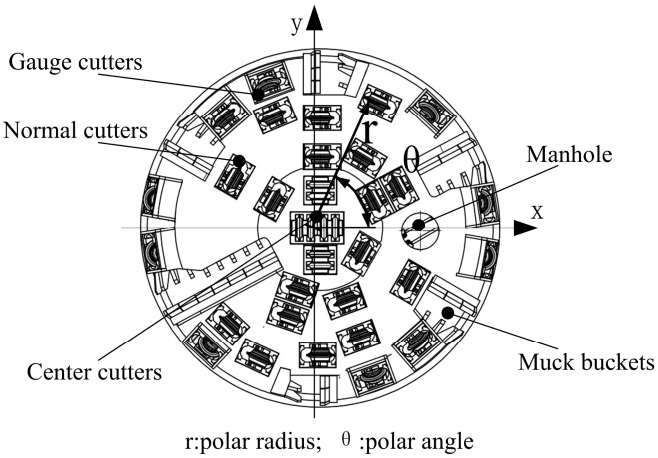

Fig. 1. Main elements on a cutter head

2.1 Polar Radius Optimization Method

As shown in Fig.1, the position of the muck buckets and manhole is fixed. The polar radius and polar angle of a cutter are determined separately. The polar radius is optimized firstly and the best layout got in this step will be set as the input for the polar angle optimization. Steps of the optimization method are as follows:

(1) Input the layout parameters of the cutters to be optimized.
(2) Obtain a group of cutter layout schemes.
(3) Obtain the objective matrix of each scheme.
(4) Select the best layout using grey relational analysis to the matrixes above.

2.1.1 Scheme Sets Establishment

The constraints of polar radius are as follows according to the cutter head structure and technical requirements of cutter layout.

(1)Number of disc cutters is kept constant.
(2)Diameter of the cutter head is kept constant.
(3)Cutter spacing decreases from center cutter to gauge cutter.

(4)Normal cutter spacing is larger than that of gauge cutter, but smaller than that of center cutter.

The constraints can be formulated as follows:

$$\begin{cases} x_1 + x_2 + ... + x_k = N_n \\ x_1 y_1 + x_2 y_2 + ... + x_k y_k = r_n \\ y_k \geq y_{k-1} \geq ... \geq y_1 \\ y_1 < S_c \\ y_k > S_s \\ x_1, x_2, ..., x_k \geq 1 \end{cases} \tag{1}$$

Where k is the number of districts of normal cutters; x_k, y_k are number of disc cutters and there cutter spacing in district k respectively; N_n is number of normal cutters; r_n is the radius distance between the outermost center cutter and the outermost normal cutter; S_c, S_s are cutter spacing of center cutter and the innermost gauge cutter respectively.

2.1.2 The Non-interference Constrains

The scheme sets are firstly selected by non-interference constraints in order to avoid interference between cutters. As shown in Fig.2, we simplify the cutter hole as its external enveloping circle if the cutter hole is rectangle, and we calculate the center distance directly if the cutter hole is round. The overlapping constraints can be formulated as follows:

$$\mathrm{A} = \left\{ (X_i, Y_i) \middle| \sqrt{(X_i - X_j)^2 + (Y_i - Y_j)^2} > d, i, j \in \{1...N\} \right\} \tag{2}$$

Where $P(X_i, Y_i)$ is the position of cutter i under rectangular coordinate system; d is the diameter of the simplified cutter hole; N is the number of disc cutters.

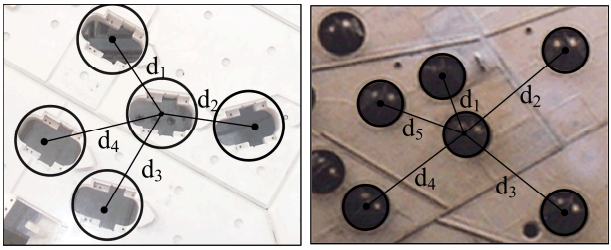

(a)rectangle cutter hole (b)round cutter hole

d1-d5:center distance between cutters

Fig. 2. Schematic diagram of the overlapping constraints

2.1.3 Grey Relational Analysis

After the scheme sets are selected by overlapping constraints, 4 technical requirements which be described as the cutter head eccentric force, the cutter head eccentric moment, the position error of the centroid of the cutters and the variance of the muck amount by each cutters are defined as main attributes to assess the performance of the cutter head. Here the 4 attributes are recorded as C_1, C_2, C_3 and C_4. The 4 attributes are minimum polarity since they are expected to be as small as possible. The standard mode is as follow.

$$\omega_0 = (\omega_0(1), \omega_0(2), \omega_0(3), \omega_0(4)) \tag{3}$$

$$\omega_0(l) = \min \omega_j(l) \tag{4}$$

Where l is the attributes alternative; j is scheme sets alternative; ω_0 is the standard mode vector; $\omega_0(l)$ is the standard mode of attribute l; $\omega_j(l)$ is the value of the lth attribute for the jth alternative.

The standard grey target is defined as follow.

$$x_0 = (x_0(1), x_0(2), x_0(3), x_0(4)) = (1,1,1,1) \tag{5}$$

Where x_0 is the standard grey target vector; $x_0(l)$ is the standard grey target of the lth attribute.

The grey relation is generated as follow.

$$x_j(l) = \frac{\min\left\{\omega_j(l), \omega_0(l)\right\}}{\max\left\{\omega_j(l), \omega_0(l)\right\}} \tag{6}$$

Where $x_j(l)$ is the target value of the lth attribute for the jth alternative.

The grey relation space can be written as follow.

$$\Delta_{GR} = (\Delta, \xi, \max(\Delta_{0j}), \min(\Delta_{0j})) \tag{7}$$

Where $\Delta = \left\{\Delta_{0j}(l) \mid j \in I = \{1,2,...,m\}, l \in L = \{1,2,3,4\}\right\}$,

$\Delta_{0j}(l) = \left|x_0(l) - x_j(l)\right| = \left|1 - x_j(l)\right|, x_0(l) \in x_0$

$\max(\Delta_{0j}) = \max_j\{\max_l \Delta_{0j}(l)\}$, $\min(\Delta_{0j}) = \min_j\{\min_l \Delta_{0j}(l)\}$

ξ is the distinguishing coefficient, $\xi \in [0,1]$.

The grey relational coefficient can be calculated by Eq. (8).

$$\gamma(x_0(l), x_j(l)) = \frac{\min(\Delta_{0j}) + \xi \max(\Delta_{0j})}{\Delta_{0j}(l) + \xi \max(\Delta_{0j})} \tag{8}$$

After calculating the entire grey relational coefficient $\gamma(x_0(l), x_j(l))$, the grey relational grade can be then calculated using Eq.(9).

$$\gamma(x_0, x_j) = \sum_{l=1}^{4} \gamma(x_0(l), x_j(l))\varpi_l \tag{9}$$

In Eq. (9), $\gamma(x_0, x_j)$ is the grey relational grade between x_0 and x_j. It represents the level of correlation between the reference sequence and the comparability sequence. ϖ_l is the weight of attribute *l* and are calculated using AHP method. In addition, $\sum \varpi_l = 1$.

The grey relational grade indicates the degree of similarity between the comparability sequence and the reference sequence, therefore, if a comparability sequence for an alternative gets the highest grey relational grade with the reference sequence, it means that the comparability sequence is most similar to the reference sequence, and that alternative would be the best choice.

2.2 Polar Angle Optimization Method

After optimization of polar radius, a relatively best layout pattern is got. Then this pattern is set as input for polar angle optimization. The optimization process is focused on the normal and gauge cutters since the position of the center cutters are fixed. A method of grouping the cutters from the inside out is adopted. Since the adjacent 4 disc cutters are basically distributed in the 4 quadrant under rectangular coordinate system, the number of disc cutters in each group is determined by Eq. (10).

$$p=4m \ (m=1, 2) \tag{10}$$

Where *p* is the number of disc cutters in a group.

In order to reduce adjustment to the original design layout pattern, micro-adjustment of an integral multiple of 1 degree is exerted for a cutter in a group, which form the set of possible polar angle of this cutter. And the elements number of the set is defined as *q*. The scheme sets of a group are got after micro-adjustment is exerted for polar angle of every cutter in it. Then the same method which was adopted in polar radius optimization is used here to make the overlapping selection and grey relational analysis. The cutters which have been optimized in the *i*th group are also considered to optimize cutters in the *(i+1)* th group.

3 Results and Comparison

3.1 Parameters Setting

The TB880E TBM cutter layout pattern are optimized. Its cutter head geometry, cutter geometry, cutting geometry, operational parameters and rock properties are described in Table 1. Attributes weights are set to be (0.3063; 0.5857; 0.0540; 0.0540)[9].

Table 1. Parameters setting

Content	Value
Uniaxial compressive strength of rock (Mpa)	150
Punch shear strength of rock (Mpa)	6
Cutter head radius (m)	4.4
Rotational speed of cutter head (r/min)	5.4
Diameter of each cutter (mm)	432
Mass of each cutter (kg)	200
Cutter penetration (mm)	9
Number of the center cutter	6
Number of the normal cutter	51
Number of the gauge cutter	14

3.2 Polar Radius Optimization

Based on parameters in Table 1 and Fig. 3, formula (1) can be solved, and cutter layout scheme sets are got.

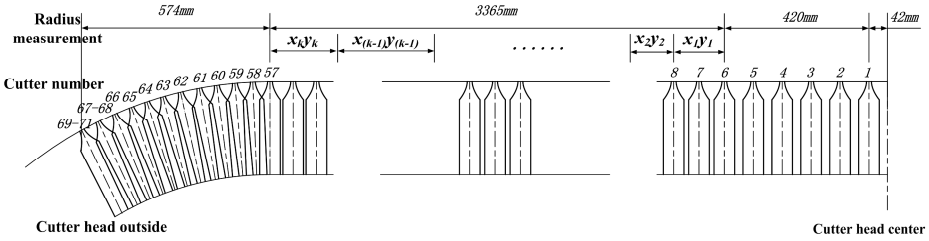

Fig. 3. Cutters overlay graph of TB880E TBM cutter head on radial direction

In Fig.3, cutters with number 1-6 are center cutters, 7-57 are normal cutters and 58-71 are gauge cutters. In order to express the change of attributes C_1-C_4 before and after optimization, 4 dimensionless variables are defined as D_1-D_4.

Where $D_1 = \frac{C_1}{10\mathrm{KN}}$, $D_2 = \frac{C_2}{100\mathrm{KN.m}}$, $D_3 = \frac{C_3}{10\mathrm{mm}}$, $D_4 = \frac{C_4}{1\times10^6\mathrm{cm}^6}$.

In Fig. 4, D_{1x} and D_{1d}, D_{2x} and D_{2d}, D_{3x} and D_{3d}, D_{4x} and D_{4d} are the minimal and maximal value of variable D_1, D_2, D_3 and D_4 respectively.

5 groups of scheme sets, from group 2 to 6, which correspond to the value of k set from 2 to 6 in formula (1) were adopted for polar radius optimization. Group 1 shows the value of 4 attributes of original TB880E TBM cutter head. From Fig. 4, there are no significant difference between group 2 to 6 and 1, which indicates that polar radius optimization does not influence attributes of cutter head significantly.

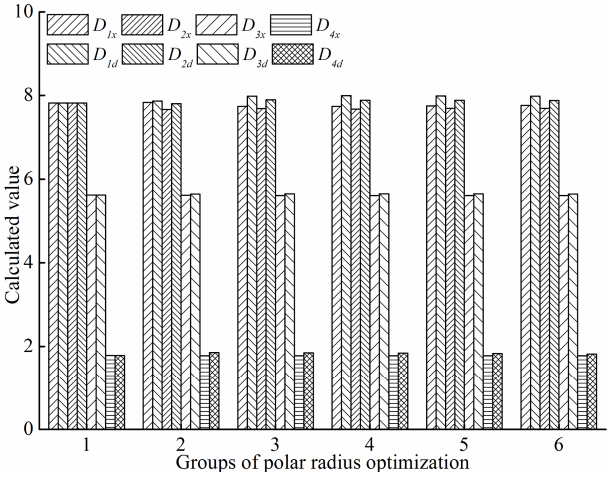

Fig. 4. Attribute results comparison of polar radius optimization

3.3 Polar Angle Optimization

The layout pattern got in polar radius optimization when k is 5 is selected as input for polar angle optimization. 5 combinations of p and q which can be expressed as (p, q)=(4,3;4,5;4,7;8,3;8,5) are adopted. Attributes results are displayed in Fig.5 and Table 2. In Fig.5, groups 1-16 stand for disc cutters of 7-10, 11-14, 15-18, 19-22, 23-26, 27-30, 31-34, 35-38, 39-43, 44-47, 48-51, 52-55, 56-59, 60-63, 64-67, 68-71, and the ordinate values are the best results of attributes C_1-C_4 in each group. The short black line in Fig. 5 stand for the attributes results of original TB880E cutter head.

As can be seen in Fig.5, attributes C_1, C_2, C_3 decrease to 0 gradually before group 8, which results from the symmetrical layout pattern of cutters in these groups. In group 9, attributes results go by a sudden jump to high values, because 5 cutters are distributed in this group asymmetrically which is restricted by manufacturing process requirements of the original layout pattern. Comparing with the original layout pattern, for 5 combinations of p and q, attributes C_1, C_2, C_3 in group 16 which also means the final results of optimization calculation decrease in some degree, however attribute C_4 keep constant basically. Of the 5 combinations, attributes are best when p=8 and q=5, in which C_1 decreases at 21%, C_2 at 65% and C_3 at 37%.

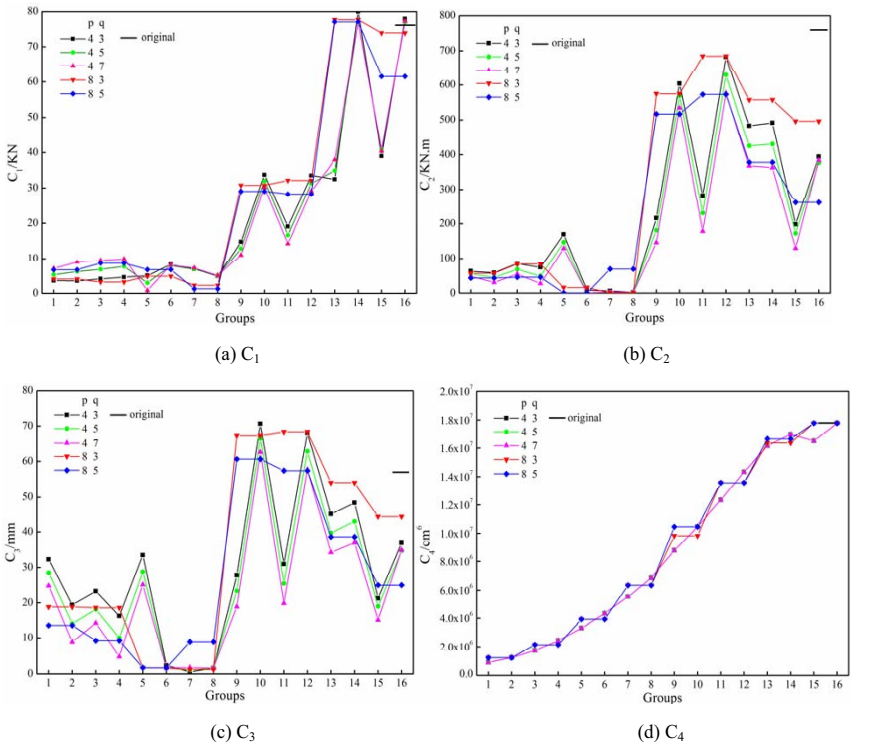

Fig. 5. Attribute results comparison of polar angle optimization

Table 2. Attribute results comparison before and after optimization

attributes	original	optimized				
		p=4, q=3	p=4, q=5	p=4, q=7	p=8, q=3	p=8, q=5
C1/KN	76.54	77.95	76.98	77.25	73.87	61.55
C2/KN.m	750	394	376	384	496	260
C3/mm	56	37	35	35	44	25
C4/cm^6	1.78×10^7	1.78×10^7	1.78×10^7	1.78×10^7	1.78×10^7	1.78×10^7

3.4 Deformation and Stress of Cutter Head

Fig. 6 shows the obtained stress and deformation distributions of original and optimized cutter head under normal load condition. As shown in Fig. 6(a), (b), the maximum deformation value occurred in the center of the cutter head, and the deformation value decreases from the cutter head center to outside. As shown in Fig. 6(c), (d), the maximum stress value of the optimized cutter head is smaller than that of the original cutter head, which means that no harm has been done on cutter head stiffness after optimization of disc cutters layout.

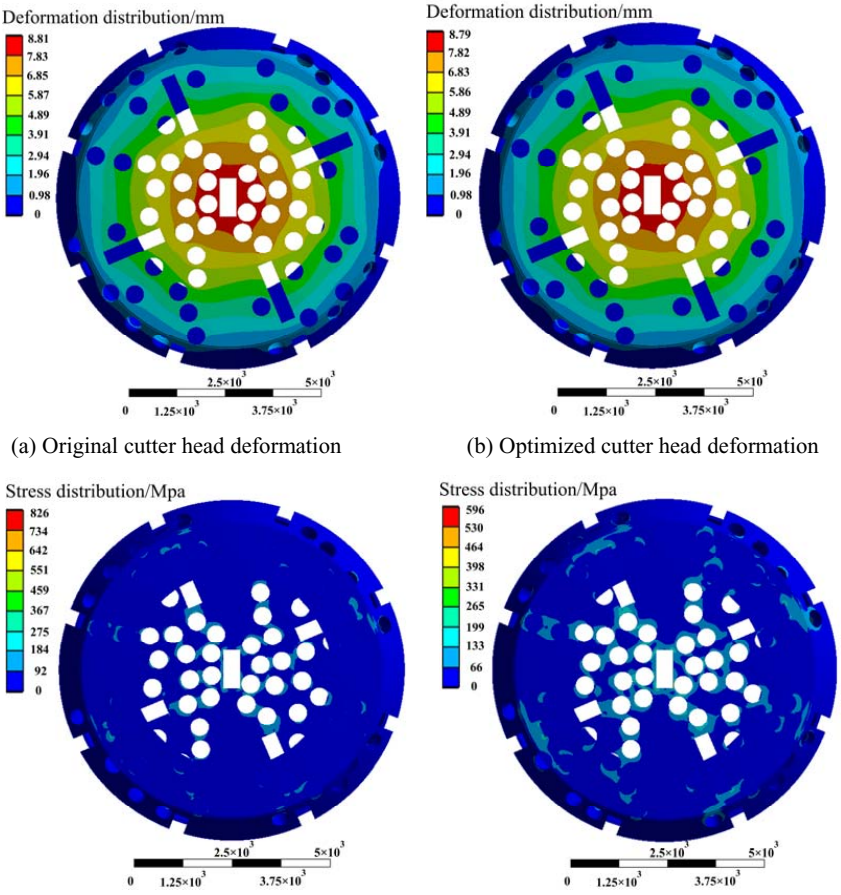

(a) Original cutter head deformation

(b) Optimized cutter head deformation

(c) Original cutter head stress

(d) Optimized cutter head stress

Fig. 6. The obtained stress and deformation distributions of original and optimized cutter head under normal load condition

4 Conclusions

A cutter layout optimization strategy for TBM which is based on grey relational analysis is proposed in this paper. Through exerting micro-adjustments for cutters, better layout pattern which expressed as smaller attributes values are got. The computational results showed that:

(1) Through the computational process, optimization of the polar angle is found to play a more important role than polar radius in cutters layout. The attributes values of C_1, C_2, C_3 and C_4 will not change significantly in polar radius optimization process, however the attributes values change significantly in polar angle optimization process.

(2) Through analysis to the process of polar angle optimization, the cutters original layout pattern makes an important influence on cutter head performance which is expressed as attributes values of C_1, C_2, C_3 and C_4 in this paper. The cutters in a group are suggested to layout symmetrically.

(3) From the calculation results, attributes C_1, C_2 and C_3 are found to be sensitive to micro-adjustment of cutter position, however attribute C_4 not, which indicates that attribute C_4 can be ignored or replaced by other technical requirements in cutters layout optimization.

(4) Through structure deformation and stress calculation of cutter head before and after cutter layout optimization, no significant change of the deformation and stress value were found, which also means the method proposed in this paper will not do any harm to the structure stiffness of the cutter head since the optimization process is done by exerting micro-adjustments for cutters.

Acknowledgements. This work was supported by the National Key Basic Research Program of China (973 Program) under Grant Nos. 2013CB035400.

References

[1] Gertsch, R.E.: Rock toughness and disc cutting, pp. 35–36. University of Missouri-Rolla, Missouri (2000)

[2] Rostami, J., Ozdemir, L., Nilsen, B.: Comparison between CSM and NTH hard rock TBM performance prediction models. In: Proceedings of Annual Technical Meeting of the Institute of Shaft Drilling Technology, Las Vegas, NV, p. 11 (1996)

[3] Zhang, Z., Qiao, Y.: Research on the layout of TBM disc cutter. Engineering Mechanics 28(5), 172–177 (2011)

[4] Zhang, H.: Study on numerical simulations of performance of tunnel boring machines (TBM). Tunnel Construction 26(A02), 1–7 (2007)

[5] Huo, J., Sun, W., Chen, J.: Optimal disc cutters plane layout design of the full-face rock tunnel boring machine (tbm) based on a multi-objective genetic algorithm. Journal of Mechanical Science and Technology 24(2), 521–528 (2010)

[6] Deng, J.: The primary methods of grey system theory. Huazhong University of Science and Technology Press, Hubei (1987)

[7] Chang, L., Zhang, X., Li, M.: Weapon System of System Technology Contribution Evaluation Based on Grey Target Theory. Ordnance Industry Automation 29(010), 13–15 (2010)
[8] Li, J., Zhao, J., Zheng, R., et al.: A grey target theory based method for state assessment of power transformer. Journal of Jilin University: Engineering and Technology Edition 38(1), 201–205 (2008)
[9] Saaty, T.L.: A scaling method for priorities in hierarchical structures. Journal of Mathematical Psychology 15(3), 234–281 (1977)

Author Index

Afzal, Muhammad Raheel I-154
Aghaei, Morteza II-54
Aghili, Farhad II-121
Ahmad, Mehran II-569
Ahmed, Ishtiaq I-693
Aljanaideh, Omar II-635

Ba, Z. II-397
Ba, Zhengyu I-649
Bae, Joonbum II-257
Baek, Joo-Won II-327
Baek, Ju-Won II-320
Baek, Seung-Hwa I-8
Bashir, Ali Kashif I-105, II-454
Bouzouia, Brahim I-679
Broecker, Bastian II-108
Butt, Khurram II-569

Cai, Hui II-513
Cai, Maojiao II-535
Chai, Xinxue I-730
Chang, Hyunjin I-540
Chen, Genliang I-384
Chen, Puwei II-503
Chen, Qiaohong I-730
Chen, Ran I-661
Chen, Weidong I-295, I-307, II-535
Chen, Wenbin I-339
Chen, Xinkai II-666
Chen, Zhiyong II-525
Chen, Zichen I-475
Cheng, Liling I-129, I-500
Cheng, Pi-Ying I-258
Cheng, Xiaoying I-500
Cheon, Byungsik I-237
Cho, Chullhee II-310
Cho, Hyunhak I-615
Cho, Kyu-Jin II-302
Choe, Yungeun I-584
Choi, Byunghun I-594
Choi, Hyeung-Sik II-289
Choi, Joon-Young I-267
Choi, Seunghwan I-66
Choi, Seung Y. I-693
Choi, Tae Yong II-74, II-155
Choi, Wan Sik I-105
Chung, Kwangcho II-155
Chung, Myung Jin I-584
Chung, TaeChoong I-693
Chwa, Dongkyoung I-668
Claes, Daniel II-108
Cui, Yuding I-484
Czeczot, Jacek II-178

Dadkhah, Mohammad I-177
Dai, Mengyuan I-520
Dai, Yu I-475
Defoort, M. II-202
Deng, Hua I-415
Deng, W.H. II-189
Ding, Han II-365, II-397, II-491, II-503, II-525, II-592
Do, Hyun-Min II-74, II-155
Du, Yuheng I-463
Duan, Xiaogang I-415

Fang, Yinfeng I-405
Farshchi, Seyyed Mohammad Reza II-54
Fei, Ling II-470
Feng, Mingchi II-417
Feng, Pingfa II-614
Feng, Ying II-623
Fossel, Joscha II-108
Fu, Xin I-129, I-427, I-500, I-509
Fu, Z. II-16, II-189, II-214

Gao, Feng I-718, II-132
Gao, Ming I-520
Ge, Yang II-470
Glowa, Christoph II-84
Go, Seok-Jo II-442
Gong, Liang I-661
Gonzalez, Jose I-318
Gu, Dong-Yun I-273
Gu, Guo-Ying II-385, II-644, II-678
Gulraiz, Shiraz II-1

Guo, Weizhong II-41
Guo, Yalei II-41

Ha, Hyunuk I-45
Haider, Nauman K. II-1
Han, HyeYoung II-375
Han, Sung Hyun II-265
Han, Youngjae I-97
Hashizume, Makoto I-237
Hassan, Syed I-154, I-204
He, Jiayuan I-396
Hennes, Daniel II-108
Hentout, Abdelfetah I-679
Heo, Seong-Min I-38
Heo, Shin-nyeong I-562
Hong, Jaesung I-237
Hu, Liang I-509
Huan, Zhang II-720
Huang, Feng I-427
Huang, Qi I-216
Huang, Xinda II-491
Huo, Junzhou II-700
Hur, Kook-Sung I-1
Hussain, Irfan I-165
Hussain, Sajjad I-105
Hwang, Seungik I-562
Hwang, Won Jun II-265

Imamoglu, Nevrez I-318
Izhar, Umer II-1
Izumi, Kiyotaka II-96

Jan, Yasir I-154
Jeong, Dong-Keun II-327
Jeong, Heein I-330
Jeong, Jae-Hun I-1
Jeong, Yang Keun I-136
Jeong, Yongseop I-625
Ji, DaeKeun I-237
Jia, L. II-397
Jia, Lei I-649
Jiang, Hua II-166
Jiang, Jun II-429
Jiang, Li I-216
Jiang, Ning II-63
Jin, Taeseok I-540
Jin, Yi II-417
Jirattigalachote, Wisit I-434
Jo, Jeongmin I-97
Jun, Du II-727

Jung, Seul II-274
Jung, Sung Won I-136
Jung, Yeongtae II-257

Kamashima, Tsutomu I-532
Kang, Eun Uk II-265
Kang, Sun-Kyun I-56, I-85
Kim, Byoung-Ho I-742
Kim, Byung In II-74
Kim, Cheol-Joong I-668
Kim, Chi Yen I-227
Kim, Dong-Hyun I-25, I-31
Kim, Dong-Il I-576
Kim, Doo-Hyung II-155
Kim, Hee-Je I-1, I-8, I-18, I-25, I-31, I-38, II-320, II-327, II-334, II-338, II-345
Kim, H. Jin I-594
Kim, Ho-Sung II-320
Kim, Hyoung-Woo I-267
Kim, Hyun-Min I-8
Kim, Jaeyong I-615
Kim, Jonggeun II-375
Kim, Jong-Hyun II-320, II-334
Kim, Jongmoo I-45
Kim, Kijung I-66
Kim, Ki-Ryong I-25, I-31, I-38
Kim, Kyung-Sik II-310
Kim, Min-Ho I-605
Kim, Myeong Ok I-204
Kim, Myong-hwan I-18
Kim, Sungshin I-615, II-375
Kim, Tae-Jin II-338
Kim, Yeoun-Jae II-237
Kim, Yunki I-66
Klopot, Tomasz II-178
Klopot, Witold II-178
Kumar, Naveen I-177
Kwak, Dong Jun I-594
Kweon, In So I-625
Kyung, Jin Ho II-74

Lai, Lei-Jie II-385, II-644
Lai, Po-Ying I-258
Laskar, Md Nasir Uddin I-693
Laszczyk, Piotr II-178
Lee, Changyoung I-97
Lee, Dong-Hyuk I-56, I-85
Lee, Hansoo II-375

Lee, Hee-Mu I-605
Lee, Jangmyung I-45, I-56, I-66, I-77, I-85, I-145, I-562, I-330
Lee, Jinho I-97
Lee, Jong-Pil II-338, II-345
Lee, Joon-Yong II-237
Lee, Ju-Jang II-237
Lee, Kok-Meng I-509
Lee, Kyoung-Jun II-338, II-345
Lee, Min-Cheol I-227, I-605
Lee, Sang-Hyo II-310
Lee, Sang-Il II-454
Lee, Sang-Seob II-289
Lee, Sangyong I-330
Lee, Woo Song II-265
Lee, Wongryol II-454
Lee, Young-Jin II-442
Li, Bin II-513
Li, Chun-Xia II-644, II-678
Li, Kang I-295, I-307, II-470, II-535
Li, Meng II-535
Li, Qinchuan I-730
Li, Weimin II-63
Li, Wen-long II-555
Li, Xiuliang II-409
Li, Zhi II-656
Li, Zicheng II-545
Liang, Guanhao I-475
Liao, Wenlong I-295
Lim, Hyun-Seop I-562
Lim, Jeong Geun II-274
Lin, Chin-Teng I-246
Lin, Sen II-481
Lin, Zhongqin I-384
Ling, Jingxiu II-700
Liu, Chao II-33, II-353
Liu, Chengliang I-661
Liu, Guoqing II-143
Liu, Hong I-216
Liu, Honghai I-405
Liu, Huan I-463
Liu, J.H. II-189
Liu, Jia II-353
Liu, Kai I-363
Liu, Pin-kuan II-365
Liu, Sining II-656
Liu, Wei-ting I-129, I-500, I-509
Liu, Yizhi II-481
Liu, Yong-Hua II-623
Liu, Yuzhang I-373
Luo, Bo II-513
Luo, Tao II-417

Ma, Jigang I-730
Mai, Ba-Loc II-289
Manurung, Auralius I-165
Mao, Jianyu II-41
Mao, Xinyong II-513
Mehmood, Ayaz II-1
Mei, Deqing I-475
Meng, Jianjun I-453
Merat, Pooya II-121
Mertsching, Bärbel I-117, I-550
Messous, Mohamed Ayoub I-679
Metzger, Mieczyslaw II-178
Miao, Yunjie II-132
Mirabdollah, Mohammad Hossein I-117, I-550
Moon, Seong-eun I-532
Moon, Wae-Shik II-580
Mou, Haikuo II-491
Mu, Hua I-520
Munawar, Majid II-569

Nagai, Isaku II-96
Nakadai, Kazuhiro I-532
Nergui, Myagmarbayar I-318, I-532
Nie, Hua II-246
Noh, Kyung-Wook I-56

Oh, Mingyun I-188
Otake, Mihoko I-532
Oukid, Saliha I-679

Pan, Dalei I-718, II-132
Pan, Lizhi I-493
Pan, Minghua II-710
Pan, Xianfei I-520
Park, Chanhun II-74
Park, Chan-Ik I-145
Park, In Man I-136
Park, Jang Sik II-450
Park, Jinseop II-454
Park, Kang-Il I-145
Park, Kyoung-Taik I-85
Park, Kyung-Taik II-155
Park, Min-Kyu II-436, II-442, II-466
Park, Moonho I-615
Park, Moon Yeol I-136
Park, Myong-Soon I-105, II-454

Park, Yong-Jai II-302
Peng, Fangyu II-481, II-513
Prasad, Mukesh I-246
Pyo, Sanghun I-188

Qi, Geng II-727
Qian, Wenwei I-427
Qian, Yang I-706
Qin, Guohua II-246
Qiu, Dong I-351
Qiu, Zhongyi I-444

Rahmani, Ahmed I-706
Rakheja, Subhash II-635
Rath, J.J. II-202
Ren, Jie II-41
Ren, Yong II-226
Rovetta, Alberto II-281
Ruan, Xiaodong I-427
Ryu, Myung-Hyo II-320, II-327, II-334
Ryuh, Youngsun II-310

Saxena, Amit I-246
Schlegl, Thomas II-84
Seo, Jonghyun I-77
Shah, Sayed Chattan II-454
Shah, Sayed Chhattan I-105
Shahzad, Waseem II-569
Shan, Qingchuan I-500
Shao, Chengjun II-409
Shen, Hui-Min I-509
Sheng, X. II-397
Sheng, Xinjun I-396, I-453, I-463, I-493, I-649
Shim, Byung Kyun II-265
Shin, Dongsul II-338, II-345
Shin, Hang Bong I-136
Shu, Xiaokang I-453
Shull, Pete B. I-434
Song, Hajun I-615
Song, Jae-Bok I-576
Song, Jong Kwan II-450
Su, Chun-Yi II-121, II-623, II-635, II-656, II-666
Su, Hongye II-409
Sun, Ronglei I-484, II-246
Sun, Wei II-700
Sung, Ji-Hun II-580
Sung, Ki Won II-265
Sung, Kum-Gil II-466
Sung, Young-Hoon II-580
Szkodny, Tadeusz I-637

Takagi, Kentaro I-532
Tao, Yuebang I-129
Tesar, Delbert II-436
Tomikawa, Morimasa I-237
Tran, Ngoc-Huy II-289
Tuyls, Karl II-108

Ullah, Ikram I-204

Veluvolu, K.C. II-202

Wang, Can I-373
Wang, Gang I-373
Wang, Hao I-384, II-33
Wang, Hesheng II-535
Wang, Hui II-353
Wang, Huiyu I-307
Wang, Jingcheng II-470
Wang, Jingchuan I-295, I-307
Wang, Shuangyuan I-661
Wang, Xiaohui II-63
Wang, Y. II-16
Wang, Yancheng I-475
Wang, You I-351
Watanabe, Keigo II-96
Wei, Jian-He I-273
Wei, Zhixuan I-295, I-307
Wu, Jian-hua II-353, II-365
Wu, Xinyu I-373
Wu, Yu I-273

Xie, Le II-429
Xiong, Caihua I-339, I-363, I-484
Xiong, You-lun II-545, II-555
Xiong, Zhenhua I-649, II-353, II-397
Xu, Jiahang II-166
Xu, Kai I-351, I-463, II-143

Yan, Hua I-284
Yan, Rong II-481
Yan, W.X. II-16, II-189, II-214
Yan, Yonghua II-166
Yang, Canjun I-284
Yang, Chien-Ting I-246
Yang, Dapeng I-216
Yang, Gi-Hun II-310
Yang, Mei-Ju II-678

Yang, Sheng II-481
Yao, Jin II-720
Yao, Lin I-453
Yao, Yan-An II-33
Yasuda, Gen'ichi II-602
Yi, Hyun-Chul I-267
Yimin, Xia II-720
Yin, Zhouping II-545
Yiping, Tang II-727
Yongliang, Cheng II-720
Yoon, Byung Woo II-450
Yoon, Jungwon I-154, I-165, I-177, I-188, I-204
Yoon, Sung Min I-227
Yoshida, Yuki I-318
Yousaf, Kamal II-569
Yu, Haidong II-690
Yu, Hailong II-429
Yu, Huiyang II-246
Yu, Jungwon II-375
Yu, Pin I-500
Yu, Wenwei I-318
Yuan, X. II-397
Yuan, Xin I-649
Yun, Hyeok-Jin II-334

Zain, Zainah Md. II-96
Zhai, Chao II-417
Zhai, Jie II-503
Zhai, Mei-Li II-33
Zhan, S.T. II-189, II-214
Zhang, Chuncao II-710
Zhang, D. II-202
Zhang, Dingguo I-396, I-444, I-493, II-226
Zhang, Gang II-365
Zhang, Hai-Tao II-503, II-525
Zhang, Jianbo II-710
Zhang, Jianfu II-614
Zhang, Jianjun II-63
Zhang, Jianrong II-166
Zhang, Langwen II-470
Zhang, Mingyong II-166
Zhang, Q. II-202
Zhang, Qing II-226
Zhang, Wenxi I-295
Zhang, Xiaoming II-491, II-503, II-592
Zhang, Xu II-700
Zhao, Chunzhang II-690
Zhao, Yanmin II-614
Zhao, Yan-Zheng II-16, II-189, II-214
Zhao, Yong II-690
Zheng, Duan I-373
Zhengying, Wei II-727
Zhou, Hang II-385
Zhou, H.F. II-16
Zhou, Li-ping II-555
Zhou, Maoying I-129
Zhu, Gaoke I-415
Zhu, Guoli II-710
Zhu, Li-Min II-385, II-644, II-678
Zhu, Xiangyang I-396, I-405, I-434, I-444, I-453, I-463, I-493
Zhuang, Kejia II-592